CORROSION ENGINEERING

Principles and Solved Problems

CORROSION ENGINEERING

Principles and Solved Problems

BRANKO N. POPOV
University of South Carolina,
301, Main Street
Department of Chemical Engineering
Swearingen Engineering Center
Columbia, SC 29208
popov@cec.sc.edu

ELSEVIER
AMSTERDAM • BOSTON • HEIDELBERG • LONDON • NEW YORK • OXFORD
PARIS • SAN DIEGO • SAN FRANCISCO • SINGAPORE • SYDNEY • TOKYO

Elsevier
Radarweg 29, PO Box 211, 1000 AE Amsterdam, Netherlands
The Boulevard, Langford Lane, Kidlington, Oxford OX5 1GB, UK
225 Wyman Street, Waltham, MA 02451, USA

Notices

Knowledge and best practice in this field are constantly changing. As new research and experience broaden our understanding, changes in research methods, professional practices, or medical treatment may become necessary.

Practitioners and researchers must always rely on their own experience and knowledge in evaluating and using any information, methods, compounds, or experiments described herein. In using such information or methods they should be mindful of their own safety and the safety of others, including parties for whom they have a professional responsibility.

To the fullest extent of the law, neither the Publisher nor the authors, contributors, or editors, assume any liability for any injury and/or damage to persons or property as a matter of products liability, negligence or otherwise, or from any use or operation of any methods, products, instructions, or ideas contained in the material herein.

ISBN: 978-0-444-62722-3

British Library Cataloguing in Publication Data
A catalogue record for this book is available from the British Library

Library of Congress Cataloging-in-Publication Data
A catalog record for this book is available from the Library of Congress

ACKNOWLEDGMENT

To my wife, Snezana, daughters, Irena and Biljana, son, Nestor, and grandchildren, Filip, Fabijana, and Erina.

I appreciate the support and collaboration provided throughout my career as a researcher and teacher by my mentors Professor H. A. Laitinen, University of Illinois, Urbana-Champaign, Illinois; Professor Branko Lovrecek, University of Zagreb, Croatia; Professor Dragutin Drazic, University of Belgrade, Serbia; and Professor Pance Kirkov, University of Kiril and Metodij, Republic of Macedonia.

I also express appreciation to Professor Ralph White, University of South Carolina; Professor Howard W. Pickering, Pennsylvania State University; Professor J. Bruce Wagner Jr., Arizona State University; Professor Arsov Ljubomir, University Kiril and Metodij, Macedonia; Professor Slavkov Dragan, University Kiril and Metodij, Macedonia; Professor Sveto Hadji-Jordanov, University Kiril and Metodij, Macedonia; Dr. Radoslav Adzic, Brookhaven National Laboratory; Dr. Ron Guidotti, Sandia National Laboratory; Dr. Ken Chen, Sandia National Laboratory; Dr. Yuri Podrazinsky, Enrev Corporation; Professor Alfred Anderson, Case Western University; Professor Richard Griffin, Texas A&M University; Professor D. Morris, Texas A&M University; Dr. Z. Mao, Professor Jakov Ivschin, Chemical and Technological Institute, Kazan; Professor Yin Ken-Ming, Yuan Zee University; Professor Andrzej Lasia, University of Sherbrook, Quebec, Canada; Professor Doron Aurbach, Bar-Ilan University, Israel; Professor Masaharu Nakayama, Yamaguchi University, Japan; Professor Hansung Kim, Yonsei University, South Korea; Professor Francis Gadala-Maria, University of South Carolina; Professor John Weidner, University of South Carolina; Professor John Van Zee, University of Alabama; and Professor Sehkyu Park, Kwangwoon University, South Korea.

I express my gratitude for the hard work and determination of my graduate students and postdoctorates, whose research on corrosion and the stability of catalyst materials in power sources have been referenced in this book: Dr. Godfrey Sikha (Tesla Motors, California); Dr. Swaminatha P. Kumaraguru (General Motors, Michigan); Dr. Tony Duarte (Murphy Oil); Dr. D. H. Coleman, Dr. G. Zhang, Dr. Pankaj Arora (Du Pont); Dr. Murali Ramasubramanian, Dr. Bala S. Haran (IBM); Dr. Anand Durairajan (Intel); Dr. Anand Krishniyar, Dr. Manikandan Ramani (General Electric); Dr. Basker Veeraragavan (IBM); Dr. Ping Yu, Dr. Ramadass Premanand (Celgard); Dr. Hector Colon-Mercado (Savannah River National Laboratory); Dr. Lingyun Liu (Ford); Dr. Nalini Subramanian (Apple Inc.); Dr. Hansung Kim (Yonsei University); Dr. Ramaraja P. Ramasamy (University of Georgia); Dr. Swaminatha P. Kumaraguru (General Motors); Dr. Godfrey Sikha (Tesla Motors); Dr. Sehkyu Park (Kwangwoon University); Dr. Subasri Ayyadurai (University of Cincinnati); Dr. Durga Nallathambi (Intel); Tae-keun Kim (University of South

Carolina); Tianyuan Xie (University of South Carolina); Wonsuk Jung (University of South Carolina); Joseph Rotchford (University of South Carolina); Dr. Jongwon Lee (Samsung); Dr. Yunseok Choi (Ohio University); Dr. Akos Kriston (European Commission); Dr. Prabhu Ganesan (University of South Carolina); and Dr. Selvarani Ganesan (Michigan State University).

For more than 20 years, my research has benefited from the financial support of the Office of Naval Research (Dr. A. John Sedriks), United States Army Corps of Engineers, National Reconnaissance Office (NRO), Sandia National Laboratory, South Carolina Department of Transportation (SCDOT), American Electroplaters and Surface Finishers Society (AESF), United States Department of Energy, National Air and Space Administration, National Science Foundation, Defense University Research Instrumentation Program (DURIP), and private industries, including United Technologies (UTC), ELISA Co., General Electric, Farasis, and Faraday Technology.

I also thank my undergraduate student Frank Risalvato, who assisted in creating graphs, schematics, and line drawings for the book chapters, as well as Dr. Prabhu Ganesan, Assistant Research Professor at USC, who helped by reproducing graphs, schematics, and line drawings; arranging references; obtaining permission from various sources to reuse figures and tables; organizing figures and tables according to the publisher's guidelines; and coordinating with the publisher.

I thank my current graduate students Xie Tianyuan, Joseph Rotchford, Kim Tae-keun, and Jung Won Suk for proofreading the solved problems, exercises, and case studies included in the book, and I express my gratitude to many of my above-listed friends who provided proofreading and technical editing for the manuscript. Excellent review comments on selected chapters have come from Dr. Ganesan Prabhu, Dr. Francis Gadala-Maria, Joseph Rotchford, and Dr. Thomas Stanford.

I thank God for giving me health and strength to finish the book.

PREFACE

Corrosion Engineering–Principles and Solved Problems is based on the author's experience teaching undergraduate and graduate corrosion courses entitled Corrosion Engineering, Advanced Corrosion Engineering, and Electrochemical and Corrosion Techniques at the University of South Carolina. The book provides an extensive and in-depth theoretical analysis of thermodynamics kinetics, mass transfer, potential theory, and passivation, creating a foundation for understanding the electrochemical nature of the corrosion process and corrosion protection strategies discussed in the book's second part. Around the world, the students who currently attend corrosion-engineering courses are enrolled in different engineering programs. This fact requires additional topics to be included in the book, and to this end, the book reviews the corrosion processes, protection strategies, and testing for civil-engineering structures; corrosion in chemical process engineering; mechanical and nuclear corrosion engineering; and metallurgy. The fundamental principles of corrosion and related protection strategies are explained through solved problems, exercises, and case studies, and the book helps upper-level undergraduate and graduate students learn the subject through an extensive theoretical description of corrosion theory, passivity, corrosion prevention strategies, and corrosion protection system design. The author has attempted to organize the book so the instructor can use it as the basis for a course in corrosion engineering for undergraduate students and also graduate students.

With a bibliography citing more than 1350 studies published in the last 10 years, the book is also designed to serve as a valuable scientific resource for professionals working in the fields of corrosion, electrochemical, chemical, metallurgical, mechanical, electrical, manufacturing, and nuclear engineering, as well as graduate students and material scientists.

Chapters 1 to 3 describe the theory of corrosion engineering and offer analyzed case studies and solved problems in the thermodynamics of corrosion processes, the relevance of electrochemical kinetics to corrosion, low field approximation theory, concentration polarization, the effects of polarization behavior on corrosion rate, the effect of mass transfer on electrode kinetics, and diffusion-limited corrosion rates.

Chapter 4 presents the fundamentals of passivity; the film and adsorption theories of passivity; criterion for passivation; methods for spontaneous passivation; factors affecting passivation, such as the effect of solution velocity and acid concentration; alloy evaluation; anodic protection systems; and design requirements. A full discussion on stainless steel composition and crystalline structure, oxidizer concentration, and alloy evaluation is included. The chapter also considers anodic protection to establish a basis for anodic

protection systems and designs. By the end of the chapter, case studies, solved problems, and exercises illustrate passivation and anodic protection system design.

The basics of corrosion measurements are outlined in Chapter 5, which describes polarization methods for measuring corrosion rates, the oxidizing power of the environment, and corrosion protection effectiveness. The chapter starts by explaining corrosion measurement basics and corrosion rate determination by linear polarization using the Stern-Geary equation and Tafel extrapolation. The advantages of corrosion inhibitor evaluation, corrosion monitoring in process plants, and corrosion characteristics are also described, and the chapter considers potentiodynamic polarization for determining passivation and critical current density. At the end of the chapter, a detailed review of recent literature explains electrochemical impedance spectroscopy. Solved and exercise problems illustrate electrochemical techniques in corrosion rate measurements.

Chapter 6, which is on galvanic corrosion, describes theoretical galvanic corrosion aspects, mixed potential theory, galvanic series, and novel testing methods suggested by the literature. A detailed discussion on galvanic corrosion, polarization, and prevention provides information on materials, minimizing cathode-anode area ratio, coatings and inhibitors, and environmentally friendly sacrificial materials. A literature review also describes novel testing methods in galvanic corrosion, novel alloys for automotive applications, and galvanic corrosion inhibition in both concrete structures and dental magnetic attachments. Galvanic corrosion theory and evaluation are explained through case studies, solved problems, exercises, and numerical modeling.

In Chapter 7, the book addresses pitting potential analyses in connection with new alloys with low pitting corrosion susceptibility. In addition, the chapter considers the recent literature on pitting mechanisms and crevice corrosion evaluation as they relate to corrosion severity control, main variables, and experimental data consistency in particular systems. Electrochemical kinetics such as charge transfer, mass transport, and ohmic effects explain pit growth and arrest, and the discussion of pitting inhibition and crevice corrosion is focused on new alloys and alloy composition effects for decreased pitting corrosion susceptibility, conversion coating, inhibitor development, and cathodic and anodic protection. Crevice and filiform corrosion are also described via initiation and propagation processes, and the case study and exercise problems illustrate pitting and crevice mechanisms and corrosion protection strategies for inhibiting pitting corrosion.

Hydrogen permeation in metals is introduced for the first time in Chapter 8 of this book, which describes hydrogen permeation and hydrogen-induced damage and prevention in metals and alloys. To this end, the chapter discusses hydrogen evolution kinetics, theoretical diffusion solutions, and basic hydrogen permeation models. Models are used as a diagnostic tool for determining the effectiveness of various metals and alloys as hydrogen permeation inhibitors. Through case studies, the chapter then explains the experimental determination of atomic hydrogen permeation transients and the evaluation of hydrogen absorption rate constants and diffusivity into metals. A discussion on

hydrogen embrittlement, hydrogen-induced cracking, hydrogen blistering, and hydrogen stress cracking then shows the relationship between hydrogen permeation and hydrogen-induced cracking mechanisms previously described in the chapter. The most recent research related to hydrogen kinetic parameters is also reviewed, and the case studies and solved problems illustrate models for developing alloys that reduce hydrogen ingress.

The discussion of stress corrosion in Chapter 9 begins with a definition and characteristics for stress corrosion cracking (SCC), testing methods common to SCC and hydrogen-induced cracking, principles and techniques of fracture mechanics, and corrosion fatigue testing. These methods have been updated with references published in the last 20 years. SCC metallurgy is explained through case studies on SCC variables such as solid solution composition, grain boundary segregation, alloy phase transformation and associated solute-depleted zones, duplex structures, and cold work. From 2000 to 2013, more than 200 published studies have analyzed electrochemical effects such as chloride-induced localized corrosion in stainless steels, SCC due to dealloying, and hydrogen-induced SCC in high-strength alloys. The chapter continues with corrosion fatigue cracking and detection. SCC failure prevention methods are discussed at the end of the chapter. In addition, the fundamental principles of SCC, the nature of the processes, and related protection strategies are explained through solved exercise problems from fracture mechanics and case studies published in the last decade.

Chapter 10 on atmospheric corrosion describes basic atmospheric corrosion principles resulting from metal exposure at ambient and near-ambient temperatures in humid air. It starts by presenting environment classification, common industrial pollutants, atmospheric corrosion factors, and atmospheric corrosion classifications according to the International Standard Organization. Atmospheric pollutants, such as sulfur-containing compounds, chlorine-containing compounds, and nitrates, are discussed in the chapter through a review of recent literature, and the chapter concludes by showing the role of industrial pollutants in controlling atmospheric corrosion, through a discussion of iron and low-alloy steel corrosion, as well as the atmospheric corrosion of nickel, magnesium alloys, zinc, and bare and anodized aluminum. The influence of alloying elements such as copper, tin, zinc, and lead on bronze corrosion and prevention is also explained through recent literature.

Chapter 11 introduces high-temperature corrosion, considering basic metal and alloy corrosion principles at elevated temperatures in air and other oxidizing gases. It starts by explaining high-temperature corrosion thermodynamics, the Pilling-Bedworth ratio, electrochemical oxidation processes, oxide-layer formation, microstructure, and oxidation kinetics. Parabolic, logarithmic, and linear rate equations and the combination of those equations also show the relationship between corrosion and oxide-layer formation at high temperatures. Hot metal-oxide corrosion is explained using molten halide, molten nitrite, and molten carbonate interactions. To further explain this interaction, a case

study on molten halides is included. The chapter concludes by considering conventional and recently developed methods for hot corrosion protection and high-temperature vacuum plasma spraying (VPS), high-velocity oxy-fuel (HVOF) thermal spraying, platinum and aluminide coatings, silicon diffusion layers, chemical additions, ion implantation, and preformation of oxide layers. In addition, case studies, solved problems, and exercises on protective coatings illustrate engineered alloy protection designed for elevated temperature service.

Corrosion in concrete structures is addressed in Chapter 12, which starts by explaining engineering alloy composition and heterogeneity, steel reinforcement degradation in an alkaline environment, corrosion mechanisms, chloride-induced corrosion, and surface depassivation with carbon dioxide. The chapter describes electrochemical techniques used for concrete reinforcement corrosion evaluation, such as corrosion potential measurements, linear polarization, Tafel polarization, and electrochemical impedance spectroscopy, and it considers mineral admixtures, commercial coatings, calcium nitrite and organic inhibitors, pozzolans, sacrificial zinc coatings, durability assessments for internal chloride in corrosion control, and service life. Simulations using SimCorr^{TM} then illustrate corrosion initiation time and crevice life prediction as a function of concrete structural and environmental parameters.

Chapters 13 to 15 describe corrosion protection methods. Chapter 13 introduces organic coating constituents, coating composition, underlying metal surface preparation, additives and fillers, metal surface prepainting treatments, and exposure testing. To this end, the chapter explains resins used in the paint industry, including vinyl resin, acrylics, alkyd (oil base), modified alkyds, chlorinated rubber, urethanes resin, and polyester resin, in the context of actual service life evaluation. The properties of paint pigments and their roles in providing color and opacity, mechanical and barrier properties, and water transport are discussed, as are the ASTM standards for pigment specification, surface preparation specifications, paint and paint material chemical analysis standards, paint application tool standards, and accelerated testing standards for coatings, with the information summarized in nine tables. The second part of the chapter discusses testing and coating evaluation, and a full discussion of physical and chemical aging mechanisms is included to show the relationship between corrosion and coating detachment or cracking, underlying metal degradation, and coating disintegration. In addition, the chapter provides a review of the recent literature on organic coatings.

Chapter 14 introduces corrosion inhibitor physicochemical and electrochemical properties. The chapter explains inhibitor classification according to mechanism, inhibitor application (pickling, acid cleaning, descaling, etc.), and inhibitor chemical nature (inorganic and organic). The chapter concludes by discussing the chemical and electrochemical properties related to anodic, passivating, and cathodic inhibitors (including cathodic poisons, cathodic precipitates, and oxygen scavengers), as well as adsorption of organic inhibitors, precipitation inhibitors, ohmic inhibitors, and vapor phase

inhibitors. A literature review is provided for recent organic, inorganic, and green corrosion inhibitor development with "zero" environmental impact.

Chapter 15 outlines the fundamentals, criteria, field data, and design aspects of cathodic protection (CP), providing detailed descriptions for monitoring methods such as potential surveys, (PS), close interval potential surveys (CIPS), direct current voltage gradient surveys (DGVG), and corrosion rate measurement methods. The discussion of sacrificial protection system design illustrates total circuit resistance evaluation, anode output, number of anodes, and anode life. Impressed current systems (ICS) design is illustrated for a pipeline designed by the author, and anode, rectifier, and ground bed selection is explained, as is ground bed resistance calculation, rectifier output, number, and service life. Finally, case studies and solved problems illustrate sacrificial and impressed current cathodic protection system design.

CHAPTER 1

Evaluation of Corrosion

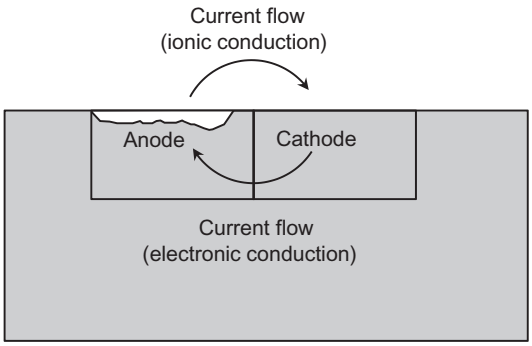

Chapter Contents

Corrosion Engineering
http://dx.doi.org/10.1016/B978-0-444-62722-3.00001-X

1.1 SIGNIFICANCE AND COST OF CORROSION

Corrosion compromises structure safety and is a leading factor in the catastrophic failure in bridges, nuclear facilities, airplane components, and equipment used in chemical, petrochemical, transportation, and construction industries. Corrosion is a spontaneous, slow-progressing phenomenon. The rate is mainly governed by the environment, metal composition, and metallurgical, chemical, and electrochemical properties. Because it takes a long time to evaluate the extent of corrosion, it is often underestimated in industrial equipment and structure design.

Corrosion is a major expense in estimating production cost and investments in any industry. According to a recent study, the direct cost of corrosion is estimated to be approximately $276 billion in the United States [1]. These losses are sustained by industry and government and constitute 3.2% of the gross domestic product (GDP). The direct cost of corrosion is considered the cost of replacing corroded structures and labor. Indirect losses add billions of dollars. The following losses are considered indirect costs: product loss, shutdown, efficiency loss, product contamination, metal and food and structure and equipment over design, for example, using more expensive, overqualified materials.

1.2 DEFINITION

Corrosion is the spontaneous destruction of metals and alloys caused by chemical, biochemical, and electrochemical interaction between metals and alloys and the environment. Corrosive environments include moisture, oxygen, inorganic and organic acids, high pressure, temperature, and chlorides. During corrosion, metals tend to convert to more thermodynamically stable compounds such as oxides, hydroxides, salts, or carbonates. Recovering the original compounds (minerals and ores) from metals by spontaneous corrosion as the result of a decrease in free energy. Hence, the energy used for metal winning from ore or alloying is emitted during corrosion reactions [2,3].

Corrosion processes are classified as chemical, biochemical, and electrochemical corrosion. In order for corrosion to proceed as a chemical reaction, the reacting particles must come into contact to transfer the electrons. Thermodynamically, the reaction is governed by the ratio of internal energy to activation energy. The laws of heterogeneous chemical reactions control spontaneous metal destruction. Examples of chemical corrosion are destructive metal interaction with nonconductive organic compounds and high-temperature corrosion in the presence of aggressive gases.

Microbial activities that produce sulfides, organic, or inorganic acids causing direct metal oxidation are major driving forces in biocorrosion. Biochemical corrosion is enhanced by stagnant water, soil, and organic products.

Electrochemical corrosion is governed by electrochemical kinetics. The rate of charge transfer reactions is determined by Faraday's law. Corrosion may affect the entire metal surface (general corrosion) or locally, resulting in pitting or stain corrosion. It attacks metals exposed in electrolytes (liquid corrosion), soils (soil corrosion), and gas in the presence of moisture on the metal surface (atmospheric corrosion). Corrosion caused by an external electric current is a special case of electrochemical corrosion. This includes stray current corrosion of underground metal structures when current is applied from bare electric lines. The potential difference is established between two electrochemically active areas of a metal structure; a cathodic area that receives current from the external circuit, and an anodic area that flows current to the soil or any other conductive medium. Electrochemical corrosion consists of two partial electrochemical reactions, an anodic partial reaction (oxidation/dissolution of the metal) and a cathodic partial reaction (reduction of water, hydrogen, or oxygen gas). The energy change of the partial corrosion reaction provides the driving force for the reaction and controls direction. The corrosion reaction activation energy and kinetic properties depend on chemical potential, temperature, and electrocatalytic properties of reactants. Depending on the metal or alloy properties, electrochemical corrosion occurs uniformly (carbon steel) or locally (hard alloys such as Inconel or Monel). In localized corrosion, the corrosion proceeds through the formation of narrow cracks or pits after penetrating the grains of the metal. Destruction may also occur along the grain boundaries, known as intercrystalline corrosion.

1.3 CONDITIONS FOR THE INITIATION OF CORROSION

Corrosion processes have features differentiating them from irreversible electrode processes. Corrosion does not require the application of an external current. The overall corrosion reaction of iron in neutral or alkaline solutions is described as:

$$2Fe + 2H_2O + O_2 \rightarrow 2Fe^{2+} + 4OH^- \rightarrow 2Fe(OH)_2 \tag{1.1}$$

The corrosion reaction (Eq. 1.1) can be separated into anodic and cathodic reactions:

$$2Fe \rightarrow 2Fe^{2+} + 4e^- \text{ Anodic reaction} \tag{1.2}$$

$$O_2 + 2H_2O + 4e^- \rightarrow 4OH^- \text{ Cathodic reaction} \tag{1.3}$$

In acidic solutions, oxygen depolarization reaction (Eq. 1.3) is:

$$O_2 + 4H^+ + 4e^- \rightarrow 2H_2O \tag{1.4}$$

In Eq. (1.2), each iron atom liberates two electrons increasing its valence state from 0 to 2. The cathodic partial reactions consist of dissolved oxygen reduction in alkaline or neutral

solutions, (Eq. 1.3), and acidic solutions, (Eq. 1.4). The other cathodic depolarization reactions are:

Hydrogen evolution reaction : $2H^+ + 2e^- \rightarrow H_2$ (1.5)

Metal deposition in galvanic corrosion : $M^+ + e^- \rightarrow M$ (1.6)

Metal ion reduction : $M^{3+} + e^- \rightarrow M^{2+}$ (1.7)

In absence of other depolarization reactions water will be reduced by

$$2H_2O + 2e^- \rightarrow H_2 + 2OH^- \quad (1.8)$$

Metals corrode through anodic reactions such as:

$$Zn \rightarrow Zn^{2+} + 2e^-$$

$$Co \rightarrow Co^{2+} + 2e^-$$

$$Al \rightarrow Al^{3+} + 3e^-$$

Corrosion may be initiated by electrochemical reactions in the following metals or alloys:

1. *Technical metals that contain metal impurities*: Examples are zinc or tin that contains silver or iron impurities. Silver and iron are cathodically protected by zinc or tin due to their potential difference. Corrosion may also occur as a result of crystal orientation or grain boundaries in the metal.
2. *Identical metals in contact with different concentrations*: In this case, the metal immersed in a dilute solution is dissolved from the electrode and deposited on the electrode immersed in a more concentrated solution. The other type of electrochemical concentration cell is known as a *differential aeration cell*. In this case, the electrode potential difference occurs when the electrode is immersed in the same electrolyte with different oxygen partial pressures. Differential aeration initiates crevice corrosion in aluminum or stainless steel when exposed to a chloride environment.
3. *Identical metals each exposed to a different temperature*: When a metal is in electrical contact with the same metal exposed to a lower temperature, the metal dissolves at the lower temperature (anode) and deposits at the higher temperature (cathode).

1.4 ELECTROCHEMICAL POLARIZATION

When a metal (M) is immersed in a solution containing its ions (M^+), several reactions may occur. The metal may lose an electron (corrosion) to form metal ions or the metal ions in solution gain electrons (reduction) and enter the solid metal state. The equilibrium across the metal-solution interface controls which reaction, if any, will occur at the metal-electrolyte interface. Because the equilibrium is determined by the equality of the partial Gibbs free-energy or chemical potentials (μ) on either side of the electrode interface (i.e., $\mu_{solution} = \mu_{electrode}$), when any metal is immersed in the electrolyte, thermodynamics

would favor interfacial electron transfer until the electrochemical potentials on both sides are balanced. The charge transfer rate at the electrode-electrolyte interface depends on the electric field across the interface as well as the chemical potential gradient. At equilibrium, the rates of both the corrosion reaction and the reduction reaction become equal, the net current is zero. The difference between the applied potential, E_{app}, when a net current flows through the corrosion cell and the corrosion potential, E_{corr}, is called the electrode polarization, overpotential, or overvoltage, η. The η term represents the extent to which the electrode-solution interface departs from the corrosion potential value.

$$\eta = E_{app} - E_{corr} \tag{1.9}$$

Overvoltage depends on the current density. When a cathodic current is applied to the electrode, the electrons accumulate in the metal as a result of slow charge transfer. This phenomenon causes cathodic polarization, η_c, to be negative. Conversely, when electrons are removed from the metal like anodic polarization (corrosion), the polarization is positive.

Equilibrium is disturbed when a net forward or backward reaction occurs, producing current in the external circuit. The current induces a potential change and causes polarization. Charge conservation requires the total rate of oxidation be equal to the total rate of reduction for any corrosion process. To avoid accumulation charge in the electrode, the sum of anodic currents must equal the sum of cathodic currents.

The concept of polarization in a corrosion cell could be well explained by an Evans diagram considering a simple galvanic cell, such as the Daniel cell, which has copper and zinc electrodes given in Fig. 1.1. This diagram helps visualize the basics of underlying corrosion kinetics. The graphical construction and analytical solutions of the Evans diagram are discussed in more detail in Chapter 3. The open circuit potential of copper in a copper ion solution and zinc in a zinc ion solution are represented, respectively, as $e_{eq,C}$ and $e_{eq,Zn}$ and the currents corresponding to the open circuit potentials are the current densities of either electrode reaction. For this cell, thermodynamics favors the reduction of copper and the oxidation of zinc, and the criterion for a spontaneous reaction ($\Delta G = -n\mathrm{Fe}^{o}$) holds.

Upon polarization of either electrode, the cell potential moves along the oxidation and reduction curves as shown in Fig. 1.1. When the current through the cell is i', the potential of the copper and zinc electrodes is $e_{1,Cu}$ and $e_{1,Zn}$; and each of the electrodes have been polarized by ($e_{eq,Cu} - e_{1,Cu}$) and ($e_{eq,Zn} - e_{1,Zn}$). Upon further polarization, the anodic and cathodic curves intersect at a point where the external current is maximized. The measured output potential in a corroding system, often termed the mixed potential or the corrosion potential (E_{corr}), is the potential at the intersection of the anodic and the cathodic polarization curves. The value of the current at the corrosion potential is termed the corrosion current (I_{corr}) and can be used to calculate corrosion rate. The corrosion current and the corrosion potential can be estimated from the kinetics of the individual redox reactions such as standard electrode potentials and exchange current densities for a specific system. Electrochemical kinetics of corrosion and solved case studies are discussed in Chapter 3.

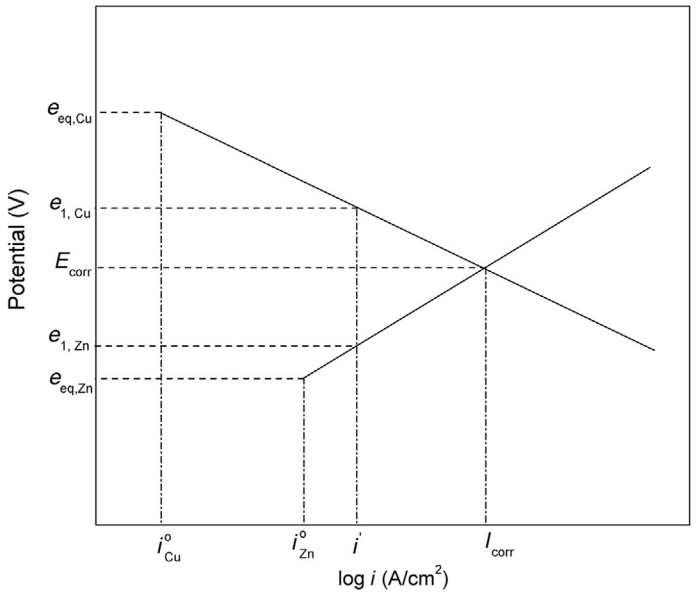

Fig. 1.1 Schematic showing the anode and cathode polarization curves with the mixed potential (Evans diagram).

For example, the corrosion current and corrosion potential of Fe in a solution of pH 7 saturated with oxygen (1 atm) can be calculated graphically or analytically if the following electrochemical kinetic parameters are known:

(a)	[Fe] = 0.7 M	pH = 7	$P_{O_2} = 1$ atm
(b)	$b_a = 0.08$ V/decade $i^{o}_{Fe} = 10^{-5}$ A/cm^2	$b_c = -0.11$ V/decade $i^{o}_{OH^-} = 10^{-6}$ A/cm^2	

Graphical and analytical determination of the corrosion current is explained in detail in Chapter 3. The Evans diagram for an iron system in an oxygen-saturated solution with a pH of 7 is shown in Fig. 1.2.

1.5 PASSIVITY

A metal is passive if it resists corrosion in strong oxidizing solutions or at applied anodic polarization [4–9]. Active-passive metal passivates through interaction with oxidizing agents or anodic polarization. A metal is defined as active-passive if it possesses three regions in the polarization curve: active, passive, and a transpassive region. A typical anodic polarization curve of an active-passive metal is shown in Fig. 1.3.

In the active region, the anodic electrochemical reaction is metal oxidation. Mixed potential theory governs the alloy corrosion in this region. The corrosion potential and

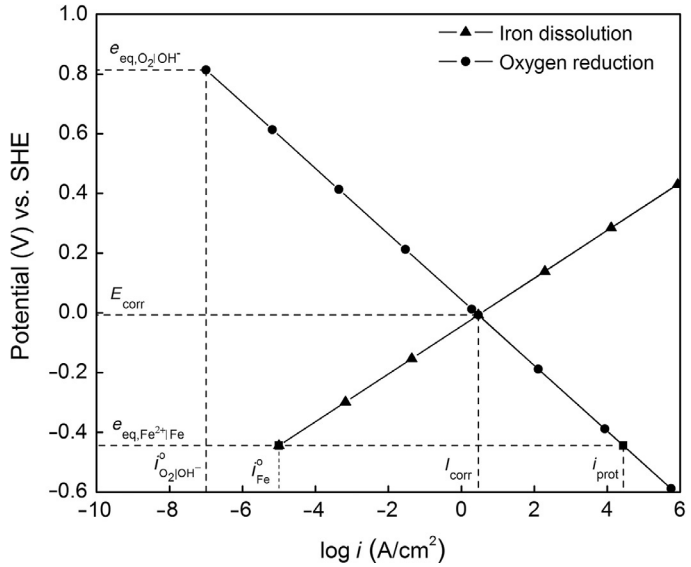

Fig. 1.2 Evans diagram for iron system in oxygen-saturated solution.

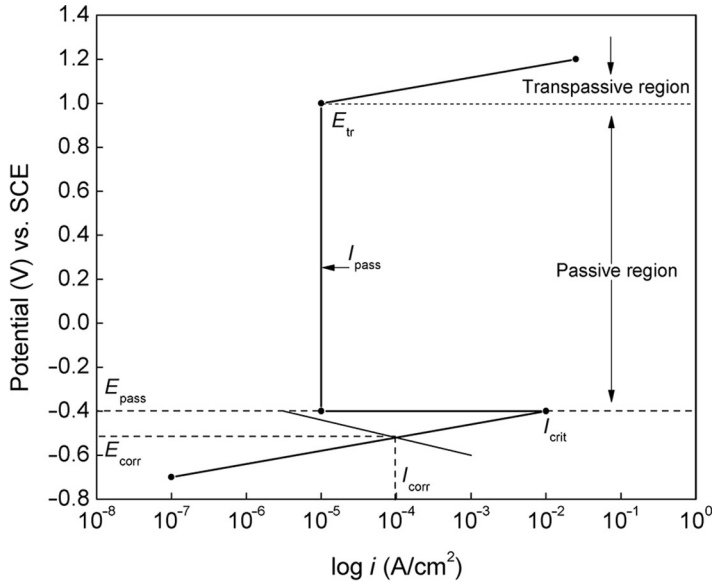

Fig. 1.3 Polarization curve for active-passive metal.

current are controlled by the Tafel kinetics of individual redox reactions. The cathodic polarization reactions are reduction of the oxidizer, hydrogen, or oxygen evolution. In the active state, the corrosion current increases with further polarization.

In the passive region, polarization increase in Fig. 1.3 results in a sudden corrosion current decrease. At the passivation potential, E_{pp}, a sufficient critical current density,

I_{crit}, is provided to the system to form a passive film on the surface. At this point, current stops increasing and starts decreasing to the passivation current, I_{pass}, several orders of magnitude smaller than the active metal surface.

Mixed potential theory is used to calculate the critical passivation current density and construct the polarization curve for the active-passive metal in Fig. 1.3 with the following electrochemical parameters: $E_{corr} = -0.5$ V vs. SCE, $E_{pp} = -0.4$ V vs. SCE, $I_{corr} = 10^{-4}$ A/cm^2, $b_a = 0.05$, $I_{pass} = 10^{-5}$ A/cm^2, and $E_{tr} = +1.0$ V vs. SCE.

The critical passivation current density is calculated by subtituting the anodic current density, i_a, with I_{crit} and the anodic potential, E, with E_{pp} in Tafel equation:

$$
\begin{aligned}
i_a &= I_{corr} 10^{(\eta_a / b_a)} \\
\eta_a &= E - E_{corr} \rightarrow E = E_{pp} \\
\eta_a &= E_{pp} - E_{corr} = -0.4 - (-0.5) \\
I_{crit} = i_a &= I_{corr} 10^{(\eta_a / b_a)} \rightarrow I_{crit} = 10^{-4} \times 10^{(0.1/0.05)} = 10^{-2}\,\mathrm{A/cm^2}
\end{aligned}
$$

The critical current density and passivation potentials are important characteristics that control metal passivation properties. In the transpassive region, E_{tr}, the current starts to increase due to oxygen evolution or passive film breakdown. In Fig. 1.3, the passive region is more anodic than the active region. This property of the active-passive metal or alloy is not observed in the case of normal metals and is only used to define passivity.

1.6 TYPES OF CORROSION

Various classifications of corrosion have been suggested in the literature [3,10–12]. Corrosion was classified by the nature, environment chemical composition and electrochemical properties, temperature, corrosion attack, and attack rate. Different forms of corrosion are:

- Uniform attack
- Galvanic corrosion
- Pitting
- Crevice corrosion
- Stress corrosion cracking
- Intergranular corrosion
- Selective leaching
- Erosion corrosion
- Hydrogen damage

Dilon [12] grouped corrosion into two categories.

Group I: Corrosion detected by visual examination:

- Uniform corrosion characterized by uniform loss of metal from the surface
- Localized corrosion mostly occurring on discrete surface areas resulting in pitting or stain corrosion

- Galvanic corrosion by electrical contact between metals with different standard potentials in an electrolyte

Group II: Corrosion distraction that requires a means of examination and identification:

- Erosion corrosion caused by high velocity flow, fretting caused by vibration of two surfaces in close contact, and cavitation caused by very high flow
- Intergranular corrosion at metal grain boundaries
- Dealloying resulting in alloy composition change due to the selective dissolution
- Environmental cracking with induced brittle failure in ductile material under stress and corrosion fatigue
- Microbial activities producing sulfides, organic, or inorganic acids causing direct metal oxidation

1.7 BRIEF DESCRIPTION OF DIFFERENT TYPES OF CORROSION

1.7.1 Uniform corrosion

Uniform corrosion proceeds over a large fraction of the metal surface area and results in uniform thickness reduction. The corroding metal must be compositionally and metallurgically uniform. Because there are no preferential corrosion sites, both the cathode and anode are not a fixed location, resulting in uniform corrosion. Corrosion rates are measured by electrochemical corrosion techniques or weight loss [13]. This type of corrosion is controlled by corrosion inhibitors, metallic and organic coatings, and cathodic protection. An example of uniform corrosion is atmospheric corrosion. The spontaneous corrosion of materials in atmospheric corrosion is controlled by temperature, relative humidity, time of wetness, pH of the electrolyte, presence of contaminants such as chlorides, NH_3, SO_2, NO_2, and acidic fogs. Corrosion rate in a wet atmosphere is similar to metals during immersion in aerated water containing 10-12 ppm of dissolved oxygen. In most cases reported in the literature, rate equations have limited validity due to different local atmospheric conditions. Metals spontaneously form a solid metal oxide film when exposed to dry atmospheres with almost no humidity. The barrier oxide film reaches a maximum thickness of 2-5 nm [14–16]. Atmospheric corrosion of a railway bridge in Vietnam is shown in Fig. 1.4 [17].

1.7.2 Galvanic corrosion

The potential difference established when two metals (alloys) are electrically connected in a conducting medium produces electron flow and causes the metal (alloy) with more negative potential to preferentially corrode. The more positive metal (alloy) becomes a cathode and is protected by the negative metal (alloy), which becomes an anode (Fig. 1.5). Because the driving force for corrosion is the potential difference between the metals (alloys), this form of corrosion is called galvanic corrosion. Steel fasteners in an aluminum foil, the solder on a copper pipe, and stainless steel in contact with

Fig. 1.4 Atmospheric corrosion of a railway bridge in Vietnam [17].

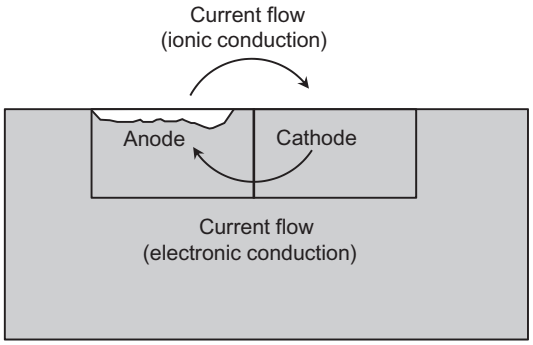

Fig. 1.5 Schematic representation of galvanic corrosion.

galvanized steel are examples of galvanically coupled dissimilar metals. Galvanic corrosion also occurs when the same metal is in contact with an electrolyte of two different concentrations or with different levels of aeration (differential aeration cell). Soil with varying salinity or pH in contact with a buried iron pipe creates galvanic cells in which the anodic part of the pipe corrodes faster.

The corrosion rate of metals is determined by established potential difference, soil conductivity, and relative anodic and cathodic areas [18–20]. Composite polarization diagrams are used to predict galvanic current. They consist of potentiostatic cathodic and anodic polarization curves for different metals and alloys in deaerated 1 N H_2SO_4 and aerated 3% NaCl. Galvanic corrosion prediction for longer time periods from data obtained in short time periods is not accurate due to surface conditions and impurities.

Galvanized steel is a common example of galvanic coupling where steel (Fe) with a standard electrode potential of −0.440 V vs. SHE is cathodically protected by a coating of zinc with a more active standard electrode potential of −0.763 V. Obviously, zinc is not a corrosion-resistant metal and cannot be classified as a barrier coating. It protects the steel from corrosion because of its sacrificial properties. Because zinc is less noble than steel, it acts as the anode. The sacrificial anode is continuously consumed by anodic dissolution and protects the more positive metal from corrosion. In practice, sacrificial anodes are

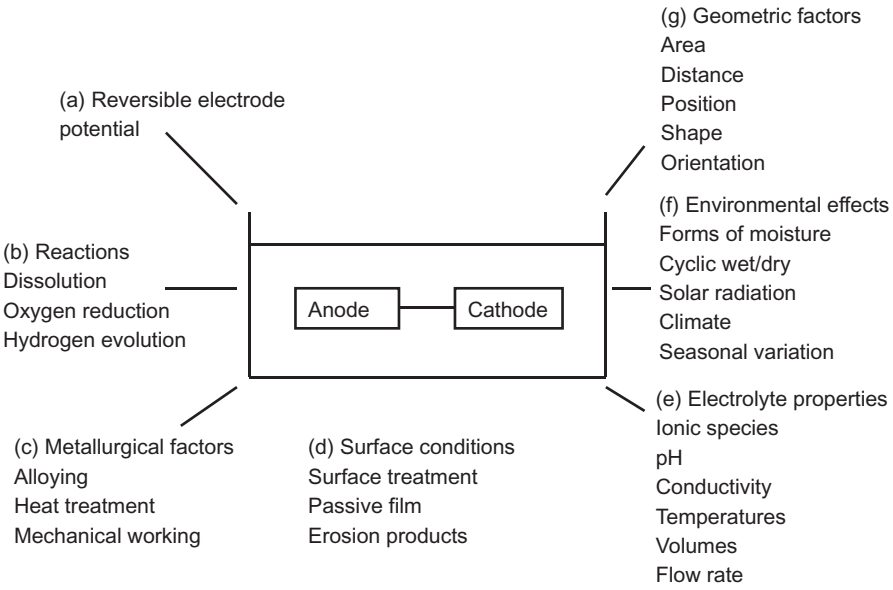

Fig. 1.6 Factors controlling galvanic corrosion [21]. *This material is reproduced with permission of John Wiley & Sons, Inc.*

comprised of zinc, tin, magnesium alloys, or aluminum. Factors that control bimetallic galvanic corrosion are summarized in Fig. 1.6 [21].

An example of iron and nickel galvanic corrosion is shown in Fig. 1.7. The corrosion potential and corrosion current for iron and nickel when coupled and uncoupled can be estimated graphically and analytically using the following electrochemical parameters for both metals: the standard equilibrium dissolution potentials (e_{eq}) for nickel and iron are -0.25 and -0.44 V vs. SHE, respectively. The exchange current density for nickel dissolution is 1×10^{-7} A/cm^2 and Fe is 1×10^{-6} A/cm^2. The concentrations of $[Ni^{2+}] = 4.13 \times 10^{-4}$ M and that of $[Fe^{2+}] = 1$ M. The exchange current densities for hydrogen evolution on nickel and iron are 4×10^{-6} and 1×10^{-6} A/cm^2, respectively. It is assumed that all Tafel constants are ± 0.1 V. A photograph of galvanic corrosion of stainless steel under grip panel area in Series 80 Colt Gold Cup 1911 pistol is shown in Figure 1.8 [22].

1.7.3 Pitting corrosion

Pitting represents an extremely localized attack that produces holes in the metal or alloy. It is one of the most destructive, localized forms of corrosion. The pits are small cavities or holes with a depth greater than or equal to the surface diameter. They penetrate the metal, causing equipment failure due to preformation with minimal weight loss. The severity of pitting corrosion is controlled by environment, chloride concentration,

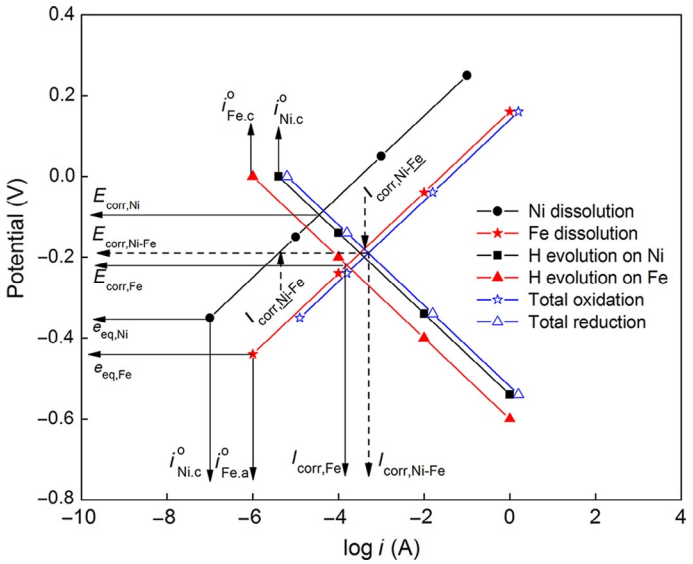

Fig. 1.7 Galvanic couple between iron and nickel.

Fig. 1.8 Galvanic corrosion of stainless steel under grip panel area in Series 80 Colt Gold Cup 1911 pistol [22]. http://ravelingroup.com/wordpress1/tag/colt-gold-cup/.

electrolyte acidity, oxidizer concentration, temperature, structural characteristics, metal or alloy composition, dissolved oxygen concentration, potential, and potential scan rates [23–26]. Surface pitting is proportional to the logarithm of chloride concentration in the electrolyte. To initiate pitting corrosion, the electrolyte must act as a strong oxidizer to favor the passive state. Oxidizing metal ions such as ferric and cupric halides act as electron acceptors (cathodic reactants) and are very aggressive because they do not require oxygen to initiate and propagate pitting corrosion. Localized mechanical or chemical damage to a passive oxide, insufficient inhibitor coverage, and nonuniformities in the metal structure due to nonmetallic impurities contribute to pitting corrosion. Pitting potential is defined by ASTM as the potential beyond which pitting propagates. An example of pitting corrosion of 304 stainless steel is shown in Fig. 1.9 [27].

Pitting analyses and potential can be used to (i) develop new alloys, (ii) perform alloy ranking, (iii) do failure analysis, (iv) evaluate process parameters, and (v) predict pitting penetration rates. Pitting corrosion is initiated by chloride migration from the electrolyte to the metal film interface. The chloride ions adsorb on the outer surface of the passive film, permeate the metal oxide passive layer, and interact with the underlying metal. An image of copper pitting corrosion in a drinking water system is shown in Fig. 1.10 [28].

The redox reaction occurring at the interface increases the potential close to the pitting potential, resulting in a local chloride concentration increase due to electrostatic attraction between the negatively charged chloride ions and the positive surface [29]. Pitting corrosion occurs through the following steps: (i) passive film breakdown and nucleated pit formation, (ii) embryonic pit formation, (iii) metastable pit development, (iv) stable pit formation and pit growth, and (v) pit arrest [30]. The stainless steel critical pitting potential shifts in the anodic

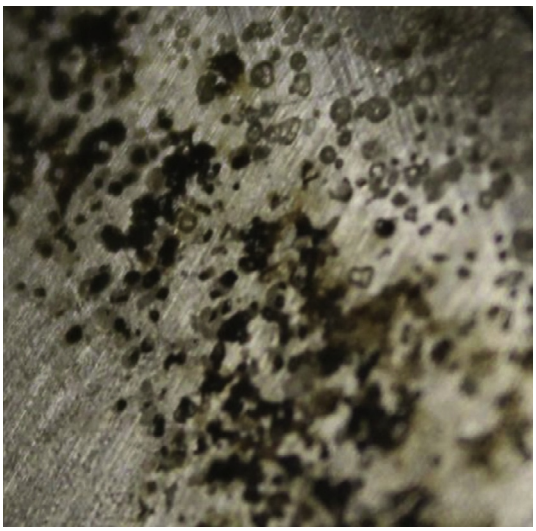

Fig. 1.9 Pits on 304 stainless steel after exposure to simulated marine environment (3.5 g/L NaCl) [27].

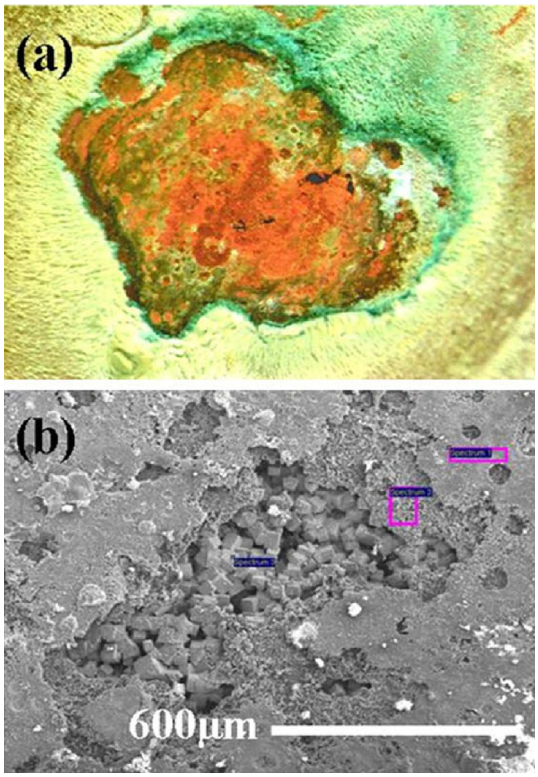

Fig. 1.10 Copper pitting corrosion in drinking water system: (a) stereomicrography of perforated membrane and (b) scanning electron micrograph of perforated pit [28].

direction when chromium content increases above the critical 12% value needed to produce stainless steel [31]. An alloying element in stainless steel such as nickel and molybdenum reduces pitting susceptibility [32,33]. Because chromium and titanium show a more positive potential than the oxygen electrode in air, they don't undergo pitting corrosion in chloride solutions at 25 °C. Mo is enriched in the surface film, which is formed in the active region and blocks the active sites during metal dissolution [34]. Pitting can be inhibited by (i) decreasing environment aggressiveness, (ii) alloy composition, (iii) temperature, (iv) alloy structure, (v) alloy protection with conversion coatings, (vi) cathodic or anodic protection, and (vii) inorganic inhibitors. Solution aggressiveness is reduced by decreasing electrolyte temperature, chloride concentration, and acidity at the interior of the pit.

1.7.4 Crevice corrosion

Crevices are formed at welds, in condensers, and between metal surfaces and valves. This type of corrosion is initiated by small volumes of solution captured in crevices under bolt

gasket rivets or surface deposits. It destroys mechanical joint integrity in structures constructed from stainless steel, aluminum, titanium, and copper. For corrosion to occur, the aggressive solution must permeate the crevice and be sufficiently narrow to keep corrosion products inside the crevice. In the case of corrosion by dissolved oxygen, active-passive short circuits are formed between the aggressive solution in the crevice, which becomes oxygen depleted (anode), and the external metal surface (cathode). The initiation of crevice corrosion is based on pH decrease in the bottom of the crevice. The positive metal ions formed in the crevice in the absence of oxygen reduction attract chloride ions and initiate acidification through water hydrolysis. The corrosion reaction within the crevice increases with decreasing pH and cathodically protects the external cathodic metal surface. Separation between the anodic reaction in the crevice and the cathodic reaction on the external passive metals surface is a precondition for crevice corrosion initiation by the IR voltage drop mechanism suggested by Pickering et al. [35,36]. Figure 1.11 shows the optical microscope image of crevice corrosion damage on Ni-Cr-Mo-W alloy-22 under a constant current of 40 μA [37].

Electropolished surfaces mitigate crevice corrosion by lowering cathodic current densities during polarization in sea water. Manganese sulfide removal by pickling increases crevice corrosion resistance. Sulfide inclusions act as pitting sites for crevice corrosion. Pickling also removes chromium-depleted layers formed during annealing at high temperature and decreases crevice corrosion susceptibility.

1.7.5 Filiform corrosion

Filiform corrosion is observed under thin organic coatings on aluminum, steel, aircraft structures exposed to humid atmosphere, beverage cans, flanges, gaskets, dis-bonded

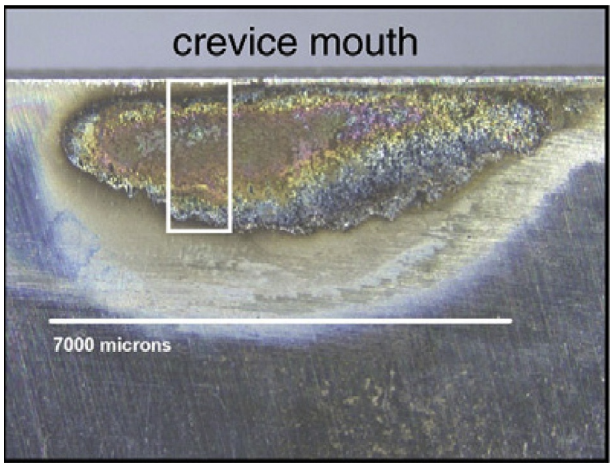

Fig. 1.11 Optical images of creviced alloy-22 corroded at a constant current of 40 μA to an accumulated charge of 7 C [37].

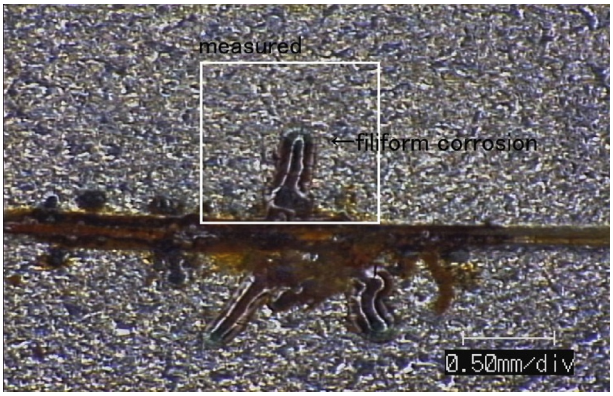

Fig. 1.12 Appearance of filiform corrosion tracks [38].

underlying metals coated with organic coatings weld zones, and so forth. Corrosion-resistant alloys of stainless steel, copper, and titanium are not susceptible to filiform corrosion. Figure 1.12 shows filiform corrosion of steel substrates painted with clear acryl paint [38]. Filiform corrosion was induced by knife-scored specimens exposed to 5% NaCl and humidity (40% and 80% RH). The corrosion of the underlying metal was clearly observed through the clear paint surface. The line in the center represents the knife-score. The filiform corrosion grew in both directions from the line and is composed of a head and the tail. The head and the tail are filled with a $FeCl_2$ solution and corrosion products, respectively [39].

1.7.6 Stress corrosion cracking

Stress corrosion cracking (SCC) is defined as crack growth due to simultaneous tensile stress and corrosive environments on active metals or alloys. In order for SCC to occur, the metal should be susceptible to SCC and be in a corrosive environment such as chloride ions, water, oxygen, pH, and so on. SCC leads to catastrophic failure in aircraft structures, nuclear facilities, boilers, and liquid or gas transmission pipes. Stress is induced by heat treatment, welding, machining, grinding, and cold work. The required tensile stresses may occur in the form of residual stress, applied load (directly applied stress), monotonic straining, or low amplitude cycling. The rate of crack propagation is affected by stress levels, temperature, and corrosion solution concentration. Corrosion products in the alloy matrix may also generate stress. Only a specific combination of active alloys, stresses, and environments create conditions for SCC. The stress should be above the threshold value. Typical SCC is due to sensitization and residual stress. Crack length has been observed reaching several dozens of mm. The cracks can be created by initiation and growth of corrosion pits and microcracks. The crack initiation in the alloy and coalescence of microcracks result in subcritical crack propagation to large crack formation. SCC of austenitic stainless steel is shown in Fig. 1.13 [40].

Fig. 1.13 Stress corrosion cracking of austenitic stainless steel [40]. http://www.metallurgicalviability.com/SCC.htm.

The cracks penetrate the material's microstructure as transgranular or intergranular morphology. Chloride SCC is intergranular and occurs in austenitic stainless steel, a great concern for the nuclear industry. Stress corrosion occurs at high temperatures in the presence of chloride ions and oxygen. Caustic SCC has been observed on Inconel alloy tubing. Extensive cracking is generated in a matter of hours for combinations like type 304 stainless steel in a boiling $MgCl_2$ solution.

Standard SCC testing has been reviewed by Sedriks and Turnbull [41,42]. The following techniques have been used to evaluate SCC: surface flawed (SF), cantilever bend (CB), creviced bent-beam tests, double cantilever beam (DCB), and compact tension (CT) specimens. These techniques are time-consuming, expensive, and require bulky specimens that restrict the use of the commonly used techniques for SCC monitoring. Testing methods that are common to SCC and hydrogen-induced cracking, fracture mechanics, and corrosion fatigue are discussed in detail in Chapter 9.

1.7.7 Metallurgy of SCC

SCC in alloys is controlled by the alloy solid solution composition, grain boundary segregation, alloy phase transformation, duplex structure, and cold work. SCC metallurgy is discussed in detail in Chapter 9.

1.7.8 Solid solution composition and grain boundary segregation

Solid solution composition determines the nature of austenitic stainless steels [41,42]. Intergranular cracking proceeds along grain boundaries, whereas transgranular cracking does not have preferences for boundaries. In the case of transgranular SCC, cracks advance across specific crystal planes with low indices. Intergranular corrosion (IGSCC) or intergranular attack (IGA) occurs in many alloy systems due to reactive impurity segregation or chromium depletion at the grain boundaries. A scanning electron microscope (SEM) image of stainless steel wire intergranular stress corrosion is shown in Fig. 1.14 [43].

Corrosion at grain boundaries or adjacent regions can be very severe dropping grains out of the surface. Chromium carbides precipitation ($Cr_{23}C_6$) in the grain boundaries enhances heat-treated austenitic steel intergranular SCC by depleting the grain boundary and adjacent regions of chromium. The alloys corrode at high rates when chromium is below 10%. When carbide distribution is widely spread in the alloy, SCC susceptibility decreases. Alloys are more susceptible to SCC than metals. Susceptibility increases with increasing alloy strength. Stainless steel thermal treatment produces carbides in the grain boundaries and chromium depletion from the grain boundaries causes intergranular corrosion sensitization. Figure 1.15 shows SCC in the return pipes of a heating system [44]. The pipes were exposed to slow strain. Temperature changes in the pipe caused intergranular SCC near the weld joints.

1.7.9 Alloy phase transformation and associated solute depleted zones

The phase at the alloy's grain boundary controls alloy reactivity or enhances reactivity of the associated solute depleted zone (SDZ) [45]. The aerospace alloy Al-Zn-Mg (7000) series exhibits SCC susceptibility when alloyed with Cu. Cu segregation and grain

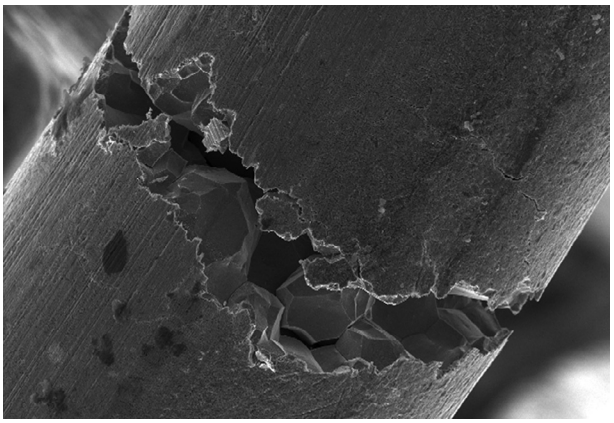

Fig. 1.14 SEM image of intergranular stress corrosion of stainless steel wire [43]. http://www.rcrd.manchester.ac.uk/materials/a-sem-image-stainless-steel-wire-intergranular-stress-corrosion/.

Fig. 1.15 Stress corrosion cracking near the weld of heating pipes [44].

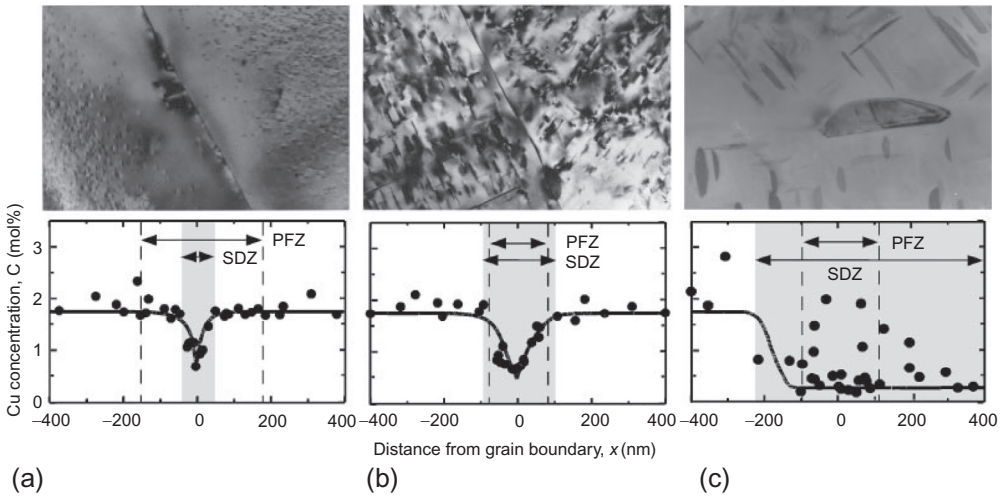

Fig. 1.16 Electron microscopy images and EDX profiles around grain boundaries of the Al-Cu alloy aged at 433 K for 7.2 ks. (a) under-aged, (b) 90 k (peak-aged), and (c) 1728 ks (over-aged). The average widths of precipitate free zone (PFZ) and solute depletion zone (SDZ) are indicated by arrow [46].

boundary phase precipitation that contain Cu (noble region) result in pitting corrosion triggered by galvanic corrosion with an adjacent Cu depleted anodic region.

Figure 1.16 illustrates a transmission electron microscope (TEM) image showing the formation of a precipitate free zone (PFZ) along a grain boundary of the under-aged alloy [46]. The precipitates were identified as plate-like Guinier-Preston zones (GP zones) with an average size of approximately 15 nm. The EDX profile in Fig. 1.16a indicated that in the PFZ zone, the concentration of Cu is in the range of 1.7 mol%. The depletion mechanism initiates after a later stage of aging. Figure 1.16b and c shows a decrease in Cu concentration

within the PFZ, indicating growth in grain boundary precipitates. The width of the PFZ zone decreases and then increases with aging time, while the SDZ increases in width and becomes identical to the width of the PFZ at ~30 ks. At high aging temperatures, only an increase in PFZ width was observed due to faster grain boundary precipitate formation [46].

Thermomechanical treatment showed superior corrosion resistance on AA5083 corrosion compared to as-received samples. Precipitates such as Al-(Fe, Si, Mn, Cr), Al-13Fe_4, Al_6(Fe, Mn), and Mg_2Si together with the β-phase post-sensitization were identified using SEM, EDS, and TEM. Dislocation networks showed better corrosion resistance than the matrix [47].

1.7.10 Duplex structure

Alloy microstructures that contain two phases in comparable ratios are defined as duplex structures. Duplex structures exhibit combined strength, low susceptibility to SCC, and good microstructural control when welded [48].

Figure 1.17 shows SCC of a 2205 DSS sand separator cone in a pulp mill [49]. Duplex stainless steels possess a high-threshold stress intensity value, K_{th}. The duplex stainless steels that contain ferrite and austenite phases have better localized corrosion resistance than single-phase austenitic stainless steels in chloride-containing solutions and are used as structural materials in petrochemical, chemical, pulp and paper, power generation, oil, and gas industries.

1.7.11 Cold work

Cold work, through work hardening or strain hardening, causes plastic deformation and permanent change in the crystalline structure of a metal. Cold work reduces ductility while increasing yield-strength and hardness. Since the metal becomes less ductile, when subjected to high stress, the probability to fracture becomes higher when compared to

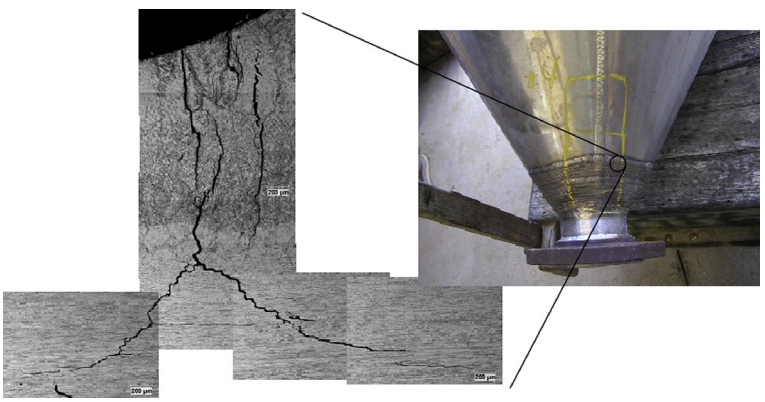

Fig. 1.17 Stress corrosion cracking of 2205 DSS sand separator cone in pulp mill [49].

bending. The most common cold working method is cold rolling. The metal is squeezed through narrow gaps between two rotating rolls causing deformation by compression. The metal may also be shaped via cold forging by pressing it into a die with a hammer. Cold heading is used to produce bolts and other fasteners. The effect of cold work on intergranular SCC susceptibility of Alloy 600 in low dissolved oxygen (DO) has been studied in pressurized water reactors (PWR) [50]. Cold work does not have a large effect on the increase of SCC velocity. However, it reduces the alloy ductility, fracture toughness, and threshold stress intensity. Moderate amounts of cold work are more detrimental than severe amounts of cold work. Crack growth rates (CGRs) are increased by one order of magnitude from only 5% cold work. Because cold work increases yield strength, an effect similar to cold work on CGRs is also observed for yield strength. CGR increases with an increase in yield stress. The effect of cold work on the SCC growth rates results from dislocation density and deformation behavior ahead of the crack tip. Fe-Cr-Ni alloy SCC susceptibility has been correlated with dislocation arrangements in the metal. Planar dislocation structures lead to transgranular SCC, and intergranular SCC is observed in materials with high stacking fault energy.

1.7.12 Hydrogen embrittlement

Hydrogen embrittlement (HE) occurs from alloy exposure during welding operations, casting, pickling, or cathodic protection. The brittle properties of observed cracks in SCC are controlled by the hydrogen atom-induced cracking mechanism. Because hydrogen solubility in the molten alloy is higher than solid, hydrogen contamination begins in the early stages of metallurgical processing. Damage occurs when hydrogen accumulates in defects (hollow spaces) in the interstitial lattice positions. The concentrated areas of adsorbed hydrogen recombine to form molecular hydrogen in the traps, which drastically increases localized pressure in the structure.

Figure 1.18 shows a boiler rupture caused by HE [51]. The irreversible accumulation of hydrogen within the metal lattice leads to mechanical property deterioration. Part of the adsorbed hydrogen diffuses into the substrate crystalline lattice where it reacts with the metal atoms to form brittle metal hydrides and causes the structure to fail far below the yield strength. Hydrogen-induced cracking (HIC) has been accepted as the controlling failure mechanism for less ductile, high-strength steels such as titanium, high-strength iron, and some aluminum alloys that have the highest susceptibility to HE.

Figure 1.19 illustrates HE of zinc-plated bolts showing intergranular damage and secondary cracking [52]. Hydrogen susceptibility drastically increases when steel strength increases. Interaction between atomic hydrogen and atomic metal structures inhibit the ability to stretch under load and become brittle. Hydrogen may also act as a grain boundary surfactant creating microcracks within the steel due to a decrease of the surface film energies at the grain boundaries. Hydrogen reduces the adhesion and cleavage

Fig. 1.18 Rupture caused by hydrogen embrittlement [51]. http://www.gewater.com/handbook/boiler_water_systems/fig14-10.jsp0.

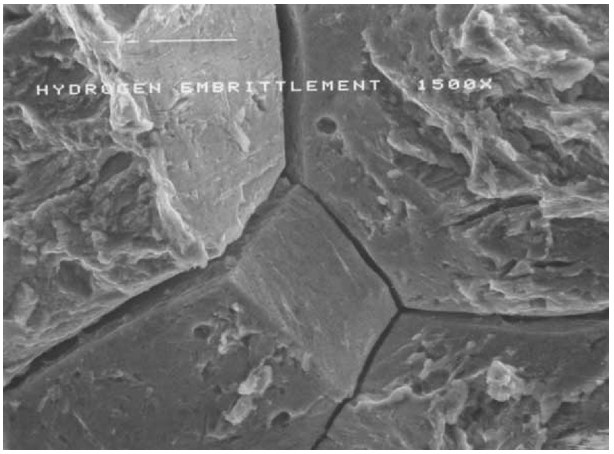

Fig. 1.19 SEM micrograph of the fractured surface of zinc specimen [52]. http://www.quali-tech-inc.com/HydrogenE.html.

strength of the alloy. The resistance to shear slip significantly reduces in the presence of hydrogen atoms.

1.7.13 Corrosion fatigue cracking

High-strength material fatigue present in titanium alloys, aluminum alloys, and steel are susceptible to SCC when exposed to a corrosive environment. Fatigue cracking is mechanical degradation (brittle failure) when exposed to corrosion and cycling loading. Corrosion fatigue cracking (CFC) should not be confused with SCC, because the only

requirement for CFC is exposure under tensile stress. Figure 1.20 shows a view of the Y488 bulkhead's RHS outboard flange and adjoining web in an aircraft [53].

Figure 1.21 illustrates longitudinal corrosion fatigue cracks in preexisting copper tube defects [54]. Low corrosion rates of metal and alloy have no effect on fatigue life in air. Fatigue cracks propagate after a certain number of cycles and below yield stress and stops propagating until the material separates by overload fracture. At this point, the load applied to the material exceeds the ultimate tensile stress. The corrosive environment effect on fatigue is evaluated by variation of fatigue fractures stress as a function of number of cycles applied in the corrosive environment and in air (*S*-*N* curves). *S*-*N* curves

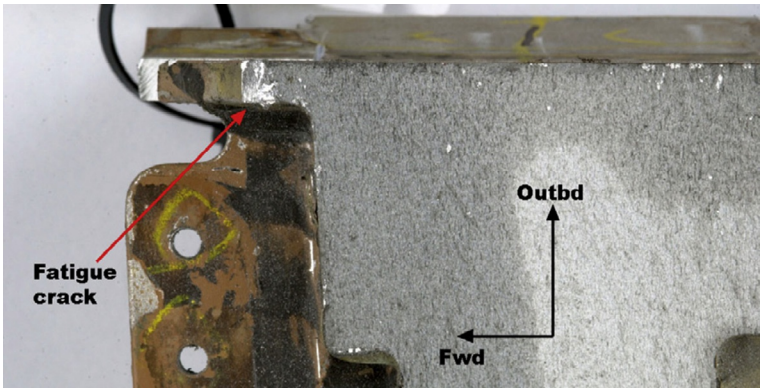

Fig. 1.20 A view of Y488 bulkhead's RHS outboard flange and adjoining web in an aircraft. The location of the fatigue crack in the forward flange is highlighted [53].

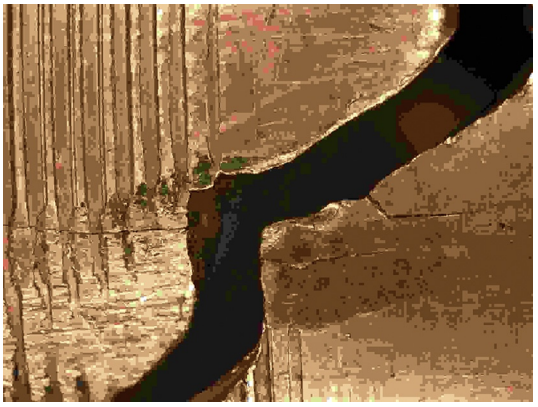

Fig. 1.21 Longitudinal corrosion fatigue cracks in preexisting notches of copper tubes in a subcooler [54]. http://www.corrosionlab.com/Failure-Analysis-Studies/30038.corrosion-fatigue-cu-tube.htm. *Photo provided courtesy of Corrosion Testing Laboratories, Inc., Newark, DE.*

indicate the variation of the fatigue fracture stress (S) with the number of cycles applied (N). In practice, the alloys are evaluated by comparing the stress at which no failure occurs after 10^8 cycles.

1.8 CORROSION RATE DETERMINATION

Electrochemical corrosion techniques are essential to predict service life in chemical and construction industries. The following direct current (dc) electrochemical methods are used in corrosion engineering practice: linear polarization technique, Tafel extrapolation, and open circuit potential vs. time measurements. The alternating current (ac) technique is electrochemical impedance spectroscopy (EIS). This technique uses alternating current to measure frequency-dependent processes in corrosion and estimates the change of polarization resistance as a function of time.

Linear polarization measurements are executed rapidly. The currents in linear polarization measurements are measured in the potential range between 10 and 20 mV from the equilibrium potential. The E-I dependence in this potential range follows a linear relationship. The slope of the plot, dE/di, represents the polarization resistance. The corrosion current is calculated using the Stern-Geary equation for known values of the anodic and cathodic Tafel slopes. The ratio of the overpotential to the current represents the resistance in Ohm's law and is often termed the charge transfer resistance or the polarization resistance, R_p.

$$R_p = \frac{RT}{nF} \times \frac{1}{i^o} \tag{1.10}$$

A higher exchange current density implies increased reaction rate, while lower exchange current density (higher polarization resistance) indicates sluggish corrosion kinetics. Equation (1.10) can be written in terms of charge transfer resistance as:

$$\eta = R_p i \tag{1.11}$$

1.8.1 Calculation of corrosion rate form corrosion current

The Stern-Geary equation is used to calculate corrosion current [55]:

$$I_{corr} = \frac{b_c b_a}{2.3(b_c + b_a)} \frac{1}{R_p} \tag{1.12}$$

where $\Delta E/\Delta i$ is the slope of the polarization curve, also called the polarization resistance, R_p. b_a and b_c and are anodic and cathodic Tafel constants.

The corrosion current in A or A/m^2 can be used to determine the amount of corroded material as a result of the corrosion process. Current can be directly converted into mass using Faraday's law.

$$\mathrm{CR\,(cm/s)} = \frac{I_{\mathrm{corr}}(\mathrm{EW})}{\mathrm{d}FA} \tag{1.13}$$

Corrosion rate calculated in milli-inches per year (mpy) is:

$$\mathrm{CR(mpy)} = \frac{I_{\mathrm{corr}}\,(\mu\mathrm{A/cm^2})\,(\mathrm{EW})}{d\,\dfrac{\mathrm{g}}{\mathrm{cm^3}} \times 96,487\,\dfrac{\mathrm{C}}{\mathrm{eq}} \times 1\,\mathrm{cm^2}} \times \frac{1\,\mathrm{C/s^2}}{10^6\,\mu\mathrm{A}} \times \frac{3600\,\mathrm{s}}{1\,\mathrm{h}} \times \frac{24\,\mathrm{h}}{\mathrm{day}} \times \frac{365\,\mathrm{days}}{\mathrm{year}} \times \frac{1\,\mathrm{in}}{2.54\,\mathrm{cm}} \times \frac{1000\,\mathrm{milli}}{1\,\mathrm{in}} \tag{1.14}$$

$$\mathrm{CR\,(mpy)} = \frac{0.13 \times I_{\mathrm{corr}}(\mathrm{EW})}{d} \tag{1.15}$$

where mpy = milli-inches per year; I_{corr} = corrosion current density ($\mu\mathrm{A/cm^2}$); EW = equivalent weight of the corroding species, (g); d = density of the corroding species, ($\mathrm{g/cm^3}$).

Corrosion rate calculations are illustrated for tin corrosion ($d = 7.3\ \mathrm{g/cm^3}$) in a corrosive solution with the linear polarization resistance, R_{p}, of $2\ \mathrm{mV/(\mu A/cm^2)}$ and $b_{\mathrm{a}} = b_{\mathrm{c}} = \pm 0.1\ \mathrm{V}$.

$$I_{\mathrm{corr}} = \frac{b_{\mathrm{a}} \times b_{\mathrm{c}}}{2.3(b_{\mathrm{a}} + b_{\mathrm{c}})} \times \frac{1}{R_{\mathrm{p}}};\quad R_{\mathrm{p}} = \frac{\Delta E}{\Delta i}$$

$$I_{\mathrm{corr}} = \frac{b_{\mathrm{a}} \times b_{\mathrm{c}}}{2.3(b_{\mathrm{a}} + b_{\mathrm{c}})} \times \frac{\Delta i}{\Delta E} = \frac{0.1\,\mathrm{V} \times 0.1\,\mathrm{V}}{2.3(0.1 + 0.1)\,\mathrm{V}} \times \frac{1\,\mu\mathrm{A/cm^2}}{2\,\mathrm{mV}}$$

$$I_{\mathrm{corr}} = \frac{(0.01\,\mathrm{V})^2}{0.46\,\mathrm{V}} \times \frac{1\,\mu\mathrm{A/cm^2}}{2\,\mathrm{mV}} \times \frac{1000\,\mathrm{mV}}{1\,\mathrm{V}} = 10.87\,\mu\mathrm{A/cm^2}$$

$$\mathrm{CR} = \frac{0.13 \times I_{\mathrm{corr}} \times \mathrm{EW}}{d} = \frac{0.131[10.87\,\mu\mathrm{A/cm^2}]\left[\dfrac{118.710\,\mathrm{g/mol}}{2}\right]}{7.3\,\mathrm{g/m^3}} = 11.57\,\mathrm{mpy}$$

Tafel extrapolation provides direct corrosion rate and potential measurements. This technique is very useful for predicting corrosion properties of various systems. It measures extremely low corrosion rates with accuracy equal to weight loss methods. The rapid determination of corrosion rates with Tafel plots can be advantageous for inhibitor evaluation and alloy comparison. The disadvantage is the large potential ranges associated with the cathodic and anodic Tafel plots that result in changing surface properties of the corroding metal. A new specimen is always required to complete the polarization studies. The corrosion measurements are performed by a potentiostat connected with the electrochemical cell. The metal specimen (working electrode) is polarized 150–300 mV in the positive and negative directions from the open circuit potential. The voltage step is

between 5 and 10 mV. Potentiostat and corrosion measurement software packages are available from electrochemical equipment manufacturers.

The open circuit potential as a function of time is a qualitative method that evaluates sacrificial coating stability. The sacrificial metal removal rate in the corroding solution is controlled by the potential difference of the underlying metal and the sacrificial coating, corroding solution, and sacrificial coating thickness. The open circuit potential changes to the protected metal when the sacrificial metal is completely removed.

EIS is the response of corrosion systems to "ac" excitations. It has been used in corrosion research to estimate corrosion rates or study the metal passivation, corrosion protection using inhibitors, sacrificial barrier properties, and polymer coating performance on metals. EIS only estimates polarization resistance. As with linear polarization, the corrosion current is calculated using the Stern-Geary equation for known values of the anodic and cathodic Tafel slopes.

REFERENCES

[1] E.D. Verink, Economics of corrosion, in: R.W. Revie (Ed.), Uhlig's Corrosion Handbook, John Wiley & Sons, New York, 2011, pp. 11–25.
[2] K.B. Veronika, Knowledge about metals in the first century, Korroz. Figy. 48 (2008) 133–137.
[3] M.G. Fontana, Corrosion Engineering, third ed., McGraw-Hill, New York, 1986.
[4] N. Sato, An overview on the passivity of metals, Corros. Sci. 31 (1990) 1–19.
[5] J.S. Leach, B.R. Parson, Crystallization in anodic oxide films, Corros. Sci. 28 (1988) 43–56.
[6] F.P. Fehlner, N.F. Mott, Low-temperature oxidation, Oxid. Met. 2 (1970) 59–99.
[7] T.L. Barr, An ESCA study of the termination of the passivation of elemental metals, J. Phys. Chem. 82 (1978) 1801–1810.
[8] H. Uhlig, The adsorption theory of passivity and the flade potential, Z. Elektrochem. 62 (1958) 626–632.
[9] U.R. Evans, Some factors in anodic processes on corroding metal, J. Electrochem. Soc. 99 (1927) 212–218.
[10] P. Roberge, Handbook of Corrosion Engineering, McGraw-Hill, New York, 2000.
[11] H.H. Uhlig, R.W. Revie, Corrosion and Corrosion Control, third ed., John Wiley & Sons, New York, 2008.
[12] C. Dilon, Forms of Corrosion: Recognition and Prevention, NACE International, Houston, TX, 1982.
[13] B. Isecke, M. Schutze, H.H. Strehblow, Corrosion, in: H. Czichos, T. Saito, L. Smith (Eds.), Springer Handbook of Metrology and Testing, Springer, Berlin, 2011, pp. 667–741.
[14] C. Leygraf, T. Graedel, Atmospheric Corrosion, John Wiley & Sons, New York, 2000.
[15] J. Weissenrieder, C. Kleber, M. Schreiner, C. Leygraf, In situ studies of sulfate nest formation on iron, J. Electrochem. Soc. 151 (2004) B497–B504.
[16] T.E. Graedel, R.P. Frankenthal, Corrosion mechanisms for iron and low alloy steels exposed to the atmosphere, J. Electrochem. Soc. 137 (1990) 2385–2393.
[17] D.T. Hai, Current status of existing railway bridges in Vietnam: an overview of steel deficiencies, J. Constr. Steel Res. 62 (2006) 987–994.
[18] K.B. Deshpande, Experimental investigation of galvanic corrosion: comparison between SVET and immersion techniques, Corros. Sci. 52 (2010) 2819–2826.
[19] E. Tada, K. Sugawara, H. Kaneko, Distribution of pH during galvanic corrosion of a Zn/steel couple, Electrochim. Acta 49 (2003) 1019–1026.
[20] R.M. Souto, Y. Gonzalez-Garcia, A.C. Bastos, A.M. Simoes, Investigating corrosion processes in the micrometric range: a SVET study of the galvanic corrosion of zinc coupled with iron, Corros. Sci. 49 (2007) 4568–4580.

[21] X.G. Zhang, Galvanic corrosion, in: R.W. Revie (Ed.), Uhlig's Corrosion Handbook, John Wiley & Sons, New York, 2000, pp. 137–164.
[22] http://ravelingroup.com/wordpress1/tag/colt-gold-cup/.
[23] G.T. Burstein, C. Liu, R.M. Souto, S.P. Vines, Origin of pitting corrosion, Corros. Eng. Sci. Technol. 39 (2004) 25–30.
[24] M.G. Fontana, N.D. Greene, Corrosion Engineering, McGraw Hill, New York, 1967.
[25] P.S. Pistorius, G.T. Burstein, Growth of corrosion pits on stainless steel in chloride solution containing dilute sulfate, Corros. Sci. 33 (1992) 1885–1897.
[26] G.S. Frankel, Pitting corrosion of metals: a review of critical factors, J. Electrochem. Soc. 145 (1998) 2186–2198.
[27] S. Caines, F. Khan, J. Shirokoff, Analysis of pitting corrosion on steel under insulation in marine environments, J. Loss Prev. Process Ind. 26 (2013) 1466–1483.
[28] D.A. Lytle, M.N. Nadagouda, A comprehensive investigation of copper pitting corrosion in a drinking water distribution system, Corros. Sci. 52 (2010) 1927–1938.
[29] B.E. Wild, Chloride ion adsorption and pit initiation on stainless steels in neutral media, in: R. W. Staehle, H. Okada (Eds.), Passivity and its Breakdown in Iron Based Alloys, NACE, Houston, 1976, pp. 129–130.
[30] B. Baroux, Further insights on the pitting corrosion of stainless steels, in: P. Marcus (Ed.), Corrosion Mechanism in Theory and Practice, second ed., Marcel Dekker, New York, 2004.
[31] J. Horvath, H.H. Uhlig, Critical potentials for pitting corrosion of nickel, chromium-nickel, chromium-iron, and related stainless steels, J. Electrochem. Soc. 115 (1968) 791–795.
[32] Z. Szklarska-Smialovska, Pitting Corrosion of Metals, NACE, Houston, Texas, 1986.
[33] H. Ogawa, H. Omata, I. Itoh, H. Okada, Auger electron spectroscopic and electrochemical analysis of the effect of alloying elements on the passivation behavior of stainless steels, Corrosion 34 (1978) 52–60.
[34] K. Hashimoto, K. Asami, K. Teramoto, An X-ray photo-electron spectroscopic study on the role of molybdenum in increasing the corrosion resistance of ferritic stainless steels in HCl, Corros. Sci. 19 (1979) 3–14.
[35] M. Wang, H.W. Pickering, Y. Xu, Potential distribution, shape evolution, and modeling of pit growth for Ni in sulfuric acid, J. Electrochem. Soc. 142 (1995) 2986–2995.
[36] M.I. Abdulsalam, H.W. Pickering, Effect of the applied potential on the potential and current distributions within crevices in pure nickel, Corros. Sci. 41 (1999) 351–372.
[37] P. Jakupi, J.J. Noel, D.W. Shoesmith, The evolution of crevice corrosion damage on the Ni-Cr-Mo-W alloy-22 determined by confocal laser scanning microscopy, Corros. Sci. 54 (2012) 260–269.
[38] K. Honda, H. Nomura, Electric potential distribution measurement of under-film corrosion by scanning Kelvin probe, J. Corros. Sci. Eng. 2 (1999) Extended Abstract No. 17. http://www.jcse.org/volume2/extabs/ea17.php.
[39] W.H. Slabaugh, M. Grother, Mechanism of filiform corrosion, Ind. Eng. Chem. 46 (1954) 1014–1016.
[40] http://www.metallurgicalviability.com/SCC.htm.
[41] J. Sedriks, Stress corrosion cracking test methods, NACE, Houston, 1990.
[42] A. Turnbull, Test methods for environment assisted cracking, Br. Corros. J. 27 (1992) 271–289.
[43] http://www.rcrd.manchester.ac.uk/materials/a-sem-image-stainless-steel-wire-intergranular-stress-corrosion/.
[44] W. Huijbregts, T. Beijers, R. Leferink, A. Zeijseijnk, J. Peters, P. Verbeek, R. Bilsen, Stress corrosion cracking in district heating pipes, Euroheat & Power/Fernwårme Intern. (2001) 52–58.
[45] R.C. Newman, A theory of secondary alloying effects on corrosion and stress-corrosion cracking, Corros. Sci. 33 (1992) 1653–1657.
[46] S. Hirosawa, Y. Oguri, T. Sato, Experimental and computational investigation of formation of precipitate free zones in an Al-Cu alloy, Mater. Trans. 46 (2005) 1230–1234.
[47] L. Tan, T.R. Allen, Effect of thermomechanical treatment on the corrosion of AA5083, Corros. Sci. 52 (2010) 548–554.
[48] J. Hochmann, A. Desestret, P. Jolly, R. Mayoud, Properties of high-chromium ferritic stainless steels and austeno-ferritic stainless steels, in: R.W. Staehle, J. Hochmann, R.D. McCright, J.E. Slater (Eds.),

Stress Corrosion Cracking and Hydrogen Embrittlement of Iron-Base Alloys, NACE, Houston, 1977, pp. 956–1002 NACE-5.
[49] A. Bhattacharya, Stress corrosion cracking of duplex stainless steels in caustic solutions (Ph.D. thesis), Georgia Institute of Technology, Atlanta, GA, 2008, pp. 1–3.
[50] D.H. Lee, J.H. Han, K.M. Kim, J.S. Kim, U.C. Lee, Effect of cold work on primary water stress corrosion cracking of Inconel Alloy 600 nuclear power steam generator tube material, Han'guk Chaelyo Hakhoechi 8 (1998) 726–732.
[51] http://www.gewater.com/handbook/boiler_water_systems/fig14-10.jsp.
[52] http://www.quali-tech-inc.com/HydrogenE.html.
[53] S.A. Barter, L. Molent, Fatigue cracking from a corrosion pit in an aircraft bulkhead, Eng. Fail Anal. 39 (2014) 155–163.
[54] http://www.corrosionlab.com/Failure-Analysis-Studies/30038.corrosion-fatigue-cu-tube.htm.
[55] M. Stern, A.L. Geary, Electrochemical polarization: I. A theoretical analysis of the shape of polarization curves, J. Electrochem. Soc. 104 (1957) 56–63.

CHAPTER 2

Thermodynamics in the Electrochemical Reactions of Corrosion

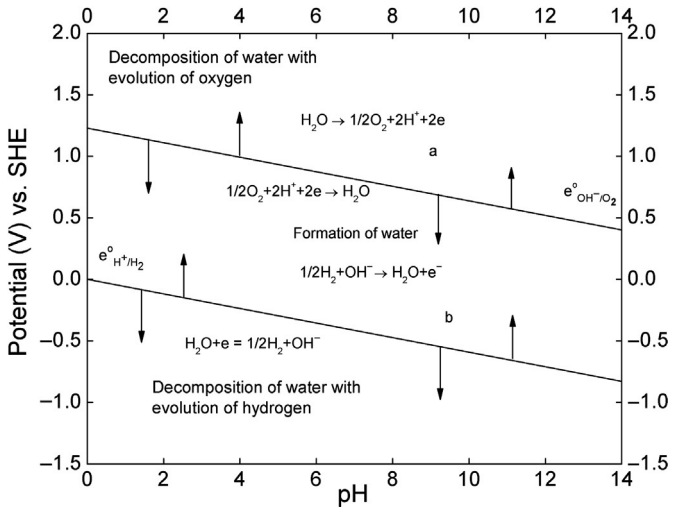

Chapter Contents

Corrosion Engineering
http://dx.doi.org/10.1016/B978-0-444-62722-3.00002-1

2.1 INTRODUCTION

Corrosion is spontaneous dissolution or destruction of metals due to electrochemical, chemical, or biochemical interactions with aqueous or organic environments. Corrosive environments include moisture, oxygen, inorganic and organic acids, pressure, temperature, and the presence of chlorides. The simplest and most common example of corrosion is the oxide (rust) formation on reinforcing steel rebars in structural concrete. Corrosion is a nonequilibrium electrode process occurring under open circuit conditions without the application of an external current. During the corrosion process, metals tend to convert to more thermodynamically stable compounds such as oxides, hydroxides, salts, or carbonates.

2.2 ELECTROCHEMICAL CORROSION

The electrochemical corrosion process consists of two partial electrochemical reactions: the anodic partial reaction, consisting of oxidation/dissolution of the metal, and the cathodic partial reaction, consisting of the reduction of water, hydrogen, or oxygen gas. The energy change of the partial corrosion reactions provides a driving force for the process and controls its direction. Electrochemical corrosion reactions have different thermodynamic and kinetic properties than chemical reactions. For example, if a redox reaction proceeds as a chemical reaction, it is necessary for the reacting particles to come into contact with each other so that electrons can be transferred from one reactant to the other. Thermodynamically, the reaction is controlled by the ratio of the internal energy of the reactants to their activation energy. The collisions of the particles are not limited in

the reaction space and may occur in any direction. As a consequence, the electrons also move in any direction in the reaction space. The only requirement is that the path of the charge transfer must be very small. With an electrochemical reaction, the activation energy of corrosion reactions and their kinetic properties depend not only on activity, chemical potential, and temperature, but also on the electrocatalytic properties of the materials.

The thermodynamics of corrosion processes provides a tool to determine the theoretical tendency of metals to corrode. Thus, the role of corrosion thermodynamics is to determine the conditions under which the corrosion occurs and how to prevent corrosion at the metal/environment interface. Thermodynamics, however, cannot be used to predict the rate at which the corrosion reaction will proceed [1–6]. The corrosion rate must be estimated by Faraday's law and is controlled by the kinetics of the electrochemical reaction.

Depending on the nature of the metal, the oxidation reaction may occur uniformly (as in carbon steel) or may be localized (as in hard alloys such as Inconel or Monel). In localized corrosion (pitting), the corrosion proceeds through the formation of narrow cracks after penetrating the grains of the metal. Corrosion occurs along the grain boundaries of the metal, known as intercrystalline corrosion. Besides the hydrogen evolution reaction, there are other cathodic depolarization reactions such as:

$$\text{Oxygen reduction in alkaline or neutral solutions}: O_2 + 2H_2O + 4e^- \rightarrow 4OH^- \quad (2.1)$$

$$\text{Oxygen reduction in acidic solutions}: O_2 + 4H^+ + 4e^- \rightarrow 2H_2O \quad (2.2)$$

$$\text{Metal deposition in galvanic corrosion}: M^+ + e^- \rightarrow M \quad (2.3)$$

$$\text{Reduction of metal ions}: M^{3+} + e^- \rightarrow M^{2+} \quad (2.4)$$

The overall anodic reaction for the corrosion of iron in neutral or alkaline solutions is described as:

$$2Fe + 2H_2O + O_2 \rightarrow 2Fe^{2+} + 4OH^- \rightarrow 2Fe(OH)_2 \quad (2.5)$$

Ferrous hydroxide produced in Eq. (2.5) is oxidized to ferric salts according to:

$$Fe(OH)_2 + H_2O \rightarrow Fe(OH)_3 + H^+ + e^- \quad (2.6)$$

Corrosion reactions also occur as a replacement reaction:

$$Ni^{2+} + Fe \rightarrow Fe^{2+} + Ni \quad (2.7)$$

Electrochemical corrosion may occur in aqueous electrolytes, gas atmosphere in the presence of moisture on the metal surface (atmospheric corrosion), or as soil corrosion (Fig. 2.1). Corrosive failure may also occur due to electrocorrosion, which is caused by an external electric current.

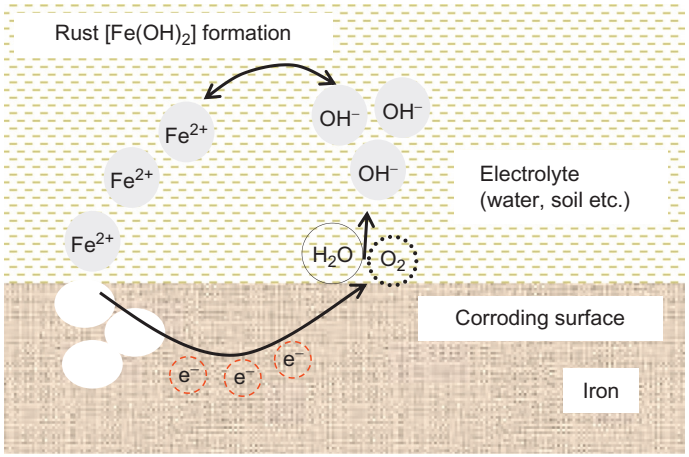

Fig. 2.1 Corrosion cell formed as a result of rusting of iron.

Corrosion is initiated by electrochemical reactions in:

1. *Technical metals that contain impurities of other metals*: Examples are technical metals such as zinc and tin, which contain silver or iron as impurities. The standard electrode potentials of silver and iron are more electropositive than those of zinc or tin, causing zinc and tin to corrode through a form of galvanic corrosion, while the impurities remain intact. Because of their more positive electrode potentials, silver and iron are cathodically protected by zinc or tin.
2. *Identical metals in contact with solutions of different concentrations*: The metal dissolves from the electrode immersed in a dilute solution, and is deposited on the electrode that is immersed in a more concentrated solution. The corrosion stops when the electrolyte concentration is homogeneous at the interfaces of both of electrodes. The other type of electrochemical concentration cell is known as a *differential aeration cell*. The electrode potential difference in this case results from different oxygen aeration of the electrodes. This type of corrosion initiates crevice corrosion in aluminum or stainless steel when exposed to a chloride environment.
3. *Identical metals each exposed to a different temperature*: The driving force for this type of corrosion results from each electrode having a different temperature when they are immersed in a homogeneous electrolyte. The metal exposed to the higher temperature acts as a cathode. When this metal is in electrical contact with a metal exposed to the lower temperature (anode), the metal dissolves from the lower-temperature electrode (anode) and is deposited on the higher-temperature electrode (cathode).

2.3 THERMODYNAMICS OF CORROSION PROCESSES

The energy change of the partial corrosion reactions provides the driving force for the overall reaction and controls its spontaneous direction. Corrosion thermodynamics

establishes the quantitative relationship between the electrical energy produced or consumed during the corrosion processes and the chemical energy. The corrosion of iron in an acid environment occurs according to the following reaction:

$$\mathrm{Fe} + 2\mathrm{HCl} \overset{\pm ne}{\rightleftarrows} \mathrm{FeCl_2} + \mathrm{H_2} \tag{2.8}$$

The dissolution of iron in an acidic solution releases hydrogen without the formation of any oxide barrier films on the surface. The reaction shown in Eq. (2.8) may be separated into two partial reactions:

$$\mathrm{Fe} \rightarrow \mathrm{Fe}^{2+} + 2\mathrm{e}^- \,(\text{anodic partial reaction}) \tag{2.9a}$$

$$2\mathrm{H}^+ + 2\mathrm{e}^- \rightarrow \mathrm{H_2} \,(\text{cathodic partial reaction}) \tag{2.9b}$$

In Eq. (2.9a), the iron atoms are transformed into iron ions while the electrons produced are consumed during the reduction of hydrogen ions to hydrogen gas.

In Eq. (2.8), "n" represents the number of elementary charges, $e = 4.803 \times 10^{-10}$ (1.602×10^{-19} coulombs) or electrostatic units exchanged during the anodic and cathodic charge transfer reactions. According to sign convention, the stoichiometric numbers are positive for the products and negative for the reactants. For the corrosion reaction presented in Eq. (2.8), the changes in the number of moles of the species in the reaction are proportional to their stoichiometric numbers.

The quantity of electricity produced as a result of the chemical reaction is equal to the product of nFE, where E is the electromotive force measured in the case of reversible reactions. The quantity F is the Faraday constant, which can be estimated from the product, $F = N_\mathrm{A}\mathrm{e}$ where $N_\mathrm{A} = 6.02 \times 10^{23}$ (Avogadro's number) and "e" is the elementary charge. The absolute value of the Faraday constant equals 96,485 C (coulomb).

For any isothermal process, the reaction described in Eq. (2.8), when performed at constant pressure, decreases the Gibbs free-energy (G). Assuming that the corrosion process proceeds at constant pressure, the change of Gibbs free-energy is the focal point for any thermodynamic analysis of corrosion reactions. The change in the Gibbs free-energy represents the maximum useful work for an isothermal and isobaric conversion for the reaction in Eq. (2.8).

$$G = H + TS \tag{2.10}$$

According to the second law of thermodynamics, Eq. (2.10) can be expressed as the difference between two equilibrium states:

$$\mathrm{d}G = -S\mathrm{d}T + V\mathrm{d}P, G = f(T, P) \tag{2.11}$$

Fundamental thermodynamic aspects are discussed in detail in [7,8]. According to convention, the dG is a negative quantity for the spontaneous direction of any reaction. When the Gibbs free-energy reaches its minimum, the dG is equal to zero. In this state,

the system is in equilibrium where the rate of the reaction in the forward direction is the same as that in the reverse. Besides the fact that the corrosion process is irreversible in nature, the equilibrium conditions are used to derive all thermodynamic and kinetic expressions.

The system can be subjected to both mechanical work (PV) and electrical work (W). Thus, the Gibbs free-energy in Eq. (2.11) can be expressed as:

$$dG = -SdT + VdP - dW \tag{2.12}$$

According to convention, the negative sign for the electrical work, dW, in Eq. (2.12) means that work is done by the system. For processes occurring at constant pressure and temperature, Eq. (2.12) can be expressed as:

$$-dG_{T,P} = dW \tag{2.13}$$

The decrease in Gibbs free-energy in Eq. (2.13) is equal to the electrical work W. Because the electrical work is expressed as:

$$W = nFE \tag{2.14}$$

$$dW = nFdE \tag{2.15}$$

and

$$dG_{T,P} = -nFdE \tag{2.16}$$

Electrical work is the product of charge multiplied by the electromotive force (emf) potential (E) of the cell. If the work done results from an electrochemical reaction with cell potential, E, and if the charge is defined for one mole of reaction in which "n" moles of electrons are transferred, then the electrical work ($-W$) done by the cell is equal to nFE. The Faraday constant F (96,485 C/mole) in Eq. (2.16) is necessary to convert moles of electrons to coulombs.

During the corrosion process, the concentration of the oxidizing and reducing species change, so the thermodynamic properties of the system must depend on the composition as well as on temperature and pressure. The Gibbs free-energy, nG, is a function of the number of moles of the reduced and oxidized species participating in the corrosion reaction through the following equation:

$$d(nG) = (nV)dP - (nS)dT + \sum_i \left[\frac{\delta(nG)}{\delta n_i}\right]_{P,T\,n_j} dn_i \tag{2.17}$$

The derivative of nG in Eq. (2.17) with respect to the number of the moles of the oxidized and reduced species participating in the corrosion reaction is defined as the chemical potential μ_i.

$$\mu_i = \left[\frac{\delta(nG)}{\delta n_i}\right]_{P,T\,n_j} \tag{2.18}$$

The general equation for d(nG) expressed in terms of the chemical potential μ_i is:

$$\mathrm{d}(nG) = (nV)\mathrm{d}P - (nS)\mathrm{d}T + \sum_i \mu_i \mathrm{d}n_i \tag{2.19}$$

Equation (2.19) is used as a foundation to build the structure of corrosion solution thermodynamics. For one mole, $n = 1$ of participating reacting species, it can be written in the form in which n_i is replaced by a mole fraction x_i:

$$\mathrm{d}G = V\mathrm{d}P - S\mathrm{d}T + \sum_i \mu_i \mathrm{d}x_i \tag{2.20}$$

At constant temperature and pressure, Eq. (2.19) becomes:

$$\mathrm{d}(nG)_{T,P} = \sum \left(\frac{\delta nG}{\delta n_i}\right)_{P,T,n_j} \mathrm{d}n_i = \sum \mu_i \mathrm{d}n_i \tag{2.21}$$

After integration

$$G_{T,P} = \sum \mu_i n_i \tag{2.22}$$

Equations (2.16) and (2.21) can be written for electrochemical process as:

$$\Delta G_{T,P} = -nF\mathrm{d}E = \sum \mu_i \mathrm{d}n_i \quad \text{or} \quad nFE = -\sum \mu_i n_i \tag{2.23}$$

2.4 EQUILIBRIUM ELECTRODE POTENTIALS

At standard states, all reactants and products in any electrochemical process are at unit activity. Departure from unit activity can be determined using the Nernst equation, which is derived by assuming that the reaction proceeds isothermally and reversibly in a corrosion system [2,9–11].

$$[\nu_\mathrm{A}]\mathrm{A} + [\nu_\mathrm{B}]\mathrm{B} + \cdots \overset{\pm nF}{\leftrightarrow} [\nu_\mathrm{C}]\mathrm{C} + [\nu_\mathrm{D}]\mathrm{D} + \cdots \pm \mathrm{Q} \tag{2.24}$$

According to Eq. (2.16), the reversible potential of the corrosion system $E_{T,P}$ is defined as:

$$E_{T,P} = -\frac{\Delta G_{T,P}}{nF} \tag{2.25}$$

The general equation for d(nG) is expressed in terms of the chemical potential μ_i by Eq. (2.19). Each dn_i in Eq. (2.19) may be replaced by the product $\nu_i a\varepsilon$, where "a" represents the activity of the reactants, ε is the reaction coordinate and characterizes the extent of the corrosion reaction. In the above equation, "ν_i" is the stoichiometric number

for the species with a chemical potential μ_i. Thus, at constant pressure and temperature and unit activity, Eq. (2.19) becomes:

$$\mathrm{d}(nG) = \sum_i \mu_i \mathrm{d}v_i \mathrm{d}\varepsilon \tag{2.26}$$

Because nG is a state function, the right-hand side of the Eq. (2.19) represents an exact differential expression, it follows that:

$$\sum \mu v_i = \left[\frac{\delta(G)}{\delta\varepsilon}\right]_{T,P} \tag{2.27}$$

In fact, the quantity $\sum \mu v_i$ represents the rate of the change of the total Gibbs free-energy for the corrosion (electrochemical) process, with the extent of the reaction ε at constant T and P. This quantity is zero at the equilibrium state. Thus, according to Eq. (2.22),

$$\Delta G = \sum \mu_i v_i. \tag{2.28}$$

Because the chemical potential is a partial property of the Gibbs free-energy, its value can be calculated from the equation:

$$\mu_i = \mu_i^{\circ} + RT \ln(a_i) \tag{2.29}$$

where μ_i^o is the standard chemical potential, and a_i is the activity of the species in the corrosion reaction. Instead of Eq. (2.28), one may write:

$$\Delta G = \sum \mu_i^{\circ} v_i + RT \sum v_i \ln a_i \tag{2.30}$$

or

$$\Delta G = \sum \mu_i^{\circ} v_i + RT \ln \frac{a_{\mathrm{C}}^{v_{\mathrm{C}}} a_{\mathrm{D}}^{v_{\mathrm{D}}}}{a_{\mathrm{A}}^{v_{\mathrm{A}}} a_{\mathrm{B}}^{v_{\mathrm{B}}}} \tag{2.31}$$

Assuming that the reactants and the products are in their standard states, the activities of the species participating in the reaction are equal to unity. Under these conditions, the Gibbs free-energy ΔG is equal to the standard Gibbs free-energy ΔG° and the absolute value is equal to the natural logarithm of the equilibrium constant K.

$$\Delta G = \Delta G^{\circ} = \sum \mu_i^{\circ} x_i = RT \ln K \tag{2.32}$$

Because ΔG_i° is a property of pure species "i" in their standard state and at constant pressure, its value depends only on the temperature. In fact, ΔG° represents the quantity $\sum v_i G_i^{\circ}$. Therefore, this function is the difference between the Gibbs free-energies of the products and reactants and depends on their stoichiometric coefficients. It is independent of the equilibrium composition or pressure and it is fixed for any given corrosion reaction once the temperature is established. The Gibbs free-energy change is defined according to Eqs. (2.29) and (2.31) as:

$$\Delta G = RT \ln K + RT \ln \prod a_i^{v_i} \tag{2.33}$$

where Π signifies the product over all species. From Eqs. (2.24) and (2.31), it follows that:

$$E_{\text{cell}} = -\frac{RT}{nF}\ln K - \frac{RT}{nF}\ln\frac{a_{\text{C}}^{\nu_{\text{C}}} a_{\text{D}}^{\nu_{\text{D}}}\cdots}{a_{\text{A}}^{\nu_{\text{A}}} a_{\text{B}}^{\nu_{\text{B}}}\cdots} \tag{2.34}$$

The logarithmic expression in the second term on the right side of Eq. (2.32), when $a_i = 1$, is equal to zero, and:

$$E^{\text{o}} = -\frac{RT}{nF}\ln K \tag{2.35}$$

The potential in Eq. (2.35) is defined as E^{o} and is called the *standard electromotive force* of a corrosion system. According to Eq. (2.34), for any equilibrium electrochemical system, the (emf) E is the sum of the standard electromotive force, E^{o}, and the activities of the products and the reactants participating in the reaction:

$$E_{\text{cell}} = E^{\text{o}} - \frac{RT}{nF}\ln\frac{a_{\text{C}}^{\nu_{\text{C}}} a_{\text{D}}^{\nu_{\text{D}}}\cdots}{a_{\text{A}}^{\nu_{\text{A}}} a_{\text{B}}^{\nu_{\text{B}}}\cdots} \tag{2.36}$$

which is equivalent to:

$$E_{\text{cell}} = E^{\text{o}} - 2.303\frac{RT}{nF}\log\frac{a_{\text{C}}^{\nu_{\text{C}}} a_{\text{D}}^{\nu_{\text{D}}}}{a_{\text{A}}^{\nu_{\text{A}}} a_{\text{B}}^{\nu_{\text{B}}}} \tag{2.37}$$

or

$$E_{\text{cell}} = E^{\text{o}} + 2.303\frac{RT}{nF}\log\frac{a_{\text{A}}^{\nu_{\text{A}}} a_{\text{B}}^{\nu_{\text{B}}}}{a_{\text{C}}^{\nu_{\text{C}}} a_{\text{D}}^{\nu_{\text{D}}}} \tag{2.38}$$

Equations (2.37) and (2.38) are well known forms of the Nernst equation. The values of $b^{\text{o}} = 2.303\frac{RT}{F}$ in Eq. (2.36) are linear functions of T, and are presented in Table 2.1. The value of b^{o} at room temperature is 0.059 V.

2.5 ELECTROCHEMICAL HALF-CELLS AND ELECTRODE POTENTIALS

The overall charge transfer of any corrosion reaction must be the sum of two electrode potentials that are established in the half-cells. Each potential results from the change of the

Table 2.1 Values of the Factor $b^{\circ} = 2.303RT/F$ for Different Temperatures

T °C	b°	T °C	b°
−40	0.046	+25	0.059
0	0.054	+30	0.060
+5	0.055	+40	0.062
+10	0.055	+60	0.066
+15	0.057	+100	0.074

chemical energy of the respective electrode reaction occurring in the half-cell [1,2,6–11]. Thus, the value of the emf, E, for any electrochemical system at equilibrium is:

$$E = e_1 + e_2 \tag{2.39}$$

where, e_1 and e_2 are the electrode potentials of the half-cell reactions. Equation (2.24) can be now rewritten by using the half-cells of the overall corrosion reaction as follows:

$$\nu_A A + \cdots \overset{\pm nF}{\leftrightarrow} \nu_C C \tag{2.40}$$

and

$$\nu_B B + \cdots \overset{\pm nF}{\leftrightarrow} \nu_D D \tag{2.41}$$

The Nernst equation defines the single electrode (half-cell) potentials in Eqs. (2.40) and (2.41). These are defined by the Nernst equation as:

$$e_1 = e_1^o + 2.303\frac{RT}{nF}\log\frac{a_A^{\nu_A}}{a_C^{\nu_C}} \tag{2.42}$$

$$e_2 = e_2^o + 2.303\frac{RT}{nF}\log\frac{a_B^{\nu_B}}{a_D^{\nu_D}} \tag{2.43}$$

where e_1^o and e_2^o are standard electrode potentials of the half-cell reactions shown in Eqs. (2.40) and (2.41). The sum of the standard electrode potentials equals the standard electromotive force of the corrosion system:

$$E^o = e_1^o + e_2^o \tag{2.44}$$

The emf of any corrosion system is the sum of the standard emf and the activities of the half-cells of the overall corrosion reaction, Eqs. (2.42) and (2.43).

$$-\frac{\Delta G}{nF} = E_{cell} = e_1^o + 2.303\frac{RT}{nF}\log\frac{a_A^{\nu_A}}{a_C^{\nu_C}} + e_2^o + 2.303\frac{RT}{nF}\log\frac{a_B^{\nu_B}}{a_D^{\nu_D}} \tag{2.45}$$

Or

$$E = E^o + 2.303\frac{RT}{nF}\log\frac{a_A^{\nu_A}a_B^{\nu_B}}{a_C^{\nu_C}a_D^{\nu_D}} \tag{2.38}$$

2.6 ELECTROMOTIVE FORCE SERIES

The emf series of the standard half-cell electrode potential on the hydrogen scale are given in Table 2.2. The reactions in this table are written as reduction reactions from left to right at $T = 25\ ^\circ C$. They have the same polarity as the reduction potential, which is measured experimentally.

From Eq. (2.38), it is not possible to distinguish which of the participants in the reaction are the reactants (oxidized species) and which are the products (reduced species).

Table 2.2 Standard Electrode Potentials at 25 °C and Their Isothermal Temperature Coefficients [12]

	Electrode Reaction	e° (*V* vs. SHE)	$\left(\frac{dE^\circ}{dT}\right) \times 10^3 \left(\frac{V}{^\circ C}\right)$
$Li^+ \mid Li$	$Li^+ + e^- = Li$	−3.045	−0.534
$Rb^+ \mid Rb$	$Rb^+ + e^- = Rb$	−2.925	−1.245
$Cs^+ \mid Cs$	$Cs^+ + e^- = Cs$	−2.923	−1.197
$K^+ \mid K$	$K^+ + e^- = K$	−2.925	−1.080
$Ra^{2+} \mid Ra$	$Ra^{2+} + 2e^- = Ra$	−2.916	−0.59
$Ba^{2+} \mid Ba$	$Ba^{2+} + 2e^- = Ba$	−2.906	−0.395
$Ca^{2+} \mid Ca$	$Ca^{2+} + 2e^- = Ca$	−2.866	−0.175
$Na^+ \mid Na$	$Na^+ + e^- = Na$	−2.714	−0.772
$La^{3+} \mid La$	$La^{3+} + 3e^- = La$	−2.522	+0.085
$Mg^{2+} \mid Mg$	$Mg^{2+} + 2e^- = Mg$	−2.363	+0.103
$Be^{2+} \mid Be$	$Be^{2+} + 2e^- = Be$	−1.847	+0.565
$Al^{3+} \mid Al$	$Al^{3+} + 3e^- = Al$	−1.662	+0.504
$Ti^{2+} \mid Ti$	$Ti^{2+} + 2e^- = Ti$	−1.628	-
$Zr^{4+} \mid Zr$	$Zr^{4+} + 4e^- = Zr$	−1.529	-
$V^{2+} \mid V$	$V^{2+} + 2e^- = V$	−1.186	-
$Mn^{2+} \mid Mn$	$Mn^{2+} + 2e^- = Mn$	−1.180	−0.08
$Zn^{2+} \mid Zn$	$Zn^{2+} + 2e^- = Zn$	−0.762	+0.09
$Cr^{3+} \mid Cr$	$Cr^{3+} + 3e^- = Cr$	−0.744	+0.468
$SbO_2^- \mid Sb$	$SbO_2^- + 2H_2O + 3e^- = Sb + 4OH^-$	−0.670	-
$Ga^{3+} \mid Ga$	$Ga^{3+} + 3e^- = Ga$	−0.529	+0.67
$S^{2-} \mid S$	$S + 2e^- = S^{2-}$	−0.510	-
$Fe^{2+} \mid Fe$	$Fe^{2+} + 2e^- = Fe$	−0.440	+0.052
$Cr^{3+}, Cr^{2+} \mid Pt$	$Cr^{3+} + e^- = Cr^{2+}$	−0.408	-
$Cd^{2+} \mid Cd$	$Cd^{2+} + 2e^- = Cd$	−0.402	−0.093
$Ti^{3+}, Ti^{2+} \mid Pt$	$Ti^{3+} + e^- = Ti^{2+}$	−0.369	-
$Tl^+ \mid Tl$	$Tl^+ + e^- = Tl$	−0.336	−1.327
$Co^{2+} \mid Co$	$Co^{2+} + 2e^- = Co$	−0.277	+0.06
$Ni^{2+} \mid Ni$	$Ni^{2+} + 2e^- = Ni$	−0.250	+0.06
$Mo^{3+} \mid Mo$	$Mo^{3+} + 3e^- = Mo$	−0.20	-
$Sn^{2+} \mid Sn$	$Sn^{2+} + 2e^- = Sn$	−0.138	−0.282
$Pb^{2+} \mid Pb$	$Pb^{2+} + 2e^- = Pb$	−0.126	−0.451
$Ti^{4+}, Ti^{3+} \mid Pt$	$Ti^{4+} + e^- = Ti^{3+}$	−0.040	-
$H^+, H_2 \mid Pt$	$H^+ + e^- = ½\ H_2$	±0.000	±0.000 (+0.871)*
$Sn^{4+}, Sn^{2+} \mid Pt$	$Sn^{4+} + 2e^- = Sn^{2+}$	+ 0.015	-
$Cu^{2+}, Cu^+ \mid Pt$	$Cu^{2+} + e^- = Cu^+$	+ 0.153	+0.073
$Cu^{2+} \mid Cu$	$Cu^{2+} + 2e^- = Cu$	+0.337	+0.008
$Fe(CN)_6^{3-}, Fe(CN)_6^{4-} \mid Pt$	$Fe(CN)_6^{3-} + e^- = Fe(CN)_6^{4-}$	+0.360	-
$OH^-, O_2 \mid Pt$	$½\ O_2 + H_2O + 2e^- = 2OH^-$	+0.401	−0.440
$Cu^+ \mid Cu$	$Cu^+ + e^- = Cu$	+0.521	−0.058
$I^- \mid I_2, Pt$	$I_2 + 2e^- = 2I^-$	+0.535	−0.148
$MnO_4^-, MnO_4^{2-} \mid Pt$	$MnO_4^- + e^- = MnO_4^{2-}$	+0.564	-

Continued

Table 2.2 Standard Electrode Potentials at 25 °C and Their Isothermal Temperature Coefficients [12]—cont'd

Electrode Reaction		e° (*V* vs. SHE)	$\left(\frac{dE^\circ}{dT}\right) \times 10^3 \left(\frac{V}{^\circ C}\right)$
$Fe^{3+}, Fe^{2+} \mid Pt$	$Fe^{3+} + e^- = Fe^{2+}$	+0.771	+ 1.188
$Hg_2^{2+} \mid Hg$	$Hg_2^{2+} + 2e^- = 2Hg$	+0.788	-
$Ag^+ \mid Ag$	$Ag^+ + e^- = Ag$	+0.799	−1.000
$Hg^{2+} \mid Hg$	$Hg^{2+} + 2e^- = Hg$	+0.854	-
$Hg^{2+}, Hg^+ \mid Pt$	$Hg^{2+} + e^- = Hg^+$	+0.910	-
$Pd^{2+} \mid Pd$	$Pd^{2+} + 2e^- = Pd$	+0.987	-
$Br^- \mid Br_2$, Pt	$Br_2 + 2e^- = 2Br^-$	+1.065	−0.629
$Pt^{2+} \mid Pt$	$Pt^{2+} + 2e^- = Pt$	+1.200	-
$Mn^{2+}, H^+ \mid MnO_2$, Pt	$MnO_2 + 4H^+ + 2e^- = Mn^{2+} + 2H_2O$	+1.230	−0.661
$Cr^{3+}, Cr_2O_7^{2-}, H^+ \mid Pt$	$Cr_2O_7^{2-} + 14H^+ + 6e^- = 2Cr^{3+} + 7H_2O$	+1.330	−1.263
$Cl^- \mid Cl_2$, Pt	$Cl_2 + 2e^- = 2Cl^-$	+1.359	−1.260
$Pb^{2+}, H^+ \mid PbO_2$, Pt	$PbO_2 + 4H^+ + 2e^- = Pb^{2+} + 2H_2O$	+1.455	−0.238
$Au^{3+} \mid Au$	$Au^{3+} + 3e^- = Au$	+1.498	-
$MnO_4^-, H^+ \mid MnO_2$, Pt	$MnO_4^- + 4H^+ + 3e^- = MnO_2 + 2H_2O$	+1.695	−0.666
$Ce^{4+}, Ce^{3+} \mid Pt$	$Ce^{4+} + e^- = Ce^{3+}$	+1.610	-
$SO_4^{2-}, H^+ \mid PbSO_4, PbO_2$, Pb	$PbO_2 + SO_4^{2-} + 4H^+ + 2e^- = PbSO_4 + 2H_2O$	+1.682	+0.326
$Au^+ \mid Au$	$Au^+ + e^- = Au$	+1.691	-

The following rules were adopted by the International Union of Pure and Applied Chemistry (IUPAC) in Stockholm in 1953 to solve the question of the signs of electrode potential and to determine which substances should be considered as the reactants and which as products. Any electrochemical cell, according to this agreement, is written from left to right as follows: (i) the material of one of the two electrodes, (ii) the solution in contact with one electrode, (iii) the solution in contact with the second electrode, and (iv) the material of the second electrode. In the written expression, the electrodes are separated from the solutions by a single bar, while the solutions are separated by a double bar, indicating that there is no diffusion potential between the solutions in the cell.

Of the two half-cell electrode potentials, only the cell potential *E* can be measured experimentally. Therefore, it is not possible to measure the absolute values of any single half-cell electrode potential. To solve this problem, Nernst suggested that the potential of

the hydrogen electrode at a hydrogen pressure of 1 atm and at unit concentration of hydrogen ion was to serve as an arbitrary zero potential. In Table 2.2, all listed potentials are on the hydrogen scale, in which the half-cell potential of the hydrogen electrode $e^{o}_{H^+|H_2}$ is at standard state, and has been arbitrarily taken as a zero reference point in the electromotive force series. The Gibbs free-energy for the hydrogen evolution reaction is not zero.

$$2H^+ + 2e^- \rightarrow H_2 \tag{2.9b}$$

The zero value of the hydrogen reference electrode has been adopted by IUPAC as suggested by Nernst for convenience, in order for the standard hydrogen electrode (SHE) to serve as a reference potential. By using this scale, the electrode potential can be determined at all temperatures. However, the arbitrary zero will be different at different temperatures [12–14].

A half-cell potential of any redox corrosion reaction is measured when the half-cell is coupled with the SHE. An example of measuring the half-cell potential is given for an $Sn|Sn^{2+}$ electrode in Fig. 2.2. Tin metal is immersed in 1M standard solution of Sn^{2+} in hydrochloric acid and is separated through a membrane from a $H_2|H^+$ reference electrode. This connection establishes a galvanic cell that, according to IUPAC agreement, is written as:

$$Pt, H_2|HCl||Sn^{2+}|Sn \tag{2.46}$$

$$Sn + 2H^+ \rightarrow Sn^{2+} + H_2 \tag{2.47}$$

Both Sn and Sn^{2+} in the corrosion reaction are at standard state. The potential measured for the $Sn|Sn^{2+}$ electrode is 0.138 V with $Sn|Sn^{2+}$ negative vs. the hydrogen reference electrode. Because the potential of the SHE is defined as zero, the standard potential of the $Sn^{2+}|Sn$ redox system is $e^o = -0.138\,V$, as presented in Table 2.2. Electrodes shown

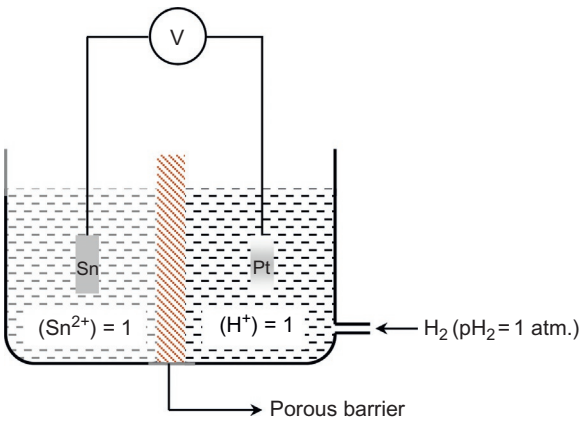

Fig. 2.2 Schematic of electrochemical cell showing the measurement of cell potential.

in Table 2.2 with a large negative e^o with respect to a standard hydrogen electrode are strongly reducing. They undergo oxidation and transfer electrons to the other half-cell reaction, where the reduction process occurs at the interface. Electrodes such as $Au|Au^{3+}$ or $Pt|Pt^{2+}$ are positive with respect to SHE. They are strongly oxidizing and capture electrons from the other half-cell.

In a spontaneous reaction between two half-cells, the half-cell with the more positive potential in Table 2.2 undergoes reduction, while the one with the more negative potential undergoes oxidation. The charge transfer changes the standard electrode potential due to the change of the composition of the electroactive species in the electrolyte. When a final ratio of the activities of the reactive species, as defined in Eq. (2.38), is equal to the equilibrium constant of the reaction, the system will be in equilibrium.

2.7 DETERMINATION OF ELECTROCHEMICAL/CORROSION REACTION DIRECTION BY GIBBS ENERGY

The energy change in the partial reactions provides the driving force and determines the direction of the spontaneous reaction. When there are no net current flows in a reversible electrochemical or corrosion cell, Eq. (2.16) is valid:

$$dG = -nFdE \tag{2.16}$$

Under standard conditions, the standard free-energy of the cell reaction ΔG^o is directly related to the standard potential difference across the cell E^o:

$$\Delta G^o = -nFE^o \tag{2.48}$$

where $\Delta G^o = \sum \nu_i G_i^o$ is the difference between the Gibbs energy of the products and the reactants of the electrochemical reaction, (weighted by their stoichiometric coefficients) or

$$\Delta G^o = \sum \Delta G_f^o(\text{products}) - \Delta G_f^o(\text{reactants}) \tag{2.49}$$

Each of the products and reactants is in its standard state as a pure substance at standard temperature and at a fixed pressure. ΔG^o is fixed for a given electrochemical reaction and it is independent of equilibrium pressure and composition once the temperature is established. The free-energy of formation of the pure elements arbitrarily is taken to be zero. The values of ΔG_{form}^o that are defined at 298 K can be corrected to the reaction temperature of interest $\Delta G_{\text{form}}^o(T)$. The equilibrium Gibbs free-energy is calculated from ΔG_{form} by using Eq. (2.31), which corrects the standard Gibbs free-energy concentrations (defined in the standard state of the pure substances at fixed pressure) with the concentrations of the products and reactants at equilibrium state (actual state of the reaction). The negative sign of the Gibbs free-energy in Eq. (2.16) follows the convention that a

positive potential, E, results in a negative free-energy change for a spontaneous electrochemical reaction. Accordingly, ΔG is calculated from ΔG^{o} data from which the potential of the reversible electrochemical cell is estimated. Conversely, the cell potential can be measured experimentally as described above; once the potential is known, ΔG is calculated using Eq. (2.16).

Example 2.1

Predict whether or not Sn will dissolve spontaneously in hydrochloric acid.

To solve the problem it is necessary to separate the corrosion reaction

$$\mathrm{Sn} + 2\mathrm{HCl} \rightarrow \mathrm{SnCl_2} + \mathrm{H_2} \quad E_{\mathrm{cell}} = 0.138\,\mathrm{V} \tag{2.50}$$

into its half-cell reactions:

$$\mathrm{Anodic}: \mathrm{Sn} \rightarrow \mathrm{Sn}^{2+} + 2\mathrm{e}^{-} \quad e^{o} = 0.138\,\mathrm{V} \tag{2.51}$$

$$\mathrm{Cathodic}: 2\mathrm{H}^{+} + 2\mathrm{e}^{-} \rightarrow \mathrm{H_2} \quad e^{o} = 0\,\mathrm{V} \tag{2.9b}$$

If reaction in Eq. (2.50) proceeds from left to right, the Gibbs free-energy change must be negative according to Eq. (2.48). To evaluate the Gibbs free-energy change, it is necessary to calculate the electrode potential, E, which is the sum of the half-cell potentials:

$$E = e_{\mathrm{a}} + e_{\mathrm{c}} \tag{2.39}$$

In order for the overall corrosion reaction in Eq. (2.50) to proceed as written, one should substitute the potential of the anodic reaction in Eq. (2.39), which as shown in Eq. (2.51) is oxidation of tin to tin oxide. According to IUPAC convention, the sign of the half-cell electrode potential must be reversed from cathodic $e^{o} = -0.138$ V in Table 2.2 to $e^{o} = +0.138$ V. The potential of the anodic reaction has the same magnitude but the opposite sign of the cathode half-cell reaction in Table 2.2. Because the potential of the SHE is set to zero, the cell potential for reaction (2.50) is:

$$E = 0.138 + 0 = 0.138\ \mathrm{V\ vs.\ SHE}$$

The calculated Gibbs free-energy using Eq. (2.48) is negative, indicating that the reaction in Eq. (2.50) proceeds spontaneously as written. Therefore, Sn will dissolve spontaneously in hydrochloric acid.

Example 2.2

Calculate the tendency for corrosion to occur in the following metal electrolyte systems: (a) silver in cupric acid and (b) nickel in silver nitrate.

(a)

$$\mathrm{Anodic}: 2\mathrm{Ag} \rightarrow 2\mathrm{Ag}^{+} + 2\mathrm{e}^{-} \quad e^{o}_{\mathrm{Ag|Ag^{+}}} = -0.799\,\mathrm{V\ vs.\ SHE}$$

$$\mathrm{Cathodic}: \mathrm{Cu}^{2+} + 2\mathrm{e}^{-} \rightarrow \mathrm{Cu} \quad e^{o}_{\mathrm{Cu^{2+}|Cu}} = 0.337\,\mathrm{V\ vs.\ SHE}$$

$$\mathrm{Corrosion\ reaction}: 2\mathrm{Ag} + \mathrm{Cu}^{2+} \rightarrow \mathrm{Cu} + 2\mathrm{Ag}^{+} \quad E_{\mathrm{cell}} = -0.462\ \mathrm{V\ vs.\ SHE}$$

Because the cell potential is negative according to Eq. (2.48), the Gibbs free-energy is positive, indicating that the corrosion process will not proceed spontaneously as written.
(b)

$$\text{Anodic}: \text{Ni} \rightarrow \text{Ni}^{2+} + 2\text{e}^- \quad e^{\circ}_{\text{Ni}|\text{Ni}^{2+}} = 0.250\ \text{V vs. SHE}$$

$$\text{Cathodic}: 2\text{Ag}^+ + 2\text{e}^- \rightarrow 2\text{Ag} \quad e^{\circ}_{\text{Ag}^+|\text{Ag}} = 0.799\ \text{V vs. SHE}$$

$$\text{Corrosion reaction}: \text{Ni} + 2\text{Ag}^+ \rightarrow 2\text{Ag} + \text{Ni}^{2+} \quad E_{\text{cell}} = 1.049\ \text{V vs. SHE}$$

Corrosion will occur with the displacement of silver ions from the electrolyte in the presence of Ni metal, which has more negative standard potential than silver.

Example 2.3

Predict the spontaneous direction for the reaction:

$$4\text{OH}^- + 2\text{Fe}^{2+} \rightarrow \text{O}_2 + 2\text{Fe} + 2\text{H}_2\text{O} \tag{2.52}$$

The half-cell reactions are:

$$\text{O}_2 + 2\text{H}_2\text{O} + 4\text{e}^- \rightarrow 4\text{OH}^-, \quad e^{\circ}_{\text{O}_2|\text{OH}^-} = 0.401\ \text{V vs. SHE} \tag{2.53}$$

and

$$\text{Fe}^{2+} + 2\text{e}^- \rightarrow \text{Fe}, \quad e^{\circ}_{\text{Fe}^{2+}|\text{Fe}} = -0.440\ \text{V vs. SHE} \tag{2.54}$$

Assuming that reaction in Eq. (2.52) proceeds from left to right, the half-cell potential for reaction in Eq. (2.53) written as oxidation is $e^{\circ}_{\text{O}_2|\text{OH}^-} = -0.401\ \text{V vs. SHE}$. According to IUPAC convention, the sign must be reversed because the positive sign for this half-cell reaction in Table 2.2 is written for the reduction reaction. The half-cell potential for the reaction in Eq. (2.54) $e_{\text{Fe}^{2+}|\text{Fe}} = -0.440\ \text{V vs. SHE}$ is correct because the half-cell reaction is a reduction. The cell potential is then $E_{\text{cell}} = -0.401 + (-0.440) = -0.841\ \text{V}$ vs. SHE. The potential is negative and reaction in Eq. (2.52) as written does not proceed spontaneously. The opposite reaction in Eq. (2.55) proceeds as:

$$\text{O}_2 + 2\text{Fe} + 2\text{H}_2\text{O} \rightarrow 4\text{OH}^- + 2\text{Fe}^{2+} \tag{2.55}$$

The cell potential for reaction in Eq. (2.55) is 0.841 V vs. SHE resulting in negative Gibbs free-energy. Thus, for iron corroding in water near a neutral pH, the half-cell reactions are written as:

$$\text{Fe} \rightarrow \text{Fe}^{2+} + 2\text{e}^- \quad \text{Anode Reaction}$$

$$\text{O}_2 + 2\text{H}_2\text{O} + 4\text{e}^- \rightarrow 4\text{OH}^- \quad \text{Cathode Reaction}$$

The metals with cell potentials that are more negative than the oxygen electrode potential are not thermodynamically stable when in contact with water and air, and a spontaneous reaction occurs in which oxygen will be converted into water.

2.8 REFERENCE ELECTRODES OF IMPORTANCE IN CORROSION PROCESSES

2.8.1 Determination of reversible potential of the hydrogen electrode

The half-cell of the hydrogen reference electrode consists of platinum foil, which serves as a conductor. The platinum foil is in contact with a sulfuric acid solution that contains H^+ cations of unit activity, in equilibrium with H_2 gas, in its standard state of 1 atm [12–17]. The standard hydrogen electrode may be represented as:

$$H^+|H_2, Pt$$

The charge transfer reaction is:

$$2H^+ + 2e^- \rightarrow H_2 \tag{2.9b}$$

According to the Nernst equation:

$$e_{H^+|H_2} = e^o_{H^+|H_2} + 2.303\frac{RT}{2F}\log\frac{(a_{H^+})^2}{P_{H_2}}$$

$$e_{H^+|H_2} = e^o_{H^+|H_2} + 0.059\log a_{H^+}$$

$$e_{H^+|H_2} = -0.059(pH) \tag{2.56}$$

The hydrogen electrode potential depends on the hydrogen activity and the partial hydrogen pressure. Under standard conditions, the hydrogen pressure is one atmosphere; thus, its activity is equal to 1 and, therefore, according to IUPAC convention, the hydrogen reference electrode potential is zero. The schematic of a SHE is shown in Fig. 2.3.

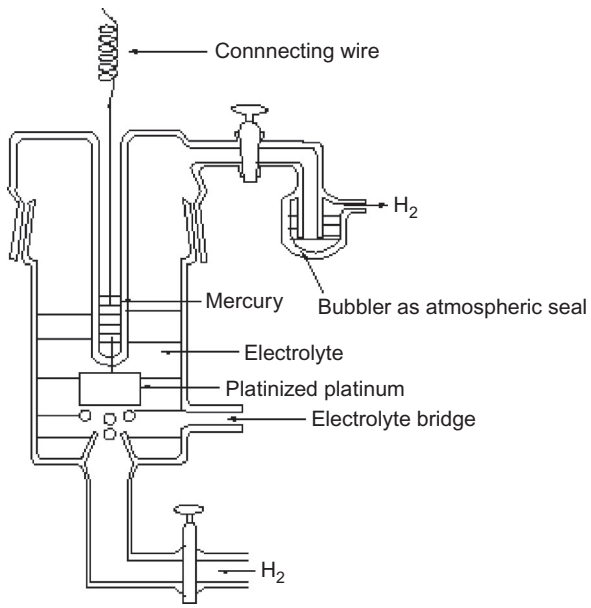

Fig. 2.3 Schematic of the standard hydrogen electrode.

The hydrogen reference electrode is connected to the other redox system through a solution bridge. The bridge consists of a porous glass membrane that permits only charge transfer, without interference of the mass transfer of the acid solution at the electrode interface. The platinum electrode in Fig. 2.3 serves only as a catalyst for the hydrogen evolution reaction, and has the function of establishing the potential on the surface. The SHE is the primary reference electrode. Its half-cell potentials presented in Table 2.2 are expressed on the basis of the standard hydrogen scale, in which the emf of any cell is equal to the potential of the redox system, relative to the potential of the SHE, which is set equal to zero.

Example 2.4

Determine whether zinc is stable in aqueous solutions of hydrochloric acid with pH between 0 and 5. The initial concentration of $ZnCl_2$ is 10^{-6} M. Plot the driving emf and the Gibbs free-energy as a function of pH for the overall corrosion reaction. The activity coefficients are assumed to be 1. The hydrogen pressure = 1 atm.

Zinc is oxidized at the anode and the H^+ is reduced at the cathode. For the overall reaction:

$$Zn + 2H^+ \rightarrow Zn^{2+} + H_2$$

the only terms that should be considered are the Zn^{2+} and the H^+ concentrations. The activities of metal Zn and H_2 are assumed to be unity. Because Zn^{2+} is the product, it will appear in the numerator of the logarithmic term, and the H^+ (reactant) will appear in the denominator. The problem requires changing the pH in order to calculate the cell potential at different pH values.

Cell Notation: $Zn\,|\,Zn^{2+}, Cl^-, H^+\,|\,H_2\,|\,Pt$

In the given reaction, Zn is oxidized at the anode according to: $Zn \rightarrow Zn^{2+} + 2e^-$

The hydrogen is evolved at the cathode according to: $2H^+ + 2e^- \rightarrow H_2$

The overall reaction can be written as: $Zn + 2H^+ \rightarrow Zn^{2+} + H_2$

The Nernst equation for the anodic reaction can be written as:

$$e_{H^+|H_2} = e^{o}_{H^+|H_2} - \frac{2.303RT}{2F}\log\frac{a_{H_2}}{(a_{H^+})^2}$$

$$e_{Zn|Zn^{2+}} = e^{o}_{Zn|Zn^{2+}} - \frac{0.059}{2}\log(a_{Zn^{2+}})$$

At pH = 0, the $e_{Zn|Zn^{2+}}$ electrode potential is calculated as

$$e_{Zn|Zn^{2+}} = 0.762 - \frac{0.059}{2}\log\left(10^{-6}\right)$$

$$e_{Zn|Zn^{2+}} = 0.940\,\text{V vs. SHE}$$

$$E_{cell} = e_a + e_c$$

$$E_{cell} = e^{o}_{H^+|H_2} + e^{o}_{Zn|Zn^{2+}} - 2.303\frac{RT}{2F}\log\left(\frac{a_{Zn^{2+}}}{(a_{H^+})^2 a_{Zn}}\right)$$

Table 2.3 The Cell Potential and Gibbs Free-Energy for the Reaction $Zn_{(s)} + 2HCl_{(aq)} \rightarrow ZnCl_{2(aq)} + H_{2(g)}$

$e_{Zn\|Zn^{2+}}(V)$	pH	E_{cell} (V)	$\Delta G\left(\frac{kJ}{mol}\right)$
0.94	0	0.940	−181.42
0.94	1	0.881	−170.03
0.94	3	0.763	−147.26
0.94	5	0.645	−124.48

The cell potential as a function of pH is calculated using the equation:

$$E_{\text{cell}} = e_{Zn|Zn^{2+}} - 0.059\text{pH}$$

The Gibbs free-energy is calculated by using Eq. (2.45):

$$-\frac{\Delta G}{nF} = \left[e^{o}_{H^+|H_2} + \frac{RT}{nF}\ln\frac{(a_{H^+})^2}{P_{H_2}}\right] - \left[e^{o}_{M^{n+}|M} + \frac{RT}{nF}\ln a_{M^{n+}}\right] \tag{2.45}$$

or $\Delta G = -nFE_{\text{cell}}$; the results are presented in Table 2.3.

As shown in Fig. 2.4a and b, for a pH increase of 1, the cell potential decreases by 59 mV. The Gibbs energy change decreases linearly with increase from pH 0-5. For pH where the Gibbs free-energy is negative, the process proceeds spontaneously. Zinc is unstable in solutions with pH 0-5.

2.8.2 Determination of reversible potential of the oxygen electrode

An oxygen gas electrode is represented by:

$$O_2, Pt|OH^-$$

The charge transfer reaction is written as:

$$O_2 + 2H_2O + 4e^- \rightarrow 4OH^-$$

According to the Nernst equation:

$$e_{O_2|OH^-} = e^{o}_{O_2|OH^-} + 2.303\frac{RT}{4F}\log\left(\frac{P_{O_2}}{(a_{OH^-})^4}\right)$$

$$e_{O_2|OH^-} = e^{o}_{O_2|OH^-} + \frac{0.059}{4}\log(P_{O_2}) - 0.059\log(a_{OH^-})$$

$$e_{O_2|OH^-} = 0.401 - 0.059\log(a_{OH^-}) \tag{2.57}$$

The oxygen electrode is classified as a metal oxide electrode of the second kind. Due to the tendency of oxygen to react with metals and produce oxides, it is very difficult to construct an oxygen electrode with the potential as described by Eq. (2.57).

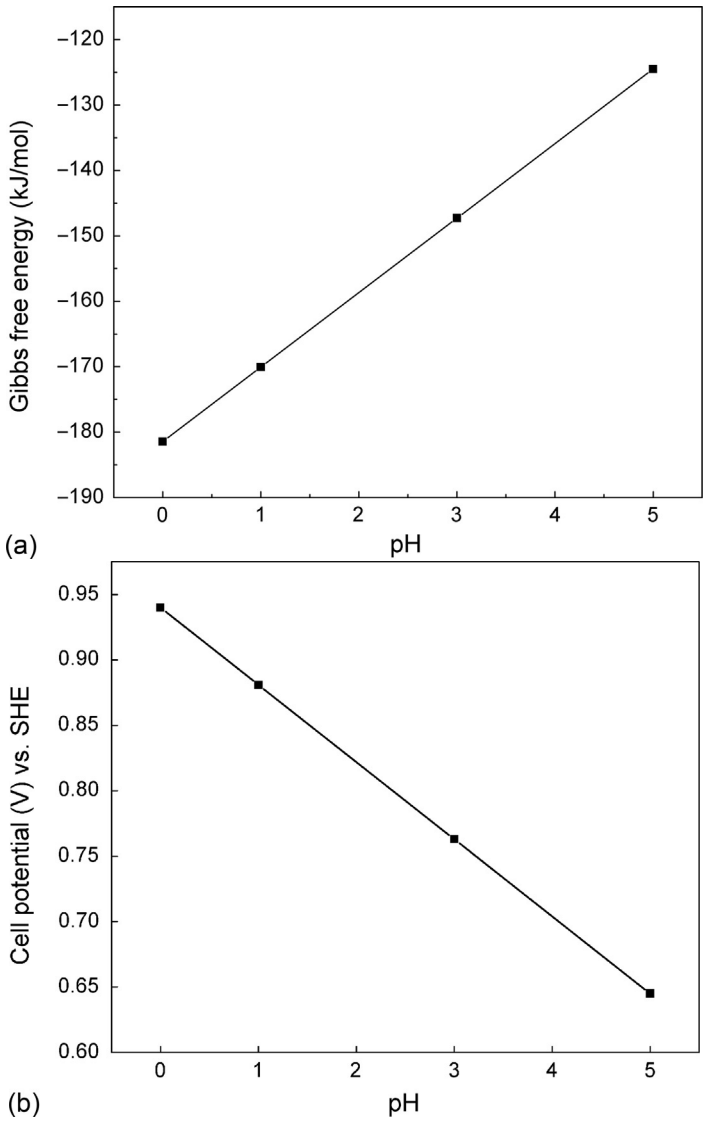

Fig. 2.4 (a) pH vs. Gibbs free-energy (b) pH vs. cell potential for the Zn corrosion cell.

2.8.3 Determination of cell potential of the hydrogen-oxygen cell (fuel cell)

In a hydrogen/oxygen fuel cell shown in Fig. 2.5, the electrical energy results from chemical energy that has been released when water is formed:

$$H_2 + \frac{1}{2}O_2 \rightarrow H_2O$$

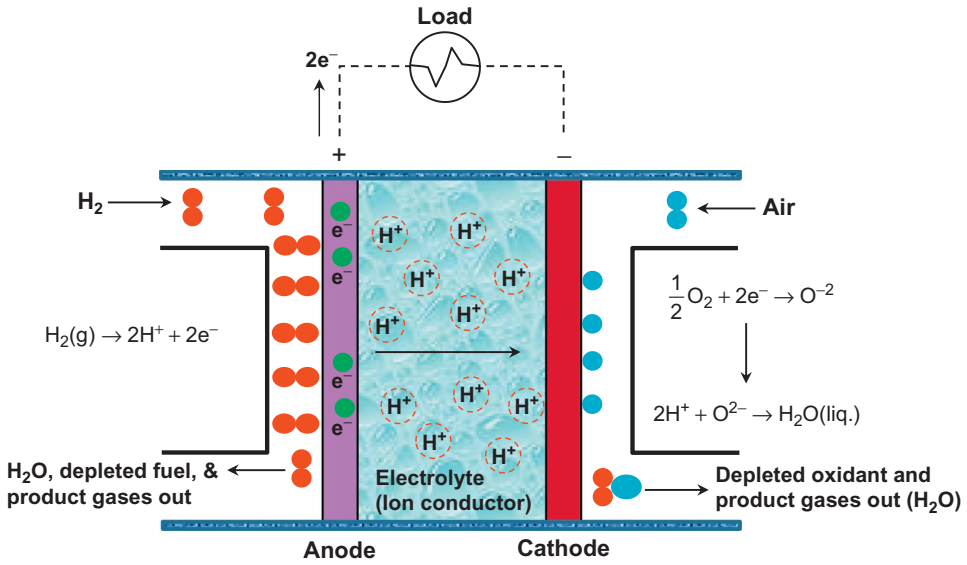

Fig. 2.5 Schematic of the hydrogen/oxygen fuel cell.

The cell potential is estimated using equation:

$$E_{H_2,O_2|H_2O} = E^{o}_{H_2,O_2|H_2O} + 2.303\frac{RT}{4F}\log\left(P_{H_2}(P_{O_2})^{\frac{1}{2}}\right)$$

This equation was derived considering the partial electrode reaction of hydrogen oxidation and oxygen reduction,

$$H_2 \rightarrow 2H^+ + 2e^-$$

$$\frac{1}{2}O_2 + H_2O + 2e^- \rightarrow 2OH^-$$

The overall reaction is:

$$H_2 + \frac{1}{2}O_2 + H_2O \rightarrow 2H^+ + 2OH^- \tag{2.58}$$

According to the Nernst equation:

$$E_{cell} = E^{o}_{cell} + 2.303\frac{RT}{4F}\log\left(\frac{P_{H_2}(P_{O_2})^{1/2}a_{H_2O}}{(a_{H^+})^2(a_{OH^-})^2}\right)$$

$$a_{H^+}a_{OH^-} = K_w$$

$$E_{cell} = E^{o}_{cell} - 2.303\frac{RT}{F}\log(K_w) + 2.303\frac{RT}{2F}\log\left(P_{H_2}(P_{O_2})^{1/2}\right)$$

$$E_{\text{cell}} = e^{\circ}_{H^+|H_2} + e^{\circ}_{OH^-|O_2} - 2.303\frac{RT}{F}\log(K_w) = 0.00 + 0.401 - 0.059\log\left(10^{-14}\right)$$

$$E_{\text{cell}} = 0.00 + 0.41 + 0.83 = 1.23\ \text{V}$$

$$E_{\text{cell}} = 1.23 + \frac{0.059}{2}\log\left(P_{H_2}(P_{O_2})^{1/2}\right) \tag{2.59}$$

According to Eq. (2.59), the potential of the fuel cell increases by the log of the partial pressure of both oxygen and hydrogen, and is independent of the pH of the solution.

2.8.4 Determination of electrode potential of a standard Weston cell

The overall reaction in the Weston cell as presented in Fig. 2.6a and b is $Cd, Hg \mid CdSO_4 \mid CdSO_4 \mid Hg_2SO_4, Hg$.

The potential of this cell is very stable with a small temperature coefficient. The left half-cell (anode) reaction in the Weston cell is reversible to cadmium ions,

$$Cd(Hg) \rightarrow Cd^{2+} + 2e^-$$

while the right-hand side (cathode) is reversible to sulfate ions:

$$Hg_2SO_4 + 2e^- \rightarrow 2Hg + SO_4^{2-}$$

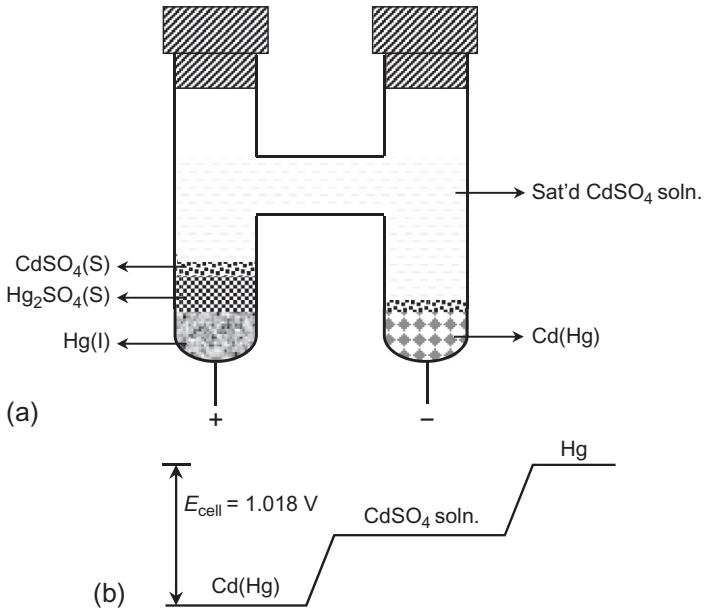

Fig. 2.6 (a) Schematic of the standard Weston cell and (b) hypothetical electric potential profile in the Weston cell.

The overall reaction in the cell is:

$$\mathrm{Cd(Hg) + Hg_2SO_4 \rightarrow Cd^{2+} + SO_4^{2-} + 2Hg}$$

The emf of the Weston cell is:

$$E_{\text{cell}} = e_{\mathrm{Hg_2SO_4|Hg}} - e_{\mathrm{Cd^{2+}|Cd}}$$

$$e_{\mathrm{Cd^{2+}|Cd}} = e^{\circ}_{\mathrm{Cd^{2+}|Cd}} - 2.303\frac{RT}{nF}\log\left(\frac{a_{\mathrm{Cd}}}{a_{\mathrm{Cd^{2+}}}}\right)$$

$$e_{\mathrm{Hg_2SO_4|Hg}} = e^{\circ}_{\mathrm{Hg_2SO_4|Hg}} - 2.303\frac{RT}{nF}\log\left(\frac{a_{\mathrm{Hg^{2+}}}\,a_{\mathrm{SO_4^{2-}}}}{a_{\mathrm{Hg_2SO_4}}}\right)$$

$$E_{\text{cell}} = E^{\circ}_{\text{cell}} - 2.303\frac{RT}{nF}\log\left(\frac{a_{\mathrm{Cd^{2+}}}\,a_{\mathrm{Hg^{2+}}}\,a_{\mathrm{SO_4^{2-}}}}{a_{\mathrm{Cd}}\,a_{\mathrm{Hg_2SO_4}}}\right)$$

Because the activities of the solid substances in the above equation are constant and equal to unity, the potential of the standard Weston cell is defined by Eq. (2.60).

$$E_{\text{cell}} = E^{\circ}_{\text{cell}} - 2.303\frac{RT}{nF}\log\left(a_{\mathrm{CdSO_4}}\right) \tag{2.60}$$

2.8.5 Determination of electrode potentials for electrodes of the second kind

The half-cell reaction of electrodes of the second kind consists of a metal covered by a low solubility compound of the same metal, (MA), such as a salt, a hydroxide, or an oxide, and is immersed in a solution that contains the same anions as the compound of the metal. Therefore, an electrode of the second kind is represented as:

$$\mathrm{A^{n-}|MA, M}$$

The electrode reaction is expressed as:

$$\mathrm{MA} + ne^{-} \rightarrow \mathrm{M} + \mathrm{A^{n-}}$$

The Nernst equation written for the electrode potential is:

$$e_{\mathrm{A^{n-}|\,MA}} = e^{\circ}_{\mathrm{A^{n-}|MA}} + 2.303\frac{RT}{nF}\log\left(\frac{a_{\mathrm{MA}}}{a_{\mathrm{A^{n-}}}\,a_{\mathrm{M}}}\right) \tag{2.61}$$

Because the solubility of MA is low, the activity of the metal, M, and the solid substance, MA, in Eq. (2.61) are constant. Thus, the equation may be simplified to:

$$e_{\mathrm{A^{n-}|MA}} = e^{\circ}_{\mathrm{A^{n-}|MA}} + 2.303\frac{RT}{nF}\log\left(a_{\mathrm{A^{n-}}}\right) \tag{2.62}$$

The electrode potential of this type of electrode is defined by the concentration (activity) of the anions. They are used in corrosion engineering as standard half-cells or reference electrodes. In corrosion engineering practice they are called secondary reference electrodes to differentiate them from the hydrogen electrode, which is a primary reference electrode. The following electrodes of the second kind are of interest in electrochemical and corrosion studies: calomel electrode, silver-silver chloride electrode, and mercury-mercurous electrode.

2.8.6 Calomel electrode

The calomel electrode shown in Fig. 2.7 consists of a pool of mercury covered with a paste of mercury and calomel (mercurous chloride), immersed in an electrolyte containing a solution of potassium chloride. The reaction of the electrode is a reduction of calomel to metallic mercury and chloride anions.

$$Cl^{-}Hg_2Cl_2|Hg$$

$$Hg_2Cl_2 + 2e^{-} \rightarrow 2Hg + 2Cl^{-}$$

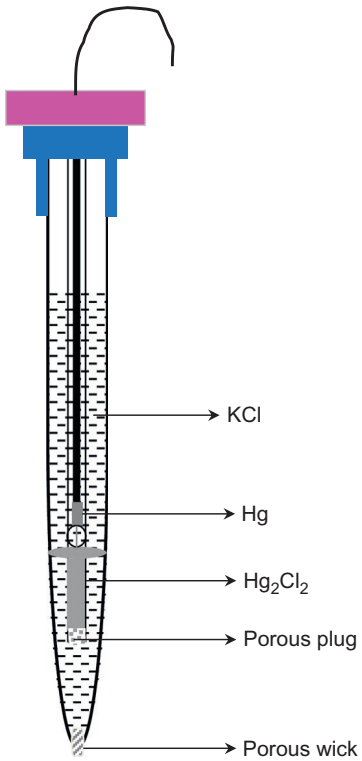

Fig. 2.7 Schematic of the calomel electrode.

The electrode potential is reversible with respect to the chloride ions.

$$e^{o}_{Hg_2Cl_2|Hg,Cl^-} = 0.268 - 0.059\log(a_{Cl^-}) \tag{2.63}$$

The saturated calomel electrodes are convenient for corrosion measurements because the diffusion potential initiated at the interface of the saturated potassium chloride solution and the electrolyte is insignificant and can be ignored. The electrode potential of the saturated calomel electrode of 0.241 V is lower than the potential of the standard half reaction of $e^{o} = 0.268$ V because of the higher chloride activity.

2.8.7 Silver-silver chloride electrode

The silver-silver chloride electrode shown in Fig. 2.8 is based on the following redox reaction:

$$AgCl|Ag, Cl^-$$

$$AgCl + e^- \rightarrow Ag + Cl^-$$

The potential of this electrode is defined by the Nernst equation:

$$e_{AgCl|Cl^-} = e^{o}_{AgCl|Cl^-} - 2.303\frac{RT}{nF}\log(a_{Cl^-})$$

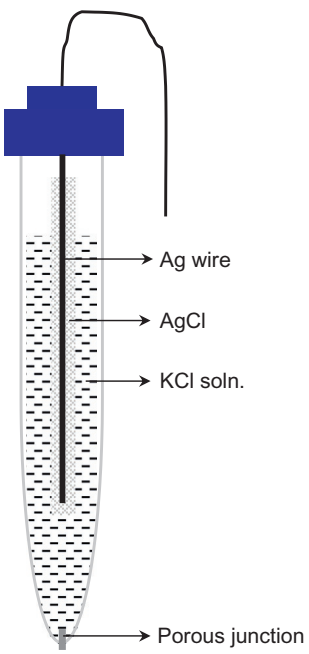

Fig. 2.8 Schematic of the silver-silver chloride electrode.

At 25 °C:

$$e_{AgCl|Cl^-} = 0.222 - 0.059\log(a_{Cl^-}) \tag{2.64}$$

2.8.8 Copper-copper sulfate electrode

The copper-copper sulfate reference electrode consists of copper metal immersed in a saturated copper sulfate solution, as shown in Fig. 2.9. A porous frit or wooden plug serves as an electrolytic contact with the cell. The electrode reaction is:

$$Cu^{2+} + 2e^- \rightarrow Cu$$

The electrode potential is given by:

$$e_{Cu^{2+}|Cu} = 0.337 + \frac{0.059}{2}\log(a_{Cu^{2+}})$$

This electrode has a very simple design and is frequently used in corrosion engineering practice to evaluate the corrosion potential of buried pipelines and other buried metallic structures. The disadvantage of using this electrode is its low precision. The conversion of potential from one reference point to another is done by using addition or subtraction.

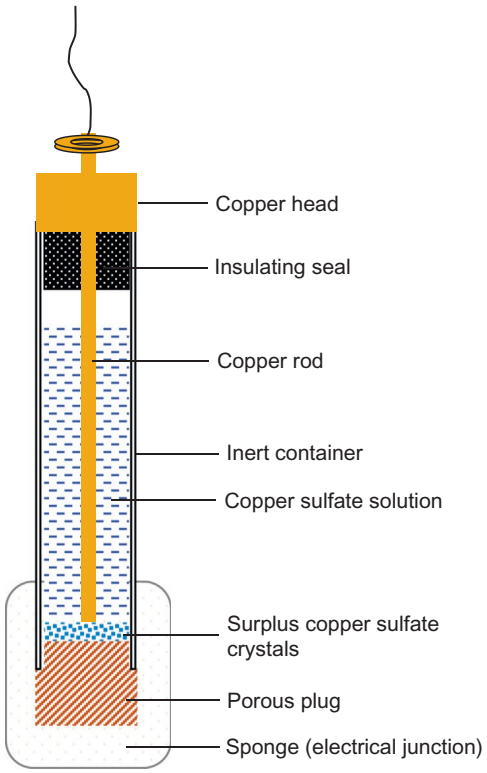

Fig. 2.9 Schematic of the copper-copper sulfate reference electrode.

Table 2.4 Equilibrium Potential Values for Commonly Used Reference Electrodes

Reference Electrode	Half-Cell Reaction	Potential *V* vs. NHE
Standard hydrogen	$2H^+ + 2e^- \rightarrow H_2$	0.000
Calomel	$Hg_2Cl_2 + 2\ e^- \rightarrow 2Hg + 2Cl^-$	0.283 (1 M KCl, NCE) 0.241 (Sat'd KCl, SCE) 0.236 (Sat'd NaCl, SCCE)
Silver-silver chloride	$AgCl + e^- \rightarrow Ag + Cl^-$	0.222 (KCl, Standard) 0.197 (NaCl, Sat'd)
Mercury-mercurous sulfate	$HgSO_4 + 2e^- \rightarrow Hg + SO_4^{2-}$	0.615 (Standard) 0.680 (0.5 M H_2SO_4)
Mercury-mercury oxide	$HgO + H_2O + 2e^- \rightarrow Hg + + OH^-$	0.165 (0.1 M NaOH)
Copper-copper sulfate	$CuSO_4 + 2e^- \rightarrow Cu + SO_4^{2-}$	0.318 (Sat'd $CuSO_4$)

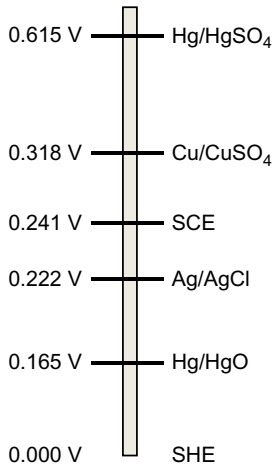

Fig. 2.10 Hydrogen electrode scale.

For example, the equilibrium reduction potential of iron, which is −0.44 V vs. NHE, will be −0.681 V vs. SCE (saturated calomel electrode). Similarly, a metal that shows a potential of −0.331 V vs. Ag|AgCl will have a potential of −0.109 V vs. SHE and −0.427 V vs. Cu|$CuSO_4$. The potentials of various reference electrodes are given in Table 2.4 and are compared in Fig. 2.10 with respect to the NHE.

2.9 MEASUREMENT OF REVERSIBLE CELL POTENTIAL WITH LIQUID JUNCTION POTENTIAL

The potential of two reversible cells can be accurately measured by using the experimental cell setup shown in Fig. 2.11. The cell contains pure zinc and pure platinum electrodes

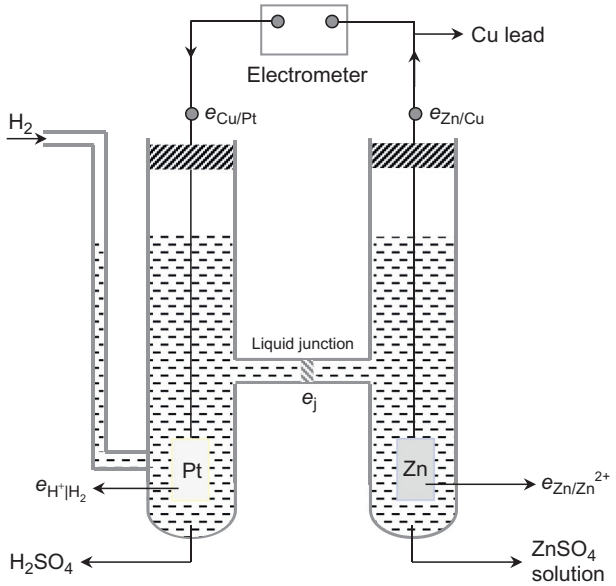

Fig. 2.11 Schematic of the experimental setup for measuring reversible cell potential.

immersed in zinc sulfate and sulfuric acid solutions, both of unit activity. The cell potential measured by using this apparatus has individual potential contributions from $e^{o}_{Zn|Zn^{2+}}$, $e^{o}_{H^+|H_2}$, $e_{Zn|Cu}$, $e_{Cu|Pt}$, and liquid junction potential, e_j.

Negligible quantities of contact potentials are also added to the total cell potentials of Zn | Cu and Cu | Pt couples because of the energy required when moving electrons from one metal to another. In most of the cases, their contribution is canceled out because of their opposite signs. However, the half-cell potentials reported in Table 2.2 are incorporated with very small contributions from contact potentials. The liquid junction e_j is generated across two solutions of differing concentrations and/or composition due to the migration of ionic species into the solution of lower concentration from higher concentration.

2.10 MEASUREMENT OF CORROSION POTENTIAL

The potential of the corroding surface can be monitored periodically by means of a reference electrode. One such example is the corrosion potential measurement of reinforced steel rebar in concrete structures. Corrosion of the steel in reinforced concrete is a major factor in the deterioration of highway and bridge infrastructure. A survey of the condition of a reinforced concrete structure is the first step toward its rehabilitation. A rapid, cost-effective, and nondestructive condition survey offers key information to evaluate the corrosion, aids in quality assurance of concrete repair and rehabilitation,

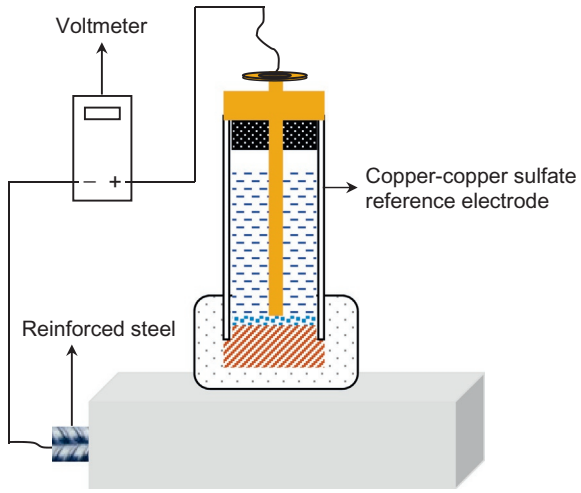

Fig. 2.12 Corrosion potential measurement of reinforced steel rebar in concrete.

and assists in the prediction of the remaining service life of the material. An effective way to assess the severity of steel corrosion is to measure the corrosion potential because it is qualitatively associated with the steel corrosion rate. Figure 2.12 illustrates the basics of corrosion potential measurements. The reference electrode and the reinforced steel are connected to the positive and negative terminals of a high-resistance ($>10\,M\Omega$) voltmeter. One measures the potential difference between a standard portable half-cell standard reference electrode, normally a copper/copper sulfate and the steel by placing the electrode on the surface of the concrete containing the steel reinforcement underneath.

2.11 CONSTRUCTION OF POURBAIX DIAGRAMS

The dissolution of a metal and the stability of the products in aqueous solutions depend on the nature of the metal, the solution's oxidizing power, and the pH of the solution. The stability of different metals is estimated by using potential-pH diagrams suggested by Marcel Pourbaix [18,19]. These diagrams are constructed from calculations based on the Nernst equation and the solubility (activity) data for various metal compounds. Pourbaix diagrams predict the reaction products of the metal that exist at equilibrium at a given electrode potential and pH. The only conditions for constructing the diagram are that all the necessary reactions should be at a given pH and be at a potential of interest. They show the values of pH and potential conditions at which the metal reacts to form complex anions or oxides or where the metal is immune to corrosion.

The Pourbaix diagrams are used to (i) predict the spontaneous direction of reactions, (ii) determine the potential/pH regions in which the metal is stable and where the

corrosion is thermodynamically impossible, (iii) estimate the nature and the composition of corrosion products, and (iv) evaluate the equilibrium conditions of the metal/electrolyte interface.

Because the potential-pH diagrams characterize equilibrium thermodynamic properties only, they cannot be used to predict the rates of reactions. They can evaluate the conditions for formation of barrier films on the metals, but they cannot estimate their effectiveness in protecting the metal in different environments. It should be noted that the Nernst equation is used to estimate the electrode potentials and is based on thermodynamic equations, which are not accurate when the concentration of the electroactive species is close to zero. All metals have a limiting critical value of their activities, (a concentration of $<10^{-6}$ g-ions per liter), below which the Nernst equation does not agree with the experimentally measured Gibbs free-energy.

2.11.1 Regions of electrochemical stability of water

Figure 2.13 shows the thermodynamic stability of water at 25 °C and at standard pressure, as a function of the potential and the pH of the electrolyte.

The regions of electrochemical stability of water are used to predict the properties of a metal in aqueous solutions when the metal's potential is known at given pH. In Fig. 2.13, the reversible potential of the hydrogen line, line "b" electrode is constructed using the reversible potential for the hydrogen evolution reaction in an acidic solution:

$$2H^+ + 2e^- \rightarrow H_2$$

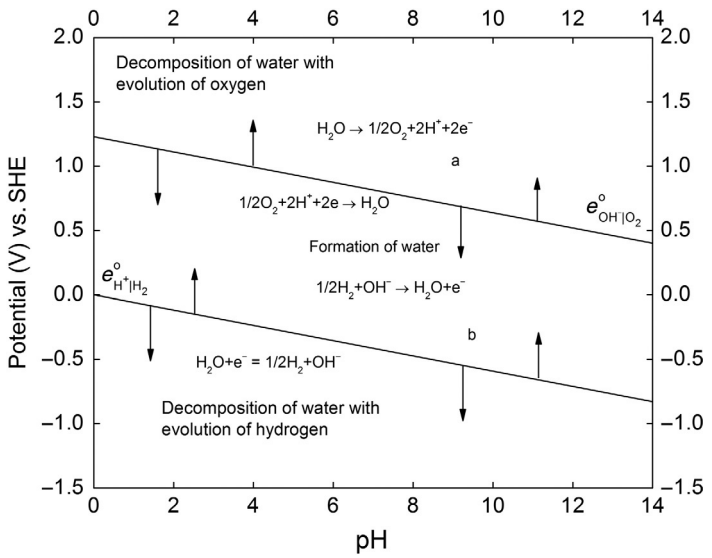

Fig. 2.13 Regions of electrochemical stability of water.

In an alkaline solution, the equivalent reaction is:

$$2H_2O + 2e^- \rightarrow H_2 + 2OH^-$$

The half-cell electrode potential as a function of the pH of the solution is given as:

$$e_{H^+|H_2} = e^o_{H^+|H_2} - 0.059\,pH$$

The area below line "b" corresponds to the area where the water decomposition with hydrogen evolution reaction occurs.

The area in Fig. 2.13 between the oxygen equilibrium potentials (line "a") and the hydrogen line (line "b") is where the water is stable. In this region, water may be synthesized from oxygen and hydrogen. The area above line "a" corresponds to the region where the water decomposes with the formation of oxygen:

$$2H_2O \rightarrow O_2 + 4H^+ + 4e^-$$

and

$$4OH^- \rightarrow O_2 + H_2O + 4e^-$$

The Nernst equation for the oxygen equilibrium potentials is defined as:

$$e_{O_2|H_2O} = e^o_{O_2|H_2O} - 0.059(pH)$$

At pH 0, the equilibrium electrode potential for the reaction is 1.22 V vs. SHE, while that of OH^- at pH 14, as shown in Table 2.2, is 0.401 V vs. SHE at unit activity. The area above line "a" corresponds to the region where the water decomposition proceeds with formation of oxygen.

2.11.2 Construction of pourbaix diagram for zinc

The zinc system is used to demonstrate the basic principles for the construction of Pourbaix diagrams. Any metal, "M," reacts anodically in the presence of water through the following general reactions:

1. Oxidation of the metal to aqueous cations:

$$M \rightarrow M^{n+} + ne^- \tag{2.65}$$

2. Oxidation of the metal to oxide or hydroxide:

$$M + nH_2O \rightarrow M(OH)_n + nH^+ + ne^- \tag{2.66}$$

3. Oxidation of the metal to aqueous anions:

$$M + nH_2O \rightarrow MO_n^{n-} + 2nH^+ \tag{2.67}$$

Thus, the oxidation of zinc to its aqueous solutions is described by the reaction:

$$Zn \rightarrow Zn^{2+} + 2e^-$$

Substituting the zinc standard potential and the zinc concentration into the Nernst equation:

$$e_{Zn|Zn^{2+}} = e^{o}_{Zn|Zn^{2+}} + \frac{0.059}{n}\log\left(\frac{a_{Zn^{2+}}}{a_{Zn}}\right)$$

we obtain:

$$e_{Zn|Zn^{2+}} = -0.762 + \frac{0.059}{n}\log\left(a_{Zn^{2+}}\right)$$

For zinc concentration of 1 M, the electrode potential from Table 2.2 is $e^{o}_{Zn|Zn^{2+}} = -0.762$ V vs. SHE. As shown in Fig. 2.14, if the concentration of zinc ions is unity, the zinc standard potential is constant at all pH. However, the standard concentration represents an unrealistically high concentration of (Zn^{2+}) in corrosion solution. More realistic for corrosion process would be lower value at the metal/electrolyte interface such as (Zn^{2+}) = 10^{-6} M resulting in $e_{Zn|Zn^{2+}} = -0.94$ V vs. SHE at all pH. The half-cell potential for formation of zinc cation is independent of pH because hydrogen cation is not involved in zinc dissolution reaction. Rather, it depends on the concentration of zinc ions in the solution. Thus, the two horizontal straight lines in Fig. 2.14 result from two different concentrations of zinc in the electrolyte.

The zinc oxidation reaction to zinc oxide is expressed by the following equation:

$$Zn + H_2O \rightarrow ZnO + 2H^+$$

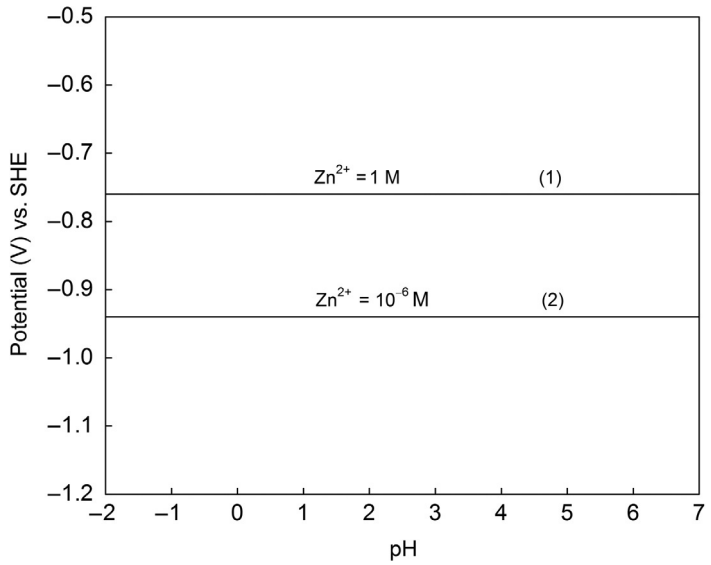

Fig. 2.14 Potential-pH diagram showing the cation formation reaction [Zn^{2+}] of 1 and 10^{-6} M.

The reduced and oxidized species, Zn and ZnO, are solids. Their activities in the Nernst equation are unity, which eliminates their contribution to the overall electrode potential. The Nernst equation reduces to:

$$e_{Zn|ZnO} = e^{o}_{Zn|ZnO} - 0.059\text{pH}$$

$$e_{Zn|ZnO} = -0.439 - 0.059\text{pH}$$

where $e^{o}_{Zn\,|\,ZnO} = -0.439$ V vs. SHE.

In Fig. 2.15, this equation represents a straight line with a slope of −0.059. At pH = 0, the potential corresponds to the standard zinc $e^{o}_{Zn\,|\,ZnO}$ electrode potential of −0.439 V vs. SHE.

The lines representing the cation and the oxide formation are labeled in Fig. 2.15 as (1) and (2) and they intercept each other at different pH values. The intercept depends on the concentration of Zn^{2+}. In fact, above these concentrations, the Zn^{2+} cations react with water to form zinc oxide:

$$Zn^{2+} + H_2O \rightarrow ZnO + 2H^{+} \tag{2.68}$$

Below this pH, the zinc oxide dissolves to Zn^{2+} cations. Notice that the charge transfer reaction does not occur in reaction shown in Eq. (2.68) because the oxidation state of Zn^{2+} does not change. The equilibrium of this reaction is determined by the concentration (activities) of the zinc cations and is independent of the potential. The pH at equilibrium where line (1) and line (2) intersect is estimated by using the value of the equilibrium constant for the reaction in Eq. (2.68) of $K = (a_{H^+})^2/(a_{Zn^{2+}}) = 10^{-10.96}$.

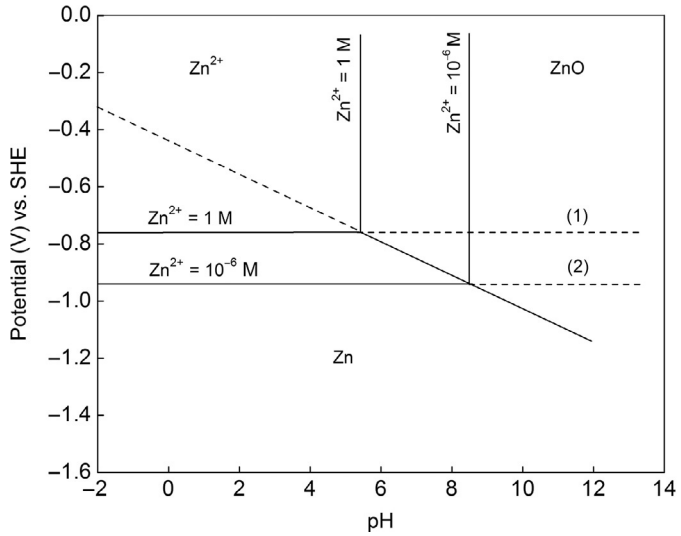

Fig. 2.15 Potential-pH diagram showing ZnO superimposed on Fig. 2.14.

Thus, for Zn^{2+} activities of 10^{-6} M, the pH value of 8.48 is calculated from the known value of the equilibrium constant:

$$\log(a_{Zn^{2+}}) = 10.96 - 2\text{pH} \tag{2.69}$$

$$\log(K) = 2\log(a_{H^+}) - \log(a_{Zn^{2+}}) = -2\text{pH} - \log(a_{Zn^{2+}})$$

$$\text{pH} = \frac{-\log(K)}{2} - \frac{\log(a_{Zn^{2+}})}{2} = \frac{10.96}{2} + \frac{6}{2} = 8.48$$

The lines in Fig. 2.15 are vertical because the pH is independent of the potential. At high potentials, the zinc cations are stable at pH lower than 8.48, while ZnO is stable at pH higher than 8.48.

The reaction that corresponds to the formation of aqueous for zinc is:

$$Zn + 2H_2O \rightarrow ZnO_2^{2-} + 4H^+ + 2e^-$$

The Nernst equation is:

$$e^o_{Zn|ZnO_2^{2-}} = 0.441 - 0.118\text{pH} + \frac{0.059}{2}\log\left(a_{ZnO_2^{2-}}\right)$$

The Nernst potential, as shown in Fig. 2.16, depends on the pH and the concentration of (ZnO_2^{2-}) anions. Lines for an anion concentration of 10^{-6} M, and an anion concentration of 1 M, are shown in Fig. 2.16. The pH slopes for both concentrations are −0.118. The standard value of $e^o_{Zn|ZnO_2^{2-}}$, estimated from the intercept at pH = 0, is equal to 0.441 V vs. SHE.

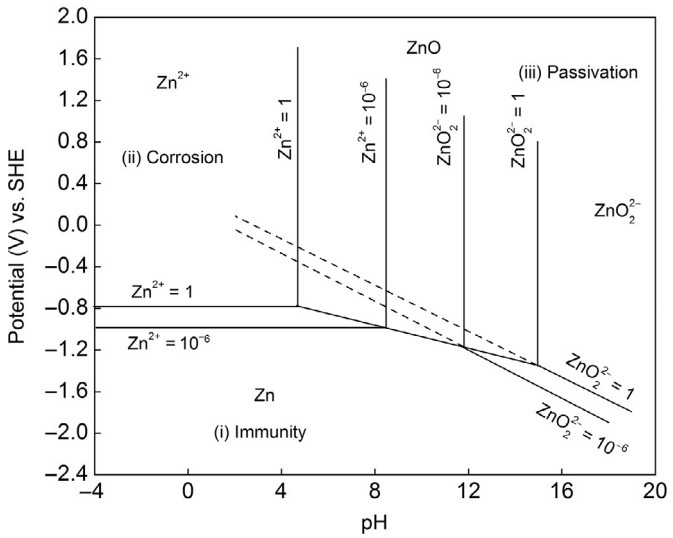

Fig. 2.16 Potential-pH diagrams showing aqueous anion formation for Zn metal.

At pH values higher than 11, ZnO dissolves to form ZnO_2^{2-}, according to the reaction:

$$Zn + 2H_2O \rightarrow ZnO_2^{2-} + 2H^+$$

Because there is no charge transfer or a valence change, this reaction is independent of the potential. Thus, the transition from ZnO to ZnO_2^{2-} is calculated from the equilibrium constant. The equilibrium pH in Fig. 2.16 is estimated to be 11.89 and 14.89 for concentrations of $a_{ZnO_2^{2-}} = 10^{-6}$ M and 1 M, respectively, independent of potential.

$$\log\left(a_{ZnO_2^{2-}}\right) = -29.78 + 2(\text{pH})$$

$$\text{for}\left(a_{ZnO_2^{2-}}\right) = 1, \quad \text{pH} = 14.89$$

$$\text{for}\left(a_{ZnO_2^{2-}}\right) = 10^{-6}, \quad \text{pH} = 11.89$$

When $(Zn^{2+}) = 10^{-6}$ M, the equilibrium is represented as straight vertical lines at pH = 11.89. In Fig. 2.16, at high potentials, the oxides are stable below a pH of 11.89 and the anion is stable above this pH. At unit activity, the zinc anion is stable above pH = 14.89.

The following regions are clearly outlined in Fig. 2.16: (i) immunity, in which the metal is considered to be immune from corrosion attack; (ii) corrosion region, in which the metal corrodes and forms soluble species; and (iii) passive region, in which the metal is coated with oxide or hydroxide. By decreasing the potential (cathodic protection), the metal can move from the active corrosion region to the immunity region. Zinc, because of its equilibrium potential, is used as a sacrificial anode to protect the iron from corrosion.

2.11.3 Construction of Pourbaix diagram for tin

The Pourbaix diagram for tin was constructed by using six reduction and oxidation reactions over a pH range of 0-14. All dissolved species were assumed to have activities of 10^{-6} M. The diagram is plotted at 25 °C. The following reactions were considered in the construction of the diagram:

$$SnH_4 \rightarrow Sn + 4H^+ + 4e^- \quad e^o_{SnH_4|H^+} = -1.076\,\text{V vs. SHE}$$

$$Sn \rightarrow Sn^{2+} + 2e^- \quad e^o_{Sn|Sn^{2+}} = -0.136\,\text{V vs. SHE}$$

$$Sn + 2H_2O \rightarrow HSnO_2^- + 3H^+ + 2e^- \quad e^o_{Sn|H^+,HSnO_2^-} = 0.333\,\text{V vs. SHE}$$

$$Sn^{2+} + 2H_2O \rightarrow SnO_2 + 4H^+ + 2e^- \quad e^o_{Sn^{2+}|H^+} = -0.077\,\text{V vs. SHE}$$

$$Sn + 2H_2O \rightarrow SnO_2 + 4H^+ + 4e^- \quad e^o_{Sn|H^+} = -0.106\,\text{V vs. SHE}$$

$$HSnO_2^- \rightarrow SnO_2 + H^+ + 2e^- \quad e^o_{HSnO_2^-|H^+} = -0.546\,\text{V vs. SHE}$$

Derivation of Equilibrium Equations: The Nernst equations were used to derive the equilibrium potentials as a function of pH.

Equilibrium (1)

$$SnH_4 \rightarrow Sn + 4H^+ + 4e^- \quad e^o_{SnH_4|H^+} = -1.076\,V \text{ vs. SHE}$$

$$e_{SnH_4|H^+} = e^o_{SnH_4|H^+} + \frac{0.059}{4}\log\left((a_{H^+})^4\right) - \frac{0.059}{4}\log\left(a_{SnH_4}\right)$$

$$e_{SnH_4|H^+} = -1.076 - 0.059pH - \frac{0.059}{4}\log\left(a_{SnH_4}\right)$$

Equilibrium (2)

$$Sn \rightarrow Sn^{2+} + 2e^- \quad e^o_{Sn|Sn^{2+}} = -0.136\,V \text{ vs. SHE}$$

$$e_{Sn|Sn^{2+}} = e^o_{Sn|Sn^{2+}} + \frac{0.059}{2}\log\left(a_{Sn^{2+}}\right)$$

$$e_{Sn|Sn^{2+}} = -0.136 + \frac{0.059}{2}\log\left(a_{Sn^{2+}}\right)$$

Equilibrium (3)

$$Sn + 2H_2O \rightarrow HSnO_2^- + 3H^+ + 2e^- \quad e^o_{Sn|H^+,HSnO_2^-} = 0.333\,V \text{ vs. SHE}$$

$$e_{Sn|H^+,HSnO_2^-} = e^o_{Sn|H^+,HSnO_2^-} + \frac{0.059}{2}\log\left((a_{H^+})^3\right) + \frac{0.059}{2}\log\left(a_{HSnO_2^-}\right)$$

$$e_{Sn|H^+,HSnO_2^-} = 0.333 - \frac{3\times 0.059}{2}pH + \frac{0.059}{2}\log\left(a_{HSnO_2^-}\right)$$

Equilibrium (4)

$$Sn^{2+} + 2H_2O \rightarrow SnO_2 + 4H^+ + 2e^- \quad e^o_{Sn^{2+}|H^+} = -0.077\,V \text{ vs. SHE}$$

$$e_{Sn^{2+}|H^+} = e^o_{Sn^{2+}|H^+} + \frac{0.059}{2}\log\left((a_{H^+})^4\right) - \frac{0.059}{2}\log\left(a_{Sn^{2+}}\right)$$

$$e_{Sn^{2+}|H^+} = -0.077 - 2\times 0.059pH - \frac{0.059}{2}\log\left(a_{Sn^{2+}}\right)$$

Equilibrium (5)

$$Sn + 2H_2O \rightarrow SnO_2 + 4H^+ + 4e^- \quad e^o_{Sn|H^+} = -0.106\,V \text{ vs. SHE}$$

$$e_{Sn|H^+} = e^{o}_{Sn|H^+} + \frac{0.059}{4}\log\left((a_{H^+})^4\right)$$

$$e_{Sn|H^+} = -0.106 - 0.059\,pH$$

Equilibrium (6)

$$HSnO_2^- \rightarrow SnO_2 + H^+ + 2e^- \quad e^{o}_{HSnO_2^-|H^+} = -0.546\,V \text{ vs. SHE}$$

$$e_{HSnO_2^-|H^+} = e^{o}_{HSnO_2^-|H^+} + \frac{0.059}{2}\log(a_{H^+}) + \frac{0.059}{2}\log\left(a_{HSnO_2^-}\right)$$

$$e_{HSnO_2^-|H^+} = -0.546 - \frac{0.059}{2}pH + \frac{0.059}{2}\log\left(a_{HSnO_2^-}\right)$$

The various regions in potential-pH diagram are determined using the equilibrium equations. The following regions exist in Figs. 2.17 and 2.18: (i) immunity region, in which the metal is considered immune to corrosion attack; (ii) passive region, in which the metal is coated with oxide or hydroxide, serving as a barrier film against corrosion; and (iii) corrosion region, in which the metal corrodes and forms soluble species.

In addition to the six reactions described above, other chemical reactions may occur, such as:

$$SnO_2 + H_2O \rightarrow SnO_3^{2-} + 2H^+$$

Because there is no charge transfer or valence change in this reaction, it is independent of the potential. The pH, where the transformation of SnO_2 to SnO_3^{2-} occurs, is calculated from the equilibrium constant.

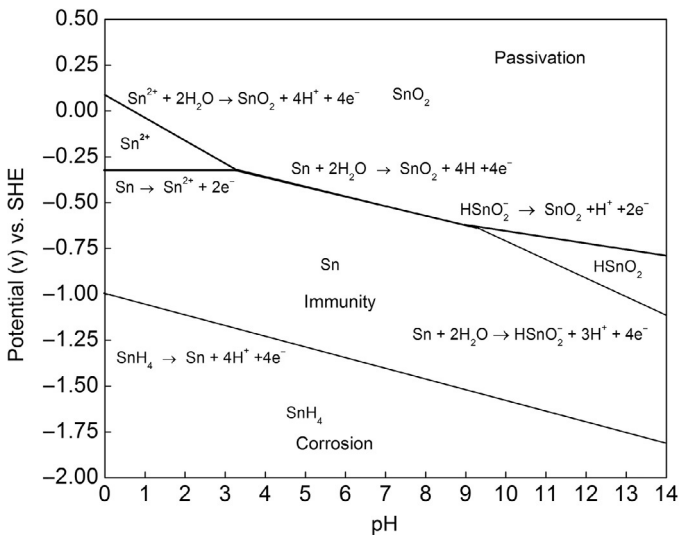

Fig. 2.17 Pourbaix diagram for tin.

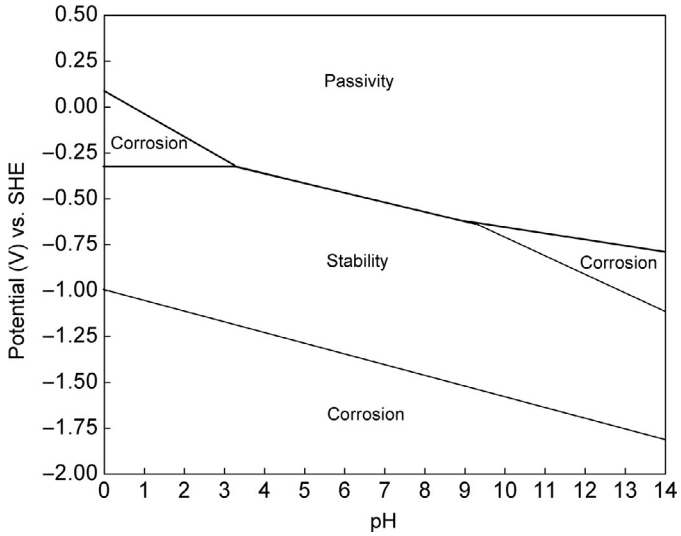

Fig. 2.18 Areas of stability, passivity, and corrosion for tin.

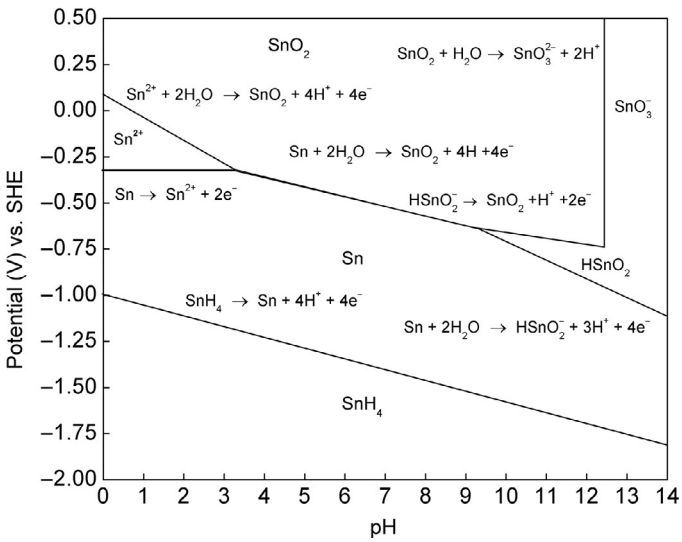

Fig. 2.19 Pourbaix diagram for tin with added chemical reactions.

$$\log\left(a_{\mathrm{SnO_3^{2-}}}\right) = -31.16 + 2\mathrm{pH}$$

For a concentration of 10^{-6} M, this equation is a vertical line at pH = 12.58. The resulting Pourbaix diagram is shown in Fig. 2.19, while the regions of corrosion, passivity, and stability are given in Fig. 2.20.

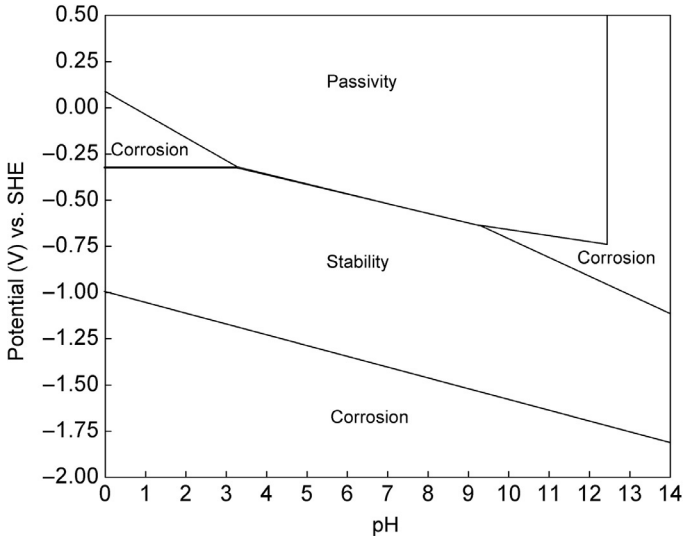

Fig. 2.20 Regions of stability, corrosion, and passivity for tin.

2.11.4 Pourbaix diagram for iron

The Pourbaix diagram for iron is constructed by using nine reduction and oxidation reactions over a pH range of 0–14. All dissolved species are assumed to have activities of 1 M. The diagram is plotted at 25 °C. The following reactions were used to construct the diagram:

Reaction (1)

$$\mathrm{Fe} \rightarrow \mathrm{Fe}^{2+} + 2\mathrm{e}^{-}$$

$$e_{\mathrm{Fe}|\mathrm{Fe}^{2+}} = -0.440 + \frac{0.059}{2}\log\left(a_{\mathrm{Fe}^{2+}}\right)$$

Reaction (2)

$$\mathrm{Fe} + 2\mathrm{H_2O} \rightarrow \mathrm{Fe(OH)_2} + 2\mathrm{H}^{+} + 2\mathrm{e}^{-}$$

$$e_{\mathrm{Fe}|\mathrm{Fe(OH)_2}} = -0.047 + 0.059\mathrm{pH}$$

Reaction (3)

$$\mathrm{Fe} + 2\mathrm{H_2O} \rightarrow \mathrm{HFeO_2^{-}} + 3\mathrm{H}^{+} + 2\mathrm{e}^{-}$$

$$e_{\mathrm{Fe}|\mathrm{HFeO_2^{-}}} = 0.493 - \frac{3 \times 0.059}{2}\mathrm{pH} + \frac{0.059}{2}\log\left(a_{\mathrm{HFeO_2^{-}}}\right)$$

Reaction (4)

$$\mathrm{Fe} + 2\mathrm{H_2O} \rightarrow \mathrm{Fe(OH)_2} + 2\mathrm{H}^{+}$$

$$\mathrm{pH} = 6.65 - 0.5\log\left(a_{\mathrm{Fe}^{2+}}\right)$$

Reaction (5)

$$Fe(OH)_2 \rightarrow HFeO_2^- + H^+$$

$$pH = 14.30 - \log\left(a_{HFeO_2^-}\right)$$

Reaction (6)

$$Fe^{2+} + 3H_2O \rightarrow Fe(OH)_3 + 3H^+ + e^-$$

$$e_{Fe^{2+}|Fe(OH)_3} = 1.057 - 3 \times 0.059pH - 0.059\log\left(a_{Fe^{2+}}\right)$$

Reaction (7)

$$Fe^{2+} + 3H_2O \rightarrow Fe(OH)_3 + 3H^+$$

$$pH = 1.613 - \frac{1}{3}\log\left(a_{Fe^{2+}}\right)$$

Reaction (8)

$$HFeO_2^- + H_2O \rightarrow Fe(OH)_3 + 2e^-$$

$$e_{HFeO_2^-|Fe(OH)_3} = -0.810 - 0.059\log\left(a_{HFeO_2^-}\right)$$

Reaction (9)

$$Fe(OH)_2 + H_2O \rightarrow Fe(OH)_3 + H^+ + e^-$$

$$e_{Fe(OH)_2|Fe(OH)_3} = 0.271 - 0.059pH$$

Iron does not corrode below the horizontal line at −0.44 V vs. SHE. The vertical lines in Reaction (4) represent a chemical reaction without the exchange of electrons. The pH at which this reaction occurs is calculated from the equilibrium constant. The sloping lines in Fig. 2.21a and b are constructed from the processes described in Reactions (2), (3), (6), (7), and (9). The stability of iron in this region increases as the solution pH increases.

2.11.5 Construction of Pourbaix diagram for nickel

The equilibrium equations for a nickel system used to construct the boundaries of the areas presented in Fig. 2.22a and b are given in Table 2.5. The boundaries between areas represent the equilibrium between the stable chemical species and the chemical species that participate in the chemical reaction. The regions in Fig. 2.22a and b are labeled as immunity, corrosion, and passivation regions. Nickel possesses typical metallic properties with high electrical and thermal conductivities. It is resistant to attack by air or

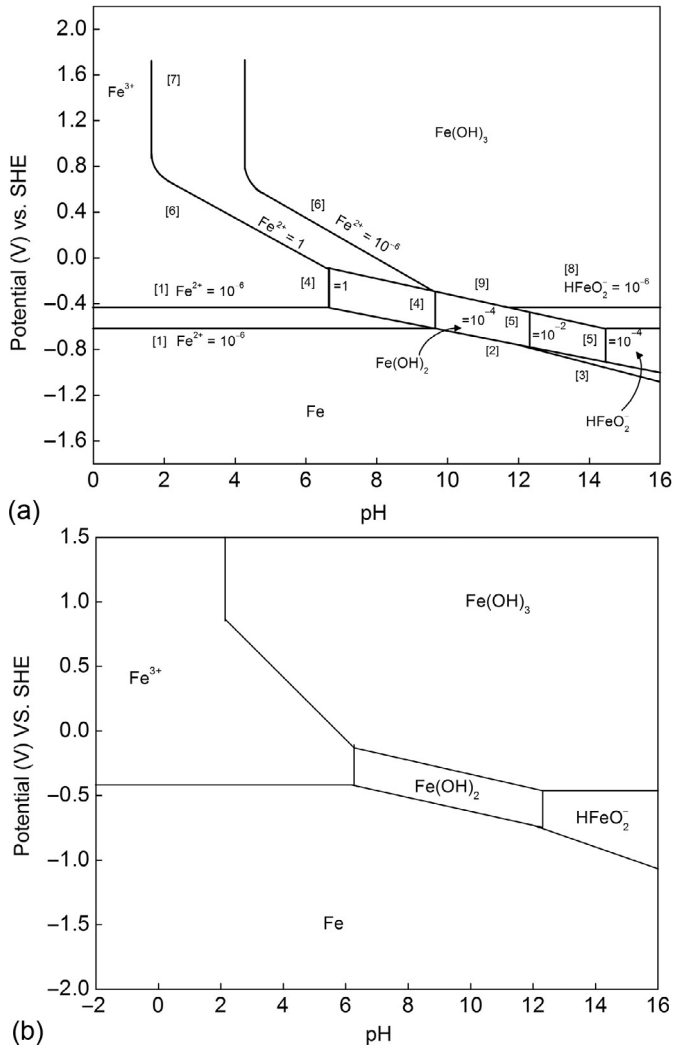

Fig. 2.21 (a and b) Pourbaix diagrams for iron.

water at ordinary temperatures and is used as a protective coating in the galvanizing industry.

The metal dissolves in dilute mineral acids. It passivates only in nitric acid. At low nonoxidizing potentials, Ni is stable and immune to corrosion attack. The corrosion areas represent regions where the metal is susceptible to corrosion, and is transformed into stable cationic (Ni^{2+}) or anionic species ($HNiO_2^-$). In the passive region, the Ni is coated with oxides NiO_2 or Ni_2O_3. NiO_2 is insoluble in water, but dissolves in acids at

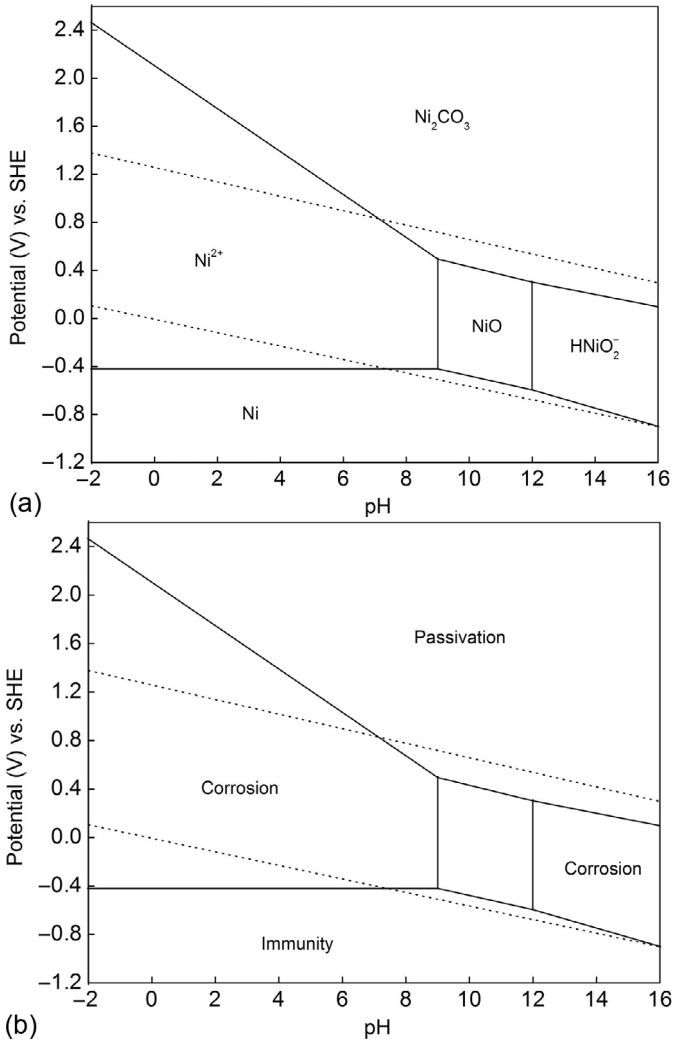

Fig. 2.22 (a and b) Pourbaix diagram for nickel showing the immunity, corrosion, and passivation regions.

Table 2.5 Various Equilibrium Reactions for the Ni System

Reaction	Relationship Between *E* and pH
(1) $Ni = Ni^{2+} + 2e^-$	$E = -0.250 + 0.0296\log[Ni^{2+}]$
(2) $Ni + 2H_2O = HNiO_2^- + 3H^+ + 2e^-$	$E = 0.648 + 0.0296\log[HNiO_2^-] - 0.0887pH$
(3) $Ni + H_2O = NiO + 2H^+ + 2e^-$	$E = 0.110 - 0.0591pH$
(4) $2Ni_2^+ + 3H_2O = Ni_2O_3 + 6H^+ + 2e^-$	$E = 1.753 - 0.0591\log[Ni^{2+}] - 0.1774pH$
(5) $2NiO + H_2O = Ni_2O_3 + 2H^+ + 2e^-$	$E = 1.020 - 0.0591pH$
(6) $Ni^{2+} + 2H_2O = HNiO^{2-} + 3H^+$	$\log[HNiO^{2-}]/[Ni^{2+}] = -30.40 + 3pH$
(7) $Ni^{2+} + H_2O = NiO + 2H^+$	$\mathrm{Log}[Ni^{2+}] = 12.18 - 2pH$
(8) $NiO + H_2O = HNiO^{2-} + H^+$	$\log[HNiO^{2-}] = -17.99 + pH$
(a) $2H_2O + 2e^- = H_2 + 2OH^-$	$E = -0.0591pH$
(b) $O_2 + 2H_2O + 4e^- = 4OH^-$	$E = 1.229 - 0.0591pH$

potentials higher than 0.4 V vs. SHE. NI^{2+} cation is stable at a low pH, while $HNiO_2^-$ anion is stable at high pH. NiO is stable at pH between 9 and 12.

2.12 CASE STUDIES

2.12.1 Activity coefficients

The dissociation constant of a weak acid is defined as:

$$K_{HA} = \frac{a_{H^+}\, a_{A^-}}{a_{HA}} \tag{2.70}$$

Equation (2.70) contains the ions activity a_{H^+} and a_{A^-} instead of the concentration of the ions C^+ and C^- [2,20]. Once the activity coefficients are defined, the dissociation constant remains the same and does not depend on the total concentration of the electrolyte. Table 2.6 summarizes the methods used to define the activities in electrolytes.

The activity is defined as a product of the concentration and the variable defined as activity coefficient. Ionic activities of the individual ions are given by:

$$a_+ = n_+ f_\pm (m_{salt}/m_o) \tag{2.71}$$

$$a_- = n_- f_\pm (m_{salt}/m_o) \tag{2.72}$$

where n_+ is the number of cations, $f_\pm$ is the mean molal activity coefficient, and the ratio (m_{salt}/m_o) is the molal concentration. The activity coefficients cannot be determined from experimental data. Also, the activity of the single ionic species cannot be estimated using the activity equations. Using the equations, one can calculate only the product of the activities of all ions of a given electrolyte. The mean activity is a geometrical mean activity of the positive and negative ions in the electrolyte. If any electrolyte dissociates into A^+ positive and B^- negative ions, the mean activity is defined as:

$$a_\pm = \left(a_+^{A^+}\, a_-^{B^-}\right)^{1/(A^+ + B^-)} \tag{2.73}$$

For a binary electrolytes, the above expressions simplifies to:

$$a_\pm = \sqrt{(a_+ a_-)} \tag{2.74}$$

Table 2.6 Methods Used to Define the Composition of the Electrolyte

Unit	Definition	Concentration	Activity
Molarity	Mole/liter of solution	C	a_c
Molality	Mole/kg of solvent	m	a_m
Mole fraction	Number of moles of solute/total number of moles in solution	N	a_N

The mean molal activity coefficients of any electrolyte that dissociates into A^+ positive and B^- negative ions are estimated using a similar equation:

$$f_{\pm} = \left(f_{+}^{A^+} a_{f_-}^{B^-}\right)^{1/(A^+ + B^-)} \tag{2.75}$$

or for binary electrolytes:

$$f_{\pm} = \sqrt{(f_{+} f_{-})} \tag{2.76}$$

Problem 2.1

Using the mean molal activity coefficients listed in Table 2.7, calculate the activities of the following ions at 298 K in:

(a) 0.01 molal aqueous solutions of HNO_3
(b) 0.01 molal aqueous solutions of $ZnCl_2$
(c) 0.1 molal aqueous solutions of $MgCl_2$

Table 2.7 Mean Molal Activity Coefficients at 25 °C

m_{salt}/m_o	0.001	0.003	0.01	0.03	0.1	0.3	1	3	10
HNO_3	0.97	0.94	0.9	0.85	0.79	0.74	0.72	0.91	
$LiNO_3$	0.97	0.94	0.9	0.85	0.79	0.74	0.74	0.97	2.44
$AgNO_3$		0.94	0.9	0.84	0.73	0.61	0.43	0.25	0.11
$Cu(NO_3)_2$					0.51	0.44	0.46	0.90	
$Al(NO_3)_3$					0.20	0.15	0.19	1.02	
LiOH			0.91	0.83	0.76	0.67	0.55	0.49	
NaOH				0.85	0.77	0.71	0.68	0.78	3.23
HCl	0.97	0.94	0.90	0.84	0.80	0.76	0.81	1.32	10.40
LiCl	0.96	0.94	0.90	0.84	0.79	0.74	0.80	1.34	9.40
NH_4Cl	0.97	0.94	0.90	0.83	0.77	0.69	0.60	0.56	
NaCl	0.97	0.94	0.90	0.85	0.78	0.71	0.66	0.71	
KCl		0.94	0.90	0.85	0.77	0.69	0.60	0.57	
$MgCl_2$					0.53	0.48	0.57	2.32	
$CuCl_2$		0.82	0.72	0.62	0.51	0.43	0.42	0.52	
$ZnCl_2$		0.81	0.71	0.62	0.52	0.43	0.34	0.29	0.90
$FeCl_2$					0.52	0.45	0.51		
$NiCl_2$					0.52	0.46	0.54	1.69	
$AlCl_2$					0.34	0.30	0.54		
H_2SO_4	0.83	0.61	0.54	0.40	0.27	0.18	0.13	0.14	
Li_2SO_4					0.47	0.36	0.28	0.29	
Na_2SO_4	0.89	0.82	0.71	0.59	0.45	0.32	0.20	0.14	
K_2SO_4	0.89	0.81	0.71	0.59	0.44	0.32			
$MgSO_4$					0.15	0.09	0.05	0.05	0.56
$CuSO_4$	0.74	0.63	0.44	0.25	0.15	0.08	0.04	0.04	
$ZnSO_4$	0.70	0.54	0.39	0.24	0.15	0.08	0.04	0.04	
$NiSO_4$					0.15	0.08	0.04		
$Al_2(SO_4)_3$					0.04	0.02	0.02		

Solution:

(a) $HNO_3 \rightleftarrows H^+ + NO_3^-$

$a_+ = n_+ f_\pm (m_{salt}/m_o)$

$a_- = n_- f_\pm (m_{salt}/m_o)$

$a_{H^+} = 1 \times 0.9 \times 0.01 = 0.009$

$a_{NO_3^-} = 1 \times 0.9 \times 0.01 = 0.009$

(b) $ZnCl_2 \rightleftarrows Zn^{2+} + 2Cl^-$

$a_{Zn^{2+}} = 1 \times 0.71 \times 0.01 = 0.0071$

$a_{Cl^-} = 2 \times 0.71 \times 0.01 = 0.0142$

(c) $MgCl_2 \rightleftarrows Mg^{2+} + 2Cl^-$

$a_{Mg} = 1 \times 0.53 \times 0.1 = 0.053$

$a_{Cl^-} = 2 \times 0.53 \times 0.1 = 0.106$

2.12.2 Evaluation of theoretical tendency of metals to corrode

Problem 2.2

Using the free-energy data given in Table 2.8, calculate the standard equilibrium potentials of:

(a) Pb^{2+}/Pb

(b) Zn^{2+}/Zn

(c) Ni^{+2}/Ni

Solution:

(a)

$Pb^{2+} + 2e^- = Pb$

$$\Delta G^o = \left(\sum n_i \mu_i\right)_{\text{Products}} - \left(\sum n_i \mu_i\right)_{\text{Reactants}}$$

$\Delta G^o = \mu_{Pb} - \mu_{Pb^{2+}}$

$\Delta G^o = 0 - (-24.3) = 24.3\,\text{kJ/mol}$

$\Delta G^o = -nFE^o$

$$e^o_{Pb^{2+}|Pb} = -\frac{\Delta G^o}{nF} = -\frac{24.3 \times 1000}{2 \times 96485} = -0.126\,\text{V vs. SHE}$$

Table 2.8 Standard Chemical Potentials (kJ/mol) of Ions in Aqueous Solution at 25 °C Relative to the Hydrogen Ion

Cation	μ^m	Anion	μ^m
Ag^+	+77.1	Br^-	−102.8
Al^{3+}	−483.1	Cl^-	−131.1
Au^{3+}	+ 410.8	F^-	−274.8
Ca^{2+}	+ 555.1	I^-	−51.6
Cd^{2+}	−77.6	OH^-	−157.2
Cr^{2+}	−164.6	S^{2-}	+98.0
Cr^{3+}	−205.0	HS^-	+12.3
Cu^+	+ 50.4	CN^-	+163.7
Cu^{2+}	+ 66.6	CO_3^{2-}	−528.7
Fe^{2+}	−84.9	ClO_4^- MnO_4^-	−44.8
Fe^{3+}	−10.6	CrO_4^-	−717.0
Hg(I) as Hg_2^{2+}	+162.5		−420.8
Mg^{2+}	−450.9	NO_2^-	−35.3
NH_4^+	−79.3	NO_3^-	−109.8
Na^+	−261.8	PO_4^{3-}	−1008.0
Ni^{2+}	−48.2	SO_4^{2-}	−736.6
Pb^{2+}	−24.3		
Pb^{4+}	−824.1		
Pt^{2+}	+231.0		
Sn^{2+}	−26.3		
Sn^{4+}	+ 2.9		
Ti^{2+}	−157.0		
Zn^{2+}	−147.2		

(b)

$$Zn^{2+} + 2e^- \rightarrow Zn$$

$$\Delta G^o = \mu_{Zn} - \mu_{Zn^{2+}}$$

$$\Delta G^o = 0 - (-147.2) = +147.2 \frac{kJ}{mol}$$

$$e^o_{Zn^{2+}|Zn} = -\frac{\Delta G^o}{nF} = -\frac{147.2 \times 1000}{2 \times 96485} = -0.763 V \text{ vs. SHE}$$

(c)

$$Ni^{2+} + 2e^- \rightarrow Ni \quad \Delta G^o = \mu_{Ni} - \mu_{Ni^{2+}}$$

$$\Delta G^o = 0 - (-48.2) = 48.2 \frac{kJ}{mol}$$

$$e^o_{Ni^{2+}|Ni} = -\frac{\Delta G^o}{nF} = -\frac{48.2 \times 1000}{2 \times 96485} = -0.250 V \text{ vs. SHE}$$

Problem 2.3

Calculate the standard equilibrium single potentials using Gibbs free-energy data given in Table 2.8 for:
(a) Cu^{2+}/Cu
(b) Fe^{2+}/Fe

Solution:

(a)

$$Cu^{2+} + 2e^- \rightleftarrows Cu$$

$$\Delta G^o = \mu_{Cu} - \mu_{Cu^{2+}} = 0 - 66.6 = -66.6\,kJ/mol \rightarrow \Delta G^o = -nFe^o$$

$$e^o = -\Delta G^o/nF = \frac{66.6 \times 1000}{2 \times 96485} = 0.345\,V \text{ vs. SHE}$$

(b)

$$Fe^{2+} + 2e^- \rightleftarrows Fe$$

$$\Delta G^o = -nFe^o$$

$$\Delta G^o = \mu_{Fe} - \mu_{Fe^{2+}} = 0 - (-84.9) = +84.9\,kJ/mol$$

$$e^o_{Fe^{2+}|Fe} = -\Delta G^o/nF = -\frac{84.9 \times 1000}{2 \times 96500} = -0.44\,V \text{ vs. SHE}$$

Problem 2.4

Calculate the half-cell potential of Ni in 0.1 M $NiCl_2$ solution. The half-cell is represented as: $Ni\,|\,Ni^{2+}$, Cl^- (0.1 M).

Solution:

$$Ni^{2+} + 2e^- \rightarrow Ni \quad e^o_{Ni^{2+}|Ni} = -0.250\,V \text{ vs. SHE}$$

$$e_{Ni^2|Ni} = e^o_{Ni^{2+}|Ni} - 2.303\frac{RT}{2F}\log\left(\frac{a_{Ni}}{a_{Ni^{2+}}}\right) = -0.250 + \frac{0.059}{2}\log(a_{Ni^{2+}})$$

$$e_{Ni^2|Ni} = -0.250 + \frac{0.059}{2}\log(0.1\,M) = -0.280\,V \text{ vs. SHE}$$

Problem 2.5

If one mole of tin is consumed in the corrosion cell $Sn/Sn^{2+}//Cu^{2+}/Cu$, calculate the change of the Gibbs free-energy, ΔG.

Solution:

$$Sn^{2+} + 2e^- \rightarrow Sn \quad e^o_{Sn^{2+}|Sn} = -0.138\,V \text{ vs. SHE}$$
$$Cu^{2+} + 2e^- \rightarrow Cu \quad e^o_{Cu^{2+}|Cu} = 0.337\,V \text{ vs. SHE}$$

Tin will corrode when coupled with the copper.

$$E^o_{cell} = e^o_{Cu^{2+}|Cu} - e^o_{Sn^{2+}|Sn} = 0.337 + 0.138 = 0.475\,V \text{ vs. SHE}$$

The Gibbs free-energy change when one mole of tin is consumed is:

$$\Delta G = -nFE^o = -2 \times 96,485 \times 0.475 = -91.7\,kJ$$

Problem 2.6

Estimate the equilibrium constant for the reaction:

$$2Fe^{3+} + Zn^{2+} \rightarrow 2Fe^{2+} + Zn$$

Solution:

The half cell reactions are:

$$Fe^{3+} + e^- \rightarrow Fe^{2+} \quad e^o_{Fe^{3+}|Fe^{2+}} = 0.771 \text{ V vs. SHE}$$
$$Zn^{2+} + 2e^- \rightarrow Zn \quad e^o_{Zn^{2+}|Zn} = -0.762\,V \text{ vs. SHE}$$

Because

$$\Delta G^o = -2.303RT \ln K = -nFE^o_{cell},$$

$$\log K = \frac{nE^o_{cell}}{0.059}$$

The electrode potentials for the individual half-cell reactions are:

$$e_{Fe^{3+}|Fe^{2+}} = 0.771 - 2.303\frac{RT}{2F}\log\left(\frac{a_{Fe^{2+}}}{a_{Fe^{3+}}}\right)$$

$$e_{Zn^{2+}|Zn} = -0.762 - 2.303\frac{RT}{2F}\log\left(\frac{a_{Zn}}{a_{Zn^{2+}}}\right)$$

Because the equilibrium constant is a ratio between the activities of the products and reactants, it follows that:

$$0.771 - 2.303\frac{RT}{2F}\log\left(\frac{a_{Fe^{2+}}}{a_{Fe^{3+}}}\right) = -0.762 - 2.303\frac{RT}{2F}\log\left(\frac{a_{Zn}}{a_{Zn^{2+}}}\right)$$

$$\log\left(\frac{a_{Fe^{2+}} + a_{Zn^{2+}}}{a_{Fe^{3+}} + a_{Zn}}\right) = \frac{(0.771 + 0.762) \times 2}{0.059} = 52 = \log(K)$$

$$K = 10^{52}$$

Problem 2.7

What is the emf of a cell constructed from a lead electrode in lead sulfate of pH = 1 with activity of $Pb^{2+} = 0.01$ and a hydrogen electrode?

Solution:

Cell Notation: $Pb\,|\,Pb^{2+}, SO_4^{2-}, H^+\,|\,H_2$

Cell Reactions (assumption):

$$Pb \rightarrow Pb^{2+} + 2e^- \text{ (anode)}$$

$$2H^+ + 2e^- \rightarrow H_2 \text{ (cathode)}$$

$$Pb + 2H^+ \rightarrow Pb^{2+} + H_2 \text{ (overall)}$$

$$e_{H^+|H_2} = 0 - 2.303\frac{RT}{2F}\log\left(\frac{P_{H_2}}{(a_{H^+})^2}\right)$$

$$e_{Pb|Pb^{2+}} = 0.126 - 2.303\frac{RT}{2F}\log\left(\frac{a_{Pb^{2+}}}{a_{Pb}}\right)$$

$$E_{cell} = 0.126 - 2.303\frac{RT}{2F}\log\left(\frac{a_{Pb^{2+}}}{(a_{H^+})^2}\right)$$

$$E_{cell} = 0.126 - \frac{0.059}{2}\log\left(\frac{0.01}{(0.1)^2}\right) = 0.126 \text{ V vs.SHE}$$

The cell potential is positive, indicating that the reaction proceeds spontaneously. The lead will corrode, while the hydrogen electrode will serve as the cathode.

Problem 2.8

Determine whether tin is stable in 10^{-6} M Sn^{2+} acid solution of pH = 2. Estimate (a) the Gibbs free-energy change and (b) the cell potential for the corrosion cell. The activity coefficients are assumed to be 1. The hydrogen pressure is 1 atm.

Solution:

Half-cell reactions:

$$Sn^+ \rightarrow Sn^{2+} + 2e^- \text{ (anode)}$$

$$2H^+ + 2e^- \rightarrow H_2 \text{ (cathode)}$$

$$Sn + 2HCl \rightarrow SnCl_2 + H_2 \text{ (overall)}$$

$$e_{H^+|H_2} = 0 - 2.303\frac{RT}{2F}\log\left(\frac{P_{H_2}}{(a_{H^+})^2}\right)$$

$$e_{Sn|Sn^{2+}} = 0.138 - 2.303\frac{RT}{2F}\log\left(\frac{a_{Sn^{2+}}}{a_{Sn}}\right)$$

$$E_{cell} = e_a + e_c$$

$$E_{\text{cell}} = 0 + 0.138 - 2.303\frac{RT}{2F}\log\left(\frac{P_{H_2}a_{Sn^{2+}}}{(a_{H^+})^2 a_{Sn}}\right)$$

$$E_{\text{cell}} = 0.138 - \frac{0.059}{2}\log\left(\frac{10^{-6}}{(10^{-2})^2}\right) = 0.197\,\text{V vs. SHE}$$

The Gibbs free-energy is calculated by using the Eq. (2.45):

$$-\frac{\Delta G}{nF} = E_{\text{cell}} = \left[e^{o}_{H^+|H_2} + \frac{RT}{nF}\ln\left(\frac{a^2_{H^+}}{P_{H_2}}\right)\right] - \left[e^{o}_{M^{n+}|M} + \frac{RT}{nF}\ln\left(a_{M^{n+}}\right)\right] \qquad (2.45)$$

or

$$\Delta G_{Sn} = -nFE_{\text{cell}} = -2 \times 96{,}500 \times 0.197 = -38.021\,\frac{\text{kJ}}{\text{mol}}$$

Because Gibbs free-energy change is negative, tin dissolves at pH = 2.

Problem 2.9

For the cell at 25 °C, $Cu\,|\,Cu^{2+}$ $(a=1)//Fe^{2+}\,|\,Fe$ $(a=1)$ determine if the reaction will proceed spontaneously as written?

Cell Reactions:

Solution:

$$Cu \rightarrow Cu^{2+} + 2e^-$$

$$Fe^{2+} + 2e^- \rightarrow Fe$$

$$E^{o}_{\text{cell}} = e^{o}_{Fe^{2+}|Fe} + e^{o}_{Cu|Cu^{2+}} = -0.440 - 0.337 = -0.777\,\text{V vs. SHE}$$

$$\Delta G^{o} = -nFE^{o}_{\text{cell}} = -2 \times 96{,}485 \times (-0.777) = 150\,\frac{\text{kJ}}{\text{mol}} > 0$$

The reaction will not proceed spontaneously as written.

The spontaneous reaction is:

$$Cu^{2+} + Fe \rightarrow Cu + Fe^{2+}$$

Problem 2.10

Determine whether Fe is stable in 10^{-6} M aerated water solution of Fe^{2+} at a pH of 8. Estimate (a) the Gibbs free-energy change and (b) the cell potential of the corrosion cell. The activity coefficients are assumed to be 1. The hydrogen pressure is 1 atm.

Solution:

$$\mathrm{Fe} \rightarrow \mathrm{Fe}^{2+} + 2\mathrm{e}^- \quad (\text{anode})$$

$$\frac{1}{2}\mathrm{O_2} + \mathrm{H_2O} + 2\mathrm{e}^- \rightarrow 2\mathrm{OH}^- \quad (\text{cathode})$$

$$\mathrm{Fe(s)} + 1/2\mathrm{O_2(g)} + \mathrm{H_2O(l)} \rightarrow \mathrm{Fe(OH)_2(aq.)} \quad (\text{overall})$$

$$e_{\mathrm{O_2|OH^-}} = 0.401 - 2.303\frac{RT}{2F}\log\left(\frac{\left(a_{\mathrm{OH^-}}\right)^2}{\mathrm{P_{O_2}}}\right)$$

$$e_{\mathrm{Fe|Fe^{2+}}} = 0.440 - 2.303\frac{RT}{2F}\log\left(\frac{a_{\mathrm{Fe^{2+}}}}{a_{\mathrm{Fe}}}\right)$$

$$E_{\mathrm{cell}} = 0.401 + 0.440 - 2.303\frac{RT}{2F}\log\left(\frac{\left(a_{\mathrm{OH^-}}\right)^2 a_{\mathrm{Fe^{2+}}}}{\mathrm{P_{O_2}}\, a_{\mathrm{Fe}}}\right)$$

This simplifies to:

$$E_{\mathrm{cell}} = 0.841 - \frac{0.059}{2}\log\left(10^{-6}\left(10^{-6}\right)^2\right) = 1.372\,\mathrm{V\ vs.\ SHE}$$

The Gibbs free-energy is calculated by using the Eq. (2.45)

$$-\frac{\Delta G}{nF} = E_{\mathrm{cell}} = \left[e^{\mathrm{o}}_{\mathrm{H^+|H_2}} + \frac{RT}{nF}\ln\left(\frac{a_{\mathrm{H^+}}{}^2}{\mathrm{P_{H_2}}}\right)\right] - \left[e^{\mathrm{o}}_{\mathrm{M^{n+}|M}} + \frac{RT}{nF}\ln\left(a_{\mathrm{M^{n+}}}\right)\right]$$

$$\Delta G_{\mathrm{Fe|O_2}} = -nFE = -2 \times 96{,}485 \times 1.372 = -264.8\,\frac{\mathrm{kJ}}{\mathrm{mol}}$$

Because the Gibbs free-energy is negative, the reaction will proceed spontaneously as written. Iron will dissolve in aerated solution at pH of 8.

Problem 2.11

Estimate the theoretical tendency for zinc to corrode (emf) when immersed in 10^{-6} to 10^{-1} M $ZnCl_2$ solution at pH of 3. The corrosion cell is described as:

$$\mathrm{Zn(s)} + 2\mathrm{HCl(aq)} \rightarrow \mathrm{ZnCl_2(aq)} + \mathrm{H_2(g)}$$

Solution:

The overall reaction can be written as:

$$\mathrm{Zn} + 2\mathrm{H}^+ \rightarrow \mathrm{Zn}^{2+} + \mathrm{H_2}$$

The Nernst equations for the anode, cathode, and overall reactions are as follows:

$$e_{\mathrm{Zn|Zn^{2+}}} = e^{\mathrm{o}}_{\mathrm{Zn|Zn^{2+}}} - 2.303\frac{RT}{2F}\log\left(\frac{a_{\mathrm{Zn^{2+}}}}{a_{\mathrm{Zn}}}\right) \quad (\text{anode})$$

$$e_{\mathrm{H^+|H_2}} = e^{\mathrm{o}}_{\mathrm{H^+|H_2}} - 2.303\frac{RT}{2F}\log\left(\frac{a_{\mathrm{H_2}}}{\left(a_{\mathrm{H^+}}\right)^2}\right) \quad (\text{cathode})$$

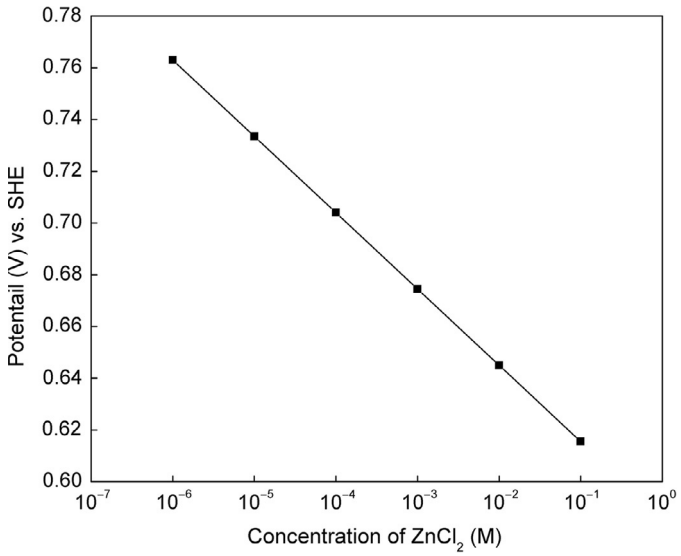

Fig. 2.23 Plot of $ZnCl_2$ concentrations vs. cell potential for the Zn corrosion cell.

$$E_{\text{cell}} = e_{H^+|H_2} + e_{Zn|Zn^{2+}} = e^{o}_{H^+|H_2} + e^{o}_{Zn|Zn^{2+}} - 2.303\frac{RT}{2F}\log\left(\frac{a_{H_2}a_{Zn^{2+}}}{(a_{H^+})^2 a_{Zn}}\right) \quad \text{(overall)}$$

$$E_{\text{cell}} = 0 + 0.762 - \frac{0.059}{2}\log\left(\frac{a_{Zn^{2+}}}{(a_{H^+})^2}\right)$$

For pH 3, the above equation can be written as:

$$E_{\text{cell}} = 0.762 - \frac{0.059}{2}\log(a_{Zn^{2+}}) - 0.059\text{pH}$$

By substituting the $ZnCl_2$ concentrations at pH = 3 in the above expression, the tendency of zinc to corrode in volts was calculated and presented in Fig. 2.23. The results indicate that the tendency of zinc to corrode increases with decreasing the concentration of zinc ions at the electrode interface.

Problem 2.12

Estimate the hydrogen pressure (fugacity) necessary to stop the corrosion of cobalt in 0.1 M Co^{2+} solution at pH of 1, 3, 5, and 7.

Solution:

To stop the corrosion process, the EMF of the cell should be zero or positive. The standard equilibrium potential for the reaction:

$$Co \rightarrow Co^{2+} + 2e^- \text{ is } 0.277\,V \text{ vs. SHE.}$$

The Nernst equation for the reaction:

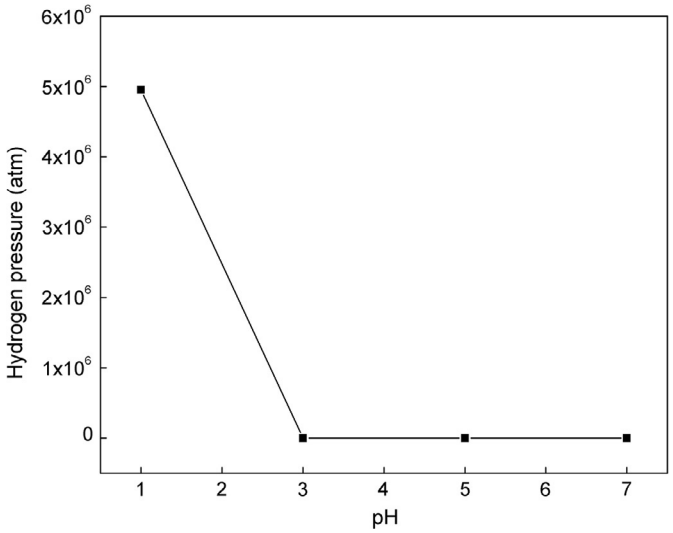

Fig. 2.24 Dependence of fugacity on pH for the cobalt system.

$$Co + 2H^+ \rightarrow Co^{2+} + H_2$$

is written as:

$$E_{cell} = e^{o}_{Co|Co^{2+}} + e^{o}_{H^+|H_2} - 2.303\frac{RT}{2F}\log\left(\frac{a_{Co/Co^{2+}}\,P_{H_2}}{[a_{H^+}]^2}\right)$$

$$E_{cell} = 0.277 - \frac{0.059}{2}\log\left(\frac{[0.1]\times P_{H_2}}{[a_{H^+}]^2}\right) = 0$$

$$P_{H_2} = \frac{10^{\frac{0.277\times 2}{0.059}}(a_{H^+})^2}{0.1}$$

The hydrogen pressure necessary to stop corrosion of Co is calculated by substituting appropriate pH values in the above equation and equating to zero. The plot of pH vs. hydrogen pressure (Fig. 2.24) indicates that below pH = 3, the hydrogen pressure cannot stop cobalt from corroding. Thus, increasing hydrogen pressure is not a feasible solution to stop the corrosion of cobalt in acidic solutions.

Problem 2.13

Determine the tendency of zinc to corrode in 0.6 M $ZnCl_2$ solution at pH between 0 and 5.
Cell notation: $Zn|Zn^{2+}, Cl^-, H^+|H_2|Pt$

Cell reactions: $Zn \rightarrow Zn^{2+} + 2e^-$ (anode)

$$2H^+ + 2e^- \rightarrow H_2\,(\text{cathode})$$

Solution:

Zinc is oxidized at the anode and the H^+ is reduced at the cathode. The only terms that one should consider are those for the $Zn^{2+}$and the H^+ concentrations. The activities of

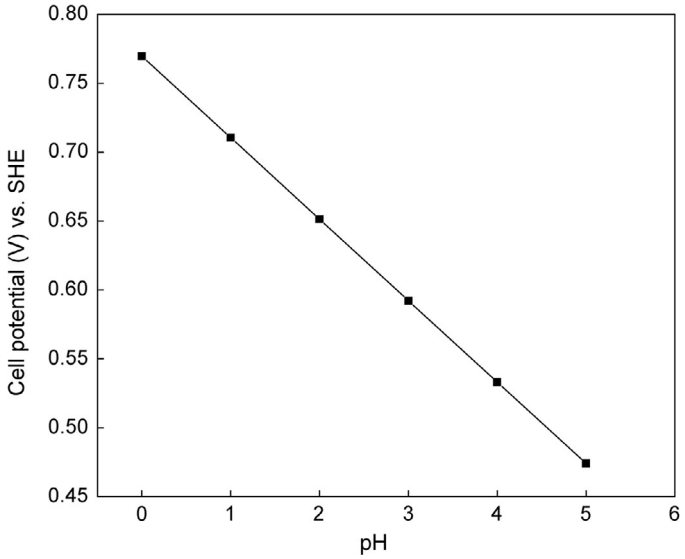

Fig. 2.25 Dependence of cell potential on pH for the Zn system.

metallic Zn and H_2 are assumed to be unity. Because Zn^{2+} is formed (product), it will appear in the numerator of the logarithmic term, and the H^+ (reactant) will appear in the denominator. The problem requires changing the H^+ concentration in line with the pH in order to calculate the cell potential at different pH values. The general Nernst equation for the overall reaction is:

$$E_{\text{cell}} = e^{\text{o}}_{\text{H}^+|\text{H}_2} + e^{\text{o}}_{\text{Zn}|\text{Zn}^{2+}} - 2.303\frac{RT}{2F}\log\left(\frac{a_{\text{Zn}^{2+}}}{(a_{\text{H}^+})^2}\right)$$

$$E_{\text{cell}} = 0 + 0.762 - \frac{0.059}{2}\log\left(\frac{a_{\text{Zn}^{2+}}}{(a_{\text{H}^+})^2}\right)$$

$$E_{\text{cell}} = 0.762 - \frac{0.059}{2}\log(0.6) - 0.059\text{pH}$$

$$E_{\text{cell}} = 0.769\,\text{V vs. SHE} \quad (\text{for pH} = 0)$$

The plot of pH vs. the cell potential (Fig. 2.25) indicates that, for an increase of the pH of 1, there is a decrease in the cell potential of 0.059 mV.

Problem 2.14

Calculate the theoretical tendency of nickel to corrode (in volts) with evolution of hydrogen when immersed in 0.02 M $NiCl_2$, acidified to pH = 6.

$$\text{Cell Notation}: \text{Ni}|\text{Ni}^{2+}, \text{Cl}^-, \text{H}^+|\text{H}_2|\text{Pt}$$

$$\text{Cell Reactions}: \text{Ni} \rightarrow \text{Ni}^{2+} + 2\text{e}^- \ (\text{anode})$$

$$\text{H}_2 \rightarrow 2\text{H}^+ + 2\text{e}^- \ (\text{cathode})$$

$$\text{Ni} + 2\text{H}^+ \rightarrow \text{Ni}^{2+} + \text{H}_2 \ (\text{overall})$$

Solution:

The Nernst equation for the overall reaction can be written as:

$$E_{\text{cell}} = e_{\text{H}^+|\text{H}_2} + e_{\text{Ni}|\text{Ni}^{2+}} = e^{\text{o}}_{\text{H}^+|\text{H}_2} + e^{\text{o}}_{\text{Ni}|\text{Ni}^{2+}} - 2.303\frac{RT}{2F}\log\left(\frac{\text{P}_{\text{H}_2} a_{\text{Ni}^{2+}}}{(a_{\text{H}^+})^2 a_{\text{Ni}}}\right)$$

$$E_{\text{cell}} = 0 + 0.250 + 2.303\frac{RT}{2F}\log\left(\frac{(a_{\text{H}^+})^2}{a_{\text{Ni}^{2+}}}\right)$$

$$E_{\text{cell}} = 0.250 + \frac{0.059}{2}\log\left(\frac{(10^{-6})^2}{0.02}\right)$$

$$E_{\text{cell}} = -0.05\,\text{V vs. SHE}$$

The Gibbs free-energy is calculated by using the expression:

$$\Delta G = -nFE$$

$$\Delta G = -2 \times 96,485 \times (-0.05) = 9.65\,\text{kJ/mol}$$

Nickel does not corrode at pH = 6.

Problem 2.15

Calculate the driving emf for the corrosion cell and write the spontaneous reaction for the following cell:

$$\text{Pt}||\text{Fe}^{3+}(\text{activity} = 0.1), \text{Fe}^{2+}(\text{activity} = 0.001), \text{Zn}^{2+}(\text{activity} = 0.01)\,||\,\text{Zn}$$

The iron redox reaction is assumed to be the cathode.

The half-cell reactions and the overall reaction are:

$$\text{Zn} \rightarrow \text{Zn}^{2+} + 2\text{e}^- \ (\text{anode})$$

$$2\text{Fe}^{3+} + 2\text{e}^- \rightarrow 2\text{Fe}^{2+} \ (\text{cathode})$$

$$\text{Zn} + 2\text{Fe}^{3+} \rightarrow \text{Zn}^{2+} + 2\text{Fe}^{2+} \ (\text{overall})$$

Solution:

The Nernst equations for the anode, cathode, and overall reactions are as follows:

$$e_{Zn|Zn^{2+}} = e^{o}_{Zn|Zn^{2+}} - 2.303\frac{RT}{2F}\log\left(\frac{a_{Zn^{2+}}}{a_{Zn}}\right) \quad \text{(anode)}$$

$$e_{Fe^{3+}|Fe^{2+}} = e^{o}_{Fe^{3+}|Fe^{2+}} - 2.303\frac{RT}{2F}\log\left(\frac{(a_{Fe^{2+}})^2}{(a_{Fe^{3+}})^2}\right) \quad \text{(cathode)}$$

$$E_{cell} = e_{Fe^{3+}|Fe^{2+}} + e_{Zn|Zn^{2+}}$$

$$= e^{o}_{Fe^{3+}|Fe^{2+}} + e^{o}_{Zn|Zn^{2+}} - 2.303\frac{RT}{2F}\log\left(\frac{(a_{Fe^{2+}})^2 a_{Zn^{2+}}}{(a_{Fe^{3+}})^2}\right) \quad \text{(overall)}$$

$$E_{cell} = 0.762 + 0.771 + 2.303\frac{RT}{2F}\log\left(\frac{(0.001)^2 0.01}{0.1}\right)$$

$$E_{cell} = 1.326\,\text{V vs. SHE}$$

The Gibbs free-energy is calculated by using the expression:

$$\Delta G = -nFE_{cell}$$

Because ΔG is negative, the Fe^{3+}cation will oxidize zinc to zinc ion by reducing itself to Fe^{+2}.

Problem 2.16

Calculate the theoretical tendency of cobalt to corrode (in volts) in deaerated water of pH = 5, 6, 7, and 8. Assume corrosion products are hydrogen and $Co(OH)_2$. The solubility product: $K_{sp}^{Co(OH)_2} = [Co^{2+}][OH^-]^2 = 1.6 \times 10^{-17}$.

$$\text{Cell Notation}: Co|Co^{2+}, H^+|H_2$$

Cell Reactions:

$$Co(OH)_2 \rightarrow Co^{2+} + 2OH^-$$

$$K_{sp}^{Co(OH)_2} = \left[Co^{2+}\right][OH^-]^2 = 1.6 \times 10^{-17}$$

$$\left[Co^{2+}\right] = \frac{1.6 \times 10^{-17}}{[10^{-pH}]^2}$$

$$Co \rightarrow Co^{2+} + 2e^- \text{ (anode)}$$

$$2H^+ + 2e^- \rightarrow H_2 \text{ (cathode)}$$

$$Co + 2H^+ \rightarrow Co^{2+} + H_2 \text{ (overall)}$$

$$e_{H^+|H_2} = 0 - 2.303\frac{RT}{2F}\log\left(\frac{P_{H_2}}{(a_{H^+})^2}\right)$$

Table 2.9 pH and Corresponding Potential of Cobalt System

pH	Potential (*V*) vs. SHE
5	0.132
6	0.014
7	−0.104
8	−0.222

$$e_{\mathrm{Co|Co^{2+}}} = 0.227 - 2.303\frac{RT}{2F}\log\left(\frac{a_{\mathrm{Co^{2+}}}}{a_{\mathrm{Co}}}\right)$$

$$E_{\mathrm{cell}} = 0.227 - 2.303\frac{RT}{2F}\log\left(\frac{a_{\mathrm{Co^{2+}}}}{(a_{\mathrm{H^{+}}})^2}\right) \tag{2.77}$$

Solution:

The Co^{2+} concentration is estimated at different pH from the K_{sp}. Next, the potential is calculated using Eq. (2.77) and presented in Table 2.9. Cobalt is stable at pH values 7 and 8 and starts to corrode at a pH of 6, as indicated by the positive potential.

Problem 2.17

Tin is immersed in a solution of $CuCl_2$ with activity of $Cu^{2+} = 0.2$. Determine the concentration of Sn^{2+} at which the corrosion will stop.

Solution:

$$\mathrm{Sn} \rightarrow \mathrm{Sn^{2+}} + 2\mathrm{e^-}$$

$$\mathrm{Cu^{2+}} \rightarrow 2\mathrm{e^-} + \mathrm{Cu}$$

$$\mathrm{Sn} + \mathrm{Cu^{2+}} \rightarrow \mathrm{Cu} + \mathrm{Sn^{2+}}$$

$$E^{\mathrm{o}}_{\mathrm{cell}} = e^{\mathrm{o}}_{\mathrm{Sn|Sn^{2+}}} + e^{\mathrm{o}}_{\mathrm{Cu^{2+}|Cu}}$$

$$E_{\mathrm{cell}} = E^{\mathrm{o}}_{\mathrm{cell}} - \frac{0.059}{2}\log\left(\frac{a_{\mathrm{Sn^{2+}}}}{a_{\mathrm{Cu^{2+}}}}\right)$$

The reaction stops when the cell emf is zero.

$$E_{\mathrm{cell}} = E^{\mathrm{o}}_{\mathrm{cell}} - \frac{0.059}{2}\log\left(\frac{a_{\mathrm{Sn^{2+}}}}{a_{\mathrm{Cu^{2+}}}}\right) = 0 \quad \frac{2\times 0.475}{0.059} = \log\left(\frac{a_{\mathrm{Sn^{2+}}}}{a_{\mathrm{Cu^{2+}}}}\right)$$

$$a_{\mathrm{Sn^{2+}}} = 10^{\frac{0.95}{0.059}} \times a_{\mathrm{Cu^{2+}}} = 2.53\times 10^{16}\,\mathrm{M}$$

The corrosion will stop when Sn^{2+} concentration reaches 2.53×10^{16} M at the electrode interface.

Problem 2.18

(a) Calculate the pressure (fugacity) of hydrogen required to stop corrosion of nickel immersed in 0.05 M $NiCl_2$, pH = 2.
(b) Compare the results for the fugacity to stop the corrosion of iron immersed in 0.05 M $FeCl_2$ at a pH of 2.

Solution:

(a) Ni in $NiCl_2$ at pH = 2
Cell Notation

$$Ni \rightarrow Ni^{2+} + 2e^- \text{ (anode)}$$
$$2H^+ + 2e^- \rightarrow H_2 \text{ (cathode)}$$
$$Ni + 2H^+ \rightarrow Ni^{2+} + H_2 \text{ (overall)}$$
$$e_{H^+|H_2} = 0 - 2.303\frac{RT}{2F}\log\left(\frac{P_{H_2}}{(a_{H^+})^2}\right)$$
$$e_{Ni|Ni^{2+}} = 0.250 - 2.303\frac{RT}{2F}\log\left(\frac{a_{Ni^{2+}}}{a_{Ni}}\right)$$
$$E_{cell} = 0 + 0.250 - 2.303\frac{RT}{2F}\log\left(\frac{P_{H_2}a_{Ni^{2+}}}{(a_{H^+})^2 a_{Ni}}\right)$$

This simplifies to:

$$E_{cell} = 0 = 0.250 + \frac{0.059}{2}\log\left(\frac{P_{H_2}a_{Ni^{2+}}}{(a_{H^+})^2}\right) = 0.250 - \frac{0.059}{2}\log\left(\frac{0.05P_{H_2}}{(a_{H^+})^2}\right)$$
$$\frac{0.500}{0.059} = \log\left(\frac{0.05P_{H_2}}{(10^{-2})^2}\right)$$
$$P_{H_2} = \frac{\left(10^{0.500/0.059}\right)(10^{-2})^2}{0.05} = 5.965 \times 10^5 \text{ atm}$$

(b) For $FeCl_2$ at a pH of 2:
Cell Notation:

$$Fe \rightarrow Fe^{2+} + 2e^- \text{ (anode)}$$
$$2H^+ + 2e^- \rightarrow H_2 \text{ (cathode)}$$
$$Fe + 2H^+ \rightarrow Fe^{2+} + H_2 \text{ (overall)}$$
$$e_{H^+|H_2} = 0 - 2.303\frac{RT}{2F}\log\left(\frac{P_{H_2}}{(a_{H^+})^2}\right)$$
$$e_{Fe|Fe^{2+}} = 0.440 - 2.303\frac{RT}{2F}\log\left(\frac{a_{Fe^{2+}}}{a_{Fe}}\right)$$

$$E_{\text{cell}} = 0 + 0.440 - 2.303\frac{RT}{2F}\log\left(\frac{P_{H_2} a_{Fe^{2+}}}{(a_{H^+})^2 a_{Fe}}\right)$$

This simplifies to:

$$E_{\text{cell}} = 0 = 0.440 + \frac{0.059}{2}\log\left(\frac{P_{H_2} a_{Fe^{2+}}}{(a_{H^+})^2}\right) = 0.440 - \frac{0.059}{2}\log\left(\frac{0.05 P_{H_2}}{(10^{-2})^2}\right)$$

$$\frac{0.880}{0.059} = \log\left(\frac{0.05 P_{H_2}}{(10^{-2})^2}\right)$$

$$P_{H_2} = \frac{\left(10^{\frac{0.880}{0.059}}\right)(10^{-2})^2}{0.05} = 1.645 \times 10^{12}\,\text{atm}.$$

The pressure to stop the Ni corrosion cell is much less than the pressure to stop the iron corrosion cell. Iron is more thermodynamically active with standard potential of −0.44 V vs. SHE when compared with nickel with standard electrode potential of $e^{o} = -0.250$ V vs. SHE.

2.12.3 Hydrogen and oxygen electrodes

Problem 2.19

Plot the half-cell potential for a hydrogen electrode at pH 0-14, pressure of hydrogen of 1 atm, and temperatures of 25, 30, 40 and 50 °C.

Solution:

For a hydrogen electrode, the reaction can be written as:

$$2H^+ + 2e^- \rightarrow H_2$$

The Nernst equation for this reaction is:

$$e_{H^+|H_2} = e^{o}_{H^+|H_2} - 2.303\frac{RT}{2F}\log\left(\frac{P_{H_2}}{(a_{H^+})^2}\right)$$

At 25 °C, the Nernst equation for the reaction becomes:

$$e_{H^+|H_2} = 0 - 0.059\text{pH}$$

By substituting the given temperature and pH values, the half-cell potential of the hydrogen electrode can be calculated. The results are presented in Table 2.10 and graphically shown in Fig. 2.26a and b.

Table 2.10 pH and Potential Relationship of the Hydrogen Electrode at Different Temperatures

pH	*E* (25 °C)	*E* (30 °C)	*E* (40 °C)	*E* (50 °C)
1	−0.059	−0.060	−0.062	−0.064
2	−0.118	−0.120	−0.124	−0.128
3	−0.177	−0.180	−0.186	−0.192
4	−0.237	−0.240	−0.248	−0.256
5	−0.296	−0.301	−0.311	−0.320
6	−0.355	−0.361	−0.373	−0.385
7	−0.414	−0.421	−0.435	−0.449
8	−0.473	−0.481	−0.497	−0.513
9	−0.532	−0.541	−0.559	−0.577
10	−0.591	−0.601	−0.621	−0.641
11	−0.650	−0.661	−0.683	−0.705
12	−0.710	−0.721	−0.745	−0.769
13	−0.769	−0.782	−0.807	−0.833
14	−0.828	−0.842	−0.869	−0.897

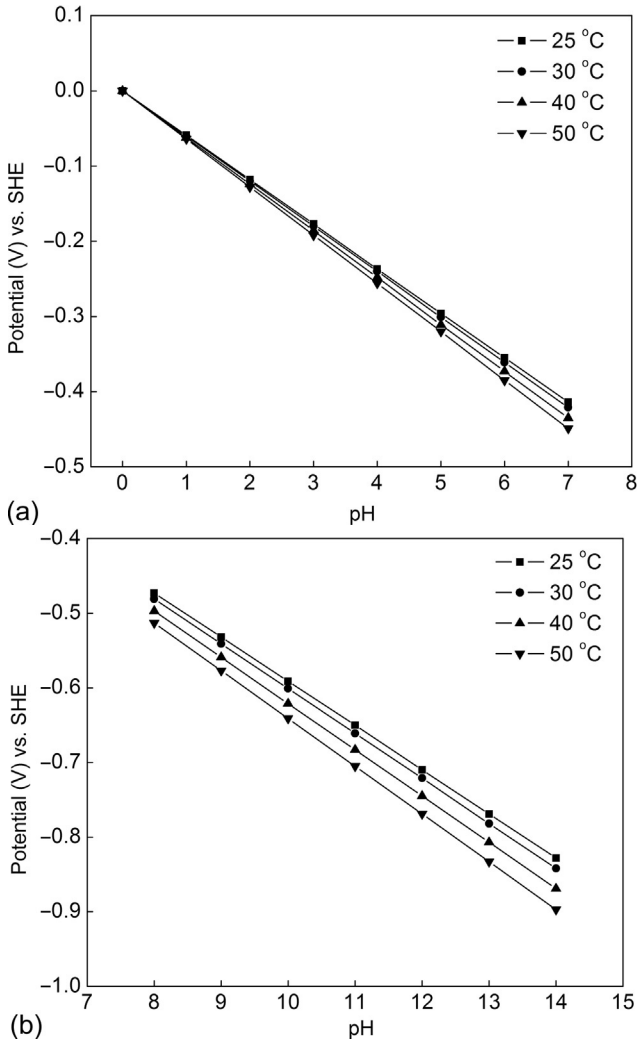

Fig. 2.26 Plot of pH vs. cell potential for the hydrogen electrode. (a) pH = 0-7 and (b) pH = 8-14.

Problem 2.20

The oxygen discharge electrode reactions at pH = 0 and pH = 14 are as follows:

$$2H_2O \rightarrow O_2 + 4H^+ + 4e^- \quad (pH = 0)$$
$$4OH^- \rightarrow O_2 + 2H_2 + 4e^- \quad (pH = 14)$$

For unit activity of H^+, the standard potential for the first discharge reaction is $e_1^o = 1.229$ V vs. SHE. Calculate the standard potential for the oxygen electrode, e_2^o, at pH = 14.

Solution:

The oxygen electrode reactions taking place at different pH values are as follows:

$$2H_2O \rightarrow O_2 + 4H^+ + 4e^- \ (pH = 0)$$
$$4OH^- \rightarrow O_2 + 2H_2O + 4e^- \quad (pH = 14)$$

The electrode potentials for the respective oxygen electrodes can be represented as:

$$e_1 = e^o + 0.059\log(a_{H^+}) \quad (pH = 0)$$
$$e_2 = e_2^o - 0.059\log(a_{OH^-}) \quad (pH = 14)$$

Because both reactions represent the oxygen electrode:

$$e_2 - e_1 = 0 = e_2^o - e_1^o + 0.059\log(a_{OH^-})(a_{H^+})$$
$$(a_{H^+})(a_{OH^-}) = K_w = 10^{-14}$$
$$e_2^o - e_1^o + 0.059\log\left(10^{-14}\right) = 0$$
$$e_2^o - e_1^o = +0.8288$$
$$e_1^o = e_2^o - 0.8288 = 0.401\,V$$
$$e_1^o = 1.2298 - 0.8288 = 0.401\ V \text{ vs. SHE}$$

The electrode potential, e^o, for the reaction $4OH^- \rightarrow O_2 + 2H_2O + 4e^-$ is 0.401 V vs. SHE.

Problem 2.21

Plot the half-cell potential of the hydrogen electrode in a solution of pH 7 with partial pressures of hydrogen of 0.5, 1, 1.5, 2, 3, and 5 atm at 25 °C. The cell notation is $Pt|H_2|H^+$

Solution:

The H_2/H^+ standard potential is equal to zero. By substituting the hydrogen partial pressure values in the Nernst equation one can obtain the potential of a hydrogen electrode under the conditions described in the problem. The general Nernst equation for the half-cell electrode reaction is:

$$e_{H^+|H_2} = e^o_{H^+|H_2} - 2.303\frac{RT}{2F}\log\left(\frac{(P_{H_2})}{(a_{H^+})^2}\right)$$

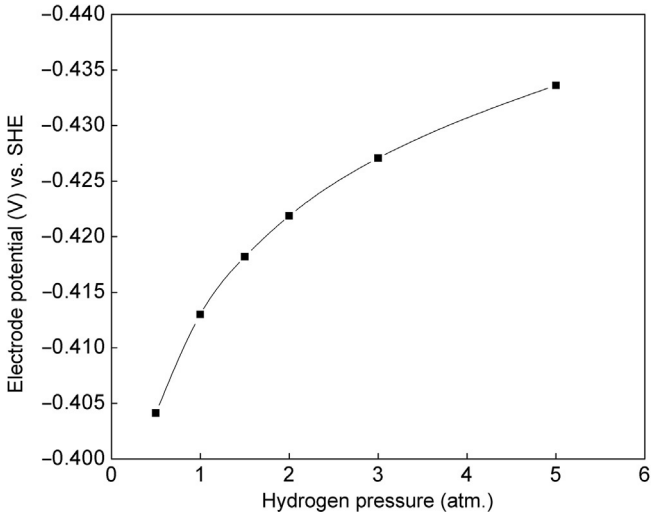

Fig. 2.27 Dependence of the hydrogen electrode potential on hydrogen pressure at pH 7.

Because under standard conditions, $e^{o}_{H^+|H_2} = 0$

$$e_{H^+|H_2} = 0 - 2.303\frac{RT}{2F}\log\left(\frac{P_{H_2}}{(10^{-7})^2}\right)$$

For the case of hydrogen partial pressure of 0.5 atm., the equation becomes:

$$e_{H^+|H_2} = 0 - \frac{0.059}{2}\log\left(\frac{0.5}{10^{-14}}\right)$$

$$e_{H^+|H_2} = -0.405 \text{ V vs. SHE}$$

Substituting the other hydrogen partial pressure values in the above equation, the respective half-cell potential values are obtained and shown in Fig. 2.27. The results indicate that by increasing the pressure from 0.5 to 5 atm., the hydrogen reference potential decreases by 30 mV at pH of 7.

EXERCISES

E2.1. Calculate the half-cell potential of cadmium in 0.1 M $CdCl_2$.

E2.2. Calculate the theoretical tendency of tin to corrode (in volts) with the evolution of hydrogen when immersed in 0.01 M $SnCl_2$ acidified to pH = 2, 3, 4, and 5.

E2.3. Plot the hydrogen pressure (fugacity) necessary to stop corrosion of nickel in 0.1 M Ni^{2+} solution at pH = 1, 3, 5, and 7.

E2.4. Plot the hydrogen pressure (fugacity) necessary to stop corrosion of tin in 0.1 M Sn^{2+} solution at pH = 1, 3, 5, and 7.

E2.5. Determine which electrode will corrode in a cell made up of iron and zinc electrodes when the cell is short circuited. The electrodes are immersed in a solution of Fe^{+2} and Zn^{+2} of equal activity.

E2.6. A cell, constructed from tin (anode) and a hydrogen electrode (cathode), is immersed in 0.2 M $SnCl_2$ solution. Estimate the cell potential as a function of pH (pH = 1, 3, 5, and 7).

E2.7. Calculate the theoretical tendency of zinc to corrode (in volts) with the evolution of hydrogen when immersed in 0.05 M $ZnCl_2$ at pH = 1 through 5.

E2.8. Plot the emf of an electrode constructed of zinc (anode) and a hydrogen electrode (cathode) immersed in 0.6 M $ZnCl_2$ at pH 0, 1, 2, 3, 4, and 5.

E2.9. Calculate the concentration of Zn^{2+} ions required to stop zinc corrosion when Zn is immersed in a solution of $FeCl_2$ with activity of $Fe^{2+} = 0.1$ M.

E2.10. (a) Calculate the cell potential of a concentration cell constructed from a zinc electrode in 0.2 M $ZnSO_4$ and 0.6 M $ZnSO_4$ solution. Neglect the liquid junction potential.

(b) Write the spontaneous reaction of the cell and indicate which electrode is the anode.

E2.11. If the concentration of H^+ decreases from 0.5 to 10^{-6} M, estimate how much the oxidizing power of the (MnO_4^-/Mn^{2+}) couple will be reduced.

E2.12. Determine whether iron is stable in an aqueous solution at pH = 3, 5, and 7. Plot the driving EMF and the Gibbs free-energy as a function of pH. Assume $P_{H_2} = 1$ atm. and $[Fe^{2+}] = 10^{-6}$ M.

REFERENCES

[1] H.H. Uhlig, R. Winston, Corrosion and Corrosion Control, third ed., John Wiley & Sons, New Jersey, 1985.

[2] L.I. Antropov, Theoretical Electrochemistry, Translated from Russian by Artavaz BeknazarovMir Publishers, Moscow, 1972.

[3] R.H. Perry, D. Green, Perry's Chemical Engineers' Handbook, seventh ed., McGraw-Hill, New York, 1997.

[4] J.M. West, Basics Corrosion and Oxidation, second ed., Holsted Press: A Division of John Wiley & Sons, New York, 1986.

[5] J.M. West, Electrodeposition and Corrosion Processes, D. Van Nostrand Co., New York, 1965

[6] D.R. Gaskell, Introduction to Metallurgical Thermodynamics, Taylor and Francis, United Kingdom, 1981.

[7] J.M. Smith, H.C. Van Ness, M.M. Abbot, Introduction to Chemical Engineering. Thermodynamics, seventh ed., McGraw Hill, New York, 2005.

[8] S.I. Sandler, Chemical and Engineering Thermodynamics, third ed., John Wiley & Sons, New York, 1999.

[9] D.A. Jones, Principles and Prevention of Corrosion, second ed., Prentice Hall, New Jersey, 1996.

[10] M.G. Fontana, Corrosion Engineering, McGraw Hill, New York, 1986.

[11] L.L. Shrier, Corrosion Control, second ed., Newnes-Butterworths, Sevenoaks, Kent, England, 1976.
[12] A.H. Bard, R. Parsons, J. Jordan, Standard Potentials in Aqueous Solutions, Marcel Dekker, New York, 1985.
[13] D.J.G. Ives, G.J. Janz, Reference Electrodes, NACE International, Houston, 1996.
[14] D.R. Lide, Handbook of Physics and Chemistry, CRC Press, New York, 1997.
[15] J.O.M. Bockris, R.A. Fredlein, A Workbook of Electrochemistry, Plenum Press, New York, 1973.
[16] H. Kaesche, Metallic Corrosion, NACE Publication. NACE International, Houston, 1985.
[17] D.J.G. Ives, G.J. Janz, Reference Electrodes: Theory and Practice, Academic Press, New York, 1961.
[18] M. Pourbaix, Atlas of Electrochemical Equilibria in Aqueous Solutions, NACE, Houston, 1974.
[19] M. Pourbaix, Lectures on Electrochemical Corrosion, Plenum Press, New York, 1971.
[20] J.O.M. Bockris, A.K.N. Reddy, Modern Electrochemistry, Plenum Press, New York, 1971.

CHAPTER 3

Electrochemical Kinetics of Corrosion

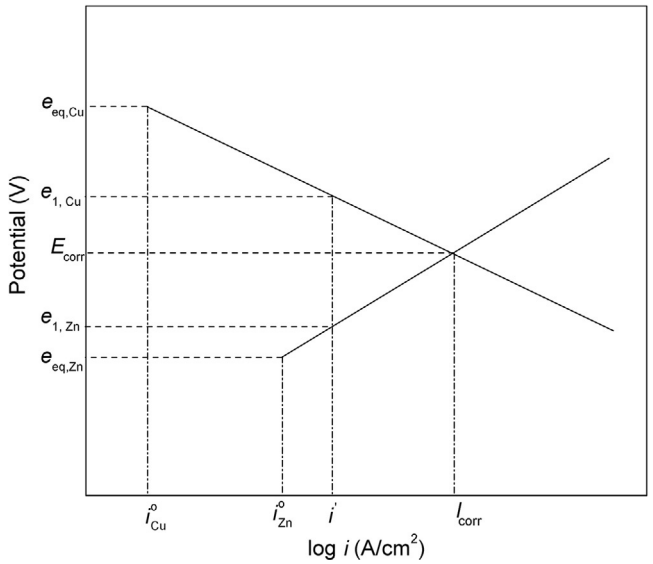

Chapter Contents

Corrosion Engineering
http://dx.doi.org/10.1016/B978-0-444-62722-3.00003-3

3.1 INTRODUCTION

This chapter outlines the basic aspects of interfacial electrochemical polarization and their relevance to corrosion. A discussion of the theoretical aspects of electrode kinetics lays a foundation for the understanding of the electrochemical nature of corrosion. Topics include mixed potential theory, reversible electrode potential, exchange current density, corrosion potential, corrosion current, and Tafel slopes. The theoretical treatment of electrochemistry in this chapter is focused on electrode kinetics, polarization behavior, mass transfer effects, and their relevance to corrosion. Analysis and solved corrosion problems are designed to understand the mechanisms of corrosion processes, learn how to control corrosion rates, and evaluate the protection strategies at the metal-solution interface [1–7].

3.2 OHMIC POLARIZATION

The passage of an electric current in any electrochemical corrosion system is associated with the change of the electrode potential from its initial equilibrium value. The potential of an electrolytic cell, E_{ec}, at any current density is higher than the equilibrium cell potential, E_{cell}.

$$E_{ec} \geq E_{cell} \tag{3.1}$$

The difference between the electrolytic cell potential and the potential (voltage) when the current passes in the external circuit is due to ohmic losses. The main sources of ohmic losses are the resistance of the electrolyte, contact resistances of the leads, and the film formed on the electrode-electrolyte interface. The circuit ohmic resistance decreases the equilibrium potential by an amount equal to iR, where "i" is the current passing between the working and counter electrode and R is the net resistance in the circuit. Current passes through the cell only when the voltage applied to the system consists of thermodynamically controlled equilibrium potential and the potential drop that compensates for the ohmic losses. The potential drop is not thermodynamically controlled and depends on the current density and the resistance in the circuit. It approaches zero when the current is shut off, and increases immediately when the current is switched on [8,9]. The iR drop in volts is equal to $i^{o}l/k$, where "i^{o}" is the current density in A/cm^2, "l" is the thickness of the electrolyte in cm, and "k" is the specific conductivity of the electrolyte $1/\Omega$ cm. Various techniques are employed to measure the ohmic losses in an electrochemical cell. These measurement techniques include current interruption and four probe methods, among others that are discussed later in the book [8–10].

If the electrochemical system generates a current (galvanic cell), then the experimentally observed cell potential decreases with the passage of current. In this case, the resistance in the galvanic cell controls the voltage drop, which compensates for the resistance inside the cell and introducing a loss in electrical energy production. When a net current

flows through any corrosion system, the main factor causing a change in the cell voltage is not the voltage drop, but rather the variation of the potential with respect to the applied current density, which is also called the electrode polarization.

3.3 ELECTROCHEMICAL POLARIZATION

When a metal, M, is immersed in a solution containing its ions, M^+, several reactions may occur. The metal atoms may lose electrons (oxidation reaction) to become metallic ions, or the metal ions in solution may gain electrons (reduction reaction) to become solid metal atoms. The equilibrium conditions across the metal-solution interface controls which reaction, if any, will take place. When the metal is immersed in the electrolyte, electrons will be transferred across the interface until the electrochemical potentials or chemical potentials (Gibbs free-energies) on both sides of the interface are balanced, that is, $\mu_{\text{solution}} = \mu_{\text{electrode}}$ until thermodynamic equilibrium is reached. The charge transfer rate at the electrode-electrolyte interface depends on the electric field across the interface and on the chemical potential gradient. At equilibrium, the net current is zero and the rates of the oxidation and reduction reactions become equal. The potential when the electrode is at equilibrium is known as the reversible half-cell potential or equilibrium potential, e_{eq}. The net equivalent current that flows across the interface per unit surface area when there is no external current source is known as the exchange current density, i^{o}.

The difference between the potential, E, when a net current flows through the electrochemical cell and the reversible half-cell potential, e_{eq}, is called the electrode polarization or simply the overpotential or overvoltage, η. The overvoltage represents the extent to which the electrode solution interface departs from the equilibrium potential value.

$$\eta = E - e_{\text{eq}} \tag{3.2}$$

The overvoltage depends on the current density. When there is no net current flow, the overvoltage is equal to zero. Electrochemical processes are heterogeneous reactions consisting of consecutive steps. The overvoltage controls the kinetics of the charge-transfer reaction at the interface and is associated with the slowest step, abbreviated as the rate determining step.

Electrochemical polarization experiments are performed to study the kinetics of charge-transfer reactions at the electrode-electrolyte interface. When cathodic current is applied to the electrode, the electrons accumulate in the metal as a result of the slow charge transfer. This phenomenon causes the cathodic polarization, η_{c}, to be always negative. Conversely, when electrons are removed from the metal as in the case of anode polarization, the polarization is always positive.

The transport of reactants to and from the electrode-electrolyte interface occurs during any electrochemical process. The electrode reactions involve at least one charge

transfer across the electrode-electrolyte interface. Due to the passage of current, these steps control the concentration of the reactants near the electrode. The change in composition alters the electrode potential resulting in electrode polarization. The concentration overvoltage, η_{conc}, results from a slow transport of reactants to and from the electrode interface and from the chemical transformation preceding the transport of ions. A special case of concentration polarization occurs when mass transport is an irreversible process, corresponding to the transport overpotential or diffusion overpotential, η_d. When a slow chemical reaction causes concentration polarization and all other processes proceed reversibly, it is called chemical or reaction overvoltage, η_r. When all the steps of the electrode reaction except the charge transfer proceed reversibly, the electrode polarization is called the charge transfer or electrochemical overpotential, η_e. If the rate-determining step is the incorporation of metallic ions in the electrode crystal lattice, the electrode polarization is called the phase overpotential, η_{ph}. The departure of the operating electrode potential from the equilibrium potential value results from superposition of all types of overpotentials,

$$\eta = \eta_d + \eta_r + \eta_e + \eta_{ph} \tag{3.3}$$

The electrochemical (η_e) and the phase overpotentials (η_{ph}) are called the activation polarization, η_{ac}. The overall overvoltage is the sum of the concentration polarization and the activation polarization:

$$\eta = \eta_{conc} + \eta_{ac} \tag{3.4}$$

where η_{conc} is the sum of the diffusion and the reaction overpotential.

The rate of any electrochemical reaction, and consequently the current, is controlled, in part, by the rate of the charge-transfer reaction and the rate of transport of the electroactive species to the electrode surface. In this chapter, we will assume that the solution is homogeneous, so that the surface concentration of the ions is equal to the concentration in the bulk solution. This would approximately be the case when the solution is stirred and the transport of the ions to the electrode is fast. Under these conditions, the current is controlled only by the rate of the electron transfer at the electrode. If the electron transfer reaction is described by Eq. (3.5), the rate of the cathodic reaction is first order in concentration of oxidized species at the electrode-electrolyte interface.

$$O + e^- \underset{k_a}{\overset{k_c}{\rightleftarrows}} R \tag{3.5}$$

O and R are oxidized and reduced species, respectively. The cathodic rate is defined by $k_c C_O$, where k_c is the cathodic reaction rate constant and C_O is the concentration of oxidized species. The rate of oxidation at the anode is first order in the concentration of reduced species at the electrode-electrolyte interface, R, and is given by $k_a C_R$, where k_a is the anodic reaction rate constant and C_R is the concentration of reduced species.

The heterogeneous rate constants, k_a and k_c, have units of m/s. The net flux of "O" at the electrode surface (conversion rate of O to R) is the difference between the cathodic and the anodic rates, which is proportional to the net current, i, that passes in the circuit. Thus,

$$\text{Net conversion rate} = k_c C_O - k_a C_R \tag{3.6}$$

or

$$i = FA[k_c C_o - k_a C_R] \tag{3.7}$$

F in Eq. (3.7) is Faraday's constant, while A is the electrode surface area. At equilibrium, the net current flow is equal to zero; that is, the current flow for the forward reaction (product formation) is equal to the current flow for the reverse reaction (reactant formation from the products) in an electrochemical reaction involving oxidation and reduction reactions. At equilibrium, the current flow is not zero for the forward and reverse reactions. The passage of current in either forward or reverse reaction is equal to the exchange current density of the overall redox reaction.

In most cases, the reaction rate constants "k" follows the Arrhenius equation:

$$k = Z\exp\frac{-\Delta G^*}{RT} \tag{3.8}$$

where Z is the preexponential factor, ΔG^* is the activation energy, R is the universal gas constant, and T is the absolute temperature. If this is the case, and the activation energy is independent of temperature, then a plot of lnk vs. $1/T$ would be a straight line with a slope $-\Delta G^*/R$.

The exponential term in Eq. (3.8) is related to the probability of surmounting the energy barrier defined by the standard free energy of activation ΔG_o^*. The preexponential factor, Z, is known as the frequency factor, which indicates the number of attempts needed to surmount the standard free energy of activation. In this chapter, Z is treated as an empirical parameter with units of m/s.

From transition state theory, the temperature dependence of anodic and cathodic rate constants is given by:

$$k_c = Z\exp\frac{-\Delta G_c^*}{RT} \tag{3.9a}$$

$$k_a = Z\exp\frac{-\Delta G_a^*}{RT} \tag{3.9b}$$

Under equilibrium conditions, the ratio of the concentration of the oxidized and reduced species is given by the Nernst equation:

$$e_{eq} = e^o + \frac{RT}{F}\ln\frac{C_O}{C_R} \tag{3.10}$$

where e_{eq} and e^o are the equilibrium and standard half-cell potentials, respectively. Taking the logarithm of Eqs. (3.9a) and (3.9b) and substituting into Eq. (3.8), one obtains:

$$\frac{\Delta G_c^* - \Delta G_a^*}{RT} = \frac{C_O}{C_R} = \left(\frac{k_a^o}{k_C^o}\right) \exp^{(nF/RT)\left(e_{eq} - e^o\right)} \tag{3.11}$$

In Eq. (3.11) n is the number of electrons, while k_a^o and k_c^o are rate constant at zero current.

Combining Eq. (3.11) with the Nernst equation, one obtains:

$$\Delta G_c^* - \Delta G_a^* = nF\left(e_{eq} - e^o\right) \tag{3.12}$$

The electrochemical free energy change at equilibrium and reduction is depicted in Fig. 3.1. As shown in Fig. 3.1a, the difference between the cathodic and anodic activation

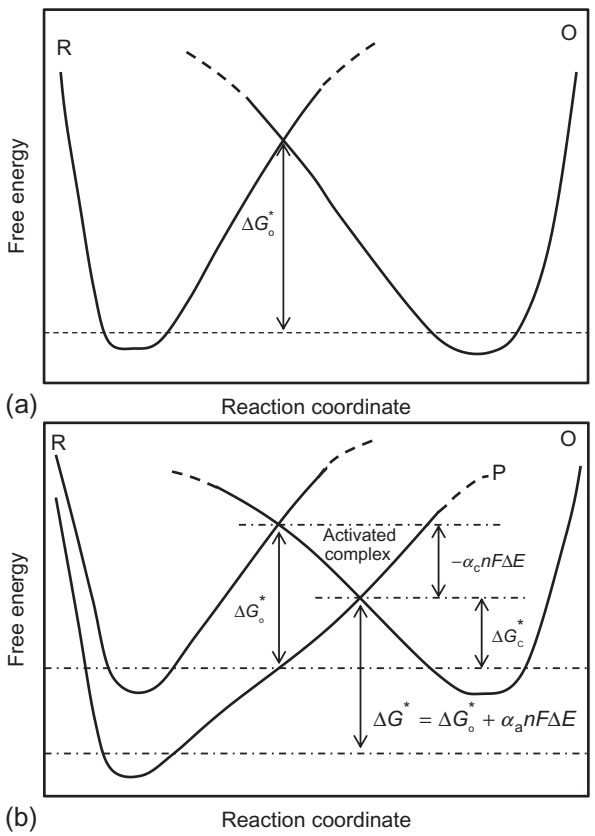

Fig. 3.1 Electrochemical free energy change (a) at equilibrium and (b) when the oxidized species are reduced.

free energies for the redox reaction in Eq. (3.5) is equal to the standard free energy. Curve "R" represents the potential energy curve of reduced species at the equilibrium potential of the redox couple, while curve "O" stands for the potential energy curve for the species in their oxidized form.

The rates of the cathodic and anodic reaction, shown in Eq. (3.12), depend on the electrode potential. If the electrode potential shifts in the cathodic direction, favoring the cathodic reaction in Eq. (3.5), the free energy of the redox system changes by an amount of $-nF\Delta E$, lowering the potential energy curve of the reduced species to a new position represented by curve P in Fig. 3.1b.

For the cathodic and anodic activation energies, one can assume simple linear relationships:

$$\Delta G_c^* = \Delta G_o^* + \alpha_c nF\left(e_{eq} - e^o\right) \tag{3.13}$$

$$\Delta G_a = \Delta G_o^* - \alpha_a nF\left(e_{eq} - e^o\right) \tag{3.14}$$

In Eq. (3.13), α_c is the fraction of the total free energy ($-nF\Delta E$) that decreases the energy barrier for the cathodic reaction, while $\alpha_a = 1 - \alpha_c$ is the fraction that increases the anodic potential barrier in Fig. 3.1b. The parameters α_c and α_a are called the cathodic and anodic transfer coefficients. As shown in Fig. 3.1b, they are a measure of energy barrier symmetry of the cathodic and anodic potential energy curves. If under equilibrium conditions, the cathodic and anodic activation free energies are substituted into Eqs. (3.9a) and (3.9b), one obtains:

$$k_c^o = k_o \exp\frac{-\alpha_c nF\left(e_{eq} - e^o\right)}{RT} \tag{3.15}$$

$$k_a^o = k_o \exp\frac{-\alpha_a nF\left(e_{eq} - e^o\right)}{RT} \tag{3.16}$$

where

$$k_o = Z\exp\frac{-\Delta G_o^*}{RT} \tag{3.17}$$

Current flows through the corrosion system (electrochemical cell) only when the redox reaction is not at equilibrium. The difference between the operating electrode potential, E, and the equilibrium potential, e_{eq}, is defined as the electrode polarization, ΔE. Thus, the electrode polarization is a deviation from the equilibrium potential in the presence of current. When a cathodic current is imposed, the potential is displaced to the negative side, causing cathodic polarization to be negative. When an anodic current is applied, polarization is positive. The electrode polarization and defined nature of the limiting step is called electrode overpotential or overvoltage.

$$\eta = E - e_{eq} \tag{3.18}$$

The rate constants at nonequilibrium conditions are defined as:

$$k_c = k_c^o \exp\frac{-\alpha_c nF\eta}{RT} \tag{3.19}$$

$$k_a = k_a^o \exp\frac{\alpha_a nF\eta}{RT} \tag{3.20}$$

Thus the rate of the anodic and cathodic reactions can be expressed as:

$$i_a = Fk_a^o C_R \exp\left(\frac{\alpha_a F\left(E - e_{eq}\right)}{RT}\right) \tag{3.21a}$$

$$i_c = Fk_c^o C_O \exp\left(\frac{-\alpha_c F\left(E - e_{eq}\right)}{RT}\right) \tag{3.21b}$$

Substituting the rate constant at nonequilibrium conditions into Eq. (3.7):

$$i = FA\left[k_c^o C_o \exp\frac{-\alpha_c F\eta}{RT} - k_a^o C_R \exp\frac{\alpha_a F\eta}{RT}\right] \tag{3.22}$$

or

$$i = i^o\left[\frac{C_O}{C_O^b}\exp\frac{-\alpha_c F\eta}{RT} - \frac{C_R}{C_R^b}\exp\frac{\alpha_a F\eta}{RT}\right] \tag{3.23}$$

where i^o is the exchange current density, while C_O^b and C_R^b are the concentrations of the oxidized and reduced species in the bulk of the solution at equilibrium. At equilibrium conditions:

$$i_c = i_a = i^o \tag{3.24}$$

$$i = \overrightarrow{i} - \overleftarrow{i} = 0 \tag{3.25}$$

$$i^o = i_{c,eq} = FAk_o C_o^b \exp\frac{-\alpha_c F\left(e_{eq} - e^o\right)}{RT} \tag{3.26}$$

$$i^o = -i_{a,eq} = FAk_o C_R^b \exp\frac{\alpha_a F\left(e_{eq} - e^o\right)}{RT} \tag{3.27}$$

In the case of energy producing power sources, the equilibrium shifts to one side, resulting in the flow of net current and the subsequent loss of equilibrium at the electrode. A system of this nature is said to be polarized. The net current that flows through the polarized system at any given overpotential is $i = (i_a - i_c)$. Assuming fast transport, the concentrations of the electroactive species in the bulk and at the electrode interface are equal which reduces Eq.(3.23) to the Butler-Volmer equation (3.28), which is a fundamental equation in electrode kinetics.

$$i = \overrightarrow{i} - \overleftarrow{i} = i^{o}\left\{\exp\left(\frac{-\alpha_c F\eta}{RT}\right) - \exp\left(\frac{\alpha_a F\eta}{RT}\right)\right\} \tag{3.28}$$

The exchange current density, i^{o}, represents the oxidation and the reaction rates at equilibrium. Exchange current densities for hydrogen and oxygen evolution reaction on different metals are given in Table 3.1 [1]. The magnitude of the exchange current density varies in Table 3.1 depending on the metal electrode. The experimentally measured exchange current density for hydrogen evolution on Ni in 1 M HCl is 2×10^{-11} A/cm^2, while Pt is eight orders of magnitude higher at 10^{-3} A/cm^2. The exchange current density is a function of the ratio of the oxidized and reduced species and the temperature. Because it is expressed in terms of geometric surface area, the exchange current density also depends on the surface roughness.

3.3.1 Special cases of Butler-Volmer equation-high field approximation

The electrode overpotentials, η, and its effect on current, i, are very significant in electrochemistry and corrosion engineering. When η is large, one of the exponential terms of the Butler-Volmer equation will be negligible as compared to the other. For example, when the overpotential is large and cathodic (negative), the anodic term in Eq. (3.28) is negligible, and we can approximate Eq. (3.28) using the form:

$$i_c = i^{o}\exp\frac{-\alpha_c F\eta}{RT} \tag{3.29}$$

or

$$\eta = \frac{2.3RT}{\alpha_c nF}\log i^{o} - \frac{2.3RT}{\alpha_c nF}\log i_c = -\frac{2.3RT}{\alpha_c nF}\ln\frac{i_c}{i^{o}} \tag{3.30}$$

Equation (3.30) is the Tafel equation, named for the German scientist who discovered the relationship between the current equivalent to the rate of a single reaction on a metal surface and the potential of the metal. By defining the Tafel constants

$$a_c = 2.3\frac{RT}{\alpha_c nF}\log i^{o} \tag{3.31a}$$

and

$$b_c = -2.3\frac{RT}{\alpha_c nF} \tag{3.31b}$$

Equation (3.30) can be simplified to:

$$\eta = a_c + b_c \log i \tag{3.32}$$

Plots of η vs. logi (called Tafel plots) at high overpotentials would be straight lines, from which the constants a_c and b_c could be evaluated. Tafel plots have been long known to fit

Table 3.1 Electrode Kinetic Parameters [1]

Electrode	Solution	i_o (A/cm^2)	b_c (V)	b_a (V)	Reference
Reaction:	$2H^+ + 2e^- \rightarrow H_2$				
Pt	1 N HCl	10^{-2}	0.03		[11]
	0.1 N NaOH	0.7×10^{-3}	0.11		[11]
Pd	0.6 N HCl	2×10^{-3}	0.03		[11]
Mo	1 N HCl	10^{-5}	0.04		[11]
Au	1 N HCl	10^{-5}	0.05		[11]
Ta	1 N HCl	10^{-4}	0.08		[11]
W	5 N HCl	10^{-4}	0.11		[11]
Ag	0.1 N HCl	5×10^{-6}	0.09		[11]
Ni	0.1 N HCl	8×10^{-6}	0.31		[11]
	0.12 N H_2SO_4	4×10^{-6}	0.10		[11]
Bi	1 N HCl	10^{-6}	0.10		[11]
Nb	1 N HCl	10^{-6}	0.10		[11]
Fe	1 N HCl	10^{-5}	0.15		[11]
	0.52 N H_2SO_4	2×10^{-5}	0.11		[12]
	4% NaCl, pH 1-4	10^{-6}	0.10		[13]
Cu	0.1 N HCl	2×10^{-6}	0.12		[11]
	0.15 N NaOH	10^{-5}	0.12		[11]
Sb	2 N H_2SO_4	10^{-8}	0.10		[11]
Al	2 N H_2SO_4	10^{-9}	0.10		[11]
Be	1 N HCl	10^{-8}	0.12		[11]
Sn	1 N HCl	10^{-7}	0.15		[11]
Cd	1 N HCl	10^{-6}	0.20		[11]
Zn	1 N H_2SO_4	2×10^{-10}	0.12		[11]
Hg	0.1 N HCl	7×10^{-12}	0.12		[11]
	0.1 N H_2SO_4	2×10^{-12}	0.12		[11]
	0.1 N NaOH	3×10^{-14}	0.10		[11]
Pb	0.01-8 N HCl	2×10^{-12}	0.12		[11]
Reaction:	$O_2 + 4H^+ + 4e^- \rightarrow 2H_2O$				
Pt	0.1 N H_2SO_4	9×10^{-11}	0.10		[11]
Reaction:	$O_2 + 2H_2O + 4e^- \rightarrow 4OH^-$				
Pt	0.1 N NaOH	4×10^{-12}	0.05		[11]
Au	0.1 N NaOH	5×10^{-12}	0.05		[11]
Reaction:	$Cl_2 + 2e^- \rightarrow 2Cl^-$				
Pt	1 N HCl	5×10^{-3}	0.11	0.130	[11]
Reaction:	$M \rightarrow Mn^+ + ne^-$				
Pt	0.52 N H_2SO_4	10^{-7}		0.060	[12]
	0.52 N H_2SO_4	10^{-10}		0.039	[12]
	0.63 N $FeSO_4$	3×10^{-9}		0.060-0.075	[14]
	4% NaCl, pH 1-4			0.068	[15]
	0.3 N H_2SO_4			0.100	[16]
	0.5 M $FeSO_5$, 0.1 M $NaHSO_4$	3×10^{-10}		0.030	[17]
	Perchlorate			0.030	[18]
Cu	0.001 N $Cu(NO_3)_2$	10^{-9}			[11]

experimental data obtained in studies of activation overpotential (such as the evolution of hydrogen and oxygen at various electrodes). Equation (3.32) may also be written in the form

$$\eta = b_c \log\left(\frac{i}{i^o}\right) \tag{3.33}$$

The overpotential, η, is occasionally called the activation overpotential and ignores the contribution of the overpotential changes due to concentration gradients. The use of activation overpotential normally occurs when the concentration of ions in solution is very high or when there is enough forced convection to minimize concentration gradients. These conditions are approached in experimental setups like rotating disk electrodes.

Similar expressions are obtained when the overpotential is large and anodic (positive), resulting in the cathodic term being eliminated. When the anodic process takes place,

$$i = -i_a = \overleftarrow{i} \tag{3.34}$$

then,

$$i_a = i^o \exp^{\frac{(1-\alpha)nF\eta}{RT}} \tag{3.35}$$

and

$$\eta = \frac{2.3RT}{(1-\alpha)nF}\log i^o + \frac{2.3RT}{(1-\alpha)nF}\log i_a \tag{3.36}$$

The Tafel relationship for the anodic process becomes:

$$\eta = a_a + b_a \log i \tag{3.37}$$

where

$$a_a = -2.3\frac{RT}{(1-\alpha)nF}\log i^o \tag{3.38a}$$

and

$$b_a = 2.3\frac{RT}{(1-\alpha)nF} \tag{3.38b}$$

Comparison of the anodic and cathodic Tafel constants shows that when $\alpha = 0.5$, $a_c = -a_a$; $b_c = -b_a$. Tables 3.2 and 3.3 list values of the Tafel constants for cathodic hydrogen evolution at $T = 20 \pm 2\,^{\circ}C$ on different metals and the effect of electrode materials and solution composition on oxygen overpotential [21]. The Tafel equation has been confirmed for numerous cathodic and anodic reactions, and its use is illustrated in the examples and case studies that follow.

Table 3.2 Values of Tafel Constants for Cathodic Hydrogen Evolution on Different Metals, $T = 20 \pm 2$ °C [21]

Metal	Acidic Solutions		Alkaline Solutions	
	a	b	a	B
Ag	0.95	0.100	0.73	0.12
Al	1.00	0.100	0.64	0.14
Au	0.40	0.120	-	-
Be	1.08	0.120	-	-
Bi	0.84	0.120	-	-
Cd	1.40	0.120	1.05	0.16
Co	0.62	0.140	0.60	0.14
Cu	0.87	0.120	0.96	0.12
Fe	0.70	0.120	0.76	0.11
Ge	0.97	0.120	-	-
Hg	1.41	0.114	1.54	0.11
Mn	0.8	0.100	0.90	0.12
Mo	0.66	0.080	0.67	0.14
Nb	0.8	0.100	-	-
Ni	0.63	0.110	0.65	0.10
Pb	1.56	0.110	1.36	0.25
Pd	0.24	0.030	0.53	0.13
Pt	0.10	0.030	0.31	0.10
Sb	1.00	0.110	-	-
Sn	1.20	0.130	1.28	0.23
Ti	0.82	0.140	0.83	0.14
Tl	1.55	0.140	-	-
W	0.43	0.100	-	-
Zn	1.24	0.120	1.20	0.12

Table 3.3 The Effect of Electrode Material and Solution Composition on Oxygen Overpotential [21]

Metal	Solution	T (°C)	Current Density (A/cm^2)	b/2.303	a
Pt	0.005-0.05 N H_2SO_4	25	10^{-7}-10^{-4}	(3/2 RT)/F	0.95
Pt	0.1 N H_2SO_4	35	10^{-7}-10^{-2}	2RT/F	1.08
Pt	0.1 N NaOH	25	-	RT/F	-
Au	0.1-1.0 N H_2SO_4	25	3×10^{-5}-10^{-2}	(3/4 RT)/F	0.99
Au	0.1 N NaOH	25	-	RT/F	-
Pb	3.8 N H_2SO_4	30	-	2RT/F	1.10
Pt, PbO_2 (α)	4.4 N H_2SO_4	31.8	10^{-4}-2×10^{-3}	(3/4 RT)/F	0.72
Pt, PbO_2 (β)	4.4 N H_2SO_4	31.8	7×10^{-5}-2×10^{-3}	2RT/F	1.17
Ni	7.5 N KOH	25	5×10^{-6}-10^{-3}	(1/2 RT)/F	0.35
Ni	7.5 N KOH	25	10^{-3}-5×10^{-2}	3RT/F	1.30
Ni	7.5 N KOH	25	5×10^{-2}-3×10^{-1}	RT/F	1.08
Fe	pH = 2	5	3×10^{-6}-10^{-4}	(1/2 RT)/F	0.66

Example 3.1

The potential of an iron electrode when polarized as a cathode in an aqueous medium is −0.716 V vs. SCE. What would be the value of the hydrogen overpotential of this electrode in an electrolyte with a pH of 2.0?

Solution:

The hydrogen overpotential, η, is the difference between the potential of iron electrode ($E = -0.716$ V vs. SCE) and the potential of the hydrogen reaction.

$$\eta = E - e_{eq}$$

For the hydrogen reaction $2H^+ + 2e^- \rightarrow H_2$, $e^o_{H^+|H_2} = 0.00\,V$ vs. SHE or $e^o_{H^+|H_2} = -0.241$ vs. SCE

$$\begin{aligned} e_{eq,H^+|H_2} &= e^o_{H^+|H_2} - 0.059(pH) = -0.241 - (0.059 \times 2) \\ &= -0.359\,V \text{ vs. SCE} \end{aligned}$$

The hydrogen overpotential is the difference of the potential of iron electrode (−0.716 V vs. SCE) and the potential of the hydrogen reaction.

$$\eta = -0.716 - (-0.359) = -0.357\,V$$

Example 3.2

The potential of an iron electrode when cathodically polarized in an aqueous medium is −0.75 V vs. SHE. Determine the hydrogen overpotential in electrolytes with pH between 1 and 6.

Solution:

$$2H^+ + 2e^- \rightarrow H_2 \quad e^o_{H^+|H_2} = 0.00\,V \text{ vs. SHE}$$

$$e_{eq,H^+|H_2} = e^o_{H^+|H_2} - 2.303\frac{RT}{nF}\log\left(\frac{a_{H_2}}{(a_{H^+})^2}\right)$$

The hydrogen overpotential is the difference of the potential of the iron electrode and the potential of hydrogen reaction.

$$\begin{aligned} \eta &= E - e_{eq} \\ \eta_{eq.H^+|H_2} &= 0 - 0.059(pH) \\ e_{eq.H^+|H_2} &= -0.059(pH) \\ \eta_{H_2} &= -0.75 - e_{eq,H^+|H_2} \\ \eta_{H_2} &= -0.75 + 0.059(pH) \end{aligned}$$

At a pH of 1,

$$\eta_{H_2} = -0.75 + 0.059(1) = -0.691\ V$$

The effect of pH on the hydrogen overpotential of the iron electrode in an aqueous medium is shown in Fig. 3.2.

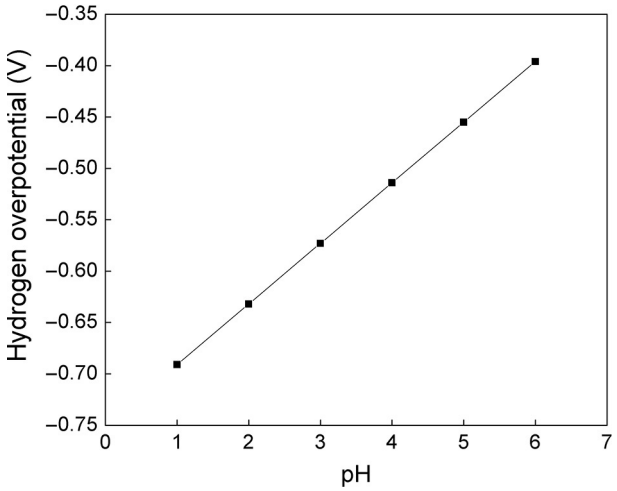

Fig. 3.2 The effect of pH on the hydrogen overpotential on iron electrode in aqueous medium.

Example 3.3

Oxygen evolves at a platinum anode at pH 8 when a potential of 0.515 V with respect to the saturated calomel electrode is applied. The reaction occurs at unit pressure of oxygen. The potential of the standard calomel electrode is 0.241 V vs. SHE.

(a) Calculate the overpotential of the oxygen evolution reaction and predict whether or not the reaction will take place at this potential.

(b) Calculate the overpotential of the reaction at pH 6, 7, 9, and 10 and determine whether the oxygen reduction reaction will occur if the applied potential of the platinum remains at 0.515 V vs. SCE. Given: The standard electrode potential for oxygen evolution reaction at pH 14 is 0.401 V vs. SHE.

Solution:

(a) The standard electrode potential for oxygen evolution reaction at pH 14 is 0.401 vs. SHE. At pH = 8,

$$e_{\mathrm{eq,O_2|OH^-}} = e^{\mathrm{o}}_{\mathrm{O_2|OH^-}} - \frac{0.059}{n}\log\left(a_{\mathrm{OH^-}}\right) = 0.401 + 0.059(14 - \mathrm{pH}) = 0.401 + 0.059(14 - 8)$$

$$e_{\mathrm{eq,O_2|OH^-}} = 0.755\ \mathrm{V\ vs.\ SHE}$$

The oxygen equilibrium potential at a pH of 8 is estimated to be 0.755 vs. SHE. Because the potential of Pt electrode is 0.515 V vs. SCE when normalized to the SHE scale, it becomes 0.756 vs. SHE. The oxygen overpotential is only 0.001 V and the oxygen evolution reaction will occur at pH slightly above 8.

(b) A plot of pH vs. oxygen overpotential is constructed using the following expression:

$$\eta = E - e_{\mathrm{eq,O_2|OH^-}}$$

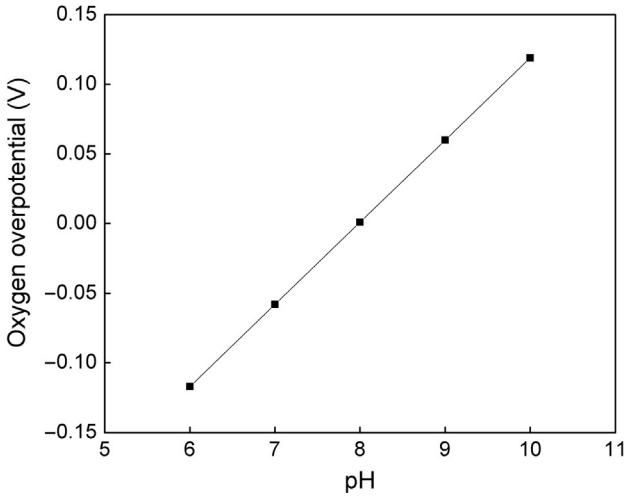

Fig. 3.3 Overpotential vs. pH for oxygen evolution reaction on Pt electrode.

For example, at pH = 6, the overpotential, η, is,

$$\eta = -0.756 - e_{\mathrm{eq,O_2|OH^-}}$$
$$\eta = -0.756 - [0.401 + 0.059(14 - 6)]$$
$$\eta = -0.117\,\mathrm{V}$$

The overpotential at pH 7, 9, and 10 are −0.058, 0.06, and 0.119 V, respectively.

Figure 3.3 shows the oxygen overpotential dependence on pH. Assuming that the applied potential of platinum remains at 0.515 V vs. SCE, the oxygen reduction reaction occurs only when the pH is less than or equal to 8.

3.3.2 Low-field approximation

Another special case of the Butler-Volmer equation, Eq. (3.28), occurs when the overpotential is extremely small; under this condition, one can consider the value of $F\eta/RT$ to be small. In such a case, Eq. (3.28) can be approximated, based on the relations $[(e^x - e^{-x})/2 = \sinh x]$ and $[\sinh x = x, \text{ when } x \to 0]$, to

$$i = i^{\mathrm{o}} \frac{nF}{RT}\eta \tag{3.39}$$

The ratio of the overpotential to the current in the above equation is called the charge-transfer resistance. This equation adds more physical meaning to the exchange current density, i_{o}, and can be viewed as a parameter to estimate the resistance of an electrochemical (corrosion) reaction. A high value of the exchange current density implies high reaction rate, while a low exchange current density value indicates sluggish corrosion kinetics.

Based on low-field approximation, a simple procedure for the evaluation of corrosion currents and corrosion rates was developed in 1938 by Wagner and Traud [22]. Stern and Geary [23] and Stern [24,25] developed an experimental procedure for measuring the corrosion rates known as the linear polarization technique. This technique will be discussed in detail in Chapter 5.

Example 3.4

Calculate the hydrogen overpotential of an iron electrode and the corrosion current of iron for pH between 2 and 8. The potential of the iron electrode at unit hydrogen concentration (pH = 0), $V = -0.75$ V vs. SCE. The Tafel slope for the hydrogen evolution reaction is $b_c = -0.12$ V/decade. The exchange current density of hydrogen on iron i^o_{Fe} is 10^{-4} A/cm^2. Assume that the corrosion potential is -0.5225 V vs. SHE.

Solution:

Hydrogen overpotential:

$$2H^+ + 2e^- \rightarrow H_2, \quad e^o_{H^+|H_2} = 0.00\,\text{V vs. SHE}$$

$$e_{eq,H^+|H_2} = 0 - 2.303\frac{RT}{2F}\log\left(\frac{a_{H_2}}{(a_{H^+})^2}\right)$$

$$e_{eq,H^+|H_2} = \frac{0.059}{2}\log\left[(a_{H^+})^2\right]$$

$$e_{eq,H^+|H_2} = -0.059(\text{pH})$$

$$\eta_c = -0.75 - e_{eq,H^+|H_2}$$

$$\eta_c = -0.75 - (-0.059(\text{pH}))$$

At a pH of 2, $\eta_c = -0.75 + (0.059 \times 2) = -0.632$ V

η_c is plotted as a function of pH in Fig. 3.4a.

Corrosion current:

Using Eq. (3.33),

$$E_{corr} - e_{H^+|H_2} = b_c \log\left(\frac{I_{corr}}{i^o_{H_2}}\right)$$

$$\frac{E_{corr} - e_{H^+|H_2}}{b_c} = \log\left(\frac{I_{corr}}{i^o_{H_2}}\right)$$

$$I_{corr} = i^o_{H_2} \times 10^{\left(E_{corr} - e_{H^+|H_2}\right)/b_c}$$

For example, at pH = 2,

$$I_{corr} = i^o_{H_2} \times 10^{(-0.5225-(-0.059\times 2))/-0.12}$$

$$I_{corr} = 10^{-4} \times 10^{-0.4045/-0.12}$$

$$I_{corr} = 0.235\,\text{A/cm}^2$$

Similarly, the corrosion current for other pH values are calculated and plotted in Fig. 3.4b

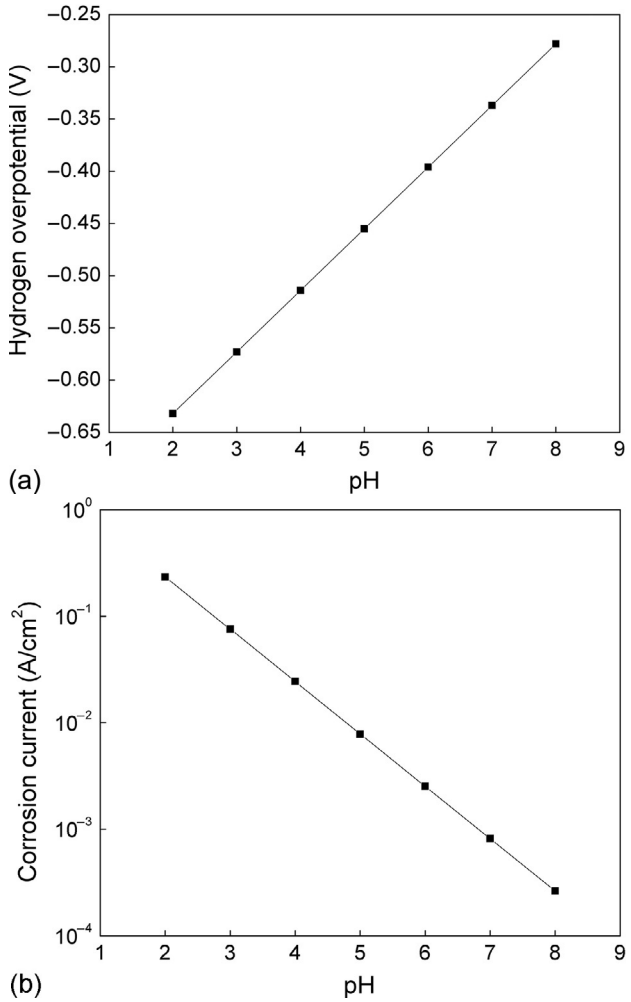

Fig. 3.4 Plot of (a) pH vs. hydrogen overpotential and (b) pH vs. corrosion current for the iron electrode.

Example 3.5

The potential of platinum polarized in the cathodic direction in deaerated H_2SO_4 at a pH of 1.0 at 0.01 A/cm^2 is -0.334 V vs. SCE. At 0.10 A/cm^2 the potential is -0.364 V. Derive expression for the exchange current density, $i^{o}_{H_2}$ in terms of the overpotential and currents. Calculate b_c (the Tafel constant) and $i^{o}_{H_2}$ (the exchange current density)for a discharge of H^+ on platinum in this solution.

Solution:

The Tafel expressions for the two current densities are:

$$\eta_{c_1} = b_c \log\left(\frac{i_{1,H_2}}{i^o_{H_2}}\right)$$

$$\eta_{c_2} = b_c \log\left(\frac{i_{2,H_2}}{i^o_{H_2}}\right)$$

Next, one should estimate η_{c_1} and $i^o_{H_2}$. Because the two Tafel expressions for η_{c_1} and η_{c_2} are for the same reaction, the Tafel constant, b_c, is the same. Exchange current density, $i^o_{H_2}$, is calculated by eliminating b_c from the equations:

$$\left(\frac{\eta_{c_1}}{\eta_{c_2}}\right)\log\left(\frac{i_{2,H_2}}{i^o_{H_2}}\right) = \log\left(\frac{i_{1,H_2}}{i^o_{H_2}}\right)$$

$$\left(\frac{\eta_{c_1}}{\eta_{c_2}}\right)\log(i_{2,H_2}) - \left(\frac{\eta_{c_1}}{\eta_{c_2}}\right)\log\left(i^o_{H_2}\right) = \log(i_{1,H_2}) - \log\left(i^o_{H_2}\right)$$

$$\left(\frac{\eta_{c_1}}{\eta_{c_2}}\right)\log(i_{2,H_2}) - \log(i_{1,H_2}) = \left[\left(\frac{\eta_{c_1}}{\eta_{c_2}}\right) - 1\right]\log\left(i^o_{H_2}\right)$$

$$\log\left(\frac{i_{2,H_2}^{\left(\eta_{c_1}/\eta_{c_2}\right)}}{i_{1,H_2}}\right) = \log\left(i^{o\left[\left(\eta_{c_1}/\eta_{c_2}\right)-1\right]}_{H_2}\right)$$

The expression for the exchange current density is

$$i^o_{H_2} = \left[\frac{i_{2,H_2}^{\left(\eta_{c_1}/\eta_{c_2}\right)}}{i_{1,H_2}}\right]^{1/\left[\left(\eta_{c_1}/\eta_{c_2}\right)-1\right]} \tag{A}$$

The equilibrium potential of hydrogen ions in solution is estimated using the Nernst equation and can be expressed in terms of the pH of the solution.

$$\eta = E - e_{eq}$$

$$2H^+ + 2e^- \rightarrow H_2, \quad e^o_{H^+|H_2} = 0.00\,\text{V vs. SHE}$$

$$e_{eq,H^+|H_2} = 0.059(\text{pH}) = -0.059\,\text{V vs.SHE, at pH} = 1;\ \text{or} -0.059 - 0.241 = -0.300\,\text{V vs. SCE}$$

The overpotentials are:

$$\eta_{c_1} = -0.334 - (-0.300) = -0.034\,\text{V}$$
$$\eta_{c_2} = -0.364 - (-0.300) = -0.064\,\text{V}$$

The exchange current density is calculated using the expression (A):

$$i^o_{H_2} = \left[\frac{0.1^{(-0.034/-0.064)}}{0.01}\right]^{1/((-0.034/-0.064)-1)} = 7.364 \times 10^{-4}\,\text{A/cm}^2$$

Calculation of cathodic Tafel constant:

$$\eta_{c_1} = b_c \log\left(\frac{i_{1,H_2}}{i^o_{H_2}}\right)$$

$$b_c = \frac{\eta_{c_1}}{\log\left(\frac{i_{1,H_2}}{i^o_{H_2}}\right)} = \frac{(-0.034)}{\log\left(\frac{0.01}{7.364\times10^{-4}}\right)} = -0.030\,\text{V/decade}$$

3.4 CONCENTRATION POLARIZATION

The previous discussion assumed that the reacting species concentration is always present in excess, and no limitations exist on the availability of the species (an ideal system). In real electrochemical reactions, the concentration of the species at the electrode continues to change as the reaction proceeds. This change in concentration is a result of the slow transport of species from the bulk solution to the surface of the electrode. Because the electrode potential is governed by the solution composition near the electrode surface, a change in the activity of species at the interface alters the equilibrium potential. Thus, the concentration polarization can be defined as shift of cell voltage due to concentration changes while current is passing. The overpotential developed as a result of such concentration polarization is called the diffusion overpotential (η_d), as discussed previously. Nernst's law describes the diffusion overpotential phenomenon. If the activities of the oxidized and the reduced species at the start are a_{M^+} and a_M, respectively, and change to a'_{M^+} and $a_M{}'$ after the passage of current, then Nernst's law allows the equilibrium potential at the start (e_{eq}) and after the passage of current (e'_{eq}) to be expressed as:

$$e_{eq} = e^o + \frac{RT}{nF}\ln\left(\frac{a_{M^+}}{a_M}\right) \tag{3.40}$$

$$e'_{eq} = e^o + \frac{RT}{nF}\ln\left(\frac{a'_{M^+}}{a'_M}\right) \tag{3.41}$$

and the concentration overpotential, η_{conc}, is given by

$$\eta_{conc} = e'_{eq} - e_{eq} = \frac{RT}{nF}\ln\left(\frac{a'_{M^+}}{a'_M}\frac{a_M}{a_{M^+}}\right) \tag{3.42}$$

These relations are based on the fact that the potential loss due to charge-transfer reactions are negligible (the activation overpotential approaches zero). The diffusion overpotential is usually negative during cathodic processes and positive during anodic processes. The effects of concentration polarization are usually pronounced at high current densities, when a reaction species at the interface is consumed at a faster rate than it can be

replenished by transport from the bulk solution. As the current density increases, the polarization increases until the concentration of the species at the surface approaches zero. The current density at which this occurs is called the limiting current density, i_L. Eq. (3.42) can now be written in terms of the limiting current density as [7,19,20]:

$$\eta_{conc} = \frac{RT}{nF} \ln\left(\frac{i_L - i}{i_L}\right) \tag{3.43}$$

where "i" is the current passing through the electrode when the surface concentration of the metal species is a_{M^+}. The limiting current density is given by

$$i_L = -\frac{DnFC_b}{\delta} \tag{3.44}$$

where δ is the diffusion layer thickness and D is the diffusion coefficient of the reacting species. Equation (3.43) also assumes that the linear part of the concentration profile is extrapolated to intersect the asymptotically approaching bulk value. Changes in the surface concentration of species can also occur due to chemical reactions.

3.5 RELEVANCE OF ELECTROCHEMICAL KINETICS TO CORROSION

The equilibrium of processes occurring at the electrode are disturbed when a net reaction occurs and produces current in the external circuit. The current induces a potential change and subsequently causes polarization of the electrode. The principle of charge conservation requires that the total rate of oxidation must be equal to the total rate of reduction for any corrosion process. To avoid the accumulation of charge on the electrode, the sum of anodic currents must equal the sum of cathodic currents. The electrochemical reaction at the anode is the oxidation (loss of electrons) of the metal, corrosion.

$$M \rightarrow M^{n+} + ne^-$$

At the cathode, electrons are gained. Examples of cathodic reactions are:

Evolution of hydrogen from acidic, neutral, or alkaline solution:

$$2H^+ + 2e^- \rightarrow H_2 \text{ (acid solutions)}$$

$$2H_2O + 2e^- \rightarrow H_2 + 2OH^- \text{ (neutral and alkaline solutions)}$$

Evolution of dissolved oxygen in acid, neutral, or alkaline solution:

$$O_2 + 4H^+ + 4e^- \rightarrow 2H_2O \text{ (acid solutions)}$$

$$O_2 + 2H_2O + 4e^- \rightarrow 4OH^- \text{ (neutral and alkaline solutions)}$$

Reduction of oxidizer,

$$Fe^{3+} + e^- \rightarrow Fe^{2+}$$

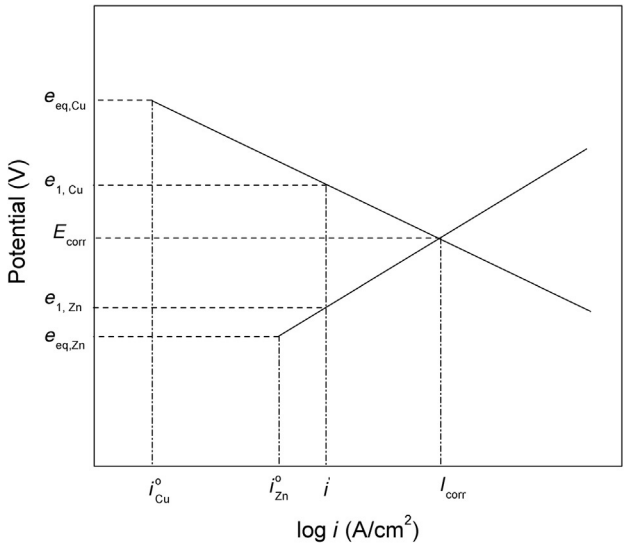

Fig. 3.5 Schematic showing the anode and cathode polarization with the mixed potential (Evans diagram).

The concept of polarization in a corrosion cell can be explained by considering a simple galvanic cell, such as a Daniel cell, with copper and zinc electrodes. The Evans diagram of a Daniel cell shown in Fig. 3.5 is the basis for understanding the underlying corrosion process kinetics [26,27].

The open circuit potential of copper in a copper ion solution and zinc in a zinc ion solution are represented as $e_{eq,Cu}$ and $e_{eq,Zn}$, respectively, in Fig. 3.5. The currents corresponding to the open circuit potentials are the exchange current densities of the electrode reactions. For such a cell, thermodynamics favors the reduction of copper and the oxidation of zinc and the criterion for a spontaneous reaction ($\Delta G = -nFE^{o}$) is valid.

Upon the polarization of either electrode, the cell potential moves along the oxidation and reduction curves as shown in Fig. 3.5. When the current through the cell is i', the potential of the copper and zinc electrodes is $e_{1,Cu}$ and $e_{1,Zn}$, and each of the electrodes have been polarized by an amount of $(e_{eq,Cu} - e_{1,Cu})$ and $(e_{eq,Zn} - e_{1,Zn})$.

Upon further polarization, the anodic and cathodic curves intersect at a point where the potentials are the same (E_{corr}) and the external current is maximized. The electrode potentials at this point are numerically equal for copper and zinc and the current is I_{corr}. Physically, this point on Fig. 3.5 is attained when the load in the external circuit is extremely low or when the system is short circuited. Systems undergoing corrosion can be explained on a very similar basis. The measured output potential in a corroding system, often called the mixed potential or the corrosion potential (E_{corr}), is the potential at the intersection of the anodic and the cathodic polarization curves.

The value of the current at the corrosion potential is called the corrosion current (I_{corr}) and can be used to calculate the rate at which the metal will corrode. To predict the corrosion current or the corrosion potential, we need information about the kinetics of the individual redox reactions, the standard electrode potentials, and the exchange current densities for a specific system.

The Evans diagram is also very useful in estimating the current required in the external circuit to stop the process of corrosion. If an external current is applied cathodically (negative current), the potential on the cathodic polarization line crosses the equilibrium potential of the anode and the anodic reaction is not thermodynamically feasible. Thus, the corrosion process stops. This process is the basis of cathodic protection and is discussed in Chapter 15.

3.6 CONSTRUCTION OF EVANS DIAGRAMS

Originally developed by Evans [26,27], the Evans diagram plots the potential vs. the log of the current density, generating a polarization diagram of a corroding metal. Evans diagrams are very useful in predicting the corrosion behavior of electrochemical systems. If polarization data is available, the Evans diagram can be used to estimate the exchange current densities of the anodic and cathodic reactions. When the exchange current densities and the equilibrium potentials of the anodic and cathodic reactions are known, Evans diagrams can be used to estimate the mixed potential (corrosion potential) of a system. A typical three-electrode electrochemical cell containing a working, counter, and reference electrode can be used to obtain polarization data [4–7].

Measurements are made by applying a current and monitoring the potential after a relaxation time and repeating the procedure for different anodic and cathodic currents. The experimental procedure for obtaining the polarization diagram of a corroding system requires the initial measurement of the open circuit potential of the system. The open circuit potential value falls between the equilibrium potentials of the anodic and cathodic reactions. When there is no current in the external circuit, an open circuit potential value is equal to the corrosion potential.

The second step in the procedure requires the working electrode to be anodically polarized, yielding one of the dashed lines shown in Fig. 3.6. The electrode is then cathodically polarized, and the other dashed line from Fig. 3.6 is obtained. The anodic polarization usually results in the oxidation of the metal species, while the reaction resulting from cathodic polarization depends on the medium. In an aerated solution, the oxygen reduction reaction may be the prime cathodic reaction, while, in the case of deaerated aqueous solutions, hydrogen reduction could be the dominant reaction. In Fig. 3.6, the redox reaction is represented by a general reaction

$$M^{n+} + ne^{-} \rightarrow M$$

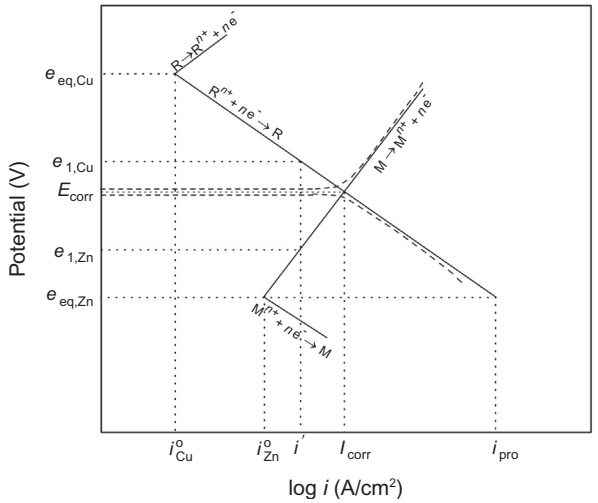

Fig. 3.6 Schematic showing the anodic and the cathodic parts of a corrosion reaction.

At significantly large overpotentials (>100 mV) the anodic and the cathodic polarization curves become linear. Linear extrapolation of the curves will yield a point of intersection at the corrosion potential with the corresponding current being the corrosion current. The experimental procedure above can also be performed potentiostatically using modern potentiostats that are capable of automatically handling the process.

As an alternative to generating an entire polarization diagram, we can use the exchange current densities and the equilibrium potentials of the anodic and cathodic reactions to estimate the corrosion potential and corrosion current by extrapolating the cathodic and anodic polarization lines of the corroding system. At the corrosion potential, the anodic and cathodic currents are equal. The schematic shown in Fig. 3.6 represents a case for which the anode and the cathode area are the same; once the corrosion current is known, the rate of deterioration of the electrode can be estimated. The accurate prediction of the corrosion (mixed) potential depends on the polarization behavior of the specific electrode.

Once the corrosion (mixed) potential is known, the estimation of the cathodic protection current is relatively simple; the cathodic Tafel line is extended until the ordinate reaches the anode equilibrium value. The current corresponding to that ordinate value is the minimum value of the external current that must be supplied to stop the corrosion process. For processes in which there are multiple species undergoing cathodic or anodic reactions, the resultant cathodic and anodic Tafel curves are calculated by adding the individual polarization curves within the respective potential range.

Case Study 3.1—Construction of the Evans Diagram for the Corrosion of Zinc

Construct the Evans diagram for the corrosion of zinc in a hydrochloric acid solution with a pH of 1 and a Zn^{2+} concentration of 10^{-5} M. The cathodic ($b_c = \partial\eta_c/\partial \log i$) and anodic Tafel slope ($b_a = \partial\eta_a/\partial \log i$) are -0.12 and 0.15 V/decade, respectively. The exchange current densities for the cathodic and anodic reactions are $i^{o}_{H_2} = 10^{-8}$ and $i^{o}_{Zn} = 2 \times 10^{-10}$ A/cm^2, respectively.

(a) Calculate the corrosion potential and the corrosion current. Also evaluate the protection current required for the system. Assume that charge-transfer kinetics controls the reaction rate and that the high-field approximation applies.

(b) Calculate the corrosion potential when the pH of the solution is doubled, and the activity of the Zn^{2+} ion is squared.

Solution:

(a) According to Tafel kinetics and mixed potential theory:

$$\eta_a = b_a \log\left(\frac{I_{corr}}{i^{o}_{Zn}}\right) = E_{corr} - e_{eq,Zn^{2+}|Zn}$$

$$\eta_c = b_c \log\left(\frac{I_{corr}}{i^{o}_{H_2}}\right) = E_{corr} - e_{eq,H^{+}|H_2}$$

The values for b_a, b_c, i^{o}_{Zn}, and $i^{o}_{H_2}$ are known. The equilibrium potential for the two reactions is estimated using the Nernst equation.

$$\begin{aligned} e_{eq,Zn|Zn^{2+}} &= e^{o}_{Zn|Zn^{2+}} + \frac{0.059}{2}\log\left(a_{Zn^{2+}}\right) \\ &= -0.762 + \frac{0.059}{2}\log\left(10^{-5}\right) = -0.91\,\text{V vs. SHE} \end{aligned}$$

At a pH of 1, the equilibrium hydrogen potential is:

$$\begin{aligned} e_{eq,H^{+}|H_2} &= e^{o}_{H^{+}|H_2} + \frac{0.059}{2}\log\left(a_{H^{+}}\right)^2 \\ &= -0.059(\text{pH}) = -0.059\,\text{V vs. SHE} \end{aligned}$$

Graphical construction:

(i) Refer to Fig. 3.7. Use a marker for each of these points ($i^{o}_{Zn}, e_{eq,Zn}$) and ($i^{o}_{H_2}, e_{eq,H_2}$) on an E vs. i, semilogarithmic graph with logarithmic values for the current.

(ii) From the points marked, draw straight lines with the slope b_c from ($i^{o}_{H_2}, e_{eq,H_2}$) and b_a from ($i^{o}_{Zn}, e_{eq,Zn}$).

(iii) The two straight lines intersect at the point (I_{corr}, E_{corr}), giving the corrosion current and corrosion potential.

(iv) Extend the cathodic polarization line until it reaches the anodic equilibrium potential on the ordinate. The corresponding current on the abscissa gives the value of the external current required to stop the corrosion process.

From Fig. 3.7, the following values are estimated:

$$E_{corr} = 0.631\,\text{V}, \quad I_{corr} = 1.76 \times 10^{-6}\,\text{A/cm}^2, \quad i_{prot} = 9.3 \times 10^{-5}\,\text{A/cm}^2$$

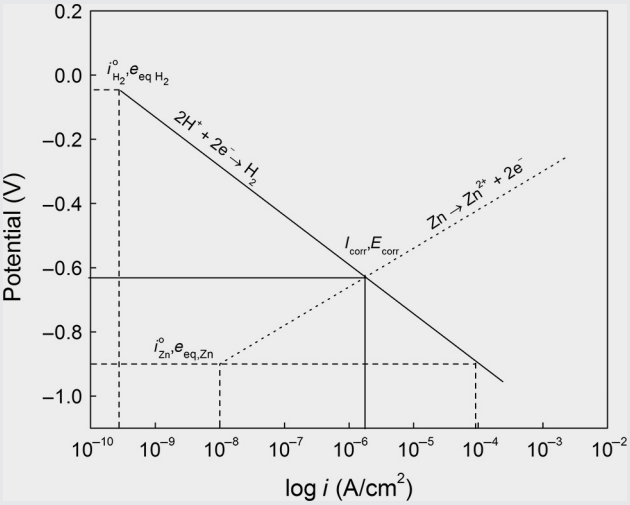

Fig. 3.7 Evans diagram for zinc in hydrochloric acid.

(b) When the pH of the system is doubled, and the activity of zinc is squared, the kinetic parameters remain the same but the equilibrium potential shifts based on the Nernst equation. Thus,

$$e_{\mathrm{eq,Zn}} = e^{\mathrm{o}}_{\mathrm{Zn}} + \frac{0.059}{2}\log\left(a_{\mathrm{Zn^{2+}}}\right) = -0.76 + \frac{0.0591}{2}\log\left(10^{-10}\right) = -1.055\mathrm{V}$$

From Fig. 3.8, the following values are estimated:

$$E_{\mathrm{corr}} = -0.33\mathrm{V},\ I_{\mathrm{corr}} = 1.65 \times 10^{-6}\mathrm{A/cm^2},\ i_{\mathrm{prot}} = 0.13\mathrm{A/cm^2}$$

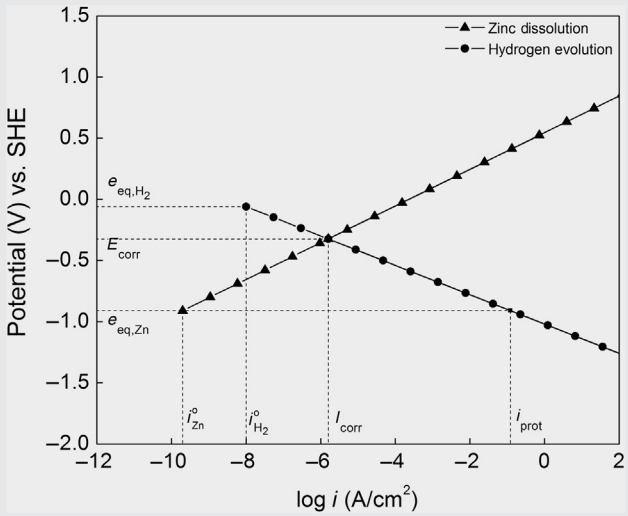

Fig. 3.8 Evans diagram for zinc in hydrochloric acid, and the graph is drawn again as per the described procedure.

Case Study 3.2—Analytical Evaluation of the Corrosion Rate

The graphical construction performed in Case Study 3.1 may also be carried out in Case Study 3.2. Below is the derivation for the corrosion rate, I_{corr}. Rearranging Eq. (3.28), the Tafel kinetics for the anodic and the cathodic processes can be represented as:

$$\eta_a = b_a \log\left(\frac{i_a}{i^o_{Ox}}\right) = E_{corr} - e_{eq,Ox} \tag{3.45}$$

$$\eta_c = b_c \log\left(\frac{i_c}{i^o_{R}}\right) = E_{corr} - e_{eq,R} \tag{3.46}$$

Rewriting the equations for the corrosion potential, we obtain:

$$\begin{aligned} E_{corr} &= e_{eq,Ox} + b_a \log\left(\frac{i_a}{i^o_{Ox}}\right) \\ E_{corr} &= e_{eq,R} + b_c \log\left(\frac{i_c}{i^o_{R}}\right) \end{aligned} \tag{3.47}$$

At the point where the anodic and cathodic polarization curves intersect, the anodic (i_a) and the cathodic (i_c) currents are equal to the corrosion current (I_{corr}), and so the set of Eq. (3.47) take the form:

$$\begin{aligned} E_{corr} &= e_{eq,Ox} + b_a \log\left(\frac{I_{corr}}{i^o_{Ox}}\right) \\ E_{corr} &= e_{eq,R} + b_c \log\left(\frac{I_{corr}}{i^o_{R}}\right) \end{aligned} \tag{3.48}$$

where I_{corr} and E_{corr} are the only variables; the equilibrium potentials are calculated through the Nernst equation and the transfer coefficients are known parameters.

$$e_{eq,Ox} + b_a\left[\log(I_{corr}) - \log\left(i^o_{Ox}\right)\right] = e_{eq,R} + b_c\left[\log(I_{corr}) - \log\left(i^o_{R}\right)\right]$$

$$e_{eq,R} - e_{eq,Ox} = b_a\left[\log(I_{corr}) - \log\left(i^o_{Ox}\right)\right] - b_c\left[\log(I_{corr}) - \log\left(i^o_{R}\right)\right]$$

$$E_{cell} = \log(I_{corr})(b_a - b_c) + b_c \log\left(i^o_{R}\right) - b_a \log\left(i^o_{Ox}\right)$$

where $E_{cell} = e_{eq,R} - e_{eq,Ox}$.

Solving this equation and substituting Eq. (3.49) into either equation of Eq. (3.48), we obtain Eq. (3.50).

$$I_{corr} = \exp\left[\frac{\left(E_{cell} - b_c \log\left(i^o_{R}\right) + b_a \log\left(i^o_{Ox}\right)\right)}{b_a - b_c}\right] \tag{3.49}$$

$$E_{corr} = \frac{b_a b_c\left(\log\left(i^o_{Ox}\right) - \log\left(i^o_{R}\right)\right) + \left(b_a e_{eq,R} - b_c e_{eq,Ox}\right)}{b_a - b_c} \tag{3.50}$$

Example 3.6

Determine the corrosion potential, the corrosion rate, and the protective current of zinc in 1 N hydrochloric acid. Assume that the entire zinc surface acts as a cathode, Tafel slopes are $b_a = 0.1$ V/decade and $b_c = -0.1$ V/decade, and the exchange current densities for zinc dissolution and for hydrogen evolution on zinc are 10^{-5} and 10^{-8} A/cm^2, respectively.

Additional information:

$$e^{o}_{Zn^{2+}|Zn} = -0.762\,\text{V vs. SHE} \quad e^{o}_{H^{+}|H_2} = 0.00\,\text{V vs.SHE}$$

$$i^{o}_{Zn} = 10^{-5}\,\text{A/cm}^2 \quad i^{o}_{H_2} = 10^{-8}\,\text{A/cm}^2$$

Solution:

Writing the Tafel equations for both the cathodic and anodic parts, we obtain:

$$E_{corr} - (-0.762) = 0.1 \log\left(\frac{I_{corr}}{10^{-5}}\right)$$

$$E_{corr} - 0.0 = -0.1 \log\left(\frac{I_{corr}}{10^{-8}}\right)$$

These two equations can be solved simultaneously for E_{corr} and I_{corr}.
Adding both equations, we obtain:

$$2E_{corr} + 0.762 = 0.1 \log\left(\frac{I_{corr}}{10^{-5}}\frac{10^{-8}}{I_{corr}}\right)$$

$$E_{corr} = -0.531\,\text{V vs.SHE}$$

Substituting in the value of E_{corr} in one of the Tafel equations, one obtains:

$$I_{corr} = 2.04 \times 10^{-3}\,\text{A/cm}^2$$

Because the protective potential is equal to the equilibrium potential or $E_{prot} = e_{eq,\,Zn^{2+}|Zn} = -0.762\,\text{V vs.SHE}$, the overvoltage necessary to stop the corrosion is:

$$\eta_{prot} = E_{prot} - e_{eq,\,H^{+}|H_2} = -0.762 - 0.0 = -0.762\,\text{V vs.SHE.}$$

The protective current at protective potential is calculated by using the Tafel equation:

$$-0.762 - 0.0 = -0.1 \log\left(\frac{i_{prot}}{10^{-8}}\right)$$

$$i_{prot} = 0.42\,\text{A/cm}^2$$

Case Study 3.3

Calculate: (a) the corrosion rate of iron in an oxygen-free solution at a pH of 3.1, (b) the exchange current density for hydrogen evolution on iron, and (c) the cathodic current required to reduce the corrosion of iron to zero.

The concentration of the iron at the electrode interface is 0.02 M. The exchange current density for iron dissolution is $i^{o}_{Fe} = 9 \times 10^{-7} A/cm^2$ and the anodic slope $b_a = 0.04$ V/decade; the corrosion potential of iron is -0.215 V vs. RHE and $e^{o}_{Fe^{2+}|Fe} = -0.44 V$ vs. SHE. For hydrogen evolution reaction (HER), the cathodic slope $b_c = -0.12$ V/decade.

The required quantities can be obtained from an Evans diagram for the corrosion of iron in hydrogen-saturated, oxygen-free solution. Assume that charge-transfer kinetics controls the reaction rates and that the high-field approximation applies. In this example, iron corrodes by the electrochemical reaction producing iron ions at the anode:

$$Fe \rightleftharpoons Fe^{2+} + 2e^{-}$$

and hydrogen is reduced at the cathode:

$$2H^{+} + 2e^{-} \rightleftharpoons H_2$$

According to mixed potential theory, any electrochemical reaction consists of partial reduction and oxidation reactions. In any redox reaction, such as the corrosion of a metal, there is no net accumulation of electric charge and the rate of the oxidation must equal the rate of reduction. At the intersection of the cathodic and anodic kinetic lines (see Fig. 3.8), the rates of oxidation and reductions are equal. This point represents the corrosion potential, E_{corr}, and the corrosion current, I_{corr}. At the corrosion potential, the rate of iron dissolution is equal to the rate of hydrogen evolution. Note in Fig. 3.8, these rates are expressed in terms of current density.

Solution:

According to the Butler-Volmer equation, we have:

$$i = \overrightarrow{i} - \overleftarrow{i} = i^{o}\left\{\exp\left(\frac{-\alpha_c F\eta}{RT}\right) - \exp\left(\frac{\alpha_a F\eta}{RT}\right)\right\} \tag{3.28}$$

where

$$\eta_{Fe} = E_{corr} - e_{Fe^{2+}|Fe};\ \eta_{H_2} = E_{corr} - e_{H^{+}|H_2}$$

According to mixed potential theory:

$$I_{corr} = i_{Fe} = i_{H_2}$$

When the system departs very slightly from equilibrium

$$\left(E_{corr} - e_{Fe^{2+}|Fe}\right) \gg 59 mV$$

and

$$\left(E_{corr} - e_{H^{+}|H_2}\right) \ll 59 mV$$

The Butler-Volmer equation can be simplified for the anodic and cathodic reactions to:

$$i_{H_2} = i^{o}_{H_2} \exp\left(\frac{-\alpha_c nF}{RT}\eta_{H_2}\right) \tag{3.51}$$

$$i_{Fe} = i^{o}_{Fe} \exp\left(\frac{\alpha_a nF}{RT}\eta_{Fe}\right) \tag{3.52}$$

According to Eq. (3.52), the Tafel semilogarithm expressions are:

$$\eta_{Fe} = -\frac{RT}{\alpha_a nF}\ln i^{o}_{Fe} + \frac{RT}{\alpha_a nF}\ln i_{Fe}$$

$$a_a = -2.3\frac{RT}{\alpha_a nF}\log i^{o}_{a} \text{ and } b_a = 2.3\frac{RT}{\alpha_a nF}$$

and

$$\eta_{H_2} = \frac{RT}{\alpha_c nF}\ln i^{o}_{H_2} - \frac{RT}{\alpha_c nF}\ln i_{H_2}$$

$$a_c = 2.3\frac{RT}{\alpha_c nF}\log i^{o}_{c} \text{ and } b_c = -2.3\frac{RT}{\alpha_c nF}$$

(a) Calculation of corrosion rates:

$$b_a = \frac{2.3\,RT}{\alpha_a nF} = \frac{d\eta_{Fe}}{d\log i} = 0.04\,V/\text{decade}$$

$$a_a = -\left(\frac{2.3\,RT}{\alpha_a nF}\right)\log i^{o}_{Fe} = -b_a \log i^{o}_{Fe}$$

$$= -0.04\log\left(9\times10^{-7}\right) = 0.242V$$

$$a_a = 0.242V$$

$$e_{Fe^{2+}|Fe} = -0.44 + \frac{0.05916}{2}\log(0.02) = -0.490V \text{ vs. SHE}$$

$e_{Fe^{2+}|Fe}$ is in standard hydrogen electrode (SHE) scale and it needs to be converted into RHE scale before calculating η:

$$e^{o}_{H^+|H_2} = 0 - 0.05916\,pH = 0 - 0.05916\times3.1 = -0.183V \text{ vs. SHE}$$

$$e_{Fe^{2+}|Fe} = -0.490 - (-0.183) = -0.307V \text{ vs. RHE}$$

$$\eta_{Fe} = E_{corr} - e_{Fe^{2+}|Fe} = -0.215 - (-0.307) = 0.092V$$

$$\eta_{Fe} = a_a + b_a \log i_{Fe}$$

$$\log I_{corr} = -3.75$$

$$I_{corr} = 1.78\times10^{-4}\,A/cm^2$$

(b) Calculation of exchange current density for the hydrogen evolution reaction on iron:

$$\eta_{H_2} = a_c + b_c \log i_{H_2}$$

$$b_c = -\frac{2.3RT}{\alpha_c nF} = \frac{d\eta_{H_2}}{d\log i} = -0.12V$$

$$a_c = \left(\frac{2.3RT}{\alpha_c nF}\right)\log i^{o}_{H_2} = -b_c \log i^{o}_{H_2}$$

$$E_{corr} = -0.215\,\mathrm{V}$$

$$e^{o}_{H^+|H_2} = 0\,\mathrm{V\,vs.RHE}$$

$$\eta_{H_2} = -0.215\,\mathrm{V\,vs.RHE}$$

$$a_c = \eta_{H_2} - b_c \log \mathrm{I}_{corr} = -0.215 - (-0.12)\log\left(1.78 \times 10^{-4}\right) = -0.665\ V$$

$$log\, i^{o}_{H_2} = -\frac{a_c}{b_c} = -\left(\frac{-0.665}{-0.12}\right) = -5.54.$$

(c) Calculation of protection current:
To stop the corrosion of Fe, it is necessary to shift the iron corrosion to its equilibrium potential value $e_{eq,Fe^{2+}|Fe}$. Thus, $E_{prot} = e_{eq,Fe^{2+}|Fe} = -0.49\,\mathrm{V\,vs.SHE}$. At this potential, the corrosion reaction is reversed and the overvoltage for iron dissolution is equal to zero.

$$\eta_{prot} = e_{Fe^{2+}|Fe} - e_{H^+|H_2};\ \eta_{Fe} = 0$$

$$\eta_{prot} = -0.490 + 0.183 = -0.307\,\mathrm{V}$$

The cathodic current required to shift the iron electrode potential to its reversible value is calculated using the Tafel equation or:

$$\log i_{cathode} = \left(\eta_{H_2} - a_c\right)/b_c = (-0.307 + 0.665)/(-0.12) = -2.98;$$

$$i_{cathode}\left(i_{prot}\right) = 0.001\,\mathrm{A/cm^2}$$

As shown in Fig. 3.9, to eliminate corrosion a cathodic current of $0.001\ \mathrm{A/cm^2}$ should be applied to an iron electrode to shift the $Fe\,|\,Fe^{2+}$ electrode potential to -0.490 V vs. SHE, where the electrode is at equilibrium.

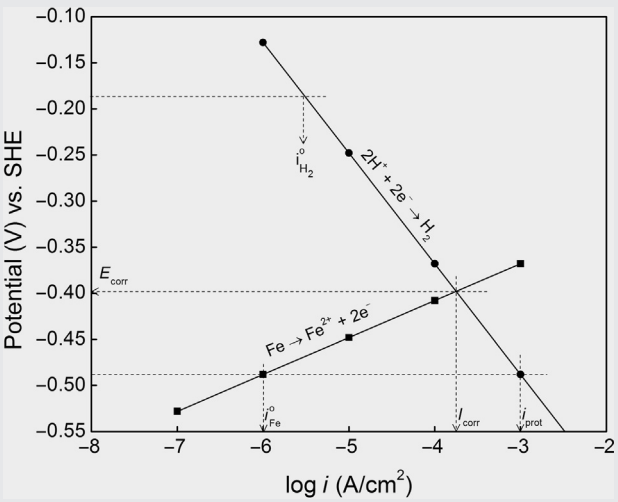

Fig. 3.9 Evans diagram for the iron dissolution in hydrogen-saturated oxygen-free solution of pH = 3.1.

Example 3.7 Iron corrosion in oxygen-saturated solution and evaluation of impressed current-cathodic protection system.

(a) Consider iron in a solution with a pH of 7 saturated with oxygen and a partial pressure of oxygen, $P_{O_2} = 1\,\text{atm}$. Calculate the corrosion current and the corrosion potential.
(b) Estimate the protection current required to reduce the corrosion current to zero:

Additional information:

$$\left[Fe^{2+}\right] = 0.7\text{M} \quad P_{O_2} = 1\text{ atm}$$
$$b_a = 0.08\text{V/decade} \quad b_c = -0.11\text{V/decade}$$
$$i^o_{Fe} = 10^{-5}\text{A/cm}^2 \quad i^o_{OH^-} = 10^{-6}\text{A/cm}^2$$

Solution:

Calculating the potentials:

$$2Fe^{2+} + 4e^- \rightarrow 2Fe,\ e^o_{Fe^{2+}|Fe} = -0.440\text{V vs. SHE}$$
$$O_2 + 2H_2O + 4e^- \rightarrow 4OH^-,\ e^o_{O_2|OH^-} = 0.401\text{V vs. SHE}$$
$$e_{eq,O_2|OH^-} = e^o_{O_2|OH} - 2.303\frac{RT}{nF}\log\left(\frac{\left(a_{OH^-}\right)^4}{P_{O_2}}\right)$$
$$e_{eq,O_2|OH^-} = 0.401 + 0.059(14-7)$$
$$e_{eq,O_2|OH^-} = 0.814\text{V vs. SHE}$$
$$e_{Fe^{2+}|Fe} = e^o_{Fe^{2+}|Fe} - 2.303\frac{RT}{nF}\log\left(\frac{a_{Fe}}{\left(a_{Fe^{2+}}\right)^2}\right)$$
$$e_{Fe^{2+}|Fe} = -0.440 - \frac{0.059}{4}\log\left(\frac{1}{(0.7)^2}\right)$$
$$e_{Fe^{2+}|Fe} = -0.445\text{V vs. SHE}$$

Calculation of E_{corr} and I_{corr}:

$$\eta = b\log\left(\frac{i}{i^o}\right)$$
$$\eta_c = b_c\log\left(I_{corr}\right) - b_c\log\left(i^o_{OH^-}\right)$$

$$\eta_a = b_a\log\left(I_{corr}\right) - b_a\log\left(i^o_{Fe}\right)$$
$$E_{corr} = e_{O_2|OH^-} + b_c\log\left(\frac{I_{corr}}{i^o_{OH^-}}\right)$$
$$E_{corr} = e_{eq,Fe^{2+}|Fe} + b_a\log\left(\frac{I_{corr}}{i^o_{Fe}}\right)$$

I_{corr} and E_{corr} are calculated using Eqs (3.49) and (3.50):

$$\log(I_{corr}) = \left[\frac{\left(E_{cell} - b_c \log\left(i^o_{OH^-}\right) + b_a \log\left(i^o_{Fe}\right)\right)}{(b_a - b_c)}\right]$$

$$I_{corr} = 10^{\left[\left(E_{cell} - b_c \log\left(i^o_{OH^-}\right) + b_a \log\left(i^o_{Fe}\right)\right)/(b_a - b_c)\right]}$$

$$= 10^{[(1.259-(-0.11)\log(10^{-6}) + 0.08\log(10^{-5}))/(0.08-(-0.11))]}$$

$$I_{corr} = 11.2\ \text{A/cm}^2$$

Using the analytical solution for the corrosion potential, Eq. (3.50),

$$E_{corr} = \frac{b_a b_c\left(\log\left(i^o_{Fe}\right) - \log\left(i^o_{OH^-}\right)\right) + \left(b_a e_{eq,O_2|OH^-} - b_c e_{eq,Fe^{2+}|Fe}\right)}{(b_a - b_c)}$$

$$E_{corr} = \frac{(0.08 \times (-0.11)(\log(10^{-5}) - \log(10^{-6})) + (0.08 \times 0.814) - (-0.11) \times -0.45)}{(0.08 - (-0.11))}$$

$$E_{corr} = 0.039\,\text{V vs. SHE}$$

Shifting the iron corrosion potential to the equilibrium potential value will stop the corrosion of Fe, $E_{prot} = e_{eq,Fe^{2+}|Fe} = -0.45$ V vs.SHE. To reverse the corrosion reaction, the overvoltage for iron dissolution must be zero, $\eta_{Fe} = 0$;

$$\eta_{prot} = E_{prot} - e_{O_2|OH^-};\ \eta_{Fe} = 0$$

$$\eta_{prot} = -1.259\,\text{V vs.SHE}$$

The cathodic current that is applied to the iron electrode to shift the iron electrode potential to its reversible value is calculated using the Tafel equation:

$$\log\left(i_{prot}\right) = \frac{\eta_{prot} - a_c}{b_c}$$

$$i_{prot} = 10^{\left(\eta_{prot} - a_c\right)/b_c}$$

According to Eqs. (3.31a) and (3.31b),

$$a_c = 2.3\frac{RT}{\alpha_c nF}\log i^o_c$$

and

$$b_c = -2.3\frac{RT}{\alpha_c nF}$$

or

$$a_c = -b_c \log\left(i^o_c\right)$$

$$a_c = 0.11\log\left(10^{-6}\right)$$

$$a_c = -0.66\,\text{V vs.SHE}$$

$$i_{prot} = 10^{(-1.259 + 0.66)/-0.11}$$

$$i_{prot} = 2.79 \times 10^5\ \text{A/cm}^2$$

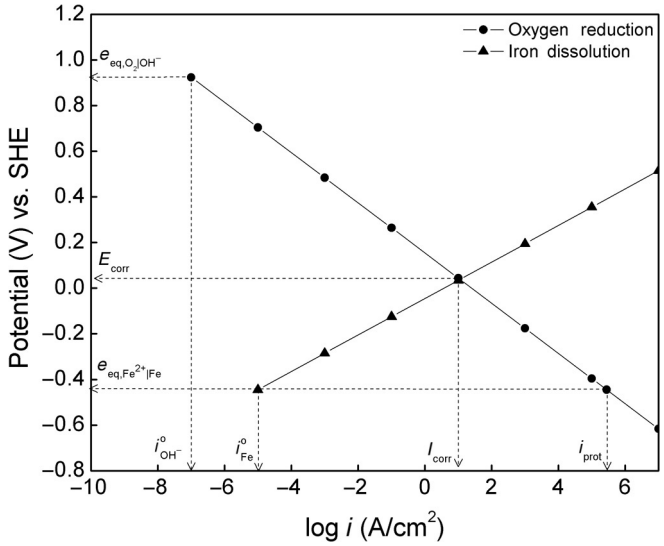

Fig. 3.10 Evans diagram for iron in oxygen-saturated solution.

A cathodic current of 3.03×10^5 A/cm^2 should be applied to the iron electrode to shift the Fe/Fe^{2+} electrode potential to its reversible value of -0.449 V vs. SHE, where the electrode is at equilibrium as shown in Fig. 3.10. The effect of electrode material and solution composition on oxygen overpotential is given in Table 3.3.

3.7 EFFECTS OF POLARIZATION BEHAVIOR ON THE CORROSION RATE

The mixed potential depends on the polarization behavior of the anodic and cathodic reactions. More precisely, specific parameters determine whether the mixed potential is close to the equilibrium value of the anode reaction or the cathode reaction. These parameters include the exchange current density and anodic and cathodic reaction transfer coefficients, which determine the Tafel slope. Based on these criteria, when the cathode is a highly polarizable electrode in comparison to the anode or when the Tafel slope for the cathodic reaction is much larger than the anodic reaction, the system is said to be cathodically controlled. In such a case, the corrosion potential of the system is very close to the anode equilibrium potential and is represented in Fig. 3.11a.

Conversely, when the anode is highly polarized in comparison to the cathode, the mixed potential lies close to the cathode equilibrium potential and such systems are anodically controlled. This type of corroding system is described in Fig. 3.11b.

A corroding system may be anodically or cathodically controlled based on the polarization of the corroding electrode in the specific medium. In some cases, the electrolyte resistance is so high that the electrodes will not be sufficiently polarized. In these cases, the corrosion current is controlled by the ohmic resistance in the solution.

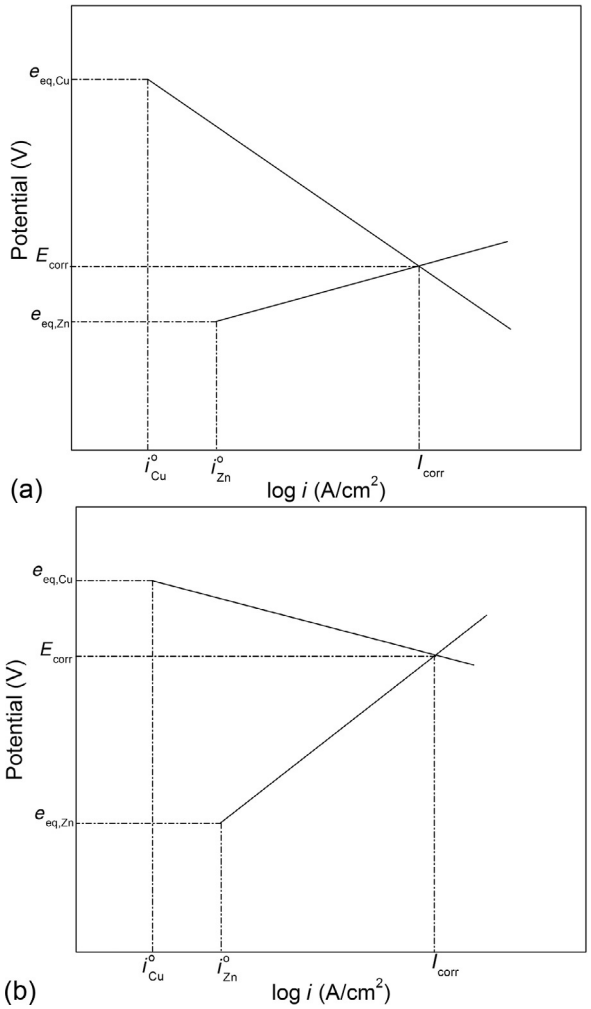

Fig. 3.11 Effect of the polarization curve on the mixed potential of a corroding system: (a) cathodically controlled, (b) anodically controlled.

Example 3.8—Effects of Polarization Behavior on the Corrosion Rate

For the following reactions:

$$2H^+ + 2e^- \rightarrow H_2(\text{Hydrogen Evolution})$$
$$M \rightarrow M^{2+} + 2e^-(\text{Metal Dissolution})$$

show that

(a) The corrosion current can be expressed as:

$$I_{corr} = \left\{ \left(i^o_M\right)^{b_a} \left(i^o_{H_2}\right)^{-b_c} \exp\left(2.303\left(e_{eq,H^+|H_2} - E_{eq,M^{2+}|M}\right)\right) \right\}^{1/(b_a - b_c)}$$

(b) When the exchange current densities for both the reactions are equal and the ratio of the transfer coefficients is 1/2 (i.e., $\alpha_a = \alpha_c = 1/2$), the corrosion potential is given by

$$E_{corr} = \frac{E_{eq,M^{2+}|M} + 2E_{eq,H^+|H_2}}{3}$$

Solution:

(a) The anodic and the cathodic processes occur according to the Tafel equations and intersect at the corrosion potential. Therefore,

$$\eta_a = b_a \log\left(\frac{I_{corr}}{i^o_M}\right) = E_{corr} - e_{eq,M^{2+}|M}$$

$$\eta_c = b_c \log\left(\frac{I_{corr}}{i^o_{H_2}}\right) = E_{corr} - e_{eq,H^+|H_2}$$

Eliminating E_{corr}, we obtain:

$$-e_{eq,M^{2+}|M} + e_{eq,H^+|H_2} = \log\left(\left(\frac{I_{corr}}{i^o_M}\right)^{b_a}\left(\frac{I_{corr}}{i^o_{H_2}}\right)^{-b_c}\right)$$

$$-e_{eq,M^{2+}|M} + e_{eq,H^+|H_2} = \log\left(\frac{(I_{corr})^{b_a - b_c}}{(i^o_M)^{b_a}\left(i^o_{H_2}\right)^{-b_c}}\right)$$

$$I_{corr} = \left\{(i^o_M)^{b_a}\left(i^o_{H_2}\right)^{-b_c}\exp\left(2.303\left(E_{eq,H^+|H_2} - E_{eq,M^{2+}|M}\right)\right)\right\}^{\frac{1}{b_a - b_c}}$$

If $\left(\frac{\alpha_a}{\alpha_c} = \frac{1}{2}\right)$, then $\left(\frac{b_a}{b_c} = -2\right)$; $\left\{b_c = -2.3\frac{RT}{\alpha_c nF},\ b_a = -2.3\frac{RT}{\alpha_a nF}\right\}$

Because $\eta_a = b_a \log\left(\frac{I_{corr}}{i^o_M}\right) = E_{corr} - e_{eq,M^{2+}|M}$; $\eta_c = b_c \log\left(\frac{I_{corr}}{i^o_{H_2}}\right) = E_{corr} - e_{eq,H^+|H_2}$

Rearranging the equations, we obtain:

$$\frac{E_{corr} - e_{eq,M^{2+}|M}}{b_a} = \log\left(\frac{I_{corr}}{i^o_M}\right)$$

$$\frac{E_{corr} - e_{eq,H^+|H_2}}{b_c} = \log\left(\frac{I_{corr}}{i^o_{H_2}}\right)$$

Because the exchange current densities are equal, $i^o_M = i^o_{H_2}$, the above equations become

$$E_{corr} - e_{eq,M^{2+}|M} = \frac{b_a}{b_c}\left(E_{corr} - e_{eq,H^+|H_2}\right)$$

from which

$$E_{corr} = \frac{e_{eq,M^{2+}|M} + 2e_{eq,H^+|H_2}}{3}$$

3.8 EFFECTS OF MASS TRANSFER ON ELECTRODE KINETICS

Under well-stirred conditions, when the currents are kept low enough for the concentration gradients in the electrolyte to be minimized, and the concentration at the electrode-electrolyte interface and the bulk do not vary significantly, Eq. (3.28) is valid. In real-time electrochemical applications, appreciable concentration gradients between the bulk and the interface always exist, and one often desires a rate expression that includes the concentration terms. At equilibrium, the rates of the forward and backward reactions are equal, and Eqs. (3.21a) and (3.21b) can be written as:

$$i_c = i_a = i^o \tag{3.24}$$

and

$$Fk_c^o C_o \exp\left(\frac{-\alpha_c F\left(E - e_{eq}\right)}{RT}\right) = Fk_a^o C_R \exp\left(\frac{\alpha_a F\left(E - e_{eq}\right)}{RT}\right) \tag{3.53}$$

At equilibrium, the bulk concentration and the surface concentration are the same, and Eq. (3.53) can be written as:

$$i^o = Fk_o C_o^b \exp\left(\frac{-\alpha_c F\left(e_{eq} - e^o\right)}{RT}\right) = Fk_o C_R^b \exp\left(\frac{\alpha_a F\left(e_{eq} - e^o\right)}{RT}\right) \tag{3.54}$$

where C_o^b and C_R^b are the concentrations of the oxidized species and reduced species in the bulk of the electrolyte at equilibrium. The current is the difference between the rates of the forward and the reverse reactions, which yields:

$$i = Fk_c^o C_O \exp\left(\frac{-\alpha_c F\left(E - e_{eq}\right)}{RT}\right) - Fk_a^o C_R \exp\left(\frac{\alpha_a F\left(E - e_{eq}\right)}{RT}\right) \tag{3.55}$$

Combining Eqs. (3.54) and (3.55), we obtain:

$$\frac{i}{i^o} = \frac{Fk_C^o C_O \exp\left(\frac{-\alpha_c F\left(E - e_{eq}\right)}{RT}\right)}{Fk_o C_O^b \exp\left(\frac{-\alpha_c F\left(e_{eq} - e^o\right)}{RT}\right)} - \frac{Fk_a^o C_R \exp\left(\frac{\alpha_a F\left(E - e_{eq}\right)}{RT}\right)}{Fk_o C_R^b \exp\left(\frac{\alpha_a F\left(e_{eq} - e^o\right)}{RT}\right)} \tag{3.56}$$

Upon rearranging, the concentration dependent Butler-Volmer equation is obtained.

$$i = i^o \left\{ \frac{C_O}{C_O^b} \exp\left(\frac{-\alpha_c F\left(E - e_{eq}\right)}{RT}\right) - \frac{C_R}{C_R^b} \exp\left(\frac{\alpha_a F\left(E - e_{eq}\right)}{RT}\right) \right\} \tag{3.57}$$

When there is no significant concentration gradient between the interface and the bulk, $C_R = C_R^b$ and $C_O = C_O^b$, Eq. (3.57) takes the form of Eq. (3.27). Based on the definition of limiting current (concentration at the interface is zero), one can evaluate the ratio of the concentration at the surface and the bulk to be:

$$\frac{C_R}{C_R^b} = 1 - \frac{i}{i_{a,L}} \tag{3.58a}$$

$$\frac{C_O}{C_O^b} = 1 - \frac{i}{i_{c,L}} \tag{3.58b}$$

where $i_{a,L}$ and $i_{c,L}$ are the anodic and cathodic limiting current densities, respectively. Thus, Eq. (3.57) may be more conveniently written in terms of limiting current density as:

$$i = i^o \left\{ \left(1 - \frac{i}{i_{c,L}}\right) \exp\left(\frac{-\alpha_c F\left(E - e_{eq}\right)}{RT}\right) - \left(1 - \frac{i}{i_{a,L}}\right) \exp\left(\frac{\alpha_a F\left(E - e_{eq}\right)}{RT}\right) \right\} \tag{3.59}$$

The effect of mass transfer on electrode kinetics is shown in Fig. 3.12. Many useful kinetic rate expressions based on Tafel conditions, mass transport limitations can be developed from Eq. (3.59). Prediction of mass transfer effects may be useful in corrosion systems depending on the system's corrosion conditions. The mass transport limitations in corrosion systems may alter the mixed potential of a corroding system. Under Tafel conditions (anodic or cathodic), Eq. (3.59) can be written as:

$$\left.\begin{aligned} i_a &= -i^o \left(1 - \frac{i}{i_{a,L}}\right) \exp\left(\frac{\alpha_a F\left(E - e_{eq}\right)}{RT}\right) \\ i_c &= i^o \left(1 - \frac{i}{i_{c,L}}\right) \exp\left(\frac{-\alpha_c F\left(E - e_{eq}\right)}{RT}\right) \end{aligned}\right\} \tag{3.60}$$

3.8.1 Diffusion-limited corrosion rate

The relationship between the potential and the logarithmic current density is not always linear (Tafel expression). In the case of a reacting species that is diffusion controlled, the logarithm of current density does not increase proportionally beyond a certain value of

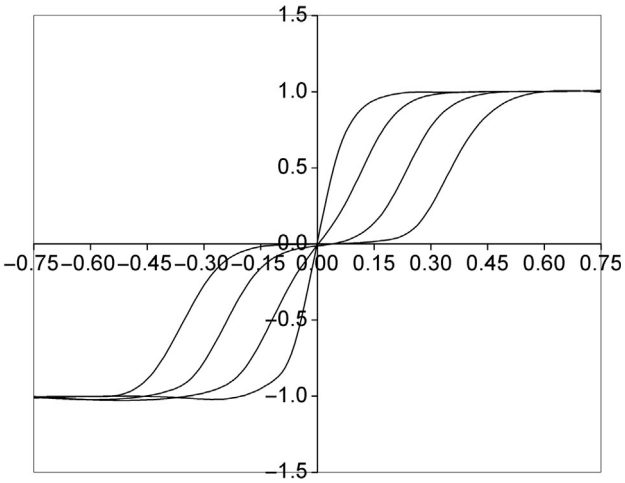

Fig. 3.12 Effect of concentration polarization.

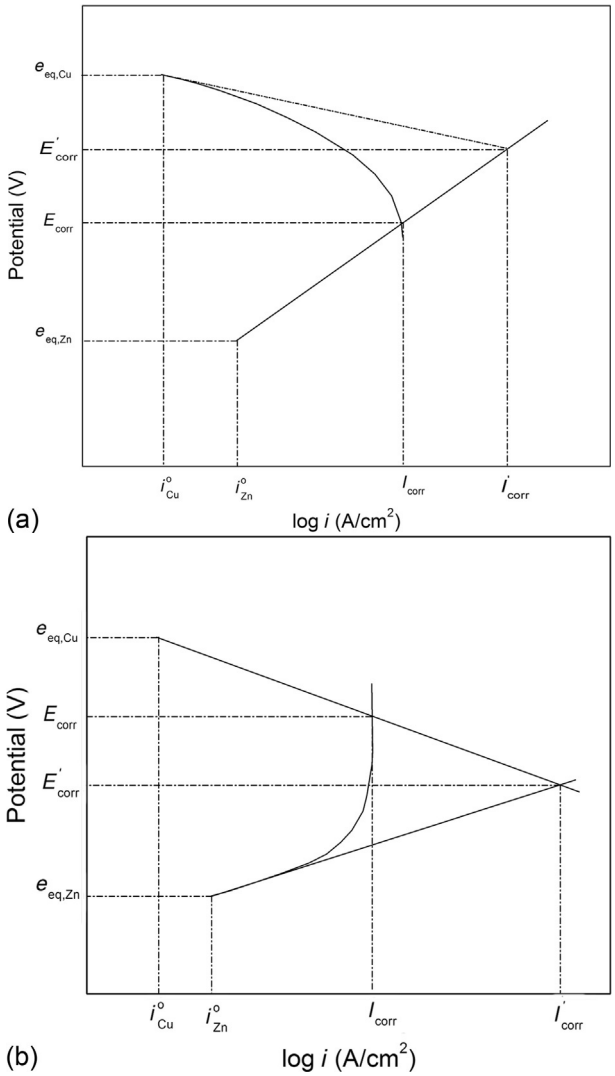

Fig. 3.13 Influence of diffusion-controlled polarization curves on the mixed potential of corroding systems: (a) cathodic diffusion control and (b) anodic diffusion control.

the overpotential. In such a case, the Evans diagram looks qualitatively like those in Fig. 3.13a or b, which represent a cathodically diffusion-limited system and an anodically diffusion-limited process (both the anodic and cathodic currents can be diffusion limited). The mixed potential in a diffusion-limited process is denoted by E_{corr}, while the mixed potential without diffusion limitations is represented by E'_{corr}; the corrosion currents for cases with and without diffusion limitations are denoted in a similar manner. Due to the

system's departure from linearity, the corrosion current and thus the corrosion rate for a diffusion-controlled system is lower than that of a system with linear kinetics (as shown by the dotted lines). Equation (3.32) for a diffusion-limited case would be:

$$\eta = b_c \log \frac{i}{i^o\left(1 - \frac{i}{i_{c,L}}\right)} \tag{3.61}$$

When the limiting current density, $i_{c,L}$, is large, Eq. (3.61) reduces to Eq. (3.32). Diffusion limitations can be suppressed by vigorously stirring the electrolyte solution. The mixing reduces the concentration gradients and increases species availability at the interface, thereby allowing the reactions to take place at a higher rate.

3.8.2 Rotating disk electrode

The rotating disk electrode is one of the most popular convective electrode systems and is widely used for research purposes to study the kinetics of electrochemical reactions. This is because it provides uniform concentration gradients along the electrode surface during electrochemical processes. The frequency of electrode rotation is controlled to adjust the extent of convection in the system. The hydrodynamics of the rotating disk electrode have been studied extensively [28–37] and an important result is the Levich equation:

$$i_L = 0.62nFD_o^{2/3}\omega^{1/2}\nu^{-1/6}C_b \tag{3.62}$$

where i_L is the current density that would be obtained in the limiting case when the concentration of the reaction species at the surface of the electrode is equal to zero. The term ω is the angular velocity, C_b is the concentration of the species in the bulk (far from the rotating disk electrode surface), ν is the kinematic viscosity, and D_o is the diffusivity of the species in the electrolyte. The Levich equation [28] takes into account both the rate of diffusion across the stagnant layer and the complex flow pattern near the rotating disk electrode surface. In particular, the Levich equation gives the peak current observed in rotating disk voltammetry. The limiting current thus obtained may be relevant to corrosion in that it changes the mixed potential and corrosion current, depending on the rotation speed. As shown in Fig. 3.14, increased angular velocity of the rotating disk electrode increases the corrosion rate to the point where the cathodic limiting current reaches the intersection of the cathodic and anodic polarization curves for the Tafel case. When the cathodic limiting current is greater than the Tafel case intersection, the effect of velocity does not affect the corrosion potential or the corrosion current. The cathodic polarization in Fig. 3.14 is diffusion limited, while the anodic polarization is of the Tafel type, without concentration limitations.

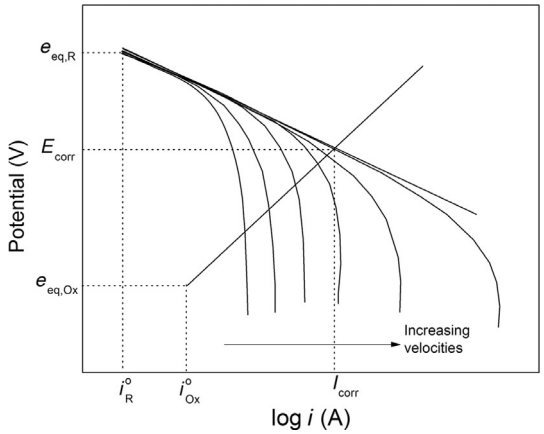

Fig. 3.14 Plot showing the effect of velocity of the fluid on the corrosion current and the corrosion potential of a corroding system.

Case Study 3.4—Effect of Limiting Current Density on the Corrosion Potential and Corrosion Current

For a system 10^{-3} M Cr^{3+} in hydrochloric acid at a pH of 1:

(a) Determine the corrosion current and potential

(b) Evaluate the corrosion current and potential if the mass transport limitation for a hydrogen reaction limits the maximum current to 10^{-5} A/cm^2.

(c) How would the corrosion potential and current change if the limiting current density for the hydrogen evolution reaction was 10^{-3} A/cm^2?

(d) Plot the Evans diagram for the three cases.

The values of the cathodic (b_c) and anodic (b_a) Tafel slopes are -0.10 V/decade and 0.12 V/decade, respectively. The exchange current densities for both the anodic and cathodic reactions are given to be 10^{-6} and 10^{-8} A/cm^2.

Additional information:

$$b_a = 0.12\,\text{V/decade} \quad b_c = -0.1\,\text{V/decade}$$

$$\left(i^o_{Cr^{2+}} = 10^{-6}\,\text{A/cm}^2 \quad i^o_{H_2} = 10^{-8}\,\text{A/cm}^2\right)$$

Solution:

The half-cell equilibrium potentials are calculated based on the Nernst equation:

$$e_{eq,Cr^{3+}|Cr^{2+}} = e^o_{Cr^{3+}|Cr^{2+}} + \frac{0.059}{3}\log\left(a_{Cr^{3+}}\right) = -0.744 + \frac{0.059}{3}\log\left(10^{-3}\right) = -0.803\,\text{V vs. SHE}$$

$$e_{eq,H^+|H_2} = e^o_{H^+|H_2} + \frac{0.059}{3}\log\left(a_{H^+}\right)^3 = -0.059(\text{pH}) = -0.059\,\text{V vs. SHE}$$

(a) Writing the Tafel equations for both the cathode and anode, we obtain:

$$E_{corr} - (-0.059) = -0.1 \log\left(\frac{I_{corr}}{10^{-8}}\right)$$

$$E_{corr} - (-0.803) = 0.12 \log\left(\frac{I_{corr}}{10^{-6}}\right)$$

Solving the above equations
$E_{corr} = -0.506$ V vs. SHE
$I_{corr} = 2.97 \times 10^{-4}$ A/cm^2.

(b) When the cathodic current is limited by diffusion to a maximum of 10^{-5} A/cm^2 then the mixed potential will be on the anodic line where the current is 10^{-5} A/cm^2 ($I_{corr} = 10^{-5}$ A/cm^2)

Thus, the mixed potential in this case would be:

$$E_{corr} - (-0.803) = 0.12 \log\left(\frac{10^{-5}}{10^{-6}}\right);\ E_{corr} = -0.683\,\text{V vs. SHE}$$

(c) When the cathodic limiting current density is 10^{-3} A/cm^2, more than when there was no diffusion limitation (part a), then the effect of limiting current density does not influence the corrosion current or the corrosion potential and so the analysis of part (a) is not affected and the results are the same:

$$E_{corr} = -0.506\,\text{V vs.SHE}$$

$$I_{corr} = 2.97 \times 10^{-4}\,\text{A/cm}^2$$

The Evans diagrams for the three cases are shown in Fig. 3.15a–c.

(d) The effect of the limiting current density on the corrosion potential and corrosion current is shown in Fig. 3.15a and b.

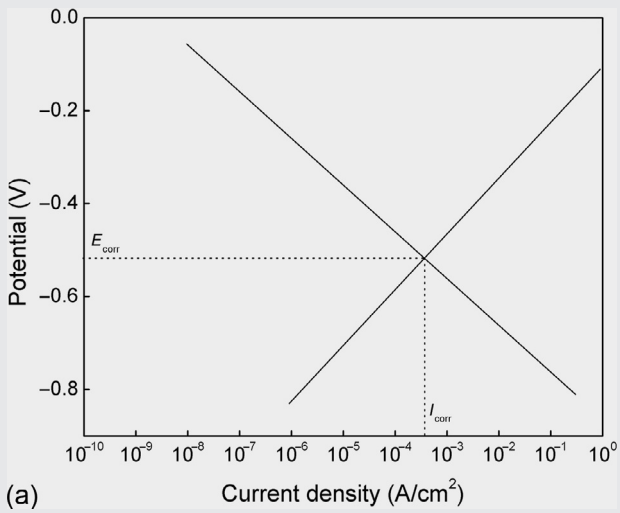

Fig. 3.15 Evans diagram showing the effect of limiting current density on the corrosion potential and corrosion current.

Continued

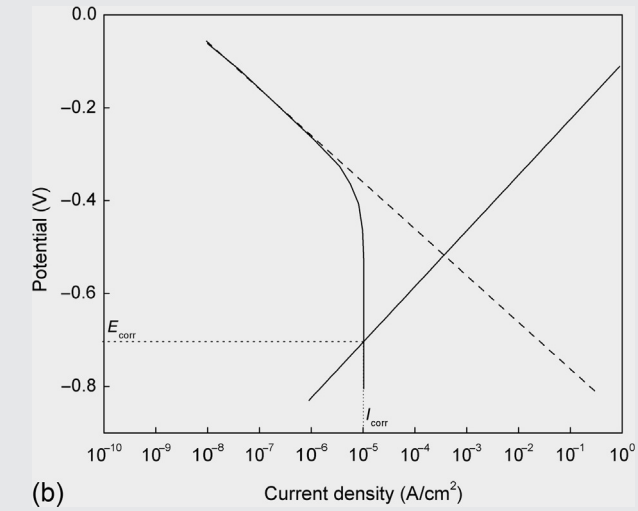

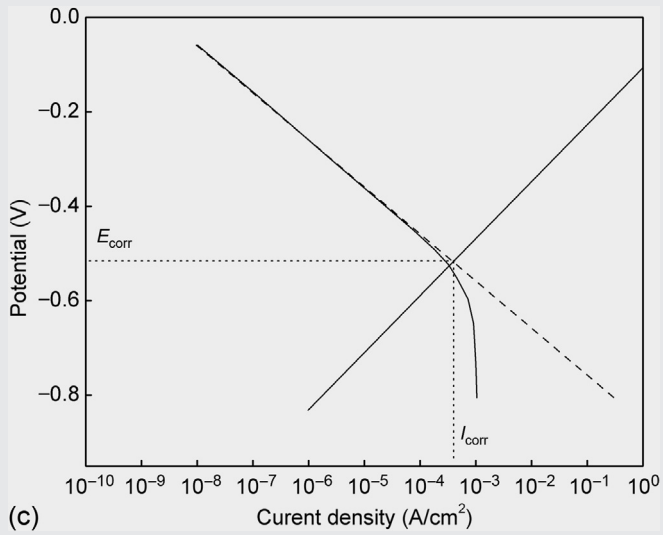

Fig. 3.15—cont'd

Case Study 3.5—The Effect of Rotation Speed on the Corrosion Potential

In a rotating disk system of iron in sulfuric acid maintained at a pH of 1, the limiting cathodic current density due to the evolution of hydrogen changes with rotation speed. As a result, the corrosion potential of the system also changes. (a) Plot the modified Evans diagram, showing the effect of limiting current on the corrosion potential and corrosion current for various rotation speeds. Show how the corrosion potential varies as a function of the rotating speed and evaluate the critical velocity

beyond which the corrosion potential of this system equals the corrosion potential of a similar system with no diffusion limitations.

Additional information:

The cathodic and anodic reaction parameters are $\partial\eta_c/\partial\log i = -0.05$ V/decade, $\partial\eta_a/\partial\log i = 0.05$ V/decade, $i^o_{H_2} = 10^{-8}\,A/cm^2$, $i^o_{Fe} = 10^{-6}\,A/cm^2$. Assume the concentration of Fe^{2+} in the system to be equal to 0.3 M, $D_o = 10^{-12}\,m^2/s$, $\nu = 1$ cP.

Solution:

The half-cell equilibrium potentials are calculated based on the Nernst equation.

$$e_{eq,Fe^{2+}|Fe} = e^o_{Fe^{2+}|Fe} + \frac{0.059}{2}\log(a_{Fe^{2+}}) = -0.440 + \frac{0.059}{2}\log(0.3) = -0.455\,V\,vs.SHE$$

$$e_{eq,H^+|H_2} = e^o_{H^+|H_2} + \frac{0.059}{2}\log(a_{H^+})^2 = -0.059(pH) = -0.059\,V\,vs.SHE$$

The corrosion potential and corrosion current when there are no diffusion limitations or the rotating speed tends to infinity are calculated by solving the anodic and cathodic Tafel equations. Writing the Tafel equations for both the cathodic and anodic parts, we obtain:

$$E_{corr} + 0.059 = -0.05\log\left(\frac{I_{corr}}{10^{-8}}\right)$$

$$E_{corr} + 0.4554 = 0.05\log\left(\frac{I_{corr}}{10^{-6}}\right)$$

Solving the above equations, we obtain:

$$E_{corr} = -0.307\,V\,vs.SHE$$

$$I_{corr} = 9.21 \times 10^{-4}\,A/cm^2$$

The limiting current density is then calculated as a function of rotation speed using the Levich equation. From Eq. (3.62) we obtain: $i_L = 0.62nFD_o^{2/3}\omega^{1/2}\upsilon^{-1/6}C_b = 0.62 \times 2 \times 96487 \times (10^{-12})^{2/3}\omega^{1/2}(10^{-3})^{-1/6}0.3 \times 10^3\,A/cm^2$

$$i_L = 1.135 \times 10^{-4}\omega^{1/2}\,A/cm^2$$

Rewriting the Tafel equations and considering the cathodic diffusion limitations, we obtain using Eq. (3.61):

$$E_{corr} - (-0.059) = -0.05\log\frac{I_{corr}}{10^{-8}\left(1 - \frac{I_{corr}}{i_L}\right)}$$

$$E_{corr} - (-0.4554) = 0.05\log\left(\frac{I_{corr}}{10^{-6}}\right)$$

Utilizing the expression for the cathodic limiting current density as a function of the rotation speed, the Tafel equations take the form:

$$E_{corr} + 0.059 = -0.05\log\frac{I_{corr}}{10^{-8}\left(1 - \frac{I_{corr}}{1.135 \times 10^{-4}\omega^{1/2}}\right)}$$

$$E_{corr} + 0.4554 = 0.05 \log\left(\frac{I_{corr}}{10^{-6}}\right)$$

Solving these two equations for a particular value of angular velocity, we obtain the corrosion potential and the corrosion current. Figure 3.16 shows the Evans diagram plotted for various angular velocities. As noted from the plot, below 600 rpm the anodic and the cathodic slopes intersect closer to the equilibrium potential of iron, while beyond 600 rpm, no matter how much the rotation speed is increased, the corrosion potential is always equal to the corrosion potential of the system when there are no diffusion limitations (shown in the cathodic dark line).

The effect of rotation speed on the corrosion potential of a system is shown in Fig. 3.17. This figure shows that beyond about 600 rpm, the corrosion potential remains the same.

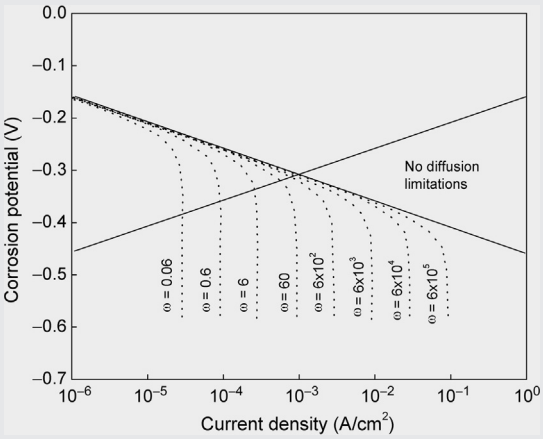

Fig. 3.16 Evans diagram showing the effect of rotation speed on the corrosion potential.

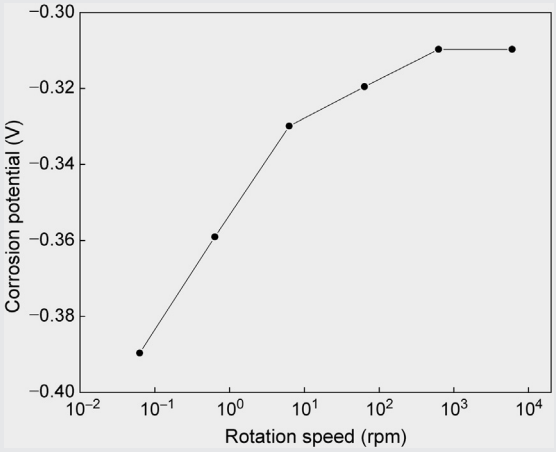

Fig. 3.17 Effect of rotation speed on the corrosion potential of a system.

Case Study 3.6—Effect of Rotational Speed on Corrosion Potential

Consider iron immersed in an aerated corrosive solution saturated with oxygen. The oxygen reduction in this system is diffusion controlled. Table 3.4 shows the variation of the limiting current of oxygen with the velocity of the electrolyte.

Table 3.4 Limiting Cathodic Current Data as a Function of Electrolyte Velocity

Electrolyte Velocity (m/s)	Limiting Current (A/cm^2)
0(1)	0.001
10(2)	0.010
20(3)	0.100
30(4)	1.000
40(5)	10.00

(a) Construct the cathodic and anodic Tafel plots for the above system under each case. Also, calculate the corrosion current and corrosion potential for each case. Plot the corrosion current vs. velocity, and explain the effect of the electrolyte velocity.
(b) To protect the above system, a sacrificial Zn-Mn alloy with an equilibrium potential of −1.0 V vs. SHE is coupled to the system. Estimate the galvanic current, corrosion potential, and corrosion current of the system for the above plots when the sacrificial anode is coupled to iron.

Given:

$$b_a = 0.1, \quad b_c = -0.1 \quad P_{O_2} = 1\,\text{atm}, \quad \left[Fe^{2+}\right] = 0.5\,\text{M}, \quad \text{pH} = 10$$

$$i^{o}_{O_2|OH^-} = 10^{-7}\,\text{A/cm}^2 \quad i^{o}_{Fe^{+2}|Fe} = 10^{-5}\,\text{A/cm}^2 \quad e_{eq,Fe^{2+}|Fe} = -0.4606\,\text{V vs. SHE}$$

$$i^{o}_{Zn-Mn}\text{anode} = 10^{-5}\,\text{A/cm}^2 \quad e_{eq,Zn|Mn} = -1.0\,\text{V vs. SHE}$$

Solution:

(a) The cathodic reaction is:

$$O_2 + 2H_2O + 4e^- \rightarrow 4OH^-$$

The equilibrium potential for cathodic reaction is calculated using the Nernst equation:

$$e_{O_2|OH^-} = 1.227 - 0.059(\text{pH})$$

The anodic Tafel equation for iron dissolution is:

$$\eta_a = b_a \log\left(\frac{i_a}{i^{o}_a}\right)$$

where

$$\eta_a = E_{corr} - e_{eq,Fe^{+2}|Fe}$$

$$\eta_c = b_c \log\left(\frac{i_c}{i^{o}_c}\right)$$

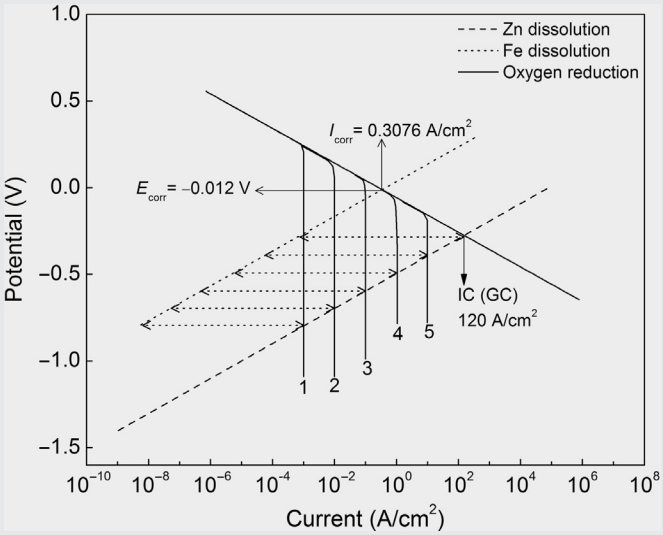

Fig. 3.18 Evans diagram showing the effect of electrolyte velocity on the corrosion potential.

where

$$\eta_c = E_{corr} - e_{eq,O_2|OH^-}$$

The corrosion currents and potentials presented in Fig. 3.18 are obtained by constructing the Evans diagram. The points $(e_{eq,Fe^{2+}|Fe}, i^o_{Fe^{2+}|Fe})$ and $(e_{eq,O_2|OH^-}, i^o_{O_2|OH^-})$ are marked on a semilogarithmic graph of E vs. i. From the points marked, straight lines with the slope b_c from $(e_{eq,O_2|OH^-}, i^o_{O_2|OH^-})$ and b_a from $(e_{eq,Fe^{2+}|Fe} i^o_{Fe^{2+}|Fe})$ are extended. The two straight lines intersect at the point (E_{corr}, I_{corr}) giving the corrosion potential and the corrosion current, respectively. The corrosion current and the corrosion potential can also be estimated analytically by simultaneously solving the anodic and cathodic Tafel equations.

As shown in Fig. 3.18, similar cathodic Tafel plots are constructed for each limiting current. The point of intersection of the anodic and cathodic curves provides the corrosion current and corrosion potential as a function of the electrolyte velocity for the oxygen-iron system. Note that the value of the sacrificial current increases with increased electrolyte velocity.

From the plots, it is seen that the corrosion current increases as the angular velocity increases from 0 to 30. However, when the velocity is increased further, the reduction of oxygen becomes activation controlled. As a result, the corrosion rate becomes independent of velocity. Table 3.5 summarizes the corrosion current and the corrosion potential as a function of electrolyte angular velocity. The data were taken from Fig. 3.18.

(b) To estimate the corrosion current and the corrosion potential when sacrificial Zn-Mn alloy is short circuited with iron, the anodic Tafel line for Zn-Mn sacrificial alloy is plotted in Fig. 3.19. The point of intersection of the Zn-Mn dissolution line and cathodic oxygen Tafel line provides the value of the galvanic current (GC) or impressed current (IC) and the corrosion potential.

The intersection of the anodic Zn-Mn alloy dissolution line and the cathodic oxygen reduction line for different electrolyte velocities gives a new value for E_{corr} and

Table 3.5 Estimated Corrosion Current and Corrosion Potential as a Function of Electrolyte Velocity

Electrolyte Velocity (m/s)	Corrosion Current (A/cm^2)	Corrosion Potential (V)
0	0.001	−0.260
10	0.010	−0.160
20	0.100	−0.060
30	0.307	−0.012
40	0.307	−0.120

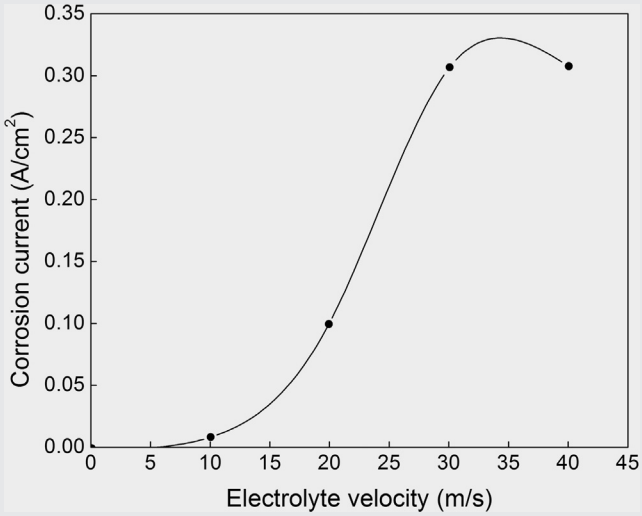

Fig. 3.19 Corrosion current as a function of electrolyte velocity.

Table 3.6 Corrosion Current and Corrosion Potential as a Function of Electrolyte Velocity in Zn-Mn Sacrificial Alloy

Electrolyte Velocity (m/s)	Corrosion Current (A/cm^2)	Corrosion Potential (V vs. SHE)
0	4.05×10^{-8}	−0.8
10	4.05×10^{-7}	−0.7
20	4.05×10^{-6}	−0.6
30	4.05×10^{-6}	−0.5
40	4.05×10^{-5}	−0.4

galvanic current provided by Zn-Mn. Figure 3.19 and Table 3.6 indicate that by decreasing the limiting current of oxygen, the cathodic polarization due to the sacrificial anode is increased. Also, the galvanic current needed to protect the system decreases. For each oxygen diffusion limiting current, the corrosion current and the corrosion potential for the iron dissolution system were estimated from Fig. 3.19 and are summarized in Table 3.6 for the for the iron dissolution system.

The results indicate that the system is underprotected when the velocity of the electrolyte is greater than or equal to 40 m/sec, and it is overprotected when the velocity is less than or equal to 30 m/s.

EXERCISES

E3.1. The potential of a zinc electrode on which Zn deposits from a 0.1 M $ZnSO_4$ solution is −1.1 V vs. SCE.
(a) Determine the zinc deposition potential on the hydrogen scale.
(b) Determine whether oxidation or reduction occurs at this potential.

E3.2. Copper is immersed in a solution of AgCl where the activity of Ag^+ is 0.01 M. The following ion exchange reaction occurs during corrosion of copper:

$$Cu + 2Ag^+ \rightarrow Cu^{2+} + 2Ag.$$

Estimate the concentration of Cu^{2+} that would trigger the copper corrosion to stop.

E3.3. Calculate the anodic exchange current density for tin for an overpotential of 0.2 V if the corrosion current is 0.5 A/cm^2. The anodic Tafel slope, b_a, is 0.05 V/decade.

E3.4. Using the Tafel equations, derive:
(a) The corrosion current equation (dependence of I_{corr} on $i^o_{H_2}$ and i^o_M).
(b) The corrosion potential equation (dependence of E_{corr} on $i^o_{H_2}$ and i^o_M).

E3.5. Construct an Evans diagram (E vs. log i) for the corrosion of silver in a hydrogen-saturated 0.1 M HCl solution where the activity of Ag^{2+} is 10^{-18} M. The corrosion reaction data is as follows:

$$\left[Ag^{2+}\right] = 10^{-18}\,\text{M} \quad [H^+] = 0.1\,\text{M}$$

$$a_c = -0.0824\,\text{V vs. SHE} \quad b_a = 0.100\,\text{V/decade} \quad b_c = -0.100\,\text{V/decade}$$

$$i^o_{Ag} = 0.8\,\text{A/cm}^2 \quad i^o_{H_2} = 0.15\,\text{A/cm}^2$$

Calculate:
(a) Equilibrium potentials of the hydrogen and Ag redox reaction.
(b) Corrosion current and corrosion potential.
(c) Protection current to prevent corrosion.

E3.6. A lead electrode is immersed in an oxygen-saturated 0.1 M $PbSO_4$ solution. Calculate and plot the corrosion current at pH between 3 and 6. The Tafel constants are $b_a = -b_c = 0.10$ V/decade and the exchange current densities for lead and oxygen reduction are 10^{-1} and 10^{-2} A/cm^2, respectively.

E3.7. Iron corrodes in a solution saturated with oxygen. The pH of the solution is 7 and the partial pressure of oxygen is 1 atm.
(a) Calculate the corrosion current and corrosion potential of the system.
(b) Calculate the protection current required to reduce the corrosion current to zero.

Additional information:

$$[\mathrm{Fe}] = 0.7\,\mathrm{M} \quad \mathrm{pH} = 7 \quad P_{O_2} = 1\ \mathrm{atm}$$

$$b_a = 0.08\,\mathrm{V/decade} \quad b_c = -0.11\,\mathrm{V/decade}$$

$$i^{o}_{Fe} = 10^{-5}\,\mathrm{A/cm^2} \quad i^{o}_{OH^-} = 10^{-6}\,\mathrm{A/cm^2}$$

E3.8. Derive an expression for the slope of the corrosion rate vs. pH for zinc in a 0.01 M $ZnCl_2$ solution. Assume that all zinc acts as a cathode and assume that there is no concentration polarization.

E3.9. The exchange current density and the cathodic Tafel slope, b_c, of platinum in a deaerated H_2SO_4 solution with a pH of 2.0 are 7.6×10^{-6} and -0.025 V/decade, respectively. Calculate the current in A/cm^2 when platinum is polarized cathodically at -0.334 V vs. SCE.

E3.10. Calculate the limiting current density for oxygen reduction in alkaline solution if the oxygen concentration is 0.4 mol/m^3, the diffusion coefficient, D_{O_2}, is equal to 5.0×10^{-10} m^2/s, and the diffusion layer thickness is 195.3 μm.

E3.11. Nickel is deposited at a current density of 75 A/m^2. Calculate the limiting current if the reduction occurs at a concentration overpotential of -150 mV.

E3.12. Calculate the corrosion potential, corrosion current, and protection current needed to stop corrosion for cadmium in a corrosive deaerated medium.

Additional information:

$$\left[Cd^{2+}\right] = 10^{-5}\,\mathrm{M} \quad \mathrm{pH} = 1 \quad a_c = -0.360\,\mathrm{V\ vs.\ SHE}$$

$$b_a = 0.100\,\mathrm{V/decade} \quad b_c = -0.120\,\mathrm{V/decade} \quad i^{o}_{Cd} = 10^{-3}\,\mathrm{A/cm^2}$$

REFERENCES

[1] H.H. Uhlig, R.W. Revie, Corrosion and Corrosion Control, third ed., John Wiley & Sons, New York, 1985.
[2] K.J. Vetter, Electrochemical Kinetics: Theoretical and Experimental Aspects, Academic Press, New York, 1967.
[3] W.H. Smyrl, in: J.O.M. Bockris (Ed.), Comprehensive Treatise of Electrochemistry, Electrochemical Materials Science, vol. IV, Plenum Press, New York, 1997, p. 97.
[4] A.J. Bard, L.R. Faulkner, Electrochemical Methods, Wiley, New York, 1980.
[5] H. Kaesche, Metallic Corrosion, English translation of: Die Korrosion der Metalle, second ed., NACE, Huston, Texas, 1985.
[6] S. Glasstone, Text-book of Physical Chemistry, Van Nostrand, NewYork, 1943.
[7] J. Newman, K.E. Thomas-Alyea, Electrochemical Systems, Prentice Hall, New Jersey, 1991.
[8] D. Jones, Polarization in high resistivity media, Corros. Sci. 8 (1968) 19–27.
[9] B.E. Wilde, Corrosion measurements in water-cooled nuclear reactor environments, Corrosion 23 (1967) 379–384.
[10] P.J. Morgan, Auxillary electrode method for determination of ohmic resistance, Corrosion 42 (1986) 432–434.
[11] B.E. Conway, Electrochemical Data, Elsevier, New York, 1952.

[12] A.C. Makrides, Dissolution of iron in sulfuric acid and ferric sulfate solutions, J. Electrochem. Soc. 107 (1960) 869–877.
[13] M. Stern, The electrochemical behavior, including hydrogen overvoltage, of iron in acid environments, J. Electrochem. Soc. 102 (1955) 609–616.
[14] W. Roitar, W. Jura, E. Polujan, Electrochemical polarization of metallic electrodes. I. Mechanism of the polarization of the iron electrode, Acta Physicochim. 10 (1939) 389–414.
[15] M. Stren, R.M. Roth, Anodic behavior of iron in acid solutions, J. Electrochem. Soc. 104 (1957) 390–392.
[16] G. Okamoto, M. Nagayama, N. Sato, Application of the "rapid" method for the measurement of polarization characteristics of iron in acid solutions, in: International Committee of Electrochemistry, Thermodynamics and Kinetics, 8th Meeting, Madrid, 1956, Butterworth's, Sevenoaks, Kent, England, 1958, , pp. 72–89.
[17] T.P. Hoar, T. Hurlen, Kinetics of the $Fe|Fe_{aq}^{++}$ electrode, in: International Committee of Electrochemistry, Thermodynamics and Kinetics, 8th Meeting Madrid, 1956, Butterworth's, Sevenoaks, Kent, England, 1958, pp. 445–447.
[18] K. Bonhoeffer, H. Heusler, Anodic solution of iron, Z. Elektrochem. Angew. P. 61 (1957) 122–123.
[19] J. Tafel, Cathodic polarization in diluted sulfuric acid, Z. Elektrochem. Angew. P. 8 (1902) 604–607.
[20] J. Tafel, K. Schmitz, On the reducing action of lead and mercury cathodes in sulphuric acid solutions, Z. Elektrochem. Angew. P. 8 (1902) 281–285.
[21] L.I. Antropov, Theoretical Electrochemistry, Translated from Russian, MIR Publishers, Moscow, 1972.
[22] C. Wagner, W. Traud, On the interpretation of corrosion processes through superposition of electrochemical partial processes and on the potential of mixed electrodes, Z. Elektrochem. 44 (1938) 391–393.
[23] M. Stern, A.L. Geary, Electrochemical polarization I. A theoretical analysis of the shape of polarization curves, J. Electrochem. Soc. 104 (1957) 56–63.
[24] M. Stern, A method for determining corrosion rates from linear polarization data, Corrosion 14 (1958) 440t–444t.
[25] M. Stern, Surface area relations in polarization and corrosion, Corrosion 14 (1958) 329t–332t.
[26] U.R. Evans, Distribution and velocity of the corrosion of metals, J. Franklin Inst. 298 (1929) 45–58.
[27] U.R. Evans, Corrosion and Oxidation of Metals, Edward Arnold, London, 1960.
[28] V.G. Levich, Physicochemical Hydrodynamics, Prentice Hall, Englewood Cliffs, New Jersey, 1962.
[29] J.N. Agar, Diffusion and convection at electrodes, Disc. Faraday Soc. 1 (1947) 26–37.
[30] J. Maruyama, M. Inaba, Z. Ogumi, Rotating ring-disk electrode study on the cathodic oxygen reduction at Nafion®-coated gold electrodes, J. Electroanal. Chem. 458 (1998) 175–182.
[31] U.A. Paulus, A. Wokauna, G.G. Scherer, T.J. Schmidt, V. Stamenkovic, N.M. Markovic, P.N. Ross, Oxygen reduction on high surface area Pt-based alloy catalysts in comparison to well defined smooth bulk alloy electrodes, Electrochim. Acta 47 (2002) 3787–3798.
[32] E. Ahlberg, A.E. Broo, Oxygen reduction at sulphide minerals. 1. A rotating ring disc electrode (RRDE) study at galena and pyrite, Int. J. Miner. Process. 46 (1996) 73–89.
[33] R.H. Castellanos, A. Campero, O. Solorza-Feria, Synthesis of W-Se-Os carbonyl electrocatalyst for oxygen reduction in 0.5 M H_2SO_4, Int J. Hyd. Energy 23 (1998) 1037–1040.
[34] T.J. Schmidt, H.A. Gasteiger, G.D. Stäbc, P.M. Urbanc, D.M. Kolb, R.J. Behm, Characterization of high-surface-area electrocatalysts using a rotating disk electrode configuration, J. Electrochem. Soc. 145 (1998) 2354–2358.
[35] O. Solorza-Feria, S. Ramírez-Raya, R. Rivera-Noriega, E. Ordoñez-Regil, S.M. Fernández-Valverde, Kinetic studies of molecular oxygen reduction on $W_{0.013}Ru_{1.27}Se$ thin films chemically synthesized, Thin Solid Films 311 (1997) 164–170.
[36] T.J. Schmidt, U.A. Paulus, H.A. Gasteiger, N. Alonso-Vante, R.J. Behm, Oxygen reduction on $Ru_{1.92}Mo_{0.08}SeO_4$, Ru/carbon, and Pt/carbon in pure and methanol-containing electrolytes, J. Electrochem. Soc. 147 (2000) 2620–2624.
[37] M. Lefevre, J. Dodelet, Fe-based catalysts for the reduction of oxygen in polymer electrolyte membrane fuel cell conditions: determination of the amount of peroxide released during electroreduction and its influence on the stability of the catalysts, Electrochim. Acta 48 (2003) 2749–2760.

CHAPTER 4

Passivity

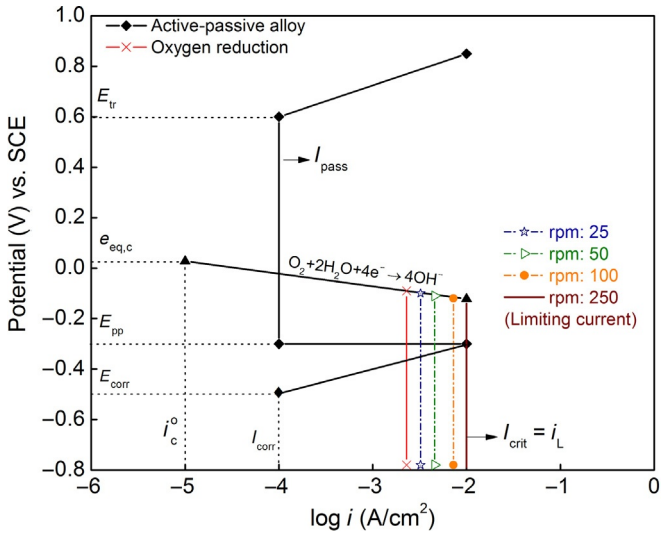

Chapter Contents

Corrosion Engineering
http://dx.doi.org/10.1016/B978-0-444-62722-3.00004-5

4.1 ACTIVE-PASSIVE CORROSION BEHAVIOR

A metal is in a passive state if its rate of anodic dissolution in a corrosive environment decreases with the increase in the applied potential toward more noble values or with the increase in the concentration of an oxidizing agent in the solution [1–3]. Faraday was the first to observe that iron substantially resists corrosion after its initially very high dissolution in concentrated nitric acid. The observed stability of iron in concentrated nitric acid was defined as the passive state of the metal [4]. The metal passivates through interaction with oxidizing agents such as nitric acid, an oxidizing redox couple such as $Fe^{3+}|Fe^{2+}$, or by anodic polarization. An active-passive metal possesses active, passive, and transpassive regions in the polarization curve. A typical anodic polarization curve of an active-passive metal is shown in Fig. 4.1.

In the active region, the anodic electrochemical reaction is the metal oxidation. In this region, the corrosion potential and corrosion current are defined by Tafel kinetics of individual redox reactions. The corrosion rate, I_{corr}, and the corrosion potential, E_{corr},

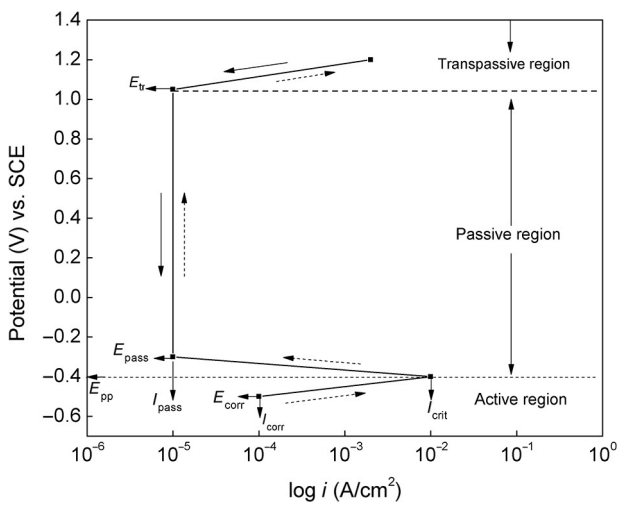

Fig. 4.1 Potentiostatic polarization curves (forward and reverse scan).

are controlled by the standard electrode potentials and exchange current densities of the individual redox reactions. The cathodic polarization reactions are the reduction of the oxidizer and hydrogen or oxygen evolution reactions. In the active state, the corrosion current increases upon further polarization from the corrosion potential. In this region, the current increases exponentially with the applied potential and appears as a straight line when presented in the semilogarithmic plot (Fig. 4.1). In the passive region, further increase of the potential results in a sudden decrease of corrosion current. At the passivation potential, E_{pp}, a sufficient critical current density, I_{crit}, is provided to the system to form a passive film on the surface. At this point, the current stops increasing and starts decreasing toward the passivation current, I_{pass}, which is several orders of magnitude smaller than that observed on the active surface. The thickness and composition of the passive film depend on the potential, time, temperature, and the composition of the electrolyte. The part of the potentiostatic curve connecting the active state region and the passive region in Fig. 4.1 is termed as the prepassivating state. A thick insulating film is formed on the stainless steel surface in this state. With time, this film starts to dissolve and a much thinner, more corrosion-resistant passive film forms on the surface. The critical current density and the passivation potential determine the passivation properties of the active-passive metal surface. The surface is more easily passivated when the active-passive metal has a lower critical current density and a more negative passivation potential in the electrolyte. In the transpassive region, the current increases due to the oxygen evolution reaction or the breakdown of the passive film. Figure 4.1 was constructed by using the following electrochemical parameters; $E_{corr} = -0.5$ V vs. SCE; $I_{corr} = 1 \times 10^{-4}$ A/cm^2; $b_a = 0.05$ V/decade; $E_{pp} = 1 \times 10^{-5}$ A/cm^2; and $E_{tr} = 1.0$ V vs. SCE. The critical current density to passivate the surface is calculated by assuming that corrosion takes place only in the Tafel region. The overvoltage of the anodic Tafel curve is:

$$\eta = a + b_a \log(i) \tag{4.1}$$

where η is the overpotential of the anodic reaction and b_a is the anodic Tafel constant. The same expression can be used at both points (I_{corr}, E_{corr}) and at (I_{crit}, E_{pp}) in Fig. 4.1.

$$E_{corr} - e_{eq,a} = a + b_a + \log(i) \tag{4.2}$$

$$E_{pp} - e_{eq,a} = a + b_a \log(I_{crit}) \tag{4.3}$$

Combining Eqs. (4.2) and (4.3), one obtains:

$$E_{pp} - E_{corr} = b_a \times \log(I_{crit}) - b_a \times \log(I_{corr}) \tag{4.4}$$

The critical current required to passivate the surface, calculated from Eq. (4.4), is 10^{-2} A/cm^2.

In the back scan in Fig. 4.1 (solid arrows), the potential is lowered from positive (anodic) to negative (cathodic) values resulting the active-passive metal to shift from the transpassive region to the passive region and finally reaches the active state. The passive film is depassivated by removing the anodic applied potential or by shifting the passivation potential in the cathodic direction. The potential that triggers the rapid decay to the active state was defined by Flade [5] and is called the activation potential or the Flade potential, (ϕF). Franck [6] found a linear dependence of the Flade potential with pH. At 25 °C, ϕ_F in volts vs. SHE is given by:

$$\phi_F = +0.63 - 0.059\text{pH} \tag{4.5}$$

It has been suggested that the following redox reaction occurs during anodic passivation [5–7]:

$$M + H_2O \rightarrow OM + 2H^+ + 2e^- \tag{4.6}$$

where OM qualitatively describes the presence of oxygen in the passive film and does not represent the stoichiometry of the oxide that defines the standard Flade potential. The Flade equation for the redox reaction, Eq. (4.6) is defined as:

$$\phi_F = \phi_F^\circ - 0.059\text{pH} \tag{4.7}$$

Equation (4.7) corresponds to the potential variation of a metal electrode of the second kind as a function of pH. The Flade potential is used to evaluate the conditions for passive film formation and to determine the stability of the passive film. The reversible Flade potential of three important engineering materials is approximately: +0.63 V for iron, +0.2 V for nickel, and −0.2 V for chromium [7,8]. The negative value of the Flade potential for chromium (−0.2 V) indicates that chromium has favorable Gibbs free-energy for the formation of passive oxide film on its surface. The oxide film is formed at much lower potentials than in other engineering materials.

The Flade potential for iron (+0.63 V) indicates that only very strong and concentrated oxidizing agents will form passive films on its surface. However, even weak oxidizing agents form thin and very stable corrosion-resistant surface films on chromium. The 12-30% chromium content in stainless steel gives excellent corrosion resistance properties to steel due to formation of a stable chromium oxide passive film on its surface. Figure 4.2 shows the standard Flade potential measured for stainless steels with different chromium contents.

As the chromium content in the alloy increases from 8% to 13%, the corrosion rate of iron decreases from ~0.08 mm/year to very low values [9]. The Flade potentials of chromium-iron alloys in 4% NaCl solutions increases from −0.57 V (vs. SHE) in the absence of chromium to +0.17 V (vs. SHE) for the alloy with 12% chromium [7,10]. The critical current density for the passivation of Cr-Fe alloys at pH = 7 reaches a

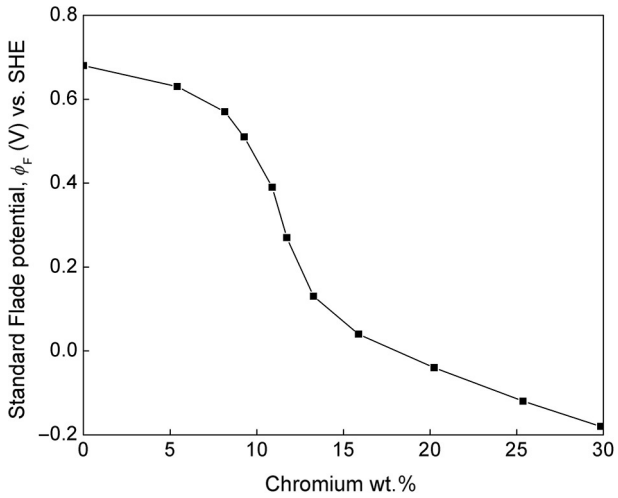

Fig. 4.2 Standard Flade potentials measured for stainless steel [8]. *This material is reproduced with permission of John Wiley & Sons, Inc.*

minimum of $\sim 1.1 \times 10^{-3}$ mA/cm^2 at 12 wt.% chromium and levels off at higher chromium contents [11].

Other metals that have favorable reversible Flade potentials and form passive film on their surfaces include titanium, silicon, aluminum, tantalum, and niobium. Naturally formed aluminum oxide protects the underlying aluminum metal at pH between 4 and 8. Titanium possesses very high oxidizing potentials and is used to manufacture anodes for cathodic protection systems for the chlorine-alkali process (production of hydrogen, chlorine, and sodium hydroxide) and many other applications.

4.2 APPLICATIONS OF POTENTIOSTATIC POLARIZATION MEASUREMENTS

The potentiostatic polarization technique is used to determine the potential region in which the metal is passive when exposed to a particular environment. Figure 4.3 shows the potentiostatic circuit with the three-electrode cell used to generate polarization curve. This technique estimates the ability of the metal surface to passivate by determining the critical current density necessary for passivation, the corrosion in the active region, the onset of passivation, the primary passive potential, the value of the current in the passive region, the voltage span of the passive region, and the transpassive potential.

The working electrode (WE) in Fig. 4.3 is the sample under investigation. The applied potential is controlled by a potentiostat. The potential is applied between the WE and the reference electrode (REF). The REF has a stable potential and is not polarized.

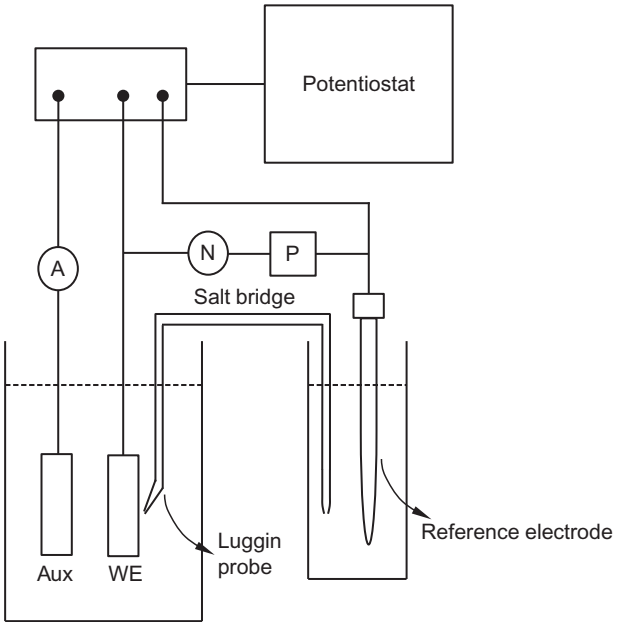

Fig. 4.3 Potentiostatic circuit used to generate anodic polarization curve.

The current is measured in the circuit depicted in Fig. 4.3, while the potential is increased in steps (potentiostatically) or continuously (potentiodynamically) from the corrosion potential of the WE to a preset final potential.

Figure 4.4 shows an anodic polarization curve obtained under potentiostatic conditions. The current is allowed to reach a steady state value at each potential.

Potentiodynamic and potentiostatic anodic polarization curves obtained at the same sweep rate are identical. They identify corrosion properties of passivating metals and alloys and are very useful in predicting the corrosion properties of materials. Figure 4.5 shows potentiostatic polarization curve of an active-passive metal with more than one passivation potential.

4.3 GALVANOSTATIC ANODE POLARIZATION

The galvanostatic polarization curve shown in Fig. 4.6 was obtained using a galvanostatically (constant current) controlled circuit.

In this mode, the current, $I_{app} = i_a - i_c$, is applied in the anodic direction starting from the corrosion potential of the WE. The potential is measured at each galvanostatically controlled step. Above the critical current density, the applied current increases the potential into the transpassive region of the anodic curve and it does not follow the

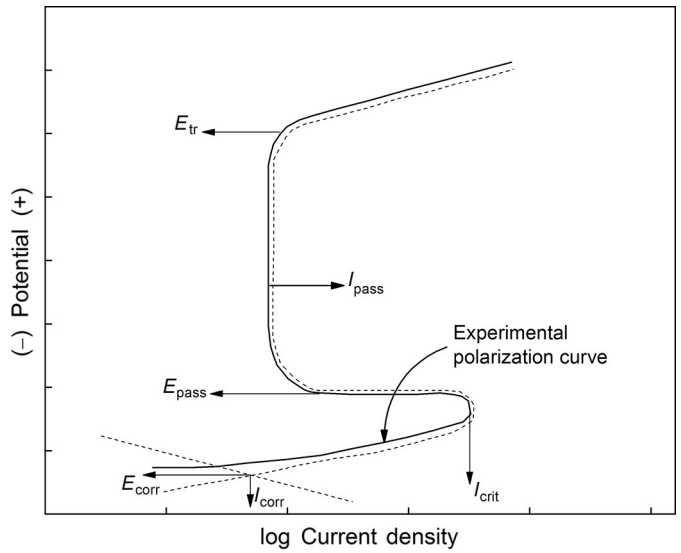

Fig. 4.4 Potentiostatic polarization curve of an active-passive metal obtained with controlled potential.

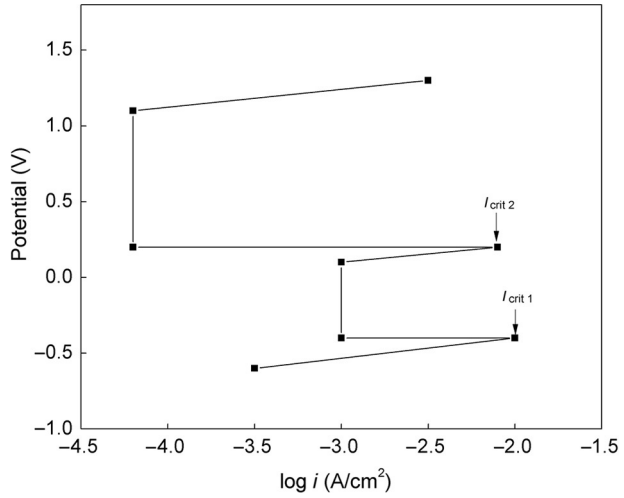

Fig. 4.5 Potentiostatic polarization curve of an active-passive metal with more than one passivation potential.

current decay of the anodic curve in the passive region. In the back scan, the applied current shifts the potential into the active region. Because, in galvanostatic mode the potential is not a single-valued function of current, the galvanostatic procedure cannot adequately define the corrosion properties of an active-passive metal in corrosion environment.

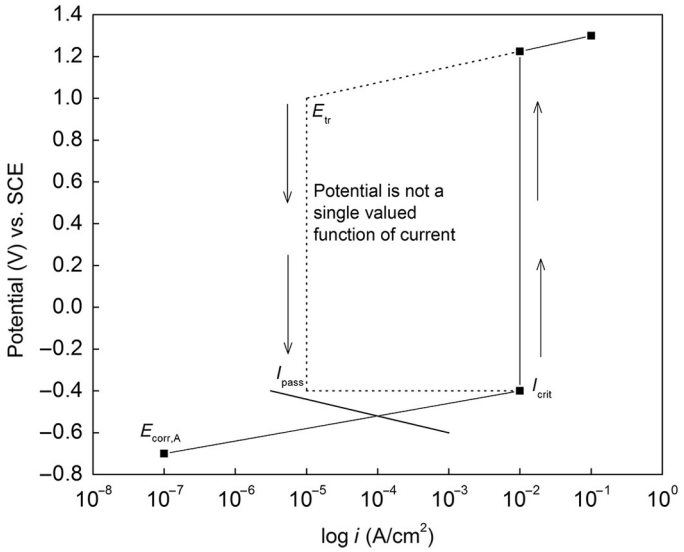

Fig. 4.6 Galvanostatically controlled polarization curve of an active-passive metal.

4.4 FUNDAMENTALS OF PASSIVITY

4.4.1 The film and adsorption theories of passivity

Film and adsorption theories explain the nature of passivity. The film theory assumes the formation of a metal oxide thin film that acts as a barrier layer protecting the underlying metal from interacting with the corrosion medium. The thickness of the oxide layer is estimated to be in the range of several monolayers, proving the molecular nature of the passive films [12,13]. Oxide passive films are amorphous when thin, but partially crystalline when the film grows [14]. According to their structure and composition, Fehlner and Mott [15] and Bar [16] divided the passive oxide films into two groups: network glass oxides consisting of Al, Ti, Zr, Mo, or Si, and network modifiers Pt, Ni, Cu, Co, or Fe. The network glass oxides are characterized by the formation of passive oxide films in one oxidation state, such as Al/Al_2O_3 or Ti/Ti_2O_3. The passive oxide films form compact and completely dehydrated oxide layers with no impurities from the electrolyte. The oxides grow by inward diffusion, forming passive layers with excellent barrier properties and very low conductivities.

In the network modifiers, the metals at high anodic potentials form mixed stable oxide films that are combinations of low- and high-oxidation state oxides. The lower valence oxides usually have poor barrier properties. Examples of such mixed oxides are $Cu/Cu_2O/CuO$ and $Co/CoO/Co_2O_3$. The poor corrosion-resistance properties of these mixed oxides results from the outward metal ion diffusion growth, which incorporates anions and impurities from the electrolyte [14].

Lead, copper, and platinum metal oxides act as electrodes of the second kind. The passivation and activation potentials of these metals are equal to the reversible potentials of their corresponding metal oxide electrodes, proving the validity of film theory. When immersed in solution, they have the same electrolyte anion in the surface oxide of the electrode. However, the reversible Flade potentials calculated using the Gibbs free-energy of formation of barrier layers of FeO and Fe_2O_3 are 0.051 and 0.085 V, respectively, are not consistent with the experimentally measured value of the Flade potential of 0.6 V vs. SHE [17]. A Flade potential of 0.57 V vs. SHE for iron oxides, close to the experimentally measured value of 0.6 V vs. SHE, is calculated by substituting enthalpy for O_2 ($\Delta H^o = -75$ kcal/mol) and entropy values for the chemisorption of oxygen on Fe ($\Delta S^o = -46.2$ cal/mol) in Eq. (4.10).

$$2FeO + 4H^+ + 4e^- \leftrightarrow 2Fe + 2H_2O \tag{4.8}$$

$$2Fe + O_2 \leftrightarrow 2FeO \tag{4.9}$$

$$\Delta G^o(2FeO) = \Delta H^o(2FeO) - T\Delta S^o(2FeO) \tag{4.10}$$

The adsorption theory is based on a decrease in the metal dissolution rate by adsorbed oxygen atoms [17,18]. The monomolecular passive layer formed by adsorbed oxygen atoms inhibits the hydration of metal ions by increasing the overvoltage of the anodic reaction, thus electrochemically retarding the metal dissolution. Initial partial coverage of the metal surface with oxygen causes an abrupt change in metal dissolution resulting in an increase of polarization and a shift in potential in the anodic direction. Consequently, the increase of the positive surface charge creates conditions that further increase the area covered with a continuous monomolecular layer of oxygen. This mechanism of selective adsorption continuously increases the passive layer and decreases metal dissolution. The adsorbed oxygen film does not act as a barrier film; rather, it increases the polarization resistance resulting in a decrease in the exchange current density of the metal dissolution reaction. The strong adsorption of oxygen on transition metals is caused by the uncoupled electrons in their "d" shell orbital [19]. In addition to the ionic bonding, the oxygen with unpaired electrons bonds with "d" orbital of the transition metal creating a covalent bond. Due to high energies for the adsorption of oxygen on transition metals, passivation of stainless steel and chromium occurs by chemisorption of oxygen from solution or directly from the air.

4.4.2 Thermodynamics

The dissolution of a metal and the existence of a passivation potential and stability of the passive products in an aqueous solution depend on the nature of the metal, the solution's pH, and the solutions' oxidizing power. The stability of different metals is estimated by using potential-pH diagrams (Pourbaix diagrams) as suggested by Pourbaix [20]. Pourbaix diagrams show the values of pH and the potential at which the metal reacts to form

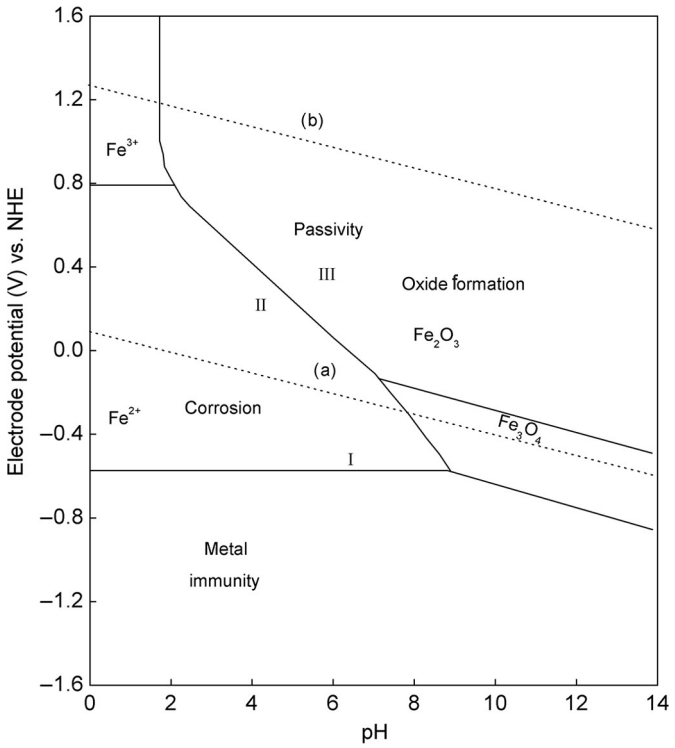

Fig. 4.7 Pourbaix diagram for iron constructed for concentration of Fe^{2+} of 10^{-6} mol/l.

complex anions or oxides. They also indicate where metal passivates or is immune to corrosion. Construction of these diagrams is based on the Nernst equation and the solubility (activity) data for various metal compounds. The only condition for constructing the diagram is that all the necessary reactions be at pH and at potentials of interest. The Pourbaix diagram for iron, Fig. 4.7, shows the combination of potential and pH where the corrosion is thermodynamically impossible and iron is stable, (region I). In region II, spontaneous dissolution of iron occurs.

Oxide formation and passivation occurs in region III. This region describes the nature and the composition of the oxides formed as corrosion products. By using the Pourbaix diagrams, it is possible to identify the combinations of potential and pH that will stop the corrosion of metals and form passive oxide layers. At any given pH, it is possible to describe conditions at the metal-electrolyte interface that help to evaluate the equilibrium potential as a function of pH.

Because the potential-pH diagrams characterize equilibrium thermodynamic properties only, the Pourbaix diagrams cannot be used to predict the rates of reactions. They can be used to evaluate the conditions for the formation of barrier oxide films but not

the thickness and the passive film effectiveness in protecting the metal in different environments.

4.4.3 Kinetics of passivation processes

The nature, the growth rate, and the stability of electrochemically passivated [21,22] and air-formed films [23] have been investigated in acidic and borate buffer solutions. The passive film properties were found to depend on the passivation potential [24,25], solution temperature [26], solution pH [24], and time of exposure in the corrosive media [21,22]. The film becomes more passive during air exposure due to change in the structure of the film from an amorphous phase to long-range ordered structure [27]. The mechanism is controlled by reductive dissolution of iron into Fe^{2+} in the solution [22,23] and by the film structure that forms after exposure to air [28,29].

The diffusion of cation vacancies from the solution interface to the metal-film interface has been assumed to be the rate-determining step in iron oxidation [21]. Extensive literature exists on the growth and breakdown of passive films. Only a brief summary will be provided in this chapter. The growth of thickness, δ_{pass} of passive film with time, t, in the passive region above E_{pp} can be explained by the logarithmic rate law, Eq. (4.11) or the inverse logarithmic law Eq. (4.12):

$$\delta_{pass} = A + B \ln t \tag{4.11}$$

$$\frac{1}{\delta_{pass}} = C - D \ln t \tag{4.12}$$

A, B, C, and D in Eqs. (4.11) and (4.12) are constants. Experimentally, the rate laws fit the data for most metals and alloys exposed to corrosion under oxidizing conditions and for the passive film grown under anodic polarization (anodic protection) or at open-circuit potentials [30]. The thickness of the passive layer is between 1 and 3 nm due to the dielectric breakdown that occurs in most of the metals and alloys at high anodic potentials. The dielectric breakdown for tantalum, titanium, and zirconium takes place at high anodizing potentials because of the much thicker, highly resistive films formed on these metals. Both the cathodic reaction and the anodic metal oxidation reactions occur on the metal surface under corroding conditions during the formation of the passive film. The cathodic depolarization reaction $O_2 \rightarrow O^{2-}$ takes place at the oxide-electrolyte interface (outer interface). Oxide formation and film growth are controlled by the diffusion of the anions from the oxide solution interface to the inner metal-oxide interface and by the transfer of electrons from the metal surface to the oxide-electrolyte interface.

One of the first mechanistic models of the kinetics of passive film formation was described by Cabrera and Mott [31]. The passive film thickness in their model is controlled by the transport of the metal cations from the underlying metal to the

film-solution interface. This model has been used extensively to explain the results of passive film growth on substrate surfaces.

Fehlner and Mott [32] modified Cabrera and Mott's model [31] by assuming that anion diffusion controls the film growth. However, the experimental evidence indicated that the interfacial reaction between oxygen and hydrogen cations is very fast and is not the rate-limiting step as suggested in Fehlner and Mott's model. To explain the rate-limiting law, Sato and Cohen [33] proposed an exchange mechanism at the metal-solution interface, which had limited application because this model becomes less accurate as film thickness increases.

An excellent review of the history of the point defect model (PDM) for the growth and breakdown of passive films was written by Macdonald [34,35]. The first-generation point defect model (PDM-I) was developed by Chao et al. [36–38] by assuming that the passive film consists of a single defective layer with cation and oxygen vacancies. The model provides quantitative description of the film growth on iron and nickel in phosphate and borate solutions. The model successfully predicts the inverse logarithmic law. It explains that passivity breakdown is a result of local condensation of cation vacancies at the metal-film interface. Also, it explains why the barrier layer stops to grow into the metal. However, the model can neither account for the experimentally observed properties of the passive states on metals interfaced with aqueous solutions nor explain the development of multilayer passive films.

The second-generation point defect model (PDM-II) [39] addressed the deficiencies of the previous model by incorporating a bilayer structure of the film consisting of a defective oxide layer on the metal surface and an outer layer that is formed by precipitation of products from the reaction of transmitted cations from the underlying metal with species in the environment. PDM-II assumed that the barrier layer controls the passive current and recognized the barrier layer dissolution and the need to distinguish whether the reactions are lattice conservative or nonconservative. The model also introduced the metal interstitials to the suite of defects. The model is in agreement with experimental results. Model PDM-III extends the application of the PDM model and addresses the formation of multiple passive layers at the outer layer [40].

4.5 FACTORS AFFECTING PASSIVATION

Solution pH, velocity, and oxidizer concentration change the properties of the anodic curve of the active-passive metal. For example, the equilibrium potential of the cathodic reaction shifts according to the Nernst equation in the noble direction by increasing the oxidizer concentration. Mixed potential theory, in this case, may predict the intersection of the cathodic and anodic Tafel lines and corrosion rate or extent of passivation of the metal.

4.5.1 Effect of acid concentration on passivity of an active-passive metal

The effect of acid concentration on polarization of active-passive metals is shown in Fig. 4.8. Higher hydrogen ion concentration increases the critical anodic current density and decreases the passive potential range. Severe corrosion conditions present at higher acidity also increase current densities and corrosion rates at all potentials. Figure 4.9 presents the data for iron passivation in phosphoric acid/phosphate buffer solutions of

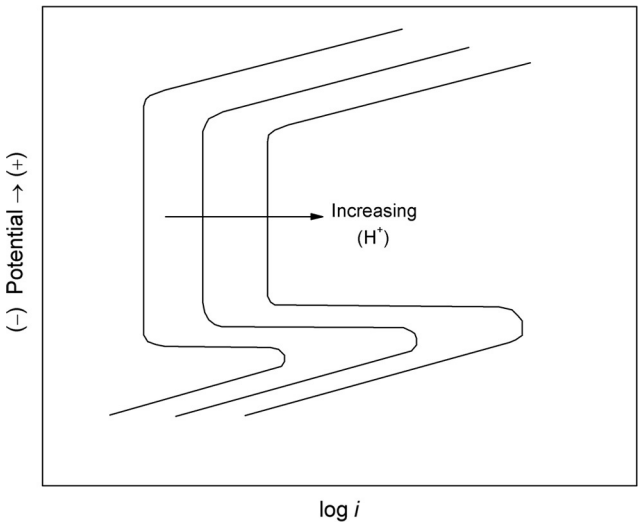

Fig. 4.8 Effect of acid concentration on polarization of active-passive metal.

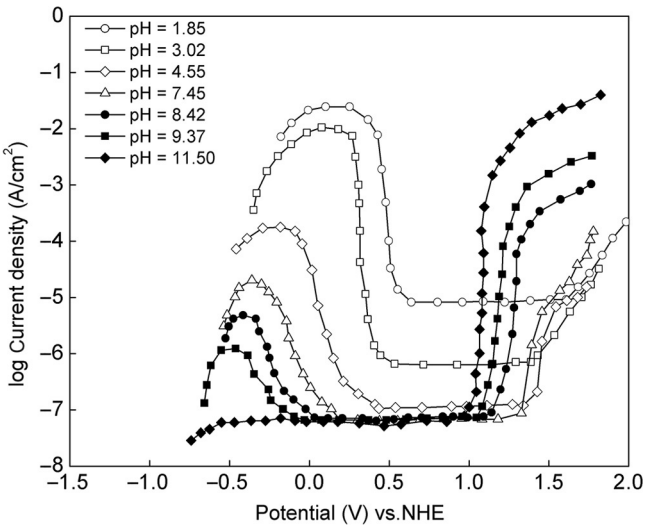

Fig. 4.9 Anodic potentiostatic polarization curves for iron in 0.15 M Na_3PO_4 solution of different pH [41]. *Reproduced by permission of The Electrochemical Society.*

different pH [41]. Increasing the applied potential in the positive direction increases current exponentially in the active region, where the charge-transfer reaction is metal dissolution. Both the corrosion current and the potential in this region increase with increasing solution acidity. The critical current density drastically increases from $\sim 10^{-6}$ to 5×10^{-2} A/cm^2 when the pH decreases from 9.35 to 1.85. At the critical current density in Fig. 4.8, the dissolution current decreases to a passivation current density plateau that has a voltage span of approximately 1.0 V. In the prepassivation region, the precipitation of iron hydroxide is the predominant process, followed by the formation of a thin passive film of iron oxide in the passive region [41].

In the transition region, the current increases due to the oxygen evolution reaction. It is evident from Fig. 4.9 that the overvoltage for the oxygen evolution reaction decreases as the pH increases. This shift in the overvoltage is due to the change in the oxygen electrode potential with pH.

Figure 4.10 shows the activation reduction processes at three different exchange current densities for the hydrogen evolution reaction on three different passive-active metals A, B, and C in acidic solution. The mixed potential theory is applied in all three cases in Fig. 4.10 to evaluate the corrosion rate of the active-passive metal. In the active state of metal A, the corrosion current increases upon further polarization from the corrosion potential to intersection 1. Mixed potential theory applied to passive-active metal B results in three intersection points where the total rate of hydrogen reduction is equal to that of metal oxidation. Intersection 2 is in the active polarization region of the active-passive metal and corresponds to a high corrosion rate. Point 3 is not stable. A small shift of the potential in either direction results in a transition to the active or passive region at this point. The third intersection at point 4 is in the passive region. From an

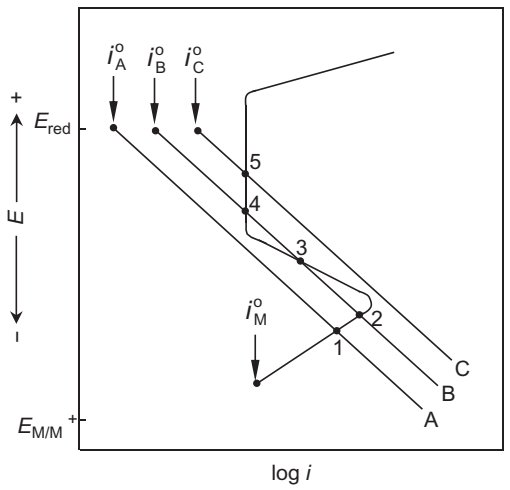

Fig. 4.10 Reduction processes with three different exchange current densities on passive-active metals exposed to acidic solution.

engineering viewpoint, the active-passive metal B is not desirable because a sudden transition from the passive to the active region will result in rapid corrosion damage. The active-passive metal C intersecting at Point 5 spontaneously passivates and is the most desirable for anodic protection and engineering applications. The stability of the system in this region is controlled by the voltage span of the passive region. Titanium and stainless steel behave like metal C and are typical examples of an active-passive metal exposed to aerated solutions, ferric salts or in oxidizing acidic solutions.

4.5.2 Effect of solution velocity on active-passive metals and alloys—construction of polarization curve for stainless steel alloy in aerated solution

The cathodic reaction in deaerated neutral solutions is water reduction. Under deaerated conditions, the hydrogen evolution reaction is slow and results in low corrosion rates of the active-passive metal. In aerated natural fresh waters or in solutions with high pH, the concentration of hydrogen ion is too low for the hydrogen evolution reaction to control the corrosion rate. The cathode reaction rate is controlled only by the rate of the oxygen reduction reaction, Eq. (4.13):

$$O_2 + 2H_2O + 4e^- \rightarrow 4OH^- \quad e_c^o = 0.401\,V \text{ at } pH = 14 \tag{4.13}$$

The solution velocity in this case is one of the major factors that control the corrosion potential and the corrosion rate in the active state of the alloy. The effect of mass transfer on electrode kinetics is discussed in detail in Chapter 3. Figure 4.11 correlates the

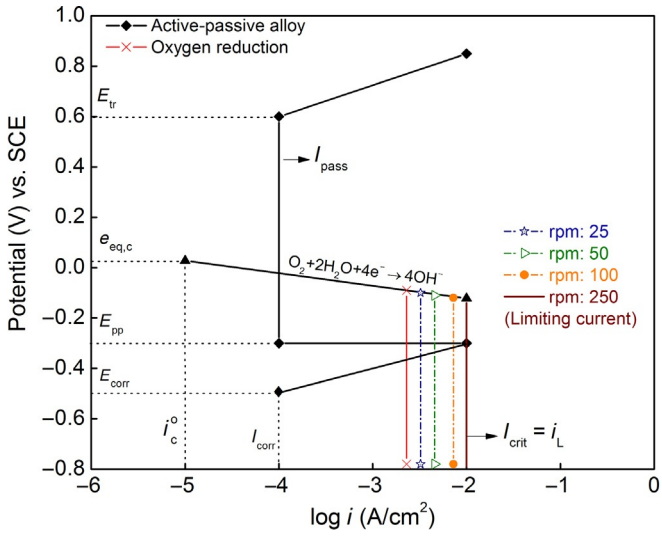

Fig. 4.11 Effect of solution velocity on corrosion of active-passive alloy in deaerated and aerated alkaline solution (pH = 11).

potential current relationship of the active-passive alloy with respect to different solution velocities. An increase in the solution velocity increases the limiting diffusion current to the critical anodic current density. At this point, the corrosion potential increases to the passivation potential and the corrosion rate decreases to the passivation current, I_{pass}.

Case Study: Velocity Effects on Corrosion of Active-Passive Stainless Steel

Effect of velocity on the corrosion of active-passive stainless is analyzed using a rotating disk electrode (RDE) technique. The hydrodynamics of the rotating disk electrode have been studied extensively [42–46]. The Levich equation provides the limiting current density as a function of angular velocity of the electrode [42]:

$$i_L = 0.62nFD_o^{2/3}\omega^{1/2}\upsilon^{-1/6}C_b \tag{4.14}$$

In the Levich equation, i_L is the current density obtained when the concentration of the species at the surface of the electrode is equal to zero at a particular rotating speed ω; υ is the kinematic viscosity and C_b is the bulk concentration of oxygen, and D_o is the diffusivity of the species in the electrolyte. The Levich equation takes into account both the rate of diffusion of oxygen across the stagnant layer and the complex solution flow pattern; in particular, this equation gives the peak current observed in rotating disk voltammetry. The limiting current is relevant to corrosion and changes the mixed potential and corrosion current, depending on the rotation speed. The only cathode reaction is the reduction of oxygen in the solution having an oxygen concentration of 10^{-3} M and pH 11. The limiting current is calculated for angular velocities of 25, 50, 100, and 250 rpm. Numerical and graphical evaluation of the oxygen limiting current, the critical passivation potential, and the passivation current density are shown in Fig. 4.11 for an active-passive alloy immersed in partially oxygen-aerated solution. The diffusion coefficient of O_2 is 10^{-6} cm^2/s. The kinematic viscosity, υ, of the solution is 0.02 cm^2/s. Table 4.1 and Table 4.2 summarize the oxygen electrochemical kinetic parameters and the parameters for the active-passive metal, respectively.

Mixed potential theory and the Levich equation are used to construct the anodic and cathodic polarization curve of the active-passive alloy and to estimate the value of the oxygen limiting diffusion current when a spontaneous passive film is formed on the surface. Figure 4.11 correlates the relationship between potential and current for the

Table 4.1 Oxygen Reduction Parameters

b_c (V/decade)	i_c^o (A/cm^2)	[O_2] (mol/l)	α_c	α_a
−0.05	10^{-5}	1.0×10^{-3}	0.5	0.5

Table 4.2 Parameters for the Active-Passive Alloy

I_{corr} (A/cm^2)	b_a (V/decade)	E_{corr} (V vs. SCE)	E_{pp} (V vs. SCE)	I_{pass} (A/cm^2)	E_{tr} (V vs. SCE)
10^{-4}	0.1	−0.5	−0.3	1×10^{-4}	0.6

active-passive alloy in an aerated and deaerated alkaline solution with a pH of 11. The active region of the anodic polarization curve is constructed by using the values of the corrosion potential, E_{corr}, the corrosion rate, I_{corr} and the Tafel slope $b_a = 0.1$ V/decade given for the active-passive metal. The critical current density in the active region, I_{crit}, is calculated using the parameters for the active-passive alloy given in Table 4.2 and by setting $I = I_{crit}$ in the Tafel equation.

$$\eta_a = E - E_{corr} = a + b_a \log(i) = b_a \log\left(\frac{I_{crit}}{I_{corr}}\right) \rightarrow I_{crit} = I_{corr} \times 10^{\left[\left(E_{pp} - E_{corr}\right)/b_a\right]} \quad (4.15)$$

$$I_{crit} = 10^{-4} \times 10^{[(-0.3-(-0.5))/0.1]} = 10^{-2}\,\mathrm{A/cm^2}$$

The cathodic polarization curve is constructed using the oxygen electrode equilibrium potential and the cathodic slope, $b_c = -0.05$ V/decade. The equilibrium cathode potential, $e_{eq,c}$ is calculated by applying the Nernst equation to the oxygen reduction reaction, Eq. (4.13), for an oxygen concentration of 1.0×10^{-3} mol/l at pH = 11.

$$e_{eq,c} = e_c^o + \frac{RT}{4F} \ln\left(\frac{[O_2][H_2O]}{[OH^-]^4}\right) \rightarrow 0.401 + \frac{0.059}{4} \log\left(\frac{[10^{-3}] \times 1.0}{[10^{-3}]^4}\right)$$

$$e_{eq,c} = 0.268\,\mathrm{V\ vs.\ SHE\ or\ } 0.028\,\mathrm{V\ vs.\ SCE}$$

The limiting current is relevant to the corrosion of an active-passive metal. It changes with the rotation speed of the electrode, resulting in a change of the mixed potential and the corrosion current. (See also Figs. 3.15a–c and Case Study 3.4 in Chapter 3.) The graphical evaluation of the oxygen limiting current, the critical passivation potential, and the passivation current density is shown in Fig. 4.11.

In the active state of the alloy, the available charge reaction in deaerated solutions is water reduction

$$2H_2O + 2e^- \rightarrow H_2 + 2OH^- \quad (4.16)$$

The alloy corrodes in the absence of a concentration limitation region. In Fig. 4.11, the active state region is defined with $E_{corr} = -0.5$ V vs. SCE and a corrosion current, I_{corr} of 10^{-4} A/cm^2. In the aerated solution, the cathodic polarization reaction at 0.028 V vs. SCE is the reduction of oxygen. The limiting current for rotation speeds of 25, 50, 100, and 250 rpm are calculated using Eq. (4.14) for $D_{o_2} = 10^{-6}\,\mathrm{A/cm^2}$; $\upsilon = 0.02$ cm^2/s and $C_b = 1.0 \times 10^{-3}$ mol/l. The cathode charge-transfer reaction is diffusion limited, while the anodic polarization is of the Tafel type and without concentration limitations. An increase in the fluid velocity increases the corrosion rate until the point where the cathodic limiting current reaches the intersection with the anodic polarization curve. For the oxygen reduction reaction in aerated solutions, the initial cathodic limiting current at a rotation speed of 25 rpm is greater than the Tafel case intersection for water reduction and does not affect the corrosion potential nor the corrosion current at $E_{corr} = -0.5$ V vs. SCE. As the potential decreases, the kinetics of the oxygen reduction in aerated solutions is limited by both charge transfer and diffusion limitations.

At high cathodic potentials in Fig. 4.11, depending on the angular velocity, the oxygen reduction reaction is controlled by diffusion. Increasing the velocity from 25

to 250 rpm, the thickness, δ, of the diffusion layer decreases at the active-passive metal-solution interface. A decrease of the diffusion layer thickness results in an increase of the limiting current.

$$i_L = \frac{nFDC}{\delta} \tag{4.17}$$

Also, an increase in the oxygen concentration to the surface of the active-passive metal increases the oxygen limiting diffusion current with a subsequent increase of the corrosion rate. For a limiting current of $I_{crit} = 0.01\ A/cm^2$, the rotation speed ω is calculated to be $474\ s^{-1}$ with a diffusion layer thickness of $\delta = 1.6 D_{O_2}^{1/3} \omega^{-(1/2)} \nu^{1/6} = 0.183\,cm$.

4.5.3 Criterion for passivation

As shown in Fig. 4.11, an increase in the oxygen diffusion limiting current results in an increase in the passivation potential of the active-passive film. At this potential, a sufficient anodic critical current density of $10^{-2}\ A/cm^2$ is provided to the system that causes the corrosion rate to decrease to the passivation current density of $10^{-4}\ A/cm^2$, due to formation of a passive oxide film on the surface. When the cathodic limiting current is greater than the anodic critical current density, the angular velocity does not affect the corrosion potential or the corrosion current of the passive region of the active-passive metal. This statement generally defines the criterion for passivation: *the passive film of an active-passive alloy is stable only when the cathodic current density or oxygen diffusion limiting current density is greater than the anodic critical current*. One of the objectives of corrosion engineering is to determine the composition of an active-passive alloy that is more easily passivated. Such an alloy should possess very negative (cathodic) passivation potential, and a very low critical current density.

4.5.4 Effect of oxidizer concentration on passivity

The critical current density for passivation of an active-passive metal strongly depends on the oxidizing power of the solution. The redox potential in Fig. 4.12 increases according to the Nernst equation from points 1 to 7 due to the increase in the concentration of the oxidizing agent. Mixed potential theory can be applied to the system to find the intersection points where the total rate of hydrogen reduction equals the metal dissolution. In the active region of the active-passive metal, represented by intersection points 1 through 3, the corrosion increases with an increase of the oxidizing agent concentration. The active-passive metal is not stable for the oxidizer concentration at intersection point 3. At this point, a small shift of the potential in either direction results in transition of the system to active region 3 or passive region 3a. With further increase of the oxidizer concentration, the corrosion current decreases to the passivation current

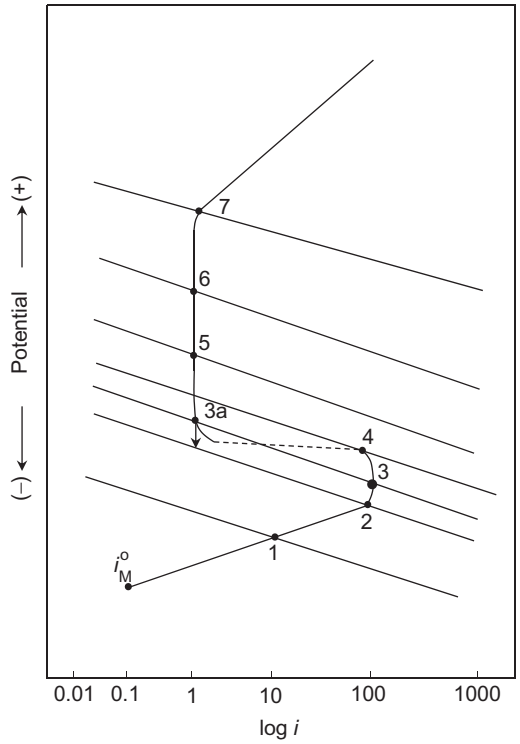

Fig. 4.12 Effect of oxidizer concentration on current density of an active-passive metal.

observed at intersection 5 and 6. At intersection 7, the corrosion current starts to increase in the transpassive region due to the oxygen evolution reaction and breakdown of the passive film.

The effect of the oxidizer on the corrosion rate is shown in Fig. 4.13. In regions 1 through 3, both active and passive states are present. At the critical current density (the passivation potential), point 4, the corrosion current drops to passivation current. The stability of the system in this region is controlled by the voltage span of the passive region. In the transpassive state, the corrosion current starts to increase at point 7.

In the back scan in Fig. 4.13, the corrosion rate decreases from point 8, by decreasing the concentration of the oxidizer. The active-passive metal passes from the transpassive to its passive state. The passivity in the back scan is retained at concentrations 4-3a-2, lower than those necessary for the formation of the passive film. Thus, the region 4-3a-2 represents borderline passivity, where decreasing or increasing the oxidizer concentration results in a transition of the system to the active or passive region, respectively. The passivity decays within a short period of time to the normal active state of the active-passive metal.

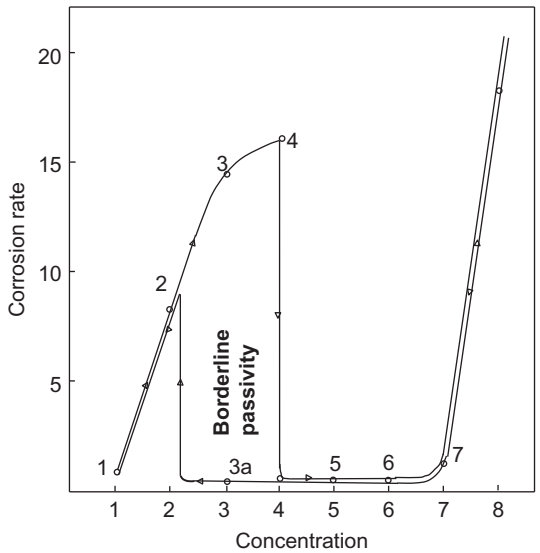

Fig. 4.13 Corrosion rate of the active-passive metal as a function of the oxidizer concentration.

4.6 METHODS FOR SPONTANEOUS PASSIVATION OF METALS

Passivation is crucially important to numerous technologies and industries that depend on the use of metals and alloys with high corrosion resistance. The development of stainless steel in the first half of the twentieth century accelerated the growth of modern technologies in the transportation, construction, chemical, and pharmaceutical industries. The development of semiconductor devices relied on the superior passive films formed on silicon. A better understanding of the nature of passivity and discovery of new processes for achieving passivity in metallic materials provide engineers with new materials with superior corrosion properties. A major objective of corrosion engineering is to determine the composition of an active-passive alloy that is more easily passivated. Such an alloy should possess a more negative (cathodic) passivation potential and a lower critical current density. Spontaneous passivation is achieved when, for example, an increase in the oxygen diffusion limiting current results in a shift in the corrosion potential to the passivation potential. At this potential, sufficient anodic critical current density is provided to the system to cause the corrosion rate to decrease to the passivation current density due to the formation of a passive oxide film on the surface. The limiting diffusion current density of oxygen in air-saturated solutions is 100 $\mu A/cm^2$. Some active-passive metals have lower critical current density than 100 $\mu A/cm^2$, and the oxygen dissolved in the solution causes spontaneous passivation on their surfaces. Oxidizing agents, such as ferric chloride, concentrated nitric acid, or chromate passivate and maintain passivity on some metals. Surface pretreatments can be performed to decrease the critical current density and

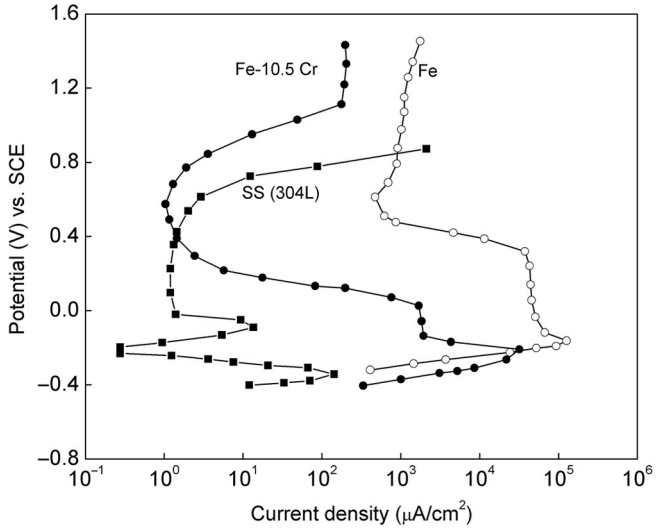

Fig. 4.14 Anodic polarization curves for Fe-10.5%C and SS (304 L) in 1 N sulfuric acid [47]. *Reproduced by permission of The Electrochemical Society.*

spontaneously passivate stainless steel, nickel, and titanium. Impressed anodic potential shifts the corrosion potential from the active to passive region of an active-passive metal and maintains the passivation current above the passivation potential. As shown in Fig. 4.14, iron in 1 N sulfuric acid has a very large critical current density of 10^5 μA/cm^2 and cannot be passivated in acidic solutions [47]. The addition of 10.5% chromium to iron decreases the critical current density in 1 N sulfuric acid to 10^4 μA/cm^2, still very high. The addition of chromium and nickel to iron in the case of 304 L stainless steel (^{18}Cr-^{8}Ni) decreases the passivation critical current density to 100 μA/cm^2 [47,48].

As shown in Fig. 4.15, the anodic polarization curves obtained for steels with chromium content between 3.54% and 19.20% indicates that increasing the chromium content enhances the Fe-Cr-Ni alloy passivation ability by decreasing the critical current density of the alloys from 10^6 to 10^2 μA/cm^2 [49]. The passive current also decreases from 50 μA/cm^2 for 3.54% Cr alloy in sulfuric acid to 10^{-2} μA/cm^2 for the alloy with 19.2% Cr.

A schematic summary of the alloying metals that affect the anodic polarization curve of stainless steel is shown in Fig. 4.16. The addition of 8% nickel to an alloy containing 18% chromium forms austenitic structure SS Type 304. The addition of Mn and N increases the stability of austenitic steel. The chromium content of stainless steel affects the anodic polarization curves as shown in Fig. 4.16. Nickel promotes repassivation in a corrosive environment, but concentrations higher than 30% reduces the passivation current, the critical current density, and increases the critical pitting potential. Nitrogen

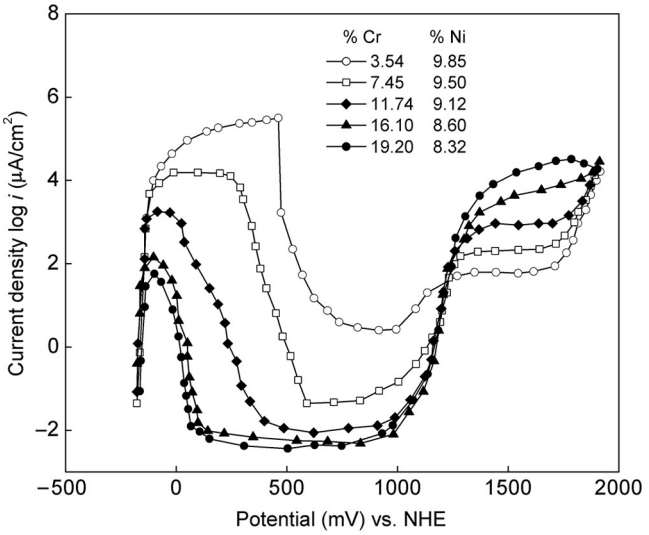

Fig. 4.15 Anodic polarization curves for Fe-Cr-Ni alloys with different contents of Cr and Ni [49].

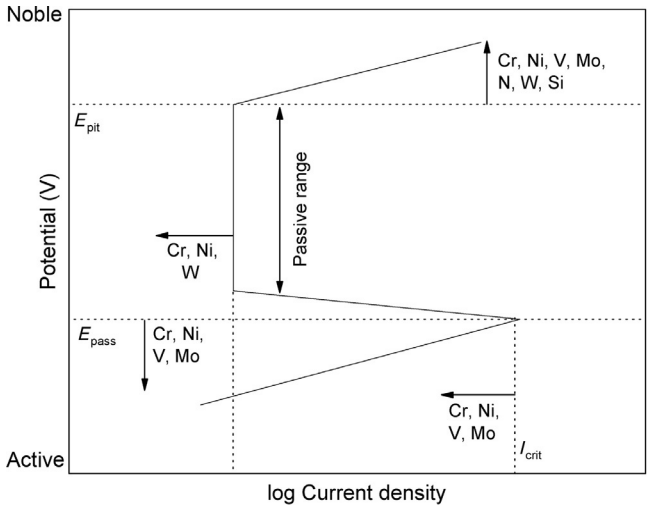

Fig. 4.16 Effect of alloying elements on stainless steel anodic polarization curve.

added to austenitic stainless steel up to 0.2 wt.% stabilizes and prompts the strength of the austenitic phase [50–54].

Molybdenum in combination with chromium increases the corrosion-resistant properties of ferritic stainless steel in chloride electrolytes and is effective in increasing the resistance to pitting and crevice corrosion. Cr-Ni-Mo-Cu alloys increase the passivity in sulfuric acid concentrations with concentrations between 20% and 70%. Nickel

contents higher than 30% increase the alloy's corrosion resistance in 75% sulfuric acid [55]. Alloys with ^{29}Cr-^{4}Mo-^{2}Ni provide excellent resistance to pitting, chloride stress corrosion cracking (SCC), crevice corrosion, intergranular corrosion, and general corrosion in acidic solutions. These alloys possess excellent ductility, weldability, and strength [56].

4.7 ALLOY EVALUATION

Potentiostatic anodic polarization technique is used to evaluate the corrosion properties of active-passive metals and alloys and to test galvanic corrosion, pitting corrosion, and intergranular localized corrosion. The corrosion rate in the active region of the active-passive metal is determined by Tafel kinetics. The rate is proportional to the anodic current density. Desirable active-passive metals or alloy should have a low corrosion rate in the active region. Spontaneous passivation of the active-passive metal occurs when the applied current density exceeds the critical current density for passivation. The alloy with the more negative (cathodic) passivation potential and lower critical current density is more susceptible to passivation. Under oxidizing conditions, the stability of the passive state is essential in judging the corrosion resistance of metals and alloys. A desirable active-passive metal should have low corrosion rates and a large voltage span of the passive region. In the case of a small passive voltage span, a slight variation in the applied protection potential may cause a transition from the passive to the active corrosion region, resulting in a drastic increase in corrosion rate. Finally, to avoid localized corrosion, one should not use a active-passive metal or alloy whose passive films breakdown in corrosive solutions.

Hypothetical alloys A, B, and C are used in Fig. 4.17 to illustrate the evaluation of alloys under reducing and oxidizing conditions. For reducing (or active state of the alloy) conditions represented by line 1, alloy C is superior because its corrosion rate is the lowest in the active region. For modestly oxidizing conditions represented by line 2, alloy C is not recommended because the critical passivation current density is higher than the reduction line 2. The intersection 2C indicates that this alloy is in the state of borderline passivity. Both, the active and passive states are possible. Alloy C is recommended in highly oxidizing conditions because the critical passivation current density does not exceed the reduction line 3. Also, this alloy has the lowest passivation current density.

Alloy B is superior in highly oxidizing conditions, represented by curves 2 and 3, because reduction curves 2 and 3 exceed their critical passivation current density values. Alloy A has very high critical current density for passivation and is very difficult to passivate. It is not recommended in oxidizing conditions, curve 2, because the reduction line 2 is below the critical passivation current density. In strongly oxidizing conditions, curve 3, this alloy is in the state of borderline passivity.

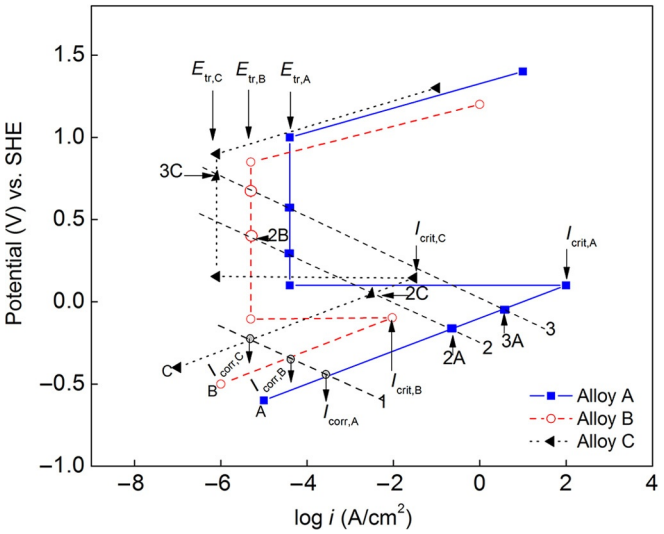

Fig. 4.17 Anodic polarization curves of hypothetical alloys.

4.8 ANODIC PROTECTION

Figure 4.18 illustrates the principles based on an impressed anodic protection system. An active-passive metal possesses three regions in the polarization curve: the active, the passive, and the transpassive regions. In the active region, the corrosion potential and corrosion current are controlled by the Tafel kinetics of the individual redox reactions.

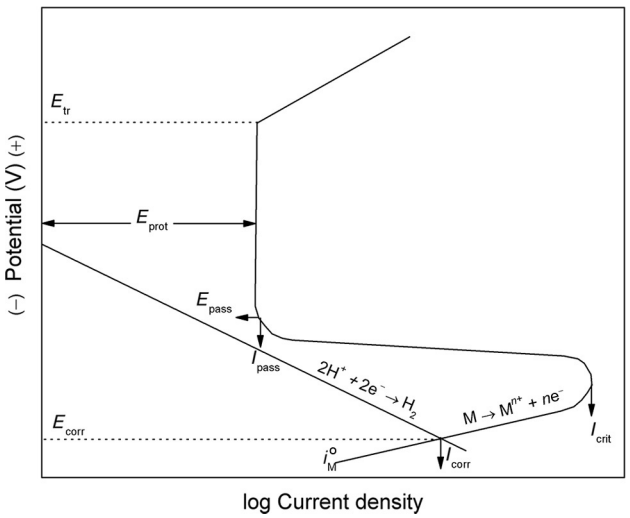

Fig. 4.18 Anodic protection with impressed anodic current of an active-passive metal.

An increase in the anodic potential or increase of solution oxidizing power moves the system into the passive region, in which the corrosion current is low and independent of the potential. Onset of the passivation region is defined by the passivation potential, where a sufficient critical current density is provided for the formation of the passive film. The thickness and the composition of the passive film are determined by the potential, time, temperature, and composition of the electrolyte. In the passivation region, corrosion rate is equal to passivation current. The corrosion rate starts to increase again in the transpassive region due to the oxygen evolution reaction or the breakdown of the passive film. The corrosion rate of the active-passive metal significantly decreases by shifting the corrosion potential to anodic potentials in the passive region by applying necessary current using an external power source. The impressed anodic current must be greater than the critical current density for passivation. Impressed anodic potential also maintains the passivation current above the passivation potential. Once the system is anodically protected, a small current density corresponding to passivation current is necessary to maintain the passivity.

The polarization behavior of the substrate is used to optimize the anodic protection parameters. The surface of the active-passive alloy is easier to passivate by an impressed anodic current when the active-passive metal has a lower critical current density and a higher cathodic passivation potential. A desirable active-passive metal should have a passive region with a large voltage range and a low corrosion rate in the corrosive solution. The optimum applied anodic potential should be midway in the passive region. Otherwise, in the case of an alloy with a small voltage range of the passive region, a slight variation of the applied protection potential may cause a transition from passive to active corrosion and result in a drastic increase of corrosion rate.

4.8.1 Anodic protection systems

Anodic protection has been most extensively used to protect steel in sulfuric acid. The advantages of anodic protection are low cost, low current requirements, and applicability in aggressive acidic solutions. It extends the life of the equipment with substantial cost savings. Besides being capable of reducing the corrosion rate of active-passive metals and alloys in acids by several orders of magnitude, it also hinders the hydrogen evolution reaction, which minimizes hydrogen permeation and subsequent hydrogen embrittlement of hard alloys.

The impressed current anodic protection system of a steel storage vessel containing sulfuric acid is shown in Fig. 4.19. The design parameters and the operating conditions for anodic protection are determined by experimental polarization measurements. The power supply protects the storage tank by applying constant potential between the tank and the $Hg/HgSO_4$ REF. The applied voltage is the sum of the cathodic overvoltage, the anodic overvoltage of the structure, and the ohmic losses.

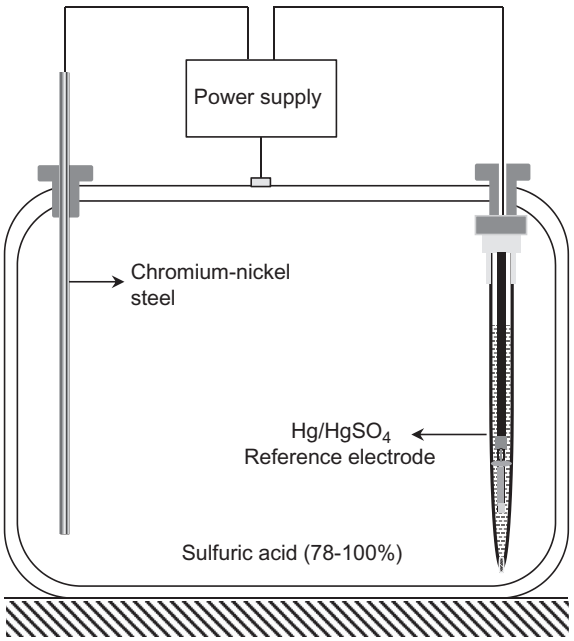

Fig. 4.19 Schematic for anodic protection system for sulfuric acid storage tank.

The protective potential is determined by the experimentally obtained potentiodynamic polarization curve. Anodic protection systems are equipped with continuous proportional type controls [57]. The control measures the potential between the storage tank and the REF and compares the measured value to a preset optimum protective potential value. Next, the system sends a signal to the power supply to provide the required protective potential and current between the cathode and the tank. The potential of the REF is stable with respect to time and should not be polarized. Some of the standard REFs used for anodic protection are calomel electrode $Hg/HgCl_2$, $Hg/HgSO_4$, and Ag/Ag/Cl. The potential in an anodic protection system is distributed uniformly on the structure due to the low currents and high conductivity of the electrolyte. The impressed current flows between the storage tank and the chromium-nickel steel cathode. The cathode should be inert in the corrosive solution and electrochemically stable. The resistance of the system is dominated by the cathode because of the large surface area of the anode and the high conductivity of the solution. To minimize the hydrogen evolution and permeation in the bulk of the alloy, the cathode materials must have a low hydrogen overvoltage. Examples of cathode materials that have been used in anodic protection include chromium-nickel steel in 90-100% sulfuric acid environment, Hastelloy C in sulfuric acid, and platinum-clad brass in sulfuric of various concentrations.

4.8.2 Design requirements

The following are the requirements for designing anodic protection systems:

- The polarization potential should be determined from the potentiodynamic polarization curve. The variation of the protective potential with time must be determined accurately.
- Avoid polarizing the system at a high rate through the passivation potential E_{pass}, because of a drastic increase of the critical current density, I_{crit}, at a high polarization rate.
- The cathode should be inert in the corrosive solution and electrochemically stable.
- The cathode materials must have low hydrogen overvoltage and small surface area to minimize hydrogen permeation and embrittlement.
- The solution resistivity should be very low. The overall system resistivity should be controlled by the cathode surface area.
- The system should be designed to avoid surface irregularities in the structure that may create a nonuniform current distribution.
- The active-passive metal or alloy should have a low critical passivation current density

4.8.3 Applications

Some of the alloys that are protected by anodic protection are stainless steel in phosphoric acid, steel in sulfuric acid, nickel in nitric acid, nickel alloys in nitrate solutions, and titanium in ammonia solution. Recently, anodic protection has been used to protect stainless steel heat exchangers used in the production of sulfuric acid [57]. The current requirement for some of the steels on which anodic protection has been applied is summarized by Sudbury and Locke [58]. Anodic protection has also been used in plants for the manufacture, storage, and transport of sulfuric acid. It reduces the iron dissolution in sulfuric acid to 1 ppm per day of storage. Portable anodic protection systems are used to stop iron dissolution during the transportation of sulfuric acid in trucks [57].

4.9 COMPOSITION AND STRUCTURE OF IRON PASSIVE FILMS

The initial stages of the electrochemical growth of the passive film on iron were studied in borate solutions using in situ electrochemical scanning tunneling microscopy (ECSTM) [59]. ECSTM analysis indicated that in the Tafel region, at −0.9 V vs. Ag/AgCl REF, iron converts into iron hydroxide. With further anodic polarization at potentials between −0.8 and −0.4 V, the iron cations are over the saturation limit, resulting in precipitation and the formation of a Fe(II) hydroxide passive film on the iron surface.

The passive layer on iron has been suggested to be a bilayer consisting of an inner layer of magnetite (Fe_3O_4) and an outer layer of maghemite (γ-Fe_2O_3) [60]. A two-layered structure of inner oxide layer and an outer hydrated film was suggested by Tjong and Yeager [61]. A single-layer passive film of Fe_2O_3 was suggested by Ogura and Sato [62]. However, surface-enhanced Raman spectroscopy confirms the existence of the bilayer oxide film [63].

The presence of a hydrated film (FeOOH) was found to depend on the concentration of iron cations at the passive layer-solution interface [64]. In situ surface X-ray diffraction studies indicated that the film consists of a spinel crystal structure [65].

The structure and the composition of the passive film on iron was studied using in situ methods such as Mössbauer [66], extended X-ray absorption fine structure (EXAFS) [67], scanning tunneling microscopy (STM) [68], and Raman spectroscopy [69]. The results from these studies indicate that both Fe_3O_4 and γ-Fe_2O_3 have non-stoichiometric inverse spinel structures. The film stoichiometry varies with distance from the metal-film interface. In magnetite, one-third of the tetrahedral positions are occupied by Fe^{3+} ions, while the other two-thirds are shared evenly by Fe^{3+} and Fe^{2+} ions. In γ-Fe_2O_3, iron is in the trivalent state and one-ninth of the octahedral sites are vacant [70]. The film is cation-deficient Fe_3O_4 with continuous stoichiometry between Fe_3O_4 and γ-Fe_2O_3 [71]. Thus, cation-deficient Fe_3O_4 is considered to be the passive film formed on iron.

The corrosion properties of nitrided (570 °C, 4 h) and untreated iron were examined in a borate solution of pH 8.4 with and without chlorides or ammonia [72]. Enhanced pitting resistance and enhanced anodic currents were observed for nitrided Fe and also for untreated Fe in the presence of ammonia. The observed increase of the magnetite in the passive layer is due to the ammonia-promoted conversion of:

$$\mathrm{FeOOH} + \mathrm{Fe(II)} \rightarrow \mathrm{Fe_3O_4} \tag{4.18}$$

It was assumed that the enhanced pitting resistance of nitrided Fe results from binding of chloride anions into a Fe-NH_3-Cl complex.

4.9.1 Stainless steel

The nature of passive films grown on Fe-Cr alloys has been reviewed [73–75]. Iron is passivated when alloyed with chromium by the formation of electronically conductive passive films. The corrosion rate of iron drastically decreases from ~0.08 mm/year to 0 when chromium content in the alloy increases from 8% to 13% [9]. The Flade potentials of chromium-iron alloys in 4% NaCl solutions increase from −0.57 V in the absence of chromium to +0.17 V in an alloy with 12% chromium [10,11]. The critical passivating current for Cr-Fe alloys at pH = 7 reaches a minimum of $\sim 2 \times 10^{-3}$ mA/cm^2 at 12% chromium [76]. The small critical passivation current density observed for Fe-Cr alloys explains why these alloys are easily passivated in aerated aqueous solutions. Later experimental studies identified the existence of critical chromium concentration on the passivation behavior of the alloys [76].

More stable and thicker passive films were obtained when a 24% Cr-Fe alloy was passivated potentiostatically in 1 N sulfuric acid for long periods of time [77]. A decrease in the critical current density for the passivation of Fe-9% Ni alloy in 1 M sulfuric acid and

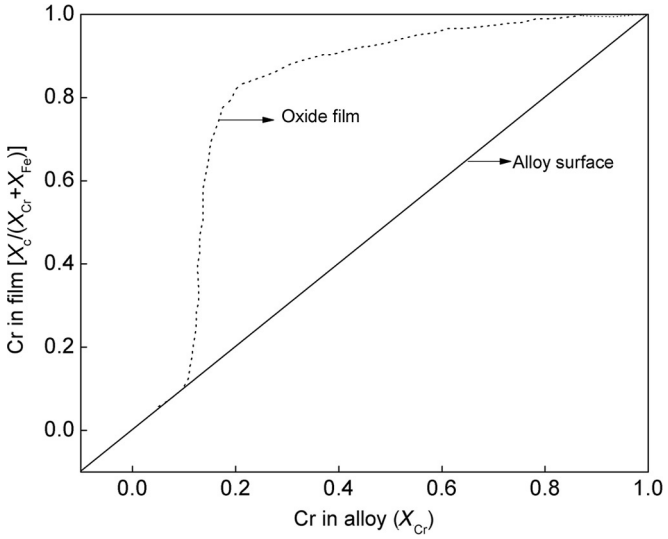

Fig. 4.20 Cationic fraction of chromium in the passive film as a function of chromium fraction in the alloy [78].

an increase of the passive region in the anodic polarization curve was observed when the chromium content in the alloy was increased, indicating an increase in the protective nature of the passive film [49].

Early studies provided evidence that for the formation of passive films on the alloy surface it should contain at least 12% Cr [9–11]. Later, surface passive layer studies on Fe-Cr confirmed that the cationic fraction of chromium in the passive film increases when the chromium atomic fraction in the alloy is higher than 12%, and, as shown in Fig. 4.20, levels off at Cr atomic fraction in the alloy of 50% [78].

Increasing the atomic fraction of Cr in the range between 14% and 18% provides resistance in acid environments. An increase in the minimum chromium content in the alloy contributes to a further reduction in general corrosion rates. Increasing chromium content from 12% to 25% in Fe-Cr and Fe-10% Ni-Cr alloys reduces the corrosion rate of the alloys in an oxidizing environment by 99.44% [56]. The tests were performed in boiling sulfuric acid containing ferric sulfate for 15 min. There is general agreement in the literature that the passive film formed on stainless steel alloys consists of Fe^{2+}, Fe^{3+}, and Cr_2O_3 [79]. The film composition changes with the applied electrode potential. At high anodic potentials (in the transpassive region), some Cr^{3+} is converted to the soluble Cr^{6+} species [80]. Also, an increase of chromium-oxyhydroxide in the passive film was observed at higher anodic potentials [81,82]. In situ ellipsometry and potential modulated UV-visible reflection was used to study the effect of the film thickness and pH on the composition of the passive film formed on Fe-Cr and Fe-Cr-Ni alloys [83]. The chromium enrichment in the passive layer increases with an increase of the film thickness.

However, a continuous decrease of the Cr^{3+} content in the film was observed at higher anodic potentials.

Using radiotracer studies, two classes of bound water M-H_2O and M-OH (aquo and olation groups) and MO or M-OOH with oxo and olation bridges were identified in the passive film [84–86]. The nature of the water was found to be critical to the dynamic rupture and self-repair of the film.

4.9.2 Crystalline structure

Oxide passive film formation on metals and their crystalline structure have been reviewed recently [73,87]. The nanometer-scale chemical and structural aspects have been reviewed by Maurice and Marcus [88]. The growth of 2-D anodic oxide films and the nanostructure of 3-D films are considered in this review. The structures of stainless steels [27,89], Co- [90], Ni- [91], and Cu-based alloys [92,93] have been studied with atomic force microscopy (AFM) and scanning tunneling microscopy (STM).

The crystalline structure of austenitic or 200 and 300 series stainless steels at temperatures ranging from the cryogenic to the melting point is face-centered cubic. The alloys contain a minimum of 16% chromium and a maximum of 0.15% carbon and nickel and/or manganese, which help the alloys to retain an austenitic structure.

Super austenitic stainless steels, such as AL-6XN and 254SMO alloys, have high resistance to localized corrosion. Chloride pitting and crevice corrosion in these alloys is very low due to the presence of high molybdenum content (>6%) and nitrogen additions. Steels with higher nickel content exhibit better resistance to stress corrosion cracking than austenitic stainless steels.

Ferritic stainless steels contain between 10.5% and 27% chromium with small amounts of nickel or lead; some alloys may contain aluminum or titanium. These alloys have reduced corrosion resistance when compared to austenitic alloys because of their lower chromium and nickel content. Examples of these alloys are ^{29}Cr-^{4}Mo, ^{18}Cr-^{2}Mo, ^{29}Cr-^{4}Mo-^{2}Ni, ^{26}Cr-^{1}Mo, and ^{29}Cr-^{4}Mo.

Martensitic stainless steels contain between 12% and 14% chromium, less than 2% nickel, between 0.2% and 1% molybdenum, and between 0.1% and 1% carbons. These alloys exhibit lower corrosion resistance when compared to austenitic or ferritic alloys. However, they are very strong and can be hardened by heat treatment.

Precipitation-hardening martensitic stainless steels contain 17% chromium and 4% nickel. Their corrosion resistance is comparable to austenitic steels. They can be precipitation hardened to higher strengths than the martensitic stainless steels.

Duplex stainless steels have a mixed microstructure of ferrite and austenite with chromium content in the range between 19% and 32%, molybdenum up to 5%, and lower nickel contents than austenitic stainless steels. They exhibit better corrosion resistance to pitting, stress corrosion cracking, and crevice corrosion than austenitic stainless steels, and are approximately twice as strong.

EXERCISES

E4.1. Calculate and construct, using mixed potential theory, the critical passivation current density (a) potentiostatic and (b) galvanostatic polarization curve for anodic dissolution for active-passive metal that has the following electrochemical parameters: $E_{corr} = -0.5$ V vs. SCE, $E_{pp} = -0.4$ V vs. SCE, $I_{corr} = 10^{-4}$ A/cm^2, $b_a = 0.05$, $I_{pass} = 10^{-5}$ A/cm^2, and $E_{tr} = +1.0$ V vs. SCE.

E4.2. For active-passive alloys A and B with the following prameters given in Table E4.1, calculate the critical passivation current density and determine which is more easily passivated.

Table E4.1 Electrochemical Parameters for Active-Passive Alloys A and B

	I_{corr} (A/cm^2)	b_a (V/decade)	E_{corr} (V vs. SCE)	E_{pp} (V vs. SCE)
Alloy A	1×10^{-9}	+0.1	−0.300	0.2
Alloy B	7×10^{-8}	+0.1	−0.100	0.1

E4.3. Construct an anodic polarization curve and calculate the critical passivation current density of an active-passive alloy using mixed potential theory with the following electrochemical parameters: $E_{corr} = -0.55$ V vs. SCE; $I_{corr} = 10^{-4}$ A/cm^2; $b_a = 0.1$, $E_{pp} = -0.3$ V vs. SCE; and $I_{pass} = 10^{-7}$ A/cm^2, $E_{tr} = +0.9$ V.

E4.4. Parameters of an active-passive metal are given in Table E4.2:

(a) Calculate the critical current density to passivate the metal.

(b) Calculate the equilibrium potential of the corroding species given the exchange current density of the metal, $i^o = 10^{-9}$ A/m^2.

(c) Calculate the concentration of the metal-ion species at the equilibrium potential. Assume that one electron transfer reaction occurs during the corrosion of the metal-ion species and the standard electrode potential of this reaction is −0.25 V vs. SCE.

(d) Assuming the corrosive media is acidic, calculate the cathodic exchange current density if the cathodic reduction is hydrogen. The pH of the solution is 2 and the cathodic Tafel slope is −0.12 V.

(e) Construct the Evans diagram using the electrochemical parameters of the active-passive metal.

Table E4.2 Electrochemical Parameters of an Active-Passive Metal

E_{corr} (V vs. SCE)	I_{corr} (A/cm^2)	b_a (V/decade)	E_{pp} (V vs. SCE)	I_{pass} (A/cm^2)	E_{tr} (V vs. SCE)
−0.5	10^{-4}	0.05	−0.4	10^{-5}	1.0

E4.5. Plot the polarization curve for anodic dissolution of the active-passive metal that has the electrochemical parameters given in Table E4.3.

(a) Calculate the critical current density to passivate the metal,

(b) Calculate the equilibrium potential of the anodic dissolution reaction if the exchange current density of the anodic reaction is 10^{-5} A/cm^2.

(c) Assuming that the hydrogen evolution reaction is the only cathodic reaction in an acidic media with activity of H^+ and H_2 equal to 1.0, calculate the exchange current density for the hydrogen evolution reaction on the active-passive metal.

Table E4.3 Electrochemical Parameters of Anodic Dissolution of an Active-Passive Metal

E_{corr} (V vs. SCE)	I_{corr} (A/cm^2)	E_{pp} (V vs. SCE)	b_a (V/decade)	b_c (V/decade)	I_{pass} (A/cm^2)	E_{tr} (V vs. SCE)
−0.5	10^{-4}	−0.4	0.05	0.1	10^{-5}	1.05

E4.6. Hypothetical active-passive alloys A and B have the electrochemical parameters given in Table E4.4:

(a) Construct the polarization curves for both alloys and estimate their critical passivation current densities.

(b) Discuss the following:

1. Which alloy will be more easily protected by anodic protection?

2. Which will be more corrosion resistant in the reducing condition?

3. Which will be more corrosion resistant in the passive state?

4. Which will be more easily passivated by dissolved oxidizers?

Table E4.4 Electrochemical Parameters for Hypothetical Active-Passive Alloys A and B

	E_{corr} (V vs. SCE)	I_{corr} (A/cm^2)	b_a (V/decade)	E_{pp} (V vs. SCE)	I_{pass} (A/cm^2)	E_{tr} (V vs. SCE)
Alloy A	−0.5	1.0×10^{-7}	0.1	0.1	1×10^{-6}	+0.9
Alloy B	−2.3	7.0×10^{-8}	0.1	0.25	1×10^{-7}	+1.1

E4.7. Active-pasive alloys A, B, and C have electrochemical parameters given in Table E4.5:

Calculate the critical current density and determine:

(a) Which alloy would be more easily protected by anodic protection?

(b) Which is more easily passivated in oxydizing electrolytes?

(c) Which will be the more corrosion resistant in the passive state?

(d) Which will be more corrosion resistant in the cative state of the alloy in the presence of oxidizing solutions?

Table E4.5 Electrochemical Parameters for Active-Passive Alloys A, B, and C

	I_{corr} (A/cm^2)	b_a (V/decade)	E_{pp} (V vs. SHE)	I_{pass} (A/cm^2)	E_{corr} (V vs. SHE)	E_{tr} (V vs. SHE)
Alloy A	2.8×10^{-4}	0.1	+0.1	3.8×10^{-5}	−0.43	1.00
Alloy B	4.4×10^{-5}	0.1	−0.1	5×10^{-6}	−0.35	0.85
Alloy C	4.5×10^{-6}	0.1	+0.14	1×10^{-6}	−0.24	0.90

E4.8. An active-passive alloy corrodes in the active state in an acidic solution in the presence of the redox couple $Fe^{3+}|Fe^{2+}$. The corrosion potential and corrosion current are $E_{corr} = -0.35$ V vs. SHE and $I_{corr} = 10\ \mu A/cm^2$. If the reduction occurs under activation control with $b_c = -0.1$ V/decade, concentration of Fe^{2+} of 10^{-6} M, and the exchange current density of the redox couple $i^o_{Fe^{3+}|Fe^{2+}} = 0.01\,\mu A/cm^2$, calculate the concentration of Fe^{3+} oxidizer necessary to passivate the alloy. Recalculate the oxidizer concentration for an exchange current density of 0.1 and 1 $\mu A/cm^2$ for the redox couple.

E4.9. Table E4.6 lists the parameters of the active-passive alloys A, B, C, and D. Calculate critical current densities of the active-passive alloys and determine:

(a) Which of the alloys will be more corrosion resistant in the reducing condition?

(b) Which will be more corrosion resistant in the passive state?

(c) Which will be more easily passivated by dissolved oxidizers?

(d) Which would be more easily protected by anodic protection?

Table E4.6 Parameters of the Active-Passive Alloys A, B, C, and D

	E_{corr} (V vs. SCE)	I_{corr} (A/cm^2)	b_a (V/decade)	E_{pp} (V vs. SCE)	I_{pass} (A/cm^2)	E_{tr} (V vs. SCE)
Alloy A	−0.4	1.0×10^{-6}	0.1	0.0	1×10^{-5}	0.7
Alloy B	−0.2	7.0×10^{-7}	0.1	0.3	1×10^{-6}	1.2
Alloy C	−0.5	5.0×10^{-7}	0.1	−0.1	8×10^{-4}	0.3
Alloy D	−0.1	1×10^{-6}	0.06	-	-	-

E4.10. As a function of chromium content, Fe in Fe-Cr alloy has the following electrochemical properties shown in Table E4.7. Assume that b_a is constant for all alloy compositions. The value of I_{corr} and b_a for pure iron are 5×10^{-5} A/cm^2 and 0.1 V/decade, respectively.

(a) Calculate the Flade potential for iron with no chromium as an alloying element.

(b) Calculate the corrosion current in the case of the alloys that contain 4% and the 8% Cr. The Flade potential of the corresponding alloys are −0.48 and −0.25 V, respectively.

(c) Plot the polarization curves.

Table E4.7 Electrochemical Properties of Fe in Fe-Cr Alloy as a Function of Chromium Content

Percentage of Cr in Fe-Cr Alloy	E_{corr} (V)	I_{crit} (A/cm^2)	I_{pass} (A/cm^2)	E_{tr} (V)
0%	−0.65	5×10^{-4}	1×10^{-5}	1.5
4%	−0.57	8×10^{-5}	1×10^{-6}	1.4
8%	−0.35	1×10^{-6}	1×10^{-8}	1.2

REFERENCES

[1] J. Keir, Experiments and observations on the dissolution of metals in acids, and their precipitations; with an account of a new compound acid menstruum, useful in some technical operations of parting metals, Phil. Trans. 80 (1790) 359–384.
[2] C. Schonbein, About the behavior of tin and iron from the nitric acid, Pogg. Ann. 37 (1836) 390–399.
[3] C. Wagner, Passivity and inhibition during the oxidation of metals at elevated temperatures, Corros. Sci. 5 (1965) 751–764.
[4] M. Faraday, in: Experimental Researches in Electricity, vol. II, Richard and John Edward Taylor, London, 1844.
[5] F. Flade, Contributions to the knowledge of passivity, Z. Physik. Chem. 76 (1911) 513–546.
[6] U.F. Franck, The anodic behavior of iron in sulfuric acid—a contribution to an understanding of the Ostwald-Lillie model of [living] nerves, Z. Naturforschung 4A (1949) 378–391.
[7] H.H. Uhlig, P.F. King, The Flade potential of iron passivated by various inorganic corrosion inhibitors, J. Electrochem. Soc. 106 (1959) 1–7.
[8] H.H. Uhlig, R. Winston Revie, Corrosion and Corrosion Control, third ed., Wiley, New York, 1985.
[9] W. Whitman, E. Chappell, Corrosion of steels in the atmosphere, Ind. Eng. Chem. 18 (1926) 533–535.
[10] H.H. Uhlig, N.E. Carr, P. Shneider, The potentials of iron-chromium alloys containing hydrogen, Trans. Electrochem. Soc. 79 (1941) 111–127.
[11] R. Oliver, Proceedings of the 6th Meeting International Committee on Electrochemistry, Thermodynamics, and Kinetics, Poitiers, Butterworth, London, 1955, p. 314.
[12] N. Sato, G. Okamoto, Electrochemical passivation of metals, in: J.O.M. Bockris, B.E. Conway, E. Yeager, R.E. White (Eds.), in: Comprehensive Treatise of Electrochemistry, vol. IV, Plenum Publishing Corp, New York, 1981, pp. 193–245.
[13] N. Sato, An overview on the passivity of metals, Corros. Sci. 31 (1990) 1–19.
[14] J.S. Leach, B.R. Pearson, Crystallization in anodic oxide films, Corros. Sci. 28 (1988) 43–56.
[15] F.P. Fehlner, N.F. Mott, Low temperature oxidation, Oxid. Met. 2 (1970) 59–99.
[16] T.L. Barr, An ESCA study of the termination of the passivation of elemental metals, J. Phys. Chem. 82 (1978) 1801–1810.
[17] H. Uhlig, The adsorption theory of passivity and the Flade potential, Z. Electrochem. 62 (1958) 626–632.
[18] U.R. Evans, The passivity of metals. I. The isolation of the protective film, J. Chem. Soc. (1927) 1020–1040.
[19] H.H. Uhlig, Passivity and its breakdown on iron and iron based alloys, in: NACE USA-Japan Seminar, NACE, Houston, 1976.
[20] M. Pourbaix, Atlas of Electrochemical Equilibria in Aqueous Solutions, second English ed., NACE, Texas, USA, 1974.
[21] J.A. Bardwell, B. MacDougal, M.J. Graham, Use of ^{18}O/SIMS and electrochemical techniques to study the reduction and breakdown of passive oxide films on iron, J. Electrochem. Soc. 135 (1988) 413–418.
[22] J.A. Bardwell, M.J. Graham, Pitting of iron by chloride in borate buffer solution: role of the anodic oxide film, J. Electrochem. Soc. 135 (1988) 2157–2161.
[23] H. Konno, M. Kawai, M. Nagayama, The mechanism of spontaneous dissolution of the air-formed oxide film on iron in a deaerated neutral phosphate solution, Surf. Technol. 24 (1985) 259–271.

[24] A.J. Davenport, L.J. Oblonsky, M.P. Ryan, M.F. Toney, The structure of the passive film that forms on iron in aqueous environments, J. Electrochem. Soc. 147 (2000) 2162–2173.
[25] H. Deng, H. Nanjo, P. Qian, A. Santosa, I. Ishikawa, Y. Kurata, Potential dependence of surface crystal structure of iron passive films in borate buffer solution, Electrochim. Acta 52 (2007) 4272–4277.
[26] P.B. Sewell, C.D. Stockbridge, M. Cohen, An electrometric and electron diffraction study of air-formed oxide films on iron, J. Electrochem. Soc. 108 (1961) 933–941.
[27] M.P. Ryan, R.C. Newman, G.E. Thompson, Atomically resolved STM of oxide film structures on Fe-Cr alloys during passivation in sulfuric acid solution, J. Electrochem. Soc. 141 (1994) L164–L165.
[28] H.H. Deng, I. Ishikawa, M. Yoneya, H. Nanjo, Reconstruction in air of an iron passive film formed at −0.4 V in a borate buffer solution, J. Phys. Chem. B 108 (2004) 9138–9146.
[29] H. Deng, H. Nanjo, P. Qian, Z. Xia, I. Ishikawa, Evolution of passivity in air exposure of an iron passive film, Electrochim. Acta 52 (2006) 187–193.
[30] F.P. Fehlner, M.J. Graham, Thin oxide film formation on metals, in: P. Marcus, J. Oudar (Eds.), Corrosion Mechanism in Theory and Practice, Dekker, New York, 1995, pp. 123–155.
[31] N. Cabrera, N.F. Mott, Theory of oxidation of metals, Rep. Prog. Phys. 12 (1949) 163–184.
[32] F.P. Fehlner, N.F. Mott, Low-temperature and anodic oxidation of metals and semiconductors, Oxid. Met. 2 (1972) 75–78.
[33] N. Sato, M. Cohen, The kinetics of anodic oxidation of iron in neutral solution: I. Steady growth region, J. Electrochem. Soc. 111 (1964) 512–519.
[34] D.D. Macdonald, The history of the point defect model for the passive state: a brief review of film growth aspects, Electrochim. Acta 56 (2011) 1761–1772.
[35] D.D. Macdonald, Some personal adventures in passivity—a review of the point defect model for film growth, Russ. J. Electrochem. 48 (2012) 235–258.
[36] C.Y. Chao, L.F. Lin, D.D. Macdonald, A point defect model for anodic passive films: I. Film growth kinetics, J. Electrochem. Soc. 128 (1981) 1187–1194.
[37] C.Y. Chao, L.F. Lin, D.D. Macdonald, A point defect model for anodic passive films: II. Chemical breakdown and pit initiation, J. Electrochem. Soc. 128 (1981) 1194–1198.
[38] C.Y. Chao, L.F. Lin, D.D. Macdonald, A point defect model for anodic passive films. III. Impedance response, J. Electrochem. Soc. 129 (1982) 1874–1879.
[39] D.D. Macdonald, Passivity – the key to our metals-based civilization, Pure Appl. Chem. 71 (1999) 951–978.
[40] D.D. Macdonald, G.R. Engelhard, The point defect model for bi-layer passive films, ECS Trans. 28 (2010) 123–144.
[41] N. Sato, in: R.P. Frankenthal, J. Kruger (Eds.), Passivity of Metals, The Electrochemical Society, NJ, 1978, pp. 1–10.
[42] V.G. Levich, Physiochemical Hydrodynamics, Prentice Hall, NJ, 1962.
[43] U.R. Evans, Corrosion and Oxidation of Metals, Arnolds, London, 1960.
[44] U.A. Paulus, A. Wokaun, G.G. Scherer, T.J. Schmidt, V. Stamenkovic, N.M. Markovic, R.N. Ross, Oxygen reduction on high surface area Pt-based alloy catalysts in comparison to well defined smooth bulk alloy electrodes, Electrochim. Acta 47 (2002) 3787–3798.
[45] T.J. Schmidt, U.A. Paulus, H.A. Gasteiger, N. Alonso-Vante, R.J. Behm, Oxygen reduction on $Ru_{1.92}Mo_{0.08}SeO_4$, Ru/carbon, and Pt/carbon in pure and methanol-containing electrolyte, J. Electrochem. Soc. 147 (2000) 2620–2624.
[46] M. Lefevre, J.P. Dodelet, Fe-based catalysts for the reduction of oxygen in polymer electrolyte membrane fuel cell conditions: determination of the amount of peroxide released during electroreduction and its influence on the stability of the catalysts, Electrochim. Acta 48 (2003) 2749–2760.
[47] R.F. Steigerwald, N.D. Greene, The anodic dissolution of binary alloys, J. Electrochem. Soc. 109 (1962) 1026–1034.
[48] M.G. Fontana, N.D. Green, Corrosion Engineering, McGraw-Hill, New York, 1967.
[49] K. Osozawa, H.J. Engel, The anodic polarization curves of iron-nickel-chromium alloys, Corros. Sci. 6 (1966) 389–393.

[50] A.J. Sedriks, Corrosion of Stainless Steels, John Wiley, New York, 1979.
[51] B.D. Craig, D.S. Anderson, Handbook of Corrosion Data, ASM International, Materials Park, Ohio, 1995.
[52] R.N. Gunn, Duplex Stainless Steel, Abigton Publishing, Cambridge, UK, 1997.
[53] R. Pierre, P.R. Roberge, Handbook of Corrosion Engineering, McGraw-Hill, New York, 2000.
[54] N.B. Pilling, D.E. Ackerman, Resistance of iron-nickel-chromium alloys to corrosion by acids, Trans. AIMME 83 (1929) 248–279.
[55] I. Class, H. Graefen, Resistance of austenitic nickel-chromium steels containing molybdenum and copper to sulfuric acid, Werkstoffe, Korros. 15 (1964) 79–84.
[56] M.A. Streicher, Austenitic and ferritic stainless steels, in: R.W. Revie (Ed.), Uhlig's Corrosion Handbook, second ed., John Wiley, New York, 2000, pp. 601–650.
[57] C.E. Locke, Anodic protection, in: Metals Handbook: Corrosion, ASM International, Materials Park, Ohio, 1987, , pp. 463–465.
[58] J.D. Sudbury, C.E. Locke, Anodic control of corrosion, Proc. Am. Petrol. Inst. Sect. III 43 (1965) 115–119.
[59] I. Diéz-Pérez, P. Gorostiza, F. Sanz, C. Müler, First stages of electrochemical growth of the passive film on iron, J. Electrochem. Soc. 148 (2001) B307–B313.
[60] D. Rahner, W. Forker, Effect of convection conditions on the stability and in-situ analytics of passive layers on iron in neutral media, Z. Phys. Chem. 18 (1978) 344.
[61] S.C. Tjong, E. Yeager, ESCA and SIMS studies of the passive film on iron, J. Electrochem. Soc. 128 (1981) 2251–2254.
[62] K. Ogura, K. Sato, Cathodic dissolution of the passive film on iron—I. Kinetics and mechanism, Electrochim. Acta 25 (1980) 857–862.
[63] V. Schroeder, T.M. Devine, Surface enhanced Raman spectroscopy study of the galvanostatic reduction of the passive film on iron, J. Electrochem. Soc. 146 (1999) 4061–4070.
[64] M. Buchler, P. Schmuki, H. Bohni, Iron passivity in borate buffer: formation of a deposit layer and its influence on the semiconducting properties, J. Electrochem. Soc. 145 (1998) 609–614.
[65] M. Buchler, P. Schmuki, H. Bohni, T. Stenberg, T. Manntyla, Comparison of the semiconductive properties of sputter-deposited iron oxides with the passive film on iron, J. Electrochem. Soc. 145 (1998) 378–385.
[66] J. Eldridge, W. Hoffman, A Mössbauer spectroscopy study of the potential dependence of passivated iron films, J. Electrochem. Soc. 136 (1989) 955–961.
[67] A.J. Davenport, M. Sansone, High resolution in-situ XANES investigation of the nature of the passive film on iron in a pH 8.4 borate buffer, J. Electrochem. Soc. 142 (1995) 725–730.
[68] E.E. Rees, M.P. Ryan, D.S. McPhail, An STM study of the nanocrystalline structure of the passive film on iron, Electrochem. Solid State Lett. 5 (2002) B21–B23.
[69] S. Joiret, M. Kedam, X.R. Novoa, M.C. Perez, C. Rangel, H. Takenouti, Use of EIS, ring-disk electrode, EQCM and Raman spectroscopy to study the film of oxides formed on iron in 1 M NaOH, Cem. Concr. Compos. 24 (2002) 7–15.
[70] A.F. Wells, Structural Inorganic Chemistry, Clarendon Press, Oxford, UK, 1984.
[71] P.A. Castro, E.R. Vago, E.J. Calvo, Surface electrochemical transformations on spinel iron oxide electrodes in aqueous solutions, J. Chem. Soc. Faraday Trans. 92 (1996) 3371–3379.
[72] I. Flis-Kabulska, T. Zakroczymski, Corrosion and passivation of iron and its nitrided layer in borate buffer, Electrochim. Acta 54 (2009) 1810–1819.
[73] C.O.A. Olsson, D. Landolt, Passive films on stainless steels—chemistry, structure and growth, Electrochim. Acta 48 (2003) 1093–1104.
[74] T. Shibata, Critical factors for controlling the stability of the passive film on stainless steels, ECS Trans. 16 (52) (2009) 331–343.
[75] P. King, H. Uhlig, Passivity in the iron-chromium binary alloys, J. Phys. Chem. 63 (1959) 2026–2032.
[76] S. Fujimoto, R.C. Newman, S.P. Kaye, H. Kheyrandish, J.S. Colligon, Passivation thresholds in iron-chromium alloys prepared by ion-beam sputtering, Corros. Sci. 35 (1993) 51–55.
[77] R. Frankenthal, On the passivity of iron-chromium alloys: I. Reversible primary passivation and secondary film formation, J. Electrochem. Soc. 114 (1967) 542–547.

[78] K. Asami, K. Hashimoto, S. Shimodaira, XPS determination of compositions of alloy surfaces and surface oxides on mechanically polished iron-chromium alloys, Corros. Sci. 17 (1977) 713–723.
[79] C. Calinski, H.H. Strehblow, ISS depth profiles of the passive layer on Fe/Cr alloys, J. Electrochem. Soc. 136 (1989) 1328–1331.
[80] J.A. Bradwell, A.J. Davenport, H.J. Isaacs, G.I. Sproule, D. MacDougall, M.J. Graham, In situ XANES detection of Cr(VI) in the passive film on Fe-^{26}Cr, J. Electrochem. Soc. 139 (1992) 371–373.
[81] H. Fischmeister, U. Roll, Passive layers on stainless steels: a survey of surface analysis results, Fresenius Z. Anal. Chem. 319 (1984) 639–645.
[82] K. Asami, K. Hashimoto, X-ray photoelectron spectroscopy for corrosion studies, Langmuir 3 (1987) 897–904.
[83] N. Harra, K. Sugimoto, In situ analysis of passive films on Fe-Cr-Ni alloy by potential-modulated UV-visible reflection spectroscopy, J. Electrochem. Soc. 138 (1991) 1594–1599.
[84] G. Okamoto, Passive film of 18-8 stainless steel structure and its function, Corros. Sci. 13 (1973) 471–489.
[85] K. Tachibana, K. Miya, K. Furuya, G. Okamoto, Changes in the power spectral density of noise current on type 304 stainless steels during the long time passivation in sulfuric acid solutions, Corros. Sci. 31 (1990) 527–532.
[86] H. Saito, T. Shibata, G. Okamoto, The inhibitive action of bound water in the passive film of stainless steel against chloride corrosion, Corros. Sci. 19 (1979) 693–708.
[87] P. Marcus, V. Maurice, Oxide passive films and corrosion protection, in: G. Pacchioni, S. Valeri (Eds.), Oxide Ultrathin Films: Science and Technology, Wiley-VCH, Weinheim, 2012, pp. 119–144.
[88] V. Maurice, P. Ph. Marcus, Passive films at the nanoscale, Electrochim. Acta 84 (2012) 129–138.
[89] H. Nanjo, R.C. Newman, N. Sanada, Atomic images of 304SS surface after electrochemical treatments, Appl. Surf. Sci. 121–122 (1997) 253–256.
[90] A. Foelske, J. Kunze, H.H. Strehblow, Initial stages of hydroxide formation and its reduction on Co(0 0 0 1) studied by in situ STM and XPS in 0.1 M NaOH, Surf. Sci. 554 (2004) 10–24.
[91] A. Machet, A. Galtayries, S. Zanna, L.H. Klein, V. Maurice, P. Jolivet, M. Foucault, P. Combrade, P. Scott, P. Marcus, XPS and STM study of the growth and structure of passive films in high temperature water on a nickel-base alloy, Electrochim. Acta 49 (2004) 3957–3964.
[92] J. Kunze, V. Maurice, L.H. Klein, H.H. Strehblow, P. Marcus, In situ STM study of the effect of chlorides on the initial stages of anodic oxidation of Cu(111) in alkaline solutions, Electrochim. Acta 48 (2003) 1157–1167.
[93] J. Kunze, V. Maurice, L.H. Klein, H.H. Strehblow, P. Marcus, In situ STM study of the anodic oxidation of Cu(0 0 1) in 0.1 M NaOH, J. Electroanal. Chem. 554–555 (2003) 113–125.

CHAPTER 5

Basics of Corrosion Measurements

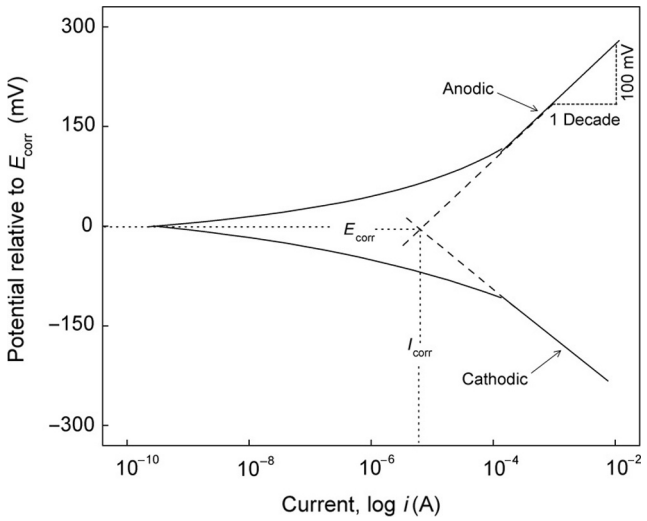

Chapter Contents

Corrosion Engineering
http://dx.doi.org/10.1016/B978-0-444-62722-3.00005-7

5.1 INTRODUCTION

Electrochemical corrosion techniques are essential in predicting the service life of metallic components used in chemical and construction industries. They measure the corrosion rates, the oxidizing power of the environment, and evaluate the effectiveness of corrosion protection strategies. The following direct current "dc" electrochemical methods are discussed in this chapter: linear polarization technique, Tafel extrapolation, and open circuit potential (OCP) vs. time measurements. Electrochemical impedance spectroscopy (EIS) is introduced as an alternating current technique "ac." This technique uses alternating current to measure frequency-dependent processes in corrosion and estimates the change of polarization resistance.

In linear polarization measurements, the current is measured at potentials between 10 and 20 mV in cathodic and anodic direction from the equilibrium potential. The dependence of current vs. potential in this potential range is linear and the slope dE/dI represents the polarization resistance. The corrosion current is calculated using the Stern-Geary equation for known values of the anodic and cathodic Tafel slopes.

The Tafel extrapolation method provides a direct measurement of the corrosion rate and the corrosion potential. It measures extremely low corrosion rates with an accuracy compared to that of weight loss methods. Tafel technique is advantageous in evaluation of corrosion inhibitors and in comparison of corrosion characteristics of alloys. This is a destructive technique due to a large polarization range required to complete the polarization. Because the surface properties of the corroding metal change during polarization, it is necessary to use new specimens to complete the corrosion evaluation studies. Measurement of the OCP as a function of time provides a qualitative method to evaluate the stability of sacrificial coatings. The removal rate of a sacrificial coating in corroding solution is controlled by the potential difference between the underlying metal and the sacrificial coating, the severity of the corroding solution, and the thickness of the coating. The OCP reaches the value for the protected metal when the sacrificial coating is completely removed from its surface.

EIS measures the response of corrosion systems to "ac" perturbations. It has been used in corrosion research to estimate the corrosion rates and to study the passivation of metals, the corrosion protection provided by inhibitors, sacrificial and barrier properties of electrodeposited coatings, and performance of polymer coatings such as paints. EIS only

estimates the polarization resistance. As in the case of the linear polarization technique, the corrosion current is calculated using the Stern-Geary equation for known values of anodic and cathodic Tafel slopes.

5.2 POLARIZATION RESISTANCE

Current-potential relationship, shown in Fig. 5.1, describes a redox system that departs slightly (10-20 mV) from its equilibrium state. As shown in the figure, the relationship between the current and the applied potential is nearly linear when measured close to the equilibrium potential. In this case, the overpotential in Butler-Volmer equation (3.28) is small and is equal to the inequality:

$$\eta \leq RT/nF$$

$$i = \vec{i} - \overleftarrow{i} = i^{o}\left\{\exp\left(\frac{-\alpha_c F\eta}{RT}\right) - \exp\left(\frac{\alpha_a F\eta}{RT}\right)\right\} \tag{3.28}$$

As described in the low-field approximation theory (Section 3.3.2, Chapter 3), the exponents in Eq. (3.28) expand using $[(e^{x} - e^{-x})/2 = \sinh x]$ and $[\sinh x = x, \text{when } x \to 0]$ resulting in:

$$\exp\left(\frac{-\alpha nF\eta}{RT}\right) = 1 - \frac{-\alpha nF\eta}{RT} \tag{5.1}$$

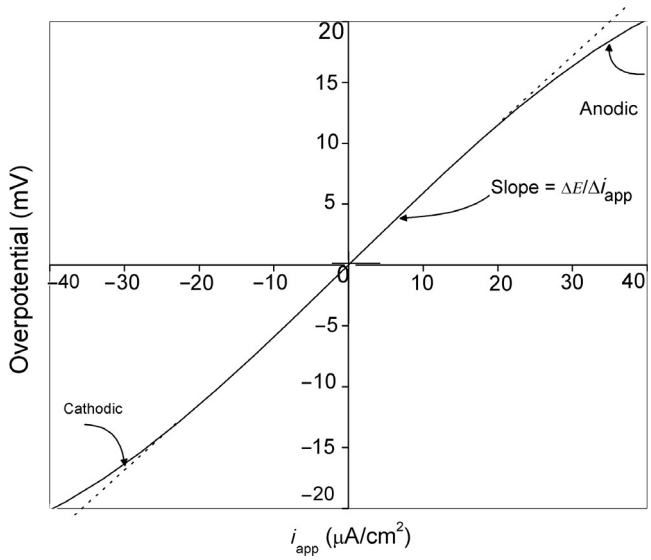

Fig. 5.1 Current-potential relationships for a redox system that shifts slightly (10-20 mV) from its equilibrium state.

and

$$\exp\left(\frac{(1-\alpha)nF\eta}{RT}\right) = 1 + \left(\frac{(1-\alpha)nF\eta}{RT}\right) \tag{5.2}$$

At overvoltage $\eta \rightarrow 0$, the difference of the current density in the forward direction (reduction) and reverse (oxidation) directions, is defined by the equation (3.39):

$$i = -i^{o}\frac{nF}{RT}\eta \tag{3.39}$$

The overvoltage is defined as:

$$\eta = -\frac{RT}{nF}\frac{i}{i^{o}} \tag{5.3}$$

The ratio of the derivative of the overpotential to the current, $\partial\eta/di$ when $\eta \rightarrow 0$, in Eq. (5.3), (the slope in Fig. 5.1), represents the resistance in Ohm's law and is often termed the charge-transfer resistance or the polarization resistance R_p.

$$R_p = \frac{RT}{nFi^{o}} \tag{5.4}$$

Equation (5.4) introduces a better physical explanation to the definition of exchange current density. The exchange current density can be viewed as a parameter that estimates the resistance of any corrosion or electrochemical reaction. A higher value of the exchange current density implies an increased reaction rate, while a lower exchange current density value (higher polarization resistance) indicates sluggish corrosion kinetics. Equation (5.4) can be written in terms of charge-transfer resistance as:

$$\eta = R_p i \tag{5.5}$$

Initial studies by Green et al. [1] and Simmons [2] suggested that the slope of the linear polarization curve is inversely proportional to the corrosion rate. According to Stern and Geary [3,4], the derivative overvoltage vs. applied current curve is linear only in a small range (10-20 mV) above and below the equilibrium electrode potential. Thus, the polarization resistance is defined as the slope of the polarization curve at the equilibrium potential (the origin of the polarization curve). The polarization resistance is imposed at the electrode surface by the finite rate of the charge transfer at the interface and represents a kinetic analog to the resistance in Ohm's law. Stern and Geary [4] developed a polarization method to measure the corrosion rates of metals by correlating Wager and Traud's [5] theoretical work to the experimental studies described by Stern [2], Skold and Larsen [6], and Bonhoeffer and Jena [7].

5.3 CALCULATION OF CORROSION RATES FROM POLARIZATION DATA-STERN AND GEARY EQUATION

Electrochemical techniques can be used to measure the oxidizing power of the environment and the corrosion rates of metals [8–11]. When a metal is immersed in a corrosive

media, both the oxidative and reductive processes occur on its surface. The corrosion reactions are divided into partial oxidation and reduction reactions. The metal, in most of the cases, is oxidized while the solution is reduced. The anode reaction is always oxidation:

$$\begin{aligned} \mathrm{Zn} &\rightarrow \mathrm{Zn}^{2+} + 2\mathrm{e}^- \\ \mathrm{Fe} &\rightarrow \mathrm{Fe}^{2+} + 2\mathrm{e}^- \\ \mathrm{M} &\rightarrow \mathrm{M}^{n+} + n\mathrm{e}^- \end{aligned} \tag{5.6}$$

The cathodic reaction is one of the following reductions:

$$\begin{aligned} \mathrm{O_2} + 4\mathrm{H}^+ + 4\mathrm{e}^- &\rightarrow 2\mathrm{H_2O}\ (\text{in acidic solutions}) \\ \mathrm{O_2} + 2\mathrm{H_2O} + 4\mathrm{e}^- &\rightarrow 4\mathrm{OH}^-\ (\text{in alkaline solutions}) \\ 2\mathrm{H}^+ + 2\mathrm{e}^- &\rightarrow \mathrm{H_2}\ (\text{hydrogen evolution}) \\ \mathrm{Cu}^{2+} + 2\mathrm{e}^- &\rightarrow \mathrm{Cu}\ (\text{reduction of metal cations}) \end{aligned} \tag{5.7}$$

Conservation of energy requires no net accumulation of electrical charge during any corrosion reaction. Thus, the total rate of oxidation is always equal to the total rate of reduction [4–7]. The conservation of energy is explained through the current-potential relationship shown in Fig. 5.2. In this figure, the equilibrium potentials of the redox reactions are labeled as $e_{\mathrm{eq,M}}$ and $e_{\mathrm{eq,H_2}}$. Equilibrium potentials of both cathode and anode

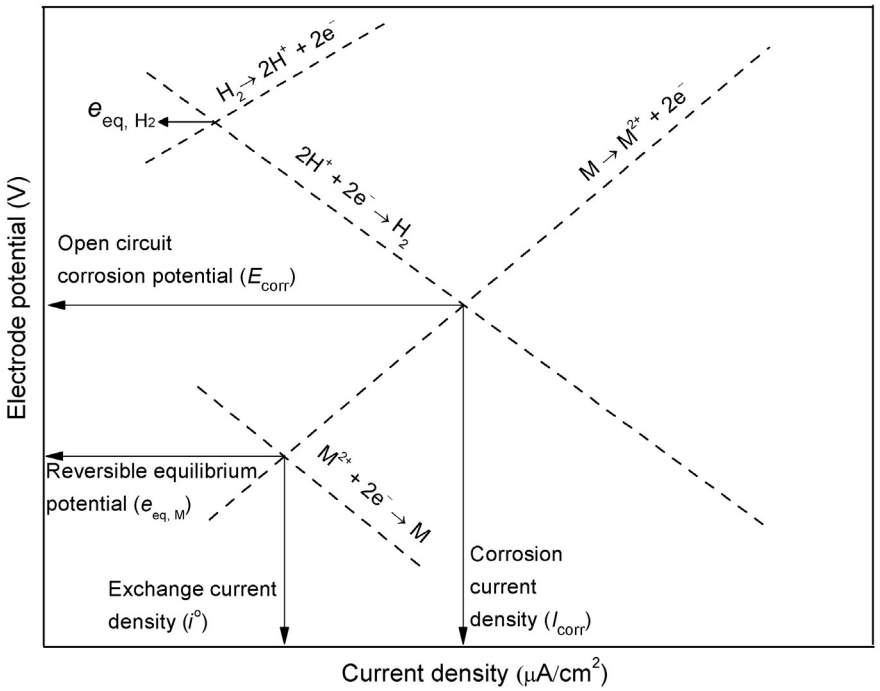

Fig. 5.2 *E* vs. *I* for a mixed electrode system.

reactions are given by the Nernst equation. The corrosion potential is defined as the potential at which the rate of oxidation of the metal, defined by current, $i_{O,M}$, is equal to the rate of reduction of H^+, defined by current, $i_{R,H}$. The point in Fig. 5.2 where both cathodic and anodic rates are equal is at the intersection of the cathodic line ($2H^+ + 2e^- \rightarrow H_2$) and anodic line ($M \rightarrow M^{2+} + 2e^-$). This point specifies the corrosion potential, E_{corr}, and the corrosion current, I_{corr}. The corrosion potential is not controlled by the thermodynamics of the redox system; rather, it is determined by the electrochemical kinetic parameters such as the exchange current density and the Tafel kinetics, that is, the cathodic and anodic intercepts and slopes in Tafel equation. Stern and Geary [3,4], Wagner and Traud [5], and (later) Oldam and Mansfeld [12,13] have provided a theoretical background for the determination of corrosion rates.

At E_{corr}, the rate of oxidation equals the rate of reduction and is equal to the corrosion rate.

$$I_{corr} = i_{O,M} = i_{R,H} \tag{5.8}$$

When the electrode is polarized, the overpotential is:

$$\eta = E_{app} - E_{corr} \tag{5.9}$$

E_{app} is the potential of an electrode under polarization. Because the overvoltage is defined as

$$\eta = b_c \log\left(\frac{i}{i^o}\right) \tag{3.33}$$

anodic and cathodic overpotentials for metal oxidation and hydrogen reduction reactions can be expressed as:

$$\eta = b_a \log\left(\frac{i_{O,M}}{I_{corr}}\right) \tag{5.10}$$

$$\eta = b_c \log\left(\frac{i_{R,H}}{I_{corr}}\right) \tag{5.11}$$

The anodic and cathodic Tafel slopes are b_a and b_c. Assigning a positive sign for anodic Tafel slope, b_a, and negative sign for the cathodic Tafel slope, b_c, and rearranging Eqs. (5.10) and (5.11), one obtains:

$$\log\left(\frac{i_{O,M}}{I_{corr}}\right) = \frac{\eta}{b_a} \tag{5.12}$$

$$\log\left(\frac{i_{R,H}}{I_{corr}}\right) = -\frac{\eta}{b_c} \tag{5.13}$$

Rearranging and combining Eqs. (5.12) and (5.13), one obtains:

$$10^{\eta/b_a} = \frac{i_{O,M}}{I_{corr}} \tag{5.14}$$

$$10^{-\eta/b_c} = \frac{i_{R,H}}{I_{corr}} \tag{5.15}$$

$$i_{meas} = I_{corr}\left(10^{\eta/b_a} - 10^{-\eta/b_c}\right) \tag{5.16}$$

The sum of anodic, $i_{O,M}$, and cathodic, $i_{R,H}$, currents is equal to i_{meas}. For small values of x, power series Eq. (5.17) can be expressed with Eq. (5.18):

$$10^x = 1 + 2.3x + \left[(2.3x)^2/2!\right] + \cdots + \left[(2.3x)^n/n!\right] \tag{5.17}$$

$$10^x \approx 1 + 2.3x \tag{5.18}$$

$$10^{\eta/b_a} = 1 + 2.3\eta/b_a \tag{5.19}$$

$$10^{-\eta/b_c} = 1 - 2.3\eta/b_c \tag{5.20}$$

Substituting Eqs. (5.19) and (5.20) into Eq. (5.16) and solving, one obtains:

$$i_{meas} = 2.3 I_{corr}\eta\frac{b_c + b_a}{b_c b_a} \tag{5.21}$$

$$\eta/i_{meas} = \frac{b_c b_a}{2.3 I_{corr}(b_c + b_a)} \tag{5.22}$$

Substituting the polarization resistance $R_p = \eta/i_{meas} = \Delta E/\Delta i$ in Eq. (5.22), one obtains:

$$I_{corr} = \frac{b_c b_a}{2.3(b_c + b_a)}\frac{\Delta i}{\Delta E} \tag{5.23}$$

or

$$I_{corr} = \frac{b_c b_a}{2.3(b_c + b_a)}\frac{1}{R_p} \tag{5.24}$$

Equation (5.24) is known as the Stern-Geary equation. Assuming that the cathodic and anodic slopes are constant for a particular metal in a given environment, then the Stern-Geary equation becomes:

$$I_{corr} = \frac{K}{R_p} \tag{5.25}$$

where

$$K = \frac{b_a b_c}{2.303(b_a + b_c)} \tag{5.26}$$

The constant, K, in Eq. (5.26) varies from 32 to 52 for a majority of the metal-solution interface systems. The polarization resistance can be determined with minimum system perturbation using the linear polarization resistance technique.

$$\log R_p = \log K - \log I_{corr} \tag{5.27}$$

A plot of log R_p vs. log I_{corr} is linear with a slope of −1 and intercept log K. Stern and Weisert [14] confirmed this relationship for the experimental corrosion rates in over six orders of magnitude. Their work contributed to the wide acceptance of the polarization method for estimating corrosion rates. A review by Mansfeld [15] provides details on the theory and application of this method.

5.3.1 Calculation of corrosion rate from the corrosion current

The corrosion current, usually denoted in A or A/m^2, can be used to determine the amount of corroded material. The current can be directly converted into the mass of the lost material by using Faraday's law:

$$Q = \frac{n\,FW}{M} \tag{5.28}$$

where Q represents charge passed in coulombs, n is the number of electrons involved in the redox reaction, W is the mass of electroactive species (g), and M is molecular weight (g/mol).

$$W = \frac{QM}{nF} \tag{5.29}$$

$$W = \frac{Q \times \mathrm{EW}}{F} \tag{5.30}$$

$$W = \frac{i \times t \times \mathrm{EW}}{F} \tag{5.31}$$

where EW represents the equivalent weight of the material, while Q is the product of total current passed in t sec. If Eq. (5.31) is divided by the density of the electrode material and geometric surface area, A (in cm^2), an expression for the corrosion penetration rate (CPR) is obtained.

$$\mathrm{CPR(cm/s)} = \frac{I_{corr} \times \mathrm{EW}}{dnF} \tag{5.32}$$

The CPR or W/t is corrosion rate in cm/s and "d" is the density of the material. Other conventional forms of corrosion rate are expressed in Table 5.1.

$$\mathrm{CR(cm/s)} = \frac{I_{corr} \times \mathrm{EW}}{dF} \tag{5.33}$$

$$\mathrm{CR(mpy)} = \frac{I_{\mathrm{corr}}(\mu\mathrm{A/cm^2}) \times \mathrm{EW}}{d(\mathrm{g/cm^3})96,485(\mathrm{C/eq})1\,\mathrm{cm^2}} \frac{1\,\mathrm{C/s}}{10^6\,\mu\mathrm{A}} \frac{3600\,\mathrm{s}}{1\,\mathrm{h}} \frac{24\,\mathrm{h}}{\mathrm{day}} \frac{365\,\mathrm{days}}{\mathrm{year}} \frac{1\,\mathrm{in.}}{2.54\,\mathrm{cm}} \frac{1000\,\mathrm{mil}}{1\,\mathrm{in.}} \tag{5.34}$$

$$\mathrm{CR\ (mpy)} = \frac{0.129 \times I_{\mathrm{corr}} \times \mathrm{EW}}{d} \tag{5.35}$$

In Eq. (5.35), mpy = mils/year; I_{corr} = corrosion current density ($\mu\mathrm{A/cm^2}$); EW = equivalent weight of the corroding species, (g/eq); and d = density of the corroding species, ($\mathrm{g/cm^3}$).

Table 5.1 summarizes the relationship of commonly used corrosion rate units and their expressions. The conversion factors are given in Table 5.2 and Table 5.3 [16]. The current density equivalent to a corrosion rate of 1 $\mathrm{g/m^2}$ day is given in Table 5.4 [16].

Table 5.1 Relationship Between Various Commonly Used Units of Corrosion Rates and Their Expressions

	mA/cm²	mm/year	mpy	g/(m² × day)
$\mathrm{mA/cm^2}$	1	$\frac{3.28M}{nd}$	$\frac{129M}{nd}$	$\frac{8.95M}{n}$
mmpy	$\frac{0.306nd}{M}$	1	39.4	$2.74d$
mpy	$\frac{0.00777nd}{M}$	0.0254	1	$0.0694d$
$\mathrm{g/m^2/day}$	$\frac{0.112n}{M}$	$\frac{0.365}{d}$	$\frac{14.4}{d}$	1

Table 5.2 Conversion Factors [16]

Metal	Density (g/cm³)	2.74 × Density	0.365/Density
Aluminum	2.70	7.40	0.135
Cadmium	8.65	23.7	0.0422
Copper	8.96	24.6	0.0407
Copper-Nickel (70-30)	8.95	24.5	0.0408
Iron	7.87	21.6	0.0464
Iron-Silicon (Duriron) (84-14.5)	7.0	19.2	0.0521
Lead (chemical)	11.35	31.1	0.0322
Magnesium	1.74	4.77	0.210
Nickel	8.90	24.4	0.0410
Nickel-Copper (Monel) (70-30)	8.84	24.2	0.0413
Silver	10.49	28.7	0.0348
Tin	7.30	20.0	0.0500
Zinc	7.13	19.5	0.0512

This material is reproduced with permission of John Wiley & Sons, Inc.
Multiply millimeters penetration per year (mm/y) by 2.74 × density ($\mathrm{g/cm^3}$) to obtain grams per square meter per day ($\mathrm{g/m^2/d}$).
Multiply $\mathrm{g/m^2/d}$ by 0.365/density to obtain millimeters per year (mm/y).
Multiply inches penetration per year (ipy) by 696 × density to obtain milligrams per square decimeter per day (mdd).
Multiply mdd by 0.00144/density to obtain ipy.

Table 5.3 Additional Conversion Factors [16]

Multiply	By	To Obtain
ipy	25.4	mmpy
mdd	0.1	gmd
mA/cm^2	10	A/m^2
A/m^2	0.093	A/ft^2
Å	0.1	nm (nanometer)

This material is reproduced with permission of John Wiley & Sons, Inc.

Table 5.4 Current Density Equivalent to a Corrosion Rate of 1 g/m^2 day [16]
1 gmd = 1.117 *n/W* A/m^2, where *W* is the gram atomic weight

Reaction	A/m^2
$Al \rightarrow Al^{3+} + 3e^-$	0.124
$Cd \rightarrow Cd^{2+} + 2e^-$	0.0199
$Cu \rightarrow Cu^{2+} + 2e^-$	0.0352
$Fe \rightarrow Fe^{2+} + 2e^-$	0.0400
$Fe \rightarrow Fe^{3+} + 3e^-$	0.0600
$Pb \rightarrow Pb^{2+} + 2e^-$	0.0108
$Mg \rightarrow Mg^{2+} + 2e^-$	0.0919
$Ni \rightarrow Ni^{2+} + 2e^-$	0.0381
$Sn \rightarrow Sn^{2+} + 2e^-$	0.0188
$Zn \rightarrow Zn^{2+} + 2e^-$	0.0342

This material is reproduced with permission of John Wiley & Sons, Inc.

5.4 ELECTROCHEMICAL TECHNIQUES TO MEASURE POLARIZATION RESISTANCE

5.4.1 Linear polarization technique

The linear polarization technique estimates instantaneous corrosion rates under various process conditions. The corrosion current, according to the Stern-Geary equation, is inversely proportional to polarization resistance, which allows the measured polarization resistance to be normalized directly into corrosion rates. Because the current follows the applied overvoltage, the polarization resistance curve is plotted automatically. Because this technique accurately measures corrosion rates <0.1 mpy, it is of a great importance in water distribution systems and food industries that face problems with traces of impurities and contamination. It can be used to measure the corrosion rates in civil engineering structures that cannot be subjected to weight loss measurements. Usually, linear polarization measurements are executed in ~10 min. As shown in Fig. 5.3, the current as a

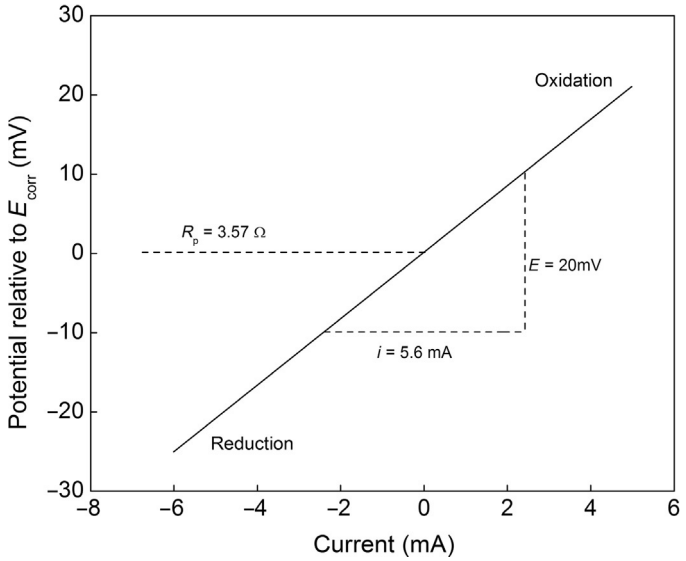

Fig. 5.3 Experimentally measured polarization resistance using linear polarization technique.

function of applied potential follows a linear trend. The slope of the *E-I* plot is the polarization resistance. The corrosion current is calculated using the Stern-Geary equation for known values of the anodic and cathodic Tafel slopes and from the estimated value of the polarization resistance obtained from the *E-I* plot.

The Stearn-Geary equation requires both the anodic and cathodic slopes to remain constant. For accurate measurements, it is necessary for the Tafel constants, b_a and b_c, to be determined independently using the Tafel technique. The slope of a linear polarization curve is controlled mainly by I_{corr}. Assuming that b_a and b_c are in the range of 120 mV, Eq. (5.24) reduces to:

$$I_{corr} = \frac{0.026}{R_p} \tag{5.36}$$

Equation (5.36) is used to calculate the corrosion rate of a system without knowledge of electrode-kinetic parameters. This approximation may not always result in accurate corrosion estimates. However, this equation provides a basis for rapid corrosion evaluation studies.

5.4.2 Galvanostatic technique

In the galvanostatic method, constant current steps are applied for a predetermined duration and to measure the overvoltage. The polarization resistance curve is constructed by plotting the values of the overvoltage as a function of applied current for each current step. The slope at the origin of the plot gives the polarization resistance. Because the metal

electrodes corrode at an unknown corrosion rate, the initial magnitude of the current steps is not known. It is necessary to conduct a preliminary trial and error testing to determine the magnitude of the current steps, in which the applied current is increased in small increments from zero to a value of current (I_1) that produces an overvoltage of 1-2 mV [17,18]. The current is then applied in small steps between $-I_1$ and I_1 and the corresponding overvoltages are measured. Tests conducted for ASTM by Mansfeld [19] indicated that the linear polarization resistance technique is more accurate and reproducible than the galvanostatic technique. The measurements of corrosion rates in different laboratories for stainless steel in 1 N H_2SO_4 were the basis for these conclusions.

5.4.3 Nonlinearity of polarization curves

Because the current-potential relationship in Eq. (5.24) must be linear, the Stern-Geary approximation is only valid for applied potentials in the range between 10 and 20 mV. This requirement for linearity has not always been observed in the literature. Some of the drawbacks of this technique include uncertainty in Tafel slopes, effect of solution and surface film resistance, scan rate, and nonlinearity of the current-potential relationship [3,20–25]. Methods of correcting for iR drop due to the resistance of surface films and the electrolyte resistance have been proposed [10,26–29].

Mansfled [30] examined the errors in measuring the corrosion rates when linearity of the overvoltage is assumed for various values of b_a and b_c. When b_a and b_c are both 0.120 V, linearity is observed near the origin. The error, as shown in Fig. 5.4a, is zero. However, at lower overvoltages, that is, when $b_a = b_c = 30$ mV, a

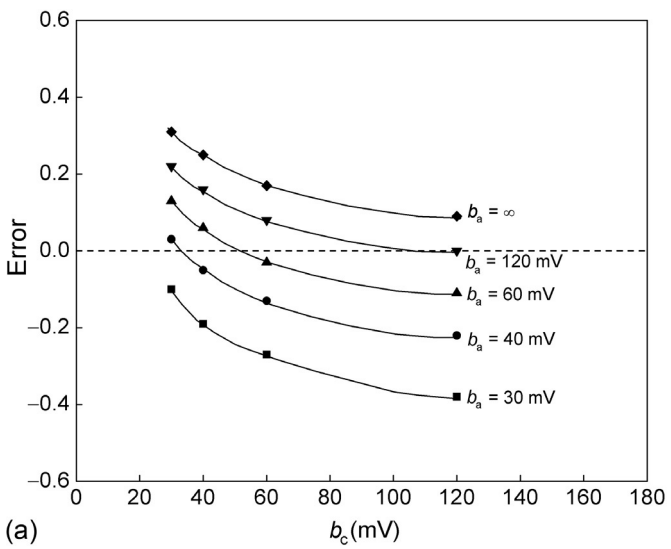

Fig. 5.4 (a) Errors due to assumed linearity of +10 mV anodic and −10 mV cathodic overvoltages for various values of b_c.

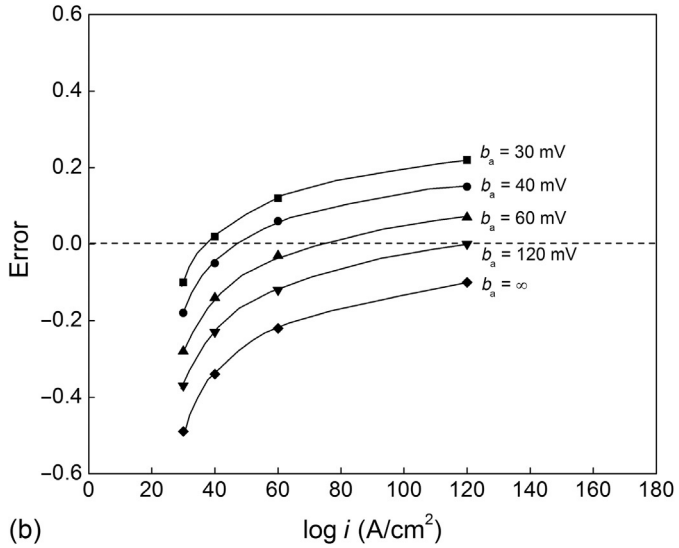

Fig. 5.4—Cont'd (b) Errors due to assumed linearity of +10 mV anodic and −10 mV cathodic overvoltages for various values of b_a [30]. © *NACE International 2003.*

departure from linearity near the origin is observed. The errors that occur from assumed linearity of 10 mV are shown in Fig. 5.4b. Notice that the errors are opposite in sign and increase when the difference between absolute values of the Tafel constants increases. In fact, there is no error for $b_a = b_c = 120$ mV. Maximum error is observed when one of the Tafel constants "b" equals to infinity, while the other is 30 mV [30].

5.5 APPLICATIONS OF LINEAR POLARIZATION TECHNIQUE—ESTIMATION OF CORROSION RATES

Numerous linear polarization studies have been carried out to estimate the corrosion rates or to study the passivation of metals; corrosion protection using inhibitors, sacrificial barrier properties, and performance of polymer coatings when deposited on metals [31–37]. One of the first papers published was from Mennenoh and Engel [31], using polarization to investigate the effectiveness of inhibitors to stop steel corrosion in pickling baths. Linear polarization studies have been used by Popov et al. [32–34] to estimate the polarization resistance and the corrosion rate of various sacrificial and barrier coatings. The potential in most of the experiments was swept from −10 mV to +10 mV vs. E_{corr} at a scan rate of 0.5 mV/s. The linear polarization plots shown in Fig. 5.5 show that Zn-Ni-Cd has higher polarization resistance (low

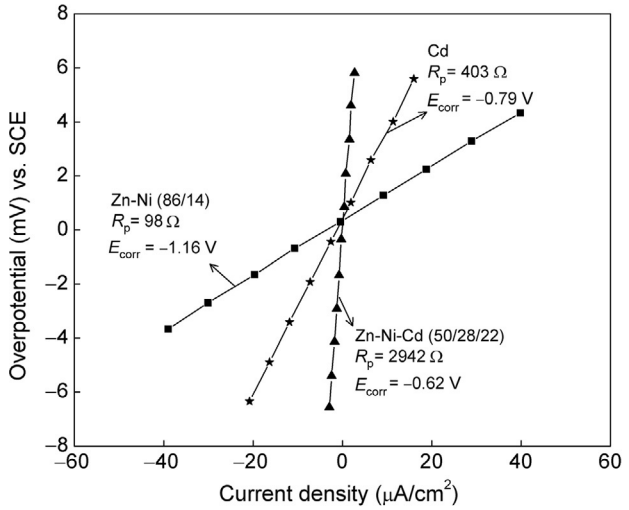

Fig. 5.5 Linear polarization plots for Zn-Ni-Cd, Zn-Ni, and Cd coatings [33].

corrosion rates) when compared to the other coatings investigated in 0.5 M H_3BO_3 + 0.2 M Na_2SO_4 solution at pH of 6.5 [33].

In another example shown in Fig. 5.6, the potential was swept from −10 mV to +10 mV vs. E_{corr} at a scan rate of 0.5 mV/s [34]. The resulting graphs of overpotential vs.

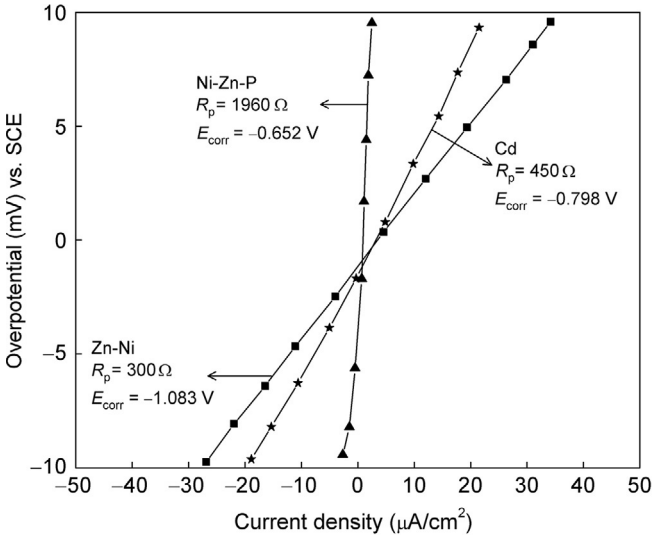

Fig. 5.6 Linear polarization studies of Ni-Zn-P, Zn-Ni, and Cd coatings in 0.5 M Na_2SO_4 + 0.5 M H_3BO_3 solution at pH [34].

Table 5.5 Variation in Corrosion potential and Corrosion Rates for the Different Coatings

Coating	E_{corr} (V vs. SCE)	I_{corr} (A/cm^2)	CR (mpy)
Ni-Zn-P	−0.652	8.6×10^{-6}	3.3
Cd	−0.798	4.0×10^{-5}	17.2
Zn-Ni	−1.083	3.8×10^{-4}	17.7

current density for different coatings are shown in Fig. 5.6. Assuming anodic and cathodic Tafel slopes of 0.12 mV/decade, the corrosion rates were estimated using the Stern-Geary equation.

Table 5.5 summarizes the corrosion potential values, E_{corr}, corrosion currents, and estimated corrosion rates of Ni-Zn-P, Zn-Ni alloys and Cd, polarization curves shown in Fig. 5.6.

Example 5.1:

The exchange current densities for a hydrogen-evolution reaction on three different metals are 5×10^{-4} A/cm^2, 3×10^{-7} A/cm^2, and 5×10^{-11} A/cm^2, respectively. Calculate the current densities and the polarization resistances if the reactions proceed at $\eta = -0.08$ V versus SHE. The electrode surface area is 1 cm^2 and $\alpha = 0.5$.

Solution:

The polarization resistance for a given area of the electrode is given by:

$$R_p = \frac{\left(\frac{d\eta}{di}\right)}{A}$$

The simplified form of the Butler-Volmer equation for the cathodic reaction can be written as:

$$\left[\frac{di}{d\eta}\right] = -i^{\circ}\frac{\alpha nF}{RT}$$

The polarization resistance is calculated using the expression (A) and the given i° values:

$$R_p = \frac{1}{A}\frac{1}{\left[\frac{di}{d\eta}\right]} = -\frac{1}{A}\frac{RT}{nFi^{\circ}} \quad \text{(A)}$$

$$R_{p_1} = 0.0513\,\text{k}\Omega$$

$$R_{p_2} = 0.0513\,\text{k}\Omega$$

$$R_{p_3} = 0.0513\,\text{k}\Omega$$

Example 5.2:

Calculate the corrosion currents for the metals in Example 5.1, using the Stearn-Geary equation for cathodic and anodic Tafel slopes of $b_c = -0.1$ V and $b_a = 0.1$ V. Estimate the corrosion rates in mpy.

Solution:

Corrosion currents:

$$I_{corr} = \frac{b_a \times b_c}{2.3(b_a + b_c)} \times \frac{1}{R_p}$$

$$I_{corr_1} = \frac{0.1\,V \times 0.1\,V}{2.3 \times (0.1\,V + 0.1\,V)} \times \frac{1}{51.3\,\Omega} = 4.24 \times 10^2\,\mu A/cm^2$$

$$I_{corr_2} = \frac{0.1\,V \times 0.1\,V}{2.3 \times (0.1\,V + 0.1\,V)} \times \frac{1}{8.56 \times 10^4\,\Omega} = 2.54 \times 10^{-1}\,\mu A/cm^2$$

$$I_{corr_3} = \frac{0.1\,V \times 0.1\,V}{2.3 \times (0.1\,V + 0.1\,V)} \times \frac{1}{5.13 \times 10^8\,\Omega} = 4.20 \times 10^{-5}\,\mu A/cm^2$$

Corrosion rates:

$$C.R_1 = \frac{0.131 \times (4.24 \times 10^2) \times (E.W_1)}{d_1}$$

$$C.R_2 = \frac{0.131 \times (2.54 \times 10^{-1}) \times (E.W_2)}{d_2}$$

$$C.R_3 = \frac{0.131 \times (4.20 \times 10^{-5}) \times (E.W_3)}{d_3}$$

Example 5.3

If the slope of the polarization curve is $R_p = \Delta E/\Delta i = 2\,mV/\mu A/cm^2$ and the cathodic and anodic Tafel slopes are $b_c = -0.1$ V and $b_a = 0.1$ V, calculate the corrosion rate of Ni ($d = 8.9\,g/cm^3$) in g/s.

Solution:

Using the Stern-Geary equation (5.24)

$$I_{corr} = \frac{b_a \times b_c}{2.3\,(b_a + b_c)} \times \frac{\Delta i}{\Delta E}$$

$$I_{corr} = \frac{0.01\,V^2}{2.3 \times 0.2\,V} \times \frac{\mu A/cm^2}{2m\,V} \times \frac{1000\,m\,V}{1\,V} = I_{corr} = 10.87\,\mu A/cm^2$$

Because

$$\frac{m}{t}=\frac{MI_{\text{corr}}}{nF}A$$

$$\text{CR}=\left[\frac{58.6934\,\text{g/mol}}{2\,\text{eq/mol}}\right]\times\left[10.87\,\mu\text{A/cm}^2\right]\times\frac{1\,\text{eq}}{96,500\,\text{C}}\times 1\,\text{cm}^2\times\frac{1\,\text{C/s}}{10^6\,\mu\text{A}}=3.3\times10^{-9}\,\text{g/s}$$

Example 5.4

The linear polarization slope for a tin electrode measured in tomato juice is 5 mV/(μA/cm^2). Calculate the corrosion rate in (g/m^2 day). Assume $b_a=b_c=\pm0.1$ V.

Solution:

$$R_p=\frac{\Delta E}{\Delta i}=5\frac{\text{mV}}{\mu\,\text{A/cm}^2}$$

$$I_{\text{corr}}=\frac{b_a\times b_c}{2.3(b_a+b_c)}\times\frac{\Delta i}{\Delta E}$$

$$I_{\text{corr}}=\frac{0.01\,\text{V}^2}{0.46\,\text{V}}\times\frac{\mu\text{A/cm}^2}{5\,\text{mV}}\times\frac{1000\,\text{mV}}{1\,\text{V}}$$

$$I_{\text{corr}}=4.348\,\mu\text{A/cm}^2$$

$$\text{CR}=\left[4.348\,\mu\text{A/cm}^2\right]\left[\frac{118.710\,(\text{g/mol})}{2\,(\text{eq/mol})}\right]\times\frac{1\,\text{cm}^2}{1\times10^{-4}\,\text{m}^2}=2.581\times10^6\,\frac{\mu\text{A g}}{\text{eq m}^2}$$

$$\text{CR}=2.581\times10^6\left(\frac{\mu\text{A g}}{\text{eq m}^2}\right)\times\left(\frac{1\,\text{eq}}{96,487\,\text{C}}\right)\times\left(\frac{1\,\text{C}}{1\times10^6\,\mu\text{A s}}\right)\times\left(\frac{3600\,\text{s}}{1\,\text{h}}\right)\times\left(\frac{24\,\text{h}}{1\,\text{day}}\right)$$
$$=2.31\,\text{g/m}^2\text{day}$$

Example 5.5

The polarization data for Ni in a solution, given in Fig. 5.7, were obtained by scanning the coupon ±20 mV from E_{corr}. The area of the coupon is 1 cm^2, b_c and b_a are ±0.1 V, and $E_{\text{corr}}=-0.218$ V vs. SCE. The polarization resistance obtained from the plot is $R_p=\Delta E/\Delta i=3.8797$ mV/(μA/cm^2). Using the equivalent weight and the density for nickel of 8.9 g/cm^3, calculate the corrosion rate for nickel in mpy by using the Stern-Geary equation.

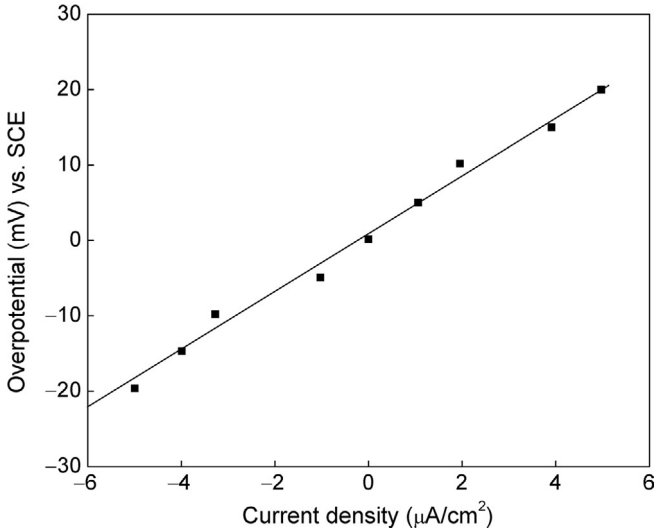

Fig. 5.7 Polarization diagram of Ni.

Solution:

Using the Stearn-Geary equation (5.24), one obtains:

$$I_{corr} = \frac{b_a \times b_c}{2.3(b_a + b_c)} \times \frac{\Delta i}{\Delta E} = \frac{(0.01\,V)}{0.46\,V} \times \frac{\mu A/cm}{3.8797\,mV} \times \frac{1000\,mV}{1\,V} = 5.60\,\mu A/cm^2$$

$$CR = \frac{0.131 \times I_{corr} \times EW}{d}$$

or

$$CR = \frac{0.131[5.60\,\mu A/cm^2]\left[\frac{58.6934\,g/mol}{2\,eq/mol}\right]}{8.9\,g/cm^3} = 2.418\,mpy$$

Example 5.6

Iron ($d = 7.8$ g/cm^3) is corroding in a solution saturated with oxygen. The partial pressure of oxygen is 1 atm, $b_c = -0.11$ V, $i_c^o = 10^{-7}$ A/cm^2, pH = 7, $b_a = 0.08$ V, $i_a^o = 10^{-5}$ A/cm^2, $(Fe^{2+}) = 0.7$ M. Calculate the corrosion potential, the corrosion current in A/cm^2, and the corrosion rate in mpy.

Solution:

(a) Calculation of oxygen electrode potential:

$$O_2 + 2H_2O + 4e^- \rightarrow 4OH^-$$

$$e_{O_2|OH^-} = e^{o}_{O_2|OH^-} - 2.303\frac{RT}{nF}\log\left(\frac{(a_{OH^-})^4}{P_{O_2}}\right)$$

Because

$$-\log(H^+) - \log[OH^-] = 14$$
$$\log(OH^-) = -14 + pH$$
$$(OH^-) = 10^{-14+pH}$$
$$e_{O_2|OH^-} = 0.814\,V \text{ vs.SHE}$$

(b) Calculation of iron electrode potential:

$$Fe^{2+} + 2e^- \rightarrow Fe$$
$$e_{Fe^{2+}|Fe} = e^{o}_{Fe^{2+}|Fe} - 2.303\frac{RT}{nF}\log\frac{a_{Fe}}{a_{Fe^{2+}}}$$
$$e_{Fe^{2+}|Fe} = -0.440 - \frac{0.059}{2}\log\left(\frac{1}{0.7}\right) = -0.445\,V \text{ vs.SHE}$$

(c) Calculation of E_{corr} and I_{corr}

$$\eta = b \times \log\left(\frac{I_{corr}}{i^o}\right)$$
$$\eta_c = E_{corr} - e_c$$
$$\eta_a = E_{corr} - e_a$$
$$\eta_c = b_c\log(I_{corr}) - b_c\log\left(i^o_c\right)$$
$$E_{corr} - e_{O_2|OH^-} = b_c\log(I_{corr}) - b_c\log\left(i^o_c\right)$$
$$E_{corr} - 0.814 = -0.11\log(I_{corr}) + 0.11\log\left(10^{-7}\right)$$
$$E_{corr} - 0.814 = -0.11\log(I_{corr}) - 0.77$$

Calculation of the anode voltage:

$$\eta_a = b_a\log(I_{corr}) - b_a\log\left(i^o_a\right)$$
$$E_{corr} - e_{Fe^{2+}|Fe} = b_a\log(I_{corr}) - b_a\log\left(i^o_a\right)$$
$$E_{corr} + 0.445 = 0.08\log(I_{corr}) - 0.08\log\left(10^{-5}\right)$$
$$E_{corr} + 0.445 = 0.08\log(I_{corr}) + 0.4$$

Solve simultaneously for E_{corr} and I_{corr}:

$$E_{corr} - 0.814 = -0.11\log(I_{corr}) - 0.77(\text{Cathode})$$
$$E_{corr} + 0.445 = 0.08\log(I_{corr}) + 0.4(\text{Anode})$$
$$E_{corr} = -0.007\,V$$
$$I_{corr} = 2.93\,A/cm^2$$

Using Eq. (5.33)

$$CR = \frac{0.131 \times I_{corr} \times (EW)}{d} = \frac{0.131 \times (2.93 \times 10^6) \times 27.82}{7.8} = 1.367 \times 10^6\,mpy$$

Example 5.7

Recalculate the values of the corrosion potential, the corrosion current in A/cm^2, and the corrosion rate in mpy, under the same conditions as given in Example 5.6, for pH 3, 5, and 9 and determine the dependence of the corrosion rate on pH.

Solution:

The same method as described in Example 5.6 is used to calculate the corrosion rate in mpy for pH in the range between 3 and 9. The results are presented in Table 5.6. The corrosion rate of iron decreases approximately one order of magnitude as the pH increases from 3 to 9. The corrosion rate (mpy) vs. pH is plotted in Fig. 5.8.

Table 5.6 Corrosion Rates Estimated for Solution pH in the Range Between 3 and 9

pH	E_{O_2/OH^-}	$E_{Fe^{2+}/Fe}$	E_{corr} (V)	I_{corr} (A/cm^2)	CR (mpy)
3	1.050	−0.445	−0.092	51.081	23,866,839
5	0.932	−0.445	−0.042	12.224	5,711,396
7	0.814	−0.445	−0.007	2.925	1,366,751
9	0.696	−0.445	−0.057	0.700	327,067

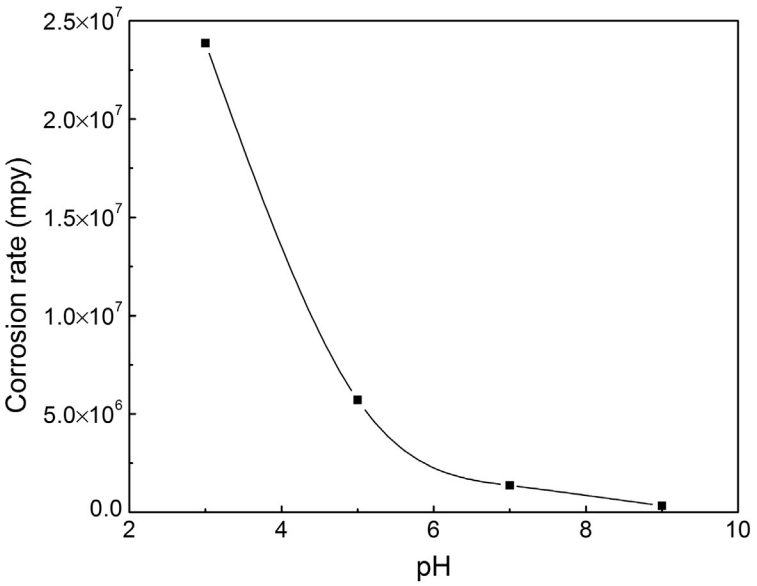

Fig. 5.8 Plot of corrosion rate (mpy) vs. pH.

5.6 CORROSION POTENTIAL MEASUREMENTS AS A FUNCTION OF TIME (OCP VS. TIME)

The change in the OCP vs. time of the corroding metal is determined by monitoring the OCP as a function of time. Figure 5.9 presents the OCPs vs. time of various sacrificial and barrier coatings that are commonly used for corrosion protection [35]. The coating stability is controlled by the severity of the corroding solution, the thickness of the coating, and the potential difference of the underlying metal and that of the sacrificial or barrier coating.

The sacrificial properties of the coatings were predicted by OCP measurements and verified using the scratch model approach. The more negative zinc coating offers high levels of sacrificial protection to underlying steel and inhibits hydrogen penetration into the bulk of the alloy. However, this coating has a very short life due to a high rate of galvanic corrosion. The OCP potential of pure zinc is approximately −1.1 V (vs. SCE). The OCP of Zn-Ni and Zn-Ni-Cd, Zn-Ni-Cu, Ni-Zn, and electroless Ni-Zn-P are slightly more positive, indicating that the inclusion of more noble components in the deposit results in an anodic shift in potentials with respect to zinc, which, in turn, decreases the galvanic corrosion.

The potentials of Zn, Zn-Ni, Cd, and Ni-Zn-P were continuously monitored by Popov et al. [32,36] with respect to SCE as a function of time in 0.5 M Na_2SO_4 + 0.5 M boric acid solution at pH 7.0. The results presented as potential-time plateaus are shown in Fig. 5.10 [34]. The OCP plots of Zn-Ni showed three distinct plateaus occurring at three different potentials, namely −1.0, −0.700, and −0.400 V. Zn-Ni alloy deposits

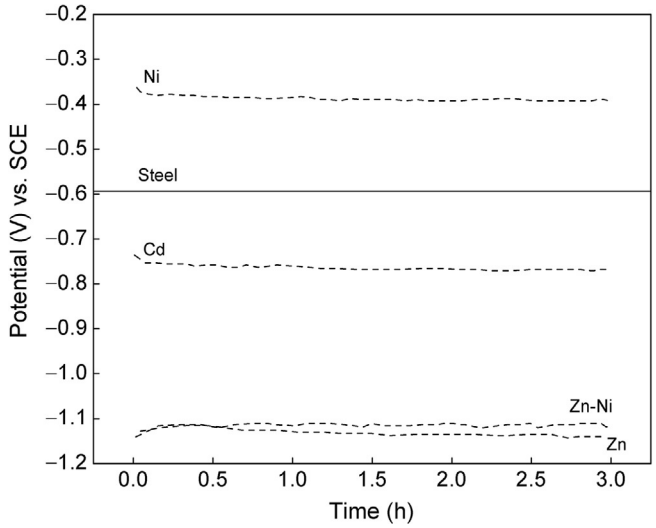

Fig. 5.9 Open circuit potential vs. time of various coatings on steel in 0.5 M Na_2SO_4 + 0.5 M boric acid solution at a pH of 7.0 [35]. *Reproduced by permission of The Electrochemical Society.*

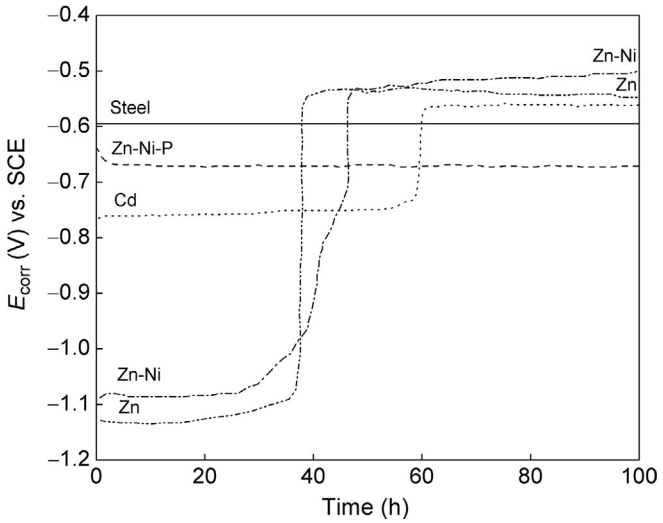

Fig. 5.10 E_{corr} vs. time plot for the various alloy coatings (thickness = 2 μm) immersed in 0.5 M Na_2SO_4 + 0.5 M boric acid solution at a pH of 7.0 [34].

exist in three phases, a Zn-rich eta (η) phase, ($E_{corr} = -1.050$ V vs. SCE), an intermediate gamma(γ) phase ($E_{corr} = -0.700$ V vs. SCE), and a nickel-rich alpha (α) phase ($E_{corr} = -0.400$ V vs. SCE).

The η phase has an E_{corr} value comparable to that of pure zinc because it is mostly composed of zinc. The Zn-rich η-phase exhibits homogenous, hexagonal crystals. Once a galvanic couple is formed, they dissolve rapidly and the surface becomes enriched in the γ-phase. The intermediate phase or the γ-phase, which has a Zn-Ni ratio of 4:1, has a body-centered cubic structure and usually exhibits good barrier resistance against dissolution. However, the thickness of this layer is small. It vanishes after a short period of time. Dissolution of the γ-phase exposes the nickel-rich phase to the environment. A small defect in the coating would lead to the preferential dissolution of the less noble metal, namely steel. Thus, an increase in the life of the protective coating depends on the life of the more electronegative phase, which is the Zn-rich η phase in the case of Zn-Ni coatings.

5.7 TAFEL EXTRAPOLATION METHOD

5.7.1 Principles of the Tafel extrapolation method

When the overpotential is large and negative (cathodic), the anodic term in the Butler-Volmer equation becomes negligible and Eq. (3.29) takes the form:

$$i_c = i^o \exp\frac{-\alpha_c F\eta}{RT} \tag{3.29}$$

or

$$\eta = \frac{2.3RT}{\alpha_c nF}\log i^o - \frac{2.3RT}{\alpha_c nF}\log i_c = -\frac{2.3RT}{\alpha_c nF}\ln\frac{i_c}{i^o} \tag{3.30}$$

Equation (3.30) is termed the Tafel approximation for the German scientist who found that the current equivalent to the rate for a single reaction on a metal surface is related to the potential of the metal [38]. Substituting for $a_c = 2.3(RT/\alpha_c nF)\log i^o$ and $b_c = -2.3(RT/\alpha_c nF)$;

Equation (3.30) becomes:

$$\eta = a_c + b_c \log i_c \tag{3.32}$$

or

$$\eta = b_c \log\frac{i}{i^o} \tag{3.33}$$

5.7.2 Tafel extrapolation procedure

The Tafel extrapolation method provides a direct measurement of the corrosion rate and of the corrosion potential, and it is very useful in predicting the corrosion properties of various corrosion systems. This technique monitors the corrosion rates with an accuracy that is equal to or greater than conventional weight loss methods. Using the Tafel extrapolation method, it is possible to measure extremely low corrosion rates. The rapid determination of corrosion rates with Tafel plots can be advantageous for the evaluation of inhibitors and the comparison of alloys. The cathodic and anodic polarization data are obtained by using a three-electrode electrochemical cell containing working, counter, and reference electrodes. The corrosion measurements are performed by using a potentiostat that is connected to the electrochemical cell. The metal specimen (working electrode) is polarized 150-300 mV above or below the OCP. The voltage step is normally between 5 and 10 mV. The potential vs. log current curves generate a polarization diagram of the corroding metal. A typical conventional three-electrode electrochemical corrosion cell is shown in Fig. 5.11.

The measurements are carried out using a standard calomel reference electrode or Hg/HgO reference electrode. The reference electrode provides a stable reference potential for the working electrode. The auxiliary (counter electrode) is made of materials that are inert in the electrolyte. Platinum or graphite rods are good choices for counter electrodes. The working electrode is the metal being tested for corrosion properties. The potential between the working and reference electrodes is increased in steps or continuously in the anodic direction, and the current between the working and the counter electrode is measured. Potentiostat and corrosion measurement software packages are commercially available. As shown in Fig. 5.12, the anodic and cathodic Tafel polarization

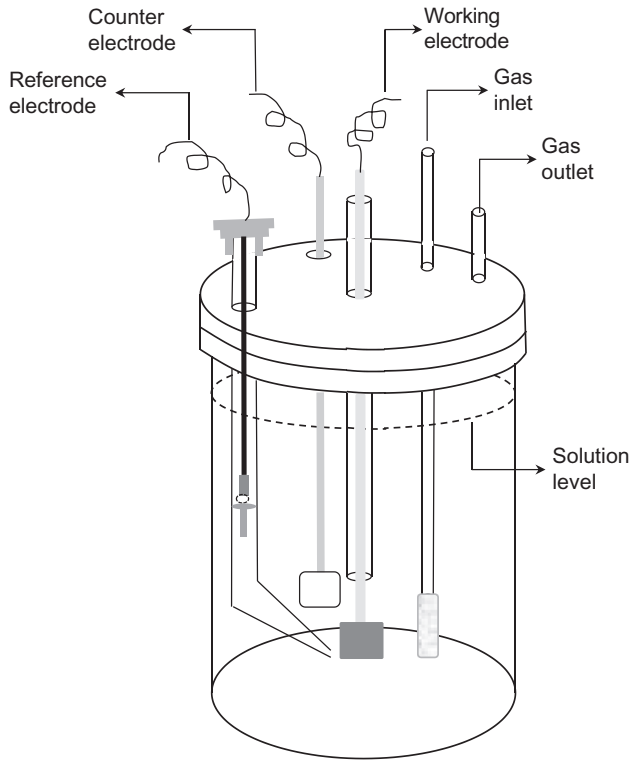

Fig. 5.11 A typical three-electrode electrochemical cell for corrosion studies.

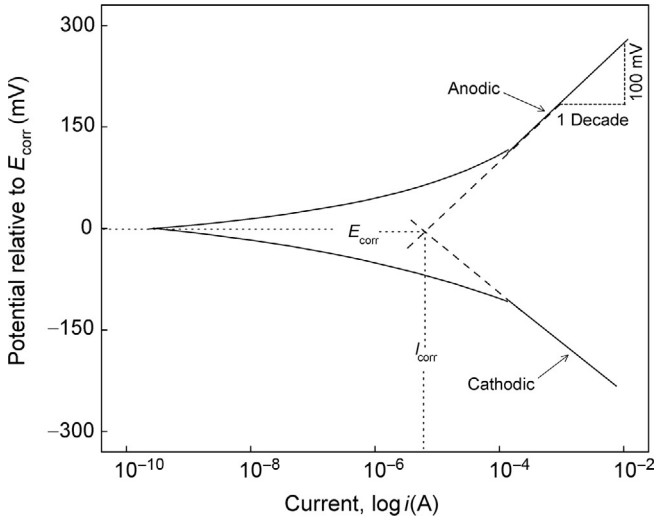

Fig. 5.12 Corrosion rate determination.

curves are extrapolated to the corrosion potential to obtain the corrosion rate from polarization measurements. At the corrosion potential, the rate of the cathodic reaction is equal to the rate of metal dissolution [16,39–41]. This point corresponds to the corrosion rate of the system expressed in terms of current density. The Tafel constants are calculated from the linear portions of the anodic and cathodic data of the Tafel plot. The units of the Tafel constants are V/decade, being one order of magnitude. A Tafel constant calculation is illustrated in Fig. 5.12. These measurements may be complicated by two interfering phenomena: resistance drop and concentration polarization effects. Resistance drops across the solution trigger nonlinear Tafel behavior at high currents: $E_{IR} = i_{meas} R_{sol}$ [42,43]. The concentration polarization effect occurs when the rate of the charge or discharge electrochemical reaction is so high that the reaction rate becomes diffusion-controlled [44–46].

A system in which the reduction process is diffusion-controlled is illustrated in Fig. 5.13. In this case, the metal follows a typical anodic dissolution reaction under activation control. The reduction process follows the following equation:

$$\eta_{red} = -b_c \log \frac{i_c}{i^o} + 2.3 \frac{RT}{nF} \log \left(1 - \frac{i_c}{i_L}\right) \tag{5.37}$$

$$i_L = \frac{D \times n \times F \times C}{\delta} \tag{5.38}$$

In Eq. (5.38), i_L is limiting diffusion current density, A/cm^2; D is diffusion coefficient, cm^2/s; C is concentration of the reacting ions on the bulk solution, moles/cm^3; δ is the

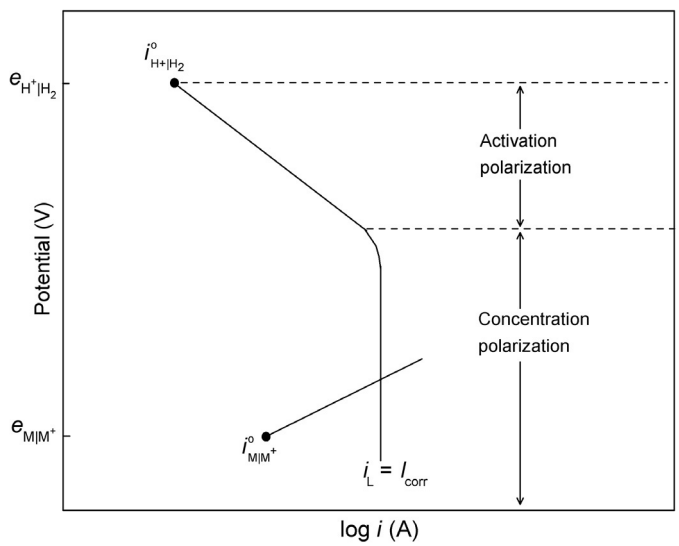

Fig. 5.13 Corrosion of metal M under diffusion-controlled conditions.

thickness of the diffusion layer, cm; and "*n*" represents the number of electrons in the redox reaction. A disadvantage of this method is the large potential range that needs to be applied during the measurements, causing a change of the surface properties of the corroding metal. Thus, more than one specimen is required to complete the polarization studies and construct the Tafel plot. Barnartt [21] developed a three-point method applicable in any potential range to obtain Tafel slopes with high accuracy. This method eliminates most of the problems in accurately estimating the anodic curve in the vicinity of the corrosion potential [43,47].

Tafel polarization studies have been used to determine the sacrificial nature and the corrosion resistance of different sacrificial coatings [32–37]. An example of the Tafel polarization behavior of different coatings tested in a 0.5 M Na_2SO_4 + 0.5 M H_3BO_3 solution at pH 7.0 is shown in Fig. 5.14 [32]. Steel exhibits an OCP of −0.59 V vs. SCE. The results shown in Fig. 5.14 indicate that all three coatings exhibit a potential more negative than that of steel and can be applied as sacrificial coatings [32]. The corrosion current of Ni-Zn-P coatings estimated from the intersection of the anodic and cathodic slopes is at least one order of magnitude lower than that of Cd and Zn-Ni coatings, indicating higher corrosion resistance.

Figure 5.15 shows that the corrosion current is one order of magnitude smaller for the pulse current-deposited (pc) Zn-Ni-Cd (7% Cd) sacrificial coatings when compared to the direct current-deposited (dc) Zn-Ni-Cd with 22% Cd in the alloy [36]. The corrosion rates of pulse current-deposited Zn-Ni-Cd sacrificial coatings that contain 7% and 3% Cd were 0.49 and 1.03 mpy, respectively; much lower than the 2.87 mpy observed for the direct current-deposited Zn-Ni-Cd alloy with 22% Cd in the alloy.

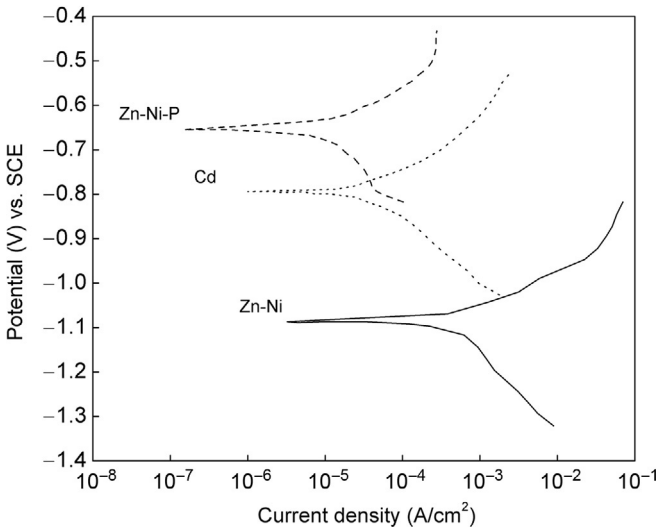

Fig. 5.14 Tafel polarization curves for Ni-Zn-P, Cd, and Zn-Ni coatings in 0.5 M Na_2SO_4 + 0.5 M H_3BO_3 solution at pH 7.0 [32]. © *NACE International 2003.*

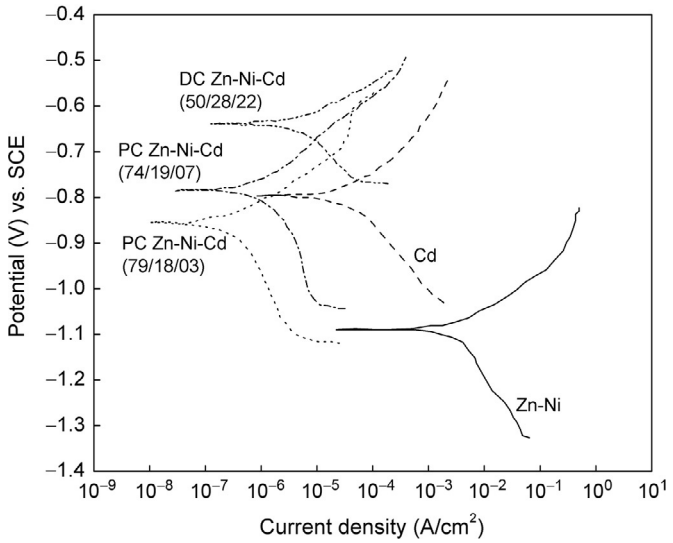

Fig. 5.15 Comparison of Tafel polarization plots for different coatings. Numbers in the parenthesis correspond to the weight percentage of metals [36].

5.8 POTENTIODYNAMIC POLARIZATION MEASUREMENTS

The potentiodynamic polarization technique is used to determine the potential region at which the alloy or the metal is passive when exposed to a particular environment. It estimates both the ability of the material to spontaneously passivate as well as the critical current density necessary for its passivation. Potentiodynamic polarization measurements identify the corrosion properties of passivating metals and alloys and are very useful in predicting how a material will behave when exposed to a corrosive environment. The method estimates the corrosion active region, the onset of passivation, the critical current density, the primary passive potential, the current in the passive region, and the voltage span of the passive region.

The potentiodynamic anodic polarization plot for 430 stainless steel is shown in Fig. 5.16. The data were obtained by recording the current as the applied potential increased continuously at a predetermined sweep rate. At small current densities, region A in Fig. 5.16, stainless steel is active and corrodes to Fe^{2+} as the applied potential increases in the anodic direction. When the critical current density for passivation is reached, region B, the passivation begins and the current drops to the passive current density. Point B is defined by two values, the critical current density for passivation, i_{crit}, and the primary passive potential, E_{pp}, or critical potential. In region C, a thick passivating film forms on the surface of the alloy. The corrosion current density in the passive region D is orders of magnitude lower when compared with the active region. In this region, the thick insulating film is replaced by thinner film. In region E, called the

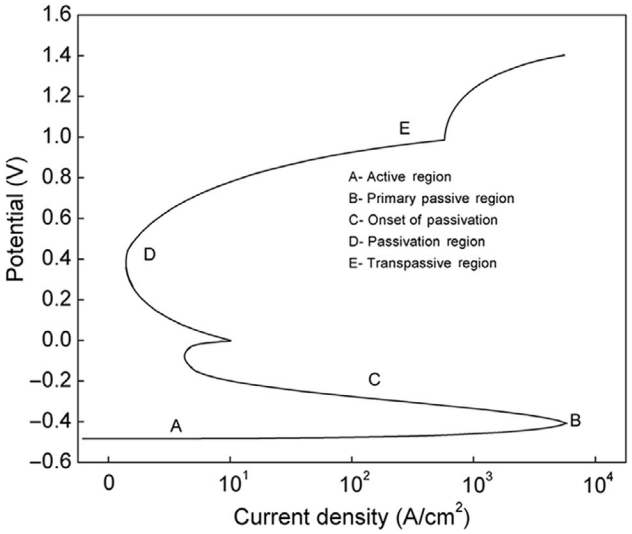

Fig. 5.16 Standard potentiodynamic anodic polarization plot of 430 stainless steel.

transpassive region, the passivating film begins to decay. At ~1.2 V vs. the standard hydrogen electrode, oxygen evolution starts and a drastic increase in the current density is observed. In this region, stainless steel alloys are prone to pitting corrosion under a corrosive environment, which is estimated using cyclic polarization [28,48,49] as described in Chapter 7.

Example 5.8

Tin ($d = 7.3$ g/cm^3) corrodes in a deaerated solution of pH 2.0. The activity of Sn^{2+} in the solution is 10^{-3} M. The value of the cathodic, b_c, and anodic, b_a, Tafel slopes are -0.12 and $+0.1$ V/decade, respectively. The exchange current density for tin and for hydrogen on tin are $i_a^o = 10^{-6}$ A/cm^2 and $i_c^o = 10^{-8}$ A/cm^2, respectively. Assume that the tin surface acts as cathode.

(a) Calculate the corrosion potential, the corrosion density current in A/cm^2, and the corrosion rate in grams per square meter per day (gmd) and mils per year (mpy).

(b) Recalculate the values of the parameters estimated in (a) for pH of 4, 6, and 8, and plot the dependence of the corrosion rate on pH.

Solution:

(a)

$$\text{Anode}: \ Sn^{2+} + 2e^- \rightarrow Sn \quad e^o_{Sn^{2+}|Sn} = -0.136\text{V vs. SHE}$$

$$e_{Sn^{2+}|Sn} = e^o_{Sn^{2+}|Sn} - \frac{0.059}{n}\log\left(\frac{1}{(Sn^{2+})}\right) = -0.136 - \frac{0.059}{2}\log\left(\frac{1}{10^{-3}}\right) = -0.225 \text{ vs. SHE}$$

$$\text{Cathode}: \ 2H^+ + 2e^- \rightarrow H_2 \quad e^o_{H^+|H_2} = 0.00\text{V vs. SHE}$$

$$e_{H^+|H_2} = e^o_{H^+|H_2} - \frac{0.059}{n}\log\left(\frac{1}{(H^+)^2}\right) = 0.00 - \frac{0.059}{2}\log\left(\frac{1}{(10^{-2})^2}\right) = -0.118 \text{ vs. SHE}$$

$$\eta = E_{corr} - e_{eq} = b \times \log\left(\frac{I_{corr}}{i^{o}}\right)$$

$$\eta_a = E_{corr} - e_a = b_a \log I_{corr} - b_a \log i_a^{o}$$

$$E_{corr} - (-0.225) = 0.1 \times \log I_{corr} - 0.1 \times \log\left(10^{-6}\right) \quad (A_1)$$

$$\eta_c = E_{corr} - e_c = b_c \log I_{corr} - b_c \log i_c^{o}$$

$$E_{corr} - (-0.118) = -0.12 \times \log I_{corr} - (-0.12) \times \log\left(10^{-8}\right) \quad (B_1)$$

Solving equations (A_1) and (B_1) simultaneously

$$I_{corr} = 2.49 \times 10^{-7}\,\mathrm{A/cm^2} = 0.249\,\mu\mathrm{A/cm^2}$$

$$E_{corr} = -0.285\,\mathrm{V}$$

$$\mathrm{CR(mpy)} = \frac{0.131 \times I_{corr} \times (\mathrm{EW})}{d} = \frac{0.131 \times (0.249) \times \left(\frac{118.710}{2}\right)}{7.30} = 0.265\,\mathrm{mpy}$$

$$\mathrm{CR\,in\,(gmd)} = 0.265\,\mathrm{mpy} \times 0.0694 \times d$$

$$\mathrm{CR\,in(gmd)} = 0.265 \times 0.0694 \times 7.30 = 0.134\,\mathrm{gmd}$$

The corrosion potential, corrosion current density, and the corrosion rates at pH 4, 6, and 8 are calculated using the method described in (a). The results are summarized in Table 5.7. The plot of corrosion rate vs. pH is shown in Fig. 5.17.

Table 5.7 Electrochemical Properties of $Sn^{2+}|Sn$ at Different pH

pH	E_a (V)	E_c (V)	E_{corr} (V)	I_{corr} (A/cm^2)	CR (mpy)	CR (gmd)
2	−0.225	−0.118	−0.285	2.49×10^{-07}	0.265	0.134
4	−0.225	−0.236	−0.339	7.23×10^{-08}	0.077	0.039
6	−0.225	−0.354	−0.393	2.1×10^{-08}	0.0224	0.0113
8	−0.225	−0.472	−0.446	6.11×10^{-09}	0.00651	0.0033

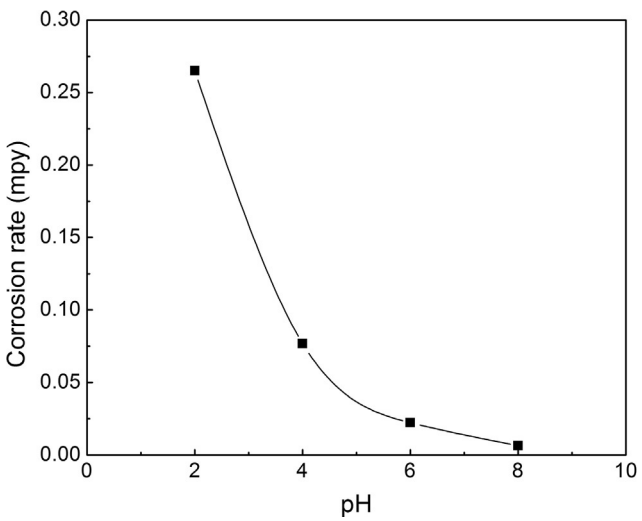

Fig. 5.17 Corrosion rate in mpy as a function of pH for tin.

Example 5.9

The zinc ($d = 7.14$ g/cm^3) corrosion rate in a deaerated solution of pH 1 is 3785 mpy. Assuming the zinc surface acts as cathode, calculate the corrosion potential of zinc vs. hydrogen reference electrode. The activity of the metal in solution is 10^{-2} M. The value of the anodic Tafel slope, b_a, is 0.1 V per decade. The exchange current density for zinc is 10^{-5} A/cm^2.

Solution:

(a)

$$\text{Anode: } Zn^{2+} + 2e^- \rightarrow Zn \quad e^o_{Zn^{2+}|Zn} = -0.76\,\text{V vs. SHE}$$

$$e_{Zn^{2+}|Zn} = e^o_{Zn^{2+}|Zn} - \frac{0.0591}{n}\log\left(\frac{1}{(Zn^{2+})}\right) = -0.76 - \frac{0.0591}{2}\log\left(\frac{1}{10^{-2}}\right)$$

$$= -0.819\,\text{V vs. SHE}$$

Calculation of the corrosion current:

$$\text{CR(mpy)} = 3\,785 = \frac{0.131 \times I_{corr} \times (\text{EW})}{d} = \frac{0.131 \times I_{corr} \times (65.4/2)}{7.14}$$

$$\text{Solving for } I_{corr} \rightarrow I_{corr} = 6309\,\mu\text{A/cm}^2$$

Calculation of corrosion potential:

$$E_{corr} - (-0.819) = 0.1\log I_{corr} - 0.1\log\left(10^{-5}\right)$$

$$E_{corr} = 0.1\log I_{corr} - 0.1\log\left(10^{-5}\right) - 0.819$$

$$E_{corr} = 0.1\log(6309) - 0.1\log\left(10^{-5}\right) - 0.819 = -0.539\,\text{V vs. SHE}$$

Example 5.10

Chromium corrodes in hydrochloric acid of pH = 1 with activity of Cr^{2+} of 10^{-3} M. The values of the cathodic (b_c) and anodic (b_a) Tafel slopes are −0.1 and 0.12 V per decade, respectively. The exchange current densities for the anodic and cathodic reactions are 10^{-6} and 10^{-8} A/cm^2, respectively.

(a) Calculate the corrosion current, corrosion potential, and corrosion rate in grams per square meter per day (gmd).
(b) Calculate the corrosion current and potential if mass limitations for hydrogen limit the measured current density to 10^{-5} A/cm^2.
(c) Repeat the same for a maximum current density of 10^{-3} A/cm^2.

Solution:

Given parameters:

$$b_a = 0.12, b_c = -0.1, i^o_{Cr} = 10^{-6}\,\text{A/cm}^2, i^o_{H_2} = 10^{-8}\,\text{A/cm}^2, e^o_{Cr^{2+}|Cr} = -0.74\,\text{V vs. SHE}$$

$$e_{eq,Cr^{2+}|Cr} = e^o_{Cr^{2+}|Cr} + \frac{0.0591}{2}\log(a_{Cr^{2+}}) = -0.74 + \frac{0.0591}{2}\log\left(10^{-3}\right) = -0.829\,\text{V vs. SHE}$$

$$e_{\mathrm{eq,H^+|H_2}} = e^{\mathrm{o}}_{\mathrm{H^+|H_2}} + \frac{0.059}{2}\log\left(a_{\mathrm{H^+}}\right)^2 = -0.0591(\mathrm{pH}) = -0.0591\,\mathrm{V\,vs.SHE}$$

(a) The cathodic and anodic Tafel equations are solved for E_{corr} and $\mathrm{I_{corr}}$.

$$E_{\mathrm{corr}} + 0.0591 = -0.1\log\left(\frac{I_{\mathrm{corr}}}{10^{-8}}\right)$$

$$E_{\mathrm{corr}} + 0.829 = 0.12\log\left(\frac{I_{\mathrm{corr}}}{10^{-6}}\right)$$

Corrosion potential $E_{\mathrm{corr}} = -0.519\,\mathrm{V}$ vs. SHE and corrosion current $I_{\mathrm{corr}} = 3.88\times10^{-4}\,\mathrm{A/cm^2}$ are calculated. The Evans diagram for chromium corrosion is presented in Fig. 5.18a.

Calculation of corrosion rate in grams per square meter per day (gmd):

$$\frac{m}{t} = \frac{M\times\mathrm{A}\times I_{\mathrm{corr}}}{nF}$$

$$\mathrm{CR} = \left[\frac{52\,\mathrm{g/mol}}{2\,\mathrm{eq/mol}}\right]\times\frac{1\,\mathrm{eq}}{96{,}500\,\mathrm{C}}\times\left[3.88\times10^{-4}\,\mathrm{A/cm^2}\right]\times\frac{10^4\,\mathrm{cm^2}}{1\,\mathrm{m^2}}\times\frac{1\,\mathrm{C/s}}{1\,\mathrm{A}}$$

$$\mathrm{CR} = 1.05\times10^{-3}\,\mathrm{g/m^2s}\times\frac{3600\,\mathrm{s}}{1\,\mathrm{h}}\times\frac{24\,\mathrm{h}}{1\,\mathrm{day}} = 90.7\,\mathrm{gmd}$$

(b) In a case when the cathodic current is limited by diffusion to a maximum of $10^{-5}\,\mathrm{A/cm^2}$, the mixed potential moves to the position on the anodic line where the current is $10^{-5}\,\mathrm{A/cm^2}$. Thus, the mixed potential (Fig. 5.18b) in this case is:

$$E_{\mathrm{corr}} + 0.829 = 0.12\log\left(\frac{10^{-5}}{10^{-6}}\right)$$

$$E_{\mathrm{corr}} = -0.709\,\mathrm{V}$$

$$I_{\mathrm{corr}} = 10^{-5}\,\mathrm{A/cm^2}$$

(c) Because the cathodic limiting current density of $10^{-3}\,\mathrm{A/cm^2}$ (Fig. 5.18c) is higher than the corrosion current under kinetic control (Fig. 5.18a), the mass limitation in this case does not affect the results of part (a).

$$E_{\mathrm{corr}} = -0.518\,\mathrm{V\,vs.\,SHE}$$

$$I_{\mathrm{corr}} = 3.88\times10^{-4}\,\mathrm{A/cm^2}$$

Example 5.11

Iron ($d = 7.8\,\mathrm{gm/cm^3}$) corrodes in a solution of pH 7.0 saturated with oxygen. The corrosion potential estimated for partial pressure of oxygen of 1 atm is −0.07 V vs. SHE. The oxygen overvoltage follows the relation:

$$E_{\mathrm{corr}} - e_{\mathrm{c}} = b\log\left(I_{\mathrm{corr}}\right) - b\log\left(i^{\mathrm{o}}_{\mathrm{c}}\right)$$

$$E_{\mathrm{corr}} - 0.814 = -0.11\log\left(I_{\mathrm{corr}}\right) - 0.77$$

Calculate the corrosion rate in mpy assuming all the iron surface acts as cathode for oxygen evolution reaction.

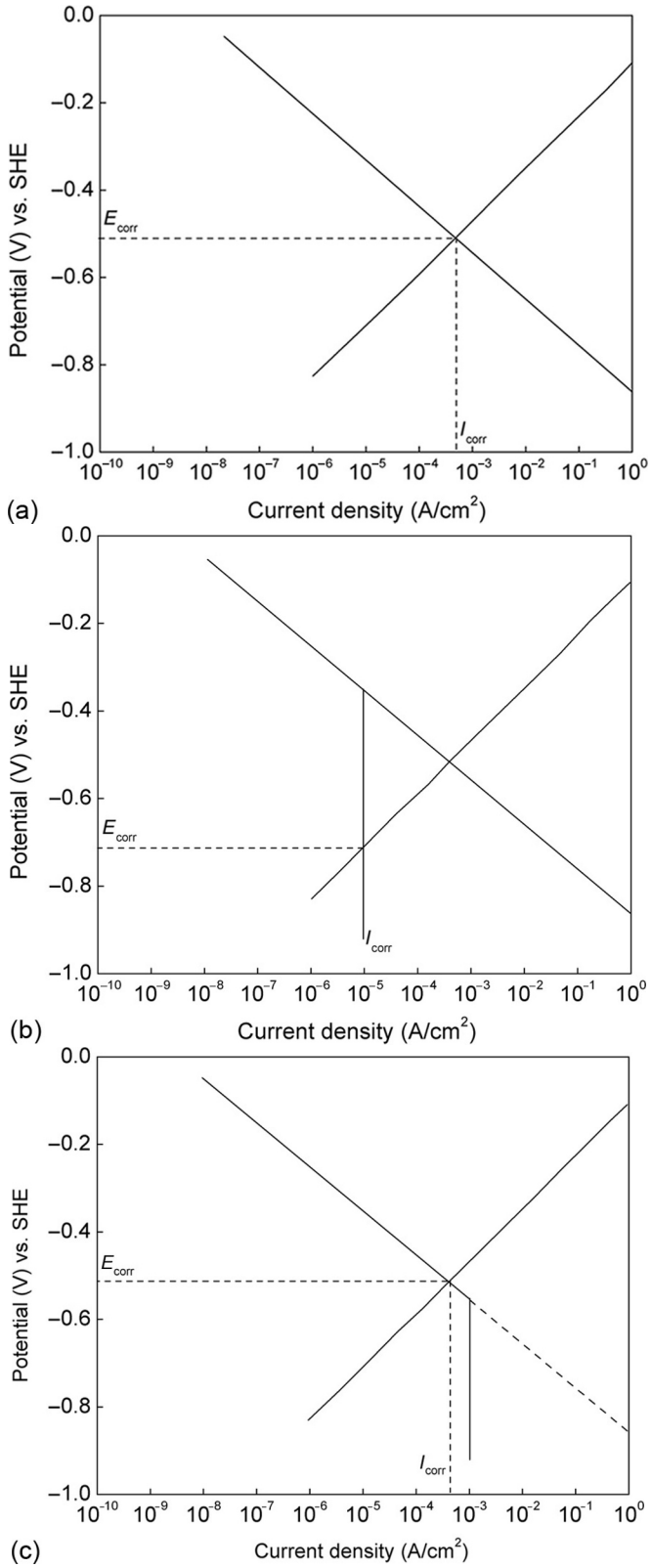

Fig. 5.18 See legend on opposite page.

Solution:
For iron corrosion,

$$E_{corr} = -0.07\,V$$

$$E_{corr} - 0.814 = -0.11\log(I_{corr}) - 0.77\,V \text{ vs. SHE}$$

$$I_{corr} = 10.87\,A/cm^2 = 1.087 \times 10^7\,\mu A/cm^2$$

Converting to mpy:

$$CR = \frac{(0.131)(I_{corr})(EW)}{d} = \frac{0.131 \times 1.087 \times 10^7 \times 27.92}{7.8}$$

$$CR = 6.47 \times 10^6\,mpy$$

Converting to mm/year:

$$CR = \frac{(3.28 \times 10^{-3})(I_{corr})(EW)}{d} = \frac{3.28 \times 10^{-3} \times 1.087 \times 10^7 \times 27.92}{7.8}$$

$$CR = 1.28 \times 10^5\,mm/year$$

5.9 ELECTROCHEMICAL IMPEDANCE SPECTROSCOPY

5.9.1 Principles of the method

EIS examines the response of the corroding system to "ac" excitations at frequencies from 100 MHz to 100 KHz. The current or voltage is measured when a small amplitude voltage or current is applied to the working electrode. The method was initially used by Dolin and Ershler [50] and developed later by Randles and Somerton [51] and Grahame [52]. In corrosion research, EIS was extensively used to study the passivation of metals [53–57] to determine corrosion rates and to study the inhibitor performance, sacrificial and barrier coating performance, and the disbondment of polymer-coated metals [9,23,58–66]. Macdonald and Mc Kubre published an excellent review on the use of EIS [67].

The corrosion cell or any electrochemical discharge reaction at the electrode interface is represented in EIS by an electronic circuit consisting of capacitors and resistors. Because the frequency is not zero in the case of "ac" excitation, Ohm's law is represented by:

Fig. 5.18—cont'd (a) Tafel polarization curves for chromium corrosion diagram showing the corrosion potential and the corrosion current. (b) The corrosion current and the potential if mass limitations for hydrogen limit the maximum current to 10^{-5} A/cm^2, and (c) to 10^{-3} A/cm^2, respectively.

$$V = IZ \tag{5.39}$$

V and I are waveform amplitudes for potential and current, respectively, and Z is defined as the impedance and represents the "ac" equivalent of resistance. The "ac" current is altered by resistors and circuit elements such as capacitors and inductors. The magnitude of impedance Z is given by:

$$Z = \frac{\Delta V}{\Delta I} \tag{5.40}$$

In the presence of only resistive components, the "ac" waveform is defined only by its magnitudes. The current response to a potential sinusoidal wave, as shown in Fig. 5.19, indicates that the potential and the current traces differ not only in magnitude but also in phase. The time-dependent current response $I(t)$ of an electrode interface is a function of sinusoidal "ac." Potential signal $V(t)$ is given in Eq. (5.41a) by frequency (ω) dependent impedance $Z(\omega)$ [68]:

$$\begin{gathered} Z(\omega) = \frac{V(t)}{I(t)} \\ I(t) = I_o \sin(\omega t + \theta) \\ V(t) = V_o \sin \omega t \end{gathered} \tag{5.41a}$$

where $I(t)$ = instantaneous current; ω = angular frequency in radians per second; I_o = maximum current amplitude; and θ = phase shift in radians [phase angle between $V(t)$ and $I(t)$].

The phase angle θ corresponds to the phase difference between the two sinusoidal signals. Vector analysis in Fig. 5.19 characterizes an "ac" waveform with both the amplitude and the phase characteristics. Impedance as a vector quantity is plotted in the

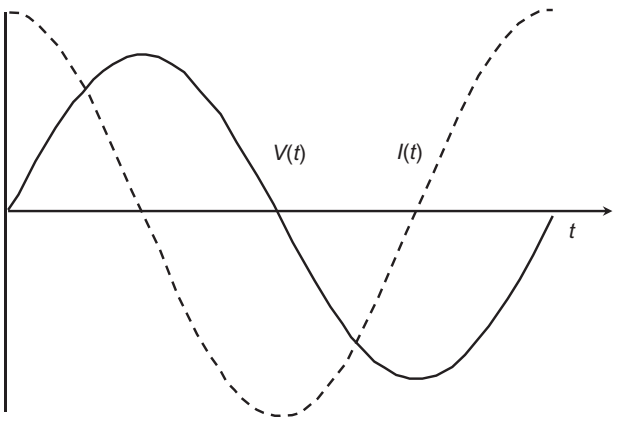

Fig. 5.19 Voltage sine wave $v(t)$ applied across resultant "ac" current waveform $i(t)$ for capacitor.

complex plane in Fig. 5.19, characterized by Z and θ. The real $Z'(\omega)$ and imaginary $Z''(\omega)$ components are projected on the x and y axes. The imaginary component is 90° out of phase. This coordinate system requires multiplying the imaginary "I" coordinate by $\sqrt{-1}$, in literature known as "j." The "ac" current is defined as the sum of its real and imaginary components:

$$I = I' + I''j \qquad j = \sqrt{-1} \tag{5.41b}$$

"ac" voltage is expressed as:

$$V = V' + V''j \tag{5.42}$$

By applying Eq. (5.39), the impedance vector is calculated as the ratio of the voltage and current vectors:

$$Z = \frac{V' + V''j}{I' + I''j} \tag{5.43}$$

The resulting "ac" impedance is:

$$Z = Z' + Z''j \tag{5.44}$$

As shown in Fig. 5.20, the absolute magnitude of the impedance vector is:

$$|Z| = \sqrt{(Z')^2 + (Z'')^2} \tag{5.45}$$

and

$$\tan\theta = \frac{Z''}{Z'} \tag{5.46}$$

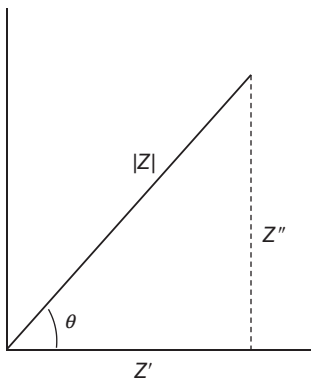

Fig. 5.20 Impedance as a vector quantity plotted in the complex plane.

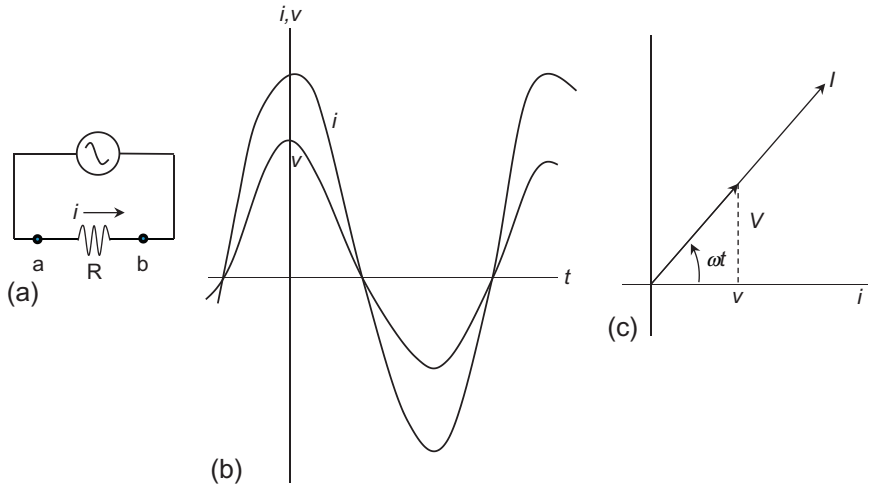

Fig. 5.21 (a) Resistance circuit, (b) Instantaneous current and voltage in phase, and (c) Vector diagram.

Figure 5.21 shows the expressions for the "ac" impedance of simple electrical circuits (Fig. 5.21a) applicable to corrosion systems. When the corrosion cell is represented only by resistance, the current is in phase with voltage, $\theta = 0$ and the impedance has no imaginary component, $Z = R$.

The instantaneous value of the current I or voltage V varies sinusoidally with time (Fig. 5.21b) and is represented by the projection in Fig. 5.21c onto the horizontal axis of a vector V or I of length corresponding to the current of voltage amplitude. The vector rotates counterclockwise with a change of angular frequency with time. Because both vectors I and V are in phase, their phasors rotate together.

The potential measured instantaneously at point "a" with respect to point "b" is $v_{ab} = V \cos \omega t$. The instantaneous current in the resistor is:

$$i = \frac{v_{ab}}{R} = \frac{V}{R} \cos \omega t \tag{5.47}$$

The maximum current amplitude is V/R, while the current as a function of the angular velocity ω is defined as:

$$i = I \cos \omega t \tag{5.48}$$

In Fig. 5.22a, a capacitor of capacitance C is connected across the source with instantaneous charge "Q" on the capacitor defined as:

$$Q = Cv_{ab} = CV \cos \omega t \tag{5.49}$$

Instantaneous current is equal to the rate of change of the capacitor charge with time, or

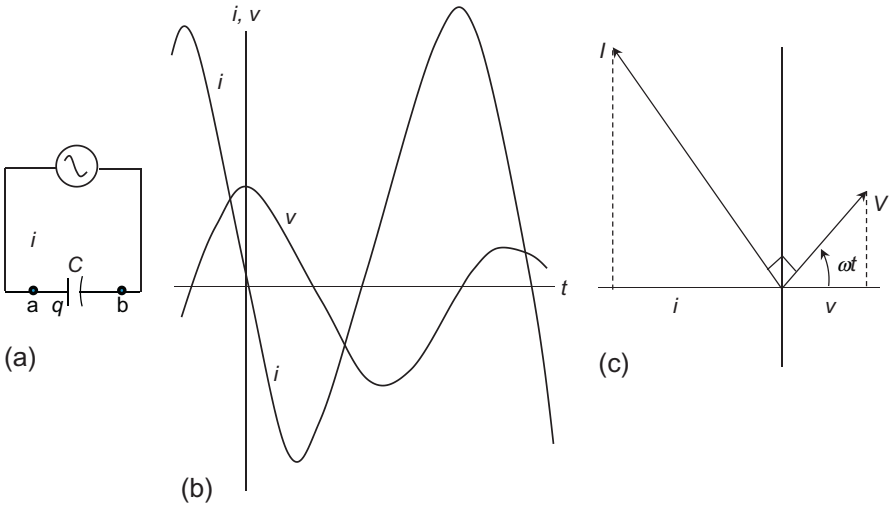

Fig. 5.22 (a) Capacitive circuit, (b) Instantaneous voltage and current, and (c) Vector diagram.

$$i = \frac{dQ}{dt} = -\omega CV \sin \omega t \tag{5.50}$$

The voltage is presented in Fig. 5.22b as a cosine function, while the current is presented as a negative sine function. The current as shown in Fig. 5.22c is not in phase with the voltage. The current vector is ahead of the voltage vector by a quarter cycle, 90°. Because $\cos(A + 90^\circ) = -\sin A$, Eq. (5.50) takes the form:

$$i = \omega CV \cos\left(\omega t + 90^\circ\right) \tag{5.51}$$

The maximum current, ωCV, can be presented in the form $I = V/R$ or $I = V/1/\omega C$ that defines a quantity, X_C, named the capacitive reactance of the capacitor with unit one volt per ampere (1 Ω):

$$X_C = \frac{1}{\omega C} \rightarrow I = \frac{V}{X_C} \tag{5.52}$$

Figure 5.23a shows a schematic of a pure inductor with self-inductance L and zero resistance connected to an "ac" source. The potential difference between "a" and "b" terminals of an inductor are:

$$L\frac{di_{ab}}{dt} = V\cos(\omega t) \tag{5.53}$$

or

$$di_{ab} = V/L\cos\omega dt \tag{5.54}$$

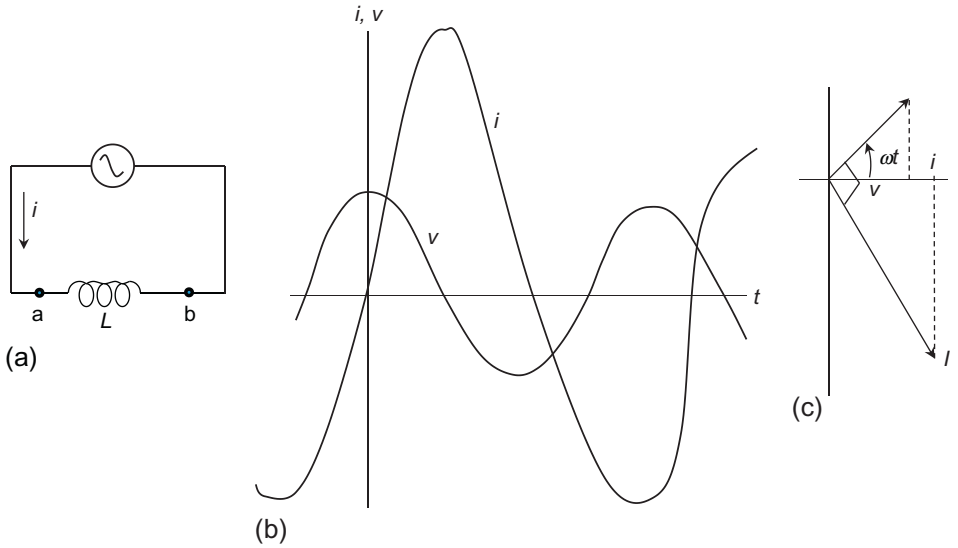

Fig. 5.23 (a) Inductance "L" circuit, (b) Instantaneous voltage and current, and (c) Vector diagram.

Integration of both sides if $I_{a,b}=0$ at 0 time and $C=0$ results in:

$$i_{ab}=\frac{V}{\omega L}\sin\omega t \tag{5.55}$$

The voltage and current with the inductor substituted in the circuit are a quarter-cycle out of phase, Fig. 5.23b. The voltage, as shown in Fig. 5.23c leads the current by 90°. Using the identity $\cos(A-90°)=\sin A$, Eq. (5.55) becomes:

$$i_{ab}=\frac{V}{\omega L}\cos(\omega t-90^{o}) \tag{5.56}$$

The maximum current is defined as:

$$I=\frac{V}{\omega L}\quad\text{and}\quad i_{a,b}=I\sin\omega t \tag{5.57}$$

Defining the inductive reactance as:

$$I=\frac{V}{X_{L}} \tag{5.58}$$

The inductive reactance is proportional to the angular velocity.

5.9.2 Expression for impedance of the R-L-C series circuit

Figure 5.24a shows a circuit that includes resistance, inductive reactance, and capacitive reactance. The phasor diagram is shown in Fig. 5.24b. The voltage phasor is the-sum of the phasors of the individual voltages. The maximum and instantaneous voltages are presented as capital V and small v, respectively. The instantaneous voltages, v, v_R, v_L, v_C are projections on the horizontal axis in Fig. 5.24b of V_R, V_L, and V_C phasors. The potential difference between the terminals in Fig. 5.24 is in phase with the current in the resistor where the voltage maximum value is $V_R = IR$.

The projection of the V_R phasor results in the instantaneous potential difference $v_R = v_{ac}$ (Fig. 5.24b). The voltage amplitude across an inductor is defined as $V_C = IX_C$. In Fig. 5.24b, the voltage in a capacitor circuit lags the current by 90°. The projection of the phasor V_C onto the horizontal axis in Fig. 5.24b results in $v_c = v_{db}$.

The potential difference "v" between terminal "a" and terminal "b" is equal to sum of the projections of the phasors V_R, V_L, and V_C. To estimate the vector sum or the source voltage V, one subtracts the phasor V_C from V_L resulting in $V_L - V_C$ as shown in Fig 5.24b. Thus, the phasor V is:

$$V = \sqrt{V_R^2 + (V_L - V_C)^2} = \sqrt{(IR)^2 + (IX_L - IX_C)^2} = I\sqrt{R^2 + (X_L - X_C)^2} \quad (5.59)$$

V/I is defined as the impedance of the circuit Z. The phasor V_L is defined as:

$$V_L = IX_L \quad (5.60)$$

The voltage in this case leads the current by 90°. The projection of phasor V_L on the horizontal axis in Fig. 5.24b results in $v_L = v_{cd}$.

The voltage amplitude across a capacitor is defined as:

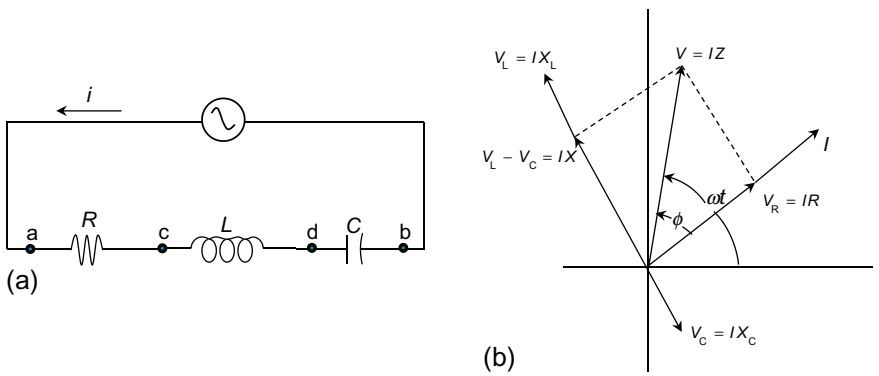

Fig. 5.24 (a) A series R-L-C circuit and (b) Vector diagram.

$$Z = \sqrt{R^2 + (X_L - X_C)^2} = \sqrt{R^2 + X^2} \rightarrow I = \frac{V}{Z} \tag{5.61}$$

$X = X_L - X_C$ is the reactance of the circuit. The impedance Z of the R-C circuit is obtained by taking $X_L = 0$ or

$$Z = \sqrt{R^2 - \left(\frac{1}{\omega C}\right)^2} \tag{5.62}$$

The expression for Z for the R-L-C circuit is:

$$Z = \sqrt{R^2 + (X_L - X_C)^2} = \sqrt{R^2 + \left[\omega L - \left(\frac{1}{\omega C}\right)^2\right]} \tag{5.63}$$

The value of the phase angle θ of the source voltage V is estimated from Fig. 5.24 by using Eq. (5.64)

$$\tan\theta = \frac{Z''}{Z'} = \frac{V_L - V_C}{V_R} = \frac{I(X_L - X_C)^C}{IR} = \frac{X}{R} \tag{5.64}$$

In summary, the source voltage is a cosine function, $v = V\cos(\omega t)$. The current lags the voltage by an angle θ between 0° and 90° represented by $i = I\cos(\omega t - \theta)$. A plot of Z' vs. Z'' represents a Nyquist plot, which can be used to evaluate the corrosion properties of metals and coatings.

5.9.3 AC impedance plots: impedance spectra with their associated equivalent circuits

The goal of "ac" impedance measurements is to determine the values of elements in the equivalent circuit. It is necessary to experimentally study the response of corrosion system to an "ac" excitation and to fit the data to an equivalent circuit model that accurately describes the corrosion process at the metal-electrolyte interface.

The "ac" excitation is applied as an "ac" current or an "ac" voltage and it is performed over a range of frequencies between 10^{-3} and 10^4 Hz. The raw data consist of the real and imaginary component of the voltage and the real and imaginary component of current. The data can be used to calculate the real impedance, the imaginary impedance, the total impedance $|Z|$, and the phase shift of response (θ) for each applied frequency. The data is plotted by using different formats to provide accurate information of the corrosion system under study.

When the corrosion cell can be represented only by a resistor, the current is in phase with the voltage, the phase shift $\theta = 0$, and the impedance has no imaginary component,

$$Z = R \tag{5.65}$$

A pure resistance is presented in Fig. 5.25a by only a point on the x-axis as a function of frequency.

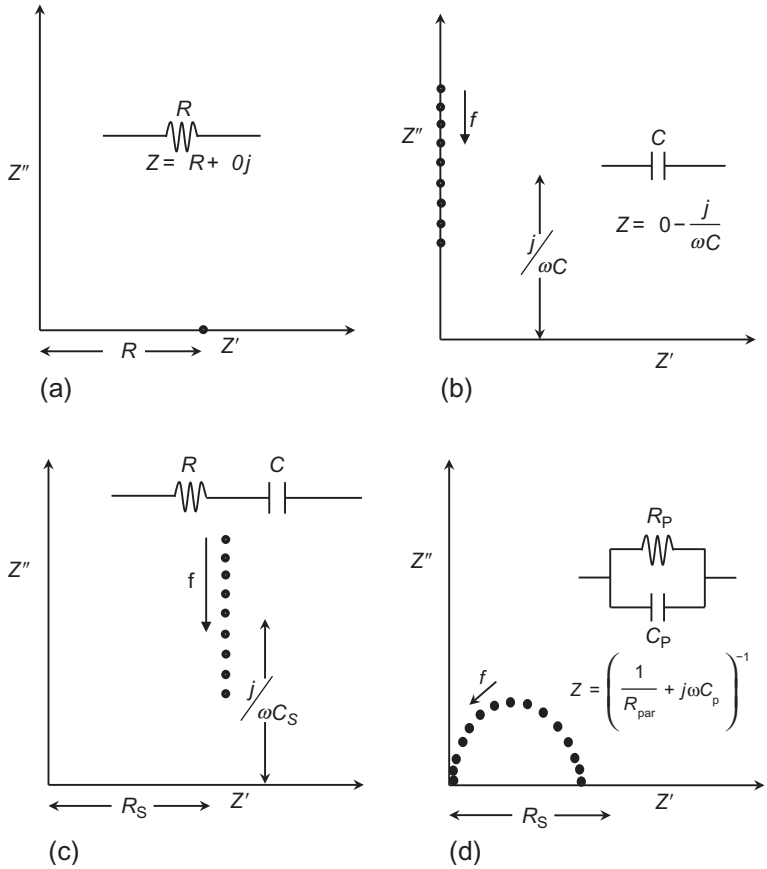

Fig. 5.25 Complex plane impedance spectra and their associated equivalent circuits: (a) resistor, (b) capacitor, (c) resistor and capacitor connected in series, and (d) resistor and capacitor connected in parallel.

If the cell can be represented by only a capacitor, (Fig. 5.25b), the phase shift, $\theta = 90°$, and the impedance, Z, will have only an imaginary component that depends on frequency through the equation:

$$Z = -\frac{j}{\omega C} \tag{5.66}$$

The points in Fig. 5.25b vary with frequency.

Figure 5.25c represents an equivalent circuit that consists of resistance and double-layer capacitance in series. Equation (5.66) is used to calculate the impedance. For an R-C circuit in series, $Z' = R_s$ and $Z'' = -(j/\omega C_s)$. The phase angle θ varies between 0° and 90°, depending on the frequency used in the measurement. Equation (5.66) when multiplied by $\sqrt{(-1)^{1/2}}$ takes the form:

$$Z = R_s - \frac{j}{\omega C_s} \tag{5.67}$$

where $j = \sqrt{-1}$.

In the case of a parallel circuit (Fig. 5.25d), the following equation can be derived for the impedance.

$$Z = \left(\frac{1}{R_{par.}} + j\omega C_p\right)^{-1} \tag{5.68}$$

A corroding metal can be represented by the equivalent circuit, shown in Fig. 5.26, consisting of R_Ω, which includes the resistance of the electrolyte, the surface films, and circuit leads. The polarization resistance at the interface is in parallel with the double-layer capacitance C_{dl}.

Figure 5.27 shows the response of the circuit in Fig. 5.26. The following equations describe the circuit elements in Fig. 5.27.

$$Z(\omega) = Z' + jZ'' = R_\Omega + \frac{R_p}{1 + j\omega R_p C} \tag{5.69}$$

$$Z = R_\Omega + \frac{R_p}{1 + \left(\omega C R_p\right)^2} - \frac{j\omega C R_p^2}{1 + \left(\omega C R_p\right)^2} \tag{5.70}$$

The frequency f (Hz) of the AC signal is given by $\omega = 2\pi f$. When ω is very large, the real term (Z') becomes simply R_Ω, while the imaginary term (Z'') approaches

$$\frac{-1}{\omega C} \tag{5.71}$$

Equation (5.71) is best expressed by considering the admittance Y:

$$\frac{1}{Z} = Y = Y' + jY'' \tag{5.72}$$

where

$$Y = \frac{R_\Omega + R_p + \left(\omega C R_\Omega R_p\right)^2}{\left(R_\Omega + R_p\right)^2 + \left(\omega C R_\Omega R_p\right)^2} \tag{5.73a}$$

and

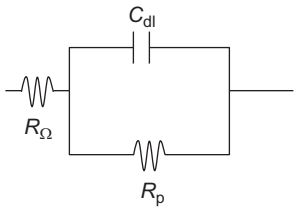

Fig. 5.26 The equivalent circuit of the electrochemical cell with solution/electrolyte resistance, R_Ω.

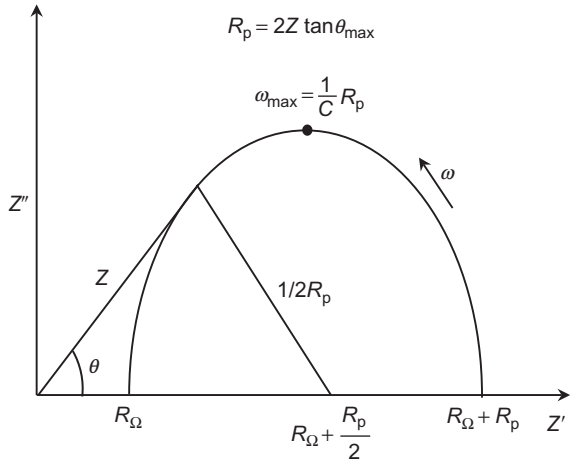

Fig. 5.27 Complex plane impedance spectra (Nyquist plot) for corroding metal.

$$Y'' = \frac{CR_p^2}{\left(R_\Omega + R_p\right)^2 + \left(\omega C R_\Omega R_p\right)^2} \tag{5.73b}$$

The relationships between impedance and admittance are:

$$Z' = \frac{Y'}{Y'^2 + Z''^2} \tag{5.74a}$$

and

$$Z'' = -\frac{Y''}{Y'^2 + Z''^2} \tag{5.74b}$$

Elimination of ω in Eq. (5.70) leads to:

$$\left[Z' - \left(R_\Omega + \frac{1}{2}R_p\right)\right]^2 + (Z'')^2 = \left(\frac{R_p}{2}\right)^2 \tag{5.75}$$

At the apex of the semicircle in the Nyquist plot:

$$\omega_{max} = \frac{1}{R_p C} \tag{5.76}$$

The Ohmic resistance, R_Ω, in Fig. 5.26 is the uncompensated resistance between the reference electrode and the working electrode. The polarization resistance, R_p, is defined as resistance at the electrode/solution interface. The capacitance, C_{dl}, represents the double-layer capacitance at the interface. Evaluation of polarization resistance, R_p, calculates the corrosion rates.

Capacitance measurements evaluate the rates of film formation on metallic surfaces, adsorption and desorption, and the durability of organic coatings [69,70]. The Nyquist plot in Fig. 5.27 is also known as the complex impedance plane diagram and the Cole-Cole plot. For each frequency, the imaginary component $Z''(\omega)$ in this format is plotted vs. the real component $Z'(\omega)$. As shown in the figure, the frequency in the Nyquist plot increases in the counterclockwise direction. At very high frequency, the imaginary component $Z' = 0$. Z is at the intersection of the nearby end of the semicircle of the Nyquist plot with the Z' axis, and Z is equal to the ohmic resistance, R_Ω. At the other end of the semicircle, at very low frequencies, the imaginary impedance is again $Z'' = 0$ and the real impedance Z' is equal to the sum of the ohmic resistance, R_Ω, and the faradaic resistance or polarization resistance, R_p. Thus, at high frequencies the uncompensated resistance, R_Ω, defines the real impedance, while at low frequencies the real impedance is the sum of the faradic and the ohmic resistances, $R_\Omega + R_p$.

The ohmic resistance, R_Ω, is the same at all frequencies. The polarization resistance can also be measured by a DC technique and can be used to calculate the corrosion rates of any metal in a given corrosion environment.

The impedance of a corroding metal also can be expressed as Bode plots, $|Z|$ vs. frequency and $\log(\theta)$ vs. frequency in cycles/s (hertz), as shown in Fig. 5.28.

The Bode plot is another method to analyze the frequency dependence of the absolute value $|Z| = \sqrt{Z'^2 + Z''^2}$ and the phase angle θ defined as:

$$\tan\theta = \frac{Z''}{Z'} = (\omega C_S R_S)^{-1} \tag{5.77}$$

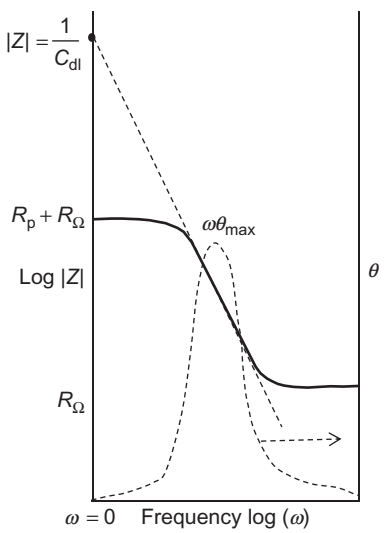

Fig. 5.28 Bode plot showing the impedance and the phase angle as a function of frequency.

The double-layer capacitance, C_{dl}, can be calculated by using Eq. (5.78):

$$\omega_{(\theta=\max)} = \sqrt{\left(\frac{1}{C_{dl}R_p}\right)\left(\frac{1+R_p}{R_\Omega}\right)} \tag{5.78}$$

Extrapolating the straight line with a slope -1 in the Bode plot yields the value of C_{dl} from Eq. (5.79).

$$\log|Z| = \log\frac{1}{\omega C_{dl}} \tag{5.79}$$

The absolute impedance $|Z|$ is estimated by using Eq. (5.79). The capacitance plots at intermediate frequencies are linear with a slope of -1 and maximum phase angle θ. As shown in Fig. 5.28, one can estimate a compensated value of R_p by subtracting the R_Ω measured at high frequencies from the sum of $R_\Omega + R_p$ measured at low frequencies. Thus, the $\log|Z|$ vs. $\log\omega$ curve can be used to estimate the values of R_p and R_Ω. At the break point (intermediate frequencies) of the straight line in Fig. 5.28 the slope is -1. One can calculate the double-layer capacitance by extrapolating this line to the $\log|Z|$ at $\omega = 1$ ($\log\omega = 0$) using Eq. (5.79):

$$\begin{aligned}\log|Z| &= -\log(\omega C_{dl}) = -\log(\omega) - \log(C_{dl}) \\ &= -\log(2\pi f) - \log(C_{dl}) = -\log(2\pi) - \log(f) - \log(C_{dl})\end{aligned}$$

At the point where $f = 0.16$ Hz, $\omega = 2\pi f = 1$, $\log(2\pi f) = 0$ resulting:

$$\log(|Z|) = -\log(C)\,\text{when}\, f = 0.16\,\text{Hz}$$

or

$$|Z_{(f=0.16)}| = \frac{1}{C_{dl}} \tag{5.80}$$

The plot θ vs. log ω exhibits a peak at frequency corresponding to $\omega^{\theta\max}$. At this frequency, the capacitance of the double layer is calculated using Eq. (5.80) [23]:

$$\omega^{\theta\max} = \frac{1}{CR_p}\sqrt{1+\frac{R_p}{R_\Omega}} \tag{5.81}$$

where $\omega^{\theta\max} = 2\pi f^{\theta\max}$.

In the case of charge-transfer processes controlled by diffusion (concentration polarization) in the electrolyte, the impedance spectra are represented in Fig. 5.29, where Z_W in Eq. (5.82) is the Warburg impedance.

For a reversible system under pure diffusion control, the mass transfer impedance (Warburg), Z_W, is given by:

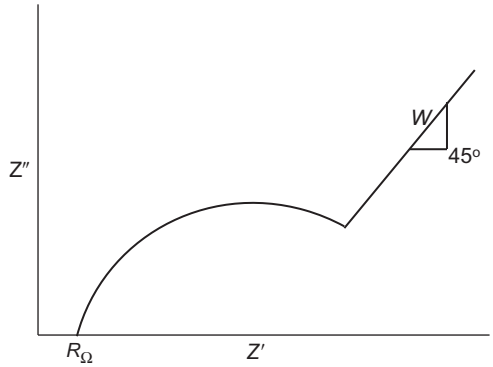

Fig. 5.29 Complex plane impedance spectra, Nyquist plot in case of charge-transfer processes controlled by diffusion in the electrolyte.

$$Z_W = \frac{(2\sigma)^{1/2}}{\omega} \tag{5.82}$$

The parameter σ is the Warburg coefficient, from which the diffusion coefficient is calculated.

5.9.4 Application of electrochemical impedance to corrosion studies

Figure 5.30 shows a comparison of Nyquist responses obtained for Zn, Zn-Ni, Cd, Zn-Ni-Cu, nano Ni-Zn, and electroless Ni-Zn-P coatings. The solution resistance remains the same for all frequencies. This is to be expected because the studies were done under similar conditions in pH 7.0. R_p values can be approximately determined by fitting the Nyquist response to a simple equivalent circuit consisting of ohmic resistance, double-layer capacitance, and polarization resistance.

The electrodeposited Ni-Zn alloy and electroless Ni-Zn-P offers a barrier resistance in the order of 2000 Ω, which is five times higher than the typical Cd deposit. The increase in the barrier resistance of these coatings is an outcome of the increase in nickel content in the deposit.

EIS has been used to predict the life of organic coatings used for corrosion protection [58,60,71–73]. It has been proven to be a powerful tool to obtain system-specific parameters for evaluating the initial duration of their capacitive behavior and deterioration of the barrier coatings properties [58,71,72]. The change in the capacitance of the coating was found to correlate with the uptake of water [66]. The change of the resistance has been explained in terms of ionic species penetration from the electrolyte [74]. EIS was used to evaluate the degree of delamination of the epoxy primer electrocoated on phosphate treated cold-rolled steel in 3.5% NaCl exposed to air [64]. Coating parameters were

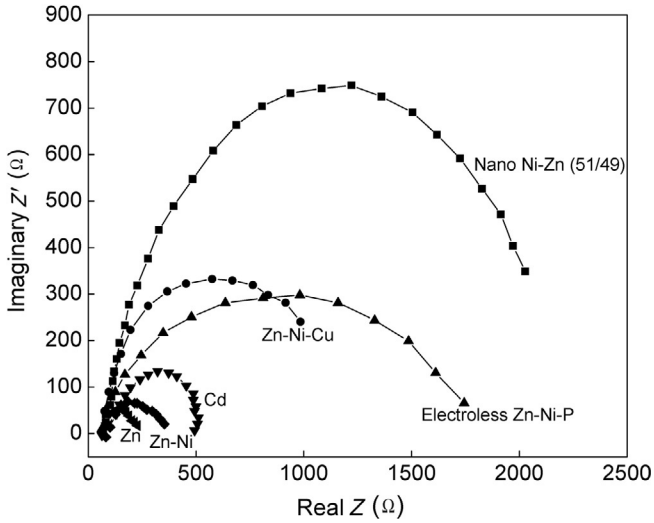

Fig. 5.30 Nyquist plots obtained for various coatings in 0.5 M Na_2SO_4 + 0.5 M H_3BO_3 solution at pH 7.0 solution [Popov, Unpublished data].

obtained using a circuit analog model. The delamination area was estimated using pore resistance and the break point frequency. The results were compared with the corroded area determined visually. EIS has successfully estimated the barrier properties of epoxy/phenolic and epoxy/amine thick-coated mild steel exposed to 3.5% NaCl solution in air [65]. A special electrochemical cell shown in Fig. 5.31 was used to estimate the coating properties [65]. Good agreement was obtained between calculated capacitance using a mathematical model and measured coating capacitance.

An analytical impedance model was developed by Popov and coworkers to calculate the diffusion coefficient of hydrogen in metal [75]. From the slope of the Nyquist plots in the transition region, the diffusion coefficient of hydrogen was calculated. Figure 5.32 presents the effect of varying the diffusion coefficient on the impedance of the hydride electrode [75]. The semi-infinite diffusion, transition, and infinite diffusion regions are shown in the plot. The value of the diffusion coefficient affects not only the magnitude of the impedance but also the transition from semi-infinite to complete diffusion control. As the diffusion coefficient decreases, the transition is also shifted to lower frequencies. This is expected because lowering the diffusion coefficient reduces the rate of transport of hydrogen across the particle. Because the frequency is inversely proportional to time, the transition and diffusion regions appear even later.

Figure 5.33 presents the effect of particle size on the Nyquist impedance behavior of the electrode [75]. The plot shows that the effect of particle size is opposite to that of the diffusion coefficient, that is, a decrease in the particle radius shifts the appearance of the transition region to higher frequencies. In smaller particles, hydrogen needs to travel only

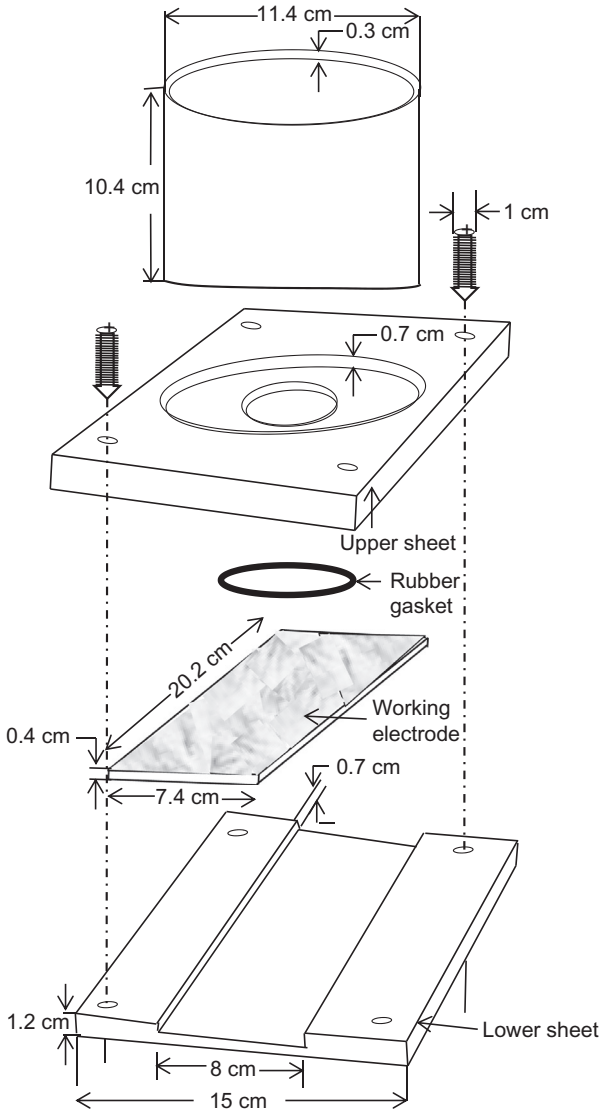

Fig. 5.31 Schematic of organic coating test cell [65]. *Reproduced by permission of The Electrochemical Society.*

a short distance and the time for diffusion is smaller. Hence, the diffusion regime appears at higher frequencies. The simulations were done at a diffusion coefficient value of 2.0×10^{-10} cm^2/s. The charge-transfer resistance and Warburg coefficient were set to 18 Ω and 1 Ω/s$^{1/2}$, respectively. Decrease in the particle size or increase in the diffusion coefficient shifts the onset of the transition region to a higher frequency.

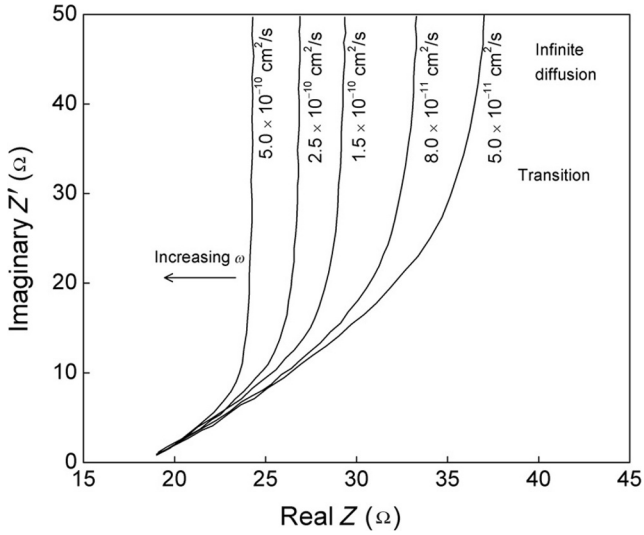

Fig. 5.32 Nyquist plots of the hydride electrode simulated for different values of the diffusion coefficient [75].

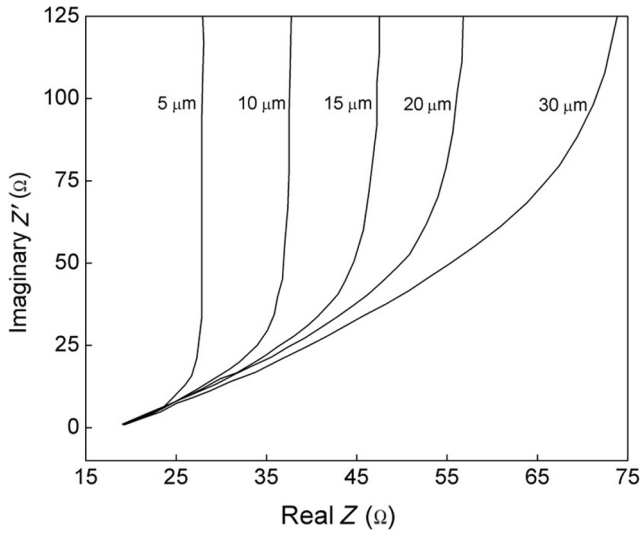

Fig. 5.33 Change in the Nyquist impedance due to variation in the average particle size of the metal hydride electrode. The simulations were done at a diffusion coefficient value of 2.0×10^{-10} cm^2/s [75].

The first principles model [75] was used by Popov et al. to study the pulverization and corrosion of bare and cobalt encapsulated metal hydride electrodes [76]. EIS under zero current conditions enables the determination of the oxidation resistance and the evaluation of alloy corrosion without interference of any of the ohmic resistances. The total

resistance of the electrode is the sum of the following resistances: (i) the electrolyte, (ii) between the current collector and the electrode pellet, (iii) the alloy particle to particle contact, and (iv) polarization, which is related to the electrode reaction on the alloy surface and is inversely proportional to the electrode active surface area. The equivalent circuit used to determine the various resistances is shown in Fig. 5.34. The alloy resistance at the electrode-electrolyte interface was evaluated using this circuit.

Figure 5.35 shows the impedance response of a bare and a cobalt-coated metal-hydride electrode. Two semicircles are seen in the Nyquist plot initially for the bare alloy and Co-coated alloy. After 50 charge/discharge cycles of the electrode for the bare alloy, the two semicircles merge and a significant increase in the alloy resistance is observed. The increase in resistance for the Co-coated alloy is comparatively less even after 120 cycles [76]. Alloy oxidation is responsible for the increase of the particle-to-particle resistance observed in the bare alloy in Fig. 5.35.

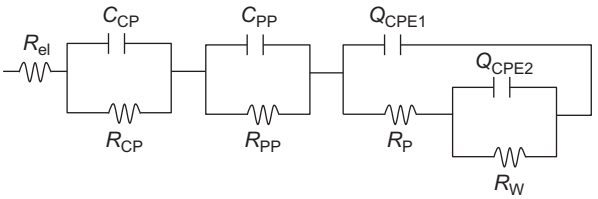

Fig. 5.34 Schematic of the equivalent circuit for the metal hydride electrode.

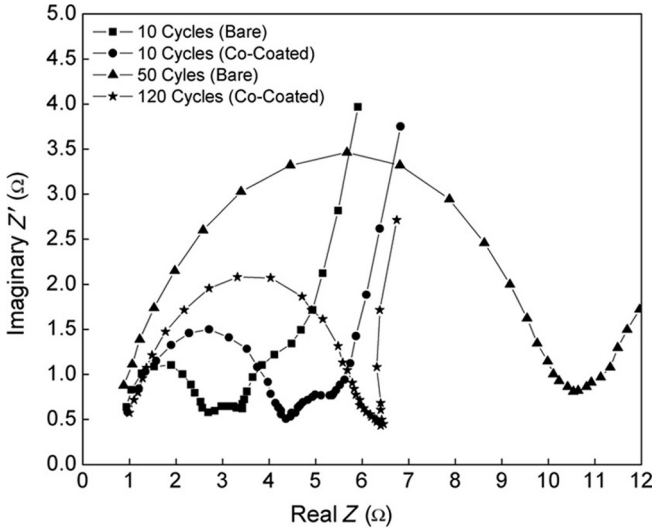

Fig. 5.35 Nyquist plot of the impedance response of bare and cobalt-coated metal hydride alloy at different charge-discharge cycles [76].

5.10 ADVANTAGES AND LIMITATIONS OF EIS

EIS is a powerful nondestructive technique capable of covering a broad range of frequencies and isolating and studying the electrochemical, chemical, and physical phenomena at the metal-electrolyte interface in a single experiment [77,78]. EIS is a steady state technique that requires an application of a small perturbation of the current or potential without significantly affecting the electrochemical processes in an electrochemical cell. It provides valuable information for processes occurring in electrolytes of low conductivity because this method is free of potential errors present in direct current methods with potential scans to evaluate the processes at the metal-electrolyte interface. It has been applied with high accuracy and reproducibility to estimate the electrode capacitance and charge-transfer kinetics, providing mechanistic information for electrochemical and corrosion processes. EIS measures the polarization resistance, R_p, with high accuracy. Measurement of the capacitance of corrosion processes at different rates is also possible by using multifrequencies excitations.

Impedance data may be analyzed directly from impedance plots (Bode and Nyquist plots). Alternatively, the capacitances and the resistances are varied until the model predicted "ac" behavior matches the experimental data using a circuit analog model. These electrical properties are then interpreted as the properties of the system.

Macdonald summarized the limitations of EIS technique when used to measure the corrosion current (corrosion rates) of metals [79]. A high level of mathematics is required to analyze data and interpret properties of the corrosion system. Analysis of impedance data results in determination of the polarization resistance. However, it requires obtaining a large number of low-frequency data for an accurate estimate. It is necessary to extract the noise from the data obtained at low frequency ranges to obtain meaningful mechanistic information. To calculate the corrosion rate using the Stern-Geary equation, the Tafel method should be used to estimate the Tafel slopes as a function of time. Due to the variation of porosity of corrosion products on metals, the corrosion products (oxides and hydroxides) contributions to the overall impedance spectra are difficult to evaluate.

5.11 RECENT CORROSION RESEARCH

Because EIS is a microscopic technique, the localized corrosion processes occurring at grain boundaries such as cracks and pits are very difficult to evaluate. Currently, localized electrochemical impedance spectroscopy (LEIS), scanning Kelvin probe (SKP), and scanning electrochemical microscopy (SECM) are aggressively used to study localized corrosion initiation [80,81] and passive film properties [82,83]. LEIS is based on spatially resolved electrochemical spectroscopy and has been used to evaluate the efficiency of inhibitors to stop corrosion, wear tests, pit growth, and coating delamination studies. With this technique, changes of the impedance are measured locally and AC current

is measured during the pit growth [84,85]. The factors that control the limiting spatial resolution and the mathematical foundation of this technique have been addressed in the literature [86–91] and reviewed by Huang [92]. Although a large number of papers have been published in this area, a better understanding of the current distribution is necessary to explain the processes in localized corrosion.

Macdonald published an excellent review reflecting on the history of EIS starting with the foundations established in the late nineteenth century by Heaviside in the form of linear system theory [78]. The EIS technique has been successfully used to evaluate the initial change of coating properties from their initial capacitive behavior [60]. An extensive review by Mansfield [93] summarizes the use of EIS for the study of protection polymer coatings and the models for the simulation and analysis of EIS data for polymer-coated metals and alloys. An alternative model based on the substitution of the constant pulse element by Warburg impedance was developed by Skale et al. [94] for fitting electrochemical impedance spectra of protective coating. A review by Cano et al. [95] summarizes the use of EIS for the evaluation of the protective properties of coatings and general EIS and its application in corrosion research in areas such as the study of corrosion inhibitors, cathodic protection, metallic coatings, passive films, biomedical systems, reinforced concrete, and microbiologically influenced corrosion. A new impedance technique, described by Darowicki et al. [96] and Krakowiak et al. [97], is dynamic electrochemical impedance spectroscopy (DEIS), which is used under nonstationary conditions. It is based on the current dynamic electrochemical techniques such as cyclic voltammetry or pulse voltammetry. The method is capable of estimating the rate of creation and repassivation of metastable pits.

EXERCISES

E5.1. For iron ($d = 7.8$ gm/cm^3) in a corrosive solution, the linear polarization slope at low current densities is 2 mV/μAcm^2. Assuming $b_a = b_c = \pm 0.1$ V/decade, calculate the corrosion current in mpy.

E5.2. Zinc (d = 7.14 g/cm^3) corrosion rate in a deaerated solution of pH 1 is 2500 mpy. Calculate the corrosion potential of zinc vs. hydrogen reference electrode. The activity of the metal in the solution is 10^{-5} M. The value of the anodic (b_a) Tafel slope is 0.1 V/decade. The exchange current density for zinc is 10^{-5} A/cm^2.

E5.3. For tin ($d = 7.3$ g/cm^3) in a corrosive solution, the linear polarization, R_p, is 2 mV/(μA/cm^2). Assuming $b_a = b_c = \pm 0.1$ V/decade, calculate the corrosion rate in mpy.

E5.4. By polarizing a corrosion redox system, a change in current of 8 mA was measured for a potential change of 2 mV. If the corrosion current is 1 A/m^2, estimate

the electrochemically active area and the polarization conductance. (Assuming $b_a = b_c = \pm 0.1$ V/decade.)

E5.5. Assuming $b_a = b_c = \pm 0.1$ V/decade, $R_p = 4$ mV/(μA/cm^2), calculate the corrosion rate of zinc in a corrosive interface in gmd (grams per day).

E5.6. Determine the corrosion potential, the corrosion current, and the corrosion rate in mpy for zinc ($d = 7.14$ g/cm^3) in a solution of pH = 1. The activity of the metal in the solution is 10^{-2} M. The values of both the cathodic and the anodic Tafel slopes are ±0.1 V/decade. The exchange current densities for the anodic and cathodic reactions are 10^{-5} and 10^{-7} A/cm^2, respectively.

E5.7. Calculate the corrosion rate in gmd for zinc ($d = 7.14$ g/cm^3) in a solution of pH 3. The activity of the metal in the solution is 10^{-4} M. The values of the cathodic and the anodic Tafel slopes are −0.12 and 0.1 V/decade, respectively. The exchange current densities for hydrogen evolution on zinc and zinc dissolution are 10^{-7} and 10^{-4} A/cm^2, respectively.

E5.8. Calculate the corrosion current and the corrosion rate if a tin ($d = 7.3$ g/cm^3, EW = 118.71 g/mol) sample with surface area of 100 cm^2 is exposed in a deaerated solution of pH 2 for 24 h loses 34 mg.

E5.9. Cadmium ($d = 8.65$ g/cm^3) activity in a deaerated corrosive solution with a pH of 4 is 10^{-1} M. The values of the cathodic and the anodic Tafel slopes are −0.12 and +0.1 V/decade, respectively. The cathodic intercept is $a_c = -1.4$ V. The exchange current density for cadmium, i^o, is 3×10^{-11} A/cm^2. Standard potential for hydrogen and cadmium are $e^o_{H^+|H_2} = 0$ V vs. SHE and $e^o_{Cd|Cd^{2+}} = 0.403$ V vs. SHE, respectively. Assume that all the cadmium surface acts as cathode. Calculate the hydrogen exchange current density, corrosion potential, and the corrosion rate in mm/year.

E5.10. Calculate the corrosion potential and the corrosion rate of silver in grams per square meter per day (gmd). The concentration of silver in a 0.3 N H_2SO_4 is 10^{-26} M. The values of the cathodic and the anodic Tafel slopes are −0.09 and +0.12 V, respectively. The exchange current density for silver and hydrogen are $i^o_{Ag} = 5 \times 10^{-6}$ A/cm^2 and $i^o_{H_2} = 5 \times 10^{-7}$ A/cm^2, respectively. Standard potential for hydrogen and silver are 0 V vs. SHE and 0.799 V vs. SHE, respectively. Assume that all the silver surface acts as cathode.

E5.11. Calculate the corrosion current (A/cm^2) and corrosion rate in mm/year of Sn dissolution if the potential of the tin ($d = 7.3$ g/cm^3) anode undergoing corrosion is −0.08 V vs. SHE in 0.5 M $SnSO_4$. The standard electrode potential is e^o_{Sn} is −0.13 V vs. SHE. The anodic Tafel constant is 0.1 V/decade and exchange current density, $i^o = 10^{-8}$ mA/cm^2.

E5.12. For an overpotential of 0.2 V, calculate the corrosion rate of zinc (7.14 g/cm^3) in mpy if the exchange current density is 5×10^{-3} A/m^2. (The anodic Tafel constant is 0.045 V/decade.)

E5.13. If the slope of the polarization curve for Ni is 2 mV/(μA/cm^2), assuming $b_a = b_c = \pm 0.1$ V/decade, calculate the corrosion rate in grams per second (g/s).

REFERENCES

[1] N.D. Green, G.A. Saltzman, Effect of plastic deformation on the corrosion of iron and steel, Corrosion 20 (1964) 293t–299t.
[2] E.J. Simmons, Use of the Pearson Bridge in corrosion inhibitor evaluation, Corrosion 11 (1955) 255t–260t.
[3] M. Stern, A method for determining corrosion rates from linear polarization data, Corrosion 14 (1958) 440t–444t.
[4] M. Stern, A.L. Geary, Electrochemical polarization I. A. Theoretical analysis of the shape of polarization curves, J. Electrochem. Soc. 104 (1957) 56–63.
[5] C.W. Wagner, W. Traud, Concerning the evaluation of corrosion reactions by superposition of electrochemical partial reactions and concerning the potential formation on mixed electrodes, Z. Electrochemica 144 (1938) 391–402.
[6] R.V. Sklod, T.E. Larsen, Measurement of the instantaneous corrosion rate by means of polarization data, Corrosion 13 (1957) 139t–142t.
[7] K.F. Bonhoeffer, W. Jena, The electromotive behavior of iron, Z. Elektrochemica 55 (1951) 151–154.
[8] S.N. Popova, B.N. Popov, R.E. White, Determination of corrosion properties of lacquered tinplate in citrate solutions by DC and AC electrochemical methods, Corrosion 46 (1990) 1007–1014.
[9] D.A. Jones, Polarization in high resistivity media, Corros. Sci. 8 (1968) 19–27.
[10] J.R. Park, D.D. MacDonald, The fast-growth mechanism of magnetite on carbon steel in oxidizing high-temperature aqueous solutions, Corrosion 45 (1989) 563–571.
[11] R.L. Leroy, Evaluation of corrosion rates from nonlinear polarization data, J. Electrochem. Soc. 124 (1977) 1006–1012.
[12] K.B. Oldham, F. Mansfeld, On the so-called linear polarization method for measurement of corrosion rates, Corrosion 27 (1971) 434–436.
[13] F. Mansfeld, K.B. Oldam, A modification of the Stern-Geary linear polarization equation, Corros. Sci. 11 (1971) 787–796.
[14] M. Stern, E.D. Weisert, Experimental observations on the relation between polarization resistance and corrosion rate, Proc. ASTM 59 (1959) 1280–1291.
[15] F. Mansfeld, The polarization resistance technique for measuring corrosion currents, M.G. Fontana,R. W. Staehle (Eds.), Advances in Corrosion Science and Technology, vol. VI, Plenum Press, New York, 1976, pp. 163–262.
[16] H.H. Uhlig, R.W. Revie, Corrosion and Corrosion Control, John Wiley & Sons, New York, 1985.
[17] D.A. Jones, The advantages of galvanostatic polarization resistance measurements, Corrosion 39 (1983) 444–448.
[18] D.A. Jones, N.D. Greene, Electrochemical measurement of low corrosion rates, Corrosion 22 (1966) 198–205.
[19] F. Mansfeld, Polarization resistance measurements—experimental procedure and evaluation of test data, in: R. Baboian (Ed.), Electrochemical Techniques for Corrosion Engineering, NACE, Houston, 1977, p. 67.
[20] L.I. Antropov, Correlation between kinetics of corrosion and the mechanism of inhibition by organic compounds, Corros. Sci. 7 (1967) 607–620.
[21] S. Barnartt, Tafel slopes for iron corrosion in acidic solutions, Corrosion 27 (1971) 467–470.
[22] W.J. Lorenz, C. Mayer, H. Fisher, Galvanostatic current change method for differentiation between primary and secondary surface boundary inhibition of electrode reactions I. Theory of the method, Z. Phys. Chem. 52 (1967) 180–192.
[23] F. Mansfeld, M.W. Kending, T. Tsai, Recording and analysis of AC impedance data for corrosion studies II. Experimental approach and results, Corrosion 38 (1982) 570–579.

[24] F. Mansfeld, S.L. Jeanpaquet, M.W. Kending, The evaluation of corrosion protection measures for metal matrix composites, Corros. Sci. 26 (1986) 727–734.
[25] F. Mansfeld, S.L. Jeanpaquet, M.W. Kending, An electrochemical impedance spectroscopy study of reactions at the metal/coating interface, Corros. Sci. 26 (1986) 736–742.
[26] G. Lauer, R.A. Osteryoung, Effect of uncompensated resistance on electrode kinetic and absorption studies by chronocoulometry, Anal. Chem. 38 (1966) 1106–1112.
[27] F. Mansfeld, The effect of uncompensated IR-drop of polarization resistance, Corrosion 32 (1976) 143–146.
[28] D.T. Sawyer, J.L. Roberts Jr., Experimental Electrochemistry for Chemists, John Wiley & Sons, New York, 1974.
[29] B.E. Wilde, Adaptation of linear polarization techniques for in-situ corrosion measurements in water cooled nuclear reactor environments, Corrosion 23 (1967) 379–384.
[30] F. Mansfeld, Some errors in linear polarization measurements and their correction, Corrosion 30 (1974) 92–96.
[31] S. Mennenoh, H.J. Engel, A method for measuring the effectiveness of inhibitors in pickling baths, Stahl Eisen. 82 (1962) 1796–1801.
[32] B. Veeraraghavan, H. Kim, B. Haran, B. Popov, Comparison of mechanical, corrosion and hydrogen permeation properties of electroless Ni-Zn-P alloys with electrodeposited Zn-Ni and Cd, Corrosion 59 (2003) 1003–1010.
[33] H. Kim, B. Popov, K.S. Chen, Comparison of corrosion resistance and hydrogen permeation properties of Zn-Ni, Zn-Ni-Cd and Cd coatings on low carbon Steel, Corros. Sci. 45 (2003) 1505–1521.
[34] B. Veeraraghavan, H. Kim, B.N. Popov, Optimization of electroless Ni-Zn-P deposition process: experimental study and mathematical modeling, Electrochim. Acta 49 (2004) 3143–3154.
[35] A. Durairajan, B.S. Haran, R.E. White, B.N. Popov, Development of a new electrodeposition process for plating of Zn-Ni-X (X = Cd, P) alloys: Corrosion characteristics of Zn-Ni-Cd ternary alloys, J. Electrochem. Soc. 147 (2000) 1781–1786.
[36] P. Ganesan, S.P. Kumaraguru, B.N. Popov, Development of Zn-Ni-Cd coatings by pulse electrodeposition process, Surf. Coat. Tech. 201 (2006) 3658–3669.
[37] P. Ganesan, Y.I. Choi, S.P. Kumaraguru, B.N. Popov, Development of corrosion-resistant silica coatings on surface modified zinc-coated steel, J. Appl. Surf. Finish. 2 (2007) 20–28.
[38] J. Tafel, Polarization during cathodic hydrogen development, Z. Phys. Chem. 50 (1904) 641–712.
[39] H. Kaesche, Metallic Corrosion, NACE, Houston, 1985.
[40] J.O.M. Bockris, A.K.N. Reddy, Modern Electrochemistry, Plenum Press, New York, 1970.
[41] M.G. Fontana, N.D. Greene, Corrosion Engineering, second ed., McGraw-Hill, New York, 1978.
[42] J.R. Scully, in: R. Baboian (Ed.), Corrosion Tests and Standards, ASTM International, Philadelphia, PA, 1995.
[43] R. Bandy, D.A. Jones, Analysis of errors in measuring corrosion rates by linear polarization, Corrosion 32 (1976) 126–134.
[44] R.H. Hausler, Practical experiences with linear polarization measurements, Corrosion 33 (1977) 117–128.
[45] D.A. Jones, Principles and Prevention of Corrosion, second ed., Macmillan, New York, 1992.
[46] B. Poulson, Electrochemical measurements in flowing solutions, Corros. Sci. 23 (1983) 391–430.
[47] M. Stern, R.M. Roth, Anodic behavior of iron in acid solutions, J. Elecrochem. Soc. 104 (1957) 390–392.
[48] E.A. Lizlovs, A.P. Bond, Anodic polarization behavior of high-purity 13 and 18% Cr stainless steels, J. Electrochem. Soc. 122 (1975) 719–722.
[49] R.L. Leroy, The range of validity of the linear polarization method for measurement of corrosion rates, Corrosion 29 (1973) 272–275.
[50] P. Dolin, B. Ershler, Kinetics of processes on the platinum electrode: I. The kinetics of the ionization of hydrogen adsorbed on a platinum electrode, Acta Physicochim. URSS 13 (1940) 747–778.
[51] J.E.B. Randles, K.W. Somerton, Kinetics of rapid electrode reactions. Part 4. Metal ion exchange reaction at amalgam electrodes, Trans. Faraday Soc. 48 (1952) 951–955.
[52] D.C. Grahame, Mathematical theory of the faradic admittance: pseudocapacity and polarization resistance, J. Electrochem. Soc. 99 (1952) 370C–385C.

[53] K. Sugimoto, Y. Sawaka, The effect of some alloying elements on the corrosion resistance of lead-antimony alloys—II. Silver, Corros. Sci. 17 (1977) 415–417.
[54] S. Haruyama, K. Masamura, The dissolution of magnetite in acidic perchlorate solutions, Corros. Sci. 18 (1978) 263–274.
[55] I. Epelboin, M. Keddam, The dissolution and passivation of iron and iron-chromium alloys in acidified sulfate medium. Influences of pH and chromium content, Corros. Sci. 19 (1979) 1105–1112.
[56] G. Lewis, The Adsorption of benzotriazole onto cuprous oxide surface: an electrode impedance study, Corrosion 34 (1978) 424–428.
[57] J.J. Dickinson, S. Lofti, The anodic dissolution of tin in sodium hydroxide solutions, Electrochim. Acta 23 (1978) 513–519.
[58] F. Mansfeld, Don't be afraid of electrochemical techniques—but use them with care, Corrosion 44 (1988) 856–868.
[59] J.N. Murray, P.G. Moran, Influence of moisture on corrosion of pipeline steel in soils using in situ impedance spectroscopy, Corrosion 45 (1989) 34–43.
[60] J. Titz, G.H. Wanger, H. Spahn, M. Ebert, K. Juttner, W.J. Lorenz, Characterization of organic coatings on metal substrates by electrochemical impedance spectroscopy, Corrosion 46 (1990) 221–229.
[61] W.J. Lorenz, F. Mansfeld, Determination of corrosion rates by electrochemical DC and AC methods, Corros. Sci. 21 (1981) 647–672.
[62] D.D. Macdonald, Transient Techniques in Electrochemistry, Plenum Press, New York, 1977.
[63] I. Epelboin, M. Jousselin, M. Wiart, Impedance measurements for nickel deposition in sulfate and chloride electrolytes, J. Electroanal. Chem. 119 (1981) 61–71.
[64] S.A. McCluney, S.N. Popova, B.N. Popov, R. White, Comparing EIS methods for estimating the degree of delamination of organic coatings on steel, J. Electrochem. Soc. 139 (1992) 1556–1560.
[65] B.N. Popov, M.M.A. Alwohaibi, R.E. White, Using electrochemical impedance spectroscopy as a tool for organic coating solute saturation monitoring, J. Electrochem. Soc. 140 (1993) 947–951.
[66] J.R. Scully, Electrochemical impedance of organic-coated steel: correlation of impedance parameters with long-term coating deterioration, J. Electrochem. Soc. 136 (1989) 979–990.
[67] D.D. Macdonald, M.C.H. Mc Kubre, Electrochemical impedance techniques in corrosion science, in: F. Mansfeld, U. Bertocci (Eds.), Electrochemical Corrosion Testing, STP 272, ASTM International, Philadelphia, PA, 1981, pp. 110–149.
[68] A.J. Bard, L.R. Faulkner, Electrochemical Methods, Wiley, New York, 1980.
[69] F. Mansfeld, M.W. Kendig, S. Tsai, Application of acoustic emission to detection of reinforcing steel corrosion in concrete, Corrosion 38 (1982) 9–14.
[70] J.C. Padget, J.P. Moreland, Use of A.C. impedance in the study of the anticorrosive properties of chlorine-containing vinyl acrylic latex copolymers, J. Coat. Technol. 55 (1983) 39–51.
[71] M.W. Kending, F. Mansfeld, S. Tsai, Determination of the long term corrosion behavior of coated steel with AC impedance measurements, Corros. Sci. 23 (1983) 317–329.
[72] W.J. Lorenz, F. Mansfeld, Corrosion inhibition in neutral, aerated media, J. Electrochem. Soc. 132 (1985) 290–296.
[73] M.W. Kending, J.R. Scully, Basic aspects of electrochemical impedance application for the life prediction of organic coatings on metals, Corrosion 46 (1990) 22–29.
[74] S.W. Tait, Using electrochemical measurements to estimate coating and polymer film durability, J. Coat. Technol. 75 (2003) 45–50.
[75] B.S. Haran, B.N. Popov, R.E. White, Determination of hydrogen diffusion coefficient in metal hydrides by impedance spectroscopy, J. Power Sources 75 (1998) 56–63.
[76] A. Durairajan, B.S. Haran, R.E. White, B.N. Popov, Pulverization and corrosion studies of bare and cobalt-encapsulated metal hydride electrodes. *J*, Power Sources 87 (2000) 84–91.
[77] D.D. Macdonald, S.I. Smedley, Characterization of vacancy transport in passive films using low-frequency electrochemical impedance spectroscopy, Corros. Sci. 31 (1990) 667–672.
[78] D.D. Macdonald, Reflections on the history of electrochemical impedance spectroscopy, Electrochim. Acta 51 (2006) 1376–1388.
[79] D.D. Macdonald, Some advantages and pitfalls of electrochemical impedance spectroscopy, Corrosion 46 (1990) 229–242.

[80] B.B. Katemann, A. Schulte, E.J. Calvo, M. Koudelka-Hep, W. Schuhmann, Localized electrochemical impedance spectroscopy with high lateral resolution by means of alternating current scanning electrochemical microscopy, Electrochem. Commun. 4 (2002) 134–138.
[81] K. Eckhard, H. Shin, B. Mizaikoff, W. Schuhmann, C. Kranz, Alternating current (AC) impedance imaging with combined atomic force scanning electrochemical microscopy (AFM-SECM), Electrochem. Commun. 9 (2007) 1311–1315.
[82] A. Schulte, S. Belger, M. Etienne, W. Schuhmann, Imaging localized corrosion of NiTi shape memory alloys by means of alternating current scanning electrochemical microscopy, Mater. Sci. Eng. A378 (2002) 523–526.
[83] P.M. Diakowski, A.S. Baranski, Positive and negative AC impedance feedback observed above conductive substrates under SECM conditions, Electrochim. Acta 52 (2006) 854–862.
[84] I. Annergren, F. Zou, D. Thierry, Application of localized electrochemical techniques to study kinetics of initiation and propagation during pit growth, Electrochim. Acta 44 (1999) 4383–4393.
[85] S. Ningshen, U.K. Mudali, R. Baldev, Corrosion assessment of nitric acid grade austenitic stainless steels, Corros. Rev. 51 (2009) 493–531.
[86] C. Blanc, M.E. Orazem, N. Pebere, B. Tribollet, V. Viver, S. Wu, The origin of the complex character of the ohmic impedance, Electrochim. Acta 55 (2010) 6313–6321.
[87] S. Wu, M.E. Orazem, B. Tribollet, V. Vivier, Impedance of a disk electrode with reactions involving an adsorbed intermediate: experimental and simulation analysis, J. Electrochem. Soc. 156 (2009) C214–C221.
[88] L.A. Schneider, D. Kramer, A. Wokaun, G.G. Scherer, Spatially resolved characterization of PEFCs using simultaneously neutron radiography and locally resolved impedance spectroscopy, Electrochem. Commun. 7 (2005) 1393–1397.
[89] S. Lima-Neto, J.P. Farias, L.F. Herculano, H.C. de Miranda, W.S. Arujo, J.B. Jorcin, N. Pebere, Determination of the sensitized zone extension in welded ISI 304 stainless steel using non-destructive electrochemical techniques, Corros. Sci. 50 (2008) 1149–1155.
[90] G. Baril, C. Blanc, M. Kedam, N. Pebere, Local electrochemical impedance spectroscopy applied to the corrosion behavior of an AZ91 magnesium alloy, J. Electrochem. Soc. 150 (2003) B488–B493.
[91] R. Oltra, V. Vignal, Recent advances in local probe techniques in corrosion research—analysis of the role of stress on pitting sensitivity, Corros. Sci. 49 (2007) 158–165.
[92] V.M. Huang, S. Wu, M.E. Orazem, N. Pebere, B. Tribollet, V. Vivier, Local electrochemical impedance spectroscopy: a review and some recent developments, Electrochim. Acta 56 (2011) 8048–8057.
[93] F. Mansfeld, The use of electrochemical impedance spectroscopy (EIS) for the study of corrosion protection by polymer coatings—a review, J. Appl. Electrochem. 25 (1995) 187–202.
[94] S. Skale, V. Dolecek, M. Slemnik, Substitution of the constant phase element by Warburg impedance for protective coatings, Corros. Sci. 49 (2007) 1045–1055.
[95] E. Cano, D. Laufente, D.M. Bastidas, Use of EIS for the evaluation of the protective properties of coatings for metallic cultural heritage: a review, J. Solid State Electrochem. 38 (2010) 381–391.
[96] K. Darowicki, S. Krakowiak, P. Slepski, The time dependence of pit creation impedance spectra, Electrochem. Commun. 6 (2004) 860–866.
[97] S. Krakowiak, H. Darowicki, P. Slepski, Impedance of metastable pitting corrosion, J. Electroanal. Chem. 575 (2005) 33–38.

CHAPTER 6

Galvanic Corrosion

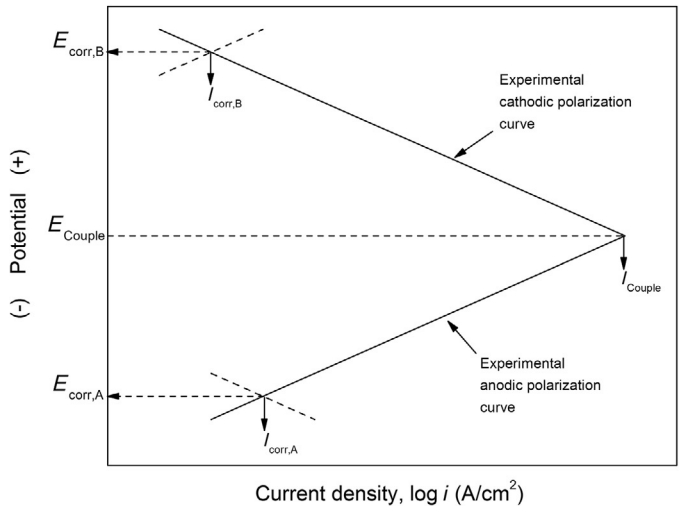

Chapter Contents

Corrosion Engineering
http://dx.doi.org/10.1016/B978-0-444-62722-3.00006-9

6.1 DEFINITION OF GALVANIC CORROSION

The potential difference between two metals in contact through a conducting medium produces electron flow. The metal with a more negative potential preferentially corrodes. The more positive metal acts as a cathode and is cathodically protected by the more negative metal, which becomes the anode. Because the driving force is the potential difference, this form of corrosion is called galvanic corrosion. Steel fasteners in an aluminum sheet, solder on a copper pipe, and stainless steel with galvanized steel are examples of galvanically coupled dissimilar metals. Galvanic corrosion also occurs when the same metal is in contact with an electrolyte at two different concentrations or with different aeration levels (differential aeration cell). Soil with varying salinity or pH, in contact with a buried iron pipe, creates galvanic cells. The metal corrosion rate is determined by the established potential difference, soil conductivity, and relative anodic and cathodic area.

6.2 GALVANIC SERIES

The reversible potentials listed for metals in Table 6.1 represent the half-cell potentials for each metal with respect to the standard hydrogen reference electrode [1–3].

Table 6.1 Standard emf Series for Metals

	Metal/Metal-Ion Equilibrium	Electrode Potential vs. SHE at 25 °C (V)
Noble or Cathodic	Au^{3+}/Au	1.50
	Pt^{2+}/Pt	1.20
	Cu^{2+}/Cu	0.34
	H^{+}/H_2	0.00
	Sn^{2+}/Sn	−0.14
	Ni^{2+}/Ni	−0.25
	Cd^{2+}/Cd	−0.40
	Fe^{2+}/Fe	−0.44
	Zn^{2+}/Zn	−0.76
	Al^{3+}/Al	−1.66
Active or Anodic	Mg^{2+}/Mg	−2.36

The reversible potentials can be used to predict the corrosion tendency of the metal when the metal and the electrolyte are under standard thermodynamic conditions described in Chapter 2, Section 2.12.2. Table 6.1 is written as reduction reactions following the guidelines suggested by the International Union of Pure and Applied Chemistry (IUPAC) during the Stockholm Convention in 1953. The procedure for estimating half-cell potential is presented in Chapter 2. In an electrochemical cell, the electrode with a smaller standard potential in Table 6.1 undergoes oxidation and transfer electrons to the electrode with a larger standard potential, which is reduced at the interface. In redox systems, the electrodes, such as $Au|Au^{3+}$ or $Pt|Pt^{2+}$, are positive with respect to the SHE and are strong oxidizers. These electrodes accept electrons from the other half-cell that is more active and undergoes rapid oxidation. As a result of charge transfer at both interfaces, the redox system composition will change and the electrode potentials will no longer correspond to their standard values. A new thermodynamic equilibrium will be established when the electrode potentials become equal after the changes in composition. Electrolyte composition and temperature variation may reverse corrosion tendencies.

Galvanized steel is a common example of galvanic coupling where steel (Fe), with a standard electrode potential of -0.440 V vs. SHE, is cathodically protected by zinc, which has a more active standard electrode potential of -0.763 V. Obviously, zinc is not a corrosion-resistant metal and cannot be classified as a barrier coating. It protects steel from corrosion through its sacrificial properties. Because zinc is less noble than iron in terms of the standard electrode potentials, it acts as an anode. The sacrificial anode (zinc) is continuously consumed by anodic dissolution reaction and protects the underlying metal (iron in steel) from corrosion. In practice, sacrificial anodes are comprised of zinc, magnesium alloys, or aluminum.

Figure 6.1 shows the corrosion potentials vs. saturated calomel electrode (SCE) of various metals and alloys controlled by electrochemical kinetic parameters such as Tafel slope and exchange current density [3,4]. The potentials listed in Fig. 6.1 are not thermodynamically controlled [4]. They depend on electrochemical kinetic parameters of the cathodic reaction (hydrogen evolution or oxygen reduction) and metal dissolution (anodic reaction). The metal with the more active corrosion potential (more negative) will exhibit accelerated corrosion, while metal corrosion for the less active potential (more positive) will slow down. The hydrogen evolution exchange current density, the exchange current density of the corroding metal, Tafel slopes, electroactive surface, and temperature are some of the factors that control metal corrosion rate. Hence, the corrosion potentials shown in Fig. 6.1 should not be confused with the standard emf series potentials for metals given in Table 6.1. Corrosion potential is obtained by the polarization of two or more half-cell reactions on a corroding surface. The potentials in the galvanic series are measured under real corrosion conditions and are listed with respect to SCE. The dark boxes in Fig. 6.1 indicate the active behavior for listed active-passive alloys. The values in the galvanic series cannot be used to reliably predict

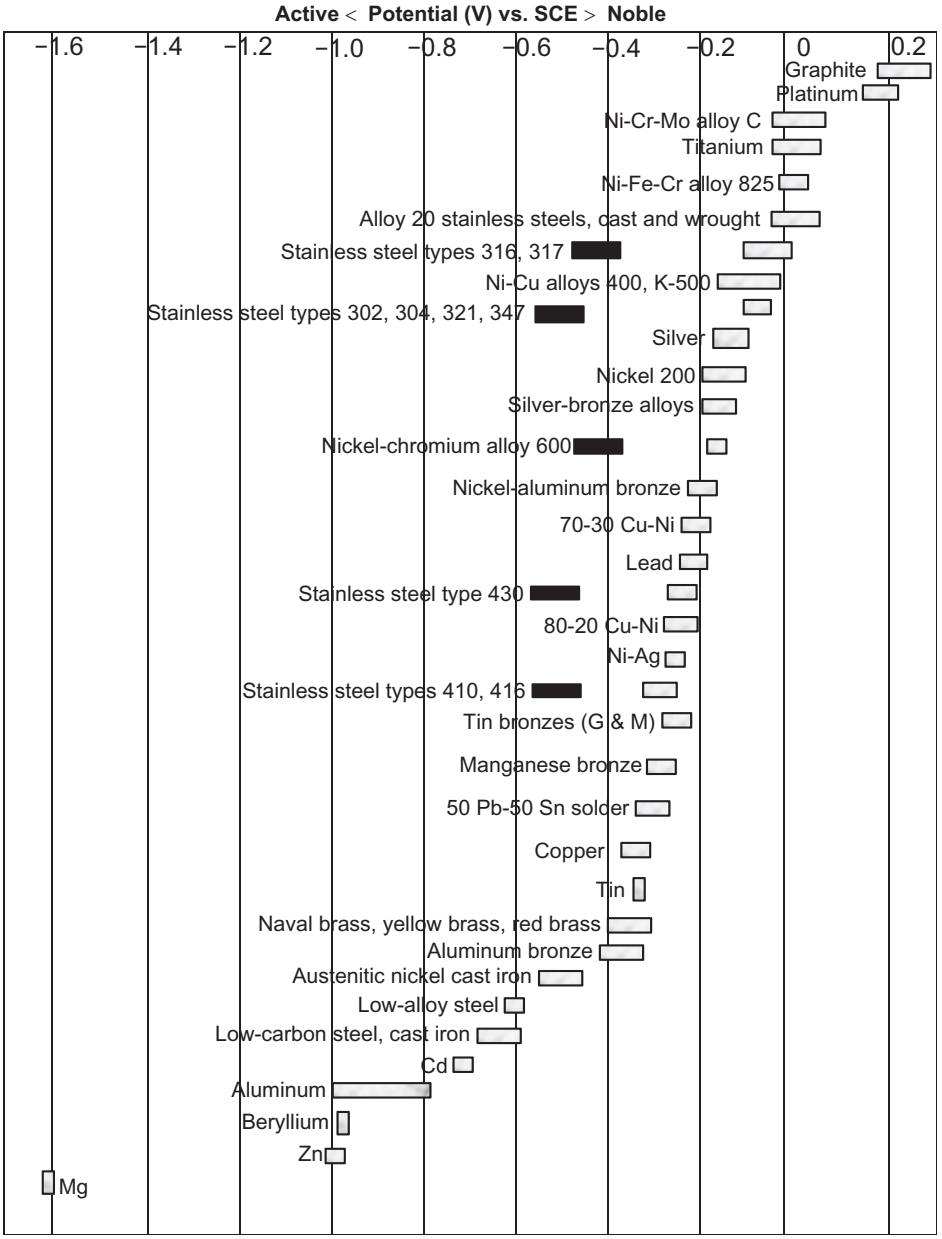

Fig. 6.1 Galvanic series in sea water. The dark boxes indicate the active behavior for listed active-passive alloys [4]. *Reprinted with permission of ASM International, Materials Park, OH. www.asminternational.org*.

corrosion behavior or extent (rate) of corrosion. They only qualitatively indicate galvanic corrosion tendency. As a general rule, the most active metal (that with the smaller or more negative corrosion potential) will exhibit accelerated corrosion rate, while the less active metal (that with the larger or more positive corrosion potential) will exhibit slower corrosion rate.

6.3 EXPERIMENTAL MEASUREMENTS

6.3.1 Polarization in galvanic couples

Galvanic current, I_{couple}, and corrosion potential, E_{couple}, are located at the intersection of the cathodic and anodic polarization curves shown in Fig. 6.2. In the absence of polarization exerted by an external power source, galvanic current polarizes the metal surface. Mixed potential theory applies to galvanic couples as in the case of single metal polarization. $E_{corr,A}$ and $E_{corr,B}$ represent the uncoupled anode and cathode corrosion potentials.

The anode and cathode corrosion currents, $I_{corr,A}$ and $I_{corr,B}$, respectively, are estimated at the intersection of the cathode and anode polarization of uncoupled metals A and B. Conventional electrochemical cells as well as the polarization systems described in Chapter 5 are used to measure electrochemical kinetic parameters in galvanic couples. Galvanic corrosion rates are determined from galvanic currents at the anode. The rates are controlled by electrochemical kinetic parameters like hydrogen evolution exchange current density on the noble and active metal, exchange current density of the corroding metal, Tafel slopes, relative electroactive area, electrolyte composition, and temperature.

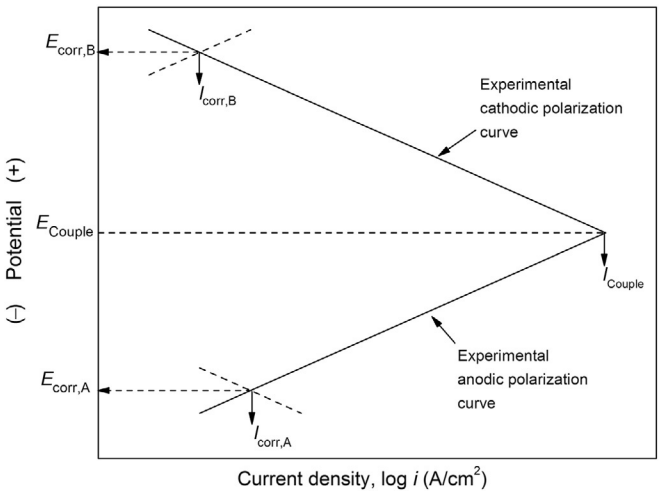

Fig. 6.2 Experimental polarization of anode and cathode in a galvanic couple.

Other factors that control galvanic corrosion are electrolyte properties such as pH, conductivity, temperature, geometric factors, anodic and cathodic area, distance between anode and cathode, and electrode location and structure geometry (two-dimensional or three-dimensional). Stray currents in the vicinity of the structure and mechanical stress also play an important role in galvanic corrosion. The case studies outlined in this chapter explain the factors that control galvanic corrosion. Composite polarization diagrams are available in the literature [5,6] to predict galvanic current. They consist of potentiostatic cathodic and anodic polarization curves for different metals and alloys in deaerated 1 N H_2SO_4 and aerated 3% NaCl. Galvanic corrosion prediction for long periods of time from polarization data obtained in short periods of time is not accurate due to surface conditions and impurities. It has been shown that long-term galvanic behavior prediction in sea water improves if the initial polarization experiment on the galvanic system is performed at low scan rates (in mV/s) [6].

6.3.2 Zero resistance ammeter

When two dissimilar metals in an aqueous environment are connected (or short circuited), it results in surface polarization. The galvanic current, I_{couple}, cannot be measured by placing a conventional ammeter in the circuit due to voltage drop across the ammeter. As shown in Fig. 6.3, the ammeter separates the anode and the cathode potentials. This results in a measurable current, I, smaller than the galvanic couple current,

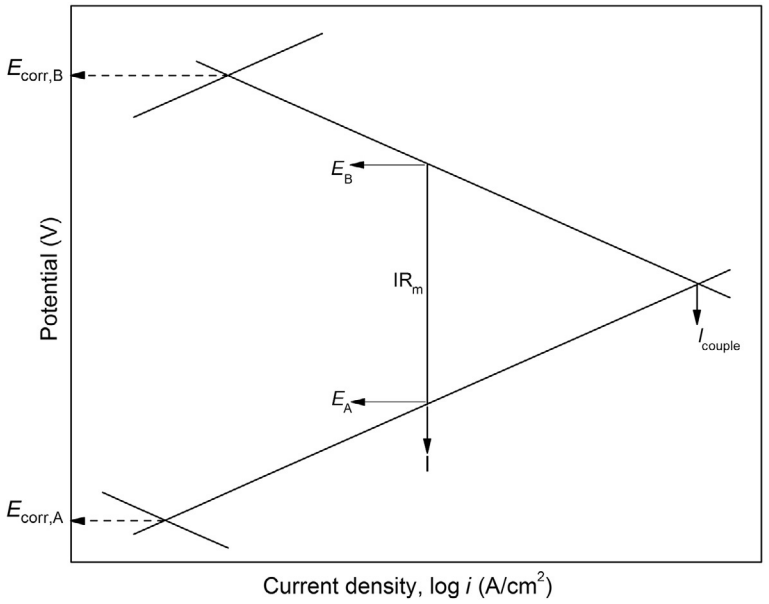

Fig. 6.3 Potential difference between the cathode and anode when measuring a galvanic current, I, with ammeter of resistance, R_m.

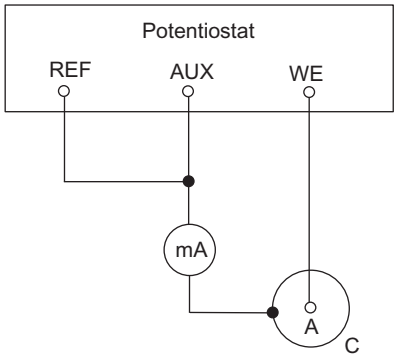

Fig. 6.4 Schematic of zero-resistance ammeters capable to measure the galvanic current.

I_{couple}. A zero-resistance ammeter (ZRA) can estimate the desired I_{couple} [7]. ZRA is based on the potential difference established when two metals (or alloys) are electrically connected in a conducting medium, producing electron flow that causes the metal (or alloy) with a more negative potential in the galvanic series to preferentially corrode. The more positive metal (or alloy) becomes a cathode and is protected by the sacrificial anode. The ZRA is a current-to-voltage converter that produces a voltage proportional to the current between the input terminals and creates a zero voltage drop in the external circuit. Because the cathode, anode, and galvanic polarization behavior varies with time, the measured current must be continuously changed to maintain the cathode and anode potential difference at zero.

A schematic of a commercial potentiostat capable of continuously measuring galvanic current is shown in Fig. 6.4. When the anodic reaction is stable, the galvanic current monitors the response of the cathodic reaction. When the cathodic reaction is stable, the anodic reaction response is monitored to control anode fluctuations. The potentiostat monitors the difference between the counter electrode (AUX) and reference electrode (REF) terminals in Fig. 6.4 and corrects any change by varying the current between the AUX and working electrode (WE) terminals [7]. The zero-resistance experiment is performed by short circuiting the REF and AUX terminals, enabling the potentiostat to control the potential difference between the cathode, C, and anode, A [8]. When the potential difference is zero, the potentiostat will automatically display galvanic current, I_{couple}.

6.3.3 Scanning vibrating electrode technique

The scanning vibrating electrode technique (SVET) uses a microelectrode capable of measuring potential gradients in the corrosion solution near localized corrosion. It locates and measures corrosion at specific points of the corroding surface [9]. This technique performs in situ localized corrosion measurements occurring on the surface. During the measurement, the microelectrode vibrates perpendicular to the surface. The tip of the

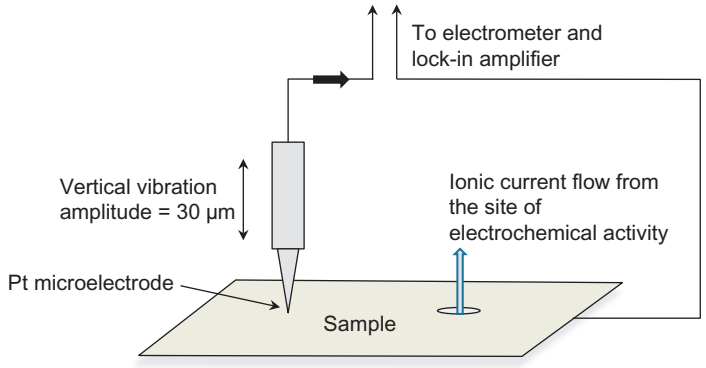

Fig. 6.5 Schematic representation of SVET measurement.

electrode is positioned as shown in Fig. 6.5, a few hundred microns above the sample. A sinusoidal AC potential signal is generated and recorded at the vibration amplitude maximum. Next, the AC signal is measured by a lock-in amplifier at the probe vibration frequency. By using a simple calibration procedure, the measured DC potential gradients in solution are converted to current density [9]. Initially, SVET was developed to measure the extracellular currents near living cells [10,11]. Isaacs later developed a procedure to study 304 stainless steel stress corrosion cracking [12] and corrosion inhibition by cerium salts [13]. The SVET technique has been successfully used to measure coil-coated steel corrosion [14,15].

6.4 PREVENTION OF GALVANIC CORROSION

The following guidelines have been used to minimize or prevent galvanic corrosion [16–18]:

(i) Select materials similar in galvanic series.
(ii) Minimize cathode-anode area ratio to minimize galvanic coupling and galvanic current density.
(iii) Apply a cathode coating to decrease available area for cathodic reactions.
(iv) Do not coat the anode. Severe corrosion may occur on coating defects that may cause pitting or crevice corrosion.
(v) Insulate dissimilar metals to eliminate galvanic coupling.
(vi) Use environmentally friendly sacrificial materials, such as Zn or Sn, to protect the galvanic assembly. Replaceable anodes are advisable using this approach. Only the corroded anodes need to be replaced.
(vii) Use cathodic inhibitors to combat cathodic depolarization reactions, minimizing galvanic corrosion.

6.5 THEORETICAL ASPECTS

6.5.1 Effect of exchange current density on galvanic current in Fe-Zn galvanic couple

Galvanized steel is a common galvanic coupling where steel (Fe), with standard electrode potential of −0.44 V vs. SHE, is cathodically protected by zinc with a lower (more active) standard electrode potential of −0.76 V vs. SHE. In this section we will use technical zinc, which contains 2% iron, to explain zinc corrosion kinetics when electrically connected with iron. The iron impurity occupies 2% of the zinc surface and establishes a galvanic couple with zinc when immersed in an acidic corrosive solution. Pure zinc and iron corrosion kinetics can explain the corrosion kinetics in the couple. The corrosion potential of pure zinc is between zero, according to mixed potential theory (the standard hydrogen electrode potential), and the zinc equilibrium potential of −0.76 V vs. SHE. Because the exchange current densities for zinc and hydrogen evolution on zinc are $\sim 10^{-5}$ and 10^{-10} A/cm^2, respectively, the zinc corrosion potential at a pH of 0 reduces to its equilibrium potential. Using the hydrogen overpotential of −0.76 V vs. SHE on zinc, the Tafel constants for hydrogen evolution on zinc at a pH of 0 from Table 3.2 in Chapter 3 of $a = -1.24$ and $b_c = -0.12$ V/decade and by substituting these values into the Tafel equation:

$$\eta = a + b_c \log i_{H_{Zn}} \tag{3.32}$$

the hydrogen evolution current density and corrosion current of pure zinc $i_{H_{Zn}} = I_{corr,Zn} = 10^{-4}$ A/cm^2 is calculated. For pure iron, the exchange current density of iron dissolution is $\sim 10^{-9}$ A/cm^2 with a standard equilibrium potential of −0.44 V vs. SHE. Compared to zinc, hydrogen evolution on iron is four orders of magnitudes higher, reaching a value of $\sim 10^{-6}$ A/cm^2. High hydrogen evolution on iron causes the corrosion potential to shift toward the hydrogen evolution equilibrium potential. Iron acts as a hydrogen electrode in acidic media due to its high hydrogen evolution current density and low iron dissolution exchange current density. Assuming technical zinc is immersed in an acidic corroding solution with a pH of 0 and an activity, $a_{Zn^{2+}}$, of 1, hydrogen evolution occurs on both zinc and iron impurities on the zinc surface. The total hydrogen evolution and zinc dissolution is controlled by hydrogen evolution reaction kinetics on zinc and 2% iron. Using hydrogen evolution kinetic data for zinc and iron in Table 3.2, the following equations are obtained for the hydrogen evolution overpotentials on zinc and iron:

$$\begin{aligned} \eta_{H_{Zn}} &= -1.24 - 0.12 \log i_{H_{Zn}} \\ \eta_{H_{Fe}} &= -0.70 - 0.12 \log i_{H_{Fe}} \end{aligned} \tag{6.1}$$

Note that hydrogen evolution occurs on zinc and iron on 98% and 2% of the entire surface area, respectively. Hydrogen evolution on the total surface area and the corrosion rate I_{corr} is:

$$I_{corr} = i_{H_2} = 0.98\, i_{H_{Zn}} + 0.02\, i_{H_{Fe}} \tag{6.2}$$

Assuming the entire specimen surface is equipotential, hydrogen evolution on iron can be expressed through hydrogen evolution on zinc:

$$\eta_{H_{Fe}} = \eta_{H_{Zn}} = E_{corr,Zn} - e_{eq,H^+|H_2} \tag{6.3}$$

Applying the zinc and iron kinetic parameters to the Tafel equation obtains:

$$-1.24 - 0.12\log i_{H_{Zn}} = -0.70 - 0.12\log i_{H_{Fe}} \tag{6.4a}$$

or,

$$\begin{aligned} &\frac{i_{H_{Fe}}}{i_{H_{Zn}}} = 10^{-((0.70-1.24)/0.12)} = 10^{4.5} \\ &I_{corr} = \left(0.98 i_{H_{Zn}} + 0.02 \times 10^{4.5} i_{H_{Zn}}\right) = 633 i_{H_{Zn}} \\ &\text{or} \\ &I_{corr} = 633 \times 10^{-4}\,\text{A/cm}^2 \end{aligned} \tag{6.4b}$$

The above corrosion increase is smaller due to formation of inter metallic compounds between iron and zinc.

Case Study 6.1—Effect of the Ratio of the Surface Area of the Cathode to the Surface Area of the Sacrificial Anode on Galvanic Corrosion of the Tin-Platinum Galvanic Couple

Hydrogen evolution rate on the tin surface increases when tin is coupled with inert platinum. The observed increase in Fig. 6.6 results from the exchange current density difference of the coupled metals. The intersection between the tin dissolution polarization curve and the polarization curve for hydrogen evolution on tin results in $I_{corr,Sn}$. When equal surface area of tin (1 cm^2) and platinum (1 cm^2) are coupled, the sum of the rates of hydrogen evolution reactions on both metals is equal to the total rate of hydrogen evolution.

Because hydrogen evolution exchange current density is very low (10^{-8} A/cm^2) on Sn and very high on platinum (10^{-3} A/cm^2), the total rate of hydrogen evolution is approximately equal to the hydrogen evolution on platinum. The polarization curves for hydrogen evolution on 1 and 10 cm^2 are marked as Sn-Pt (1 cm^2) and Sn-Pt (10 cm^2) in Fig. 6.6. The figure clearly illustrates that coupling tin to platinum shifts the corrosion potential of Sn from $E_{corr,Sn}$ to $E_{corr,\underline{Sn}-Pt(1\,cm^2)}$ and shifts the corrosion rate of Sn from $I_{corr,Sn}$ to $I_{corr,\underline{Sn}-Pt(1\,cm^2)}$. The rate of hydrogen evolution on Sn decreases from $I_{corr,Sn}$ to $I_{H_2,\underline{Sn}-Pt(1cm^2)}$. The rate of hydrogen evolution on 1 cm^2 Pt is equal to the corrosion current of Sn when coupled with 1 cm^2 of platinum, $I_{corr,\underline{Sn}-Pt(1\,cm^2)}$. 10 cm^2 platinum coupled with 1 cm^2 tin increases the hydrogen current magnitude,

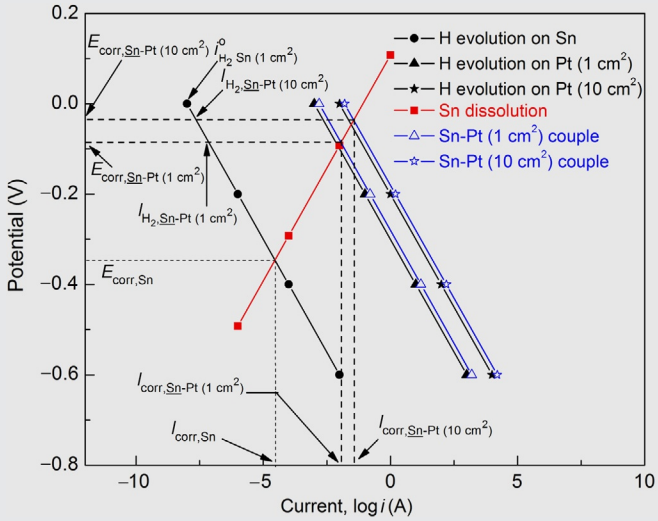

Fig. 6.6 Effect of the cathode-sacrificial anode surface area on galvanic corrosion of a tin-platinum galvanic couple.

resulting in Sn corrosion rate increase to $I_{\text{corr},\underline{\text{Sn}}-\text{Pt}(10\,\text{cm}^2)}$. Hydrogen evolution on Sn, as shown in Fig. 6.6, decreases to $I_{\text{H}_2,\underline{\text{Sn}}-\text{Pt}(10\,\text{cm}^2)}$. Hydrogen evolution on tin coupled with 1 cm^2 of platinum is estimated at the intersection of line for tin $i^{\text{o}}_{\text{H}_2,\text{Sn}(1\,\text{cm}^2)}$ and the line for couple's corrosion potential $E_{\text{corr},\underline{\text{Sn}}-\text{Pt}(1\,\text{cm}^2)}$.

Case Study 6.2—Effect of the Exchange Current Density on Galvanic Corrosion of Tin-Platinum and Tin-Gold Couples

Comparing Galvanic couples of tin-platinum and tin-gold illustrates the exchange current density effect on the overall corrosion rate. The reversible potential of $\text{Au}|\text{Au}^{3+}$ in the emf series is +1.50 V vs. SHE, more positive than $\text{Pt}|\text{Pt}^{2+}$ (+1.20 V vs. SHE).

Figure 6.7 compares the corrosion rates for tin-platinum and tin-gold galvanic couples with the following electrochemical characteristics and assumptions: hydrogen evolution exchange current densities for tin, gold, and platinum are 10^{-8}, 10^{-6}, and 10^{-3} A/cm^2, respectively. The cathodic slope (b_c) for the hydrogen evolution reaction on Sn, Pt, and Au is −0.1 V/decade. The concentration of dissolved $[\text{Sn}^{2+}]$ species is 10^{-12} M and exchange current density for Sn dissolution is 1×10^{-6} A/cm^2. Sn equilibrium potential, $e^{\text{o}}_{\text{Sn}^{2+}|\text{Sn}}$, is −0.14 V vs. SHE. Assume gold and platinum dissolution is negligible. Considering the values of exchange current densities, if equal areas of platinum and tin are coupled, the observed corrosion rate increase is greater than if equal areas of gold and tin are galvanically coupled, as shown in Fig. 6.7. The corrosion rate of a Sn-Au couple is ∼30 times smaller when compared to Sn-Pt. Higher hydrogen exchange current density on Pt contributes to the severe galvanic effect compared to gold despite gold's more positive reversible potential. Thus, only the reversible potentials cannot be

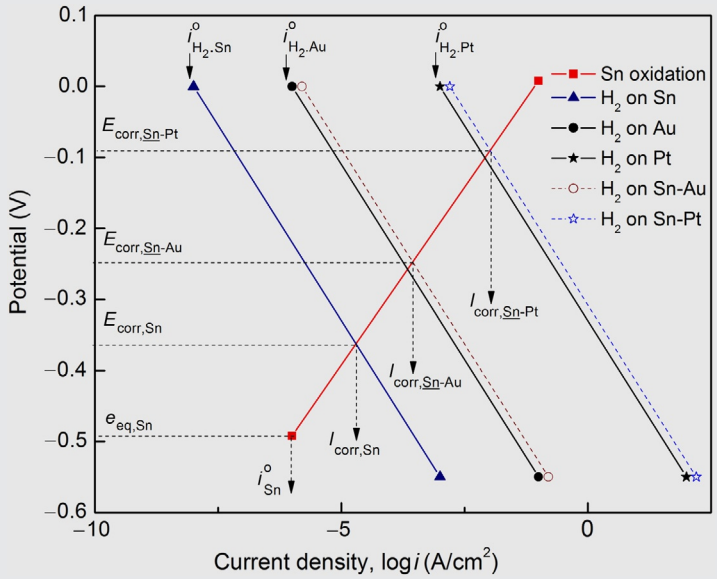

Fig. 6.7 Comparison of corrosion rates of tin-gold and tin-platinum galvanic couples.

used accurately to predict the galvanic corrosion behavior. The corrosion rate of a galvanic couple is determined by exchange current densities, the electrode potentials and the relative surface areas of both metals.

Case Study 6.3—Galvanic Corrosion between Two Corroding Metals

Mixed potential theory estimates galvanic couple corrosion for metals P and Q (Fig. 6.8). Metal P has a more positive corrosion potential and lower corrosion current, $I_{corr(P)}$, due to lower hydrogen evolution current density, $i^{o}_{H_2(P)}$. Metal Q has a more negative and active corrosion potential and corrodes at higher rates $I_{corr(Q)}$ due to higher hydrogen evolution current density of $i^{o}_{H_2(Q)}$. When P and Q are coupled, the new corrosion potential and corrosion current is established based on mixed potential theory at the point where the total oxidation rate of the metals P and Q equals their total reduction rate. The new galvanic corrosion potential and corrosion current shown in Fig. 6.8 is in between the individual corrosion potentials. When coupled, the corrosion potential and corrosion current of the more active metal Q increases to $I_{corr(P\text{-}\underline{Q})}$, while the corrosion potential and corrosion rate of metal P decreases to $I_{corr(\underline{P}\text{-}Q)}$. Galvanic current and potential calculation using mixed potential theory is outlined in Case Study 6.4.

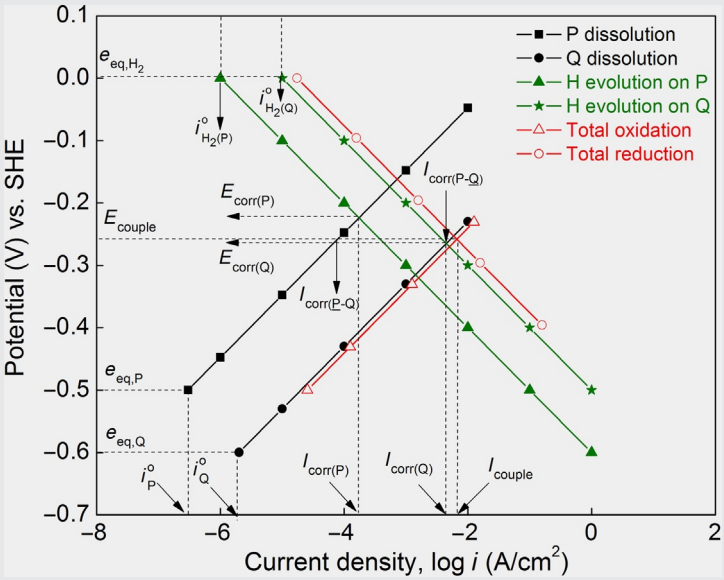

Fig. 6.8 Galvanic coupling between two corroding metals.

Under steady state conditions, mixed potential theory can be used to evaluate galvanic corrosion rate and potential. To maintain electroneutrality at the electrode interfaces, this theory requires the rate of oxidation at the anode be equal to the reduction at the cathode. Under these conditions, the potential of both electrodes is equal to the corrosion potential, while the current density represents the corrosion current density. The corrosion current of two electrically connected dissimilar metals is proportional to the galvanic corrosion current. Graphical evaluation using mixed potential theory is illustrated for two coupled corroding metals in Fig. 6.8.

Case Study 6.4—Calculation of Galvanic Current and Potential Using Mixed Potential Theory

Numerical evaluation using mixed potential theory is described for two corroding metals A and B with standard equilibrium dissolution potentials −0.36 and −0.53 V vs. SHE, respectively. The corresponding exchange current densities are 2.1×10^{-8} and 5×10^{-7} A/cm^2. The dissolved species concentrations are $[A^{2+}] = 3 \times 10^{-6}$ M and $[B^{2+}] = 0.9$ M. The exchange current densities for hydrogen evolution reaction on A and B are $i^{\circ}_{H,A} = 4 \times 10^{-6}$ and $i^{\circ}_{H,B} = 1 \times 10^{-6}$ A/cm^2, respectively. Assume all Tafel constants are ±0.1 V/decade. Mixed potential theory in this example is used to calculate:

(a) Corrosion current and corrosion potential of A and B when not coupled.
(b) Corrosion current and corrosion potential when coupled.

(c) Galvanic corrosion rate of the metal that corrodes at a higher rate.
(d) Effect of two dissolved species concentration while changing the concentration of A from 3×10^{-6} to 1 M.

Solution:

(a) Corrosion current and the corrosion potential of metals A and B when they are not coupled.

(i) Calculation of anode equilibrium potentials:

$$\text{Cathode standard potential}: e_c^o = 0.0\,\text{V vs. SHE}$$

$$\text{Anode equilibrium potential}: e_{eq,a(A)} = e_A^o + \frac{0.059}{2}\log\left(3 \times 10^{-6}\right) = -0.523\,\text{V}$$

$$e_{eq,a(B)} = e_B^o + \frac{0.059}{2}\log(0.9) = -0.531\,\text{V}$$

(ii) Corrosion current and the corrosion potential for metal A
Anodic polarization:

$$E_{corr,A} - (-0.523) = 0.1\log\left(\frac{I_{corr,A}}{2.1 \times 10^{-8}}\right) \tag{6.5}$$

Cathodic polarization:

$$E_{corr,A} - 0 = -0.1\log\left(\frac{I_{corr,A}}{4 \times 10^{-6}}\right) \tag{6.6}$$

Solving Eqs. (6.5) and (6.6):

$$E_{corr,A} = -0.148\,\text{V},\ I_{corr,A} = 1.21 \times 10^{-4}\,\text{A/cm}^2$$

(iii) Corrosion current and the corrosion potential for metal B
Anodic polarization:

$$E_{corr,B} - (-0.531) = 0.1\log\left(\frac{I_{corr,B}}{5 \times 10^{-7}}\right) \tag{6.7}$$

Cathodic polarization:

$$E_{corr,B} - 0 = -0.1\log\left(\frac{I_{corr,B}}{10^{-6}}\right) \tag{6.8}$$

Solving Eqs. (6.7) and (6.8): $E_{corr,B} = -0.25\,\text{V}$, $I_{corr,B} = 3.16 \times 10^{-4}\,\text{A/cm}^2$

(b) Total corrosion current and the corrosion potential when A and B are coupled:
When the metals are coupled, a new corrosion potential and its corresponding corrosion current is established based on the mixed potential theory at the point where the total oxidation rate of A and B equals the total reduction rate.

The total couple cathode exchange current density is the sum of the corresponding exchange current densities for A and B:

$$i_{couple,c}^o = 4 \times 10^{-6} + 10^{-6} = 5 \times 10^{-6}\,\text{A/cm}^2$$

Cathodic polarization:

$$E_{\text{corr, couple}} - 0 = -0.1 \log \left(\frac{I_{\text{corr, couple}}}{i^{\text{o}}_{\text{couple, c}}} \right)$$

$$E_{\text{corr, couple}} = -0.1 \log \left(I_{\text{corr, couple}} \right) + 0.1 \log \left(5 \times 10^{-6} \right) \tag{6.9}$$

Considering the equilibrium potential of metal A, $e_{\text{eq,a(A)}} = -0.523\,\text{V}$ vs. SHE, is one point on the galvanic couple polarization line, one can calculate the current for metal B at this potential by using the overvoltage between the anode equilibrium potential of −0.523 V and $e_{\text{eq,a(B)}} = -0.531\,\text{V}$ vs. SHE applying to Eq. (6.7).

$$\eta = -0.523 - (-0.531) = 0.1 \log \left(\frac{i_{\text{B}}}{5 \times 10^{-7}} \right) \rightarrow i_{\text{B}} = 6.01 \times 10^{-7}\,\text{A/cm}^2$$

(b_1) Total anodic current of the couple at −0.523 vs. SHE:

$$i_{\text{T, A}} = i^{\text{o}}_{\text{A}} + i_{\text{B}} = 2.1 \times 10^{-8} + 6.01 \times 10^{-7} = 6.22 \times 10^{-7}\,\text{A/cm}^2$$

The anodic polarization line is:

$$E_{\text{corr, couple}} - e_{\text{A}} = 0.1 \log \left(\frac{I_{\text{corr, couple}}}{i_{\text{TA}}} \right)$$

$$E_{\text{corr, couple}} - (-0.523) = 0.1 \log \left(I_{\text{corr, couple}} \right) - 0.1 \log \left(6.22 \times 10^{-7} \right) \tag{6.10}$$

The couple corrosion potential and galvanic current is calculated at the anodic and cathodic polarization curve intersection. From Eqs. (6.9) and (6.10):
$E_{\text{corr,couple}} = -0.216\,\text{V}$ vs. SHE and $I_{\text{corr,couple}} = 7.23 \times 10^{-4}\,\text{A/cm}^2$

(c) Which metal will corrode at a higher rate when coupled? (see Fig. 6.8).

By substituting $E_{\text{corr,couple}} = -0.216\,\text{V}$ into Eqs. (6.5) and (6.7), one estimates the corrosion rates of A and B after coupling:

$$(-0.216) - (-0.523) = 0.1 \log \left(\frac{I_{\text{corr, }\underline{\text{A}}-\text{B}}}{2.1 \times 10^{-8}} \right) \Rightarrow I_{\text{corr, }\underline{\text{A}}-\text{B}} = 2.47 \times 10^{-5}\,\text{A/cm}^2$$

$$(-0.216) - (-0.531) = 0.1 \log \left(\frac{I_{\text{corr, A}-\underline{\text{B}}}}{5 \times 10^{-7}} \right) \rightarrow I_{\text{corr, A}-\underline{\text{B}}} = 7.06 \times 10^{-4}\,\text{A/cm}^2$$

Because the corrosion potential of B is more negative and its corrosion current is higher than that of metal A. *Metal B corrodes at a higher rate when coupled with A.*

(d) Estimate the effect of dissolved species concentration while changing the concentration of A from 3×10^{-6} to 1 M.

When A and B are uncoupled:

$$\text{On the cathode} : e^{\text{o}} = 0.0\,\text{V vs. SHE}$$

$$\text{On the anode} : e_{\text{eq, a(A)}} = e^{\text{o}}_{\text{A}} + \frac{0.059}{2} \log (1) = -0.36\,\text{V}$$

$$\text{Anodic polarization curve} : E_{\text{corr, A}} - (-0.36) = 0.1 \log \left(\frac{I_{\text{corr, A}}}{2.1 \times 10^{-8}} \right) \tag{6.11}$$

$$\text{Cathode polarization curve}: E_{\text{corr,A}} - 0 = -0.1\log\left(\frac{I_{\text{corr,A}}}{4\times10^{-6}}\right) \tag{6.12}$$

Solving Eqs. (6.11) and (6.12) obtains the corrosion potential and current for A when the concentration of metal A increases to 1 M:

$$E_{\text{corr,A}} = -0.066\,\text{V} \text{ and } I_{\text{corr,A}} = 1.83\times10^{-5}\,\text{A/cm}^2$$

In summary, by increasing the concentration of A, both the equilibrium and the corrosion potential increase (more anodic) while the corrosion rate of A decreases.
When metal A and metal B are coupled, there is no change on the cathode:

$$E_{\text{corr, couple}} = -0.1\log\left(I_{\text{corr, couple}}\right) + 0.1\log\left(5\times10^{-6}\right) \tag{6.9}$$

At the anode at $e_{\text{eq,a(A)}} = -0.36\,\text{V}$ vs. SHE, use Eq. (6.7)

$$-0.36-(-0.531) = 0.1\log\left(\frac{i_{\text{B}}}{5\times10^{-7}}\right);$$
$$i_{\text{B}} = 2.56\times10^{-5}\,\text{A/cm}^2 \text{ at } e_{\text{eq,a(A)}} = -0.36\,\text{V vs. SHE.}$$

$$\begin{aligned} i_{\text{T,A}} &= i_{\text{A}}^{\text{o}} + i_{\text{B}} \\ &= 2.1\times10^{-8} + 2.56\times10^{-5} \\ &= 2.56\times10^{-5} \end{aligned}$$

Therefore

$$E_{\text{corr, couple}} - e_{\text{eq,a(A)}} = 0.1\log\left(\frac{I_{\text{corr, couple}}}{i_{\text{T,A}}}\right)$$

$$E_{\text{corr, couple}} - (-0.36) = 0.1\log\left(I_{\text{corr, couple}}\right) - 0.1\log\left(2.56\times10^{-5}\right) \tag{6.13}$$

Solving Eqs. (6.9) and (6.13)
$E_{\text{corr,couple}} = -0.215$ V and $I_{\text{corr,couple}} = 7.06\times10^{-4}\,\text{A/cm}^2$

Case Study 6.5—Evaluation of Corrosion Current in Active-Passive Metal

Mixed potential theory is used to estimate the galvanic current and the galvanic potential in an active-passive metal that passivates at potentials less noble than the reversible hydrogen potential. A galvanic couple between titanium and platinum of equal area of 1 cm^2 is exposed to 1 M HCl. The electrochemical parameters for the active-passive alloy are $e_{\text{eq,Ti}} = -1.63\,\text{V}$ vs. SHE; anodic Tafel, $b_{\text{a,Ti}} = 0.1$; exchange current density, $i_{\text{Ti}}^{\text{o}} = 10^{-7}\,\text{A/cm}^2$; passivation potential, $E_{\text{pp}} = -0.73$ V; passivation current, $I_{\text{pass}} = 10^{-2}\,\text{A/cm}^2$; transpassive potential, $E_{\text{tr}} = 0.4$ V vs. SHE; and activity of dissolved species $[\text{Ti}^{2+}] = 1$ M. The exchange current densities, $i^{\text{o}}_{\text{H}^+|\text{H}_2}$, on platinum and titanium are 10^{-3} and $10^{-8}\,\text{A/cm}^2$, respectively. The cathodic Tafel slopes for both platinum and titanium are $b_c = -0.14$ V/decade.

Solution:

The corrosion rate and corrosion potential are estimated using electrochemical kinetic parameters such as exchange current density for hydrogen evolution reaction on titanium and platinum, reversible potentials, and cathodic and anodic slopes.

(a) Ti corrosion potential and rate for Ti metal using the Tafel equation:

$$\text{Standard cathode potential}: e_c^o = 0.0\,\text{V vs. SHE}$$

$$\text{Equilibrium anode potential}: e_{eq,a(Ti)} = e_{Ti}^o + \frac{0.059}{2}\log(1) = -1.63\,\text{V vs. SHE}$$

$$\text{Anodic polarization curve}: E_{corr,Ti} - (-1.63) = 0.1\log\left(\frac{I_{corr,Ti}}{10^{-7}}\right) \tag{6.14}$$

$$\text{Cathodic polarization curve}: E_{corr,Ti} - 0 = -0.14\log\left(\frac{I_{corr,Ti}}{10^{-8}}\right) \tag{6.15}$$

Solving Eqs. (6.14) and (6.15), the corrosion potential and current are:

$$E_{corr,Ti} = -1.009\ \text{V vs. SHE};\ I_{corr,Ti} = 0.162\,\text{A/cm}^2$$

(b) Galvanic potential and current in the platinum-titanium couple:
According to mixed potential theory, the hydrogen evolution exchange current density on the cathode is the sum of the hydrogen evolution on platinum and hydrogen evolution on titanium: $i_{c,couple} = 10^{-3} + 10^{-8}\ \text{A/cm}^2 = 10^{-3}\ \text{A/cm}^2$

$$\text{Cathodic polarization curve}: E_{corr,couple} - 0 = -0.14\log\left(\frac{I_{corr,couple}}{i_{c,couple}}\right)$$

$$E_{corr,couple} = -0.14\log\left(I_{corr,couple}\right) + 0.14\log\left(10^{-3}\right) \tag{6.16}$$

Anodic polarization curve, Eq. (6.14):

$$E_{corr,couple} - (-1.63) = 0.1\log\left(I_{corr,couple}\right) - 0.1\log\left(10^{-7}\right) \tag{6.17}$$

Subsituting the passivation current of $10^{-2}\ \text{A/cm}^2$ into Eq. (6.16), the couple corrosion potential and current are calculated.

$$E_{corr,Ti\text{-}Pt} = -0.14\,\text{V vs.SHE}$$
$$I_{corr,couple} = 10^{-2}\,\text{A/cm}^2$$

The results indicate when titanium is in the active state and corrodes at $I_{corr,Ti} = 0.162\ \text{A/cm}^2$. Titanium passivates at $I_{pass} = 10^{-2}\,\text{A/cm}^2$ at a critical pasivating potential of $E_{crit} = -0.73$ V vs. SHE when coupled with Pt. The critical passivation potential is more negative than the corrosion potential of the couple $E_{corr,Ti\text{-}Pt} = -0.14$ V vs. SHE. The corrosion rate of the couple decreases to $0.01\ \text{A/cm}^2$ from $0.162\ \text{A/cm}^2$ observed at the titanium corrosion potential, $E_{corr,Ti} = -1.009$ V due to Ti passivation at −0.73 V when coupled with Pt.

In summary, when a metal with a more negative corrosion potential (such as Ti) is galvanically coupled with a more positive metal (such as Pt), the corrosion rate of the more negative metal is accelerated. However, the anomalous behavior observed in Fig. 6.9 is explained by titanium passivation in the absence of oxidizers at more active critical potentials (negative) than the reversible hydrogen potential.

Table 6.2 summarizes the corrosion current and potential before and after coupling.

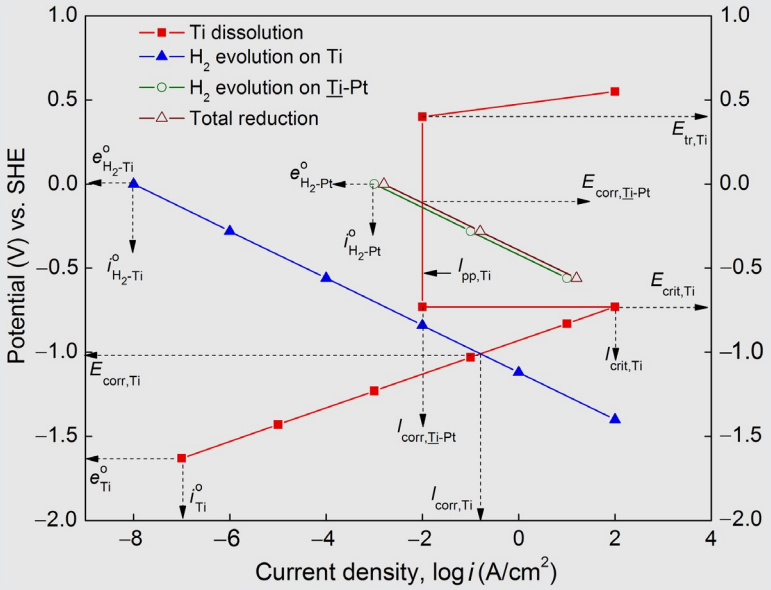

Fig. 6.9 Spontaneous passivation of titanium by coupling to platinum.

Table 6.2 The Corrosion Current and the Corrosion Potential of Titanium Before and After Coupling With Platinum

	Corrosion Current (A/cm^2)	Corrosion Potential (volts)
Titanium (before coupling)	0.162	−1.009
Titanium (after coupling)	0.010	−0.14

Case Study 6.6—Evaluation of Corrosion Current in Active-Passive Metal When the Passive Metal Passivates at Potentials More Noble Than the Reversible Hydrogen Potential

Figure 6.10 illustrates a metal (Fe) in an acid solution before and after coupling with platinum. Because the metal (Fe) passivates at more noble potentials than the reversible hydrogen potential, this system is different from the previous example.

The following parameters were used to calculate corrosion current and potential before and after coupling: Tafel slope, $b_a = 0.1$ V/decade; exchange current density, $i^o_{Fe} = 10^{-6}$ A/cm^2, $E_{pp} = 0.1$ V vs. SHE; passivation current, $I_{pp} = 3.3 \times 10^{-4}$ A/cm^2; transpassive potential, $E_{tr} = 0.7$ V; and dissolved specie activity, $[Fe^{2+}] = 1$. Hydrogen evolution exchange current density on platinum and iron are 10^{-3} and 10^{-4} A/cm^2, respectively. A cathodic Tafel slope of −0.1 V/decade is assumed for iron and platinum.

The corrosion currents and potentials before and after coupling are summarized in Table 6.3. Because the corrosion current of iron coupled with platinum ($I_{corr(Fe\text{-}Pt)}$) is smaller than the critical current density, I_{crit}, a passive film is not formed on the surface of the metal (Fe).

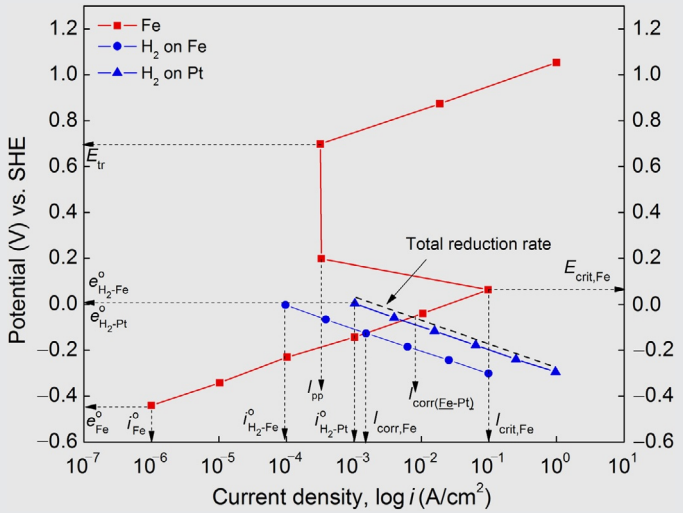

Fig. 6.10 Galvanic couple between platinum and active-passive metal Fe in air-free acidic solution.

Table 6.3 The Corrosion Current and the Corrosion Potential of Iron Before and After Coupling with Platinum

	Corrosion Current (A/cm^2)	Corrosion Potential (V)
Iron (before coupling)	0.0016	−0.120
Iron (after coupling)	0.0053	−0.068

Consequently, the corrosion rate of Fe coupled with platinum increases. Critical current density of $\sim I_{pp} = 0.1$ A/cm^2 is necessary to increase corrosion rate to I_{crit}. However, this critical current density is provided to the system only at very high Pt/Fe surface ratios.

6.5.2 Differential aeration: oxygen concentration cell

Concentration cells occur when metal surfaces contact common electrolytes with different concentrations (activities). One important example is the oxygen concentration cell, involved in pitting and crevice corrosion.

Thermodynamics of oxygen differential aeration cell: The oxygen electrode is classified as a metal oxide electrode of the second kind. It is represented by a platinized platinum electrode immersed in an oxygen-saturated solution. The charge-transfer reaction in the oxygen electrode is not reversible due to metal oxidization. Oxide films result in electrode potentials that are not reproducible. Oxygen differential aeration cells are established due to different oxygen partial pressures on the corroding surface. The electrode is defined as:

$$OH^-|O_2, Pt$$

The corresponding charge-transfer reaction is:

$$4OH^- \rightarrow O_2 + 2H_2O + 4e^- \tag{6.18}$$

The Nernst equation is for Eq. (6.18) is:

$$E_{OH^-|O_2} = e^o_{OH^-|O_2} + 2.303\frac{RT}{4F}\log\left(\frac{P_{O_2}}{a_{OH^-}}\right) \tag{6.19a}$$

or

$$E_{OH^-|O_2} = 0.401 - 0.059\log\left(\frac{a_{OH^-}}{(P_{O_2})^{1/4}}\right) \tag{6.19b}$$

Equations (6.19a) and (6.19b) can be used to estimate the oxygen electrode potential as a function of pressure. To explain the thermodynamics of the oxygen differential aeration cell, a cell is considered with two oxygen electrodes in aqueous solutions exposed to different oxygen pressures at 25 °C. This example outlines the methodology to estimate the electrode polarity of the electrodes. The oxygen pressure at the left electrode of the cell is varied from 760 to 50 mm Hg, while the right electrode is varied from 50 to 760 mm Hg. The left electrode is assumed to be anode and the right electrode is assumed to be the cathode. The cell notation is:

$$O_2(760\,mm\,Hg), Pt|H_2O|O_2(76\,mm\,Hg), Pt$$

The problem is solved for $P = 760$ mm Hg at the left electrode and $P = 76$ mm Hg at the right electrode. The left electrode with higher pressure is assumed to be anode and the right electrode is assumed to be the cathode

$$OH^- \rightarrow 1/2H_2O + 1/4\,O_2\,(760\,mm\,Hg) + e^-(anode) \tag{6.20a}$$

$$1/2H_2O + 1/4O_2(76\,mm\,Hg) + e^- \rightarrow OH^-(cathode) \tag{6.20b}$$

Thus, the differential aeration cell reaction is:

$$1/2H_2O + 1/4O_2(76\,mm\,Hg) + OH^- \rightarrow OH^- + 1/2H_2O + 1/4O_2(760\,mm\,Hg)\,(overall) \tag{6.21}$$

$$E_{cell} = e^o_{OH^-|O_2} + e^o_{O_2|OH^-} - 0.059\log\left(\frac{760^{1/4}}{76^{1/4}}\right) = -0.0147\,V\,vs.SHE \tag{6.22}$$

Because Gibbs free-energy is positive (the cell potential is negative), the overall reaction will not proceed spontaneously as written. The results indicate that the electrode in contact with lower partial pressure (76 mm Hg) is the anode and the electrode in contact with higher partial pressure (760 mm Hg) is the cathode for a common electrolyte of the same activity. Because the same species are in the numerator and denominator of the Nernst equation, only changes in the oxygen partial pressure affect the potential. The

Table 6.4 Oxygen Partial Pressure and Cell Potential of Oxygen Differential Aeration Cell

Left Electrode (Assumed to be the Anode) $OH^- \rightarrow 1/2\,H_2O + 1/4\,O_2(\text{pressure}) + e^-$ **Oxygen Partial Pressure (mm Hg)**	**Right Electrode (Assumed to be the Cathode)** $1/2\,H_2O + 1/4\,O_2(\text{pressure}) + e^- \rightarrow OH^-$ **Oxygen Partial Pressure (mm Hg)**	**Cell Potential (V)**
760	50	−0.017
700	100	−0.012
600	200	−0.007
550	300	−0.004
500	400	−0.001
400	500	0.001
300	550	0.004
200	600	0.007
100	700	0.012
50	760	0.017

equilibrium differential cell potential is equal to 0 V because the two electrodes are the same. The differential aeration cell potential as a function of pressure is presented in Table 6.4. The minus sign for the cell potential indicates the polarity of the electrodes should be reversed to proceed spontaneously.

Electrochemical kinetics of the oxygen differential aeration cell: The differential aeration cell shown in Fig. 6.11 consists of identical iron electrodes placed in a two-compartment cell separated by a membrane. Two electrically connected iron electrodes of equal area are

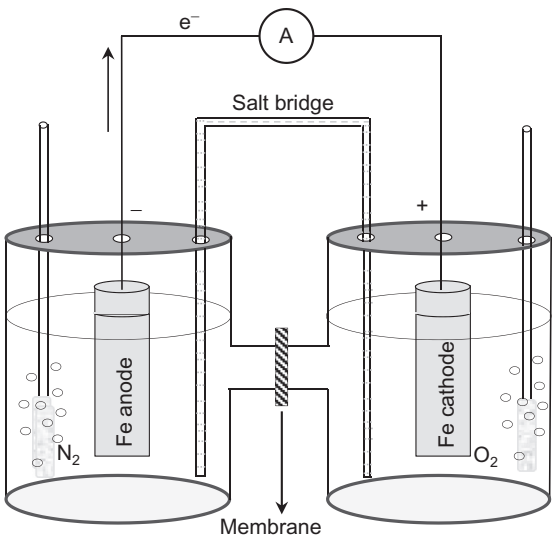

Fig. 6.11 Schematic of a differential aeration cell.

immersed in the compartments filled with 0.1 N NaCl solution. The membrane allows limited mass transfer and does not allow any change of oxygen content in the electrolyte on either side. On one side, nitrogen is purged though the solution in the compartment. On the other compartment of the cell, compressed air is purged through the solution, providing high dissolved oxygen content in contact with the iron electrode. A difference in pressure is established in the cell due to different content of dissolved oxygen, thus forming a thermodynamic differential aeration cell in a common electrolyte of the same activity. The constant air and nitrogen pressure maintains constant solution composition at both compartments of the cell.

Figure 6.12 compares the corrosion rates and potentials of an uncoupled and galvanically coupled differential aeration cell of equal electrode area. The corrosion rates were estimated by mixed potential theory. With two uncoupled electrodes, on the nitrogen side of the differential aeration cell the anodic reaction is iron dissolution:

$$Fe \rightarrow Fe^{2+} + 2e^{-} \tag{6.23}$$

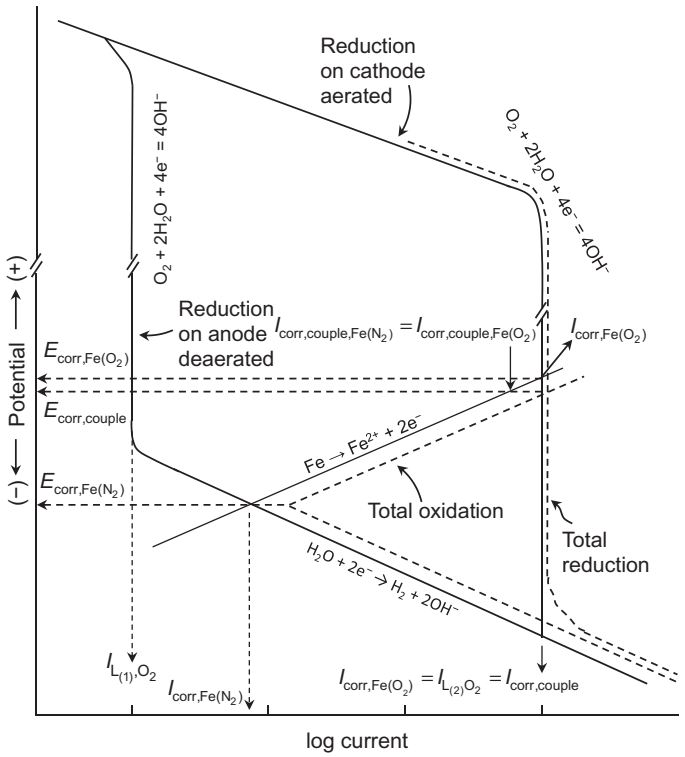

Fig. 6.12 Evaluation of corrsoion current and corrosion potential of the differential aeration on iron electrodes.

In absence of oxygen on this side, the cathodic reaction is water reduction:

$$2H_2O + 2e^- \rightarrow 2OH^- + H_2 \tag{6.24}$$

The corrosion rate and potential are predicted using electrochemical kinetic parameters for iron dissolution and water reduction. The corrosion potential and current of uncoupled oxygen differential cell on the nitrogen side (anode) of the cell, $E_{corr,Fe(N_2)}$ and $I_{corr,Fe(N_2)}$, are at the intersection point where the iron oxidation rate equals water reduction. In Fig. 6.12, the oxygen diffusion limiting current $\left(I_{L_{(1)}O_2}\right)$ is assumed to be negligible due to very low dissolved oxygen at the anode compartment.

On the aerated electrode, the corresponding cathode charge-transfer reaction is oxygen reduction:

$$O_2 + 2H_2O + 4e^- \rightarrow 4OH^- \tag{6.25}$$

The anodic charge-transfer reaction on the aerated side is the same iron dissolution charge-transfer reaction (6.23) with equal electrode area as the electrode in the deaerated side of the compartment.

The corrosion current of the uncoupled cathode on the aerated side, $I_{corr,Fe(O_2)}$, is controlled by oxygen limiting current, I_{L_2,O_2}, or $I_{corr,Fe(O_2)} = I_{L_2,O_2}$. The uncoupled corrosion potential on the aerated electrode is located at the point $E_{corr,Fe(O_2)}$ where the iron oxidation rate equals to the limiting current of dissolved oxygen reduction, I_{L_2,O_2}.

When the two electrodes in the differential cell are coupled together, the electrode area and the current of the iron dissolution reaction (6.23) increase by a factor of two. However, the overall current of the couple continuous to be controlled by the limiting oxygen current of the aerated electrode because the oxygen reduction current of the anode in the deaerated electrolyte is negligible. As shown in Fig. 6.12, the corrosion potential of the couple, $E_{corr,couple}$, and the corrosion current of the couple, $I_{corr,couple}$, are at intersection of the total oxidation current of iron dissolution and the total reduction. Note that the cathode current of the couple is controlled by the reduction current in the aerated electrolyte, since the cathodic current in deaerated electrolyte is negligible. Thus, the value of $I_{corr,couple} = I_{L_2,O_2} = I_{corr,Fe(O_2)}$. The value of $E_{corr,couple}$ is between nonaerated corrosion potential, $E_{corr,Fe(N_2)}$, and the aerated corrosion potential, $E_{corr,Fe(O_2)}$. The corrosion current of the uncoupled anode on the nitrogen side, $I_{corr,Fe(N_2)}$, increases to $I_{corr,couple,Fe(N_2)}$. On the cathode side, the corrosion current of the uncoupled cathode on the aerated side, $I_{corr,Fe(O_2)}$, decreases to $I_{corr,couple,Fe(O_2)}$. Assuming uniform current distribution in the oxygen differential aeration cell, as shown in Fig. 6.12, the anodic corrosion rate increases to match the overall cathode polarization. Due to polarization differences on the anode and cathode, a nonuniform current distribution causes corrosion to be faster near the deaerated and aerated separation.

6.6 TESTING METHODS IN GALVANIC CORROSION

6.6.1 Scanning vibrating electrode technique

AE44 (Mg alloy)-mild steel and AE44 (Mg alloy)-AA6063 (Al alloy) galvanic corrosion was investigated using the SVET and an immersion technique [9]. Magnesium is used in

Table 6.5 The Maximum Corrosion Rate Estimated from the SVET Experiments for AE44—Mild Steel and AE44—AA6063 Couples [9]

Galvanic Couple	Peak SVET Output (mV)	Anodic Peak Current Density (A/m^2)	Maximum Corrosion Rate	
AE44—mild steel	98	81.7	6.24	197
AE44—AA6063	21	17.5	1.34	42

Table 6.6 Maximum Corrosion Rate Estimated from the Immersion Experiments for AE44-Mild Steel and AE44-AA6063 Couples [9]

Galvanic Couple	Maximum Pit Depth (after 3 Days of Immersion (mm))	Maximum Corrosion Rate	
		Nm/s	Mm/y
AE44—mild steel	2	7.72	243
AE44—AA6063	0.43	1.66	52

the automotive industry to reduce an automobile's weight. However, it increases the risk of galvanic corrosion because of the large potential difference between magnesium and steel. The SVET, as AC method, measures the potential difference between two probe vibration extremes. This technique requires placing the sample in solution for three days, then slicing and photographing it with a high-resolution camera. This cross-section is then analyzed to determine the extent of corrosion, shown in Tables 6.5 and 6.6 [9].

The precipitated corrosion product morphology formed on the zinc/steel galvanic couple has been studied as a function of pH distribution and galvanic corrosion potential [19]. The experimental setup used for pH distribution measurements is shown in Fig. 6.13 [19]. The zinc/steel sample is immersed in a 0.01 M NaCl solution. The pH measurements are performed above the sample at 0.3 mm increments using a scanning tungsten electrode.

The regions over the Zn section in Fig. 6.14 have a higher pH than the regions farther away because most of the corrosion is near zinc [19]. Vertical pH changes were found to exist only in a small region (1.5 mm above the sample). Horizontally, the low pH regions were over the zinc layer and well into the steel area. Zinc corrosion products were found at low pH over the steel, but not in the regions of high pH. Galvanic zinc corrosion coupled with iron was studied in 0.1 M Na_2SO_4 solution using SVET [20]. The samples consisted of iron (99.5%) and zinc (99.95%). After being filled with electrolyte, the scanner was set to a 20×20 matrix over the sample. From the scan, three-dimensional representations of the anodic and cathodic current maps were developed. The data was integrated to give the three-dimensional plot shown in Fig. 6.15 [20]. SVET provided excellent spatial resolution, making it possible to determine zinc oxidation in localized regions.

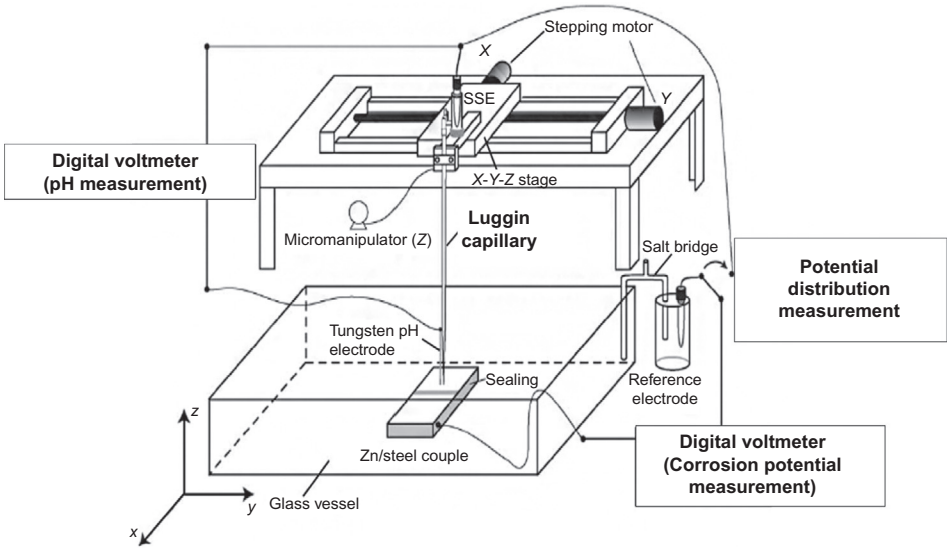

Fig. 6.13 Experimental setup used for the pH distribution measurements [19].

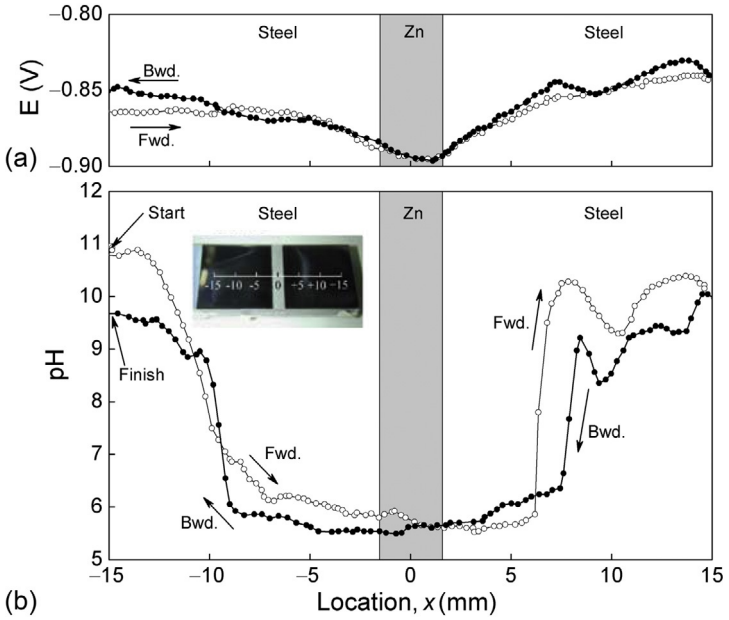

Fig. 6.14 Horizontal distribution of the (a) potential and (b) pH over the surface of a zinc/steel couple after a 4.5 ks immersion in 0.01 M NaCl. The photograph in the inset was taken just before measuring the distribution [19].

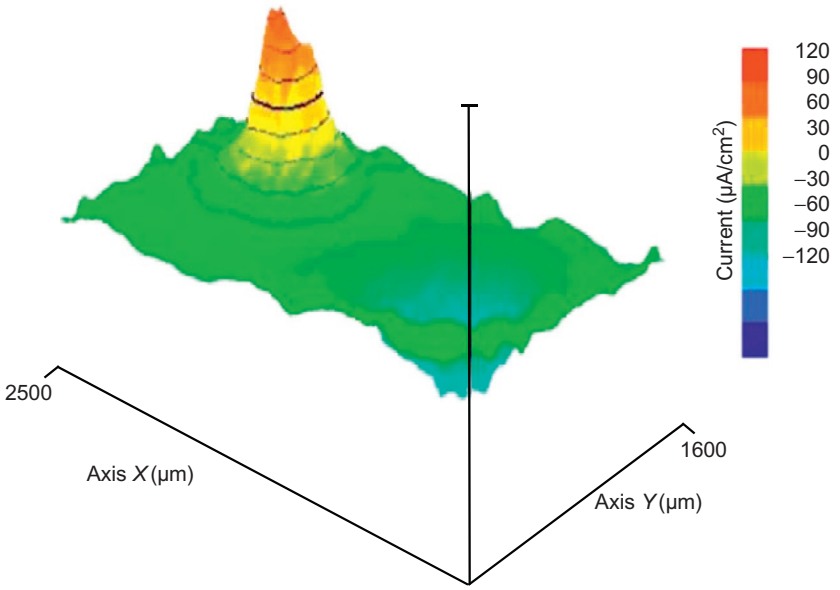

Fig. 6.15 Ionic current maps determined above the galvanic couple in 0.1 M Na_2SO_4 [20].

6.6.2 Shadowgraphy and Mach-Zehnder interferometry

Shadowgraphy and Mach-Zehnder interferometry have been used to investigate the concentration profile above a zinc-steel couple immersed in 0.01 M NaCl. Concentration profiles of Zn^{2+} 0.3 mm above the Zn/steel couple surface were measured at several immersion times using optical visualization [21]. The experimental apparatus is shown in Fig. 6.16 [21]. Because shadowgraphy and Mach-Zehnder interferometry techniques are based on optical visualization methods, there are several advantages over more conventional scanning probe techniques. Optical techniques are faster than scanning probe methods and do not disturb the system. The concentration profile in Fig. 6.17 shows the growth of Zn^{2+} layer with time. It also shows the location of zinc concentration increase directly over the zinc area [21]. This concentration profile was found in good agreement with the scanning probe methods used previously.

6.6.3 Other methods

A new method was developed using a modified polishing device for measuring galvanic corrosion during chemical mechanical planarization (CMP) of copper and tantalum [22]. CMP is used to polish on a microscopic scale. In most cases, this is done using a colloidal slurry of abrasive microscopic particles.

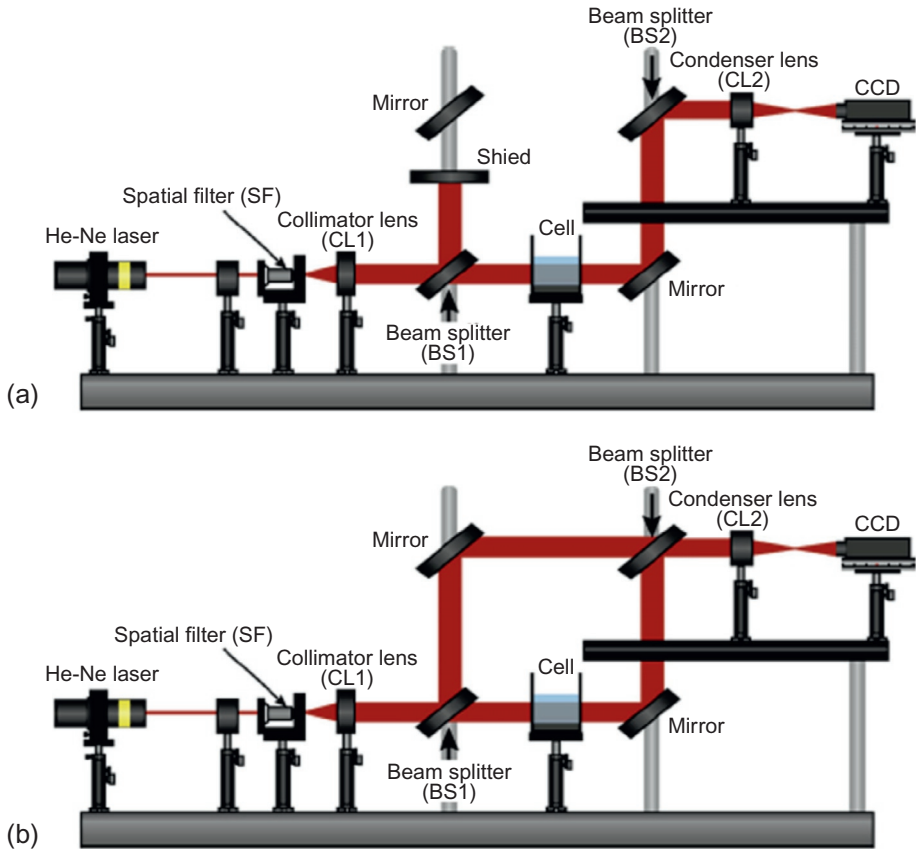

Fig. 6.16 Schematic of optical arrangments for Shadowgraphy and Mach-Zehnder interferometry [21].

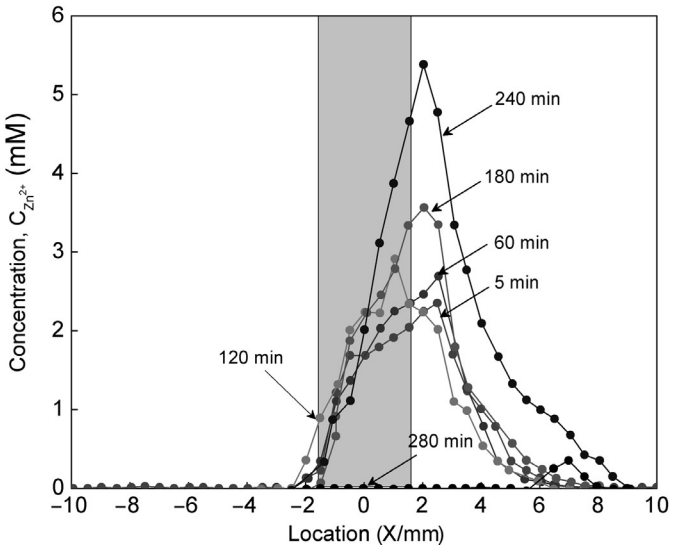

Fig. 6.17 Concentration profiles of Zn^{2+} at 0.3 mm high above the surface of a Zn/steel couple measured at several immersion time [21].

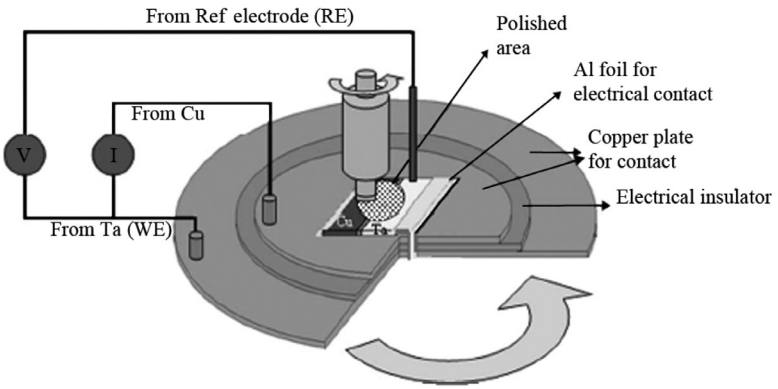

Fig. 6.18 Modified electrochemical polishing cell for measuring galvanic corrosion potential and current density abrasion [22]. *Reproduced by permission of The Electrochemical Society.*

Copper is electrodeposited on the silicon dioxide wafer surface. Prior to the main copper deposition, a thin layer of copper and tantalum is deposited in the large trenches of the wafer. Above this layer another layer of copper is applied. This layer of copper is polished using the colloidal slurry. Slurry chemistry plays an important role in the extent of corrosion. Slurries consisting of hydrogen peroxide or hydroxylamine were examined. Figure 6.18 shows the galvanic corrosion measurement setup [22]. The setup was also used to measure the single-metal currents by replacing the plates with a single plate of either copper or tantalum. This technique estimates the galvanic couple strength by first measuring the corrosion current of each metal separately. The estimated values for galvanic corrosion were fairly accurate at high pH but significantly less accurate at low pH. The corrosion current density of tantalum increases drastically in 0.5 M hydroxylamine and 1.2 M hydrogen peroxide during abrasion.

Inconel 718 galvanic corrosion was studied after electron beam welding [23] with specific objectives to study the effects of galvanic corrosion in welds. The Inconel 718 had been solution annealed and precipitation-hardened. Galvanic corrosion was tested in a 3.5 wt% NaCl solution at 30 °C. Inconel 718 was developed to meet high temperature and strength requirements in aerospace and nuclear industries. Inconel 718 alone has very high corrosion resistance, but the deficiency is in weld resilience. The study found galvanic corrosion between the fusion zone, the heat-affected zone, and the base metal under these conditions. Marked galvanic corrosion occurred at the fusion zone after very short anodic polarization. The authors recommended precipitation-hardening treatment after welding to reduce the corrosion potential.

Corrosion of laser welded AA6061 aluminum alloy parts has been studied in an aerated 3.5% NaCl solution at room temperature [24]. Welding changes the physical structure and corrosion properties of the metal at the weld. Welding tends to create a

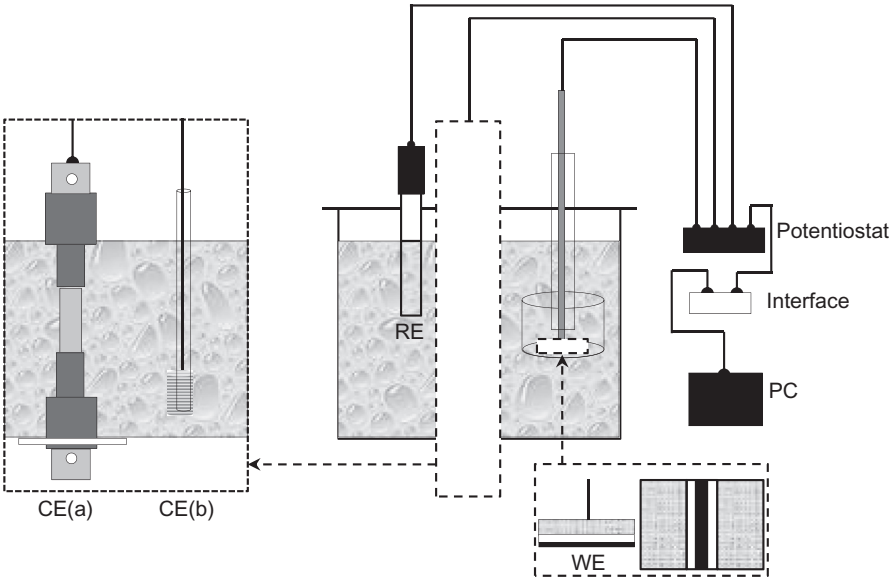

Fig. 6.19 Schematic of the experimental setup [24].

cathodically polarized region compared to the base metal. The experimental cell and the setup are shown in Fig. 6.19 [24].

The counter electrode, CE(a), consists of the base metal and is used for potentiodynamic polarization measurements. CE(b) is a conventional platinum counter electrode. The reference electrode, RE, is a saturated calomel electrode. The inset at the bottom right depicts the WE as a vertical view of a bead-on-plate weld showing the weld fusion zone at the center surrounded by the heat zone and base metal. Figure 6.20 shows

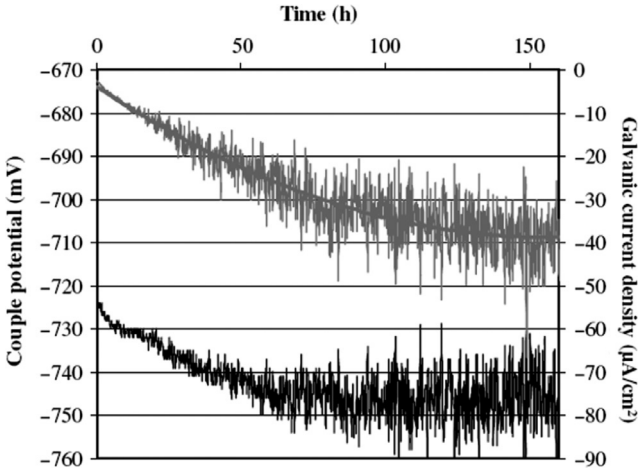

Fig. 6.20 Galvanic corrosion current density (top trace) and the galvanic potentials (bottom trace) [24].

galvanic current density (top trace) and galvanic potential (bottom trace) of the weld fusion zone (cathode) and the base metal (anode) [24]. Results indicate potential differences between the different zones cause galvanic corrosion on the metal. Galvanic current value increases with time until it approaches a maximum value. The base metal corrosion potential becomes more negative as the weld fusion zone moves to a more positive value. Base metal corrosion current does not change with time but the corrosion current of the weld zone does.

6.7 AUTOMOTIVE APPLICATIONS

The galvanic corrosion properties of MgO in an engine coolant have been studied as a function of coating thickness [25]. The authors also studied the effect of adding an oxide coating to the magnesium using plasma electrolytic oxidation (PEO). The use of magnesium in the automotive industry is increasing due to low density and high strength. In particular, research is conducted to fabricate the engine block out of magnesium.

Current engine coolants are highly corrosive to pure magnesium, so it is necessary to develop coatings that increase corrosion resistance. Discs of magnesium were placed into the apparatus shown in Fig. 6.21 [25]. This apparatus simulates the engine block, which employs aluminum heads and a magnesium block. The sample was evaluated using immersion tests to measure disk weight loss exposed to a long-life automotive coolant. Magnesium was evaluated without coating and with five different coating thicknesses. The uncoated magnesium weight loss was extremely high. Oxide coatings on the magnesium drastically decreased galvanic corrosion. The thermal properties of the magnesium were not affected by the coating application.

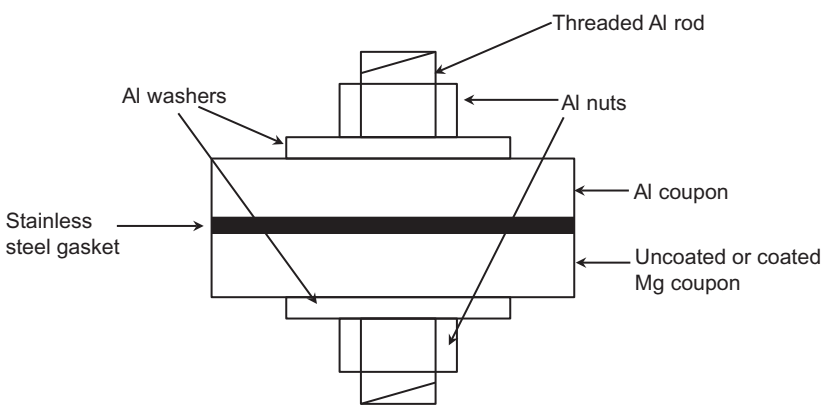

Fig. 6.21 Schematic of the galvanic corrosion test sample [25].

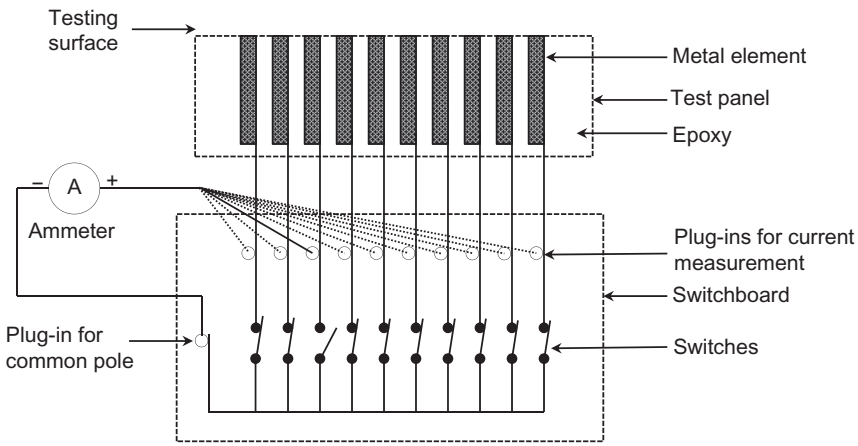

Fig. 6.22 Configuration of the test panel and switchboard for the measurement of galvanic current [26].

Magnesium alloy AZ91D galvanic corrosion in contact with aluminum alloys, steel, and zinc in a 5% NaCl solution was studied by Song et al. [26]. The authors studied couples between magnesium and aluminum alloy and between steel and zinc immersed in the test solution. A specially designed test panel was constructed to test the materials, shown in Fig. 6.22 [26]. Galvanic corrosion increases with time for all galvanic couples. An AZ91D anode with a large area coupled with a cathode of a metal with a large area will result in a dramatic increase in magnesium corrosion. Adding an insulating spacer can decrease the corrosion rate but will not eliminate it entirely. Steel, when coupled to the magnesium alloy, resulted in largest corrosion rate. A "shortcut" effect can occur where corrosion products accumulate and form a path that increases galvanic corrosion rate.

Alloy galvanic corrosion has been measured in alcohol fuel [27]. The corrosive effects of the alcohol fuels on different galvanic couples Zamak 5, low-carbon steel AISI 1010, stainless steel ABNT 420, and Al-Si alloy-4000 series were studied. Zamak was used as a permanent anode for these tests. Samples were immersion tested for three weeks at 50 °C. The alcohol fuel-water content was varied in this study and the corrosion product effect was investigated. Results indicated that higher ethanol fuel-water content was more corrosive regardless of the galvanic couples.

Jia et al. [28] analyzed the effect of geometry on AZ91D coupled with steel. The authors used a boundary element method (BEM) to evaluate cathode-anode surface area ratio, cathode-anode insulation distance, solution film depth covering the galvanic couple, and galvanic couple interactions on the corrosion rate. The results indicated that decreasing surface area ratio increased the galvanic current. Galvanic current also increased with increased solution film depth, while it decreased as insulating distance

increased. The results confirmed that BEM-based calculations adequately predict galvanic couple corrosion. In summary, the experimental data and mathematical modeling indicated galvanic current caused by galvanic interaction of two or more galvanic couples can be predicted by linear superposition of the current originated by each couple.

6.8 GALVANIC CORROSION IN CONCRETE STRUCTURES

The extent of galvanic corrosion has been measured between steel rebars and chromium containing steel rebars in concrete reinforcement [29]. The corrosion rates were estimated in both chlorinated and carbonated environments.

Galvanic corrosion rates of standard reinforcing ribbed bars (rebars) 12 mm in diameter with yield strength 550 MPa were measured in carbonated concrete by Nasser et al. [30]. The experimental apparatus is shown in Fig. 6.23 [30]. Carbonated concrete and sound concrete were placed on both sides of the test stand to establish an active and passive steel bar section. The experimental setup consists of steel rebars embedded in the concrete structure with PVC sections to allow electrical contact. The PVC sections help insulate the rebar and prevent any air corrosive effects. Weight loss measurements indicated high galvanic corrosion rates in carbonated concrete due to nonuniform carbonation forming large macrocells in the structure. Steel also contributes to large active and passive metal region formation.

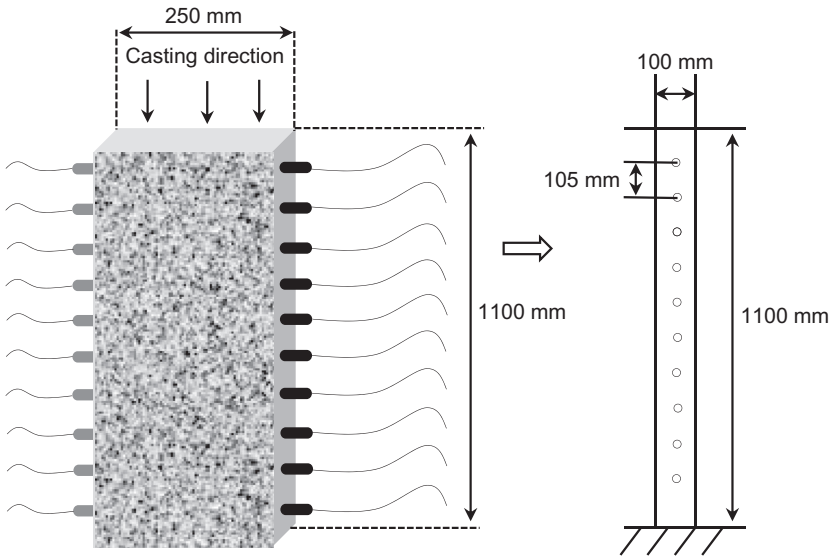

Fig. 6.23 High size concrete member location of the PVC steel bars and concrete casting direction [30].

6.9 REFRIGERATION

Refrigeration systems, besides having high energy costs, require chemicals that pollute the environment. Conventional refrigeration systems use some form of chlorofluorocarbon compound. New refrigerants have been investigated that are less harmful. Absorption refrigeration systems are also being investigated that use a lithium bromide solution. Lithium bromide solutions create new difficulties for corrosion properties of the currently used refrigerants.

Sanchez-Tovar et al. [31] attempted to measure the galvanic couple effect between copper and AISI 304 stainless steel, the two commonly used materials in absorption refrigeration systems, in a solution of LiBr under hydrodynamic conditions. The authors measured corrosion potential and corrosion current of each metal and the galvanic couple. The measurements were carried out at Reynolds numbers between 1456 and 5066 and different temperatures (25, 50, and 75 °C). The Galvanic parameters of the copper/AISI 304 stainless steel in 850 g/L LiBr solution at different temperatures and Reynolds numbers are summarized in Table 6.7 [31]. Increasing temperature increased corrosion rate, I_{corr}, for both copper and stainless steel. Increasing the Reynolds number only increased corrosion rate for copper. Copper acts as a sacrificial anode for stainless steel when galvanically coupled. The galvanic current density, I_{couple}, increased with both temperature and Reynolds number; temperature having a much larger effect.

Galvanic corrosion between Grade 2 commercial titanium and titanium-titanium welds was studied in different heavy brine LiBr concentrations at temperatures of 25, 50, and 100 °C [32]. The results were obtained using a ZRA method. Figure 6.24 shows mean values of the galvanic current for different temperatures and brine concentrations [32]. The welding process alters titanium microstructure, increasing base metal and welded piece dissimilarity. This phenomenon resulted in the welded piece acting as an anode. The welded titanium remained passive throughout all temperatures and brine concentrations. The current density was higher at 50 °C than 25 °C and 100 °C in all solutions. This was attributed to breakdown/recrystallization from anatase to rutile between 50 and 70 °C. With increased bromine concentrations, the possibility of pitting increases drastically.

The galvanic coupling effects of aluminum-copper model alloy couples were studied in an aqueous solution of 0.1 M Na_2SO_4 [33]. The anodic and cathodic region metallic content was varied and corrosion current and potential were measured for each combination. The cathodic region was more susceptible to pitting. Copper content increase in the cathodic phase resulted in a pitting rate increase. Cathodic phase pitting susceptibility also increases as the copper ratio increases. In general, pitting corrosion for any region increases with copper content.

Table 6.7 Galvanic Parameters of the Copper/AISI 304 Stainless Steel in an 850 g/L LiBr Solution [31]

Re	Temperature (°C)	Material	E_{corr} ($mV_{Ag\|AgCl}$)	E_{couple} ($mV_{Ag\|AgCl}$)	E_C-E_A (mV)	I_{corr} (μA/cm²)	I_{couple} (μA/cm²)	I_{couple}/I_{corr}
1456	25	Copper	−404.17	−383.16	163.04	2.37	3.21	1.50
		AISI 304	−241.13			0.09		
	50	Copper	−393.47	−378.08	159.11	3.23	5.03	1.56
		AISI 304	−234.36			0.20		
	75	Copper	−382.16	−369.0	208.66	4.48	6.86	1.53
		AISI 304	−173.50			0.43		
3166	25	Copper	−374.31	−358.0	166.11	2.92	3.82	1.31
		AISI 304	−208.20			0.09		
	50	Copper	−396.47	−378.85	142.72	4.70	5.62	1.20
		AISI 304	−253.75			0.20		
	75	Copper	−397.63	−379.54	248.74	6.81	9.24	1.36
		AISI 304	−136.70			0.43		
5066	25	Copper	−410.32	−393.09	186.74	3.96	6.12	1.56
		AISI 304	−223.58			0.09		
	50	Copper	−410.32	−386.93	251.60	5.42	9.32	1.72
		AISI 304	−158.72			0.20		
	75	Copper	−393.86	−375.01	257.16	8.38	11.45	1.37
		AISI 304	−148.89			0.43		

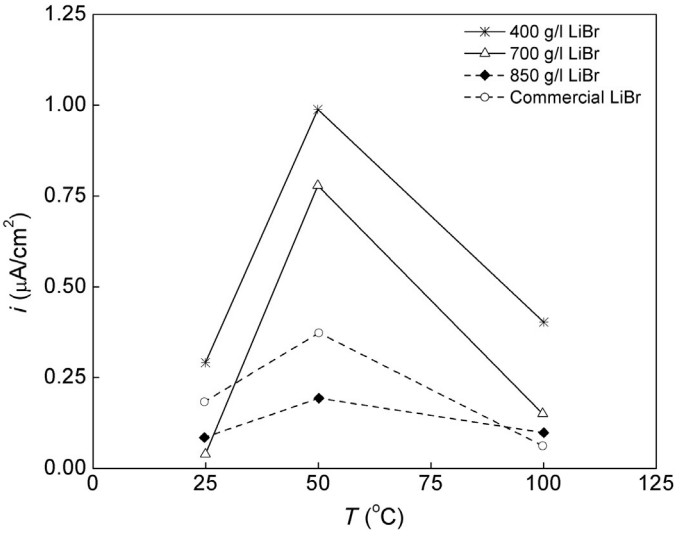

Fig. 6.24 Mean value of the galvanic current density during the 8 h immersion in the LiBr solutions at different temperatures [32]

6.10 DENTAL APPLICATIONS

Galvanic corrosion currents and potentials of several titanium-based implant materials were studied by Arslan et al. [34]. The corrosion tests were performed on couples between titanium and three alloys: a gold alloy, a Co-Cr alloy, and a Cr-Ni alloy. Each couple was tested in Ringer's solution (0.31 g sodium lactate, 0.02 g calcium chloride, 0.6 g sodium chloride, and 0.03 g potassium chloride in 100 mL of water) at 37 °C. The titanium-gold couple was found to be the best for use in dental environments.

Galvanic corrosion was studied by Nakamura et al. on ferritic stainless steels (SUS 444, SUS XM27, and SUS 447J1) used for dental magnetic attachments in contact with an iron-platinum magnet [35]. Dental instruments are frequently attached using these magnets and their corrosion properties are crucial to suitability. A 1:1 ratio and a 1:10 ratio of stainless steel to iron-platinum were used in this study. Several parameters were estimated to quantify the effects of galvanic corrosion such as released ions, rest potential, and anodic and cathodic polarization curves. The released Fe ions increased when in contact with the iron-platinum magnet. Corrosion also significantly increased as the stainless steel-magnet surface area ratio decreased. However, Fe ions release from any of the stainless steels was within the corrosion-resistance boundaries for dental use. The stainless steels with more chromium were more corrosion resistant.

6.11 CORROSION OF MICROSTRUCTURES

Ding and Hihara [36] studied galvanic corrosion in metal matrix composites containing semiconducting constituents. Several factors contribute to Al/SiC MMC corrosion behavior. The photochemical-corrosion-diode (PCD) model was used to explain the results. The study focused on the corrosion of matrix interfaces when exposed to sunlight. The authors found corrosion increased two- to threefold in the corrosion product layer when exposed to sunlight. The results indicated at open circuit conditions, a depletion-insulating layer forms on the Si. In the absence of light, this depletion layer mostly prevents galvanic corrosion. Under illuminated conditions, the type of semiconducting material dictates suppressed or accelerated corrosion.

Al/AlN composites were studied to determine the importance of microgalvanic interactions in the aluminum matrix composite (AMC) (Al reinforced with 50% AlN) [37]. AMCs are increasingly investigated as an alternative to aluminum alloys. The corrosion behavior of these metal matrices is not well understood. In this investigation, an AMC with AlN compounds as ceramic structure was studied. Potentiodynamic polarization tests were performed using a standard three-electrode glass cell. Polarization curves were obtained by varying the potential from −2 to 0 V at a scan rate of 5 mV/s. The corrosion studies were performed in a 3.5 wt% NaCl solution with pH values of 5, 8.6, and 11.6. Galvanic interaction between aluminum and AlN compounds were found to cause severe pitting corrosion.

Miller et al. [38] studied the mechanical effects of galvanic corrosion on structural polysililcon. In structural polysilicon components manufacture, hydrofluoric acid is frequently used to remove unwanted, sacrificial, silicon dioxide. When immersed in aqueous HF environment, the components are subjected to galvanic corrosion. In this study, the decrease in microcantilever beam mechanical resonance frequency (f_R) is used to observe polysilicon crystal corrosion. In aqueous solutions, these polysilicon crystals are in contact with gold components via aqueous HF solution. In addition to frequency, changes in modulus, hardness, retained energy ratio, and K_{exp} loading were analyzed. The resonant frequency measurements for microcantilever beams and comb drives were subjected to various HF-based mixtures. The resonant frequency tends to decrease with immersion time, and the greatest decrease in resonant frequency occurred during direct electrical contact with the gold components. The observed decrease was attributable to galvanic corrosion. Materials not tested with gold found differences in chemistry can cause a galvanic couple between different polysilicon structures. Other factors tested did not have a strong impact on resonant frequency. The authors also gave physical experiments that connect the resonant frequency decrease to autonomous polysilicon dissolution. These results indicate HF solution composition in manufacturing can have an impact on the final polysilicon product.

In micromachined polysilicon structure manufacturing, galvanic corrosion is becoming an increasing problem. The relation between morphology, etch rate, surface wetting,

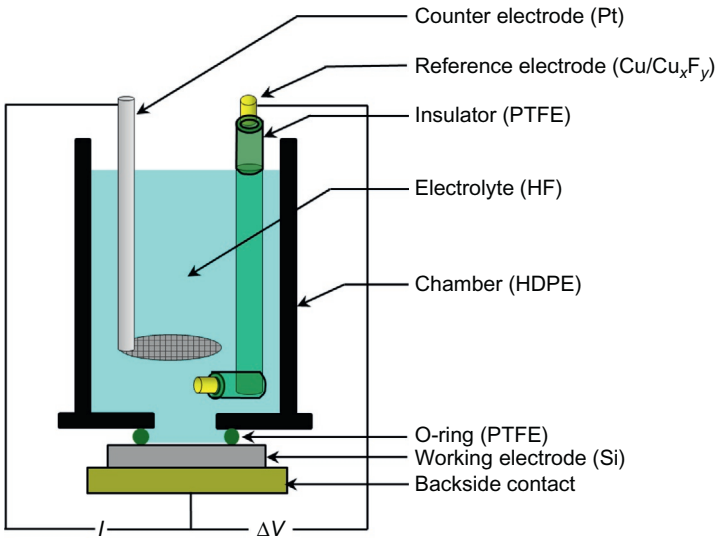

Fig. 6.25 Schematic showing cross-sectional view of the custom three-electrode fixture used for electrochemical characterization [39]. *Reproduced by permission of The Electrochemical Society.*

and electrochemical characteristics for micromachined silicon subject to galvanic corrosion was studied by Miller et al. [39]. The galvanic corrosion rate was studied using morphology, resistive probe, surface wetting, and electrochemical characterization. Three acid solutions were used: undiluted (UD) 48% HF, UDHF:H_2O, and UDHF:Triton X-100. Figure 6.25 shows the test apparatus [39]. The authors found that the measured porosity for corroded silicon ranged from 20% to 47%. The amount of metal directly affected porosity and thickness. When water was added to the acid solution, additional hydroxide ions increase corrosion rate and porosity. The resistive probe indicated corrosion current eventually decreased to zero. Corrosion current also varies exponentially with the amount of metal.

Galvanic corrosion of polyacrylnitrile (PAN) and pitch-based short carbon fibers in polyetheretherketone (PEEK) composites were studied by Gebhard et al. [40]. Galvanic corrosion of carbon-fiber compounds can occur in contact with a steel electrode. The effects ranged from initial breakdown and cracking, to complete dissolution.

6.12 GALVANIC COATINGS

The practical use of steel and high-strength alloys is limited by corrosion and cracking hazards due to hydrogen penetration and hydrogen accumulation in the bulk. A cadmium galvanic coating on steel has many advantages such as good lubricity, solderability,

and low galvanic corrosion with aluminum [41]. Cadmium plating offers effective sacrificial protection to steel components under corroding conditions. However, cadmium deposition from cyanide baths gives rise to unacceptably high hydrogen intake by high-strength plated components, leading to hydrogen embrittlement [42]. Environmental concerns and performance criteria led research to cadmium-coating alternatives. Efforts have been made to develop alternative, noncyanide baths for cadmium plating based on sulfamate, flouborate, and chloride. However, these baths have not been satisfactory due to many factors like coating quality and performance under a corroding environment.

To increase barrier properties of galvanic zinc coating, research has been aimed at developing effective galvanic zinc-based coatings by alloying zinc with a more noble metal such as nickel [43–47]. Deposition characteristics of sacrificial Zn-Ni alloys as compared to conventional galvanic zinc include extended corrosion resistance and significantly harder deposits. Nickel presence also imparts good barrier resistance. Several studies have been done to optimize Zn-Ni alloy composition based on corrosion performance [45]. Electrodeposited sacrificial zinc alloy formed with other metals such as cobalt [48–50], iron [51], tin [52], and manganese [53,54] are also of interest. Due to high zinc content in the deposit, these alloys have more negative potentials than cadmium and dissolve rapidly in many corrosive environments. Typical Zn-Ni alloys contain ~10-15% Ni and any further increase in nickel composition is based on plating baths with a higher Ni/Zn ratio. A noble metal composition enhancement would lead to a more anodic open circuit potential, which in turn reduces the driving force for galvanic corrosion. Also, barrier properties associated with such deposits will be superior to other coatings.

Zn coating service life can be enhanced through passivation such as phosphating, trichrome, and silicating [55,56]. Zn corrosion-resistant properties can also be improved by alloying with other transition metals such as Co, Sn, and Cr. Various Zn-based binary and ternary electrodeposition coatings like Zn-Fe [57,58], Zn-Ni-Cd [59–61], and Zn-Ni-P [62–64] have been reported in the literature. Corrosion resistance was improved by an order of magnitude compared to bare Zn coatings. The corrosion potential of different galvanic coatings after 1 and 24 h exposure in a H_3BO_3 solution at pH 3 are given in Table 6.8 [62]. The dissolution rate is very high due to the high corrosion potential

Table 6.8 Corrosion Potential Values of Selected Coatings Determined in 0.5 M H_3BO_3 Solution at 25 °C [62]

	E_{corr} (mV vs. SCE)	
Coating	**1 h**	**24 h**
Ni	−360	−360
Cd	−798	−798
Zn	−1140	−1124
Zn-Ni	−1127	−745
Zn-Ni-P	−1035	−748

differences between the underlying metal (steel) and zinc. Nickel possesses excellent barrier properties, but is susceptible to hydrogen embrittlement and cracking. Sacrificial properties predicted by open circuit potential (OCP) measurements were verified using the scratch-model approach [62]. The more negative zinc coatings offer good sacrificial protection and inhibit the hydrogen penetration in the bulk. This coating does have a very short life due to high galvanic corrosion rate. The potential of pure zinc was stable at −1.1 V (vs. SCE) whereas Zn-Ni, Zn-Ni-P, and Zn-Ni-Cd were more positive, indicating that more noble components in the deposit results in an anodic shift with respect to zinc, decreasing galvanic corrosion.

Corrosion current for selected coatings in 0.5 M H_3BO_3 solution at 25 °C are shown in Table 6.9. Table 6.9 indicates that the zinc coating had the highest I_{corr} value after 1 h. The Zn-Ni and Zn-Ni-P coatings had higher I_{corr} than cadmium, suggesting they will provide less efficient barrier protection. After exposing samples for 240 h at 6 pH, the corrosion rates of Zn-Ni and Zn-Ni-P decreased due to dezincification. The Zn-Ni-Cd coatings gave the best performance with stable and significantly lower corrosion current. The I_{corr} observed for Zn-Ni-Cd was about one order of magnitude smaller than pure cadmium due to significant nickel presence in the alloy. I_{corr} value obtained for pure nickel coating is given for comparison.

Among various zinc-based alloy coatings, there is a growing interest in zinc-manganese (Zn-Mn). In contrast alloying elements such as Ni, Co, and Cr, Mn has more negative potential $\left(e^{o}_{Mn^{2+}|Mn} = -1.185\ V \text{vs.SCE}\right)$ compared to Zn. However, this alloy shows synergy with better corrosion resistance than the individual metals. In addition, the alloying elements are nontoxic and environmentally friendly. Zn-Mn alloy coatings are thermodynamically less noble than pure Zn and show passivating behavior under severely corroding environments due to insoluble compounds on the corroding surface that affect catalytic cathodic oxygen reduction activity [65–72]. Galvanic Zn-Mn alloy is reported to exhibit optimal protective characteristics, especially where Mn content is up to ~10-11 wt.% [65,68–70].

Thermal-sprayed galvanic coatings offer excellent corrosion and wear protection [73–75] and have been used in various industrial applications [76]. For the purpose of

Table 6.9 Corrosion Current Values of Selected Coatings Determined in 0.5 M H_3BO_3 Solution at 25 °C Using the Tafel Extrapolation Method

Coating	I_{corr} (μA/cm^2)
Ni	0.77
Cd	5.0
Zn	17.5
Zn-Ni	8.0
Zn-Ni-P	5.78
Zn-Ni-Cd	1.53

efficiency and reducing fuel consumption in an aircraft turbine engine, the gap between rotating and stationary parts should be small as possible. Abradable sealing coatings reduce fuel cell consumption by minimizing blade-tip clearance in compressors and turbines [77,78]. The coating should possess high erosion resistance, abradability, porosity, sufficient bond strength to substrate, and high temperature stabilization [79]. These coatings consist of a self-lubricating, nonmetallic phase and a metallic matrix.

Flame sprayed Ni/graphite abradable sealing coating and air plasma Ni-Al coatings coupled with different aluminum contents were investigated with OCP and polarization tests [80]. Ti-6Al-4V alloy (Ti-6.2Al-4.1V-0.3Fe 0.1C0.05N-0.015H-0.20 wt.%) was used as the substrate material. The galvanic corrosion testing was performed in 5 wt.% NaCl solution by using a ZRA.

Four types of couples were prepared: (I) Ni_{80}-Al_{20} coating/(Ni/graphite) coating; (II) Ni_{85}-Al_{15} coating/(Ni/graphite) coating; (III) Ni_{90}-Al_{10} coating/(Ni/graphite) coating; and (IV) Ni_{95}-Al_{05} coating/(Ni/graphite) coating. The couple potentials were simultaneously monitored with respect to the saturated calomel electrode. Galvanic current density of the Ni/graphite coating/(Ni-Al coating) couples in oxygen-saturated 5% NaCl solution after 20 h of exposure are shown in Fig. 6.26 [80]. The negative current observed for (I), (II), and (III) indicate Ni-Al coatings act as anodes. The coatings with higher aluminum content exhibited higher galvanic corrosion density. In the case of (IV), the Ni_{95}-Al_{05} coating acted as the cathode while the Ni/graphite coating corroded. Scanning electron microscope (SEM) images of the coupled anodic surface are shown Fig. 6.27 [80]. The pictures were taken after 20 h in 5%wt.% NaCl solution saturated with oxygen at 35 °C. As shown in Fig. 6.27, increasing Al content in the galvanic couples (I), (II), and (III), drastically decreases Ni-Al coatings corrosion resistance with severe

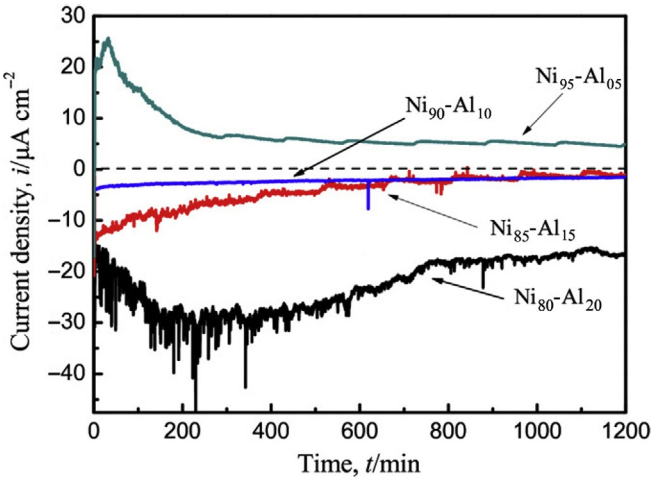

Fig. 6.26 Galvanic current density of the Ni-Al bond coatings to Ni/graphite abradable coating pair in oxygen-saturated 5 wt.% NaCl solution at 35 °C [80]

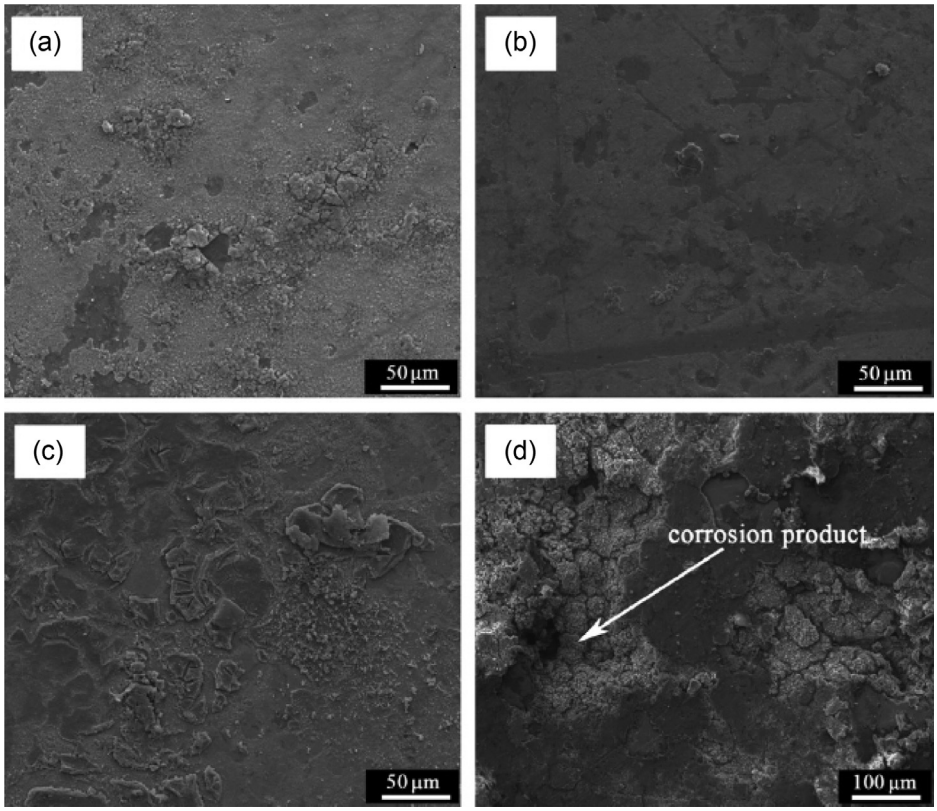

Fig. 6.27 SEM analysis of anode coating top surfaces after the 20 h galvanic corrosion test: (a) Ni_{80}-Al_{20}; (b) Ni_{85}-Al_{15}; (c) Ni_{90}-Al_{10}; (d) Ni/graphite coupled to Ni_{95}-Al_{05} [80].

damage along the lamellae boundaries with mainly white Al_2O_3 determined by energy dispersive analysis of X-ray (EDAX) measurement [80]. For (I), (II), and (III), the Ni-Al coating is anodic. Their corrosion potential is more active than the corrosion potential of Ni/graphite. The galvanic corrosion test indicated that Ni-Al coatings with higher Al contents (Ni_{80}-Al_{20}, Ni_{85}-Al_{15}, and Ni_{90}-Al_{10}) act as anodes in the galvanic couple while the Ni_{95}-Al_{05} coating acted as a cathode. The Ni/graphite coating, when coupled with Ni_{95}-Al_{05}, showed corrosion products on the pore walls. Green corrosion products were formed on the Ni/graphite coating surface when coupled to the Ni_{95}-Al_{05} coating. No corrosion products were observed on the Ni_{95}-Al_{05} coating.

6.13 NUMERICAL MODELING OF GALVANIC CORROSION COUPLES

Some of the factors that control corrosion rate in galvanic couples are the corrosion potential difference between dissimilar metals, hydrogen evolution exchange current

density, exchange current density of the corroding metal, Tafel slopes, relative electrode area, electrolyte composition, conductivity, and temperature. Mixed potential theory has been used to quantitatively estimate galvanic current and potential, effect of cathode-sacrificial anode electrode surface area, and exchange current density of the individual corroding metals. These are some parameters that can be accurately determined using this theory. Numerical models that consider polarization behavior provide quantitative means to estimate galvanic couple corrosion rate. Numerical models based on electrochemical kinetic parameters and thermodynamic properties of individual metals in the couple can supplement experimental results and provide galvanic couple corrosion rates.

Early numerical galvanic corrosion modeling has been reviewed by Munn [81], Zamani [82], De Giorgy [83,84], and Addey and Niku [85]. These authors derived the partial differential equations that govern the electric potential distribution in the electrolytes. Boundary conditions were developed to account for nonlinear electrochemical kinetics. To include mixed potential theory in electrochemical modeling, a finite element formulation was developed consistent with charge conservation. Other methods, such as Boundary Element Model, BEM, have been routinely used in the last 20 years for galvanostatic corrosion studies [84–87]. An excellent review by Verbrugge [88] summarizes the accomplishments in advancing the theoretical foundation to solve current distribution for complicated practical galvanic systems. The Laplace equation has been accepted as a governing equation for potential distribution in modeling galvanic couple systems. For simple mathematical analysis, the galvanic couples can be treated as semi-infinite or infinite surfaces. For low corrosion rates, it was possible to assume linear kinetics for simplified mathematical problems. A boundary element model with nonlinear polarization curves as boundary conditions was used to estimate galvanic current distribution in Mg-alloys when coupled with steel [28,89]. The BEM approach with nonlinear polarization curves as boundary conditions resulted in a better galvanic current distribution estimate than a linear boundary condition. The potential and current distribution of a one-dimensional galvanic corrosion system was applied to a steel-Al joint exposed to biofuel E85. The galvanic couple was separated by a passive spacer and organic coating [90]. The approach examined modeled galvanic corrosion accuracy. Microgalvanic corrosion numerical modeling was used to evaluate microstructural effects on corrosion and localized corrosion in different galvanic couples [91–95]. The effect of cross-sectional microstructure on the corrosion behavior of Mg alloys has been investigated using a moving mesh technique in COMSOL Multi-Physics^{R} [96].

EXERCISES

E6.1. Predict the possibility of galvanic corrosion in sea water for the following coupled pairs of alloys and metals: (i) aluminum alloys and aluminum brass, (ii) cadmium and manganese bronze, (iii) zinc and tin, (iv) low alloy steel and stainless steel 410, (v) low alloy steel and stainless steel 430, (vi) nickel 200 and Ni-Cr-Mo-Cu-Si

alloy G, (vii) nickel cast iron and nickel 200, (viii) manganese bronze and silver bronze alloys, (ix) graphite and Ni-Cr-Mo alloy C, and (x) zinc and lead.

E6.2. Predict whether or not galvanic corrosion will cause the following alloys to be subjected to leaching: (i) carbon and carbon steel alloys in an oxidizing atmosphere, (ii) steel rivets in aluminum drain gutters, (iii) copper-nickel alloy in refinery condenser tubes, (iii) graphite fiber-reinforced aluminum composites, (iv) brass in water, (v) iron-chromium alloys, and (vi) carbon steel pipe in contact with the weld to stainless steel pipe.

E6.3. Estimate the effect of 1% impurity of platinum on the corrosion rate of zinc in acidic and alkaline solutions. Use the values of Tafel constants for the hydrogen evolution on the respective metals from Table E6.1.

Table E6.1 Tafel Constants for the Hydrogen Evolution on the Respective Metals

Metal	Zn Acidic Solution	Pt Acidic Solution	Zn Alkaline Solution	Pt Alkaline Solution
Tafel constant, a	−1.24	−0.10	−1.20	−0.31
Tafel constant, b	−0.12	−0.12	−0.12	−0.12

E6.4. Assuming that the surface of the alloy is equipotential under corroding conditions, by what factors do the corrosion rates of the following alloys increase/decrease in comparison with the pure iron (100% Fe) in acidic medium? Use the values of Tafel constants for the hydrogen evolution on the respective metals from Table E6.2.

Alloy A: (25% Fe, 25% Zn, 25% Ag, 25%Pb)
Alloy B: (50% Fe, 25% Zn, 12.5% Ag, 12.5%Pb)
Alloy C: (5% Fe, 25% Zn, 30% Ag, 40%Pb)

Table E6.2 Tafel Constants for Each of the Metals in the Alloy

Metal	Fe	Zn	Ag	Pb
Tafel constant, a	−0.7	−1.24	−0.95	−1.56
Tafel constant, b	−0.12	−0.12	−0.12	−0.12

E6.5. Sn and Pt are immersed in an acidic solution with unit hydrogen ion activity. Using the electrochemical parameters listed below, calculate the galvanic corrosion rate.

(a) When 1 cm^2 Sn is coupled to 1 cm^2 of Pt in acidic solution.
(b) When 10 cm^2 Pt is coupled to 1 cm^2 of Sn in the same solution.

The Tafel slope for tin dissolution is $b_a = 0.1$ V/decade. The cathodic Tafel slope for hydrogen evolution reaction on both Sn and Pt is $b_c = -0.1$/decade.

Exchange current density for hydrogen evolution on Sn, $i^{o}_{H_2,Sn} = 1 \times 10^{-8}$ A/cm^2 and on Pt, $i^{o}_{H_2,Pt} = 1 \times 10^{-3}$ A/cm^2. The concentration of dissolved species of [Sn^{2+}] = 10^{-12} M. Exchange current density for Sn dissolution is $i^{o}_{Sn} = 1 \times 10^{-6}$ A/cm^2. Tin equilibrium potential is −0.138 V vs. SHE. Assume that platinum dissolution is negligible.

E6.6. Sn and Pt are immersed in an acidic solution with unit hydrogen ion activity. Using the electrochemical parameters listed below, construct the Evans diagram and evaluate the effect of the cathode-sacrificial anode electrode surface area ratio on galvanic corrosion of a tin-platinum galvanic couple (see Case Study 6.1).

(a) Determine the corrosion potential $E_{corr,Sn}$ and corrosion rate for tin when tin is not coupled $I_{corr,Sn}$.

(b) Estimate the corrosion potential $E_{corr,\underline{Sn}-Pt(1\ cm^2)}$ and the galvanic corrosion rate $I_{corr,\underline{Sn}-Pt(1\ cm^2)}$ when 1 cm^2 of Sn is coupled with 1 cm^2 of platinum in the same solution.

(c) Estimate the corrosion potential $E_{corr,\underline{Sn}-Pt(10\ cm^2)}$ and the galvanic corrosion rate $I_{corr,\underline{Sn}-Pt(10\ cm^2)}$ when 1 cm^2 of Sn is coupled with 10 cm^2 of platinum in the same solution.

(d) Estimate the hydrogen evolution current density $i_{H_2,\underline{Sn}-Pt(1\ cm^2)}$ on tin when 1 cm^2 of Sn is coupled with 1 cm^2 of platinum in the same solution.

(e) Estimate the hydrogen evolution current density $i_{H_2,\underline{Sn}-Pt(10\ cm^2)}$ on tin when 1 cm^2 of Sn is coupled with 10 cm^2 of platinum in the same solution.

Tafel slope for tin dissolution is $b_a = 0.1$ V/decade. The Tafel slopes for hydrogen evolution reaction on both tin and platinum is $b_c = -0.1$/decade. Exchange current density for hydrogen evolution on Sn, $i^{o}_{H_2,Sn} = 1 \times 10^{-8}$ A/cm^2 and on Pt, $i^{o}_{H_2,Pt} = 1 \times 10^{-3}$ A/cm^2. The concentration of dissolved species of [Sn^{2+}] = 10^{-12} M. Exchange current density for Sn dissolution is $i^{o}_{Sn} = 1 \times 10^{-6}$ A/cm^2. Platinum dissolution is negligible. Sn equilibrium potential is −0.138 vs. SHE and that of hydrogen, e^{o}, is 0.00 vs. SHE. Assume that platinum dissolution is negligible.

E6.7. Tin and gold are immersed in acidic solution with unit hydrogen ion activity. Using the electrochemical parameters listed below, calculate the galvanic corrosion rate when 1 cm^2 of Sn is coupled to 1 cm^2 of Au in acidic solution. Compare the results with those obtained in problem E6.6 when 1 cm^2 Sn is galvanically coupled with 1 cm^2 Pt. For Sn, the anodic Tafel constant, b_a, is 0.1 V/decade. The cathodic slopes for hydrogen evolution reaction on both Sn and Au is $b_c = -0.1$/decade. Hydrogen evolution current density on Sn is 1×10^{-8} A/cm^2 and on Au 1×10^{-6} A/cm^2. The concentration of dissolved species of [Sn^{2+}] = 10^{-12} M. Exchange current density for Sn dissolution is 1×10^{-6} A/cm^2. Sn equilibrium potential is $e^{o}_{Sn^{2+}|Sn} = -0.138$V vs. SHE. The hydrogen

reversible potential on tin is 0.00 vs. SHE. Assume that gold dissolution is negligible.

E6.8. Equal 1 cm^2 areas of nickel and iron are immersed in 1 M acidic solution. Using the electrochemical parameters listed below:

(a) Calculate the corrosion potential and the corrosion rate for each metal, when they are uncoupled.

(b) Determine the potential and current passing in the galvanic couple when nickel and iron are electrically coupled.

(c) Determine the corrosion rates for nickel and iron when they are galvanically coupled.

The standard equilibrium dissolution potentials for nickel and iron are -0.25 and -0.44 V vs. SHE, respectively. The exchange current density for nickel dissolution is 1×10^{-7} A/cm^2 and that for Fe is 1×10^{-6} A/cm^2. The concentrations of dissolved species of $[Ni^{2+}]$ is 4.13×10^{-4} M and that of $[Fe^{2+}]$ is 1 M. The exchange current densities for the hydrogen evolution reaction on nickel is 4×10^{-6} A/cm^2 and on iron is 1×10^{-6} A/cm^2. Assume Tafel constants of ± 0.1 V/decade for the anodic and cathodic reactions.

E6.9. Construct the Evans diagram for a nickel and iron galvanic couple immersed in 1 M acidic solution. Using the electrochemical parameters listed in Exercise E6.8, estimate graphically the following parameters and tabulate the results:

(a) The corrosion potential and the corrosion rate for each metal, when they are uncoupled.

(b) The corrosion potential, $E_{corr,Ni\text{-}Fe}$, and the current passivating the galvanic couple, $I_{corr,Ni\text{-}Fe}$.

(c) The individual corrosion rates for nickel, $I_{corr,\underline{Ni}-Fe}$, and iron, $I_{corr,Ni-\underline{Fe}}$, when they are galvanically coupled.

REFERENCES

[1] A.H. Bard, T. Parsons, J. Jordan, Standard Potentials in Aqueous Solutions, Marcel Dekker, Inc., New York, 1985.

[2] L.I. Antropov, Theoretical Electrochemistry, MIR Publishers/Imported Publications, Moscow/Chicago, 1972.

[3] M.G. Fontana, Corrosion Engineering, third ed., McGraw-Hill, New York, 1986.

[4] H.P. Hack, Evaluating Galvanic Corrosion, in: Corrosion: Fundamentals, Testing and Protection, ninth ed., in: ASM Handbook, Vol. 13A, ASM, Metals Park OH, 1987, pp. 562–567.

[5] P.E. Morris, R.M. Kain, An electrochemical approach to alloy protection, Chem. Eng. Prog. 73 (1977) 103–104.

[6] H.P. Hack, J.R. Scully, Galvanic corrosion prediction using long- and short-term polarization curves, Corrosion 42 (1986) 79–90.

[7] D.A. Jones, N.D. Greene, Electrochemical measurement of low corrosion rates, Corrosion 22 (1966) 198–204.

[8] D.A. Jones, Polarization studies of brass-steel galvanic couples, Corrosion 40 (1984) 181–185.

[9] K.B. Deshpande, Experimental investigation of galvanic corrosion: comparison between SVET and immersion techniques, Corros. Sci. 52 (2010) 2819–2826.
[10] P.W. Davies, Membrane potential and resistance of perfused skeletal muscle fibers with control of membrane current, Fed. Proc. 25 (1966) 332–336.
[11] L.F. Jaffe, R. Nucitelli, An Ultrasensitive vibrating probe for measuring steady extracellular currents, J. Cell Biol. 63 (1974) 614–628.
[12] H.S. Isaacs, Initiation of stress corrosion cracking of sensitized type 304 stainless steel in dilute thiosulfate solution, J. Electrochem. Soc. 135 (1988) 2180–2183.
[13] H.S. Isaacs, A.J. Davenport, A. Shipley, The Electrochemical response of steel to the presence of dissolved cerium, J. Electrochem. Soc. 138 (1991) 390–393.
[14] F. Zou, C. Barreau, R. Hellouin, D. Quantin, D. Thierry, Application of scanning vibrating electrode techniques to study the degradation of coil coated steel at edges, in: Proceedings of the 3rd International Conference on Zinc and Zinc Alloy Coated Steel Sheet, 1995, pp. 837–843, Galvatech'95, Chicago.
[15] D.A. Worsley, H.N. McMurray, A. Belghazi, Determination of localized corrosion mechanisms using a scanning vibrating reference electrode technique, Chem. Commun. (1997) 2369–2370.
[16] Z. Ahmad, Principles of Corrosion Engineering and Corrosion Control, first ed., Elsevier, Great Britain, 2006.
[17] D.A. Jones, Principles and Prevention of Corrosion, second ed., Prentice Hall Inc., New Jersey, 1992.
[18] D.A. Jones, B.E. Wilde, Galvanic reactions during localized corrosion on stainless steel, Corros. Sci. 18 (1979) 631–643.
[19] E. Tada, K. Sugawara, H. Kaneko, Distribution of pH during galvanic corrosion of a Zn/steel couple, Electrochim. Acta 49 (2003) 1019–1026.
[20] R.M. Souto, Y. Gonzalez-Garcia, A.C. Bastos, A.M. Simoes, Investigating corrosion processes in the micrometric range: a SVET study of the galvanic corrosion of zinc coupled with iron, Corros. Sci. 49 (2007) 4568–4580.
[21] E. Tada, H. Kaneko, Optical visualization of concentration field of Zn^{2+} during galvanic corrosion of a Zn/steel couple, Corros. Sci. 52 (2010) 3421–3427.
[22] S. Tamilmani, W. Huang, S. Raghavan, Galvanic corrosion between copper and tantalum under CMP conditions, J. Electrochem. Soc. 153 (2006) F53–F59.
[23] C.A. Huang, T.H. Wang, W.C. Han, C.H. Lee, A Study of the galvanic corrosion behavior of Inconel 718 after electron beam welding, Mater. Chem. Phys. 104 (2007) 293–300.
[24] A.B. Rahman, S. Kumar, A.R. Gerson, Galvanic corrosion of laser weldments of AA6061 aluminium alloy, Corros. Sci. 49 (2007) 4339–4435.
[25] P. Zang, X. Nie, D.O. Northwood, Influence of coating thickness on the galvanic corrosion properties of Mg oxide in an engine coolant, Surf. Coat. Techol. 203 (2009) 3271–3277.
[26] G. Song, B. Johannesson, S. Hapugoda, D. StJohn, Galvanic corrosion of magnesium alloy AZ91D in contact with an aluminum alloy, steel and zinc, Corros. Sci. 46 (2004) 955–977.
[27] A.R.P. Ambrozin, M.R. Monteiro, A.O. Santos, S.E. Kuri, Evaluation of galvanic corrosion of a Zn alloy in alcohol fuel, Fuel Process. Technol. 91 (2010) 1687–1690.
[28] J.X. Jia, G. Song, A. Atrens, Influence of geometry on galvanic corrosion of AZ91D coupled to steel, Corros. Sci. 48 (2006) 2133–2153.
[29] S. Tae, Probability of galvanic corrosion of Cr-bearing rebars in concrete, ISIJ Int. 49 (2009) 1206–1211.
[30] A. Nasser, A. Clement, S. Laurens, A. Castel, Influence of steel-concrete interface condition on galvanic corrosion currents in carbonated concrete, Corros. Sci. 52 (2010) 2878–2890.
[31] R. Sanchez-Tovar, M.T. Montanes, J. Garcia-Anton, The effect of temperature on the galvanic corrosion of the copper/AISI 204 pair in Li-Br solutions under hydrodynamic conditions, Corros. Sci. 52 (2010) 722–733.
[32] M.E. Blasco-Tamarit, A. Igual-Munoz, J. Garcia-Anton, D.M. Garcia-Garcia, Galvanic corrosion of titanium coupled to welded titanium in Li-Br solutions at different temperatures, Corros. Sci. 51 (2009) 1095–1102.
[33] J. Idrac, G. Mankowski, G. Thompson, P. Skeldon, C. Blanc, Y. Kihn, Galvanic corrosion of aluminum-copper model alloys, Electrochim. Acta 52 (2007) 7626–7633.

[34] H. Arslan, H. Celikkan, N. Ornek, O. Ozan, M.L. Aksu, A.E. Ersoy, Galvanic corrosion of titanium-based dental implant materials, J. Appl. Electrochem. 38 (2008) 853–859.
[35] K. Nakamura, Y. Takada, M. Yoda, K. Kimura, O. Okuno, Galvanic corrosion of ferritic stainless steels used for dental magnetic attachments in contact with an iron-platinum magnet, Dent. Mater. 27 (2008) 203–210.
[36] H. Ding, H. Hihara, Galvanic corrosion in metal-matrix composites containing semiconducting constituents, J. Electrochem. Soc. 156 (2009) C422–C427.
[37] Z. Liu, B. Wu, M. Gu, An investigation of micro-galvanic corrosion in Al/AlNp composites, Mater. Chem. Phys. 102 (2007) 43–46.
[38] D.C. Miller, W.L. Hughes, Z. Wang, K. Gall, C. Stoldt, Mechanical effects of galvanic corrosion on structural polysilicon, J. Microelectromech. Syst. 16 (2007) 87–101.
[39] D.C. Miller, C.R. Becker, C.R. Stoldt, Relation between morphology, etch rate, surface wetting, and electrochemical characteristics for micromachined silicon subject to galvanic corrosion, J. Electrochem. Soc. 155 (2008) F253–F265.
[40] A. Gebhard, T. Bayerl, A.K. Schlarb, K. Friedrich, Galvanic corrosion of polyacrylnitrile (PAN) and pitch-based short carbon fibers in polyetheretherketone (PEEK) composites, Corros. Sci. 51 (2009) 2524–2528.
[41] V.C.R. McLoughlin, The replacement of cadmium for the coating of fasteners in aerospace applications, Trans. Inst. Met. Finish. 57 (1979) 102–104.
[42] A. Ashur, J. Sharon, I.E. Klein, Hydrogen embrittlement of cadmium-plated high-strength steels, Plat. Surf. Finish. 83 (1996) 58–60.
[43] N. Zaki, Zinc-nickel alloy plating, Metal Finish. 87 (1989) 57–60.
[44] D.E. Hall, Electrodeposited zinc-nickel alloy coatings: a review, Plat. Surf. Finish. 70 (1983) 59–65.
[45] M. Ramasubramanian, B.N. Popov, R.E. White, Characterization of hydrogen permeation through zinc-nickel alloys under corroding conditions: mathematical model and experimental study, J. Electrochem. Soc. 145 (1998) 1907–1913.
[46] B.N. Popov, M. Ramasubramanian, S.N. Popova, R.E. White, K.M. Yin, Galvanostatic pulse and pulse reverse plating of zinc-nickel alloys from sulfate electrolytes on a rotating disc electrode, Trans. Faraday Soc. 92 (1996) 4021–4028.
[47] P. Ganesan, S.P. Kumaraguru, B.N. Popov, Development of compositionally modulated Zn-Ni multilayer deposits as replacement for cadmium, Surf. Coat. Techol. 201 (2007) 7896–7904.
[48] K.R. Baldwin, C.J.E. Smith, Some cadmium replacements for use on aircraft components, Prod. Finish. 45 (1992) 12–18.
[49] N.R. Short, A. Abibsi, J.K. Dennis, Corrosion resistance of electroplated zinc alloy coatings, Trans. Inst. Met. Finish. 67 (1991) 73–77.
[50] ASTM B840, Standard specification for electrodeposited coatings for Zn-Co alloys deposits, ASTM International, Philadelphia, PA, 1994.
[51] T. Tsuchida, I. Suzuki. U. S. Patent 4,581,110, U.S. Patent and Trademark Office, Washington, DC, 1986.
[52] L. Sziraki, A. Cziraki, Z. Vertesy, I. Kiss, V. Ivanova, G. Raichevski, S. Vitkova, S. Marinova, T. Marinova, Zn and Zn-Sn alloy coatings with and without chromate layers. Part I: corrosion resistance and structural analysis, J. Appl. Electrochem. 29 (1999) 927–937.
[53] M. Eyraud, A. Garnier, F. Mazeron, J. Crousier, Morphology and composition of electrodeposited zinc-manganese alloys, Plat. Surf. Finish. 82 (1995) 63–70.
[54] M. Sagiyama, T. Urakawa, T. Adaniya, T. Hara, Y. Fukuda, Electrodeposition of zinc-manganese on steel strip, Plat. Surf. Finish. 74 (1987) 77–82.
[55] B. Veeraraghavan, D. Slavkov, S. Prabhu, M. Nicholson, B. Haran, B. Popov, B. Heimann, Synthesis and characterization of novel non-chrome electrolytic surface treatment process to protect zinc coatings, Surf. Coat. Techol. 167 (2003) 41–51.
[56] S.P. Kumaraguru, B. Veeraraghavan, B.N. Popov, Development of novel electroless process for deposition of corrosion resistant silica coatings, J. Electrochem. Soc. 153 (2006) B253–B259.
[57] C.J. Lan, W.Y. Liu, S.T. Ke, T.S. Chin, Potassium salt-based alkaline bath for deposition of Zn-Fe alloys, Surf. Coat. Techol. 201 (2006) 3103–3108.

[58] A.P. Yadav, H. Katayama, K. Noda, H. Masuda, A. Nishikata, T. Tsuru, Effect of Fe-Zn alloy layer on the corrosion resistance of galvanized steel in chloride-containing environments, Corros. Sci. 49 (2007) 3716–3731.
[59] H. Kim, B.N. Popov, K.S. Chen, A novel electrodeposition process for plating Zn-Ni-Cd Alloys, J. Electrochem. Soc. 150 (2003) C81–C88.
[60] H. Kim, B. Popov, K.S. Chen, Comparison of corrosion resistance and hydrogen permeation properties of Zn-Ni, Zn-Ni-Cd and Cd coatings on low carbon steel, Corros. Sci. 45 (2003) 1505–1521.
[61] P. Ganesan, S.P. Kumaraguru, B.N. Popov, Development of Zn-Ni-Cd coatings by pulse electrodeposition process, Surf. Coat. Techol. 201 (2006) 3658–3669.
[62] A. Durairajan, A. Krishnaiyer, B. Haran, R.E. White, B.N. Popov, Characterization of hydrogen permeation through a corrosion-resistant zinc-nickel-phosphorus alloy, Corrosion 56 (2000) 283–288.
[63] B. Veeraraghavan, B. Haran, S. Prabhu, B. Popov, Corrosion protection of steel using non-anomalous Ni-Zn-P alloys, J. Electrochem. Soc. 150 (2003) B131–B139.
[64] B. Veeraraghavan, H. Kim, B.N. Popov, Optimization of electroless Ni-Zn-P deposition process: experimental study and mathematical modeling, Electrochim. Acta 49 (2004) 3143–3154.
[65] N. Boshkov, K. Petrov, D. Kovacheva, S. Vitkova, S. Nemska, Influence of the alloying component on the protective ability of some zinc galvanic coatings, Electrochim. Acta 51 (2005) 77–84.
[66] M. Bucko, J. Rogan, S.I. Stevanovic, A. Peric-Grujic, J.B. Bajat, Initial corrosion protection of Zn-Mn alloys electrodeposited from alkaline solution, Corros. Sci. 53 (2011) 2861–2871.
[67] C. Savall, C. Rebere, D. Sylla, M. Gadouleau, P. Refait, J. Creus, Morphological and structural characterization of electrodeposited Zn-Mn alloys from acidic chloride bath, Mater. Sci. Eng. A 430 (2006) 165–171.
[68] N. Boshkov, Galvanic Zn-Mn alloys: electrodeposition, phase composition, corrosion behavior and protective ability, Surf. Coat. Techol. 172 (2003) 217–226.
[69] N. Boshkov, K. Petrov, S. Vitkova, G. Raichevsky, Galvanic alloys Zn-Mn composition of the corrosion products and their protective ability in sulfate-containing medium, Surf. Coat. Techol. 194 (2005) 276–282.
[70] N. Boshkov, K. Petrov, G. Raichevski, Corrosion behavior and protective ability of multilayer galvanic coatings of Zn and Zn-Mg alloys in sulfate-containing medium, Surf. Coat. Techol. 200 (2006) 5995–6001.
[71] B. Bozzini, E. Griskonis, A. Fanigliulo, A. Sulcius, Electrodeposition of Zn-Mn alloys in the presence of thiocarbamide, Surf. Coat. Techol. 154 (2002) 294–303.
[72] P. Díaz-Arista, G. Trejo, Electrodeposition and characterization of manganese coatings obtained form an acidic chloride bath containing ammonium thiocyanate as an additive, Surf. Coat. Techol. 201 (2006) 3359–3367.
[73] H. Chen, C.X. Ding, P.Y. Zhang, P.Q. La, S.W. Lee, Wear of plasma-sprayed nanostructured zirconia coatings against stainless under distilled-water conditions, Surf. Coat. Techol. 173 (2003) 144–149.
[74] H. Singh, D. Puri, S. Prakash, An overview of Na_2SO_4/V_2O_5 induced hot corrosion of Fe- and Ni-based super-alloys, Surf. Coat. Techol. 192 (2007) 27–38.
[75] J. Jayaraj, D.J. Sordelet, D.H. Kim, Y.C. Kim, E. Fleury, Corrosion behavior of Ni-Zr-Ti-Si-Sn amorphous plasma-spray coating, Corros. Sci. 48 (2006) 950–964.
[76] M. Gell, L.D. Xie, E.H. Jordan, N.P. Padture, Mechanisms of spallation of solution precursor plasma spray thermal barrier coatings, Surf. Coat. Techol. 188–189 (2004) 101–106.
[77] H.I. Faraoun, T. Grosdidier, J.L. Seichepine, D. Goran, H. Aourag, C. Coddet, J. Zwick, N. Hopkins, Improvement of thermally-sprayed abradable coating by microstructure control, Surf. Coat. Techol. 201 (2006) 2303–2312.
[78] H.I. Faraoun, J.L. Seichepine, C. Coddet, H. Aourag, J. Zwick, N. Hopkins, D. Sporer, M. Hertter, Modelling route for abradable coatings, Surf. Coat. Techol. 200 (2006) 6578–6582.
[79] J. Matejicek, B. Kolman, J. Dubsky, K. Neufuss, N. Hopkins, J. Zwick, Alternative methods for determination of composition and porosity in abradable materials, Mater Charact 57 (2006) 17–29.
[80] C. Xu, L. Du, B. Yang, W. Zhang, The effect of Al content on the galvanic corrosion behavior of coupled Ni/graphite and Ni-Al coatings, Corros. Sci. 53 (2011) 2066–2074.

[81] R.S. Munn, Computer modeling in corrosion, in: R.S. Munn (Ed.), ASTM STP 1154, ASTM International, Philadelphia, PA, 1992, pp. 215–228.
[82] N.G. Zamani, Boundary element simulation of the cathodic Protection system in a prototypic ship, Appl. Math. Comp. 26 (1988) 119–134.
[83] V.G. DeGiorgi, E.D. Thomas, A.I. Kaznoff, Computer modeling in corrosion, in: R.S. Munn (Ed.), ASTM STP 1154, ASTM International, Philadelphia, PA, 1992, pp. 265–267.
[84] V.G. DeGiorgi, A review of computational analyses of ship cathodic protection systems, in: Boundary Elements XIX, Computational Mechanics Publications, South Hampton, 1997, pp. 829–838.
[85] R.A. Adey, S.M. Niku, Computer modeling of corrosion using the boundary element method, in: R. S. Munn (Ed.), ASTM STP 1154, ASTM International, Philadelphia, PA, 1992, pp. 248–263.
[86] Y.G. Kim, Y.C. Kim, Y.T. Kho, BEM application for thin electrolyte corrosion problem, in: in: A. J. Kasaab, C.A. Brebbia (Eds.), Boundary Element Technology XIV, Vol. 27, Wessex Institute, United Kingdom, 2001, pp. 88–94.
[87] K.S. Yeung, The effect of protective coatings on galvanic corrosion for bolted components, in: in: A. J. Kasaab, C.A. Brebbia (Eds.), Boundary Element Technology XIV, Vol. 27, Wessex Institute, United Kingdom, 2001, pp. 273–283.
[88] M. Verbrugge, Galvanic corrosion over a semi-infinite, planar surface, Corros. Sci. 48 (2006) 3489–3512.
[89] J. Jia, G. Song, A. Atrens, D. St. John, J. Baynham, G. Chandler, Evaluation of the BEASY program using linear and piecewise linear approaches for the boundary conditions, Mater. Corros. 55 (2004) 845–852.
[90] G. Song, Potential and current distributions of one-dimensional galvanic corrosion systems, Corros. Sci. 52 (2010) 455–480.
[91] G. Ballerini, U. Bardi, R. Bignucolo, G. Ceraolo, About some corrosion mechanisms of AZ91D magnesium alloy, Corros. Sci. 47 (2005) 2173–2184.
[92] T.R. Thomaz, C.R. Weber, T. Pelegrini, L.F.P. Dick, G. Knornschild, The negative difference effect of magnesium and of the AZ91 alloy in chloride and stannate-containing solutions, Corros. Sci. 52 (2010) 2235–2243.
[93] S. Amira, M. Shehata, D. Dube, R. Tremblay, E. Ghalli, Corrosion behavior of die-cast and thixocast AXJ530 magnesium alloy in chloride medium, Adv. Mater. Res. 15–17 (2007) 449–454.
[94] H.S. Isaacs, The measurement of the galvanic corrosion of soldered copper using the scanning vibrating electrode technique, Corros. Sci. 28 (1998) 547–558.
[95] A.M. Simoes, A.C. Bastos, M.G. Ferrira, Y. Gonzalez-Garcia, S. Gonzalez, R.M. Souto, Use of SVET and SECM to study the galvanic corrosion of an iron-zinc cell, Corros. Sci. 49 (2007) 726–739.
[96] K.B. Deshpande, Numerical modeling of micro-galvanic corrosion, Electrochim. Acta 56 (2011) 1737–1745.

CHAPTER 7

Pitting and Crevice Corrosion

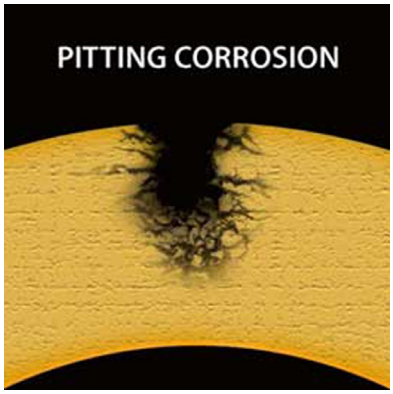

Chapter Contents

Corrosion Engineering
http://dx.doi.org/10.1016/B978-0-444-62722-3.00007-0

7.1 INTRODUCTION

Pitting mechanism and crevice corrosion evaluation is discussed in this chapter by reviewing recent literature through corrosion severity control, main variables, and experimental data consistency in particular systems. Electrochemical kinetics such as charge transfer, mass transport, and ohmic effects explain pit growth and arrest. Pitting inhibition and crevice corrosion is focused on new alloys and alloy composition effects for decreased pitting corrosion susceptibility, conversion coating and inhibitor development, and cathodic and anodic protection. Crevice and filiform corrosion are described by initiation and propagation processes. The case study and exercise problems illustrate pitting and crevice mechanisms and corrosion protection strategies.

Pitting represents extremely localized corrosion and is one of the most destructive forms of corrosion. Corrosion pits are small cavities or holes similar to or deeper than its surface diameter. The pits grow with a porous cover that appears as a white deposit on the surface with minimal base metal loss, and are very difficult to detect. Removing the white deposits reveals small holes or pits on the surface. They penetrate the metal, causing equipment failure due to preformation with minimal weight loss.

Pitting corrosion severity is controlled by parameters such as corrosive environment, chloride concentration, electrolyte acidity, oxidizer concentration, temperature, structural characteristics, metal or alloy composition, low dissolved oxygen concentrations, and potential scan rate [1–11]. Localized mechanical or chemical damage to a passive oxide, insufficient inhibitor coverage, and nonuniformities in the metal structure due to impurities contribute to pitting corrosion [1–4]. The most common aggressive species are halogen ions. Chloride is the anion of a strong acid and is very soluble with high diffusivity. Chloride in the electrolyte prevents passive film formation or breakdown passive films on many metals and alloys including aluminum, iron, nickel, and stainless steel. Surface pitting extent is reportedly proportional to the logarithm of chloride concentration in the electrolyte [12–14]. The electrolyte must act as a strong oxidizer and favor the passive state to initiate pitting corrosion. Oxidizing metal ions such as ferric and cupric halides act as electron acceptors (cathodic reactants) and do not require oxygen to initiate and propagate pitting corrosion [4,12,14]. Other ions, such as $S_2O_3^-$, may cause pitting corrosion. Pitting corrosion also initiates by nonmetallic inclusions or second-phase intermetallics in the stainless steel surface microstructure [1–3]. MnS inclusion dissolution at the MnS/matrix is the initial step in stainless steel pit formation [15]. Dissolved oxygen in the electrolyte causes a less stable stainless steel protective film and, in the presence of chloride ions, initiates pitting corrosion.

7.2 CRITICAL PITTING POTENTIAL AND EVALUATION OF PITTING CORROSION

Pitting potential is defined by the American Society for Testing and Materials (ASTM) as the potential beyond which pitting propagates. Stable pits form at potentials more noble

than the critical pitting potential. The potential where current sharply increases during cyclic polarization in the anodic direction is defined as the pitting potential (E_P) or critical pitting potential. This potential is also called breakdown potential (E_b) because it is not clear which form of localized corrosion occurs: pitting, intergranular, or crevice corrosion. Cyclic polarization measures the specimen's pitting tendency in a given metal-electrolyte system. This technique estimates pitting potential and critical protection potential (E_{prot}) [5]. Critical protection potential is defined as the most noble potential where neither pitting nor crevice corrosion will propagate.

Figure 7.1 shows a typical cyclic polarization curve for stainless steel. In a pitting experiment, a potential scan is applied in the anodic direction beginning at E_{corr} until a large current increase [16]. The potential is controlled by a potentiostat and is commonly measured using a saturated calomel reference electrode and a Pt counter electrode. The final potential of the scan should be negative with respect to the protection potential E_{prot}. A preliminary scan is usually performed to estimate the final potential. The polarization curve in Fig. 7.1 illustrates a protective passive film present at the alloy corrosion potential E_{corr}. The passive film breaks down at the pitting potential. The pit starts to grow above the critical pitting potential. The potential where the loop closes on the reverse scan in Fig. 7.1 is the passivation or protection potential. The protection potential can be estimated by extrapolating the reverse scan to zero current when the loop of the polarization curve does not close. The larger the hysteresis loop, the higher probability that localized corrosion will propagate if pitting corrosion is initiated. If the protection and pitting potential are the same, there will be little tendency to pit. If the protection

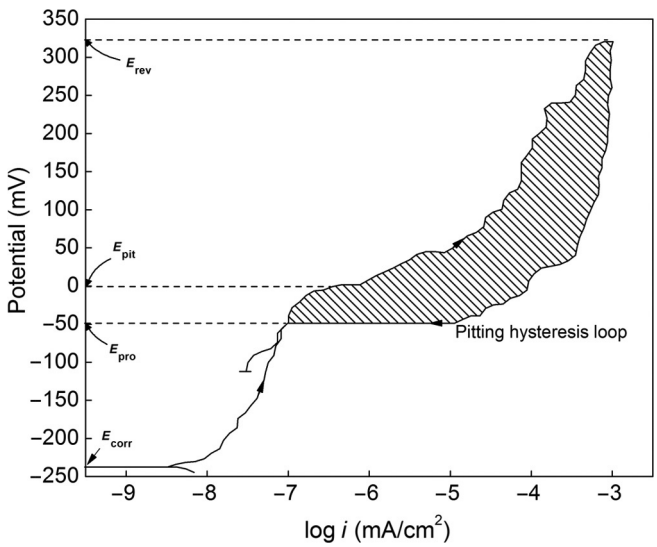

Fig. 7.1 Typical cyclic polarization plot for stainless steel that shows the corrosion potential, E_{corr}, critical pitting potential, E_{pit}, protection potential, E_{prot}, and metastable pitting region.

potential is more positive (anodic) than the pitting potential, there will be no pitting. Furthermore, higher E_{prot} value for an alloy indicate its tendency to repassivate more easily.

The difference between pitting and protective potential is used to estimate pitting corrosion susceptibility for materials [6,7,15]. If protection is more negative than the pitting potential, as shown in Fig. 7.1, the pitting probability is greater [6,7]. When the open circuit or corrosion potential is above the pitting potential, the material spontaneously pits at the corrosion potential.

Figure 7.2 shows how pitting potential can be determined from the anodic polarization curve. A drastic current increase is observed when the pitting potential is reached. Pitting potential is less noble in the presence of chlorides. Pitting potentials have been compared to maximum and minimum corrosion potentials for stainless steel alloys: Types 430, 304, and 116; Carpenter 20Cb; Incoloy 825; and Hastelloy C in the $Fe^{3+}|Fe^{2+}$ redox couple [7]. Pitting was always observed when the maximum corrosion potential was higher (nobler) than the pitting potential. Only Hastelloy C, where the maximum corrosion potential was below pitting potential, did not pit in the electrolyte in the presence of strong oxidizing agents.

Figure 7.3 presents stainless steel pitting potential with 13% and 18% chromium as a function of molybdenum content in the presence of 1 M NaCl at 20 °C. Pitting potential increases with an increase of Cr or Mo content, resulting in a decrease of pitting corrosion [8]. Pitting analyses is used to: (i) develop new alloys, (ii) rank alloys, (iii) perform failure

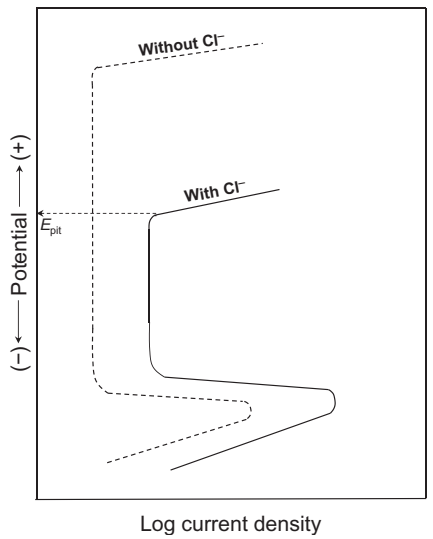

Fig. 7.2 Determination of the critical pitting potential from anodic potentiodynamic curve.

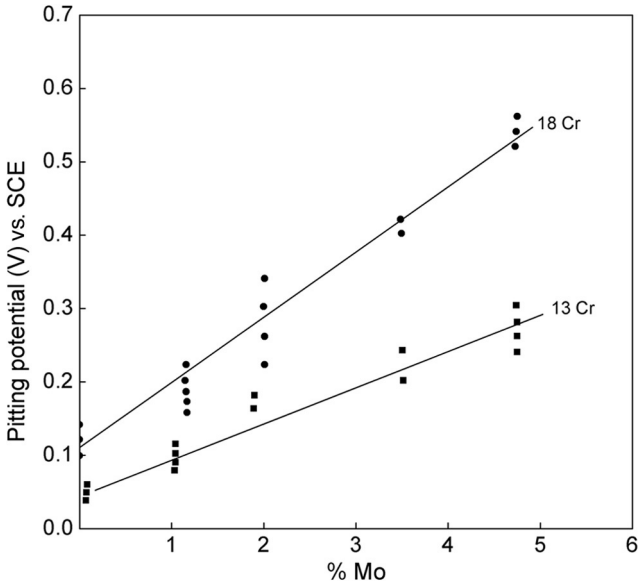

Fig. 7.3 Pitting potentials for the 13% and 18% Cr ferritic stainless steels in 1 M NaCl at 20 °C [8]. *Reproduced by permission of The Electrochemical Society.*

analysis, and (iv) predict pitting penetration rates. However, localized corrosion evaluation through cyclic polarization is insufficient to fundamentally understand pitting corrosion [17–19].

Depending on the potential, chloride concentration in the electrolyte, structure of the alloy, passive film thickness, and the chemical composition of the corrosion environment, pits may appear in various morphologies as illustrated in Fig. 7.4.

A ferric chloride test for evaluation of pitting corrosion has been standardized as ASTM Practice G 46-76. The test solution contains 100 g of reagent-grade ferric chloride ($FeCl_3.6H_2O$) in 900 ml distilled water (a solution of about 6 wt.% $FeCl_3$). Sample exposures are performed at 22 or 50 °C. Environment aggressiveness increases with temperature. Pitted specimen evaluation may include taking photographs or weight loss measurements. ASTM Practice G 46-94 includes more detailed examination such as pit density, surface size, and pit depth. Measurements are compared using standard charts, as shown in Fig. 7.5. For example, a pit characterized as A-3, B-2, and C-1 would have an average surface density of 5×10^4 pits/cm^2, a surface area of 2.0 mm^2, and a depth of 0.4 mm.

Weight measurements are not useful to evaluate pitting corrosion since a small number of pits can penetrate the reactor wall and cause failure with very small weight loss. Table 7.1 lists pit depth measurement methods according to ASTM G 46-94 [5].

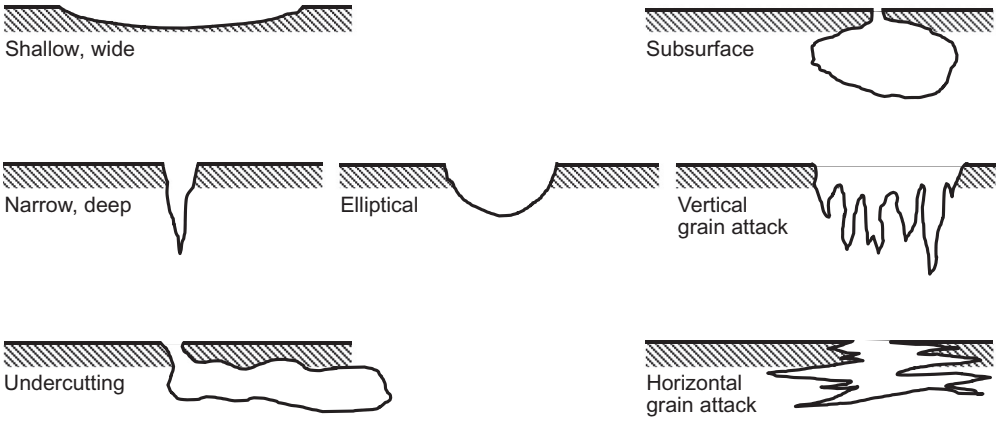

Fig. 7.4 Cross-sectional shapes of pits [5]. *Reprinted, with permission, from ASTM G 46-94, Standard Guide for Examination and Evaluation of Pitting Corrosion, copyright ASTM International, West Conshohocken, PA.*

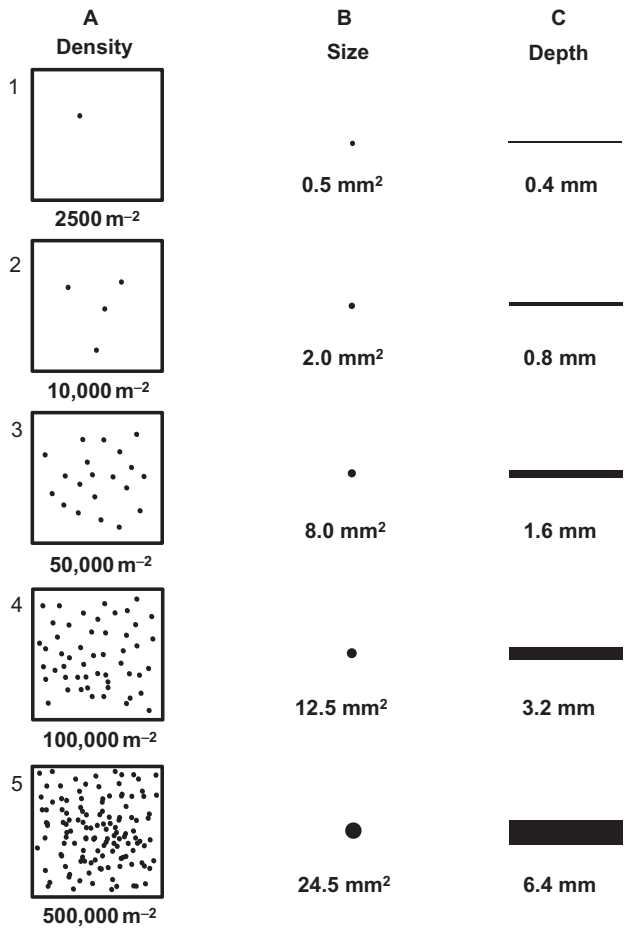

Fig. 7.5 Standard rating charts for pits [5]. *Reprinted, with permission, from ASTM G 46-94, Standard Guide for Examination and Evaluation of Pitting Corrosion, copyright ASTM International, West Conshohocken, PA.*

Table 7.1 Methods of Measuring Pit Depth [5]

Method	Description	Remarks
Metallographic	Sectioning at maximum depth Polish through selected pit followed by microscopic measurements	Large uncertainty in selecting deepest pits and time consuming and sectioning at maximum depth
Machining	Measure depth where no evidence of pits remains	The sample is destroyed. Requires sample of regular shape
Micrometer Depth Gauge	With needle probe compare readings between surface and pit bottoms	Cannot be used for undercut or directionally oriented pits. Only pits with large opening are used
Microscopic	Calibrated fine focus should be used to determine depth difference between surface and pit bottoms	Light must reach pit bottom

Reprinted, with permission, from ASTM G 46-94, Standard Practice for Examination and Evaluation of Pitting Corrosion, copyright ASTM International, West Conshohocken, PA

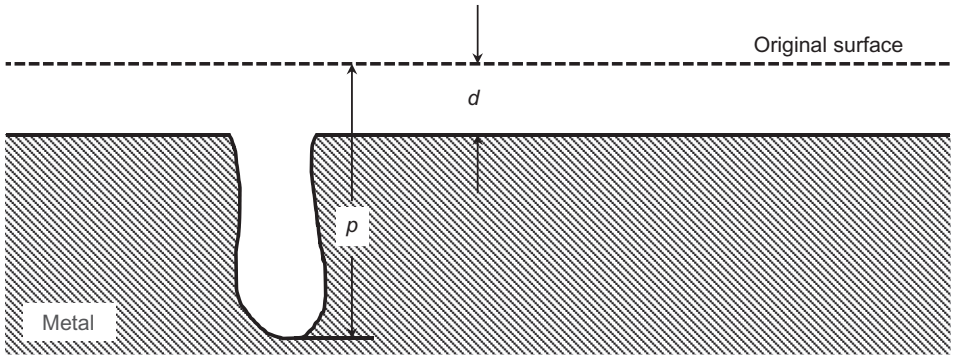

Fig. 7.6 Definition of the pitting factor, *p*/*d*.

Pit attack extent, shown in Fig. 7.6, is measured using the pitting factor, p/d, where p is the maximum penetration from the original surface determined using microscopy and d is the average penetration estimated by weight loss. For low average penetration, this method is inappropriate because the pitting factor tends to infinity.

7.3 MECHANISM OF PITTING CORROSION

Pitting corrosion is initiated by chloride migration from the electrolyte to the metal-passive film interface. Chloride ions adsorb on the outer metal oxide surface, permeate and interact with the underlying metal [9,10]. Redox reaction at the interface increases

the potential toward pitting potential resulting in a local chloride concentration increase due to electrostatic attraction between the negatively-charged chloride ions and the positively-charged surface [11]. Pitting takes place in several steps: (i) passive film breakdown-nucleated pit formation, (ii) embryonic pit formation, (iii) metastable pit development, (iv) stable pit and pit growth, and (v) pit arrest [1–4,14], as discussed below.

7.3.1 Passive film breakdown

Three main mechanisms for passive film breakdown and pit initiation have been suggested in the literature through penetration, adsorption, or film breaking [20–22]. These mechanisms apply to pure metal systems because they do not consider second-phase particles in the passive film matrix, which very often initiates pitting. For example, as already discussed, dissolution of MnS inclusion at the MnS/matrix is the initial pit formation step in steel [15]. In the absence of chloride ions, the protective hydrated iron passive film slowly converts into dissolved ferric ions:

$$FeOOH + H_2O \rightarrow Fe^{3+} + 3OH^- \tag{7.1}$$

In the presence of chloride ions, the outer layers of the passive film are displaced due to catalytic Fe^{3+} formation. The overall reaction (7.1) takes place in two steps and much more rapidly, with intermediate FeOCl displaced to chloride islands on the passive film surface as shown in Fig. 7.7.

$$FeOOH + Cl^- \rightarrow FeOCl + OH^- \tag{7.2}$$

$$FeOCl + H_2O \rightarrow Fe^{3+} + Cl^- + 2OH^- \tag{7.3}$$

The reaction in Eq. (7.3) removes the passive film at the active pitting site and initiates underlying iron dissolution to Fe^{2+}.

In the early 1970s, Galvele modeled ion transport in a one-dimensional pit geometry based on metal dissolution and hydrolysis [23,24]. The model suggested that passive film pitting potential is determined by small pit propagation (metastable pits) below pitting potential. As shown in Fig. 7.8 [23], the model suggests that the pit growth is initiated when the pit interior is acidified by metal dissolution, diffusion, and hydrolysis in addition to passive film penetration by the electrolyte.

Galvele and his coworkers [25–27] defined the critical factor that controls the pitting current density and the pit penetration as the product of current density, i, and pit depth, x. The critical value (ix) maintains the pH at the pit bottom sufficient to sustain metal dissolution and pit propagation. A Galvele model [23] used for pit depth, diffusion length, and interface metal concentration values that are too low. The model arbitrarily used 10^{-6} mol/L for the metal ion concentration in equilibrium with the metal oxide. Most experimental results indicate ion concentration in a stable pit is considerably higher and

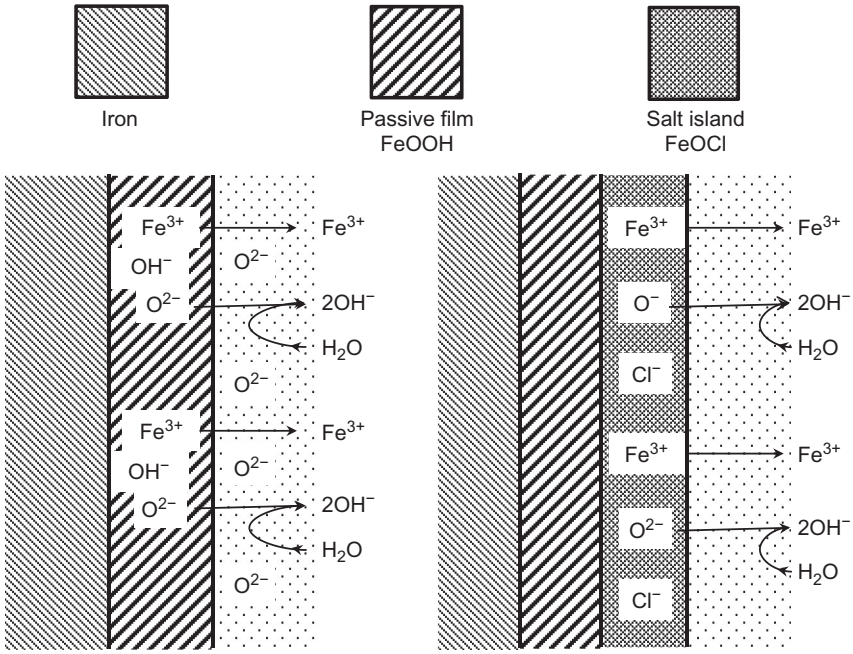

Fig. 7.7 Accelerated dissolution at a chloride islands resulting in formation of Fe^{3+}.

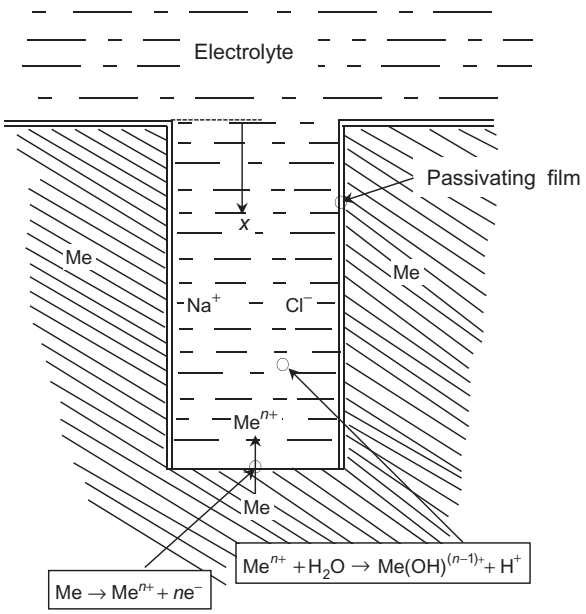

Fig. 7.8 Galvele's model pit geometry [23]. *Reproduced by permission of The Electrochemical Society.*

the effective diffusion length is between 0.1 and 1 μm. As shown in Fig. 7.8, metal dissolution and hydrolysis occur at the pit bottom. Assuming a critical pH value for pit initiation, the model explains pH effect on pitting potential, pitting inhibition potential, and pitting protection potential. Mass transport analysis inside the pit indicated that the pitting potential changes with chloride concentration as follows:

$$E_{pit} = E^{o}_{pit} - B\log[Cl^{-}] \tag{7.4}$$

where $B = 0.059$ at room temperature [28].

Chloride ions decrease the overvoltage by increasing the exchange current density for metal dissolution. Vera Cruz *et al.* [29] observed a sudden open circuit potential (OCP) drop when pitting initiates in the presence of chlorides. Small surface area anodes are formed on the metal surface in contact with large surface area passive film cathodes. The active-passive cell potential (0.5 V vs. SHE) triggers a high anodic current density due to the much smaller electroactive surface areas of the anodes. Figure 7.9 shows polarization curves for the cathode surface and anode crevice using the potentiostatic method. The low anode crevice polarization is attributed to the absence of extensive ohmic polarization resistance [30]. Metal cations hydrolysis, due to metal dissolution shown in Fig. 7.10, results in a local pH decrease and chloride concentration increase at the pitting initiation site according to Eq. (7.5).

$$Fe^{2+} + 2H_2O + 2Cl^{-} \rightarrow Fe(OH)_2 + 2HCl \tag{7.5}$$

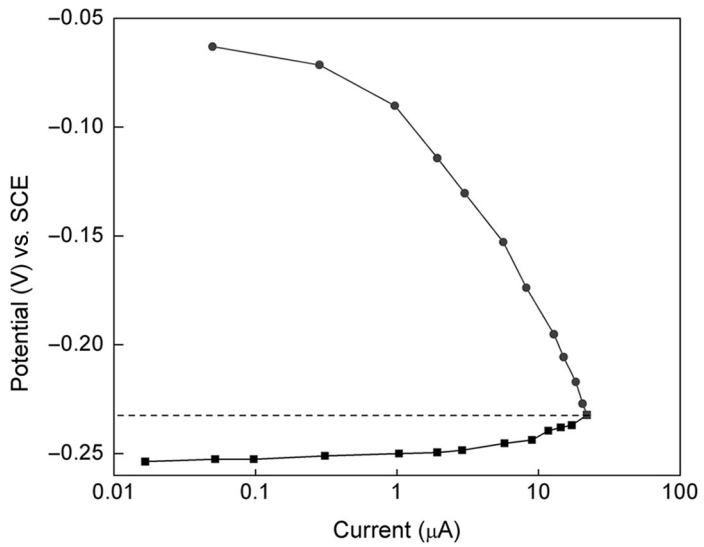

Fig. 7.9 Simultaneous anodic polarization of crevice and cathodic polarization of passive surface for type 304 stainless steel determined by using potentiostatic method [30].

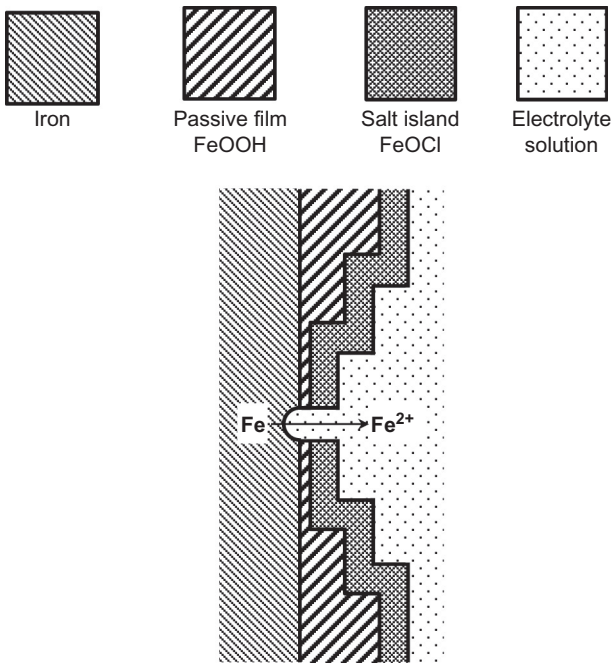

Fig. 7.10 Anodic dissolution of underlying metal at a pit initiation site forming Fe^{2+}.

7.3.2 Autocatalytic mechanism of pit growth

7.3.2.1 Formation of nucleated pits

Nucleated pits represent the initial pitting corrosion step. They are either passivated by surrounding cathode areas or propagate due to local saturated chloride salt solution concentration increase [1–4,20,21]. The nucleated pit formed in the initial step propagates due to localized solution areas on the metal surface initiating the second step, the embryonic pit formation [1]. Under high anodic current densities and high metal ions penetration rates in the electrolyte, the embryonic pit develops into a metastable pit, the third step in the pitting corrosion mechanism. Metastable pits are formed below critical pitting potential and their formation precedes stable pit formation above the critical pitting potential [1–4]. Because they cannot control the diffusion of the aggressive species to the pit interface, metastable pits grow for a short period of time and are repassivated by the surrounding cathode. They are microns in size and have a lifetime of seconds. During potentiostatic or galvanostatic anodic polarization, metastable pit formation in stainless steel is characterized by anodic current or potential transients [12,31]. Localized electrochemical metal dissolution and inclusions such as MnS in the metal matrix in the presence of chlorides initiates metastable pits [4,15,32–34]. Stable pits survive the metastable stage,

continue to propagate, and stabilize at a bigger size in anodic currents above the critical pitting potential. Stable pit formation is irreversible, resulting in stable pit growth, the last step of pitting corrosion [1–4].

7.3.2.2 Propagation pit growth

An iron pit growth model in alkaline chloride solutions (pH 9) is shown in Fig. 7.11. Pit growth at low potentials is controlled by electrochemical kinetic parameters such as charge transfer, mass transport, or ohmic effects. Chloride or oxidizer mass transport in the bulk pit interior controls pit growth at high potentials. During pit growth, oxygen reduction occurs at the passive region, while ferrous ions formed at the anode penetrate the solution beneath the hydrated oxide film. Anodic metal dissolution rate is controlled by oxygen reduction at the passive cathode exterior surfaces. Positively charged ferrous ions attract negatively charged chloride ions from the bulk solution and accumulate on the initial pitting site. Potential gradient established at the pit interface drives chloride electromigration due to voltage drop between the pit interior and cathodic sites of passive film. Oxygen also diffuses through the rust membrane and oxidizes ferrous ions that

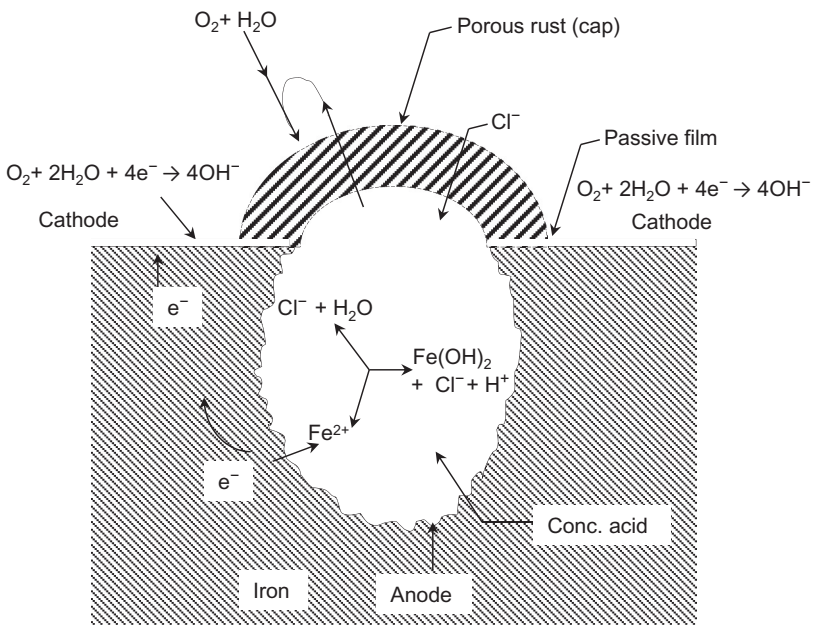

Fig. 7.11 Schematic of pit propagation in iron.

diffuse from the acidic pit bottom to the pit mouth, where it produces $Fe(OH)_3$ as a corrosion product at the insoluble porous rust cap.

The acidity developed in the pit is not neutralized by the cathodic reaction because of the distance between the cathode and the anode. Oxygen reduction occurs on the passive film, while the anodic reaction takes place at the interior of the pit. During pitting, the pit is acidified, enriched with chlorides and metal cations, while oxygen is depleted from the pit interior.

The porous cap allows chlorides to penetrate and maintains a high acid chloride concentration at the pit bottom. Low pH, aggressive chloride, and oxidizing agents in the pit interior prevent repassivation and promote pit growth in most metals. Because the cathode reaction controls the pit growth, pits are distributed randomly in aerated chloride solutions due to limited oxygen solubility in the electrolyte (10-12 ppm). Low oxygen solubility in the electrolyte requires large cathode areas to support pit growth. Chloride concentration decreases to the saturation value and is controlled by the equilibrium constant between the chloride concentration in the electrolyte and the chloride concentration in the layered film. Pit growth under supersaturation conditions is mass-transport controlled by chloride diffusion out of the pit. The pits formed under these conditions are hemispherical with polished surfaces.

7.3.2.3 Pit arrest

As pit depth increases with time, so does the ohmic path length between the pit bottom and the passive film on the outer surface of the pit. As a result of ohmic voltage drop, the outer surface potential is higher than the dissolving pit wall. The local pit potential decreases with pit growth, causing a decrease in pit current density and, consequently, a decrease in metal dissolution rate. Figure 7.12 shows the potential profile using microprobe measurements [35].

Chloride concentration at the pit bottom is controlled by migration into or out of the pit. This phenomena occurs when the pit electrolyte is saturated with chloride. If the pit cover is lost, repassivation may occur due to chloride transport out of the pit. Chloride concentration in the pit electrolyte would decrease due to a decrease in metal dissolution because of the voltage drop at the pit bottom [4].

7.3.2.4 MnS inclusions

MnS inclusions have been extensively investigated as a pitting corrosion initiation site in steel [36–38]. MnS inclusion dissolution formed in a MnS/matrix is the initial pit formation step. Various reaction products such as HSO_3^-, $S_2O_3^{2-}$, SO_4^{2-}, S, and H_2S are suggested to form during MnS dissolution [36,38–43]. Dissolution of MnS inclusions in the presence of chloride solutions causes the metal matrix to be exposed and attacked by sulfur-containing compounds and chloride ions. MnS dissolution initiates a microcrevice at the MnS inclusion site and there is a high probability for the microcrevice to grow into

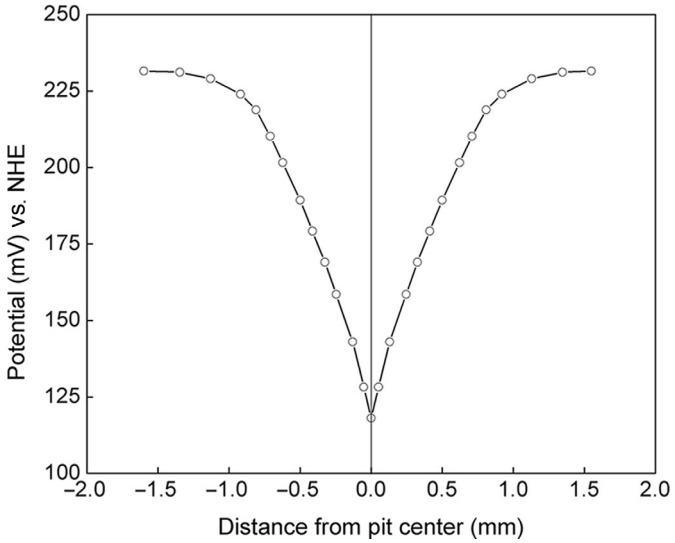

Fig. 7.12 Potential across a pit obtained using microprobe measurements [35].

a stable pit, as evidenced by microelectrochemical methods [41,43–50]. Webb *et al.* [46] predicted 1 μm critical microcrevice depth is required to initiate stable pit formation. An electrochemical microcell technique was used to investigate the electrochemical dissolution of MnS inclusions and the resulting pit initiation processes on type 303 stainless steel [51]. Field emission scanning electron microscopy (FE-SEM) was used to observe the initiation site and the morphology of metastable and stable pits. Electrochemical dissolution of MnS inclusions occurred at 0.1-0.3 V vs. the Ag/AgCl reference electrode in 1 M Na_2SO_4. The dissolution of MnS was followed by the initiation and formation of a hemispherical and smooth wall pit at the MnS/matrix boundary. In the presence of Na_2SO_4, the dissolution products of MnS inclusions initiate a localized electropolishing. The onset potential of electrochemical dissolution of MnS inclusions in 0.1 M NaCl is between 0.3 and 0.4 V. Stable pit growth was observed at approximately 0.5 V vs. the Ag/AgCl reference electrode. If the polarization measurements are stopped immediately after stable pit formation, field emission electron microscopy indicates the formation of many metastable pits at the MnS/matrix boundary that are similar to flat-walled etched pits observed when the experiments were performed in a Na_2SO_4 solution. Metastable pits have a polygonal shape diameter of 1 μm and formed at MnS inclusion sites when stainless steel is in contact with NaCl solutions. Other investigators have also observed metastable pits of similar size [44,46]. The dissolution products of MnS inclusions and chloride ions attack the newly exposed metal surface.

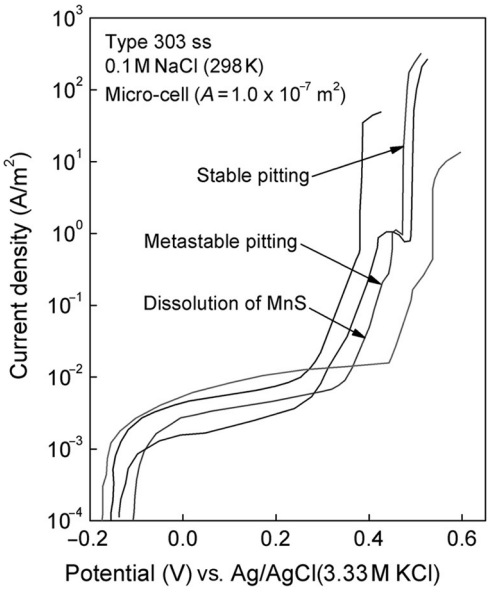

Fig. 7.13 Polarization curves measured on type 303 SS in 0.1 M NaCl using an electrochemical microcell at 298 K [51]. *Reproduced by permission of The Electrochemical Society.*

Figure 7.13 shows microscopic polarization curves of type 303 stainless steel in 0.1 M NaCl solution at 298 K [51]. The first current transient on the polarization curve corresponds to metastable pit initiation. MnS starts to dissolve from 0.1 to 0.2 V indicating that MnS is not directly associated with pit initiation. The species resulting from the dissolution of MnS inclusions were assumed to affect the initiation of metastable pitting at MnS inclusions. The onset potentials for MnS dissolution and stable pitting vary for different experiments. The fact that the critical current for stable pit growth is of the same order of magnitude (in the range of 43-80 nA) indicates the possibility that the dissolution products of MnS initiates the formation of stable pitting. Figure 7.14 summarizes the pit initiation mechanism at MnS/matrix inclusions in the presence of chloride [51].

Pitting corrosion proceeds through the following steps: (i) MnS dissolves at 0.3-0.4 V vs. the Ag/AgCl reference electrode, releasing sulfur-containing products; (ii) the synergistic effect between chloride ions and sulfur-containing species depassivates and exposes the alloy surface to corrosion; (iii) a polygonal metastable pit forms on the exposed surface; (iv) the metastable pit grows to a stable pit due to the accumulation of dissolution products of MnS inclusions; and (v) the electropolishing reaction inside the stable pit forms a large hemispherical pit.

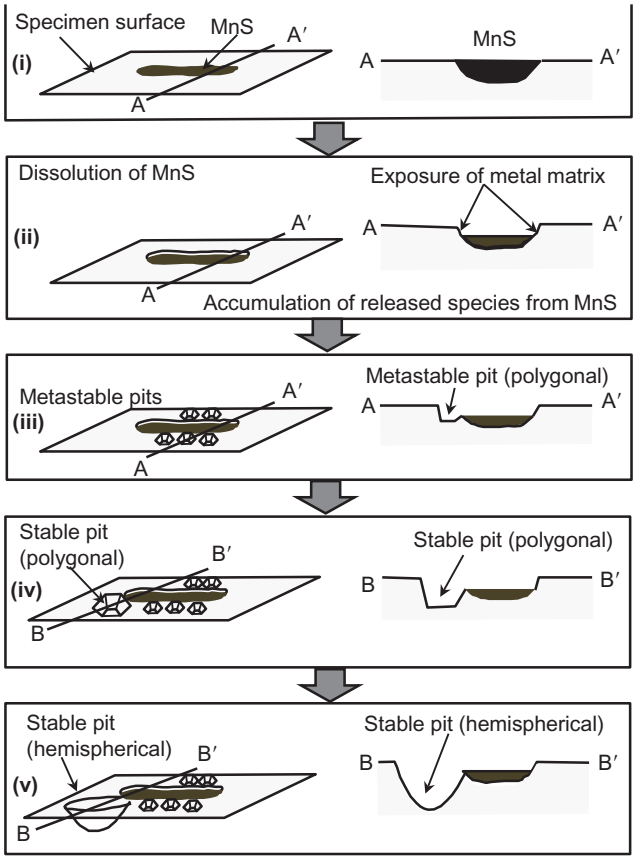

Fig. 7.14 Schematic of the steps of pitting corrosion at MnS inclusions in the presence of chloride solutions [51]. *Reproduced by permission of The Electrochemical Society.*

7.4 EFFECT OF TEMPERATURE

The concept of critical pitting temperature (CPT) was suggested by Bringham and Tozer [52] and is a criterion for evaluating pitting susceptibility in stainless steels. The CPT is defined as the minimum temperature in °C that initiates pitting corrosion at a given potential. Pitting temperature dependence can be evaluated by varying temperature at a fixed applied potential and monitoring pit initiation. Experiments are also performed at constant temperature while varying applied potential. The CPT in duplex steel was measured by Salinas-Bravo and Newman [53] using a zero ammeter and plotting breakdown potential as a function of temperature [54]. Burstein and Moloney [55] introduced cyclic thermammetry to determine aluminum re-passivation temperature in stainless steel. Pitting initiation and propagation is monitored as a function of temperature using this method.

CPT is used to rank the susceptibility of metals and alloys to pitting corrosion. Higher estimated CPT represents more resistance to localized corrosion. Deng *et al.* [56] used cyclic thermammetry to investigate CPT and critical repassivation temperature (T_r) of duplex stainless steels UNS S31803 and UNS S32750 in chloride solutions. They observed hysteresis in the cyclic thermammetry curve indicating that propagating pits repassivate during the cooling part of the cycle. Pitting was preferentially observed in the austenite phase. CPT was determined as the temperature where current density first exceeded 100 μA/cm^2 during the heating part of the cycle. The repassivation temperature was determined as the temperature where current density fell below 100 μA/cm^2 during the cooling part of the cycle. Figure 7.15 shows a cyclic thermammogram of UNSS31803 at a potential of 750 mV. Increasing the temperature above the CPT suddenly increases the current density, indicating stable pit formation [56].

During initial heating, the observed current density was low (in the range of 1 μA) indicating a passive film on the alloy. As temperature increases, metastable pits form on the alloy below the CPT as found previously [57] while stable pits form above the CPT. Upon increasing the temperature above CPT, the current density continues to increase, indicating stable pit formation. The heater was switched off when the current density reached 5 mA/cm^2. Besides the fact that temperature begins to decrease, the current density continuously increases and reaches a maximum value of 8 mA/cm^2, indicating pitting corrosion is still taking place in the alloy. As the temperature continues to decrease, the current density quickly decreases to 400 μA/cm^2, and at a slightly lower temperature, the current density reaches the repassivation region. The observed repassivation temperature is lower than the CPT, indicating pitting exhibits thermal

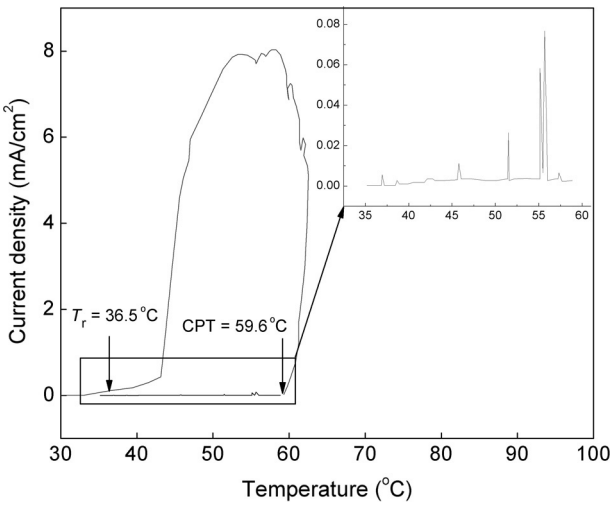

Fig. 7.15 Cyclic thermammogram of UNS S31803 in 1 M NaCl at a potential of 750 mV. Arrows mark the CPT of 59.6 °C and the T_r of 36.5 °C [56].

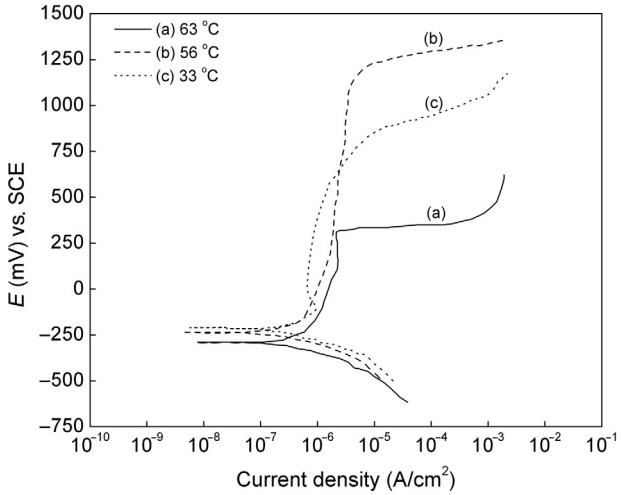

Fig. 7.16 Anodic polarization curves for UNS S31803 in 1 N NaCl with potential scan rate of 1 mV/s at different temperatures [56].

irreversibility. The authors use the difference CPT–(T_r) as a parameter to evaluate stainless steel repassivation performance. Previously, Abd *et al.* [58] suggested using $\Delta E = E_p - E_{rp}$ as criteria to measure the susceptibility of stainless steel to pitting corrosion. Typical anodic polarization curves between 33 and 63 °C are shown in Fig. 7.16 [56]. At 63 °C, the current density suddenly increases to a value of 15 mA when the potential reaches 320 mV, indicating pitting corrosion. A well-defined passive region with a current density of 2×10^{-6} A/cm^2 was observed at 56 °C. The current density of the polarization curve obtained at 33 °C (below T_r) was still in the passive region. The transpassive region occurred at 850 mV, indicating 33 °C is lower than the repassivation temperature of 36 °C. Figure 7.17 shows SEM pictures of pits formed at 750 mV during the cycling test in 1 N NaCl [56]. The size of observed metastable pits in Fig. 7.17 was in the range of 2 μm, consistent with previously estimated metastable pit size.

7.5 EFFECTS OF ALLOY COMPOSITION ON PITTING CORROSION

Critical pitting potential shifts in the anodic direction when chromium content increases above the critical value of 12% needed to produce stainless steel [59–64]. The following critical pitting potentials of Ni (0.28 V vs. SHE) [59], 30% Cr-Fe (0.2 V vs. SHE) [59], and Cr (>0.1 V vs. SHE) [62] in 0.1 N NaCl were reported in the literature. Alloying elements such as nickel [59] and molybdenum [65,66] reduce the susceptibility of stainless steel to pitting. Because chromium and titanium show more positive potentials than the oxygen electrode in air, they do not undergo pitting corrosion in chloride solutions at 25 °C. Mo accumulates in the surface film formed in the active region and blocks active

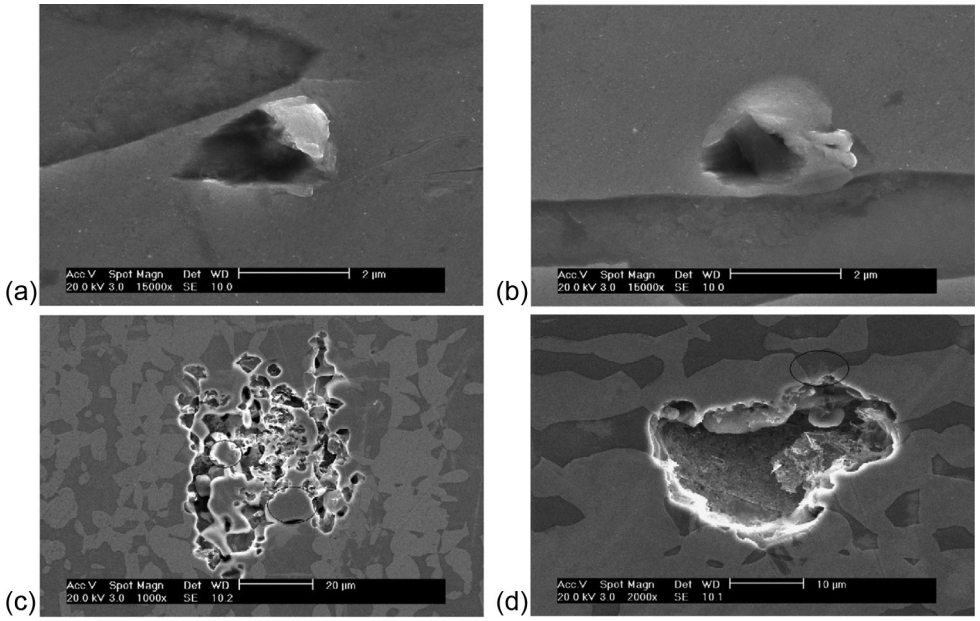

Fig. 7.17 SEM pictures showing the morphologies of pits formed on the specimens during the cyclic thermammetry test at 750 mV/SCE in 1 M NaCl: (a) metastable pit formed on UNS S31803, (b) metastable pit formed on UNS S32750, (c) stable pit formed on UNS S31803, and (d) stable pit formed on UNS S32750 [56].

sites during metal dissolution [66,67]. It has been suggested that Mo increases the overvoltage needed for metal dissolution, resulting in a decrease in pitting current density at a given potential [68].

Small amounts of tungsten and nitrogen in the alloy decrease susceptibility of stainless steel to pitting. Sedriks [69] introduced pitting resistance equivalent number (PREN) as an index for stainless steel:

$$\mathrm{PREN} = \%\mathrm{Cr} + 3.3(\%\mathrm{Mo}) + 16(\%\mathrm{N})\ (\text{in wt.}\%) \tag{7.6}$$

The equation is valid for nitrogen up to 30%. Between 1980 and 2000, research on stainless steel pitting corrosion was aimed at defining the transition from metastable to stable pitting [3,4,31,51,70–76]. Pit stability product was defined as *ir* for stable pit growth in type 304 stainless steel by Pistorius and Burstein [77] where "*i*" and "*r*" are current density and the pit radius, respectively. Pit growth in 80Ni-20Fe sputtered tin films was studied by analyzing the pit images [78]. Piting current density increased with pitting potential until a limiting current density was reached. Limiting current density increases as the film thickness decreases. Voltage component calculations agreed with experimental data and indicated pit growth below the limiting current density is limited by ohmic concentration and surface activation.

Tsutsumi *et al.* [79–81] found stainless steel pitting corrosion (SS304) in a marine environment is initiated between 35% and 75% relative humidity (RH) with approximately 6 M chloride concentration in the electrolyte. Pitting onset was determined from the sudden OCP drop. Chloride concentration at the alloy interface was controlled by varying the RH. The chloride concentration required to initiate pitting corrosion increased with increasing drying rate [81]. Studies were also performed on the influence of electrolyte drop size on pitting corrosion [82]. Susceptibility of an alloy to pitting under chloride solution droplets with a diameter lower than 5 mm was drastically reduced due to negligible cathodic current density at the alloy interface. Maier and Frankel [83] studied pitting corrosion of stainless steel 304 (SS304) under chloride solution droplets using a Kelvin probe (KP). Three different volumes of 0.44 M $MgCl_2$ (2, 4, and 6 μL) were used in this study. KP operation is described by Frankel *et al.* [84]. Pitting initiation was estimated by the abrupt OCP decrease. When droplets with initial concentration of 0.88 M Cl^- were used, the chloride concentration at pitting initiation was between 3.0 and 8.4 M. Both, the anodic current required for pit growth at the OCP and the cathodic current decreased with time.

Lin *et al.* [85] developed scanning electrochemical probes to monitor *in situ* localized corrosion processes occurring on reinforcing steel in NaCl solutions. Chloride ions were found to preferentially adsorb and accumulate at defective sites with MnS inclusions, resulting in pit initiation and propagation.

7.6 INHIBITION OF PITTING CORROSION

Pitting can be inhibited by (i) decreasing the aggressiveness of the environment, (ii) alloy composition, (iii) temperature, (iv) alloy structure, (v) protecting the alloys with conversion coatings, (vi) cathodic or anodic protection, and (vii) inorganic inhibitors.

Solution aggressiveness can be decreased by decreasing the electrolyte temperature, chloride concentration, and acidity at the pit interior. Inorganic inhibitors including nitrates, chromates, molybdates, and sulfates mitigate pitting corrosion. They adsorb at active sites, slowing down pit growth. Sulfates provide a supporting electrolyte that reduces chloride electromigration into the pit. The addition of Na_2SO_4, $NaNO_3$, or $NaClO_4$ shifts the critical potential in the positive direction [86,87]. At a critical concentration of Na_2SO_4, the critical potential shifts in the positive direction to a more noble value than the corrosion potential mitigating pitting corrosion of the alloy, as shown in Fig. 7.18 [13]. Uhlig and Gilman [86] found the addition of 3% $NaNO_3$ to 10% $FeCl_3$ mitigated pitting in 18-8 stainless steel for 25 years. In the absence of $NaNO_3$, under the same conditions, the alloy corroded within a few hours. The addition of 3% $NaNO_3$ shifts the critical potential to a more positive value than the OCP of the alloy. Equation (7.7) defines the minimum anion activity needed to mitigate pitting of 18-8 stainless steel and aluminum in chloride electrolyte:

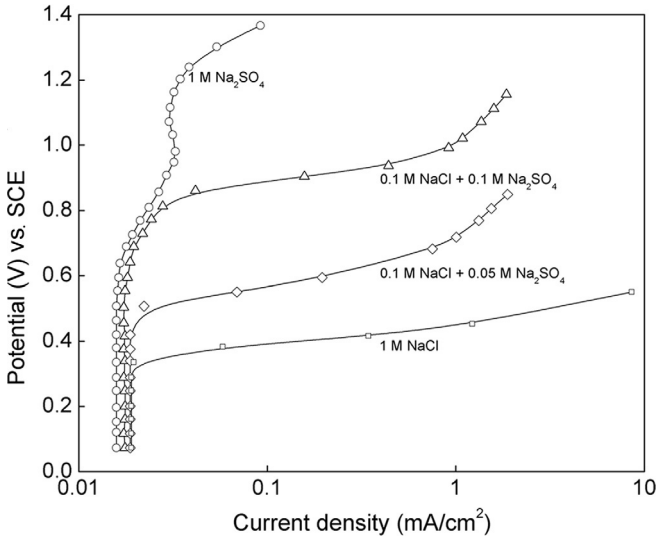

Fig. 7.18 Polarization curves for 18-8 stainless steel in 0.1 M NaCl showing shifting the critical potential to more positive values with addition of Na_2SO_4 [13]. *Reproduced by permission of The Electrochemical Society.*

$$\log Cl^- = k\log(\text{anion}) + \text{const.} \tag{7.7}$$

This expression was derived assuming the Freundlich adsorption isotherm [86] and estimates the concentration ratio of the inhibitor to chloride that destroys passivity is more important to initiate pitting than the absolute value of inhibitor concentration. In the initial pitting stages, replacement of aggressive ions from the adsorption layer by inhibiting anions explains the inhibition mechanism.

Because the pH at the interior of the pit is one factor that initiates pitting corrosion, hydroxide ions also act as an inhibitor. For example, nitrate ions are reduced in the pit interior of Al by consuming protons and mitigating pitting corrosion by increasing pH [87]. Anion inhibiting efficiency is controlled by anion type and its activity in the electrolyte. Leckie and Uhlig [13] and Lockie [88] found anions activities necessary to inhibit pitting for 18-8 CrNi steel for a given chloride activity are as follows:

$$\log a_{Cl^-} = 1.88\log\left(a_{NO_3^-}\right)_{crit} + 1.18 \tag{7.8}$$

$$\log a_{Cl^-} = 1.62\log\left(a_{OH^-}\right)_{crit} + 1.84 \tag{7.9}$$

$$\log a_{Cl^-} = 0.85\log\left(a_{SO_4^{2-}}\right)_{crit} - 0.05 \tag{7.10}$$

$$\log a_{Cl^-} = 0.83\log\left(a_{ClO_4^-}\right)_{crit} - 0.44 \tag{7.11}$$

These equations assume equilibrium adsorption exists at the passive film interface. Island-type adsorption instead of the uniform adsorption assumed in these equations has also been suggested. The standard coating based on chromate conversion layers is used to protect high-strength Al alloys. The primer may contain chromate pigments that enhance protection. The chromium protection mechanism is described by Edeleanu and Evans [89].

7.7 CREVICE CORROSION

Crevices are formed at welds in condensers between metals and valves. This corrosion is initiated by small solution volumes captured under bolt gasket rivets or surface deposits. It destroys the integrity of mechanical joints in engineering structures constructed from stainless steel, aluminum, titanium, and copper. For corrosion to occur, the crevice must allow the entry of the aggressive solution and be sufficiently narrow to keep the corrosion products inside the crevice. In the case of corrosion by dissolved oxygen, active-passive short circuits are formed between the aggressive solution in the crevice, which becomes depleted in oxygen (anode) and the external metal surface (cathode). Crevice corrosion is described by initiation and propagation. The short-circuit current between anode and cathode results in electrolytic chloride migration that initiates pit formation in the crevice. As discussed in pitting corrosion, metal dissolution in a crevice is followed by electrolyte hydrolysis and acidification at the pit interior. Figure 7.19 illustrates crevice corrosion and propagation. The crevice corrosion reaction involves oxygen reduction and metal dissolution:

$$O_2 + 2H_2O + 4e^- \rightarrow 4OH^- \quad (\text{oxygen reduction}) \tag{7.12}$$

$$Fe \rightarrow Fe^{2+} + 2e^- \quad (\text{iron oxidation}) \tag{7.13}$$

The oxygen in the crevice is depleted with time due to limited oxygen diffusion, resulting in a drastic decrease in the oxygen reduction rate. However, the overall oxygen reduction rate does not change because it continues on the external surface area and is orders of magnitude larger than the area within the crevice.

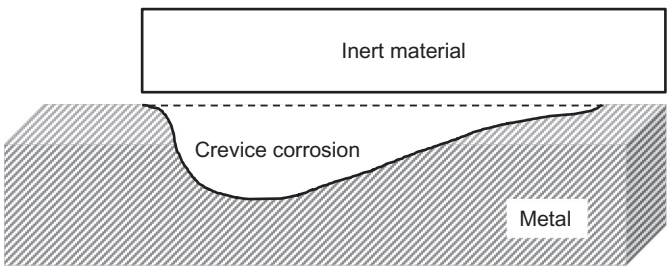

Fig. 7.19 Illustration of crevice corrosion propagation.

7.7.1 Mechanism of crevice corrosion

Crevice corrosion initiation is based on a pH decrease at crevice bottom due to Eq. (7.5). Positive metal ions formed in the absence of oxygen reduction attract chloride into the crevice, initiating acidification (water hydrolysis):

$$Fe^{2+} + 2H_2O + 2Cl^- \rightarrow Fe(OH)_2 + 2HCl \tag{7.5}$$

$$Fe^{3+} + 3H_2O + 3Cl^- \rightarrow Fe(OH)_3 + 3HCl \tag{7.14}$$

$$Cr^{2+} + 2H_2O + 2Cl^- \rightarrow Cr(OH)_2 + 2HCl \tag{7.15}$$

$$Cr^{3+} + 3H_2O + 3Cl^- \rightarrow Cr(OH)_3 + 3HCl \tag{7.16}$$

$$Ni^{2+} + 2H_2O + 2Cl^- \rightarrow Ni(OH)_2 + 2HCl \tag{7.17}$$

The rate of corrosion reaction within the crevice increases with decreasing pH and cathodically protects the external cathodic metal surface. Separation between the anodic reaction in the crevice and the cathodic reaction on the external passive metals surface is a precondition for crevice corrosion initiation by the IR voltage drop mechanism suggested by Wang *et al.* [90], Cho *et al.* [91], and Abdulsalam and Pickering [92]. The IR voltage drop results in an electrode potential shift on the crevice wall in the negative direction, which increases with external metal surface and crevice distance [93]. Walton *et al.* [94] developed a mathematical model for potential distribution in crevices that shows good agreement with experimentally measured potential distributions by Sawford *et al.* [95] and Valdes and Pickering [96]. The distance into the crevice, "x_{pass}" where the transition from passive to active dissolution in the crevice wall occurs, is located at E_{pass} [95–100]. Equation (7.18) predicts the location of x_{pass} [101].

$$\Delta\Phi = E_{x=0} - E_{pass} = IRx_{pass} \tag{7.18}$$

where $\Delta\Phi$ is the potential drop, $E_{x=0}$ is the passive applied potential at the crevice mouth, "I" represents the crevice current, and $R = \frac{\rho_e}{A}$, where A is the electrolyte cross section area in the crevice and ρ_e is the electrolyte resistance.

Shu *et al.* [102] found that corrosion on the passive crevice wall of iron in a sulfate/chromate solution was initiated in the pit near the bottom of the crevice. In the induction period, more pits were formed higher on the crevice wall. Gas bubbles observed in the pits indicated pitting is initially a local cell process with hydrogen evolution and metal dissolution. Corrosion across the crevice width occurred by transition from merging pits to stable IR type crevice corrosion attack resulting in increasing current. The crevice wall polarization curve is presented in Fig. 7.20 [102]. $\Delta\Phi^*$ represents the difference between the active-passive transition electrode potential on the crevice wall, $E_x = E_{A/P}$, and the applied potential in the passive region, $E_{app} = E_x$, at the crevice opening where $x = 0$. Stable corrosion occurs in the crevice wall between $x = L$ and $x_{A/P}$ where the voltage

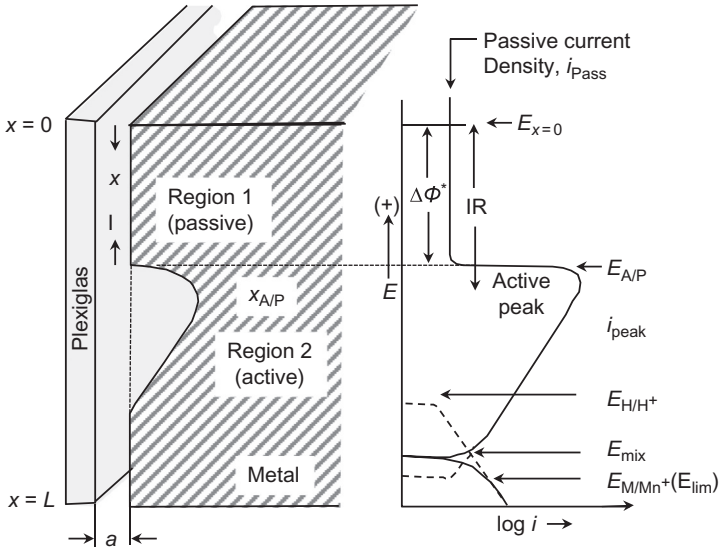

Fig. 7.20 Schematic drawing showing the corrosive attack on the crevice wall during crevice corrosion [102].

drop $IR > \Delta\Phi^*$ [103]. The observed current in the crevice results from the potential gradient in the crevice electrolyte $\Delta\Phi^*$. Because $\Delta\Phi_e = IR_e$ is the potential difference in the electrolyte, it is a function of distance x into the crevice. The potential difference increases with increasing distance x and corresponds to a range of E_x on the crevice wall. During the induction period, the potential difference between $x = 0$ and $x = L$ is small and $\Delta\Phi_e = IR_e$. Consequently, ΔE_x between $x = 0$ and $x = L$ is also small and causes only a small passive region to exist at $E_{x=0}$. In fact, ΔE_x is too small to introduce an active loop in the polarization curve even at low pH and explains why crevice corrosion does not occur on the crevice wall during the induction period. For large potential difference between $x = 0$ and $x = L$ and a large ΔE_x, the polarization curve in Fig. 7.20 extends from $E_{x=0}$ to E_{mix} at $x = L$ and to the crevice wall [102]. In this case, active metal dissolution occurs, resulting in stable crevice corrosion [99,104]. The induction period is discussed in more detail by Shu *et al.* [102].

Cyclic potentiodynamic polarization and constant-potential tests were used to study crevice corrosion for a Fe-based bulk metallic glass alloy (SAM1651) and a Ni-Cr-Mo crystalline alloy (C-22) in a 4 M NaCl solution at 100 °C [105]. The results indicated SAM 1651 has a more positive breakdown potential and repassivation potential than C-22 and requires a more positive oxidizing potential to initiate crevice corrosion in constant-potential tests. C-22 corrosion propagation was more localized near the crevice

border. Corrosion products from both alloys contained a high amount of O and were enriched with Mo and Cr. A Cr-rich oxide passive film was formed on both alloy surfaces and corroded congruently in the areas exhibiting crevice corrosion damage.

7.7.2 Inhibition of crevice corrosion

Electropolished surfaces mitigate crevice corrosion by lowering cathodic current densities during cathodic polarization in sea water [71]. MnS inclusion removal by pickling from the metal surface increases crevice corrosion resistance. Sulfide inclusions act as sites for pitting and crevice corrosion [106]. Pickling also removes chromium-depleted layers formed during annealing and decreases susceptibility to crevice corrosion. Lu and Ives [107] found that doping the surface of type 316 steel with cerium by ion implantation or by immersion in 0.05 M cerium nitrate [108] inhibits crevice corrosion when tested using ASTM G 48, practice B (10% ferric chloride, 24 h at 22 °C). They found that a crevice corrosion test on stainless steel types 904L, 304L, and 316L doped with cerium immersion did not show crevice corrosion initiation after three weeks of exposure in sea water. Crevice corrosion of stainless steel decreases when it is cathodically protected with sacrificial anodes [109]. Aluminum and zinc sacrificial anodes have been suggested for crevice corrosion protection in 254SMO stainless steel [110]. Type 6X, 26-1, 22-13-5, and 216 stainless steels were effectively protected by zinc sacrificial anodes [69]. ASTM Practice G 48, Method B and Method D, Materials Technology Institute Method MTI-2, Materials Technology Institute Methods MTI-4, Multiple Crevice Assembly Test, Tests Employing-Type Crevice Formers, Specialized Test with Separated Anode, and Cathode and Perspex Crevice Assembly Test are described by Sedriks [69]. Crevice corrosion can be minimized by coating the cathode area with a more crevice corrosion-resistant alloy. Crevice-forming paints such as epoxy coatings should be avoided.

Case Study 7.1—Corrosion Evaluation of Crevice Exposed to Differential Acidity in the Absence of Chlorides or Other Dissolved Oxidizers

Assume that a crevice is exposed to a differential in acidity between the bottom of the crevice and its outer surface in the absence of chlorides or other dissolved oxidizers. The crevice bottom acts as an anode, consuming hydrogen ions through active metal corrosion. The anodic reaction depletes acid concentration in the crevice. The outer crevice surface is passivated and acts as a cathode. On the cathode, hydrogen evolution occurs by hydrogen reduction in solution. Assume the cathode surface area is 10 times larger than the anode surface area.

Construct polarization diagrams and determine if acid depletion will cause crevice corrosion.

Calculate:

(i) the corrosion potential of uncoupled cathode, $E_{corr,C}$

(ii) the corrosion current of uncoupled cathode, $I_{corr,C}$
(iii) the corrosion potential of uncoupled anode, $E_{corr,A}$
(iv) the corrosion current of the uncoupled anode $I_{corr,A}$
(v) the corrosion potential of the couple, $E_{corr,couple}$
(vi) the corrosion current of the coupled anode, $I_{corr,A,couple}$
(vii) the corrosion current of coupled cathode, $I_{corr,C,couple}$.

Use the following electrochemical parameters to construct polarization curves for: Corrosion current of the coupled anode, $I_{corr,couple}$ and corrosion current of coupled cathode, $I_{corr,C,couple}$.

I. Cathodic electrochemical parameters
(i) Equilibrium potential for hydrogen evolution reaction, $e_{eq,H^+|H_2,C} = 0.55$ V.
(ii) Equilibrium current for hydrogen evolution reaction, $\log i_{eq,H^+|H_2,C} = 1.845$ mA.
(iii) $b_{c,C} = -0.12$ V/decade.
(iv) Equilibrium potential of the metal dissolution, $e_{eq,M,C} = 0.1$ V.
(v) Equilibrium current for metal dissolution, $\log i_{eq,M,C} = 2$ mA.
(vi) Anodic slope of metal dissolution, $b_{a,C} = 0.1$ V/decade.

II. Anodic electrochemical parameters
(i) Equilibrium potential for hydrogen evolution reaction, $e_{eq,H^+|H_2,A} = 0.35$ V.
(ii) Equilibrium current for hydrogen evolution reaction, $\log i_{eq,H^+|H_2,A} = 0.7$ mA.
(iii) Cathode slope for hydrogen evolution reaction, $b_{c,A} = -0.12$ V.
(iv) Equilibrium potential of the metal dissolution, $e_{eq,M,A} = 0.1$ V.
(v) Equilibrium current for metal dissolution, $\log i_{eq,M,C} = 1$ mA.
(vi) Anodic slope of metal dissolution, $b_{a,A} = 0.1$ V/decade.

III. Crevice electrochemical parameters
(i) Equilibrium potential of the total metal dissolution, $e_{eq,M,T} = 0.1$ V.
(ii) Equilibrium current for total metal dissolution, $\log I_{eq,M,T} = 2.47$ mA.
(iii) Anodic slope of total metal dissolution, $b_{a,T} = 0.1$ V/decade.

Figure 7.21 shows polarization diagrams for the uncoupled crevice anode, uncoupled crevice cathode, and estimated polarization diagram of the couple. Table 7.2 summarizes the values obtained from Fig. 7.21 for corrosion potentials and currents of the uncoupled crevice anode and cathode and the coupled crevice.

Estimated corrosion currents are $I_{corr,A,couple} = 562$ mA/cm^2 and $I_{corr,C,couple} = 575$ mA/cm^2. Cathode current is an order of magnitude larger than the anodic current. However, cathode surface area is one order of magnitude larger than that of the anode, so the coupled current densities are the same. Because the outer metal surface of the crevice is passive, it polarizes the small active anode from a corrosion potential of 0.2-0.275 V, as shown in Fig. 7.21, and passivates the anode. The corrosion potential of the coupled anode is slightly active in reference to the passive corrosion potential of the uncoupled cathode. This corrosion evaluation indicates acid depletion will not cause crevice corrosion.

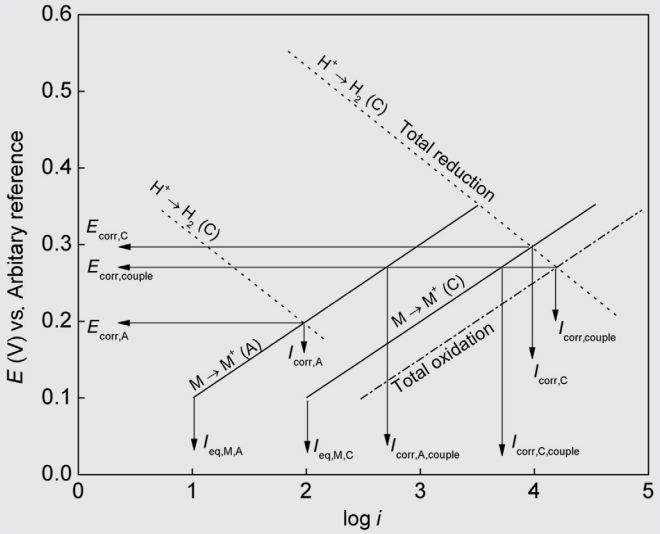

Fig. 7.21 Polarization diagram that illustrates (i) corrosion potential of the noncoupled cathode, $E_{corr,C}$, (ii) the corrosion current of the noncoupled cathode, $I_{corr,C}$, (iii) the corrosion potential of the noncoupled anode, $E_{corr,A}$, (iv) the corrosion current of the uncoupled anode, $I_{corr,A}$, (v) the corrosion potential of the couple, $E_{corr,couple}$, (vi) the corrosion current of the coupled anode, $I_{corr,A,couple}$, and (vii) the corrosion current of the coupled cathode, $I_{corr,C,couple}$.

Table 7.2 Electrochemical Parameters of Coupled Device

	***E* (V)**	**log(*I*) (mA)**	***I* (mA/cm^2)**
$E_{corr,C}$	0.3	4	–
$E_{corr,couple}$	0.275	4227	–
$E_{corr,A}$	0.2	2.0	–
$I_{corr,A,couple}$	–	2.75	562
$I_{corr,C,couple}$	–	3.76	575

7.8 FILIFORM CORROSION

Filiform corrosion is observed under thin organic coatings (typically 0.1 mm) on aluminum and steel exposed to a humid atmosphere. It has been observed in aircraft structures, beverage cans, flanges, gaskets, and weld zones [111–113]. Corrosion-resistant alloys of stainless steel, copper, and titanium are not susceptible to filiform corrosion. Metals with thin organic coatings are in contact with water from the humid atmosphere.

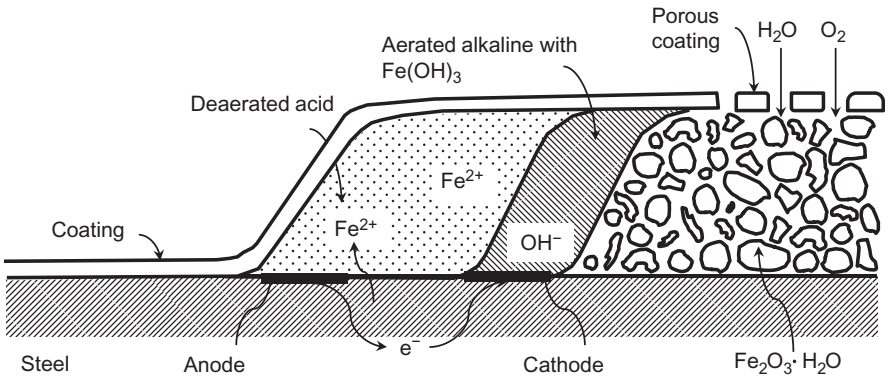

Fig. 7.22 Electrochemical processes during filiform corrosion in steel.

Filiform corrosion initiates at the defects of organic coatings and is accelerated by soluble sulfates, chlorides, and carbon dioxide, which enhance acidification at the corrosion site [111]. The filament cell structure consists of an actively corroding site and an inactive tail saturated with corrosion products. As shown in Fig. 7.22, water diffuses under the coating into the delaminated area.

Oxygen is reduced at the actively corroding site or at the filament head. The mechanism is the same as crevice corrosion. A differential aeration cell is established between a deaerated acidified anode at the filament head and an alkaline cathode at the filament tail, saturated with water and oxygen [112]. The metal oxidation is followed by hydrolysis and acidification down to pH 1 [113]. $Fe(OH)_3$, shown in Fig. 7.22, is formed from Fe^{2+} reacting with the aerated solution in the tail and diffuses through the microcracks in the coating.

7.9 PREVENTION

Organic films, such as epoxy coatings with very low water permeability, may drastically prevent filiform corrosion. Decreasing water and oxygen transport disrupts filament cell propagation. Decreasing RH below 60% and using multiple coatings may minimize filiform corrosion.

EXERCISES

E7.1. The radius, '*r*', of a growing hemispherical pit increases linearly with the time, *t*, while the true current density, I_{pit}, for metal dissolution in the pit remains constant with time. Derive the following relationship between the anodic current, I'_{pit}, and pit growth rate,

Table E7.1 The Dependence of Apparent Pitting Current for Steel

Time (min)	Apparent Pitting Current for Steel (μA)
0	0.000
3	0.001
5	0.0025
7	0.02
9	0.01
11	0.05
13	0.110
15	0.240

$$I'_{\text{pit}} = 2\pi r^2 (nF/V_{\text{Me}}) \frac{\mathrm{d}r}{\mathrm{d}t}$$

where V_{Me} is the atomic volume of the metal (1.4137×10^{-29} m^3 for Fe). The growth rate of the pit is equal to the rate of the volume change of the pit divided by the atomic volume of the metal $= (\mathrm{d}V/\mathrm{d}t)(1/V_{\text{Me}})$ [105].

E7.2. If the true current density, I_{pit}, is constant with time, estimate from the dependence of the apparent pitting current for steel on time (shown in Table E7.1) how rapidly the pit grows.

E7.3. A pit in an alloy exposed to a chloride solution grows to a depth of 0.25 cm in one month. Assuming an alloy density of 7.2 g/cm^3, calculate the current density, I_{pit}, at the interior of the pit. I_{pit} for metal dissolution remains constant with time. The alloy's molecular weight is 56 g/mol.

E7.4. If the radius of an iron atom is 1.5 Å and the thickness of iron corroding for five minutes is 15 Å, calculate the steady state passive current density for iron in 0.5 M HCl. The pitting current, I_{pit}, remains constant with time.

E7.5. Corrosion of passive metals occurs by pitting in chloride solutions. This pitting can be prevented by the addition of anionic inhibitors. At a critical ratio of adsorbed chloride ions to adsorbed anion, the passive film is displaced by chlorides, allowing a pit to initiate.

(a) Derive an equation relating the minimum amount of anion necessary to inhibit pitting of a passive metal in chloride solutions to the activity of chloride ions.

(b) A set of experimental data relating the critical activity of nitrate anions inhibiting pitting of 18-8 stainless steel in $FeCl_3$ solutions and chloride activity is given in Table E7.2. Check if these experimental data fit the equation derived in (a) [86].

Table E7.2 Critical Activity of Nitrate Anions for the Inhibition of Pitting in 18-8 Stainless Steel

Activity of Nitrate Anions (M)	Activity of Chloride Ions (M)
0.049	0.069
0.103	0.265
0.16	0.62
0.27	1.23

(c) Relate the critical ratio of adsorbed chloride ions to adsorbed anion to the Freundlich adsorption isotherm constants.

E7.6. A set of experimental data relating critical activity of hydroxide anions inhibiting pitting of 18-8 stainless steel in $FeCl_3$ solutions and chloride activity are listed in Table E7.3 [13].

(a) Plot a graph of $\log(a_{OH^-})$ vs. $\log(a_{Cl^-})$ and determine the linearity. Estimate the slope and intercept value

(b) Calculate the critical concentration of the anion needed to suppress pitting when the activity of chloride ions is 0.15 M.

Table E7.3 Critical Activity of Hydroxide Anions for the Inhibition of Pitting in 18-8 Stainless Steel

Activity of Hydroxide Anions (M)	Activity of Chloride Ions (M)
0.033	0.26
0.1	1.55
0.2	5.12
0.32	9.89

E7.7. A set of experimental data relating critical activity of sulfate anions inhibiting pitting of 18-8 stainless steel in $FeCl_3$ solutions and chloride activity is given in Table E7.4.

(a) Plot $\log(a_{SO_4^{2-}})$ vs. $\log(a_{Cl^-})$ and check the linearity. Calculate the slope and intercept values.

(b) Estimate the activity of Cl^- ions when the minimum amount of the anion to suppress pitting is 0.2 M

Table E7.4 Critical Activity of Sulfate Anions for the Inhibition of Pitting in 18-8 Stainless Steel

Activity of Sulfate Anions (M)	Activity of Chloride Ions (M)
0.031	0.046
0.1	0.12
0.16	0.19
0.31	0.32

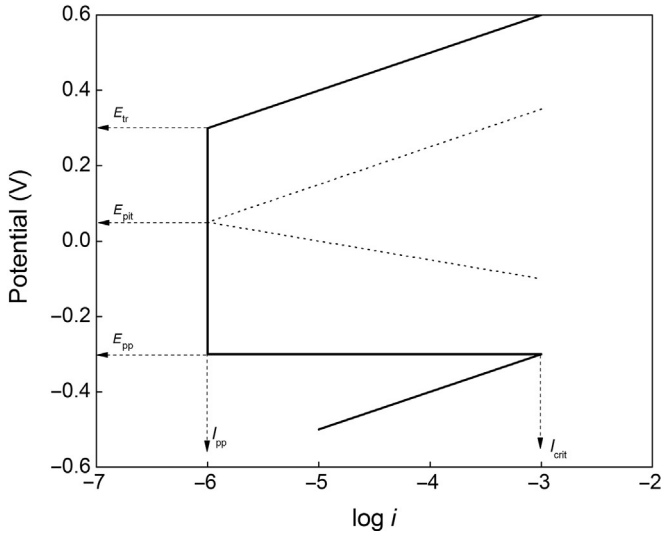

Fig. 7.23 Polarization curve of active-passive alloy in the presence of chloride ions.

E7.8. Electrokinetic parameters of an active-passive alloy are given in Table E7.5 and the anodic polarization curve of the active-passive alloy in the presence of chloride ions is shown in Fig. 7.23. Pitting corrosion initiation occurs at 0.045 V vs. SHE.

Hint: Assume the amount of ion adsorbed per unit area follows the Freundlich adsorption isotherm [86].

Using the data given in Table E7.5 and Fig. 7.23,

(a) Determine the range of $[H^+]$ where the alloy is passive. The cathodic reaction is hydrogen evolution with the following kinetics parameters:

$$i_c^o = 5 \times 10^{-5}[H^+]; \quad b_c = -0.05$$

(b) Estimate the pH value at the critical pitting potential of 0.045 V at which the alloy cannot be passivated.

Table E7.5 Electrokinetic Parameters of an Active-Passive Alloy

$I_{corr,a}$ (A/cm^2)	b_a (V/decade)	$E_{corr,a}$ (V)	E_{pp} (V)	I_{pp} (A/cm^2)	E_{tr} (V)
1×10^{-5}	0.1	−0.5	−0.3	1×10^{-6}	0.3

E7.9. Pitting inhibitor effectiveness depends strongly on type and anion concentration. The thermodynamic (critical) activity, a_I, required to inhibit pitting corrosion for a given activity of the aggressive anion is described by [13]:

$$\log(Cl^-) = a\log\left(a_{I(crit)}\right) + b$$

Table E7.6 Activities of Cl^- and ClO_4^- Anions

Cl^- (M)	ClO_4^- (M)
0.001	0.001
0.01	0.013
0.033	0.056
0.04	0.07
0.1	0.21
0.25	0.64
0.4	1.13

(a) From the data given in Table E7.6, estimate the minimum amount of anion necessary to suppress pitting when the activity of the Cl^- ions is 0.15 M.

(b) Calculate pitting inhibition potential for $(Cl^-) = 0.2$ M. $E_{pit(i)}$ is related to the concentrations of the Cl^- ion and the inhibitor as $E_{pit(i)} = +1.56 + 0.38 \log[(Cl^-/ClO_4^-)]$ [13].

E7.10. Compare pitting characteristics of the alloys listed in Table E7.7 [7], determine which alloy would pit, and why?

E7.11. The critical activity of an inhibitor $a_{crit,anion}$ essential for a given activity of chloride ions is given by an expression of the form:

$$\log(Cl^-) = a\log\left(a_I^{crit}\right) + b$$

The values of Freundlich isotherm parameters "*a*" and "*b*" for (Cl^-) concentrations between 0.1 and 1.00 M in the above equation are given in Table E7.8. Arrange the inhibitor anions in the order of increasing effectiveness.

Hint: The smaller the amount of anion required to passivate the metal for the chosen concentration of Cl^- the more efficient it is. Choose any value of (Cl^-) activity between 0.1 and 1.0 M. For example, 1.0 M and estimate the value of $\log(a_{crit,anion})$ for each of the anions.

Table E7.7 Pitting Characteristics of Various Alloys [7]

Alloy Designation	E_{pit} (V vs. SCE)	Corrosion Potential (V vs. SCE)	
		Maximum	Minimum
Type 430 SS	−0.130	0.230	−0.310
Type 304 SS	−0.020	0.280	−0.140
Type 316 SS	0.100	0.385	0.090
Carpenter 20 Cb	0.050	0.520	0.120
Incoloy 825	0.525	0.530	0.180
Hastelloy C	0.900	0.530	0.530

Table E7.8 Values of Freundlich Isotherm Parameters "*a*" and "*b*" for Cl^- Concentrations Between 0.1 and 1.0 M

Anion	*a*	*b*
Nitrate	1.88	1.18
Sulphate	0.85	−0.05
Hydroxide	1.62	1.84
Perchlorate	0.83	−0.44

REFERENCES

[1] G.T. Burstein, C. Liu, R.M. Souto, S.P. Vines, Origin of pitting corrosion, Corros. Eng. Sci. Technol. 39 (2004) 25–30.
[2] M.G. Fontana, N.D. Greene, Corrosion Engineering, McGraw Hill, New York, 1967.
[3] P.C. Pistorius, G.T. Burstein, Growth of corrosion pits on stainless steel in chloride solution containing dilute sulfate, Corros. Sci. 33 (1992) 1885–1897.
[4] G.S. Frankel, Pitting corrosion of metals: a review of critical factors, J. Electrochem. Soc. 145 (1998) 2186–2198.
[5] ASTM G 46-94, Standard Guide for Examination and Evaluation of Pitting Corrosion, ASTM International, West Conshohocken, PA, 2013.
[6] B.E. Wilde, E. Williams, The use of current/voltage curves for the study of localized corrosion and passivity breakdown on stainless steel sin chloride Media, Electrochim. Acta 16 (1971) 1971–1985.
[7] B.E. Wilde, E. Williams, On the correspondence between electrochemical and chemical accelerated pitting corrosion tests, J. Electrochem. Soc. 117 (1970) 775–779.
[8] E.A. Lizlovs, A.P. Bond, Anodic polarization behavior of high purity 13 and 18% Cr stainless steel, J. Electrochem. Soc. 117 (1975) 719–722.
[9] B.E. Lumsden, R.W. Staehle, Application of auger electron spectroscopy to the determination of the composition of passive films on type 316 SS, Scr. Metall. 6 (1972) 1205–1208.
[10] Z. Szklarska-Smialowska, H. Vierfhaus, M. Janik-Czakor, Electron spectroscopy analysis of in-depth profiles of passive films formed on iron in Cl^- containing solutions, Corros. Sci. 16 (1976) 649–652.
[11] B.E. Wilde, Chloride ion adsorption and pit initiation on stainless steels in neutral media, in: R. W. Staehle, H. Okada (Eds.), Passivity and its Breakdown in Iron Based Alloys, NACE, Houston, 1976, pp. 129–130.
[12] G.S. Frankel, L. Stockert, F. Hunkeler, H. Boehni, Metastable pitting of stainless steel, Corrosion 43 (1987) 429–436.
[13] H.P. Leckie, H.H. Uhlig, Environmental factors affecting critical potential for pitting in 18-8 stainless steel, J. Electrochem. Soc. 113 (1966) 1262–1267.
[14] B. Baroux, Further insights on the pitting corrosion of stainless steels, in: P. Marcus (Ed.), Corrosion Mechanism in Theory and Practice, second ed., Marcel Dekker Inc., New York, 2004.
[15] M.A. Baker, J.E. Castle, The initiation of pitting corrosion at MnS inclusions, Corros. Sci. 34 (1993) 667–682.
[16] ASTM G 61-86, Standard Test Method for Conducting Cyclic Potentiodynamic Polarization Measurements for Localized Corrosion Susceptibility of Iron-, Nickel-, or Cobalt-Based Alloys, ASTM International, West Conshohocken, PA, 2003.
[17] N. Sridhar, G.A. Cragnolino, Applicability of repassivation potential for long-term prediction of localized corrosion of alloy 825 and type 316L stainless steel, Corrosion 49 (1993) 885–894.
[18] D.S. Dunn, P. Pan, G.A. Cragnolino, Stress corrosion cracking, passive and localized corrosion of alloy 22 high level radioactive waste containers, Report Paper 00206, Corrosion, NACE, 2000.
[19] R.W. Revie, Uhlig's Corrosion Handbook, second ed., John Wiley & Sons, New York, 2000.
[20] H.H. Strehblow, Nucleation and repassivation of corrosion pits for pitting on iron and nickel, Werkst. Korros. 27 (1976) 792–799.

[21] H.H. Strehblow, P. Marcus, Mechanisms of pitting corrosion, in: P. Marcus (Ed.), Corrosion Mechanisms in Theory and Practice, Marcel Dekker Inc., New York, 2012, pp. 349–393.
[22] K.E. Heusler, L. Fisher, Kinetics of pit initiation at passive iron, Werkst. Korros. 27 (1976) 551, 697–788.
[23] J.R. Galvele, Transport processes and the mechanism of pitting of metals, J. Electrochem. Soc. 123 (1976) 464–474.
[24] J.R. Galvele, Transport processes in passivity breakdown—II. Full hydrolysis of metal ions, Corros. Sci. 21 (1981) 551–579.
[25] S.M. Gravano, J.R. Galvele, Transport processes in passivvity breakdown—III. Full hydrolysis plus ion migration plus buffers, Corros. Sci. 24 (1984) 517–534.
[26] M.G. Alvarez, J.R. Galvele, The mechanism of pitting of high purity iron in NaCl solutions, Corros. Sci. 24 (1984) 27–47.
[27] A.D. Keitelman, S.M. Gravano, J.R. Galvele, Localized acidification as the cause of passivity breakdown of high purity zinc, Corros. Sci. 24 (1984) 535–545.
[28] R.C. Newman, Diffusion-coupled active dissolution in the localized corrosion of stainless steels, J. Electrochem. Soc. 130 (1983) 1621–1624.
[29] R.P. Vera Cruz, A. Nishikata, T. Tsuru, Pitting corrosion mechanisms of stainless steels under wet-dry exposure in chloride-containing environments, Corros. Sci. 40 (1998) 125–139.
[30] D.A. Jones, B.E. Wilde, Galvanic reactions during localized corrosion on stainless steel, Corros. Sci. 18 (1978) 631–643.
[31] P.C. Pistorius, G.T. Burstein, Aspects of the effects of electrolyte competition on the occurrence of metastable pitting on stainless steel, Corros. Sci. 36 (1994) 525–538.
[32] D.E. Williams, R.C. Newman, Q. Song, R.G. Kelly, Passivity breakdown and pitting corrosion of binary alloys, Nature 350 (1991) 216–219.
[33] M.P. Ryan, N.J. Laycock, R.C. Newman, H.C. Isaacs, The pitting behavior of iron-chromium thin film alloys in hydrochloric acid, J. Electrochem. Soc. 145 (1998) 1566–1571.
[34] M.P. Ryan, D.E. Williams, R.J. Chatter, B.M. Hutton, D.C. McPhail, Why stainless steel corrodes, Nature 415 (2002) 770–774.
[35] I.L. Rosenfeld, I.S. Danilov, Electrochemical aspects of pitting corrosion, Corros. Sci. 7 (1967) 129–132, IN1-IN3, 133-142.
[36] G. Eklund, Initiation of pitting at sulfide inclusions in stainless steel, J. Electrochem. Soc. 121 (1974) 467–473.
[37] Z. Szklarska-Smialowska, Influence of sulfide inclusions on the pitting corrosion of steels, Corrosion 28 (1972) 388–396.
[38] G. Wranglen, Pitting and sulfide inclusions in stainless steel, Corros. Sci. 14 (1974) 331–349.
[39] S.E. Lott, R.C. Alkire, The role of inclusions on initiation of crevice corrosion of stainless steel, J. Electrochem. Soc. 136 (1989) 973–979.
[40] J.E. Castle, R. Ke, Studies by auger spectroscopy of pit initiation at the site of inclusions in stainless steel, Corros. Sci. 30 (1990) 409–428.
[41] T. Suter, T. Peter, H. Böhni, Microelectrochemical investigation of MnS inclusions, Mater. Sci. Forum 25 (1995) 192–194.
[42] C.S. Brossia, R.G. Kelly, Occluded chemistry control and the effects of alloy sulfur in the initiation of crevice corrosion of austenitic stainless steel, Corros. Sci. 40 (1998) 1851–1871.
[43] E.G. Webb, R.C. Alkire, Pit initiation at single sulfide inclusions in stainless steel. II. Detection of local pH, sulfide, and thiosulfate, J. Electrochem. Soc. 149 (2002) B280–B285.
[44] T. Suter, H. Böhni, A new microelectrochemical method to study pit initiation on stainless Steels, Electrochim. Acta 42 (1997) 3275.
[45] H. Böhni, T. Suter, A. Schreyer, Micro and nano techniques to study localized corrosion, Electrochim. Acta 40 (1995) 1361–1368.
[46] E.G. Webb, T. Suter, R.C. Alkire, Microelectrochemical measurements of the dissolution of single MnS inclusions and the prediction of the critical conditions for pit initiation on stainless steel, J. Electrochem. Soc. 148 (2001) B186–B195.
[47] E.G. Webb, R.C. Alkire, Pit initiation of single sulfide inclusions in stainless steel. I. Electrochemical microcell measurements, J. Electrochem. Soc. 149 (2002) B272–B279.

[48] H. Krawiec, V. Vignal, O. Heintz, R. Oltra, Influence of the dissolution of MnS inclusions under free corrosion and potentiostatic conditions on the composition of passive films and the electrochemical behavior of stainless steels, Electrochim. Acta 51 (2006) 3235–3243.
[49] T. Suter, E.G. Webb, H. Böhni, R.C. Alkire, Pit initiation on stainless steels in 1M NaCl with and without mechanical stress, J. Electrochem. Soc. 148 (2001) B174–B185.
[50] J.O. Park, S. Matsch, H. Böhni, Effects of temperature and chloride concentration of pit initiation an early pit growth on stainless steel, J. Electrochem. Soc. 149 (2002) B34–B39.
[51] I. Muto, Y. Izumiyama, N. Hara, Microelectrochemical measurements of dissolution of MnS inclusions and morphological observation of metastable and stable pitting on stainless steel, J. Electrochem. Soc. 154 (2007) C439–C444.
[52] R.J. Brigham, E.W. Tozer, Effect of alloying additions on the pitting resistance of 18% of Cr austenitic stainless steel, Corrosion 30 (1974) 161–166.
[53] V.M. Salinas-Bravo, R.C. Newman, An alternative method to determine critical pitting temperature of stainless steels in ferric chloride solution, Corros. Sci. 36 (1994) 67–77.
[54] R. Qvarfort, Critical pitting temperature measurements of stainless steels with an improved electrochemical method, Corros. Sci. 29 (1989) 987–993.
[55] G.T. Burstein, J.J. Moloney, Cyclic thermammetry, Electrochem. Commun. 6 (2004) 1037–1041.
[56] B. Deng, Y. Jiang, J. Gong, C. Zhong, J. Gao, J. Li, Critical pitting and repassivation temperatures for duplex stainless steel in chloride solutions, Electrochim. Acta 53 (2008) 5220–5225.
[57] M.H. Moayed, R.C. Newman, Evolution of current transients and morphology of metastable and stable pitting on stainless steel near critical pitting temperature, Corros. Sci. 48 (2006) 1004–1018.
[58] E.A. Abd, E.I. Meguid, N.A. Mahmoud, V.K. Gouda, Pitting corrosion behavior of UNS N08904 stainless steel in chloride-sulfide solutions, Br. Corros. J. 32 (1997) 68–71.
[59] J. Horvath, H.H. Uhlig, Critical potentials for pitting corrosion of Ni, Ni-Cr, Cr-Fe, and related stainless steel, J. Electrochem. Soc. 115 (1968) 791–795.
[60] H. Böhni, H. Uhlig, Environmental factors affecting the critical pitting potential of aluminum, J. Electrochem. Soc. 116 (1969) 906–910.
[61] Y. Kolotyrkin, Pitting corrosion of metals, Corrosion 19 (1963) 261t–268t.
[62] N. Greene, C. Bishop, M. Stern, Corrosion and electrochemical behavior of chromium-noble metal alloys, J. Electrochem. Soc. 108 (1961) 836–841.
[63] C. Hall Jr., N. Hackerman, Charging process on anodic polarization of titanium, J. Phys. Chem. 77 (1953) 262–268.
[64] H. Uhlig, R.R. Winston, Corrosion and Corrosion Control, John Wiley & Sons, New York, 1985.
[65] Z. Szklarska-Smialovska, Pitting Corrosion of Metals, NACE, Houston, Texas, 1986.
[66] H. Ogawa, H. Omata, I. Itoh, H. Okada, Auger electron spectroscopic and electrochemical analysis of the effect of alloying elements on the passivation behavior of stainless steels, Corrosion 34 (1978) 52–60.
[67] K. Hashimoto, K. Asami, K. Teramoto, An X-ray photo-electron spectroscopic study on the role of molybdenum in increasing the corrosion resistance of ferritic stainless steels in HCl, Corros. Sci. 19 (1979) 3–14.
[68] R.C. Newman, The dissolution and passivation kinetics of stainless alloys containing molybdenum—II. Dissolution kinetics in artificial pits, Corros. Sci. 25 (1985) 341–350.
[69] A.J. Sedriks, Corrosion of Stainless Steels, Wiley-Interscience, New York, 1996.
[70] H. Böhni, L. Stockert, The importance of metastable pitting corrosion in the case of high-alloy steels, Werkst. Korros. 40 (1989) 63–71.
[71] H. Böhni, Breakdown of passivity and localized corrosion processes, Langmuir 3 (1987) 924–930.
[72] F. Hunkeler, G.S. Frankel, H. Böhni, On the mechanism of localized corrosion, Corrosion 43 (1987) 189–191.
[73] D.E. Williams, C. Westcott, M. Fleischman, Stochastic models of pitting corrosion of stainless steels: I. Modeling of the initiation and growth of pits at constant potential, J. Electrochem. Soc. 132 (1985) 1796–1804.
[74] D.E. Williams, C. Westcott, M. Fleischman, Stochastic models of pitting corrosion of stainless steels: II. Measurement and interpretation of data at constant potential, J. Electrochem. Soc. 132 (1985) 1805–1811.

[75] N.J. Laycock, R.C. Newman, Localized dissolution kinetics, salt films and pitting potentials, Corros. Sci. 39 (1997) 1771–1790.
[76] N.J. Laycock, R.C. Newman, Temperature dependence of pitting potentials for austenitic stainless steels above their critical pitting temperature, Corros. Sci. 40 (1998) 887–902.
[77] P.C. Pistorius, G.T. Burstein, Metastable pitting corrosion of stainless steel and the transition to stability, Philos. Trans. R. Soc. London A 341 (1992) 531–542.
[78] G.C. Frankel, J.O. Dukovic, V. Brusic, B.M. Rush, C.V. Jahnes, Pit growth in Ni-Fe thin films, J. Electrochem. Soc. 139 (1992) 2196–2201.
[79] Y. Tsutsumi, A. Nishikata, T. Tsuru, Monitoring of rusting of stainless steels in marine atmospheres using electrochemical impedance technique: corrosion, passivation, and anodic films, J. Electrochem. Soc. 153 (2006) B278–B282.
[80] Y. Tsutsumi, A. Nishikata, T. Tsuru, Pitting corrosion mechanism of type 304 stainless steel under a droplet of chloride solutions, Corros. Sci. 49 (2007) 1394–1407.
[81] Y. Tsutsumi, A. Nishikata, T. Tsuru, Initial stage of pitting corrosion of type 304 stainless steel under thin electrolyte layers containing chloride ions corrosion, passivation, and anodic films, J. Electrochem. Soc. 152 (2005) B358–B363.
[82] S. Hastuty, A. Nishikata, T. Tsuru, Pitting corrosion of type 430 stainless steel under chloride solution droplet, Corros. Sci. 52 (2010) 2035–2043.
[83] B. Maier, G.S. Frankel, Pitting corrosion of bare stainless steel 304 under chloride solution droplets, J. Electrochem. Soc. 157 (2010) C302–C312.
[84] G.S. Frankel, M. Stratmann, M. Rohwerder, A. Michalik, B. Maier, J. Dora, M. Wicinski, Potential control under thin aqueous layers using a Kelvin probe, Corros. Sci. 49 (2007) 2021–2036.
[85] B. Lin, R. Hu, C. Ye, Y. Li, C. Lin, A study on the initiation of pitting corrosion in carbon steel in chloride-containing media using scanning electrochemical probes, Electrochim. Acta 55 (2010) 6542–6545.
[86] H. Uhlig, J. Gilman, Pitting of 18-8 stainless steel in ferric chloride inhibited by nitrates, Corrosion 20 (1964) 289t–292t.
[87] S.B. de Wexler, J.R. Galvele, Anodic behavior of aluminum straining and a mechanism for pitting, J. Electrochem. Soc. 121 (1974) 1271–1276.
[88] H. Lackie, A contribution to the applicability of critical pitting potentials, J. Electochem. Soc. 117 (1970) 1152–1154.
[89] C. Edeleanu, U.R. Evans, The causes of the localized character of corrosion on aluminum, Trans. Faraday Soc. 47 (1951) 1121–1135.
[90] M. Wang, H.W. Pickering, Y. Xu, Potential distribution, shape evolution, and modeling of pit growth for Ni in sulfuric acid, J. Electrochem. Soc. 142 (1995) 2986–2995.
[91] K. Cho, M.I. Abdulsalam, H.W. Pickering, The effect of electrolyte properties on the mechanism of crevice corrosion in pure iron, J. Electrochem. Soc. 145 (1998) 1862–1869.
[92] M.I. Abdulsalam, H.W. Pickering, Effect of the applied potential on the potential and current distributions within crevices in pure nickel, Corros. Sci. 41 (1999) 351–372.
[93] M.I. Abdulsalam, Significance of temperature change on the behavior of crevice corrosion, Corrosion 58 (2002) 364–369.
[94] J.C. Walton, G. Cragnolino, S.K. Kalandros, A numerical model of crevice corrosion for passive and active metals, Corros. Sci. 38 (1996) 1–18.
[95] M.K. Sawford, B.G. Ateya, A.M. Abdullah, H.W. Pickering, The role of oxygen on the stability of crevice corrosion, J. Electrochem. Soc. 149 (2002) B198–B205.
[96] A. Valdes, H.W. Pickering, On the roles of corrosion products in local cell processes, in: H. Isaacs, U. Bertacci, J. Kruger, Z. Smialowska (Eds.), Advances in Localized Corrosion, NACE-9, Houston, TX, 1990, pp. 393–401.
[97] H.W. Pickering, The significance of the local electrode potential within pits crevices and cracks, Corros. Sci. 29 (1989) 325–341.
[98] H.W. Pickering, On the roles of corrosion products in local cell processes, Corrosion 42 (1986) 125–140.

[99] M.I. Abdulsalam, H.W. Pickering, The effect of crevice-opening dimension on the stability of crevice corrosion for nickel in sulfuric acid, J. Electrochem. Soc. 145 (1998) 2276–2284.
[100] J. Al-Khamis, H.W. Pickering, IR mechanism of crevice corrosion for alloy T-2205 duplex stainless steel in acidic-chloride media, J. Electrochem. Soc. 148 (2001) B314–B321.
[101] B.D. Force, H.W. Pickering, A clearer view of how crevice corrosion occurs, JOM 47 (1995) 22–27.
[102] H. Shu, F.M. Al-Faqeerb, H.W. Pickering, Pitting on the crevice wall prior to crevice corrosion: iron in sulfate/chromate solution, Electrochim. Acta 56 (2011) 1719–1728.
[103] W. Pickering, Important early developments and understanding of the IR mechanism of localized corrosion, J. Electrochem. Soc. 150 (2003) K1–K13.
[104] A.M. Al-Zahrani, H.W. Pickering, IR voltage switch in delayed crevice corrosion and active peak formation detected using a repassivation-type scan, Electrochim. Acta 50 (2005) 3420–3435.
[105] X. Shan, H. Ha, J.H. Payer, Comparison of crevice corrosion of Fe-based amorphous metal and crystalline Ni-Cr-Mo alloy, in: Metallurgical and Materials Transactions, vol. 40, Springer, Boston, 2009, p. 1324.
[106] G.E. Coates, Effect of some surface treatments on corrosion of stainless steel, Mater. Performance 29 (1990) 61–67.
[107] Y.C. Lu, M.B. Ives, The improvement of the localized corrosion resistance of stainless steel by cerium, Corros. Sci. 34 (1993) 1773–1781, 1783-1785.
[108] Y.C. Lu, M.B. Ives, Chemical treatment with cerium to improve the crevice corrosion resistance of austenitic stainless steels, Corros. Sci. 37 (1995) 145–155.
[109] T.P. May, H. Humble, Effectiveness of cathodic currents in reducing crevice corrosion of several materials in seawater, Corrosion 8 (1952) 50–56.
[110] R. Holthe, E. Bradal, P.O. Gartland, Time dependence of cathodic properties of materials in seawater, Mater. Performance 28 (1989) 16–23.
[111] C. Hahin, Filiform corrosion, in: Corrosion, in: Metals Handbook, vol. XIII, ASM International, Metals Park, OH, 1987, pp. 104–122.
[112] H. Kaesche, Electrochemical characteristics of atmospheric corrosion, Werkst. Korros. 15 (1959) 379–390.
[113] H. Kaesche, Metallic Corrosion, NACE, Houston, TX, 1985, pp. 216-219.

CHAPTER 8

Hydrogen Permeation and Hydrogen-Induced Cracking

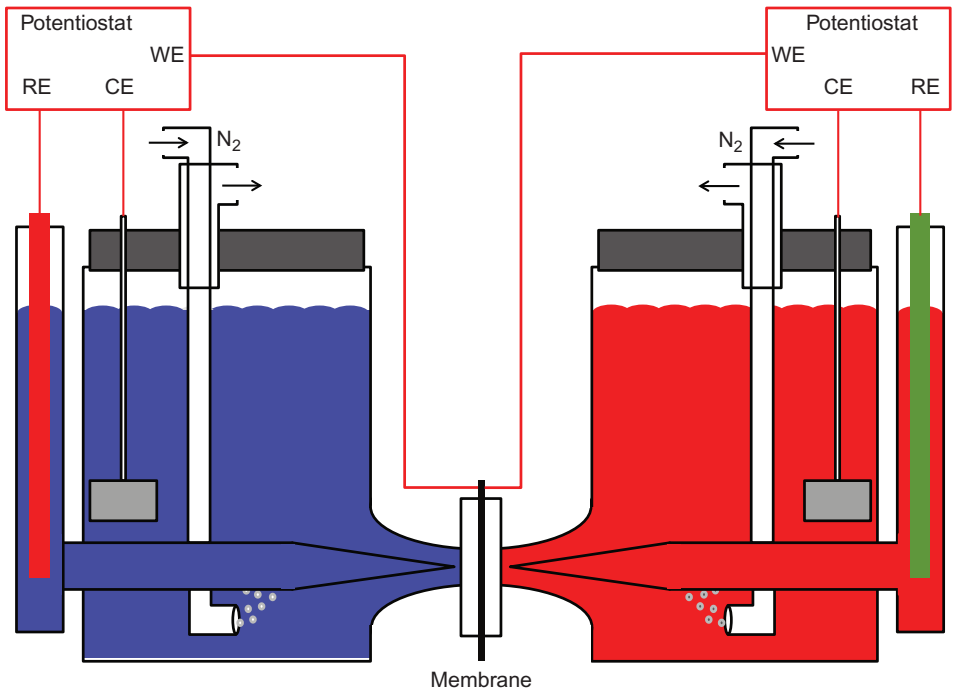

Chapter Contents

Corrosion Engineering
http://dx.doi.org/10.1016/B978-0-444-62722-3.00008-2

8.1 INTRODUCTION

The use of ultra-strength alloys is limited by their tendency to crack due to hydrogen penetration and hydrogen accumulation in the bulk. Hydrogen evolution and permeation are encountered during electroplating, corrosion, and cathodic protection. Hydrogen accumulates in areas of high stress and may reach a critical concentration, potentially causing fractures and catastrophic damage.

In this chapter, the nature and mechanisms of hydrogen-induced cracking (HIC) of metals, hydrogen embrittlement, hydrogen blistering, hydrogen stress cracking (HSC), and electrochemical hydrogen absorption assessment are discussed. The chapter starts by discussing kinetics of hydrogen evolution reaction (HER), theoretical diffusion solutions, and basic models for hydrogen permeation. Basic mechanistic hydrogen permeation mathematical models are used as a diagnostic tool for determining the effectiveness of various metals and alloys as hydrogen permeation inhibitors. The models provide an estimation of hydrogen discharge rate constant values for the recombination, adsorption reactions, and hydrogen entry inhibition efficiency. The barrier properties of metallic and alloy coatings that successfully reduce the hydrogen ingress into the metal structures are discussed. Solved exercise problems illustrate the use of the model for these purposes. Case studies are used to explain evaluation of atomic hydrogen permeation transients and hydrogen absorption rate constants and diffusivity into metals. The most recent research of hydrogen embrittlement, HIC, hydrogen blistering, and HSC is reviewed in the chapter.

8.2 HYDROGEN EVOLUTION REACTION

The overall HER occurs in two steps:

$$2H_3O^+ + 2e^- \rightarrow H_2 + 2H_2O \tag{8.1}$$

In the first step, hydrogen ions are discharged and hydrogen atoms are adsorbed onto the metal surface:

$$2H_3O^+ + 2M + 2e^- \rightarrow 2MH_{ads} + 2H_2O \tag{8.2}$$

The second step involves hydrogen recombination, electrochemical desorption, or emission of the adsorbed hydrogen. Hydrogen molecules are formed when the discharge reaction is controlled by the recombination of adsorbed hydrogen atoms, which simultaneously desorb from the metal surface.

$$2MH_{ads} \rightarrow H_2 + 2M \tag{8.3}$$

According to the electrochemical desorption mechanism, the metal serves as catalyst, while adsorbed hydrogen atoms are discharged and removed:

$$MH_{ads} + H_3O^+ + e^- \rightarrow H_2 + H_2O + M \tag{8.4}$$

Adsorbed hydrogen atoms first desorb from the catalyst surface and then recombine into molecules:

$$H_{ads} \rightarrow H \tag{8.5}$$

The slowest of the following processes at the metal interface controls the hydrogen overvoltage and the reaction mechanism: (i) electroactive species transport to the electrode interface; (ii) discharge reaction; (iii) desorption from the metal surface including catalytic desorption, electrochemical desorption, or emission; and (iv) gaseous hydrogen formation.

The following mechanisms are discussed [1–4]:

1. The Volmer-Tafel mechanism corresponds to the case where the discharge reaction is the rate-determining step, while the recombination step is fast.

$$2H_3O^+ + 2M + 2e^- \rightarrow 2MH_{ads} + 2H_2O \tag{8.6}$$

$$2MH_{ads} \leftrightarrow H_2 + 2M \tag{8.7}$$

2. The Volmer-Heyrovsky mechanism corresponds to slow discharge and fast electrochemical desorption:

$$H_3O^+ + M + e^- \rightarrow MH_{ads} + H_2O \tag{8.8}$$

$$MH_{ads} + H_3O^+ + e^- \leftrightarrow H_2 + M + H_2O \tag{8.9}$$

3. The Tafel-Horiuti mechanism corresponds to fast discharge and slow hydrogen recombination:

$$2H_3O^+ + 2M + 2e^- \rightarrow 2MH_{ads} + 2H_2O \tag{8.10}$$

$$2MH_{ads} \leftrightarrow H_2 + 2M \tag{8.11}$$

4. The Heyrovski-Horiuti mechanism is based on fast discharge and slow electrochemical desorption:

$$H_3O^+ + e^- \rightarrow MH_{ads} + H_2O \tag{8.12}$$

$$MH_{ads} + H_3O^+ + e^- \rightarrow H_2 + M + H_2O \tag{8.13}$$

5. Coupled discharge-electrochemical desorption is defined as:

$$H_3O^+ + e^- \rightarrow MH_{ads} + H_2O \tag{8.14}$$

$$MH_{ads} + H_3O^+ + e^- \rightarrow H_2 + M + H_2O \tag{8.15}$$

6. Coupled discharge-recombination mechanism:

$$H_3O^+ + e^- \rightarrow MH_{ads} + H_2O \tag{8.16}$$

$$MH_{ads} + MH_{ads} \rightarrow H_2 + 2M \tag{8.17}$$

Fast hydrogen evolution in the first four mechanisms is at equilibrium (the reaction rates of the forward and reverse reactions are equal). In the last two mechanisms, the rates of both forward reactions are equal and the rates of both reverse reactions are negligible.

8.2.1 Kinetics of HER

Hydrogen evolution rate constants have been derived assuming hydrogen evolution occurs by the slow discharge-fast recombination mechanism, (Eqs. 8.18 and 8.19). This mechanism requires the cathodic reaction to be first order in oxidized species concentration at the electrode-electrolyte interface:

$$1/2\,H_2 \rightleftharpoons H \text{ (Equilibrium)} \tag{8.18}$$

$$H \rightleftharpoons H^+ + e^- \text{ (RDS)} \tag{8.19}$$

Because Eq. (8.18) is at equilibrium, the hydrogen atom concentration is:

$$[H] = K[H_2]^{1/2} \tag{8.20}$$

where K is the equilibrium constant. The net conversion of hydrogen ions to molecules is the difference between the rates of the anodic and cathodic steps and is equal to the current "i" in Eq. (8.21):

$$i = F\left[k_1^o e^{E/b_a} K[H_2]_b^{1/2} - k_{-1}^o e^{-E/b_c}[H^+]_s\right] \tag{8.21}$$

where k_1^o and k_{-1}^o are the rate constants. At equilibrium, $i = i^o$, $E = e_{eq}$, or:

$$i^o = F\left[k_1^o e^{e_{eq}/b_a} K[H_2]_b^{1/2} - k_{-1}^o e^{-e_{eq}/b_c}[H^+]_s\right] \tag{8.22}$$

The rate constants at equilibrium are:

$$k_1^o = \frac{i^o e^{-e_{eq}/b_a}}{FK[H_2]_b^{1/2}}; \quad k_{-1}^o = \frac{i^o e^{e_{eq}/b_c}}{F[H^+]_b} \tag{8.23}$$

Substituting rate constants into Eq. (8.21), one obtains:

$$i = i^{o}\left\{\frac{[H_2]_s^{1/2} e^{(E-e_{eq})/b_a}}{[H_2]_b^{1/2}} - \frac{[H^+]_s}{[H^+]_b} e^{-(E-e_{eq})/b_c}\right\} \tag{8.24}$$

where i^{o} is the exchange current density, $[H_2]_b^{1/2}$ and $[H^+]_b$ are hydrogen molecule and cation concentrations in the bulk of the solution at equilibrium, respectively. $[H_2]_s^{1/2}$ and $[H^+]_s$ are hydrogen molecule and hydrogen ion surface concentrations, respectively. Assuming fast transport, the concentration in the bulk is equal to the electrode surface, Eq. 8.24 results in Eq. 8.25:

$$i = i^{o}\left(e^{(E-e_{eq})/b_a} - e^{-(E-e_{eq})/b_c}\right) \tag{8.25}$$

8.2.2 Theoretical diffusion solution

Evaluation of hydrogen absorption and permeation provides valuable information on the hydrogen evolution and hydrogen embrittlement mechanism. Devanathan-Stachurski [5,6] developed a technique to measure hydrogen permeation though metallic membranes. This technique is based on the assumption that the following conditions are established at each surface of the membrane under potentiostatic control:

(i) Adsorbed hydrogen surface coverage is constant on the input side and zero on the exit side.
(ii) Hydrogen entry kinetics is fast enough to maintain equilibrium at the input surface.
(iii) Hydrogen at the exit is immediately oxidized and maintained at approximately zero concentration.

By assuming hydrogen diffusion through metal is the rate-determining step, hydrogen permeation transients are obtained by Fick's laws in one-dimensional form:

$$\frac{\partial C}{\partial t} = D\frac{\partial^2 C}{\partial^2 x} \tag{8.26}$$

and

$$j_t = -FD\left(\frac{\partial C}{\partial x}\right)_{x=L} \tag{8.27}$$

where C is the concentration of hydrogen, t is time, D is the diffusion coefficient, j_t is the diffusional flux, x is the position across the membrane, F is the Faraday constant, and L is the membrane thickness.

When carrying out experiments with a bipolar membrane, the hydrogen penetration steady state rate in diffusion mode can be represented by the following equations obtained for two typical boundary conditions [7–11]:

(1) Hydrogen concentration at the entry side of the membrane is constant [11]:

$$j_t \frac{-^t j_o}{j_\infty - j_o} = 1 - 2\sum_{n=1}^{\infty} (-1)^n \exp\left(-n^2\pi^2\tau\right) \tag{8.28}$$

(2) Hydrogen flux entering the membrane is constant:

$$\frac{j_t - j_o}{j_\infty - j_o} = 1 - \frac{4}{\pi}\sum_{n=0}^{\infty} \frac{(-1)^n}{(2n+1)} \exp\left\{-\frac{(2n+1)^2\pi^2\tau}{4}\right\} \tag{8.29a}$$

In Eq. (8.28), j_t is transition hydrogen permeation current density, (A/cm^2); j_o is initial hydrogen permeation current density, (A/cm^2); j_∞ is the steady state hydrogen permeation current density, (A/cm^2);

$$\tau = tD/L^2 \tag{8.29b}$$

τ is dimensionless time; t is time, s; D is the diffusion coefficient, cm^2 s^{-1}; and L is thickness of the membrane, cm. The hydrogen diffusivity in the metal membrane is determined by fitting the theoretical solution to the experimental permeation transients.

8.2.3 Evaluation of diffusivity

Transients are typically characterized by four parameters [12]: half-rise time ($t_{1/2}$), inflection point time (t_i), breakthrough time (t_b), and time lag (t_L).

(a) *Half-Rise Time*: A common approach is to measure $t_{1/2}(0.51\ j_\infty)$ (see Fig. 8.1) required for the current to reach so that D can be evaluated from:

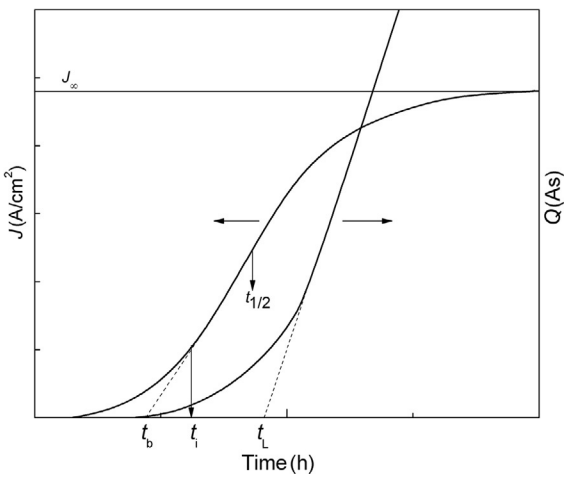

Fig. 8.1 Evaluation of hydrogen diffusivity using anodic rising transients [12].

$$t_{1/2} = \frac{0.14L^2}{D} \tag{8.30}$$

(b) *Inflection Point Time*: Inflection point time for the rising anodic transient are by represented by:

$$t_i = 0.924\frac{L^2}{\pi^2 D} \tag{8.31}$$

(c) *Breakthrough Time*: The breakthrough time, t_b is the time needed for hydrogen to arrive at the output side. It is obtained by extrapolating the tangent at the inflection point to the initial output current, and is related to the diffusivity by:

$$t_b = 0.924\frac{L^2}{\pi^2 D} \tag{8.32}$$

(d) *Time Lag*: The time lag t_L corresponds to the time required to obtain a steady state flow through the sample after charging. As shown in Fig. 8.1, when the current reaches steady state on the anodic site, charge follows a linear dependence. The time lag, t_L is determined by extrapolation to the intercept on the time axis.

$$t_L = \frac{L^2}{6D} \tag{8.33}$$

Time characteristics are proportional to the square of the membrane thickness only under diffusion control. The above equations verify that permeation rate is controlled by diffusion rather than surface kinetics.

8.2.4 Basic model for hydrogen permeation: the Iyer-Pickering-Zamanzadeh (IPZ) model

A basic hydrogen permeation mechanistic model was developed by Iyer, Pickering, and Zamanzadeh [13–15] on the basis of the following assumptions:

(i) Hydrogen evolution is a coupled discharge-recombination process.
(ii) $\eta \gg RT/F$ so backward reactions are negligible.
(iii) Surface coverage is low so the Langmuir isotherm can be used to describe hydrogen coverage.
(iv) Intermediate hydrogen adsorption-absorption reaction is in local equilibrium.
(v) Hydrogen permeation current density through the membrane without trapping is described by a simple diffusion model once steady state is reached [13,14].

With these assumptions, one can derive the following relationships [13]:

$$i_c = i_o'(1-\theta_H)e^{-(F\alpha\eta/RT)} \tag{8.34}$$

$$i_r = Fk_3\theta_H^2 \tag{8.35}$$

$$i'_o = \frac{i^o}{1-\theta_e} \tag{8.36}$$

$$j_\infty = \frac{k''\theta_H}{b} \tag{8.37}$$

$$j_\infty = \frac{k''}{b\sqrt{Fk_3}}\sqrt{i_r} \tag{8.38}$$

$$k'' = \frac{k_{abs}}{k_{ads} + \dfrac{D}{L}} \tag{8.39}$$

$$i_c e^{a\alpha\eta} = -\frac{bi'_o}{k''} j_\infty + i'_o \tag{8.40}$$

where i_c is the cathodic current density; (A/cm^2) i_r is the hydrogen recombination current density; $i_r = i_c - j_\infty$ (A/cm^2); F is the Faraday constant; 96,487 C/eq; α is the transfer coefficient, (dimensionless); η is the overpotential, $[E_{app} - E_{eq}]$ V; R is the gas constant, 8.3143J (mol K)$^{-1}$; T is the absolute temperature, K; j_∞ is the steady state hydrogen permeating current density, (A/cm^2); k_3 is the recombination constant, mol (cm^2 s)$^{-1}$; θ_H is the hydrogen surface coverage, dimensionless; i'_o is modified exchange current density (A/cm^2); i^o is the exchange current density, (A/cm^2) and θ_e equilibrium hydrogen coverage, dimensionless; $b = L/FD$ (A cm)$^{-1}$, L is the membrane thickness (cm), D is diffusion thickness, cm^2 s^{-1} and k'' is the thickness-dependent adsorption-absorption constant, (mol/cm^3).

Using the model and data obtained from hydrogen permeation experiments one can compute hydrogen surface coverage and the rate constants. This model is only applicable for coupled discharge-recombination hydrogen evolution with constant cathodic side hydrogen concentration on the membrane.

8.2.5 Experimental determination of hydrogen permeation parameters

The Devanathan-Stachurski permeation technique is commonly used to determine hydrogen permeation rate through metal or alloy membranes with ~4 cm^2 and thicknesses between 0.15 and 0.025 mm. If extremely thin membranes are chosen, grain boundary effects become dominant, localizing the hydrogen adsorption and absorption processes and short circuit hydrogen diffusion [14]. A permeation cell schematic is shown in Fig. 8.2. The cell consists of two compartments separated by a bipolar metal membrane. Under potentiostatic conditions, hydrogen permeation current through the membrane is recorded continuously as a function of time by keeping the anodic side overpotential (the side from which the hydrogen emerges) positive enough to oxidize atomic hydrogen. The absorbed hydrogen concentration on the anodic side of the

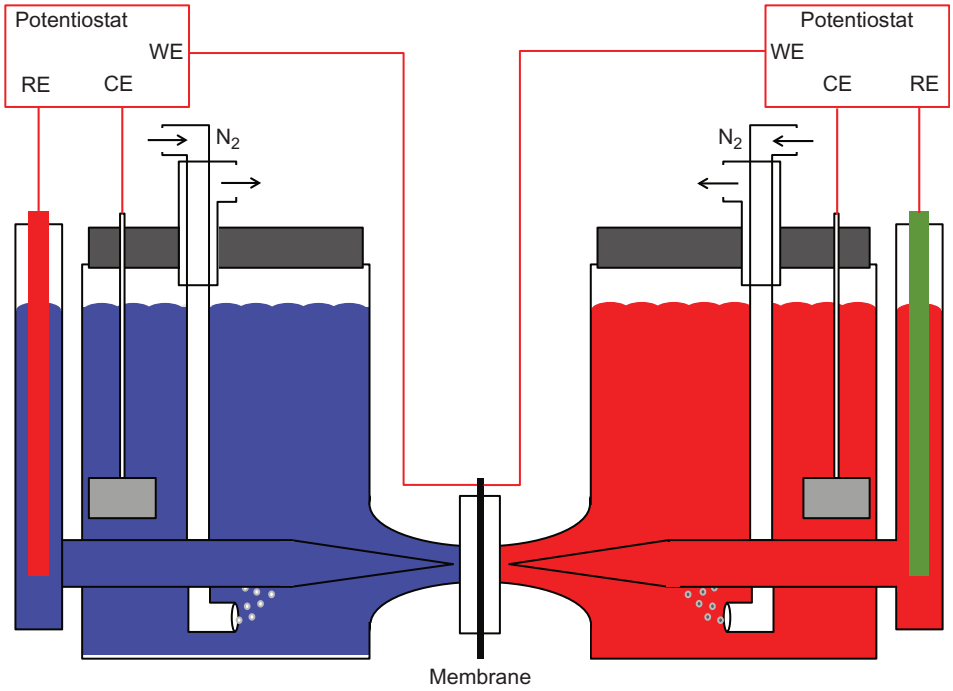

Fig. 8.2 Schematic of a hydrogen permeation cell.

membrane is practically zero. The steel membrane on the cathodic side of the cell is polarized potentiostatically, creating conditions for hydrogen evolution. Membrane permeation rate is measured by setting the potential on the "diffusion side" of the membrane (the side from which the hydrogen emerges) at a fixed value (−0.3 V vs. Hg/HgO reference electrode). This value corresponds to an almost zero concentration of absorbed hydrogen on the surface.

The membrane on the cathodic side of the cell is polarized potentiostatically using a Pt counter electrode. Prior to permeation studies, the metal or alloy membrane is mechanically polished with 600 grade sandpaper and 0.5 μm high-purity alumina powder to a mirror finish. The membrane (working electrode) is cleaned in an ultrasonic cleaning bath and saturated with hydrogen in a 0.1 M H_2SO_4 solution by maintaining a cathodic current density of 10 mA/cm^2. Next, the membrane is removed from the cell, etched for 20 s in a solution containing methyl alcohol and 1% H_2SO_4, rinsed with deionized water, dried in air, and fitted into the permeation cell. The anodic side of the membrane is electroplated with a thin layer (0.15-0.20 μm) of palladium to avoid passivation. The deposition is carried out in an electrolyte containing 2×10^{-5} M $Na_2Pd(NO_2)_4$ using a current density of 100 $\mu A/cm^2$ for two hours. The electrolyte is drained off and the compartment is washed with deionized water and filled with anodic solution (0.2 M NaOH).

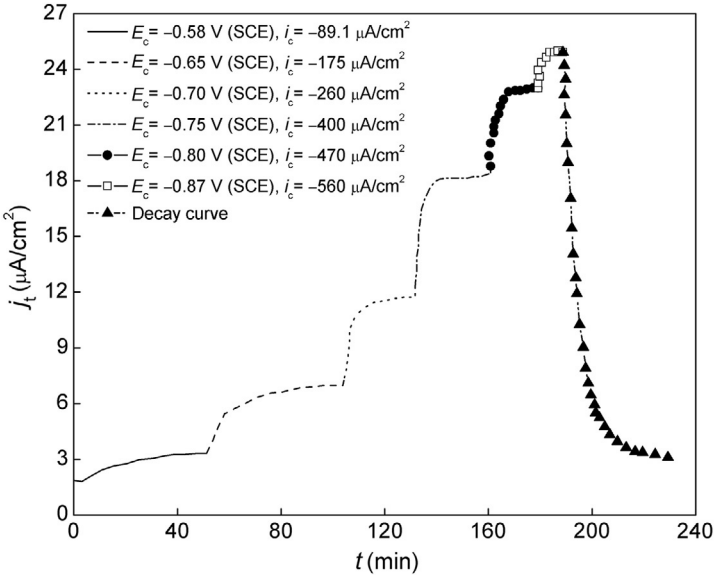

Fig. 8.3 Atomic hydrogen permeation transients through a HY-130 steel membrane as a function of time for different applied cathodic potentials in a catholyte containing 1 M $NaSO_4$, 0.4 M NaCl, and 1 M H_3BO_3. The thickness of the membrane = 0.15 mm [16]. *Reproduced by the permission of The Electrochemical Society.*

To keep electrolyte impurities at the lowest possible level, the anodic solution is pre-electrolyzed for at least 24 h in a separate electrolytic cell. The electrolyte is kept at −0.3 V vs. the Hg/HgO reference electrode until the background current in the anodic compartment is reduced to below 3 μA/cm^2. Next, the cathodic compartment is filled with a supporting electrolyte containing 0.5 M Na_2SO_4 and 0.5 M H_2SO_4. Prepurified nitrogen is bubbled through both compartments to keep the system free of dissolved oxygen. At the beginning of each experiment, as with HY-130 steel permeation studies, the cathodic site of the steel membrane is held at a constant potential of −0.58 V vs. SCE (Fig. 8.3) [16]. Next, the potential is stepped to more negative values after the hydrogen permeation current density reaches a steady state value. After the potential stabilizes at about −0.87 V vs. SCE, the potential is switched off and the decay curve is recorded.

Case Study 8.1—Evaluation of the Atomic Hydrogen Permeation Transients Through an AISI 4340 Membrane

IPZ analysis of the experimentally measured steady state hydrogen permeation rates through AISI 4340 steel are used to estimate hydrogen kinetic diffusion constants and hydrogen diffusivity within the alloy. Atomic hydrogen permeation transients through an AISI 4340 membrane for different applied potentials were studied in an electrolyte

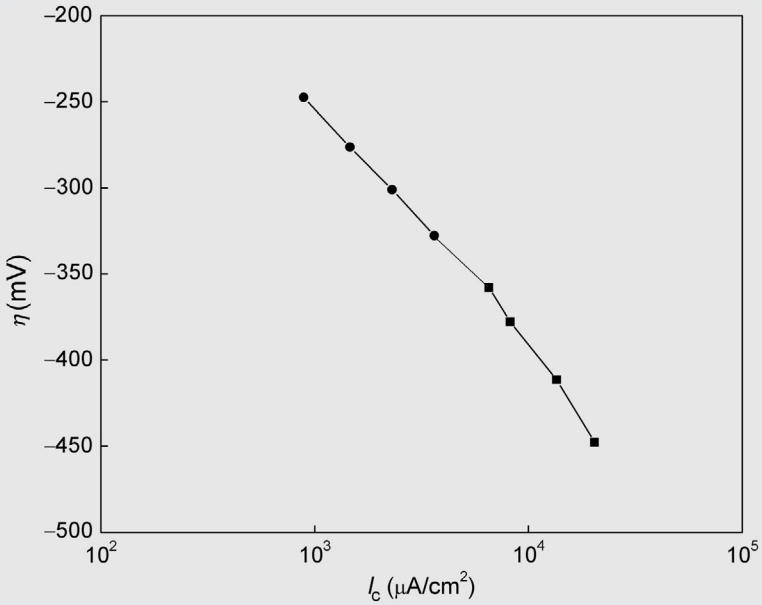

Fig. 8.4 Cathodic current-overpotential relationship for hydrogen evolution reaction obtained on AISI 4340 steel membrane in an electrolyte containing 0.5 M $HClO_4$ and 0.25 M $NaClO_4$ (pH 0.3) [3]. *Reproduced by the permission of The Electrochemical Society.*

containing 0.5 M $HClO_4$ and 0.25 M $NaClO_4$ at a pH 0.3 and experimental results were compared in two typical theoretical solutions [3]. The current-potential relationship is presented in Fig. 8.4 [3]. At low overpotentials, the slope $\partial\eta/\partial \log i_c$ is -118 mV/decade, indicating the hydrogen evolution mechanism is a coupled discharge-recombination with hydrogen coverage following a Langmuir isotherm [17]. At higher overpotentials, the current-vs.-potential plot gives a slope 177 mV/decade, which indicates the HER has the same mechanism but hydrogen coverage follows a Temkin isotherm. The transfer coefficient calculated using the data at low and high overpotentials are 0.52 and 0.50, respectively. Hydrogen permeation current densities vs. time for different cathodic potentials are presented in Fig. 8.5 [3].

The steady state hydrogen permeation current increases to -0.600 V (SCE). The diffusion coefficient of atomic hydrogen through the AISI 4340 steel membrane is evaluated by using Eq. (8.30). For $L=0.3$ mm and $t_{1/2}=426$ s, the permeation transient curve gives $E_c=-0.60$ V (SCE). This value corresponds to the permeation curve half rise presented in Fig. 8.5. It is used to calculate the atomic hydrogen diffusion coefficient 2.9×10^{-7}cm^2/s. The experimental dimensionless permeation curves are compared to the two theoretical solutions for hydrogen permeation, Eqs. (8.28) and (8.29a). The results are presented in Fig. 8.6 [3].

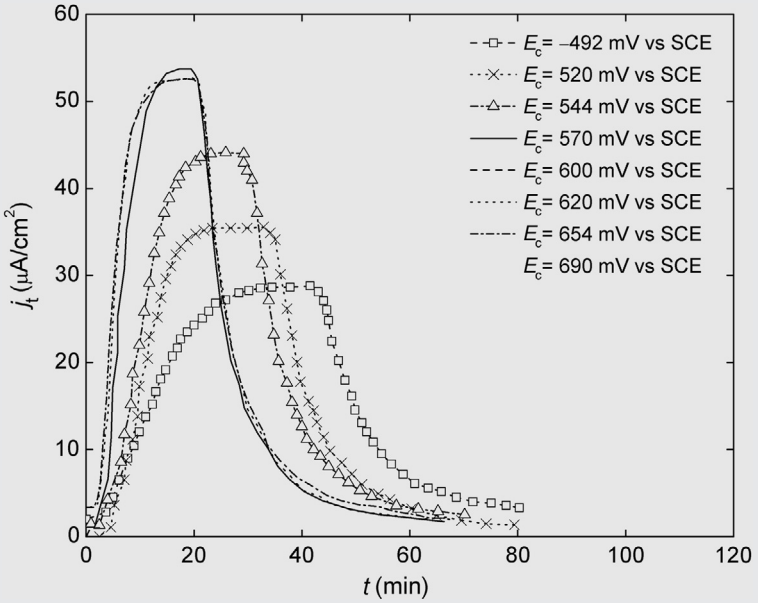

Fig. 8.5 The atomic hydrogen permeation transition through an AISI 4340 membrane as a function of time for different applied cathodic potentials in an electrolyte containing 0.5 M $HClO_4$ and 0.25 M $NaClO_4$ (pH 0.3) and the membrane thickness = 0.3 mm [3]. *Reproduced by the permission of The Electrochemical Society.*

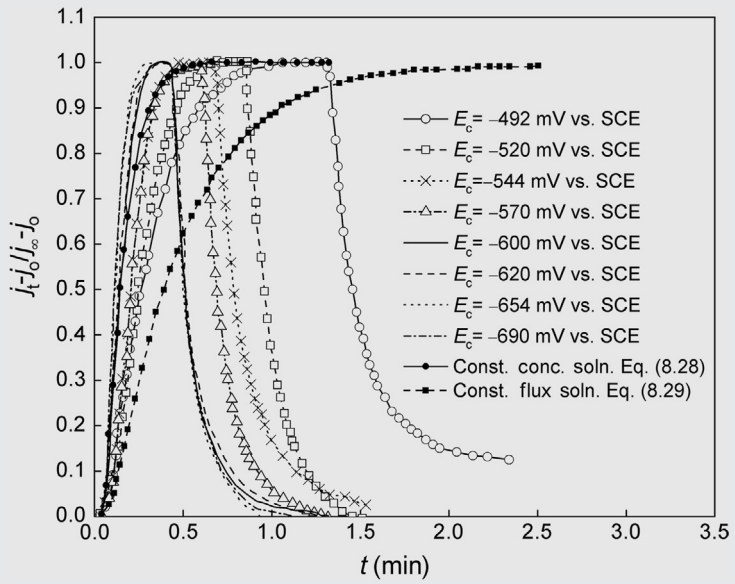

Fig. 8.6 The comparison of the experimental results given in Fig. 8.5 with the theoretical solutions for the two typical theoretical solutions in dimensionless forms [3]. *Reproduced by the permission of The Electrochemical Society.*

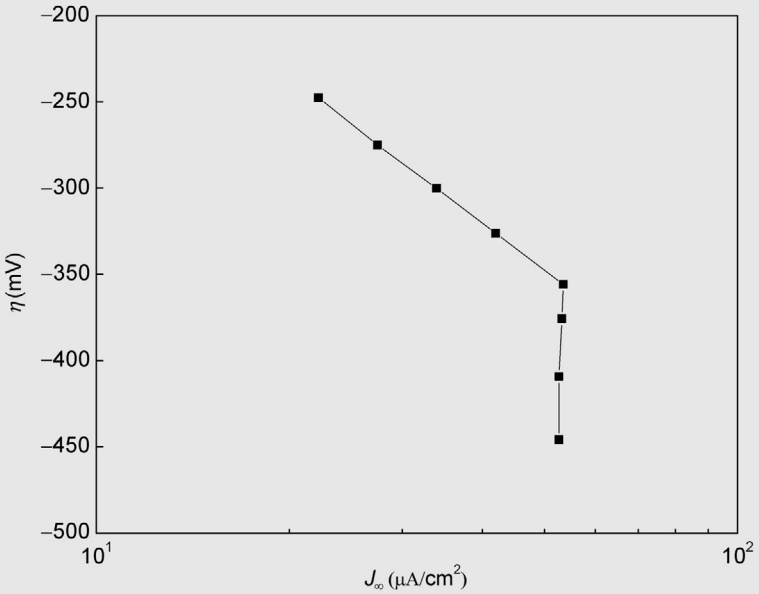

Fig. 8.7 Hydrogen permeation current-overpotential dependence obtained on an AISI 4340 steel membrane in an electrolyte containing 0.5 M $HClO_4$ and 0.25 M $NaClO_4$ (pH 0.3) and the membrane thickness = 0.3 mm [3]. *Reproduced by the permission of The Electrochemical Society.*

Data indicate that experimental permeation curves are close to the theoretical curve obtained at high cathodic potentials where the boundary condition is a constant hydrogen concentration at the entry side of the membrane. The experimental permeation transients at lower cathodic potentials are approaching the theoretical curve obtained using constant hydrogen flux boundary conditions entering the membrane. Figure 8.7 shows the hydrogen permeation current effect on applied overpotential [3]. The slopes in Fig. 8.7 provide diagnostic criteria to identify the hydrogen ion discharge mechanism on the membrane. At lower overpotentials, the slope is 273 mV/decade, approximately equal to $2.3 \times 4RT/F$ (when $T = 298.15$ K), indicating a coupled discharge-recombination mechanism [17].

Hydrogen surface coverage and surface concentration, hydrogen absorption, discharge, recombination rate constants, HER coverage-dependent transfer coefficient, α, and the exchange current density, i^o, were calculated using the steady state hydrogen permeation current values, cathodic charging current, hydrogen diffusivity, hydrogen overvoltage, and Eqs. (8.34)–(8.39) [13–15]. The square root of the hydrogen recombination current density effect on hydrogen permeation current in a solution containing 0.5 M $HClO_4$ and 0.25 M $NaClO_4$, at pH 0.3 for a membrane thickness of 0.3 mm, is shown in Fig. 8.8 [3].

The linear relationship obtained in Fig. 8.8 is consistent with Eq. (8.38). A plot of $i_c e^{a\alpha\eta}$ as a function of hydrogen permeation through an AISI 4340 steel membrane in a solution containing 0.5 M $HClO_4$ and 0.25 M $NaClO_4$ (pH 0.30) in Fig. 8.9 yields a straight line [3]. Using the intercept and slopes obtained from Figs. 8.8 and 8.9 and

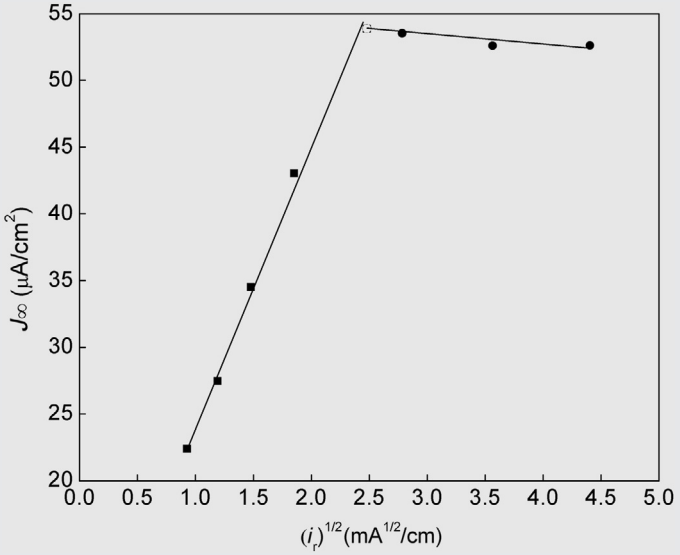

Fig. 8.8 Plot of hydrogen permeation current vs. square root of the hydrogen recombination current density in an electrolyte containing 0.5 M $HClO_4$ and 0.25 M $NaClO_4$ at pH 0.3 and the membrane thickness = 0.3 mm [3]. *Reproduced by the permission of The Electrochemical Society.*

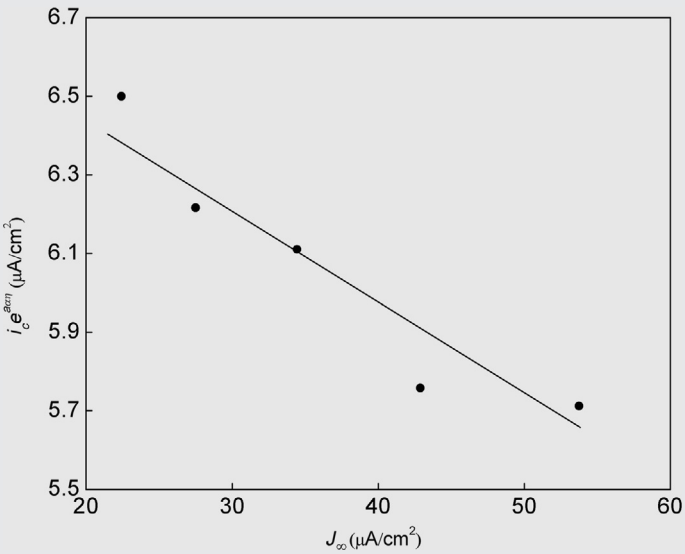

Fig. 8.9 Plot of $i_c e^{\alpha\chi\eta}$ as a function of hydrogen permeation through an AISI 4340 steel membrane in an electrolyte containing 0.5 M $HClO_4$ and 0.25 M $NaClO_4$ and the membrane thickness = 0.3 mm [3]. *Reproduced by the permission of The Electrochemical Society.*

Eqs. (8.38) and (8.39), i'_o, k'', and k_3 were calculated to be 7.2×10^{-6} A/cm^2, 4.1×10^{-4} mol/cm^3, and 1.1×10^{-6} mol/cm^2 s, respectively.

Substituting the experimentally measured value of $i_r = (i_c - j_\infty)$ and the calculated value of k_3 into Eq. (8.35), the hydrogen surface coverage can be estimated as a function of the overpotential.

8.2.6 Evaluation of rate constants for hydrogen absorption and diffusivity into metals

Bagotskaya [18], and later Frumkin [19], proposed a mechanism where hydrogen atoms directly enter a metal membrane without going through an intermediate adsorbed state. The proposed mechanism is:

$$H^+ + M + e^- \underset{k_{-1}}{\overset{k_1}{\rightleftarrows}} MH_{abs} \tag{8.41}$$

$$H^+ + M + e^- \xrightarrow{k_2} MH_{ads} \xrightarrow{k_3} \frac{1}{2}H_2 + M \tag{8.42}$$

where k_1, k_{-1}, k_2, and k_3 are rate constants. The direct atom mechanism was analyzed by Zheng *et al.* [16]. The developed expression, Eq. (8.43), indicates hydrogen permeation current density, j_∞, is independent of metal membrane thickness and is directly proportional to cathodic current density only when i_c is small.

$$j_\infty = i_c^{\,c}\frac{Fk_1 e^{-(\alpha_2-\alpha_1)a\eta}}{i^o} \tag{8.43}$$

In Eq. (8.43), α_1 and α_2 are transfer coefficients for reactions (8.41) and (8.42), i_c is the cathodic current density and $a = F/RT$. If $\alpha_1 = \alpha_2$, the hydrogen permeation current is directly proportional to the cathodic current. This expression is consistent with experiment [16] for atomic hydrogen permeation transients through a HY-130 steel membrane as a function of time for different applied potentials and other experimental data [20–27].

Ramasubramanian and Popov [28] developed a mathematical model for hydrogen permeation characterization into metals and alloys under corroding conditions. The model requires corrosion-rate knowledge for the given metal or alloy in various pH solutions. It provides quantitative recombination values and the rate constants for hydrogen discharge and adsorption. This model serves as diagnostic criteria for determining various metals and alloys as hydrogen permeation inhibitors' effectiveness and hydrogen entry inhibition efficiency. Abd Elhamid *et al.* [29,30] studied hydrogen absorption into iron (steel) membranes using the IPZ analysis of steady state hydrogen permeation rates obtained for different membrane thicknesses. Their analyses resulted in evaluation of hydrogen surface coverage, exchange current density, and HER rate constants. HER polarization data on metals with very low hydrogen permeability were used to calculate hydrogen surface coverage and rate constants for hydrogen discharge and recombination [30].

Zhang *et al.* [31] used constant concentration (CC), constant flux (CF), flux continuity (FC), and flux continuity-constant concentration (FCCC) hybrid boundary conditions to evaluate hydrogen diffusivity from permeation tests on commercial pure iron

samples with different thicknesses and surface treatments. The diffusivities estimated by the CF model were three times higher than the CC model. Diffusivities calculated with both CF and CC models were dependent on sample thickness and surface treatments. Hydrogen diffusion, trapping behavior, and solubility in nitrogen containing austenitic alloys were evaluated using electrochemical permeation and thermal desorption spectroscopy. Hydrogen diffusion decreased when nitrogen concentration is higher than 0.38 wt. % [32]. Hydrogen transport and embrittlement of 200S stainless steel was evaluated using hydrogen permeation [33]. Lattice diffusion in the ferritic phase caused higher permeation rates and diffusion. Brittle fracture and degradation was observed on hydrogen precharged for both ferritic and austenitic phases.

Hydrogen permeation and absorption in duplex stainless steel (austenitic and ferritic phases) were used to evaluate hydrogen diffusivity and diffusion paths in the ferrite phase. Absorbed hydrogen in the ferrite phase consists of hydrogen dissolved in the matrix as diffusible hydrogen. In the austenitic phase, hydrogen was reversibly trapped [34]. Hydrogen permeation and absorption in zirconium oxide scale was studied to evaluate hydrogen diffusivity. Hydrogen diffusivity increased as the precipitate area fraction increased. An inverse relationship was observed between the tetragonal phase amount and hydrogen diffusivity. Modeling data indicated that precipitates in the metallic state served as trapping sites. The tetragonal to monoclinic transition provided a fast transport route for hydrogen [35].

Akamatsu *et al.* [36] developed a dc-polarization technique for measuring hydrogen permeability through metals at high temperature based on limiting current measurements. The method is based on diffusion being the rate-limiting step for hydrogen permeation. The two-electrode electrochemical cell consists of a membrane as the working electrode and a palladium membrane as the counter electrode. The high-temperature molten salt electrolyte is a 1:1 ratio of KOH and NaOH. A standard gas mixture of Ar and H_2 is introduced from the working (anode) electrode. The hydrogen gas dissociates on the working electrode side and diffuses into the membrane. A constant potential is applied to the anode that oxidizes atomic hydrogen on the anode/molten electrolyte interface:

$$H + OH^- \rightarrow H_2O + e^- \tag{8.44}$$

The cathodic reaction that occurs on the molten salts/Pd counter electrode interface is:

$$H_2O + e^- \rightarrow H + OH^- \tag{8.45}$$

The current is measured for each applied potential under steady state conditions. The polarization measurements are performed at different potentials to obtain a current-potential curve. The measured current is a function of atomic hydrogen flux through the membrane, j_H:

$$I = FAj_H \tag{8.46}$$

A plateau (limiting current) is observed in the *I-E* curve. At this point, the permeation current is related to the thickness of the membrane according to Fick's law:

$$j_H = D_H \frac{\Delta C_H}{L} \tag{8.47}$$

where ΔC_H is the hydrogen concentration gradient in the sample. When the limiting current is reached, the concentration of hydrogen at the anode-electrolyte interface is close to zero, and

$$j_H = D_H \frac{C_H}{L} \tag{8.48}$$

According to Sievelts' law, the hydrogen concentration at the gas-membrane interface is defined as:

$$C_H = K P_{H_2}^{1/2} \tag{8.49}$$

where the hydrogen solubility is constant and P_{H_2} is the applied hydrogen partial pressure. The limiting current is expressed as:

$$I_L = \frac{FA}{L} D_H K P_{H_2}^{1/2} \tag{8.50}$$

The hydrogen permeability ($\Phi = D_H K$) is calculated using Eq. (8.51):

$$\Phi = I_L \frac{L}{FA} P_{H_2}^{-1/2} \tag{8.51}$$

The electrochemical cell used by Akamatsu *et al.* [36] to measure hydrogen permeability is shown in Fig. 8.10. A gas mixture of hydrogen and argon is introduced at the sample/gas interface. Polarization measurements are performed in the potential range between −100 and 600 mV, so the palladium cathode is not oxidized. Hydrogen partial pressures range from 0.10 to 20.5 kPa.

8.3 HYDROGEN-INDUCED DAMAGE

8.3.1 Hydrogen-induced cracking

HIC is a major problem in the gas and oil industries, causing severe equipment failure. It occurs in low-strength, low-carbon steels used in pipelines, reactors, and pressure vessels in contact with acidic hydrocarbons [37]. Hydrogen is evolved during processes such as electroplating, corrosion, and cathodic protection. Hydrogen-induced damage results in internal cracks caused by hydrogen recombination into gaseous molecules in bulk steel

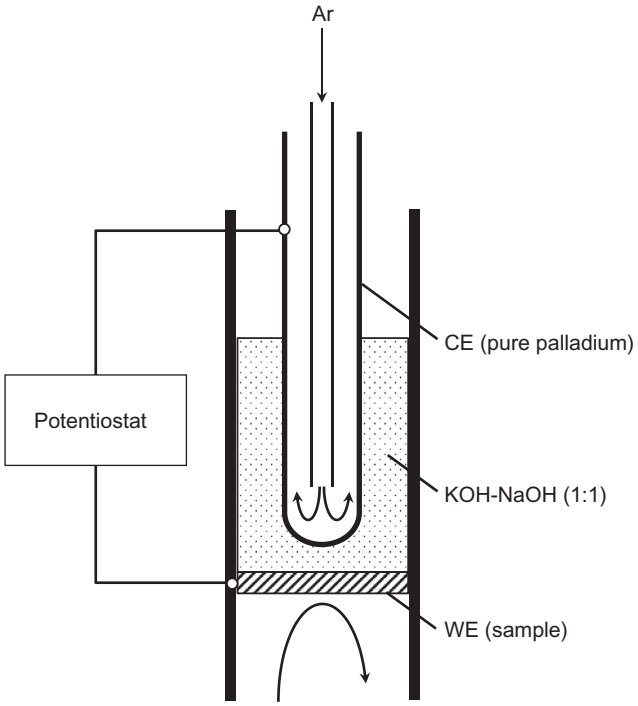

Fig. 8.10 Electrochemical cell for measuring the hydrogen permeability [36].

voids. It occurs without external stress and is strictly internal. Stress-sorption cracking mechanism has been suggested in the literature. According to this mechanism, cracking is caused by hydrogen adsorption at defects at the crack apex, resulting in metal atom surface energy reduction to a tensile force. HIC alloy resistance deceases as strength or defect density strength increases [38,39]. In general, steels with high defect density or hard matrixes are susceptible to HIC and brittle cracking. The critical minimum internal stress to trigger cracking decreases with increasing hydrogen concentration. However, baking carbon steel decreases hydrogen concentration in the alloy bulk, increasing minimum internal stress required for cracking [40,41]. HIC susceptibility is controlled by steel composition and process parameters. Alloy fabrication and nonmetallic inclusions increase the alloy's ability to absorb and trap hydrogen. HIC resistivity of an alloy is controlled by sulfur content and total sulfide inclusion length [42]. Al and Ca oxides in the alloy help initiate nucleation in HIC [43]. HIC is also reportedly controlled by alloy microstructure [44]. Acicular ferrite was a very effective microstructure for hydrogen trapping [45]. Alloying elements such as Cu (0.2%) increase HIC alloy resistance [46].

HIC has been enhanced through sulfur content reduction in alloys, uniform microstructure, and controlling inclusion morphology [47]. HIC is controlled by diffusible

hydrogen reversibly trapped in the bulk alloy voids. Steel susceptibility HIC increases with diffusible hydrogen content in the alloy, which increases with applied load in the elastic region [43,48]. Carpenter Technology developed AerMet 100 alloy [49] to replace 300 M steel. AerMet 100 is a low-C, Fe-Ni martensitic alloy that attains strength through precipitation of M_2C (M = Mo or Cr) [50,51]. AISI 4340 is another high-strength quenched-and-tempered steel that has been reviewed for similar applications [52–54]. However, HIC susceptibility increases with alloy strength [55,56].

8.3.2 Hydrogen embrittlement

Hydrogen embrittlement results from alloy exposure to hydrogen in processes such as welding, casting, pickling, or cathodic protection. Because hydrogen solubility in an alloy is higher in the liquid state than the solid state, hydrogen contamination begins in the early stages of metallurgical processing. Damage occurs when hydrogen accumulates in interstitial defects (hollow spaces) of the lattice. During electrochemical reactions, some evolved atomic hydrogen is adsorbed on the metallic surface, the extent of which depends on surface adsorption kinetics. Atomic level embrittlement occurs as low as 10 ppm due to hydrogen adsorbing in unstable crystalline lattice areas. In areas of high concentration, adsorbed hydrogen recombines to form molecular hydrogen, causing high localized pressures. Irreversible hydrogen accumulation within the metal lattice leads to the mechanical property deterioration. Steels lose ductility, resulting in hydrogen embrittlement [57]. Some adsorbed hydrogen diffuses into the crystalline substrate lattice where it reacts with metal atoms to form brittle metal hydrides, causing the structure to fail far below the yield strength. High-strength steels have the highest susceptibility to hydrogen embrittlement. Hydrogen susceptibility drastically increases with steel strength increase. The atomic hydrogen and metallic atomic structure interaction inhibits the ability to stretch under load, causing steel to become brittle. Hydrogen may also act as a grain boundary surfactant, creating microcracks within the steel due to surface film energy decrease at the grain boundaries. Cracking due to hydrogen embrittlement is caused by hydrogen evolution at the interface and increases with increasing cathodic current. Hydrogen embrittlement is different from stress corrosion cracking (SCC), which only occurs under applied anodic current.

8.3.3 Hydrogen blistering

The pressure exerted by molecular hydrogen and atomic hydrogen in most cases is high enough to cause blisters and ultimately failure. In the carbon steel wall of a reactor, blistering can cause local deformation and wall failure. Carbon removal from steel at high temperatures (decarburization) decreases steel tensile strength, increasing hydrogen-induced damage susceptibility. Hydrogen blistering occurs when the reactor

interior is exposed to an acid electrolyte while the exterior is in contact with air. The acid and interior wall produces molecular and atomic hydrogen. Adsorbed hydrogen diffuses into the alloy crystalline lattice where it combines to form defects (voids). Because hydrogen molecules cannot diffuse, the concentration increases with time, increasing the pressure. Molecular hydrogen pressure in equilibrium with atomic hydrogen may increase to several hundred thousand atmospheres, causing a reactor wall rupture or structure failure. Several high-strength iron and nickel-based alloys are less susceptible to hydrogen blistering and have been developed specifically for such applications.

8.3.4 Hydrogen stress cracking

HSC, also named sulfide stress cracking (SSC), occurs in the presence of hydrogen sulfide. This cracking failure requires applied stress because it initiates from the steel surface [58,59]. According to the NACE task group, SSC is divided into type I SSC, called stress-oriented hydrogen-induced cracking (SOHIC) due to hydrogen-induced blister cracks (HIBCs) parallel to applied stress [60], and type II SSC, typical hydrogen embrittlement [61].According to Takahashi and Ogawa [62], hydrogen-induced failure in type I SSC occurs in two steps. In the first step, HIBC forms parallel to applied stress. In the second step, the blister crack connects perpendicular the applied stress as in type II SSC.

8.3.5 Recent studies on hydrogen-induced damage

HIC does not require stress to occur, while HIBC in type I SSC requires applied stress and starts at the surface. Both HIC and HIBC are explained by internal pressure theory [63] and propagate after crack nucleation in the rolling direction. The relationship between HIC and type I sulfide stress high-strength line pipe steel cracking was studied using cathodic charging. HIC was found as an initial crack type I SSC or HIBC [64]. SSC severity regions as a function of environmental severity depends on hydrogen sulfide partial pressure and pH at the interface. In Fig. 8.11, SCC increases from region 0, where SSC is least severe, to region 3, where SSC is most severe [65].

A comparative assessment of pipeline steel electrochemical hydrogen absorption with different strength indicated that hydrogen absorption resistance decreases with decreasing steel strength [66]. Mendibide and Sourmail [67] investigated commercial steel SSC resistance effect when alloyed with Nb, Cr, V, and Cu. Ascowell C steel grade microalloyed with Nb is more SSC resistant than standard grades (Fig. 8.12). Hydrogen permeation studies indicated that Nb addition decreases hydrogen charging in acidic media. Copper content increase increases alloy resistance to SSC at pH 2.7 and 5.

To evaluate the hydrogen trapping ability of API X65 line pipe steels, hydrogen permeability and apparent diffusivity was measured in their various microstructures

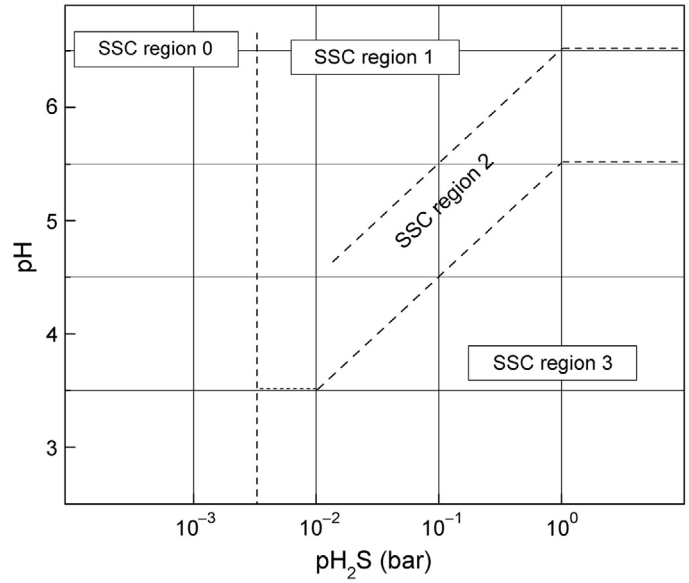

Fig. 8.11 SSC regions of corrosion severity according to ISO 15156-20 [65]. © *NACE International 2003*.

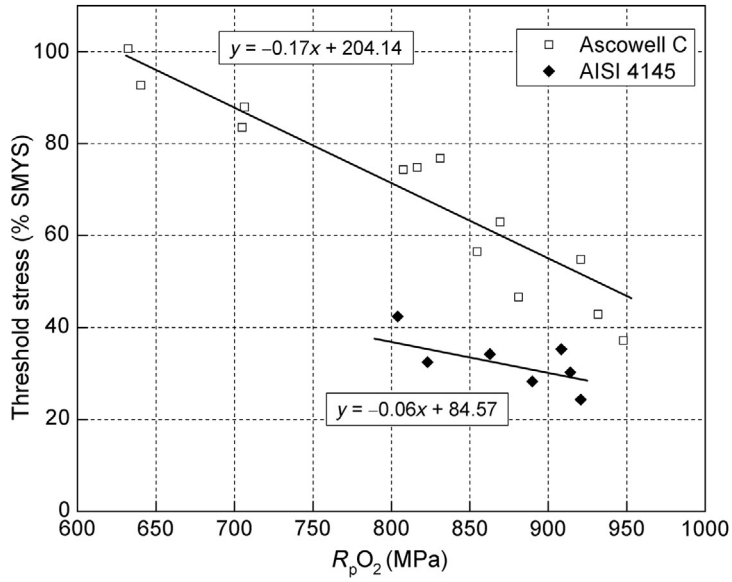

Fig. 8.12 Evaluation of the threshold stress for SSC vs. the actual yield stress for the industrial grades AISI 4145 and Ascowell C [67].

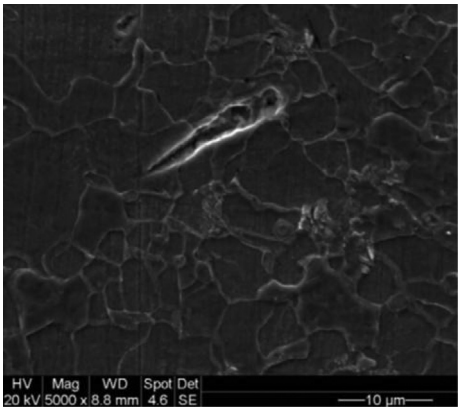

Fig. 8.13 A transgranular crack induced by hydrogen in the steel [69].

constituents such as ferrite/degenerated pearlite (F/DP), ferrite/acicular ferrite (F/AF), and ferrite/bainite (F/B). DP, AF, BF and martensite/austenite (M/A) constituents affected hydrogen trapping efficiency and apparent diffusivity. Hydrogen trapping efficiency increased in the order DP, BF, and AF. Steel F/AF or F/B microstructures initiated HIC at the local M/A region [68].

X80 pipeline steel microstructure consisted of a polygonal ferrite and bainitic ferrite matrix with martensite/austenite (M/A) constituents distributed along grain boundaries (Fig. 8.13). The alloy inclusions are Si, Al oxide, Si-ferric carbide, and Al-Mg-Ca-O mixture. Hydrogen cracks are initiated even in the absence of external stress. Cracks are initiated in the presence of Si and Al oxide-enriched inclusions [69].

HIC of commercial pure titanium (Ti) was investigated as a function of applied stress and test temperature in sulfuric and hydrochloric acids using a constant-load method. HIC nature is hydrogen embrittlement (HE) related to titanium hydride fracture [70]. Immersion testing and hydrogen permeation measurements were used to evaluate HIC in line pipe steel [41]. HIC extent at constant pH and hydrogen sulfide partial pressure $\left(p_{H_2S}\right)$ depended on exposure time until a stable level was reached. The time to reach stability depended on pH and hydrogen sulfide partial pressure. Permeation experiments confirmed that HIC is controlled by hydrogen concentration at the steel surface. HIC resistance of pipeline steels increases when strong {1 1 1} ND fiber textures are produced by warm-rolling schedules [71]. Cathodic charging initiated hydrogen blistering and HIC in Ni-P coatings. Hydrogen blister nucleation is facilitated by hydrogen atom diffusion. As hydrogen pressure increases, shear bands appeared on the hydrogen blister surface, initiating HIC propagating along the blister wall as shown in Figs. 8.14 and 8.15 [72].

The embrittlement properties of 2205 duplex stainless steels with two different grain sizes were investigated by slow strain-rate testing by applying cathodic potentials in

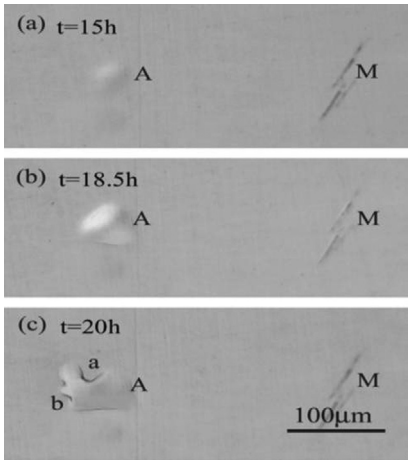

Fig. 8.14 Hydrogen blister (a and b) imitating from the wall of the blister during charging at $i = 50$ mA/cm^2 and (c) cracks [72].

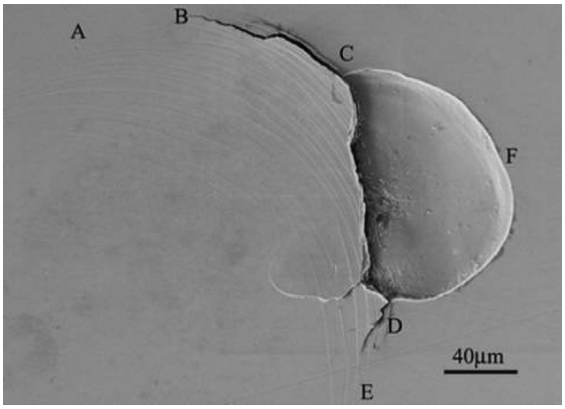

Fig. 8.15 Hydrogen-induced cracking initiate along the wall of a hydrogen blister ABCD [72].

26 wt.% NaCl (pH = 2) electrolyte. Permeation rate and effective hydrogen diffusivity were evaluated using electrochemical permeation [73]. The susceptibility of duplex stainless steel to HIC increases with increasing grain size and precharging time, as shown in Fig. 8.16 [74]. After cathodic charging in H_2SO_4 solution, transgranular and intergranular microcracks were observed in X70 pipeline steel. Cracks appear at the polygonal ferrite grain boundary, as evidenced in Fig. 8.17. It has been demonstrated that heating can heal the cracks [74].

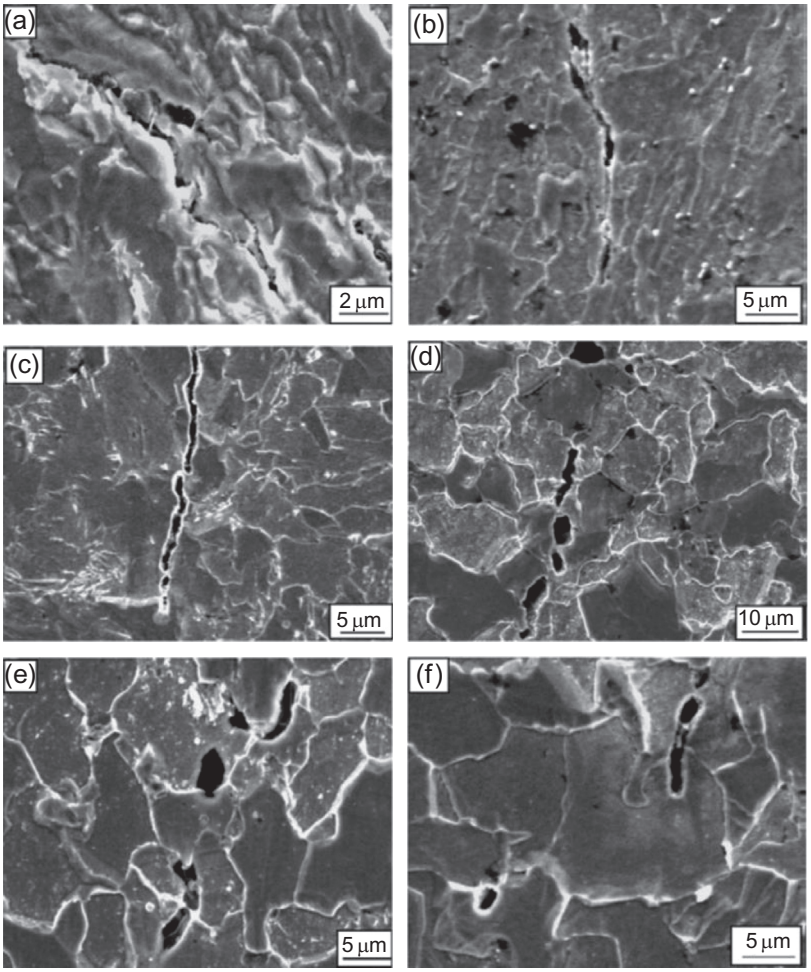

Fig. 8.16 The morphology of cracks (a) cracks induced by hydrogen charging for 1 h at the current density of 200 mA/cm^2; (b) specimens heat treated at 600 °C for 10 h; (c) specimens heat treated at 800 °C for 10 h; (d) specimens heat treated at 1000 °C for 6 h; (e) specimens heat treated at 1000 °C for 10 h; (f) specimens cyclic heat treated at 1000 °C for 10 h [74].

8.4 PREVENTING HYDROGEN DAMAGE IN METALS

Various methods have been proposed in the literature to decrease HIC [75–78]. These methods include post-heat treatment, alloying, laser surface modification, and shot preening. Baking is an efficient method to decrease hydrogen embrittlement. These methods do not reduce hydrogen entry below the cracking hazard threshold level. On the other hand, coating the hard alloy with a suitable metal/alloy can successfully reduce the hydrogen ingress [79]. The coatings can be metallic or consist of metallic

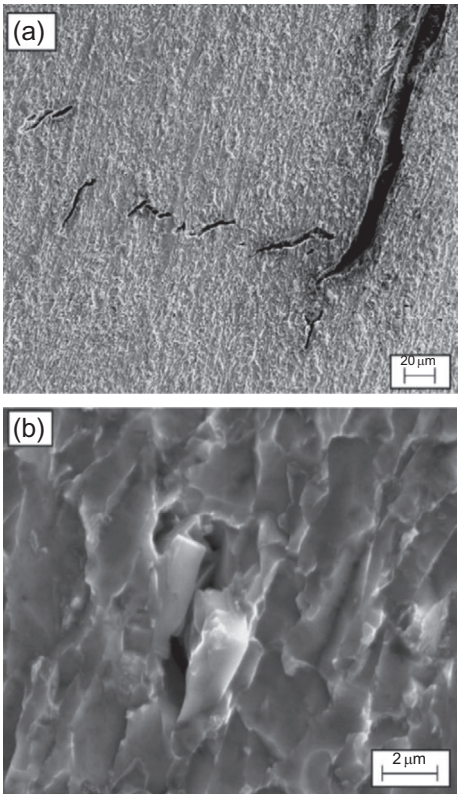

Fig. 8.17 (a) Intergranular and transgranular microcracks (b) a microcrack in and around. No inclusions can be found [74].

particles bonded in an inorganic matrix, often phosphates and/or chromates. The coating should provide sacrificial protection if the substrate is exposed to corrosion environment. Methods suggested by Popov and coworkers [3,19,28,80–94] for hydrogen permeation reduction include underpotential deposition of metals and the electrochemical deposition of metals, alloys (such as Zn-Ni), or resistive coatings on the surface. Deposited alloys or coatings reduce hydrogen embrittlement by acting as a barrier film for hydrogen entry by changing the hydrogen evolution kinetics at the surface. Deposition of thin Zn, Ni, Sn, and Cd layers have been shown to reduce the amount of hydrogen permeation into iron. Zn-Ni alloys, which are widely used as corrosion protective coatings on steel, are also studied as hydrogen permeation inhibitors. Additionally, experiments have been carried out to determine the suitability of using Zn-Ni alloys as inhibitive layers for hydrogen permeation on steel. They showed that Zn-Ni alloys impart desirable qualities in a hydrogen permeation inhibitor, such as a low adsorption-absorption constant, which suggests a high recombination rate. The two main issues to be considered in choosing

a coating are coating damage and subsequent local hydrogen uptake on exposed steel and slow corrosion of the coating (with or without local damage) leading to some hydrogen generation by water reduction and subsequent hydrogen permeation. Based on this, the optimal coating has low corrosion rates and prevents hydrogen evolution on the surface. In the presence of monolayer coverage of Pb on a membrane surface made of AISI 4340 steel, the hydrogen evolution currents were reduced twofold compared to bare steel, and steady state hydrogen permeation flux through the steel membranes was reduced by 71% [3]. Figure 8.18 shows hydrogen permeation transients through an AISI 4340 steel membrane at $E = -0.6$ V vs. SCE in the absence and presence of underpotential deposited lead. $C_{Pb^{2+}} = 2 \times 10^{-3}$ M, membrane thickness = 0.45 mm [3].

Polarization experiments and a potentiostatic pulse technique show that monolayer zinc coverage effectively mitigates hydrogen absorption into Monel K500. Both hydrogen evolution rate and hydrogen ingress flux were reduced by 60% [80]. A Zn monolayer on HY-130 steel reduced hydrogen evolution current by 58% compared with bare HY-130 steel [82]. Observed effects are explained by the suppression of hydrogen absorption by the deposited monolayers and the kinetic limitations for the hydrogen discharge reaction. A mass transfer term was introduced into the permeation model to help interpret experimental data. Hydrogen entry rate constant and entry efficiency are reduced by 74% and a factor of three, respectively, by zinc monolayers. A monolayer of lead [83] effectively inhibited the HER and hydrogen penetration through type 718 (UNS N07718)

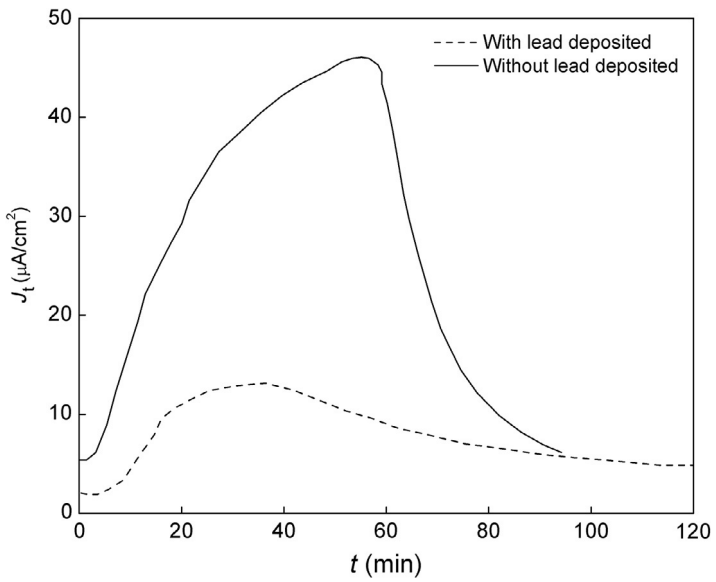

Fig. 8.18 Hydrogen permeation transients through an AISI 4340 steel membrane at $E = -0.6$ V vs. SCE in the absence and presence of underpotential deposited lead. $C_{Pb^{2+}} = 2 \times 10^{-3}$ M, membrane thickness = 0.45 mm [3]. *Reproduced by the permission of The Electrochemical Society.*

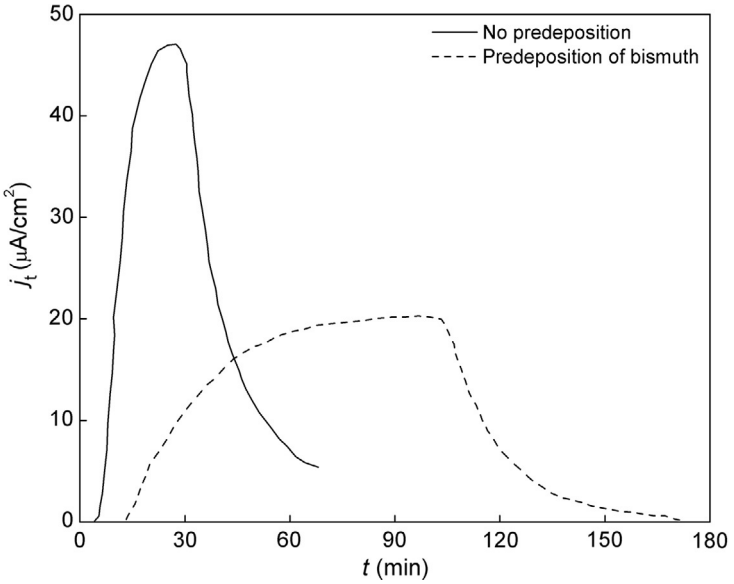

Fig. 8.19 Hydrogen permeation transients through type 4340 steel membrane at $E_c = -0.60$ V vs. SCE in the presence and absence of bismuth on the substrate ($L = 0.45$ mm) [85]. © *NACE International 1995*.

alloy. Polarization and permeation experiments showed that a thin layer of electroplated bismuth (1-2 μm thick) inhibited the evolution and penetration of hydrogen through nickel-chromium alloy 718 (UNS N07718) and type 4340 (UNS G43400) steel [85]. The HERs on alloy 718 and type 4340 steel were inhibited by 28% and 85%, respectively. Hydrogen permeation rates through these alloys were reduced by 76% and 65%, respectively (Fig. 8.19).

The Devanathan-Stachurski permeation technique was used to investigate hydrogen permeation through an iron membrane with consecutively electroplated zinc layers [86]. Hydrogen evolution rates and permeation rates were followed as functions of time at different applied potentials. Zinc layers were deposited using the same constituents as the cathodic solution (i.e., 1.0 M H_3BO_3, 1.0 M Na_2SO_4, and 0.4 M NaCl) with the addition of 0.05 M $ZnSO_4$. Each layer was deposited galvanostatically at 1 mA for 10, 20, or 40 s. Assuming 100% current efficiency, this corresponds to ~0.03 μm for each 40 s of plating time. Plating times shown are cumulative plating times. Cathodic current and permeation current measurements at different applied cathodic potentials, E, were performed on bare iron and after each zinc layer was plated. Hydrogen evolution and permeation decreased with each successive zinc layer until reaching an average decrease of 93% and 96%, respectively, compared with bare iron. Table 8.1 summarizes the average percent decrease in i_c and j_∞ with zinc layers vs. bare iron. The reduction in the

Table 8.1 Average Percent Decrease in i_c and j_∞ with Zinc Layers vs. Bare Iron

Plating Time (s)	20	40	60	80	100	120	160
i_c (%)	86	90	92	93	92	93	93
j_∞ (%)	61	82	91	93	95	96	96

permeation rate of hydrogen through the iron membrane was due to a decrease in the hydrogen discharge rate and the suppression of hydrogen absorption and adsorption on the deposited zinc layers.

The effectiveness of 5-(4-pyridyl)-2,7-nonadiene, and 1 phenyl-2-propyn-ol (PP) on inhibiting the HER on a 1010 steel membrane and on the degree of hydrogen ingress into the membrane was determined to be in the range of 98% and 95%, respectively [87,88]. The inhibition of hydrogen permeation by Zn-Ni electrodeposited alloy was investigated using the Devanathan-Stachurski permeation technique [89]. Hydrogen evolution rates and hydrogen permeation rates were followed as functions of time at different applied potentials. Zinc-nickel alloy electroplates showed hydrogen discharge kinetics substantially different from Zn or Ni electroplates. For thin Zn-Ni electroplates with negligible diffusion resistance compared to the substrate, the permeation inhibition was ~80%, while the average cathodic current inhibition was only 19%. Zn-Ni electroplated for 20 and 40 min at 10 mA/cm^2 inhibited hydrogen permeation more than 95% compared to bare iron. For thicker electroplates, inhibition was due to kinetics and barrier effects caused by membrane diffusion resistance.

Electrodeposited Zn-Ni-Cd alloy coating produced in a sulfate electrolyte inhibits hydrogen discharge on carbon steel [90]. Newly developed ternary alloys have approximately ten times higher corrosion resistance than the Zn-Ni alloy. Hydrogen permeation characteristics of Zn-Ni-Cd alloy coatings were also studied and compared with bare and Zn-Ni alloy coated steel. The transfer coefficient, α, exchange current density, i^o, thickness-dependent adsorption-absorption rate constant, k'', recombination rate constant, k_3, and surface hydrogen coverage, θ_H, were obtained by fitting the mathematical model to experimental results. Alloys obtained from baths containing $CdSO_4$ at concentrations higher than 3 g/L in the sulfate plating bath had superior permeation inhibition properties compared to Zn-Ni alloy coating and bare steel. The hydrogen permeation current was zero under normal corroding conditions for Zn-Ni-Cd alloy and increased to 0.3 μA/cm^2 at a cathodic overpotential of 250 mV. The hydrogen permeation current density for steel and Zn-Ni alloy under similar conditions were 62.1 and 1.3 μA/cm^2, respectively. Figure 8.20 compares cathodic and permeation current densities for different alloys [90].

Hydrogen permeation characteristics of a new Zn-Ni-P alloy were studied and compared with a Zn-Ni alloy [91,92,94]. The Zn-Ni-P alloy was deposited from an acid sulfate bath containing 0.5 M $NiSO_4$, 0.2 M $ZnSO_4$, 0.5 M Na_2SO_4, and

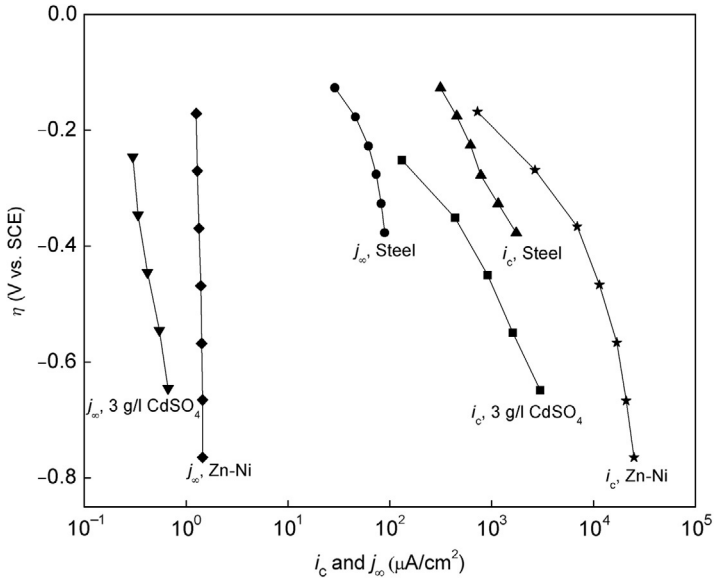

Fig. 8.20 Comparison of cathodic and permeation current densities for Zn-Ni-Cd, Zn-Ni, and steel [90]. *Reprinted by permission of The Electrochemical Society.*

100 g/L NaH_2PO_2 at pH 3. The permeation characteristics of the alloy were studied and compared qualitatively with Zn-Ni alloy under cathodically polarized and corroding conditions. The Zn-Ni-P alloy had better permeation inhibition characteristics in terms of efficiency. The IPZ model (Section 8.2.4) was used to quantitatively estimate various kinetic parameters associated with hydrogen permeation for the Zn-Ni-P alloy under polarized conditions. The Zn-Ni-P alloy had superior permeation inhibition properties compared to the Zn-Ni alloy (Fig. 8.21) [91].

Corrosion and hydrogen permeation characteristics of Zn-Ni-Cd alloy coatings electrodeposited from an alkaline bath were studied and compared with Cd and Zn-Ni coatings obtained using commercial baths [93]. Zn-Ni-Cd alloy was electroplated from an alkaline sulfate bath under potentiostatic conditions. The corrosion potential of this Zn-Ni-Cd coating was −0.62 V vs. SCE, still negative compared to iron. The corrosion rate of Zn-Ni-Cd coated steel was 0.073 mm/year estimated in a 0.5 M Na_2SO_4 + 0.5 M H_3BO_3 solution at pH 7. This is much lower than Zn-Ni alloy (0.502 mm/year) and Cd (0.306 mm/year) coatings deposited from commercial baths. Zn-Ni-Cd alloys also demonstrated superior hydrogen permeation inhibition properties compared to Cd and Zn-Ni coatings.

Effective diffusivity, permeation rate, and apparent solubility of hydrogen in a series of Fe-Al binary alloys at 25 °C were studied by Luu *et al.* [95] using electrochemical hydrogen permeation measurements. Both hydrogen diffusivity and permeation rate in these

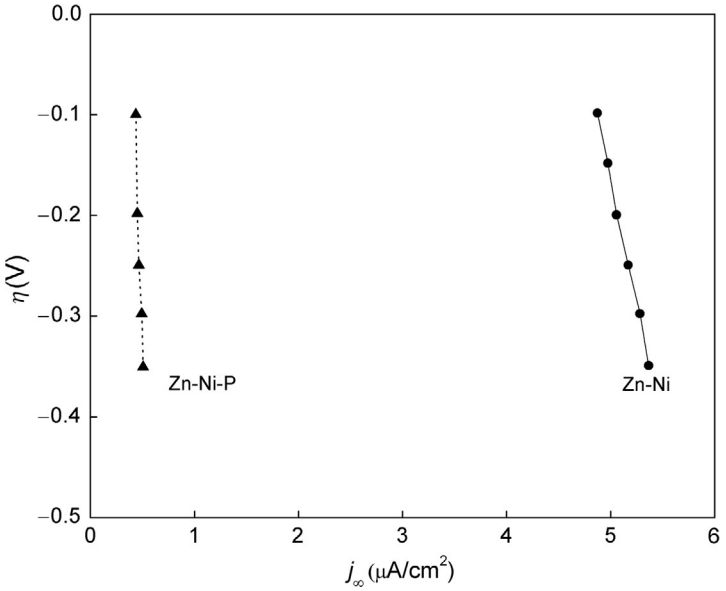

Fig. 8.21 Permeation current density as a function of applied overpotential for Zn-Ni and Zn-Ni-P alloys [91]. © *NACE International 2000.*

alloys drastically decreased when Al content in the alloy was higher than 15–20 wt.%. The observed hydrogen transport retardation factor in Fe-Al alloys is due to structural order and aluminum oxide layer presence.

Adding carbon to a Fe_3Al aluminum alloy was studied using electrochemical permeation technique [96]. The addition of 1 wt.% carbon to Fe-16 wt.% causes a perovskite $Fe_3AlC_{0.5}$ carbide phase to precipitate in the Fe_3Al-based matrix, resulting in a 50% hydrogen permeability and diffusivity decrease.

Electrochemical techniques were used to study hydrogen permeation caused by MCM 430 high-strength steel corrosion under wet-dry SO_2 cycles. Hydrogen permeation in multiphase alloys of ternary Ni-Ti-Nb was investigated in the range of 523–673 K [97]. Hydrogen embrittlement made it impossible to measure hydrogen permeation through the as-cast alloys with Ti and Ni of 20 mol%. Hydrogen permeability of the ductile B_2-NiTi phase was estimated to be 10^{-10} mol H_2 m^{-1} s^{-1} Pa$^{-0.5}$ and increased when alloyed with Nb. Similar results were obtained for the $Ni_{30}Ti_{31}Nb_{39}$ alloy. Results indicated that the eutectic phases played a major role in preventing NbTi-phase hydrogen brittleness of the NbTi phase. Cheng [98] analyzed electrochemical permeation through X-65 pipeline steel and its applications on pipeline SSC. Hydrogen permeation current through X-65 steel was tested in electrolytes simulating soil conditions that trigger near-neutral pH SCC in pipelines. Hydrogen permeation transients were analyzed using the constant concentration model. It was found that AQDS,

a chemical that stimulates the organic compound in the soil, was found to inhibit hydrogen permeation by decreasing subsurface hydrogen concentration. In the presence of sulfide, subsurface hydrogen concentration increases and promotes hydrogen permeation by inhibiting hydrogen recombination. SCC in pipeline steel in soil solutions containing high subsurface hydrogen concentration indicate hydrogen is involved in near-neutral pH SCC. Hydrogen promotes steel cracking and subsequent anodic dissolution on crack sides. Thin Al-Cr-O films have been proposed as hydrogen permeation barriers for reduced activation on ferritic martensitic steel EUROFER 97 [99]. The films are deposited by pulsed arc evaporation in a batch-type production system at substrate temperatures of 550 °C. Gas permeation experiments indicated that layers having a thickness of a few microns are capable of suppressing hydrogen permeability by a factor of 2000 to 3500 at 700 °C. The observed results are attributed to excellent efficiency of the dense layer morphology formed on the alloy surface and the possible (pre)-formation of solid solutions in a corundum-type structure.

Kanezaki *et al.* [100] studied the effect of hydrogen on stainless steel fatigue crack growth properties. The investigation evaluated microscopic fatigue mechanisms, martensitic transformation, and hydrogen content. The hydrogen-charged SUS304 and SUS316 showed accelerated fatigue growth rate compared to crack growth rates in uncharged specimens. Crack growth rate in the hydrogen-charged SUS316L was slightly higher than the uncharged SUS316L. In hydrogen-charged and uncharged specimens SUS304, SUS316, and SUS316L, martensitic transformation was detected on the fatigue fracture using X-ray diffraction. An increase in martensitic transformation also showed increased fatigue crack growth acceleration due to hydrogen. Martensitic transformation increases local hydrogen diffusion in the vicinity of fatigue cracks, which contributes to crack growth rate.

Hydrogen permeation and electrochemical corrosion behavior of the X80 pipeline steel weld was investigated with optical scanning electron microscopy and electrochemical permeation techniques. The smallest hydrogen permeation rate and largest hydrogen trapping density were observed at the heat-affected zone. The base steel was found to have the lowest hydrogen trapping [101].

EXERCISES

E8.1. Values of the hydrogen cathodic current density, i_c, and steady state hydrogen permeation current, j_∞, as a function of the overpotential, η, measured using the Devanathan-Stachurski technique are given in Table E8.1.

Using the IPZ mechanistic model [13,14], calculate:

(a) The hydrogen diffusivity (D, cm^2/s) in AISI 4340 steel.

(b) The modified exchange current density ($i_o^{'}$, A/cm^2).

Table E8.1 Kinetic Data for Hydrogen Evolution and Hydrogen Permeation in AISI 4340 Steel

η (mV)	i_c (μA/cm^2)	j_∞ (μA/cm^2)
−248	894	22.5
−276	1491	27.5
−300	2360	34.5
−326	3727	43.5
−356	6708	53.7

List of parameters:

Membrane thickness (L) = 0.01 cm
Temperature (T) = 293 K
Faraday constant (F) = 96,484 C/mol
Gas constant (R) = 8.314 J/(mol K)
Transfer coefficient (α) = 0.5
Half-rise time ($t_{1/2}$) = 52.43 s

E8.2. Using the IPZ model and measured values of hydrogen cathodic current density, i_c, and steady state hydrogen permeation current, j_∞, as a function of the overpotential, η, given in Table E8.1, calculate:

(a) The thickness-dependent absorption-adsorption rate constant, (k'', mol/cm^3).
(b) The recombination rate constant, (k_3, mol/cm^2 s).

List of parameters:

Membrane thickness (L) = 0.01 cm
Temperature (T) = 293 K
Faraday constant (F) = 96,484 C/mol
Gas constant (R) = 8.314 J/(mol K)

$$D = 2.67 \times 10^{-7}\,\text{cm}^2/\text{s}$$

$$b = L/FD$$

Transfer coefficient (α) = 0.5
Half-rise time ($t_{1/2}$) = 52.43 s

E8.3. Using the IPZ model and measured values of hydrogen cathodic current density, i_c, and steady state hydrogen permeation current, j_∞, as a function of the overpotential, η, given in Table E8.1, calculate the hydrogen surface coverage, (θ_H).

List of parameters:

Membrane thickness (L) = 0.01 cm
Temperature (T) = 293 K

Faraday constant (F) = 96,484 C/mol
Gas constant (R) = 8.314 J/(mol K)
Transfer coefficient (α) = 0.5
Half-rise time ($t_{1/2}$) = 52.43 s

E8.4. The hydrogen kinetic parameters were calculated by fitting the experimental data to the IPZ model. The results for samples A and B are presented in Table E8.2.

Table E8.2 Kinetic Data for Hydrogen Evolution and Hydrogen Permeation for Samples A and B

Sample	i_o' (A/cm^2)	k'' (mol/cm^3)	k_3 (mol/s cm^2)
A	9.17×10^{-7}	1.11×10^{-6}	7.38×10^{-6}
B	6.30×10^{-5}	2.10×10^{-5}	5.73×10^{-6}

Predict which sample shows better resistance to hydrogen permeation.

E8.5. Use the hydrogen atom direct mechanism [18,19] discussed in Ref. [16] to explain why the steady state hydrogen permeation current density, j_∞, is directly proportional to the cathodic current density, i_c, and is independent of the membrane thickness when the cathodic current density is small.

E8.6. The resistance to hydrogen permeation in Cd deposited on steel was evaluated by using the Devanathan-Stachurski technique. The hydrogen evolution current, i_c, and the permeation current, j_∞, were measured as a function of overpotential and are listed in Table E8.3.

Table E8.3 Data for Hydrogen Evolution and Hydrogen Permeation for Cd Deposited on Steel

η (mV)	i_c (μA/cm^2)	j_∞ (μA/cm^2)
−300	6.6	2.20
−400	51.0	4.83
−450	133.3	6.50
−500	317.6	8.0
−550	666.6	9.03

Determine the applicability of the IPZ model to this data.

E8.7. Using the Frumkin-Temkin (F-T) corrections to the IPZ model in exercise E8.6, calculate:

(a) The HER coverage-dependent transfer coefficient, α.
(b) The modified exchange current density, i_o' (A/cm^2).
(c) The thickness-dependent absorption-adsorption rate constant, k'' (mol/cm^3).
(d) The recombination rate constant, k_3 (mol/cm^2 s).

Use the following parameters:

Membrane thickness (L) = 0.01 cm
Temperature (T) = 293 K
Faraday constant (F) = 96,484 C/mol
Gas constant (R) = 8.314 J/(mol K)

$b = L/FD$

Diffusion coefficient (D) = 2.67×10^{-7} cm^2/s
f = 4.5

E8.8. Plot the hydrogen surface coverage for Cd deposited on steel as a function of overpotential. Use the data for permeation current and hydrogen evolution current as a function of overpotential listed in Table E8.3. The hydrogen surface coverage for Cd deposited steel was calculated using Eq. (E8.5) [81].

$$\theta_s = \frac{\left[k_{ads} + \left(\frac{D}{L}\right)\right]}{k_{abs}} C_s = \frac{C_s}{k''} = \frac{bj_\infty}{k''} \tag{E8.5}$$

where $b = L/FD$, membrane thickness (L) = 0.01 cm, temperature (T) = 293 K, Faraday constant (F) = 96,485 C/mol, gas constant (R) = 8.314 J/(mol K), diffusion coefficient (D) = 2.67×10^{-7} cm^2/s. Thickness-dependent absorption-adsorption constant, k'', calculated in Problem E8.5 = 7.32×10^{-6} mol/cm^3.

REFERENCES

[1] J.O.M. Bockris, A.K.N. Reddy, Modern Electrochemistry, Plenum Press, New York, 1970.
[2] J.O.M. Bockris, S. Subramanyan, The equivalent pressure of molecular hydrogen in cavities within metals in terms of the overpotential developed during the evolution of hydrogen, Electrochim. Acta 16 (1971) 2169–2179.
[3] G. Zheng, B.N. Popov, R.E. White, Surface treatment for mitigation of hydrogen absorption and penetration into AISI 4340 steel, J. Electrochem. Soc. 140 (1993) 3153–3198.
[4] L.I. Antropov, Theoretical Electrochemistry, Mir Publishers, Moscow, 1972, Translated from the Russian by Artavaz Beknazarov.
[5] M.A.V. Devanathan, L. Stachurski, The adsorption and diffusion of electrolytic hydrogen in palladium, Proc. Royal Soc. 270 (1962) 90–102.
[6] M.A.V. Devanathan, L. Stachurski, Mechanism of hydrogen evolution on iron in acid solutions by permeation rates, J. Electrochem. Soc. 111 (1964) 619–623.
[7] C. Kato, H.J. Grabke, B. Egert, G. Pranzer, Electrochemical and surface analytical studies on hydrogen permeation with Fe-Cu alloys in sulfuric acid with and without H_2S, Corros. Sci. 24 (1984) 591–611.
[8] N. Boes, H. Zuechner, Study of the solubility behavior of hydrogen in vanadium, niobium and tantalum using an electrochemical method, Ber. Bunsenges. Phys. Chem. 80 (1976) 22–27.
[9] B.S. Chaudary, T.T. Radhakrishhan, Boundary conditions during the electropermeation of hydrogen through pure iron, Corros. Sci. 30 (1990) 1219–1234.
[10] E. Wu, A mathematical treatment of the electrochemical method of hydrogen permeation and its application in hydrogen traps and embrittlement, J. Electrochem. Soc. 134 (1987) 2126–2133.

[11] M.A.V. Devanathan, Z. Stachurski, W. Beck, A technique for the evaluation of hydrogen embrittlement characteristics of electroplating baths, J. Electrochem. Soc. 111 (1963) 886–890.
[12] N. Boes, H. Zuechner, Electrochemical methods for studying diffusion permeation and solubility of hydrogen in metals, J. Less Common Met. 223 (1976) 24–49.
[13] R.N. Iyer, H.V. Pickering, M. Zamanzadeh, Analysis of hydrogen evolution and entry into metals for the discharge-recombination process, J. Electrochem. Soc. 136 (1989) 2463–2470.
[14] R.N. Iyer, H.V. Pickering, Mechanism and kinetics of electrochemical hydrogen entry and degradation of metallic systems, Annu. Rev. Mater. Sci. 20 (1990) 299–338.
[15] S. Chatterjee, B.G. Ateya, H.W. Pickering, Effect of electrodeposited metals on the permeation of hydrogen through iron membranes, Metall. Trans. A 9 (1978) 389–395.
[16] G. Zheng, B.N. Popov, R.E. White, Hydrogen atom direct entry mechanism into a metal membrane, J. Electrochem. Soc. 142 (1995) 154–156.
[17] P.K. Subramanyan, Electrochemical aspects of hydrogen in metals, in: in: J.O.M. Bockris, B. E. Conway, E.A. Yeager, R.E. White (Eds.), Comprehensive Treatise of Electrochemistry, vol. IV, Plenum Press, New York, 1981, pp. 411–462.
[18] I.A. Bagotskaya, Effect of composition of a solution on the rate of diffusion of electrolytic hydrogen through a metallic membrane. I. Diffusion of hydrogen through an iron membrane, Zhurn. Fiz. Khim. 36 (1962) 2667–2673.
[19] A.N. Frumkin, in: P. Delahay (Ed.), in: Advances in Electrochemistry and Electrochemical Engineering, vol. III, Interscience Publishers, New York, 1963, p. 287.
[20] J.G. Early, Hydrogen diffusion in palladium by galvanostatic charging, Acta Metall. 26 (1978) 1215–1223.
[21] H.R. Heath, An experimental investigation of the diffusion of electrolytic hydrogen through metals, Br. J. Appl. Phys. 3 (1952) 13–18.
[22] W. Raczynski, Hydrogen diffusion through iron sheets at 20-90°, Arch. Hutnictwa 3 (1958) 59–78.
[23] T. Zakroczymski, Z. Szklarska-Smialowks, M. Smialowski, Effect of arsenic on permeation of hydrogen through steel membranes polarized cathodically in aqueous solution, Werkst. Korros. 26 (1975) 17–24.
[24] A.F. Evseev, Mechanism of the penetration of hydrogen into iron cathodes from sulfuric acid solutions, Elektrokhimiya 6 (1970) 841–844.
[25] J.P. Hoare, S. Schuldiner, Mechanisms of hydrogen producing reactions on palladium: IV—electrochemical kinetics of the α-palladium-hydrogen system in acid solutions, J. Electrochem. Soc. 104 (1957) 564–568.
[26] S. Schuldiner, J.P. Hoare, Mechanisms of hydrogen producing reactions on palladium: II – diffusion of electrolytic hydrogen through palladium, J. Electrochem. Soc. 103 (1956) 178–181.
[27] J. Bowker, G.R. Piercy, The use of palladium to obtain reproducible boundary conditions for permeability measurements using galvanostatic charging, Metall. Trans. 6A (1985) 715–719.
[28] M. Ramasubramanian, B.N. Popov, R.E. White, Characterization of hydrogen permeation through zinc-nickel alloys under corroding conditions: mathematical model and experimental study, J. Electrochem. Soc. 145 (1998) 1907–1913.
[29] M.H. Abd Elhamid, B.G. Ateya, H.W. Pickering, Determination of the rate constants of hydrogen absorption into metals, J. Electrochem. Soc. 147 (2000) 2959–2963.
[30] M.H. Abd Elhamid, B.G. Ateya, K.G. Weil, H.W. Pickering, Calculation of the hydrogen surface coverage and rate constants of the hydrogen evolution reaction from polarization data, J. Electrochem. Soc. 147 (2000) 2148–2150.
[31] T.Y. Zhang, Y.P. Zheng, Q.Y. Wu, On the boundary conditions of electrochemical hydrogen permeation through iron, J. Electrochem. Soc. 146 (1999) 1741–1750.
[32] S. Ningshen, M. Uhlmann, F. Schneider, H.S. Khatak, Diffusion behaviour of hydrogen in nitrogen containing austenitic alloys, Corros. Sci. 43 (2001) 2255–2264.
[33] W.C. Luu, P.W. Liu, J.K. Wu, Hydrogen transport and degradation of a commercial duplex stainless steel, Corros. Sci. 44 (2002) 1783–1791.
[34] T. Zakroczymski, E. Owczarek, Electrochemical investigation of hydrogen absorption in a duplex stainless steel, Acta Mater. 50 (2002) 2701–2713.

[35] B.H. Lim, H.S. Hong, K.S. Lee, Measurements of hydrogen permeation and absorption in zirconium oxide scales, J. Nucl. Mater. 312 (2003) 134–140.
[36] T. Akamatsu, Y. Kume, K. Komiya, H. Yukawa, M. Morinaga, S. Yamaguchi, Electrochemical method for measuring hydrogen permeability through metals, J. Alloy Compd. 393 (2005) 302–306.
[37] M.T. Shehata, M. Elboujdain, W. Revie, Initiation of stress corrosion cracking and hydrogen induced cracking in oil and gas line-pipe steels, in: G. Pluvinage, M.H. Elwant (Eds.), Safety, Reliability and Risks Associated with Water, Oil and Gas Pipelines, Springer, The Netherlands, 2008, pp. 115–128.
[38] S. Jin, A. Atrens, ESCA—studies of the structure and composition of the passive film formed on stainless steels by various immersion times in 0.1 M NaCl solution, Appl. Phys. A 42 (1987) 149–165.
[39] A. Atrens, Z.F. Wang, Stress corrosion cracking, Mater. Forum 19 (1995) 9–34.
[40] T. Hara, H. Asahi, H. Ogawa, Conditions of hydrogen induced corrosion occurrence of X-65 grade line pipe steels in sour environments, Corrosion 60 (2004) 1113–1121.
[41] J. Kittel, V. Smanio, M. Fregonese, L. Garnier, X. Lefebvre, Hydrogen induced cracking testing of low alloy steel in sour environment: impact of time exposure on the extent of damage, Corros. Sci. 52 (2010) 1386–1392.
[42] G. Domizzi, G. Anteri, J.O. Garcia, Influence of sulphur content and inclusion distribution on the hydrogen induced blister cracking in pressure vessel and pipeline steels, Corros. Sci 43 (2001) 325–339.
[43] W.K. Kim, S.U. Koh, B.Y. Yang, K.Y. Kim, Effect of environmental and metallurgical factors on hydrogen induced cracking of HSLA steels, Corros. Sci. 50 (2008) 3336–3342.
[44] M. Elboujdaini, V.S. Sastri, J.R. Perumareddi, Studies on inhibition of hydrogen-induced cracking of linepipe steels, Corrosion 62 (2006) 29–34.
[45] G.T. Park, S.U. Koh, H.G. Jung, K.Y. Kim, Effect of microstructure on the hydrogen trapping efficiency and hydrogen induced cracking of linepipe steel, Corros. Sci. 2008 (50) (2008) 1865–1871.
[46] M.F. Galis, D. Petelot, International Conference on Interaction of Steel with Hydrogen in Petroleum Industry Pressure Vessel Service MPC, Paris, France, March 28, 1989, p. 109.
[47] M.A. Al-Anezi, S. Rao, Challenges in procurement of HIC resistant steels pipes, J. Failure Anal. Preven. 11 (2011) 385–392.
[48] U. Hadam, T. Zakroczymski, Absorption of hydrogen in tensile strained iron and high-carbon steel studied by electrochemical permeation and desorption techniques, Int. J. Hyd. Energy 34 (2009) 2449–2459.
[49] R.M. Hemphill, D.E. Wert, High strength, high fracture toughness structural alloy, US Patent 5 087 415, U.S. Patent and Trademark Office, Washington, DC.
[50] G.R. Speich, Absorption of hydrogen in tensile strained iron and high-carbon steel studied by electrochemical permeation and desorption techniques, Metall. Trans. 4 (1973) 303–315.
[51] P.M. Novotny, J.M. Dahl, AerMet 100 alloy for aerospace structural applications, in: Proceedings of the 32nd Mechanical Working and Steel Processing Conference, vol. 28, 1991, pp. 275–281.
[52] J.D. Gates, A. Atrens, I.O. Smith, Microstructure of as-quenched 3.5 NiCrMoV rotor steel. Part I. General structure and retained austenite, Z. Werkstoftech 18 (1987) 165–170.
[53] J.D. Gates, A. Atrens, I.O. Smith, Microstructure of as-quenched 3.5 NiCrMoV rotor steel. Part II. Double diffraction, Z. Werkstoftech 18 (1987) 179–185.
[54] J.D. Gates, A. Atrens, I.O. Smith, Microstructure of as-quenched 3.5 NiCrMoV rotor steel. Part III. Carbide precipitation, Z. Werkstoftech 18 (1987) 344–353.
[55] M.O. Speidel, in: M.O. Speidel, A. Atrens (Eds.), Corrosion in Power Generating Equipment, Plenum, New York, 1984, p. 85.
[56] R.M. Pedrazzoli, M.O. Speidel, in: S.M. Bruemmer, E.I. Meletis, R.H. Jones, W.W. Gerberich, F. P. Ford, R.W. Staehle (Eds.), Parkins Symposium on Fundamental Aspects of Stress Corrosion Cracking, Metallurgical Society of AIME, Warrendale, PA, 1992, p. 341.
[57] M.A. Al-Anezi, G.S. Frankel, A.K. Agrawal, Susceptibility of conventional pressure vessel steel to hydrogen-induced cracking and stress-oriented hydrogen-induced cracking in hydrogen sulfide-containing diglycolamine solutions, Corrosion 55 (1999) 1101–1109.
[58] C.M. Liao, J.L. Lee, Effect of molybdenum on sulfide stress cracking resistance of low-alloy steels, Corrosion 50 (1994) 695–704.

[59] L.W. Tsay, Y.C. Chen, S.L.I. Chen, Sulfide stress corrosion cracking and fatigue crack growth of welded TMCP API 5 L X65 pipe-line steel, Int. J. Fatigue 23 (2001) 103–113.
[60] NACE Technical Committee, Task Group T-1F-23, Stress corrosion cracking resistance of pipeline welds: a special report on sulfide stress cracking resistance of pipeline welds, Mater. Perform. 32 (1993) 58–64.
[61] NACE standard MR0175, Sulfide Stress Cracking Resistant Metallic Materials for Oilfield Equipment, NACE International, Houston, Texas, USA, 1993.
[62] A. Takahashi, H. Ogawa, Influence of microhardness and inclusion on stress oriented hydrogen induced cracking of line pipe steels, ISIJ Intl. 36 (1996) 334–340.
[63] R. Thomson, Lattice theory of fracture and crack creep, J. Appl. Phys. 44 (1973) 2051–2063.
[64] W.K. Kim, H.G. Jung, G.T. Park, S.U. Koh, K.Y. Kim, Relationship between hydrogen induced cracking and type I sulfide stress cracking of high-strength line-pipe steel, Scripta Mater. 62 (2010) 195–198.
[65] NACE MR0 175/ISO 15156-2, Petroleum and natural gas industries—materials for use in H_2S containing environments in oil and gas production – Part 2: cracking-resistant carbon and low alloy steel, and the use of cast iron, NACE International, Texas, USA, 2003.
[66] J. Capelle, I. Dmytrakh, G. Pluvinage, Comparative assessment of electrochemical hydrogen absorption by pipeline steels with different strength, Corros. Sci. 52 (2010) 1554–1559.
[67] C. Mendibide, T. Sourmail, Composition optimization of high-strength steels for sulfide stress cracking resistance improvement, Corros. Sci. 51 (2009) 2878–2884.
[68] R.A. Oriani, P.H. Josephic, Equilibrium aspects of hydrogen-induced cracking of steels, Acta Metall. 22 (1974) 1065–1074.
[69] H.B. Xue, Y.F. Cheng, Characterization of inclusions of X80 pipeline steel and its correlation with hydrogen induced cracking, Corros. Sci. 53 (2011) 1201–1208.
[70] R. Nishimura, J. Shirono, A. Jonokuchi, Hydrogen-induced cracking of pure titanium in sulfuric acid and hydrochloric acid solutions using constant load method, Corros. Sci. 50 (2008) 2691–2697.
[71] V. Venegas, F. Caleyo, T. Baudin, J.H. Espina-Hernandez, J.M. Hallen, On the role of crystallographic texture in mitigating hydrogen-induced cracking in pipeline steels, Corros. Sci. 53 (2011) 4204–4212.
[72] Q.J. Zhou, L.J. Qiao, H.B. Qi, J.X. Li, J.Y. He, W.Y. Chu, Hydrogen blistering and hydrogen-induced cracking in amorphous nickel phosphorous coating, J. Non-Cryst. Solids 353 (2007) 4011–4014.
[73] S.L. Chou, W.T. Tsai, Effect of grain size on the hydrogen assisted cracking in duplex stainless steel, Mater. Sci. Eng. A 270 (1999) 219–224.
[74] C.F. Dong, X.G. Li, Z.Y. Liu, Y.R. Zhang, Hydrogen Induced cracking and healing behavior of X70 steel, J. Alloy Compd. 484 (2009) 966–972.
[75] B.E. Wilde, T. Shimada, Surface modification: a potential new approach to combating hydrogen-induced fracture in steel, Scripta Metall. 22 (1988) 551–556.
[76] P.J. Grobner, D.L. Sponseller, D.E. Diesburg, Effect of molybdenum content on the sulfide stress cracking resistance of AISI 4130-type steel with 0.035% Cb, Corrosion 35 (1979) 240–249.
[77] M. Manohar, Laser surface modification to impede hydrogen ingress into steel (Ph.D. thesis), The Ohio State University, Columbus, OH, 1990.
[78] B.E. Wilde, L. Chattoraj, The effect of shot peening on hydrogen absorption by and hydrogen permeation through AISI 4130 steels, Scripta Metall. Mater. 26 (1992) 627–632.
[79] K.R. Baldwin, C.J.E. Smith, Advances in replacements for cadmium plating in aerospace applications, Trans. Inst. Met. Finish. 74 (1996) 202–209.
[80] G. Zheng, B.N. Popov, R.E. White, Use of underpotential deposition of zinc to mitigate hydrogen absorption into Monel-K500, J. Electrochem. Soc. 141 (1994) 1220–1224.
[81] G. Zheng, B.N. Popov, R.E. White, The role of thallium as hydrogen entry promoter on cathodically polarized HY-130 steel, J. Electrochem. Soc. 141 (1994) 1526–1532.
[82] B.N. Popov, G. Zheng, R.E. White, The underpotential deposition of zinc for mitigation of hydrogen absorption and penetration into HY-130 steel, Corros. Sci. 36 (1994) 2139–2153.
[83] B.N. Popov, G. Zheng, R.E. White, Surface treatment for inhibition of corrosion and hydrogen penetration of type 718 alloy, Corrosion 50 (1994) 613–619.

[84] G. Zheng, B.N. Popov, R.E. White, Surface treatment for mitigation of hydrogen penetration into AISI 4340 steel and Inconel 718 alloy, J. Appl. Electrochem. 25 (1995) 212–218.
[85] B.N. Popov, G. Zheng, R.E. White, Electroplating of thin films of bismuth onto AISI 4340 steel and Inconel 718 to prevent hydrogen embrittlement, Corros. Sci. 51 (1995) 429–435.
[86] D.H. Coleman, G. Zheng, B.N. Popov, R.E. White, The effects of multiple electroplated zinc layers on the inhibition of hydrogen permeation through an iron membrane, J. Electrochem. Soc. 143 (1996) 1871–1874.
[87] H.A. Duarte, D.M. See, B.N. Popov, R.E. White, The effects of organic compounds on inhibition of hydrogen permeation through a mild steel membrane, J. Electrochem. Soc. 144 (1997) 2313–2317.
[88] H.A. Duarte, D.M. See, B.N. Popov, R.E. White, Organic compounds as effective inhibitors for hydrogen permeation of type 1010 steel, Corros. Sci. 54 (1998) 187–193.
[89] D.H. Coleman, B.N. Popov, R.E. White, Hydrogen permeation inhibition by thin Layer Zn-Ni alloy electrodeposition, J. Appl. Electrochem. 28 (1998) 889–894.
[90] A. Durairajan, B.S. Haran, R.E. White, B.N. Popov, Development of a new electrodeposition process for plating of Zn-Ni-X (X = Cd, P) alloys: permeation characteristics of Zn-Ni-Cd ternary alloys, J. Electrochem. Soc. 147 (2000) 4507–4511.
[91] A. Durairajan, A. Krishniyer, B.S. Haran, R.E. White, B.N. Popov, Characterization of hydrogen permeation through a corrosion-resistant zinc-nickel-phosphorus alloy, Corrosion 56 (2000) 283–288.
[92] A. Durairajan, D. Slavkov, B.N. Popov, Development of corrosion and hydrogen permeation resistant Zn-Ni-X (X = P, Cd) ternary alloy coatings, Bull. Chem. Technol. Macedonia 20 (2001) 3–17.
[93] H. Kim, B. Popov, K.S. Chen, Comparison of corrosion resistance and hydrogen permeation properties of Zn-Ni, Zn-Ni-Cd and Cd coatings on low carbon steel, Corros. Sci. 45 (2003) 1505–1521.
[94] B. Veeraraghavan, H. Kim, B. Haran, B. Popov, Comparison of mechanical, corrosion and hydrogen permeation properties of electroless Ni-Zn-P alloys with electrodeposited Zn-Ni and Cd, Corrosion 59 (2003) 1003–1010.
[95] W.C. Luu, J.K. Wu, Influence of aluminum content on retarding hydrogen transport in Fe-Al binary alloys, Corros. Sci. 43 (2001) 2325–2333.
[96] N. Parvathavarthini, U. Prakash, R.K. Dayal, Effect of carbon addition on hydrogen permeation in Fe_3Al-based intermetallic alloy, Intermetallics 20 (2002) 329–332.
[97] K. Hashi, K. Ishikawa, T. Matsuda, K. Aoki, Hydrogen permeation characteristics of multi-phase Ni-Ti-Nb alloys, J. Alloy Compd. 368 (2001) 215–220.
[98] Y.F. Cheng, Analysis of electrochemical hydrogen permeation through X-65 pipeline steel and its implications on pipeline stress corrosion cracking, Int. J. Hyd. Energy 32 (2007) 1269–1276.
[99] D. Levchuk, H. Bolt, M. Döbeli, S. Eggenberger, B. Widrig, J. Ramm, Al-Cr-O thin film as an efficient hydrogen barrier, Surf. Coat. Tech. 202 (2008) 5043–5047.
[100] T. Kanezaki, C. Narazaki, Y. Mine, S. Matsuoka, Y. Murakami, Effects of hydrogen on fatigue crack growth behavior of austenitic stainless steels, Int. J. Hyd. Energy 33 (2008) 2604–2619.
[101] H.B. Xue, Y.F. Cheng, Hydrogen permeation and electrochemical corrosion behavior of the X80 pipeline steel weld, J. Mat. Eng. Perform. 22 (2013) 170–175.

CHAPTER 9

Stress Corrosion Cracking

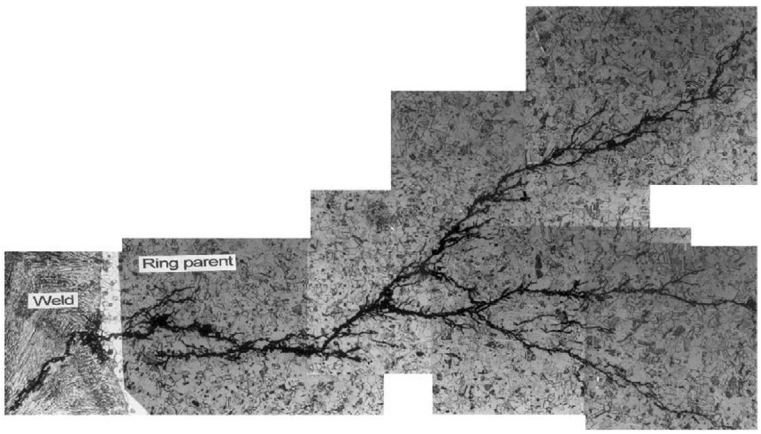

Chapter Contents

Corrosion Engineering
http://dx.doi.org/10.1016/B978-0-444-62722-3.00009-4

9.1 DEFINITION AND CHARACTERISTICS OF STRESS CORROSION CRACKING

Environmentally induced cracking (EIC) is a brittle mechanical failure from the combined action of tensile stress and corrosion environments. Depending on the failure mechanism, EIC is divided into stress corrosion cracking (SCC), corrosion fatigue cracking (CFC), and hydrogen-induced cracking (HIC) or hydrogen embrittlement (HE).

SCC is defined as the growth of cracks due to the simultaneous action of tensile stress and a corrosion environment on active metals or alloys. Besides the residual stress, to initiate SCC, the metal should be in contact with a corrosion environment such as chloride ions, water, oxygen, and pH. SCC is difficult to detect until extensive corrosion has already developed, leading to catastrophic failure such as in an aluminum alloy used in an aircraft structure, shown in Fig. 9.1, explosion of boilers, and ruptures of liquid or gas transmission pipes. The stress is induced by heat treatment, welding, machining, grinding, and by cold work. The required tensile stresses may occur in the form of residual stress, applied load (directly applied stress), monotonic straining, or low amplitude cycling, causing cracking in many metallic systems. The rate of crack propagation is affected by stress levels, temperature, and concentration of the corrosion solution. Because SCC is controlled by tensile stress, it also accelerates with time. Only specific

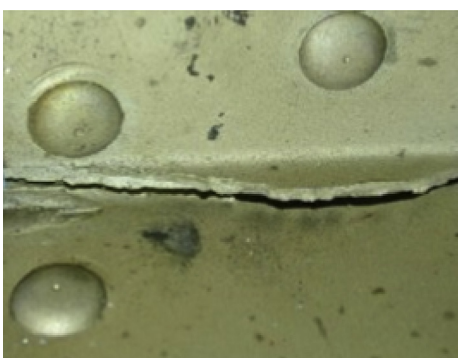

Fig. 9.1 SCC in aluminum alloy used in aircraft.

combinations of an active alloy, stress, and environment create conditions for SCC. Also, the stress should be above the threshold value of the metallic systems.

Typical SCC of alloys is due to sensitization and residual stress. Inclusion of corrosion products in the alloy matrix may also generate stress. The cracks are created by initiation and growth of corrosion pits and the coalescence and propagation of micro- and macrocracks [1–3]. Depending on the alloy and the corrosive environment, the cracks penetrate into the materials' microstructure as a transgranular or an intergranular morphology. Chloride SCC is intergranular corrosion occurring in austenitic stainless steel, which is of a great concern for the nuclear industry.

Addition of caustic soda to boiler feed waters reduces the corrosion of mild steel. However, caustic SCC has also been observed on tubing made from the Inconel alloy. Extensive cracking is generated in a matter of hours for combinations such as type 304 stainless steel in a boiling $MgCl_2$ solution. SCC failures are seen in pressure vessel piping, in shroud supports, and heavily stressed components. SCC around weld patches result when the structures are exposed to corrosive environments and residual stress caused by welding or sensitization. Most SCC occurs in primary loop recirculation pipes in boiling water reactors (BWRs), in weld heat-affected zones (HAZs), and in 316L stainless steels without sensitization [4,5]. The initiation and growth of pits, transition from pit to crack properties of microcracks, and coalescence conditions due to SCC on smooth surfaces have been investigated using constant-load tests, creviced bent-beam tests and slow strain rate tensile (SSRT) tests in simulated environments [6,7]. SCC crack propagation evaluation on precracked specimens performed by fracture mechanics [8] are described in this chapter.

HIC or HE of the material is caused by the uptake of atomic hydrogen from a corrosive environment. HIC was introduced and discussed in Chapter 8. Briefly, hydrogen atoms are generated during the cathodic protection of pipelines, galvanic corrosion, or welding. They diffuse into the metal and are trapped at the grain boundaries and dislocations. Synergy between the critical tensile stress and the susceptibility of the microstructure to hydrogen degradation results in HE and failure. Hydrogen decreases the alloy toughness and drastically decreases the fracture resistance. Examples are HIC of carbon and low-alloy steel (LAS) pipelines, HE of prestressed steel, HE of titanium, cracking of cold worked duplex stainless steel (DSS), and cracking of offshore structural steel in marine environments.

9.2 TESTING METHODS

The standard testing for SCC has been reviewed by Sedriks [9] and Turnbull [10]. The following techniques have been used to estimate the SCC: surface flawed, cantilever bend, creviced bent-beam tests, double cantilever beam, and compact tension specimens.

These techniques are time-consuming, expensive, and require bulky specimens that restrict the use of common techniques for SCC monitoring.

Stress corrosion outlined in this section is defined as an attack on a metal or alloy caused by the combined action of tensile stress and environment resulting in the formation of a crack. Threshold stress describes the stress intensity above which stress corrosion cracks are initiated and grow as a function of the conditions existing at the metal interface. Crack initiation time is defined as the time elapsed from the start of a test and the first detection of the crack. The threshold stress intensity factor stands for stress intensity above which stress corrosion cracks will initiate under plane strain conditions [9]. The stress concentration factor is the factor by which the stress is locally increased. The observed increase results from geometrical discontinuities and occurs beyond the nominal stress estimated from minimum cross-sectional area and load. Average crack velocity stands for the maximum depth of cracks divided by the stress time. Time to failure stands for the period of time between the start of the test and the first appearance of cracking or total separation of the sample. Testing methods described in this section are common to SCC and HIC. Fracture mechanics testing is discussed in Section 9.3 while corrosion fatigue testing is discussed in Section 9.9.

9.2.1 Constant deformation tests

The specimen in these tests is kept at constant deformation stress. The following shapes of the specimens are used [11,12]:

(i) C-ring
(ii) U-bend
(iii) Bend beam
(iv) Tensile specimen.

Once the elastic limit is crossed, due to the fixed stress, the stress-strain relationship is nonlinear, which is a major disadvantage using these methods. The stress is applied by tightening the nuts. A strain gauge is used to evaluate the applied stress. The susceptibility to SCC is estimated by measuring the time to fail at the applied stress. Fixed time tests are used, in which fixed stress is applied for a time period to assure the quality of the materials.

The C-ring specimens, shown in Fig. 9.2, are fabricated using sized tubing. The experimental standard for a C-ring is given in ASTM G 38-01 [11]. The amount of applied deformation controls the variable stress above and below the yield strength, which is one of the advantages of using the C-ring specimen. C-ring specimens can be used to measure the susceptibility to cracking of various alloys. They are used for testing plates in the short transverse direction and tubing, bars, and rods in the long transverse direction. C-ring specimens are also used in testing steam generator (SG) tubing in nuclear power plants. These specimens are stressed to predetermined levels by applying a constant load or constant strain. Specimen preparation and stressing is described in detail by Sedriks [9].

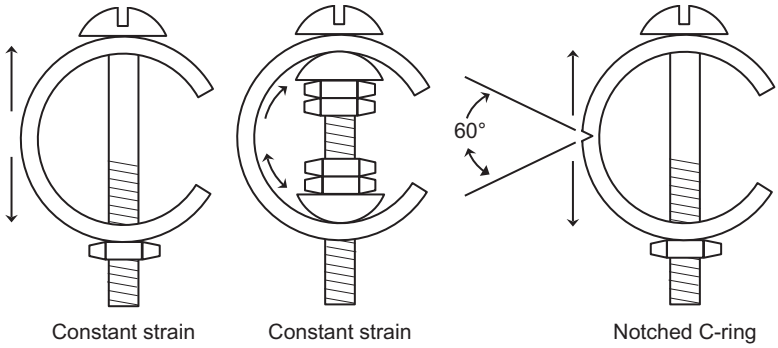

Fig. 9.2 C rings used in constant deformation tests [11]. *Reprinted, with permission, from ASTM G 38-01 Standard Practice for Making and Using C-Ring Stress-Corrosion Test Specimens, copyright ASTM International, West Conshohocken, PA.*

Stressing with strain gages attached is performed by attaching circumferential and transverse electrical strain gages to the surface stressed in tension. The bolt is then tightened until the strain measurement indicates the desired stress. Both the circumferential (σ_c) and transverse (σ_T) stresses within the elastic range are calculated using the following equations:

$$\sigma_c = \frac{E}{(1-\mu^2)(\varepsilon_c + \mu\varepsilon_T)} \tag{9.1}$$

$$\sigma_T = \frac{E}{(1-\mu^2)(\varepsilon_T + \mu\varepsilon_c)} \tag{9.2}$$

where E is Young's modulus of elasticity, μ is Poisson ratio, ε_c is circumferential strain, and ε_T is transverse strain. The degree of elastic strain is predicted using the procedure described by Sedriks [9], ASTM STP 425 [13], and Graig *et al.* [14].

U-bend shapes are shown in Fig. 9.3 [15]. They consist of a bar or sheet plastically deformed over a mandrel by a 180° bend. The ends of the specimen are constrained by a bolt. The U-bend specimens are used to evaluate the resistance of alloys under various corrosive solutions. However, it is very difficult to reproduce the stress conditions for the new specimen because the stress distribution within the specimen is not known. Fabrication of U-bend specimens is given in the ASTM G 30-97 standard method [15].

Alloys that are ductile in nature are used to form a U-shape specimen in order to avoid mechanical cracking of the sample. They are made from sheet strips or machined from bars, plates, weldments, or castings. Rectangular sheet coupons can be used to fabricate bend specimens, as shown in Fig. 9.3. The stress conditions in most of the cases are not known, because ranges of stresses are present in a single specimen. These types of

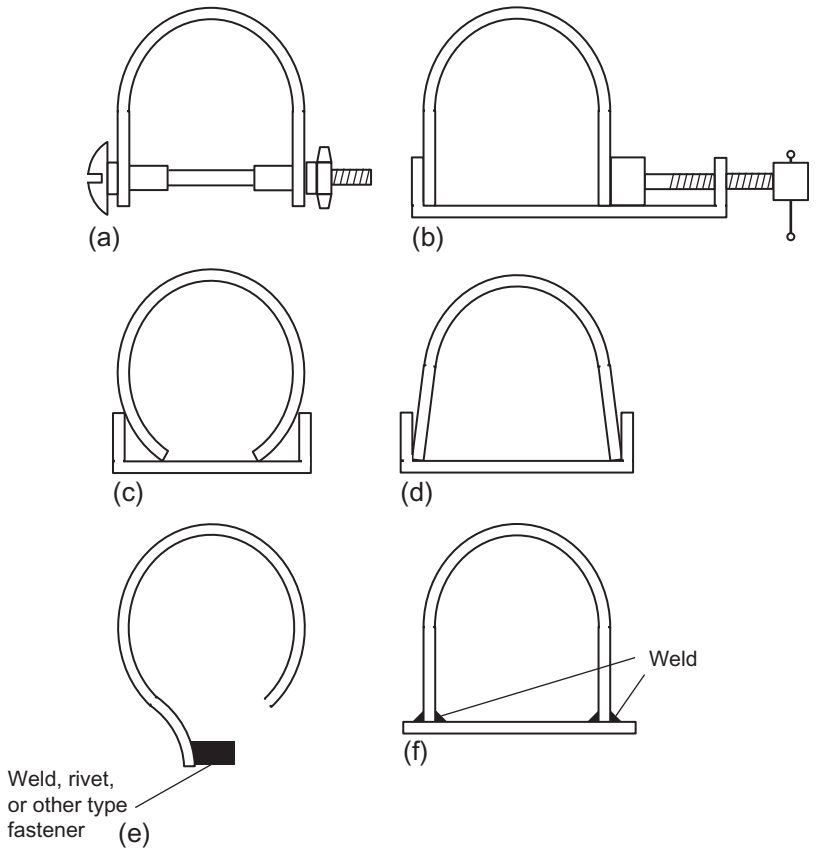

Fig. 9.3 U-bends used in constant deformation test [15]. *Reprinted, with permission, from ASTM G 30-97 Standard Practice for Making and Using U-Bend Stress-Corrosion Test Specimens, copyright ASTM International, West Conshohocken, PA.*

specimens are not suitable to evaluate the effect of different applied stresses on SCC. The total strain (ε) in the outer material of the bend is in the plastic region and is given by:

$$\varepsilon = \frac{T}{2R} \quad \text{when } T << R \tag{9.3}$$

where T is specimen thickness and R is radius of bend.

The stress-strain curve of the test material is used to obtain the value of the outer fiber stress using the strain value estimated by Eq. (9.3). The testing procedure is explained in detail by Sedriks [9].

Bend-beam specimens provide a quantitative estimate of the maximum stress in the outer fibers of the bent beam when stressed below the yield stress. Experimental standards for bent beam specimen are given in ASTM G 39-99 [16]. In this test, both the specimen

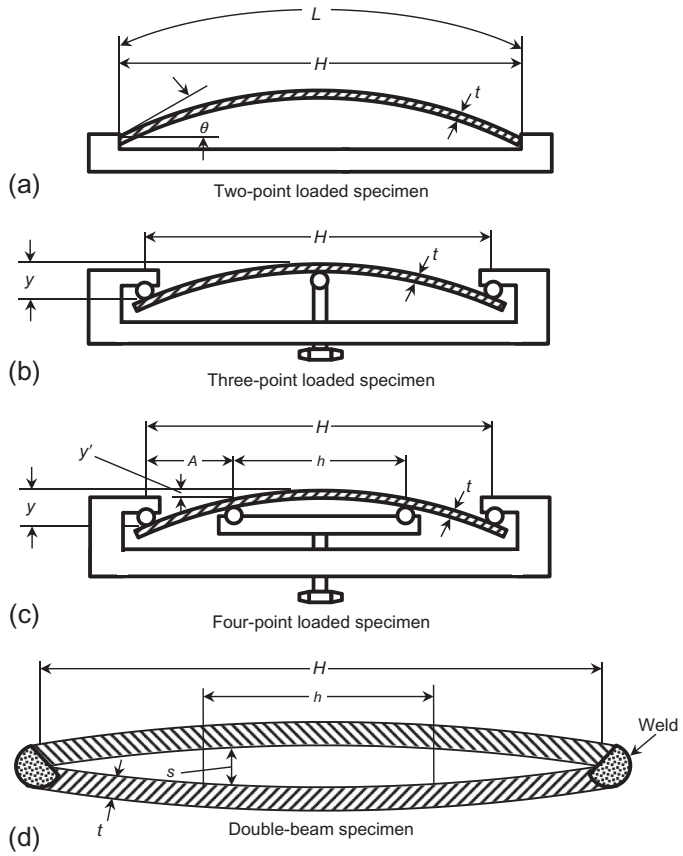

Fig. 9.4 Bend beams specimen used in constant-deformation test [16]. *Reprinted, with permission, from ASTM G 39-99 Standard Practice for Preparation and Use of Bent-Beam Stress-Corrosion Test Specimens copyright ASTM International, West Conshohocken, PA.*

and the holder are exposed to a corrosion environment. A bend-beam specimen is shown in Fig. 9.4 [16]. The testing is performed by bending the sample using a stressing jig. The formulas suggested for estimating the stress in bent beams are valid only in the elastic range [16].

9.2.1.1 Two-point loaded specimens

The two-point loaded specimen schematic is shown in Fig. 9.4a [16]. The maximum stress occurs at the midpoint of the specimen convex. It is zero at the ends. The elastic stress at the midpoint of the convex surface is estimated from Eq. (9.4):

$$L = \left(\frac{ktE}{\sigma}\right)\sin^{-1}\left(\frac{H\sigma}{ktE}\right) \tag{9.4}$$

where L is the specimen length, E is modulus of elasticity, H is holder span, t is thickness of specimen, and $k = 1.280$, an empirical constant. The equation is solved by trial and error or by using a computer model [17].

9.2.1.2 Three-point loaded specimen

A three-point loaded specimen schematic is shown in Fig. 9.4b [16]. A disadvantage using this sample is the possibility of the pressure generated in the central support to create unknown biaxial stresses. When three-point loaded specimens are used, there is a possibility of crevice corrosion at the central support, which is closer to the maximum tensile stress that cathodically protects the specimen and prevents crack formation.

The elastic stress in the outer fibers is estimated using Eq. (9.5).

$$\sigma = \frac{6Et\gamma}{H^2} \tag{9.5}$$

where σ is maximum tensile stress, E is modulus of elasticity, t is thickness of the specimen, γ is a maximum deflection, and H is distance between outer supports.

9.2.1.3 Four-point loaded specimen

A four-point loaded specimen, shown in Fig. 9.4c, provides uniform longitudinal tensile stress in the convex surface [16]. The stress decreases to zero from the inner to the outer support. This specimen is especially suitable for welded materials. Four-point loaded specimens are advantageous compared to the two- or three-point loaded specimens due to the large area of uniformly stressed material. The elastic stress of the mid-portion is estimated by Eq. (9.6).

$$\sigma = \frac{12Et\gamma}{3H^2 - 4A^2} \tag{9.6}$$

where σ is maximum tensile stress, E is modulus of elasticity, t is thickness of specimen, γ is maximum deflection, H is distance between outer supports, and A is distance between inner and outer supports. Dimensions in Eq. (9.6) are chosen so that $A = \frac{H}{4}$. A special case of Eq. (9.6) for $A = 0$ is Eq. (9.7):

$$\sigma = \frac{4Et\gamma'}{h^2} \tag{9.7}$$

where h is distance between the inner supports and γ' is deflection between inner supports.

9.2.1.4 Double beam specimen

A double beam specimen, shown in Fig. 9.4d, consists of two flat strips bent against each other over a centrally located spacer [10,16]. This specimen provides an uniform longitudinal stress in the convex space between the lines of contact with the spacer. The stress decreases linearly to zero at the ends of the specimen. The elastic stress in the convex between the lines of contact is estimated by Eq. (9.8).

$$\sigma = \frac{3\,Ets}{H^2\left(1-\frac{h}{H}\right)\left(1+\frac{2h}{H}\right)} \tag{9.8}$$

where σ is maximum tensile stress, E is modulus of elasticity, t is thickness of specimen, s is thickness of spacer, H is distance of specimen, and h is length of the spacer.

If $H=2h$, then, Eq. (9.8) simplifies to:

$$\sigma = \frac{3\,Ets}{H^2} \tag{9.9}$$

Eqs. (9.8) and (9.9) are based on small deflections ($s/H<0.2$).

A schematic of a conventional tensile specimen is shown in Fig. 9.5 [17]. This specimen is a small loading frame provided with nuts. The applied stress is controlled

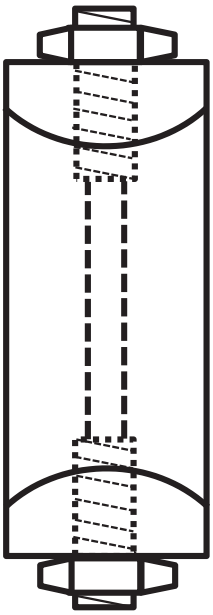

Fig. 9.5 Tensile specimen used in constant-deformation test [17]. *Reprinted, with permission, from ASTM G 49-85 Standard Practice for Preparation and Use of Direct Tension Stress-Corrosion Test Specimens, copyright ASTM International, West Conshohocken, PA.*

to provide precise stress measurements. Fabrication and experimental standards for tensile specimens are given in ASTM G 49-85 [17]. The reduced section of the specimen (gage length) has the smallest cross-section and experiences the greatest stress. Thus, the crack will be initiated in the reduced section. The specimen has a transition region between the thicker ends and the gage length. Because the specimen is more compliant due to crack extension, the applied stress decreases as the crack grows during the test. The test can be performed in stiff tensile testing machines by loading the specimen to the desired stress level, while the moving beam is locked in position.

9.2.2 Sustained load tests

A constant load specimen with a compressed spring is shown in Fig. 9.6 [11]. A constant load is applied to the specimen during the test. The stress is applied though a dead weight load hung from one end of the specimen. The net cross-sectional area of the sample decreases upon initiation of a crack. The stress increases under sustained load with the advancement of the crack and results in total fracture. In the load test, the growth portion of the crack is eliminated. Proving ring assembly for the measurement of sustained load is shown in Fig. 9.7 [17]. Due to the presence of a small plastic deformation before the fracture of the specimen, the device in Fig. 9.7 applies a constant test load that is measured accurately by the elastic deformation of the ring. The time to failure can be measured accurately using a microswitch tripped by the specimen holder at fracture.

9.2.3 Slow strain rate tensile testing

In the SSRT testing, creep stands for time-dependent deformation of the sample after the load application. Maximum load is defined as the load that results in the failure of one component. The strain rate is the initial rate of increase of the gage length of an initial

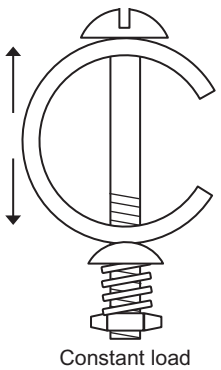

Fig. 9.6 Sustain load specimen with a compressed spring [11]. *Reprinted, with permission, from ASTM G 38-01 Standard Practice for Making and Using C-Ring Stress-Corrosion Test Specimens, copyright ASTM International, West Conshohocken, PA.*

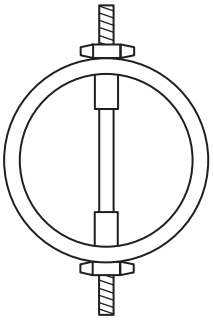

Fig. 9.7 Proving ring assembly for measurement of sustained load to a tensile specimen [17]. *Reprinted, with permission, from ASTM G 49-85 Standard Practice for Preparation and Use of Direct Tension Stress-Corrosion Test Specimens, copyright ASTM International, West Conshohocken, PA.*

plain tensile sample. The slow strain rate test is a tensile stress test performed on a conventional smooth bar tensile specimen, slowly pooled at a constant strain rate in the presence of a corrosion environment until failure [18]. The crosshead speeds are in the range of 10^{-4}–10^{-7} cm/s. The test produces fracture by SCC or mechanical failure. The strain rate testing apparatus consists of a motor-driven crosshead in a load frame. The load-cell measures the load on the specimen continuously. The crosshead travel is a measure of strain in the tensile specimen. Nominal stress elongation curves are obtained by plotting the nominal stress estimated from the instantaneously applied load and the original cross-section area of a specimen vs. the elongation of gage length. In the testing procedure, the specimens are tested to the point of total failure in an inert environment as well as in the corrosive environment at the same temperature. The inert conditions are provided to obtain a comparative assessment to the corrosive environment. The samples should be exposed to the same environment without applied strain rate because the alloys' mechanical properties may deteriorate in contact with the corrosive environment in the absence of applied strain. Intergranular corrosion or pitting may occur in the absence of strain, which requires the effect of the applied strain to be assessed in comparison with the corrosion properties of unstrained samples. Temperature variation at elevated temperatures during SSRT testing may change the strain rate, resulting in erroneous experimental results. The susceptibility to cracking is assessed by the departure of the ratio between the results obtained from the test environment and the inert environment by applying the parameters at the same initial strain rate. These parameters include (i) time of failure, (ii) the maximum value of the load achieved during the test performed to total failure, (iii) ductility determined by reduction in area or elongation fracture, and (iv) reduction of the area bounded by the normal stress/elongation curve.

A pair of stress-strain rate curves for carbon steel was investigated by Parkins [19]. The stress vs. strain curves are compared in an inert (hot oil) atmosphere and in boiling 4 N

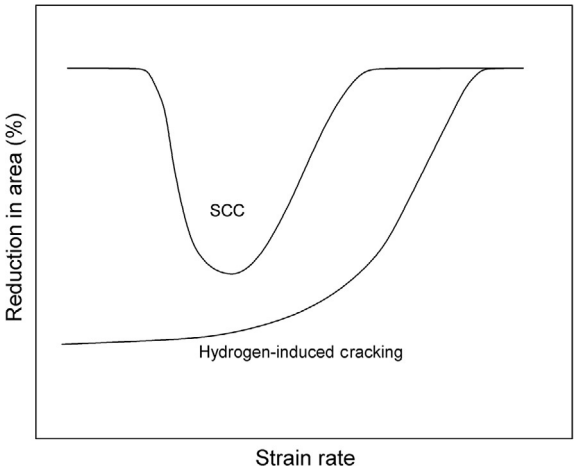

Fig. 9.8 Effect of strain rate ductility in SSRT testing for HIC and SCC [20]. *Reprinted, with permission, from ASTM STP 665, Stress corrosion cracking – the slow strain rate technique, Copyright ASTM International, West Conshohocken, PA [20].*

sodium nitrate solution initiating SCC at the same temperature. The specimen exposed in the nitrate indicated lower time or strain to failure.

Kim and Wilde [20] investigated the effect of strain rate on ductility in SSRT testing for SCC and HIC. The results are shown in Fig. 9.8 [20].

In the case of HIC, hydrogen diffuses into the lattice at all strain rates tested and no ductility is observed on the reduction in the area vs. strain rate plot. At the critical strain rate, in the case of SCC, the film formation cannot inhibit the ductile rupture [20]. Threshold stresses can also be determined by SSRT tests. The test is performed by using a number of samples that are subjected to different ranges of stress at a given strain rate. A plot of stress range vs. average crack velocity could be used to evaluate the threshold stress [20].

9.3 FRACTURE MECHANICS TESTING

Stress Intensity Factor: In fracture mechanics, the stress intensity factor, K, predicts the stress intensity near the tip of a crack caused by a load or residual stress. The stress intensity provides a failure criterion for brittle materials and estimates the damage tolerance. The magnitude of K depends on the size and location of the crack, the magnitude and the distribution of loads on the material, and the sample geometry. According to linear elastic theory, the stress distribution magnitude, σ_{ij}, near the crack tip in polar coordinates (r, θ) with the origin at the crack tip is given as:

$$\sigma_{ij}(r,\theta) = \frac{K}{2\pi r^{1/2}} f_{ij}(\theta)^{ij} + \text{higher order terms} \tag{9.10}$$

where K is the stress intensity factor (with units of stress × length$^{1/2}$) and "f_{ij}" is a dimensionless quantity that depends on the geometry and load. For small polar coordinate "r" (close to the tip of the crack), the expression breaks down resulting in the stress distribution going to ∞. The estimation of stress intensity factors depends on three independent cracking modes used in fracture mechanics, as shown in Fig. 9.9.

SCC of alloys occurs at low stress and high rates. The crack velocity varies with the mode I stress intensity factor, K_I, defined as:

$$K_I = \sigma(\pi a)^{1/2} \tag{9.11}$$

where σ is the stress and "a" is the crack length [21]. The critical stress intensity, K_{Ic}, is necessary to propagate an initiated crack or flaw and represents fracture toughness. The subscript "I" stands for mode crack displacement shown in Fig. 9.9. Models II and III represent loading in which the shear stress initiates cracking and propagates in plane shear (mode II) and out of plane (shear tearing) (mode III). K_{Ic} is lower than the stress intensity factors estimated for modes II and III. The dependence of specimen thickness on K_c to propagate a crack in aluminum alloy 7075 is shown in Fig. 9.10 [22]. The stress intensity, K_c, in Fig. 9.10 shows that initial crack propagation levels off with increasing thickness. When the strain is confined to the x-y plane (plane strain conditions), the minimum specimen thickness, B, to create the required critical lateral constraints is given by Brown and Strawley [23]:

$$B \geq 2.5\left[\frac{K_{Ic}}{\sigma_{ys}}\right]^2 \tag{9.12}$$

where σ_{ys} defines high yield strength. Decreasing the fracture toughness or increasing the high yield strength and low sample thicknesses satisfy the requirement for plain strain conditions.

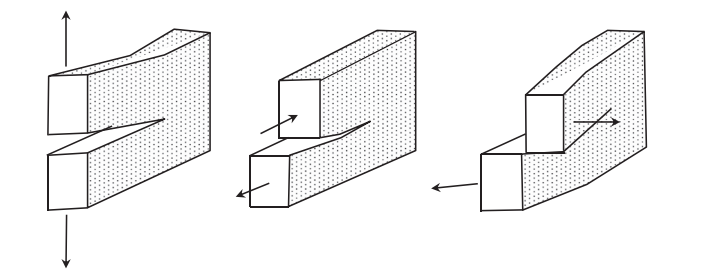

Fig. 9.9 Crack surface displacement modes during crack growth.

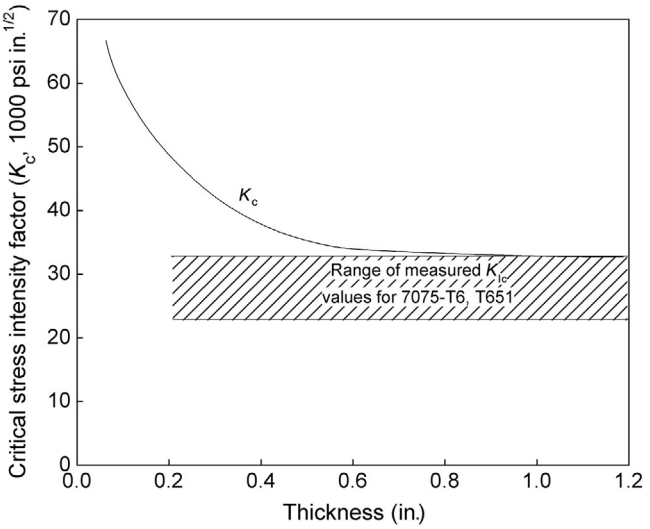

Fig. 9.10 Effect of critical stress intensity factor on the thickness of the specimen to propagate a crack in aluminum alloy 7075 [22]. *Reprinted, with permission, from ASTM STP 463, Review of Developments in Plane Strain Fracture Toughness Testing, copyright ASTM International, West Conshohocken, PA.*

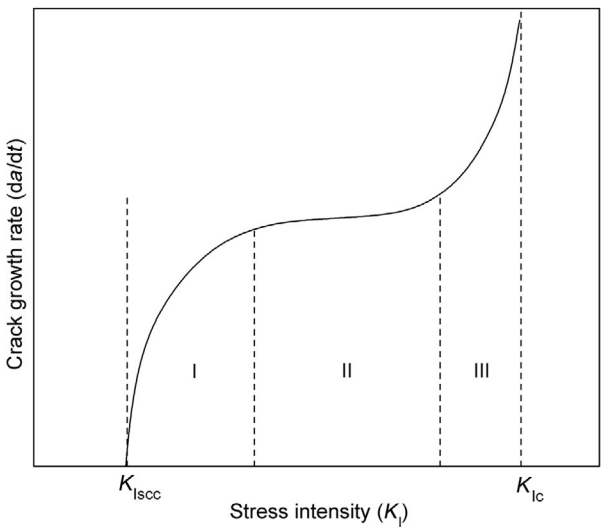

Fig. 9.11 Dependence of the CGR, d*a*/d*t*, per unit time on the stress intensity, K_I, during SCC.

The dependence of the crack growth d*a*/d*t* on the stress intensity, K_I, in the presence of SCC is shown in Fig. 9.11. Crack growth in the subcritical region could occur in a corrosive environment at a reduced rate above the stress intensity and below the fracture toughness factor, K_{Ic}. Subcritical crack growth is caused by SCC with a threshold value labeled in the figure as K_{ISCC} (Fig. 9.11). In region III, the cracks grow at high constant stress intensity at critical velocity above the fracture toughness value K_{Ic}.

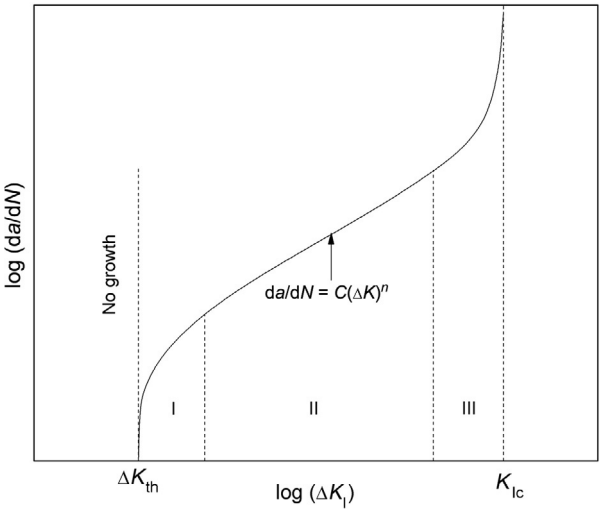

Fig. 9.12 Dependence of the CGR, d*a*/d*N*, per stress cycle during CFC.

The effects of corrosion and fatigue on crack growth rate (CGR) are presented in Fig. 9.12. The increment of growth during each fatigue cycle $\frac{da}{dN}$ is defined as the CGR and is given in Eq. (9.13) as a function of stress-intensity amplitude, ΔK, by the power law relationship:

$$\frac{da}{dN} = C(\Delta K)^n \tag{9.13}$$

The power law relationship is valid in region II for corrosion fatigue and corrosion absent fatigue. When the crack no longer grows, K_{Ic} is reduced to K_{th} and K_{Icfc}, the threshold values for fatigue and corrosion fatigue, respectively.

9.3.1 Test methods

Rising stress cantilever beam configuration was first introduced by Braun and Beachem [24] to analyze HIC. In this method, a load is applied from the end of the notched cantilever beam. The specimen's notched area is immersed in a cell with corrosive solution. Rolfe and Barsom [25] defined the stress intensity, K_I, by Eq. (9.14).

$$K_I = \frac{6M}{(BB_N)^{1/2}(W-a)^{3/2}}F \tag{9.14}$$

where M is the bending moment, B is the specimen width, B_N is the net specimen width subtracting side grooves, "a" is the crack length, W is the specimen depth, and $F(a/W) = 0.36$ when the value of a/W is 0.05. The cross-section and the stress intensity increase during the test due to the crack growth, resulting in an increase in the crack length "a". Stress intensity higher than HIC, (K_{Ihic}) initiates a continuous increase of stress, which

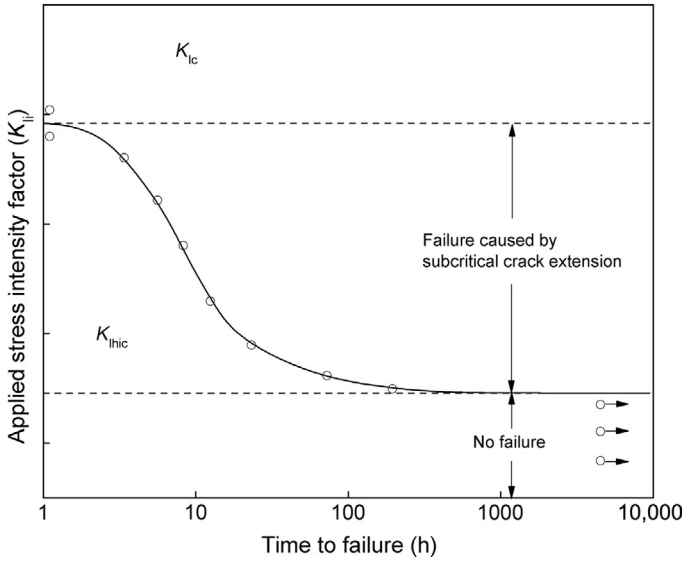

Fig. 9.13 Determination of K_{Ihic} by cantilever testing [24].

reaches the critical value of the stress intensity K_{Ic}. Fast cracking after K_{Ic} results in a complete specimen failure (fracture). Figure 9.13 shows evaluation of K_{Ihic} by cantilever beam testing [24]. K_{Ii} in Fig. 9.13 represents applied stress intensity factor.

9.3.2 Precracked cantilever beam specimens

The components of a precracked beam test are shown in Fig. 9.14 [9]. The precracked cantilever beam specimen is used to estimate stress susceptibility in the presence of stress-raising defects in the precrack sample. Plane strain stress intensity factor K_I is calculated using Eq. (9.15):

$$K_I = \frac{4.12 M_o \sqrt{\frac{1}{\alpha^3} - \alpha^3}}{B W^{3/2}} \tag{9.15a}$$

$$\alpha = 1 - \frac{a}{W} \tag{9.15b}$$

Range of applicability: $0.2 \leq \frac{a}{W} \leq 0.6$, where "$a$" is crack length, W is specimen width, and B is thickness.

The plane strain conditions and specimen preparation are described in detail by Sedriks [9]. In fracture toughness testing, the value of plane strain fracture toughness factor K_{Ic} is measured in the plane strain fracture region. For accurate K_{Ic} determination, the

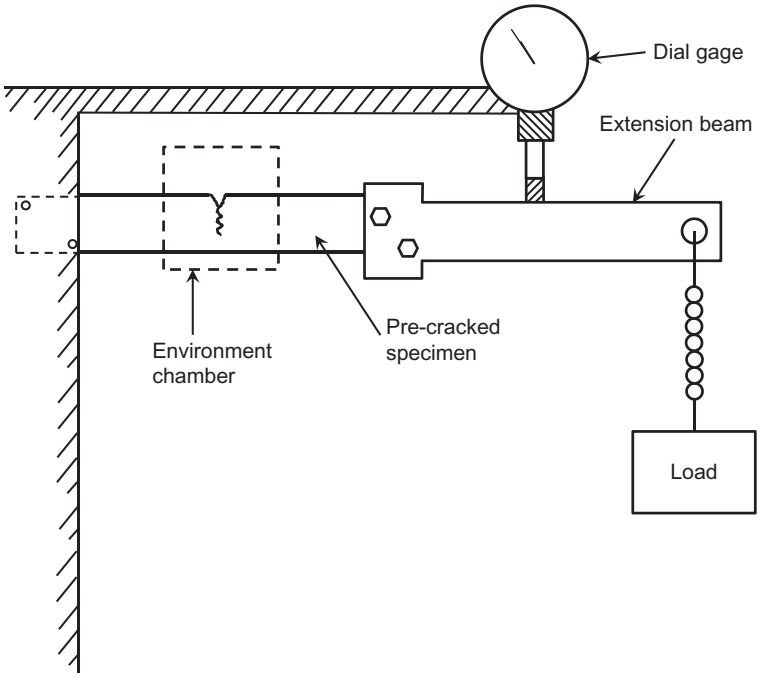

Fig. 9.14 Components of a precracked cantilever beam test [9]. © *NACE International 1990.*

crack length "a" and thickness "B" should be less than $2.5(K_{Ic}/\sigma_{ys})^2$, where σ_{ys} is 0.2% yield stress [9]. To ensure adequate constraint for large specimens, it is necessary for both "a" and "B" to be $4(K_{Ic}/\sigma_{ys})^2$. For measurements of K_{ISCC}, similar criteria are employed regarding specimen dimensions. Both "a" and "B" should be less than $2.5(K_I/\sigma_{ys})^2$ and $4(K_I/\sigma_{ys})^2$, where K_I is stress intensity. The calculation of K_I for a precracked cantilever is shown in Fig. 9.15a [9].

In the plane strain fracture toughness measurements, the ratio of yield stress (σ_{ys}) to Young's modulus should be used for selecting sample size. The testing is performed in precracked cantilever beam specimens by weight loading and hydraulic loading. The thickness, B, width, W, the crack length, "a", and length of the lever arm (distance between the precrack sample and the load attachment) should be measured before testing. The product of the lever arm length and the load defines the bending moment M_o. The load necessary to produce the initial stress intensity K_{Ii} is estimated using Eq. (9.15a). To determine accurately the value of K_{ISCC}, the initial stress intensifies until failure occurs and is plotted against the test time. As shown in Fig. 9.15b, K_{ISCC} is estimated at the point where the stress intensity at which failure occurred becomes asymptotic to a line parallel to the time axis [9].

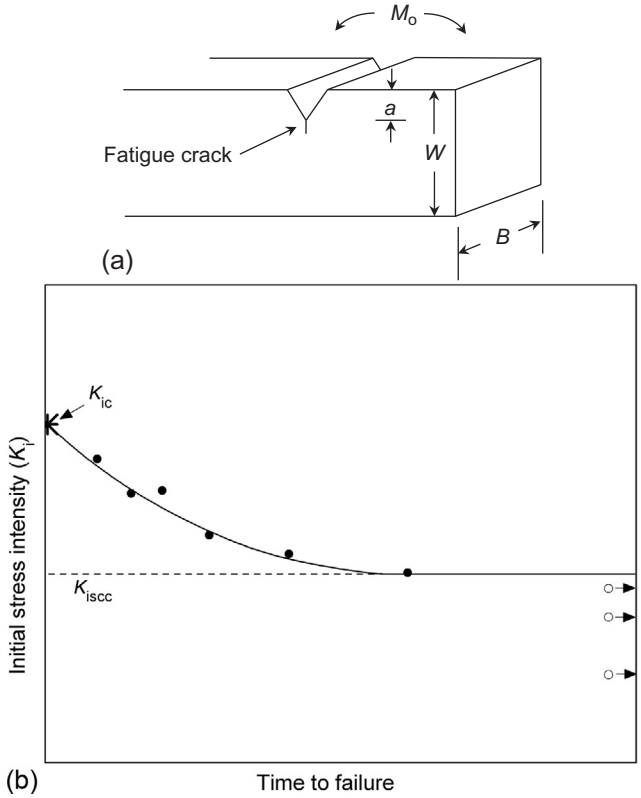

Fig. 9.15 (a) Calculation of K_I for a precracked cantilever beam specimen. M_o represents bending moment. (b) K_{ISCC} illustration of a time to failure plot in the determination of K_{ISSC} [9]. © *NACE International 1990.*

9.3.3 Linearly increasing stress test

In linearly increasing stress test (LIST), a linearly increasing engineering stress is applied to plain unnotched specimens exposed to a corrosion environment. A linear increase of the load is accomplished by means of a lever principle, as shown in Fig. 9.16 [26]. The load is moving on the right side of the lever. The horizontal position of the lever is maintained by using a linear actuator and a servocontroller with a displacement signal from the end of the lever arm. The specimen is connected to one side of the lever beam. The other side has a mass of 14 kg, which moves away from the fulcrum and increases for the standard test; the load on the specimen at 0.019 MPa/s. The applied stress is estimated from the position of the mass at any time and the original cross section of the specimen. Experiments are repeated at various applied stress rates, and the parameters measured include SCC initiation stress, average crack velocity, and fracture stress. The LIST is load

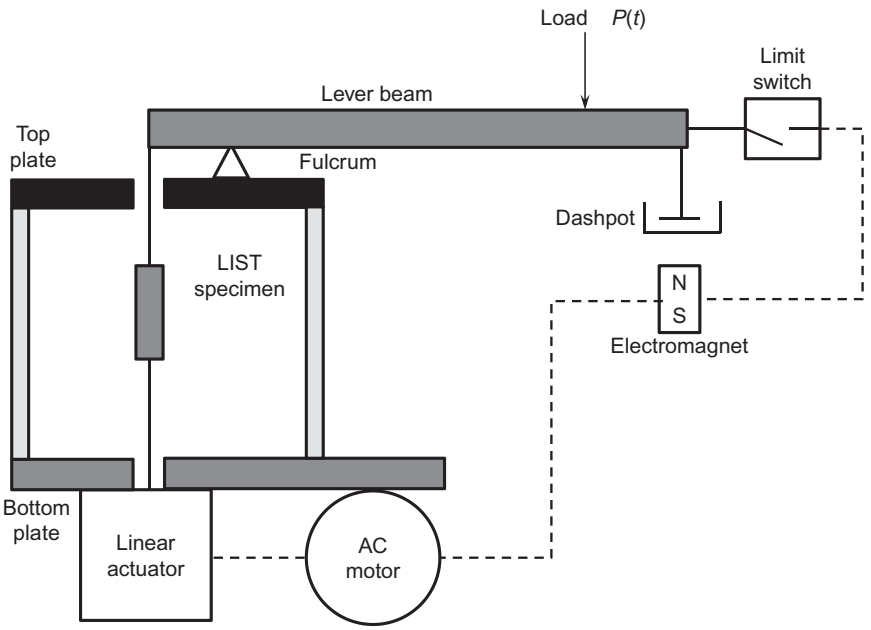

Fig. 9.16 Schematic of LIST [26]. *Reproduced, with permission from, IOP Publishing Ltd.*

controlled and used at service conditions of loaded structures and parts. Once the crack is initiated, the failure time is controlled by crack propagation. At a critical length, rapid failure occurs on the specimen. [26–29].

9.4 EXAMPLES OF STRESS CORROSION CRACKING

Table 9.1 summarizes environmental alloy combinations that have been shown to produce SCC. The test temperature accelerates the SCC for most of the systems listed in Table 9.1. Electrochemical methods and stress corrosion tests should be performed to evaluate possible corrosion environments for a given alloy. More information on these and additional systems may be found in the ASM Metals Handbook [30]. Other significant alloys include nickel alloys [31], austenitic stainless steel [30], carbon steels [32], copper alloys [33], ferritic, martensitic, duplex [31,32], titanium alloys [33], and aluminum alloys [34].

9.5 SCC MODELS

Numerous SCC mechanisms have been proposed specific to certain alloys in specific environments. An excellent review written by Newman [35] is recommended for additional information on different stress corrosion mechanism. There is no universal model that explains various mechanisms proposed for SCC because of the inconsistency in SCC

Table 9.1 Environment-Alloy-Environment Combinations that Produce SCC

Alloy	Environment	Temp.
Nickel-Cr-Fe Alloys 600, 800, 690	Caustic alkaline solution	315 °C
	Polythionic acids and thiosulfate solutions, sensitized alloys with excess carbon	RT
	High-temperature chloride solution; DO, H_2S, free sulfur	>205 °C
Ni-Cu Monel Alloy 400	Acidic fluoride solutions, H_2S, hydrofluosilicic acid	RT
Nickel Alloy 200, 201	Caustic alkaline solutions, fused caustic soda	290 °C
Carbon steels	Caustic NaOH solutions	>50 °C
	$NaOH$-$NaSiO_2$ solutions carbonates	>255 °C
	Calcium, ammonium and sodium nitrate solutions	Boiling
	Mixed acids (H_2SO_4-HNO_3), acidic H_2S solutions, seawater, anhydrous liquid ammonia, amine, HCN solutions, acidified	RT
Austenitic stainless steels	Hot acid chloride solutions such as $MgCl_2$ and $BaCl_2$	60-200 °C
	$NaCl$-H_2O_2 solutions, neutral halides: Br-, I-, F-, seawater, alkaline $CaCl_2$, sulfuric acid acid	
	Concentrated caustic solutions	>120 °C
	$NaOH$-H_2S solutions, condensing steam from chloride waters	
	For sensitized alloys:	
	Polythionic acids ($H_2S_nO_6$), sulfurous acid	RT
	Pressurized hot water containing 2 ppm DO	300 °C
Ferritic stainless steels	NH_4Cl, NH_4NO_3, hypochlorite, H_2S,	
DSSs	Susceptible to same environments as austenitic stainless steels but more corrosion resistant	
Martensitic stainless steel	Caustic NaOH solutions. Susceptible to HE	
Al alloys	Chlorides, moist air, sea water and water vapor, $NaCl$-H_2O_2, caustic soda	RT
Mg alloys	Chloride-chromate mixtures, moist air, nitric acid, fluorides, sodium hydroxide, coastal atmospheres	RT
Gold alloys	$FeCl_3$ solutions, acetic acid-salt solutions	RT
Ti alloys	Halides, methanol, red fuming nitric acid, N_2O_4, HCl, meatnol	RT
Cu alloys	Ammonia vapors, moist air, moist sulfur dioxide amines, water vapor, nitrate solutions	RT

data. The electrochemical methods used to study the SCC mechanism assume that the passive film present on the surface of engineering alloys breaks, resulting in the formation of anodic sites. Similar to pitting corrosion, both the anodic dissolution of the metal at the bottom of the crack and the repassivation rate control the crack advancement. It is generally assumed that the chemical or mechanical breakdown of the passive film is the first

step of initiation of SCC [36]. It has been reported that bound water, which occupies active sites for corrosion, initiates pitting corrosion [37]. Zhang *et al.* [38,39] suggested that the same model could be applied to explain the inhibition and acceleration of anions [38] and cations [39] for the initiation of SCC.

Based on the proposed band structure model, Rangel *et al.* [40] found that the susceptibility of 304 stainless steel to SCC in boiling chloride containing aqueous solution is caused by local changes of the semiconducting properties of the passive film in the potential region close to the flat band potential. In the conduction band, only the cathodic processes are controlled by the applied potential. In the valence band, voltage controls the anodic processes [41]. In the case of stainless steel under SCC conditions, the cracking failure is controlled by the space charges formed in annealed and cold worked regions of the sample. However, it is still unclear how the corrosion potential, flat band potential, and susceptibility to SCC are interrelated. The following mechanisms have been proposed for SCC: film rupture-slip dissolution (FRSD) [42,43], film-induced cleavage (FIC) [44], localized surface plasticity (LSP) [45], atomic surface mobility (ASM) [46,47], and HE.

9.5.1 Film rupture model

Logan [42] suggested a film rupture or slip-step dissolution model for SCC mechanism where the crack is initiated by localized anodic dissolution. This mechanism postulates that plastic strain in the metal at the crack tip causes a fracture of the oxide barrier film. The film rupture model (FRM) assumes a repetitive, cycling process of film rupture, dissolution of the underlying metal, and repassivation.

The relationship between crack propagation, da/dN, on K_I during SCC on precracked specimens has been investigated using fracture mechanics [8,9]. The film rupture corrosion model was used to evaluate the materials crack propagation properties. According to Parkins [48–50], the frequency of the passive film rupture (PFR) is controlled by the strain rate, while the crack growth velocity is correlated to the anodic current density on the metal surfaces. Charge-transfer reactions may initiate the mechanical cracking process and crack growth. Forty and Humble [51] observed that the crack growth occurs discontinuously, resulting in periodic crack arrests and surface markings. However, electrochemical crack growth would result in a smooth increase of the crack length [52]. Other models, such as the slip dissolution-repassivation model [53], slip dissolution model [54], slip oxidation mechanism [55], film rupture mechanism [56], and a new film rupture and repassivation model [57] were used to explain the FRM.

The inconsistency of FRM of SCC from a mechanistic and quantitative standpoint is addressed by Gutman [58]. Since slip dissolution develops without any films, it is not applicable to FRM because the brittle films may or may not break under conditions of small strain before the underlying metal's yield. Furthermore, FRM does not contain

parameters of slip dissolution. It could be applied to loadings of a whole sample below the yield stress only when the fracture strain is smaller than the elastic limit of the metal. This phenomenon is only observed for brittle oxide films present on the metal surface [56]. FRM and other suggested models contain fundamental inconsistencies because they do not take into account the slip parameters and stress tensor components. The stress intensity coefficient is a function of the stress and the crack length. Thus, a single mechanism cannot be used to explain the whole range of stress corrosion processes [58]. Because FRM is based on a real physical phenomenon, it also contains a fundamental deficiency. It does not take into account both the role of stress to the supply of strain rate that ruptures the surface oxide film and the mechanochemical effect in acceleration of metal dissolution [58].

9.5.2 Fracture-induced cleavage model

Edeleanu *et al.* [44] suggested the FIC model to explain that the dezincification of α-brass in an ammonia solution could initiate a fracture of the substrate with lengths of a few micrometers. According to the authors, the cracked material was embrittled by short-range ordering. The crack-jumping phenomenon was confirmed by Pugh using scanning electron microscopy [59]. Anodic dissolution of the metal is necessary to form the brittle surface film. The model explains the observed discontinuous transgranular crack growth through the presence of brittle surface films. When the crack reaches sufficient velocity at the passive film/metal interface, it propagates into the metal followed by crack arrest and reformation of the passive film before a new brittle crack burst occurs. Thus, in FIC, anodic current creates a condition for the formation of brittle film followed by a discontinuous brittle cracking.

Later, Sieradzki and Newman [60] proposed the FIC mechanism to explain high transgranular CGRs and discontinuous transgranular crack growth. When a brittle film coats a ductile material, a crack could be initiated in that film that propagates into the ductile material for a short distance before ductile blunting arrests the crack growth. Dealloyed layers in brass cause the formation of brittle films that trigger FIC. When the brittle film is formed by a corrosion reaction, the process is repeated by reforming on the blunted crack tip. The FIC process is expected to give a transgranular fracture. Figure 9.17 shows a crack growth by FIC in a face-centered cubic metal [59].

9.5.3 Localized surface plasticity model

The LSP mechanism proposes that SCC results from the effect of the structure ahead of the crack tip [61]. This mechanism assumes that a galvanic corrosion between active sites (weakened passive site) and surrounding passive surfaces produces large anodic currents at the rupture site. Repassivation of the active sites is prevented by the presence of weakened passive films on the surface. It has been suggested that the weakened passive film

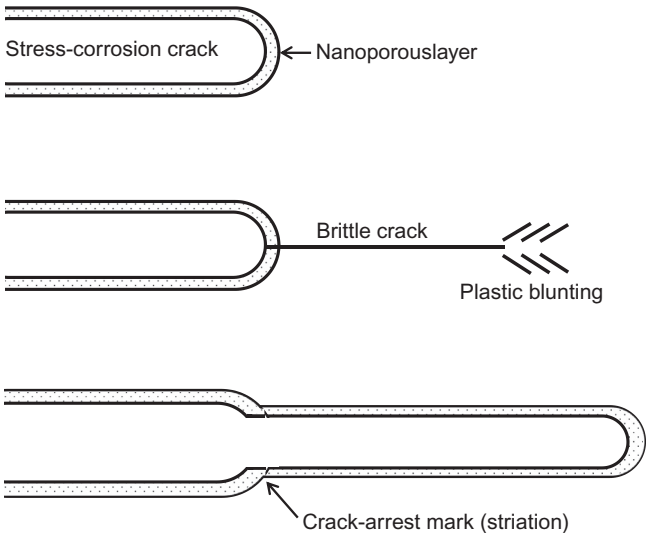

Fig. 9.17 Crack growth by FIC [59]. *Reproduced, with kind permission, from Springer Science+Business Media B.V.*

exists at critical passivation potentials near the interface of the passive film. The high-density anodic currents form a defect structure due to a small anodic surface area, which becomes a rupture site. The softened structure of the rupture sites plastically deforms on the microscopic volume ahead of the crack. This process is enhanced by the presence of surrounding passive material, which possesses high hardness. Softened and constrained crack tip volume creates a triaxial stress state that results in the propagation of brittle crack [61].

Forty and Humble [51] suggested the presence of vacancy-saturated defect structure modes. According to this model, the vacancies are injected into the crack during anodic dissolution of the alloy caused by galvanic corrosion. These vacancies create conditions for the formation of a crack structure that may initiate SCC of brass. Revie and Uhlig [62] found that vacancies were causing increased creep by the galvanic anodic reactions.

9.5.4 Atomic surface mobility model

Figure 9.18 shows Galvele's ASM model [46,47]. The model predicts SCC in metals and has been also applied to liquid metal embrittlement. According to this model, the cracks grow by the surface diffusion of metals and ions from the crack tip to the crack walls. The mechanism predicts that the surface mobility atoms are enhanced by the presence of low-melting surface compounds compared to diffusion in the metal crystal. SCC occurs at temperatures below $0.5T_m$, where T_m is the melting point of the metal. The crack velocity, ν, in this model is given by:

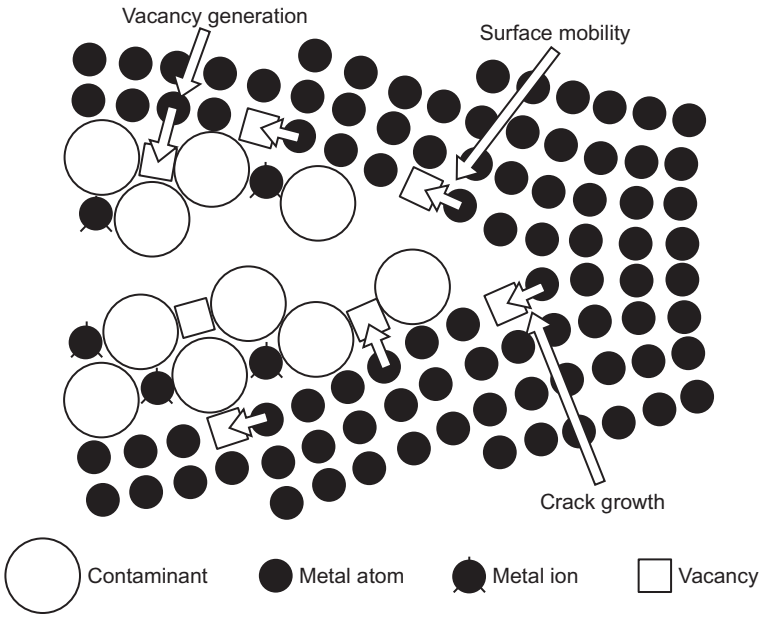

Fig. 9.18 Galvele's surface mobility model for SCC [46].

$$\nu = \frac{D_s}{L}\left(e^{\sigma a^3/kT} - 1\right) \tag{9.16}$$

where D_s is the surface self-diffusion coefficient, L is the diffusion length, σ is the surface stress in the lattice tips, and a^3 is the volume of the vacancy.

According to Sieradzki and Friedersdorf [63], the vacancy equilibrium concentration could be increased by normal stress. They suggested the following equation for the crack velocities that result from surface atom mobility:

$$\nu = \frac{D_s N_s \Omega^2}{kT}\frac{2}{\pi}\frac{1}{r^2}\left(\frac{\sigma_{\gamma\gamma}^2}{2E} - \gamma\kappa\right) \tag{9.17}$$

In Eq. (9.17), the chemical potential of the vacancy includes a capillary contribution $\frac{\gamma a^3}{r}$, where γ is surface energy and "r" is crack tip radius. N_s is the number of lattice sites/cm^2, Ω is the atomic volume (a^3), and $\kappa = 1/r$ represents curvature for the crack tip.

There is experimental evidence reported in the literature that carbon steel cracks in nitrates that form low melting compounds with iron; however, it also cracks when in contact with the high melting point magnetite [64]. Other experimental evidence provided by Oriani [65] shows that the flow of the surface atoms and ions is toward the crack tip instead of the crack walls. It has also been discussed in the literature whether there is enough force to drive diffusion of metals and the surface vacancy formation [45].

9.6 METALLURGY OF STRESS CORROSION CRACKING

SCC in alloys is controlled by solid solution composition, grain boundary segregation, alloy phase transformation, duplex structure, and cold work [66]. The cracks are normal to the tensile component of stress and exhibit little to no plastic deformation.

9.6.1 Solid solution composition

Solid solution composition plays an important role in SCC propagation. In many cases, the composition determines the nature of SCC in austenitic stainless steels [67]. In the case of brasses, dealloying controls the SCC mechanism [68].

Intergranular cracking proceeds along the grain boundaries whereas transgranular cracking does not have preferences for boundaries [69]. In the case of transgranular SCC, the cracks advanced across the specific crystal planes with low indices [70]. Intergranular stress corrosion cracking (IGSCC) is more common than transgranular SCC.

The mechanism for IGSCC of pipeline steels (APIX65) is based on the presence of hydroxyl ions at the steel/electrolyte interface, which are formed by the applied cathodic current to protect the structure [71]. The hydroxyl ions react with the dissolved CO_2 producing a complex carbonate-bicarbonate solution [72]. When the carbonate concentration in the electrolyte is sufficiently high to passivate the pipe surface, intergranular cracking occurs by the anodic dissolution mechanism [73]. The crack propagates due to the presence of plastic strain ahead of the crack tip and prevents the formation of the protective passive layer. Depending on the alloy and the corrosion environment, the cracks penetrate into the materials' microstructure as transgranular or intergranular morphology. Chloride SCC is intergranular corrosion and occurs in austenitic stainless steel; a great concern for the nuclear industry. This form of corrosion occurs at high temperature in the presence of chloride ions and oxygen. Stainless steel with a Ti/C ratio of 6.14 showed high tensile strength at the sensitization treatment. Pitting and intergranular corrosion resistance increased with the increase in Ti/C ratio. On the other hand, the tensile strength decreased with the increase in the Ti/C ratio in a solid solution. The reactivity of grain boundaries, disturbed areas at grain surfaces and deforming zones, increases with increasing solute content up to a maximum of 50% [74]. Susceptibility of nickel-based alloys to IG cracking increases due to the segregation of S, which reduces the grain boundary strength of the alloy [75]. Alloy composition changes the alloy properties such as hot cracking resistance, the microstructure and chemistry of the grain boundary, the ductility of the solidifying weld metal, the solidification temperature range, and the amount and distribution of liquid at the terminal stage of solidification [76,77].

Niobium, when added to Alloy 182, stabilizes the carbon content and prevents the precipitation of Cr carbides at the grain boundary [78]. C, P, Si, and S segregate or precipitate at the grain boundary and are critical to hot-cracking resistance of nickel-based weld metals [79]. When Si segregates at the grain boundaries of austenitic stainless steel,

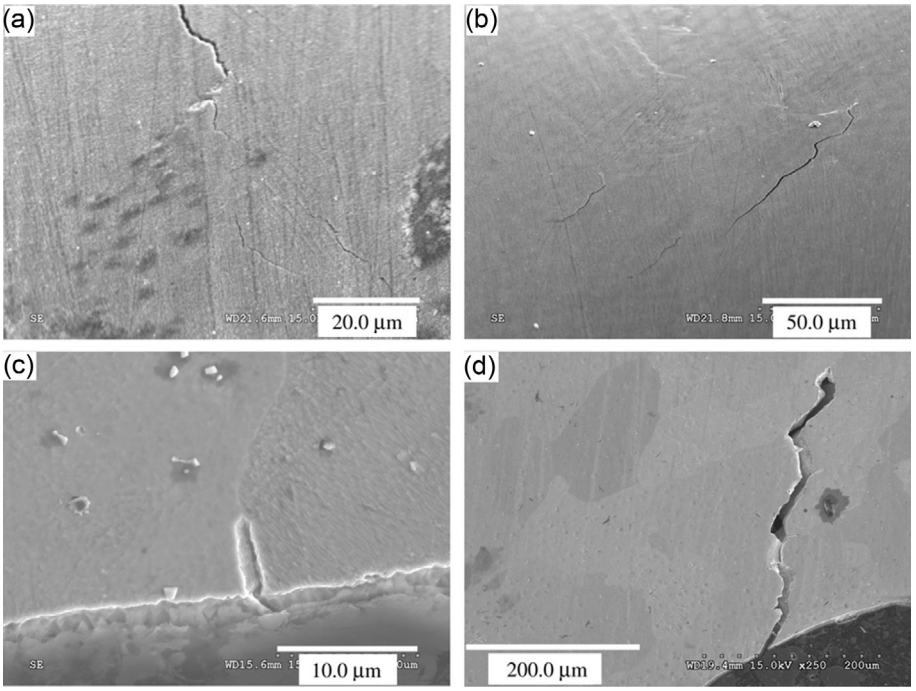

Fig. 9.19 SEM observations of SCC in Alloys 182-1 (a, c) and 182-2 (b, d). (a, b) observations on the surface and (c, d) observations on cross sections of the specimen [82].

IGSCC growth rate increases in high-temperature water [80]. Intergranular cracking resistance of the Alloy 182 reduces with precipitation of Cr-carbides due to Cr-depletion at the grain boundaries in high-temperature oxygenated water [81]. Peng *et al*. [82] investigated the effect of chemical composition on grain boundary microchemistry and SCC in Alloy 182-1 and Alloy 182-2. Alloy 182-1 has higher concentrations of P and Si than Alloy 182-2. The results indicated that Alloy 182-1 has a higher susceptibility to hot-cracking. However, this alloy showed a lower susceptibility to SCC in primary water than Alloy 182-2 (Fig. 9.19) [82]. The results are explained by the enhanced creep resistance of the grain boundary. Higher density of the precipitate at the grain boundary resulted in more tortuous grain boundaries and a stronger locking effect on grain boundary sliding [82].

9.6.2 Grain boundary segregation

The primary mechanism of SCC in the high strength 2xxx (Al-Cu-Mg) series has been suggested to be anodic dissolution associated with precipitates along the grain boundaries [83,84]. Galvanic corrosion between anodic particles with cathodic matrix surrounding causes dissolution of anodic particles [85–87]. Localized corrosion sites and cracks are

initiated by absorption of hydrogen into the aluminum alloy, which triggers HE and possible crack propagation [88].

Alloys are more susceptible to SCC than metal and susceptibility increases with the increase in the strength of the alloy. As mentioned earlier, intergranular cracking proceeds along the grain boundaries, whereas transgranular cracking does not have preferences for boundaries [69,89]. Effects of materials' yield strength on the threshold SCC, K_{ISCC} of LASs in aqueous environments was analyzed by Bulloch [90]. The increase in the yield strength in the range from 600 to 1200 MPa reduced the value of K_{ISCC}. SCC transgranular fracture was observed at yield strength values below 1200 MPa. Above this value, the fracture was intergranular in nature. The transition from transgranular to IGSCC coincided with the point at which the yield strength effects were reduced. Figure 9.20 shows yield strength-K_{ISCC} dependence of transgranular, intergranular, and mixed SCC transitions observed for LASs [90]. A sudden change in the fracture path occurred at approximately the yield strength value of 1300 MPa. The dependence of the yield stress on K_{ISCC} is explained by the HE mechanism. The critical concentration of hydrogen is governed by the yield strength, the initial hydrogen concentration, the temperature, and the stress state that controls the mechanism. When the equilibrium hydrogen concentration at the crack tip attains the critical concentration, the applied stress intensity is equal to K_{ISCC}.

Nair and Tien [91] explained the effects of yield strength on K_{ISCC} through hydrogen-induced fracture resulting from the plastic flow on a localized scale in the crack tip plastic zone. The suggested cause of SCC was isolated and unstable local fracture events in the crack plastic zone controlled by the local embrittlement due to adsorbed hydrogen [92].

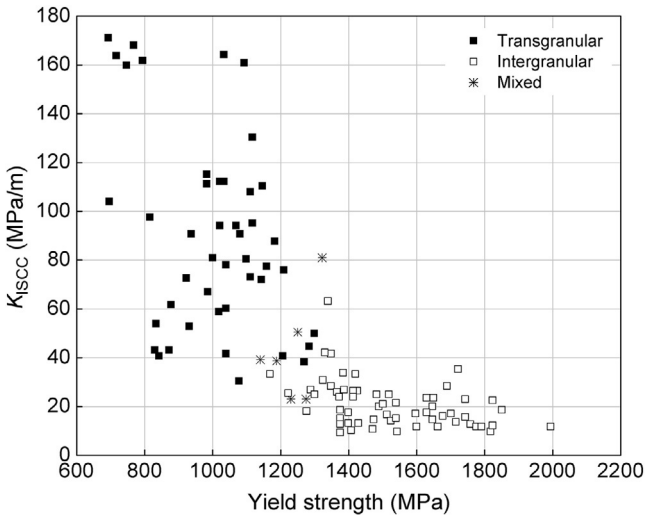

Fig. 9.20 Yield strength-K_{ISCC} dependence for LASs for transgranular, intergranular, and mixed SCC [90].

Thermal treatment of stainless steel produces grain boundary carbides and depletion of chromium from the grain boundaries, causing the alloy to become sensitized to intergranular corrosion. A sensitization diagram for type 304 stainless steel with various carbon compositions is shown in Fig. 9.21 [93].

Davidson *et al.* [93] investigated sensitization of 18 Cr-8Ni SS of varying carbon content. Sensitization is caused by chromium depletion and carbide formation at high temperatures. Precipitation of carbides is facilitated by the presence of Ni in the alloy, which increases the activity of carbon in solid solution. The as-received and sensitized austenitic stainless steels showed susceptibility to stress corrosion in boiling aqueous 45 wt.% $MgCl_2$ solution. The mean values of the stress corrosion intensity limit factor, K_{ISCC}, for not treated and treated steels were 15 MPa $\sqrt{m}$ and 7.8 MPa $\sqrt{m}$ respectively. Propagation of the main crack was transgranular in the as-received stainless steel, and an intergranular mode of failure in the sensitized stainless steel is shown in Fig. 9.22 [94]. Propagation of the main crack was transgranular in the as-received stainless steel and an intergranular mode of failure in the sensitized stainless steel. The crack propagation rate curves as a function of the stress intensity of as-received steel in 45 wt.% $MgCl_2$ at 154 °C are shown in Fig. 9.23 [94].

IGSCC or intergranular attack occurs in many alloy systems due to the segregation of reactive impurities or depletion of chromium at the grain boundaries. The corrosion at the grain boundaries or in adjacent regions could be very severe, causing drop grains out of the surface. The IGSCC of heat-treated austenitic steels enhances as a result of the precipitation of chromium carbides ($Cr_{23}C_6$) in the grain boundaries, depleting the grain

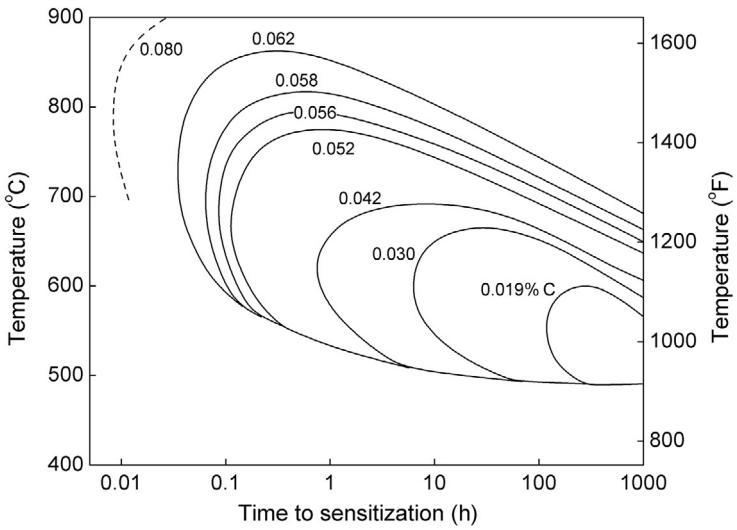

Fig. 9.21 Sensitization diagram for 18Cr-8Ni SS of varying carbon content [93]. *Reprinted with permission of ASM International, Materials Park, OH. www.asminternational.org.*

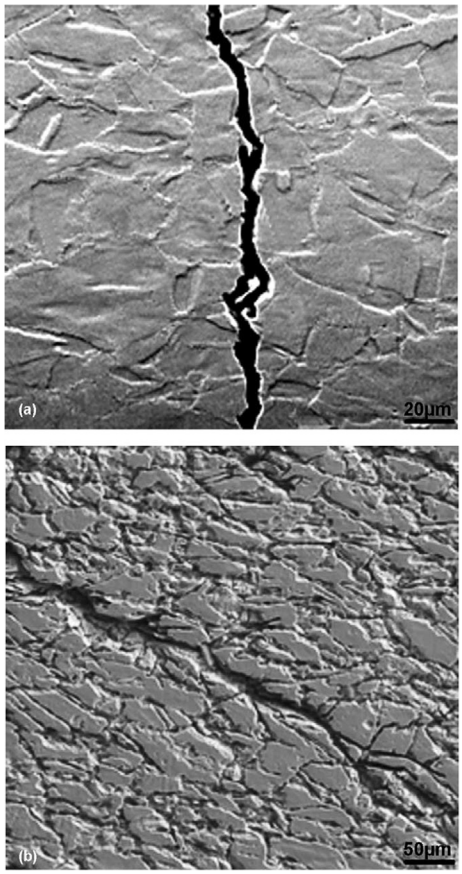

Fig. 9.22 SEM micrograph showing crack propagation modes (a) in as-received stainless steel and (b) in sensitized stainless steel [94].

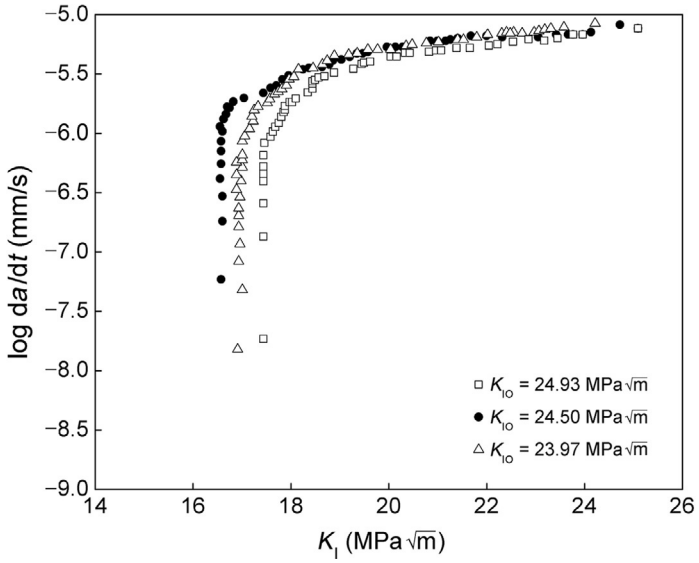

Fig. 9.23 Crack propagation rate curves as a function of the stress intensity of as-received steel in 45 wt.% $MgCl_2$ at 154 °C [94].

boundary and adjacent regions of chromium. The alloys corrode at high rates when chromium is depleted below 10% in the alloy. When the carbide distribution is widely spread in the alloy, the susceptibility of the material to SCC decreases [95].

Figure 9.24 shows an illustration of carbide precipitation at the grain boundary during sensitization in the temperature range of 425-815 °C resulting in intergranular corrosion in stainless steel. In a BWR corrosion environment, the austenitic type 304 stainless steel and Alloy 600 wrought exhibit IGSCC by a range of mechanisms. IGSCC was observed in weld-sensitized stainless steel, in piping, and cold work components such as nozzles [45]. According to Horn *et al.* [96], highly oxidizing environments contribute IGSCC over time in BWR plants. The experimental analysis indicated that the mechanisms that trigger SCC are thermal aging-induced grain boundary segregation, surface cold work, and highly oxidizing environment. Figure 9.25 shows cold work at the crack initiation site [96]. The cracking occurs in all of the stainless steel shroud weld HAZs.

Nishimura *et al.* [97] investigated the SCC of a commercial austenitic stainless steel type 316 as a function of the sensitizing temperature (750-1300 K) and test temperature (333-373 K) in 0.82 kmol/m^3 hydrochloric acid solution using a constant load method. The results indicated that the steady state elongation rate i_{ss} can be used to predict the time interval of SCC-dominated failure, t_f. In the SCC-dominated region, the logarithm of i_{ss} was a linear function of the logarithms of t_f irrespective of test temperature or applied stress. However, the slope was found to depend on the sensitizing temperature. At a

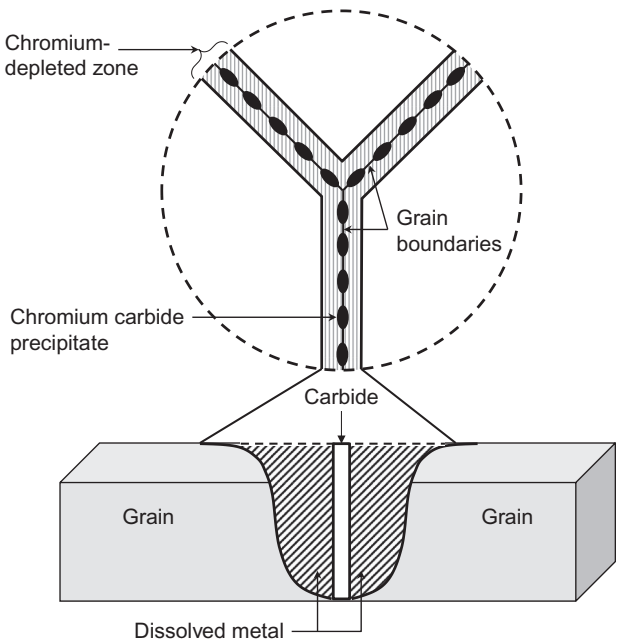

Fig. 9.24 Illustration of carbide precipitation at the grain boundary during sensitization to IGC in stainless steel.

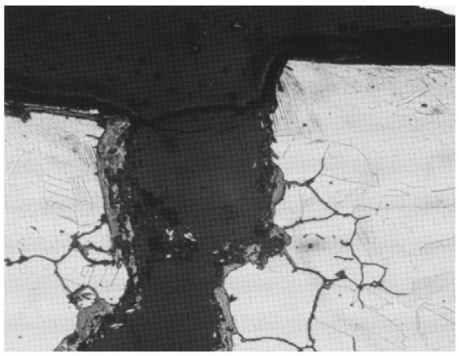

Fig. 9.25 Surface of IGSCC initiation showing the cold work layer and heavy oxides at the crack mouth [96].

sensitizing temperature of approximately 1000 K, the slope of log i_{ss} vs. log t_f showed a minimum (the value of $\frac{t_{ss}}{t_f}$ was at maximum), and the fracture appearance was an IGSCC mechanism.

Figure 9.26 shows maximum and minimum stress (σ_{max} and σ_{min}) in the SCC region as a function of sensitizing temperature [97]. Triangle symbols stand for solution-annealed samples. The maximum stress becomes larger than the solution-annealed samples in the sensitizing temperature range of 750-1250 K and exhibit a maximum at approximately 1000 K. The minimum stress was constant and independent of the sensitizing temperature. The increase of the maximum stress was related to the ultimate tensile strength.

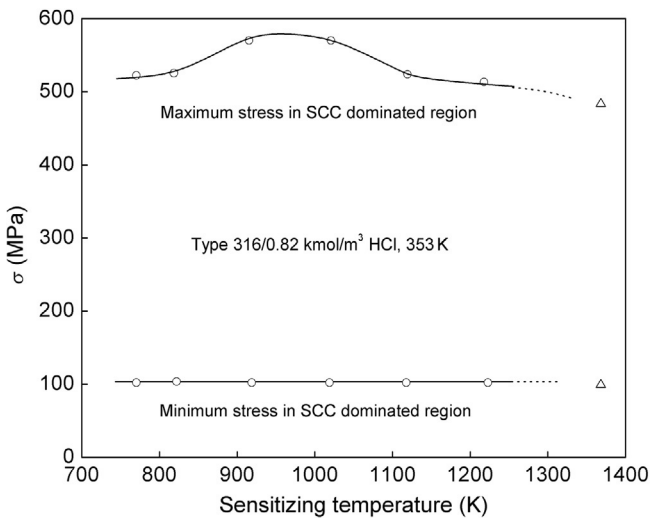

Fig. 9.26 Maximum and minimum stress (σ_{max} and σ_{min}) in the SCC region as a function of sensitizing temperature [97].

Figure 9.27 shows the relation between the values of $\frac{t_{ss}}{t_f}$ and sensitizing temperature [97]. The value of $\frac{t_{ss}}{t_f}t_s$ becomes larger than that for the solution-annealed specimens in the sensitizing temperature range of 750–1250 K. The maximum is observed at a sensitizing temperature of approximately 1000 K, corresponding to that of maximum stress as shown in Fig. 9.27.

Transgranular cracking occurs on copper in sodium nitrate [98] and on iron in anhydrous ammonia [99]. Carbon and LAS are used for piping and pressure vessels in nuclear light water and fossil reactors. Environmentally-assisted cracking (EAC) occurs in BWR in LAS piping. EAC is transgranular in nature and has been observed in weld HAZs in weld-affected zones [100,101]. The corrosion mechanism of EAC is based on oxidizing conditions due to the presence of oxygen, dynamic straining, high local stress in the range of high-temperature yield strength, pitting corrosion during shutdown periods, and secondary/residual stress (welding defects) [100,102]. Hiroki *et al.* [103] observed that, when stress was applied parallel to the elongated grains, the stress perpendicular to the grain boundary was low. The SCC resistance is improved when the applied stress perpendicular to the grain boundary is small. The SCC resistance is high for the alloys having fiber-like grain elongated in the extrusion direction because the stress is distributed along the length of the grain. However, the elongation of grain size increases the frequency of stacking fault, which in turn decreases the SCC resistance. The reduction in random boundaries due to higher structural order improves the resistance to SCC.

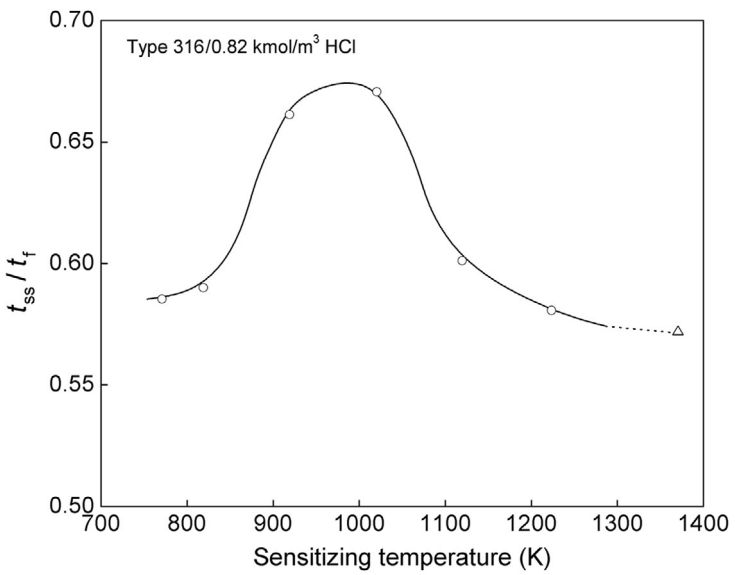

Fig. 9.27 Relation between the values of t_{ss}/t and the sensitizing temperature [97].

9.6.3 Alloy phase transformation and associated solute depleted zones

The phase formed at the alloy-grain boundary controls the reactivity of the alloy or could enhance the reactivity of associated solute-depleted zone [104]. Aerospace alloy's (Al-Zn-Mg) susceptibility to SCC increases with increasing Cu content in the alloy. Commercial aluminum 5000-series, Al-Mg (3-6 wt.%) alloys exhibit excellent resistance to corrosion, weldability, formability, and a high strength to weight ratio [105]. However, at elevated temperatures (50-200 °C), these alloys are susceptible to intergranular corrosion and SCC [106]. The susceptibility to SCC results from the formation of the grain boundary, α-phase Al_3Mg_2, anodic to the Al matrix [107,108]. Exposure of Al-Mg-based alloys to seawater results in corrosion and structural failure due to the anodic dissolution of the grain boundary phase. Yukawa *et al*. [109] found that the formation of a Mg-depleted region closer to the three-phase grain boundary results in the increase of the alloy's SCC susceptibility. β-phase has also been observed to nucleate and grow intragranularly in the Al-Mg alloys [110,111].

The aerospace alloy Al-Zn-Mg 7000 series becomes susceptible to SCC when alloyed with Cu. The segregation of Cu and precipitation of grain boundary phases that contain Cu (noble region) result in pitting corrosion triggered by galvanic corrosion with adjacent Cu depleted anodic regions. The effect of thermomechanical treatment on the corrosion of AA5083 showed superior corrosion resentence compared to the as-received samples. Precipitates such as Al-(Fe,Si,Mn,Cr), Al-13Fe_4, Al_6(Fe,Mn), and Mg_2Si, together with the β-phase after sensitization were identified using SEM, EDS, and TEM. Dislocation networks showed better corrosion resistance than the matrix [112].

Complex α/β/κ nickel-aluminum bronzes are susceptible to cracking in natural sea water in monotonic strain rate or cyclic loading tests near the corrosion potential [113]. Increasing strain rates from 10^{-8} to 10^{-6} s^{-1} appeared to decrease the threshold stress for cracking [114]. Addition of nickel and iron in copper-aluminum alloys solidifies as a "high temperature β-phase" alloy, which contains precipitates of iron-rich particles named κ_I. The β-phase transforms to α-phase in the case of slow cooling. Globular κ_{II} (principally iron) and lamellar κ_{III} (nickel-base) precipitate at the grain boundaries. Iron-rich κ_{IV} is formed in the α-grains at lower temperatures [114]. High temperature β-phase is retained as martensitic structure in the case of slow cooling. The so-called tempered-martensite, a mixture of α and κ-phases with Ni-Al precipitates, can be synthesized with a tempering treatment of martensitic structure at approximately 600 °C for 2-5 h. The role of the second phase in the SCC of a $CuAl_9Ni_3Fe_2$ bronze in saline water was investigated using an SSRT test [115]. Cracking was mainly intergranular and was controlled by the morphology of the alloy microstructure (the electrochemical interaction between α-matrix and the second phases). SCC susceptibility increases with the amount of second phase in the grain boundaries. Selective dissolution of aluminum was observed reaching areas due to galvanic corrosion (aluminum is anodic with respect

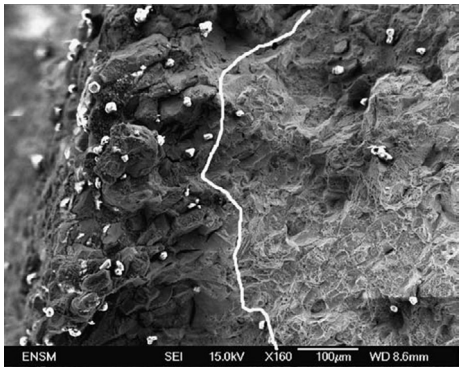

Fig. 9.28 Intergranular fracture surface of a sample with martensitic second phase at open circuit potential. The extent of the brittle zone is delimited by the line [115].

to the α-matrix). Cathodic polarization was found to enhance the detrimental effect on the mechanical properties by decreasing the number of cracks. Figure 9.28 shows the intergranular fracture surface of a sample with martensitic second phase at open circuit potential [115]. The extent of the brittle zone is delimited by the line. In Fig. 9.29, the cracks are transcrystalline in the martensite or along the interface between the martensite and α-grains [115]. The microcracks are initiated by the dissolution of particles, which contain high aluminum concentration. Figure 9.30 shows the preferential dissolution of the aluminum-rich areas (in dark) within the martensite [115].

In the case of cathodically protected samples, there is no superficial attack and cracks were not observed. The sample has brittle surface with precipitates and porosity on the facets of the α-grains, as shown in Fig. 9.31 [115]. Only one transgranular fracture in the martensite is observed in the upper part of the micrograph. The porous areas were formed

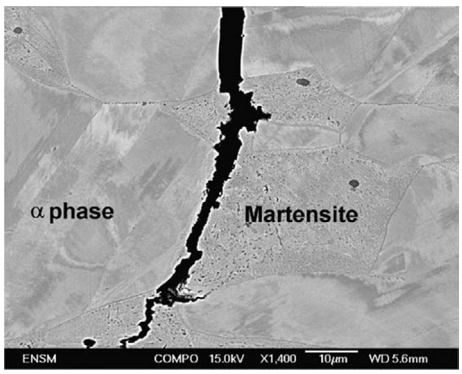

Fig. 9.29 Microsection of a failed sample with martensitic second phase. Sample tested at free potential. Note the crack path following the α/martensite interface or crossing through the martensite [115].

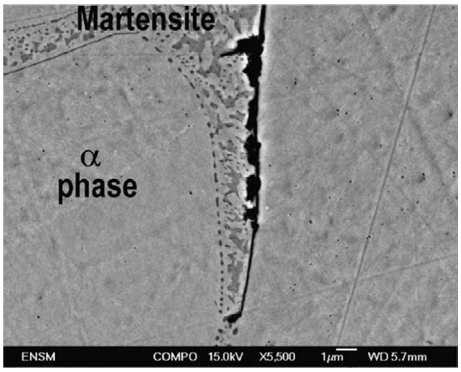

Fig. 9.30 Microsection of a crack showing the preferential dissolution of the aluminum-rich areas (in dark) within the martensite [115].

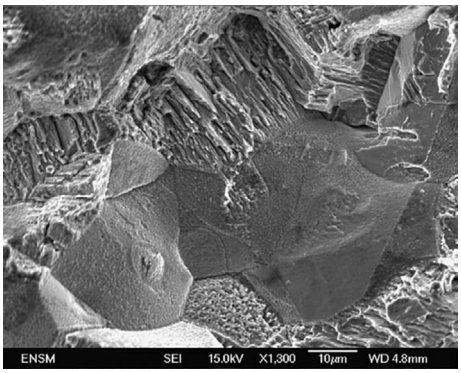

Fig. 9.31 Fracture surface of a specimen with a martensitic second phase tested under cathodic protection at −650 mV vs. SCE [115].

due to the removal of NiAl (dissolution of Al-rich areas) and κ-phase precipitates from the martensite. The upper part of the micrograph shows a transgranular fracture in the martensite. Precipitates and porosity are observed on the facets of the α-grain.

A201 aluminum alloy, Al-4.6Cu-0.3Mg-0.6Ag, is a high-strength as-cast alloy that is strengthened by Ω and θ phases. SCC susceptibility of various Ag-containing Al-4.6Cu-0.3Mg alloys in a 3.5% NaCl solution indicated that continuous grain boundary precipitations and the high Ag-concentration alloy and high density of the Ω and θ phases caused a susceptibility to high SCC [116].

Ishibashi *et al*. [117] experimentally proved that grain boundary character distribution (GBCD) controls suppressed IGSCC initiation or propagation. The cracks were predominantly propagated along the random grain boundaries. The experimental data indicated that induced lower coincidence site lattice (CSL) boundaries result in high resistance to IGSCC. The GBCD explains the distribution uniformity of CSL boundaries

and boundary network in a material. Shimada *et al.* [118] suggested that GBCD of a material can be improved by slight prestrain annealing at a relatively low temperature. The optimum distribution is formed by the introduction of low energy segments on migrating random boundaries during boundary-boundary reactions in the grain growth without generating new random boundaries.

9.6.4 Duplex structures

Alloy microstructures with two phases in comparable ratios are defined as duplex structures. Duplex structures combine strength, show low susceptibility to SCC, and good microstructural control when welded [119]. DSSs possess high value of threshold stress intensity K_{th}. The DSSs that contain ferrite and austenite phases have better localized corrosion resistance than single-phase austenitic stainless steels in chloride-containing solution and are used as structural materials in petrochemical, chemical, pulp and paper, power generation, oil, and gas industries.

Solomon and Devine [120] defines DSS as a Fe-Cr-Ni alloy that has a two-phase structure, both phases being above 30% in volume fraction. The alloy's mechanical property and corrosion resistance are dependent upon the proper austenite-ferrite balance, approximately 1:1, and high Cr-content together with the high Mo and N contents [121]. During welding process, the austenite to ferrite ratio may change with precipitation of intermetallic compounds such as χ-phase, σ-phase, γ_2-phase, $Cr_{23}C_6$, and Cr_2N [122]. These changes reduce the ductility, toughness, and the corrosion resistance of the alloy [123]. Nitrogen improves the mechanical and corrosion properties and increases the strength of DSS [124,125]. Nitrogen also improves the passivation properties of DSS by increasing the pitting potential and facilitates the repassivation process on the alloy surface [126].

Liou *et al.* [127] studied the effects of nitrogen content and cooling rate on the reformation of austenite in the Gleeble simulated HAZ of 2205DSSs. SCC behavior in the HAZ of 40 wt.% $CaCl_2$ solution was investigated at 100 °C. Grain boundary austenite (GBA), Widmanstatten austenite (WA), intergranular austenite (IGA), and partially transformed austenite were present in the HAZ. The pitting corrosion and selective dissolution was suggested to assist the crack initiation in the HAZ of DSSs. The presence of WA and IGA has a beneficial effect on SCC resistance. IGSCC was found in the HAZ when GBA was present. The transformation from IGSCC to TGSCC occurred as GBA was gradually replaced by WA or IGA. The types and amounts of reformed austenite in the HAZ that control the mode of crack propagation depends on the nitrogen content in the DSS and the cooling rate. The presence of GBA was found to promote intergranular corrosion cracking. The SCC resistance of the HAZ was found to increase with increasing nitrogen content in the DSS, and it increases with decreasing cooling rate. Figure 9.32 shows the SEM of SCC cracking resulting from the cross-link of pitting and U-bend test

Fig. 9.32 SEM showing SCC crack resulting from cross-link of pit, U-bend test, *t*, for an HAZ DSS in 40 wt.% $CaCl_2$ solution [127].

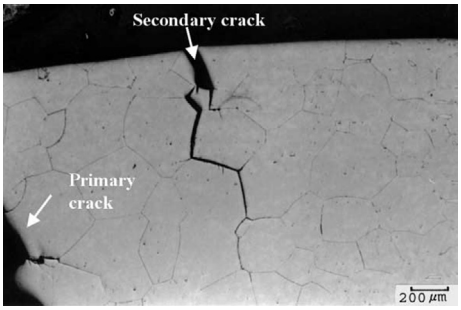

Fig. 9.33 The cross-sectioned crack propagation path in the HAZ of 0.096 wt.% DSS after SCC testing in the 40 wt.% $CaCl_2$ solution [127].

for an HAZ DSS in 40 wt.% $CaCl_2$ solution [127]. The pits were formed on the surface with microfissures induced in the vicinity of pits that cross-linked. This indicated that pitting-assisted SCC controls the fracture at the HAZ of DSS.

The types and amounts of the reformed austenites in the HAZ depended on the nitrogen content in the DSS and the cooling rate employed. The SCC resistance in the HAZ was higher than that of the solution-annealed DSS. SCC susceptibility of the HAZ in 40 wt.% $CaCl_2$ solution at 100 °C decreased as the amount of reformed austenite increased. The cross-section crack propagation path of a secondary crack in simulated HAZ of DSS with 0.096 wt.% N in 40 wt.% $CaCl_2$ solution at 100 °C is shown in the Fig. 9.33 [127]. In the early stage, the crack propagated in a transgranular manner followed by IGSCC in the latter stage. The crack initiation was not confined to the grain boundary, besides the fact that the crack might have propagated intergranularly.

Figure 9.34 shows the time of failure of the HAZ as a function of austenite content [127]. The testing was performed using the U-bend test in 40% $CaCl_2$ solution

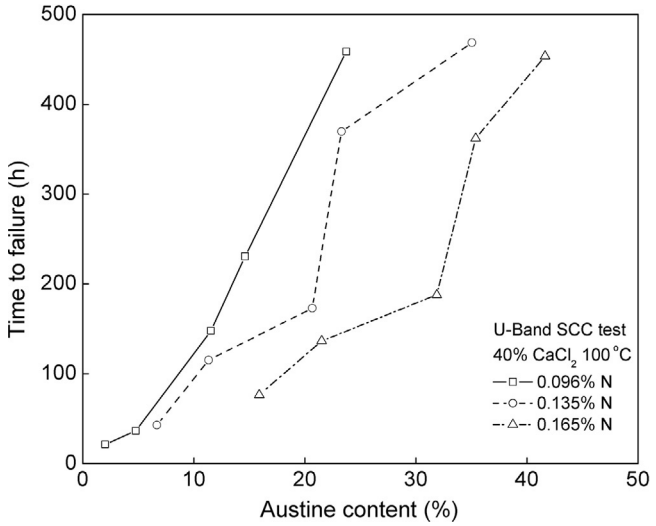

Fig. 9.34 Effect of austenite content on the time-to-failure in 40 wt.% $CaCl_2$ solution (100 °C) of solution-annealed matrix and simulated HAZs with various nitrogen contents of DSSs [127].

at 100 °C. The results indicated that the time to failure increased with increasing austenite content. Because the quantity of Cr_2N decreased with increasing austenite content in the HAZ, the authors suggested that the SCC susceptibility of the HAZ increased with increasing Cr_2N precipitation.

The SCC susceptibility of Alloy 690 in 0.01 M $Na_2S_2O_3$ has been investigated using SSRT tests. The alloy was solution-annealed at 1100 °C and water quenched, followed by sensitization at 700 °C for 5, 12, 24, 36, 48, and 72 h [128]. The maximum susceptibility toward corrosion was associated with the chromium-depleted zone along the grain boundaries. Consumption of carbon during sensitization resulted in chromium diffusion in the depleted zone, recovering resistance to SCC. The observed increase of the alloy resistance to SCC is due to the presence of a continuous network of grain boundary carbides in the specimen sensitized for 72 h. The susceptibility of intergranular attack and SCC increased with sensitization time with a maximum observed after 48 h at 700 °C.

The role of addition of nitrite ions on the susceptibility of a super DSS, SAF 2507, to SCC was investigated in a chloride environment [129]. The testing was performed using SSRT tests in 30 wt.% $MgCl_2$ solution. At lower concentrations, nitrate additions decrease the susceptibility to SCC. At higher concentrations, it has an accelerating effect on SCC. In Fig. 9.35, the ratios of t_f(corrosion)/t_f(inert) in chloride solutions (with different levels of NO_2^-) and in paraffin oil (inert) has been plotted against the (NO_2^-) content [129].

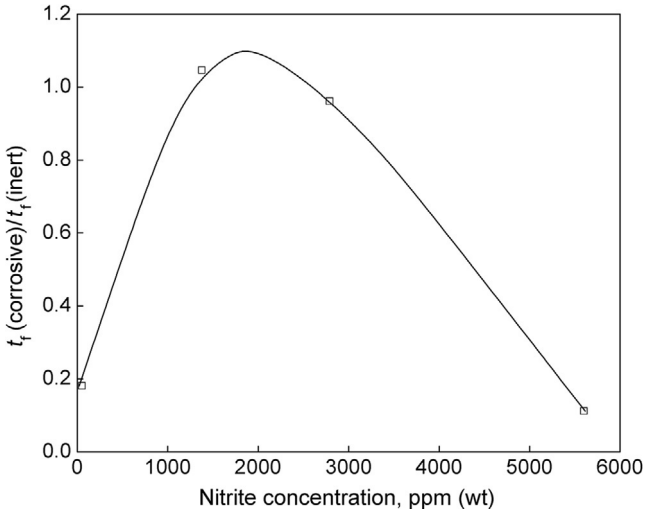

Fig. 9.35 SCC susceptibility (expressed as ratios of time to failure (t_f) in chloride solutions and in paraffin oil) as a function of the (NO_2^-) content [129].

9.6.5 Cold work

High mechanical stress is applied in cold work to the metal through a process called work-hardening or strain-hardening. This causes plastic deformation and permanent change in the crystalline structure. The cold work reduces the ductility of the metal while increasing its yield strength and hardness. As the metal becomes less ductile, the probability of the metal to fracture becomes higher when compared to bending if subjected to high stress. The most common cold working method is cold rolling. In this method, the metal is squeezed through narrow gaps between rotating rolls causing deformation by compressing the material. The metal also may be shaped by cold forging by pressing it into a die with a hammer. Cold heading is used to produce bolts and other fasteners.

Nickel-based alloys used in nuclear plants are susceptible to EAC. IGSCC of Alloy 600 was the main failure observed for the SG tubes. Yield strength and the degree of cold work were found to affect the primary water reactors stress corrosion cracking (PWSCC) behavior [130–133]. The effect of cold work on the PWSCC growth behavior of Alloy 600 was investigated using both bolt-loaded and actively loaded fracture mechanics specimens. SCC growth rates of prior-deformed Alloy 600 materials were studied in a simulated pressurized water reactor (PWR) primary water environment. Prestraining and cold rolling were used to increase the yield strength of Alloy 600. The alloy was treated by welding or cold working. The Vickers hardness of Alloy 600 weld HAZs and in the worked (CW) Alloy 600 was higher than that of the base metal. Electron backscatter diffraction results show significant plastic strains in the alloy

materials. The cold work and the crack growth orientation had a significant effect on CGR. Generally CGR increased with increasing the degree of cold work or yield strength (YS) [134]. The HAZ of Alloy 600, 8% and 20% CW Alloy 600 specimens showed extensive IGSCC in the Alloy 600. The 20% CW Alloy 600 exhibited higher CGR than 40% CW Alloy 600. The CGR in the Alloy 600 HAZ was similar to that in the 8% CW base metal. However it is much higher than the as-received base metal. Figure 9.36 shows the dependence of the crack growth with testing time for 20% CW and 40% CW Alloy 600MA materials [134]. During the SCC tests, CGR was relatively constant in these two materials, indicating that the crack growth estimated by dividing the total crack growth by the total SCC rest time is close to the steady state growth rate. The fracture surfaces after SCC in simulated PWR water at 320° are shown in Figs. 9.37 and 9.38 [134]. The facture surface of 20% Alloy 600 HAZ shows extensive IGSCC. The fracture of 40% CW Alloy 600 shows mixed intergranular-transgranular SCC with local IGSCC secondary cracks.

The effect of cold work on Alloy 600 susceptibility to IGSCC has been studied in low dissolved oxygen (DO) PWRs environments [135]. Cold work does not have a large effect on the increase of SCC velocity. However, it reduces the alloy ductility, the fracture toughness, and the threshold stress intensity. Moderate amounts of cold work are more detrimental than severe amounts of cold work. The CGRs are increased by one order of magnitude from only 5% cold work. Because the cold work increases the yield strength of the material, an effect similar to that of cold work on CGRs is also observed

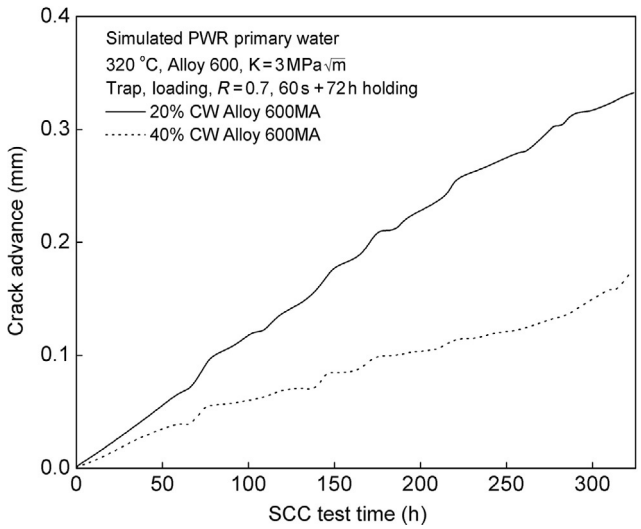

Fig. 9.36 The crack length as a function of SCC test time for 20% and 40% CW Alloy 600 materials in a simulated PWR primary water at 320 °C [134].

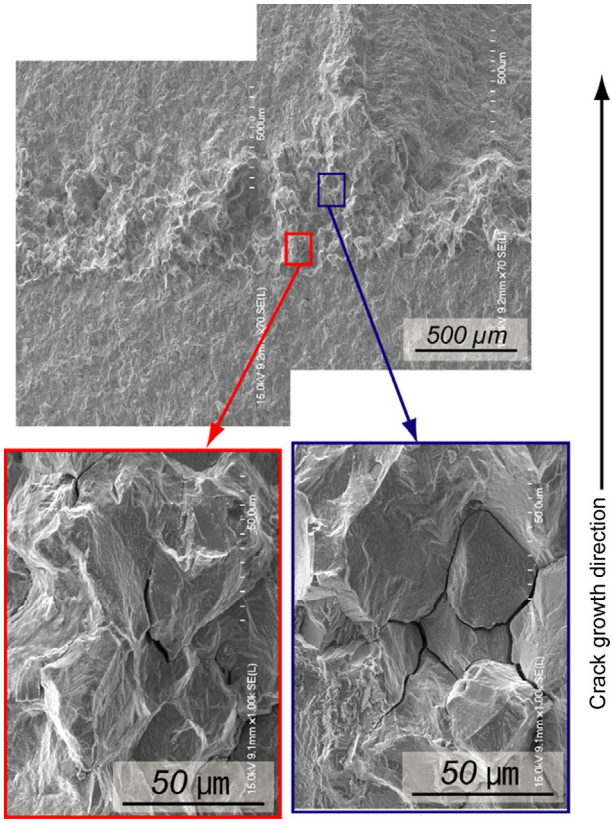

Fig. 9.37 The fracture surface of the 20% cold worked Alloy 600MA specimen after the SCC test in a simulated PWR primary water at 320 °C [134].

for yield strength on CGRs. CGRs increase with an increase in the yield stress. The effect of cold work on SCC growth rates results from dislocation density and the deformation behavior ahead of the crack tip. The SCC susceptibility of Fe-Cr-Ni alloys has been correlated with the dislocation arrangements in the metal. Planar dislocation structures lead to transgranular SCC, whereas IGSCC is observed in materials with high stacking fault energy. Rock bolt SCC was investigated using LISTs. The threshold stress was determined for various bolt metallurgies (900 MPa for 1355AXRX and 800 MPa for MAC and MA840 steels). SCC only occurred in the presence of hydrogen on the sample surface, leading to HE and SCC. Cold work increased the resistance of the steel to SCC. It was found that rock bolt rib geometry does not have a direct impact on the SCC resistance properties of the bolt. However, the process by which the ribs are produced may introduce tensile stresses into the bolt, lowering its resistance to SCC [136].

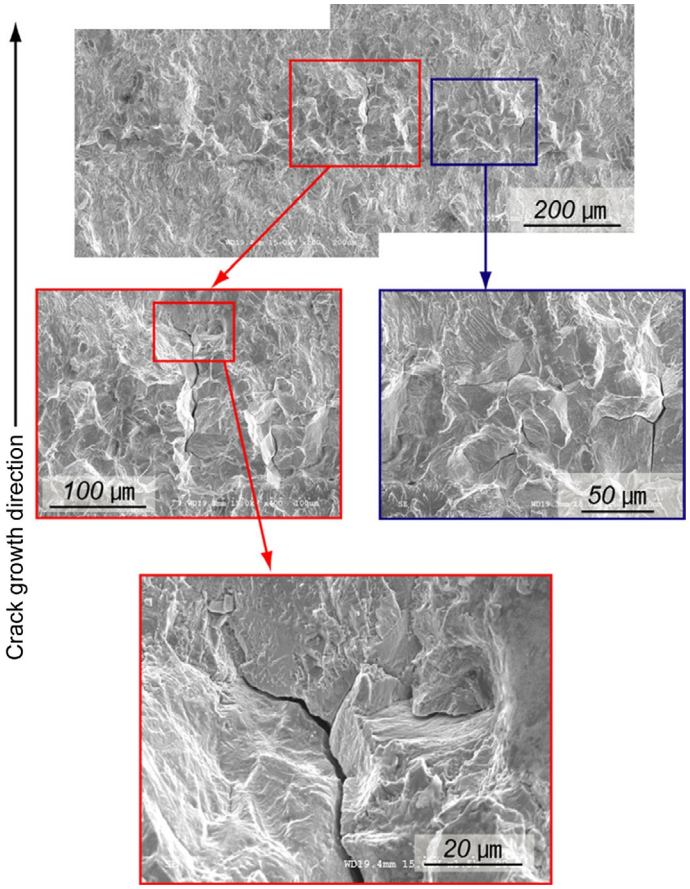

Fig. 9.38 The fracture surface of the 40% cold worked Alloy 600MA specimen after the SCC test in a simulated PWR primary water at 320 °C [134].

The effect of cold work (prestraining) in the range between 2.3% and 56% on SCC of 304 and 316L stainless steel in boiling $MgCl_2$ was investigated using a constant load method [137]. The results indicated that SCC was transgranular. The prestraining and the increase in the initially applied stress facilitated the transition in crack morphology to intergranular mode.

The SCC behavior of cold worked AISI type 316L (UNS S31603) stainless steel in a concentrated lithium salt solution at elevated temperature was investigated by Zheng and Bogaerts [138]. Using the SSRT technique, SCC experiments were performed under controlled electrochemical potential on 20% and 40% cold worked materials in a solution

containing 10 g lithium hydroxide (LiOH) and 100 cm^3 H_2O at 95 °C. The results indicated that the SCC behavior of the cold worked steel was different from that of the solution-annealed steel. The cold work significantly improved the resistance of 316L SS to IGSCC in a hot LiOH environment. The effect of cold work on SCC of Alloy 600 SG tubes was investigated in simulated PWR primary water environments [132,139,140]. SSRT tests or other constant displacement tests indicated an enhancing effect of cold work on SCC behavior.

The effect of cold work on thick plates of Alloy 600 materials [133,141] was investigated using fracture mechanics specimens. A small amount of cold work was found to have a significant effect on crack growth. CGR increases at a high rate in the first 5% of deformation and levels off with a further increase in cold work. Yield stress increases from 470 to 880 MPa and increases the CGR fourfold [142].

Cold work increases the material yield strength and ultimate strength. However, cold work decreases the materials' ductility. The plastic deformation of polycrystalline alloys affects the microstructure, which reduces the crystallite size and increases the dislocation density and the microstrain in the crystallites [143,144]. No dislocations were observed in the nondeformed materials. Dislocations were found to increase with the amount of plastic deformation. Prior deformation increases the material strength, increases the dislocation density, and creates disorientation and microstrain when large strains are used in the subdivision of grains. It was suggested that the observed decrease of crack growth and 40% cold work Alloy 600 may be caused by the change of submicrostructure, which in turn is caused by the cold work.

The SCC properties and growth kinetics for a warm-rolled 316L stainless steel (CW 316 SS) were continuously tested in high purity water at DO levels and different temperatures under a K (or K_{max}) of 30 MPa $m^{0.5}$ [145]. CGR increased in the range between 110 and 288 °C. The measurements were performed in oxygenated high-purity water at different temperatures using a contoured double cantilever beam specimen that allows constant K under constant loading for a long crack advance [146]. The crack growth was continuously monitored using an alternating current potential drop (ACPD) machine equipped with a data-logging system. After *in situ* precracking, the specimen was subjected to trapezoidal (Trap.) wave loading with 12 h constant load plus 60 s unloading/reloading ($R = 0.7$) at $K_{max} = 30$ MPa $m^{0.5}$. Very high CGR was observed at temperatures as low as 150 and 110 °C. Figure 9.39 shows the crack growth during *in situ* precracking in 2 ppm DO water at 288 °C [145]. At each R ratio, a very well-defined corrosion fatigue crack was observed. The CGR decreases with increasing R ratio. Figure 9.40 shows the advance in crack length vs. test time curve monitored by ACPD for CW316L SS in 2 ppm DO water at different temperatures [145].

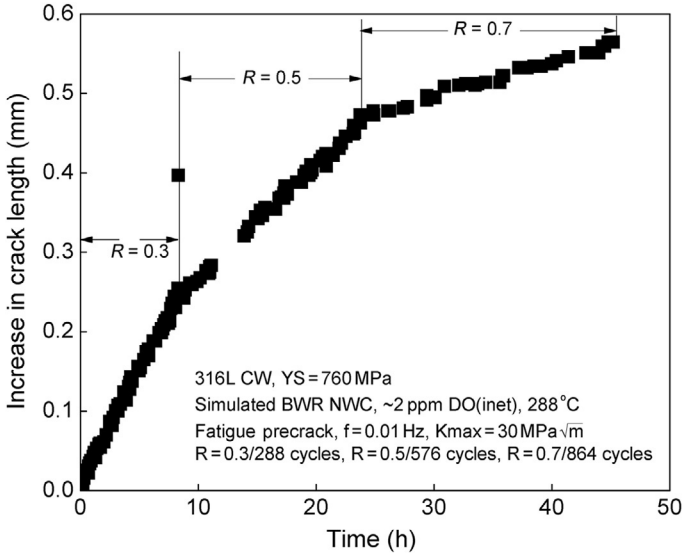

Fig. 9.39 Crack advance vs. time curve monitored by ACPD for CW316L SS in 2 ppm DO water at 288 °C under triangular wave loading [145].

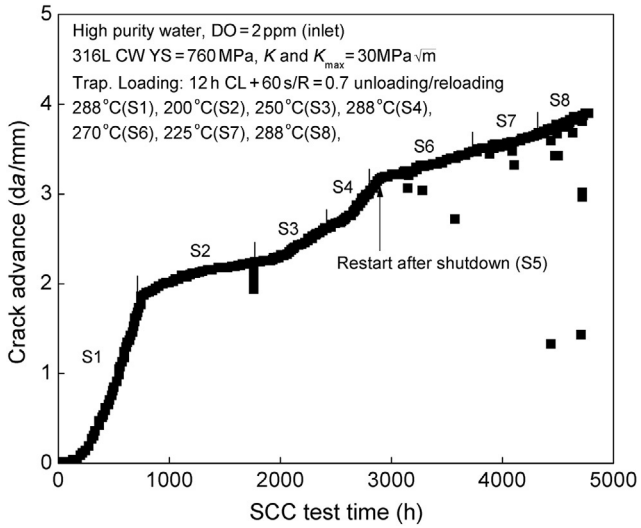

Fig. 9.40 SCC crack advance vs. time monitored by ACPD for CW316L SS in 2 ppm DO water at various temperatures [145].

9.7 ELECTROCHEMICAL EFFECTS

Electrochemical conditions that could lead to SCC in corrosion environments include:

(a) Chloride-induced localized corrosion in stainless steels, titanium, and aluminum alloys [147,148].
(b) Presence of weak passive film near a passive-active transition [64].
(c) SCC due to dealloying.
(d) Formation of surface films, which may cause intergranular corrosion and cracking at high temperatures [149].
(e) Hydrogen-induced SCC in high-strength alloys [150].

Figure 9.41 shows a typical potentiodynamic anodic polarization curve for active-passive alloys with zones where SCC occurs on susceptible alloys in a corrosive environment [151]. The arrows indicate potential ranges critical to SCC of active-passive alloy. The presence of a passive film on the metal surface is a precondition for SCC. The zones in the potentiodynamic anodic curves, which show the susceptibility to SCC, are in the potential ranges where the alloys have unstable passivity. Corrosion and SCC in Zone 1 are due to potential overlapping of SCC and chloride-induced localized pitting corrosion of steel, aluminum, and titanium alloys. In this region, Alloy 690 is susceptible to IGSCC and to pitting corrosion in caustic aqueous environments containing chloride or the thiosulfate ion [152,153]. Crack corrosion in chloride-induced localized corrosion in an acid environment occurs in an active state. The corrosion at the crack tip occurs by the anodic dissolution of metals in the alloy. The range of potentials at which this occurs is between

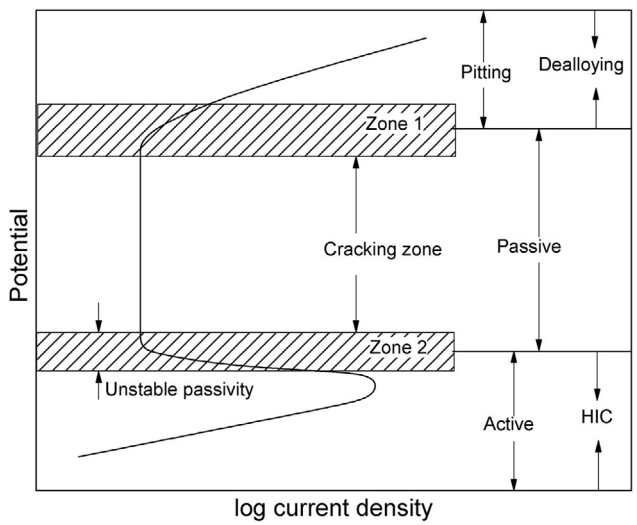

Fig. 9.41 Zones of susceptibility to stress corrosion cracking [151]. © *NACE International 1977.*

the passivation potential of the alloy and the potential at which the localized corrosion rate is equal to the crack velocity [151].

SCC in this potential range may also result from hydrogen generation in the crack in the case of martensitic steels [151]. The synergistic effect of chloride ions and thermal stresses from welding was identified as the cause for observed SCC of stainless steel below the satellite launch vehicle propellant tank assembly [154]. Chloride ions initiated transgranular cracking with a root branching and thermal stress arising while welding due to irregular heat input providing the necessary threshold stress [155]. Figure 9.42 shows a photomicrograph of crack initiation from the pit at the weld fusion line and propagation in transgranular mode with tree root morphology [155].

Austenitic stainless steels are susceptible to sensitization, which involves chromium depletion at grain boundaries. They also suffer from pitting corrosion and transgranular stress corrosion cracking in chloride-containing solutions [45]. Austenitic nickel-based alloys have better corrosion resistance and mechanical properties. However, the Alloy 600 used as tubing in PWRs is susceptible to intergranular corrosion and IGSCC due to the carbide distribution in the alloy microstructure [156,157], pH value of the environment [158,159], and stress condition [160]. Alloy 690 has a similar composition to that of Alloy 600, with almost double chromium content (30 wt.% Cr) that provides very good corrosion resistance in aqueous environments. This alloy is still susceptible to IGSCC in an alkaline environment in the presence of chlorides and thiosulfates [134,151–153,161,162].

Chen *et al.* [163] investigated the effects of solution pH, chloride concentration, and temperature on the susceptibility of Alloy 690 to SCC. SCC was found to be initiated in a NaCl concentration higher than 1 at a pH of 1. SCC susceptibility of Alloy 690 in 1 M

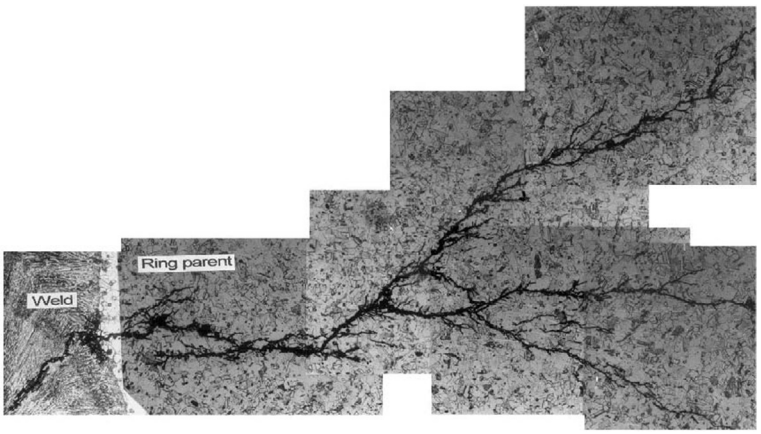

Fig. 9.42 Photomicrograph showing crack initiation from the pit at weld fusion line and propagation in transgranular mode with tree root morphology 75× [155].

NaCl at pH 1 was found to be sensitive to a variation in the solution temperature. A decrease of the solution pH and the increase of chloride concentration at 25 °C increased the polarization current while decreasing the passive region. The mechanical properties, such as the maximum tensile strength (MTS), fracture strain (FS), and reduction in area (RA), decreased at pH < 3 in 5 M NaCl at 25 °C. SCC was also found to be initiated in NaCl solutions at pH 1 in the presence of chloride concentrations higher than 1 M. The results of the SSRT test and the SCC susceptibility of Alloy 690 in 1 M NaCl at pH 1 were found to depend on the solution temperature. Figure 9.43a shows the stress-strain

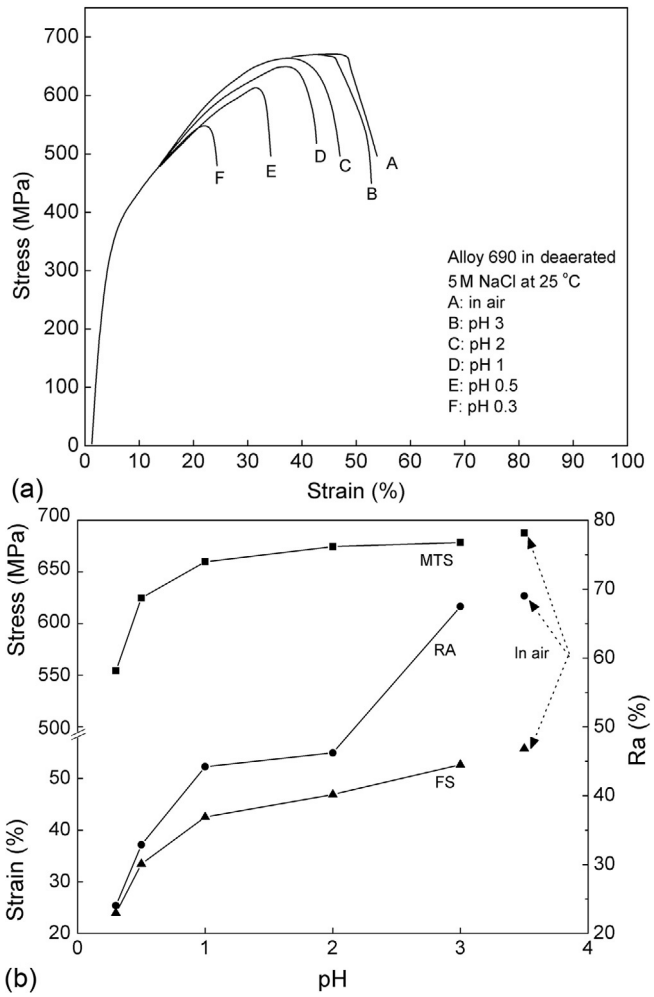

Fig. 9.43 (a) Stress-strain curves of Alloy 690 obtained in deaerated 5 M NaCl solutions of various pH values at 25 °C, and (b) effect of solution pH on MTS, FS, and RA of Alloy 690 in deaerated 5 M NaCl solutions at 25 °C [163].

curves for Alloy 690 obtained in 5% NaCl solution with various pH values at 25 °C. The effect of pH on the mechanical properties is shown in Fig. 9.43b [163].

Figure 9.44a and b shows stress-strain curves of Alloy 690 obtained in solutions with different concentrations of NaCl at pH 1 in comparison with the results obtained in air [163]. The effect of chloride concentrations on the mechanical properties of Alloy 690 in deaerated NaCl solutions at pH 1 is also shown in the figures.

Results of the SSRT tests of type 321 stainless steel in a simulated petrochemical environment containing sulfides and chlorides indicated that the effects of environmental

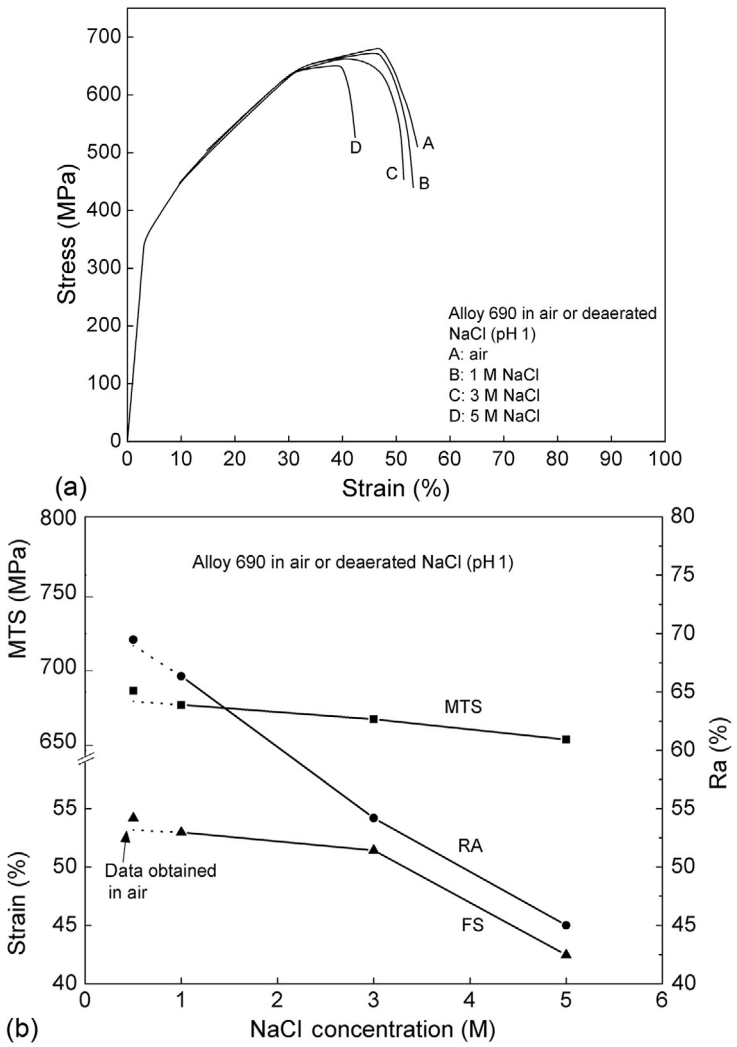

Fig. 9.44 (a) Stress-strain curves of Alloy 690 obtained in solutions with different concentrations of NaCl at pH 1 in comparison with that obtained in air, and (b) effect of chloride concentrations on the mechanical properties of Alloy 690 in deaerated NaCl solutions at a pH of 1 [163].

factors such as chlorides, thiosulfate ($S_2O_3^{2-}$), pH, and temperature, on the SCC susceptibility of type 321 decreased in the following order:

$$\text{Temperature effect} > \text{pH effect} > Cl^- \text{ concentration effect}$$

The U-bend tests indicated that the susceptibility of type 321 to SCC decreases with increasing temperature, which is related to the more compact surface film containing chromic oxide (Cr_2O_3) and magnetite (Fe_3O_4) that forms at higher temperatures. SCC of 321 stainless steel in an environment containing H_2 and chloride (20 wt.% NaCl + 0.01 M $Na_2S_2O_3$) aqueous solution was found to be initiated by pitting [164].

SCC occurs due to the presence of a weak passive film in the active potential region [48,49,165]. SCC of carbon steel in hot carbonate/bicarbonate solution is an example of zone 2 SCC in the active potential region [166]. Proportionality between CGR and anodic dissolution current was studied by Parkins [48,49]. As shown in Fig. 9.45, a linear correlation was found between CGRs and anodic current densities [49].

Seifert and Ritter [166] studied strain-induced corrosion cracking (SICC) of low alloy reactor pressure vessels (RPV), piping steels, and RPV HAZs materials under simulated BWR vs. normal water chemistry conditions. The experiments were also performed on precracked fracture mechanics specimens by using SSRT and very low-frequency fatigue tests. A minimum value of K_I of 25 MPa/m^2 is necessary to initiate SCC in SSRT tests. SICC increased above this value with an increase in the loading rate, dK_I/dt. A maximum SICC initiation susceptibility was observed at intermediate temperatures of approximately 200-250 °C. The SICC tests were performed in stainless steel autoclaves equipped with integrated electromechanical loading systems and high-temperature water loops. The electrochemical corrosion potential of the specimens and the redox potential (platinum probe)

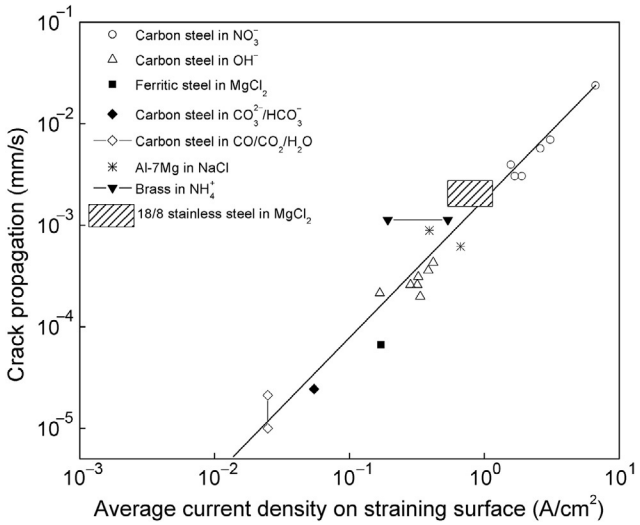

Fig. 9.45 Relationship between CGR and alloy anodic dissolution [49].

were continuously monitored by use of an external Ag/AgCl/0.01 M KCl or a $Cu/Cu_2O/ZrO_2$-membrane reference electrode. Crack advance was continuously monitored using the reversed direct current potential drop method. K_I value was calculated using ASTM E 399 by the measured load and the length of the crack $a_o + \Delta a_{SICC}$.

Figure 9.46a and b shows the crack growth initiation stress intensity factor, K_I, and SICC growth rate, da/dt_{SICC}, as a function of the crack opening displacement (COD)

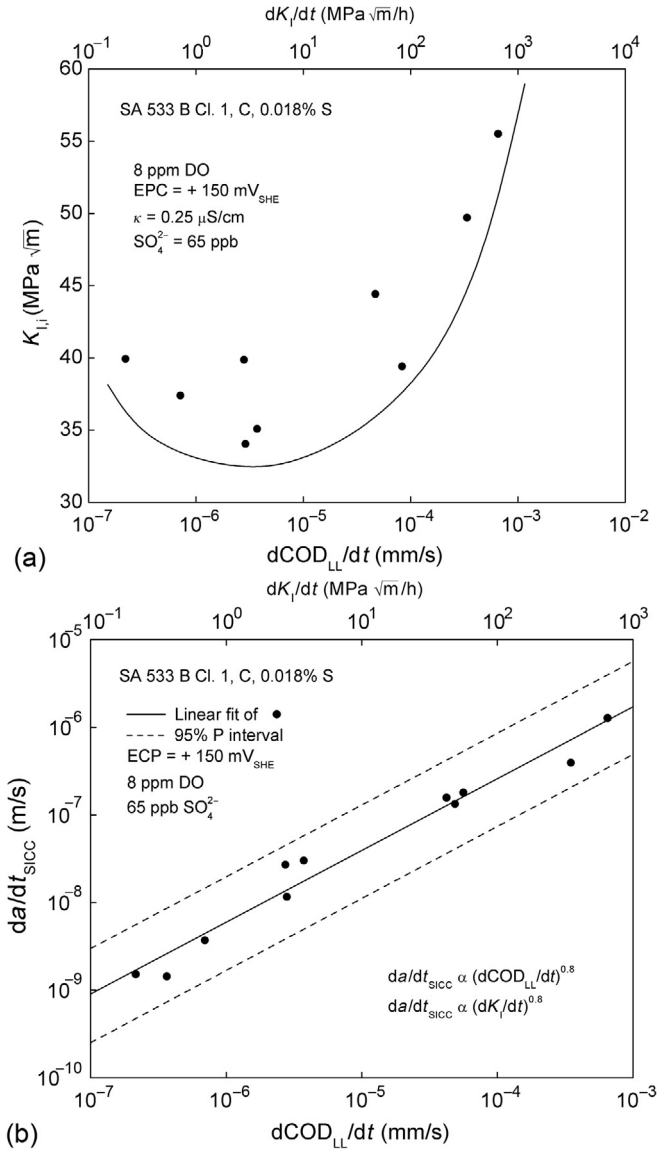

Fig. 9.46 Effect of loading on SICC initiation (a) and crack growth (b) in high-sulfur steel C [166].

rate at the load line, $dCOD_{LL}/dt$ and stress intensity factor, dK_I/dt, for high-sulfur steel [166]. The tests were performed at a DO content of 8 ppm. The stress intensity factor K_I decreases with decreasing loading rate and increases at lower loading rates at a low displacement rate of approximately 10^{-6} mm/s, corresponding to an estimated crack tip strain rate of 5×10^{-5} to 10^{-4} s. The CGR is constant when measured as a function of the rising load. A power law relationship with an exponent of 0.8 was estimated between SICC and COD. SICC initiation and growth were strongly dependent of the applied loading rates.

SCC, due to imperfect passivity near an active-passive transition, was observed for pipeline steel (APIX65) [71–73]. The mechanism for IGSCC of pipeline steels is discussed in Section 9.6.1. The crack propagates due to the presence of plastic strain ahead of the crack tip, and prevents the formation of the protective passive layer.

The effect of plasma electrolytic oxidation (PEO) treatment on the SCC of surface-modified magnesium alloys was studied [167]. PEO coating offered improved corrosion resistance. However, the barrier film did not improve the SCC resistance in ASTM D 1384 test solution. The SCC of PEO-coated specimens was attributed to the development of microcracks in the coating, leading to substrate cracking under SSRT test conditions [167].

Zirconium and zircaloy-4 in 1 M NaCl, 1 M KBr, and 1 M aqueous KI solutions were found susceptible to SCC only above the pitting potential (zone 1) [168]. Zirconium alloy SCC in aqueous halide solutions occurs as a result of electrochemical passive film breakdown followed by intergranular attack due to anodic dissolution (dealloying assisted by stress). The final step was a fast transgranular propagation. A surface-mobility SCC mechanism was suggested to explain experimental results. Figure 9.47 shows

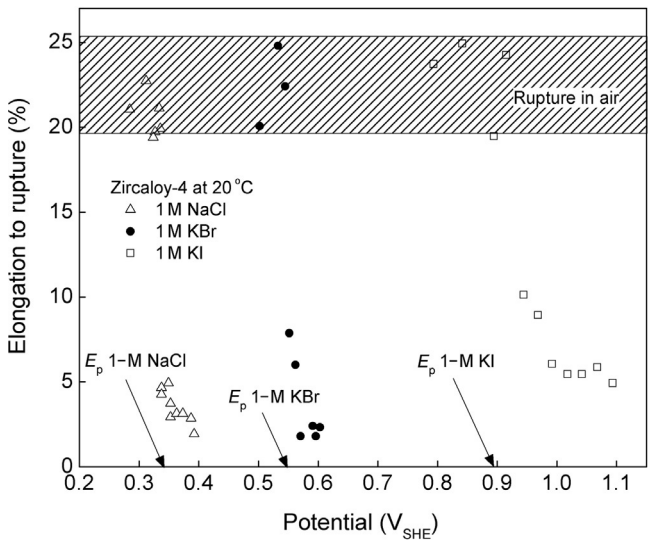

Fig. 9.47 Elongation to rupture of Zry-4 strained in 1 M NaCl, 1 M KBr, and 1 M KI aqueous solutions at room tempearure as a function of the applied potential. Strain rate (SR) $= 4.7 \times 10^{-6}$/s [168].

elongation and rupture of Zry-4 strained in 1 M NaCl, 1 M KBr, and 1 M KI aqueous solutions at room temperature as a function of applied potential [168]. Latteral surface of a Zry-4 wire strained in 1 M KBr solution at 0.60 V vs. SHE is shown in Fig. 9.48 [168]. A typical fracture surface of a Zry-4 specimen strained at room temperature in 1 M KBr solution at 0.62 V vs. SHE is shown in Fig. 9.49 [168].

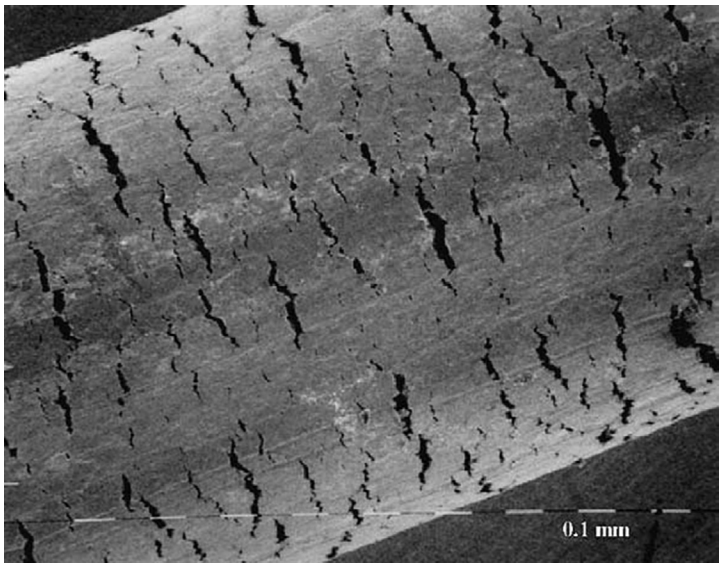

Fig. 9.48 Lateral surface of a Zry-4 wire strained in 1 M KBr solution at 0.60 V vs. SHE SR: 4.6×10^{-6}/s [168].

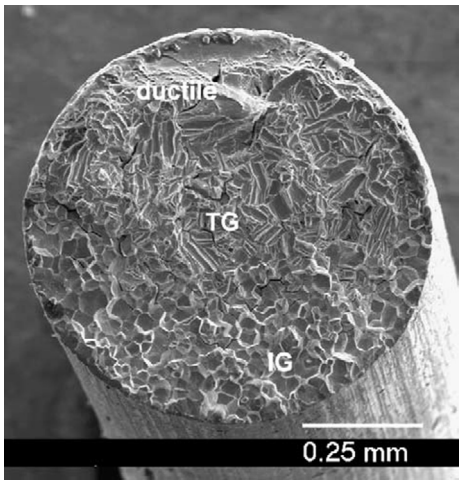

Fig. 9.49 A typical fracture surface of a Zry-4 specimen strained at room temperature in 1 M KBr solution at 0.62 V vs. SHE, showing the intergranular (IG), transgranular (TG), and ductile zones. SR: 4.6×10^{-6}/s [168].

Surface dealloying SCC has been observed for the following alloys: Cu-Al, Cu-Zn, and Au-Ag. Dealloying and cracking in these alloys occur in an oxide free surface. An example of surface dealloying is the SCC of brass in ammonia [169]. Bianchi [170] reported the cracking of silver alloys in aqueous and gaseous environments. In many cases, the composition determines the nature of dealloying and SCC of austenitic stainless steels [67] and brasses [68].

The formation of surface films may cause intergranular corrosion and cracking at high temperatures. Kanematsu *et al.* [171] investigated the SCC of an Al-Zn-Mg alloy in a 0.6 M NaCl solution. The results indicated that the IGSCC was found to initiate a crack in the brittle aluminum alloy oxide film.

9.8 HYDROGEN EMBRITTLEMENT

HE is classified in this book as part of HIC and hydrogen damage effects, and is discussed in detail in Chapter 8. HE results from the exposure of an alloy in the chemical processes during welding operations, casting, pickling, or cathodic protection. The brittle properties of the observed cracks in SCC are controlled by the hydrogen atom-induced cracking mechanism. Because hydrogen solubility in the molten alloy is higher than the solid, the hydrogen contamination begins in the early stages of the metallurgical processing of the metal/alloy. The damage occurs when the hydrogen accumulates in the defects (hollow spaces) in the interstitial positions of the lattice.

A small part of the evolved atomic hydrogen is adsorbed on the metallic surface. The atomic level embrittlement occurs at hydrogen concentrations as low as 10 ppm by adsorbing in the certain areas of unstable crystalline lattice. The concentrated areas of adsorbed hydrogen recombine to form molecular hydrogen, which drastically increases localized pressure in the structure. The irreversible accumulation of hydrogen within the metal lattice leads to the deterioration of mechanical properties of the metal. Steel loses ductility resulting in HE [172]. A part of adsorbed hydrogen subsequently diffuses into the crystalline lattice of the substrate, where it reacts with the metal atoms to form brittle metal hydrides, causing the structure to fail far below the yield strength.

HIC has been accepted as the controlling mechanism of failure for the less ductile, high-strength steels such as titanium, high-strength iron, and some aluminum alloys, which have the highest susceptibility to HE. The susceptibility to hydrogen drastically increases with the increase in the strength of the steel. Interaction between atomic hydrogen and the metallic atomic structure inhibits the ability to stretch under load. Thus, steel becomes brittle under load. Hydrogen may also act as a grain boundary surfactant, creating microcracks within the steel due to a decrease in the surface film energies at the grain boundaries. Hydrogen reduces the adhesion and cleavage strength of the alloy. The resistance to shear slip significantly reduces in the presence of hydrogen atoms.

Hydrogen failure in steels has been suggested to be caused by mechanisms such as hydrogen-enhanced decohesion (HEDE) [173,174], hydrogen-enhanced localized

plasticity (HELP) [175], and hydrogen-assisted intergranular cracking, which is facilitated by grain boundary precipitates and carbides, interface decohesion, and cleavage of grain boundary carbides [176]. Cracking due to HE is caused by the hydrogen evolution reaction at the interface and increases with an increase in the cathodic current. HE is distinguished from SCC by occurring with applied anodic current.

Detailed reviews of HE mechanisms of Mg alloys and iron alloys have been reported [177–179]. The HEDE mechanism was suggested by Gangloff for high-strength alloys that do not form hydrides [177]. The mechanism is based on the reduction of electron charge density between metal atoms in the alloy. Hydrogen accumulation by stress-assisted diffusion in the region ahead of the crack tip results in weakening the bonds and tensile separation of neighboring atoms. Delayed hydride cracking is based on stress-assisted diffusion of hydrogen atoms, hydride precipitation, and brittle fracture of formed hydrides. Birnbaum [178] and Lynch [179] suggested HELP through interactions between hydrogen at dislocations and obstacles to dislocation motion, which enhances the dislocation mobility. As a result of dislocation mobility, microvoid coalescence occurs and is more localized in inert environments. This phenomenon requires high hydrogen diffusivity in order to move with their dislocations. Subsequently, they reconfigure when interacting with other hydrogen atmospheres and stress fields.

Winzer *et al.* [180] investigated SCC of Mg-Al alloys AZ91, AZ31, and AM30 using constant extension rate tests and LISTs. AZ91 consists of an α-matrix with extensive β-particles. AZ31 and AM30 alloys consist of an α-matrix and Al-concentration similar to that in AZ91. The presence of β-particles in AZ91 resulted in a lower threshold stress, σ_{SCC}, (55-75 MPa) when compared to AZ31 (105-170 MPa) and AM30 (130-140 MPa); and a different SCC initiation mechanism for AZ91 relative to AZ31 and AM30. The SCC velocity, V_c, for AM30 (3.6×10^{-10} to 9.3×10^{-10} m/s) was lower than AZ91 (1.6×10^{-9} to 1.2×10^{-8} m/s) and AZ31 (1.2×10^{-9} to 6.7×10^{-9} m/s). The observed difference was attributed to the presence of Zn and second-phase particles, which are more concentrated in AZ31, and the diffusivity of H in the α-matrix. The mechanism for SCC initiation suggested by Winzer *et al.* [180] in AZ31 and AM30 specimens is based on localized dissolution at stresses significantly higher than AZ91. AZ91 precharged in gaseous H_2 at 3 MPa for 14 h at 300 °C fractured just above the yield stress, σ_Y. The SCC mechanism is based on fracture of a brittle hydride phase. Figure 9.50 shows failure of material caused by HE and SCC of bars made from stainless steel (AISCI, 304) used to suspend a dead concrete ceiling over the pool [181]. The branched cracks are shown in Fig. 9.51 [181].

Formation of the martensitic phase and strain-induced transformation of austenite to martensite increases the susceptibility of 304 stainless steel to HE [182,183]. In the presence of hydrogen, more transformed martensite is formed, increasing the ductile loss of the material [184]. Caskey [185] observed that large grain sizes deteriorate the FS of austenitic stainless steel due to the presence of hydrogen. Tsay *et al.* [186] evaluated the

Fig. 9.50 Fracture surface of broken hanger of dead concrete roof, made from stainless steel [181].

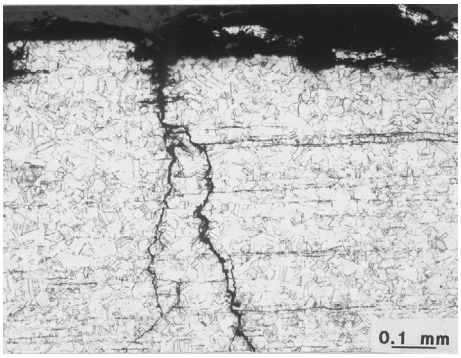

Fig. 9.51 Branched cracks of stainless steel bar shown in Fig. 9.50 [181].

fatigue behavior of 304 stainless steel specimens with and without laser processing (welding and surface treatment) in air and gaseous hydrogen using the fatigue crack growth test. Transgranular fatigue fracturing of the flat facets and a small amount of intergranular fracture were observed on the steel pelted samples. The extent of quasi-cleavage (QC) fracture resulted from the formation of strain-induced martensite that increases fatigue crack growth in the presence of gaseous hydrogen.

Commercial purity titanium is susceptible to HE when hydrogen is absorbed at elevated temperatures, resulting in the formation of hydrides upon cooling. The hydrides lead to a decrease in the elongation and material failure [187]. When the total hydrogen concentration is larger than 3310 ppm and current density is larger than 20 mA/cm^2, blistering or a combination of blistering and microcracks appears during charging without loading in the $Zr_{41.2}Ti_{13.8}Ni_{10}Cu_{12.5}Be_{22.5}$ bulk metallic glass. The critical pressure, P_i, for forming a stable blistering with radius of 15 nm was 3.6 GPa, while the critical pressure for cracking of the blistering, P_C, was 3.9 GPa [188]. Figure 9.52 shows blistering and microcracks in a bulk metallic glass specimen, precharged with 50 mA/cm^2 [188].

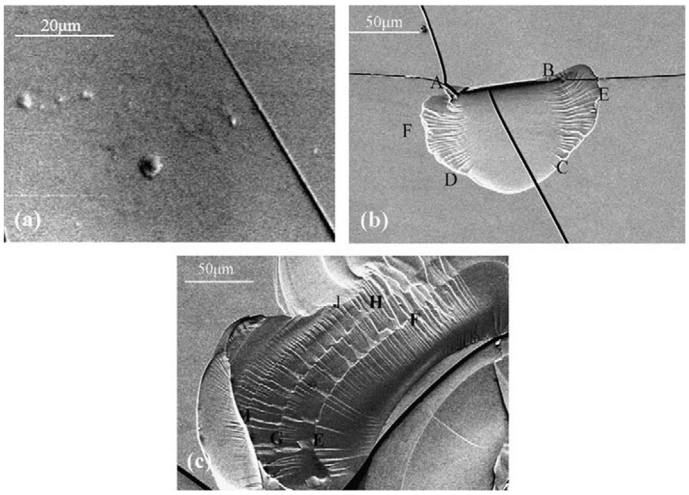

Fig. 9.52 Hydrogen blistering and microcracks in the specimen precharged with $i = 50$ mA/cm^2 for 30 h; (a) unbroken blisterings; (b) broken blistering with cracking, AFD and BEC are the fracture surface of the blistering cracks; and (c) arrest lines EF, GH, and IJ on the fracture surface of the blistering crack [188].

High pH SCC and near-neutral pH SCC have been identified as pipeline SCC modes by Beavers and Harle [189], who pointed out that SCC occurred due to anodic dissolution and then propagated by a mechanism of HIC. High pH SCC for pipelines has been explained on the basis of anodic dissolution mechanism [190–193]. The combined effect of hydrogen and stress on the dissolution of steel near neutral pH SCC was suggested by Parkins *et al.* [194]. Recent studies confirmed the synergy of HE and steel dissolution at the crack tip [195–199]. Cheng *et al.* [195–197] quantified the contributions of stress, hydrogen, and their synergy on steel dissolution at the crack tip in the near-neutral pH solution.

SCC for aluminum alloys can be explained through PFR, anodic dissolution causing IGSCC, and HIC [200]. The cast and heat-treated Al-6%Zn-1%Mg (Al-6-1) and Al-6% Zn-1%Mg-1%Ag (Al-6-1-1) metal matrix composites were evaluated using continuous immersion techniques. Al-6-1-1 composites exhibit longer lifetimes compared to the Al-6-1when tested under various SCC conditions. Fractography and scanning electron microscopy studies indicated the dissolution and hydrogen embrittling mechanisms control the initiation and propagation of stress corrosion cracks within these materials [201].

The effect of hydrogen on SCC of an as-cast $MgAl_9Zn_1$ magnesium alloy in 0.1 M Na_2SO_4 solution was investigated using an SSRT test. The HE was the main mechanism for SCC of a $MgAl_9Zn1$ alloy. Hydrogen diffused to the interior of the matrix, formed a hydride at the β-phase, and initiated cracking. The main crack propagated by coalescence of the existing microcracks [202]. SCC for austenitic stainless steels is caused by film

rupture [203], active dissolution [204], or HE [205]. Austenitic steels of type 304 and 316 SCC due to hydrogen charging or applied stress exhibit phase transformation from $\gamma \rightarrow \alpha$ martensite [206].

SCC and HE of the sensitized stainless steels of types 304, 310, and 316 were investigated as a function of the test temperature in boiling, saturated-magnesium chloride solutions under a constant applied stress condition [207]. The temperature dependence of fracture appearance and the parameters such as time to failure, t_f, steady state elongation rate, l_{ss}, and transition time to time to failure ratio, (t_{ss}/t_f), indicated that type 304 alloy is susceptible to SCC and HE. Type 316 alloy is only susceptible to HE, while type 310 alloy only to SCC. Only type 316 alloy showed a difference between sensitized and solution-annealed specimens. The dependence of the steady state elongation rate on the logarithms of the time to failure is a straight line for all stainless steels. The slopes depended upon the fracture mode: −2.0 for SCC and −1.5 for HE. The steady state elongation rate can be used as the parameter for predicting the time to failure for stainless steels in the $MgCl_2$ solutions. The results obtained were explained in terms of hydrogen entry and martensite transformation. Intergranular cracking was observed for sensitized type 316 at 406 K and transgranular cracking for sensitized type 316 stainless steel at 418 K.

Figure 9.53 shows fracture time of AISI 4340 steel baked at 150 °C for various times after initial cathodic charging [208]. After cathodic charging, DO escapes after heating at 150 °C. The incubation time, as shown in Fig. 9.53, before cracking decreases with

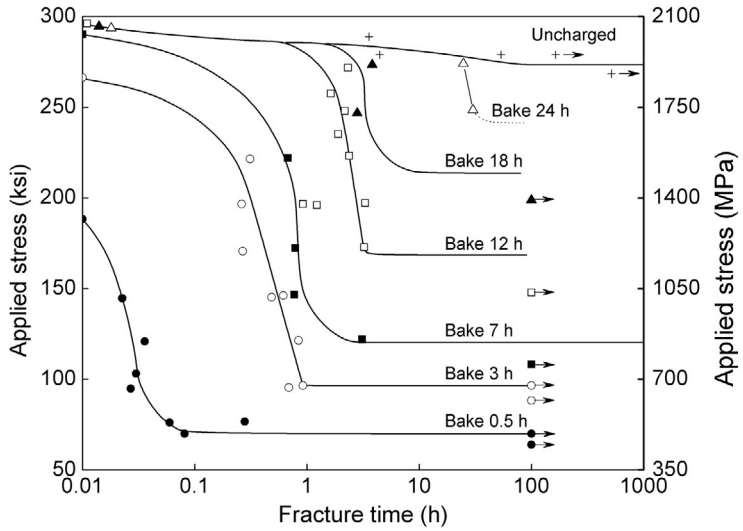

Fig. 9.53 Fracture of AISI 4340 steel baked at 150° obtained after applying cathodic current [208]. *Reprinted with permission of ASM International, Materials Park, OH. www.asminternational.org.*

increasing applied stress. Intergranular cracking from HE is caused by strain-induced formation of martensite along the interface of the grain boundaries, while transgranular cracks were initiated and propagated by dissolution at the slip steps [207,209].

9.9 CORROSION FATIGUE CRACKING

CFC is mechanical degardation (brittle failure) of the materials when exposed to both corrosion and cycling loading. Fatigue of high-strength materials such as titanium alloys, aluminum alloys, and steel are susceptible to SCC when exposed to a corrosive environment. CFC propagates perpendicular to the principle tensile stress. However, CFC should not be confused with SCC, because the only requirement for this type of failure is exposure under tensile stress. Low corrosion rates of metals and alloys have no effect over fatigue life in air. When the passive alloys are exposed at low corrosion rates, the fatigue life decreases. The crack initiation triggers higher dissolution rates at the slip bans due to film rupture [210]. Fatigue cracks propagate after a certain number of cycles and at stresses below the yield stress and stops propagating when the material separates by overload fracture. At this point, the load applied to the material exceeds the ultimate tensile stress. Figure 9.54 shows the stress-time relationship and defines the range, the alternating stress, the minimum stress, the mean stress, and the maximum stress on the oscillating curve [210,211]. In the fatigue test, one measures the time of failure of the material under conditions of applied stress of various amplitudes.

The effect of the corrosion environment on fatigue is evaluated by the variation of fatigue fractures stress as a function of number of cycles applied in the corrosion

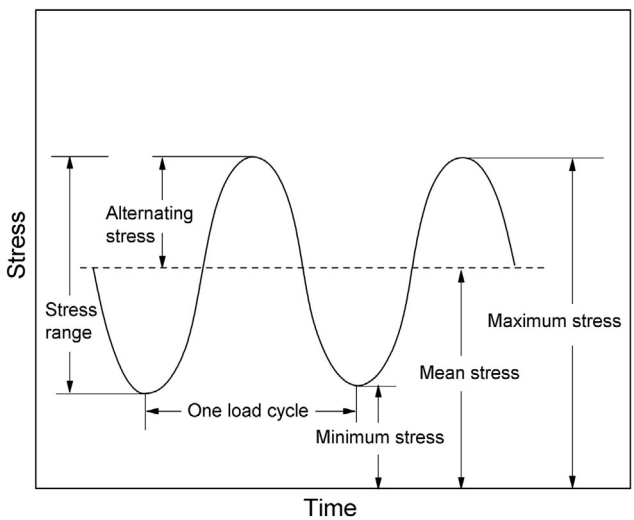

Fig. 9.54 Stress vs. time cycling in fatigue testing [210]. © *NACE International 1972.*

environment and in air (*S*-*N* curves). *S*-*N* curves indicate the variation of fatigue fracture stress (*S*) with the number of cycles (*N*) applied. In practice, to determine a corrosion fatigue limit by long lasting tests, the alloys are evaluated by comparing the stress at which no failure occurs after 10^8 cycles. The results are compared as corrosion fatigue stress (CFS) by specifying the cycle number [212]. The fatigue crack length "*a*" is measured as a function of applied number of loading cycles, *N*, to determine the CGR/ΔK plots. The CGR plots show the crack length growth per load cycle. The Paris equation is used to measure the CGR [213].

$$\frac{da}{dN} = C\Delta K^n \tag{9.18}$$

where "*a*" is the crack length, *n* is number of cycles, and ΔK is the linear elastic stress intensity factor in units MPa $\sqrt{m}$. *C* and *n* are constants that depend on the material listed in Table 9.2 for air, sea water, and 3% NaCl solution [211].

Plot of log $\frac{da}{dN}$ vs. log ΔK is used to determine the value of "*n*" from the slope, while *C* is estimated from the intercept of the Paris equation (extrapolating the value of ΔK to 10). ΔK is the range of the linear elastic stress intensity factor defined as K_{max}-K_{min} and represents the maximum and the minimum values in the load cycle of the stress intensity factor *K*. By using the Paris equation, the CGR and the linear elastic stress ΔK can be determined at any particular cycle number. Corrsion fatigue of AISI 4340 steel in a sodium chloride solution as a function of stress intensity is shown in Fig. 9.55. Lower frequencies of the cycling stress have greater crack propagations per cycle [214].

Table 9.2 List of Paris Constant C and the Paris Exponent *n*, for Various Hardening Stainless Steels[a] [211].

Material[b]	Environment	*C*	*n*
17-4 PH, VM, H1050	Air	1.1×10^{-10}	2.2
	Seawater, −0.3 V Ag/AgCl	1.6×10^{-9}	2.0
	Seawater, −0.65 V Ag/AgCl	1.6×10^{-9}	2.0
17-4 PH, AOD, H1050	Air	1.7×10^{-10}	2.4
	Seawater, −0.2 V Ag/AgCl	3.9×10^{-9}	2.1
	Seawater, −0.65 V Ag/AgCl	2.9×10^{-8}	1.6
17-4 PH, AOD, H1150	Air	3.1×10^{-10}	2.3
	Seawater, −0.2 V Ag/AgCl	9.6×10^{-9}	2.2
	Seawater, −0.65 V Ag/AgCl	3.1×10^{-10}	2.0
PH 13-8 Mo, VM, H1050	Air	5.5×10^{-9}	2.64
	3% NaCl solution	4.0×10^{-7}	1.67

[a] da/dN in meters/cycle and ΔK in MPa $\sqrt{m}$.
[b] AOD is argon-oxygen-decarburizaion; VM is vacuum melted; H1050 is hardened at 1050 °F; and H1150 is hardened at 1150 °F.

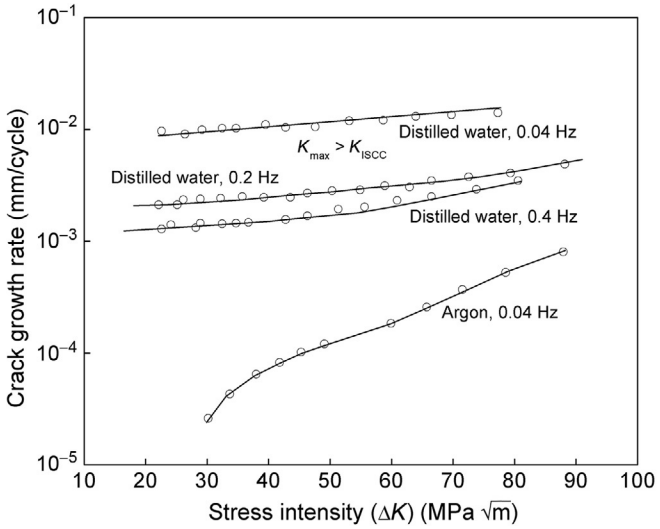

Fig. 9.55 Corrsion fatigue of AISI 4340 steel in sodium chloride solution [214].

The HE susceptibility of 304 stainless steel (304 SS) increases with the formation of martensite during deformation [215]. The strain-induced transformation of austenite to martensite causes the reduction in fracture stress in 304 SS [182]. Phase transformation during plastic deformation can also be enhanced by electrolytically charging hydrogen into 304 SS [183]. The fracture initiates through the martensite phase [216]. The martensitic transformation in a metastable stainless steel is caused by the induced strain ahead of the fatigue crack tip. The fatigue resistance increases significantly and the threshold stress intensity rises with martensitic transformation [217].

The fatigue crack growth rate (FCGR) of 302 SS increases in gaseous hydrogen. A large amount of martensite produced by cycling was found near the fatigue-fracture surface [218]. The crack propagates through martensite formed at the crack tip in the case of SCC of 304 SS in $MgCl_2$ boiling solution at 154 °C [219]. The fatigue-fractured surface morphoogy of 304 SS was observed to consist of reflective flat facets associated with twin boundary and intergranular separations [220]. Okamoto and Nakamura [221] found that the residual compressive stresses improves the fatigue life. However, residual tensile stresses enhance the fatigue crack growth of many alloys [222].

Fatigue crack growth tests were performed to evaluate fatigue behavior of 304 SS specimens with and without laser processing (welding and surface treatment) in air and gaseous hydrogen [186]. The results indicated that the laser-processed specimens exhibited a higher resistance to crack growth in the low stress-intensity factor range, ΔK, than the as-received steel plates regardless of testing environments. Fatigue-fractured

appearance of the steel plate tested in air was composed of transgranular fatigue fracture. A small number of facets exhibited intergranular fractures. QC fracture and a few twin boundary separations were observed for the same specimen in hydrogen. The extent of QC fracture was related to the formation of strain-induced martensite, which contributes to an increased FCGR of all specimens in gaseous hydrogen. The QC fracture was explained through the formation of strain-induced martensite. Fatigue fractographs of as-received (AR) specimens showing (a) transgranular fatigue fracture in air are shown in Fig. 9.56 [186]. The morphology in air is mainly composed of transgranular fatigue

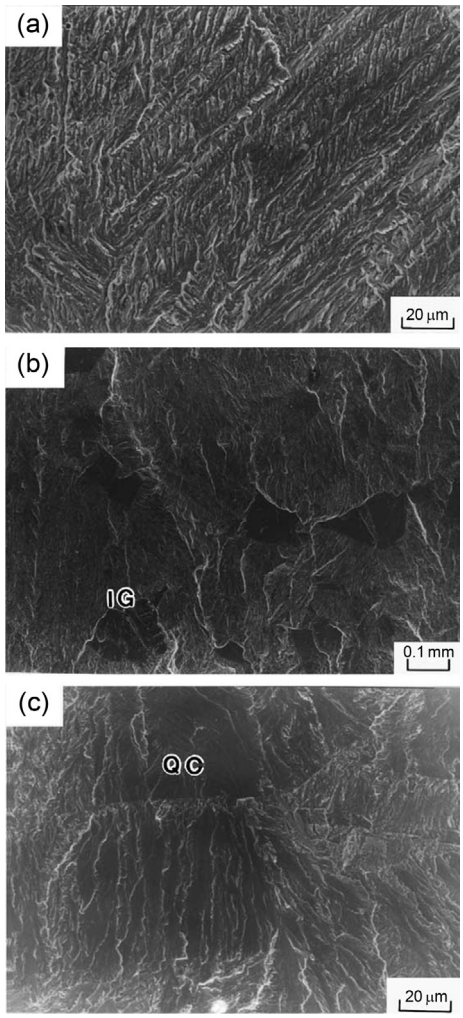

Fig. 9.56 Fatigue fractographs of as-received (AR) specimens showing (a) transgranular fatigue fracture in air, (b) twin boundary separations and intergranular (IG) fracture in air, and (c) QC fracture in hydrogen [186].

fracture indicating the presence of martensite (Fig. 9.56a) with a small number of flat facets of twin boundary separation and intergranular fracture in air (Fig. 9.56b) and QC fracture in hydrogen (Fig. 9.56c). The presence of QC fracture was due to the formation of strain-induced martensite, which is expected to increased FCGR of all specimens tested in hydrogen.

Figure 9.57 shows the fatigue crack growth behavior of the specimen with the crack growth parallel to or along the surface-heated zone (PS) [186]. The AR specimen was the same in air and hydrogen, indicating a small influence of the residual stresses on the FCGR for the PS. However, the accelerated FCGR in AR and PS specimens in hydrogen, da/dN values increased drastically when compared to those in the air [186].

Austenitic stainless steel can be made less susceptible to CFS by increasing its chromium, nitrogen, and molybdenum contents. Also, CFC of these alloys decreases by decreasing the grain size [223]. Ferritic stainless steels (type 430 SS) have high fatigue crack propagation rates due to their low toughness and low ductility. High chromium 26-1 ferritic stainless steel with composition Fe-26.2Cr-1.03Mo-0.001C-0.007 has shown high CFC in an aerated 3% NaCl solution at 3×10^7 cycles. Figure 9.58 shows that type 430 SS alloy increases the CGR in the presence of 3% NaCl solution [224].

Kaewkumsai *et al.* [225] investigated CFC of AISI 316L SS screen mesh. The screen mesh failed by pitting corrosion followed by CFC. Figures 9.59 and 9.60 show the surface appearance and surface morphology of the rupture site of AISI 316L SS [225]. The cracking was initiated by the presence of chlorides from PVC powder in combination with the residual and cyclic stress concentration present at the pits.

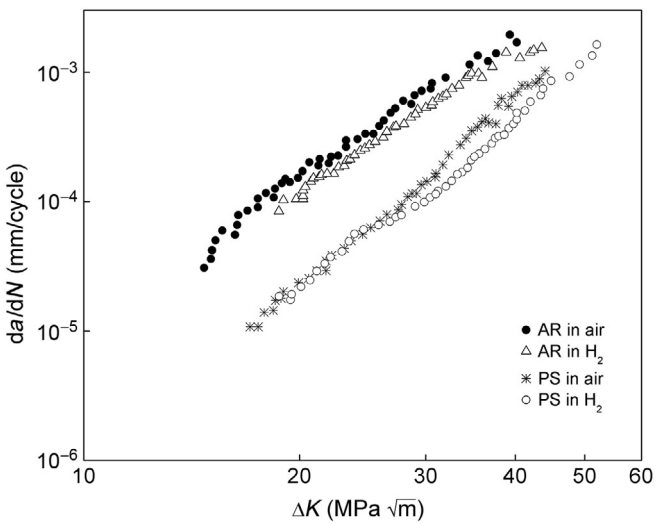

Fig. 9.57 The da/dN vs. ΔK curves for AR and PS specimens [186].

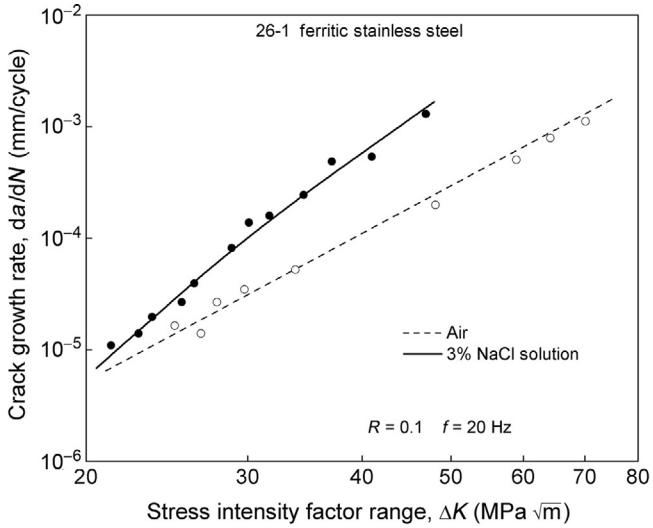

Fig. 9.58 FCGRs in 3% NaCl solution and in air for a ferritic stainless steel [224]. *Reprinted, with permission, from ASTM STP 642, Corrosion-Fatigue Technology, copyright ASTM International, West Conshohocken, PA.*

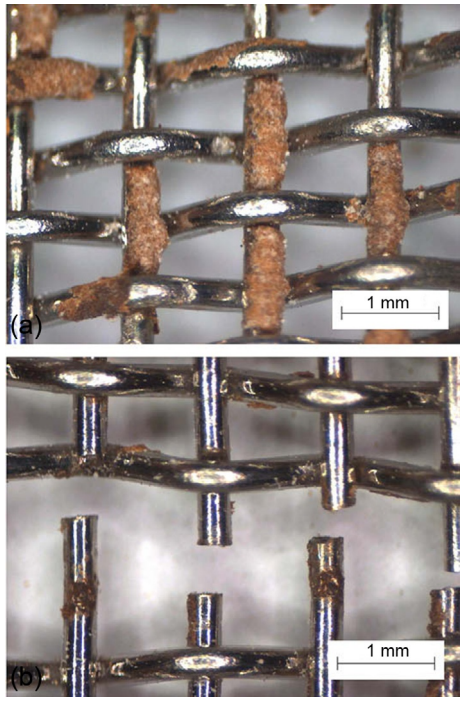

Fig. 9.59 Surface appearances in the rupture site: (a) excessively worn surface and (b) fracture sites of wires [225].

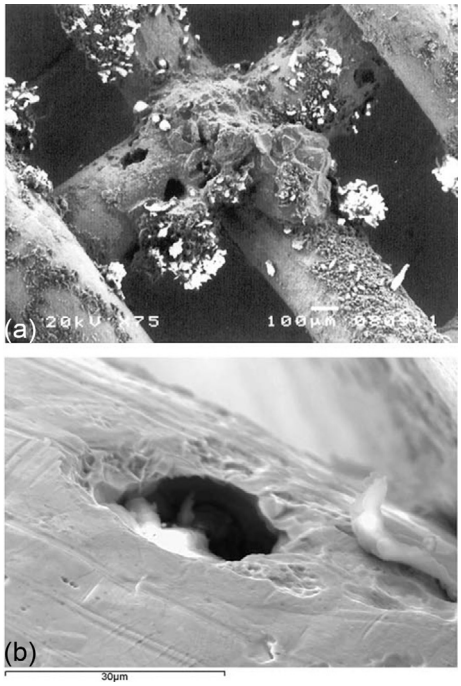

Fig. 9.60 Surface analysis: (a) SEM macrograph shows pitting corrosion under contaminants and (b) SEM micrograph showing pitting corrosion [225].

Tada [226] investigated the electrochemical responses to monitor crack initiation and propagation. Cyclic stress was applied to the sample under corrosion fatigue conditions. The electrochemical responses (current or potential) were obtained with a strain response [227–229]. CFC was investigated by analyzing current responses induced by cyclic stressing in a borate buffer solution containing 5 mM NaCl. Figure 9.61 shows the schematic of the approach for the detection of corrosion fatigue cracks [226].

To detect crack initiation, the harmonic components in the current responses as well as the decrease in phase shift between strain and current responses were evaluated. After crack initiation, the current response due to depassivation and repassivation at crack tips merged into the current response due to charging and discharging of an electric double layer. The crack initiation was detected by monitoring the phase shift between strain and current during a corrosion fatigue test or by the evolution of harmonics in the current responses. Smith *et al.* [230] developed a simulation procedure for CFC based on an intergranular corrosion/thermal stress interactive initiation mechanism and an environmentally assisted fatigue crack propagation mechanism. The simulation reproduced the high temperature CFC of low alloy Cr-Mo boiler tube steels. The results indicated that the crack was initiated by an intergranular surface corrosion/thermal stress mechanism. The crack growth was controlled by the environmentally assisted thermal fatigue crack propagation.

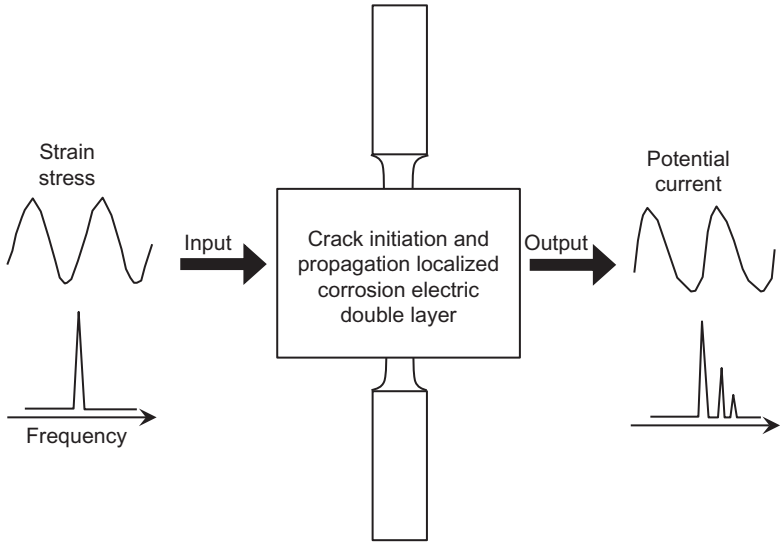

Fig. 9.61 Schematic drawing of approach to detection of corrosion fatigue cracks [226].

Corrosion fatigue can be reduced by increasing the tensile strength of a metal or alloy. However, once the crack is initiated in high tensile strength material, it advances at a faster rate when compared to the low-strength material. Reducing the stress of the material by stress relieving heat-treatment may result in the elimination of corrosion fatigue. Electrodeposited coatings such as zinc, copper, nickel, and nitrides that do not produce hydrogen or tensile stress during electrodeposition increase the corrosion fatigue resistance. Corrosion inhibitors also reduce or inhibit the corrosion fatigue.

9.10 PREVENTION OF STRESS CORROSION CRACKING

Identification of the cause of failure and the mechanism allows a recommendation to prevent future failures. EIC results in brittle mechanical failure (brittle fracture in alloys) under the condition of low uniform corrosion combined with synergistic interaction of the tensile stress, the specific corrosion environment, and the material. Thus, tensile stress, alloy susceptibility to SCC, and the critical environment are required for SCC. Eliminating any one of these factors may result in SCC prevention. Lowering the stress below the threshold value in the critical parts may be done by thickening the critical parts, reducing the load, or annealing in the case of residual stress. Removal of residual stresses allows sufficient creep to relax loads. However, it cannot be applied to stainless steels susceptible to SCC (intergranular attack) at high temperatures.

Cathodic protection should be designed not to overprotect the structure to avoid a high rate of hydrogen evolution and, consequently, HE. Environmental control can be achieved by eliminating the oxidizing agents and critical species by demineralization,

distillation, and gasification with nitrogen. The corrosion initiated by the environment can be controlled by adding inhibitors such as phosphates or other inorganic and organic inhibitors. Tarnish films [51,231] or dezincification layers are formed during the SCC of brass in ammonia solutions [232]. The dezincification layer and rupture of the tarnish film are factors that control SCC [51,231]. The strategy to inhibit the SCC of brass would be to inhibit the formation of tarnish films and dezincification layers. The addition of P, As, Sb [233], and Sn [234] inhibits the SCC formation by passivation of alloy surfaces. Phosphates are effective nontoxic inhibitors for inhibition of Cu in alkaline solutions [235–238]. The presence of phosphate inhibited the dissolution of brass by the formation of a passive zinc phosphate layer.

The effect of phosphates on SCC susceptibility of α-brass was studied by Ashour and Ateya [239]. The results indicated that disodium hydrogen phosphate (DHP) inhibits the SCC in brass by the formation of zinc phosphate. SSRT and electrochemical tests were used to study the SCC properties of H62 brass in Mattsson's solution (MS) containing various concentrations of DHP by Du *et al.* [240]. MS was used as an accelerated SCC test environment for H62 brass. The susceptibility of brass to SCC and film-induced stress decreased with increasing DHP concentrations. Electrochemical measurements confirmed that DHP inhibits SCC by forming a copper phosphate and zinc phosphate film on the brass surface. The film inhibits dezincification and decreases film-induced stress and reduces the susceptibility of brass to SCC. As shown in Fig. 9.62a, tarnishing

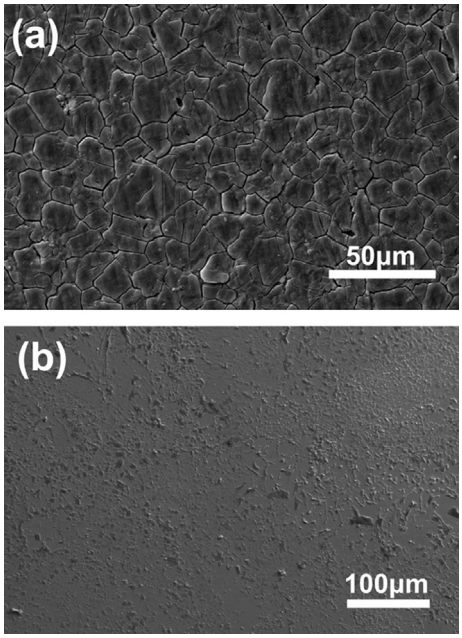

Fig. 9.62 SEM micrograph of the surface of H62 brasses formed by immersing samples in MS without DHP (a), containing 0.08 M DHP (b) for 6 h [240].

film forms on the bare surface in MS resulting in film cracks after immersing the sample for 6 h in the MS solution [240]. The surface, as shown in Fig. 9.62b, is crack free in the MS solution in the presence of 0.08 M DHP. Energy dispersive spectroscopy analysis indicated that the film formed in the presence of the inhibitor was enriched in Cu, Zn, O, and P [240]. Figure 9.63 shows the SCC susceptibility of H62 brass in MS containing various concentrations of DHP [240]. With the increase in the DHP concentration in the solution, the relative plasticity loss significantly decreases because the film-induced stress changes from tensile to compressive.

IGSCC is induced in sensitized type 304 SS exposed to contaminated water in nuclear reactors. The susceptibility to SCC of 304 sensitized SS increases with the kind of anion in the water in the following order [241]:

$$NO_3^- < B_4O_7^{2-} < CO_3^{2-} < Cl^- < PO_4^{3-} < HPO_4^{2-} < SiO_3^{2-} < OH^- < ASO_2^- < SO_4^{2-} < S_2O_3^{2-} < S^{2-} < SO_3^{2-}$$

The IGSCC propagation process was controlled by solution conductivity, while the crack initiation process was controlled by the type of anion, solution pH, and buffer capacity [38]. The addition of metal cations such as zinc ions into high-temperature water suppresses the corrosion of type 404 SS and avoids the accumulation of radioactive cobalt [242]. Addition of zinc also inhibits the IGSCC of sensitized 304 SS and Ni-based alloys [243,244]. Zhang *et al.* [39] investigated the inhibiting effect of Na^+, Ca^{2+}, Mn^{2+}, and Zn^{2+} on the IGSCC properties of sensitized 304 SS using the SSRT technique. Metal

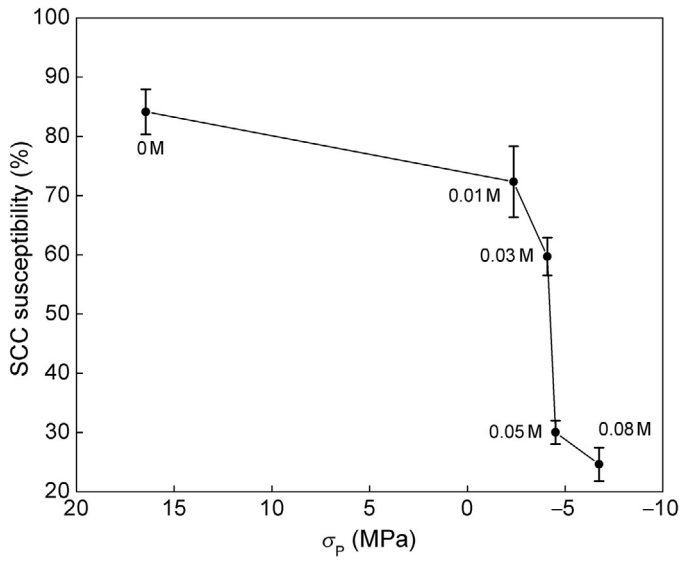

Fig. 9.63 SCC susceptibility of H62 brass in MS containing various concentrations of DHP [240].

cations investigated by Andersen and Angeliu [245] have high hardness data. The testing was performed in a deaerated water solution at 95 °C. The cations were characterized by hardness based on the hard and soft acids and bases concept. The hard metal cations present in the solution decreased the mean crack initiation frequency (MCIF) by increasing the crack initiation time, inhibiting the initiation time of the IGSCC. The effect of hardness of the metal cation on maximum stress, crack initiation time, and on MCIF is shown in Figs. 9.64–9.66, respectively [39]. As shown in the figures, increasing the metal cation hardness increases the maximum stress of the alloy by suppressing the IGSCC.

Huang [246] investigated the SCC of AISI 321 stainless steel in acidic chloride solutions by the SSRT technique and fracture mechanics. It was found that the cleavage fracture characterizes the fracture surface. The active dissolution mechanism controls the SCC of AISI 321 stainless steel in acidic chloride solutions and can be inhibited by using KI. The inhibition effect of KI on the SCC is due to inhibition of the anodic reaction of the corrosion process.

The beneficial effect of nitrogen to decrease the localized corrosion and SCC of austenitic SS welds has been reported in the literature [247–249]. Low-angle boundaries and coincidence boundaries inhibit the intergranular fracture [249]. Random high-angle boundaries are preferential sites for the crack nucleation and propagation. The type and structure of grain boundary existing in front of a propagating crack controls the change in fracture mode between intergranular and transgranular. A better grain boundary design would improve the SCC resistance of the structures.

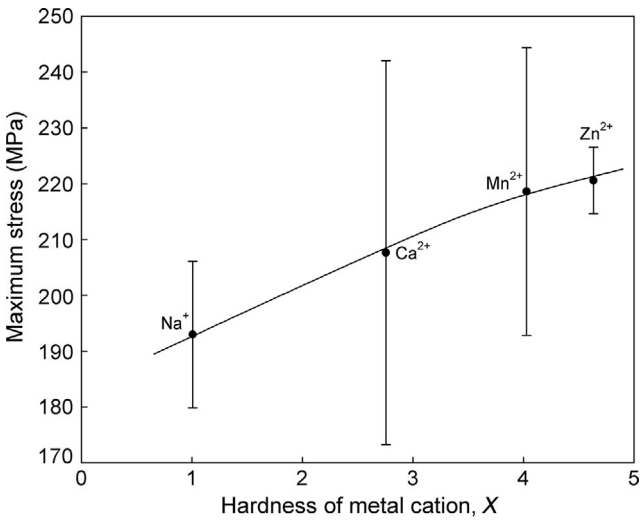

Fig. 9.64 Effect of hardness of metal cation on maximum stress obtained from the SCC tests [39].

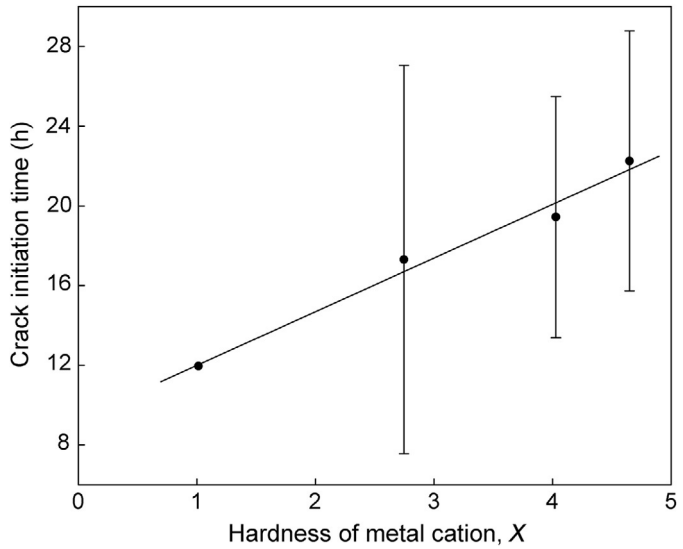

Fig. 9.65 Effect of hardness of metal cation on crack initiation time [39].

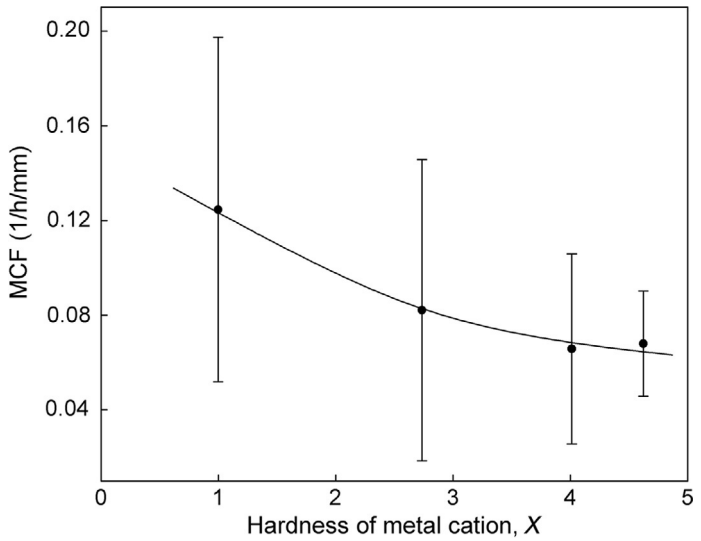

Fig. 9.66 Effect of hardness of metal cation on MCIF [39].

Case Study 9.1

The effect of sensitizing temperature on SCC of type 316 ausenitic stainless steel in hydrochloric acid was investigated by Nishimura *et al.* [97] by using a constant load method. The authors form the applied stress dependence of three parameters: steady state elongation rate, (i_{ss}), time interval of SCC-dominated failure, (t_{ss}), time of failure, (t_f), and divided the relationship between stress and the parameters into three regions.

(a) Identify the processes that dominate the regions defined by the authors.

(b) Define the relationship between $\frac{t_{ss}}{t_f}$. Is this ratio independent of applied stress and test temperature?

(c) Is it possible to use the steady state elongation rate (i_{ss}) as a parameter for prediction of time to failure?

(d) Is the fracture mode predominantly intergranular or transgranular at a sensitizing temperature of approximately 1000 K?

Case Study 9.2

SCC of zirconium and zircaloy-4 in aqueous halide solutions was investigated by Farina *et al.* [168].

(a) At which potential did the authors find that zirconium and zircaloy-4 are susceptible to SCC in an aqueous halide solution?

(b) Which of the following steps: (i) electrochemical breakdown of the passive film, (ii) intergranular attack due to anodic dissolution assisted by stress, or (iii) fast transgranular propagation are identified as "true" SCC process?

(c) Which of the SCC mechanisms explains the experimental results in this publication?

Case Study 9.3

Inhibition effect of metal cations for IGSCC of sensitized type 304 stainless steel was investigated using SSRT technique with a dynamic crack observation system by Zhang *et al.* [39].

(a) Addition of the metal cations with larger hardness into the electrolyte suppresses the initiation process of the IGSCC. Explain the effect of metal cation on crack initiation.

(b) Is the crack propagation affected by the addition of metal cations with larger hardness? Explain your response.

Case Study 9.4

Fonlupt *et al.* [115] investigated the role of the second phase in the SCC of a nickel-aluminum-bronze alloy using strain rate tests in synthetic sea water.

(a) Define the conditions at which the alloy is sensitive to SCC.

(b) Explain why the cracking path is controlled by the morphology of the alloy microstructure.

(c) Define the process between phases that triggers selective dissolution of the most electronegative phase.
(d) SCC decreases or increases with the amount of second phase in α-grain boundaries. Explain.
(e) Define the key parameter that controls the cracking mechanism under cathodic polarization.

Case Study 9.5

Factors affecting the electrochemical behavior and SCC of Alloy 690 in a chloride environment were investigated by Chen *et al.* [164] using a cyclic polarization method and a SSRT test.

(a) Define the pH values at which: (i) the alloy corrodes from general corrosion and (ii) the alloy is in passive state.
(b) Explain why the alloy is susceptible to pitting corrosion at very low pH values at higher applied potentials.
(c) What causes the maximum tensile strength (MTS) and FS measured by SSRT to decrease at pH lower than 3?

Case Study 9.6

Transient and steady state crack growth kinetics for SCC of cold worked 316 stainless steel on oxygenated pure water at different temperatures was investigated by Lu *et al.* [145].

(a) Define the crack growth kinetics identified in the paper depending on the previous test conditions and temperature.
(b) Explain why the SCC growth for the cold worked 316L stainless steel in oxygenated, high purity water is controlled by thermally activated processes.
(c) Explain why the combined effects of the crack tip reaction constants and the interface properties are affecting the time-lag crack growth after changing the temperature.

EXERCISES

E9.1. The critical stress intensity, K_{Ic}, is related to the magnitude of the stress, σ, at the tip of the crack by Eq. (E9.1)

$$K_{Ic} = Y\sigma\sqrt{\pi a} \tag{E9.1}$$

or

$$\sigma = \frac{K_{Ic}}{Y\sqrt{\pi a}}$$

where Y is a function of specimen crack geometry and "a" is crack length. Using Eq. (E9.1), calculate the critical stress intensity (materials fracture toughness) K_{Ic} of a specimen with a surface crack "a" of 0.45 mm exposed to a stress of $\sigma = 850$ MPa. Assume $Y = 1$.

E9.2. If a material with fracture toughness, K_{Ic}, of 40 MPa $\sqrt{m}$ is exposed to stress (σ) levels of 600, 800, 1000, and 1200 MPa, compute the length of the surface cracks and correlate the estimated surface cracks values vs. the stress levels. Assume $Y = 1$.

Use Eq. (E9.2):

$$a = \frac{1}{\pi}\left(\frac{K_{Ic}}{Y\sigma}\right)^2 \tag{E9.2}$$

E9.3. Using Eq. (E9.3):

$$Y = \frac{K_{Ic}}{\sigma\sqrt{\pi a}} \tag{E9.3}$$

(a) Estimate the parameter Y for a specimen with fracture toughness, K_{Ic}, (plane strain fracture) of 30 MPa $\sqrt{m}$, and stress level of 420 MPa. The surface crack length is 1.5 mm.

(b) Estimate the parameter Y values for the same specimen with surface cracks of 0.5, 1, 2, and 3 mm.

(c) For the same specimen in (a), the same crack length of 1.5 mm, and the same parameter Y as calculated in (a), compute the fracture toughness, K_{Ic}, under 550 MPa of stress.

E9.4. Compute the following:

(a) A specimen with a fracture toughness, K_{Ic}, of 60 MPa $\sqrt{m}$ is exposed to stress of 700, 900, 1100, and 1200 MPa. Assuming $Y = 1$ and the largest surface crack of 1 mm, compute if the given stress levels between 700 and 1200 MPa will fracture the specimen.

(b) For the same conditions, estimate if the given stress levels in (a) will fracture the specimen when the largest surface cracks are 0.5 and 2.0 mm.

E9.5. An alloy specimen with a plane strain fracture toughness of 50 MPa $\sqrt{m}$ cracks with the maximum (critical internal crack length) of $2a = 3.0$ mm. Estimate the applied stress assuming $Y = 1$.

E9.6. The magnitude of the maximum stress existing at the tip of an external crack (σ_m) is defined by Eq. (E9.4):

$$\sigma_m = 2\sigma_o\left(\frac{a}{\rho_t}\right)^{1/2} \tag{E9.4}$$

where σ_o is tensile stress, "a" is the crack length, and ρ_t is the radius of the curvature. Estimate the value of the maximum stress σ_m that exists at the tip of an

external crack with a radius of curvature ρ_t of 8.5×10^{-5} mm and critical crack length $2a = 3.0 \times 10^{-2}$ mm when a tensile stress σ_o of 220 MPa is applied.

E9.7. Compute the following:

(a) An alloy specimen with a plane strain fracture toughness of 80 MPa $\sqrt{\text{m}}$ cracks under stress with a minimum length of the surface crack of 35 mm, which initiates formation of a fracture. Estimate the tensile stress. Assume a value of 1 for Y.

(b) An alloy specimen that exhibits a plane strain fracture toughness of 75 MPa $\sqrt{\text{m}}$ is exposed to a tensile stress of 300 MPa. Compute the minimum (critical) length (a_c) of the surface crack that initiates a fracture. Assume a value of 1.5 for Y.

Use Eq. (E9.5):

$$K_{Ic} = Y\sigma\sqrt{\pi a_c} \rightarrow a_c = \frac{1}{\pi}\left(\frac{K_{Ic}}{Y\sigma}\right)^2 \tag{E9.5}$$

where a_c is critical crack length.

E9.8. In order to perform K_{Ic} testing on standard specimens, the following equation has been adopted:

$$a, B(W-a) \geq 2.5\left(\frac{K_{Ic}}{\sigma_{ys}}\right)^2 \tag{E9.6}$$

The quantity $\left(\frac{K_{Ic}}{\sigma_{ys}}\right)^2$ is proportional to the plastic zone size. The minimum requirement for the specimen thickness, B, the crack length, "a", and ligament length, $(W-a)$, where W is the specimen width, should ensure that the plastic zone is sufficiently small for fracture to be controlled by the intensity of stress ahead of the crack tip, K_{Ic}. Materials with high-yield stress σ_{ys} and low-fracture toughness should have low thickness to satisfy the requirement of Eq. (E9.6) for the plane strain condition. HE, SCC, and corrosion fatigue reduce the stress intensity. The methods used in linear elastic fracture mechanics developed in the last two decades can be used to test HE, SCC, and corrosion fatigue. These processes reduce the stress intensity to advance brittle cracks to low values of K_{Ic}. If a stainless steel alloy has yield strength, σ_{ys}, of 345 MPa and plain strain linear elastic fracture toughness, K_{Ic}, of 80 MPa $\sqrt{\text{m}}$, estimate the minimum specimen dimensions: a, B, W.

E9.9. Corrosion fatigue testing is performed using a sinusoidal stress function. The stress cycle is characterized by the stress ratio, R, of minimum to maximum stress, $\left(R = \frac{S_{min}}{S_{max}}\right)$. The tensile stress and the compressive stress are taken as positive and negative, respectively. In the case when the stress is completely reversible ($S_{max} = S_{min}$), $R = -1$. R is a negative fraction if the stress is partially reversed. If both maximum and minimum stresses are tensile, R is a positive fraction. By

cycling from tension to no load, R is equal to 0. A rotating cantilever beam apparatus is used for corrosion testing. The maximum stress level is defined as:

$$\sigma_m = \frac{\sigma_{max} + \sigma_{min}}{2} \tag{E9.7}$$

The stress amplitude is given by Eq. (E9.8)

$$\sigma_a = \frac{\sigma_{max} - \sigma_{min}}{2} \tag{E9.8}$$

The magnitude of the stress range, σ_r, is determined using Eq. (E9.9)

$$\sigma_r = \sigma_{max} - \sigma_{min} \tag{E9.9}$$

Single rotation of the bent-beam specimen shown in the figure represents one fatigue cycle. The specimen rotation results in tensile and compressive stress ($S_{max} = S_{min}$), $R = -1$. The results of the test as discussed under Corrosion Fatigue Testing in the chapter are plotted as the S-N curves as a maximum tensile stress vs. the number of cycles to failure. Example calculations are given for a fatigue test in which the stress amplitude, σ_a, is 180 MPa and the mean stress, σ_m, is 65 MPa. Calculations are performed using Eqs. (E9.7) through (E9.9) to estimate (a) the maximum and minimum stress levels, (b) the stress ratio, and (c) the magnitude of the stress range.

E9.10. In the cantilever beam apparatus shown in Fig. 9.67, a sample of stainless steel is exposed to a corrosion environment. If the minimum load of 20 kg is applied to a momentum arm of 2 m, estimate the fracture toughness value, K_{Ihic}, if the

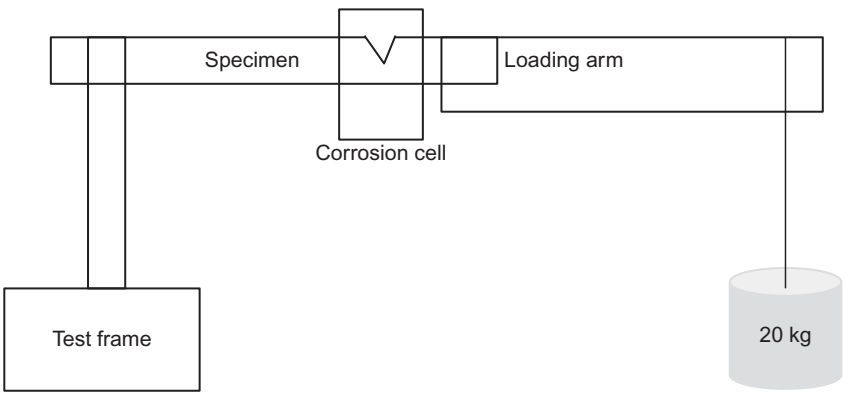

Fig. 9.67 Schematic of cantilever beam apparatus.

maximum crack length of 30 mm is caused from the applied stress. Assume the following specimen dimensions: width $B = 30$ mm, depth $W = 60$ mm, and reduced width across the side grooves $B_N = 15$ mm.

Use Eq. (E9.10) to calculate the fracture toughness value, K_{Ihic}:

$$K_{Ihic} = \frac{6MF}{\sqrt[3/2]{W-a}\sqrt{BB_N}} \tag{E9.10}$$

where, M is bending moment, B is specimen width, B_N is net specimen with subtracting side grooves, a is crack length, and W is specimen width (Table E9.1).

Table E9.1 Dependence of a/W and $F(a/W)$

a/W	$F(a/W)$
0.05	0.36
0.1	0.49
0.2	0.60
0.5	0.72

E9.11. The material toughness properties are controlled by loading rate and constrained through:

K_c is the critical stress intensity factor for plain-stress conditions of variable constraint in the case of static loading. The value of K_{Ic} depends on specimen thickness, geometry, and on the crack size.

K_{Ic} is the critical stress intensity factor for static loading and plain-strain conditions of maximum constraint represents a minimum value for thick plates.

$$K_c, K_{Ic} = C\sigma\sqrt{a} \tag{E9.11}$$

where C is is a function of specimen and crack geometry, σ is nominal stress (MPa), and "a" is flaw size, in (mm). Estimating the critical value of K_{Ic} for specific material with a given thickness, temperature, and loading rate, one can determine the flaw size for a given design stress level.

To estimate the crack growth in steel using fracture-mechanics, it is necessary to:

(i) Estimate the maximum initial flow size a_o and K.

(ii) With given value of K_c or K_{Ic} and the maximum stress, calculate the critical flaw size a_c that would cause a brittle fracture.

(iii) The following expression can be used to estimate the FCGR per cycle of the steels:

$$\frac{\mathrm{d}[a(m)]}{\mathrm{d}N} = 1.354 \times 10^{-10} \left(\Delta K_{\mathrm{I}} \left(\mathrm{MPa}\sqrt{\mathrm{m}}\right)\right)^{2.25} \tag{E9.12}$$

where $\frac{\mathrm{d}a}{\mathrm{d}N}$ represents fatigue crack growth per cycle of loading, ΔK_{I} is the stress intensity range, $(\mathrm{MPa}\sqrt{\mathrm{m}})$.

Assuming the following design specifications: $\sigma_{ys} = 700$ MPa; $K_{Ic} = 150\,\mathrm{MPa}\sqrt{\mathrm{m}}$; $a_o = 8.0$ mm; $\sigma_{max} = 350$ MPa; $\sigma_{min} = 170$ MPa; $\Delta\sigma = 180$ MPa (live-load stress range); $\Delta a = 2.0$ mm; and $K_{\mathrm{I}} = 1.12\sigma\sqrt{\pi a}$ and $\frac{\mathrm{d}[a(m)]}{\mathrm{d}N} = 1.354 \times 10^{-10} \left[\Delta K_{\mathrm{I}} \left(\mathrm{MPa}\sqrt{\mathrm{m}}\right)\right]^{2.25}$.

Estimate:

(a) The critical flaw size (a_c) using the nominal maximum design stress K_{Ic} that would cause failure by brittle fracture.

(b) Derive ΔK_{I} using the appropriate expression.

(c) Numerically integrate the CGR expression between a_o and a_c to estimate the life of the structure before failing.

To calculate the critical flaw size (a_c) use Eq. (E9.13) derived from Eq. (E9.5).

$$a_c = \frac{1}{\pi}\left(\frac{K_{Ic}}{1.12\sigma_{max}}\right)^2 \tag{E9.13}$$

REFERENCES

[1] R.N. Parkins, The application of stress corrosion crack growth kinetics to predicting life times of structures, Corros. Sci. 29 (1989) 1019–1038.

[2] Y.Z. Wang, K. Ebtehaj, D. Hardie, R.N. Parkins, The behavior of multiple stress corrosion cracks in a Mn-Cr and Ni-Cr-Mo-V steel: I, Metall. Corros. Sci. 37 (1995) 1651–1675.

[3] A. Turnbull, L.N. McCartney, S. Zhou, A model to predict the evolution of pitting corrosion and the pit-to-crack transition incorporating statistically distributed input parameters, Corros. Sci. 48 (2006) 2084–2105.

[4] S. Suzuki, K. Kumagayi, C. Shitara, J. Mizutani, A. Sakashita, H. Tokuma, H. Yamashita, Introduction of repair and maintenance technology against SCC in core shroud, Maintenology 3 (2004) 65–70.

[5] T. Shoji, Progress in the mechanistic understanding of BWR SCC and its implication to the prediction of SCC growth behavior in plants, in: Proceedings of the 11th International Symposium Environmental Degradation Materials Nuclear Power Systems-Water Reactors, American Nuclear Society, 2003, pp. 588–598.

[6] M. Kamaya, T. Haruna, Crack initiation model for sensitized 304 stainless steel in high temperature water, Corros. Sci. 48 (2006) 2442–2456.

[7] M. Kamaya, T. Haruna, Influence of local stress on initiation behavior of stress corrosion cracking for sensitized 304 stainless steel, Corros. Sci. 49 (2007) 3303–3324.

[8] Q.J. Peng, J. Kwon, T. Shoji, Development of a fundamental crack tip strain rate equation and its application to quantitative prediction of stress corrosion cracking of stainless steels in high temperature oxygenated water, J. Nucl. Mater. 324 (2004) 52–61.

[9] J. Sedriks, Making and using precracked cantilever beam specimens, in: Stress Corrosion Cracking Test Methods, National Association of Corrosion Engineers (NACE), Houston, TX, 1990, pp. 37–45.

[10] A. Turnbull, Test methods for environment assisted cracking, Br. Corros. J. 27 (1992) 271–289.

[11] ASTM G 38-01, Standard Practice for Making and Using C-Ring Stress-Corrosion Test Specimens, ASTM International, West Conshohocken, PA, 2007.
[12] D.O. Sprowls, Evaluation of stress-corrosion cracking, in: Metals Handbook, in: Corrosion, vol. XIII, ASM International, Metals Park, OH, 1987, pp. 245–282.
[13] Stress corrosion testing methods, in: Stress Corrosion Testing, ASTM STP 425 ASTM International, West Conshohocken, PA, 1967, pp. 3–20.
[14] H.L. Graig, D.O. Sprowls, D.E. Piper, W.H. Ailor (Ed.), Handbook of Corrosion Testing and Evaluation, John Wiley and Sons, Inc., New York, 1971, pp. 231–240.
[15] ASTM G 30-97, Standard Practice for Making and Using U-Bend Stress-Corrosion Test Specimens, ASTM International, West Conshohocken, PA, 2009, pp. 1-7.
[16] ASTM G 39-99, Standard Practice for Preparation and Use of Bent-Beam Stress Corrosion Test Specimens, ASTM International, West Conshohocken, PA, 2011, pp. 1-8.
[17] ASTM G 49-85, Standard Practice for Preparation and Use of Direct Tension Stress-Corrosion Test Specimens, ASTM International, West Conshohocken, PA, 2011, pp. 1-6.
[18] G. Haaijer, A.W. Loginow, Stress analysis of bent-beam stress corrosion specimen, Corrosion 21 (1965) 105–112.
[19] R.N. Parkins, Development of strain-rate testing and its implications, in: G.M. Ugiansky, J.H. Payer (Eds.), Stress Corrosion Cracking—The Slow Strain Rate Technique, ASTM STP 665, ASTM International, West Conshohocken, PA, 1979, pp. 5–25.
[20] C.D. Kim, B.E. Wilde, A review of the constant strain-rate stress corrosion cracking test, in: G. M. Ugiansky, J.H. Payer (Eds.), Stress Corrosion Cracking—The Slow Strain Rate Technique, ASTM STP 665, ASTM International, West Conshohocken, PA, 1979, pp. 97–112.
[21] J.I. Dickson, A.J. Russell, D. Tromans, Stress corrosion crack propagation in annealed and cold worked 310 and 316 austenitic stainless steels in boiling (154 °C) aqueous magnesium chloride solution, Can. Metall. Q. 19 (1980) 161–167.
[22] J.G. Kaufman, Progress in fracture testing of metallic materials: thickness as a problem, in: W. F. Brown Jr. (Ed.), Review of Developments in Plane Strain Fracture Toughness Testing, ASTM STP 463, ASTM International, West Conshohocken, PA, 1970, pp. 7–20.
[23] B.F. Brown Jr., J.E. Strawley, Commentary on present practice, in: W.F. Brown Jr. (Ed.), Review of Developments in Plane Strain Fracture Toughness Testing, ASTM STP 463, ASTM International, West Conshohocken, PA, 1967, pp. 216–249.
[24] F. Braun, C.D. Beachem, A study of the stress factor in corrosion cracking by use of the pre-cracked cantilever beam species, Corros. Sci. 5 (1965) 745–750.
[25] S.T. Rolfe, J.M. Barsom, Fracture and Fatigue Control in Structures, Prentice Hall, New Jersey, 1977, pp. 294-299.
[26] A. Atrens, C.C. Brosnan, S. Ramamurthy, A. Oehlert, I.O. Smith, Linearly increasing stress test (LIST) for SCC research, Meas. Sci. Technol. 4 (1993) 1281–1292.
[27] N. Winzer, A. Atrens, W. Dietzel, V. Song, K.U. Kainer, Comparison of the linearly increasing stress test and the constant extension rate test in the evaluation of transgranular stress corrosion cracking of magnesium, Mater. Sci. Eng. A 472 (2008) 97–106.
[28] E. Villalba, A. Atrens, Metallurgical aspects of rock bolt stress corrosion cracking, Mater. Sci. Eng. A 491A (2008) 8–18.
[29] N. Winzer, A. Atrens, W. Dietzel, V. Song, K.U. Kainer, Stress corrosion cracking in magnesium alloys: characterization and prevention, JOM 59 (2007) 49–53.
[30] K.F. Krysiak, Corrosion of weldaments, in: Metal Handbook, Corrosion, vol. XIII, ASM International, Metals Park, OH, 1987, pp. 343–368.
[31] D.L. Graver, Corrosion Data Survey, Metals Section, sixth ed., NACE, Houston, TX, 1985.
[32] W.L. Williams, Chloride and caustic stress corrosion of austenitic stainless steel in hot water and steam, Corrosion 13 (1957) 539t–545t.
[33] N. Pessal, G.P. Airey, B.P. Lingenfelter, The influence of thermal treatment on the stress corrosion cracking behavior of Inconel 600 at controlled potential in 10% caustic soda solutions at 315 °C, Corrosion 35 (1979) 100–107.
[34] J.H. Prayer, W.E. Berry, W.K. Boyd, Evaluation of slow strain-rate stress corrosion tests results, in: J.B. Wheeler, H.M. Hoersch, E.J. McGlinchey, H.P. Mahy (Eds.), Stress Corrosion

Cracking—The Slow Strain Rate Technique, ASTM STP 665, ASTM International, West Conshohocken, PA, 1970, pp. 61–80.
[35] R.C. Newman, Stress corrosion cracking mechanisms, in: P. Marcus, J. Oudra (Eds.), Corrosion Mechanisms in Theory and Practice, Marcel Dekker, Inc., New York, 1995, pp. 311–320
[36] R.W. Staehle, J. Hochmann, R.D. McCright, Stress Corrosion Cracking and Hydrogen Embrittlement of Iron-Based Alloys, in: J.E. Slater (Ed.), NACE-5, NACE, Houston, TX, 1977, pp. 180–190.
[37] G. Okamoto, T. Shibata, Desoprtion of tritiated bound-water from the passive film formed on stainless steels, Nature 296 (1965) 1350.
[38] S. Zhang, T. Shibata, T. Haruna, Contribution of solution pH and buffer capacity to suppress intergranular stress corrosion cracking of sensitized type 304 stainless steel at 95 °C, Corrosion 55 (1999) 462–468.
[39] S. Zhang, T. Shibata, T. Haruna, Inhibition effect of metal cations to intergranular stress corrosion cracking of sensitized type 304 stainless steel, Corros. Sci. 47 (2005) 1049–1061.
[40] C.M. Rangel, T.M. Silva, M. da Cunha Belo, Semiconductor electrochemistry approach to passivity and stress corrosion cracking susceptibility of stainless steels, Electrochim. Acta 50 (2005) 5076–5082.
[41] H. Gerisher, Semiconductor electrode reactions, in: P. Delahay (Ed.), Advances in Electrochemistry and Electrochemical Engineering, vol. 1, Willey-Interscience, New York, 1961.
[42] H.L. Logan, Film-rupture mechanism of stress corrosion, J. Res. Natl. Bur. Stand. 48 (1952) 99–105.
[43] P.L. Andresen, F.P. Ford, Life prediction by mechanistic modeling and system monitoring of environmental cracking of iron and nickel alloys in aqueous systems, Mater. Sci. Eng. A 103 (1988) 167–184.
[44] C. Edeleanu, A.J. Forty, Some observations on the stress corrosion cracking of α-brass and similar alloys, Philos. Mag. 58 (1960) 1029–1040.
[45] D.A. Jones, Principles and Prevention of Corrosion, second ed., Prentice-Hall Inc., Upper Saddle River, NJ, 1996, pp. 279–286.
[46] J.R. Galvele, A stress corrosion cracking mechanism based on surface mobility, Corros. Sci. 27 (1987) 1–33.
[47] G.S. Duffo, J.R. Galvele, Surface-mobility stress corrosion cracking mechanism in silver alloys, in: R.P. Gangloff, M.B. Ives (Eds.), Environment-induced Cracking of Metals, NACE, Houston, TX, 1990, pp. 261–264.
[48] R.N. Parkins, Predictive approaches to stress-corrosion cracking failure, Br. Corros. J. 14 (1979) 5–14.
[49] R.N. Parkins, Predictive approaches to stress-corrosion cracking failure, Corros. Sci. 20 (1980) 147–166.
[50] R.N. Parkins, Factors influencing stress corrosion crack growth kinetics, Corrosion 43 (1987) 130–139.
[51] A.J. Forty, P. Humble, The influence of surface tarnish on stress-corrosion of brass, Philos. Mag. 8 (1963) 247–264.
[52] E.N. Pugh, Progress toward understanding the stress corrosion problem, Corrosion 41 (1985) 517–526.
[53] T. Nakayama, M. Takano, Application of a slip dissolution-repassivation model for stress corrosion cracking of AISI 304 stainless steel in a boiling 42% $MgCl_2$ solution, Corrosion 42 (1986) 10–15.
[54] P.L. Andresen, Environmentally assisted growth rate response of nonsensitized AISI 316 grade stainless steels in high temperature water, Corrosion 44 (1988) 450–460.
[55] F.P. Ford, Quantitative prediction of environmentally-assisted cracking, Corrosion 52 (1996) 375–395.
[56] A.P. Jivkov, Strain-assisted corrosion cracking and growth rate inhibitors (Ph.D. thesis), Lund University, Malmo, Sweden, 2002, pp. 13-16.
[57] K.S. Raja, Stress corrosion cracking studies, Report TR-03-007, SIR-UNR-014, US, 2004, pp. 1-77.
[58] E.M. Gutman, An inconsistency in "film rupture model" of stress corrosion cracking, Corros. Sci. 49 (2007) 2289–2302.

[59] E.N. Pugh, On the propagation of transgranular stress-corrosion cracks, in: R.M. Latanison, J.R. Pickens (Eds.), Atomistics of Fracture, Plenum Press, New York, 1983, pp. 997–1010.
[60] K. Sieradzki, R.C. Newman, Brittle behavior of ductile metals during stress-corrosion cracking, Philos. Mag. 51 (1985) 95–132.
[61] D.A. Jones, The contribution of localized surface plasticity to the mechanism of environment-induced cracking, in: R.P. Gangloff, M.B. Ives (Eds.), Environmental-Induced Cracking of Metals, NACE, Houston, TX, 1990, pp. 265–270.
[62] R.W. Revie, H.H. Uhlig, Effect of applied potential and surface dissolution on the creep behavior of copper, Acta Metall. 22 (1974) 619–627.
[63] K. Sieradzki, F.J. Friedersdorf, Notes on the surface mobility mechanism of stress-corrosion cracking, Corros. Sci. 36 (1994) 669–676.
[64] R.N. Parkins, Stress corrosion cracking, in: R.P. Gangloff, M.B. Ives (Eds.), Environment-Induced Cracking of Metals, NACE, Houston, TX, 1990, pp. 1–20.
[65] R.A. Oriani, Hydrogen effects in high-strength steels, in: R.P. Gangloff, M.B. Ives (Eds.), Environment-Induced Cracking of Metals, NACE, Houston, TX, 1990, pp. 439–448.
[66] R.C. Newman, Stress-corrosion cracking mechanisms, in: P. Marcus (Ed.), Corrosion Mechanisms in Theory and Practice, Marcel Dekker Inc., New York, 2002, pp. 399–450.
[67] M. Vollmer-Uebing, M. Stratmann, A surface analytical and an electrochemical study of iron surfaces modified by thiols, Appl. Surf. Sci. 55 (1992) 19–35.
[68] K. Sieradzki, J.S. Kim, A.T. Cole, R.C. Newman, The relationship between dealloying and transgranular stress-corrosion cracking of copper-zinc and copper-aluminum alloys, J. Electrochem. Soc. 134 (1987) 1635–1639.
[69] M.G. Fontana, Corrosion Engineering, McGraw-Hill, New York, 1986.
[70] R. Liu, N. Narita, C. Alsteter, H. Birnbaum, E.N. Pugh, Studies of the orientations of fracture surfaces produced in austenitic stainless steels by stress-corrosion cracking and hydrogen embrittlement, Metall. Trans. A 11A (1980) 1563–1574.
[71] B.Y. Fang, A. Atrens, J.Q. Wang, E.H. Han, Z.Y. Zhu, W.J. Ke, Review of stress corrosion cracking of pipeline steels in low and high pH solutions, Mater. Sci. 38 (2003) 127–132.
[72] E.A. Charles, R.N. Parkins, Generation of stress corrosion cracking environments at pipeline surfaces, Corrosion 51 (1995) 518–527.
[73] J.Q. Wang, A. Atrens, SCC initiation for X65 pipeline steel in the high PH carbonate/bicarbonate solution, Corros. Sci. 45 (2003) 2199–2217.
[74] H.C. Choe, Stress corrosion cracking characteristics of shot-peened stainless steel containing Ti, Han'guk Pyomyon Konghak Hoechi 37 (2004) 350–359.
[75] W.F. Savage, E.F. Nippes, G.M. Goodwin, Effect of minor elements on hot cracking tendencies of Inconel 600, Weld J. 56 (1977) s245–s253.
[76] S. Kou, Solidification and liquation cracking issues in welding, JOM 55 (2003) 37–42.
[77] A.J. Ramirez, J.W. Sowards, J.C. Lippold, Improving the ductility-dip cracking resistance of Ni-base alloys, J. Mater. Process. Technol. 179 (2006) 212–218.
[78] R. Vallent, The influence of different Nb-contents on the hot-cracking susceptibility of Ni-base weld metals type 70/20, in: T. Bollinghaus, H. Herold (Eds.), Hot Cracking Phenomena in Welds, Springer-Verlag, Berlin, 2005, pp. 141–164.
[79] A.J. Ramirez, J.C. Lippold, High temperature behavior of Ni-base weld metal Part II—insight into the mechanism for ductility dip cracking, Mater. Sci. Eng. A 380 (2004) 245–258.
[80] P.L. Andresen, M.M. Morra, Stress corrosion cracking of stainless steels and nickel alloys in high-temperature water, Corrosion 64 (2008) 15–29.
[81] Q.J. Peng, H. Yamauchi, T. Shoji, Investigation of dendrite-boundary microchemistry in Alloy 182 using auger electron spectroscopy analysis, Metall. Mater. Trans. A 34A (2003) 1891–1899.
[82] Q. Peng, J. Hou, Y. Takeda, T. Shoji, Effect of chemical composition on grain boundary microchemistry and stress corrosion cracking in Alloy 182, Corros. Sci. 67 (2013) 91–99.
[83] H. Vogt, M.O. Speidel, Stress corrosion cracking of two aluminum alloys: a comparison between experimented observations and data based on modeling, Corros. Sci. 40 (1998) 251–270.

[84] M. Ahmad, Effects of environment and microstructure on stress corrosion crack propagation in an Al Li Cu Mg alloy, Mater. Sci. Eng. A 125A (1990) 1–14.
[85] R.P. Wei, C.M. Liao, M. Gao, A transmission electron microscopy study of constituent-particle-induced corrosion in 7075-T6 and 2024-T3 aluminum alloys, Metall. Mater. Trans. A 29A (1998) 1153–1160.
[86] R.G. Buchheit, M.A. Martinez, L.P. Montes, Evidence for Cu ion formation by dissolution and dealloying the Al_2CuMg intermetallic compound in rotating ring-disk collection experiments, J. Electrochem. Soc. 147 (2000) 119–124.
[87] T. Ramgopal, P.I. Gouma, G.S. Frankel, Role of grain-boundary precipitates and solute-depleted zone on the intergranular corrosion of aluminum alloy 7150, Corrosion 58 (2002) 687–697.
[88] P.V. Petroyiannis, E. Kamoutsi, A.T. Kermanidis, S.G. Pantelakis, V. Bontozoglou, G. N. Haidemenopoulos, Evidence on the corrosion-induced hydrogen embrittlement of the 2024 aluminum alloy, Fatigue Fract. Eng. Mater. 28 (2005) 565–574.
[89] N.K. Allam, Thermodynamic and quantum chemistry characterization of the adsorption of triazole derivatives during Muntz corrosion in acidic and neutral solutions, Appl. Surf. Sci. 253 (2007) 4570–4577.
[90] J.H. Bulloch, Some effects of yield strength on the stress corrosion cracking behavior of low alloy steels in aqueous environments at ambient temperatures, Eng. Fail. Anal. 11 (2004) 843–856.
[91] S.V. Nair, J.K. Tien, A plastic flow induced fracture theory for KISCC, Metall. Trans. A 16 (1985) 2334–2340.
[92] F. Gutierrez-Solana, J. Gonzalez, J.M. Varona, M.V. Biezma, Modeling the stress corrosion cracking of low alloy steels, Corros. Sci. 35 (1993) 499–505.
[93] R.M. Davidson, T. DeBold, M.J. Johnson, Corrosion of stainless steels, in: Metals Handbook, Corrosion, vol. XIII, ASM International, Metals Park, OH, 1987, pp. 547–565.
[94] N.A. Marianoa, D. Spinelli, Stress corrosion cracking of stainless steel used in drill collars, Mater. Sci. Eng. A 385 (2004) 212–219.
[95] A. Aguilar, Proceedings of the International Conference on Hydrogen Effects on Material Behavior and Corrosion Deformation Interaction, Moran, WY, United States, September 22-26, 2002, Meeting Date 2002, 2003, pp. 733–774.
[96] R.M. Horn, G.M. Gordon, F.P. Ford, R.L. Cowan, Experience and assessment of stress corrosion cracking in L-grade stainless steel BWR internals, Nucl. Eng. Des. 174 (1997) 313–325.
[97] R. Nishimura, I. Musalam, Y. Maeda, The effect of sensitizing temperature on stress corrosion cracking of type 316 austenitic stainless steel in hydrochloric acid solution, Corros. Sci. 44 (2002) 1343–1360.
[98] K. Sieradzki, R.L. Sabatini, R.C. Newman, Stress-corrosion cracking of copper single crystals, Metall. Trans. A 15A (1984) 1941–1946.
[99] R.C. Newman, W. Zheng, R.P.M. Procter, Stress-corrosion cracking of carbon-manganese steels in methanol-ammonia environments—II. Electrochemical and fractographic studies, Corros. Sci. 33 (1992) 1033–1051.
[100] H.P. Seifert, S. Ritter, J. Hickling, Research and service experience with environmentally assisted cracking of low-alloy steel pressure-boundary components under LWR conditions, Power Plant Chem. 6 (2004) 111–123.
[101] P.M. Scott, D. Tice, Stress corrosion in low alloy steels, Nucl. Eng. Des. 119 (1990) 399–413.
[102] E. Lenz, N. Wieling, Strain-induced corrosion cracking of low-alloy steels in LWR-systems interpretation of susceptibility by means of a three-dimensional (T, ε dissolved oxygen) diagram, Nucl. Eng. Des. 9 (1986) 331–344.
[103] A. Hiroki, O. Kozo, K. Jun, Relationship between stress corrosion resistance and microstructure of rapidly solidified Al-Zn-Mg alloys, Keikinzoku 54 (2004) 69–74.
[104] R.C. Newman, A theory of secondary alloying effects on corrosion and stress-corrosion cracking, Corros. Sci. 33 (1992) 1653–1657.
[105] R.A. Sielski, Research needs in aluminum structure, Ships Offshore Struct. 3 (2008) 57–65.
[106] F.S. Bovard, Corrosion in marine and saltwater environments II, in: D.A. Shifler, T. Tsuru, P.M. Natishan, S. Ito (Eds.), Electrochemical Society Proceedings, vol. 2004-2014, Electrochemical Society, Pennington, NJ, 2005, pp. 232–243.

[107] I.N.A. Oguocha, O.J. Adigun, S. Yannacopoulos, Effect of sensitization heat treatment on properties of Al-Mg alloy AA 5083-H116, J. Mater. Sci. 43 (2008) 4208–4214.
[108] J.L. Searles, P.I. Gouma, R.G. Buchheit, Stress corrosion cracking of sensitized AA5083 (Al-4.5Mg-1.0Mn), Mater. Sci. Forum 396-402 (2002) 1437–1442.
[109] H. Yukawa, Y. Murata, M. Morinaga, Y. Takahashi, H. Yoshida, Heterogeneous Distributions of magnesium atoms near the precipitate in Al-Mg based alloys, Acta Metall. Mater. 43 (1995) 681–688.
[110] D.O. Sprowls, R.H. Brown, Stress corrosion mechanisms for aluminum alloys, in: R.W. Staehel, A. J. Forty (Eds.), Fundamental Aspects of Stress Corrosion Cracking, National Association of Corrosion Engineers, Houston, TX, 1969, pp. 466–512.
[111] M. Popovic, E. Romhanji, Characterization of microstructural changes in an Al 6.8 wt.% Mg alloy by electrical resistivity measurements, Mater. Sci. Eng. A 492 (2008) 460–467.
[112] L. Tan, T.R. Allen, Effect of thermomechanical treatment on the corrosion of AA5083, Corros. Sci. 52 (2010) 548–554.
[113] R.N. Parkins, Y. Suzuki, Environment sensitive cracking of a nickel-aluminum bronze under monotonic and cyclic loading conditions, Corros. Sci. 23 (1983) 577–599.
[114] F. Hasan, A. Jahanafrooz, G.W. Lorimer, N. Ridley, The morphology, crystallography, and chemistry of phases in as-cast nickel-aluminum bronze, Metall. Trans. A 13A (1982) 1337–1345.
[115] S. Fonlupt, B. Bayle, D. Delafosse, J.L. Heuze, Role of second phases in the stress corrosion cracking of a nickel-aluminium bronze in saline water, Corros. Sci. 47 (2005) 2792–2806.
[116] C. Changa, S. Lee, J. Lin, M. Yehc, R. Jengc, Effect of Ag content and heat treatment on the stress corrosion of Al-4.6Cu-0.3Mg alloy, Mater. Chem. Phys. 91 (2005) 454–462.
[117] R. Ishibashi, T. Horiuchi, J. Kuniya, M. Yamamoto, S. Tsurekawa, H. Kokawa, T. Watanabe, T. Shoji, Effect of grain boundary character distribution on stress corrosion cracking behavior in austenitic stainless steels, Mater. Sci. Forum 475-479 (2005) 3863–3866.
[118] M. Shimada, H. Kokawa, Z.J. Wang, Y.S. Sato, I. Karibe, Optimization of grain boundary character distribution for intergranular corrosion resistant 304 stainless steel by twin-induced grain boundary engineering, Acta Mater. 50 (2002) 2331–2341.
[119] J. Hochmann, A. Desestret, P. Jolly, R. Mayoud, Properties of high-chromium ferritic stainless steels and austeno-ferritic stainless steels, in: R.W. Staehle, J. Hochmann, R.D. McCright, J.E. Slater (Eds.), Stress Corrosion Cracking and Hydrogen Embritlement of Iron-Base Alloys, in: NACE-5NACE, Houston, TX, 1977, pp. 956–1002.
[120] H.D. Solomon, T.M. Devine, Duplex stainless steels—a tail of two phases, in: R.A. Lula (Ed.), Duplex Stainless Steels, ASM, Metals Park, OH, 1983, pp. 693–756.
[121] W.A. Baeslack, J.C. Lippold, Phase transformation behavior in duplex stainless steels weldments, Met. Constr. Br. Weld. 20 (1988) 26R–31R.
[122] J.H. Potgieter, Influence of σ-phase on general and pitting corrosion resistnace of SAF 2205 duplex stainless steel: reply to comments, Br. Corros. J. 27 (1992) 219–223.
[123] E.I. Kivineva, N.E. Hannerz, The properties of Gleeble simulated heat affected zone of SAF 2205 and SAF2507 duplex stainless steels, in: Proceedings of Duplex Stainless Steels Conference, vol. 1, paper 7, 1994, Glasgow, Scotland.
[124] P.R. Levery, A. Van Bennekom, A mechanistic study of the effects of nitrogen on the corrosion properties of stainless steels, Corrosion 51 (1995) 911–921.
[125] H. Brandis, W. Heimann, Nitrogen-bearing high strength austenitic stainless steels, in: Stainless Steel'84, The Institute of Metals, London, 1985, pp. 217–221.
[126] Y.S. Lim, J.S. Kim, S.J. Ahn, H.S. Kwon, Y. Katada, The influences of microstructure and nitrogen alloying on pitting corrosion of type 316L and 20 wt.% Mn-substituted type 316L stainless steels, Corros. Sci. 43 (2001) 53–68.
[127] H.Y. Liou, R.I. Hsieh, W.T. Tsai, Microstructure and stress corrosion cracking in simulated heat-affected zones of duplex stainless steels, Corros. Sci. 44 (2002) 2841–2856.
[128] M. Casales, V.M. Salinas-Brav, A. Martinez-Villafane, J.G. Gonzalez-Rodriguez, Effect of heat treatment on the stress corrosion cracking of Alloy 690, Mater. Sci. Eng. A 332 (2002) 223–230.
[129] R.K. Singh Raman, W.H. Siew, Role of nitrite addition in chloride stress corrosion cracking of a super duplex stainless steel, Corros. Sci. 52 (2010) 113–117.

[130] P.M. Scott, Environment-assisted cracking in austenitic components, Int. J. Press. Vessels Pip. 65 (1996) 255–264.
[131] P.M. Scott, C. Benhamou, An overview of recent observation and interpretation of IGSCC in nickel base alloys in PWR primary water, in: Proceedings of the 10th International Symposium on Environmental Degradation of Materials in Nuclear Power Systems—Water Reactors, NACE, 2001, CDROM.
[132] R.B. Rebak, Z. Xia, Z. Szklarska-Smialowska, Effect of temperature and cold work on the crack growth rate of Alloy 600 in primary water, Corrosion 51 (1995) 689–697.
[133] W.C. Moshier, C.M. Brown, Effect of cold work and processing orientation on stress corrosion cracking behavior of Alloy 600, Corrosion 56 (2000) 307–320.
[134] S. Yamazaki, Z. Lu, Y. Ito, Y. Takeda, T. Shoji, The effect of prior deformation on stress corrosion cracking growth rates of Alloy 600 materials in a simulated pressurized water reactor primary water, Corros. Sci. 50 (2008) 835–846.
[135] D.H. Lee, J.H. Han, K.M. Kim, J.S. Kim, U.C. Lee, Effect of cold work on primary water stress corrosion cracking of Inconel Alloy 600 nuclear power steam generator tube material, Han'guk Chaelyo Hakhoechi 8 (1998) 726–732.
[136] E. Gamboa, A. Atrens, Material influence on the stress corrosion cracking of rock bolts, Eng. Fail. Anal. 12 (2005) 201–235.
[137] P. Muraleedharan, H.S. Khatak, J.B. Gnanamoorthy, P. Rodriguez, Effect of cold work on stress corrosion cracking behavior of types 304 and 316 stainless steels, Metall. Trans. A 16A (1985) 285–289.
[138] J.H. Zheng, W.F. Bogaerts, Effects of cold work on stress corrosion cracking of type 316L stainless steel in hot lithium hydroxide solution, Corrosion 49 (1993) 585–593.
[139] R. Bandy, D. Van Rooyen, Stress corrosion cracking on Inconel Alloy 600 in high temperature water—an update, Corrosion 40 (1984) 425–430.
[140] R.B. Rebak, Z. Szklarska-Smialowska, The mechanism of stress corrosion cracking of Alloy 600 in high temperature water, Corros. Sci. 38 (1996) 971–988.
[141] M.O. Speidel, R. Magdowski, Stress corrosion crack growth in Alloy 600 exposed to PWR and BWR environments, paper 222, 2002, NACE, Orlando, pp. 689-697.
[142] R. Magdowski, F. Vaillant, C. Amzallag, M.O. Speidel, Stress corrosion crack growth rates of Alloy 600 in simulated PWR coolant, in: Proceedings of the 8th International Symposium on Environmental Degradation of Materials in Nuclear Power Systems—Water Reactors, American Nuclear Society, Amelia Island, 1997, pp. 333–338.
[143] N. Hansen, Cold deformation microstructures, Mater. Sci. Technol. 6 (1990) 1039–1047.
[144] V. Ji, Y.G. Zhang, C.Q. Chen, The non-destructive estimation of the superficial mechanical properties of components in the INCONEL 600 alloy by X-ray diffraction peak width, Surf. Coat. Technol. 130 (2000) 95–99.
[145] Z. Lu, T. Shoji, Y. Takeda, Y. Ito, A. Kai, S. Yamazaki, Transient and steady state crack growth kinetics for stress corrosion cracking of a cold worked 316L stainless steel in oxygenated pure water at different temperatures, Corros. Sci. 50 (2008) 561–575.
[146] H. Nakajima, T. Shoji, M. Kikuchi, H. Nitsuma, M. Shindo, Detecting acoustic emission during cyclic crack growth in simulated BWR environments, in: S.J. Hudak, R.J. Bucci (Eds.), Fatigue Crack Growth Measurement and Data Analysis, ASTM STP 738, ASTM International, West Conshohocken, PA, 1981, pp. 139–162.
[147] K. Tamaki, S. Tsujikawa, Y. Hisamatsu, Development of a new test method for chloride stress corrosion cracking of stainless steels in dilute NaCl solutions, in: H.S. Isaacs, U. Bertocci, J. Kruger, S. Smialowska (Eds.), Advances in Localized Corrosion, in: NACE-9NACE, Houston, TX, 1991, pp. 207–214.
[148] A. Turnbull, S. Zhou, Impact of temperature excursion on stress corrosion cracking of stainless steels in chloride solution, Corros. Sci. 50 (2008) 913–917.
[149] K. Sieradzki, The effect of thin film formation at crack tips on fracture, Acta Metall. 30 (1982) 973–982.
[150] M. Kimura, N. Totsuka, T. Kurisu, K. Amano, J. Matsuyama, Y. Nakai, Sulfide stress corrosion cracking of line pipe, Corrosion 45 (1989) 340–346.

[151] R.W. Staehle, Predictions and experimental verification of the slip dissolution model for stress corrosion cracking of low strength alloys, in: R.W. Staehle (Ed.), Stress Corrosion Cracking and Hydrogen Embrittlemen of Iron Base Alloys, In: NACE-5NACE, Houston, TX, 1977, pp. 180–207.
[152] D. Choi, G.S. Was, Pit growth in Alloy 600/690 steam generator tubes in simulated concentrated environments (cupric, chloride, and sulfate), Corrosion 146 (1990) 100–111.
[153] W.T. Tsai, T.F. Wu, Pitting corrosion of Alloy 690 in thiosulfate-containing chloride solutions, J. Nucl. Mater. 277 (2000) 169–174.
[154] H. Spaehn, Stress corrosion cracking and corrosion fatigue of martensitic, ferritic, and ferritic-austenitic (duplex) stainless steel, in: P. Marcus, J. Oudar (Eds.), Corrosions Mechanisms in Theory and Practice, Marcel Dekker, Inc., New York, 1995, pp. 449–487
[155] A.K. Jha, V. Diwakar, K. Sreekumar, Stress corrosion cracking of stainless steel bellows of satellite launch vehicle propellant tank assembly, Eng. Fail. Anal. 10 (2003) 699–709.
[156] R. Bandy, R. Roberge, R.C. Newman, Low-temperature stress corrosion cracking of sensitized Inconel 600 in tetrathionate and thiosulfate solutions, Corrosion 39 (1983) 391–398.
[157] M.K. Ahn, H.S. Kwon, J.H. Lee, Predicting susceptibility of Alloy 600 to intergranular stress corrosion cracking using a modified electrochemical potentiokinetic reactivation test, Corrosion 51 (1995) 441–449.
[158] R. Bandy, R. Roberge, R.C. Newman, Low-temperature stress corrosion cracking of Inconel 600 under two different conditions of sensitization, Corros. Sci. 23 (1983) 995–1006.
[159] R.C. Newman, R. Roberge, R. Bandy, Environmental variables in the low temperature stress corrosion cracking of Inconel 600, Corrosion 39 (1983) 386–390.
[160] W.T. Tsai, C.S. Chang, L.T. Lee, Effects of shot peening on corrosion and stress corrosion cracking behaviors of sensitized Alloy 600 in thiosulfate solution, Corrosion 50 (1994) 98–105.
[161] R.C. Newman, W.P. Wong, H. Ezuber, A. Garner, Pitting of stainless steels by thiosulfate ions, Corrosion 45 (1989) 282–287.
[162] Z. Lu, T. Shoji, Y. Takeda, Y. Ito, S. Yamazaki, The dependency of the crack growth rate on the loading pattern and temperature in stress corrosion cracking of strain-hardened 316L stainless steels in a simulated BWR environment, Corros. Sci. 50 (2008) 698–712.
[163] Y.Y. Chen, L.B. Chou, H.C. Shih, Factors affecting the electrochemical behavior and stress corrosion of Alloy 690 in chloride environments, Mater. Chem. Phys. 97 (2006) 37–49.
[164] Y.Y. Chen, Y.M. Liou, H.C. Shih, Stress corrosion cracking of type 321 stainless steels in simulated petrochemical process environments containing hydrogen sulfide and chloride, Mater. Sci. Eng. A 407 (2005) 114–126.
[165] R.N. Parkins, The controlling parameters in stress corrosion cracking, in: Proceeding of the 5th Symposium on Line Pipe Research, American Gas Association, Arlington, VA, 1974, p. U-1.
[166] H.P. Seifert, S. Ritter, Strain-induced corrosion cracking behavior of low-alloy steels under boiling water reactor conditions, J. Nucl. Mater. 378 (2008) 312–326.
[167] P.B. Srinivasan, C. Blawert, W. Dietzel, K.U. Kainer, Stress corrosion cracking behaviour of a surface-modified magnesium alloy, Scr. Mater. 59 (2008) 43–46.
[168] S.B. Farina, G.S. Duffo, J.R. Galvele, Stress corrosion cracking of zirconium and zircaloy-4 in halide aqueous solutions, Corros. Sci. 45 (2003) 2497–2512.
[169] R.P.M. Procter, G.N. Stevens, Formation of cuprous oxide films on a α-brass stress-corrosion fracture surfaces, Corros. Sci. 15 (1975) 349–359.
[170] G.L. Bianchi, J.R. Galvele, Stress corrosion cracking of silver alloys in gaseous environments. Bromine vapor, Corros. Sci. 36 (1994) 611–619.
[171] H. Kanematsu, M. Okido, T. Oki, Electrochemical study on stress corrosion cracking of Al-Zn-Mg alloy, J. Jpn. Inst. Light Met. 36 (1986) 333–338.
[172] M.A. Al-Anezi, G.S. Frankel, A.K. Agrawal, Susceptibility of conventional pressure vessel to hydrogen-induced cracking and stress-oriented hydrogen-induced cracking in hydrogen sulfide-containing diglycolamine solutions, Corrosion 55 (1999) 1101–1109.
[173] H.H. Johnson, J.G. Morlet, A.R. Troiano, Hydrogen, crack initiation, and delayed failure in steel, Trans. Met. Soc. AIME 212 (1958) 528–536.

[174] A.R. Troiano, The role of hydrogen and other interstitials in the mechanical behavior of metals, Trans. ASME 52 (1960) 54–80.
[175] P. Sofronis, H.K. Birnbaum, Mechanics of the hydrogen-dislocation-impurity (interactions-I). Increasing shear modulus, J. Mech. Phys. Solids 43 (1995) 49–90.
[176] H.W. Liu, Hydrogen assisted intergranular cracking in steels, Eng. Fract. Mech. 78 (2011) 2563–2571.
[177] R.P. Gangloff, Hydrogen-assisted cracking, in: I. Milne, R.O. Ritchie, B. Karihaloo (Eds.), Comprehensive Structural Integrity, vol. 6.02, Elsevier, Oxford, 2003, pp. 31–101.
[178] H.K. Birnbaum, Mechanisms of hydrogen-related fractures on metals, in: N.R. Moody, A.W. Thompson (Eds.), Hydrogen Effects on Material Behavior, TMS, Warrendale, 1990, pp. 639–660.
[179] S.P. Lynch, Mechanisms of hydrogen-assisted cracking-a review, in: N.R. Moody, A.W. Thompson, R.E. Ricker, G.W. Was, R.H. Jones (Eds.), Hydrogen Effects on Material Behavior and Corrosion Deformation Interactions, TMS, Warrendale, 2003, pp. 449–466.
[180] N. Winzer, A. Atrens, W. Dietzel, V.S. Raja, G. Songe, K.U. Kainer, Characterization of stress corrosion cracking (SCC) of Mg-Al alloys, Mater. Sci. Eng. A 488 (2008) 339–351.
[181] J. Woodtli, R. Kieselbach, Damage due to hydrogen embrittlement and stress corrosion cracking, Eng. Fail. Anal 7 (2000) 427–450.
[182] J.R. Buckley, D. Hardie, The effect of pre-straining and δ-ferrite on the embrittlement of 304L stainless steel by hydrogen, Corros. Sci. 34 (1993) 93–107.
[183] M.L. Holzworth, M.R. Louthan, Hydrogen-induced phase transformations in type 304L stainless steels, Corrosion 24 (1968) 110–124.
[184] D. Hardie, J.J.F. Butler, Effect of hydrogen charging on fracture behavior of 304L stainless steel, Mater. Sci. Technol. 6 (1990) 441–446.
[185] G.R. Caskey, Effect of hydrogen on work hardening of type 304L austenitic stainless steel, Scr. Metall. 15 (1981) 1183–1186.
[186] L.W. Tsay, M.C. Young, C. Chen, Fatigue crack growth behavior of laser-processed 304 stainless steel, Corros. Sci. 45 (2003) 1985–1997.
[187] C.L. Briant, Z.F. Wang, Hydrogen embrittlement of commercial purity titanium, Corros. Sci. 44 (2002) 1875–1888.
[188] G.B. Shan, Y.W. Wang, W.Y. Chu, J.X. Li, X.D. Hui, Hydrogen damage and delayed fracture in bulk metallic glass, Corros. Sci. 47 (2005) 2731–2739.
[189] J.A. Beavers, B.A. Harle, Mechanisms of high-pH and near-neutral-pH SCC of underground pipelines, J. Offshore Mech. Arct. Eng. 123 (2001) 147–152.
[190] F.M. Song, Predicting the mechanisms and crack growth rates of pipelines undergoing SCC at high pH, Corros. Sci. 51 (2009) 2563–2657.
[191] B.T. Lu, F. Song, M. Gao, M. Elboujdaini, Crack growth model for pipelines exposed to concentrated carbonate-bicarbonate solution with high pH, Corros. Sci. 52 (2010) 4064–4072.
[192] M.A. Arafin, J.A. Szpunar, A new understanding of intergranular stress corrosion cracking resistance of pipeline steel through grain boundary character and crystallographic texture studies, Corros. Sci. 51 (2009) 119–128.
[193] F.M. Song, Predicting the effect of soil seasonal change on stress corrosion cracking susceptibility of buried pipelines at high pH, Corrosion 66 (2010) 1–14.
[194] R.N. Parkins, W.K. Blanchard Jr., B.S. Delanty, Transgranular stress corrosion cracking of high pressure pipelines in contact with solutions of near neutral pH, Corrosion 50 (1994) 394–408.
[195] M.C. Li, Y.F. Cheng, Mechanistic investigation of hydrogen-enhanced anodic dissolution of X-70 pipe steel and its implication on near-neutral pH SCC of pipelines, Electrochim. Acta 52 (2007) 8111–8117.
[196] X. Tang, Y.F. Cheng, Micro-electrochemical characterization of the effect of applied stress on local anodic dissolution behavior of pipeline steel under near-neutral pH condition, Electrochim. Acta 54 (2009) 1499–1505.
[197] G.A. Zhang, Y.F. Cheng, Micro-electrochemical characterization of corrosion of welded X70 pipeline steel in near-neutral pH solution, Corros. Sci. 51 (2009) 1714–1724.
[198] V. Smanio, J. Kittel, M. Fregonese, T. Cassagne, B. Normand, F. Ropital, Acoustic emission monitoring of wet H_2S cracking of linepipe steels: application to hydrogen-induced cracking and stress-oriented hydrogen-induced cracking, Corrosion 67 (2011) 065002/1–065002/12.

[199] A. Eslami, B. Fang, R. Kania, B. Worthingham, J. Been, R. Eadie, W. Chen, Stress corrosion cracking initiation under the disbonded coating of pipeline steel in near-neutral pH environment, Corros. Sci. 52 (2010) 3750–3756.
[200] T.D. Burleigh, The postulated mechanisms for stress corrosion cracking of aluminum alloys. A review of the literature 1980-1989, Corrosion 47 (1991) 89–98.
[201] S.L. Winkler, H.M. Flower, Stress corrosion cracking of cast 7XXX aluminum fiber reinforced composites, Corros. Sci. 46 (2004) 903–915.
[202] J. Chen, J. Wang, E. Han, W. Ke, Effect of hydrogen on stress corrosion cracking of magnesium alloy in 0.1 M Na_2SO_4 solution, Mater. Sci. Eng. A 488 (2008) 428–434.
[203] R. Nishimura, Y. Maeda, Stress corrosion cracking of type 304 austenitic stainless steel in sulphuric acid solution including sodium chloride and chromate, Corros. Sci. 46 (2004) 343–360.
[204] T.P. Hoar, J.C. Scully, Mechanochemical anodic dissolution of austenitic stainless steel in hot chloride solution at controlled electrode potential, J. Electrochem. Soc. 111 (1964) 348–352.
[205] P.R. Rhodes, Mechanism of chloride stress corrosion cracking of austenitic stainless steels, Corrosion 25 (1969) 462–467.
[206] N. Narita, C.J. Altstetter, H.K. Birnbaum, Hydrogen-related phase transformations in austenitic stainless steels, Metall. Trans. A 13A (1982) 1355–1365.
[207] O.M. Alyousif, R. Nishimura, Stress corrosion cracking and hydrogen embrittlement of sensitized austenitic stainless steels in boiling saturated magnesium chloride solutions, Corros. Sci. 50 (2008) 2353–2359.
[208] A.R. Troiano, The role of hydrogen and other interstitials in the mechanical behavior of metals, Trans. ASM 52 (1960) 54–58.
[209] T. Pyle, V. Rollins, D. Howard, Influence of cyclic plastic strain on the transient dissolution behavior of 18/8 stainless steel in 3.7 M sulfuric acid, J. Electrochem. Soc. 122 (1975) 1445–1453.
[210] D.W. Hoeppner, Fretting fatigue and corrosion fatigue of metallic materials, in: Corrosion Fatigue, Chemistry, Mechanics and microstructure, NACE, Houston, TX, 1972, pp. 3–10.
[211] A.J. Sedriks, Corrosion of Stainless Steel, second ed., John Wiley and Sons, Inc., New York, 1996.
[212] P.C. Paris, F. Erdogan, A critical analysis of crack propagation laws, Trans. ASME, Basics Corros. Eng. 85 (1963) 528–534.
[213] J. Congleton, I.H. Craig, B.K. Denton, R.N. Parkins, Crack growth in HY80 and HY130 steels by corrosion fatigue, Metal Sci. 13 (1979) 436–443.
[214] C.S. Kortovich, Corrosion fatigue of 4340 and D6AC steels below K_{ISCC}, in: Proceedings fo the 1974 Tri-Service Corrosion Conference on Corrosion of Military Equipment, vol. 1, AFML-TR-75-42, 1975, Air Force Materials Laboratory Wright Patterson Air Force Base, pp. 283-303.
[215] C.L. Briant, Hydrogen assisted cracking of type 304 stainless steel, Metall. Trans. A 10A (1979) 181–189.
[216] N. Narita, H.K. Birnbaum, On the role of phase transitions in the hydrogen embrittlement of stainless steels, Scr. Metall. 14 (1980) 1355–1358.
[217] Z. Mei, J.W. Morris, Influence of deformation-induced martensite on fatigue crack propagation in 304-type steels, Metall. Trans. A 21A (1990) 3137–3152.
[218] G. Schuster, C. Altstetter, Fatigue of stainless steel in hydrogen, Metall. Trans. A 14A (1983) 2085–2090.
[219] S.S. Birley, D. Tromans, Stress corrosion cracking of 304L austenitic steel and the martensite transformation, Corrosion 27 (1971) 63–71.
[220] M. Gao, S. Chen, R.P. Wei, Crack paths, microstructure, and fatigue growth in annealed and cold-rolled AISI stainless steels, Metall. Trans. A 23A (1992) 355–371.
[221] A. Okamoto, H. Nakamura, The influence of residual stress on fatigue cracking, J. Press. Vessel Technol. ASME 112 (1990) 199–203.
[222] Y.B. Lee, C.S. Chung, Y.K. Park, H.K. Kim, Effects of redistributing residual stress on the fatigue behavior of ss330 weldment, Int. J. Fatigue 20 (1998) 565–573.
[223] F.L. LaQue, Marine Corrosion-Causes and Prevention, Wiley, New York, 1975.
[224] J.A. Moskovitz, R. Pelloux, Corrosion-fatigue behavior of austenitic-ferritic stainless steels, in: H.L. Craig, T.W. Crooker, D.W. Hoeppner (Eds.), Corrosion Fatigue Technology, ASTM STP 642, ASTM International, West Conshohocken, PA, 1978, pp. 133–154.
[225] S. Kaewkumsai, W. Khonraeng, A. Chainpairote, Corrosion fatigue cracking of AISI 316L stainless steel screen mesh, Eng. Fail. Anal. 17 (2010) 857–863.

[226] E. Tada, Detection of corrosion fatigue cracking through current responses induced by cyclic stressing, Corros. Sci. 49 (2007) 248–254.
[227] T. Magnin, Recent advances for corrosion fatigue mechanisms, ISIJ Int. 35 (1995) 223–233.
[228] Y.F. Li, G.C. Farrington, C. Laird, Cyclic response-electrochemical interaction in mono- and polycrystalline AISI 316L stainless steel in sulfuric acid solution—I. The influence of mechanical strain on the transient dissolution behavior during corrosion fatigue, Acta Metall. 41 (1993) 693–708.
[229] E. Tada, K. Noda, S. Kuma, T. Tsuru, Monitoring of corrosion fatigue cracking using harmonic analysis of current responses induced by cyclic stressing, J. Jpn. Inst. Met. 63 (1999) 1075–1082.
[230] B.J. Smith, C.P. Erskine, R.J. Hartranft, A.R. Marde, High-temperature corrosion-fatigue (circumferential) cracking life evaluation procedure for low alloy (Cr-Mo) boiler tube steels, Mater. Charact. 34 (1995) 81–86.
[231] C. Zhang, Y.J. Su, L.J. Qiao, W.Y. Chu, Influence of hydrogen on the tarnishing film-induced brittle cracking of brass, J. Mater. Res. 24 (2009) 3432–3438.
[232] M. Kermani, J.C. Scully, The effect of strain-rate upon stress corrosion crack velocity in α-brass in ammoniacal solutions, Corros. Sci. 19 (1978) 89–95, 97–110.
[233] F. Zucchi, G. Trabanelli, M. Fonsati, A. Giusti, Influence of P, As and Sb on the susceptibility to SCC of α-β′ brasses, Mater. Corros. 49 (1998) 864–869.
[234] S. Sohn, T. Kang, The effects of tin and nickel on the corrosion behavior of 60 Cu-40Zn alloys, J. Alloys Compd. 335 (2002) 281–289.
[235] Y.A. El-Tantawy, F.M. Al-Kharafi, A. Katrib, Nature and mechanism of anodic film by formation on Cu in alkaline phosphate media, J. Electroanal. Chem. 125 (1981) 321–331.
[236] N. Souissi, E. Triki, A chemiometric approach for phosphate inhibition of copper corrosion in aqueous media, J. Mater. Sci. 42 (2007) 3259–3265.
[237] K.H. Goh, T.T. Lim, P.C. Chui, Evaluation of the effect of dosage, pH and contact time on high-dose phosphate inhibition for copper corrosion control using response surface methodology (RSM), Corros. Sci. 50 (2008) 918–927.
[238] M.B. Valcarce, M. Vázquez, Phosphate ions used as green inhibitor against copper corrosion in tap water, Corros. Sci. 52 (2010) 1413–1420.
[239] E.A. Ashour, B.G. Ateya, The effect of phosphates on the susceptibility of abrass to stress corrosion cracking in sodium nitrite, Corros. Sci. 37 (1995) 371–380.
[240] X.S. Du, Y.J. Su, J.X. Li, L.J. Qiao, W.Y. Chu, Inhibitive effects and mechanism of phosphates on the stress corrosion cracking of brass in ammonia solutions, Corros. Sci. 60 (2012) 69–75.
[241] W.E. Ruther, W.K. Soppet, T.F. Kassner, Effect of temperature and ionic impurities at very low concentrations on stress corrosion cracking of AISI304 stainless steel, Corrosion 44 (1988) 791–799.
[242] G. Okamoto, T. Shibata, Stability of passive stainless steel in relation to the potential of passivation treatment, Corros. Sci. 10 (1970) 371–378.
[243] T.M. Angeliu, P.L. Andresen, Effect of zinc additions on oxide rupture strain and repassivation kinetics of iron-based alloys in 288 °C water, Corrosion 52 (1996) 28–35.
[244] J.N. Esposito, G. Economy, W.A. Byers, J.B. Esposito, F.W. Pement, R.J. Jacko, C.A. Bergmann, The addition of zinc to primary reactor coolant for enhanced PWSCC resistance, in: Proceedings of the 5th International Symposium on Environmental Degradation of Materials in Nuclear Power Systems—Water Reactors, vol. 1, American Nuclear Society, Pittsburgh, 1992, pp. 495–503.
[245] P.L. Andresen, T.M. Angeliu, Corrosion/95, paper no. 409, 1995, NACE, Orlando.
[246] Y. Huang, Stress corrosion cracking of AISI 321 stainless steel in acidic chloride solution, Bull. Mater. Sci. 25 (2002) 47–51.
[247] S. Ahila, B. Reynders, H.J. Grabke, The evaluation of the repassivation tendency of Cr-Mn and Cr-Ni steels using scratch technique, Corros. Sci. 38 (1996) 1991–2005.
[248] V.S. Raja, Localized corrosion behavior of austenitic stainless steel weldments and the role of nitrogen, in: Proceedings of the International Conference on Corrosion, Corcoran, Mumbai, 1997, pp. 409–420.
[249] T. Watanabe, An approach to grain boundary design for strong and ductile polycrystals, Res. Mech. 11 (1984) 47–84.

CHAPTER 10

Atmospheric Corrosion

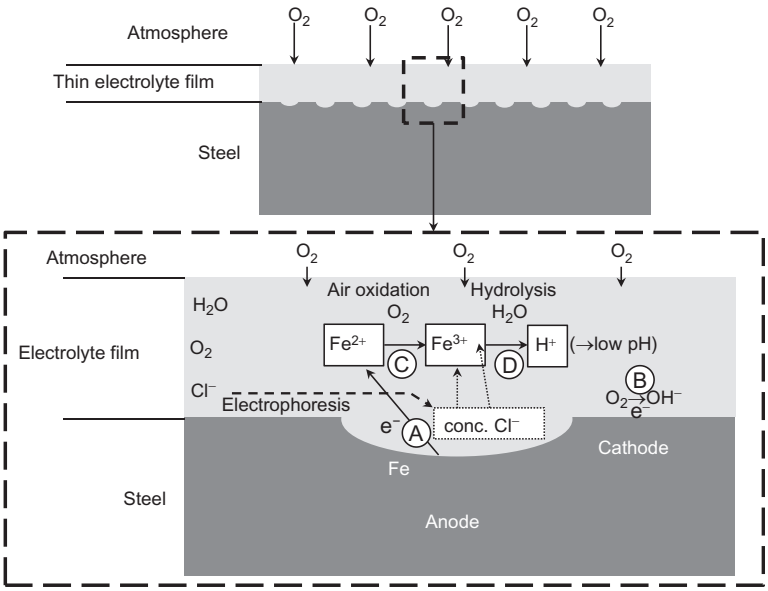

Chapter Contents

Corrosion Engineering
http://dx.doi.org/10.1016/B978-0-444-62722-3.00010-0

10.1 INTRODUCTION

Atmospheric corrosion of metals is differentiated from the other forms of corrosion due to exposure of metals to different atmospheres rather than immersion in electrolytes. The spontaneous atmospheric corrosion of materials is controlled by the temperature, the relative humidity, the time of wetness, the pH of the electrolyte, and the presence of contaminants such as chlorides, NH_3, SO_2, NO_2, and acidic fogs. In most cases, the rate equations have limited validity due to different local atmospheric conditions. Metals spontaneously form a solid metal oxide film when exposed to dry atmospheres. The barrier oxide film reaches a maximum thickness of 2-5 nm [1–6]. The corrosion rate of metals exposed to a wet atmosphere is similar to that observed during immersion in aerated water in the presence of dissolved oxygen. Atmospheric corrosion rates decrease in dry atmospheres with corrosion mechanisms that are different from those in wet atmospheres.

10.2 ATMOSPHERIC CLASSIFICATION

The environment that initiates atmospheric corrosion is classified as industrial, rural, urban, marine, and indoor. The most common industrial pollutants are SO_2 and nitrogen oxides (NO_x). Industrial processing facilities such as petrochemical, combustion of sulfur-containing coals, oil, pulp, paper industries, and smelting companies are a few sources of SO_2 and nitrogen oxide (NO_x) pollutants. Other pollutants and stimulants in atmospheric corrosion are chlorides and phosphates. Rural atmosphere is free from contaminants and is least corrosive with the exception of tropical climates. Tropical environments are subjected to accelerated atmospheric corrosion due to reoccurring moisture and large amounts of sunlight. Marine atmospheres are the extreme in atmospheric corrosion due to chlorides from sea water and salts being swept by winds. Chlorides create the most corrosive environment and are a great concern to offshore platforms and vessels. Deicing salts on highways in many cold areas create an almost equally corrosive environment.

10.3 ELECTROCHEMICAL MECHANISM

10.3.1 Corrosion of iron and low alloy steels

The electrochemical reaction begins with the formation of a thin conductive aqueous electrolyte layer on the metal surface. During iron oxidation, the cathode reaction is the reduction of oxygen:

$$2Fe = 2Fe^{2+} + 4e^{-} \tag{10.1}$$

$$O_2 + 2H_2O + 4e^{-} = 4OH^{-} \tag{10.2}$$

Figure 10.1 shows initial atmospheric corrosion of iron. The corrosion rate is determined by the alloy and electrolyte composition. Maximum generation of Fe^{2+} under atmospheric conditions occurs after ~1 h of exposure [7].

When steel or iron is exposed to an atmospheric environment, a thin layer of magnetite, Fe_3O_4, is formed, covered by a layer of FeOOH. Atmospheric oxygen then penetrates though the almost water-free, porous outer layer of FeOOH and oxidizes the magnetite to hydrated ferric oxide, Fe_2O_3, or FeOOH. The presence of Fe^{2+} in the electrolyte initiates the precipitation of various corrosion products. The electrochemical mechanism of atmospheric corrosion of iron suggested by Evans is briefly summarized in this chapter [8].

Saturated solution of ferrous ions within the pores of the magnetite react with oxygen diffusing from the atmosphere producing new layers of magnetite:

$$3Fe^{2+} + 2OH^{-} + \frac{1}{2}O_2 \rightarrow 3Fe_3O_4 + 4H_2O \tag{10.3}$$

The dissolution of iron is balanced by the reduction of hydrated ferric oxide (Fe_2O_3) or FeOOH to magnetite:

$$8FeOOH + Fe^{2+} + 2e^{-} \rightarrow 3Fe_3O_4 + 4H_2O \tag{10.4}$$

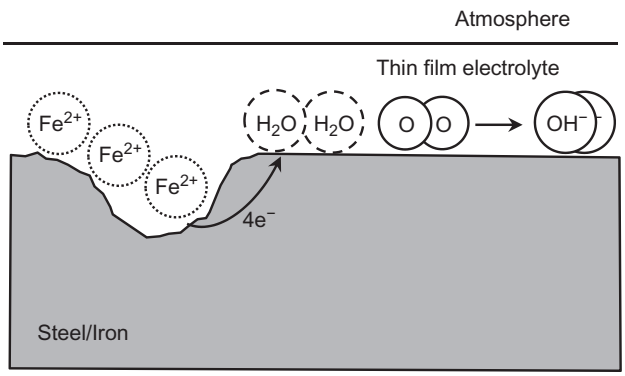

Fig. 10.1 Atmospheric corrosion of iron.

The magnetite is reoxidized to rust by the diffusion of atmospheric oxygen through open pores in the outer hydrated ferric oxide layer:

$$3Fe_3O_4 + 0.75O_2 + 4.5H_2O \rightarrow 9FeOOH \tag{10.5}$$

The rust layer usually consists of dense inner regions of amorphous FeOOH and crystalline magnetite. The outer layer consists of crystalline α-FeOOH (goethite), γ-FeOOH (lepidocrocite), and γ-Fe_2O_3 (maghemite) [9]. In summary, atmospheric corrosion of iron occurs in several steps:

(i) Less dense and moderately protective layers of mixed oxide and hydroxides are formed on the surface during the first hours.
(ii) Presence of atmospheric peroxide increases the barrier properties of the passive film.
(iii) Adsorption of water and inclusion of corrosive pollutants and gases form an electrolytic solution layer on the surface of the metal.
(iv) Charge-transfer processes result in the formation of Fe^{2+} and Fe^{3+}, creating possibilities for the formation of mixed ferrous and ferric complexes.

10.4 FACTORS AFFECTING ATMOSPHERIC CORROSION

10.4.1 Moisture

Moisture appears in several forms: rain, fog, sea breeze, and relative humidity or dew. The rain carries pollutants while adding moisture to the metal surface that accelerates the atmospheric corrosion. The onset of corrosion results from the formation of a thin water-film at certain levels of humidity. Surface moisture from condensation is also very harmful. The critical humidity level depends on the metals' tendency for forming corrosion products that absorb moisture and the presence of atmospheric pollutants [10]. The time of wetness depends on the frequency of rain, the relative humidity of the atmosphere, the temperature of the air, and the melting snow, fog, and dew. When the critical level of humidity is reached, it initiates severe and continuous atmospheric corrosion attack. Water droplets remain on the surface of the metal crevices or pits longer, increasing the time of corrosion attack. An increase in the wetting phase results in an increase in the pollutant concentration that consequently leads to an increased rate of atmospheric corrosion. However, the rain may, in some cases, have a beneficial effect by washing away the atmospheric pollutants. The rate of atmospheric corrosion is determined by the ratio of deposition of the dry and wet contaminants. The washing effect of rain decreases the corrosion rates in cases when the dry period of deposition of pollutants is greater than the wet period of deposition of surface compounds. However, in geographic areas where the air is not polluted, the rate of atmospheric metal corrosion increases with the increase in the wetness of the surface.

10.4.2 Temperature

Generally, when the temperature is below the dew point, the wetting cycle is extended. The corrosion rate of metals increases with the increase in the temperature under humid environments. The percentage of relative humidity decreases with increasing temperature. Thus, no corrosion occurs ~15° above the dew point. Because metals cool and heat slower than the ambient air, the presence of condensation process on metals is extended for much longer.

10.4.3 Atmospheric pollutants

The pollutants include SO_2, nitrogen oxides, chlorides, and phosphates. All gases in the Troposphere (Ne, Kr, He, and Xe) do not participate in atmospheric corrosion [11]. Only oxygen acts as an oxidizer in a cathodic reaction. The presence of CO_2 in the electrolyte (~300 ppm) decreases pH and increases the corrosion rate of metals.

10.4.3.1 Sulfur-containing compounds

Sulfur dioxide is the most important gaseous stimulant in atmospheric corrosion. Combustion of sulfur-containing coal and oil and emission from metal, petrochemical, and pulp and paper industries are among the most important man-made sources. Based on the environment, Calvert and Stockwell [12] suggested several ways for SO_2 to act as an oxidizer in the gas phase:

$$SO_2 + OH^{\cdot} \xrightarrow{O_2} HSO_3^{\cdot} \tag{10.6}$$

$$HSO_3^{\cdot} + O_2 \rightarrow SO_3 + HO_2^{\cdot} \tag{10.7}$$

$$SO_3 + H_2O \rightarrow H_2SO_4 \tag{10.8}$$

Gaseous SO_2 absorbs into the surface of the electrolyte layer and is hydrolyzed according to Eq. (10.6), producing $HSO_3^{\cdot}$. Oxygen interacts with $HSO_3^{\cdot}$ and produces SO_3 by decreasing the heat of reaction (10.7). Oxidation to SO_4^{2-} is a rapid process and proceeds through many paths [13]. Robin [14] suggested the following reaction mechanism for SO_2 in aqueous electrolytes:

$$SO_2 + xH_2O = SO_2 \cdot xH_2O \tag{10.9}$$

$$SO_2 \cdot xH_2O = HSO_3^- + H_3O^+ + (x-2)H_2O \tag{10.10}$$

$$HSO_3^- \xrightarrow{H_2O_2} SO_4^{2-} \tag{10.11}$$

In aqueous electrolytes, the oxidation of S(IV) to S(VI) proceeds through the reaction (10.12):

$$SO_2 + xH_2O + O_2 = H_2SO_4 \tag{10.12}$$

The oxidation of SO_2 is catalyzed at high pH or in the presence of Fe(III) or Mn(II) containing catalysts. Water electrolytes are acidified according to Eq. (10.12) and promote the dissolution of FeOOH. Figure 10.2 shows the effect of air pollution with 0.01% SO_2 and coal particles [15].

Heterogeneous corrosion of iron has been suggested to proceed through the formation of sulfate nests containing a high concentration of iron corrosion products in the electrolyte [16–18]. The corrosion products are retained by a semipermeable membrane of colloidal iron-oxyhydroxides. Water diffuses into the nest due to the high ionic concentration of the solution and burst the membrane, spreading contents to the neighboring area and triggering corrosion in the newly formed corrosion sites. However, the interaction between the rust formation and the chemistry of rusting has not been defined with a reaction mechanism. Also, there was no analytical evidence for the existence of hydroxide membranes [5]. Atmospheric corrosion of iron in the presence of sulfur-containing compounds is summarized in Fig. 10.3 [5].

The atmosphere is presented on the top of the diagram with the surface water layer in the center. The corroding metal and the corrosion products are shown at the bottom of the figure. The wavy arrows indicate the oxidation of iron to Fe^{2+}. The gas phases that enter the electrolyte are carbonyl sulfide (COS), hydrogen sulfide (H_2S), and sulfur dioxide (SO_2). Sulfate anions enter the electrolyte as part of the deposited atmospheric particles or as a component of precipitation. Several processes, such as the one outlined in

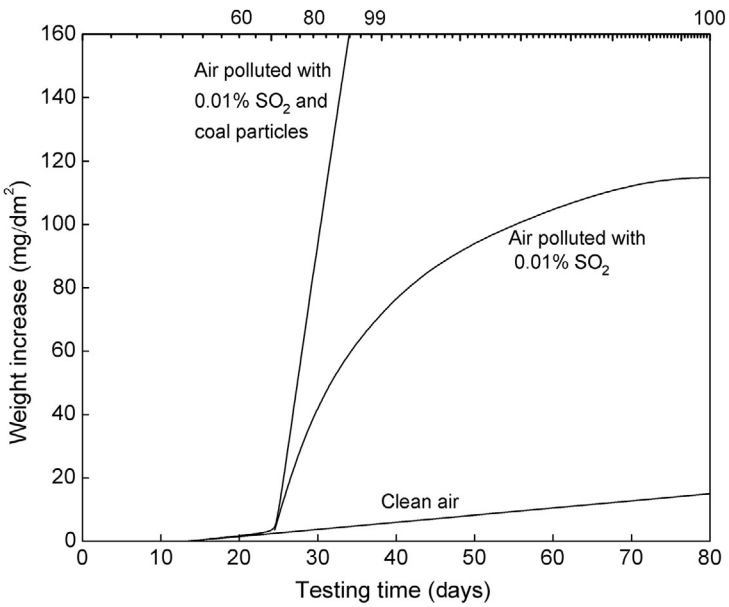

Fig. 10.2 Effect of air pollution on atmospheric corrosion of iron [15].

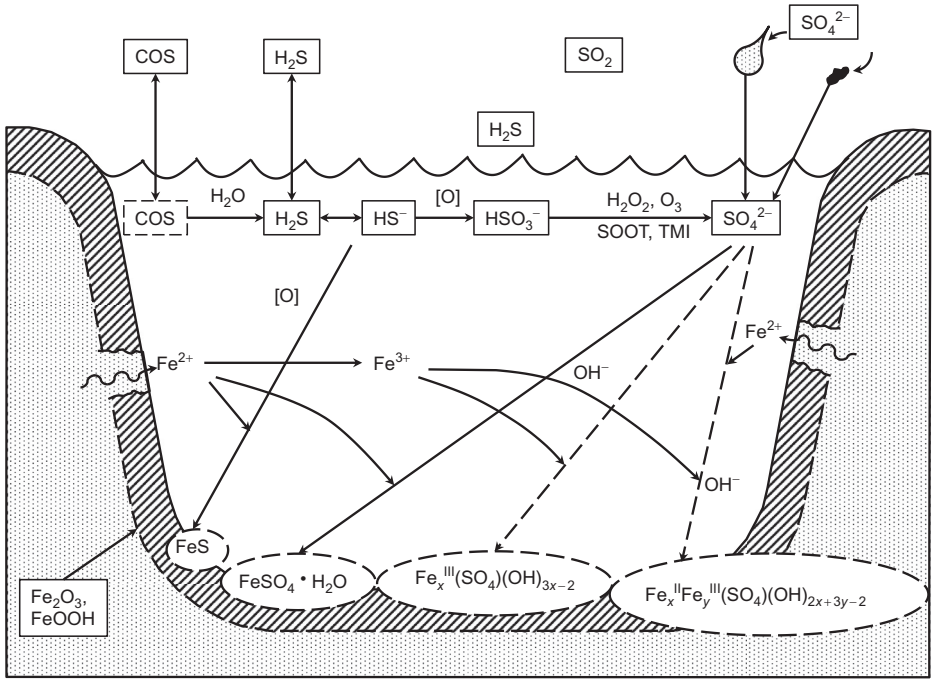

Fig. 10.3 Schematic of the sulfur chemistry present in the corrosion of atmospheric corrosion of iron and steel [5]. *Reproduced by permission of The Electrochemical Society.*

Eq. (10.12), may oxidize the dissolved SO_2 to sulfate in the outer layers. The species within rectangular boxes represent the solution constituents and those in ovals represent the corrosion products. Dotted ovals represent reactions or chemical compounds for which there is no evidence by laboratory or field studies. The chemical reactions that have been described and confirmed by laboratory studies are presented as solid arrows. The dotted arrows represent the mechanisms that are uncertain. TMI in the upper part of Fig. 10.3 stands for transition metal ions and soot catalyzes the S(IV) to S(VI). The ferrous cations react with reduced sulfur to produce several insoluble sulfides. Multistep processes including Fe(II), Fe(III), and OH^- produce hydroxysulfate mixed salts [5].

According to Weissenrieder *et al.* [4], in the absence of either NO_2 or O_3, iron passivates in 200 ppb SO_2. In the presence of oxidants, such as NO_2 or O_3 in humidified air, localized corrosion was detected by the authors and was described as "sulfate nests" [4]. The observed corrosion is autocatalytic in nature with a rapid dissolution of iron and production of Fe^{2+} and Fe^{3+} cations. Localized corrosion promotes the catalytic conversion of SO_2 to sulfate anions, which enhance the sulfate-induced corrosion of iron, thus creating more dissolved iron cations. Next, the sulfate nests distribute through increased deposition of SO_2 at high pH cathodic sites and locally create new anodic sites by decreasing the pH.

Iron sulfides are formed on steel when exposed to sea water [19]. The formation is initiated by the sulfide-reducing bacteria. According to Graedel and Frankenthal [11], H_2S reacts with $OH^{\cdot}$ to form SO_2 through reactions in Eqs. (10.13) and (10.14):

$$H_2S + OH^{\cdot} = HS^{\cdot} + H_2O \tag{10.13}$$

$$HS^{\cdot} + 2O_2 = HO_2^{\cdot} + SO_2 \tag{10.14}$$

Carbonyl sulfate and H_2S are the major atmospheric corrosion pollutants.

10.4.3.2 Nitrates

The two main nitrogen oxides produced are NO and NO_2. NO forms NO_2 by reacting with oxygen according to the reactions shown in Eqs. (10.15) and (10.16a):

$$2NO + O_2 = 2NO_2 \tag{10.15}$$

$$NO + O_3 = NO_2 + O_2 \tag{10.16a}$$

NO_2 is oxidized to nitric acid:

$$NO_2 + OH^{\cdot} \xrightarrow{GM} HNO_3 \tag{10.16b}$$

where GM stands for gaseous molecules (oxygen or nitrogen). Rice et al. [20] reported nitrogen-containing compounds in iron corrosion products. Presence of nitrates was also detected in copper patina layers [21]. Nitrite salts are soluble in water and cannot be detected in other rust layers. Figure 10.4 shows nitrate chemistry that may be involved in the corrosion of iron [5].

10.4.3.3 Chlorine-containing compounds

Atmospheric corrosion of metals is affected by contaminants such as chlorides from deicing or from airborne salt in marine atmospheres. Other sources are HCl production from the burning of chlorine-containing coals and the emission of chlorine from industrial processes. Hydrochloric acid is formed by photodissociation of chlorine, resulting in the production of chlorine radicals that are hydrogenated with organic compounds.

$$Cl_2 + h\upsilon = Cl^{\cdot} + Cl^{\cdot} (\lambda < 420\,\text{nm}) \tag{10.17}$$

$$RH + Cl^{\cdot} = R^{\cdot} + HCl \tag{10.18}$$

Chloride corrosion of steel is controlled by the environment, the concentration of oxidizer, the structural characteristics of metal, the composition of the alloy, and the presence of dissolved oxygen. The chloride ions adsorb on the outer surface of the passive film, permeate through the passive oxide film, and interact with the underlying metal.

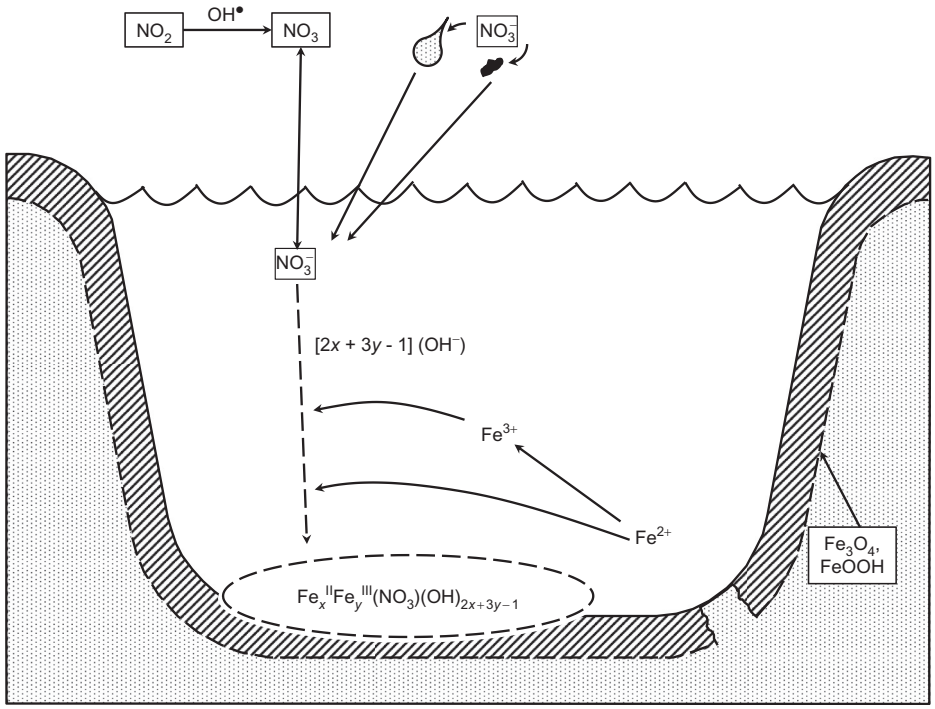

Fig. 10.4 Formation of nitrogen-containing compounds during atmospheric corrosion of iron and steel [5]. *Reproduced by permission of The Electrochemical Society.*

In the presence of chlorides, the outer layers of the passive film are displaced due to the catalytic formation of FeOCl:

$$FeOOH + Cl^- \rightarrow FeOCl + OH^- \tag{10.19}$$

FeOCl in contact with a high concentration of chlorides dissociates to Fe^{3+}.

$$FeOCl + H_2O \rightarrow Fe^{3+} + Cl^- + 2OH^- \tag{10.20}$$

10.5 ATMOSPHERIC CORROSION OF SELECTED METALS

10.5.1 Atmospheric corrosion of iron

The metals exposed to atmospheric corrosion have different electrochemical properties due to [22]:

(i) Fast transport of electroactive species at the electrode-electrolyte interface (O_2)
(ii) Quick formation of passivating films because of fast saturation of the metal cations in the thin electrolyte layer
(iii) The change in the pH in the electrolyte layer as the reaction proceeds

The anodic dissolution of iron in the presence of high water content in the pore structure of the passive film is in equilibrium (balanced) with the cathodic reaction of ferric oxide in the passive layer [23,24]. According to Stratmann *et al.* [25–31], the passive film γ-FeOOH is reduced to Fe^{2+} during wetting, which increases the conductivity of the *n*-type semiconducting passive film. During wetting cycles, the corrosion rate increases because of the largely reduced surface of γ-FeOOH. Because the composition of the rust changes, the corrosion properties of the metal are expected to change. Kamimura *et al.* [32] investigated the role of chloride on the atmospheric corrosion of steel and the corrosion resistance of Sn-bearing steel. The electrochemical cell consists of a minute anode and a cathode chamber, as shown in Fig. 10.5 [32]. The anion-selective membrane film was placed on the bottom of the anode to simulate the ion-selective permeability of a rust layer. The working electrode, Fe, was anodically dissolved. The pH of the solution (anolyte) inside the anode was measured as a function of time. Pt served as a counter electrode.

The model for atmospheric corrosion under high chloride concentration suggested by Kamimura *et al.* [32] is based on the separation of cathode and anode sites under the rust and the thin electrolyte. The pH at the anode compartment is affected by the chloride ion concentration and decreased to 1.5 by the hydrolysis of ferric ions and the formation of β-FeOOH. Chloride ions accumulate at the anode site and initiate the oxidation of ferrous ions to ferric ions. Accumulated chloride ions increase ferric ion solubility in the electrolyte and accelerate the hydrolysis of ferric ions, causing the pH at the anode to decrease. Low pH at the metal-electrolyte interface accelerated the formation of β-FeOOH. The atmospheric corrosion process is summarized as follows:

$$\text{Anodic reaction}: \ Fe \rightarrow Fe^{2+} + 2e^{-} \tag{10.21}$$

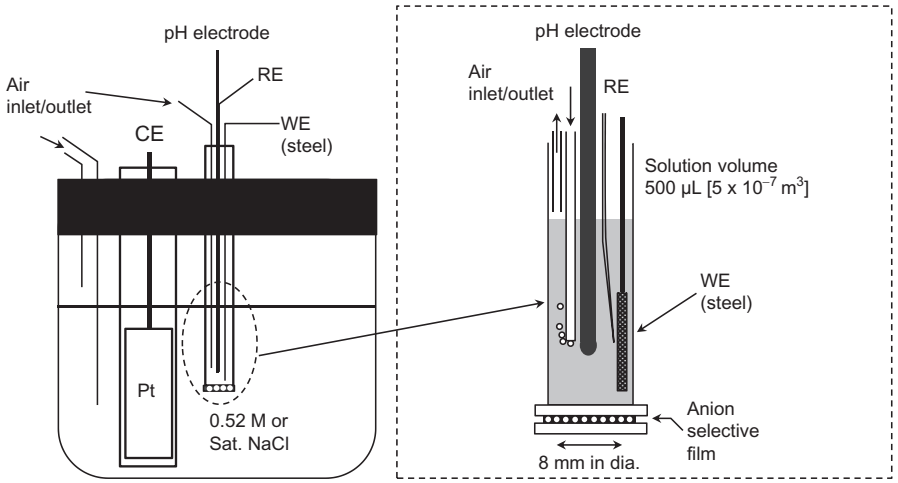

Fig. 10.5 Electrochemical cell used to simulate the local anode site under rust [32].

$$\text{Cathodic reaction}: \ H_2O + \frac{1}{2}O_2 + 2e^- \rightarrow 2OH^- \tag{10.22}$$

$$\text{Air oxidation}: \ Fe^{2+} + \frac{1}{4}O_2 + H^+ \rightarrow Fe^{3+} + \frac{1}{2}H_2O \tag{10.23}$$

Hydrolysis of Fe^{3+}:

$$\begin{aligned} Fe^{3+}H_2O &\rightarrow FeOH^{2+} + H^+ \\ Fe^{3+}H_2O &\rightarrow Fe(OH)^+ + H^+ \\ 2Fe^{3+}2H_2O &\rightarrow 2Fe(OH)^{4+} + 2H^+ \end{aligned} \tag{10.24}$$

Atmospheric corrosion of steel in the presence of chloride is summarized in Fig. 10.6 [32].

10.5.2 Atmospheric corrosion of magnesium alloy

Jönsson *et al.* [33] investigated the corrosion product formation during NaCl-induced atmospheric corrosion of the magnesium alloy AZ91D. The alloy was exposed to humid air with 95% relative humidity. A 70 μg/cm^2 NaCl was deposited on the alloy. FTIR spectroscopy and ion chromatography were used to analyze the corrosion products formed on the surface. Magnesium carbonate hydromagnesite ($Mg_5(CO_3)_4(OH)_2$ $4H_2O$) and nesquehonite ($MgCO_3$ $3H_2O$) were identified as the corrosion products. Formation of pits containing brucite $Mg(OH)_2$ covered with hydromagnesite crusts were

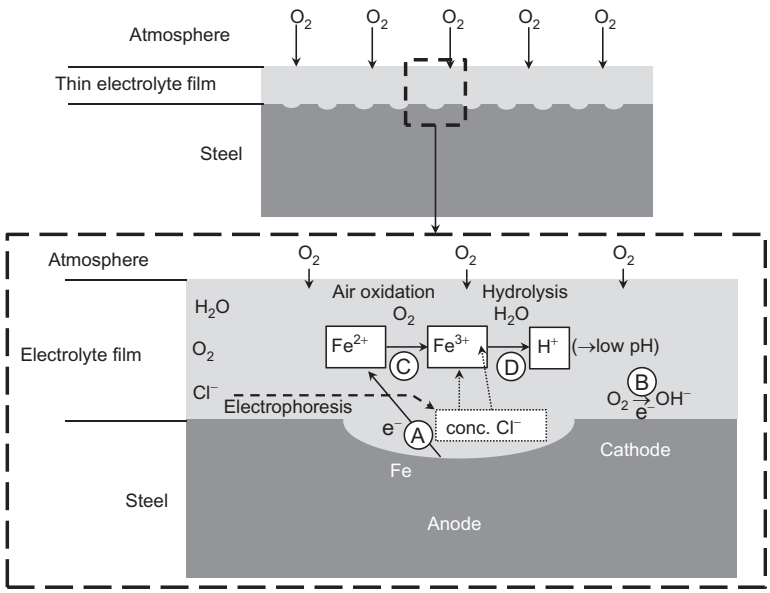

Fig. 10.6 Schematic of atmospheric corrosion of steel in the presence of chloride ion [32].

observed as corrosion products after long exposures. The hydromagnesite crust acts as a barrier film and restricts the diffusion of O_2 and CO_2 to the magnesium surface and favors the production of brucite. The corrosion of AZ91 D is controlled by the alloy microstructure and formation of carbonate-containing corrosion product that block the alloy corrosion active sites. A schematic description of the corrosion process of AZ91 D in the presence of NaCl is shown in Fig. 10.7 [34].

Jönsson *et al.* [33] also investigated corrosion of magnesium AZ91D and AM50 alloys exposed to urban, rural, and marine atmospheres. Mass loss techniques were used to determine the corrosion rates. The observed corrosion rates of AZ91D were 4.2, 2.2, and 1.8 μm/year in the marine, rural, and urban environments, respectively. The corrosion attack was initiated in the α-phase in larger grains at the boundary between the α-phase and the eutectic α/β-phase. Magnesium carbonate hydromagnesite ($Mg_5(CO_3)_4(OH)_2$ $4H_2O$) was the main corrosion product and formed at all three exposure sites. Figure 10.8 shows the corrosion rates estimated at different field-exposure sites [33]. The highest corrosion was observed for AM50 alloy. The results indicated formation of corrosion products with poor barrier properties. Samples of the alloy with

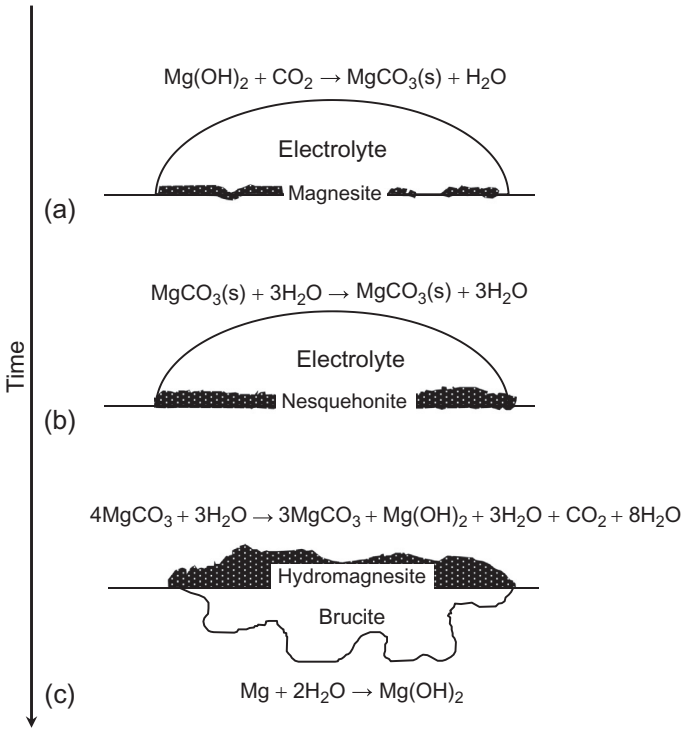

Fig. 10.7 Schematic description of the corrosion process of AZ91 D in the presence of NaCl [34].

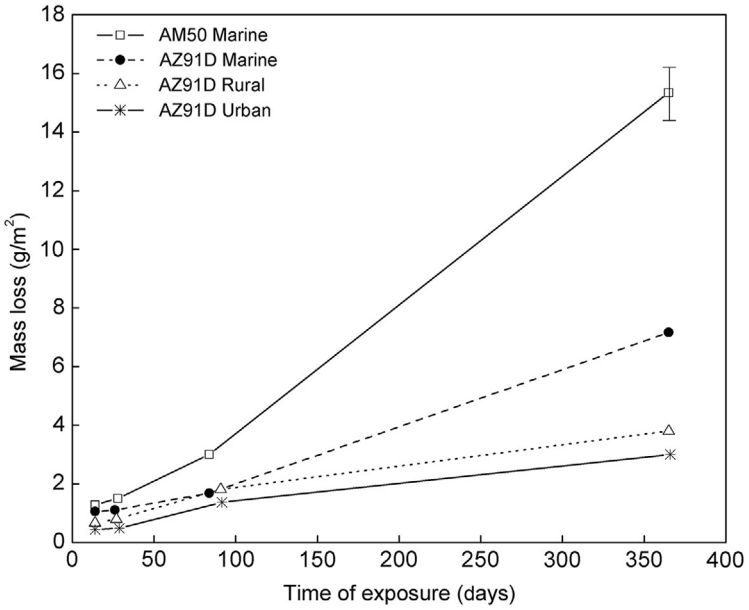

Fig. 10.8 The mass loss given in g/m^2 for magnesium alloys AZ91D and AM50 exposed for 2 weeks, 1 month, 3 months, and 12 months at three different field-exposure stations [33].

varying concentrations of aluminum were subject to various atmospheres. It was determined that the alloy is susceptible to chloride attack and doping with aluminum reduced the susceptibility to corrosion.

10.5.3 Atmospheric corrosion of nickel

In wet atmospheres, nickel initially forms NiO and $(NiOH)_2$ [35,36]. Nickel sulfates are present as corrosion products on the surface in outdoor exposures [37]. Jouen *et al.* [38] studied the atmospheric corrosion of nickel in industrial, urban, and rural atmospheres. Nickel corrodes through a pitting corrosion process. The highest corrosion rates were observed in industrial areas. The corrosion products were mainly sulfates, chlorides, and negligible amounts of nitrates surrounded by carbonate species. The pitting corrosion process occurs in two steps on nickel surfaces exposed to an outdoor atmosphere, as shown in Fig. 10.9 [38].

10.6 CLASSIFICATION OF ATMOSPHERIC CORROSION

The evaluation and classification of atmospheric metal corrosivity help develop corrosion protection strategies and optimize material service life. Two fundamental approaches are used to estimate the relationships between atmospheric corrosion rates of metals and the atmospheric variables such as pollutants' types and their concentration in the atmosphere, the temperature, and the time of wetness.

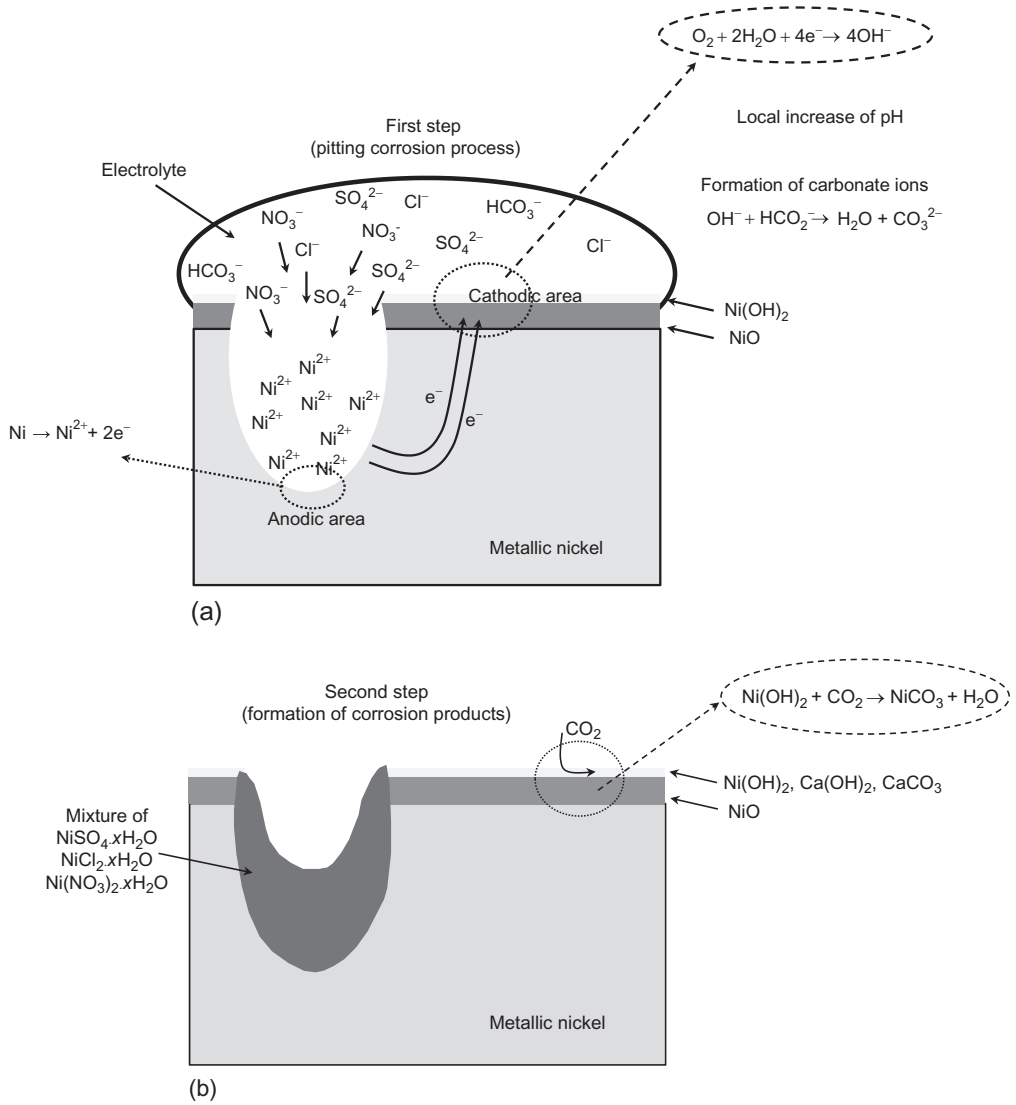

Fig. 10.9 Schematic of the pitting corrosion process occurring on nickel surfaces exposed in outdoor atmospheres: (a) pitting corrosion process and (b) formation of corrosion products [38].

10.6.1 The International Standard Organization classification of atmospheric corrosion

The International Standard Organization (ISO) developed a corrosivity classification system verified through exposure that has been carried worldwide. The ISO classification system is based on the assumptions that only the time of wetness and the concentration of pollutants in the atmosphere, SO_2 and chlorides, control the corrosion rates of metals. Table 10.1 shows the list of ISO standards related to atmospheric corrosion of metals [39].

Table 10.1 ISO Standards for Atmospheric Corrosion [39]

ISO Standard	Title
ISO 9223	Classification of the Corrosivity of Atmospheres
ISO 9224	Guiding Values for the Corrosivity Categories of Atmospheres
ISO 9225	Aggressivity of Atmospheres—Methods of Measurement of Pollution
ISO 9226	Corrosivity of Atmospheres—Methods of Determination of Corrosion Rates of Standard Specimens for the Evaluation of Corrosivity

The variables used to calculate the ISO corrosivity index are:

(a) Time of wetness

Units: hours per year (h/year) when relative humidity (RH) > 80% and $t > °C$

$TOW \leq 10$	T_1
$10 < TOW \leq 250$	T_2
$250 < TOW \leq 2500$	T_3
$2500 < TOW \leq 5500$	T_4
$5500 < TOW$	T_5

(b) Airborne salinity

Units: chloride deposition rate [mg/(m^2day)]

$S \leq 60$	S_1
$60 < S \leq 300$	S_2
$300 < S$	S_3

(c) Industrial pollution by SO_2

Two types of units are used: Concentration (μg/m^3), P_C

$P_C \leq 40$	P_1
$40 < P_C \leq 90$	P_2
$90 < P_C$	P_3

(d) Deposition rate [mg/(m^2day)], P_D

$P_D \leq 35$	P_1
$35 < P_D \leq 80$	P_2
$80 < P_D$	P_3

The corrosion categories of wetness, sulfur dioxide, and chloride are shown in Tables 10.2–10.4, respectively [40]. ISO charts are used to determine the applicable corrosivity category after categorizing the variables listed in Tables 10.3 and 10.4 [40].

Table 10.5 shows corrosion rates after 1 year of exposure predicted for different corrosivity classes [40].

Table 10.2 ISO 9223 Classification of Corrosion Rate (CR) Categories [40]

Category	Short-Term, g/(m^{2}year)	Long-Term, μg/year
C_1	$CR \leq 10$	$CR \leq 0.1$
C_2	$10 < CR \leq 200$	$0.1 < CR \leq 1.5$
C_3	$200 < CR \leq 400$	$1.5 < CR \leq 6$
C_4	$400 < CR \leq 650$	$6 < CR \leq 20$
C_5	$650 < CR$	$20 < CR$

This excerpt is taken from ISO 9223:2012, Table 2 on page 4, with the permission of ANSI on behalf of ISO. © ISO 2014—All rights reserved.

Table 10.3 ISO 9223 Classification of Time of Wetness [40]

Wetness Category	Time of Wetness (%)	Time of Wetness (h/year)	Examples of Environments
T_1	<0.1	<10	Indoor with climatic control
T_2	0.1-3	10-250	Indoor without climatic control
T_3	3-30	250-2500	Outdoor in dry, cold climates
T_4	30-60	2500-5500	Outdoor in other climates
T_5	>60	> 5500	Damp climates

This excerpt is taken from ISO 9223:2012, Table B.1 on page 10, with the permission of ANSI on behalf of ISO. © ISO 2014—All rights reserved.

Table 10.4 ISO 9223 Classification of Sulfur Dioxide and Chloride Pollution Levels [40]

Sulfur Dioxide Category	Sulfur Dioxide Deposition Rate, mg/(m^{2}day)	Chloride Category	Chloride Deposition Rate, mg/(m^{2}day)
P_0	≤10	S_0	≤3
P_1	11-35	S_1	4-60
P_2	36-80	S_2	61-300
P_3	81-200	S_3	301-1500

This excerpt is taken from ISO 9223:2012, Table B.3 on page 11 and Table B.4 on page 12, with the permission of ANSI on behalf of ISO. © ISO 2014—All rights reserved.

Table 10.5 ISO 9223 Corrosion Rates After 1 Year of Exposure Predicted for Different Corrosivity Classes [40]

Corrosion Category	Steel g/(m^{2}year)	Copper g/(m^{2}year)	Aluminum g/(m^{2}year)	Zinc g/(m^{2}year)
C_1	≤10	≤0.9	Negligible	≤0.7
C_2	11-200	0.9-5	≤0.6	0.7-5
C_3	201-400	5-12	0.6-2	5-15
C_4	401-650	12-25	2-5	15-30
C_5	651-1500	25-50	5-10	30-60

This excerpt is taken from ISO 9223:2012, Table 2 on page 4, with the permission of ANSI on behalf of ISO. © ISO 2014—All rights reserved.

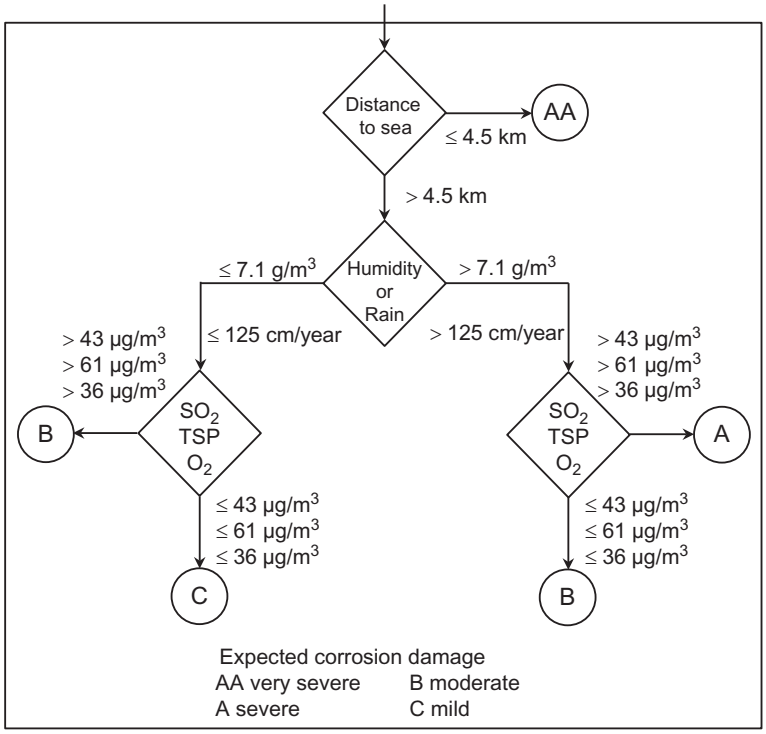

Fig. 10.10 The corrosion damage algorithm that considers distance to saltwater resulting in either the very severe AA rating or a consideration of moisture factors [42].

The ISO 9223 method does not accurately predict the atmospheric corrosion rates of metals because it does not consider the temperature and the contribution to corrosion from other contaminants such as acid rains, NO_x, and sulfides.

10.6.2 PACER LIME algorithm for atmospheric corrosion classification

Summitt and Fink [41] developed an environmental corrosion severity classification system for steel aluminum, magnesium, and titanium aircraft alloys. The corrosion damage algorithm (CDA) is shown in Fig. 10.10. This classification takes into account either the distance from saltwater or moisture levels. When the CDA considers the moisture levels in an atmosphere, the values of the concentration of the pollutants are compared with those listed in the Working Environmental Corrosion Standards (WECS) [42].

Case Study 10.1—Atmospheric Corrosion

Gonzalez *et al.* [43] and Lopez *et al.* [44] investigated the atmospheric corrosion of aluminum with different layers of anodic films in eleven different environments with estimated levels of salinity. Electrochemical corrosion techniques and electrochemical impedance spectroscopy were used to estimate the corrosion rates. The results indicated that at critical levels of anodic film thicknesses, the aluminum could be protected for a long time even when exposed to high levels of salinity.

Atmospheric corrosion studies were performed in the Spanish Canary Islands exposing zinc, copper, and carbon steel sheets to the subtropical and coastal environment for a period of 3 years [45–47]. The first part of this study was to determine the corrosion rates on each sample at different times. The study also performed an analysis of the atmospheric conditions at the thirty-five test sites on the islands. With this information, the atmospheres were classified according to ISO. Measured corrosion rates were compared with the expected ISO values. The corrosion rates obtained based on ISO were determined deficient throughout the studied region [45]. Classification of atmospheres, aggressiveness of the province of Santa Cruz de Tenerife (Canary Islands, Spain) for zinc, according to the ISO9223:2012 norm, as a function of meteorological and pollution data (classification 1) and corrosion rate (classification 2) for the first year of exposure are shown in Table 10.6 [45].

In the second part of the study, X-ray diffraction was used to determine the surface products formed on the zinc sheets as a result of corrosion through a 4-year time period [46]. The following zinc corrosion products were identified using the diffraction studies: zincite, hydrozincite, simonkolleite, zinc chlorohydroxy-sulfate, zinc oxysulfate, and zinc hydroxyl-sulfate.

Steel, copper, and aluminum were exposed to marine, industrial, rural, and indoor environments in Cuba for a period of 18 months [48]. The following parameters were monitored: chloride concentration, SO_2 concentration, relative humidity, temperature, and time of wetness. The results indicated that the ISO classification did not adequately meet the demands of the environments in the study.

The relative humidity of an environment is a significant factor in corrosion of metals under atmospheric conditions. A thin layer film is formed on metals at a critical value of relative humidity depending on the nature of the metal being corroded. Dehri and Erbil [49] studied the effect of relative humidity on the atmospheric corrosion of defective polyester-coated galvanized mild steel using impedance spectroscopy. The measurements were taken at relative humidity values between 70% and 100%. The relative humidity of the atmosphere increases the corrosion rate of the underlying metal. Figure 10.11 shows the equivalent resistance circuit used to evaluate the corrosion parameters [49].

In Figure 10.11, R_{so} represents the solution resistance, R_{pf}, the paint film resistance, C_{pf} is the paint film capacitance, Q is the differential capacitance, R_p represents the polarization resistance, R_{ct} is the charge transfer resistance, and R_{dl} represents the diffusion layer resistance. The results indicated that the mass loss calculations agree with data obtained using the EIS [49].

The EIS technique is effective for studying the atmospheric corrosion of metals in the range of 5-100% RH in the presence of chlorides [50]. This information is potentially

Table 10.6 Classification of Atmospheres, Aggressiveness of the Province of Santa Cruz de Tenerife (Canary Islands, Spain) for Zinc [45]

Test Sites		τ	P	S	Classification 1	Corrosion rate μm/year	Classification 2
Tenerife							
1	Meteorologico	τ_3	P_0	S_1	C_2	1.02	C_3
2	Policia lacal *S/C*	τ_3	P_1	S_1	C_2	1.16	C_3
3	Oceanografico	τ_3	P_0	S_1	C_2	6.29	C_5
4	Montana Ofra	τ_3	P_0	S_1	C_3	3.29	C_4
5	Quimica	τ_5	P_0	S_1	C_3	1.59	C_3
6	Pajalilos	τ_4	P_0	S_1	C_3	1.55	C_3
7	Isamar	τ_5	P_0	S_1	C_3	2.18	C_4
8	Garimba	τ_5	P_0	S_1	C_3	2.25	C_4
9	Ayuntamiento Puerto Cruz	τ_4	P_0	S_1	C_2	4.75	C_5
10	Botanico	τ_4	P_0	S_1	C_3	0.99	C_3
11	Mantaneta	τ_5	P_0	S_1	C_3	1.03	C_3
12	Buenavista	τ_4	P_0	S_1	C_3	2.89	C_4
13	El Palmar	τ_5	P_0	S_1	C_3	1.68	C_3
14	Las Raices	τ_5	P_0	S_1	C_3	1.42	C_3
15	Izana	τ_3	P_0	S_1	C_2	0.77	C_3
16	Unelco Caletillas	τ_4	P_0	S_1	C_2	5.09	C_5
17	La Planta	τ_4	P_0	S_1	C_2	3.71	C_4
18	La Oficina	τ_4	P_0	S_1	C_2	5.32	C_5
19	El Bueno	τ_4	P_0	S_1	C_2	1.68	C_3
20	Unelco Granadilla	τ_3	P_0	S_2	C_4	50.48	$>C_5$
21	Los Cristianos	τ_3	P_0	S_1	C_3	2.97	C_4
22	Vilaflor	τ_4	P_0	S_1	C_2	0.49	C_2
23	Cueva del Polvo	τ_5	P_0	S_1	C_3	3.48	C_4
24	Guia do Isora	τ_4	P_0	S_1	C_3	1.49	C_3
25	San Sebastian	τ_4	P_0	S_1	C_3	2.58	C_4
26	Valle Gran Rey	τ_4	P_0	S_1	C_2	6.48	C_5
27	El Cedro	τ_5	P_0	S_1	C_3	0.67	C_2
28	Valverde	τ_5	P_0	S_1	C_3 or C_4	7.31	C_5
29	Aeropuerto ElHierro	τ_4	P_0	S_3	C_5	223.9	$>C_5$
30	Aeropuerto La Palma	τ_4	P_0	S_1	C_3	11.78	$>C_5$
31	El Paso	τ_3	P_0	S_1	C_3	5.07	C_5
32	Pto Naos	τ_4	P_0	S_1	C_3	4.79	C_5
33	Los Llanos	τ_4	P_0	S_1	C_3 or C_4	2.13	C_4
34	Fuecaliente	τ_4	P_0	S_1	C_3 or C_4	4.4	C_5
35	San Andres y Sauces	τ_4	P_0	S_1	C_2	1.8	C_3

τ, time of wetness; *P*, sulfur dioxide deposition rate category; *S*, chloride deposition category.
[a]Corrosion categories for zinc according to the ISO 9223 norm C_1: $r_{corr} \leq 0.1$ μm/year, C_2: $r_{corr} \leq 0.7$ μm/year, C_3: $0.7 < r_{corr} \leq 2.1$ μm/year, C_4: $2.1 < r_{corr} \leq 4.2$ μm/year; C_5: $4.2 < r_{corr} \leq 8.4$ μm/year [40].
[b]C_5: Corrosion rate higher than the ones given by the ISO 9223 norm [40].

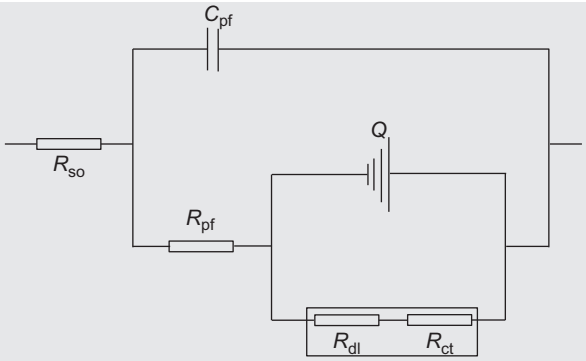

Fig. 10.11 The proposed electrical equivalent circuit model for defective polyester-coated galvanized mild steel at different relative humidity [49].

useful for the evaluation of kinetic parameters in actual service environments. The relative humidity of 70-100% in the simulated environment was obtained using ASTM D5032-97 (Standard Practice for Maintaining Constant Relative Humidity by Means of Aqueous Glycerin Solutions) [51]. The morphology of the rust layer formed at 100% RH is shown in Fig. 10.12 for different exposure times [50].

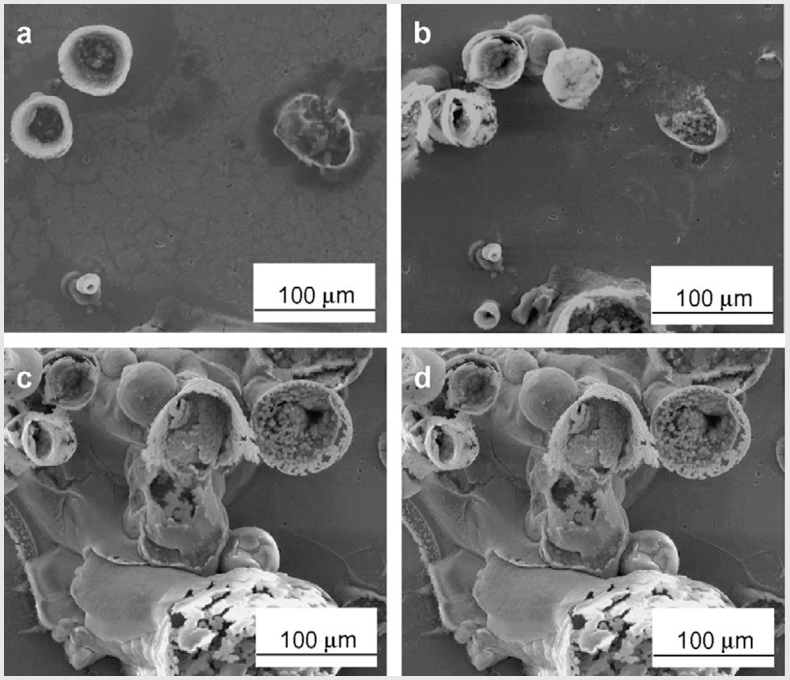

Fig. 10.12 The morphology of a rust layer on the weathering steel samples after various exposure periods at 100% RH: (a) 2 h, (b) 24 h, (c) 144 h, and (d) 216 h [50].

Relative humidity leads to the formation of a thin surface film on a metal when exposed to rain, fog, or dew formation. Xu *et al.* [52] monitored the dew formation process with a specially designed experimental arrangement. The results indicated that dust on the metal surface facilitates dew formation and increases atmospheric corrosion. Atmospheric corrosion requires both a thin film as well as some type of contaminant to initiate. The process of dew formation occurs much more rapidly in the presence of salts on the metal surface. Figures 10.13 and 10.14 compare the development and advancement of the dewing process on a clean and dust-contaminated surface, respectively [52]. Dew formation was monitored on mild steel: (i) before dewing; (ii) after 2 min; (iii) after 4 min; (iv) after 8 min; and (v) after surface drying (ambient temperature 13 °C, relative humidity 69). If the d.c. current for

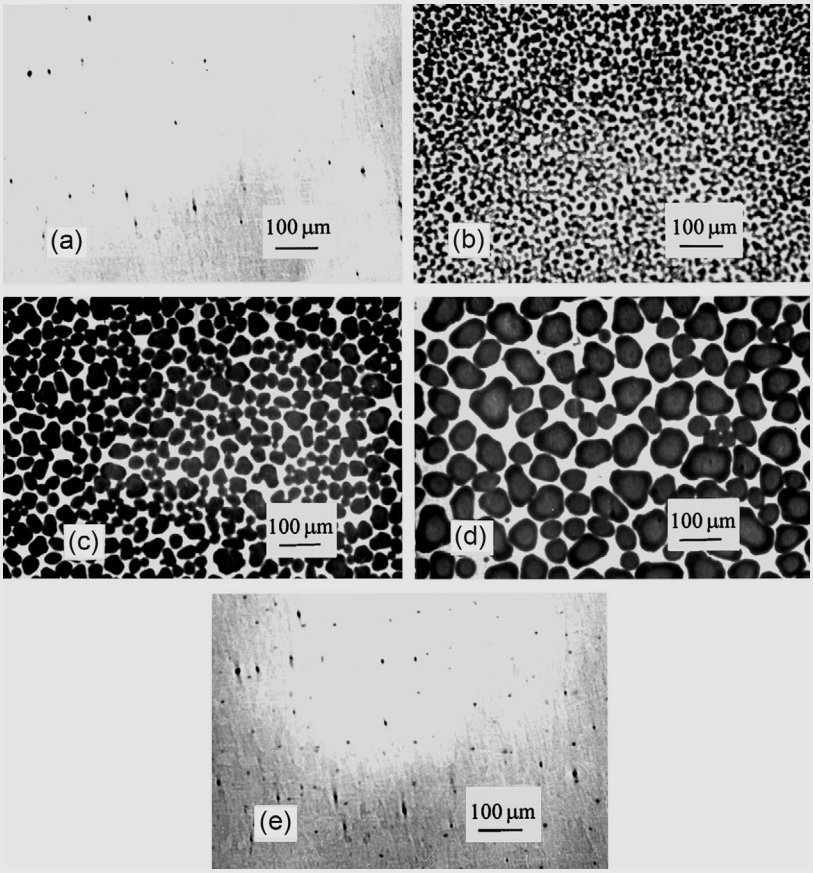

Fig. 10.13 Dewing formation on mild steel surface taken at different moments: (a) before dewing; (b) after 2 min; (c) after 4 min; (d) after 8 min; (e) after surface drying (ambient temperature 13 °C, relative humidity 69%) [52].

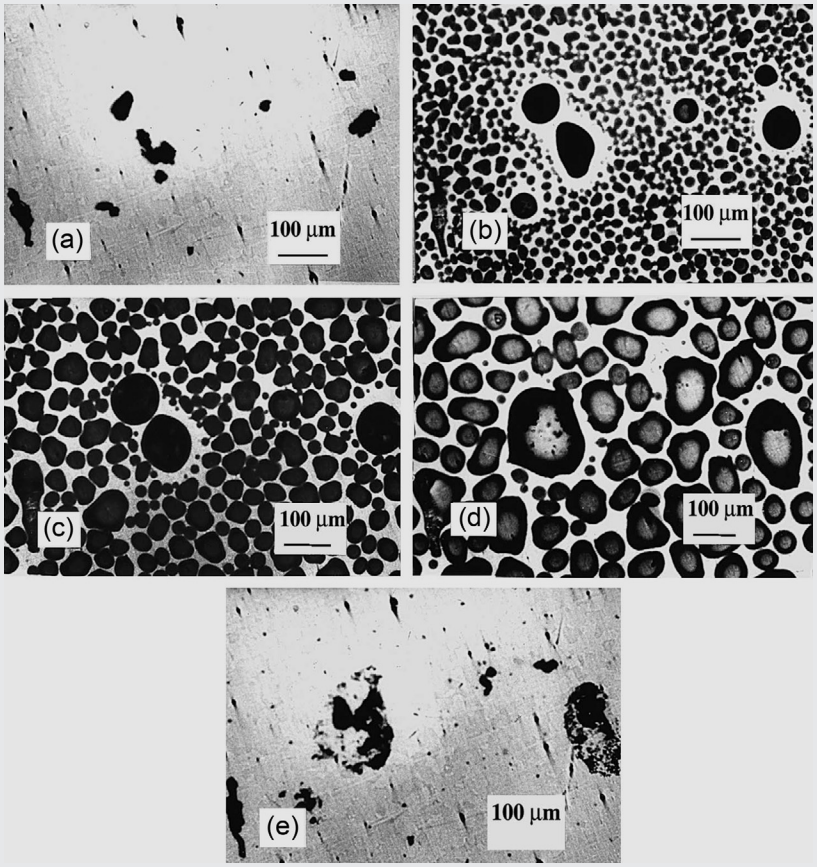

Fig. 10.14 Dewing formation on dust-covered mild steel surface taken at different moments: (a) before dewing; (b) after 2 min; (c) after 4 min; (d) after 8 min; (e) after surface drying (ambient temperature 13 °C, relative humidity 69%) [52].

cooling was cut off after the dew is fully formed, dew droplets gradually reduced in size by evaporation, indicating that a decrease of temperature is a prerequisite for dew formation.

Large dew drops form on the dust particles probably due to the condensation at the crevice between dust and the metal's surface in Fig. 10.14.

The atmospheric corrosion rate increases within the early stages for droplet formation. Tomashov [53] developed a model suggesting different corrosion mechanisms according to the thickness of the electrolyte layer, δ: dry atmospheric corrosion ($\delta < 10\,\text{nm}$), moist atmospheric corrosion ($\delta = 10\,\text{nm}$ - $1\,\mu\text{m}$), wet corrosion ($\delta = 1\,\mu\text{m}$ - $11\,\mu\text{m}$), and immersion ($\delta > 1\,\text{mm}$). Oxygen diffusion was accelerated by decreasing the electrolyte layer, enhancing the corrosion rate in the case of wet corrosion. Dry corrosion proceeds at a negligible rate.

Experimental measurements indicated that the change in the thickness of the electrolyte affects the mass transport of oxygen, hydration of dissolved metal ions, and accumulation of corrosion products [1,54–56]. Dubuisson *et al.* [57] investigated the atmospheric corrosion of galvanized steel in a micrometric electrolytic droplet containing sulfate and chloride. The measurements were performed in an electrochemical microcell through controlled

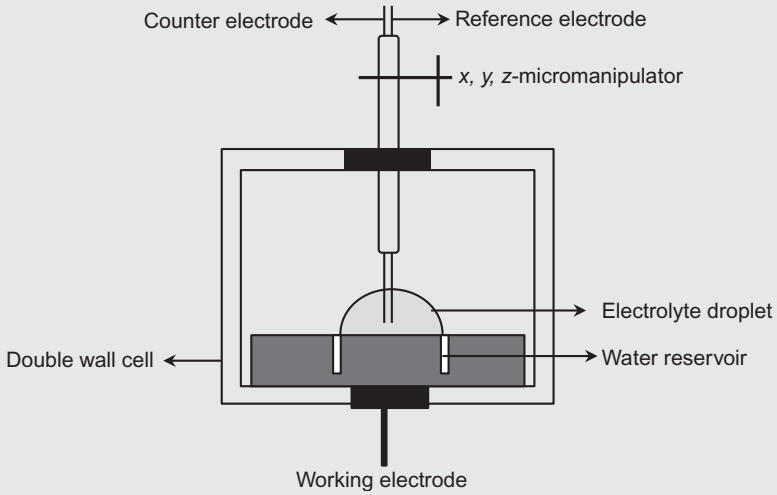

Fig. 10.15 Schematic of the electrochemical cell [57].

deposition of the electrolytic droplet on the surface of the metal. Figure 10.15 shows the electrochemical cell with a galvanized steel working electrode [57]. The reference and counter electrodes were two platinum wires.

The droplet height varied between 400 and 1100 μm. The local corrosion rates were determined by EIS and electrochemical polarization measurements. An increase in corrosion rate was observed with decreasing electrolyte thickness below 800 μm. The increase of the corrosion rate was due to the decrease of the diffusion layer thickness, resulting in an increase in oxygen reduction rate.

Experimental approaches and methodologies commonly used to understand atmospheric corrosion are based on empirical studies by testing exposure to irreproducible gaseous and electrolyte conditions. More significantly, the empirically designed approaches resulted in no instantaneous estimation of corrosion rates [58]. Cole *et al.* [58–62] found that the droplet size, shape, and chemistry at the metal-surface interface are difficult to define and result in the inability to quantitatively predict atmospheric corrosion. However, they developed a methodology capable of linking the prediction of microclimate on the surface of the metal with the nature of charge transfer occurring at the interface. The processes that control the atmospheric corrosion were found to be the deposition of marine aerosol droplets on the metal surface (2-150 μm) and the corrosion of the underlying metal [59]. However, the experimental evidence indicated that a further increase of chloride concentration did not result in the expected increase of the corrosion rate at an average estimated chloride concentration of 0.37 M [61]. The electrochemical/chemical model [62] developed to explain the processes occurring at the droplet-metal interface indicated that the Evans model [63] (anodes formed at the center of the droplet and cathodic sites forming at the droplet edge) is not applicable for small drops due to the lack of oxygen depletion in the center of the droplet. These studies clearly indicate that more corrosion studies on fine-controlled droplet size and shape are necessary to understand the mechanism of atmospheric corrosion.

Muster *et al.* [64] studied the effects of salt concentration, droplet size, and droplet shape on atmospheric corrosion of zinc. Small droplets (1-10 μL) of sea water and

sodium chloride of different concentrations were deposited onto a close-packed array of 500 μm zinc electrodes. Altered droplet contact angles were obtained by exposing the zinc electrode array to a plasma cleaning process that varied the electrodes surface energy. The microscopy image of the electrode array with overlaid spreading of 1.5 and 10 μL droplets and the temperature and humidity control during the experiment using a saturated solution of KCl and $MgCl_2$ are shown in Fig. 10.16 [64].

The plasma cleaning process enhanced the wettability of the zinc electrode array and produced droplets of identical volume but varied contact area. This approach results in more rapid drying times when the droplets of identical volume are applied to a more wetting surface. The close-packed array of zinc wires enabled the corrosion at the droplets-metal interface to be evaluated spatially across a surface that replicates planar zinc. The kinetics of the cathodic and anodic charge transfer reactions were monitored during wetting and spreading using this experimental arrangement. The influence of droplet chemistry, droplet size, and shape on the rate of corrosion was determined by evaporation over a close-pack array. The results indicated that the highest rates of zinc corrosion were not observed during the drying cycle in contrast to studies on other metals. The initial wetting and holding at relative humidity resulted in the highest measured corrosion rates. Corrosion damage while drying was accelerated for large droplets with increased electrolyte concentration and high contact angle. Figure 10.17 shows a typical shape of corrosion rate vs. time for zinc corrosion by droplets and thin films and steel corrosion [64].

The model proposed by Hœrle *et al.* [65] for the corrosion of steel is based on three regimes of wetting, wet, and drying processes. The supersaturation of metal

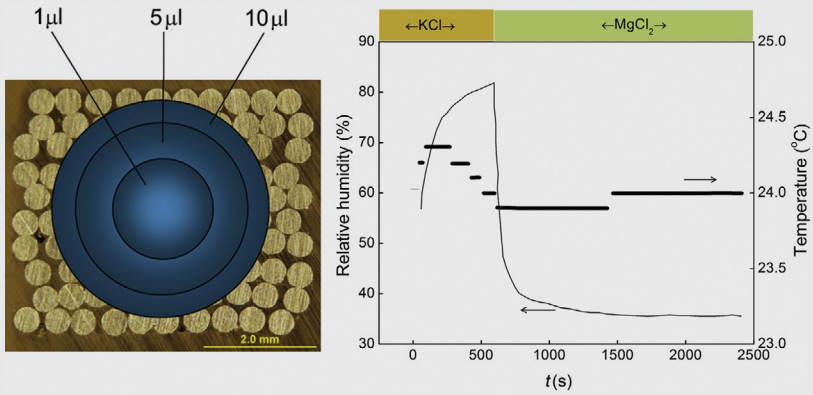

Fig. 10.16 Left: optical microscopy image of the electrode array with overlay of the spreading of 1, 5, and 10 μL droplets added after grinding of the array. Right: humidity and temperature control during droplet experiments using saturated salt solutions of KCl and $MgCl_2$ [64].

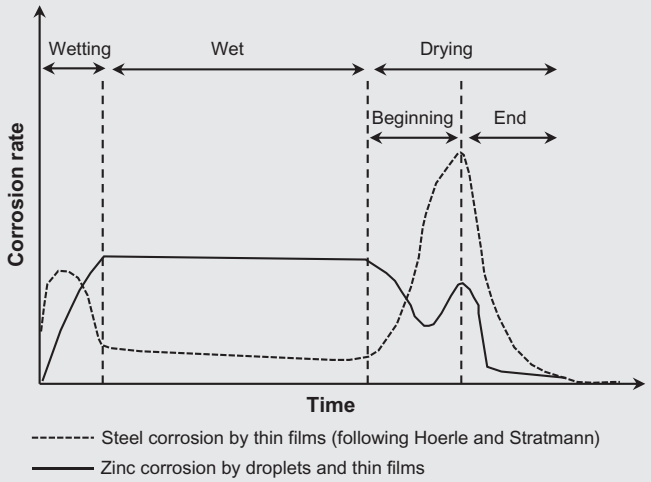

Fig. 10.17 Schematic showing typical shape of corrosion rate vs. time for zinc corrosion by droplets and thin films and steel corrosion [64].

cation-hydroxide equilibrium occurs between the beginning and end of drying. Next, the deposition of iron hydroxide moved the droplet into the anodically-controlled region, decreasing the corrosion rate at the end of drying.

In the case of zinc under wet conditions, the corrosion occurs at much higher rates and reduces under drying. High concentrations of zinc that are released into the electrolyte during the wetting initiate an earlier decrease of the corrosion current due to the precipitation of zinc hydroxide [64].

10.7 ROLE OF POLLUTANTS

Bernardi *et al.* [66] investigated the influence of alloying elements such as Cu, Sn, Zn, and Pb on the corrosion of UNSC83600 bronze subjected to acid rain. The study compared bronze samples corroded in a natural environment with those corroded in a laboratory using an artificial rain. Figure 10.18 shows the comparison of the bronze at 4 h and after 30 days of exposure [66]. A continuous dissolution of bronze was observed under a severe leaching drop effect. Sn cations remained in the patina as $SnO_x(OH)_y$. A preferential leaching of Cu and Zn was observed after several hours of exposure and formation of a Sn-rich patina [66].

The susceptibility of zinc to sulfur dioxide, a common pollutant found to cause atmospheric corrosion, was studied by Veleva *et al.* [67]. Galvanized steel and zinc plates were subjected to a humid tropical environment, inducing atmospheric corrosion during 2 years in rural and urban atmospheres. Runoff samples were taken from each of the plates and analyzed to compare the results. Runoff samples taken from the galvanized steel

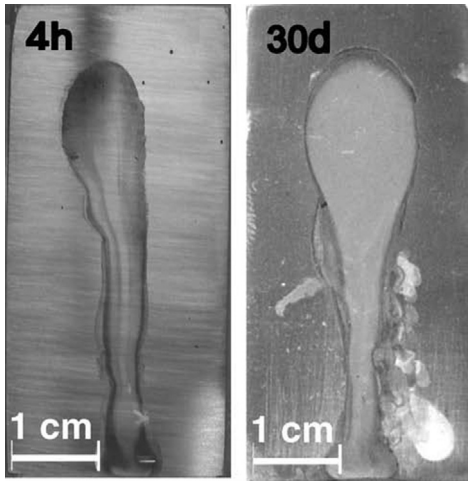

Fig. 10.18 Comparison of the bronze at 4 h and 30 days of exposure [66].

contained concentrations of both sulfur dioxides and chlorides, while the runoff samples taken from the zinc samples contained only sulfur. Zinc was highly corrodible when exposed to SO_2. The corrosion of zinc increased 47% in the second year of the test, while the zinc release was 50%. Due to the presence of zinc carbonate in the corrosion product, the concentration of carbonate ions, CO_3^{2-}, estimated in zinc runoff solutions was 1.7 times higher than those detected in rains. Figure 10.19 shows the calculated corrosion rate and experimental mass loss data for the galvanized steel [67].

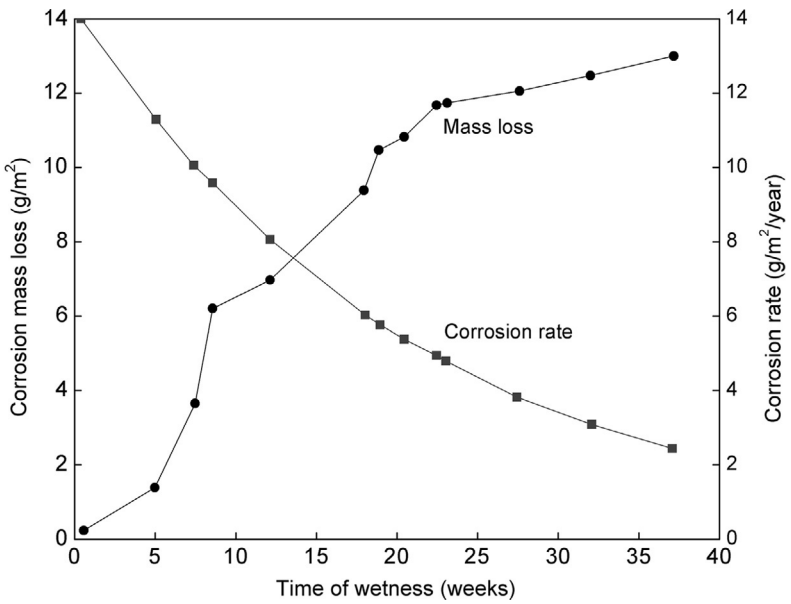

Fig. 10.19 Calculated corrosion rate and experimental mass loss data for galvanized zinc steel samples vs. time of wetness, during their exposure at rural environment [67].

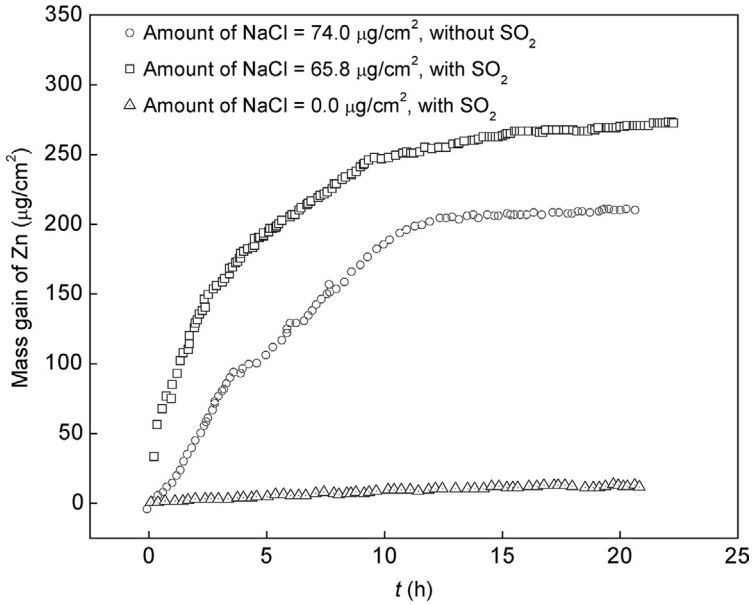

Fig. 10.20 Influence of NaCl deposition and SO_2 on atmospheric corrosion of zinc at 90% RH and 25 °C [68].

In a separate study, the effects of NaCl and SO_2 air pollutants on the corrosion of zinc were investigated by Qu *et al.* [68]. Influence of NaCl deposition and SO_2 on atmospheric corrosion of zinc at 90% RH and 25 °C is shown in Fig. 10.20 [68]. The corrosion rate decreases with time due to the large amounts of deposit buildup onto the zinc surface. NaCl increases the initial corrosion of zinc in air in the presence and absence of SO_2. Presence of only SO_2 slowly increases the initial corrosion rate. The synergistic corrosion effect was observed in the presence of both contaminants.

REFERENCES

[1] Y. Nishikata, A. Ichihara, Y. Hayashi, T. Tsuru, Influence of electrolyte layer thickness and pH on the initial stage of the atmospheric corrosion of iron, J. Electrochem. Soc. 144 (1997) 1244–1252.
[2] C. Arroyave, F.A. Lopez, M. Morcillo, The early atmospheric corrosion stages of carbon steel in acidic fogs, Corros. Sci. 37 (1995) 1751–1761.
[3] C. Leygraf, T. Graedel, Atmospheric Corrosion, John Wiley & Sons, New York, 2000.
[4] J. Weissenrieder, C. Kleber, M. Schreiner, C. Leygraf, In situ studies of sulfate nest formation on iron, J. Electrochem. Soc. 151 (2004) B497–B504.
[5] T.E. Graedel, R.P. Frankenthal, Corrosion mechanisms for iron and low alloy steels exposed to the atmosphere, J. Electrochem. Soc. 137 (1990) 2385–2393.
[6] W.H.J. Vernon, Laboratory study of the atmospheric corrosion of metals. III. Secondary product or rust (influence of sulfur dioxide, carbon dioxide and suspended particles on the rusting of iron), Trans. Faraday Soc. 31 (1933) 1678–1700.
[7] H. Leidheiser Jr., S. Music, The atmospheric corrosion of iron as studied by Mössbauer spectroscopy, Corros. Sci. 22 (1982) 1089–1096.
[8] U.R. Evans, An Introduction to Metallic Corrosion, third ed., Arnold, London, 1981.

[9] I. Suzuki, Y. Hisamatsu, N. Masuk, Nature of atmospheric rust on iron, J. Electrochem. Soc. 127 (1980) 2210–2215.
[10] V. Kucera, E. Mattson, Atmospheric corrosion, in: F. Mansfeld (Ed.), Corrosion Mechanisms, Marcel Dekker, New York, 1987.
[11] T.E. Graedel, D.T. Hawkins, L.D. Claxton, Atmospheric Chemical Compounds, Sources, Occurrence, and Bioassay, Academic Press, Florida, 1986.
[12] J.G. Calvert, W.R. Stockwell, Mechanisms and rates of the gas-phase oxidations of sulfur dioxide and nitrogen oxides in the atmosphere, in: J.G. Calvert (Ed.), SO_2, NO, and NO_2 Oxidation Mechanisms: Atmospheric Considerations, Butterworth, Woburn, MA, 1984, pp. 1–62.
[13] T.E. Graedel, M.L. Mandich, C.J. Weschler, Kinetic model studies of atmospheric droplet chemistry. 2. Homogeneous transition metal chemistry in raindrops, J. Geophys. Res. 91 (1986) 5205–5221.
[14] L.R. Robin, Kinetic studies of sulfite oxidation in aqueous solution, in: J.G. Calvert (Ed.), SO_2, NO, and NO_2 Oxidation Mechanisms: Atmospheric Considerations, Butterworth, Woburn, MA, 1984, pp. 63–100.
[15] E. Bardal, Corrosion and Protection, Springer, UK, 2003.
[16] K.J. Vlckova, J. Honzak, S.W. Dean, E.C. Rhea (Eds.), Atmospheric Corrosion of Metals, ASTM International, West Conshohocken, PA, 1982, pp. 7–44, ASTM Spec. Tech. Pub. 767.
[17] H. Schwarz, Investigations into the effect of ferrous sulfate on atmospheric corrosion and subsurface corrosion of painted surfaces, Werk. Korros. 16 (1965) 93–103.
[18] E. Mattsson, Corrosion: an electrochemical problem, Chemtech. 15 (1985) 234–243.
[19] A.M. Beccaria, E. Mor, G. Poggi, Determination of the corrosion products of iron in seawater with and without sulfides, Werk. Korros. 34 (1983) 78–83.
[20] W. Rice, R.J. Cappell, W. Kinsolving, J.J. Laskowski, Indoor corrosion of metals, J. Electrochem. Soc. 127 (1980) 891–901.
[21] T.E. Graedel, K. Nassau, J.P. Franey, Copper patinas formed in the atmosphere—I. Introduction, Corros. Sci. 27 (1987) 639–657.
[22] M. Stratmann, H. Streckel, The investigation of the corrosion of metal surfaces, covered with thin electrolyte layers-a new experimental technique, Ber. Bunsenges. Phys. Chem. 92 (1988) 1244–1250.
[23] U.R. Evans, Mechanism of rusting, Corros. Sci. 9 (1969) 813–821.
[24] U.R. Evans, C.A. Tayler, Mechanism of atmospheric rusting, Corros. Sci. 12 (1972) 227–246.
[25] M. Stratmann, K. Bohnenkamp, H.J. Engell, Attempts to understand the course of atmospheric corrosion of iron, Werk. Korros. 34 (1983) 604–612.
[26] M. Stratmann, K. Bohnenkamp, T. Ramchandran, The influence of copper upon the atmospheric corrosion of iron, Corros. Sci. 27 (1987) 905–926.
[27] M. Stratmann, K. Hoffmann, In situ Mössbauer spectroscopic study of reactions within rust layers, Corros. Sci. 29 (1989) 1329–1352.
[28] M. Stratman, The atmospheric corrosion of iron-a discussion of the physico-chemical fundamentals of this omnipresent corrosion process, Ber. Bunsenges. Phys. Chem. 94 (1990) 626–639.
[29] M. Stratmann, H. Streckel, On the atmospheric corrosion of metals which are covered with thin electrolyte layers—II. Experimental results, Corros. Sci. 30 (1990) 697–714.
[30] M. Stratmann, J. Müller, The mechanism of the oxygen reduction on rust-covered metal substrates, Corros. Sci. 36 (1994) 327–359.
[31] T. Kamimura, M. Stratmann, The influence of chromium on the atmospheric corrosion of steel, Corros. Sci. 43 (2001) 429–447.
[32] T. Kamimura, K. Kashima, K. Sugae, H. Miyuki, T. Kudo, The role of chloride ion on the atmospheric corrosion of steel and corrosion resistance of Sn-bearing steel, Corros. Sci. 62 (2012) 34–41.
[33] M. Jönsson, D. Persson, C. Leygraf, Atmospheric corrosion of field-exposed magnesium alloy AZ91D, Corros. Sci. 50 (2008) 1406–1413.
[34] M. Jönsson, D. Persson, D. Thierry, Corrosion product formation during NaCl induced atmospheric corrosion of magnesium alloy AZ91D, Corros. Sci. 49 (2007) 1540–1558.
[35] M.J. Graham, M. Cohen, The influence of on the mechanism of low-temperature oxidation (23°-450 °C) of polycrystalline nickel, J. Electrochem. Soc. 119 (1972) 879–882.

[36] S.H. Kulpa, R.P. Frankenthal, Tarnishing of nickel in air at temperatures from 23° to 200 °C and relative humidities from ambient to 95%, J. Electrochem. Soc. 124 (1977) 1588–1592.
[37] I. Odnevall, C. Leygraf, The atmospheric corrosion of nickel in a rural atmosphere, J. Electrochem. Soc. 144 (1997) 3518–3525.
[38] S. Jouen, M. Jean, B. Hannoyer, Atmospheric corrosion of nickel in various outdoor environments, Corros. Sci. 46 (2004) 499–514.
[39] S.W. Dean, Classifying atmospheric corrosivity—a challenge for ISO, Mater. Perform. 32 (1993) 53–58.
[40] ISO 9223:2012, Corrosion of Metals and Alloys—Corrosivity of Atmospheres—Classification, Determination and Estimation, International Organization for Standardization, ISO Central Secretariat, Geneva 20, 2012, Switzerland.
[41] R. Summitt, F.T. Fink, PACER LIME: an environmental corrosion severity classification system, AFWAL-TR 80 (1980) 4102.
[42] P.R. Roberge, Handbook of Corrosion Engineering, McGraw-Hill, New York, 1999.
[43] J.A. Gonzales, M. Morcillo, E. Escudero, E. Otero, Atmospheric corrosion of bare and anodized aluminum in a wide range of environmental conditions. Part 1: visual observation and gravimetric results, Surf. Coat. Tech. 153 (2002) 225–234.
[44] V. Lopez, J.A. Gonzalez, E. Otero, E. Escudero, M. Morcillo, Atmospheric corrosion of bare and anodized aluminum in a wide range of environmental conditions. Part 2: electrochemical responses, Surf. Coat. Tech. 153 (2002) 235–244.
[45] J. Morales, S. Martin-Krijer, F. Diaz, Atmospheric corrosion in subtropical areas: influences of time of wetness and deficiency of the ISO 9223 norm, Corros. Sci. 47 (2005) 2005–2019.
[46] J. Morales, F. Diaz, J. Hernandez-Borges, S. Gonzales, Atmospheric corrosion in subtropical areas: XRD and electrochemical study of zinc atmospheric corrosion products in the province of Santa Cruz de Tenerife (Canary Islands, Spain), Corros. Sci. 48 (2006) 361–371.
[47] J. Morales, F. Diaz, J. Hernandez-Borges, S. Gonzales, V. Cano, Atmospheric corrosion in subtropical areas: statistic study of the corrosion of zinc plates exposed to several atmospheres in the province of Santa Cruz de Tenerife (Canary Islands, Spain), Corros. Sci. 49 (2007) 526–541.
[48] A.R. Mendoza, F. Corvo, Outdoor and indoor atmospheric corrosion of non-ferrous metals, Corros. Sci. 42 (2000) 1123–1147.
[49] I. Dehri, M. Erbil, The effect of relative humidity on the atmospheric corrosion of defective organic coating materials: an EIS study with a new approach, Corros. Sci. 42 (2000) 969–978.
[50] C. Li, Y. Ma, Y. Li, F. Wang, EIS monitoring study of atmospheric corrosion under variable relative humidity, Corros. Sci. 52 (2010) 3677–3686.
[51] ASTM D5032-97, Standard Practice for Maintaining Constant Relative Humidity by Means of Aqueous Glycerin Solutions, ASTM International, West Conshohocken, PA, 2003.
[52] N. Xu, L. Zhao, C. Ding, C. Zhang, R. Li, Q. Zhong, Laboratory observation of dew formation at an early stage of atmospheric corrosion of metals, Corros. Sci. 44 (2002) 163–170.
[53] N.D. Tomashov, Development of the electrochemical theory of metallic corrosion, Corrosion 20 (1964) 7t–14t.
[54] G.A. El-Mahdy, Advanced laboratory study on the atmospheric corrosion of zinc under thin electrolyte layers, Corrosion 59 (2003) 505–510.
[55] M. Stratmann, H. Streckel, On the atmospheric corrosion of metals which are covered with thin electrolyte layers—I. Verification of the experimental technique, Corros. Sci. 30 (1990) 681–696.
[56] M. Stratmann, H. Streckel, K.T. Kim, S. Crockett, On the atmospheric corrosion of metals which are covered with thin electrolyte layers—III. The measurement of polarization curves on metal surfaces which are covered by thin electrolyte layers, Corros. Sci. 6–7 (1990) 715–734.
[57] E. Dubuisson, P. Lavie, F. Dalard, J.P. Caire, S. Szunerits, Study of atmospheric corrosion of galvanized steel in a micrometric electrolytic droplet, Electrochem. Commun. 8 (2006) 911–915.
[58] I.S. Cole, D.A. Paterson, W.D. Ganther, Holistic model for atmospheric corrosion. Part 1—theoretical framework for production, transportation and deposition of marine salts, Corros. Eng. Sci. Tech. 38 (2003) 129–134.
[59] I.S. Cole, D.A. Paterson, Holistic model for atmospheric corrosion. Part 5—factors controlling deposition of salt aerosol on candles, plates and buildings, Corros. Eng. Sci. Tech. 39 (2004) 125–130.

[60] I.S. Cole, D.A. Paterson, Mathematical models of dependence of surface temperatures of exposed metal plates on environmental parameters, Corros. Eng. Sci. Tech. 41 (2006) 67–76.
[61] I.S. Cole, T.H. Muster, N. Azmat, M. Venkatraman, A. Cook, Multiscale modelling of the corrosion of metals under atmospheric corrosion, Electrochim. Acta 56 (2011) 1856–1865.
[62] I.S. Cole, N.S. Azmat, A. Kanta, M. Venkatraman, What really controls the atmospheric corrosion of zinc? Effect of marine aerosols on atmospheric corrosion of zinc, Int. Mater. Rev. 54 (2009) 117–133.
[63] U.R. Evans, The Corrosion and Oxidation of Metals: Scientific Principles and Practical Applications, Edwards Arnold Ltd, London, 1960.
[64] H. Muster, A. Bradbury, A. Trinchi, I.S. Cole, T. Markley, D. Lau, S. Dligatch, A. Bendavid, P. Martin, The atmospheric corrosion of zinc: the effects of salt concentration, droplet size and droplet shape, Electrochim. Acta 56 (2011) 1866–1873.
[65] S. Hœrle, F. Mazaudier, P. Dillmann, G. Santarini, Advances in understanding atmospheric corrosion of iron. II. Mechanistic modelling of wet-dry cycles, Corros. Sci. 46 (2004) 1431–1465.
[66] E. Bernardi, C. Chiavari, B. Lenza, C. Martini, L. Morselli, F. Ospitali, L. Robbiola, The atmospheric corrosion of quaternary bronzes: the leaching action of acid rain, Corros. Sci. 51 (2009) 159–170.
[67] L. Veleva, M. Acosta, E. Meraz, Atmospheric corrosion of zinc induced by runoff, Corros. Sci. 51 (2009) 2055–2062.
[68] Q. Qu, C. Yan, Y. Wan, C. Cao, Effects of NaCl and SO_2 on the initial atmospheric corrosion of zinc, Corros. Sci. 44 (2002) 2789–2803.

CHAPTER 11

High-Temperature Corrosion

Courtesy of Power Corrosion (Consultants) Ltd.

Chapter Contents

Corrosion Engineering
http://dx.doi.org/10.1016/B978-0-444-62722-3.00011-2

11.1 INTRODUCTION

Research and development on high-temperature corrosion over the last five decades has shifted from the reaction mechanism of metal oxide to broader investigations of the corrosion of metals and alloys at high temperature including (i) the development of novel alloys with protective oxide layers stable in different corrosion environments, (ii) the study of changes in oxide properties through doping with other metals, (iii) the study of alloying, and (iv) the development of thermal barrier coatings and the development of novel methods for protection against hot corrosion such as high velocity oxy fuel (HVOF), thermal spraying, and vacuum plasma spraying (VPS). The presence of molten salts interfaced with the corroding metal drastically increases the corrosion rate. Hot corrosion between a metal/oxide and a molten salt deposit is explained by interaction with molten halides, nitrates, sulfates, and carbonates.

This chapter outlines a brief review of the literature as well as the basic principles of high-temperature oxidation of metals and engineering alloys. The chapter presents applicable thermodynamics principles, including the relationship between the oxygen partial pressure at equilibrium with the oxide and the standard energy of formation of the oxides, as well as free energy change dependence on temperature for the oxidation of metals (Ellingham diagrams). The melting point and volatility of different metal oxides are related to their protectiveness at high temperature. The Pilling-Bedworth (PB) ratio compares the volume of the oxide produced to the volume of metal consumed and represents an important parameter in predicting the protection provided by the oxide.

Oxide layers formed on metals at high temperature are the primary defense against high-temperature corrosion. The formation of oxide layers at high temperature is

explained by the oxide adsorption on the metal surface, followed by oxide formation at the interface, and oxide nucleation and growth covering the entire metal surface. Oxides have specific structural features that control their oxidation properties. They have either a deficit or an excess of oxygen relative to their stoichiometric composition. The oxide properties are discussed through p-type metal deficit oxides and n-type cation interstitial metal-excess oxide semiconductors.

At high temperatures, where the oxide layer is often the only defense against corrosion, it becomes necessary to use alloys to obtain the required corrosion resistance. The literature covering the changes of oxide properties through doping and the benefits of alloying is described in detail in this chapter. The electrochemical nature of the oxidation processes is explained in terms of n-type cation interstitial oxide growth and p-type metal-deficit oxide formation of the oxide at metal-oxide interfaces. Rate laws in the chapter are explained through their defining rate law equations and illustrated through solved exercise problems.

Thermal spraying and VPS are accepted methods of coating metals. Their application and deficiencies are explained in detail with examples using recent literature data. Also discussed in this chapter are composite coatings, corrosion protection by the addition of chemicals, ion implantation, and the preformation of oxide layers. The solved exercises problems at the end of the chapter are designed to help the reader understand the parameters that control the rate of metal oxidation at high temperatures. Additional information on the research and development of high-temperature corrosion may be found in books by Kofstad [1], Birks and Meier [2], and Lai [3].

11.2 HIGH-TEMPERATURE CORROSION THERMODYNAMICS

In corrosion engineering, oxidation is defined as a process that creates a valence state of the metal higher than the metallic state. In the case of high-temperature corrosion, oxidation refers to the creation of an oxide layer through the interaction of the metal with oxygen. It consists of two separate processes: the metal is oxidized at the metal-oxide interface,

$$M \rightarrow M^{2+} + 2e^{-} \tag{11.1}$$

and oxygen is reduced at the oxide-gas interface,

$$\frac{1}{2}O_2 + 2e^{-} \rightarrow O^{2-} \tag{11.2}$$

resulting in the overall reactions for the formation of metal oxide

$$M + \frac{1}{2}O_2 \rightarrow MO \tag{11.3}$$

The change in Gibbs free-energy is useful in analyzing corrosion reactions proceeding at constant pressure. The change in Gibbs free-energy represents the maximum useful work for an isothermal and isobaric conversion. The second law of thermodynamics defines the change in standard Gibbs free-energy between two equilibrium states as:

$$\Delta G^{\circ} = \Delta H^{\circ} - T\Delta S^{\circ} \tag{11.4}$$

when the change in standard Gibbs free-energy is negative, the reaction occurs spontaneously. When it is zero, the rate of forward reaction is the same as that for the reverse reaction and the system is at equilibrium. Although the corrosion process is irreversible in nature, the equilibrium conditions are used to derive all thermodynamic and kinetic expressions to evaluate the thermodynamic properties of corrosion process at high temperatures.

Consider the oxidation of a metal at high temperature proceeding according to this reaction:

$$\mathrm{M} + \mathrm{O_2} \rightarrow \mathrm{MO_2} \tag{11.5}$$

Assuming the reactants and products are in their standard states, the activities of the species participating in the reaction are equal to unity. Under these conditions, the Gibbs free-energy change, ΔG, is equal to the standard Gibbs free-energy change, ΔG°. The absolute value is equal to the product of RT with the natural logarithm of the equilibrium constant K.

$$\Delta G = \Delta G^{\circ} = \sum \mu_i^{\circ} x_i = RT \ln K \tag{11.6}$$

where μ_i° stands for the chemical potential of products and reactants in Eq. (11.6), and x_i is the mole fraction. Applying Eq. (11.6) to the oxidation reaction (11.5):

$$\Delta G^{\circ} = -RT \ln \left[\frac{a_{\mathrm{MO_2}}}{a_{\mathrm{M}} p_{\mathrm{O_2}}} \right] \tag{11.7}$$

Because the activities of the oxide and the metal are unity, Eq. (11.7) becomes:

$$\Delta G^{\circ} = RT \ln p_{\mathrm{O_2}} \tag{11.8}$$

or

$$\ln p_{\mathrm{O_2}} = \frac{\Delta G^{\circ}}{RT} \tag{11.9}$$

Equation (11.9) defines the relationship between the oxygen partial pressure in equilibrium with the oxide and the standard energy of formation. The oxygen partial pressure in equilibrium with the oxide can be calculated if the standard free energy of formation is known. According to Eq. (11.4), a plot of ΔG° vs. T at a given $p_{\mathrm{O_2}}$ is a straight line. The slope of this line changes at melting or boiling temperatures where new phases are

formed. Such plots for the oxide reactions at the standard state, $p_{O_2} = 1$ atm, are known as Ellingham diagrams; examples are shown in Fig. 11.1 [4]. A detailed discussion on how to construct Ellingham diagrams is described by Gaskel [5]. The equation, temperature ranges, and standard free energy changes used to construct the Ellingham diagrams shown in Fig. 11.1 are listed in Table 11.1 [6].

The oxygen partial pressures for different oxides can be easily determined from Fig. 11.1. It can be read by drawing a straight line from point "O" on the left vertical axis to the free-energy line for the oxide reaction at the temperature of interest. The line is then extended to the bottom and on the right of Fig. 11.1 where the oxygen partial pressure, p_{O_2} in equilibrium with the oxide, can be read. Using this procedure, the oxygen partial pressure for Ti at 1200 °C is estimated to be $\sim 10^{-22}$ atmospheres. Any oxygen partial pressure above that value oxidizes pure titanium. Lower oxygen partial pressures reduce titanium oxide to titanium.

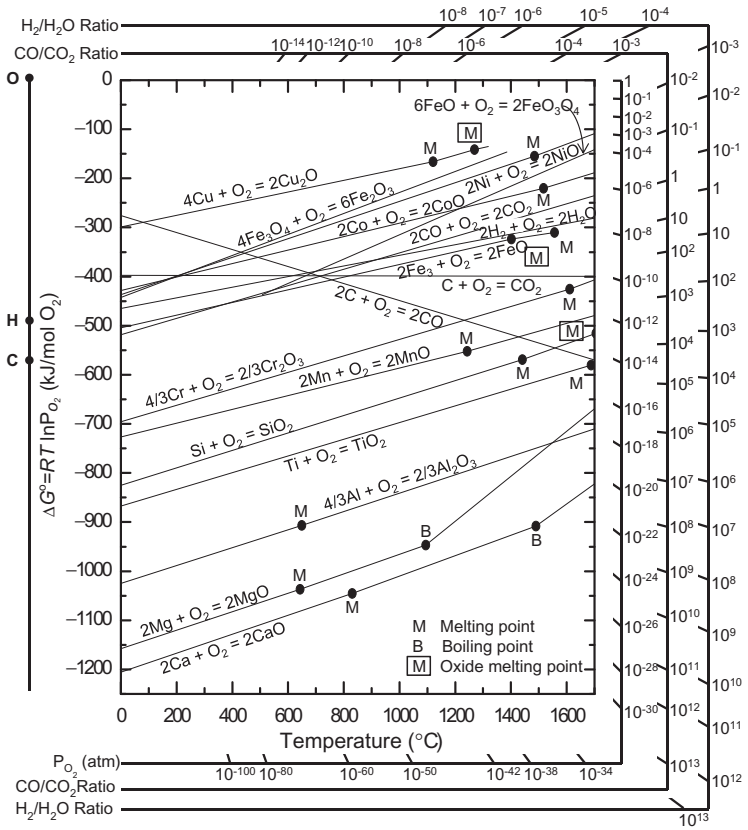

Fig. 11.1 Free energy vs. temperature for oxidation of metals (Ellingham diagrams) [4]. *Courtesy of United States Steel.*

Table 11.1 Thermodynamic Data for Reactions Involving Oxygen [6]

Range (K)	Coexistence Equation (Oxidation Reaction)	Standard Free Energy Change (J)
900–1154	$Pd + 1/2O_2 \rightarrow PdO$	$-114{,}200 + 100\ T\ (^\circ K)$
884–1126	$2\ Mn_3O_4 + 1/2O_2 \rightarrow 3\ Mn_2O_3$	$-113{,}360 + 92.0\ T$
298–1300	$3\ CoO + 1/2O_2 \rightarrow Co_3O_4$	$-183{,}200 + 148\ T$
892–1302	$Cu_2O + 1/2O_2 \rightarrow 2\ CuO$	$-130{,}930 + 94.5\ T$
1396–1723	$1.5\ UO_2 + 1/2O_2 \rightarrow 1/2\ U_3O_8$	$-166{,}900 + 84\ T$
878–1393	$U_4O_9 + 1/2O_2 \rightarrow 4/3\ U_3O_8\text{-}z$	$-164{,}400 + 82\ T$
967–1373	$2\ Fe_3O_4 + 1/2O_2 \rightarrow 3\ Fe_2O_3$	$-246{,}800 + 141.8\ T$
1489–1593	$2\ Cu + 1/2O_2 \rightarrow Cu_2O$	$-166{,}900 + 43.5\ T$
1356–1489	$2\ Cu + 1/2O_2 \rightarrow Cu_2O$	$-190{,}300 + 89.5\ T$
924–1328	$2\ Cu + 1/2O_2 \rightarrow Cu_2O$	$-166{,}900 + 71.1\ T$
992–1393	$3\ MnO + 1/2O_2 \rightarrow Mn_3O_4$	$-222{,}540 + 111\ T$
1160–1371	$Pb + 1/2O_2 \rightarrow PbO$	$-190{,}580 + 74.9\ T$
772–1160	$Pb + 1/2O_2 \rightarrow PbO$	$-215{,}000 + 96.0\ T$
911–1376	$Ni + 1/2O_2 \rightarrow NiO$	$-233{,}580 + 84.9\ T$
1173–1373	$Co + 1/2O_2 \rightarrow CoO$	$-235{,}900 + 71.5\ T$
973–1273	$10\ WO_{2.90} + O_2 \rightarrow 10\ WO_3$	$-279{,}400 + 112\ T$
973–1273	$10\ WO_{2.72} + O_2 \rightarrow 10\ WO_{2.90}$	$-284{,}000 + 101\ T$
973–1273	$1.39\ WO_2 + 1/2O_2 \rightarrow 1.30\ WO_{2.72}$	$-249{,}310 + 62.7\ T$
973–1273	$1/2\ W + 1/2O_2 \rightarrow 1/2\ WO_2$	$-287{,}400 + 84.9\ T$
949–1273	$3\ FeO + 1/2O_2 \rightarrow Fe_3O_4$	$-311{,}600 + 123\ T$
770–980	$Sn + 1/2O_2 \rightarrow SnO_2$	$-293{,}230 + 108\ T$
903–1540	$Fe + 1/2O_2 \rightarrow FeO$	$-263{,}300 + 64.8\ T$
1025–1325	$1/2\ Mo + 1/2O_2 \rightarrow 1/2\ MoO_2$	$-287{,}600 + 83.7\ T$
1050–1300	$2\ NbO_2 + 1/2O_2 \rightarrow Nb_2O_5$	$-313{,}520 + 78.2\ T$
693–1181	$Zn + 1/2O_2 \rightarrow ZnO$	$-355{,}890 + 107.5\ T$
1300–1600	$0.66\ Cr + 1/2O_2 \rightarrow 0.33\ Cr_2O_3$	$-371{,}870 + 83.7\ T$
1050–1300	$NbO + 1/2O_2 \rightarrow NbO_2$	$-360{,}160 + 72.4\ T$
923–1273	$Mn + 1/2O_2 \rightarrow MnO$	$-388{,}770 + 76.3\ T$
1539–1823	$Mn + 1/2O_2 \rightarrow MnO$	$-409{,}500 + 89.5\ T$
1073–1273	$0.4\ Ta + 1/2O_2 \rightarrow 0.2\ Ta_2O_5$	$-402{,}400 + 82.4\ T$
1050–1300	$Nb + 1/2O_2 \rightarrow NbO$	$-420{,}000 + 89.5\ T$
298–1400	$1/2\ U + 1/2O_2 \rightarrow 1/2\ UO_2$	$-409{,}500 + 89.5\ T$
1380–2500	$Mg_{(v)} + 1/2O_2 \rightarrow MgO$	$-759{,}600\ \text{-}30.83\ T \log T + 317\ T$
923–1380	$Mg_{(l)} + 1/2O_2 \rightarrow MgO$	$-608{,}200\ \text{-}1.00\ T \log T + 105\ T$
1124–1760	$Ca + 1/2O_2 \rightarrow CaO$	$-642{,}500 + 107\ T$
1760–2500	$Ca_{(v)} + 1/2O_2 \rightarrow CaO$	$-795{,}200 + 195\ T$

Figure 11.1 is also used to predict the equilibrium molar ratio of H_2 to H_2O and CO to CO_2 in mixtures of water vapor and hydrogen or carbon monoxide and carbon dioxide. In the "reducing" atmosphere created by combustion, the oxygen potential is controlled by the equilibrium ratio of p_{H_2}/p_{H_2O} or p_{CO}/p_{CO_2}.

The standard free energy of formation of water

$$2H_2 + O_2 \rightleftarrows 2H_2O \tag{11.10}$$

is determined by the partial pressures of water, hydrogen, and oxygen:

$$\Delta G^\circ = -RT \ln \left[\frac{p^2_{H_2O}}{p^2_{H_2} p_{O_2}} \right] \tag{11.11}$$

or

$$p_{O_2} = e^{\Delta G^\circ / RT} \frac{1}{\left[p_{H_2} / p_{H_2O} \right]^2} \tag{11.12}$$

Equation (11.12) can be used to determine the oxygen partial pressure as a function of p_{H_2}/p_{H_2O} ratio at different temperatures.

In the case of TiO_2, the p_{H_2}/p_{H_2O} in equilibrium with TiO_2 is estimated by drawing a line from point "H" to the point at 1200 °C on the Gibbs free-energy line for titanium and extending it to the scale marked as H_2/H_2O. The p_{H_2}/p_{H_2O} shows an equilibrium ratio for hydrogen to water vapors for titanium of about 5×10^{-6}. Any higher ratio reduces titanium oxide to metallic titanium. At a lower ratio, titanium is oxidized to titanium oxide.

The oxygen potential in carbon monoxide and carbon dioxide is controlled by p_{CO}/p_{CO_2} through the equilibrium reaction:

$$2CO + O_2 \rightleftarrows 2CO_2 \tag{11.13}$$

with the oxygen potential of:

$$p_{O_2} = e^{\Delta G^\circ / RT} \frac{1}{\left[p_{CO} / p_{CO_2} \right]^2} \tag{11.14}$$

The equilibrium, p_{CO}/p_{CO_2}, is determined from Fig. 11.1 by extending the line from point "C" to the CO/CO_2 scale.

In summary, one can obtain the oxygen potential at different atmospheres in terms of standard free energy of formation or $p_{o_2}, p_{H_2/H_2O}, p_{CO}/p_{CO_2}$. The Ellingham diagram can be used to estimate the oxygen partial pressure in equilibrium with the oxide and determine the possibility of oxide formation. These diagrams, as in the case of Pourbaix diagrams, predict equilibrium conditions and cannot be used to predict rates of corrosion at high temperatures.

The Ellingham diagram shows thermodynamic stability of the oxide at different temperatures. The more negative the standard Gibbs free-energy change in Fig.11.1, the lower the p_{O_2} or the higher p_{H_2}/p_{H_2O}, p_{CO}/p_{CO_2}, the more stable the oxide. The most stable oxides are the oxides of Ca, Mg, and Al. The least stable are the oxides of Cr, Mn, Cu, and Fe oxides. The following equations are used to calculate the enthalpy, H_T, entropy, S, and heat capacity at constant pressure, C_p, as a function of temperature. In these equations, H_{tr} and T_{tr} stand for the enthalpy change and temperature for any

phase transition that may occur between the standard temperature (298.15 K) and the temperature at which the process occurs.

$$H_{\mathrm{T}} = H_{f(298^{\circ})} + \int C_p \mathrm{d}T + H_{\mathrm{tr}} \tag{11.15}$$

where $H_{f(298^{\circ})}$ stands for enthalpy of formation at standard temperatures

$$S = S^{\circ}_{298.15} + \int_{298.15}^{T} \frac{C_{\mathrm{p}}}{T}\mathrm{d}T \sum \frac{H_{tr}}{T_{tr}} \tag{11.16}$$

$$C_{\mathrm{p}} = A + B \times T + C \times T + D \times T^3 \tag{11.17}$$

The Gibbs free-energy can be calculated for each species at the temperature of interest

$$G = H - TS \tag{11.18}$$

and is used to determine the stability of the species participating in the equilibrium.

The equilibrium constant, K_{p}, can then be calculated for the reaction of interest from

$$\log K_{\mathrm{p}} = \frac{-\Delta G^{\circ}}{2.303RT} \tag{11.19}$$

11.2.1 Melting points and volatility of oxides

Table 11.2 illustrates the melting points of oxides used to synthesize high temperature alloys. Oxides such as V_2O_5 and MoO_3 have low melting points and if their content in the alloy is large, the alloy could experience severe oxidation at high temperatures. However, vanadium and molybdenum improve the corrosion properties of alloys when used at lower temperatures in different corrosive environments. Nickel and high-strength alloys benefit from the presence of molybdenum and vanadium that increase their strength and the corrosion resistance in aqueous electrolytes at high temperatures.

Oxides with low melting points exhibit high vapor pressure at high temperatures and become less protective. Refractory metal oxides such as MoO_3, VO_2, and WO_3, have high vapor pressure at temperatures above 1000 °C. However, the volatility of these oxides does not contribute to the oxidation and is no concern of alloys if used in small quantities [7,8].

As discussed in Chapter 4, the passivation potential and the passivation critical current density of stainless steel alloys depend upon the stability of Cr_2O_3. At temperatures higher than 1000-1200 °C, Cr_2O_3 forms volatile CrO_3, which drastically decreases the alloy resistance to oxidation and its protectiveness [9,10]. The vapor pressure for oxides of refractory metals above 1000 °C are presented in Fig. 11.2 as Arrhenius plots of log (p_{MO}) vs. $1/T$ at constant oxygen pressure or $\log\left(p_{\mathrm{O}_2}\right)$ [8].

Refractory metals are used as carbide formers (vanadium) in alloys that contain insufficient chromium to form a protective layer of Cr_2O_3 (MoO_3 or WO_3 in Mo or W containing alloys) or as solution strengthening elements in Co-based alloys (Mo or W) [8].

Table 11.2 Melting Points of Oxides used to Synthesize High-Temperature Alloys

Oxide	Melting Point (°C)
α-Al_2O_3	2015
CoO	1935
Cr_2O_3	2435
FeO	1420
Mn_3O_4	1705
MoO_3	795
Nb_2O_5	1460
NiO	1990
SiO_2	1713
TiO_2	1830
V_2O_5	690
WO_3	1473

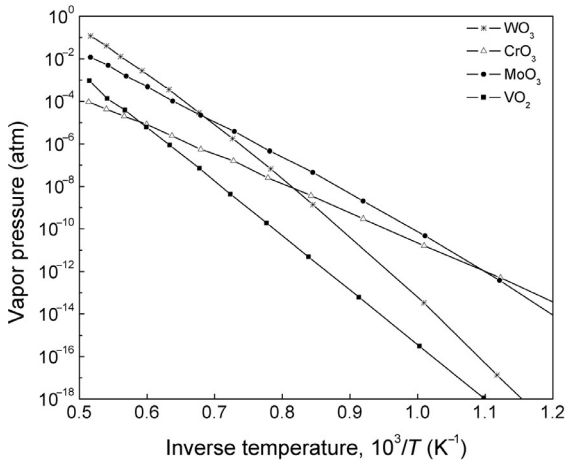

Fig. 11.2 Vapor pressures of refractory metal used in alloys at temperatures above 1000 °C [8]. *Reprinted with the permission of Cambridge University Press.*

11.3 PILLING-BEDWORTH RATIO

The Pilling and Bedworth ratio [11] compares the volume of oxide produced to the volume of metal consumed. It is an important parameter in predicting the oxide protection properties. In their model, Pilling and Bedworth [11] assumed a mechanism in which the oxide growth occurs at the metal-oxide interface by the diffusion of oxygen through the oxide. If the volume of the oxide layer is smaller than the volume lost by the metal, then the oxide layer will be subjected to high tensile stresses. On the other hand, if the volume

of the oxide layer is much larger than the volume lost by the metal, the adhesion between metal and oxide begins to decrease drastically.

Pilling and Bedworth ratios closest to unity are the most suited for protection, while those that deviate from unity would suggest an oxide layer that will crack or do not adhere effectively. The PB ratio is defined as:

$$\text{PB} = \frac{\text{volume of oxide produced}}{\text{volume of metal produced}} = \frac{Wd}{ndw} \tag{11.20}$$

where W = molecular weight of oxide, D = density of oxide, n = number of metal atoms in the oxide molecule, d = density of metal, w = atomic weight of metal.

The Pilling-Bedworth ratio for several protective and nonprotective oxides is listed in Table 11.3 [12]. It is necessary to check the actual degree of protection by an oxide layer by testing using another method. The volume ratio for alkali metals such as Li, K, and Na was found to be <1, indicating that their oxides are nonprotective. However, the experimental data disagreed. The PB ratio is a useful tool in making quick predictions. However, this principle has a limited applicability and its results cannot be taken as a certainty and must be verified using other techniques. Other factors include [13,14]:

- Oxides may grow through outward migration at the gas-oxide interface instead of inward diffusion of oxygen through the scale to the metal-oxide interface.
- Specimen and component geometries alter stress distributions in oxide layers.
- Cracks in the oxide layer may "self-heal" as oxidation continues.
- The presence of highly porous oxide layers are not accurately predicted by the PB model.
- Volatile oxides cannot be predicted by the PB model.

Table 11.3 Pilling-Bedworth Ratios [12]

Protective Oxides	PB Ratio	Nonprotective Oxides	PB Ratio
Be	1.59	Li	0.57
Cu	1.68	Na	0.57
Al	1.28	K	0.45
Si	2.27	Ag	1.59
Cr	1.99	Cd	1.21
Mn	1.79	Ti	1.95
Fe	1.77	Mo	3.40
Co	1.99	Cb	2.61
Ni	1.52	Sb	2.35
Pd	1.60	W	3.40
Pb	1.40	Ta	2.33
Ce	1.16	U	3.05
		V	3.18

Source: Data reproduced from B. Chalmers, Physical Metallurgy, John Wiley & Sons, New York, 1959.

11.4 FORMATION OF OXIDE LAYERS AT HIGH TEMPERATURE

The oxide growth on the metal surface is controlled by the rate of several processes occurring at the metal/gas-phase interface:

1. Oxygen adsorption on the metal surface
2. Oxide formation at the interface
3. Oxide nucleation and growth over the entire metal surface
4. Oxide film growth into a continuous layer and internal oxidation
5. Development of microcracks, cavities, and film porosity

Crystal defects at the metal surface, surface orientation, and metal and gas impurities control the first two processes. Oxide layers formed on the metal at high temperature are barriers in nature and provide the primary defense against high-temperature corrosion. The protectiveness of the oxide depends on the stability of the continuous layer formed in the third and fourth steps. After completion of the third step, the oxide growth proceeds through solid-state diffusion of ionic species through the oxide layer. The transport of the reactive species is determined by the concentration gradients across the oxide or by the presence of electric fields in the film or gradients of electric fields in the layer in the case of thin oxide films. Porosity and fractures may develop during the growth of the oxide layer due to micro- and macrocrack formation. Because the oxide layer is nonprotective, the contact of the oxides with the metal results in high corrosion that proceeds kinetically unhindered due to an absence of diffusion limitations. Processes occurring at the oxide-gas and oxide-film phase boundaries limit the film growth in porous oxide films. These films do not have the capability to serve as solid-state diffusion barriers between reacting ionic species. Because the electronic conductivity (ability to conduct electrons) for most oxide layers is greater than their ionic conductivity (ability to conduct ions), the protectiveness of the oxide layer is not based on its electron transfer barrier properties. The kinetics of the oxide layer growth is diffusion limited. The anion or cation diffusion determines whether the oxide layer grows on the metal-oxide interface or on the gas-oxide interface.

The oxide layer is more protective if the film growth is controlled by oxygen anions or metal cations with low diffusion coefficients. A metal's or alloy's resistance to high-temperature corrosion is based on the rate of the oxide growth, and it is possible to increase the protectiveness of the oxide layer by controlling the rate. An ideal protective layer would have a high melting point, low vapor pressure, high temperature of evaporation, and good film adherence to the substrate. A layer with a thermal expansion coefficient similar to the metal is better at resisting fractures and disbonding from the metal.

11.4.1 Oxide microstructure

Metal oxides have specific structural features that control their oxidation properties. They are far from uniform homogeneous solids and have a stoichiometric composition only at limited ranges of temperature and pressure. The oxides usually have either a deficit or an

excess of oxygen relative to their stoichiometric composition and, consequently, different structures. Small deviations from the oxide stoichiometry are compensated through the formation of single-point defects. These point defects depend upon the type of oxide deficiencies, such as interstitials or oxygen or metal vacancies. In the case of single-point defects, the structure of the oxide remains the same [1]. However, defect clusters are formed as the oxide structure increasingly deviates from its stoichiometric composition due to Coulombic interaction of point defects with opposite charges.

Nonstoichiometric oxides with metal deficits, such as $M_{1-x}O$, are p-type metal deficit oxides. Due to cation deficiencies, the defects are cation vacancies and oxygen interstitials. They are compensated through the formation of positive electronic defects (electronic holes). To maintain the charge electroneutrality, metal cations with a greater positive charge are present in the lattice or a regular cation is paired with an electron hole and results in a higher cation valence state.

An n-type cation interstitial metal-excess oxide semiconductor has an excess of interstitial cations or oxygen anion vacancies in the crystal lattice. An excess of electrons maintains the neutrality and electrical conductivity. The oxygen vacancies are created from single-point defects. The nonstoichiometric oxide MO_{2-x} with large cations is oxygen deficient and creates anion vacancies.

Examples of n-type oxides include CdO, TiO_2, Ta_2O_5, Al_2O_3, SiO_2, Cb_2O_5, and PbO_2. Interstitial ions predominate in oxides with excess metal such as $M_{1+x}O_2$. If these defects were charged, they would have positive charges. To maintain electroneutrality, the positive charges are compensated with the same formation and concentration of negative electronic defects. ZnO is representative of an n-type semiconductor.

11.4.2 Benefits of alloying

The concentration of lattice defects at the oxide-metal interface, oxide-air interface, and the rate of defects diffusion control metal oxidation and, consequently, the protectiveness of the oxide. It is possible to decrease the rate of metal oxidation and increase the oxide protectiveness by doping the oxides with other ions to decrease the concentration of lattice defects. For example, when the oxide is doped with higher-valence-state-ions (more positive), there is an increase in the number of cation vacancies because fewer electron holes are required for electroneutrality. On the other hand, doping the oxide with lower-valence-state-ions will increase the number of required electron holes, decreasing the number of cation vacancies. A lower-valence impurity (the dopant) increases resistance to ionic transport in a p-type oxide, while it decreases it in an n-type oxide. This phenomenon explains why alloying metals help prevent corrosion. In high-temperature corrosion, where the oxide layer is often the only defense against corrosion, alloys are often used to achieve better resistance to corrosion. Experimental evidence for the effect of doping on the oxide protectiveness at high temperatures has been reported [15]. The oxidation resistance of pure Zn, which forms an n-type oxide

(ZnO), is 8×10^{-10} g^2/(cm^4 h). The oxidation resistance is greater (1×10^{-11} g^2/(cm^4 h)) when doped with higher-valence ions, such as Al^{3+}, and it decreases to 2×10^{-7} g^2/(cm^4 h) when doped with lower-valence ions, such as Li^+ [15].

As seen in Table 11.4, the protectiveness of p-type nickel alloy oxide decreases when the content of Cr^{3+} ions is increased. At higher weight percentages of Cr^{3+} cations, the oxide protectiveness starts to increase due to large amounts of Cr_2O_3, an excellent defense against corrosion [16]. The nickel vacancy concentration decreases by doping NiO with Li^+ ions, resulting in a decrease in the oxidation rate.

Another example of changing oxide properties is decreasing the concentration of interstitial metal ions by doping the metal with higher-valence cations to change the ionic and electronic conductivity of the oxide. Although there are many other factors in preventing metal oxidation, the formation of a protective oxide layer is absolutely critical in controlling the oxidation rate at high temperatures.

Chromium and aluminum are known to form extremely stable oxides and are included in many alloys. Generally, 10 at.% is sufficient to provide the alloy with a continuous oxide layer. In some metals, like Co, the diffusion rate of Cr or Al is lower, and a greater concentration of Cr (25 at.%) is needed to achieve a continuous layer. If temperatures above 850 °C are anticipated, it is generally preferable to use Al in place of Cr as chromium oxides will oxidize to CrO_3, a volatile compound at elevated temperatures [17].

In addition to high-temperature stability, aluminum also has a slower rate of oxidation than chromium. Aluminum will form a more durable oxide layer than chromium. The layer will take longer to form a protective oxide layer. In a highly oxidative environment like high-temperature corrosion, this delay decreases the thickness of the oxide and its protectiveness. When alloying aluminum and chromium, the protection provided by the resulting oxide layer closely follows aluminum's oxide layer. Chromium-aluminum alloys form oxide layers much faster than an alloy with aluminum alone because chromium attracts oxygen anions that bond with the aluminum cations [17]. Figure 11.3 compares the oxidation rate of an alloy with both aluminum and chromium to alloys with only aluminum and only chromium [17].

Under induced temperature gradients, even the most protective oxide layers have difficulty in adhering to the metal. The addition of reactive metals, such as Y, Hf, and

Table 11.4 Oxidation Constants of Nickel Alloys [16]

Weight % Cr^{3+}	Parabolic Oxidation Constant k_p (mg^2/cm^4 h)
0	3.8×10^{-10}
0.3	15×10^{-10}
1	28×10^{-10}
3	36×10^{-10}
10	5×10^{-10}

Source: Data reproduced from C. Wagner, K.E. Zimens, Acta Chem. Scand. 1 (1947) 547–565.

Ce, slows the oxidation rate, slowing the diffusion rate of ions [17]. These metals also react and bond with sulfur and phosphorus impurities in the oxides. The products of these reactions impede diffusion through the metal oxide, slowing the rate of corrosion.

The oxidation rate of austenitic stainless steels decreases with the addition of nickel. The oxidation resistance of stainless steels and nickel-based alloys in air at 900 °C is shown in Fig. 11.4 [18].

The effect of chromium content on Fe-Cr alloys' oxidation (parabolic rate constant $g^2/cm^4/s$) at 1000 °C and 0.13 atm O_2 is shown in Fig. 11.5 [19]. The thickness of the chromium oxide layer increases with increasing chromium content up to 20%, resulting in a drastic decrease in oxidation rate. A continuous protective layer of Cr_2O_3 is formed on Fe-Cr alloys with a minimum content of 18% of chromium. Cr_2O_3 starts to vaporize at 1000 °C. The oxide will lose its protectiveness and a sharp increase in corrosion will occur when the oxide is not replenished from the bulk of the alloy under these conditions.

The oxidation resistance of stainless steel alloys with different compositions is compared to the oxidation resistance of carbon steel in Fig. 11.6 [4]. Carbon steels perform satisfactorily at temperatures below 500 °C. Chromium-molybdenum steels doped with up to 2% silicon have low corrosion rates up to 700 °C. Ferritic stainless and martensitic steels have superior oxidation resistance when compared to carbon and Cr-Mo steels. The corrosion rate of the alloy drastically decreased (increase in the resistance to oxidation) upon increasing the chromium content from 8% to 25%.

Alloying iron with nickel and chromium is necessary to mitigate corrosion above 900 °C. At higher temperatures, 2% Al addition increases the alloy oxidation resistance [19,20]. The oxidation rate of austenitic stainless steels (Types 309 and 310) decreases with the addition of nickel in the alloy, while the addition of tungsten, niobium, tantalum, and molybdenum increase mechanical strength, as shown in Fig. 11.7 [3].

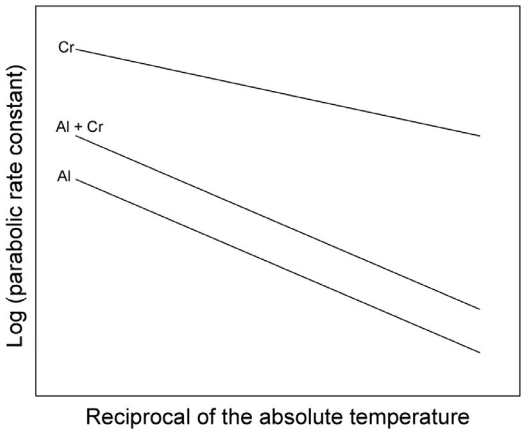

Fig. 11.3 Effect of chromium and aluminum in alloys [17].

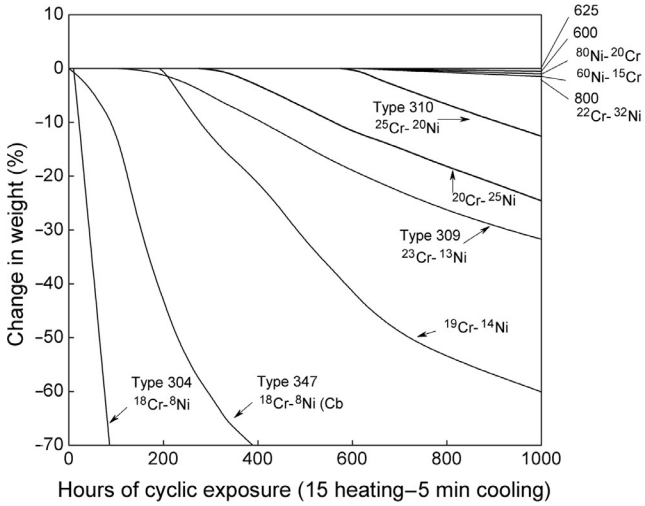

Fig. 11.4 Cyclic oxidation resistance of nickel-base alloys and stainless steels in air at 900 °C [18]. *Reprinted, with permission, from STP165 Symposium on Effect of Cyclic Heating and Stressing on Metals at Elevated Temperatures, copyright ASTM International, 100 Barr Harbor Drive, West Conshohocken, PA.*

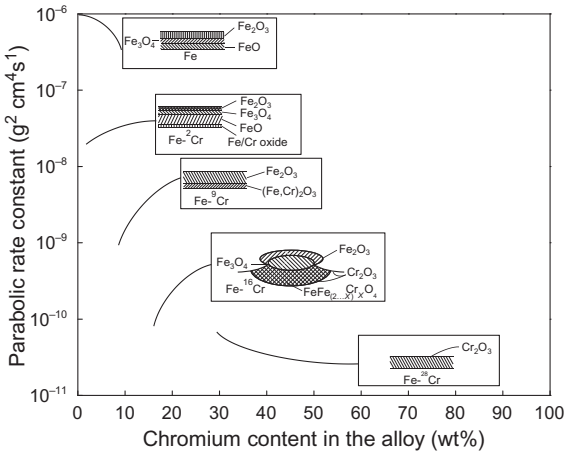

Fig. 11.5 Effect of chromium content on the oxidation (parabolic rate constant $g^2/cm^4/s$) of Fe-Cr alloys at 1000 °C and 0.13 atm O_2 [19]. *Reprinted with permission of ASM International, Materials Park, OH. www.asminternational.org.*

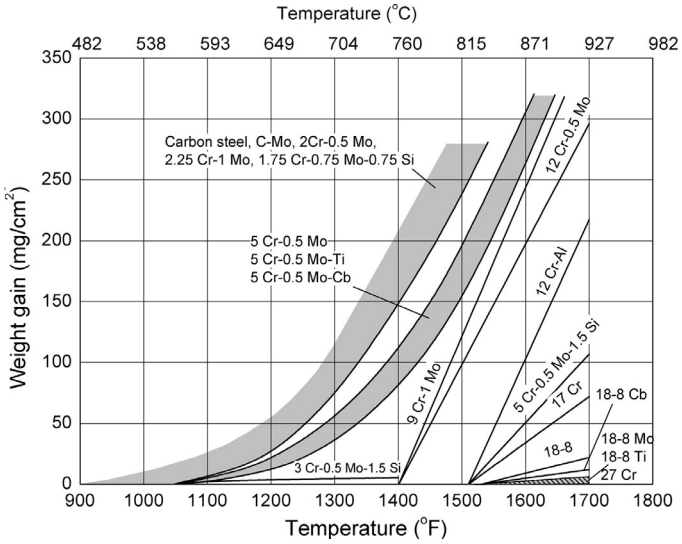

Fig. 11.6 Oxidation resistances of carbon steel and stainless steel heat-resistant alloys with different compositions after 1000 h exposure in air from 1100 to 1700 °F [4]. *Courtesy of United States Steel.*

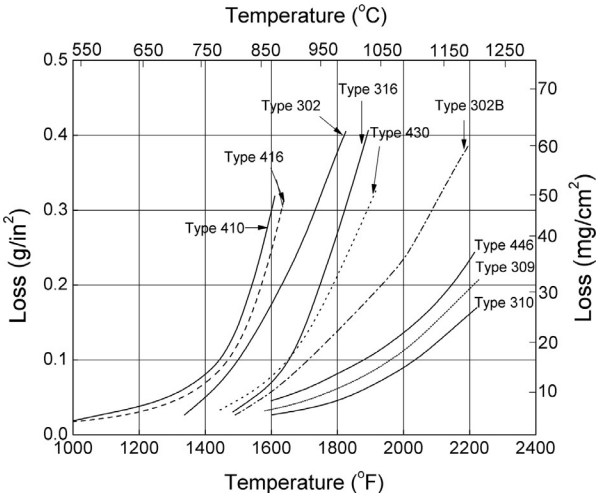

Fig. 11.7 Oxidation resistance of stainless steel at different temperatures [3]. *Reprinted with permission of ASM International, Materials Park, OH. www.asminternational.org.*

11.5 ELECTROCHEMICAL NATURE OF OXIDATION PROCESSES

As described in Section 11.2, the oxidation of metals is a process in which the valence state of the metal is higher than that in the metallic state. For high-temperature corrosion, oxidation refers to the creation of an oxide layer through the interaction of metal and

oxygen. It consists of two separate processes. The metal oxide is formed through metal oxidation at the metal-oxide interface,

$$M \rightarrow M^{2+} + 2e^{-} \tag{11.1}$$

and oxygen reduction occurs at the oxide-gas interface

$$\frac{1}{2}O_2 + 2e^{-} \rightarrow O^{2-} \tag{11.2}$$

with an overall reaction:

$$M + \frac{1}{2}O_2 \rightarrow MO \tag{11.3}$$

An electronic conductor is required in electrochemical reactions to separate the reduction reaction from the oxidation reaction during the redox processes. However, the external conductor is not necessary in high-temperature corrosion because the oxide layer conducts both ions and electrons [1,13]. Oxygen oxidation may be treated as aqueous corrosion. Electrochemical processes occur only during the change of the electrical energy resulting from electron flow in one direction (oxidation or reduction). In high-temperature oxidation, the electrons are transported from the metal-oxide interface to the oxide-gas interface where oxygen reduction takes place. The anions are transported from the oxide-gas interface to the metal-oxide interface and cations diffuse from the metal-oxide interface to the oxide-gas interface depending on the oxide interface.

An n-type cation interstitial oxide grows through interstitial cations diffusion to the oxide-gas interface (Fig. 11.8). The electrons travel to the same interface where the overall reaction, Eq. (11.3), occurs. The metal oxidation and oxide formation, Eq. (11.1), and oxygen reduction, Eq. (11.2), are shown in Fig. 11.8.

In the case of an n-type anion vacancy oxide (Fig. 11.9), the oxide film is formed at the metal-oxide interface. The conduction of the electrons and diffusion of anion vacancy are shown in the figure. The anodic reaction at the metal-oxide interface provides metal cations.

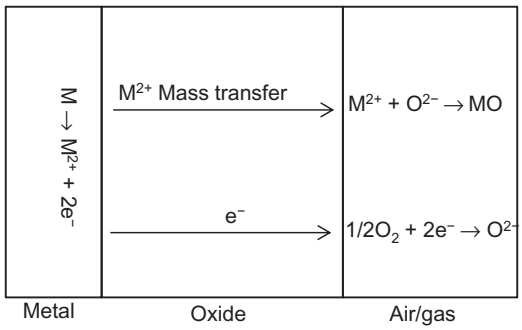

Fig. 11.8 Formation of an n-type oxide through cation diffusion at an air-gas interface.

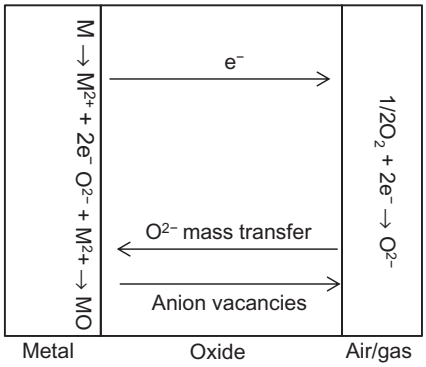

Fig. 11.9 The oxide film formation occurs at the metal-oxide interface in the case of n-type anion vacancies.

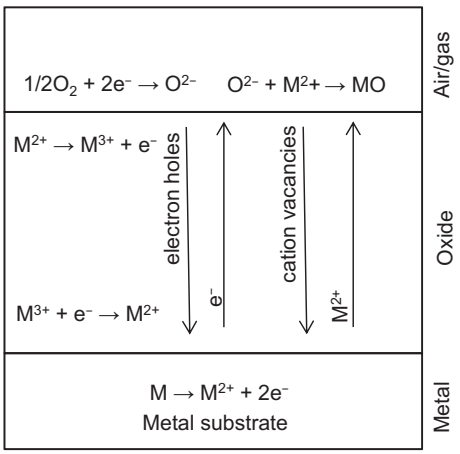

Fig. 11.10 Formation of p-type metal deficit oxides.

Figure 11.10 shows the formation of p-type metal deficit oxides; nonstoichiometric oxides with metal deficits. The defects are cation vacancies and oxygen interstitials. They are compensated through the formation of positive electronic defects (electronic holes). Electron charges are transferred to the metal-oxide interface by the movement of electron holes in the opposite direction. Metal cations diffuse at the oxide-air-gas interface, while the cation vacancies diffuse in opposite direction. The oxide film is formed at the oxide-metal interface.

11.6 OXIDATION KINETICS

High-temperature corrosion in metals has been studied in order to understand reaction rates, rate-limiting steps, reaction mechanisms, metal oxide crystal structure, oxide composition, and oxide microstructure and morphology.

The goal was to develop oxide layers with low oxidation rates and increased durability at high temperatures. Thermogravimetry has been used to study kinetics and oxidation rate by measuring the weight change of metal specimens when exposed to various gases at high temperatures. Oxide is formed on the surface resulting in a continuous increase in sample weight with time during the reaction. Weight loss of the sample is observed in the case of metal evaporation. Various types of balances have been used, such as torsion balances and microbalances with resonating quartz crystals. A schematic of an automatic recording thermobalance is shown in Fig. 11.11 [1].

The rate of oxidation and/or oxide formation has been described with linear, parabolic, logarithmic, and inverse logarithmic rate laws [1,22,23]. The generally accepted rate of oxidation is given in units of mass per area, the mass of oxide product formed per area of metal, and is denoted as W. The film thickness "x" is proportional to the weight gain.

The rates of oxide formation on metal surfaces are estimated experimentally by measuring the weight gain as a function of time and are shown in Fig. 11.12 for the four laws discussed in the following sections [1].

Figure 11.13 shows the oxidation rate of carbon steel in air at different temperatures [24]. Carbon steel showed negligible weight gain when exposed at 800 and 1000 °F for 500 h. Gradual oxidation of carbon steel was observed with increasing temperature up to 1200 °F and a linear rate was observed at 1400 °F.

11.6.1 Parabolic rate equation

The parabolic rate law is based on the assumption that cation or anion diffusion through the oxide layer is the rate-limiting step. In this case, Fick's law of diffusion serves as the starting point for any reaction rate. According to Fick's law, the flux of the diffusing

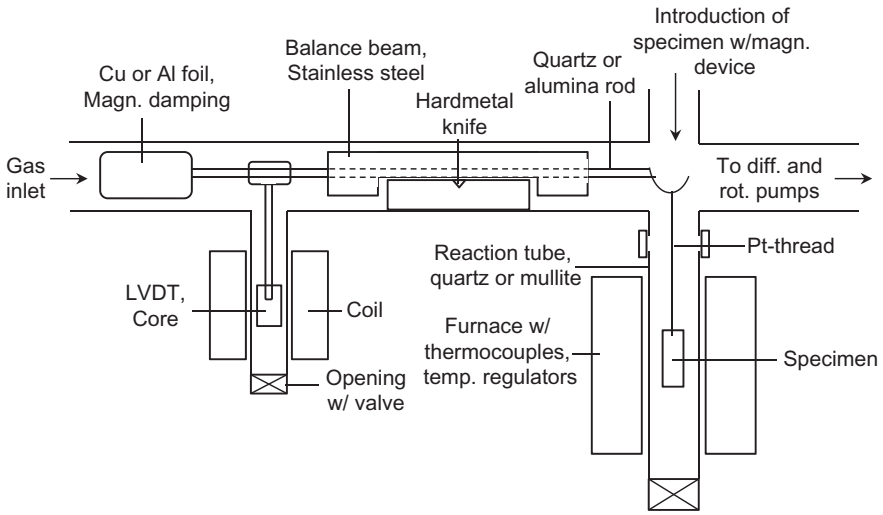

Fig. 11.11 Schematic of an automatic recording thermobalance [1].

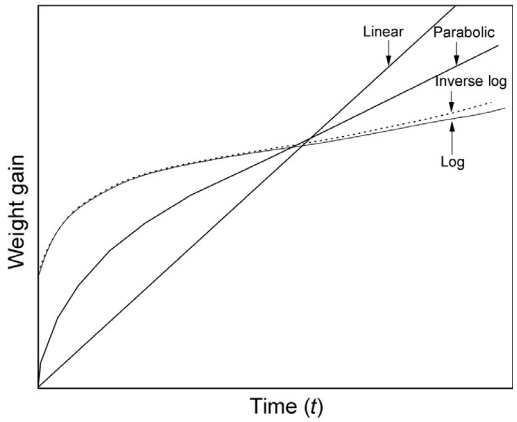

Fig. 11.12 Weight gain vs. time for the various kinetics laws for metal oxidation.

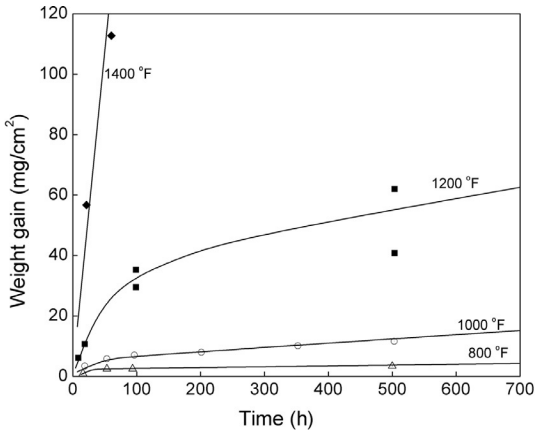

Fig. 11.13 Oxidation rate of carbon steel on air at different temperatures [24]. *Copyright © SAE International. Reprinted with permission from paper 780921.*

species equals the product of the diffusion coefficient, D, and the concentration gradient ($\Delta c/x$) and is proportional to the rate of increase of the oxide thickness with time, $\mathrm{d}x/\mathrm{d}t$:

$$-\frac{\mathrm{d}x}{\mathrm{d}t} = CD\left(\frac{\Delta c}{\mathrm{d}x}\right) \tag{11.21}$$

The mechanism is explained by Wagner [25]. Both oxygen anions and the metal cations are the rate-controlling species. The parabolic rate law has a theoretical basis and is very often encountered in high-temperature corrosion. Integration of Fick's law results to parabolic rate law equation when $k_\mathrm{p} = CD\Delta c$.

$$W^2 = k_\mathrm{p} t + C \tag{11.22}$$

where k_p and C are both constants and t is time. The parabolic law can also be defined through the square of the film thickness or:

$$x^2 = k_p t \tag{11.23}$$

The film thickness x is proportional to weight gain W and can be substituted in Eq. (11.23) with corresponding changes in the values of k_p and C. Parabolic oxidation rate yields a straight line when metal oxidation data is plotted as W^2 vs. t. A parabolic relationship between weight gain and time would indicate that the system possesses a protective oxide layer that is slowing the rate of reaction. The magnitude of the parabolic constant, k_p, for diffusion-controlled oxidation that forms a single-phase oxide is calculated from the value of the ionic self-diffusion coefficient of rate diffusion controlling ions or from the partial ionic conductivities. Figure 11.14 shows the thickness vs. time for parabolic and linear rate laws metal oxidation. If the data does not fit the parabolic rate law well, the protective oxide layer may have some defects, such as voids. Parabolic time dependence is observed for oxidation of metals at high temperatures. Under these conditions, the rate-controlling process in the oxide formation is the diffusion of the ions.

The Arrhenius equation describes the temperature dependence of the oxidation rate constants:

$$k_p = k_o \exp\left(\frac{-E_a}{RT}\right) \tag{11.24}$$

where E_a is the activation energy (cal/mol or J/mol), R (cal/mol.K or J/mol.K) is the gas constant, and T (K) is the absolute temperature. The activation energy is estimated by plotting log k_p as a function of $1/T$ with a slope given by $-E_a/2.303R$.

When the oxidation rate follows the parabolic rate law, k_p can be determined from the slope of W^2 vs. t. The rate constants determined at different temperatures can be used to find

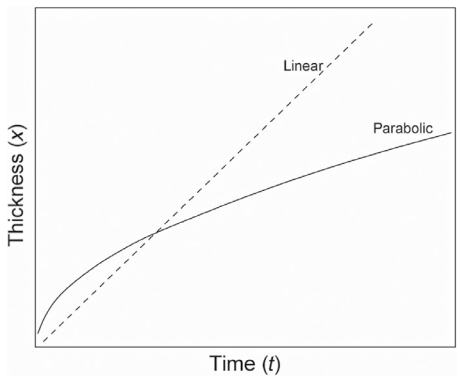

Fig. 11.14 Thickness vs. time for parabolic and linear oxidation laws.

the activation energy. The parabolic rate constant under high oxygen partial pressure and linear phase boundary-controlled reactions is related to the oxygen partial pressure as follows:

$$k_p = C p_{O_2}^{1/n} \tag{11.25}$$

where C is constant. The adsorption equilibrium shown in Eq. (11.25) is controlled by a dissociative adsorption of oxygen on the metal oxide surface:

$$O_2 = 2O_{ads} \tag{11.26}$$

The overall oxide layer growth rate is determined by the adsorbed oxygen content and diffusion processes in the oxide. The amount of adsorbed oxygen is not rate-limiting when the overall reactions are controlled by slow diffusion of the ionic species in the solid state. Thermodynamic equilibrium is assumed at both the metal-oxide interfaces and oxide-gas interfaces when high-temperature parabolic oxidation kinetics is analyzed through the diffusion of ions, electrons, or atoms. The dependence of the total reaction rate on the adsorption equilibrium of Eq. (11.26) is determined by the oxide dissociation pressure and oxide structure defects [1]. So long as the oxide has an excess of oxygen (metal deficient), the parabolic rate constant follows the relation in Eq. (11.25) and is affected by the partial pressure of oxygen and the defect structure of the oxide, determining the value of the constant "n" in the equation [1].

11.6.2 Logarithmic rate equation

The logarithmic rate law has no theoretical basis and is an empirical relationship. The logarithmic rate is given as:

$$W = k_1 \log(k_2 t + C) \tag{11.27}$$

where k_1, k_2, and are all constants. The logarithmic law of oxidation expressed through the oxide layer thickness growth is defined as:

$$x = k \log(at + 1) \tag{11.28}$$

where "k" and "a" are constants. The inverse logarithmic law can be expressed in the following form:

$$\frac{1}{x} = b - k_i \log t \tag{11.29}$$

where b and k_i are constants. The oxide thickness vs. time plot for the logarithmic and inverse logarithmic rate laws is shown in Fig. 11.15. The logarithmic relationship fits the data exceedingly well only for very thin (<1000 Å) oxide layers and moderately at low and moderate temperatures. The growth of thicker oxide layers at high temperature is controlled by parabolic law. For these reasons, the logarithmic rate law has little applicability to high-temperature corrosion.

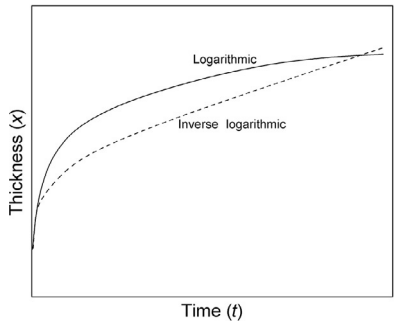

Fig. 11.15 Oxide thickness vs. time observed for logarithmic and inverse logarithmic rate laws.

11.6.3 Linear rate equation

The linear rate law is defined as:

$$W = k_L t \tag{11.30}$$

where W is weight gain per unit area, k_L is the linear rate constant, and t is time. A linear rate is the least desirable rate of oxide formation because it does not decrease with time. This high rate creates very thick oxides that eventually peel off, exposing the metal substrate to direct oxidation. A linear rate of weight gain is usually the result of oxidation kinetics. A linear fit of the data indicates that there are no diffusion limitations, or, at least diffusion is not the rate-limiting step for the oxidation. The rate of linear oxidation is constant with time. Thus, the rate is independent of whether or not the metal has been previously oxidized. Empirical weight gain data for the oxidation of metals is given in Fig. 11.12 [1]. The data that fits the linear rate law would suggest the oxide layer is completely ineffective at providing any diffusion resistance. This ineffectiveness could be the result of a nonadhesive, cracked, or highly porous oxide layer. For some metals, such as zirconium cubic, the law has been explained by metal oxidation through the formation of an oxide layer controlled by diffusion and oxygen dissolution.

11.6.4 Combination of rate equations

Figure 11.16 clearly indicates the logarithmic rate law is valid only for very thin oxide layers. Nickel oxidation follows the logarithmic law up to 200 °C. At 340 °C, the parabolic rate law better fits the data [26]. The oxidation reaction follows different rate laws at different temperatures.

The change of the rate laws in high-temperature oxidation may occur as a result of:

1. Changes in the rate-limiting reaction mechanism due to changes in the oxide film properties.
2. Changes in the reaction mechanism as a result of oxide film growth.

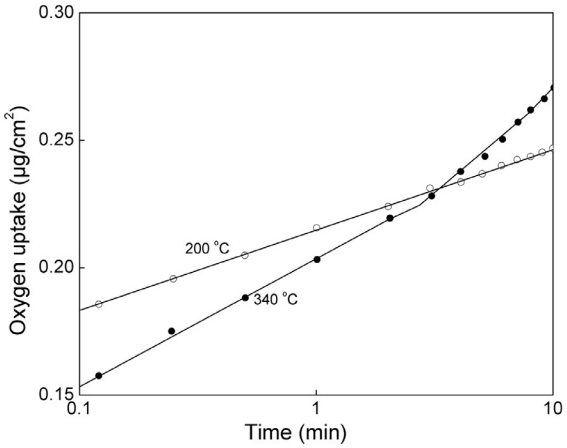

Fig. 11.16 Combination of rate equations estimated for oxidation of Ni at (a) 200 °C (logarithmic law) and (b) 340 °C (parabolic law) [26]. *Reproduced by permission of The Electrochemical Society.*

3. A reduction in the oxidation rate due to a change from the thermal diffusion of the ions to electric field -induced transport through the film. The metal oxidation becomes controlled by a combination of both the logarithmic and parabolic rate equations as a result.

When logarithmic and parabolic oxidation rates occur simultaneously, the metal oxidation may obey cubic rate law. Logarithmic and parabolic rate equations as a function of time may be distinguished by an equation:

$$x^m = k_m t + C \tag{11.31}$$

where "m" has a value of 3 or 4 depending on if the oxidation rate equation is cubic or quartic. The double logarithmic plot shown in Fig. 11.17 indicates that if the parabolic and logarithmic laws proceed simultaneously, the overall metal oxidation may follow a cubic rate [1]. Under short-exposure periods, some metals form oxides according to a cubic law:

$$W^3 = k_c t + C \tag{11.32}$$

where k_c and C are constants. For some metals, the cubic law has been explained by metal oxidation through the formation of an oxide layer controlled by diffusion and oxygen dissolution.

Catastrophic oxidation is not defined by any particular rate law. The term refers to oxidation that continues to increase as a function of time. Metals that demonstrate linear oxidation rates at lower temperatures have the potential to undergo catastrophic oxidation at higher temperatures. The oxidation reaction is an exothermic one, generating

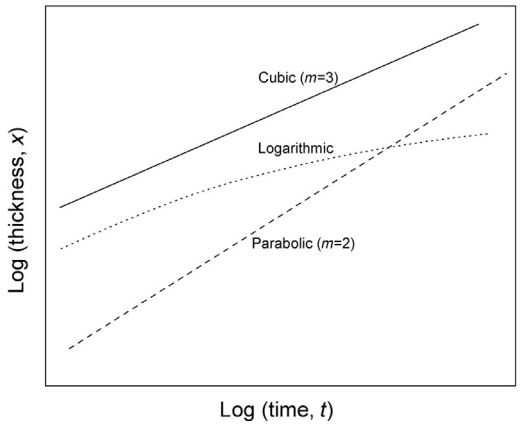

Fig. 11.17 Illustration of metal oxidation obeying cubic rate law when logarithmic and parabolic oxidations occur simultaneously [1].

heat as the reaction proceeds. At higher temperatures, the reaction rate increases, which creates heat faster. If the heat transfer from the metal surface is not sufficient to compensate for the increased heat generation, then the temperature of the metal surface will increase, further increasing the reaction and heat generation rates. At this point, the reaction has become autocatalytic and will proceed at ever higher rates and temperatures.

11.7 HOT CORROSION

Hot corrosion refers to corrosion between a metal-oxide and a molten salt deposit. It occurs at the solid-gas interface. Molten salts are extremely corrosive and their presence increases the rate of corrosion by two orders of magnitude when compared to high-temperature corrosion at similar temperatures and conditions [27–29]. They act as solvents, preventing the formation of a stable oxide, or they chemically react with the oxide layers. By transporting through, the salts may damage the protective oxide layers. Two different types of hot corrosion exist, namely, Type I and II.

Type I hot corrosion is the transport of sulfur from a sulfur deposit (a molten salt) through an existing oxide layer, where it forms stable sulfides with chromium. As time progresses, chromium fully reacts with sulfur and can no longer move through the oxide layer to provide protection against oxidative attack. Type I hot corrosion occurs from 750 to 950 °C [16].

Type II hot corrosion occurs between 600 and 850 °C and involves base-metal sulfates that require a certain concentration of sulfur trioxide for stabilization. These sulfates, when stable, react with alkali metals to form salts with low melting points and impede protective oxide layer formation [17].

In hot corrosion as well as high-temperature corrosion, metal oxidation coupled with oxygen reduction remains the primary degradation mechanism for affected metals. Oxygen in hot corrosion comes from oxygenated anions such as sulfates, carbonates, nitrates, and hydroxides. Alloying the metal with chromium generally offers a high level of protection against corrosion.

11.7.1 Molten halides

Molten halides are particularly corrosive, and this subtype of hot corrosion deserves further discussion. It is encountered in the compressor sections of turbines in ships, off-shore platforms, and aircraft operated over the seas. Salt mixed with water vapor enters the turbines, where corrosive attack takes place. Other examples of hot corrosion via molten halides are reactors or pieces of industrial equipment that contain traces of NaCl, KCl, $BaCl_2$, or other halide salts and operate at temperatures high enough to melt the salts.

The effect of molten halides on oxide layer scale formation was studied by placing various stainless steels in a KCl-NaCl-$BaCl_2$ melt at 600 °C [30]. The oxide layers formed under these conditions were porous and had poor adherence properties. Due to oxide porosity, the chromium in the stainless steel was subjected to selective leaching. The addition of certain oxyanions, such as carbonate and peroxide, helps forming a more protective oxide layer and inhibits the selective leaching of chromium [30].

Oxide formation was studied on iron, chromium, carbon steel, and other steel alloys placed in $ZnCl_2$ and KCl melts at 450 °C and pure oxygen [31,32]. The oxide formed on the iron, mostly Fe_2O_3, had very low adhesion. The chromium oxide scale peeled off and provided little defense against oxidation. Carbon steel behaved similarly to pure iron. Also, the oxide layer on stainless steel failed to adequately protect the metal. High concentrations of chromium fail to offer effective protection against molten chloride salts [32]. This is due to chromium leaching by molten salts [30]. The oxide scale may turn into $Cr_2O_2Cl_2$ under highly acidic conditions. $Cr_2O_2Cl_2$ is a very volatile substance and, at these temperatures, it evaporates away, exposing the metal beneath to oxidative attack.

Hot corrosion of various ferritic and austenitic stainless steels has been studied in molten NaCl, NaCl-$AlCl_3$, and NaCl-$Al_2(SO_4)_3$ [33]. The results indicate that initially Cr, Fe, and Ni all form oxides with Na_2O and free chlorine. Next, the chlorine begins to dissolve in Cr_2O_3, increasing the rate of solid-state oxidation. As shown in Fig. 11.18, chlorine reacts at the oxide-salt interface to form complexes with anion vacancies [32]. This leads to a decrease in anion vacancies that must be balanced by a greater consumption/generation of cation vacancies, the growth of the oxide layer. The addition of $AlCl_3$ reduces the melting temperature of the salt mix, which allows the corrosive attack to begin at a lower temperature.

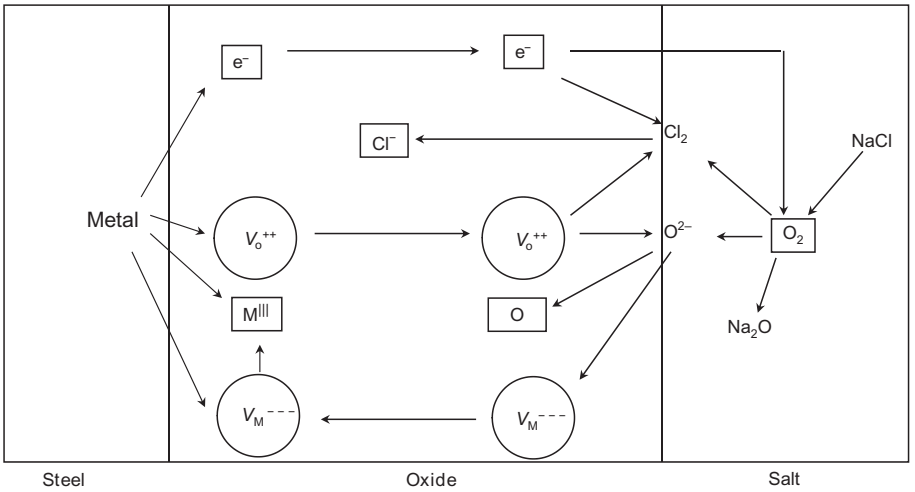

Fig. 11.18 Diagram of film growth during hot corrosion in NaCl [32].

Case Study 11.1—The Effects of Molten Halides

Corrosion of 310 SS was studied in the presence of NaCl and $NaSO_4$ salt mixtures at 750 °C [28]. Five different mixtures of NaCl/Na_2SO_4 with the following wt% were used: 100/0, 75/25, 50/50, 25/75, and 0/100. The salts were applied to specimens of 310 SS and placed in air at 750 °C. Figure 11.19 shows parabolic metal oxidation kinetics for the control specimen with no applied salt (labeled oxidation in the legend) after about 3 h [28]. The specimens that underwent hot corrosion exhibited various types of rate laws for their oxidation.

It is generally assumed that hot corrosion can only occur in the presence of molten salts. Although the experiments were conducted at 750 °C, below the melting point of pure NaCl (801 °C), the rate of corrosion is almost four orders of magnitude greater than simple oxidation. The high corrosion rate is explained by the formation of sodium chromate (Na_2CrO_4) at temperatures below the melting point of NaCl. The sodium chromate forms a eutectic with NaCl with a low melting point of 577 °C. The melting of the eutectic initiates the hot corrosion mechanism involving the NaCl and, consequently, extremely high corrosion rates are observed [28].

The melting point of all the salt mixtures is below 750 °C. However, Na_2SO_4 has a melting point of 884 °C, which accelerates the alloy corrosion rate. It is found that NaCl attacks the oxide (Cr_2O_3) and cracks it. Once the protective oxide layer is fragmented and becomes nonprotective, the sulfur from Na_2SO_4 accelerates the corrosive attack on the alloy. The presence of the molten halides hinders protective oxide layer formation. These processes result in an oxide layer that is noncontinuous and nonadhesive. Adding sulfate ions in molten halides causes internal sulfidation along oxide imperfections. If Ni is present in chromium-depleted portions of the oxide, nickel sulfides form and damage the protective oxide. Solid-state oxidation is relatively unimportant in the case of molten halides. Figure 11.20 shows the surface of an oxide layer formed on a titanium alloy that shows heavy cracking in a NaCl environment [34].

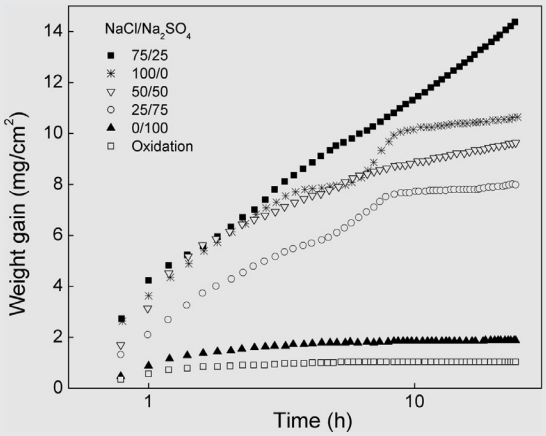

Fig. 11.19 Kinetics of hot corrosion at 750 °C as a function of square root time [28].

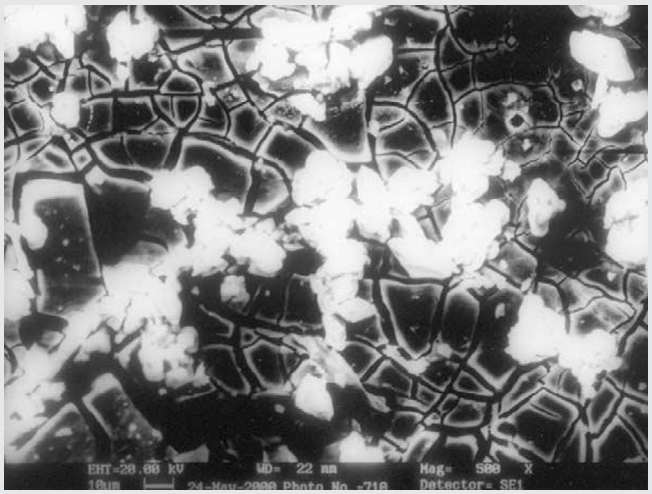

Fig. 11.20 SEM image of a cracked oxide layer on a Ti alloy under NaCl condition [34].

11.7.2 Molten nitrates

A protective oxide film, Fe_3O_4, was formed during the corrosion of stainless steels at 250–450 °C in (Na, K)NO_3 [32,35]. The rate of oxide layer formation followed the parabolic rate law. Oxides formed with molten nitrates resemble those formed in aqueous solutions and are quite stable. Solid-state oxidation is the dominant mechanism of oxide layer growth.

11.7.3 Molten sulfates

Hot corrosion induced by molten sulfates is commonly encountered on the fire side of boilers that run on conventional fossil fuels. Several different types of corrosions have

been identified for stainless steels that contain both chromium and nickel when in contact with a salt melt that contains (Li, Na, K)$_2SO_4$ [32,36]. The oxide layer lacked an inner layer and was porous and saturated with sulfides. For steels with titanium in addition to chromium and nickel, the surface became completely passivated. In the presence of a salt melt that contains (Li, Na, K)$_2SO_4$, the two-layered oxides were susceptible for both active and transpassive dissolution. The active dissolution is most likely the result of the reduction of SO_4^{2-} to S^{2-}. On the other hand, the transpassive dissolution is probably due to the reduction of SO_4^{2-} to SO_3 and O_2.

The oxide film on the lower-alloy steels in a $CaSO_4$, Na_2SO_4, K_2SO_4, $PbSO_4$, $ZnSO_4$ molten salt mixture containing vanadate and chloride additives at 600 °C has two layers [37]. The outer layer is thick and made of Fe_3O_4 and Fe_2O_3; below there is a thin inner layer of FeS with dissolved Cr from the metal. The thick outer layer was absent for steels with higher chromium and nickel percentages. In these steels, high concentrations of chromium oxide with Zn and (Fe, Ni) oxide dissolved in the molten salt mixture were found in pits.

Molten sulfates are extremely corrosive to stainless steels. The chromium-rich oxide layers formed on their surfaces are only partially protective. Other forms of protection must be explored if the metals are used in a known hot corrosive environment with molten sulfates.

The corrosion behavior of sputtered Ni-based superalloy K38 nanocrystalline coatings in molten sulfate (75 wt.% Na_2SO_4 + 25 wt.% K_2SO_4) was investigated at 900 °C in air. The results indicated that nanocrystallization triggers rapid formation of a protective oxide layer. The addition of yttrium to the coating improved its corrosion resistance [38].

11.7.4 Molten carbonates

Molten carbonates have been receiving attention due to the development of the molten carbonate fuel cell that uses CO_2 as a reactant. CO_2 easily reacts with salts and other impurities to form highly corrosive products.

The formation of an oxide layer on Fe in the presence of Li_2CO_3 and K_2CO_3 at 650 °C was explained through the mechanism shown in Fig. 11.21 [39]. The growth of the oxide layer is achieved through the formation, transportation, and consumption of oxygen vacancies in the oxide layer. Oxidation and lithiation of iron atoms in the interstitial oxide layer results in the formation of $LiFeO_2$ in the outer portion of the oxide. The formation of $LiFeO_2$ results in high stresses felt in both the metal and the oxide layers and leads to cracking.

A similar melt of Li_2CO_3 and K_2CO_3 in the presence of typical molten carbonate fuel cell feed yielded only $Li_5Fe_5O_8$ on the surface [40]. When the formation of $Li_5Fe_5O_8$ is studied using a cyclic voltammogram, two sharp, overlapping anodic spikes

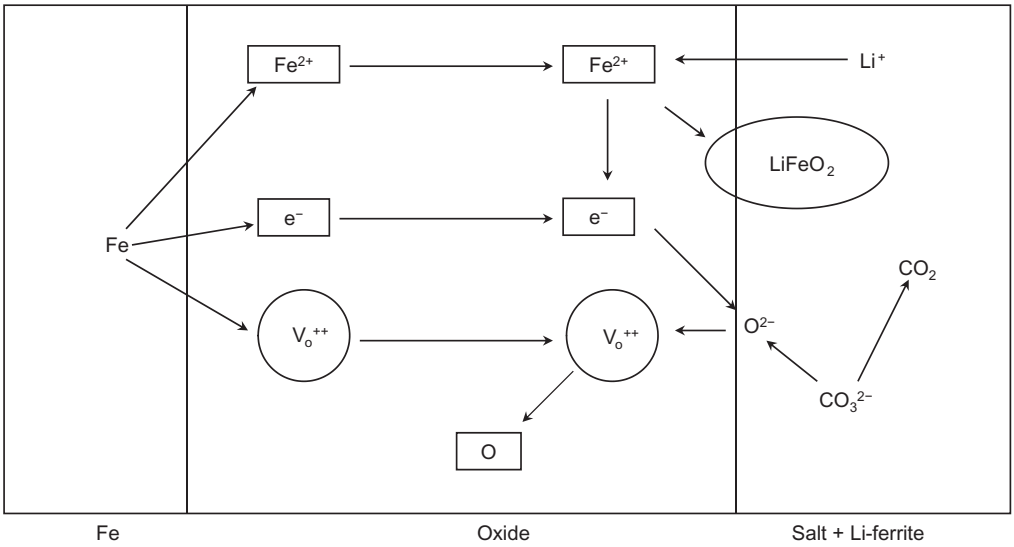

Fig. 11.21 Growth of an oxide layer on iron in molten carbonate environments [39].

are observed, consistent with the solid-state oxidation and liquid-state oxidation/lithiation mechanism. At higher anodic potentials, a $LiFeO_2$ layer is formed within the oxide layer. The $LiFeO_2$ provides a boost in protection because of its low solubility in eutectic mixtures.

Corrosion tests of AISI310 stainless steel in molten carbonate environments under the same conditions used by earlier investigators [39–41] detected the presence of $LiFeO_2$ and $LiCrO_2$. In this case, the $LiFeO_2$ had cracks in its surface and did not adequately protect the underlying metal. After a longer period of time, the oxide layer segregated into a spinel layer and a chromium-rich layer.

Keijzer *et al.* [42] studied AISI304 corrosion in a molten carbonate environment that simulates a molten carbonate fuel cell. The outer layer in the multilayered oxide was iron-rich and below that was a chromium-rich layer. The investigators believed the iron-rich layer protects the chromium layer below by mitigating catastrophic oxidation. The chromium-rich layer reduces the transport of metal ions and oxygen anions through the metal to the oxide layer. When the oxide layer is formed under load conditions in the fuel cell operation regime, it provided a greater degree of protection than when it was formed under open-circuit conditions. On the other hand, when the fuel cell was running under open circuit, FeO and $LiFeO_2$ comprised the outer layer of the oxide while $LiCrO_2$ made up the chromium-rich layer. In summary, dual layers have been seen to form in ferrous alloys with an outermost iron-rich layer followed by the chromium-rich layer next to the alloy. The chromium-rich layer acts as a strong diffusion barrier for metal

ions to the top of the oxide layer while the iron-rich layer above helps to protect the chromium layer from leaching via the formation of chromate.

Corrosion studies of austenitic alloys 316SS and 310SS and 800H in high-temperature supercritical carbon dioxide at 650 °C for 3000 h indicated 800H showed the best corrosion resistance followed by 310SS and 316SS. The oxide growth in 800H and 310SS followed the parabolic growth law [43].

11.8 METHODS OF PROTECTING AGAINST HOT CORROSION AND HIGH-TEMPERATURE CORROSION

In the presence of molten salts, hot corrosion is unavoidable. Alloy components only slowdown the corrosion process. The naturally forming oxide layers are not sufficient to completely protect against hot corrosion. Composites have been used to resist salt corrosive attack at high temperatures. These composites consist of a metal or alloy core with a coating specially designed to resist hot corrosion. The metal core provides strength and the coating provides protection.

The accepted method to coat metals is vacuum plasma spraying (VPS), but a new method called high velocity oxy-fuel (HVOF) thermal spraying has been developed and is more cost-effective and has thus made the use of composites much more practical.

Case Study 11.2—Protective Coatings

Different coatings applied through VPS and HVOF have been tested to protect Superfer 800H, a Fe-based superalloy with the following composition by weight percent: 32 Ni, 21 Cr, 0.3 Al, 0.3 Ti, 1.5 Mn, 1.0 Si, 0.1 C, balance Fe [44]. This superalloy is used in the compressor section of turbines where the material of construction must be strong as well as resistant to corrosion at extremely high temperatures and corrosive conditions. Four different coating powders were used in the investigation [44]. Three are commercially available: Ni-22Cr-10Al-1Y, Ni-20Cr, and Stellite-6. The fourth was an experimental nickel aluminide (Ni_3Al). A thermal plasma spray apparatus was used to coat the substrate. Before spaying, a NiCrAlY powder was deposited on the substrate to provide a stronger bonding. The specimens were each sprayed with a salt mix of 40% Na_2SO_4-60% V_2O_5 and run for fifty cycles of hot corrosion to test the effectiveness of these coatings against hot corrosion. Each cycle involved heating for 1 h at 900 °C and atmospheric pressure followed by 20 min. cooling at room temperature. The cyclic approach accelerated corrosion conditions. The results of these experiments are presented in Fig. 11.22 [44]. Four different coatings and a control superalloy without a protective coating were used in the experiment.

Figure 11.22 shows the impact made in protecting even the most advanced alloys from hot corrosive attack. The uncoated alloy clearly was subjected to massive attack, while the alloys that were coated with Ni-20Cr and NiAlCrY have the lowest corrosion rate. Adding a protective coating to a metal substrate considerably improves its resistance to hot corrosion under the most corrosive environments.

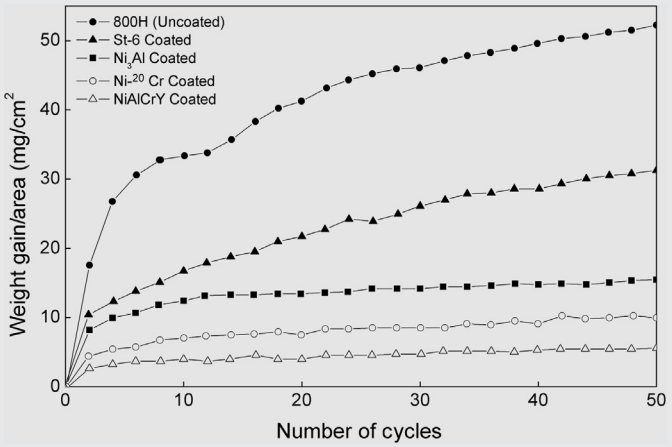

Fig. 11.22 Weight gain vs. number of hot corrosion cycles for Superfer 800H with various coatings [44].

Nanoceria (CeO_2 nanoparticles) coated 9Cr–1Mo ferritic steel in air and steam at high temperatures exhibited better oxidation resistance than the uncoated steel under similar conditions. The improved corrosion resistance was attributed to the oxide growth mechanism change in the presence of the nanoceria coating [45].

11.8.1 High velocity oxy-fuel (HVOF) basics

HVOF processes involve both thermal and kinetic energy transfer because of the melting and accelerating forces felt by the deposited particles [46]. Particles in powder form are injected into the hot gas stream resulting from the combustion of a hydrocarbon (propane, propylene, acetylene, etc.) or hydrogen. Varying the composition of fuel allows some control over the temperature of the hot gas stream. Using this process, denser and less porous coatings can be deposited. A coating applied through HVOF has a greater hardness, less porosity, lower oxide content, higher bond strength, and a higher maximum thickness than a coating applied with VPS [47,48]. Additionally, the cost of using HVOF is lower than VPS. Figure 11.23 demonstrates some of the benefits of HVOF over VPS [46].

There are several other advantages to HVOF over VPS. VPS must be run in a vacuum, but HVOF can be run at atmospheric conditions. This avoids costly and time-consuming evacuation and flooding cycles inherent to vacuum chambers. Also, a real-time control feature such as particle or substrate pyrometry is not available or very difficult to implement in vacuum situations but is easily adaptable to HVOF [3,49]. In terms of control, the particle velocity is more sensitive to changing parameters than particle temperature. It is important to control both, because using greater velocity

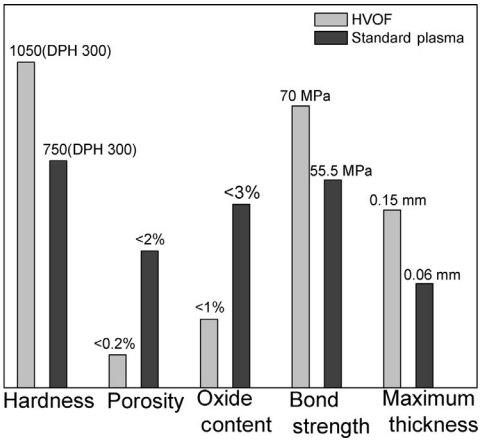

Fig. 11.23 Comparison of HVOF and VPS coatings [46].

and temperature results in coatings that are stronger, harder, and less porous. Gil and Statia [50] used a factorial design to identify the important variables in controlling the protection offered by the coating. They found that spraying distance, fuel/oxygen ratio, and powder feed rate have the most significant impact on the amount of protection against hot corrosion offered by a coating applied through HVOF.

11.8.2 Future work in HVOF

Kawakita *et al.* [51] suggested an improved design using inert gas that surrounds the high-velocity gas stream. This inert stream allows to use greater velocities (up to 750 m/s) and protects the particles in the hot gas stream from oxidation before they are deposited on the surface of the metal. A coating on a Ni-based alloy using this new method had zero porosity and about 0.2 mass% oxygen, a strong indicator of the oxidation protection imparted by the inert stream.

The effect of heat treatment and laser remelting [52,53] on this promising technology has been studied with the very common Ni-Cr-W-Mo-B coating and its response to heat treatment after deposition on the metal substrate. Heat treatment was found to offer greater protection against corrosion. The authors suspected that this increase in protection is the result of greater structural homogeneity at the microscopic scale. Similar results were reported by Uusitalo *et al.* [53] with Ni-50Cr, Ni-57Cr, Fe_3Al, Ni-21Cr-9Mo coatings and lasers to remelt the coatings after being deposited. Coatings that were not remelted proved ineffective at completely stopping corrosion on the metal substrate. After remelting with lasers, the coatings proved immune to the same corrosive attack. This improvement is attributed to removing microstructure voids as well as oxides at the boundaries of the HVOF coating [53]. HVOF is a promising technology. To date,

most of the research on this technology has been used in normal environments (air). Tests in environments that simulate extremely corrosive surroundings for alloy usage are still to be performed. Mathematical models also need to be derived to predict a coating's protection against corrosion in a variety of environments. However, the mechanisms of hot corrosion must be better understood before this can be accomplished [48].

11.8.3 Platinum and aluminide coatings

Electrochemically deposited coatings were used by Gurappa to protect titanium alloys from hot and high-temperature corrosion [34]. The high strength and low weight of Ti alloys make them ideal for turbine compressors. However, turbines are often subjected to hot corrosion conditions, and alternate coatings must be developed to decrease the corrosion damage of molten salts.

Using a titanium alloy composed of Ti, Al, Sn, Zr, Nb, Mo, Fe, O, and N, Gurappa found the alloy suffered extensive hot corrosion without any coating [34]. The composite coating structure underwent a diffusion treatment at 700 °C in the presence of argon to increase the bonding between the coating and the substrate. A platinum coating was deposited electrochemically with a thickness of 5 μm to decrease the corrosion rate of the alloy. On top of the platinum coating, aluminide was deposited at 700 °C in the presence of argon. The composite coating structure underwent a diffusion treatment at 700 °C in the presence of argon to increase the bonding between the coating and the substrate. They were tested in a high-temperature corrosive environment for 400 h at 800 °C to test the effectiveness of these coatings. Figure 11.24 shows the corrosion rate of various coatings on the titanium alloy. The lowest corrosion rates were obtained

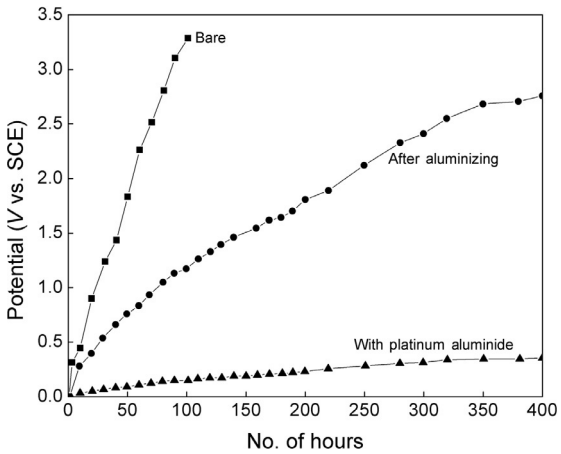

Fig. 11.24 Effect of coatings on a titanium alloy in a high-temperature corrosive environment [34].

with the platinum aluminide coating [34]. Fisher *et al.* [54] tested these coatings on nickel-based superalloys and found similar results. Srivastavaa *et al.* [55] studied the high-temperature oxidation and corrosion behavior of Ni/Ni-Co-Al composite coatings. The hot corrosion studies indicated that increasing Co content of the composite coating increases the resistance compared to Ni-rich coatings. For high-temperature corrosion resistance, the authors suggested a cobalt content of 30% in the composite coating.

The HVOF technique has also been successfully employed for coating ceramic materials to mitigate high-temperature corrosion. Recent research also focuses on the use of titania [56] and yttrium oxide-stabilized zirconium oxide composite coatings [57–59] to decrease the heat transfer to the hot parts in turbines. These coatings are applied by plasma spraying and have a high thermal expansion coefficient and low thermal conductivity. Their small grain size improves mechanical properties, increasing hardness and strength [57–59].

11.8.4 Silicon diffusion layers

High-temperature corrosion resistance in molten salts of Si diffusion layers on stainless steel was studied by Fukumoto *et al.* [60]. They used the pack-cementation method to alloy Si onto SUS430 and SUS304 stainless steels. The oxidation of the siliconized stainless steel was lower than that of nontreated stainless steel. The authors attributed this to the surface alloying of Si with stainless steel alloys, confirmed by electrochemical studies.

11.8.5 Chemical additions

HVOF and VPS coatings provide protection against high-temperature corrosion in most aggressive environments. However, they are not always applicable in boilers that use heavy fuel oils due to contamination with vanadium, sodium, sulfur, and other impurities. These impurities create exceedingly aggressive environments that can cause hot corrosion. Given the size of such boilers, coating all surfaces that might be exposed to such contaminants would be impractical. An alternative approach is to use additives in the fuel to reduce or even halt hot corrosion. These additives are divided into two categories: solid-oxides and organometallics [61,62]. Magnesium oxide slurries and oil-soluble organometallics are the most popular additives. The magnesium oxides react with the impurities over the ash at the solid-gas interface. The oil-soluble organometallics assure emission of metallic elements during the combustion. Barroso *et al.* [62] tested both magnesium-oxide slurries and an undisclosed organometallic liquid over a period of 4 years in a heavy-fuel boiler. Both the magnesium-oxide slurries and organometallics suitably reduced the rates of hot corrosion induced by impurities found in

heavy-oil fuels. However, both types of additives caused process difficulties. Better results were obtained using organometallic compounds. The investigators found an expected change in the resulting slag that includes raising the melting temperature and reducing the fouling of the heat transfer surfaces. Despite these successes, some low melting point compounds were detected through X-ray diffraction. The authors deduced that these low melting point compounds were the result of magnesium deficiency. The best results were obtained using a mixture of magnesium-oxide slurries and organometallic liquids.

11.8.6 Ion implantation

Ion implantation is less expensive than VPS or HVOF and can be used in environments that are slightly less corrosive. A concentration of 1016-1018 ions/cm^2 drastically improves corrosion resistance. Rare earth (RE) metals also improve the corrosion resistance. Rare earth metals such as Y improve oxide scale formation on alloys. This improvement is based upon the "reactive element effect" (REE), which improves resistance in several ways According to Hussey *et al.* [63], the observed increase in corrosion resistance is due to:

- Rare earth ions blocking other metals at grain boundaries
- RE ions adhering to the oxide scale at the boundary
- RE causing vacancy annihilation (further blocking metal ion diffusion)
- RE reducing oxide scale growth stresses (preventing scale cracking)
- RE enhancing the selective oxidation of Cr to form stronger Cr_2O_3 scales

Perez *et al.* [64] studied the effect of Si, Mo, and Ce implantation in AISI 304 stainless steel to test their corrosion resistance. At high temperatures, Si was found to behave similarly to a RE metal. Mo has beneficial properties in halide environments.

The ions were implanted using high electrical potentials (150 keV). After implantation, the alloys were placed in an oxidizing environment (air) at 1173 K and atmospheric pressure. The Si-implanted AISI 304 steel demonstrated greater oxidation resistance than the standard AISI 304 control. According to the author, this is because Si ions always segregated to the metal-scale interface where they help to form a homogeneous oxide layer. The Si oxidizes first at the surface of the metal. The resulting SiO_2 then serves as a nucleation site for the formation of Cr_2O_3.

Mo did not offer many benefits against high-temperature corrosion. Like Si, Mo oxidized preferentially at the beginning. Unfortunately, the resulting Mo oxides, MoO_2 and MoO_3, are volatile at temperatures above 600 °C. Figures 11.25 and 11.26 show SEM images of the Mo implantation in the alloy [64]. Figure 11.25 shows the top surface of the oxide layer. Note the pores are distributed throughout the surface. This image was taken after 48 h at 1173 K. Figure 11.26 shows a cross section of a metal and its oxide layer.

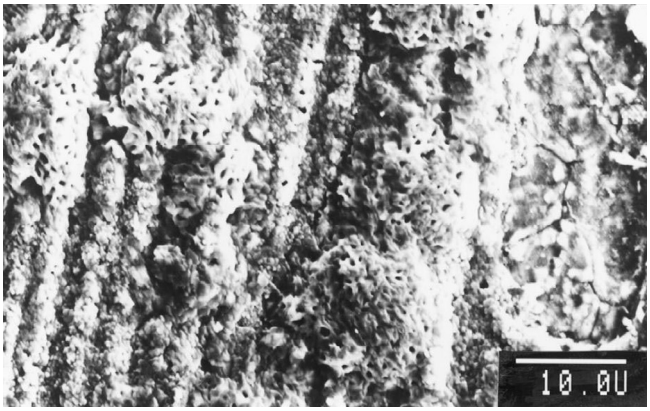

Fig. 11.25 Oxide surface with Mo-implantation after 48 h of exposure to air at atmospheric pressure and 1173 K [64].

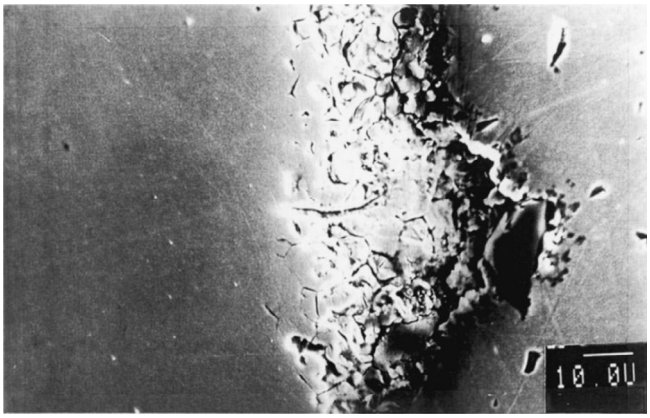

Fig. 11.26 Cross section of Mo-implanted alloy and oxide layer after 48 h of exposure in air at 1173 K [64].

Note the "blister" formation that indicates greater oxidation of the metal along the path formed by volatile Mo oxides [64].

The Ce-implanted alloys demonstrated greater oxidation resistance after several hours of oxidation. The direct oxidation of the alloy that took place in the first 8-9 h at high-temperature corrosion conditions is attributed to Cr_2O_3 layer cracking. With time, the Ce particles begin to act as nucleation sites for the formation of a stronger and more homogeneous protective oxide layer composed mostly of Cr_2O_3. Implantation of certain ions, such as Si and Ce, contributes to greater protection as a result of stronger

and more homogeneous Cr oxides that form on the nucleation sites provided by the implanted ions [64].

11.8.7 Preformation of oxide layers

Preformation of an oxide layer under carefully controlled conditions that is superior to the oxide formed under standard high-temperature conditions is another method used to fight high-temperature corrosion. This method is used to protect zirconium alloys used in nuclear reactors. The zirconium alloys act as sheaths for nuclear fuel exposed to extreme temperatures. If no pretreatment is used, the zirconium alloy rate transitions from cubic to linear [65]. As described in Section 11.6.3, a linear rate is the least desirable rate of oxide formation because it does not decrease with time. This high rate creates very thick oxides that eventually peel, exposing the metal substrate to direct oxidation. Hong *et al.* [65] tested a preformed oxide layer to determine if it would resist the rate transformation that is observed in natural forming oxide layers in the nuclear reactor environment. To test their theory, a zirconium alloy (Zircaloy-4) was annealed at 700 and 1100 °C; a gas stream of oxygen and argon flowed over the alloy to avoid hydrogen embrittlement. Oxide layers with various thicknesses (0.5–13 μm) were formed on the surface. To simulate the conditions of a nuclear reactor, an autoclave was used and operated at 360 °C and 180 bar. Specimens were placed in the autoclave for 168 days before removal and examination. The results indicated that all control specimens without preformed oxide layers oxidized much faster in the autoclave than those with protection. Specimens without the preformed oxide layer had a rate transition after ~98 days in the autoclave, while those with the preformed layer never underwent a rate transition.

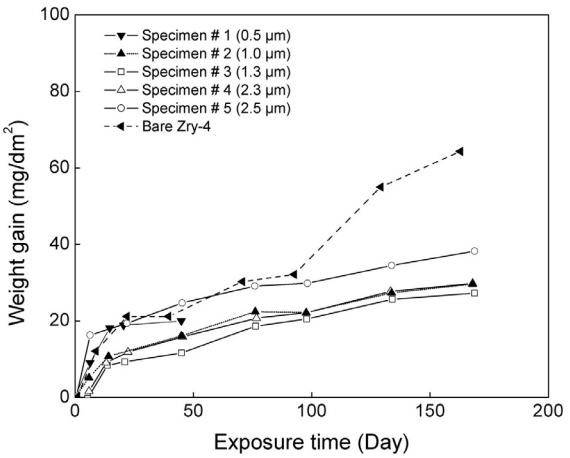

Fig. 11.27 Oxide growth on zirconium alloys under simulated nuclear reactor conditions of zirconium alloys [65].

However, not all preformed layers were equal in performance. The optimum thickness of the preformed layers was between 1 and 2.3 μm. Figure 11.27 shows the progress of oxide formation in the autoclave of preformed oxide layers of various thicknesses in addition to a control specimen that lacks a preformed layer [65].

EXERCISES

E11.1. Experimentally determined weight gain data for oxidation of cobalt at 1200 °C are given in Table E11.1. Using the data:
(a) Plot graphs for parabolic, cubic, and quartic kinetics. Determine which rate equation best fits the data.
(b) Find the rate constant (k_{1200}) from the plot constructed in (a).

E11.2. Using the rate constant for cobalt oxidation at 1200 °C obtained in exercise E11.1, calculate the rate constants at 900, 950, and 1150 °C using the Arrhenius equation. Assume that activation energy is 35 kcal/mol.

E11.3. Calculate the weight gain (mg/cm^2) expected after 5 h at 900, 950, 1150, and 1200 °C by using information from exercises E11.1 and E11.2. Plot temperature vs. weight gain for 900, 950, 1150, and 1200 °C. Discuss the effects of temperature on the oxidation of cobalt.

E11.4. The rate constants for cobalt with different temperatures are given in Table E11.2. Calculate the activation energy, E_a, in kcal/mol, and the constant, k_o, in mg^2/cm^4 h in the Arrhenius equation.

E11.5. Oxidation of nickel at high temperatures follows the parabolic kinetics law. Using the oxidation constants given in Table E11.3, calculate the weight gain

Table E11.1 Weight Gain Data for Oxidation of Cobalt at 1200 °C

Time (hour)	0	0.5	1.0	1.4	2.0	2.4	2.9	3.5	3.9	4.5	5.0
Weight gain (mg/cm^2)	0	11.1	15.6	19.2	22.4	25.2	27.7	30.3	32.2	34.1	36.4

Table E11.2 Rate Constants for Cobalt as a Function of Temperature

Temp (°C)	900	950	1050	1100	1150	1200	1350
k_p (mg^2/cm^4 h)	12.45	23.00	68.36	111.00	174.30	265.40	801.91

Table E11.3 Parabolic Oxidation Constant k_p (g^2/cm^4 h) at 900 °C for Different Weight % Cr^{3+}

Cr^{3+} Content (Wt. %)	Parabolic Oxidation Constant k_p at 900 °C (g^2/cm^4 h)
0	3.8×10^{-10}
0.3	15×10^{-10}
1	28×10^{-10}
3	36×10^{-10}
10	5×10^{-10}

Table E11.4 Oxygen Uptake ($\mu g/cm^2$) as a Function of Time for Nickel at 200 and 340 °C

200 °C	Time (min)	0.121	0.249	0.5	1.005	2.017	3.024	4.087	5.027	6.07	7.058	8.047	9.007	10
	Oxygen uptake ($\mu g/cm^2$)	0.186	0.196	0.205	0.216	0.224	0.231	0.234	0.237	0.24	0.242	0.244	0.245	0.247
340 °C	Time (min)	0.121	0.245	0.502	1.01	2.049	3.075	4.079	5.166	6.126	7.125	8.051	9.192	10.1
	Oxygen uptake ($\mu g/cm^2$)	0.158	0.175	0.188	0.203	0.219	0.228	0.238	0.244	0.25	0.257	0.262	0.266	0.271

(g/cm^2) expected after 20 h for each of the alloys and plot the results as weight gain vs. weight % of Cr^{3+} in the alloy.

E11.6. Using the information in exercise E11.5, calculate the expected weight gain (g/cm^2) after 20 h at 1200 °C for 3% Cr^{3+} in the alloy, assuming an activation energy of 47.6 kcal/mol.

E11.7. The oxidation of nickel at 200 and 340 °C was studied by Graham and Cohen [26]. The following approximate data were obtained for oxygen uptake as a function of time and presented in Table E11.4:

(a) Determine if the experimental data at 200 °C follow the logarithmic law.
(b) Determine if the experimental data at 340 °C follow the logarithmic law.
(c) If experimental data at 340 °C does not follow the logarithmic law at a whole range of data, determine the amount of oxygen uptake ($\mu g/cm^2$) at the point in the kinetic curve where the kinetics of nickel oxidation changes.

REFERENCES

[1] P. Kofstad, High Temperature Corrosion, second ed., Elsevier, New York, 1988.
[2] N. Briks, G.H. Meier, Introduction to High Temperature Oxidation of Metals, Arnold, London, 1983.
[3] G.Y. Lai, High Temperature Corrosion and Materials Applications, second ed., ASM International, Materials Park, Ohio, 2008.
[4] H.E. McGannon, Steels for elevated-temperature service, in: The Making, Shaping and Treating of Steel, United States Steel Corp, USA, 1964, pp. 1131–1140.
[5] D.R. Gaskel, Introduction to Metallurgical Thermodynamics, second ed., McGraw-Hill, New York, 1983.
[6] R.A. Rapp, High Temperature Corrosion, The American Chemical Society, Washington DC, 1980.
[7] R.C. West, Physical constants of inorganic compounds, in: Handbook of Chemistry and Physics, 65th ed., The Chemical Rubber Company, USA, 1984, pp. B68–B161.
[8] C.E. Ramberg, P. Beatrice, K. Kurokawa, W.L. Worrell, High temperature oxidation behavior of structural silicides, in: in: C.L. Briant, J.J. Petrovic, B.P. Bewlay, A.K. Vasudevan, H.H. Lipsitt (Eds.), High Temperature Silicides and Refractory Alloys, vol. 332, Martials Research Society, Pittsburgh, 1994, pp. 243–254.
[9] H. Asteman, J.E. Svenson, L.G. Johnson, M. Norell, Indication of chromium oxide hydroxide evaporation during oxidation of 304 L at 873 K in the presence of 10% water vapor, Oxid. Met. 52 (1999) 95–111.
[10] D. Caplan, M. Cohen, The volatilization of chromium oxide, J. Electrochem. Soc. 108 (1961) 438–442.
[11] N.B. Pilling, R.E. Bedworth, Oxidation of metals at high temperatures, J. Inst. Met. 29 (1923) 529–539.
[12] B. Chalmers, Physical Metallurgy, John Wiley & Sons, New York, 1959.
[13] M.G. Fontana, Corrosion Engineering, third ed., McGraw-Hill, New York, 1986.
[14] P.R. Roberge, Handbook of Corrosion Engineering, McGraw-Hill, New York, 2000.
[15] C. Gensch, K. Hauffe, Oxidation velocity of zinc alloys, Z. Phys. Chem. 196 (1951) 427–437.
[16] C. Wagner, K.E. Zimens, Die oxydationsgeschwindigkeit von nickel bei kleinen zusätzen von chrom und mangan: Beitrag zur theorie des anlaufvorganges, Acta Chem. Scand. 1 (1947) 547–565.
[17] M.J. Pomeroy, Coatings for gas turbine materials and long term stability issues, Mater. Des. 26 (2005) 223–231.
[18] H.E. Eiselstein, E.N. Skinner, The effect of composition on the scaling of iron-chromium-nickel alloys subjected to cyclic temperature conditions, in: STP 165, ASTM International, Philadelphia, PA, 1954, pp. 162–172.

[19] I.G. Write, High temperature corrosion, ninth ed., in: Metals Handbook, vol. XIII, ASM International, Metal Park, OH, 1987, pp. 97–103.
[20] A. Grodner, Stainless steel for pressure vessels, Weld. Res. Council Bull. 31 (1956) 20–30.
[21] R.H. Kane, Alloy selection for high temperature corrosives, in: B.J. Moniz, W.I. Pollock (Eds.), Process Industries Corrosion, NACE, Houston, 1986, pp. 45–65.
[22] A.T. Fromhold Jr., in: Theory of Metal Oxidation: Fundamentals, vol. I, North Holland, Amsterdam, 1976.
[23] O. Kubaschewski, B.E. Hopkins, Oxidation of Metals and Alloys, Butterworths, London, 1962.
[24] W.R. Peterson, Designing for automotive corrosion prevention, in: Proceedings of the Society of Automotive Engineers, Troy, MI, 1978, pp. 78–88.
[25] C. Wagner, Theory of tarnishing process, Z. Phys. Chem. B21 (1933) 25–41.
[26] M.J. Graham, M. Cohen, On the mechanism of low-temperature oxidation (23°-450 °C) of polycrystalline nickel, J. Electrochem. Soc. 119 (1972) 879–882.
[27] Y. Shinata, F. Takahashi, K. Hashiura, NaCl-induced hot corrosion of stainless steels, Mat. Sci. Eng. 87 (1987) 399–405.
[28] C.C. Tsaur, J.C. Rock, C.J. Wang, Y.H. Su, The hot corrosion of stainless steel with pre-coated $NaCl/Na_2SO_4$ mixtures at 750 °C, Mater. Chem. Phys. 89 (2005) 445–453.
[29] J. Stringer, The role of underlying research in corrosion control in coal conversion systems, in: D. B. Meadowcroft, M.I. Manning (Eds.), Corrosion Resistance Materials in Coal Conversion Systems, Elsevier Science Ltd, New York, 1983, pp. 407–421.
[30] H.A. Abd-El Rahman, A. Baraka, S.A. Abd-El Gwad, Effect of oxide ion donors on the corrosion and dechromization of stainless steels in KCl-NaCl-$BaCl_2$ melt, J. Appl. Electrochem. 29 (1999) 1205–1210.
[31] Y. Li, Y. Niu, W. Wu, Accelerated corrosion of pure Fe, Ni, Cr and several Fe-based alloys induced by $ZnCl_2$-KCl at 450 °C in oxidizing environment, Mater. Sci. Eng. A A345 (2003) 64–71.
[32] Tz. Tzvetkoff, J. Kolchakov, Mechanism of growth, composition, and structure of oxide films formed on ferrous alloys in molten salt electrolytes-a review, Mater. Chem. Phys. 87 (2004) 201–211.
[33] C.J. Wang, T.T. He, Morphological development of subscale formation in Fe-Cr-(Ni) alloys with chloride and sulfates coating, Oxid. Met. 58 (2002) 415–437.
[34] I. Gurappa, Protection of titanium alloy components against high temperature corrosion, Mat. Sci. Eng. A 356 (2003) 372–380.
[35] A. Baraka, A. Abdel Rahman, A. El-Hosary, Corrosion of mild steel in molten sodium nitrate-potassium nitrate eutectic, Br. Corros. J. 11 (1976) 44–46.
[36] W. Schendler, W. Schwenk, Electrochemical studies of the corrosion of heat-resistant iron and nickel-base alloys in eutectic alkali sulfate melt at 700 °C, Werkst. Korros. 32 (1981) 428–434.
[37] M. Spiegel, Influence of gas phase composition on the hot corrosion of steels and nickel-based alloys beneath a (Ca-Na-K) sulfate mixture containing $PbSO_4$ and $ZnSO_4$, Mater. Corros. 51 (2000) 303–312.
[38] P. Yu, W. Wang, F. Wang, S. Zhu, High-temperature corrosion behavior of sputtered K38 nanocrystalline coatings with and without yttrium addition in molten sulfate at 900 °C, Surf. Coat. Tech. 206 (2011) 68–74.
[39] M.S. Yazici, J.R. Selman, Oxidation-lithiation of nickel, iron and cobalt in contact with molten carbonate, Solid State Ion. 124 (1999) 149–160.
[40] P. Biedenkopf, M. Spiegel, H.J. Grabke, The corrosion behavior of iron and chromium in molten $(Li_{0.62}\ K_{0.38})_2CO_3$, Electrochim. Acta 44 (1998) 683–692.
[41] F.J. Perez, M.P. Hierro, D. Duday, C. Gomez, M. Romero, L. Daza, Hot-corrosion studies of separator plates of AISI-310 stainless steels in molten carbonate fuel cells, Oxid. Met. 53 (2000) 375–398.
[42] M. Keijzer, G. Lindbergh, K. Hemmes, P.J.J.M. Van der Put, J. Schoonman, J.H.W. De Wit, Corrosion of 304 stainless steel in molten carbonate fuel cells, J. Electrochem. Soc. 146 (1999) 2508–2516.
[43] G. Cao, V. Firouzdor, K. Sridharan, M. Anderson, T.R. Allen, Corrosion of austenitic alloys in high temperature supercritical carbon dioxide, Corros. Sci. 60 (2012) 246–255.

[44] H. Singh, D. Puri, S. Prakash, Some studies on hot corrosion performance of plasma sprayed coatings on a Fe-based superalloy, Surf. Coat. Tech. 192 (2005) 27–38.
[45] T. Sundararajan, S. Kuroda, J. Kawakita, S. Seal, High temperature corrosion of nanoceria coated 9Cr-1Mo ferritic steel in air and steam, Surf. Coat. Tech. 201 (2006) 2124–2130.
[46] J.C. Tan, L. Looney, M.S.J. Hashmi, Component repair using HVOF thermal spraying, J. Mater. Process Technol. 92–93 (1999) 203–208.
[47] M.M. Helali, M.S.J. Hashmi, in: Proc. 10th Conference of the Irish Manufacturing Committee (IMC 10), Galway, Ireland, 1992, pp. 377–387.
[48] T.S. Sidhu, R.D. Agrawal, S. Prakash, Hot corrosion of some superalloys and role of high-velocity oxy-fuel spray coatings-a review, Surf. Coat. Tech. 198 (2005) 441–446.
[49] P.J. Meyer, Economics of MCrAlY coatings, in: Thermal Spraying: Current Status and Future Trends, Proceedings of the 10th International Thermal Spray Conference, Kobe, Japan, 2004, 2004, pp. 217–222.
[50] L. Gil, M.H. Statia, Influence of HVOF parameters on the corrosion resistance of NiWCrBSi coatings, Thin Solid Films 420–421 (2002) 446–454.
[51] J. Kawakita, S. Kuroda, T. Fukushima, T. Kodama, in: C. Moreau, B. Marble (Eds.), Thermal Spray 2003: Advancing the Science and Applying the Technology, ASM International, Materials Park, OH, USA, 2003.
[52] C.H. Lee, K.O. Min, Effects of heat treatment on the microstructure and properties of HVOF-sprayed Ni-Cr-W-Mo-B alloy coatings, Surf. Coat. Tech. 132 (2000) 49–57.
[53] M.A. Uusitalo, P.M.J. Uuoristo, T.A. Mantula, High temperature corrosion of coatings and boiler steels in reducing chlorine-containing atmosphere, Surf. Coat. Tech. 161 (2002) 275–285.
[54] G. Fisher, W.Y. Chan, P.K. Datta, J.S. Burnell-Gray, Noble metal aluminide coatings for gas turbines, Platinum Met. Rev. 43 (1999) 59–61.
[55] M. Srivastavaa, J.N. Balarajua, B. Ravisankarb, C. Anandana, V.K. William Grips, High temperature oxidation and corrosion behavior of Ni/Ni-Co-Al composite coatings, Appl. Surf. Sci. 263 (2012) 597–607.
[56] R.S. Lima, B.R. Marple, High weibull modulus HVOF titania coatings, J. Therm. Spray Technol. 12 (2003) 240–249.
[57] M. Saremi, Z. Valefi, N. Abaeian, Hot corrosion, high temperature oxidation and thermal shock behavior of nano-agglomerated YSZ-alumina composite coatings, Surf. Coat. Tech. 221 (2013) 133–141.
[58] S. Ran, J. Vleugels, S. Huang, K. Vanmeensel, D.H.A. Blank, L. Winnubst, Manipulating microstructure and mechanical properties of CuO doped 3Y-TZP nano-ceramics using spark-plasma sintering, J. Eur. Ceram. Soc. 30 (2010) 889–904.
[59] A. Afrasiabi, A. Kobayashi, Hot corrosion control in plasma sprayed YSZ coating by alumina layer with evaluation of microstructure and nanoindentation data, Vacuum 88 (2013) 103–110.
[60] M. Fukumoto, C. Tachikawame, Y. Matsuzaka, M. Hara, Formation of Si diffusion layer on stainless steels and their high temperature corrosion resistance in molten salt, Corros. Sci. 56 (2012) 105–113.
[61] N.D. Tomashov, Theory of Corrosion and Prote ction of Metals: The science of Corrosion, McMillan, New York, 1966.
[62] J. Barroso, F. Barreras, J. Ballester, Behavior of a high-capacity steam boiler using heavy fuel oil: Part I. High-temperature corrosion, Fuel Process. Technol. 86 (2004) 89–105.
[63] R.J. Hussey, M.J. Graham, The influence of reactive-element coatings on the high-temperature oxidation of pure-Cr and high-Cr-content alloys, Oxid. Met. 45 (1996) 349–374.
[64] F.J. Perez, E. Otero, M.P. Hierro, C. Gomez, F. de Pedraza, J.L. Segovia, E. Roman, High temperature corrosion protection of austenitic AISI 304 stainless steel by Si, Mo and Ce ion implantation, Surf. Coat. Tech. 108–109 (1998) 127–131.
[65] H.S. Hong, Y. Yun, K.S. Lee, Corrosion characteristics of zirconium alloy with a high temperature pre-formed oxide film, J. Alloys Compd. 388 (2005) 279–283.

CHAPTER 12

Corrosion of Structural Concrete

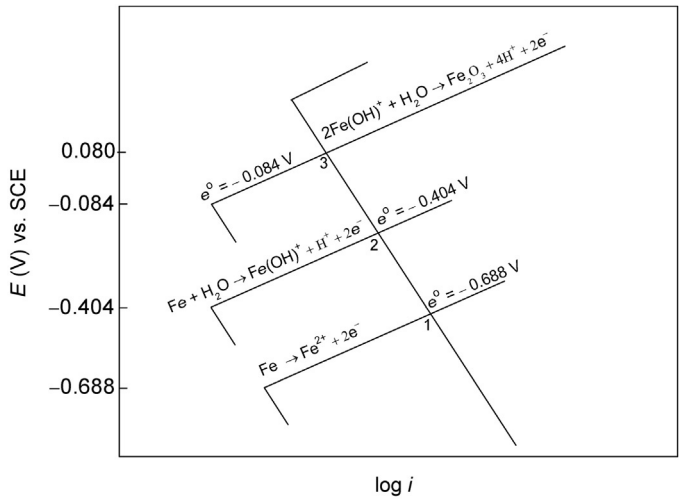

Chapter Contents

Corrosion Engineering
http://dx.doi.org/10.1016/B978-0-444-62722-3.00012-4

12.1 INTRODUCTION

Extensive concrete use began with the Roman Empire and continues to be a primary building material in modern times [1–4]. Concrete is composed of an aggregate and a binder. Depending on the desired concrete properties, aggregate size ranges from coarse gravel to fine sand. They can be natural (limestone, gravel, granite) or recycled (demolition or excavation). Portland cement, named for its similarity in color to Portland limestone, is most commonly used as a binder (cement). Cement is a mixture of silicon, calcium, and aluminum oxides. When combined with water, cement forms a paste that fills the void between the aggregate. Hydration causes the cement to harden or cure over time:

$$2Ca_3SiO_5 + 7H_2O \rightarrow 3(CaO)2(SiO_2)4(H_2O) + 3Ca(OH)_2 \tag{12.1}$$

Because concrete is heterogeneous in nature, it is mixed thoroughly before pouring into molds or casts to form structures and shapes to prevent strength gradients. Property enhancing additives or replacements such as calcium or sodium nitrite accelerates the hardening of concrete, while citric acid, sodium gluconate, glucose, and sucrose are used to retard curing. Corrosion inhibitors are added to prevent steel reinforcement rebar degradation. Because concrete has naturally high compressive strength but low tensile strength, steel reinforcement bars are used to obtain the required tensile strength [5–7]. Reinforcing steel rebars are passive because of the high-alkaline concrete environment [1]. Low permeable concrete acts as a barrier to water, chlorides, and carbon dioxide permeation. A thin passive oxide film is formed on the rebar, which is maintained only at high pH values (pH of 14). The initial passive film on the rebar surface is a tightly adherent coating of gamma-hydrated ferric oxide $Fe_2O_3.2H_2O$ (γ-FeOOH):

$$4Fe(OH)_2 + O_2 \rightarrow Fe_2O_3{\cdot}H_2O + 2H_2O \tag{12.2}$$

The passive iron oxide layer is destroyed when pH is reduced to about 11.0 or below, causing the porous oxide layer (rust) to form during corrosion.

12.2 CORROSION MECHANISM OF REINFORCEMENT IN CONCRETE

Electrochemical corrosion of steel rebar occurs in the local pore solution with the presence of oxygen.

$$\text{Anode}: Fe \rightarrow Fe^{2+} + 2e^- \tag{12.3}$$

$$\text{Cathode}: O_2 + 2H_2O + 4e^- \rightarrow 4OH^- \tag{12.4}$$

$$\text{Overall reaction}: 4Fe + 3O_2 + 2H_2O \rightarrow 2Fe_2O_3{\cdot}2H_2O \tag{12.5}$$

The overall reaction mechanism is summarized in Fig. 12.1. When reinforcing steel is immersed in the model solution, the cathodic reaction is oxygen reduction. Iron reacts through either of these two predominant reactions:

$$\mathrm{Fe} \rightarrow \mathrm{Fe}^{2+} + 2\mathrm{e}^{-} \quad e^{o} = -0.688\,\mathrm{V\,vs.SCE} \tag{12.6}$$

$$\mathrm{Fe} + \mathrm{H_2O} \rightarrow \mathrm{Fe(OH)}^{+} + \mathrm{H}^{+} + 2\mathrm{e}^{-} \quad e^{o} = -0.404\,\mathrm{V\,vs.SCE} \tag{12.7}$$

The reaction pathway for Eq. (12.7) is given as:

$$\mathrm{Fe} + \mathrm{OH}^{-} \rightarrow [\mathrm{Fe(OH)}]_{\mathrm{ads}} + \mathrm{e}^{-} \tag{12.8}$$

$$[\mathrm{Fe(OH)}]_{\mathrm{ads}} \rightarrow \mathrm{Fe(OH)}^{+} + \mathrm{e}^{-} \tag{12.9}$$

Iron hydroxide ion formation, $\mathrm{Fe(OH)}^{+}$, depends on solution pH, that is, the availability of OH^{-} ions. As bivalent Fe^{2+} ions are formed through Eq. (12.6), OH^{-} ions are transported from the bulk to the surface to maintain electroneutrality. Hydroxide ions are also produced via the cathodic oxygen reduction reaction, causing an increase in surface pH. At high pH, the formation of adsorbed $[\mathrm{Fe(OH)}]_{\mathrm{ads}}$ on the iron surface becomes more favorable than bivalent Fe^{2+} ions, Eq. (12.6). The electrode potential tends to shift into a more anodic direction to accommodate the formation of $\mathrm{Fe(OH)}^{+}$. As time increases, the $\mathrm{Fe(OH)}^{+}$ concentration at the surface increases. In the next step, $\mathrm{Fe(OH)}^{+}$ oxidizes to ferric oxide at $e^{o} = -0.084\,\mathrm{V\,vs.\,SCE}$, resulting in a barrier oxide layer:

$$2\mathrm{Fe(OH)}^{+} + \mathrm{H_2O} \rightarrow \mathrm{Fe_2O_3} + 4\mathrm{H}^{+} + 2\mathrm{e}^{-} \quad e^{o} = -0.084\,\mathrm{V\,vs.SCE} \tag{12.10}$$

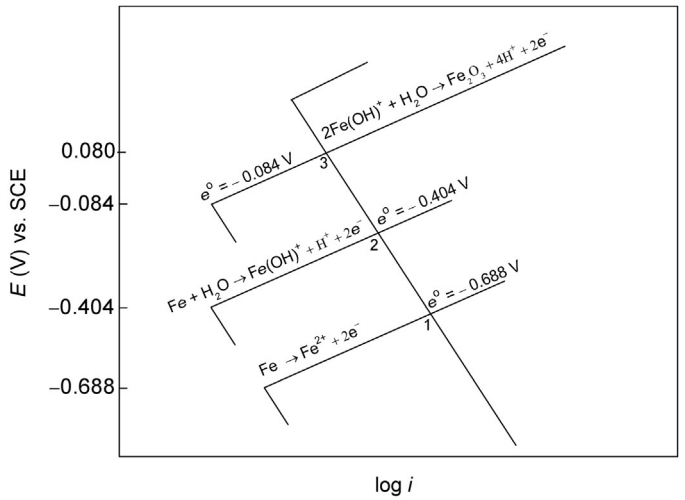

Fig. 12.1 Anodic reaction occurring during passive film formation on iron.

When steel is oxidized, the following chromium anodic reaction occurs on the surface:

$$Cr \rightarrow Cr^{2+} + 2e^{-} \quad e^{o} = -1.305\,V\ vs.SCE \tag{12.11}$$

Once the bivalent chromium ion is formed, it can be further oxidized to chromic hydroxide [$Cr(OH)_3$] or chromium trioxide:

$$Cr^{2+} + 3H_2O \rightarrow Cr(OH)_3 + 3H^{+} + e^{-} \quad e^{o} = -0.376\,V\ vs.SCE \tag{12.12}$$

Thus, steel contains a mixture of iron and chromium oxides. The predominant oxidation state for both chromium and iron ions are trivalent. Reaction (12.12) is thermodynamically favored only when pH increases. Because chromium is oxidized to bivalent chromium, OH^{-} ions migrate to the surface, increasing interface pH. The pH increase promotes chromic hydroxide formation enhancing stability of the surface by forming a protective barrier layer. Corrosion potential is a clear indication of protective layer quality. In steel corrosion, a less negative corrosion potential is related to a lower corrosion rate.

12.2.1 Chloride-induced corrosion mechanism

In the presence of chlorides, Eq. (12.6) produces an excess of positive charges near the rebar surface. Chloride ions and negatively charged hydroxide ions diffuse to the interface to maintain electroneutrality. Due to higher mobility, chloride concentration increases near the surface, saturating the interface with cations (Fe^{2+}) and (Cl^{-}). Because Cl^{-} ions replace OH^{-} ions, the formation of metal monohydroxide at the metal interface through Eq. (12.7) is reduced causing the iron-chloride complex preferentially to adsorb onto the surface. These complexes dissolve in the test solution, leading to a potential shift to a more cathodic direction. For stainless steel, OH^{-} ions with Cl^{-} ions move toward the substrate surface. Adsorbed chloride forms (CrO_2^{-}) on the surface affecting immunity and passivation.

Nitrite, an inhibitor, undergoes a chemical reaction with ferrous ion:

$$2Fe^{2+} + 2OH^{-} + 2NO_2^{-} \rightarrow 2NO + Fe_2O_3 + H_2O \tag{12.13}$$

Ferrous ion, a product of the corrosion reaction in Eq. (12.6), reacts with nitrate immediately to form a barrier oxide film through Eq. (12.13). The resulting potential would then be the potential of Fe_2O_3 in water. The anodic potential shift is due to protective film surface coverage. The observed performance improvement of chromium-containing alloys suggests that the inhibitor helps stabilize both the iron and chromium oxide layer. Nitrite ions act as anodic inhibitors by increasing barrier oxide film formation rate.

For stainless steel, a similar process can be assumed. When chromium is oxidized to Cr^{2+}, negative ions move toward the surface resulting in further oxidation of Cr.

12.2.2 Surface depassivation with carbon dioxide

Rebar corrosion in concrete is considered to occur in two phases [8]. The first phase begins with construction of the structure and ends with corrosion initiation when depassivating species reach the reinforcement. The second phase is the active corrosion that destroys the structure. Controlling rebar corrosion in this phase is very difficult. Passive film corrosion is initiated when local pore solution at the concrete-rebar interface drops below the passivation pH due to the presence of atmospheric carbon dioxide (carbonation) or chloride penetration. The following mechanism controls the carbonation process:

$$CO_2 + H_2O \rightarrow H_2CO_3 \tag{12.14}$$

Carbonic acid formation decreases local pore solution pH from 14 to ~8. This fall initiates passive hydrated ferric oxide film destruction and hydrated calcium carbonate formation:

$$H_2CO_3 = H^+ + HCO_3^- \tag{12.15}$$

$$H_2CO_3 + Ca(OH)_2 = CaCO_3 \cdot 2H_2O \tag{12.16}$$

Once $Ca(OH)_2$ is neutralized with carbonic acid, pH falls to 8. At this pH, rebar corrosion is activated with porous rust formation that causes internal expansion, damaging and eventually causing spalling.

12.3 ELECTROCHEMICAL TECHNIQUES FOR CORROSION EVALUATION OF REINFORCEMENT IN CONCRETE

Carbon steel reinforcement corrosion rates are determined using in situ electrochemical corrosion techniques. These techniques have advantages and disadvantages, and are complementary to some extent. Electrochemical impedance spectroscopy (EIS) is an AC method particularly suited for coated metal corrosion rates.

12.3.1 Corrosion potential measurements

Potential measurement techniques are used to locate reinforcing steel corrosion in concrete structures. Data are usually plotted as potential vs. time to observe corrosion onset, propagation, or passivation. Methods and interpretation are described in ASTM C876-09 (test methods for half-cell potentials of reinforcing steel in concrete) [9]. Concrete samples are often made with three different cover sizes of 5.08, 7.62, and 10.16 cm diameter and carbon steel sizes of 0.953, 1.27, and 1.90 cm, respectively. After preparation and curing, concrete samples are immersed in pH 12.5 $Ca(OH)_2$ solution. Figure 12.2a shows details of concrete cylinders. The immersed concrete cylinders are shown in Fig. 12.2b, while a front view of the cylinder is shown in Fig. 12.2c. Testing is performed in a conventional three-electrode cell with contact between the working electrode and the reference electrode via a Luggin probe. SCE, $Cu/CuSO_4$, or Hg/HgO can be used as reference

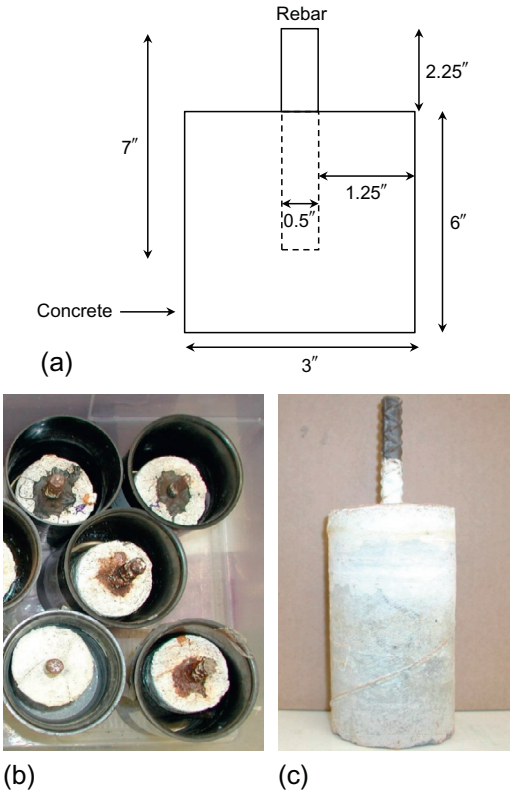

Fig. 12.2 Details of concrete cylinder tested: (a) schematic of concrete cylinder, (b) concrete cylinder with 1.27 cm diameter rebar in middle in a testing solution, and (c) front view of the cylinder.

electrodes. Platinum gauze or carbons with high surface area serve as auxiliary electrodes. The working electrode is a concrete cylinder containing a centrally placed steel rod. The top bar is set 2.25 cm from the top of the surface. The bottom bars are set 3.5 cm from the cylinder bottom to ensure uniform electrolyte diffusion during storage. The top rebar portion is exposed to the atmosphere as shown in Fig. 12.2c.

12.3.2 Linear polarization measurements

Linear polarization measurements are performed by scanning a range close to the corrosion potential. These experiments provide nondestructive information about the corrosion process occurring on reinforcing steel. The polarization resistance (R_p) of a corroding system under activation control is defined as:

$$R_p = \left(\frac{dE}{dI}\right)_{E=E_{corr}} \tag{12.17}$$

Once R_p is known, the corrosion rate can be evaluated using the Stern-Geary equation. Polarization resistance and corrosion current are determined from the current measured close to the corrosion potential. Polarization resistance can be determined with minimum system perturbation with linear polarization resistance or by using EIS. Experimentally determined potential ranges that indicate expected iron corrosion intensity for different-measured corrosion potentials are shown in Fig. 12.3.

12.3.3 Tafel polarization

When current is applied to an electrode under activation control, the potential is shifted from its initial Tafel equation value. The potential shift is termed "polarization," often referred to as $E - \log i$ testing. Because this is a destructive test, Tafel studies are performed on carbon steel rebar immersed directly in the test solution, not by using concrete samples.

12.3.4 Electrochemical impedance spectroscopy

Using EIS, the polarization resistance, R_p, and non-faradaic resistance, R_s, are determined separately. EIS consists of a small amplitude sinusoidal voltage application (5-10 mV) to the working electrode at a wide range of frequencies. The output at every frequency is another sinusoidal signal with amplitude (ΔI) and phase shift relative to the input signal. EIS data is often presented as a Nyquist plot where the imaginary component (Z'') is plotted vs. the real component (Z') for each excitation frequency. Bode-magnitude and Bode-phase plots permit absolute impedance examination. They clearly show the characteristic features of AC impedance data, especially when more than one constant

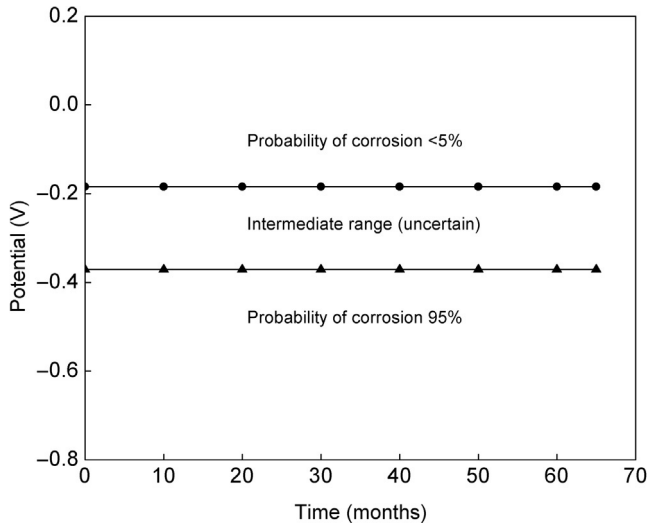

Fig. 12.3 Range of corrosion potential values.

is involved in the circuit. EIS measurements will provide information on both resistive and capacitive behavior of the interface, enabling corrosion behavior evaluation of an inhibitor-coated metal. In this analysis, the high-frequency intercept of real impedance gives the solution resistance (R_s) and the low-frequency intercept gives the sum of R_s and R_p. Polarization resistance can be calculated using the equation:

$$R_p = \frac{\Delta E}{\Delta I} - R_s \tag{12.18}$$

Once R_p is known, metal corrosion rate can be evaluated using the Stern-Geary equation (See Chapter, Section 5.3). AC impedance spectra also provides information on inhibiting layer impedance, adsorption capacitance from inhibitor presence, potential-dependent surface relaxation processes associated with inhibiting species coverage at lower frequencies, anodic intermediate species at higher frequencies, and presence and absence of diffusional processes. High-frequency data provide information on inhibitor coating characteristics controlled by adsorption capacitance. Low-frequency data provide information on Faradaic and surface relaxation processes associated with inhibitor adsorption.

12.4 CHLORIDE-INDUCED DAMAGE

The other major reinforcement corrosion problem is chloride ions in local pore solution at the concrete rebar interface. Chloride ions act as an iron dissolution catalyst and rust formation, making very small amounts of chloride ions dangerous for steel integrity. They have the ability to destroy passive ferric oxide films at high alkalinities [10–13]. The chloride required to initiate corrosion depends on solution pH. Comparatively small quantities are needed to offset Portland cement basicity. Chloride ions remain in the structure, so that there can be a steady buildup until critical concentrations (of around 500 ppm) are exceeded. Sources for chloride contamination are deicing salts, contaminated hydration, or sea water, all of which provide acidified, oxygenated pore solution that depassivates steel rebar. Chloride ions adsorb on the outer passive film surface and permeate the metal oxide layer to interact with the underlying metal. The redox reaction at the interface increases potential close to the pitting potential, resulting in an increase in the local chloride concentration due to electrostatic attraction. Chlorides in the electrolyte prevent passive film restoration. Surface pitting is proportional to the logarithm of chloride concentration in the local pore solution. Localized mechanical or chemical passive oxide damage, insufficient inhibitor coverage, and nonuniformities in the metal structure due to nonmetallic impurities contribute to pitting corrosion. Pitting corrosion represents an extremely localized attack that results in holes in the metal or alloy. Pitting corrosion severity is controlled by the environment, chloride concentration, electrolyte acidity, oxidizer concentration, temperature, structural characteristics, metal or alloy composition, and oxygen. In the presence of

chlorides, iron dissolution forms soluble iron compounds at the anode that react with water, producing $Fe(OH)_2$.

$$Fe^{2+} + 4Cl^- \rightarrow (FeCl_4)^{2-} + 2e^- \tag{12.19}$$

$$(FeCl_4)^{2-} + 2H_2O \rightarrow Fe(OH)_2 + 2H^+ + 4Cl^- \tag{12.20}$$

Reactions in Eqs. (12.19) and (12.20) destroy both ferric oxide and magnetite (Fe_3O_4) protective layers on the rebar. Hence, research is directed to improve inherent steel corrosion resistance, corrosion control parameter evaluation, implementing corrosion inhibitors that influence physical and chemical concrete and steel properties, chloride attack evaluation under severe chloride and temperature and improving corrosion, and pore solution models.

Simulated concrete pore solutions were used to test chloride-induced high-strength stainless steel (HSSS) corrosion resistance in simulated alkaline and carbonated concrete pore solutions [14]. Austenitic, martensitic HSSSs, duplex stainless steels, and pearlitic prestressing steel were investigated with cyclic polarization. Only duplex steels S32205 and S32304 exibited high corrosion resistance. Pitting corrosion was present across most samples as a result of ferrite dissolution. Admixtures such as ground granulated blast furnace slag (GGBS) have been used to retard chloride ingress [15]. Ordinary Portland cement was used as a reference for corrosion measurements. Considerable transport resistance for chloride is observed in a 70% GGBS replacement, as well as lower corrosion rates and similar corrosion potential. The reduced chloride transport was attributed to high tortuosity within the GGBS pore matrix and not chloride binding. Jaffer and Hansson [16] investigated loading impact on chloride-induced corrosion in cracked concrete. They subjected ordinary Portland cement concrete (OPCC) and high-performance concrete (HPC) to dynamic and static loading to estimate the impact on concrete durability. They found that HPC, with a lower porosity, had a longer average corrosion products spread along the rebar, leading to a higher likelihood of spalling and failure. Higher OPCC porosity led to corrosion product diffusion into the concrete, resulting in aggregate-paste detachment and cracking. Opening and closing cracks due to dynamic loading resulted in greater detachment and cracking from greater corrosion product diffusion. Morris *et al.* [17] evaluated chloride-induced corrosion in reinforcing steel by concrete resistivity measurements. Chloride threshold (Cl_{TH}) concentration increases from 0.44% to 2.32% relative to cement weight with a concrete-electrical resistivity increase from 2 to 100 kΩcm. Dehwah *et al.* [18] investigated the impact of sulfate contamination in addition to chloride penetration. By monitoring corrosion potential and current density, they show that increasing sulfate ions increased corrosion rate but did not influence corrosion initiation time.

Glass and Buenfeld [19] investigated theoretical chloride binding influence on corrosion risk in reinforced concrete. Chloride binding determines time to chloride-induced corrosion. It increases the total chloride content and impacts external chloride diffusion.

Chloride binding reduced free chloride concentration, minimizing mobile chloride within the concrete. The high concentration gradient due to bound chloride also increases external chloride diffusion velocity into the concrete. This results in a high total chloride concentration near the surface (bound plus free chlorides) and a low total chloride concentration at the center. A drop in pore solution pH releases bound chloride, facilitating a greater drop in pH and depassivation. The time to corrosion initiation for embedded steel depends on the corrosion risk presented by bound chloride relative to free chloride. It increases via binding increase, when the chloride threshold is low but the source chloride content is high. When the surface chloride threshold difference is small, the time to corrosion initiation may be reduced by a binding increase. Chloride binding may have negative or positive effects on time to corrosion initation depending on source chloride content and chloride threshold. Chloride isotherms used to predict chloride ingress were generated for low (2%), medium (8%), and high (14%) C3A-type cements to represent low, medium, and high binding capacities. The model predicted data and fitted isotherms are presented in Fig. 12.4 [19].

The best-fitted Langmuir isotherm describes the predicted data for cement containing 8% C3A. Glass and Buenfled [20] suggested a chloride diffusion model that considers the effects of a Langmuir adsorption isotherm given by the equation:

$$C_b = \frac{\alpha C}{1 + \beta C} \tag{12.21}$$

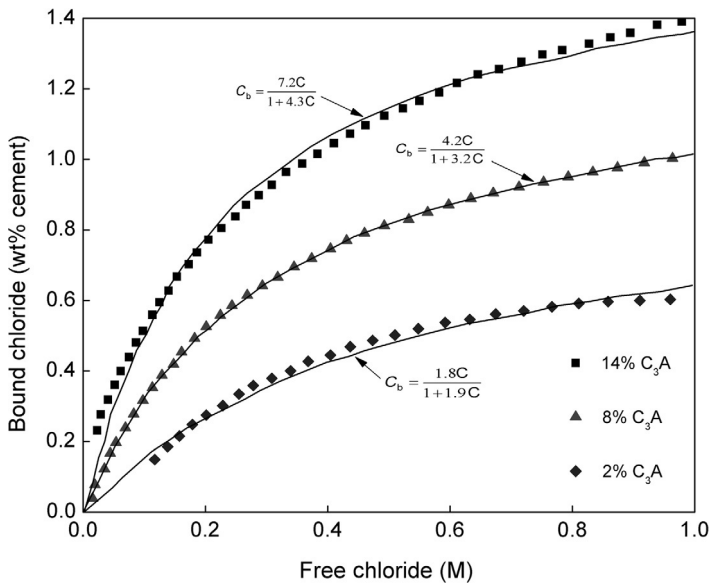

Fig. 12.4 Predicted binding data compared with the fitted Langmuir adsorption isotherms for a 0.45 w/c cement paste [19].

where C_b is bound chloride quantity, C is free chloride concentration, and α and β are constants. The predicted maximum bound chloride contents for the 2%, 8%, and 14% C3A-type cements are 0.97%, 1.32%, and 1.67% chloride by cement weight. Figure 12.5 shows total chloride buildup in the first 8 years [19]. The apparent diffusion coefficients (D_a) are also included in Fig. 12.5. They were estimated using conventional total chloride profile (C_t) fitting by the equation:

$$C_t = C_s \mathrm{erfc}\left(\frac{x}{2\sqrt{D_a t}}\right) \tag{12.22}$$

C_s in Eq. (12.2) is surface chloride content. Least squares predicted data at 1 mm depth increments.

Thangavel and Rengaswamy [21] investigated chloride/hydroxide ratio influence on corrosion rate within various environmental and concrete systems. The corrosion rate was measured gravimetrically, visually, alkalinity, and chloride content analysis. They found that the chloride/hydroxide ratio is not an accurate index for characterizing chloride-induced corrosion. Within the experiment, oxygen diffusion and initial chloride content had a significant impact on final corrosion propagation and initiation. Reddy *et al.* [22] investigated the bound chloride effect on concrete corrosion by looking at additional chloride binding systems such as calcium aluminate admixtures and sulfate resistant cement. An additional bound chloride phase was discovered that released chlorides at a relatively high pH, making bound chloride a similar corrosion risk to free

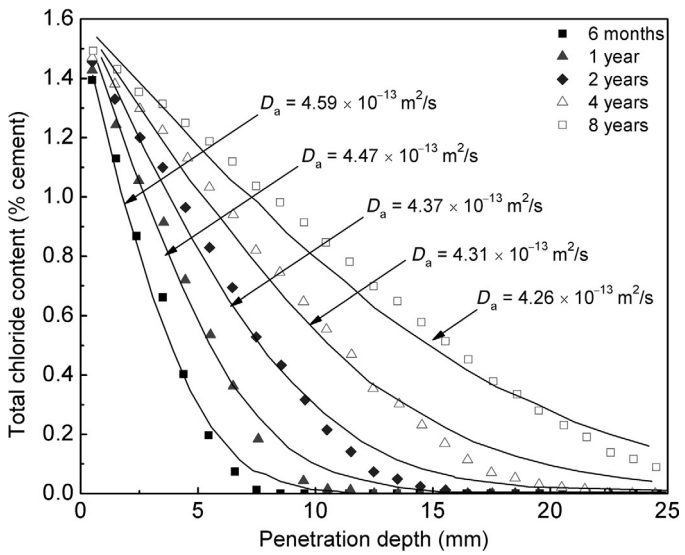

Fig. 12.5 The buildup of total chloride for eight years of exposure compared with the fitted profiles obtained by Eq. (12.22) and the associated apparent diffusion coefficients [19].

chloride. The majority of acid-soluble chloride entered the pore solution when pH fell below 11. Bound chloride, previously thought irrelevant, may have a significant contribution to corrosion despite its solid phase behavior at pH near 12.5. Cementitious binder has an impact on the resistance to pH reduction, or acid neutralization capacity. This would impact the chloride threshold that depassivates stainless steel. Ann *et al.* [23] investigated surface chloride concentration influence on theoretical chloride ingress. Constant, linear, square root, and square root with initial chloride conditions were used to describe boundaries with a constant diffusion coefficient. The model determined a linear and square root build up demonstrated the slowest chloride ingress. Yu *et al.* [24] investigated steel rebar corrosion behavior in a simulated pore solution. Open circuit potential and linear polarization resistance was recorded during stepwise chloride addition. Results indicated that the chloride and chloride/hydroxide ratio were appropriate indices for critical chloride content. Corrosion resistance also improved with increasing pH, as expected, with steel rebar repassivation. Severe pitting corrosion was found on sandblasted rebar. Suryavanshi *et al.* [25] investigated the influence of internal chloride on steel corrosion behavior. Shi *et al.* [26] addressed the recent advances in fundamental concrete durability understanding including mineral admixtures, chloride ingress, durability assessment in terms of internal chloride behavior, and service life modeling. They recognize the need for model improvements to better represent incredibly complex heterogeneous concrete environments, temperature, and moisture cycles. Concrete transport properties, corrosion propagation, geometry, environmental fluctuations, deterioration, and chloride penetration are identified as specific areas to improve. Admixtures such as fly ash, slag, and industrial by-products have significant cost savings by inhibiting chloride transport. Brenna *et al.* [27] investigated commercial concrete coatings' effectiveness to prevent chloride and water ingress, reducing steel corrosion. Coatings consisted of a polymer-modified mortar and three elastomeric coatings. By measuring corrosion potential and current over time, they compared uncovered concrete with covered concrete and found every coating increased the time to corrosion and corrosion rate after initiation to varying degrees. Polymeric containing mortar demonstrated greatest effectiveness when impairing corrosion initiation, but all coatings could be considered to lengthen concrete service life in aggressive corrosion environments. Al-Methel *et al.* [28] investigated corrosion inhibitor impact on silica fume cement concrete corrosion in both long-term and accelerated environments. Inhibitors were calcium nitrate, a proprietary calcium nitrite-based mixed inhibitor, a proprietary migrating inhibitor, and an organic mixed inhibitor. Samples with varying chloride contamination were subjected to wetting and drying cycles or immersed in chloride solution and subjected to an anodic potential of 2 V. Corrosion potential and current were measured to monitor corrosion. Increasing chloride content decreased time to initiation, while all corrosion inhibitors increased time to corrosion and time to cracking with decreased corrosion current density. Accelerated testing was determined satisfactory to evaluate

corrosion in a smaller time frame using applied anodic potential. Fajardo *et al.* [29] studied the use of pozzolans, natural volcanic material, as partial cement substitutes in reinforced mortar. The specimens containing ordinary Portland cement, 10%, and 20% pozzolanas were characterized by compressive strength, corrosion pontential, polarization resistance, resistivity, and chloride content. The pozzolan substitute had higher resistivity, increased time to corrosion initiation, and decreased corrosion rate upon initiation. These properties are suggested to be the result of pore filling by finely ground pozzolan. Pozzolan does result in an acceptable reduction in compressive strength. Fedrizzi *et al.* [30] investigated migrating corrosion inhibitors (MCIs) and repair mortars in ordinary Portland cement contaminated with 1 wt.% chlorides. Additionally, an alkanolamine-based inhibitor was applied. The inhibitors were charcterized using corrosion potential measurements, EIS, and chloride penetration analysis. Mercury intrustion porosimetry physically characterized the repair mortars. The MCI results were inconclusive on long-term corrosion prevention. Repair mortars with low porosity were much more effective in creating a barrier around the concrete and reducing corrosion rate. High-porosity repair mortars only had short-term effectiveness, retarding severe corrosion but not reducing corrosion rate in the long term.

In the presence of chlorides, the steel passive film was destroyed. Calcium nitrate on carbon steel rebars was investigated under different pH conditions in the presence and absence of chloride ions [31]. Studies indicated corrosion completion and passivation on the surface and the resulting open circuit potential depends on the relative corroding-passivating environment strength. In the absence of chloride, pH serves as a sufficient passivator. Nitrite ions act as anodic inhibitors by increasing the barrier oxide film formation rate. The nitrite ion protective action seems to be more pronounced in a highly corroding environment. This is due to the inhibition mechanism that uses unwanted corrosion products and converts them to desirable products. Protection in chloride environments depends on the Cl^- to NO_2^- ratio [31]. Song *et al.* [32] developed a corrosion model for predicting service life based on micromechanics. The significance and influence of ambient temperature as a steel reinforcement rate factor was addressed by Zivica [33].

Using ordinary and sulfate-resistant Portland cement to represent differing chloride environments, short-term electrochemical monitoring and SEM were used to characterize corrosion behavior [34]. Steel electrodes attained passivity in mortar with high levels of calcium aluminate, up to 1% wt. chloride. At 1.75% wt. chloride, steel electrodes corrode. All chloride levels resulted in steel corrosion for low levels of calcium aluminate. Pore solution was also impacted by mortar exposure conditions. Atmosphere exposure had a high influence on hydroxide concentration in pore solution but no impact on chloride concentration. Carbonation was also investigated; samples in a sealed container had a chloride/hydroxide ratio half that of unsealed samples.

Chloride-induced reinforcement corrosion and concrete cracking simulation was investigated by Chen and Mahadevan [35] using Faraday's law to develop a

reinforcement corrosion model and finite-element analysis to create a rust expansion model characterized by equivalent time-varying radial displacement boundary condition. These models, combined with a smeared cracking approach, predicted crack patterns for reinforced concrete due to chloride penetration in a constant chloride environment. Guzman *et al.* [36] used a finite element approach to model chloride-induced corrosion and subsequent concrete cover cracking. The model includes nonlinear diffusion coefficients, chloride binding, transport phenomena, and internal cracking due to expansive pressures. Progression is noted in the integration of corrosion initiation and propagation phases.

12.5 CORROSION CONTROL OF REINFORCING STEEL

One of the most severe and widespread problems in concrete structures is internal damage caused by external chlorides on embedded reinforcing steel. Corrosion on embedded steels can be lowered by applying inhibitors, zinc coatings, and thin barrier organic coatings. Frequently used organic coatings are polyurethanes, acrylics, and chlorinated rubber. Other methods for corrosion control are chloride removal, cathodic protection, and corrosion resistant or coated reinforcement.

In practice, the common method to retard corrosion under moderate to severe chloride attack is complete removal of the chloride-laden region and subsequent patching. However, active corroding sites that have not yet deteriorated are left in place, leading to chloride diffusion and new corrosion site initiation. Alternative treatments are polymer impregnation, electrochemical chloride removal, and cathodic protection. However, these suffer from problems like cost (polymer impregnation and cathodic protection), continuous monitoring (cathodic protection), and hydrogen evolution and embrittlement (electrochemical chloride removal and cathodic protection). Treatments focus on effects rather than causes of corrosion damage (chloride ions). An efficient way to combat chloride attack is through innovative rebars and/or corrosion inhibitors. Carbon steel rebars have been traditionally used for reinforcement in concrete structures. However, they suffer severe corrosion even in moderate chloride ion amounts. The corrosion rate of austenitic steel is an order of magnitude less than carbon steel in aggressive environments. Chloride tolerance is also several times higher. These characteristics make austenitic steel an attractive alternative to carbon steel. Austenitic steels are widely employed in new reinforced steel structures designed for long service life or highly aggressive environments. Their use is limited mainly to those special cases due to material cost, an order of magnitude higher than carbon steel. Steels containing 12% chromium have proven superior to carbon steel and are comparable to SS 316 and SS 304. The solution to preparing more resistant steel with affordable cost is to optimize chromium content. Such materials include solid stainless steel, stainless steel clad high-performance reinforcement, and MMFX, among others.

12.6 INHIBITORS

12.6.1 Classification of corrosion inhibitors

Corrosion inhibiting admixtures for reinforcing concrete steel are classified as anodic, cathodic, or mixed (anodic + cathodic) depending on the inhibition corrosion mechanism. These inhibitors are chromates, nitrites, benzoates, phosphates, stannous salts, and ferrous salts. Anodic inhibitors cause an anodic shift in corrosion potential, increasing anodic polarization and passivating the steel. There are two types of passivating anodic inhibitors in concrete: oxidizing anions such as nitrite, chromate, and nitrate that passivate steel in the absence of oxygen; and the nonoxidizing ions such as phosphate, tungstate, and molybdate that require oxygen in the pore solution to passivate the substrate [37–46].

Cathodic inhibitors either selectively precipitate on cathodic areas or slow the cathodic reaction by increasing hydrogen overvoltage. Other cathodic inhibitors utilize alkalinity increase at cathodic sites to precipitate insoluble compounds on the metal surface. Hydrogen evolution causes the metal-concrete interface to become more alkaline and ions such as calcium or magnesium precipitate as oxides to form a protective layer. The commercial production of stable calcium nitrite solutions with up to 40% dissolved solids encouraged the use of this corrosion inhibitor. The first results were released in 1983 by the Federal Highway Administration (FHWA). The conclusion was that calcium nitrite can reduce corrosion rate by more than an order of magnitude. Calcium nitrite was effective at chloride to nitrite ratios smaller than one based on admixed chlorides [47,48]. Increasing microsilica to reduce chloride permeability is also a popular option. Microsilica is an effective pozzolan because small particle size enables better filling and increases chemical reactivity. The small particle size helps fill the heterogeneous concrete pores, blocking external chlorides and other contaminants [49]. Calcium nitrite is compatible with microsilica and should provide protection in the presence of chloride. This combination has been used to safeguard a four-level parking garage at the Minneapolis Convention Center. The 5000 psi, high-performance concrete was specified to be a 4 by 5 combo: 4.95 L/m^3 of calcium nitrite and 5% silica fume solids by cement weight. The mix also included a retarder, water reducer, air entrainer, and superplasticizer admixture. Since completion, Grace's combo mix has been used often, mostly in parking garages. An efficient concentration of calcium nitrite in the concrete mix depends on chloride content, other admixtures, pH, temperature, and crack extent.

12.6.2 Determination of inhibitor efficiency

Corrosion inhibitors are compared by their inhibiting efficiency (IE), the percentage that corrosion is lowered, compared with corrosion rate in their absence.

$$\mathrm{IE} = \frac{I^{\mathrm{o}}_{\mathrm{corr}} - I^{\mathrm{i}}_{\mathrm{corr}}}{I^{\mathrm{o}}_{\mathrm{corr}}} \times 100 \tag{12.23}$$

I^{o}_{corr} and I^{i}_{corr} are corrosion currents in the absence and presence of the inhibitor, respectively. Inhibitor efficiency can be expressed with polarization resistance measured in the presence and absence of inhibitor in the concrete mix:

$$IE = \frac{R^{i}_{p} - R^{o}_{p}}{R^{i}_{p}} \times 100 \tag{12.24}$$

R^{i}_{p} and R^{o}_{p} are polarization resistances in the presence and absence of the inhibitor.

12.7 SACRIFICIAL ZINC COATINGS

Galvanized coatings are used to protect steel reinforcement in concrete [50–59]. Zinc dissolves in alkaline media and sacrificially protects iron [51,52]. However, the general conclusion appears to be neutral. Galvanized coatings may be insufficient in the presence of chloride, accelerating coating corrosion. Corrosion products may cause distress in the concrete, and protection ceases when the anode metal is used up. Zinc coatings are generally less appropriate than nonmetallic coatings due to high pH levels in concrete. In reality this may be due to high chloride concentrations. Reinforcement bar corrosion in soils has been primarily addressed using galvanized steel. Specifying a permissible range of physicochemical soil properties is sufficient to hold corrosion to reasonable levels. Typical specifications are pH 4.5-9.5, resistivity at least 1000 Ωm, chloride content does not exceed 0.02%, and sulfate content does not exceed 0.1%. Under these circumstances, studies have shown corrosion loss rates from buried metal are between 0.002 and 0.01 mm per year. Rates have been found to decrease with time. Because galvanization thicknesses are on the order of 0.3 mm, zinc coating life is usually predicted to be 30-50 years. Metal dimensions are usually chosen so that an additional 100-150 years' worth of corrosion can take place before the steel rebar becomes critically stressed. Galvanized rebar corrosion resistance was studied in various bridges [50]. Results indicated galvanized steel reinforcement performance was excellent in spite of chloride content and was well above the corrosion threshold for carbon steel. Zinc passivation been studied extensively under anodic passivation [54–59]. The passive film composition is a mixture of zinc oxide, peroxide, and/or hydroxide. Macias and Andrade [51,52] found that zinc was passivated bellow pH 13.3 in alkaline solutions saturated with $Ca(OH)_2$ with various additions of KOH/NaOH/$CaSO_4$/Na_2SO_4/K_2SO_4. No passivation occurs above this value, and an exponential corrosion rate increase was observed. Pitting was observed on zinc regardless of the passivation film, at excessive chloride concentration [60]. Pitting occurs in poor-quality concrete with galvanized reinforcing bars. In the case of sound concrete, zinc acts as a sacrificial anode and protects underlying steel. Sodium chromate and chromic acid were investigated as zinc coating inhibitors with and without chloride [1]. Baker *et al.* [61] studied the marine corrosion of galvanized steel for a period of

11 years. Zinc coating had an average loss of 2-3 mills. In the absence of chloride, the inhibitors passivate zinc. Chlorides additions destroy passive film formation. Galvanized carbon steel studies in $Ca(OH)_2$ and calcium nitrate indicated that zinc was not protected by nitrite in the presence of chloride ions. The inhibitor significantly reduced the steel corrosion rate [52]. Maldonado [62] investigated the chloride threshold for galvanized reinforcement corrosion exposed in the Mexican Caribbean for nine years. The time of incubation (TI) and chloride threshold (CT) were determined in concretes with water/cement (w/c) ratios of 0.4, 0.5, 0.6, and 0.7. The results indicated galvanized reinforcement resists chloride levels 6-3 times higher than carbon steel, even in poor-quality concretes. Silane-based hydrophobic admixture studies on galvanized reinforcing steel corrosion in concrete showed hydrophobic concrete protects galvanized steel reinforcement even with concrete cover cracks [63]. The major reduction reaction during galvanized steel rebar passivation by Tittarelli and Bellezze [64] show oxygen is the main oxidizing agent, initiating rapid passive layer formation on zinc coating.

Comparison studies between surface and bulk hydrophobic treatments against galvanized reinforcing steel corrosion in concrete indicated bulk hydrophobization is the most effective treatment to improve corrosion resistance in concrete even with cracks. Surface hydrophobization is very effective in the first few exposure cycles to an aggressive environment and as a restorative method for 0.5 mm wide cracks [65]. pH and chloride ion concentration effect on galvanized steel corrosion behavior in a simulated rust layer solution was investigated by Liu *et al.* [66]. Results revealed galvanized steel in simulated rust layer solution was susceptible to pitting corrosion in all chloride concentrations between 0.1 and 0.6 M.

12.8 CONCRETE PERMEABILITY

Concrete is a porous media that transmits moisture, oxygen, and aggressive ions (chlorides and sulfates) to the surface [7,67]. Chlorides penetrate the passive oxide film and form active-passive cells. Minute anodes are formed surrounded by a large cathode area, resulting in very high current densities and metal dissolution at the anodes. The metal area immediately surrounding the anode is cathodically protected.

Reinforcement protection can be achieved by selecting concrete cover and mix design so that chloride will not reach the bar surface within the expected lifetime. This requires knowledge about chloride penetration depth as a function material and environmental parameters.

Chloride ion diffusion in a one-dimensional slab has been modeled by Lin [7] subject to time-dependent surface concentration and diffusion coefficient. Bazant [68] developed a physical model to study reinforcement corrosion. Saetta *et al.* [69] considered ion diffusion coefficient variability with concrete parameters in a chloride diffusion study in partially saturated concrete. The time for corrosion initiation has been empirically

found to depend on chloride ion concentration at the rebar surface [70–72]. Results indicated corrosion begins when chloride concentration at the rebar interface reaches a threshold limit of 0.24-4%.It has been accepted in the literature that a chloride concentration of 0.2% (for the Portland cement concrete) is a good assumption as to chloride threshold limit to initiate reinforcement. Semiempirical models were used to predict concrete bridge decks' service life subject to reinforcement corrosion [73–75]. Because they lack fundamental basis, these models cannot be generalized outside the conditions they were derived for. They cannot be used to conduct comprehensive parametric studies or develop detailed quantitative design specifications. Hornbostel *et al.* [76] addressed concrete corrosion and durability through ion transport with concrete resistivity control. A clear decrease was observed in corrosion rate with increasing resistivity.

A theoretical model to study chloride diffusion in concrete has been developed by Arora and Popov [77]. Two different coordinate systems are considered to model structure geometry. A chloride ion adsorption and diffusion schematic in a one-dimensional concrete cylinder is shown in Fig. 12.6, comparable to a planar slab with one-dimensional chloride diffusion. Chloride ingress follows Fick's law of diffusion for cured concretes [77].

The splash/tidal zone of bridges and walls represent cylindrical columns immersed in water. These structures involve entry in two dimensions. Chloride ions enter concrete by adsorption at the surface, which is given by an empirical equation. The effective chloride diffusion coefficient is derived from concrete permeability, water/cement ratio, and concrete resistivity. When concentration reaches a critical value in the vicinity of steel, corrosion begins. As shown in Fig. 12.6, a boundary layer exists adjacent to the concrete

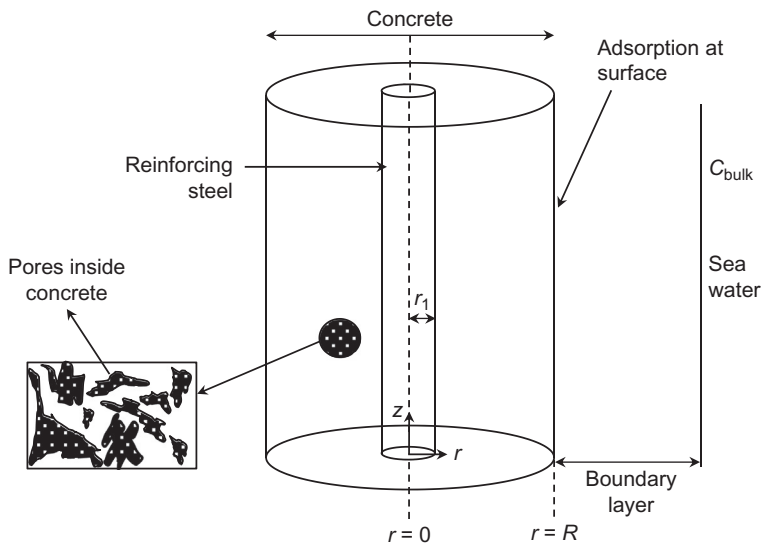

Fig. 12.6 Chloride ion adsorption and diffusion schematic in a one-dimensional concrete cylinder [77].

surface. In the model, boundary layer thickness has been assumed constant over a long period of time. Chloride ions are transported to the concrete surface by diffusion and convection. Beyond the boundary layer, natural convection maintains a uniform concentration of chloride ions at the bulk value (C_b). Chloride ions adjacent to the concrete surface are adsorbed on the surface as a function of time. If the adsorption rate is fast, the system can be described by an equilibrium adsorption isotherm. In this case, the adsorption process is slow when compared to diffusion and convection in the boundary layer. In order to validate the model, the concrete cover thickness effect on corrosion rate and initiation time has been determined.

The diffusion coefficient of chloride in concrete varies with time and the water to cement ratio. The exact rate of chloride diffusion through concrete cannot be determined due to concrete heterogeneity and concrete material differences. The relationship given by Lin [7] was used to estimate the diffusion coefficient in the model:

$$D_{Cl^-} = \left(1.249 - 5.051w + 8.941w^2\right)10^{-8}\,\mathrm{cm}^2/\mathrm{s} \tag{12.25}$$

where "w" represents the water to cement ratio and D_{Cl^-} is the chloride diffusion coefficient of in concrete. Diffusion rate is equal to the sum of adsorption, surface, and transport rates through the boundary layer. Diffusion and convection transport inside the boundary layer is very fast compared to adsorption and can be neglected. The rate-limiting steps in this process are adsorption and subsequent diffusion. The assumption and development of one-dimensional and extended one-dimensional models are described in [77].

Case Study 12.1—Prediction of Corrosion Initiation Time and Life of Rebars under Real Time (Practical) Conditions

Objective

The objective is to predict corrosion initiation time for various cases using SimCorr™. In this simulation, chloride is assumed present at the surface at all times. The model simulations are used to determine corrosion initiation time and reinforcing steel rebar life in the deck and cap beam of the bridge. SimCorr™ can be used to predict corrosion initiation time as a function of structural and environmental parameters, estimate structure life, design concrete mixes, and geometry based on lifetime calculations and optimize corrosion protection system as a function of surrounding conditions. SimCorr™ also serves as a tool for evaluation of chloride transport and underlying concrete corrosion. The simulation software is based on the first principles model described in [77].

Model Parameters

Reinforcing Steel in Concrete: Due to versatility and acceptability, steel-reinforced concrete is one of the most widely used materials for construction. Steel rebar provides mechanical strength critical to concrete performance.

Threshold Chloride Concentration: The average threshold concentration in carbon steel is 0.83 kg/m^3. If the chloride concentration rebars increases beyond this value, the passive film is destroyed.

Surface Chloride Concentration: The main source of chloride ions arises from salt added during road and bridge deicing. Sodium chloride (NaCl) and calcium chloride ($CaCl_2$) have been traditionally used as deicing salts. In the United States, 282 kg of salt are used per lane-mile. Normally the number of applications varies from less than 8 to more than 16 per year depending on climate conditions. Annual salt estimates for various states are given in Table 12.1. Rebar surface can be exposed to the following ranges of chloride concentration: moderate—3.56 kg/m^3 NaCl, high exposure—5.4 kg/m^3 NaCl, and severe exposure—7.36 kg/m^3 of sodium chloride. Coastal bridge rebar surface is exposed to moderate to high chloride levels.

Water/Cement Ratio: The concrete used in the deck and cap beam of the bridge is type *D* and has a water to cement ratio of 0.43. Unless otherwise mentioned, this value has been used in all simulations.

Table 12.1 A Rough Estimate of Different Annual Salt Applications in Various States

More than 16 applications	8-16 applications	Less than 8 applications
Connecticut	Kansas	Alabama
Illinois	Kentucky	Alaska
Indiana	Iowa	Arizona
Maine	Minnesota	Arkansas
Maryland	Missouri	California
Massachusetts	Nebraska	Colorado
Michigan	New Jersey	Delaware
New Hampshire	Pennsylvania	Florida
New York	West Virginia	Georgia
Ohio	Tennessee	Hawaii
Rhode Island		Louisiana
Vermont		Mississippi
Wisconsin		Montana
		Nevada
		New Mexico
		North Carolina
		North Dakota
		Oklahoma
		Oregon
		South Carolina
		South Dakota
		Texas
		Utah
		Washington
		Wyoming

Results and Discussion

The chloride ingress into concrete follows Fick's law of diffusion for cured concretes. Concrete mixtures and admixtures affect the diffusivity of chloride ions. Figure 12.7 shows the transport of chloride ions through the concrete deck under moderate corrosion environment. The surface chloride concentration is assumed to be equal to 3.56 kg/m^3, which corresponds to moderate corrosive conditions. Chloride diffusion follows an exponential decay into the concrete. Chloride concentration at the rebar surface increases with time.

Figure 12.8 presents the chloride concentration profiles with higher surface chloride content, (7.36 kg/m^3). A comparison reveals chloride concentration throughout the entire deck is higher with an increase in surface chloride content.

In both cases, the critical transport parameter is the chloride diffusion coefficient. The diffusion coefficient varies with water to cement ratio and time. In this model, the effective chloride diffusion coefficient is derived from concrete permeability, water/cement ratio, and concrete resistivity.

Figure 12.9 shows chloride content change at the concrete rebar surface as a function of time. Simulations were performed for a cover thickness of 5.08 cm and different surface chloride contents. It is clear that an increase in surface chloride content results in more chloride ions at the rebar surface, leading to faster corrosion initiation.

Similar studies have been carried out for the bottom of the deck, which has a cover thickness of 7.62 cm, and the results are shown in Fig. 12.10. The chloride concentration at the rebar surface increases more rapidly for 5.08 cm cover thickness compared to 7.62 cm. Because the top of the deck is not in the splash zone, the surface chloride content is lower than the bottom part. Corrosion onset will start at the bottom deck first and lead to eventual structure failure.

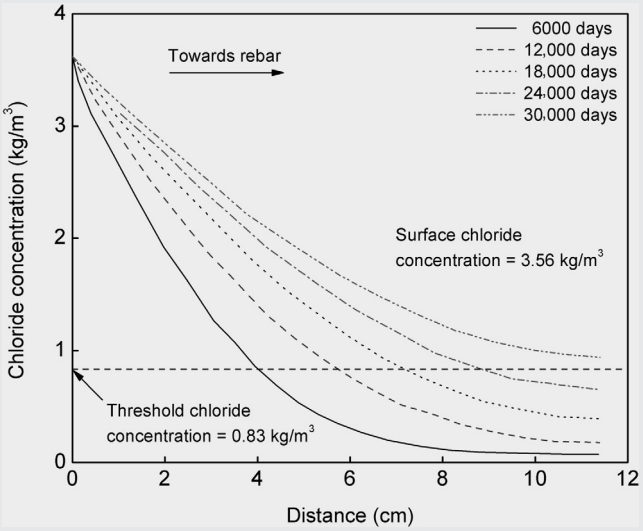

Fig. 12.7 Chloride concentration profiles under moderate corrosion environment.

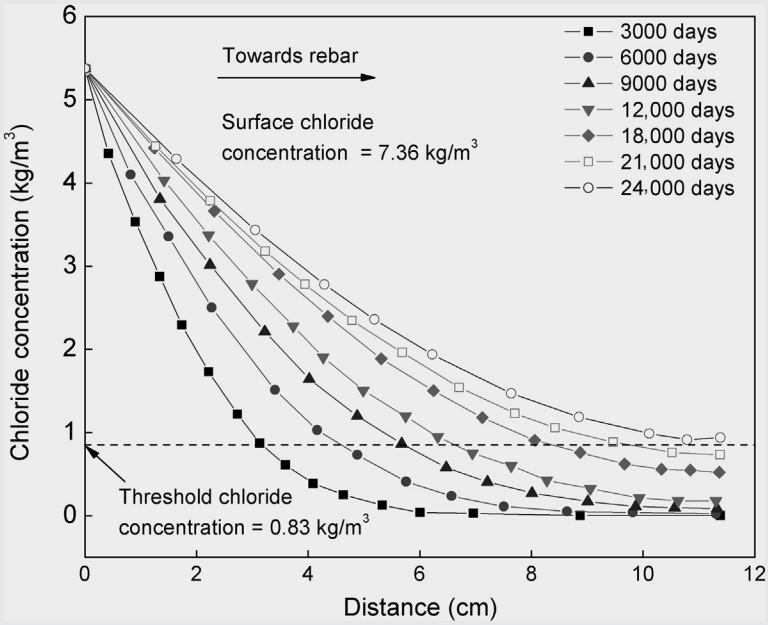

Fig. 12.8 Chloride concentration profile within the concrete.

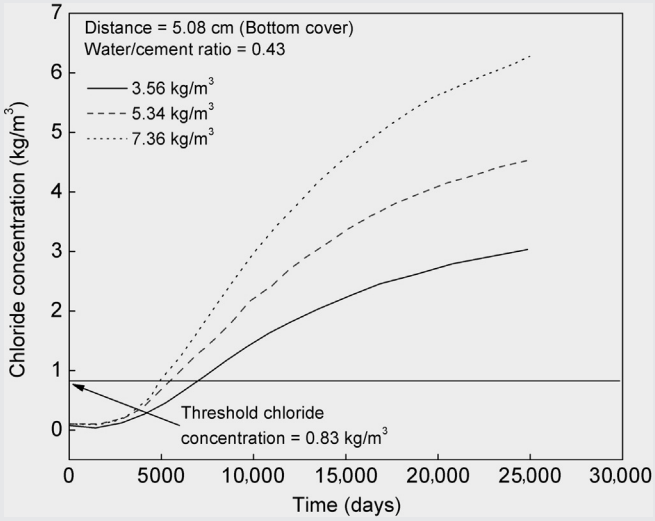

Fig. 12.9 Change in surface chloride concentration for 5.08 cm cover thickness.

Figure 12.11 presents surface chloride content change for different cover thickness at threshold concentration of 7.36 kg/m^3 NaCl. The threshold chloride content of 0.83 kg/m^3 is marked by the straight line in the plot. This graph shows rebars at the bottom of the deck will start corroding after 2500 days (~7 years), while those at the top will start

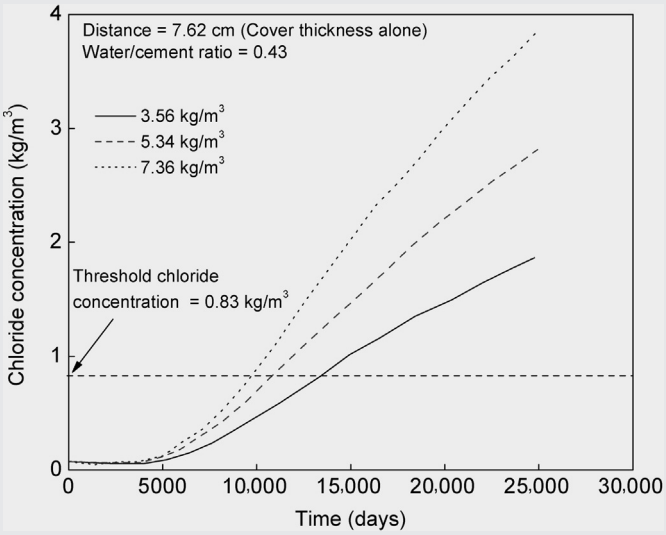

Fig. 12.10 Change in surface chloride content for 7.62 cm concrete cover thickness.

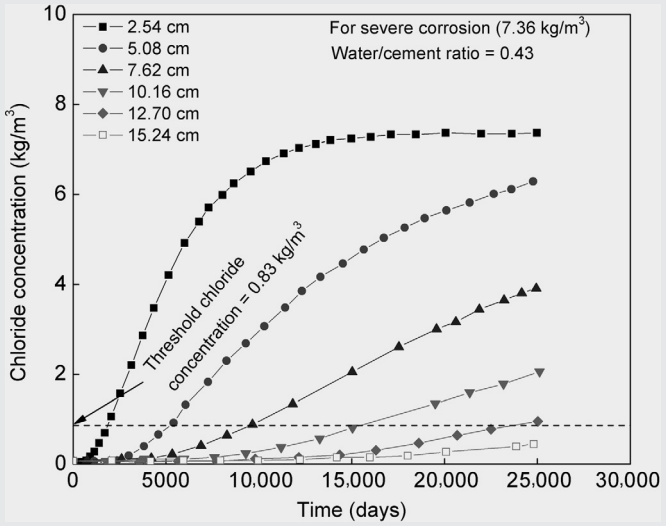

Fig. 12.11 Change in surface chloride concentration for different cover thickness at threshold concentration of 7.36 kg/m^3.

corroding after 8500 days (~23 years). The surface chloride concentration at the top is much lower than the bottom and the onset of corrosion will be delayed by several more years.

Corrosion initiation time is shown in Fig. 12.12 as a function of concrete slab thickness for various surface chloride contents. Corrosion initiation time for different water/cement

ratio is shown in Fig. 12.13. From these plots, corrosion initiation time can be directly obtained from the intersection of the x and y axes. Figure 12.12 indicates corrosion onset time increases with slab thickness and with surface chloride concentration. In Fig. 12.13, the corrosion initiation time increases when water content in the concrete reaches a maximum and subsequently decreases. The water to cement ratio affects chloride permeability. This is reflected through chloride diffusion coefficient changes.

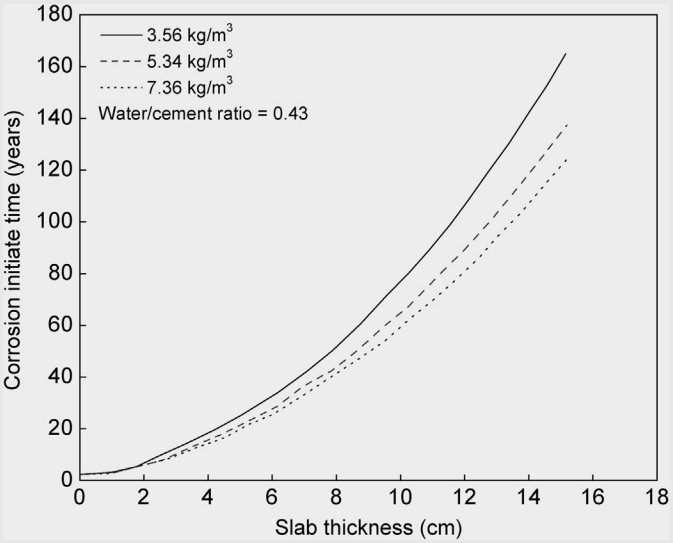

Fig. 12.12 Corrosion initiation time as a function of slab thickness.

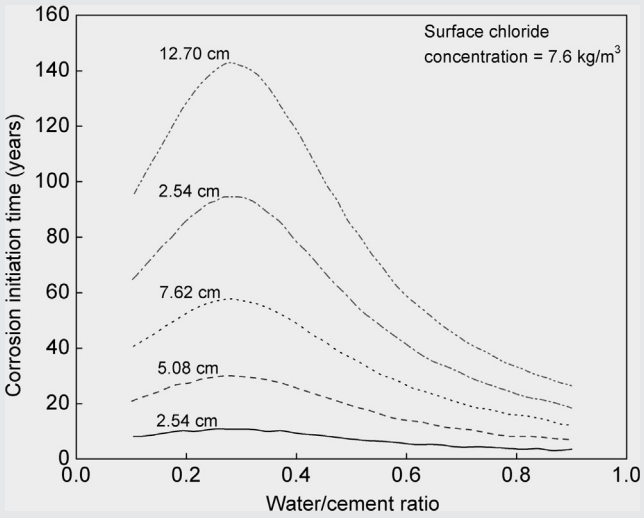

Fig. 12.13 Corrosion initiation time for different water/cement ratios.

The chloride diffusion rate is a minimum at a water/cement ratio of 0.3. Beyond this value, water content increase results in more chlorides permeating through the concrete resulting in lowering the corrosion initiation time. The above simulations have been done with a threshold concentration of 0.83 kg/m^3.

Effect of inhibitors: In the presence of nitrite inhibitor at 9.9 L/m^3 in the concrete mix, simulations were performed with a chloride threshold concentration of 3.56 kg/m^3, concrete cover thickness of 7.62 cm, and surface chloride concentration of 5.34 kg/m^3. Figure 12.14 shows the chloride concentration profile in concrete for an inhibitor concentration of 9.9 L/m^3. Comparison of Figs. 12.8 and 12.14 shows that the time needed to increase chloride concentration beyond the threshold value increases for a given thickness of concrete cover approximately fivefold.

Figure 12.15 shows corrosion initiation time as a function of water/cement ratio in the presence of an inhibitor. The simulation was carried out for a 2.54 cm concrete cover and 7.6 kg/m^3 surface chloride concentration. Comparison of Figs. 12.13 and 12.15 shows that rebars better resist chloride attack with an inhibitor for every water/cement ratio.

Model simulations for Myrtle Beach Bridge: SimCorr™ was used to predict rebar corrosion behavior in the Myrtle Beach Bridge in South Carolina. Myrtle Beach Bridge is a coastal bridge and chloride is present at all times and exposure risk to chloride is considered "severe." Surface chloride concentration of 7.36 kg/m^3 was used in all simulations. Table 12.2 summarizes the conditions used. Figures 12.16 and 12.17 show the chloride concentration profiles for cases 1 and 2 outlined in Table 12.2 for 7.36 kg/m^3 surface chloride concentration. With an inhibitor, the time required to exceed the chloride concentration threshold value increases even under "severe"

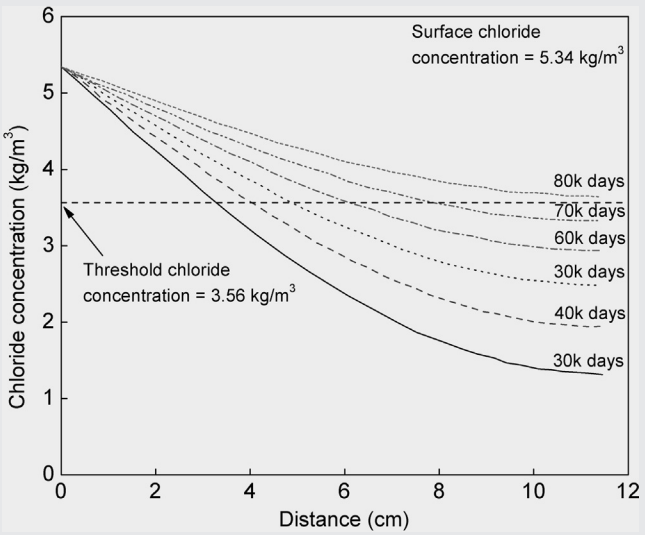

Fig. 12.14 Chloride concentration profiles in concrete under high-corrosion environment in the presence of 9.9 L/m^3 nitrite inhibitor.

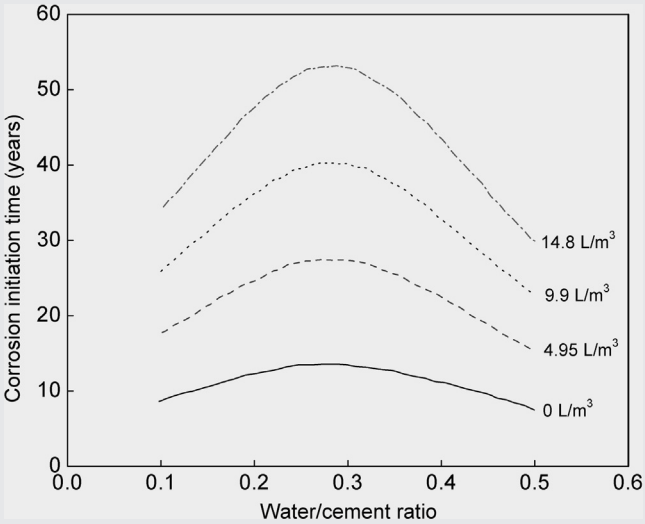

Fig. 12.15 Corrosion initiation time as a function of water/cement ratios for different inhibitor concentrations.

Table 12.2 Various Conditions Used in this Study

Case No.	Concrete Cover Thickness (inch)	*W/C* Ratio	Inhibitor (L/m^3)	Surface Chloride Concentration (kg/m^3)
1	4	0.4	0	7.36
2	4	0.4	4.95	7.36
3	4	0.4	9.9	7.36
4	4	0.4	14.8	7.36
5	4	0.4	19.8	7.36

exposure. This is due to the threshold concentration increase from 0.83 kg/m^3 for without an inhibitor, to 1.78 kg/m^3 for 4.95 L/m^3 inhibitor. The results are consistent with Figs. 12.8 and 12.14.

Figure 12.18 shows the dimensionless threshold chloride concentration as a function of time for different inhibitor concentrations. The required time to exceed chloride threshold value increases by increasing inhibitor concentration. Corrosion initiation time increases from 20 years without inhibitor to 60 years for 9.9 L/m^3 inhibitor. These results show inhibitors increase the threshold limit to a much higher value, but under aggressive chloride attack this threshold limit will eventually be reached. This dependence is given in Fig. 12.19 which illustrates the corrosion initiation time for different slab thicknesses as a function of nitrate inhibitor concentration. The plot shows corrosion initiation time as a function of concrete cover thickness for different inhibitor concentrations.

The observed data is consistent with the findings in Figs. 12.14–12.18. The plot also shows a corrosion initiation time increase for all concrete thickness values.

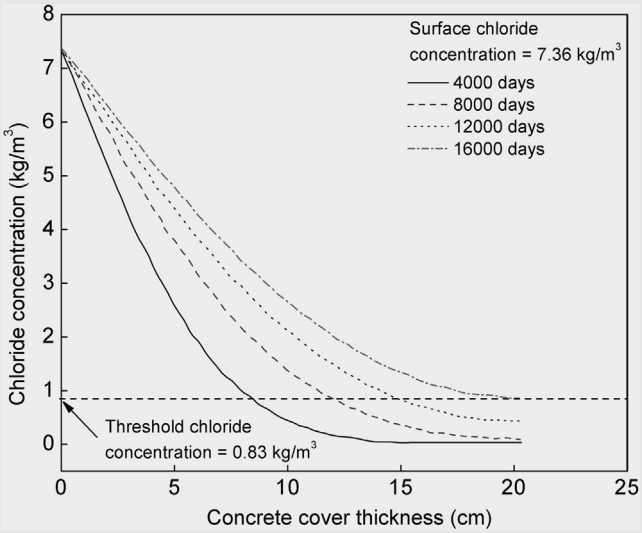

Fig. 12.16 Chloride concentration profiles in concrete under severe corrosion environment in the absence of inhibitor.

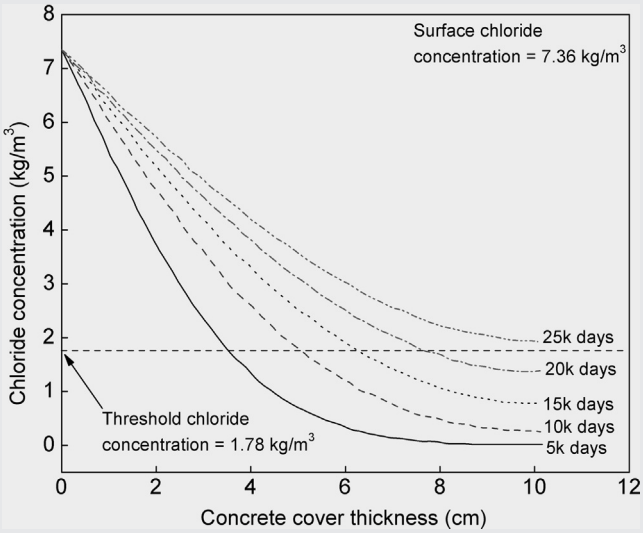

Fig. 12.17 Chloride concentration profiles in concrete under severe corrosion environment in the presence of 9.9 L/m^3 nitrate inhibitor.

Once chloride reaches the threshold, reinforcement is susceptible to corrosion. The service life of the samples was determined by using the Stern-Geary equation by adding corrosion initiation time and corrosion rate. For example, carbon steel rebar typically shows 800 Ω cm^2 corrosion resistance, while SS304 steel shows 4000 Ω cm^2 corrosion resistance.

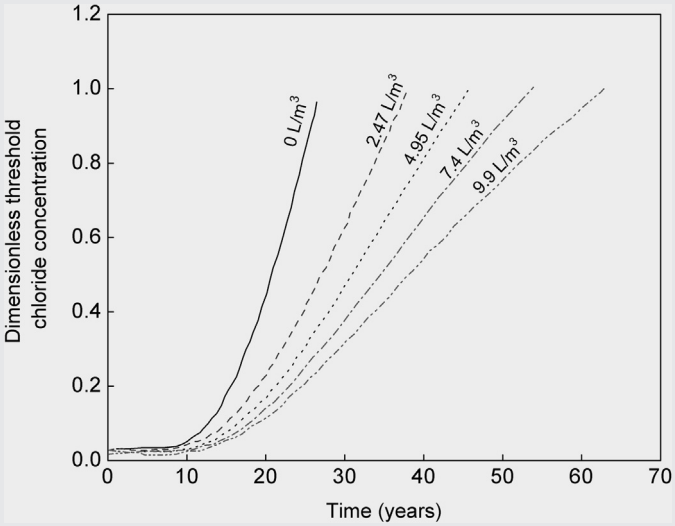

Fig. 12.18 Time required to reach dimensionless threshold chloride concentration of 1.0 for different concentrations of nitrite inhibitor.

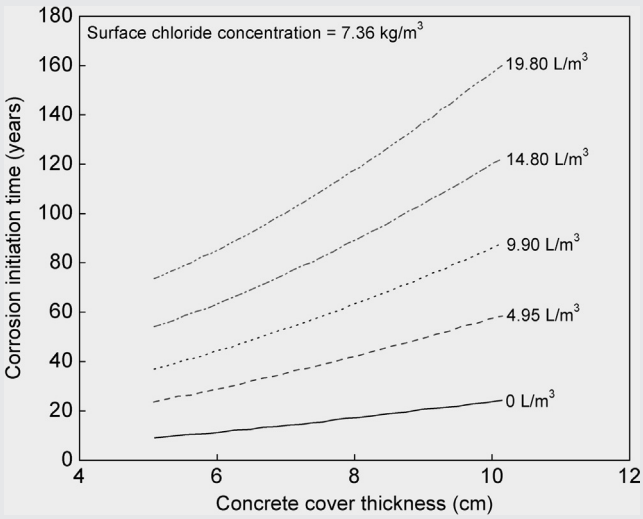

Fig. 12.19 Corrosion initiation time for different thicknesses as a function of nitrite inhibitor concentration.

Table 12.3 summarizes the life for different types of 1.27 cm thick rebars. The results are also summarized in Fig. 12.20. The plot clearly shows an increase in service life as a function of concentration for all rebars. The order of service life estimated for different reinforcements is SS316 > SS304 > carbon steel under corrosive conditions.

Table 12.3 Prediction of Service Life as Function Inhibitor Concentrations for Different Types of Steel

Case No.	Thickness (cm)	Inhibitor (L/m^3)	Service Life Under Corrosion (Year)		
			Carbon Steel (1.27 cm)	SS304 (1.27 cm)	SS316 (1.27 cm)
1	10.16	0	32.1	61.0	80.9
2	10.16	4.95	66.2	95.1	115.0
3	10.16	9.9	95.5	124.4	144.3
4	10.16	14.8	129.4	158.3	178.2
5	10.16	19.8	168.0	196.9	216.8

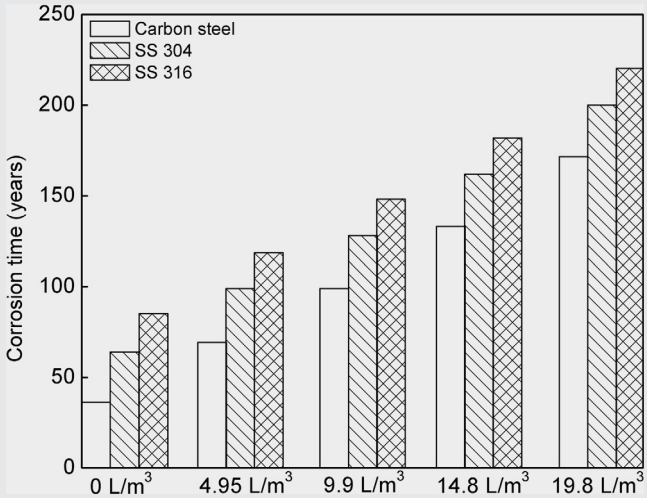

Fig. 12.20 Service life of different types of rebars under corrosive conditions as a function of nitrite inhibitor concentration.

REFERENCES

[1] D.J.H. Corderoy, H. Herog, Corrosion of reinforcing steel in concrete, in: D.E. Tonini, J.M. Gaidid (Eds.), ASTM STP 713, ASTM International, Philadelphia, PA, 1980, pp. 142–159.
[2] C. Alonso, C. Andrade, Effect of nitrite as a corrosion inhibitor in contaminated and chloride-free carbonated mortars, ACI Mater. J. 87 (1990) 130–137.
[3] S.N. Popova, B.N. Popov, R.E. White, M.F. Petrou, D. Morris, Corrosion effects of stabilized backfill on steel reinforcement, ACI Struct. J. 95 (1998) 570–577.
[4] N.S. Berke, Corrosion inhibitors in concrete, Concr. Int. 13 (1991) 24–27.
[5] C.A. Loto, Effect of inhibitors and admixed chloride on electrochemical corrosion behavior of mild steel reinforcement in concrete in seawater, Corrosion 48 (1992) 159–163.
[6] A.M. Zayed, A.A. Sagues, Corrosion at surface damage on an epoxy-coated reinforcing steel, Corros. Sci. 30 (1990) 1025–1044.
[7] S.H. Lin, Chloride diffusion in a porous concrete slab, Corrosion 46 (1990) 964–967.

[8] K. Tuutti, Corrosion of Steel in Concrete, Swedish Cement and Concrete Institute, Stockholm, 1982, pp. 17–25.
[9] ASTM C876-09, Standard Test Method for Corrosion Potentials of Uncoated Reinforcing Steel in Concrete, ASTM International, Philadelphia, PA, 2009.
[10] N.S. Berke, M.P. Dallaire, R.E. Weyers, M. Henry, J.E. Peterson, B. Prowell, Corrosion forms and control for infrastructure, in: V. Chaker (Ed.), ASTM STP 1137, ASTM International, Philadelphia, PA, 1992, pp. 300–327.
[11] S.N. Raicheva, B.V. Aleksiev, E.I. Sokolova, The effect of the chemical structure of some nitrogen- and sulfur-containing organic compounds on their corrosion inhibiting action, Corros. Sci. 34 (1993) 343–350.
[12] D.G. Kolman, S.R. Taylor, Sodium molybdate as a corrosion inhibitor of mild steel in natural waters. Part 1: flow rate effects, Corrosion 49 (1993) 622–634.
[13] D. Trejo, P.J. Monteiro, Corrosion performance of conventional (ASTM A615) and low-alloy (ASTM A706) reinforcing bars embedded in concrete exposed to chloride environments, Cem. Concr. Res. 35 (2005) 562–571.
[14] R.D. Moser, P.M. Singh, L.F. Kahn, K.E. Kurtis, Chloride-induced corrosion resistance of high-strength stainless steels in simulated alkaline and carbonated concrete pore solutions, Corros. Sci. 57 (2012) (2012) 241–253.
[15] V. Bouteiller, C. Cremona, V. Barohel-Bouny, A. Maloula, Corrosion initiation of reinforced concretes based on Portland or GGBS cements: chloride contents and electrochemical characterizations versus time, Cem. Concr. Res. 42 (2012) 1456–1467.
[16] S.J. Jaffer, C.M. Hansson, Chloride-induced corrosion products of steel in cracked-concrete subjected to different loading conditions, Cem. Concr. Res. 39 (2009) 116–125.
[17] W. Morris, A. Vico, M. Vazquez, Chloride induced corrosion of reinforcing steel evaluated by concrete resistivity measurements, Electrochim. Acta 49 (2009) 4447–4453.
[18] H.A.L. Dehwah, M. Maslehuddin, S.A. Austin, Long-term effect of sulfate ions and associated cation type on chloride-induced reinforcement corrosion in Portland cement concretes, Cem. Concr. Compos. 24 (2002) 17–25.
[19] G.K. Glass, N.R. Buenfeld, The influence of chloride binding on the chloride induced corrosion risk in reinforced concrete, Corros. Sci. 42 (2000) 329–344.
[20] G.K. Glass, N.R. Buenfeld, Theoretical assessment of the steady state diffusion cell test, J. Mater. Sci. 33 (1998) 5111–5118.
[21] K. Thangavel, N.S. Rengaswamy, Relationship between chloride/hydroxide ratio and corrosion rate of steel in concrete, Cem. Concr. Compos. 20 (1998) 283–292.
[22] B. Reddy, G.K. Glass, P.J. Lim, N.R. Buenfeld, On the corrosion risk presented by chloride bound in concrete, Cem. Concr. Compos. 24 (2002) 1–5.
[23] K.Y. Ann, J.H. Ahn, J.S. Ryou, The importance of chloride content at the concrete surface in assessing the time to corrosion of steel in concrete structures, Constr. Build. Mater. 23 (2009) 239–245.
[24] H. Yu, K.K. Chiang, L. Yang, Threshold chloride level and characteristics of reinforcement corrosion initiation in simulated concrete pore solutions, Constr. Build. Mater. 26 (2012) 723–729.
[25] A.K. Suryavanshi, J.D. Scantelbury, S.B. Lyon, Corrosion of reinforcement steel embedded in high water-cement ratio concrete contaminated with chloride, Cem. Concr. Compos. 20 (1998) 263–381.
[26] X. Shi, N. Xie, K. Fortune, J. Gong, Durability of steel reinforced concrete in chloride environments: an overview, Constr. Build. Mater. 30 (2012) 125–138.
[27] A. Brenna, F. Bolzoni, S. Beretta, M. Ormellese, Long-term chloride-induced corrosion monitoring of reinforced concrete coated with commercial polymer-modified mortar and polymeric coatings, Constr. Build. Mater. 48 (2013) 734–744.
[28] M. Al-Methel, S. Al-Dulaijan, S.H. Al-Idi, M. Shameem, M.R. Ali, M. Maslehuddin, Performance of generic and proprietary corrosion inhibitors in chloride-contaminated silica fume cement concrete, Constr. Build. Mater. 23 (2009) 1768–1774.
[29] G. Fajardo, P. Valdez, J. Pacheco, Corrosion of steel rebar embedded in natural pozzolan based mortars exposed to chlorides, Constr. Build. Mater. 23 (2009) 768–774.

[30] L. Fedrizzi, F. Azzolini, P.L. Bonora, The use of migrating corrosion inhibitors to repair motorways concrete structures contaminated by chlorides, Cem. Concr. Res. 35 (2005) 551–561.
[31] M. Ramasubramanian, B.S. Haran, S. Popova, B.N. Popov, M.F. Petrou, R.E. White, Inhibiting action of calcium nitrite on carbon steel rebars, J. Mater. Civ. Eng. 13 (2001) 10–17.
[32] H.W. Song, H.J. Kim, V. Saraswathy, T.H. Kim, Micro-mechanics based corrosion model for predicting the service life of reinforced concrete structures, Int. J. Electrochem. Sci. 2 (2007) 341–354.
[33] V. Zivica, Significance and influence of ambient temperature as a rate factor of steel reinforcement corrosion, Indian Acad. Sci. Bull. Mater. Sci. 25 (2002) 375–379.
[34] C.L. Lambert, P. Page, Investigations of reinforcement corrosion electrochemical monitoring of steel in chloride-contaminated concrete, Mater. Struct. 24 (1991) 351–358.
[35] D. Chen, S. Mahadevan, Chloride-induced reinforcement corrosion and concrete cracking simulation, Cem. Concr. Compos. 30 (2008) 227–238.
[36] S. Guzman, J.C. Galvez, J.M. Sancho, Cover cracking of reinforced concrete due to rebar corrosion induced by chloride penetration, Cem. Concr. Res. 41 (2011) 893–902.
[37] R.D. Armstrong, L. Peggs, The behavior of lead silicate as a corrosion inhibitor for iron and zinc, Corros. Sci. 36 (1994) 749–757.
[38] N. Ohno, N. Hiroshi, K. Aramaki, Electrochemical and spectroscopic studies on inhibition mechanism of benzyl thiocyanate for iron corrosion in 1 N perchloric and hydrochloric acid solutions, Corros. Sci. 36 (1994) 583–591.
[39] M.J. Franklin, D.C. White, H.S. Isaacs, A study of carbon steel corrosion inhibition by phosphate ions and by an organic buffer using a scanning vibrating electrode, Corros. Sci. 33 (1992) 251–260.
[40] S.N. Banerjee, S. Mishra, 1,10-Phenanthroline as corrosion inhibitor for mild steel in sulfuric acid solution, Corrosion 45 (1989) 780–783.
[41] M. Ajmal, A.S. Mideen, M.A. Quraishi, 2-Hydrazino-6-methyl-benzothiazole as an effective inhibitor for the corrosion of mild steel in acidic solutions, Corros. Sci. 36 (1994) 79–84.
[42] K.L.N. Phani, S. Pitchumani, S. Muralidharan, S. Ravichandran, S.V. Iyer, Polyamino-benzoquinone polymers: a new class of corrosion inhibitors for mild steel, J. Electrochem. Soc. 142 (1995) 1478–1483.
[43] N.S. Rawat, A.K. Saxena, Corrosion inhibition of mild steel in ferric ion-containing mine waters by oxalate ions, in: Int. Corros. Conf. Series, NACE-7 (Corrosion Inhibition), 1988, pp. 150–158.
[44] C.L. Page, K.W.J. Treadaway, Aspects of the electrochemistry of steel in concrete, Nature 297 (1982) 109–115.
[45] R.B. Diegle, J.E. Slater, Influence of crystallinity on corrosion behavior of ferrous alloys, Corrosion 32 (1976) 155–157.
[46] M.G. Arber, H.E. Vivian, Inhibition of the corrosion of steel embedded in mortar, Aust. J. Appl. Sci. 12 (1961) 339–347.
[47] N.S. Berke, A Review of corrosion inhibitors in concrete, Mater. Performance 28 (1989) 41–44.
[48] B.B. Hope, A.K.C. Ip, Corrosion inhibitors for use in concrete, ACI Materi. J. 86 (1989) 602–608.
[49] A.B. Poole, Alkali silica reactivity mechanisms of gel formation and expansion, in: 9th International Conference on Alkali-Aggregate Reaction in Concrete 2, 1992, pp. 782–789.
[50] R. Cook, S.F. Radtke, Recent research on galvanized steel for reinforcement of concrete, in: D.E. Tonini, S.W. Dean Jr. (Eds.), Chloride Corrosion of Steel in Concrete, ASTM STP 713, ASTM International, Philadelphia, PA, 1977, pp. 51–60.
[51] A. Macias, C. Andrade, Corrosion rate of galvanized steel immersed in saturated solution of $Ca(OH)_2$ in the pH range of 12-13.8, Br. Corros. J. 18 (1983) 82–87.
[52] A. Macias, C. Andrade, Corrosion of galvanized steel reinforcement in alkaline solutions, Br. Corros. J. 22 (1987) 113–118.
[53] B.S. Haran, B.N. Popov, M.F. Petrou, R.E. White, Studies on galvanized carbon steel in $Ca(OH)_2$ solutions, ACI Mater. J. 97 (2000) 425–431.
[54] R.D. Armstrong, M.F. Bell, Electrochemical behavior of zinc in alkaline solution, Electrochem. 4 (1974) 1–17.
[55] R.D. Armstrong, M.F. Bell, The active dissolution of zinc in alkaline solutions, J. Electroanal. Chem. 55 (1974) 201–211.

[56] M.C.H. McKubre, D.D. McDonald, The dissolution and passivation of zinc in concentrated aqueous hydroxide, J. Electrochem. Soc. 128 (1981) 524–530.
[57] R.W. Powers, M.W. Breiter, The anodic dissolution and passivation of zinc in concentrated potassium hydroxide solutions, J. Electrochem. Soc. 116 (1991) 719–729.
[58] G. Prentice, Y. Chang, Y. Shan, A model for the passivation of the zinc electrode in alkaline electrolytes, J. Electrochem. Soc. 138 (1991) 890–894.
[59] Z. Zembura, Z. Burzynska, The corrosion of zinc in deaerated 0.1 M NaCl in the pH range from 1.6 to 13.3, Corros. Sci. 17 (1977) 871–878.
[60] M. Unz, Performance of galvanized reinforcement on calcium hydroxide solution, Proc. ACI J. 3 (1978) 91–99.
[61] E.A. Baker, K.L. Money, C.B. Sanborn, Marine corrosion behavior of bare and metallic-coated steel reinforcing rods in concrete, in: D.E. Tony, S.W. Dean Jr. (Eds.), "Chloride Corrosion of Steel in Concrete" ASTM, STP629, ASTM International, Philadelphia, PA, 1977, pp. 30–50.
[62] L. Maldonado, Chloride threshold for corrosion of galvanized reinforcement in concrete exposed in the Mexican Caribbean, Mater. Corros. 60 (2009) 536–539.
[63] F. Tittarelli, G. Moriconi, The effect of silane-based hydrophobic admixture on corrosion of galvanized reinforcing steel in concrete, Corros. Sci. 52 (2010) 2958–2963.
[64] F. Tittarelli, T. Bellezze, Investigation of the major reduction reaction occurring during the passivation of galvanized steel rebars, Corros. Sci. 52 (2010) 978–983.
[65] F. Tittarelli, G. Moriconi, Comparison between surface and bulk hydrophobic treatment against corrosion of galvanized reinforcing steel in concrete, Cem. Concr. Res. 41 (2011) 609–614.
[66] S. Liu, H. Sun, L. Sun, H. Fan, Effects of pH and Cl^- concentration on corrosion behavior of the galvanized steel in simulated rust layer solution, Corros. Sci. 65 (2012) 520–527.
[67] S. Mindess, J.F. Young, Concrete, Prentice-Hall, Upper Saddle River, New Jersey, 1991.
[68] Z.P. Bazant, Prediction of concrete creep and shrinkage: past, present and future, Nucl. Eng. Des. 201 (2001) 27–38.
[69] A.V. Saetta, R.V. Scotta, R.V. Vitalini, Analysis of chloride diffusion into partially saturated concrete, ACI Mater. J. 90 (1993) 441–451.
[70] D.A. Hausmann, Criteria for cathodic protection of steel in concrete structures, Mater. Prot. 8 (1969) 23–25.
[71] R.D. Browne, Design prediction of the life for reinforced concrete in marine and other chloride environments, Durability Build. Mater. 1 (1982) 113–125.
[72] M. Funahashi, Predicting corrosion-free service life of a concrete structure in a chloride environment, ACI Mater. J. 87 (1990) 581–587.
[73] N.C. Berke, M.C. Hicks, Predicting chloride profiles in concrete, Corrosion 50 (1994) 234–239.
[74] N.S. Berke, M.C. Hicks, Estimating the life cycle of reinforced concrete decks and marine piles using laboratory diffusion and corrosion data, in: V. Chaker (Ed.), "Corrosion Forms and Control for Infrastructure" ASTM STP2137, ASTM International, Philadelphia, PA, 1992, pp. 207–230.
[75] P.S. Mangat, K. Gumsamy, Chloride diffusion in steel fiber reinforced marine concrete, Cem. Concr. Res. 17 (1987) 385–396.
[76] K. Hornbostel, C.K. Larsen, M.R. Geiker, Relationship between concrete resistivity and corrosion rate-A literature review, Cem. Concr. Compos. 39 (2013) 60–72.
[77] P. Arora, B.N. Popov, B.S. Haran, M. Rama, S.N. Popova, R.E. White, Corrosion initiation time of steel reinforcement in a chloride environment a one dimensional solution, Corros. Sci. 39 (1997) 739–757.

CHAPTER 13

Organic Coatings

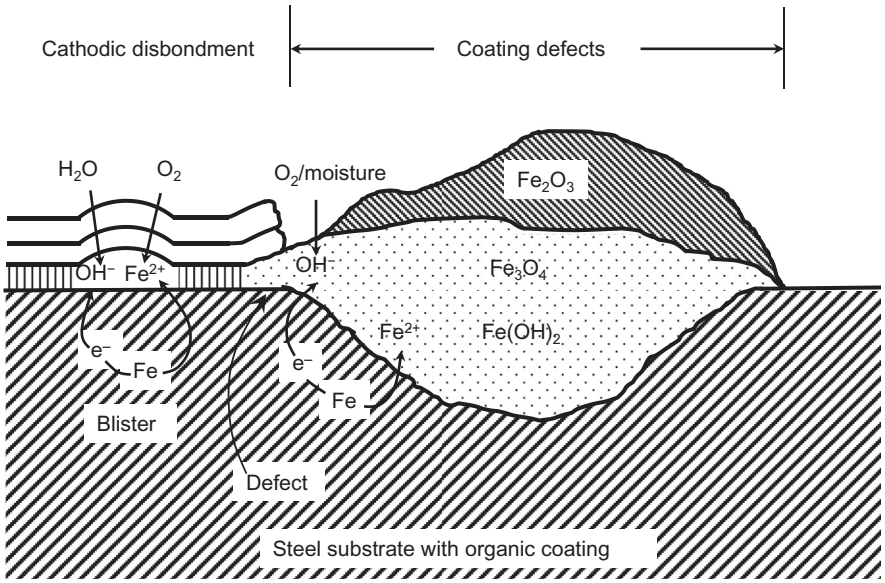

Chapter Contents

Corrosion Engineering
http://dx.doi.org/10.1016/B978-0-444-62722-3.00013-6

13.1 INTRODUCTION

Organic coatings are corrosion barriers between the underlying metal and the corrosive environment. They maintain durability of structures and provide resistance to weather, humidity, abrasion, chemical resistance, toughness, and aesthetic appearance. Organic coating efficiency depends on the mechanical properties of the coating system, type and concentration of suspended inhibitors [1,2], pretreatment of the metal surface [3], adhesion of the coating to the underlying metal base [4], and other additives that inhibit substrate corrosion. Coating formulation usually contains solvent, resin (binder), pigment, filler, and additives. When applied to the underlying metal, they provide a continuous, homogeneous coating that prevents cracking and structure breakdown during stress, water permeability, and physical aging. Protective coatings should possess low permeability, good corrosion stability, and appearance over a long period of time to justify the cost.

Organic coatings are classified according to the resin's chemical composition. The resin is dissolved or suspended in the solvent. The content and density of the resin are critical for corrosion barrier properties and oxygen and water permeability. The common resins used to manufacture single-component organic coatings are vinyls, acrylics, chlorinated rubber, alkyd (oil base), modified alkyd-silicon, amino-modified alkyd, phenolic alkyd, and epoxy ester. Two component organic coating systems are manufactured using phenolic and polyurethanes. Coating properties such as color and opacity, mechanical, and barrier properties and water transport depend on the chemical composition of the dispersed pigment, pigment volume concentration, and critical volume concentration. Besides color and opacity, the pigments protect the cured resin against UV radiation. Resins control coating properties including toughness, flexibility, time of curing, service performance, exterior weathering, and adhesion [5].

Organic solvents perform several functions. They dissolve the resin, control coating viscosity and evaporation for film formation, and affect film adhesion and coating durability. Other additives and fillers provide coating uniformity and improve coating flow, surface drying, or decrease the permeability of water and oxygen. Metal surface prepainting treatments such as phosphate and chromium conversion coatings are applied to increase adhesion of the organic coating. Before applying the top coat, it may be necessary to apply a primer coat that possesses inhibitive properties and good surface adhesion. More than one coat provides good mechanical properties, pleasant color and opacity, and good barrier properties (resistance to water and oxygen diffusion to the interface between the underlying meal and the coating). Metal corrosion rate should not exceed more than 1.2–5.0 mm/year with applied liquid coatings [6].

13.2 CLASSIFICATION OF ORGANIC COATINGS

Organic coatings are classified according to the chemical structure of the resin binder. The following resins are frequently used in the paint industry:

Vinyl resin contains the vinyl linkage group (—CH═CH_2). Vinyl coatings are copolymers of vinyl chloride and vinyl acetate with the chemical structure shown in Fig. 13.1.

Vinyl copolymers require a large amount of solvent to dissolve. Due to low solid content in the solution, vinyl coats are applied in thin coats and require several (up to five) layers to coat the substrate. Vinyl copolymer has excellent protection against acids, alkali, and water and good protection against weather. Vinyl resins are used as primers in industrial coatings with recoating intervals of over 20 years [7].

Acrylics are formulated as water-emulsion latex, thermoplastic, or thermosetting resin. They are synthesized from polymers of primarily polymethacrylate, acrylate esters, and polyethyl acrylate (Fig. 13.2). Acrylate resins are very stable in oxygen and UV light and are resistant to weathering and frequently used in the automobile industry as topcoats. Water-based acrylics are used as household paints. For ultraviolet resistance and improved weathering, acrylic resins are used as modifiers for epoxy and alkyd coatings.

Alkyd (oil base) base coatings are used in both industrial and household applications. They have excellent adhesion properties and can be used to protect against mild chemical fumes. These coatings polymerize by air oxidation at room temperature. Coatings based on alkyd resins synthesized from soybean oils possess better chemical resistance and drying times.

Modified alkyds like silicon-modified alkyds have very good gloss retention and improved heat and moisture resistance. Amino phenolic compounds increase resistance in high-humidity environments.

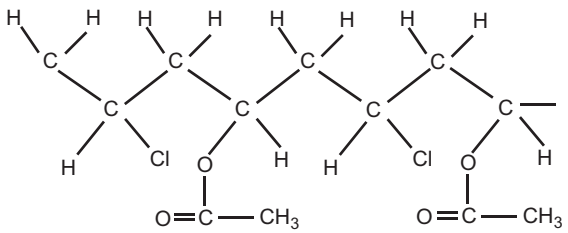

Fig. 13.1 Structure of vinyl chloride and vinyl acetate copolymer.

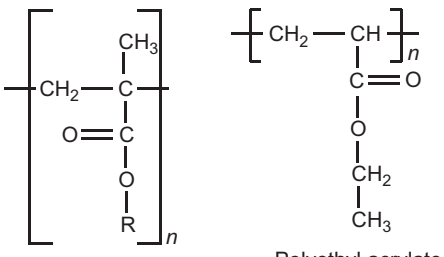

Fig. 13.2 Chemical structure of polymethacrylate and polyethyl acrylate.

Chlorinated rubber resins are produced by the chlorination of synthetic and natural rubbers. The chemical structure shown in Fig. 13.3 is synthesized by the addition of chlorine to unsaturated double bonds until the resin contains 65% chlorine. These resins have similar properties to those of vinyl resins. Plasticizers are added to increase elasticity and resin adhesion. These coatings are resistant to water but have poor resistance to sunlight.

Epoxy resins form a durable protective coating only when polymerized with amine, polyamide, or esterified fatty acids. Coal-tar epoxies are modified with coal-tar filler to improve moisture resistance. Coatings highly resistant to solvents, acids, and alkalis are based on phenolic cross-linked epoxies. These coatings are used to protect process equipment. When the phenolformaldehyde constituent of phenol is used to cross-link epoxy resin instead of amine, the coating has improved resistivity to alkalis.

Urethane resins are synthesized from isocyanates and chemical compounds with hydroxyl or urethane groups (—N—C—O—) including water, polyesters, epoxies, and acrylics [8,9]. The chemical structure of urethane coating is shown in Fig. 13.4. Polyester and epoxy have better barrier resistance to moisture and chemical attack than the acrylic polyol. Aliphatic isocyanate-based coatings are resistant to UV light and have excellent gloss and color retention.

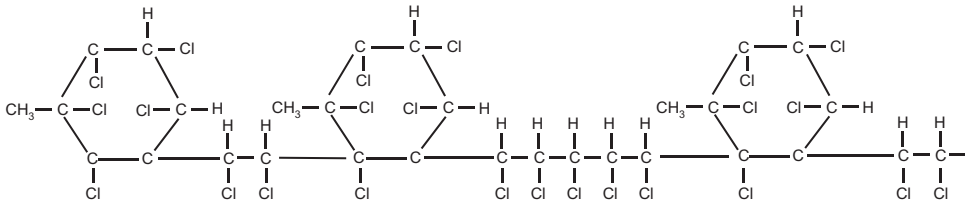

Fig. 13.3 Chemical structure of chlorinated rubber.

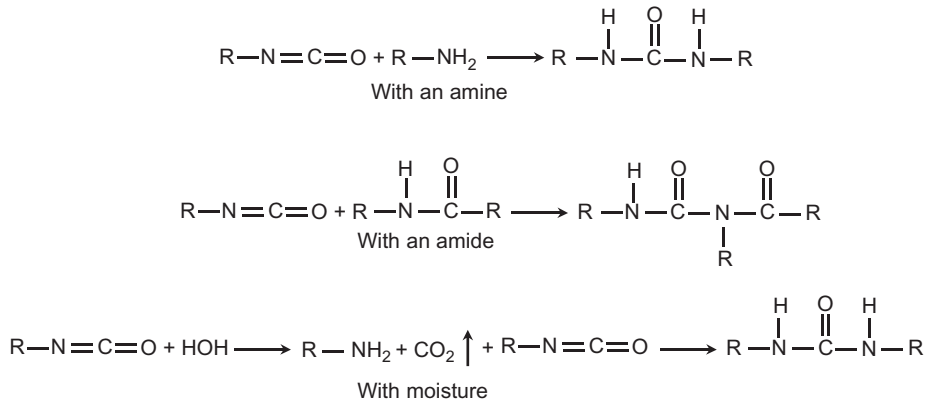

Fig. 13.4 Chemical structure of urethane coating.

Polyester resin coatings are synthesized with components that introduce unsaturation into the polymer chain (—C═C—). The paint is manufactured by mixing a dissolved polyester resin in styrene monomer with pigment and reaction inhibitor. Additional styrene and peroxide are packaged in a separate container and are mixed with the paint when applied using a dual-headed spray gun. Peroxide serves as a radical polymerization initiator for the polyester resin with monomeric styrene and cross-linking. Figure 13.5 shows the chemical structure of an isophthalic polyester resin.

13.3 PIGMENTS

Pigments provide color and opacity, decrease water permeability, and protect the cured resin against UV radiation. They also act as volume fillers to decrease the coating cost. Typical pigments materials are titanium dioxide, carbon, and iron oxides. Pigments range in size between 0.01 and 10 μm [10]. The following types of pigments are used to protect primer coatings: (i) chemically resistant pigments form barrier coatings for acidic and alkaline environment, (ii) sacrificial pigments based on zinc provide galvanic protection between pH 5 and 10, and (iii) active pigments, such as chromates, are used as inhibitors in linseed oil/alkyd primers [11–13]. Extensive studies have been performed to understand pigment properties and their role in paint formulation, application, and production. The results indicate numerous coating properties such as mechanical stress, water permeability, physical aging, glass transition temperature, and film formation are drastically changed by the pigment chemical composition, pigmentation level, particle size distribution, and pigment dispersion [14–19].

Commercial pigments provide white, black, or color covering. White pigments are zinc oxide, titanium dioxide, zinc sulfite, white lead, and lithopone, a mixture of $ZnSO_4$ and $BaSO_4$. Titanium dioxide, due to its refractive index, is the brightness pigment and is the main commercial white pigment [20]. Inorganic pigments do not absorb any light. They are known as "extender pigments" with low refractive indices. These pigments have negligible hiding power when incorporated in the binder. Inorganic pigments extensively used in the paint industry include aluminum silicates, calcium carbonates, talcs (magnesium silicates), silicon dioxide, barium sulfate, and calcium metasilicate [21]. They increase the apparent viscosity of the paint and function as thickening agents.

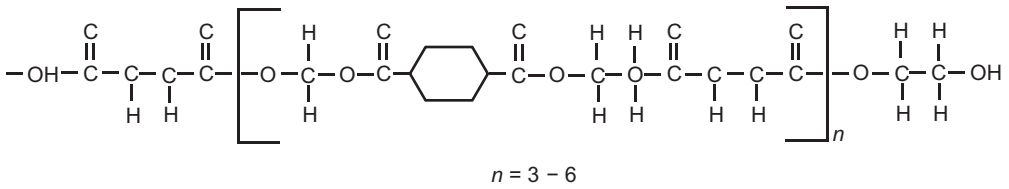

Fig. 13.5 Chemical structure of polyester coating.

Silica and alumina trihydrate are extender pigments known to reduce coating flammability and increase chemical resistance [22]. Colored inorganic pigments are yellow, red, and white iron oxides, green cadmium oxide, and chromium oxides [23]. Monoazo pigments are representative of organic colored pigments [24]. Rossi et al. [25] investigated the effect of three different color pigments (grey, red, and orange) and three different concentrations of color pigments (standard, standard +25 wt.%, and standard +50 wt.%) on appearance and corrosion protection properties of powder-deposited coatings. Figure 13.6 shows gloss variation for samples with different percentages of color pigments [25]. Increase in the percentage of color pigment results in an enhancement of the initial gloss. Because the gloss values are mainly related to the surface geometry and roughness, this observation was explained by the rheology of the polymeric paste, which can be modified by the addition of color pigments with different chemical structure [25].

"Anticorrosive pigments" used in the paint industry are imbedded in primer paints to provide "anticorrosive" properties. The coatings protect against salts, oxygen, moisture, and corrosive gases such as SO_2 and SO_3 [25,26]. The effects of pigmentation on organic coating characteristics have been reported, including curing and film formation [27], thermal expansion coefficient [28–30], mechanical properties [31–33], glass transition temperature [34,35], physical aging [36–38], water transport [39–41], and stress development [16,42–44]. Perera reviewed the effect of pigmentation on organic coating characteristics [45]. When pigment volume concentration (PVC) is smaller than critical pigment volume concentration (CPVC), increasing the pigment volume concentration results in a decrease in the thermal expansion coefficient and break strain and an increase in the elastic module, coating stress, and break stress [45]. The physical aging rate and the

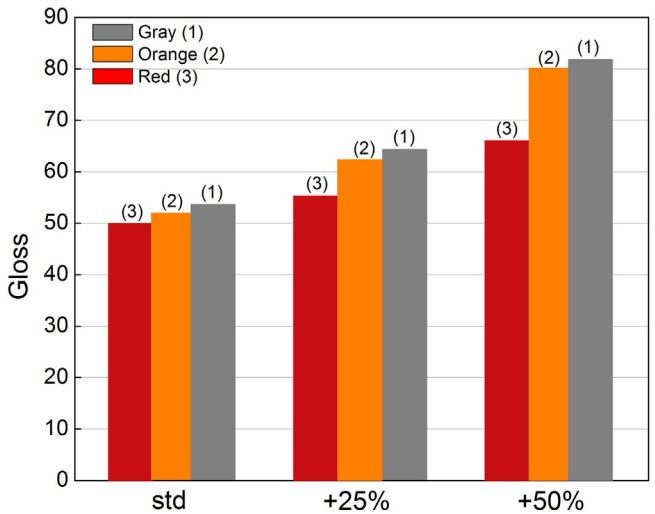

Fig. 13.6 Variation of gloss for the samples with different percentages of color pigments [25].

glass transition temperature, T_g, depends on the amount of binder adsorbed on the surface, while the water transport is controlled by the pigment volume concentration and dispersion. A summary of characteristics of various pigments for metal protective paints and outlines of the specific contributions to corrosion resistance has been discussed by Tator [46]. ASTM standards for pigments specifications are summarized in Table 13.1.

Veselý et al. [47] investigated organic coating properties' dependence on chemical composition and structure of pigment particles. Metal oxide (MO)-based pigments (M = Zn, Mg) were synthesized with different particle shapes and core-shell pigments

Table 13.1 ASTM Standards for Pigment Specification

Designation	Title
D34—08	Standard Guide for Chemical Analysis of White Pigments
D49—83(2008) e1	Standard Test Methods of Chemical Analysis of Red Lead
D50—90(2011)	Standard Test Methods for Chemical Analysis of Yellow, Orange, Red, and Brown Pigments Containing Iron and Manganese
D79—86(2009)	Standard Specification for Zinc Oxide Pigments
D81—87(2008) e1	Standard Specification for Basic Carbonate White Lead Pigment
D83—84(2008) e1	Standard Specification for Red Lead Pigment
D85—05(2011)	Standard Specification for Ochre Pigment
D126—87(2012)	Standard Test Methods for Analysis of Yellow, Orange, and Green Pigments Containing Lead Chromate and Chromium Oxide Green
D153—84(2008)	Standard Test Methods for Specific Gravity of Pigments
D185—07(2012)	Standard Test Methods for Coarse Particles in Pigments
D209—81(2012)	Standard Specification for Lampblack Pigment
D210—05(2011)	Standard Specification for Bone Black Pigment
D211—67(2012)	Standard Specification for Chrome Yellow and Chrome Orange Pigments
D263—05(2011)	Standard Specification for Chrome Oxide Green Pigment
D267—82(2008) e1	Standard Specification for Gold Bronze Powder
D279—02(2012)	Standard Test Methods for Bleeding of Pigments
D280—01(2012)	Standard Test Methods for Hygroscopic Moisture (and Other Matter Volatile Under the Test Conditions) in Pigments
D305—84(2008)	Standard Test Method for Solvent-Extractable Material in Black Pigments
D444—88(2008)	Standard Test Methods for Chemical Analysis of Zinc Yellow Pigment (Zinc Chromate Yellow)
D476—13	Standard Classification for Dry Pigmentary Titanium Dioxide Products
D478—02(2012)	Standard Specification for Zinc Yellow (Zinc Chromate) Pigments
D480—88(2008)	Standard Test Methods for Sampling and Testing of Flaked Aluminum Powders and Pastes
D520—00(2011)	Standard Specification for Zinc Dust Pigment
D521—02(2012)	Standard Test Methods for Chemical Analysis of Zinc Dust (Metallic Zinc Powder)
D561—82(2008)	Standard Specification for Carbon Black Pigment for Paint

($ZnO/CaSiO_3$ and $MgO/CaSiO_3$), and their anticorrosive properties were compared in epoxy-ester-based paints. Results indicated that MgO exhibits higher anticorrosion efficiency than zincite (ZnO). Depending on the shape, the anticorrosion efficiency for zincite particles decreases in the order:

$$\text{tetrapod ZnO} > \text{lamellar} - \text{shaped ZnO} > \text{needle} - \text{shaped ZnO}.$$

The observed anticorrosion efficiency of core-shell pigments was higher for the $MgO/CaSiO_3$ than for the zincite $ZnO/CaSiO_3$.

13.4 SOLVENTS, ADDITIVES, AND FILLERS

Solvents are used to carry dissolved or suspended resin and evaporate from the coating after application. Additives in small amounts are used as mildew inhibitors (cuprous compounds), surface-drying additives (manganese and cobalt naphthanates), and barrier-forming additives to protect the resin from heat and UV degradation. Fillers (talc and mica) decrease the permeability of oxygen and water in the coating.

13.5 SURFACE PREPARATION

Prior to paint application, the substrate should be properly prepared by removing oxides and organic impurities like oils and scales. Well-prepared metallic surfaces provide coatings with maximum protection [6,48–50]. The surface preparation procedure should follow the Steel Structure Painting Council (SSPC) standards suggested by Schweitzer [49]. Solvent cleaning (SP1), hand-tool cleaning (SP2), power-tool cleaning (SP3), white-metal blast cleaning (SP5), and pickling (SP8) are some of the commonly used methods for surface preparation prior to painting. Besides surface preparation, surface prepainting treatments such as phosphate and chromium conversion coatings are applied to increase adhesion for organic coatings and improve the barrier properties of the coatings. Conversion coatings are also used to provide corrosion inhibition by passivating the underlying metal or by inhibiting the rate of the oxygen reduction reaction. Conversion coatings are composed of chemically inert inorganic compounds capable of reducing the cathodic and anodic surface areas of the substrate.

The phosphate conversion coatings are formed by metal dissolution and phosphate precipitation. In the case of zinc phosphate film formation, iron reacts at the anodic sites through the following steps:

$$Fe + 2H_3PO_4 \rightarrow Fe\left(H_2PO_4\right)_2 + H_2 \tag{13.1}$$

In the presence of an activator:

$$2Fe + 2H_2PO_4^- + 2H^+ + 3NO_2 \rightarrow 2FePO_4 + 3H_2O + 3NO \tag{13.2}$$

$$4Fe + 3Zn^{2+} + 6H_2PO_4^{2-} + 6NO_2 \rightarrow 4FePO_4 + Zn_3(PO_4)_2 + 6H_2O + 6NO \quad (13.3)$$

At the cathodic sites, phosphophyllite $Zn_2Fe(PO_4)_2{\cdot}4H_2O$ and hopeite, $Zn_3Fe(PO_4)_2{\cdot}4H_2O$ precipitate though reactions in Eqs.(13.4) and (13.5), respectively.

$$2Zn(H_2PO_4)_2 + Fe(H_2PO_4)_2 + 4H_2O \rightarrow Zn_2Fe(PO_4)_2{\cdot}4H_2O + 4H_3PO_4 \quad (13.4)$$

$$3Zn(H_2PO_4)_2 + 4H_2O \rightarrow Zn_3(PO_4)_2{\cdot}4H_2O + 4H_3PO_4 \quad (13.5)$$

Phosphate conversion coating precipitates on the cathodic site at a pH range of 6–8, while pinholes are formed on the anodic sites. Because the phosphate conversion film is not uniformly deposited on the surface, it does not provide a good barrier protection.

Chromate conversion coatings provide improved adhesion to the organic coatings and corrosion protection to aluminum and its alloys with zinc, magnesium, and cadmium. A chromate coating forms a continuous layer of insoluble trivalent and soluble hexavalent chromium compounds. Trivalent chromic oxide provides a protective layer with excellent barrier properties, while hexavalent chromium maintains passivity by reducing to Cr(III) when the surface is damaged. This is the well-known self-healing property of chromium coatings. Hexavalent chromium reduces to Cr(III), producing hydrated hydroxides of aluminum and chromium according to Eq. (13.6):

$$6H^+ + H_2Cr_2O_7 + 6e^- \rightarrow 2Cr(OH)_3 + H_2O \quad (13.6)$$

The chromic acid-based conversion coatings and resistant barriers for decorative applications are formed according to Eq. (13.7):

$$6H_2Cr_2O_7 + 30HF + 12Al + 18HNO_3 \rightarrow 3Cr_2O_3 + Al_2O_3 + 10AlF_3 + 6Cr(NO_3)_3 + 30H_2O \quad (13.7)$$

13.6 APPLICATION

Organic coatings are applied by painting, powder coating, E-coating, plasma polymerization, and sol-gel coating [50]. The first step in painting is the selection of the primer. ASTM standards for chemical analysis of paints and paint materials are summarized in Table 13.2.

Powder coatings are applied by thermoplastics powder flame spraying or electrostatic powder spraying. In most cases, electrostatic powder spray systems are more versatile. An electrostatic charge is applied on the substrate and an opposite charge is applied to the powder in the spray head (gun). A coating film forms after heat-fusion.

E-coating or electrophoretic deposition (EDP) is a two-step process. In the first step, electrophoresis is used to transfer the charged particles to an electrode (substrate). In the

Table 13.2 ASTM Standards for Chemical Analysis of Paints and Paint Materials

Designation	Title
D564—87(2008)	Standard Test Methods for Liquid Paint Driers
D1259—06(2012)	Standard Test Methods for Nonvolatile Content of Resin Solutions
D1310—01(2007)	Standard Test Method for Flash Point and Fire Point of Liquids by Tag Open-Cup Apparatus
D1360—98(2011)	Standard Test Method for Fire Retardancy of Paints (Cabinet Method)
D1644—01(2012)	Standard Test Methods for Nonvolatile Content of Varnishes
D1978—91(2008)	Standard Guide for Analysis of Electrocoat Bath Samples
D2245—90(2011)	Standard Test Method for Identification of Oils and Oil Acids in Solvent-Reducible Paints
D2349—90(2009)	Standard Test Method for Qualitative Determination of Nature of Solvent Composition in Solvent-Reducible Paints
D2350—90(2010)	Standard Test Method for Antimony Oxide in White Pigment Separated from Solvent-Reducible Paints
D2351—90(2010)	Standard Test Method for Sulfide in White Pigment Separated from Solvent-Reducible Paints
D2352—85(2010)	Standard Test Method for Sulfur Dioxide in White Pigment Separated from Solvent-Reducible Paints
D2369—10e1	Standard Test Method for Volatile Content of Coatings
D2371—85(2010)	Standard Test Method for Pigment Content of Solvent-Reducible Paints
D2372—85(2010)	Standard Practice for Separation of Vehicle from Solvent-Reducible Paints
D2373—05(2011)	Standard Test Method for Determination of Cobalt in Paint Driers by EDTA Method
D2374—05(2011)	Standard Test Method for Lead in Paint Driers by EDTA Method
D2375—05(2011)	Standard Test Method for Manganese in Paint Driers by EDTA Method
D2613—01(2012)	Standard Test Method for Calcium or Zinc in Paint Driers by EDTA Method
D2621—87(2011)	Standard Test Method for Infrared Identification of Vehicle Solids from Solvent-Reducible Paints
D2697—03(2008)	Standard Test Method for Volume Nonvolatile Matter in Clear or Pigmented Coatings
D2698—05(2010)	Standard Test Method for Determination of the Pigment Content of Solvent-Reducible Paints by High-Speed Centrifuging
D2832—92(2011)	Standard Guide for Determining Volatile and Nonvolatile Content of Paint and Related Coatings
D3168—85(2011)	Standard Practice for Qualitative Identification of Polymers in Emulsion Paints
D3271—87(2012)	Standard Practice for Direct Injection of Solvent-Reducible Paints Into a Gas Chromatograph for Solvent Analysis

Table. 13.3 ASTM Standards for Paint Application Tools

Designation	Title
D5068—04(2013)	Standard Practice for Preparation of Paint Brushes for Evaluation
D5069—07	Standard Practice for Preparation of Paint-Roller Covers for Evaluation of Architectural Coatings
D5301—92(2012)	Standard Practice for Physical Characterization of Paint Brushes
D5913—96(2013)	Standard Test Method for Evaluation of Cleanability of Paint Brushes
D5959—12	Standard Test Method for Bulk Density of Level Paintbrush Filaments
D6337—98(2013)	Standard Practice for Physical Characterization of Woven Paint Applicator Fabrics
D6737—12	Standard Test Method for Bulk Density of Tapered Paintbrush Filaments
D6957—12	Standard Practice for Measuring Curl in Paint Brush Filling Material
D7054—04(2013)	Standard Specification for Cautionary Labeling of Extension Poles for Use with Paint Applicators Distributed In North America
D7233—08(2012)	Standard Test Method for Testing Fracture of Level Paintbrush Filaments
D7801—12	Standard Terminology for Paint Brush Application Tools
D7802—12	Standard Terminology for Paint Roller Application Tools
D7804—12	Standard Test Method for Fiber Shedding of Paint Roller Covers
D7834—13	Standard Test Method for Filling Material Shedding of Paint Brushes

second step, a compact film is formed by particle deposition [10]. ASTM standards for paint application tools are summarized in Table 13.3.

Sol-gel painting is a multistep process. In the first step a solid phase is formed through gelation of a colloidal suspension. In the second step a "dry gel," or xerogel, is formed by drying. Other steps may be used to increase the density, stabilize, introduce, or remove unwanted organic residues.

13.7 EXPOSURE TESTING

The actual service life of coatings is accurately estimated using outdoor exposure of coated specimens. In order to show any degradation in outdoor exposure, the coating testing is performed between 3 and 5 years. An accelerated testing method can be used to estimate the service life of the coating only if the method induces the same degradation mechanism as the one occurring in the field testing. Because the goal of an accelerated test is to cause corrosion in a shorter time, specimens are subjected to more severe conditions than the actual service conditions. Some of the accelerated tests suggested in the literature are immersion tests, simulated service tests, cabinet tests, electrochemical "dc" and "ac" corrosion tests, and atmospheric corrosion tests [50,51]. Attempts to speed up the natural corrosion processes were made by changing humidity, pH, UV radiation intensity, and

corrosive solution concentration. However, it is still necessary to establish a valid correlation between accelerated test performance and the actual service-life testing. ASTM standards for accelerated testing for organic coatings are summarized in Table 13.4.

The salt spray test provides testing under atmospheric corrosion conditions. The sample is exposed to a continuously sprayed salt solution in a humidified, temperature-controlled closed chamber. The chamber is composed of an atomizing nozzle and a salt solution

Table 13.4 Standards for Accelerated Testing

Designation	Title
D609—00(2012)	Standard Practice for Preparation of Cold-Rolled Steel Panels for Testing Paint, Varnish, Conversion Coatings, and Related Coating Products
D822/D822M—13	Standard Practice for Filtered Open-Flame Carbon-Arc Exposures of Paint and Related Coatings
D870—09	Standard Practice for Testing Water Resistance of Coatings Using Water Immersion
D1006/D1006M—13	Standard Practice for Conducting Exterior Exposure Tests of Paints on Wood
D1014—09	Standard Practice for Conducting Exterior Exposure Tests of Paints and Coatings on Metal Substrates
D1735—08	Standard Practice for Testing Water Resistance of Coatings Using Water Fog Apparatus
D2201—99(2011)	Standard Practice for Preparation of Zinc-Coated and Zinc-Alloy-Coated Steel Panels for Testing Paint and Related Coating Products
D2247—11	Standard Practice for Testing Water Resistance of Coatings in 100% Relative Humidity
D2248—01a(2013)	Standard Practice for Detergent Resistance of Organic Finishes
D2454—08	Standard Practice for Determining the Effect of Overbaking on Organic Coatings
D2485—91(2013)	Standard Test Methods for Evaluating Coatings for High Temperature Service
D2803—09	Standard Guide for Testing Filiform Corrosion Resistance of Organic Coatings on Metal
D3361/D3361M—13	Standard Practice for Unfiltered Open-Flame Carbon-Arc Exposures of Paint and Related Coatings
D3891—08	Standard Practice for Preparation of Glass Panels for Testing Paint, Varnish, Lacquer, and Related Products
D4141—07	Standard Practice for Conducting Black Box and Solar Concentrating Exposures of Coatings
D4585/D4585M—13	Standard Practice for Testing Water Resistance of Coatings Using Controlled Condensation
D4587—11	Standard Practice for Fluorescent UV-Condensation Exposures of Paint and Related Coatings

Table 13.4 Standards for Accelerated Testing—cont'd

Designation	Title
D5031/D5031M—01(2006)	Standard Practice for Enclosed Carbon-Arc Exposure Tests of Paint and Related Coatings
D5722—08	Standard Practice for Performing Accelerated Outdoor Weathering of Factory-Coated Embossed Hardboard Using Concentrated Natural Sunlight and a Soak-Freeze-Thaw Procedure
D5894—10	Standard Practice for Cyclic Salt Fog/UV Exposure of Painted Metal, (Alternating Exposures in a Fog/Dry Cabinet and a UV/Condensation Cabinet)
D6675—01(2011)	Standard Practice for Salt-Accelerated Outdoor Cosmetic Corrosion Testing of Organic Coatings on Automotive Sheet Steel
D6695—08	Standard Practice for Xenon-Arc Exposures of Paint and Related Coatings
D7356/D7356M—13	Standard Test Method for Accelerated Acid Etch Weathering of Automotive Clearcoats Using a Xenon-Arc Exposure Device
D7869—13	Standard Practice for Xenon Arc Exposure Test with Enhanced Light and Water Exposure for Transportation Coatings

reservoir. The test specifications are given in ASTM B117-03 (standard practice for operating salt spray (fog) apparatus) [52], ASTM G85-11 (standard practice for modified salt spray (fog) testing) [53], and ASTM D5894-10 (standard practice for cyclic salt fog/UV exposure of painted metal) [54]. The accelerated corrosion testing reported in the literature found no correlation between the salt spray testing and actual service-life testing. Service-life evaluation was improved by developing a cycling weathering test to mimic the outdoor environment. The results obtained from these tests indicated better correlation to the actual service-life coating evaluation [55]. The average relative humidity in coastal environments is ~60% during the summer. The humidity test is performed according to ASTM D 2247-02 specifications [56].

The prohesion test (ASTM G85-11) is a modified salt spray test widely used to evaluate the corrosion degradation of organic coatings [50,53]. Coated samples are placed against heated walls and exposed to a salt spray of 0.35% ammonium sulfate and 0.05% sodium chloride at 35 °C for 1 h and allowed to dry for 1 h at 40 °C. Many cycles of exposure are applied, as required, to the coated samples [57]. Skerry and Simpson [58] supplemented the prohesion test with continuous condensation and an alternate cycle of UV exposure. The Norwegian Norsok M501 is a standardized test for materials under UV exposure with salt fog, humidity, and a conditioning period at room temperature. In addition to the several thousand hours necessary to complete the test, damage evaluation of these tests is subjective and depends on the ability and experience of the operator.

Bierwagen et al. [59] and Li et al. [60] used electrochemical techniques to study the performance of organic coatings at room temperature. The authors described an experimental setup to establish the cumulative effect of degradation processes occurring during material testing that varied temperature above and below the glass transition temperature of the resin. The objective was to evaluate the cumulative effects of a thermal cycling on the organic coating properties by changing the electrochemical parameters such as electrolyte transport through the film, loss of adhesion, chemical and physical aging caused by thermal effects, and variation of dielectric constants. Thermal cycling controlled by electrochemical parameters was expected to result in the ranking of different materials by constituents and application purposes and produce reliable data in a short period of time [60].

Fedrizzi et al. [51] performed thermal cycling tests using electrochemical impedance spectroscopy (EIS) at different temperatures to determine organic coating barrier and adhesion properties. It was found that a proper fitting procedure with meaningful parameters is necessary to obtain reliable EIS data. Thermal cycling, as expected, produced accelerated degradation at high temperatures enhanced by exposure to wet environments. Water uptake contributed to the loss of adhesion from the substrate. The data evaluation method and aging procedure resulted in quick and precise evaluations of adhesion and barrier properties.

ASTM standards for evaluation of weathering effects are summarized in Table 13.5. The corrosion process of the underlying metal begins when water and dissolved oxygen

Table 13.5 ASTM Standards for Evaluation of Weathering Effects

Designation	Title
D610—08(2012)	Standard Practice for Evaluating Degree of Rusting on Painted Steel Surfaces
D660—93(2011)	Standard Test Method for Evaluating Degree of Checking of Exterior Paints
D661—93(2011)	Standard Test Method for Evaluating Degree of Cracking of Exterior Paints
D662—93(2011)	Standard Test Method for Evaluating Degree of Erosion of Exterior Paints
D714—02(2009)	Standard Test Method for Evaluating Degree of Blistering of Paints
D772—86(2011)	Standard Test Method for Evaluating Degree of Flaking (Scaling) of Exterior Paints
D1654—08	Standard Test Method for Evaluation of Painted or Coated Specimens Subjected to Corrosive Environments
D4214—07	Standard Test Methods for Evaluating the Degree of Chalking of Exterior Paint Films
D7087—05a(2010)	Standard Test Method for An Imaging Technique to Measure Rust Creepage at Scribe on Coated Test Panels Subjected to Corrosive Environments

from the environment permeate the coating. ASTM standard D1653 is used to estimate water permeability [61].

The coating adhesion tests estimate the coating adhesion to the underlying metal. Methods that are used for adhesion testing are the knife adhesion test, pull-off, scratch adhesion test, and the tape test. The abrasion resistance tests estimate coating durability under mechanical stress. It is performed with a Taber Abraser according to the ASTM standard D4060-01 [62]. Table 13.6 summarizes standardized accelerated tests such as wet and dry cycling, alternating UV/condensation cycling, wet/dry salt-spray testing, wet/dry humidity cycling [50].

Table 13.6 Overview of Standardized Accelerated Tests [50]

Test Method	Conditions
Cyclic tests	
ASTM G85—Annex 5	Wet and dry cycling (1 h of fog (0.05 wt% $NaCl^+$ 0.35 wt% $(NH_4)_2SO_4$) at ambient temperature and 1 h of drying at 35 °C)
ASTM G 154 ISO 4892-3	Coated specimens are exposed alternating UV/condensation cycles
Advanced Cyclic tests	
ASTM D5894 ISO 20340	Alternating UV/condensation cycles and wet/dry salt-spray cycles ISO 20340 includes an optional freeze cycle
GM 9540P/B (General Motors)	Wet/dry and humidify cycling. Electrolytic solution: 0.9% NaCl, 0.1% $CaCl_2$, 0.25% $NaHCO_3$, pH: 6-8 Total cycle time: 24 h the typical duration of the test is 80 cycles
CCT-I, IV (Nissan)	Wet/dry and humidity cycling. Electrolytic solution: 5% NaCl. The typical duration of the test is 200 cycles (1600 h) for CCT-I and 50 cycles (1200 h) for CCT-IV
VDA 621-415	Wet/dry and humidify cycling. High time of wetness, poor correlation for zinc pigments and galvanized steel. Also used for testing heavy in structure paints
HCT (Hoogovens Cyclic Test)	Based on actual weathering conditions in the Netherlands. The test simulates 2 years of exposure including daily and seasonal variations in 1680 h. The temperature and relative humidity varied from respectively 25 to 50 °C and 50% to 98%
Other test	
SCAB (Simulated Corrosion Atmospheric Breakdown) Test: ISO 11474	Accelerated outdoor corrosion test. Test specimens exposed outdoors are periodically sprayed with a salt solution

13.8 ELECTROCHEMICAL TECHNIQUES

The cathodic disbondment tests were developed from investigations reported by Wiggle and Stone [63,64] in the late sixties. A rapid disbondment was observed at larger defects of the coating when using cathodic polarization technique in NaCl solution. Electrochemical techniques, including electrochemical impedance spectroscopy, provide results quickly [65–70]. They can be used to predict coating performance prior to any visual manifestation of corrosion damage. The cathodic disbondment test is performed either at room temperature or at 65 °C for a period of 28 days [71,72]. In this test, current is applied between the cathode (coated sample) and the anode (platinum electrode) at a constant voltage of 1.5 V vs. SCE. An intentional hole of 3.5 mm is made on the coated sample and it is immersed in 3.5% NaCl solution. After 28 days, the measured disbonded area around the hole is converted into millimeters radius. Cathodic disbondment in the salt fog test occurs due to the reduction of oxygen and formation of hydroxide ions:

$$O_2 + 2H_2O + 4e^- \rightarrow 4OH^- \tag{13.8}$$

The corrosion process begins when water with dissolved oxygen permeates through the pores and defects of the coating and reaches the underlying metal.

$$Fe \rightarrow Fe^{+2} + 2e^- \tag{13.9}$$

The alkaline hydroxide ions disbond the coatings through saponification. Figure 13.7 shows the corrosion mechanisms when the disbondment occurs at the coating pores (microscopic coating defects) producing blisters at the defects of the coating.

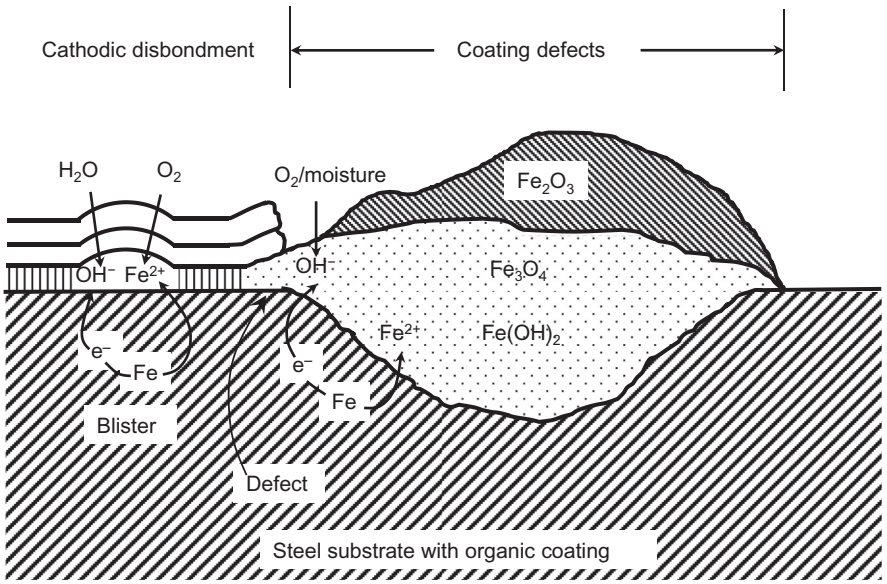

Fig. 13.7 Corrosion mechanism at the pores (microscopic coating defects) and at the defect in the coating.

13.9 EVALUATION METHODS

The ASTM standard methods for evaluation of specimens subjected to accelerated tests are summarized in Table 13.7. The performance rating depends on subjective visual observation made by the operator. Also, high corrosion resistant coatings show no visual signs of deterioration after weathering.

13.10 CHEMICAL AND PHYSICAL AGING OF ORGANIC COATINGS

Irreversible modifications in the coating are induced in chemical aging caused by temperature, UV radiation, and moisture. Chemical aging results in detachment or cracking of the coating, causing underlying metal degradation and coating disintegration [73–77]. High temperature and moisture induce hydrolysis and thermal degradation, while UV radiation oxidizes the double bonds of the polymer resulting in cross-linking and polymer chain scission. Temperature, moisture, and UV radiation change the chemical

Table 13.7 The ASTM Standard Evaluation Methods of Specimens Subjected to Accelerated Tests

Standard	Aspect	Description
ISO 4628-2 ASTM D714	Blistering	These standards describe a method for assessing the degree of blistering of coatings by comparison with pictorial standards. The ISO standard has adopted the pictorial standards from ASTM and includes the correlation between the ISO and ASTM rating systems
ISO 4628-3 ASTM D610	Rusting	These standards describe a method for assessing the degree of rusting of coated steel surfaces by comparison with pictorial standards The ISO standards includes the correlation between the ISO and ASTM rating systems
ISO 4628-4	Cracking	These standards describe a method for assessing the degree of cracking of coatings by comparison with pictorial standards
ISO 4628-5 ASTM D772	Flaking	These standards describe a method for assessing the degree of flaking (scaling) of coatings by comparison with pictorial standards
ISO 4628-6 ISO 4628-7	Chalking	These standards describe a method for assessing the degree of chalking of coatings by comparison with pictorial standards
ISO 4628-8 ASTM D1654	Delamination and corrosion	These standards describe a method for assessing delamination and corrosion around a scribe in a coating on a test panel or other test specimens. The ISO standard describes one method that involves the use of pictorial standards. Both standards include numerical rating of failure

composition of the coating, decreasing chemical stability and toughness while increasing hydrothermal stress. These properties change with chemical aging and result in poor coating adhesion and substrate cohesion [44,78,79].

Cooling organic coatings below the glass transition temperature transfers the polymer to a nonequilibrium state due to higher enthalpy, entropy, and volume values than those in the equilibrium state, causing changes in the thermal, dielectric, and mechanical properties. The material becomes more brittle and harder due to a decrease in stress relaxation and an increase in coating density [80–86]. Struik [80] defined these phenomena as physical polymer aging. Physical aging occurs because organic coatings are formulated to be in the glassy state under normal service conditions. The glassy state induces qualities in the coating such as resistance to erosion, dirt retention, blocking, and scratching. Physical aging is reversed by reheating the polymer to temperatures above the glass transition temperature.

Physical aging of organic coatings subjected to thermal and hygroscopic cycles similar to those in actual cycle-life testing was investigated by Perera [87]. The hydrothermal history was found to affect enthalpy, relaxation, and thermal stress. The physical aging rate of organic compounds increases with decreasing aging temperature and relative humidity. The observed aging rates were explained by the decrease in glass transition temperature and mobility of the polymer chain segment or an increase in relative humidity. Perera [88] reviewed the origin of physical aging and the effect of coating properties that influence coating durability such as thermal expansion, film contraction, elastic modulus, stress and strain at break, stress corrosion, and thermal stress. The reported evidence indicates that the increase in rigidity and relaxation time, decrease in ductility and fracture resistance, sometimes in combination with stress, contributes to coating contraction. Changes in these material properties are caused by physical aging due to environmental conditions, especially the difference between the real glass temperature, which is affected by the humidity, aging temperature, and change in the chemical composition of the coating such as pigmentation, structure, and cross-link density. Dependence of volume (V), enthalpy (H), and entropy ($S^{'}$) on the aging temperature (T_a) and glass transition temperature is shown in Fig. 13.8 [88]. At temperatures higher than the glass transition temperature, the high mobility of the macromolecular segments results in a decrease of V, H, and S′. The system under these conditions is in equilibrium state. At temperatures lower than the glass transition temperature (e.g., in the glassy region), the motions of the polymer chain are frozen, reducing the mobility of macromolecular segments. In this case, a decrease of thermodynamic properties cannot follow the change in temperature creating a nonequilibrium state. Because the mobility of macromolecular segments is reduced in the nonequilibrium states, a magnitude decrease of thermodynamic properties is observed at any temperature in the glassy region until they reach the equilibrium value (Fig. 13.8). The physical aging rate and magnitude of the change in coating properties is controlled by the actual aging temperature. The final magnitude change of the coating properties depends on the difference between actual aging temperature and glass transition temperature. Thermal, mechanical, optical, and transport properties of the polymer coating are controlled by the decrease of thermodynamic properties during the transition to equilibrium state [89–92].

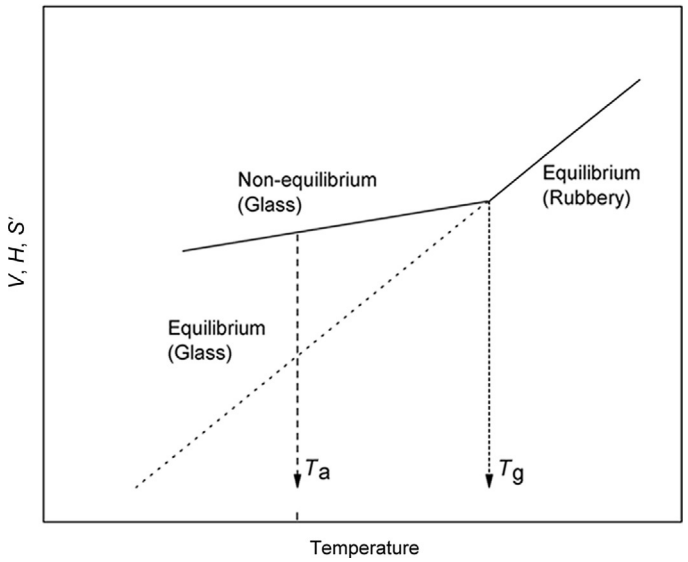

Fig. 13.8 Dependence of volume (V), enthalpy (H), and entropy (S) on aging temperature (T_a) and glass transition temperature (T_g) [88].

As shown in Fig. 13.9, physical aging causes small coating contraction [93]. Smaller differences between aging temperature and glass transition temperature resulted in a higher initial contraction rate. The contraction under equilibrium at low temperatures is more significant than at higher temperature [93].

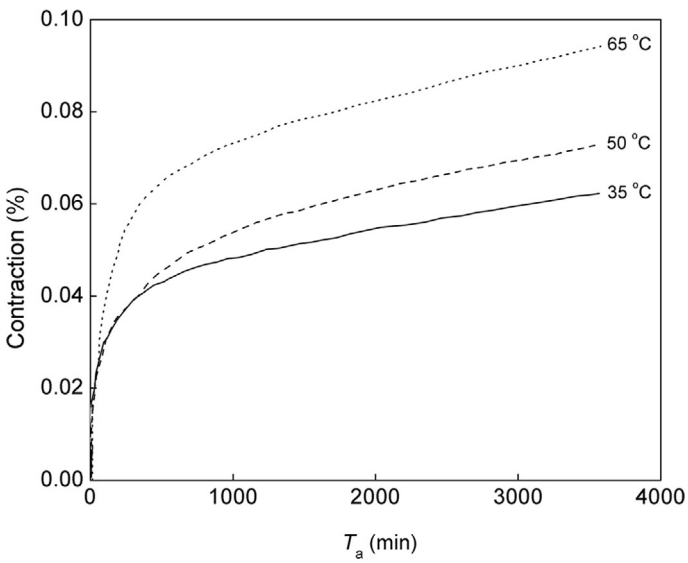

Fig. 13.9 Contraction as a function of aging time (t_a) for a nonpigmented coating at three aging temperatures T_a [93].

REFERENCES

[1] L.H. Yang, F.C. Liu, E.H. Han, Effects of P/B on the properties of anticorrosive coatings with different particle size, Prog. Org. Coat. 53 (2005) 91–98.

[2] M.V. Popa, P. Drob, E. Vasilescu, J.C. Mirza-Rosca, A. Santana-Lopez, C. Vasilescu, S.I. Drob, The pigment influence on the anticorrosive performance of some alkyd films, Mater. Chem. Phys. 100 (2006) 296–303.

[3] G. Grundmeier, B. Rossenbeck, K.J. Roschmann, P. Ebbinghaus, M. Stratmann, Corrosion protection of Zn-phosphate containing water borne dispersion coatings, Corros. Sci. 48 (2006) 3716–3730.

[4] A. Kalendova, D. Vesely, P. Kalenda, Pigments with Ti^{4+}—Zn^{2+}, Ca^{2+}, Sr^{2+}, Mg^{2+}-based on mixed metal oxides with spinel and perovskite structures for organic coatings, Pigm. Resin Technol. 36 (2007) 3–17.

[5] T.N. Bortak, Guide to Protective Coatings: Inspection and Maintenance, United States Department of the Interior Bureau of Reclamation Technical Service Center, Washington DC, 2002.

[6] K.B. Tator, J.D. Trim, K.E. Buffington, S.R. Calhoun, Influence of surface preparation upon performance of protective coatings in various atmospheres, Mater. Perform. 22 (1983) 48–55.

[7] K.B. Tator, (1987). Organic coatings and linings, in: Metals Handbook, ninth ed., in: Corrosion, Vol. XIII, ASM International, Metals Park, OH, 1987, pp. 399–418.

[8] M. Kathalewar, P. Joshi, A. Sabnis, V.C. Malshe, Non-isocyanate polyurethanes: from chemistry to applications, RSC Adv. 3 (2013) 4110–4129.

[9] J. Guan, Y. Song, Y. Lin, X. Yin, M. Zua, Y. Zhao, X. Tao, Progress in study of non-isocyanate polyurethane, Ind. Eng. Chem. Res. 50 (2013) 6517–6527.

[10] P.A. Schweitzer, Corrosion of Linings and Coatings, Taylor and Francis Group, New York, 2007.

[11] R.C. Schiek, Lead chromate pigments, in: in: T.C. Patton (Ed.), Pigment Handbook, vol. I, Willey Interscience, New York, 1973, pp. 357–370.

[12] E. Herrmann, Inorganic colored pigments, in: G.D. Parfitt, K.S.W. Sing (Eds.), Characterization of Pigment Surfaces, Academic Press, London, 1976, pp. 209–229.

[13] P. Merchak, Colored organic pigments, in: K. Joseph (Ed.), The Gardner Sward Handbook: Paint and Coating Testing Manual, 14th ed., in: ASTM Manual, Vol. XVII, ASTM International, 100 Barr Harbor Drive, West Conshohocken, PA, 1995, pp. 190–208.

[14] F.B. Stieg, Influence of PVC [pigment volume concentration] on paint properties, Prog. Org. Coat. 1 (1973) 351–373.

[15] A. Toussaint, Influence of pigmentation on the mechanical properties of paint films, Prog. Org. Coat. 2 (1974) 237–267.

[16] D.Y. Perera, E.D. Vandan, Internal stress in pigmented thermoplastic coatings, J. Coating Technol. 53 (1981) 40–45.

[17] D.Y. Perera, E.D. Vandan, Effect of pigment on internal stress in latex coatings, J. Coating Technol. 56 (1984) 47–53.

[18] A. Al-Turaif, P. Lepoutre, Evolution of surface structure and chemistry of pigmented coatings during drying, Prog. Org. Coat. 38 (2000) 43–52.

[19] A. Al-Turaif, P. Lepoutre, Effect of sintering on surface chemistry and surface energy of pigmented latex coatings, J. Appl. Polym. Sci. 82 (2001) 968–975.

[20] J.H. Braun, White pigments, in: K. Joseph (Ed.), The Gardner Sward Handbook: Paint and Coating Testing Manual, 14th ed., in: ASTM Manual, Vol. XVII, ASTM International, 100 Barr Harbor Drive, West Conshohocken, PA, 1995, pp. 159–177.

[21] R. Eppler, Extender pigments, in: K. Joseph (Ed.), The Gardner Sward Handbook: Paint and Coating Testing Manual, 14th ed., in: ASTM Manual, Vol. XVII, ASTM International, 100 Barr Harbor Drive, West Conshohocken, PA, 1995, pp. 217–224.

[22] S.H. Mansour, Polymeric composites containing alumina trihydrate and silica, J. Elastom. Plast. 32 (2000) 248–264.

[23] P.A. Lewis, Inorganic colored pigments, in: K. Joseph (Ed.), The Gardner Sward Handbook: Paint and Coating Testing Manual, 14th ed., in: ASTM Manual, Vol. XVII, ASTM International, 100 Barr Harbor Drive, West Conshohocken, PA, 1995, pp. 209–213.

[24] V.C. Malshe, A.M. Bendale, Polymeric pigments, Surf. Coat. Int. Part B: Coat. Trans. 85 (2002) 287–294.
[25] S. Rosi, M. Fedel, F. Deflorian, S. Zanol, Influence of different color pigments on the properties of powder deposited organic coatings, Mater. Des. 50 (2013) 332–341.
[26] L. Veleva, Protective coatings and inorganic anti-corrosion pigments, in: K. Joseph (Ed.), The Gardner Sward Handbook: Paint and Coating Testing Manual, 14th ed., in: ASTM Manual, Vol. XVII, ASTM International, 100 Barr Harbor Drive, West Conshohocken, PA, 1995, pp. 238–255.
[27] R.B. Prime, Thermosets, in: E.A. Turi (Ed.), second ed., in: Thermal Characterization of Polymeric Materials, vol. II, Academic Press, New York, 1997, pp. 1673–1698.
[28] L.E. Nielsen, Mechanical Properties of Polymers and Composites, Marcel Dekker, New York, 1974.
[29] K. Sato, The mechanical properties of filled polymers, Prog. Org. Coat. 4 (1976) 271–302.
[30] A. Zosel, Mechanical behavior of coating films, Prog. Org. Coat. 8 (1980) 47–79.
[31] M. Narkis, Crazing in glassy polymers. Polymer-glass bead composites, Polym. Eng. Sci. 15 (1975) 316–320.
[32] M. Narkis, Size distribution of suspension-polymerized unsaturated polyester beads, J. Appl. Polym. Sci. 23 (1979) 2043–2048.
[33] D. Quemada, Rheology of concentrated disperse systems. III. General features of the proposed non-Newtonian model. Comparison with experimental data, Rheol. Acta 17 (1978) 643–653.
[34] P. Bajaj, N.K. Jha, A. Kumar, Effect of coupling agents on thermal and electrical properties of mica/epoxy composites, J. Appl. Polym. Sci. 56 (1995) 1339–1347.
[35] R.P. Chartoff, Thermoplastic polymers, in: E.A. Turi (Ed.), second ed., in: Thermal Characterization of Polymeric Materials, Vol. I, Academic Press, New York, 1997, pp. 537–563.
[36] S.L. Simon, G.B. McKenna, Development of isotropic residual stresses during thermoset cure: effects of cure history and resin properties, Proc. Am. Soc. Compos. 15 (2000) 127–134.
[37] S.L. Simon, G.B. McKenna, Quantitative analysis of errors in TMDSC in the glass transition region, Thermochim. Acta 348 (2000) 77–89.
[38] D.Y. Perera, Physical aging of organic coatings, Prog. Org. Coat. 47 (2003) 61–76.
[39] D.Y. Perera, Water transport in organic coatings, Prog. Org. Coat. 2 (1973) 57–80.
[40] J. Crank, A theoretical investigation of the influence of molecular relaxation and internal stress on diffusion in polymers, J. Polymer Sci. 11 (1953) 151–168.
[41] N.S. Sangaj, V.C. Malshe, Permeability of polymers in protective organic coatings, Prog. Org. Coat. 50 (2004) 28–39.
[42] D.Y. Perera, Stress phenomena in organic coatings, in: K. Joseph (Ed.), The Gardner Sward Handbook: Paint and Coating Testing Manual, 14th ed., in: ASTM Manual, Vol. XVII, ASTM International, 100 Barr Harbor Drive, West Conshohocken, PA, 1995, pp. 585–602.
[43] D.Y. Perera, Internal stress and film formation in emulsion paints, J. Oil Colour Chem. As. 68 (1985) 275–281.
[44] D.Y. Perera, Internal stress in latex coatings, J. Coating Technol. 56 (1984) 111–118.
[45] D.Y. Perera, Effect of pigmentation on organic coating characteristics, Prog. Org. Coat. 50 (2004) 247–262.
[46] K.B. Tator, Coatings, in: P.A. Schweitzer (Ed.), Corrosion Resistance and Corrosion Protection Handbook, Marcel Dekker, New York, 1983, pp. 453–489.
[47] D. Veselý, A. Kalendová, P. Němec, Properties of organic coatings depending on chemical composition and structure of pigment particles, Surf. Coat. Tech. 204 (2010) 2032–2037.
[48] K.B. Tator, How coatings protect—and why they fail, Canadian Paint Finish. 8 (1977) 30–34.
[49] P.A. Schweitzer, Surface preparation and application, in: Paint and Coatings: Applications and Corrosion Resistance, Taylor & Francis Group, New York, 2006, pp. 67–87.
[50] A.S. Khanna, High-Performance Organic Coatings, Woodhead Publishing Limited, Cambridge, England, 2008.
[51] L. Fedrizzi, A. Bergo, F. Deflorian, L. Valentinelli, Assessment of protective properties of organic coatings by thermal cycling, Prog. Org. Coat. 48 (2003) 271–280.
[52] ASTM B117-03, Standard practice for operating salt spray (fog) apparatus, in: Annual Book of ASTM Standards, ASTM International, 100 Barr Harbor Drive, West Conshohocken, PA, 2003.

[53] ASTM G85-11, Standard practice for modified salt spray (fog) testing, in: Annual Book of ASTM Standards, vol. 03.02, ASTM International, 100 Barr Harbor Drive, West Conshohocken, PA, 2002.
[54] ASTM D5894-10, Standard practice for cyclic salt fog/UV exposure of painted metal (alternating exposures in a fog/dry cabinet and a UV/condensation cabinet, in: Annual Book of ASTM Standards, Vol. 06.01, ASTM International, 100 Barr Harbor Drive, West Conshohocken, PA, 2010.
[55] R. Hu, S. Zhang, J. Bu, C. Lin, G. Song, Recent progress in corrosion protection of magnesium alloys by organic coatings, Prog. Org. Coat. 73 (2012) 129–141.
[56] ASTM D2247-02, Standard practice for testing water resistance of coatings in 100% relative humidity, in: Annual Book of ASTM Standards, vol. 06.02, ASTM International, 100 Barr Harbor Drive, West Conshohocken, PA, 2002.
[57] N.D. Cremer, Cyclic methods of accelerated corrosion testing, Polym. Paint Col. J. 180 (1990) 640–642.
[58] B.S. Skerry, C.H. Simpson, Accelerated test method for assessing corrosion and weathering of paints for atmospheric corrosion control, Corrosion 49 (1993) 663–674.
[59] G.P. Bierwagen, J. Li, L. Ellingson, D.E. Tallman, Studies of a new accelerated evaluation method for coating corrosion resistance-thermal cycling testing, Prog. Org. Coat. 39 (2000) 67–78.
[60] J. Li, C.S. Jeffcoate, G.P. Bierwagen, D.J. Mills, D.E. Tallman, Thermal transition effects and electrochemical properties in organic coatings: part 1-Initial studies on corrosion protective organic coatings, Corrosion 54 (1998) 763–771.
[61] ASTM D1653, Standard test methods for water vapor transmission of organic coating film, in: Annual Book of ASTM Standards, vol. 06.01, ASTM International, 100 Barr Harbor Drive, West Conshohocken, PA, 1993.
[62] ASTM D4060-01, Standard test method for abrasion resistance of organic coatings by the Taber Abrader, in: Annual Book of ASTM Standards, vol. 06.01, ASTM International, 100 Barr Harbor Drive, West Conshohocken, PA, 2001.
[63] R.R. Wiggle, A.G. Smith, J.V. Petrocelli, Paint adhesion failure mechanisms on steel in corrosive environments, J. Paint Technol. 40 (1968) 174–186.
[64] J. Stone, Paint adhesion on a scribed surface—the PASS test, J. Paint. Technol. 41 (1969) 661–669.
[65] J. Zhang, C. Wu, Corrosion protection behavior of AZ31 magnesium alloy with cathodic electrophoretic coating pretreated by silane, Prog. Org. Coat. 66 (2009) 387–392.
[66] J. González-Guzmán, J.J. Santana, S. González, R.M. Souto, Resistance of metallic substrates protected by an organic coating containing glass flakes, Prog. Org. Coat. 68 (2010) 240–243.
[67] K. Aramaki, T. Shimura, Corrosion prevention of passivated iron in 0.1 M NaCl by coverage with an ultrathin polymer coating and healing treatment in 0.1 M $NaNO_3$, Corros. Sci. 52 (2010) 1464–1471.
[68] J.J. Santana, J. González-Guzmán, J. Izquierdo, S. González, R.M. Souto, Sensing electrochemical activity in polymer-coated metals during the early stages of coating degradation by means of the scanning vibrating electrode technique, Corros. Sci. 52 (2010) 3924–3931.
[69] F. Cadenaa, L. Irustab, M.J. Fernandez-Berridi, Performance evaluation of alkyd coatings for corrosion protection in urban and industrial environments, Prog. Org. Coat. 76 (2013) 1273–1278.
[70] Y. Zhanga, Y. Shaoa, Z. Tao, G. Menga, F. Wanga, High corrosion protection of a polyaniline/organophilic montmorillonite coating for magnesium alloys, Prog. Org. Coat. 76 (2013) 804–811.
[71] ASTM G8-96, Standard test methods for cathodic disbondmnet of pipeline coatings, in: Annual Book of ASTM Standards, vol. 06.02, ASTM International, 100 Barr Harbor Drive, West Conshohocken, PA, 1996.
[72] J.C. Holzwarth, R.F. Thomson, A.L. Boegehold, A study of nonprotective rust formation on auto-body sheet steel, SAE Trans. 64 (1956) 221–228.
[73] D.R. Bauer, D.F. Mielewski, J.L. Gerlock, Photooxidation kinetics in crosslinked polymer coatings, Polym. Deg. Stab. 38 (1992) 57–67.
[74] D.F. Mielewski, D.R. Bauer, J.L. Gerlock, Determination of hydroperoxide concentrations in crosslinked polymer coatings containing hindered amine light stabilizers, Polym. Deg. Stab. 41 (1993) 323–331.
[75] D.R. Bauer, Application of failure models for predicting weatherability in automotive coatings, ACS Symp. Series 722 (1999) 378–395.

[76] D.R. Bauer, Chemical criteria for durable automotive topcoats, J. Coating Technol. 66 (1994) 57–65.
[77] D.R. Bauer, Predicting in-service weatherability of automotive coatings: a new approach, J. Coating Technol. 69 (1997) 85–96.
[78] D.Y. Perera, M. Oosterbroek, Hygrothermal stress evolution during weathering in organic coatings, J. Coating Technol. 66 (1994) 83–88.
[79] D.Y. Perera, P. Schutyser, C. De Lame, E.D. Vanden, On film formation and physical aging in organic coatings, Polym. Mater. Sci. Eng. 73 (1995) 187–188.
[80] L.C.E. Struik, Physical Aging in Amorphous Polymers and Other Materials, Elsevier, Amsterdam, 1978.
[81] G.B. McKenna, Glass formation and glassy behavior, in: in: C. Booth, C. Price (Eds.), Polymer Properties-Comprehensive Polymer Science, vol. II, Pergamon Press, Oxford, 1989, pp. 311–322.
[82] R.C. Warren, The effect of aging and annealing on the physical properties of nitrocellulose plasticized with nitroglycerine, Polymer 31 (1990) 861–868.
[83] F. Biddelestone, A.A. Goodwin, J.N. Hay, G.C. Mouledous, The relaxation spectrum and physical aging of poly(ether imide), Polymer 32 (1991) 3119–3125.
[84] A. Celli, M. Scandola, Thermal properties and physical aging of poly(L-lactic acid), Polymer 33 (1992) 2699–2703.
[85] D.Y. Perera, P. Schutyser, C. De Lame, E.D. Vanden, Film formation and physical aging in organic coatings, ACS Symp. Series 648 (1996) 210–221.
[86] S.L. Simon, Physical aging, in: J. Kroscwitz (Ed.), Encyclopedia of Polymer Science and Technology, Wiley, New York, 2003.
[87] D.Y. Perera, Effect of thermal and hygroscopic history on physical ageing of organic coatings, Prog. Org. Coat. 44 (2002) 55–62.
[88] D.Y. Perera, Physical ageing of organic coatings, Prog. Org. Coat. 47 (2003) 61–76.
[89] C.G. Robertson, G.L. Wilkes, Physical aging behavior of miscible blends of poly(methyl methacrylate) and poly(styrene-co-acrylonitrile), Polymer 42 (2001) 1581–1589.
[90] C.G. Robertson, G.L. Wilkes, Physical aging behavior of miscible blends containing atactic polystyrene and poly(2,6-dimethyl-1,4-phenylene oxide), Polymer 41 (2000) 9191–9204.
[91] S.L. Simon, J.W. Sobieski, D.J. Plazek, Volume and enthalpy recovery of polystyrene, Polymer 42 (2000) 2555–2567.
[92] P. Tiemblo, J. Guzmàn, E. Riande, C. Mijangos, H. Reinecke, Effect of physical aging on the gas transport properties of PVC and PVC modified with pyridine groups, Polymer 42 (2001) 4817–4823.
[93] D.Y. Perera, P. Schutyser, On the curing of powder coatings, in: Proc. 23rd FATIPEC Congress, Vol. B, Budapest, Hungary, 1994, pp. B144–B153.

CHAPTER 14

Corrosion Inhibitors

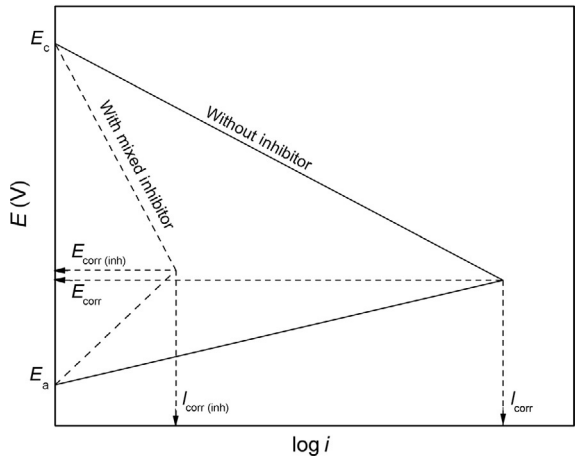

Chapter Contents

14.1 INTRODUCTION

A corrosion inhibitor is a substance that effectively reduces or prevents the corrosion of exposed metal in a corrosive environment. Inhibitors in small concentrations are added to cooling water, acid, and steam to maintain an inhibiting surface film. Different mechanisms inhibit corrosion. This chapter emphasizes corrosion inhibitors that affect anodic or

Corrosion Engineering
http://dx.doi.org/10.1016/B978-0-444-62722-3.00014-8

cathodic polarization properties or retard corrosion by surface adsorption and film formation at the metal-electrolyte interface. Organic inhibitors form barrier films that inhibit metal corrosion rate by decreasing the diffusion rate of depolarizers to the surface of the metal. Thin film adsorption with several monolayers is one of the mechanisms that inhibit corrosion. In acidic solutions, the inhibitor retards cathodic and/or anodic depolarization. In neutral solutions, the inhibitor blocks oxygen depolarization at the cathodic sites. It enhances the barrier properties of the oxide layers present on the metal surfaces. This mechanism is based on decreased oxygen transport to the metal by the formation of thin passive films. The inhibition mechanism of iron, aluminum, and zinc in neutral solutions by inorganic and organic inhibitors is based on (i) preferred inhibitor anion adsorption on the metal surface, (ii) plugging the pores of the passive oxide film, (iii) promoting reparation of damaged passivating oxide film, and (iv) decreasing metal dissolution [1]. The role of inhibitors in alkaline solutions is to stop pitting and crevice corrosion of metals such as aluminum, zinc, copper, and iron, which are known to form amphoteric oxides. Organic compounds such as gelatin and tannin, thiourea, naphtoles, and phenols have been used extensively in corrosion protection to inhibit corrosion since the middle of the twentieth century [2]. Gelatin and tannin increase the range of pH stability of hydroxide and amphoteric oxide layers or repair damaged hydroxide and oxide films on the metal surface. The inhibition mechanism of thiourea, naphtoles, and phenols involves adsorption and precipitation of metal chelate complexes and overvoltage increase by altering the kinetic properties of the cathodic and anodic reactions. Figure 14.1

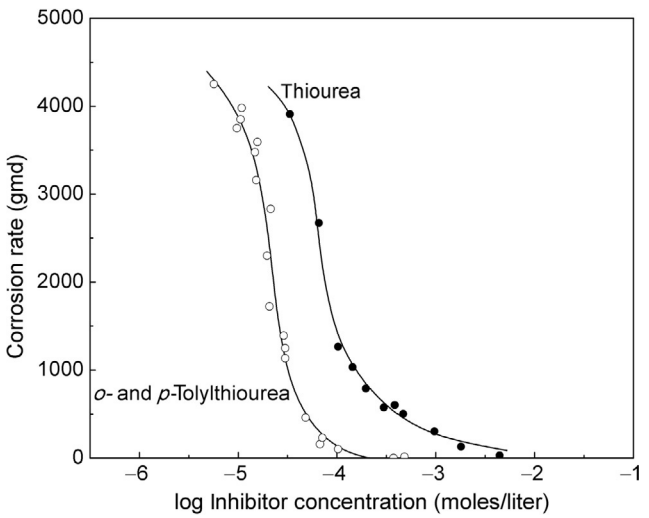

Fig. 14.1 The effect of concentration of thiourea and *o*- and *p*-tolylthiourea on corrosion of carbon steel in 5% sulfuric acid at 70 °C [2]. *Reproduced by permission of John Wiley and Sons.*

shows the effect of thiourea concentration and *o*- and *p*-tolylthiourea on the corrosion of carbon steel in 5% sulfuric acid at 70 °C.

Inhibitor efficiency is determined using Eq. (14.1):

$$I_{\text{eff}} = \frac{R_{\text{o}} - R_{\text{i}}}{R_{\text{o}}} \times 100 \tag{14.1}$$

where I_{eff} is efficiency of inhibitor %, R_{o} represents metal corrosion rate in the absence of an inhibitor, and R_{i} is the corrosion rate of metal in the presence of an inhibitor.

14.2 TYPES OF INHIBITORS

Inhibitors are classified according to their inhibition mechanism, application (pickling, acid cleaning, descaling, etc.) or chemical nature (organic or inorganic chemical substances). The following classes of inhibitors are discussed in this chapter: (i) anodic or passivating; (ii) cathodic including cathodic poisons, cathodic precipitates, and oxygen scavengers; (iii) adsorption or organic inhibitors; (iv) precipitation inhibitors; (v) ohmic; and (vi) vapor phase inhibitors.

14.2.1 Anodic passivating inhibitors

Anodic inhibitors increase anode polarization to the critical passivation potential of the metal or alloy. They are called passivating inhibitors because they drastically decrease the corrosion current. Figure 14.2a and b illustrate the polarization and passivation effect of anodic inhibitors. These inhibitors are strong oxidizing agents and shift the corrosion potential of the metal in the noble direction with the formation of a passive film.

Anodic inhibitors are also known as "dangerous" inhibitors because insufficient inhibitor concentration (below the critical value for oxidation) can cause pitting corrosion. Two types of passivating inhibitors are used to inhibit corrosion, nonoxidizing and oxidizing anions. Nonoxidizing anions require the presence of oxygen to passivate the metal; examples are tungstate, molybdate, and phosphate. Organic nonoxidizing inhibitors are sodium benzoate, sodium cinnamate, and polyphosphate [3]. They polarize the corrosion system in the passive region by enhancing the adsorption of oxygen. Oxidizing anions passivate steel in the absence of oxygen. Examples are chromate, nitrite, and nitrate. They have a tendency to be reduced by accepting electrons from metals. Sodium chromate depolarizes the cathodic curve in the anodic direction, intersecting the anodic curve in the passive region. It also adsorbs at the anodic area and forms an ionically bonded compound. This compound polarizes the anodic reaction by decreasing the critical passivation current density necessary to shift the potential in the passive region. Chromate affects the polarization curves of both the cathodic and anodic reaction and is known as a mixed inhibitor (Fig. 14.3). The corrosion potential shift is controlled by the polarization reaction (cathodic or anodic) that is affected by the inhibitor.

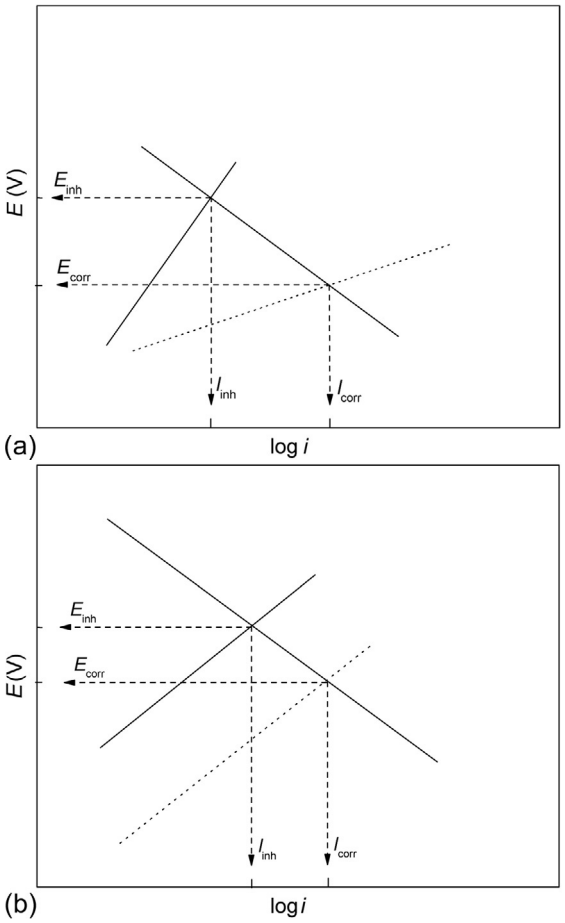

Fig. 14.2 (a) Polarization diagram illustrating the polarization effect of an anodic inhibitor and (b) polarization diagram illustrating the effect of an anodic passivation.

The critical inhibitor concentration increases with decreasing temperature or increasing chloride concentration and oxygen concentration [4,5]. For each passivating anodic inhibitor, there is a critical concentration of chlorides or sulfates that causes depassivation. A linear relationship exists between the logarithm of chromate concentration necessary for metal passivation and the logarithm of aggressive ion (chloride) concentration, $\log C_{\text{inh}} = n \log C_{\text{Cl}^-} + \text{const}$. Figure 14.4 shows the relationship between chromate concentrations required to passivate iron and chloride concentration. A polarization diagram that illustrates the effect of a passivating anodic inhibitor on critical passivation current and potential is shown in Fig. 14.5.

The electrochemical parameters I_{crit} (critical current density necessary to initiate passivation), E_{pp} (passivation potential), and I_{pass} (passivation current density) are controlled

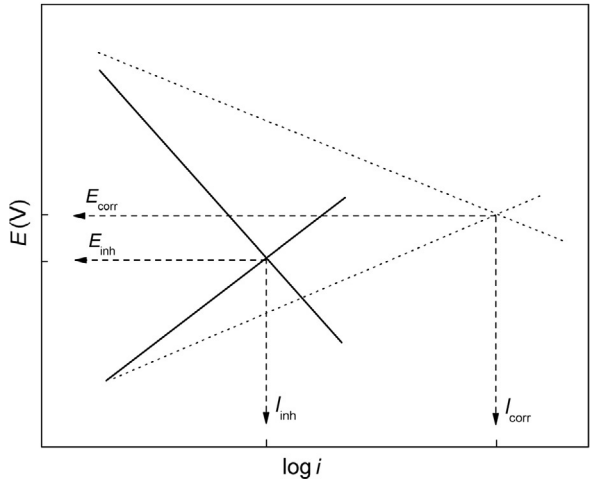

Fig. 14.3 Polarization diagram illustrating the effect of mixed inhibitors.

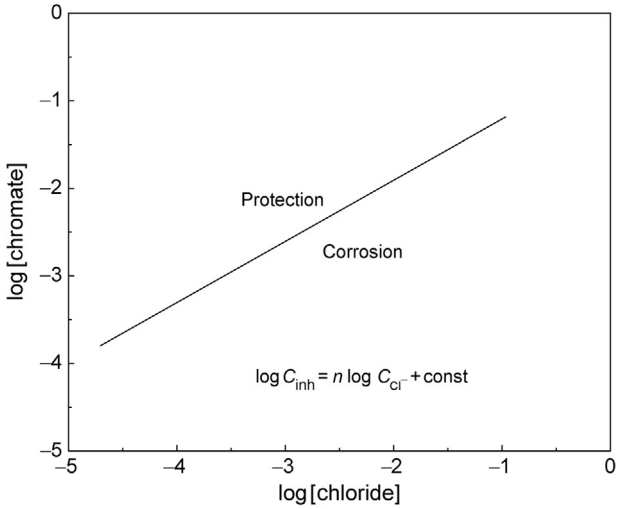

Fig. 14.4 Correlation between chromate concentration necessary to passivate iron and the concentration of chloride ion.

by inhibitor concentration in the electrolyte. The limiting cathodic current density should be greater than the critical current density to enable passivation. The points A-B-C-D represent the corrosion potentials in Fig. 14.5. At point A, the cathode polarization curve intersects the anodic curve in the active region, resulting in active metal dissolution. At point A, the inhibitor concentration is below the critical value that corresponds to the critical current density to initiate passivation. Point B is in the

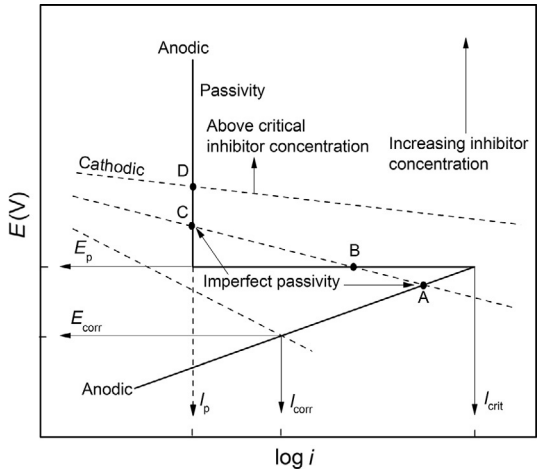

Fig. 14.5 Polarization diagram illustrating the effect of passivating anodic inhibitor.

active–passive region, where passivity is not stable. The corrosion potential of the active–passive metal shifts in the active or passive region (imperfect passivity), which increases the corrosion rate in localized areas causing pitting. Point C is located in the passive region, characterized by imperfect passivity. Point D is in the passive region with corrosion current equal to passivation current density, I_{pass}. The corrosion potential is stable with corrosion current that is several orders of magnitude lower than current observed in the active region. The cathodic polarization curve at point D does not intersect the anodic curve below the critical current density, I_{crit}. At point D, the concentration of the inhibitor is above the critical value providing stable anodic protection to the system.

14.2.2 Cathodic precipitation inhibitors

Cathodic or precipitation inhibitors decrease the corrosion rate by increasing the cathodic depolarization overvoltage (hydrogen evolution and oxygen reduction). Thick deposits form in the presence of these inhibitors and decrease depolarizer diffusion to the metal surface, inhibiting the cathodic reaction and corrosion. Cathodic inhibitors also reduce the corrosion current by inhibiting cathodic polarization. Figure 14.6a and b show polarization diagrams that illustrate cathodic polarization and passivation in the presence of cathodic inhibitors.

Depending on their inhibition mechanism, cathodic inhibitors are classified as cathodic poisons, cathodic precipitates, and oxygen scavengers. Cathodic poisons decrease the rate of hydrogen evolution reaction by adsorption or deposition (sulfides, selenides, arsenates, bismuth, and antimony) on the metal surface. Since these inhibitors inhibit hydrogen recombination, they may cause hydrogen blistering and increase metal susceptibility to hydrogen embrittlement.

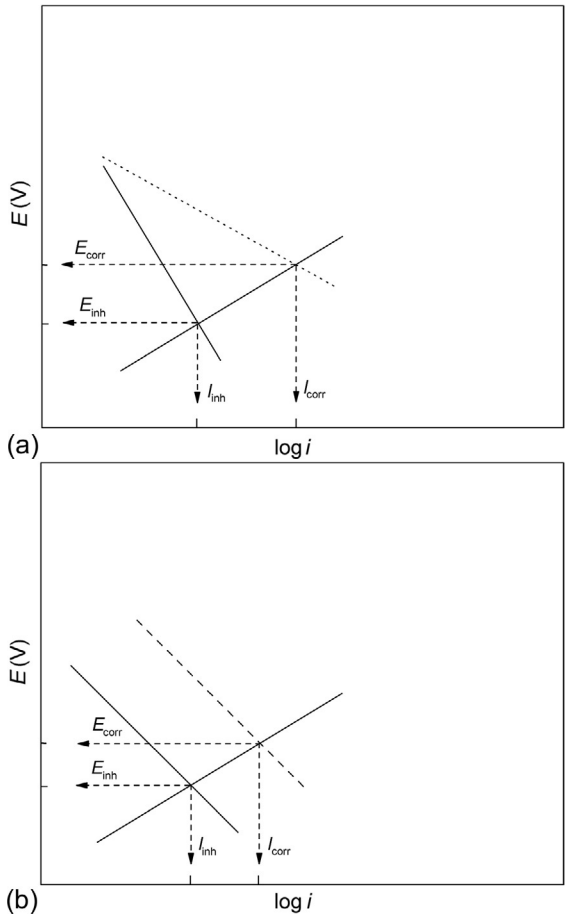

Fig. 14.6 (a) Effect of cathodic inhibitor on cathodic polarization and (b) cathodic passivation in the presence of cathodic inhibitors.

Cathodic precipitates increase cathodic site passivity with precipitation of insoluble compounds. Frequently used cathodic precipitation inhibitors are $CaCO_3$, $MgCO_3$, or zinc sulfates that precipitate as $Zn(OH)_2$. The efficiency of these inhibitors is only controlled by pH adjustment. Calcium carbonate (limestone) dissolves in water as calcium bicarbonate $Ca(HCO_3)_2$. Careful pH control forms smooth and hard calcium carbonate barrier films. Once the precipitate is formed, pH must be carefully controlled to avoid film dissolution at lower pH values:

$$Ca^{2+} + 2HCO_3^- \rightarrow Ca(HCO_3)_2 \rightarrow CaCO_3 + CO_2 + H_2O \tag{14.2}$$

In the presence of oxygen, hydroxide ions are formed through reaction (14.3)

$$O_2 + 2H_2O + 4e^- \rightarrow 4OH^- \tag{14.3}$$

The hydroxide ions formed by Eq. (14.3) enhance the rate of calcium carbonate precipitation through reaction in Eq. (14.4):

$$Ca(HCO_3)_2 + OH^- \rightarrow CaCO_3 + HCO_3 + H_2O \tag{14.4}$$

Polyphosphates are effective cathodic inhibitors for aerated cooling systems [5,6]. They are also known as condense or polymer phosphates. They bond with calcium ions to form positively charged colloidal particles that form a barrier film on the cathode (Fig. 14.7) [6]. A disadvantage of this inhibitor is hydrolysis of phosphorus oxygen bond, resulting in orthophosphate, a less desirable inhibitor.

Oxygen scavengers such as sulfite and hydrazine decrease the corrosion rate of carbon steels, copper, and cast iron used in oil production and steam generation industries by inhibiting the oxygen cathodic reaction. These inhibitors decrease the concentration of dissolved oxygen by reacting with oxygen, producing water and salts. Frequently used oxygen scavengers in water are sulfur dioxide and sodium sulfite. Cobalt or manganese is used to catalyze the reaction between oxygen and sulfites at low temperature.

Hydrazine, N_2H_4, sodium sulfite, Na_2SO_3, and ammonium sulfite, $(NH_4)_2SO_3$, have been successfully used as oxygen scavengers in boiler steam water [7,8].

$$N_2H_4 + O_2 \rightarrow N_2 \uparrow + 2H_2O \tag{14.5}$$

$$(NH_4)_2SO_3 + \frac{1}{2}O_2 \rightarrow (NH_4)_2SO_4 \tag{14.6}$$

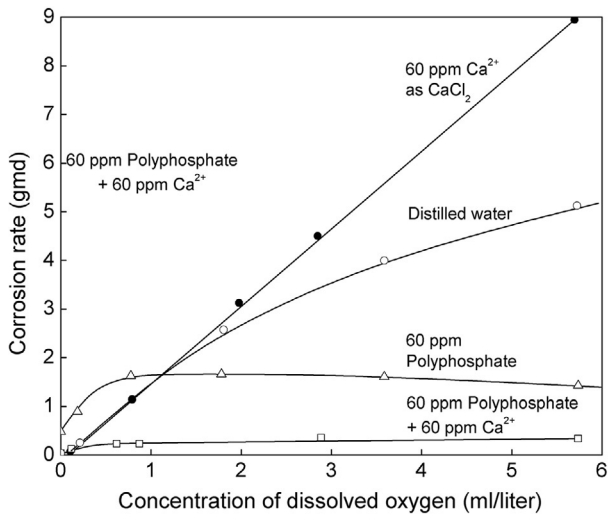

Fig. 14.7 Effect of oxygen concentration on the inhibiting efficiency of polyphosphate, illustrating the beneficial effect of dissolved calcium cation [6]. *Reproduced by permission of The Electrochemical Society.*

$$Na_2SO_3 + \frac{1}{2}O_2 \rightarrow Na_2SO_4 \tag{14.7}$$

$$NH_4HSO_3 + \frac{1}{2}O_2 \rightarrow NH_4HSO_4 \tag{14.8}$$

Hydrazine decomposes at high steam temperatures, producing ammonia or nitrogen. Because hydrazine is carcinogenic, new scavengers have been suggested such as ammonium isoascorbate and hydroquinone carbohydrazide. Silicates and phosphates are precipitation inhibitors by film formation. They decrease the corrosion rate of the metal by the combination of both cathodic and anodic polarization effects. They increase the overvoltage of both oxygen reduction and hydrogen evolution. In neutral solutions, these inhibitors cause steel passivation in the presence of oxygen as anodic inhibitors.

14.2.3 Organic inhibitors

Inorganic compounds such as nitrite, nitrate, chromate, and dichromate have been extensively investigated as inhibitors. Toxicity of these compounds limits their use in corrosion protection. Alternatives are organic corrosion inhibitors containing sulfur, nitrogen, or oxygen atoms and organic heterocyclic compounds containing polar groups [9–13]. These compounds adsorb and form a covalent bond on the metal surface [14]. Organic inhibitors cover the entire surface area of the corroding metal with a thick film consisting of several monolayers and change the structure of the double layer at the metal interface, decreasing depolarization rate. They may also act as a barrier film by blocking anodic and cathodic active sites or decreasing electroactive species transport rate to or from the metal surface. Lower inhibitor concentration is effective only for strong adsorption. The film is formed by the adsorption of positively or negatively charged soluble organic compounds. Film-forming organic compounds may exhibit anodic, cathodic, or mixed properties. Film-forming inhibitors by adsorption include amines, imidazolines, quaternaries, and acetylenic alcohols. Positively charged anodic inhibitors are primary amines, RNH_2, secondary amines, R_2NH, tertiary amines, $R\text{-}N(CH_3)_2$, diamines, $R\text{-}NHCH_2CH_2CH_2NH_2$, amides, $R\text{-}CONH_2$, and polyethoxylated compounds. Negatively charged compounds are sulfonates. Effective polar groups include hydroxyl, nitrogen, sulfur, phosphorous, or selenium. The charged ionic species initially form a physisorbed film through van Der Waals forces. The film is then stabilized through chemisorption [15].

The position of the corrosion potential with respect to its potential at zero charge (PZC) determines the surface charge of the metal. The overpotential is defined as the difference between the corrosion potential and the potential at zero charge. At negative overpotentials, cations, while at positive overpotential, anions are adsorbed. Electrostatic adsorption is due to attractive forces between inhibiting organic ions or dipoles and the charged surface of the metal. In electrostatic adsorption, the ions are not in contact with

the metal. They are separated by a layer of water molecules. The electrostatic adsorption process is almost independent of temperature and has very low activation energy.

In chemisorption, unshared electron pairs or "p" electrons from organic compounds interact with the metal orbitals to form a coordinate-type bond. The interaction proceeds in the presence of heteroatoms (P, Se, S, N, and O) that possess lone-pair of electrons and/or aromatic rings in the adsorbed molecules [16,17]. Chelate forms through a coordinate covalent bond by electron transfer from organic compounds to metal. The chemisorption has higher activation energy than electrostatic adsorption. It is a temperature-dependent phenomena, it occurs slowly, and is not reversible.

Organic molecules are chemisorbed on the surface of the metal due to unsaturated bonds on the heteroatoms. They favor electronic binding with the metal substrate [15,18,19]. Adsorption of surface active organic compounds increases with the charge of the metal surface, their molecular mass, and with the dipole moment [20]. The amount of inhibitor adsorbed on the surface increases by increasing the concentration of the inhibitor in the solution. Inhibitor effectiveness is improved by the strength of the adsorption bond and with greater molecular weight, asymmetry, and electron density [21]. Drazic *et al*. [22–27] studied the adsorption of ions and organic molecules on iron electrodes and defined corrosion-inhibiting properties of anodic reactions [22,23], cathodic reactions [24,25], or both [26,27]. The adsorption mechanism for cathodically protected surfaces is similar to the mechanism of anodically polarized surfaces.

Inhibitors such as imidazolines, amines, diamines, pyrimidines and their fatty acid, naphthenic acid and sulfonate compounds are used in refinery processes. The electron-rich polar group of these molecules adsorbs on the metal surface, while the nonpolar hydrocarbon part of the molecule forms a hydrophobic film that repels water.

A synergistic effect is observed between cathodic protection of pipeline and inhibitors. An efficiency increase is observed when the pipeline is cathodically polarized in the presence of an organic inhibitor. Organic inhibitors that contain nitrogen such as aryl and alkyl amines, aniline [28–31], imidiazoline derivatives [32,33], and ketones [33] are used in industrial acid cleaning, acid-descaling, and acid-pickling. Figure 14.8 shows the inhibitor effect on steel polarization behavior corroding in pickling acid [31]. The corrosion current drastically decreased with inhibitors added to the pickling acid solution. A mixture of nitrite and glycerophosphate are synergistic for steel protection [34].

14.2.4 Organic inhibitors used for inhibition of steel in an aqueous environment

N-heterocyclic compounds like azoles [35], benzylaminopurine, [36], Schiff base [37], pyrimidine derivatives [38], pyridine derivatives [39], pyrazole derivatives [40], bipyrazole derivatives [41], benzimidazole [42,43], and 2,3-diphenylbenzoquinoxaline [44] have been successfully used as acidic inhibitors for corrosion protection of steel in an acidic environment. Organic corrosion inhibitors decrease the corrosion rate by

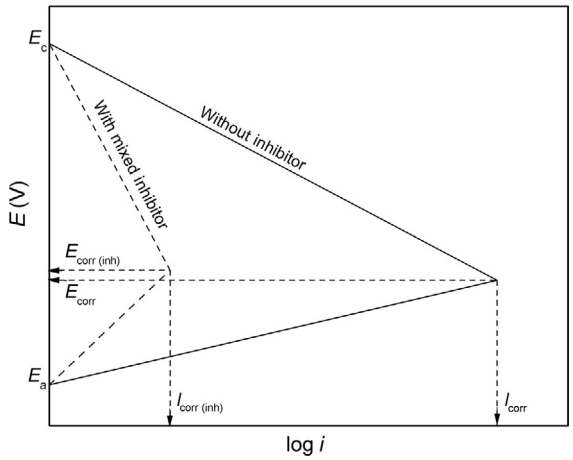

Fig. 14.8 Effect of inhibitor on polarization diagram for steel corroding in pickling acid [31]. *This material is reproduced with permission of John Wiley & Sons, Inc.*

adsorption of oxygen, sulfur or nitrogen heteroatoms, and aromatic rings on the metal. The adsorption bond strength is determined by functional group steric factor, polarizability, and the electron density of donor atoms [45]. The presence of heteroatoms cause inhibiting effects and reduce metal dissolution [46–48]. Adsorption of surface active corrosion inhibitors increases with the aliphatic chain length. Fatty acids with 16-18 C atoms were found to have good corrosion inhibition properties [49,50]. Phosphonic acid is an effective inhibitor for the inhibition of mild steel corrosion in a neutral aqueous environment. These acids have the ability to form complexes with corrosion products and have high hydrolytic stability [51,52]. Ramesh *et al.* [53] found that 3-anisalidene aminol, 2, 4-triazole phosphonate exhibits excellent corrosion inhibition efficiency.

"Green" corrosion inhibitors including amino acids have been investigated as inhibitors for Co [54], Ni [55], iron and mild steel [56] in acidic environments in the past three decades. The objective was to develop effective corrosion inhibitors with "zero" environmental impact. The inhibition effect of tryptamine (TA) was tested by Moretti *et al.* [57] for ARMCO iron protection in 0.5 M deaerated sulfuric acid. At a concentration of 10 mM, the inhibition efficiencies were between 90% and 99%.

14.2.5 Ohmic inhibitors

Ohmic inhibitors may increase the resistance by forming a nonconducting thick film on the metal surface or by potential drop in the solution. They increase the overvoltage of the anodic or cathodic reactions depending on where the film is deposited (Fig. 14.9).

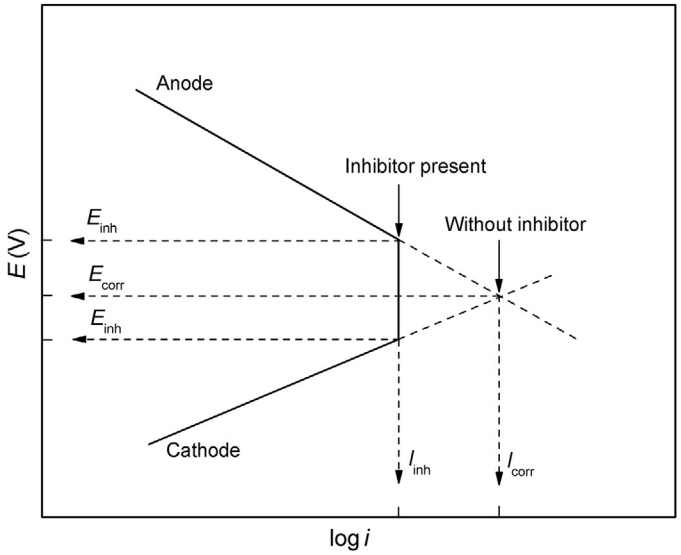

Fig. 14.9 Polarization curve showing the effect of ohmic inhibitor.

14.2.6 Vapor phase inhibitors/volatile corrosion inhibitors (VCI)

Vapor phase corrosion inhibitors are volatile compounds introduced in a closed system for corrosion protection. These inhibitors possess a high vapor pressure at normal temperature and protect the metal by forming a bond and barrier layer on the metal surface. In general, a weak volatile acid or base that easily hydrolyzes provides the most effective inhibition. Volatile alkaline compounds such as octadecylamine and morphine are introduced in boilers with steam to inhibit corrosion in condenser tubes by neutralizing the acidic carbon dioxide. Inhibiting anions such as nitrite (NO_2^-) and amine (NH_2^-) substituted into organic structures increase vapor pressure, increasing their protective ability against aggressive ions in atmospheric corrosion [58]. The inhibition mechanism of VCI is not clear. It is assumed that VCI forms a weak bond as an adsorbed monolayer that protects the surface from water inclusion and aggressive ions such as sulfates and chlorides. The adsorbed monolayer changes anodic (dissolution of the metal) and cathodic reaction kinetics [59]. Vapor phase inhibitors used in corrosion protection are summarized in Table 14.1.

14.2.7 Anodic inorganic inhibitors

Inorganic inhibitors such as chromate, nitrite, nitrates, and arsenate are very efficient for ferrous alloys. They prevent stainless steel pitting corrosion by forming a monolayer or multilayer passivating films. For chromate, the film is formed by iron oxidation (anodic

inhibitor) [60]. The passive film consists of iron and chromium oxide. Chromates are reduced to trivalent chromium according to Eq. (14.10):

$$Fe \rightarrow Fe^{2+} + 2e^{-} \tag{14.9}$$

$$2CrO_4^{2-} + 10H^{+} + 6e^{-} \rightarrow Cr_2O_3 + 5H_2O \tag{14.10}$$

Nitrites are environmentally friendly anodic inhibitors. They form a passive film with ferric oxide and inhibit the corrosion of copper, nickel, and tin alloys in alkaline environments (pH levels 9-10), but aggressive ions such as chloride and sulfate ions attack and destroy the barrier film. They reduce the rate of anodic dissolution on steel as shown in Fig. 14.10 [61]. Nitrites are used only in closed systems because they oxidize to nitrates in the presence of oxygen. They are not as efficient inhibitors as chromates.

Table 14.1 Vapor Pressure Inhibitor

Substance	Temperature (°C)	Vapor Pressure (mmHg)	Melting Point (°C)
Morpholine	20	8.0	-
Benzylamine	29	1.0	-
Cyclohexylamine carbonate	25.3	0.397	-
Diisopropylamine nitrite	21	4.84×10^{-3}	139
Morpholine nitrite	21	3×10^{-3}	-
Dicyclohexylamine nitrite	21	1.3×10^{-4}	179
Dicyclohexylamine caprylate	21	5.5×10^{-4}	-
Guanadine chromate	21	1×10^{-5}	-

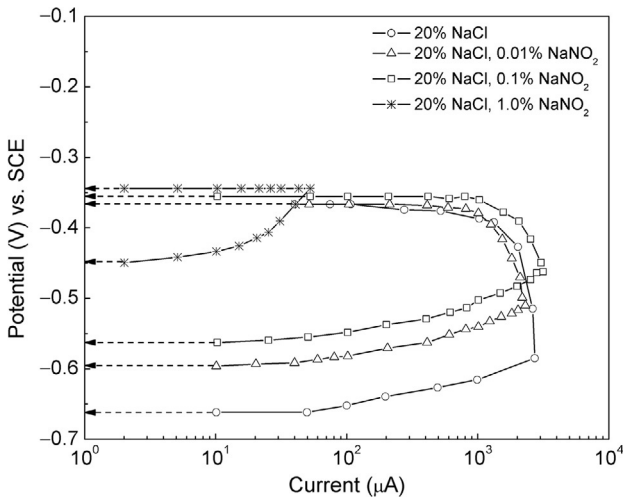

Fig. 14.10 Effect of nitrite anion on reducing the rate of anodic dissolution reaction on steel [61]. © *NACE International 1984.*

Most inorganic inhibitors are toxic and ecologically unacceptable. Molybdate inhibitors have been used in open recirculating cooling systems as a substitution for chromate-based inhibitors in neutral environments [62–66]. Nitrates have been used to inhibit corrosion of zinc [67,68], galvanized steel, and aluminum [69]. The effect of inorganic inhibitors like lithium nitrate, lithium molybdate, and lithium chromate on the corrosion behavior of 1018 carbon steel in the LiBr-ethylene glycol-H_2O mixture was studied by Samiento-Bustos *et al.* [70]. Inhibition efficiency increased with inhibitor concentration, except in the case of Li_2CrO_4, where the highest efficiency was obtained with 20 ppm of inhibitor. Regardless of inhibitor chemical composition, measured pitting potential in the presence of 5 ppm of inhibitor was observed to be more active than in the absence of inhibitor. Similar to molybdates, the toxicity of tungstate is also very low [71]. The corrosion inhibition properties of tungstate have been investigated extensively in neutral solution [72].

REFERENCES

[1] J.G.N. Thomas, The mechanism of corrosion prevention by inhibitors, in: L.L. Shreir (Ed.), Corrosion, second ed., Butterworth, London, England, 1976, pp. 18:34–18:56.
[2] T.P. Hoar, R.D. Holliday, The inhibition by quinolones and thioureas of the acid dissolution of mild steel, J. Appl. Chem. 3 (1953) 502–513.
[3] Y.I. Kuznetsov, J.G.N. Thomas, Organic Inhibitors of Corrosion of Metals, Plenum Press, New York, 1996.
[4] R.K. Frier, Industrial experience with metal oxide protective layers with the addition of oxygen, Vom Wasser 48 (1971) 443–458.
[5] B.P. Boffardi, Control of environmental variables in water-recirculating systems, in: Metals Handbook, in: Corrosion, vol. XIII, ASM International, Metals Park, OH, 1987, pp. 487–497.
[6] H.H. Uhlig, D.N. Triadis, M. Stern, Effect of oxygen, chlorides, and calcium ion on corrosion inhibition of iron by polyphosphates, J. Electrochem. Soc. 102 (1955) 59–66.
[7] M.D. Baker, V.M. Marcy, Hydrazine as an oxygen scavenger—a progress report on tests at Springdale Station, Trans. ASME 78 (1956) 299–304.
[8] H.D. Ongman, Reducing solutions at steam-boiler temperatures, Combustion 24 (1929) 40–44.
[9] S.W. Dean Jr., R. Derby, G.T. Vondembussche, Inhibitor types, Mater. Perform. 20 (1981) 47–51.
[10] L. Wang, Evaluation of 2-mercaptobenzimidazole as corrosion inhibitor for mild steel in phosphoric acid, Corros. Sci. 43 (2001) 2281–2289.
[11] M.A. Quraishi, R. Sardar, Aromatic triazoles as corrosion inhibitors for mild steel in acidic environments, Corrosion 58 (2002) 748–755.
[12] F. Bentiss, M. Lebrini, H. Vezin, M. Lagrenee, Experimental and theoretical study of 3-pyridyl-substituted 1,2,4-thiadiazole and 1,3,4-thiadiazole as corrosion inhibitors of mild steel in acidic media, Mater. Chem. Phys. 87 (2004) 18–23.
[13] E.A. Noor, The inhibition of mild steel corrosion in phosphoric acid solutions by some N-heterocyclic compounds in the salt form, Corros. Sci. 47 (2004) 33–55.
[14] G. Trabanelli, Corrosion inhibitors, in: F. Mansfeld (Ed.), Chemical Industries: Corrosion Mechanism, Marcel Dekker, New York, 1970, pp. 28–120 (chapter 3).
[15] G. Trabanelli, V. Carassiti, Mechanism and phenomenology of organic inhibitors, in: M.G. Fontaine, R.W. Stachle (Eds.), in: Advances in Corrosion Science and Technology, vol. I, Plenum Press, New York-London, 1970, pp. 147–205.
[16] M.M. Singh, R.B. Rastogi, B.N. Upadhyay, Inhibition of copper corrosion in aqueous sodium chloride solution by various forms of the piperidine moiety, Corrosion 50 (1994) 620–625.

[17] G. Quartarone, T. Bellomi, A. Zingales, Inhibition of copper corrosion by isatin in aerated 0.5 M H_2SO_4, Corros. Sci. 45 (2002) 715–733.
[18] B.B. Damaskin, O.A. Petrii, V.V. Batrakov, Adsorption of Organic Compounds on Electrodes, Plenum Press, New York-London, 1971.
[19] H. Fisher, 15 years of German research in the corrosion research program of the Federal Republic of Germany, Werkst Korros. 24 (1973) 525–535.
[20] J. De Damborenea, J.M. Bastidas, A.J. Vaquez, Adsorption and inhibitive properties of four primary aliphatic amines on mild steel in 2 M hydrochloric acid, Electrochim. Acta 42 (1997) 455–459.
[21] O.L. Riggs, Theoretical aspects of corrosion inhibitors and inhibition, in: C.C. Nathan (Ed.), Corrosion Inhibitors, NACE, Houston, Texas, 1973, pp. 7–27.
[22] V.J. Drazic, D.M. Drazic, Adsorption of inhibitors on a corroding iron surface, J. Serb. Chem. Soc. 56 (1991) 753–757.
[23] V.J. Drazic, D.M. Drazic, Competitive adsorption of water, sulfuric acid and inhibition species on a corroding iron surface, J. Serb. Chem. Soc. 57 (1992) 917–926.
[24] Lj Vracar, D.M. Drazic, Influence of chloride ion adsorption on hydrogen evolution reaction on iron, J. Electroanal. Chem. 339 (1992) 269–279.
[25] D.M. Drazic, Lj Vracar, V.J. Drazic, The kinetics of inhibitor adsorption on iron, Electrochim. Acta 39 (1994) 1165–1170.
[26] M. Lj, D. Vracar, M. Drazic, Anomalous temperature dependence of the hydrogen evolution reaction on iron, J. Electroanal. Chem. 256 (1989) 171–178.
[27] Lj.M. Vracar, D.M. Drazic, Adsorption and corrosion inhibitive properties of some organic molecules on iron electrode in sulfuric acid, Corros. Sci. 44 (2002) 1669–1680.
[28] L.V. Mavlov, N.G. Klyuchnikov, V.D. Sheludyakov, N.A. Viktorov, Corrosion behavior of steel in the presence of organosilicon nitrogen-containing compounds, in: Conf. Ingibitory Korroz. Met, Moscow, USSR, 1972, pp. 121–124.
[29] V.I. Komarov, S.A. Balezin, Protection of ferrous and nonferrous metals from acid corrosion, USSR Patent 141 049, 1961.
[30] T. Kataoka, A. Takada, Method of inhibiting the acid corrosion of metals, U. S. Patent US 3 736 098, U.S. Patent and Trademark Office, Washington, DC, 1973.
[31] H.H. Uhlig, R.W. Revie, Corrosion and Corrosion Control, third ed., John Wiley & Sons, New York, 1985.
[32] T. Kataoka, A. Takada, Protecting metal articles from acidic corrosion, Japanese Patent JP 7 415 145, 1974.
[33] R.H. Scott, H.B. Lockhart, Process for inhibiting corrosion. U. S. Patent US 3 770 377, U.S. Patent and Trademark Office, Washington, DC, 1973.
[34] C. Monticelli, A. Frignani, G. Trabanelli, G. Brunoro, A study on the inhibiting efficiency of a glycerophosphate-nitrite admixture against steel corrosion in mortars, in: Proceedings of the 8th European Symposium, vol. 1, 1995, pp. 609–620.
[35] A. Popova, M. Christov, A. Zwetanova, Effect of the molecular structure on the inhibitor properties of azoles on mild steel corrosion in 1 M hydrochloric acid, Corros. Sci. 49 (2007) 2131–2143.
[36] X. Li, S. Deng, H. Fu, G. Mu, Inhibition effect of 6-benzylaminopurine on the corrosion of cold rolled steel in H_2SO_4 solution, Corros. Sci. 51 (2009) 620–634.
[37] H.D. Lece, K.C. Emregul, O. Atakol, Difference in the inhibitive effect of some Schiff base compounds containing oxygen, nitrogen and sulfur donors, Corros. Sci. 50 (2008) 1460–1468.
[38] S.A. Abd El-Maksoud, The influence of some Arylazobenzoyl acetonitrile derivatives on the behavior of carbon steel in acidic media, Appl. Surf. Sci. 206 (2003) 129–136.
[39] M.A. Veloz, I.G. Martinz, Effect of some pyridine derivatives on the corrosion behavior of carbon steel in an environment like NACE TM0177, Corrosion 62 (2006) 283–292.
[40] A. Ouchrif, M. Zegmout, B. Hammouti, S. El-Kadiri, A. Ramdani, 1,3-Bis(3-hyroxymethyl-5-methyl-1-pyrazole) propane as corrosion inhibitor for steel in 0.5 M H_2SO_4 solution, Appl. Surf. Sci. 252 (2005) 339–344.
[41] A. Chetouani, B. Hammouti, T. Benhadda, M. Daoudi, Inhibitive action of bipyrazolic type organic compounds towards corrosion of pure iron in acidic media, Appl. Surf. Sci. 249 (2005) 375–385.

[42] A. Popova, M. Christov, T. Deligeorigiev, Influence of the molecular structure on the inhibitor properties of benzimidazole derivatives on mild steel corrosion in 1 M hydrochloric acid, Corrosion 59 (2003) 756–764.
[43] A. Popova, M. Christov, S. Raicheva, E. Sokolova, Adsorption and inhibitive properties of benzimidazole derivatives in acid mild steel corrosion, Corros. Sci. 46 (2004) 1333–1350.
[44] I.B. Obot, N.O. Obi-Egbedi, 2, 3-Diphenylbenzoquinoxaline: a new corrosion inhibitor for mild steel in sulfuric acid, Corros. Sci. 52 (2010) 282–285.
[45] S. Sankarapapavinasam, F. Pushpanaden, M.F. Ahmed, Hydrazine and substituted hydrazines as corrosion inhibitors for lead in acetic acid, Brit. Corros. J. 24 (1989) 39–42.
[46] S.S. Abd El Rehim, M.A.M. Ibrahim, K.F. Khalid, The inhibition of 4-(2′amino-5′-methylphenylazo) antipyrine on corrosion of mild steel in HCl solution, Mater. Chem. Phys. 70 (2001) 268–273.
[47] I.B. Obot, N.O. Obi-Egbedi, N.W. Odozi, Acenaphtho [1, 2-b] quinoxaline as a novel corrosion inhibitor for mild steel in 0.5 M H_2SO_4, Corros. Sci. 52 (2010) 923–926.
[48] A.S. Fouda, A.S. Ellithy, Inhibition effect of 4-phenylthiazole derivatives on corrosion of 304 L stainless steel in HCl solution, Corros. Sci. 51 (2009) 868–875.
[49] R.J. Meakins, Alkyl quaternary ammonium compounds as inhibitors of the acid corrosion of steel, J. Appl. Chem. 13 (1963) 339–345.
[50] H.F. Finley, N. Hackerman, Effect of adsorption of polar organic compounds on the reactivity of steel, J. Electrochem. Soc. 107 (1960) 259–263.
[51] E. Kalman, G. Palinkas, Mechanism of inhibition in neutral solutions, Corros. Sci. 35 (1993) 1471–1476.
[52] K. Mijos, Cyclic amines, in: Kirk-Othmer Encyclopedia of Chemical Technology, Wiley Interscience, London, 1998.
[53] S. Ramesh, S. Rajeswari, S. Maruthamuthu, Effect of inhibitors and biocide on corrosion control of mild steel in natural aqueous environment, Mater. Lett. 57 (2003) 4547–4554.
[54] S. Bilgic, A.A. Aksut, Effect of amino acids on corrosion of cobalt in sulfuric acid, Br. Corros. J. 28 (1993) 59–62.
[55] A.A. Aksut, S. Bilgic, The effect of amino acids on the corrosion of nickel in sulfuric acid, Corros. Sci. 33 (1992) 379–387.
[56] A. Oni, Mild-steel corrosion and inhibition by aromatic amino acid in hot sulfuric acid, Corros. Prevent. Control 39 (1992) 128–130.
[57] G. Moretti, F. Guidi, G. Grion, Tryptamine as a green iron corrosion inhibitor in 0.5 M deaerated sulfuric acid, Corros. Sci. 46 (2004) 387–403.
[58] L.R.M. Estevao, R.S.V. Nascimento, Modifications in the volatilization rate of volatile corrosion inhibitors by means of host-guest systems, Corros. Sci. 43 (2001) 1133–1153.
[59] J.M. Bastidas, E.M. Mora, S. Feliu, The protective action of two vapor-phase inhibitors on the corrosion of mild steel, Werkst. Korros. 41 (1990) 343–347.
[60] M.A. Igual, A.J. García, J.L. Gunon, H.V. Perez, The effect of chromate in the corrosion behavior of duplex stainless steel in LiBr solutions, Corros. Sci. 48 (2006) 4127–4151.
[61] D.A. Jones, Polarization studies of brass-steel galvanic couples, Corrosion 40 (1984) 181–185.
[62] M.J. Pryor, M. Cohen, The inhibition of the corrosion of iron by some anodic inhibitors, J. Electrochem. Soc. 100 (1953) 203–215.
[63] E.A. Lizlovs, Molybdates as corrosion inhibitors in the presence of chlorides, Corrosion 32 (1976) 263–266.
[64] D.R. Robitaile, Sodium molybdate as a corrosion inhibitor in cooling tower water, Mater. Perform. 15 (1976) 40–44.
[65] J. Jefferies, B. Bucher, A new look at molybdate, Mater. Perform. 31 (1992) 50–53.
[66] M.S. Vukasovich, J.P.G. Farr, Molybdate corrosion inhibition—a review, Mater. Perform. 24 (1985) 9–18.
[67] A. Aramaki, Treatment of zinc surface with cerium (III) nitrate to prevent zinc corrosion in aerated 0.5 M NaCl, Corros. Sci. 4 (2001) 2201–2215.
[68] D. Wang, X. Tang, Y. Qiu, F. Gan, G. Zheng Chen, A study of the film formation kinetics on zinc in different acidic corrosion inhibitor solutions by quartz crystal microbalance, Corros. Sci. 47 (2005) 2157–2172.

[69] A.M. Cabral, W. Trabelsi, R. Serra, M.F. Montemor, M.L. Zheludkevich, M.G.S. Ferreira, The corrosion resistance of hot dip galvanized steel and AA2024-T3 pre-treated with bis-[triethoxysilylpropyl] tetrasulfide solutions doped with $Ce(NO_3)_3$, Corros. Sci. 48 (2006) 3740–3758.
[70] E. Samiento-Bustos, J.G. González Rodriguez, J. Uruchurtu, G. Dominguez-Patiño, V.M. Salinas-Bravo, Effect of inorganic inhibitors on the corrosion behavior of 1018 carbon steel in the LiBr-ethylene glycol-H_2O mixture, Corros. Sci. 50 (2008) 2296–2303.
[71] J.B. Lumsden, Z. Szklarska-Smiralowska, The properties of films formed on iron exposed to inhibitive solutions, Corrosion 34 (1978) 169–176.
[72] E. Fujioka, H. Nishihara, K. Aramaki, The inhibition of pit nucleation and growth on the passive surface of iron in a borate buffer solution containing Cl^- by oxidizing inhibitors, Corros. Sci. 38 (1996) 1915–1933.

CHAPTER 15

Cathodic Protection

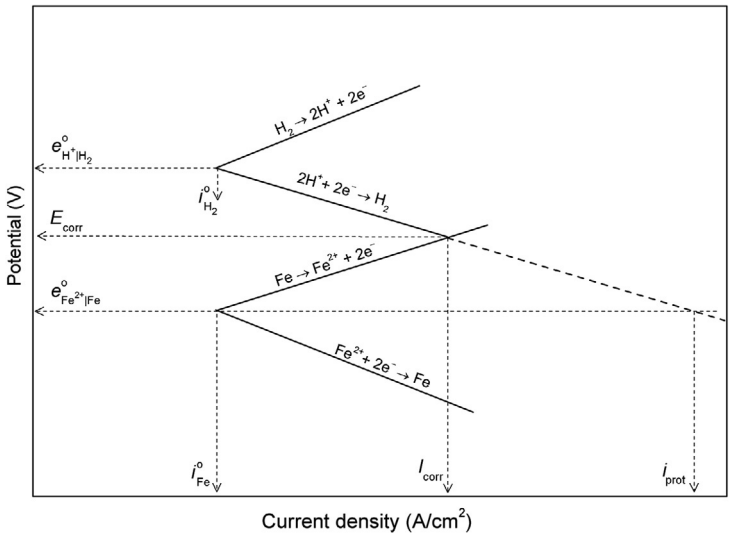

Chapter Contents

Corrosion Engineering
http://dx.doi.org/10.1016/B978-0-444-62722-3.00015-X

15.1 INTRODUCTION

Pipelines are exposed to aggressive soil environments, varying climate conditions, microorganisms, and stray currents that initiate corrosion processes. Research carried out in the last several decades indicated cathodic protection is the most promising protection method for pipelines [1,2]. Basic information on cathodic protection is well documented in several textbooks and handbooks [3–9].

Sir Humphrey Davy [10] reported in 1824 that copper could be successfully protected against corrosion by coupling it with iron or zinc. In the 1920s, cathodic protection was first used to protect buried pipelines carrying oil and gases. In successive decades, an immense development in cathodic protection systems was accomplished. In the beginning of this century, thousands of miles of buried pipelines and cables are effectively protected by cathodic protection. Cathodic protection is also applied to storage tanks, ships, offshore drilling structures, condensers, and concrete bridges.

15.2 FUNDAMENTALS

15.2.1 Principle

Cathodic protection (CP) is defined as the reduction or elimination of corrosion by making the metal a cathode by means of impressed current or sacrificial anode (usually magnesium, aluminum, or zinc) [11]. This method uses cathodic polarization to control electrode kinetics occurring on the metal-electrolyte interface. The principle of cathodic protection can be explained by the Wagner-Traud mixed potential theory [12].

For iron corroding in an aerated neutral electrolyte, the following reactions take place:

$$\mathrm{Fe} \rightarrow \mathrm{Fe}^{2+} + 2\mathrm{e}^{-} \tag{15.1}$$

$$\mathrm{O_2} + 2\mathrm{H_2O} + 4\mathrm{e}^{-} \rightarrow 4\mathrm{OH}^{-} \tag{15.2}$$

According to mixed potential theory, any electrochemical or corrosion process can be divided into two or more oxidation (Eq. 15.1) and reduction (Eq. 15.2) partial reactions with no net accumulation of electric charge during the process. Corrosion will start only when both cathodic and anodic reactions occur simultaneously. The total rate of oxidation must equal the total rate of reduction. The relationship between anodic and cathodic partial currents for the above system is presented in Fig. 15.1. In this figure, mixed potential theory and kinetic equations were used to explain iron corrosion. Iron interfaced with an electrolyte starts to dissolve (anodic reaction) with the reduction of oxygen to form a OH^- ion. As a result of corrosion, an equilibrium state is established. Under equilibrium conditions, the rate of the reduction reaction (cathodic) equals the rate of oxidation (anodic) reaction. The only point in the system in Fig. 15.1 where the total rates of oxidation and reduction are equal is at the intersection represented as the mixed or corrosion potential, E_{corr}. The current density corresponding to corrosion potential is called the corrosion current density, I_{corr}. At E_{corr}, the rate of iron dissolution is equal to the rate of oxygen reduction. Four electrons are provided by the anodic reaction to reduce one oxygen molecule to four hydroxide anions. The difference between the corrosion potential, E_{corr}, and the reversible potential, $e^{o}_{Fe^{2+}|Fe}$, of the corroding metal is the driving force for the corrosion processes. If the slopes of both polarization curves and the exchange current densities are known, it is possible to predict the corrosion rate of iron from electrochemical data. As illustrated in Fig. 15.1,

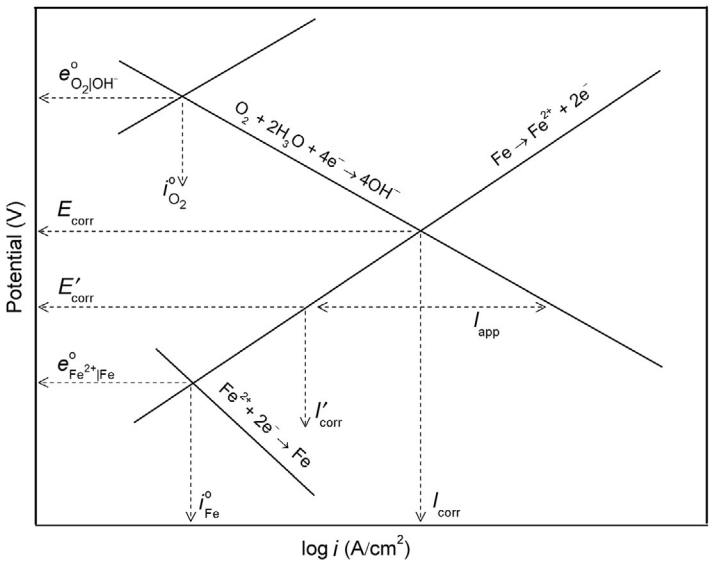

Fig. 15.1 Evans diagram—principle of cathodic protection.

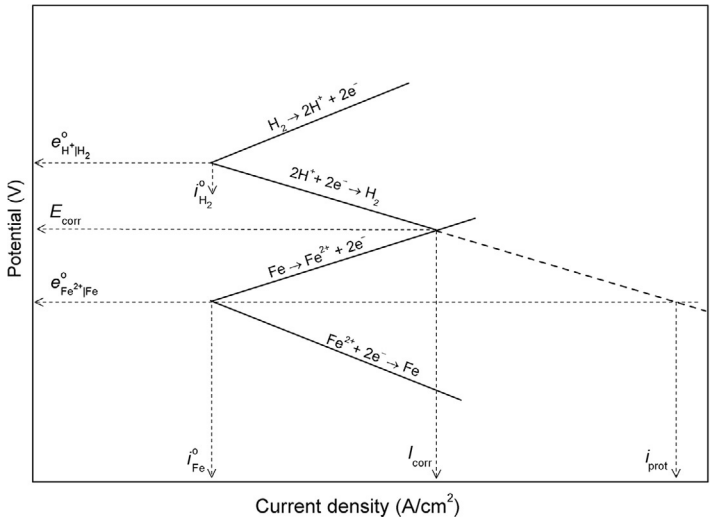

Fig. 15.2 Evans diagram showing the protection current for a corroding Fe system.

the corrosion rate decreases by cathodically polarizing the cathode in the negative direction from the corrosion potential. By polarizing the system from E_{corr} to E'_{corr} with a known applied current (I_{app}), the corrosion current decreases from I_{corr} to I'_{corr}. For complete corrosion inhibition, it is necessary to polarize the metal to its reversible potential, $e^o_{Fe^{2+}|Fe}$, as shown in Fig. 15.2. The applied current at this point is known as the protection current, i_{prot}.

Example 15.1

For steel in a corroding acidic solution, calculate (i) corrosion current and corrosion potential, (ii) impressed current density I_{app} required to bring corrosion to 10^{-6} A/cm^2, and (iii) cathodic polarization required to bring the corrosion rate from 460 to 0.46 mpy.

Given:

$i^o_a = 10^{-6}$ A/cm^2, $i^o_c = 10^{-8}$ A/cm^2, $b_c = -0.10$ V/decade, $b_a = 0.040$ V/decade.

Solution:

(i) Anodic reaction: $Fe \rightarrow Fe^{2+} + 2e^-, e^o_{Fe^{2+}|Fe} = -0.44$ V vs. SHE.

Tafel equation:

$$E + 0.44 = b_a \log \frac{i}{i^o_a} \tag{15.3}$$

Cathodic reaction: $2H^+ + 2e^- \rightarrow H_2, e^o_{H^+|H_2} = 0.0$ V vs. SHE.

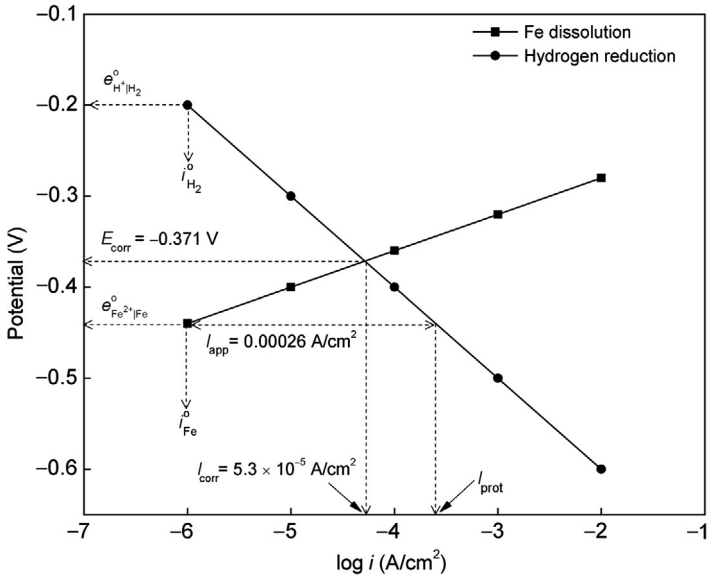

Fig. 15.3 Estimation of corrosion current, applied current for the Fe substrate protected by impressed current cathodic protection system in acidic media.

Tafel equation:

$$E + 0.0 = b_c \log \frac{i}{i_c^o} \tag{15.4}$$

By substituting the given values in Eqs. (15.3) and (15.4) and replacing $E = E_{corr}$ and $i = I_{corr}$, the following equation is obtained:

$$E_{corr} = 0.04 \times \log I_{corr} - 0.2 \tag{15.5a}$$

and for the anodic reaction

$$E_{corr} = -0.1 \times \log I_{corr} - 0.8 \tag{15.5b}$$

The values of E_{corr} and I_{corr} are calculated by solving the anodic and cathodic reactions shown in Eqs. (15.5a) and (15.5b). Also, assuming I_{corr} values from -2 to -8, one can calculate corresponding E values for the anodic and cathodic reactions. A plot of anodic and cathodic reactions is shown in Fig. 15.3.

The intersection of anodic and cathodic slopes gives the values of E_{corr} and I_{corr}.

$$E_{corr} = -0.371\ \text{V}$$

$$I_{corr} = 5.3 \times 10^{-5}\ \text{A/cm}^2$$

(ii) To bring corrosion current to 10^{-6} A/cm^2, the system should be polarized from $E_{corr} = -0.371$ V to -0.44 V vs. SHE. To polarize the system, an external impressed current of 0.00026 A/cm^2 is applied.

(iii) To decrease the corrosion rate by three orders of magnitude (from 460 mpy to 0.46 mpy), the cathodic polarization required is $3 \times b_a = 3 \times 40 = 120$ mV.

15.2.2 Types of cathodic protection

Based on the polarization used to protect the structure, the CP systems are divided into sacrificial anode and impressed current systems (ICS).

15.2.2.1 Sacrificial anode cathodic protection

In this system, corrosion protection is accomplished by coupling a less noble, that is, more electronegative metal in the galvanic series with the pipeline [7]. A schematic of the sacrificial CPs is given in Fig. 15.4. The nobler pipeline (metal) in this galvanic couple is cathodically polarized, while the less noble metal is anodically dissolved. Sacrificial anodes serve as a source of electrical energy. High purity anodes (zinc, aluminum, or magnesium) are required to avoid significant anode polarization and accumulation of insulating reaction products. The anode is packaged in a backfill consisting of 75% gypsum, 20% betonite, and 5% sodium sulfate. The backfill absorbs corrosion products and water from the soil to keep anodes active. Sacrificial anodes are coupled to the pipeline at regular intervals based on the current requirements needed to protect the pipeline.

Sacrificial anodes do not require outside power sources; rather, they provide their own power and need minimum maintenance. Sacrificial coatings are recommended with well-coated structures with minimum chance of being damaged during the pipeline's useful life.

Requirements for a Good Sacrificial Anode

(a) The potential between the anode and the corroding structure must overcome the formation of anode cathode cells on the corroding structure.
(b) When drawing current, the anode should not be polarized to a large extent.

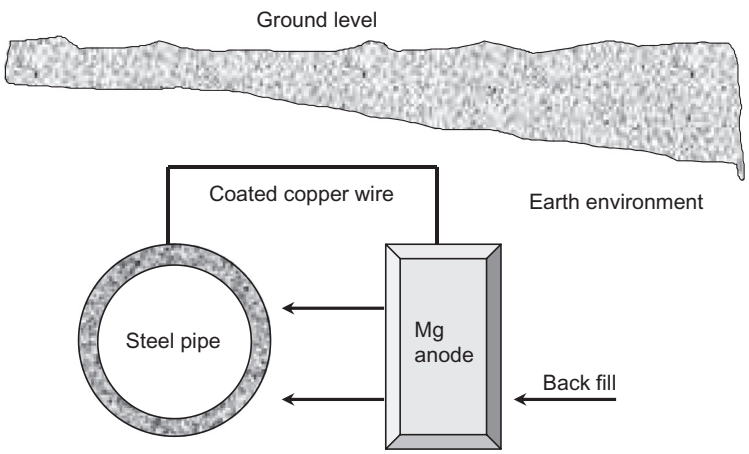

Fig. 15.4 Protection of an underground pipeline with a magnesium anode.

Table 15.1 Galvanic Anode Characteristics

Material	Theoretical Output (Ah/kg)	Actual Output (Ah/kg)	Efficiency	Consumption	
				Rate (kg/A year)	Potential to CSE[a]
Zinc type I	860	781	90%	11	1.06
Zinc type II	816	739	90%	12	1.10
Magnesium H-1 alloy	2205	551-1279	25-58%	6.8-16	1.40-1.60
Magnesium high potential	2205	992-1191	45-54%	7.3-8.6	1.70-1.80
Al/Zn/Hg	2977	2822	95%	3.1	1.06
Al/Zn/In	2977	2591	87%	3.3	1.11

[a]$Cu/CuSO_4$ reference electrode.

(c) The anode must have high anode efficiency, that is, the current produced by metal dissolution must be readily available for cathodic protection.

Magnesium and zinc are the predominantly used galvanic anodes for the cathodic protection of pipelines [13–16]. The corrosion potential difference of magnesium with respect to steel is 1 V, which limits the length of the pipeline that can be protected by one anode. Economic considerations have led to the use of aluminum and its alloys as anodes. However, aluminum passivates easily, decreasing current output. To avoid passivation, aluminum is alloyed with tin, indium, mercury, or gallium. The electrochemical properties of these alloys, such as theoretical and actual output, consumption rate, efficiency, and open circuit (corrosion) potential, are given in Table 15.1.

Example 15.2

Iron corrodes in a solution saturated with oxygen. The pH of the solution is 7 and the partial pressure of oxygen is 1.

(i) Calculate corrosion current and potential of the system.

(ii) A sacrificial zinc-manganese alloy anode is coupled with iron to protect the structure.
  (a) Calculate the sacrificial anode galvanic current and potential necessary to protect the structures.
  (b) Calculate the corrosion current of the protected structure.

(iii) Is the applied sacrificial protection system satisfactory? Does the system offer overprotection or underprotection?

Given:

$b_a = 0.1\text{V/decade}, \quad b_c = -0.1\text{V/decade}$

$P_{O_2} = 1\text{ atm.}, \quad [Fe^{2+}] = 0.29\text{ M}$

$e^{o}_{Fe|Fe^{2+}} = -0.44\text{ V vs. SHE}$

$e^{o}_{ZnMn} = -1.46\text{ V vs. SHE}$

Exchange current density for oxygen reduction $i^{o}_{O_2} = 10^{-6}\,A/cm^2$
Exchange current density for iron dissolution $i^{o}_{Fe} = 10^{-5}\,A/cm^2$
Exchange current density for zinc alloy anode $i^{o}_{ZnMn} = 10^{-5}\,A/cm^2$

Solution:

(i) Calculation of corrosion current and potential of Fe-O_2 corrosion couple.

For the given problem,

Anodic reaction:

$$Fe \rightarrow Fe^{2+} + 2e^{-}, e^{o}_{Fe|Fe^{2+}} = -0.44\,V \text{ vs. SHE}$$

Using the Nernst equation:

$$e_{eq,Fe} = -0.44 + \frac{0.059}{2}\log[0.29] \rightarrow e_{eq,Fe} = -0.4559\,V \text{ vs. SHE}$$

Tafel equation:

$$\eta_a = b_a \log\left(\frac{i_a}{i^{o}_{a}}\right) \quad \text{where } \eta_a = E_{corr} - e_{eq,Fe} \tag{15.6}$$

Cathodic reaction:

$$O_2 + 2H_2O + 4e^{-} \rightarrow 4OH^{-}$$
$$e_{eq,O_2} = 1.227 - 0.059\,pH$$
$$e_{eq,O_2} = 0.814\,V \text{ vs. SHE.}$$

Tafel equation:

$$\eta_c = b_c \log\left(\frac{i_c}{i^{o}_{c}}\right) \quad \text{where } \eta_c = E_{corr} - e_{eq,O_2} \tag{15.7}$$

Calculation of E_{corr} and I_{corr}:

Substituting $i_a = I_{corr}$ and $i_c = I_{corr}$ in Tafel expressions (15.6) and (15.7)

$$E_{corr} = e_{eq,Fe} + b_a \log\left(\frac{I_{corr}}{i^{o}_{a}}\right) = e_{eq,O_2} + b_c \log\left(\frac{I_{corr}}{i^{o}_{c}}\right)$$

The following polarization equations are obtained: $E_{corr} = 0.1 \log I_{corr} + 0.0441$ for the anodic reaction and $E_{corr} = -0.1 \log I_{corr} + 0.214$ for the cathodic reaction.

Solving the anodic and cathodic equations

$$I_{corr,Fe} = I_{corr} = 7.14\,A/cm^2$$
$$E_{corr} = 0.13\,V$$

$I_{corr,Fe}$ and E_{corr} can also be obtained graphically using the cathodic and anodic slopes and the exchange current densities of both redox reactions. The plot of E vs. $\log i$ is shown in Fig. 15.5.

(ii) Calculate the sacrificial anode galvanic current and potential necessary to protect the structure.

(a) The intersection of the oxygen reduction and zinc alloy oxidation polarization curves yields the sacrificial galvanic current and the new corrosion potential of the system. The exchange current density of the corresponding cathodic

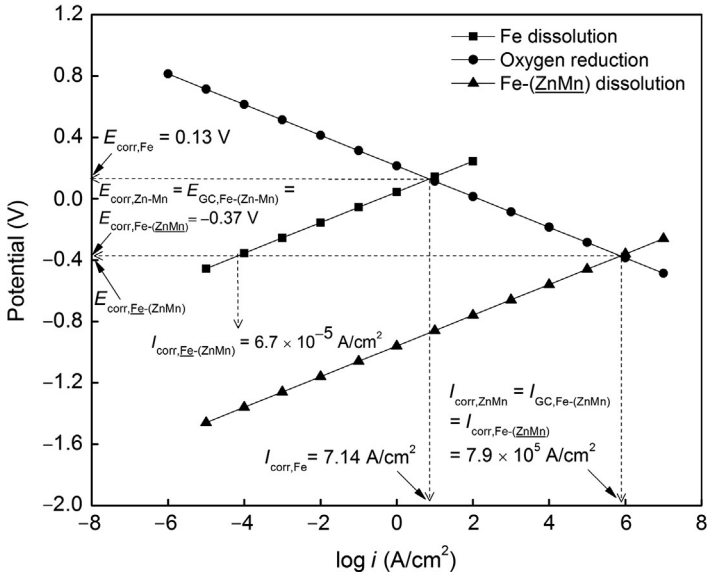

Fig. 15.5 Evans plot for the sacrificial galvanic protection system.

reaction for the ZnMn alloy anode is too small and can be neglected. Use the following kinetic parameters for ZnMn alloy in the Tafel equation:

$$b_a = 0.1\text{V/decade};\quad e^o_{ZnMn} = -1.46\,\text{V vs. SHE};\quad i^o_{ZnMn} = 10^{-5}\,\text{A/cm}^2$$

$$E_{corr,Fe-(ZnMn)} = e^o_{ZnMn} + b_a \log\left(\frac{I_{corr,Fe-(ZnMn)}}{i^o_{ZnMn}}\right) = e_{eq,O_2} + b_c \log\left(\frac{I_{corr}}{i^o_c}\right)$$

Because $I_{corr} = I_{GC,Fe-(ZnMn)}$, we get:

$$E_{corr,Fe-(ZnMn)} = 0.1 \times \log I_{corr,Fe-(ZnMn)} - 0.96$$

and

$$E_{corr,Fe-(ZnMn)} = -0.1 \times \log I_{corr} + 0.214$$

The values for $I_{corr,Fe-(ZnMn)}$ and $E_{corr,Fe-(ZnMn)}$ are obtained by solving the anodic and cathodic equations. The sacrificial anode galvanic current, $I_{GC,Fe-(\underline{ZnMn})}$, and the corrosion potential necessary to protect the structure are:

$$I_{GC,Fe-(ZnMn)} = I_{GC,Fe-(\underline{ZnMn})} = 7.9 \times 10^5\,\text{A/cm}^2$$

$$E_{corr,Fe-(ZnMn)} = -0.37\,\text{V}$$

(b) Calculate the corrosion current for the protected structure:

The corrosion current for the protected structure is calculated by substituting E_{corr} in Eq. (15.6) with $E_{corr,Fe-(ZnMn)}$:

$$E_{corr,Fe-(ZnMn)} - e_{eq,Fe} = b_a \log\left[\frac{I_{corr,\underline{Fe}-(ZnMn)}}{i^o_{Fe}}\right]$$

$$-0.373-(-0.4559)=0.1\log\left[\frac{I_{\text{corr,Fe}-(\text{ZnMn})}}{i^{o}_{\text{Fe}}}\right]$$

Corrosion current of protected structure $\rightarrow I_{\text{corr,Fe-(ZnMn)}}=6.74\times10^{-5}$ A/cm^2

(iii) The system is underprotected under the given conditions because the protection current is not sufficient to move the potential to the equilibrium potential of Fe $=-0.44$ V vs. SHE.

15.2.2.2 Impressed current cathodic protection

As shown in Fig. 15.6, external DC current is supplied from a power source such as a rectifier. The external DC current is used to cathodically polarize the pipeline. Impressed Current System (ICS) can be used to protect bare and poorly coated pipelines because of high current capacity. The anodes are made of durable materials that resist wear or dissolution. Iron with 14% silicon, carbon, and graphite are some commonly used anodes for pipeline protection [17,18]. All impressed current CPs require routine maintenance because they involve a power supply and more electrical connections than sacrificial systems.

In aerated neutral or alkaline solutions, cathodic corrosion reaction is usually the reduction of oxygen. The cathodic corrosion process is controlled by the availability of oxygen, which is related to oxygen diffusion to the cathodic corrosion site. For structures immersed in flowing water, the limiting current of oxygen varies with the flow velocity of the water. This will lead to underprotection or overprotection.

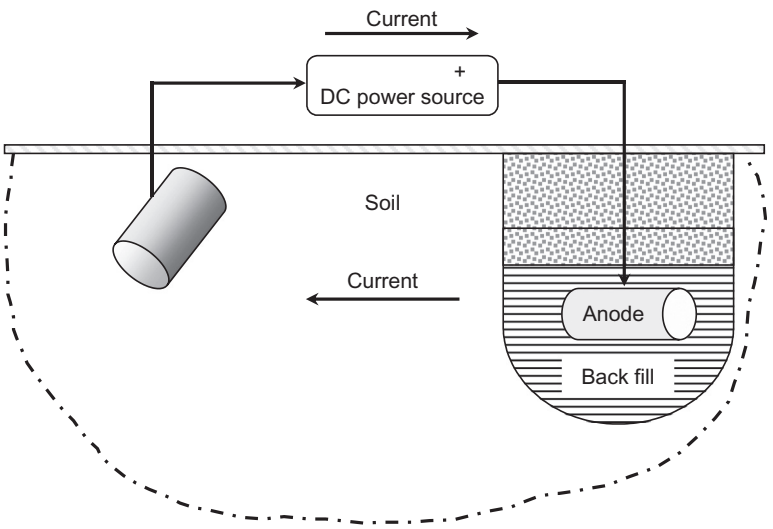

Fig. 15.6 Schematic of cathodic protection system using impressed current.

The corresponding applied current density needs to be varied accordingly, and several tedious automated controls are essential. Controlled potential systems are used in these conditions. The potential required to protect the structure is applied and the impressed current varied accordingly. Controlled potential cathodic protection is widely used for ship hulls and several sea water installations where the velocity of flowing water is a variable.

15.2.3 Selection of cathodic protection system

When selecting a cathodic protection system, the designer should consider the size of the structure and the past project experience in operating and maintaining both types of systems.

15.2.3.1 Basis for selecting a sacrificial anode system

Advantages:

(i) No need for an external power source
(ii) Less complex installation
(iii) Uniform distribution of current
(iv) Minimum maintenance
(v) Minimum cathodic interference

Limitations:

(i) Current output is limited. It has limited driving potential; therefore, the protection for the bare steel area is limited for each anode.
(ii) Poorly coated structures need more anodes.
(iii) The system is ineffective in high resistive environments.

15.2.3.2 Basis for selecting ICS

Advantages:

(i) The system can be applied with a wider range of voltage and current requirements.
(ii) High current can be impressed with a single ground bed.
(iii) Single installation can protect larger metallic surface.
(iv) Uncoated and poorly coated structures can be effectively protected.
(v) Voltage and current can be varied to meet changing conditions with time.

Limitations:

(i) Overprotection leads to coating damage and hydrogen embrittlement.
(ii) The system is affected by interference problems.
(iii) External power is necessary, thus the system is vulnerable to power failure.

Example 15.3

In a seagoing ship hull, the steel surface exposed to sea water is under diffusion control by dissolved oxygen. The limiting current for oxygen diffusion changes by an order of two when the speed of the ship increases from 10 to 15 mph. (i) How does the limiting current density for oxygen reduction vary? Calculate the cathodic current required for protection. (ii) For the above system, suggest the nature of cathodic protection that is ideal (constant current or constant potential) and why?

Given: For oxygen reduction, $i_{L,O_2} = 10^{-4}$ A/cm^2; $b_a = 0.04$ V/decade; exchange current density for Fe dissolution, $i^o = 10^{-6}$ A/cm^2.

Solution:

(i) With an increase in water velocity, the diffusion of oxygen to the steel surface increases, resulting in increased oxygen reduction and steel corrosion rate. Fig. 15.7 shows that with increased speed, the diffusion current of oxygen increases from 10^{-4} to 10^{-2} A/cm^2.

Because oxygen is in a limiting region (vertical line),

$$i_{L,O_2} = I_{corr} = i_c \text{ (to be applied)}$$

Therefore, when $i_{L,O_2} = 10^{-4}$ A/cm^2

$$I_{corr} = 10^{-4} \text{ A/cm}^2$$

$$I_{app} = i_c - i_a$$

$$I_{app} = 10^{-4} - 10^{-6}$$

$$I_{app} = 10^{-4} \text{ A/cm}^2$$

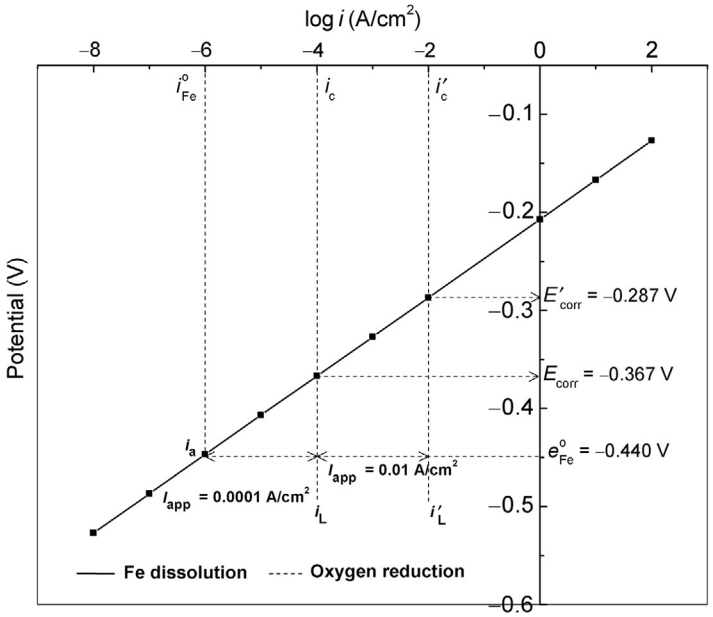

Fig. 15.7 Effect of diffusion rate of oxygen on the impressed current protection system.

When $i_{L,O_2} = 10^{-2}\,A/cm^2$

$$I_{corr} = 10^{-2}\,A/cm^2$$

$$I_{app} = i_c - i_a$$
$$= 10^{-2} - 10^{-4}$$

$$I_{app} = 0.01\,A/cm^2$$

(ii) For the above case, the limiting current of oxygen varies with the velocity of the moving water or indirectly with the velocity of the moving ship. Hence, the rate of oxygen reduction varies and leads to variation in corrosion current. A constant cathodic current impressed system will lead to overprotection or underprotection due to the variation in corrosion current. To solve this problem, ship hulls generally use a constant cathodic potential system. When the system is polarized to the equilibrium potential of iron, cathodic current varies since applied potential is maintained constant.

15.3 CATHODIC PROTECTION CRITERIA

15.3.1 Potential criteria

Kuhn [19] first postulated in 1933 that the potential needed to stop corrosion is probably in the neighborhood of −0.85 V vs. $Cu/CuSO_4$. The results obtained from extensive studies on cathodic protection [20–27] helped National Association of Corrosion Engineers (NACE) to establish criteria for cathodic protection [28]. NACE RP-01-69 specifies: "A negative (cathodic) potential of at least 850 mV vs. $Cu/CuSO_4$ should be applied to protect the structure" [28,29]. However, in the presence of sulfides, bacteria, elevated temperatures, acid environments, and dissimilar metals, the criteria of −850 mV may not be sufficient [5,30–33]. According to NACE, one should also account for the IR drop at the metal-soil interface, which is included in most practical measurements and is an uncertain value depending on the electrolyte (soil) resistance.

For other metals, such as aluminum and copper piping, NACE RP0169 suggests a minimum of 100 mV cathodic polarization between the structure surface and a stable reference electrolyte. Some of the other criteria suggested by NACE RP0169 and Gummow [20] are summarized in Table 15.2.

15.3.2 IR Drop considerations

The IR drop is caused by current flow through the soil, pipe coating, and metallic path [5]. All cathodic protection potential measurements contain an IR drop component when CP current or interference current is present. The measured potential (E_m) is the sum of polarized potential (E_p) measured near the cathode electrolyte interface and IR drop along the

Table 15.2 Criteria for Cathodic Protection

Criterion	Measurement Condition	Comments
1. Potential less than −0.85 V vs. Cu-saturated CuO_4 for steel	Current on (IR_Ω present)	Meaningful in some environments Uncertain due to IR_Ω
2. Cathodic polarization more than 300 mV active to corrosion potential of structure	Current on (IR_Ω present)	Uncertain due to interferences from IR_Ω
3. Cathodic polarization more than 100 mV active to corrosion potential of structure	Current interrupted (IR_Ω absent)	Interruption techniques difficult to implement
4. Cathodic polarization to a potential where Tafel behavior achieved	Current variable (IR_Ω present)	Difficult to determine in presence of IR_Ω
5. Net protective current flows from electrolyte into the structure surface	Unspecified	Correct in theory Difficult to determine in practice

path. On a new pipeline with a high-performance coating, a large IR drop is produced due to extremely high dielectric resistance of the coating. When the current direction is toward the structure, the polarity of the IR drop is additive and measured potential (E_m) is greater than E_p. The structure appears better protected than it really is. When the current direction is away from the structure, like stray current, the IR drop subtracts from E_p and the structure appears less protected than it really is. When the IR drop is high, both effects could be detrimental. Measuring the IR drop is crucial in evaluating the correct polarized potential. Gummow summarizes several methods that have been developed to measure the IR drop [34], namely:

(a) Extrapolation of potential measurements taken with the reference electrode placed at increasing distance from the pipe
(b) Extrapolation using a stepwise current reduction technique
(c) Interruption of current with the measurement of an "instant off" potential

Current interruption is considered to be the best IR drop correction technique. However, current interruption technique is very difficult to conduct for large structures, such as pipelines. IR (see Section 15.5.1.3) coupon technique to estimate the IR drop has been implemented worldwide.

15.3.3 Electrochemical basis for CP criteria

At the equilibrium potential, the rate of anodic reaction in Eq. (15.1) is equal to the rate of cathodic reaction while the net current flow is zero [35,36]. When polarized to the reversible potential, the corrosion rate of the metal is equal to zero. The equilibrium potential of the system can be calculated from the Nernst equation [37] as follows:

$$e_{Fe|Fe^{2+}} = -0.44 + \frac{0.059}{2}\log\left(a_{Fe^{2+}}\right) \tag{15.8}$$

The activity of Fe^{2+} in equilibrium is determined by the solubility of the covering layer of $Fe(OH)_2$.

$$a_{Fe^{2+}} = \frac{\text{solubility product}}{(OH^-)^2} \tag{15.9}$$

The concentration of OH^- is estimated assuming that its concentration at equilibrium is twice that of (Fe^{2+}) according to:

$$Fe(OH)_2 \rightarrow Fe^{2+} + 2OH^- \tag{15.10}$$

The calculated potential is -0.59 V vs. SHE, (-0.91 V vs. $Cu/CuSO_4$ reference electrode). The value of this potential is in agreement with the empirical value of -0.85 V vs. $Cu/CuSO_4$ discussed earlier.

Example 15.4

Calculate the electrochemical criteria for the cathodic protection of iron. The solubility product of iron is 1.8×10^{-15} in a neutral solution. Estimate the potential with reference to $Cu/CuSO_4$ electrode. Repeat the same for zinc, if solubility product for zinc is 4.5×10^{-17}.

Solution:

The theoretical open circuit potential is calculated by using the Nernst equation.

$$e_{Fe|Fe^{2+}} = -0.44 + \frac{0.059}{2}\log\left(a_{Fe^{2+}}\right)$$

$$a_{Fe^{2+}} = \frac{\text{solubility product}}{(OH^-)^2}$$

$$e_{Fe|Fe^{2+}} = -0.59\,\text{V vs. SHE}$$

$$e_{Fe|Fe^{2+}} = -0.91\,\text{V vs. } Cu/CuSO_4$$

Solubility product of zinc $= 4.5 \times 10^{-17}$

$$e_{Zn|Zn^{2+}} = -0.763 + \frac{0.059}{2}\log\left(a_{Zn^{2+}}\right)$$

$$a_{Zn^{2+}} = \frac{\text{solubility product}}{(OH^-)^2}$$

$$e_{Zn|Zn^{2+}} = -0.93\,\text{V vs. SHE}$$

$$e_{Zn|Zn^{2+}} = -1.25\,\text{V vs. } Cu/CuSO_4$$

15.4 FIELD DATA AND DESIGN ASPECTS

Successful application of cathodic protection depends upon the selection, design, installation, and maintenance of the system. Before designing the cathodic protection systems, adequate field data must be collected, analyzed, and evaluated. Nature and conditions of the soil are reflected by field measurements like soil resistance, hydrogen ion activity (pH), and the redox potential. To understand the nature of the pipeline, potential measurements, coating resistance, and meaningful design current requirement tests must be conducted.

15.4.1 Soil resistance

Soil resistance is one of the most important factors in selecting a ground bed location. The type of anode and number of anodes required [38], the length and diameter of the backfill column, and the voltage rating of the rectifier and power cost are all influenced by the soil resistance [39]. Marshy soils have low resistance, while rocky soils may have resistance of several thousands of Ohms [40,41]. Corrosion activity is always an inverse function of soil resistance. The current drastically increases in low resistive soils and the anode dissolution contribution increases. The corrosion activity of steel exposed to soils of varying activity is given in Table 15.3. The soil resistance can be estimated using the following methods:

15.4.1.1 Wenner four-pin method

This is the most commonly used method of measuring the soil resistance. In this method, as shown in Fig. 15.8, four pins are placed at equal distances "*a*." A current is sent through the two outer pins (C_1 and C_2) [42,43]. By measuring the voltage across the two inner pins, the soil resistance can be calculated using Ohm's law ($V = IR$). Soil resistance (ρ_s) can be determined using the equation:

$$\rho_s = 191.5 \times R \times L \tag{15.11}$$

where R is resistance in Ohms and L (Ω cm) is the length of the pin spacing.

This method gives an average *in situ* resistance at a depth equal to the pin spacing. Foreign buried structures may interfere with the measurements when using the Wenner method. Therefore, it is important to position the pins perpendicular to the underground pipeline [44]. If the pins are positioned parallel to the pipeline, it would result in lower resistance values than the actual resistance. If the specific soil resistance varies vertically

Table 15.3 Classification of Soil Corrosivity Based on Soil Resistivity

Resistivity range (Ω cm)	Corrosivity
0–1000	Very severe
1001–2000	Severe
2001–5000	Moderate
5001–10,000	Mild
10,001 +	Very mild

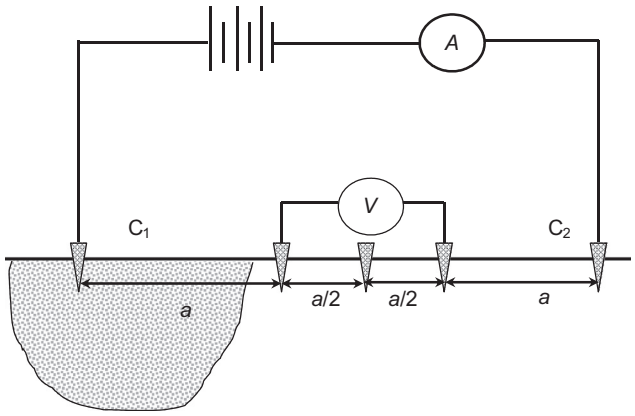

Fig. 15.8 Wenner four-pin method for measuring soil resistance.

with the depth "t," an apparent specific resistance can be obtained from a combination of the resistances of the upper and lower layers. It is recognized that the influence of the lower soil layer is only significant when $a > t$.

15.4.1.2 Soil box method

This method is based on the same principle as the Wenner four-pin test method. There are four points of electrical contact with the soil; the current is driven through the two outer points and the voltage drop is measured across the two inner points. In the soil box, however, the outer points are the metal end plates of the box, rather than pins. The inner points are pins, just as in the Wenner four-pin method. The resistance is calculated by using Ohm's law. The resistance (ρ) is given by

$$\rho_s = R\frac{w_a d_s}{l_s} \tag{15.12}$$

where w_a, d_s, and l_s are the soil box dimensions. The soil box method gives very accurate results for fluids. However, the value measured for soil samples may differ from those measured at the actual site due to variations in natural conditions including moisture, compaction, void ratio, particle size, and so forth. If the soil resistance varies with depth, the samples must be taken from an accurate map of soil resistance in the area Fig. 15.8. This method is more time-consuming than the Wenner four-pin method.

15.4.2 Hydrogen ion activity (pH)

The soil pH is a measure of the hydrogen ion activity

$$\mathrm{pH} = -\log_{10}[a_{H^+}] \tag{15.13}$$

where a_{H^+} corresponds to the activity of the hydrogen ion. pH of soils may vary in the range between 3.5 and 10. The metal corrosion rates increase with a decrease in the soil pH. It is well-known that iron passivates at pH higher than 9 [7]. The soil pH can be

determined by testing the underground water in the area of interest. In the absence of any underground water, the pH can be measured by mixing 1 volume of soil with 1 volume of distilled water. Antimony and $Cu/CuSO_4$ electrodes can be used to obtain *in situ* soil pH values.

Example 15.5

Iron corrodes in a solution saturated with oxygen. The pH of the solution plays a significant role in the corrosion of iron and the applied current needed to protect the iron. To analyze the effect of pH: (i) calculate the corrosion current and potential when the solution has a pH of 14, 10, and 7; (ii) to bring down the corrosion current to the order of 10^{-5}, calculate the impressed current needed; and (iii) Does the impressed current increase/decrease with pH? If so, why?

Given:

$b_a = 0.1$ V/decade, $b_c = -0.1$ V/decade

$p_{O_2} = 1$ atm., $[Fe^{2+}] = 0.5$ M

Exchange current density for oxygen reduction, $i^o_{O_2} = 10^{-7}$ A/cm^2

Exchange current density for iron dissolution $i^o_{Fe} = 10^{-5}$ A/cm^2

Solution:

Anodic reaction: $Fe \rightarrow Fe^{2+} + 2e^-$, $e^o = 0.44$ V

From Nernst equation $e_{eq,Fe} = -0.4488$ V

Tafel equation:

$$E - e_{eq,Fe} = b_a \log \frac{i}{i^o_{Fe}} \tag{15.14}$$

Cathodic reaction: $O_2 + 2H_2O + 4e^- \rightarrow 4OH^-$

$$e_{eq,O_2} = 1.227 - 0.059\,\text{pH} \tag{15.15}$$

(i) At pH 14, $e_{eq,O_2} = 0.401$ V

Tafel equation:

$$E - 0.401 = b_c \log \frac{i}{i^o_{O_2}}$$

At pH 10, $e_{eq,O_2} = 0.637$ V

Tafel equation:

$$E - 0.637 = b_c \log \frac{i}{i^o_{O_2}} \tag{15.16}$$

At pH 7, $e_{eq,O_2} = 0.814$ V

Tafel equation:

$$E - 0.814 = b_c \log \frac{i}{i^o_{O_2}} \tag{15.17}$$

Figure 15.9 is obtained by plotting Eqs. (15.14) through (15.17).

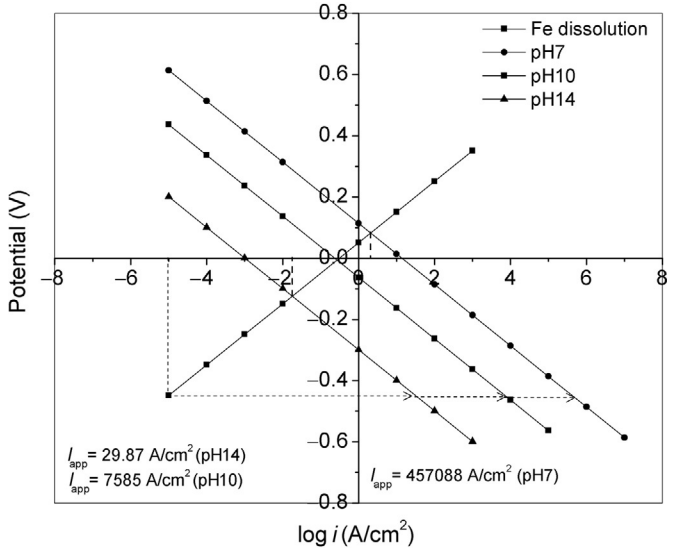

Fig. 15.9 Effect of pH on the corrosion current and applied current density.

The intersection of the anodic and cathodic slopes gives I_{corr} and E_{corr}:
pH 14: $I_{corr} = 0.0178$ A/cm^2 and $E_{corr} = -0.124$ V
pH 10: $I_{corr} = 0.269$ A/cm^2 and $E_{corr} = -0.00594$ V
pH 7: $I_{corr} = 2.06$ A/cm^2 and $E_{corr} = 0.0826$ V

(ii) From the anodic slope for iron, the potential corresponding to the corrosion current of 10^{-5} is -0.45 V. The protection potential required to bring down the corrosion current of 10^{-5} is $E_{prot} = -0.45$ V. Impressed currents required are:
pH 14: $I_{app} = 31.54$ A/cm^2
pH 10: $I_{app} = 7224$ A/cm^2
pH 7: $I_{app} = 425{,}406$ A/cm^2

(iii) The impressed current required to protect steel increases with a decrease in pH. With a decrease in pH, the equilibrium potential of the oxygen electrode goes to more positive potential; this increases the cathodic and anodic potential difference, leading to a shift in the corrosion potential to a more positive value. Therefore, the corrosion current increases with a decrease in pH. To counter this increased corrosion current, higher applied current is needed.

15.4.3 Microbiological activity and redox potential

The soils may become more aggressive in the presence of microbiological activity. Commonly observed bacteria present in the soils are sulfate reducing (Desulpho Vibrio desulpharicans). This bacterium consumes hydrogen and reduces sulfates to sulfide [45,46].

$$SO_4^{2-} + 4H_2 \rightarrow S^{2-} + 4H_2O \tag{15.18}$$

The product is hydrogen sulfide, which reacts with steel and produces black FeS. Under anaerobic conditions, the reactions are:

$$4Fe + SO_4^{2-} + 4H_2O \rightarrow 3Fe(OH)_2 + FeS + 2OH^- \quad (15.19)$$

It is explicit that hydrogen is consumed and H_2S is formed. The corrosion acceleration by bacteria is twofold. Hydrogen consumption accelerates the corrosion by decreasing the cathodic polarization. Also, iron sulfide formation increases the corrosion rate by forming a galvanic couple with bare steel [47,48]. Bacteria survive by consuming certain types of adhesives. The favorable conditions for prompting bacteriological activity include a temperature range of about 35–40 °C and pH between 5.5 and 8.5.

The presence of bacterial activity can be qualitatively established by placing a few drops of hydrochloric acid on the corrosion products. The evolution of H_2S indicates the existence of anaerobic bacteriological activity. The bacteriological existence is also established by measuring the redox potential. This can be done by placing a redox probe into freshly dug soil at the pipeline depth. The potential is measured between a clean platinum surface and a saturated calomel reference electrode [49–53]. The redox potential measurement data and the tentative anticipated bacteriological activity are shown in Table 15.4.

Sulfate reducing bacteria and sulfur oxidizing bacteria (Thiobacillus, thioxidants) may also exist in an aerated environment. These bacteria consume oxygen and oxidize sulfides to sulfuric acid (H_2SO_4) during their metabolic activity. They can produce sulfuric acids with concentrations as high as 10% (i.e., pH 0.5) [54]. In general, the microbiological activity can increase the corrosion rate by:

(a) Depolarizing the cathodes.
(b) Creating corrosion products that can be effective cathodes.
(c) Causing damage to coatings and exposing structure to environments.

15.4.4 Coating resistance

Cathodic protection is always applied as a complimentary protection to the coating. The coating reduces the amount of current necessary to be impressed for cathodic protection. Coating is usually employed to distribute current evenly so that precise protection of the structure can be accomplished. It also levels out the uneven distribution of current at

Table 15.4 Classification of Soil Resistance Based on Oxidation-Reduction Potential

Redox Potential V vs. SCE	Anaerobic Condition
Below 0.100	Severe
0.100-0.200	Moderate
0.200-0.400	Slight
Over 0.400	None

different parts of a structure. Most protection systems are coated with an insulation material that greatly reduces the current required for cathodic protection. In other systems, the insulation layer is formed during the passage of current and after a while the current required for protection is greatly reduced. In the case of steel-protected pipelines under the sea, a carbonate film is usually formed due to hard water that aids in corrosion protection. So, the coating resistance is a crucial parameter in determining the protection current to be supplied. Current requirements or current density measurements are related to the coating conductance/resistance [55,56]. The coatings used to protect pipelines include (i) coal tar and asphalt enamels, (ii) mastics, (iii) waxes, (iii) polyvinyl chloride, (iv) polyethylene tapes, (v) thermosetting epoxy resins, and (vi) epoxy coatings. A perfect coating has a coating resistance on the order of $10^{10}\ \Omega\ \text{cm}^2$. Unfortunately, coatings are not perfect; they develop holidays and deteriorate with time. Coating damages are caused by chemicals present in soil bacteriological activity, penetration by tree roots, and thermal and mechanical stresses [55,56].

15.4.4.1 Determination of coating resistance

The effective coating resistance can be determined at any section of the pipeline by applying a cathodic current [53,56]. The temporary current should be interrupted at defined time intervals (40 s with 20 s off). The current-induced difference may be found out at two different locations of the pipeline. Once these differences in pipeline current ($I = I_{on} - I_{off}$) and the difference in potential ($E = E_{on} - E_{off}$) are known at two locations, the coating resistance can be estimated by using the expression:

$$R_c = E_1 + \frac{E_2}{2(I_1 - I_2)} \tag{15.20}$$

where E_1 and E_2 are the differences in the remote electrode potential in volts, and I_1 and I_2 are the differences in pipeline current in amperes. The effective coating resistance can be estimated by multiplying by the surface area ($\Omega\ \text{cm}^2$).

15.4.5 Required current density

A critical part of design calculations for cathodic protection systems is the amount of current density (protection current) required to change the structure's potential to −0.85 V vs. $Cu/CuSO_4$. The current density required for complete protection depends on the metal being protected and the environment. This current can be estimated from the Evans plot shown in Figs. 15.1 and 15.2. However, because these measurements are based on theoretical values and laboratory experiments, application may result in significant errors. To estimate the current necessary to protect the pipeline in service one should perform a field test. The field test is performed by applying a test current to the structure and measuring the resultant change of potential. From these data, the current requirement can be estimated [29,56,57]. For a new pipeline installation, the current density

Table 15.5 Current Requirements for Cathodic Protection of Bare Steel

Environment	(mA/m^2)
Neutral soil	4.5-16.0
Well-aerated neutral soil	21.5-32.0
Highly acid soil	32.0-160.0
Soil supporting sulfate reducing bacteria	65.0-450.0
Heated soil	32.0-270.0
Stationary fresh water	11.0-65.0
Moving, oxygenated fresh water	54.0-160.0
Sea water	32.0-110.0

requirements are usually estimated from previous estimates such as those presented in Table 15.5. For coated pipelines, the amount of the exposed steel depends on the quality of the coating. An arbitrary coating efficiency of 90-95% (10-5% bare steel) is assumed in current requirement calculations. Current density requirements for soils, sea water, and a variety of other aqueous environments are available [58–61].

The total current requirement (I_c) in mA is the total area, A_c, in m^2 of the pipeline multiplied by the percent or bare metal and the current density required (I_{req}), or

$$I_c = A_c f_c I_{req} \tag{15.21}$$

where I_c is the total current requirements in milliamperes (mA); A_c is the total area of the pipeline in square meters (m^2); and f_c is the fraction of the external pipe surface exposed at coating defects and bare metal areas. The product $A_c f_c$ is surface area exposed.

15.5 MONITORING METHODS

The effectiveness of cathodic protection can be accomplished by monitoring the pipeline potential using the close interval potential survey (CIPS) method or by using direct current voltage gradient (DCVG) or IR coupon techniques. Also, physical and electrochemical methods can be used to estimate the corrosion rates of a cathodically protected system.

15.5.1 Potential surveys

Measuring the pipeline potential with reference to a nonpolarized reference electrode (e.g., Cu/$CuSO_4$) is one of the most commonly used methods for potential survey (PS) of the pipeline. This method is based on the potential criteria listed in the previous section. Presently, battery operated, inexpensive, light (50 MΩ or higher) internal resistance voltmeters with a resolution of 1 mV are widely available. Microprocessor digital recorders called data loggers are more frequently used for monitoring pipeline potential.

15.5.1.1 CIPS technique

The CIPS method is based on connecting a thin, strong cable to a monitored pipeline and performing frequent potential readings along the route [62]. The operator carries a battery-operated portable computer in a field while walking the line. Wire connected to a terminal point is reeled out through a distance counter. The potential of the buried surface is measured through a walking stick reference electrode thrust into the earth at about 1 m intervals. Potential vs. distance readings are automatically logged into the computer. Special software is used for data processing [62].

15.5.1.2 DCVG method

The DCVG method provides evaluation of CP effectiveness and detection of defects in insulation by determining the zones of inflow or outflow of polarizing current [63–66]. The impressed cathodic protection current, upon reaching the insulation defects, causes a drop in voltage in the soil. This potential difference can be detected between the two electrodes placed on the ground with a sensitive mV meter. The location of the coating defect can be determined with a precision of 10 cm. The center point of the defected area can be located by means of two perpendicular measurements series. The size of the insulation defect is characterized by a relative number, so-called % IR number, obtained from potential gradient graphs and soil resistance measurements. A distinctive feature of this technique is that even small defects can be located accurately, with claimed accuracy of about 10 cm. With the DCVG method, parallel pipelines can be inspected at the same time. It does not require extra current input. Noises from other current sources can be eliminated easily. This method is also effective in pipelines without cathodic protection by using temporary anodes and CP stations. In recent years, there have been improvements contributing to more precise monitoring of pipelines [67].

Combined methods are also used to monitor cathodic protection efficiency. In the intensive measurement described by Wessling *et al.* [68], both CIPS and DCVG are used. The worker walks the pipeline route and records the distance and the "switch on" and "switch off" potential changes vs. the portable reference electrode at small intervals. The measurements are supplemented with ON/OFF potential gradients in one or two directions perpendicular to the pipeline. The measured (real) values serve as the basis for calculating the insulation defects (% IR). Other techniques such as the intensive holiday detection method can be used to detect the coating defects in the pipelines. Implementation of the above methods has led to a considerable decrease in the number of breakdowns of underground pipelines.

15.5.1.3 IR coupons/simulation probes

Coupons have been used extensively for years in the laboratory and field environment to determine the corrosion rate of metals under various conditions [34,69,70]. They were

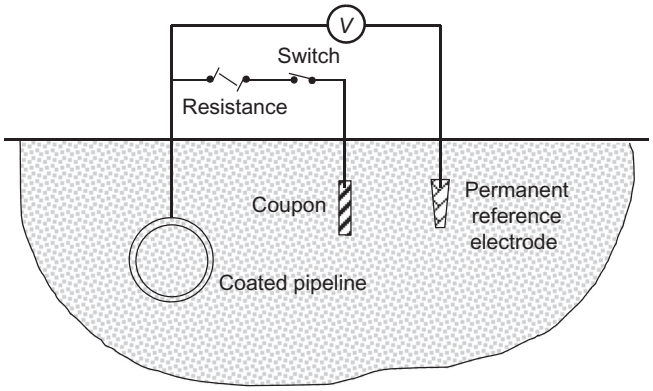

Fig. 15.10 Coupon simulator circuit to determine IR drop.

used specifically to test the effectiveness of the −850 mV (vs. $Cu/CuSO_4$ electrode) and the −100 mV polarization potential shift cathodic protection criteria.

The coupons have been used to monitor cathodic protection systems in Europe since 1960 [70]. Most of these coupons were installed since 1975. Coupons are used in the form of steel electrodes of a strictly determined shape and surface area, protected by cathodic protection together with the structure. The schematic of the coupon installation on a pipeline is shown in Fig. 15.10.

Disconnecting the coupon momentarily from the pipe interrupts the coupon current and provides an opportunity to measure the "instant off" potential. Further remnants of IR drop can be eliminated by fixing the reference electrode near the coupon or by using an electrolytic bridge [70,71]. Using these coupons, the IR-free potential can be measured without interrupting the cathodic protection to the pipeline [34]. A distinctive feature of the use of coupons is that the effects of steady state and DC transit stray currents can be measured accurately [72,73]. In 1994 Martin [74] reported the use of coupons to monitor the impressed current cathodic protection system at river crossings on a pipeline in Papua, New Guinea. More than 400 probes have been installed on the Trans Alaska pipeline systems since 1994. Uses of coupons have proven very effective for measuring the level of cathodic polarization and for detection of holidays.

15.5.2 Corrosion rate measurements

The most widely used potential monitoring measurements are based on protection potential criteria. Despite improvements in these methods, they only indicate if the pipeline is protected, underprotected, or overprotected. These methods can only estimate the corrosion rates, but should not be used to predict the life expectancy of the system. A more advantageous solution would be the introduction of kinetic CP criterion that

Table 15.6 Physical and Electrochemical Methods for Corrosion Rate Measurements

Physical Methods	Electrochemical Methods
Gravimetry	Tafel polarization
Electrical resistance	Linear polarization
Radiography	Electrochemical impedance spectroscopy
Ultrasonic	Harmonic synthesis
Eddy currents	Electrochemical noise

would allow maintaining the metal structure corrosion rate at a given level depending on actual requirements.

Several electrochemical and physical methods can be used to measure the corrosion rate of the system. Some of the commonly used methods are listed in Table 15.6. The use of these electrochemical tools in monitoring the corrosion rate of cathodically protected structures was reviewed by several researchers [75–80]. More information and the scope of corrosion rate measurements of cathodically polarized metal structures by electrochemical techniques can be obtained in the reviews by Jankowski [81,82].

15.6 DESIGN OF CATHODIC PROTECTION SYSTEMS

The ideal design for a cathodic protection system is the one that will provide desired degree of protection at the minimum total annual cost over the projected life of the structure. Design of cathodic protection systems for pipelines has been extensively studied, and several standards have evolved over the decades [56,57,83–96]. A detailed description has been illustrated in the work by Peabody [56]. The basic procedure involved in the design of cathodic protection is summarized below.

15.6.1 Choice of the CP system

It is essential to make an important decision on the selection of the CP system to be installed. The choice of the CP system is based on the environment in which the pipeline is operated. The merits of each system are illustrated in Section 15.2.3. Sacrificial protection is generally employed in environments with low soil resistance (10,000 Ω cm) with a relatively low protective current requirement because of the low driving voltage. Well-coated and isolated pipelines favor the installation of a sacrificial system in high resistive soils. On the other hand, ICS are usually installed in conditions where the current requirements are higher and for pipelines that are bare or poorly coated. In all cases, the final decision is based on the total installation and annual maintenance cost of the systems.

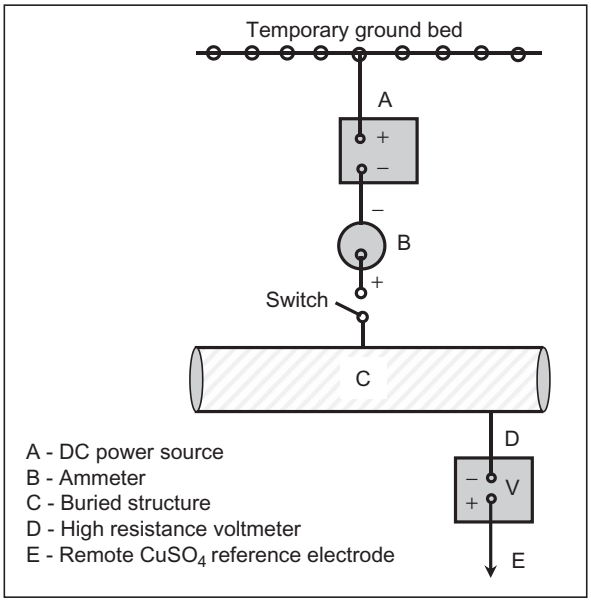

Fig. 15.11 Cathodic protection requirement test.

15.6.2 Design of sacrificial protection system

The basic design of sacrificial CP system includes calculation of cathodic protection circuit resistance, potential difference between the anode and structure, anode output, number of anodes, and the anode life expectancy. A schematic of the cathodic protection test is given in Fig. 15.11. To estimate current requirements, a test is needed to determine the current (i_c) necessary to provide adequate protection for the pipeline. This can be done by applying current using a temporary test setup and adjusting the current from the rectifier until the cathodic protection criteria is reached.

15.6.2.1 Cathodic protection circuit resistance

The cathodic protection circuit resistance includes the anode to soil resistance, resistance of the wire/cable, and the structure to soil resistance.

Anode Resistance: The anode resistance has a significant role in determining the amount of the anode material to be used [84]. The anodes use in the sacrificial cathodic protection system is of three types: vertical anodes, horizontal anodes, and grouped anodes. A typical graphite anode vertical and horizontal installation is shown in Figs. 15.12 and 15.13. The resistance of the vertical anode to earth is calculated using the Dwight formula [87].

$$R_v = \frac{\rho_s}{2\pi L}\left(\ln\frac{8L}{d_a} - 1\right) \tag{15.22}$$

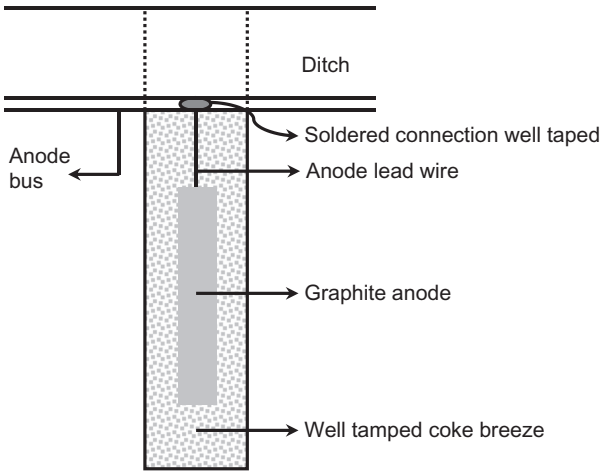

Fig. 15.12 Typical graphite anode-vertical installation.

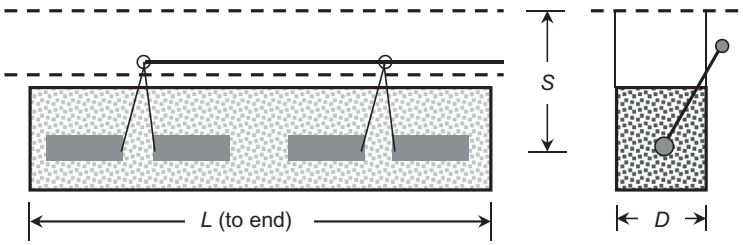

Fig. 15.13 Typical graphite anode-horizontal installation.

where R_v is the resistance to earth in Ohms (Ω), ρ_s is the soil resistance in Ohm centimeters (Ω cm), L is the anode length in centimeters (cm), and d_a is the anode diameter in centimeters.

If horizontal anodes are used, the resistance to earth is given by a modified Dwight formula [57,87].

$$R_a = \frac{\rho_s}{2\pi L}\left(\ln\left[\frac{4L^2+\sqrt{(2h)^2+L^2}}{2dh}\right]+\frac{2h}{d_a}-\frac{\sqrt{(2h)^2+L^2}}{L}-1\right) \tag{15.23}$$

where R_a is the resistance of anode to earth in Ohms (Ω), L is the anode length in centimeters (cm), d is the anode diameter in centimeters, and h is the depth below the surface to the center of the anode in centimeters.

In the case of grouped anodes, the resistance to earth is given by the Sunde equation [88]

$$R_n = \frac{\rho_s}{2\pi NL}\left(\ln\frac{8L}{d_a}-1+\frac{2L}{S}\ln 0.656N\right) \tag{15.24}$$

Table 15.7 Resistance and Current Capacity Data for Copper Cable

Size AWG[a]	dc Resistance 20 °C	Max dc Current Capacity (A)
14	8.4650	15
12	5.3152	20
10	3.3466	30
8	2.0998	45
6	1.3222	65
4	0.8334	85
3	0.6595	100
2	0.5217	115
1	0.4134	130
1/0	0.3281	150
2/0	0.2608	175
3/0	0.2070	200
4/0	0.1641	230

[a]American wire gauge (AWG).

where R_n is the resistance of anodes to earth in Ohms, L is the anode length in centimeters (cm), d_a is the anode diameter in centimeters, N is the number of anodes, and S is the center to center spacing of anodes in centimeters.

15.6.2.2 Cable resistance

The anode and structure are interconnected by copper cables. The copper cables have an inherent resistance (R_w) to current flow. Table 15.7 presents the resistance of copper cable data.

15.6.2.3 Structure to electrolyte resistance

The structure to electrolyte resistance is not very significant. Detailed information on calculating structure to electrolyte resistance can be obtained in the work by Peabody [56].

15.6.2.4 Total circuit resistance

The total cathodic protection circuit resistance, R_t is given by:

$$R_t = R_a + R_w + R_{soil} \tag{15.25}$$

where R_a is the anode resistance, R_w is wire resistance, and R_{soil} represents the soil resistance.

15.6.2.5 Anode output

The anode output depends on the anode circuit resistance and potential difference between the anode and the pipeline. The anode output is directly proportional to the potential difference between the open circuit potential of the anode ($e_{eq,A}$) and the

cathodically polarized potential of the pipeline (E_p). The current output I_a in mA is then calculated from Ohm's law:

$$I_a = \frac{(E_p - e_{eq,A})}{R_a} 1000 \tag{15.26}$$

15.6.2.6 Number of anodes and anode life

The number of anodes is calculated from the anode output and the current density requirements. The number of anodes (N) required is given by

$$N = \frac{i_c \times A_c}{I_a} \tag{15.27}$$

where A_c is the area of structure to be protected and i_c is the cathodic current density required for protection, and I_a is the anode output in amperes.

The cycle life (CL) of the anode is given by the formula [94]:

$$CL = \frac{\text{Th} \times W_a \times \varepsilon \times u}{h \times I_a} \tag{15.28}$$

where CL is cycle life in years, Th is the theoretical Ah/kg output (Table 15.1), W_a is the anode weight in kilograms, ε is the electrochemical current efficiency, u is the utilization factor, h is hours per year (8766), and I_a is the anode output in amperes. The utilization factor is usually chosen as 0.85 (85%). This means that once the anode is 85% consumed, its resistance to earth begins to increase to the point that its output is reduced significantly.

15.6.3 Design of ICS

Design of ICS primarily involves anode selection, rectifier selection, ground-bed selection, and calculation of the I-ground-bed resistance and other main parameters.

15.6.3.1 Current and potential distributions on the protected structure

An analytical approach to determine the current and potential distribution as a function of distance x along a coated pipeline of infinite length are given by the attenuation equations [95]:

$$\left.\begin{aligned} E_x &= E_o \exp(-\alpha x) \\ i_x &= I_o \exp(-\alpha x) \end{aligned}\right\} \tag{15.29}$$

where E_o and I_o are the potential and current at the point of connection to the anode, also known as the drainage point, and α is the attenuation coefficient.

$$\alpha = \frac{R_s}{R_k} \tag{15.30}$$

and R_s is the longitudinal resistance pipe resistance per unit length and $R_k = (R_s R_L)^{1/2}$ and

$$R_L = (E_x - E_o)/(I_x - I_o) \tag{15.31}$$

where R_L is defined as the leakage resistance of the pipeline and $E_x - E_o$ is the ohmic potential drop along the coating. The attenuation equations between two drainage points separated by a distance $2d$ are:

$$\left.\begin{aligned} E_x &= \frac{E_o \cosh \alpha(d-x)}{\cosh \alpha d} \\ i_x &= \frac{I_o \sinh \alpha(d-x)}{\sinh \alpha d} \end{aligned}\right\} \tag{15.32}$$

The variation of potential with distance along with the cathodic protection criteria is given in Fig. 15.14.

Attenuation curves with driving potential (ΔE) and polarization potential (ΔE_p) are given in Fig. 15.15. Driving potential is defined as a difference between the "on" potential and "off" potential, while polarization potential is defined as the difference between the "off" potential and the open circuit potential at each point.

15.6.3.2 Anode selection

Selection of the anode in the case of impressed current CP system is primarily based on the dissipation rate of the anode. Low resistance to current flow, low dissipation rate, physical robustness, fabrication, and minimal cost are the desirable properties of candidate anode materials. High silicon, chromium bearing cast iron has a low dissipation rate. Dissipation rate varies with the environment; however, 0.5 kg/A year is a typical requirement for the impressed current CP of pipelines.

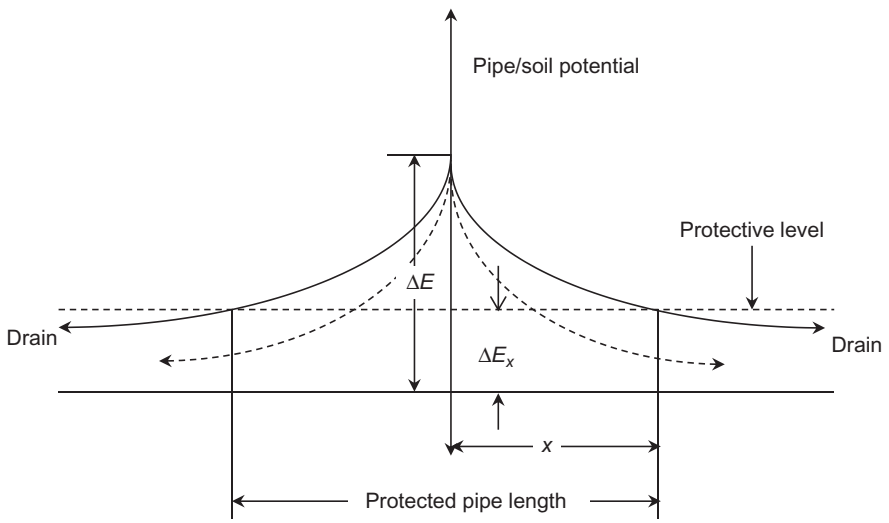

Fig. 15.14 Theoretical attenuation of potential between two drainage points on a pipeline.

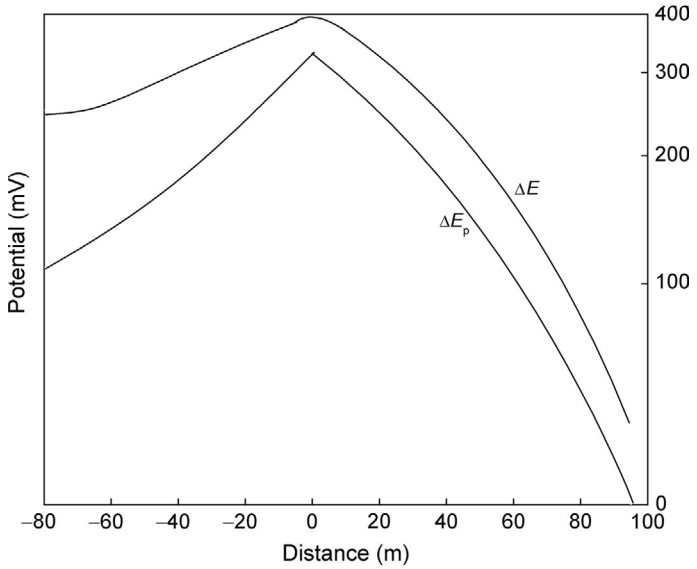

Fig. 15.15 Attenuation curves: driving voltage (ΔE) and polarization potential (ΔE_p) as a function of distance along the line.

15.6.3.3 Anode requirements

In this case of a cathodic protection system, the weight and number of anodes to be used is calculated from the cycle life of the system. Prolonged life of the anode is essential to decrease maintenance cost of the impressed current cathodic protection system. Dissipation rate of the anode is a measure of the life of the anode. For high silicon, chromium bearing cast iron, the dissipation rate is 0.5 kg/A year. The weight of the anode is given by

$$W_{a,t} = D_r \times I_c \times CL \tag{15.33}$$

where D_r is the dissipation rate in kg/A year, I_c is the current required in amperes, CL is the cycle life in years, and $W_{a,t}$ is the total weight of the anode in kilograms. The number of anodes required is given by the ratio of total weight to individual anode weight.

15.6.3.4 Ground-bed resistance

The ground-bed resistance is similar to that of the total circuit resistance calculated for the design of a sacrificial system (Section 15.6.2). In this case, multiple anodes are used and the resistance of anode to ground is calculated from Sunde equation [88].

15.6.3.5 Rectifier selection

Over the years, the quality of the coating decreases, leading to the exposure of bare steel. The current requirements increase with time for accomplishing a complete cathodic

protection. The required driving voltage determined by Ohm's law is scaled up by 1.5 times to that required normally for a newer pipeline:

$$E = \frac{I_{req}}{R_t} \times 1.5 \tag{15.34}$$

15.6.3.6 Ground-bed selection

The anodes are usually arranged horizontally or vertically depending on the nature of the soil and the proximity of nearby structures. Deep vertical ground-beds 6-12 in. in diameter and up to 100 m deep are used for pipelines, where the surface soil is dry and nonconductive and long distances must be protected [92]. Other instances where deep ground-beds are necessary include sites where the right of way surface ground-beds cannot be obtained. Figure 15.16 shows a deep anode bed. Deep ground-beds are conventionally backfilled with coke breeze for improved electrical contact to the soil or with lubricated fluidizeable coke, which can be pumped out later when the anode needs replacement [94].

15.7 COMPUTER-AIDED DESIGN OF CATHODIC PROTECTION

The last decade has seen immense development in the use of computer modeling techniques for the design of cathodic protection. Large pipelines of complex design are being installed in land and offshore environments, all of which require cathodic protection for corrosion prevention. Modeling CP systems have been useful for troubleshooting existing structures, design analysis of sacrificial and ICS, checking for interference effects,

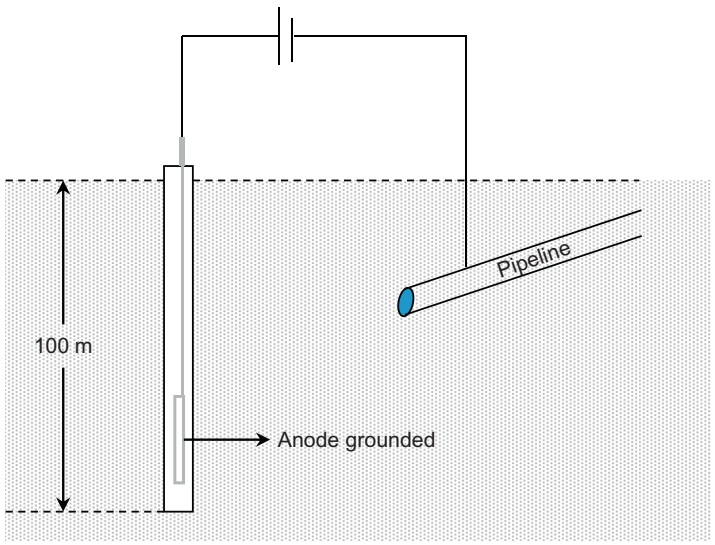

Fig. 15.16 Impressed current cathodic protection using a deep anode ground-bed.

attenuation, and prediction of life of the system [96–100]. Several numerical methods are used for the modeling of the CP systems; some being the (i) boundary element method (BEM), (ii) finite difference method, (iii) finite element method, and (iv) integral equation method [101,102]. All these methods involve the numerical solution of the Laplace equation:

$$\nabla^2 E = 0 \tag{15.35}$$

The above equation is derived from the electroneutrality law for homogeneous environments and is the governing equation to be solved for determining the potential distribution. To solve this equation, appropriate boundary conditions need to be specified. Finite element methods divide the three-dimensional electrolyte volume into a network of finite "nodes" whose electrical properties are connected to one another by linear equations. Finite element methods yield potential and current distributions within the electrolyte volume. Incorporation of polarization at the anode and cathode surfaces is difficult at volume boundaries. BEM has shown considerable promise in treating this problem. The electrode surface is divided into discrete boundary elements that are solved numerically. Unlike the finite difference methods, in the BEM only the electrode surfaces are divided into discrete elements and not the entire volume, leading to decreased computation power.

With steady development in the modeling methods and computational techniques, this approach is expected to rule the future of cathodic protection design. Development of models has lead to a widespread increase in the theoretical understanding of the system. In the future it is expected to play wide role in developing new designs without wasting money on field experimental projects.

EXERCISES

E15.1. Iron corrodes in a sea water solution of pH 7. Assuming corrosion proceeds by oxygen depolarization, calculate the minimum current required for complete cathodic protection. Exchange current density, i^o, for oxygen reduction is 10^{-8} mA/cm^2.

E15.2. Using the following data for the corrosion of iron in hydrogen-saturated, oxygen-free solution, calculate (a) the corrosion rate and (b) the exchange current density for the hydrogen evolution reaction (HER) on iron:

pH = 4; $a_{Fe^{2+}} = 0.02$ M; $i^o_{Fe} = 9 \times 10^{-7}$ A/cm^2; anodic $d\eta/d(\log i) = 0.04$ V/decade; the corrosion potential of iron is -0.215 V vs. RHE and $e^o_{Fe^{2+}|Fe} = -0.44$ V vs. SHE. For the HER, the cathodic $d\eta/d(\log i) = -0.12$ V/decade.

E15.3. Using the data given in exercise E15.2, calculate the cathodic protection current required to reduce the corrosion rate to zero. (See Case Study 3.3, Chapter 3.)

E15.4. During cathodic protection of iron under sea water conditions, the generation of OH^- leads to the calcareous deposits by reaction with calcium and magnesium ions.

(i) List the reactions for scale formation. Does the limiting current density of oxygen increase or decrease with scale formation?

(ii) After 6 months, the limiting current for oxygen reduction changes by an order of two due to the formation of deposits. Calculate the current density required for the protection of the substrate, before and after formation of the calcareous deposit.

(iii) If the applied current density is not changed, will it lead to overprotection or underprotection?

Given: In absence of calcareous deposit, $i_{L,O_2} = 10^{-3}$ A/cm^2; $b_a = 0.04$ V/decade. For anode dissolution, $i^o = 10^{-6}$ A/cm^2.

E15.5. Calculate the mass of an anode and the number of anodes required for the protection of an iron tank for 7 years if an aluminum anode weighs 13.7 kg. Maintenance current demand in amps (I_m) = 1.52 A, utilization factor (u) = 0.85, and electrochemical capacity of the anode material (ε) = 2670 Ah/kg. The number of hours per year is 8760.

E15.6. For the cathodic protection of a steel pipeline, the following information has been obtained from the potential survey shown in Table E15.1.

Table E15.1 PS Data for the Cathodic Protection of a Steel Pipeline

Parameter	Drain Point 1	Drain Point 2
Drainage current measured, I_{om} (A)	16.6	9.8
Potential increase measured at the end of the section, ΔE_L (V)	0.26	0.26
Attenuation coefficient, α (km^{-1})	0.5	0.5
Protected pipe length, L (km)	3.86	3.86
Measured potential increase at the drainage point, ΔE_{om} (V)	0.83	0.83
Drainage current coefficient, k_i	1.5	1.5
Resistance of lead wire, ρ_w (Ω mm^2 m^{-1})	0.0015	0.0015
Resistance of backfill, ρ_a (Ω mm^2 m^{-1})	0.0052	0.0052
Resistance of soil, ρ_s (Ω mm^2 m^{-1})	0.096	0.096
Length of lead wire, l_w (m)	375	375
Length of the anode, l_a (m)	1.1	1.1
Length of the anode with coke breeze backfill, l (m)	4.82	4.82
Depth of the anode ground bed, t (m)	2	2
Wire cross section, a (mm^2)	15.5	15.5
Radius of the backfill, d_{bf} (m)	1.25	1.25
Radius of the anode, d_a (m)	0.28	0.28
Weight of a single anode of Fe-Si, W_a (kg)	68	68
Anode wear rate, R (kg/A year)	0.07	0.07
Accepted current per anode, I_a (A)	5.0	5.0

(a) Calculate the following parameters:
   1. Potential at the drainage point. Compare it with the measured value
   2. Resistance of the pipe
   3. Current at drainage point
   4. Anode resistance
   5. Number of anodes in the ground-bed
   6. Resistance of the anode ground-bed
   7. Lead wire resistance
   8. Rectifier power needed
   9. The anode wear and cycling life of the system.

REFERENCES

[1] J.S. Mandke, Corrosion causes most pipeline failures in Gulf of Mexico, Oil Gas J. 29 (1990) 40–44.
[2] Improving the Safety of Marine Pipelines, Committee on the Safety of Marine Pipelines, Marine Board, National Research Council, Washington, D.C., 1994.
[3] W. Beckmann, W. Schwenk, W. Prinz, Handbook of Cathodic Corrosion Protection: Theory and Practice of Electrochemical Protection Processes, Gulf, Houston, TX, 1997.
[4] J. Morgan, Cathodic Protection, second ed., NACE, Houston, TX, 1987.
[5] D.A. Jones, Principles and Prevention of Corrosion, second ed., Prentice Hall, Upper Saddle River, NJ, 1996.
[6] R. Juchniewicz, J. Jankowski, K. Darowicki, Cathodic and anodic protection, in: M. Schutzee (Ed.), Mater. Sci. Tech., 19, 1 (Corros. Environment. Degradation) Wiley-VCH, Weinheim, Germany, (2000), pp. 383–470.
[7] B.N. Popov, S.P. Kumaraguru, Cathodic protection of pipelines, in: M. Kutz (Ed.), Handbook of Environmental Degradation of Materials, William Andrew, New York, 2005, pp. 503–521.
[8] W. Lynes, Some historical developments relating to corrosion, J. Electrochem. Soc. 98 (1951) 3c–10c.
[9] R. Burns, W. Bradley, Protective Coatings for Metals, third ed., Reinhold Publishing Corp., New York, 1967.
[10] H. Davy, On the corrosion of copper sheeting by sea water, and on the methods of preventing this effect; and on their application to ships of war and other ships, Philos. Trans. R. Soc. 114 (1824) 151–158.
[11] A.W. Peabody, M.E. Parker, Cathodic protection, in: A. de S. Brasunas (Ed.), Corrosion Basics—An Introduction, NACE, Houston, TX, 1984, pp. 179–200.
[12] C. Wagner, W. Traud, On the interpretation of corrosion processes through the superposition of electrochemical partial processes and on the potential of mixed electrodes, Corrosion 62 (2006) 844–855.
[13] P.F. George, J.J. Newport, J.L. Nichols, A high-potential magnesium anode, Corrosion 12 (1956) 627t–633t.
[14] G.W. Kurr, Zinc anodes—underground uses for cathodic protection and grounding, Mater. Performance 18 (1979) 34–41.
[15] G. Doremus, J.G. Davis, Marine anodes: the old and new cathodic protection for offshore structures, Mater. Performance 6 (1967) 30–39.
[16] C.F. Schreiber, V. Ashworth, C.J.L. Booker, Cathodic Protection Theory and Practice, Wiley (Harwood), Chichester, West Sussex, 1986.
[17] J.A. Jakobs, A comparison of anodes for impressed current systems, Mater. Performance 20 (1981) 17–23.
[18] W.T. Bryan, Selection of alloys for corrosion-resistant service, Met. Prog. 74 (1958) 102–105.

[19] R.J. Kuhn, Cathodic protection of underground pipe lines from soil corrosion, API Proc. 14 (1933) 157–167.
[20] R.A. Gummow, Cathodic protection criteria—a critical review of NACE standard RP-01-69, Mater. Performance 25 (1986) 9–16.
[21] W.J. Schwerdtfeger, O.N. McDorman, Measurement of corrosion rate of a metal from its polarizing characteristics, J. Electrochem. Soc. 99 (1952) 407–413.
[22] L.P. Sudrabin, F.W. Ringer, Cathodic protection criteria, Corrosion 12 (1957) 825t–828t.
[23] S.P. Ewing, Cathodic protection of castings in Loudon pool, Corrosion 4 (1948) 264–286.
[24] M. Romanoff, Underground Corrosion, NACE, Houston, TX, 1989.
[25] Cathodic Protection Criteria—A Literature Survey, NACE, Houston, TX, 1989.
[26] G.H. Koch, T.J. Barlo, W.E. Berry, Effect of grit-blasting on the stress corrosion cracking behavior of line pipe steel, Mater. Performance 23 (1984) 20–23.
[27] K.G. Compton, Potential criteria for the cathodic protection of lead cable sheath, Corrosion 12 (1956) 553t–560t.
[28] NACE Standard RP0169-96 Item No. 21001 Control of External Corrosion on Underground or Submerged Metallic Piping Systems, NACE, Houston, TX.
[29] R.H. Heidersbach, Cathodic protection, in: Metals Handbook, ninth ed., Corrosion, vol. XIII, ASM International, Metals Park, OH, 1987, pp. 466–477.
[30] T.J. Barlo, W.E. Berry, A reassessment of the −0.85 V and 100 mV polarization criteria for cathodic protection of steel buried in soils, Proc. Int. Congr. Met. Corros. 4 (1984) 86–91.
[31] L.P. Sudrabin, F.W. Ringer, Cathodic protection criteria, Corrosion 13 (1957) 351t–357t.
[32] K.P. Fischer, Cathodic protection in saline mud containing sulfate-reducing bacteria, Mater. Performance 20 (1981) 41–46.
[33] T. Kobayashi, Effect of environmental factors on the protective potential of steel, in: Proceedings of the 5th International Congress on Metal Corrosion, NACE, Houston, TX, 1974, pp. 627–630.
[34] R.A. Gummow, Using coupons and probes to determine cathodic protection levels, Mater. Performance 37 (1998) 24–30.
[35] D.A. Jones, Electrochemical Fundamentals of Cathodic Protection, CORROSION/87, Paper No. 317, 1987, NACE, Houston, TX.
[36] R.B. Mears, R.H. Brown, A theory of cathodic protection, Trans. Electrochem. Soc. 74 (1938) 519–528.
[37] A.J. Bard, L.R. Faulkner, Electrochemical Methods—Fundamentals and Applications, second ed., John Wiley & Sons, New York, 2001.
[38] A.W. Peabody, Use of magnesium for cathodic protection of pipelines in high soil resistive environments, Corrosion 15 (1959) 497t–502t.
[39] H.C. Van Nouhuys, Cathodic protection and high soil resistivity soil, Corrosion 9 (1953) 448–459.
[40] J.D. Palmer, Soil resistivity—measurement and analysis, Mat. Performance 13 (1974) 41–44.
[41] E.P. Marshall, E.G. Peattie, Pipeline Corrosion and Cathodic Protection, third ed., Gulf Professional Publishing, Woburn, MA, 1995.
[42] F. Wenner, A method of measuring earth resistivity. Report No. 258, U.S. Bull. Bur. Stand. 12 (1916) 469–478.
[43] A. Deb, D. Sarma, M.K. Banerjee, Significance of logarithmic averaging of soil resistivity data for underground pipelines using impressed current cathodic protection system, J. Met. Mater. Sci. 47 (2005) 169–176.
[44] ASTM G 57-95A, Standard Test Method for Field Measurement of Soil Resistivity Using the Wenner Four-Electrode Method, ASTM International, West Conshohocken, PA, 1995.
[45] C.A.H. von Wolzogen Kuhr, The corrosion of lead and copper pipes in the soil, Water 23 (1939) 215–220.
[46] J.A. Hardy, Utilization of cathodic hydrogen by sulfate-reducing bacteria, Br. Corros. J. 18 (1983) 190–193.
[47] T.R. Jack, M. Wilmott, G. Van Boven, R.G. Worthingham, R.L. Sutherby, Corrosion sequences of secondary oxidation of microbial corrosion, Corrosion 54 (1998) 246–252.
[48] R.A. King, J.D.A. Miller, Corrosion by the sulfate-reducing bacteria, Nature 233 (1971) 491–492.

[49] R.L. Starkey, K.M. Wight, Final Report of the American Gas Association Iron Corrosion Research Fellowships, American Gas Association, New York, 1945.
[50] F. Kajiyama, Apparatus for Measuring the Corrosivity of the Soil, Japanese Patent, JP 58208654, 1982.
[51] C.G. Deuber, G.B. Deuber, Development of Redox Probe, Final Report to American Gas Association, Research Project PM-20, New York, 1956.
[52] F.E. Costanzo, R.E. McVey, Development of the redox probe field technique, Corrosion 14 (1958) 268t–272t.
[53] R.L. Starkey, K.M. Wight, Anaerobic Corrosion of Iron in Soil, American Gas Association Monograph, New York, 1945.
[54] D.H. Pope, H. Daniel, T.P. Zintel, H. Aldrich, D. Duquette, Efficacy of biocides and corrosion inhibitors in the control of microbiologically influenced corrosion, Mater. Performance 11 (1990) 46–51.
[55] J.L. Banach, Evaluating design and cost of pipe line coatings: Part 1, Pipeline Ind. 62-67 (1998).
[56] A.W. Peabody, Pipeline corrosion survey techniques, Mater. Prot. 1 (1962) 62–66, 68, 70-71, 74-76.
[57] A. Kumar, Impressed Current Cathodic Protection Systems Utilizing Ceramic Anodes, U.S. Army Corps of Engineers, Construction Engineering Research Laboratories, Champaign, IN, 1990.
[58] J.A. Jakobs, F.W. Hewes, Evaluation of impressed current anode materials for use in wet soils and sediments containing chlorides and sulfates, Proc. Int. Conre. Met. Corros., Edmonton, AB, Canada, (1984), pp. 78–85.
[59] B.S. Wyatt, Cathodic protection of offshore structures, Anti-Corros. Methods Mater 24 (1977) 5–10.
[60] J.S. Gerrard, Practical applications of cathodic protection, in: in: L.L. Shreir (Ed.), Corrosion, vol. II, Newnes-Butterworths, Kent, England, 1976, pp. 11–25.
[61] T. Foster, V.G. Moores, Cathodic Protection Current Demand of Various Alloys in Sea Water, Paper No. 254, CORROSION/86, March 17-21, 1986, Houston, TX.
[62] R.L. Pawson, Technical aspects of computerized close-interval surveys, Proc. Appalachian Underground Corrosion Short Course 37 (1992) 377–384.
[63] M. Rahman, E. Naderi, M.H. Moayed, A new equation proposed for evaluation of IR drop on buried pipelines, Anti-Corros. Methods Mater. 60 (2013) 312–318.
[64] C. Ringas, J.M. Leeds, P. Osthuizen, The application of DC voltage-gradient technology to accurately determine buried pipeline rehabilitation requirements, in: Pipeline Risk Assessment, Rehabilitation and Repair Conference, Houston, Texas, September 12-15, 1994, organized by Pipeline Industry and Pipes & Pipelines International.
[65] Z. Masilela, J. Pereira, Using the DCVG technology as a quality control tool during construction of new pipelines, Eng. Fail. Anal. 5 (1998) 99–105.
[66] L. Di Biase, R. Cigna, O. Fumei, A new technique for locating coating faults on buried metallic pipelines, Adv. Mater. Res. 38 (2008) 113–122.
[67] A.A. Ivanov, System for monitoring of corrosion process in pipelines, Zashchita Okruzhayushchei Sredy v Neftegazovom Komplekse Janusz 1 (2000) 25–27.
[68] D. Wessling, K. Ostroznik, M.L. Dalganow, A. Wladimirowitsch, M. Olegowitsch, Procedure for the determination of the tubing/ground/floor/soil potential at cathodically protected pipes, German Patent DE 10021994 20011108, 2001.
[69] K.M. Lawson, N.G. Thompson, M. Islam, M.J. Schofield, Monitoring corrosion of reinforced soil structures, Br. J. Non-Destr. Test. 35 (1993) 319–324.
[70] K. Kasahara, T. Sato, H. Adachi, Results of polarization potential and current density surveys on existing buried pipelines, Mater. Performance 19 (1980) 45–51.
[71] J.L. Didas, Practical Applications and Limitations of Buried Coupons Utilized for IR drop Measuremtns, Paper No. 572, Proc. Corrosion'97, December 1, 1997, Houston, TX.
[72] M.E. Orazem, J.M. Esteban, K.J. Kennelley, R.M. Degerstedt, Mathematical models for cathodic protection of an underground pipeline with coating holidays: Part 1—theoretical development, Corrosion 53 (1997) 264–272.
[73] D.H. Boteler, W.H. Seager, Telluric currents: a meeting of theory and observation, Corrosion 54 (1998) 751–755.
[74] B.A. Martin, Cathodic protection of a remote river pipeline, Mater. Performance 33 (1994) 12–15.

[75] I. Gurrappa, Aluminum alloys for cathodic protection, Corros. Prev. Control 44 (1997) 69–80.
[76] G. Sabde, F. Gan, D.T. Chin, Cathodic protection of underground pipeline against crevice corrosion: a review, J. Chin. Inst. Chem. Eng. 24 (1993) 417–429.
[77] R. Juchniewicz, J. Janowski, Application of impedance spectroscopy to the assessment of cathodic protection effectiveness, in: in: J.M. Costa, A.D. Mercer (Eds.), Progress in Understanding and Prevention of Cathodic Protection Ineffectiveness, vol. II, EFC, London, 1993, pp. 1401–1410.
[78] L.G. Cooper, Sensing probes and instruments for electrochemical and electrical resistance corrosion monitoring, in: G.C. Moran, P. Labin (Eds.), Corrosion Monitoring in Industrial Plants Using Nondestructive Testing and Electrochemical Methods, ASTM STP 908ASTM International, West Conshohocken, PA, 1986.
[79] J. Jankowski, A new approach to harmonic analysis, in: Proceedings of the EUROCORR'99, Sep 28-Oct 1, 1998, Utrecht, The Netherlands, 1998.
[80] J. Jankowski, Application of AC electrochemical techniques for corrosion rate monitoring in cathodically protected systems, in: Proceedings of the EUROCORR'99, Aug 30-Sep 2, 1999, Aachen, Germany, 1999.
[81] J. Jankowski, Electrochemical methods for corrosion rate determination under cathodic polarisation conditions—a review part I—DC methods, Corros. Rev. 20 (2002) 159–177.
[82] A. Jankowski, Electrochemical methods for corrosion rate determination under cathodic polarisation conditions—a review part 2—AC methods, Corros. Rev. 20 (2002) 179–200.
[83] Pipeline Cathodic Protection—Part 2: Cathodic Protection of Offshore Pipelines, ISO/TC 67/SC2 NP 14489, International Standards Organization, May 1, 1999.
[84] L.I. Freiman, A theory and design of an insulating insert in a cathodically protected underground water pipeline. II. The corrosion rate of anodic zones and effectiveness of the insert, Prot. Met. 38 (2002) 277–283 (Translation of Zashchita Metallov).
[85] W.B. Russel, Cathodic isolation/protection technologies applied to underground metallic structures, Proc. Appalachian Underground Corrosion Short Course 46 (2001) 117–125.
[86] L.E. Carlson, J.H. Frrzgerald III, F.R.D. Webster, Cathodic protection design for 1,900 miles (3,050 km) of high-pressure natural gas pipeline, Mater. Performance 40 (2001) 28–32.
[87] H.B. Dwight, Calculations for coreless induction furnaces, Electr. Eng. 54 (1936) 312–314.
[88] E.D. Sunde, Earth Conduction Effects in Transmission Systems, D. Van Nostrand, New York, 1949.
[89] H. Capper, Experience of cathodic protection for structures and pipelines, Int. Mech. Eng. Conf. Publ. 7 (1979) 27–35.
[90] J. Jenkins, Cathodic protection system design 3. Sacrificial anode system design principles for underground structures. Report No. NFESC-TDS-2022-SHR, Order No. AD-A301 912/2GAR, 1995, Naval Facilities Engineering Service Center, Port Hueneme, CA, USA.
[91] W.H. Hartt, X. Zhang, W. Chu, Issues associated with expiration of galvanic anodes on marine structures, Corrosion 61 (2005) 1035–1040.
[92] T.H. Lewis Jr., Replaceable deep anode design and installation, in: Proceedings of the Corrosion and Prevention, LORESCO International, Australia, 1998, pp. 352–357.
[93] R. Baboian, P.F. Prew, K. Kawate, Design of platinum clad wire anodes for impressed current protection, Mater. Performance 23 (1984) 31–35.
[94] R.A. Jarman, L.L. Shrier, The basic principles of corrosion, Weld. Met. Fabr. 55 (1987) 370, 372, 374, 376, 378–379.
[95] H.H. Uhlig, R.W. Revie, Corrosion and Corrosion Control, John Wiley, New York, 1985.
[96] K. Bethune, W.H. Hartt, Applicability of the slope parameter method to the design of cathodic protection systems for marine pipelines, Corrosion 57 (2001) 78–83.
[97] M.E. Orazem, J.M. Esteban, K.J. Kennelley, R.M. Degerstedt, Mathematical models for cathodic protection of an underground pipeline with coating holidays: Part 2—case studies of parallel anode cathodic protection systems, Corrosion 53 (1997) 427–436.
[98] P. Pierson, K.P. Bethune, W.H. Hartt, P. Anathakrishnan, A new equation for potential attenuation and anode current output projection for cathodically polarized marine pipelines and risers, Corrosion 56 (2000) 350–360.

[99] S.H. Lee, J.S. Han, Analysis of potential distribution around pipeline under cathodic protection using boundary element method, Corrosion 25 (1996) 340–348.
[100] R.M. Degerstedt, K.J. Kennelley, M.E. Orazem, J.M. Esteban, Computer modeling aids. Traditional cathodic protection. Design methods for coated pipelines, Mater. Performance 35 (1996) 16–20.
[101] C.S. Chapra, R.P. Canale, Numerical Methods for Engineers, second ed., McGraw-Hill, New York, 1988.
[102] C.A. Brebbia, S. Walker, Boundary Element Techniques in Engineering, Newness, Butterworth, London, 1980.

SOLUTIONS GUIDE

Chapter 2: Thermodynamics in the Electrochemical Reactions of Corrosion

E2.1. Calculate the half-cell potential of cadmium in 0.1 M $CdCl_2$.

Solution:

$$\text{Cell Notation}: \mathrm{Cd}|\mathrm{Cd}^{2+}, \mathrm{Cl}^{-}\ (0.1\,\mathrm{M}\,\mathrm{CdCl_2})$$

$$\text{Cell Reaction}: \mathrm{Cd}^{2+} + 2\mathrm{e}^{-} \rightarrow \mathrm{Cd}$$

$$e_{\mathrm{Cd}^{2+}|\mathrm{Cd}} = -0.402 + \frac{0.059}{2}\log\left(a_{\mathrm{Cd}^{2+}}\right) = -0.402 + \frac{0.059}{2}\log(0.1) = -0.432\,\mathrm{V}$$

E2.2. Calculate the theoretical tendency of tin to corrode (in volts) with the evolution of hydrogen when immersed in 0.01 M $SnCl_2$ acidified to pH = 2, 3, 4, and 5.

Solution:

$$\text{Cell Notation}: \mathrm{Sn}|\mathrm{Sn}^{2+}, \mathrm{Cl}^{-}, \mathrm{H}^{+}|\mathrm{H_2}|\mathrm{Pt}$$

Cell Reactions:

$$\mathrm{Sn} \rightarrow \mathrm{Sn}^{2+} + 2\mathrm{e}^{-}(\text{anode})$$

$$2\mathrm{H}^{+} + 2\mathrm{e}^{-} \rightarrow \mathrm{H_2}(\text{cathode})$$

$$\mathrm{Sn} + 2\mathrm{H}^{+} \rightarrow \mathrm{Sn}^{2+} + \mathrm{H_2}(\text{overall})$$

$$e_{\mathrm{H}^{+}|\mathrm{H_2}} = 0 - 2.303\frac{RT}{2F}\log\left(\frac{a_{\mathrm{H_2}}}{\left(a_{\mathrm{H}^{+}}\right)^2}\right)$$

$$e_{\mathrm{Sn}|\mathrm{Sn}^{2+}} = 0.138 - 2.303\frac{RT}{2F}\log\left(\frac{a_{\mathrm{Sn}^{2+}}}{a_{\mathrm{Sn}}}\right)$$

$$E_{\mathrm{cell}} = 0 + 0.138 - 2.303\frac{RT}{2F}\log\left(\frac{a_{\mathrm{H_2}}a_{\mathrm{Sn}^{2+}}}{\left(a_{\mathrm{H}^{+}}\right)^2 a_{\mathrm{Sn}}}\right)$$

The potential pH dependence is calculated using the equation:

$$E_{\mathrm{cell}} = 0.138 - \frac{0.059}{2}\log\left(\frac{0.01}{\left(a_{\mathrm{H}^{+}}\right)^2}\right)$$

Corrosion Engineering
http://dx.doi.org/10.1016/B978-0-444-62722-3.09968-7

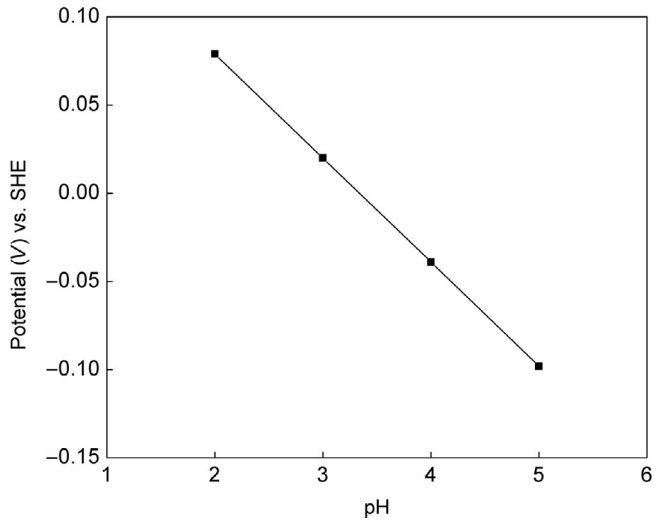

Fig. E2.1 Plot of cell potential for the tin system as a function of pH.

The cell potentials plotted in (Fig. E2.1) are negative at pH lower than 3. Therefore, tin is stable at pH values 4 and 5, and starts to corrode at pH = 3 and lower.

E2.3. Plot the hydrogen pressure (fugacity) necessary to stop corrosion of nickel in 0.1 M Ni^{2+} solution at pH = 1, 3, 5, and 7.

Solution:

Ni corrodes according to the following reaction:

$$Ni + 2H^+ \rightarrow Ni^{2+} + H_2$$

with a standard potential of 0.250 V vs. SHE.

For a Ni^{2+} concentration of 0.1 M, the equilibrium potential is

$$e_{Ni|Ni^{2+}} = e^{o}_{Ni|Ni^{2+}} - 2.303\frac{RT}{2F}\log\left(\frac{a_{Ni^{2+}}}{a_{Ni}}\right) = 0.280\,V \text{ vs. SHE}$$

The Nernst equation for the overall reaction is:

$$E_{cell} = e^{o}_{Ni|Ni^{2+}} + e^{o}_{H^+|H_2} - 2.303\frac{RT}{2F}\log\left(\frac{a_{Ni^{2+}}P_{H_2}}{(a_{H^+})^2}\right)$$

To stop the corrosion process, the cell potential should be zero or positive. The required hydrogen pressure is calculated from this equation at zero cell potential for different pH values. The results indicate that the pressure required to stop Ni corrosion decreases as the pH increases. An extremely high pressure

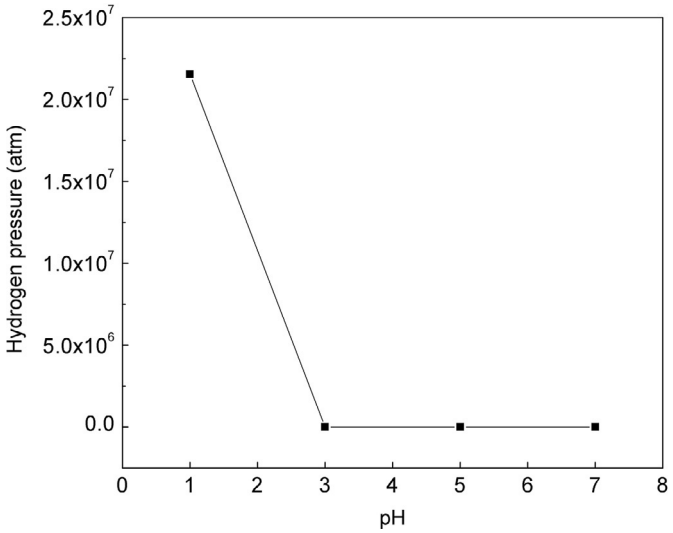

Fig. E2.2 Plot of pH vs. hydrogen pressure for the nickel system.

is required for pH = 1 (Fig. E2.2). Therefore, increasing hydrogen pressure is not a feasible solution for stopping Ni corrosion in very acidic solutions.

E2.4. Plot the hydrogen pressure (fugacity) necessary to stop corrosion of tin in 0.1 M Sn^{2+} solution at pH = 1, 3, 5, and 7.

Solution:

Sn corrodes according to reaction:

$$Sn + 2H^+ \rightarrow Sn^{2+} + H_2$$

The oxidation electrode potential for tin in 0.1 M solution is estimated from the Nernst equation:

$$e_{Sn|Sn^{2+}} = e^{o}_{Sn|Sn^{2+}} - 2.303\frac{RT}{2F}\log\left(\frac{a_{Sn^{2+}}}{a_{Sn}}\right) = 0.168\ \text{V vs.SHE}$$

The overall cell potential is:

$$E_{cell} = e^{o}_{Sn|Sn^{2+}} + e^{o}_{H^+|H_2} - 2.303\frac{RT}{2F}\log\left(\frac{a_{Sn^{2+}}P_{H_2}}{(a_{H^+})^2}\right)$$

The results indicated that the pressure required for stopping tin corrosion decreases as the pH increases (Fig. E2.3). Extremely high pressure is required for pH = 1. Thus, increasing hydrogen pressure is not a feasible solution for stopping tin corrosion in acidic solutions.

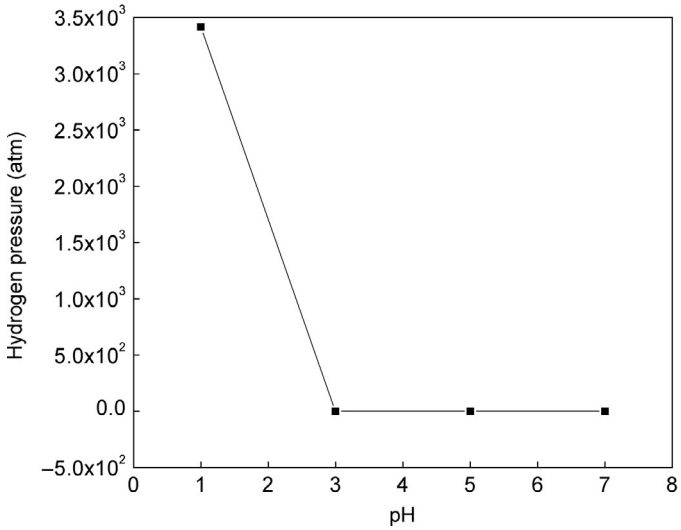

Fig. E2.3 Plot of pH vs. hydrogen pressure for the tin system.

E2.5. Determine which electrode will corrode in a cell constructed of iron and zinc electrodes when the cell is short circuited. The electrodes are immersed in a solution of Fe^{+2} and Zn^{+2} of equal activity.

Solution:

Cell Notation : $Zn|Zn^{2+}, Cl^{-}, Fe^{2+}|Fe$

Cell Reactions:

$$Zn \rightarrow Zn^{2+} + 2e^{-} \text{ (anode)}$$

$$Fe^{2+} + 2e^{-} \rightarrow Fe \text{ (cathode)}$$

$$Zn + Fe^{2+} \rightarrow Zn^{2+} + Fe \text{ (overall)}$$

The Nernst equations for the anode, cathode, and overall reactions are as follows:

$$e_{Zn|Zn^{2+}} = e^{o}_{Zn|Zn^{2+}} - 2.303\frac{RT}{2F}\log\left(\frac{a_{Zn^{2+}}}{a_{Zn}}\right)\text{(anode)}$$

$$e_{Fe^{2+}|Fe} = e^{o}_{Fe^{2+}|Fe} - 2.303\frac{RT}{2F}\log\left(\frac{a_{Fe}}{a_{Fe^{2+}|Fe}}\right)\text{(cathode)}$$

$$E_{cell} = e_{Fe^{2+}|Fe} + e_{Zn|Zn^{2+}} = e^{o}_{Fe^{2+}|Fe} + e^{o}_{Zn|Zn^{2+}} - 2.303\frac{RT}{2F}\log\left(\frac{a_{Fe}a_{Zn^{2+}}}{a_{Fe^{2+}}a_{Zn}}\right)\text{(overall)}$$

If the activity of the zinc and the iron are equal then the log of the activities is zero, so the cell potential is the standard half-cell potentials of iron and zinc added together.

$$E_{\text{cell}} = e^{\circ}_{\text{Fe}^{2+}|\text{Fe}} + e^{\circ}_{\text{Zn}|\text{Zn}^{2+}}$$

$$E_{\text{cell}} = 0.762 - 0.440$$

$$E_{\text{cell}} = 0.322 \text{ V vs. SHE}$$

The Gibbs free energy is calculated by using the expression

$$\Delta G = -nFE$$

where n is the number of electrons involved in the reaction, F is the Faraday constant, and E is the emf of the cell.

Since the ΔG is negative, the reaction occurs spontaneously. Thus, the zinc will corrode when short-circuited with iron.

E2.6. A cell, constructed from tin (anode) and a hydrogen electrode (cathode), is immersed in 0.2 M $SnCl_2$ solution. Estimate the cell potential as a function of pH (pH = 1, 3, 5, and 7).

Solution:

Cell Notation: $\text{Sn}|\text{Sn}^{2+},\text{Cl}^{-},\text{H}^{+}|\text{H}_2\,|\text{Pt}$

Cell Reactions:

$$\text{Sn} \rightarrow \text{Sn}^{2+} + 2\text{e}^{-} \text{ (anode)}$$

$$2\text{H}^{+} + 2\text{e}^{-} \rightarrow \text{H}_2 \text{ (cathode)}$$

$$\text{Sn} + 2\text{H}^{+} \rightarrow \text{Sn}^{2+} + \text{H}_2 \text{ (overall)}$$

(a)

$$e_{\text{H}^{+}|\text{H}_2} = 0 - 2.303\frac{RT}{2F}\log\left(\frac{a_{\text{H}_2}}{(a_{\text{H}^{+}})^2}\right)$$

$$e_{\text{Sn}|\text{Sn}^{2+}} = 0.138 - 2.303\frac{RT}{2F}\log\left(\frac{a_{\text{Sn}^{2+}}}{a_{\text{Sn}}}\right)$$

$$E_{\text{cell}} = 0 + 0.138 - 2.303\frac{RT}{2F}\log\left(\frac{a_{\text{H}_2}a_{\text{Sn}^{2+}}}{(a_{\text{H}^{+}})^2 a_{\text{Sn}}}\right)$$

This simplifies to:

$$E_{\text{cell}} = 0.138 - \frac{0.059}{2}\log\left(\frac{a_{\text{Sn}^{2+}}}{(a_{\text{H}^{+}})^2}\right) = 0.138 - \frac{0.059}{2}\log\left(\frac{0.2}{(a_{\text{H}^{+}})^2}\right)$$

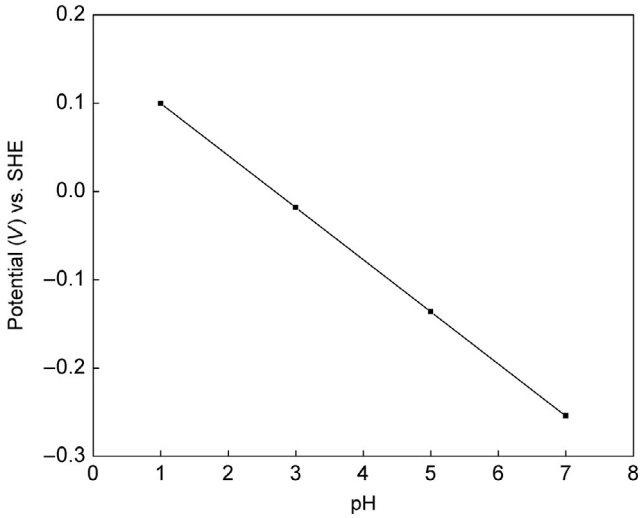

Fig. E2.4 Plot of pH vs. potential for the tin system.

The potentials at various pHs are calculated using the above equation and plotted in Fig. E2.4.

E2.7. Calculate the theoretical tendency of zinc to corrode (in volts) with the evolution of hydrogen when immersed in 0.05 M $ZnCl_2$, at pH = 1 through 5.

Solution:

Cell Notation : $Zn|Zn^{2+}, Cl^-, H^+|H_2|Pt$

Cell Reactions:

$$Zn \rightarrow Zn^{2+} + 2e^- \text{ (anode)}$$

$$2H^+ + 2e^- \rightarrow H_2 \text{ (cathode)}$$

$$Zn + 2H^+ \rightarrow Zn^{2+} + H_2 \text{ (overall)}$$

The Nernst equation for the overall reaction can be written as:

$$E_{cell} = e_{H^+|H_2} + e_{Zn|Zn^{2+}} = e^o_{H^+|H_2} + e^o_{Zn|Zn^{2+}} - 2.303\frac{RT}{2F}\log\left(\frac{a_{H_2}a_{Zn^{2+}}}{(a_{H^+})^2 a_{Zn}}\right)$$

$$E_{cell} = 0 + 0.762 + 2.303\frac{RT}{2F}\log\left(\frac{(a_{H^+})^2}{a_{Zn^{2+}}}\right)$$

$$E_{cell} = 0.762 + \frac{0.059}{2}\log\left(\frac{0.1^2}{0.05}\right) \text{ (for pH} = 1)$$

$$E_{cell} = 0.741 \text{ V vs. SHE}$$

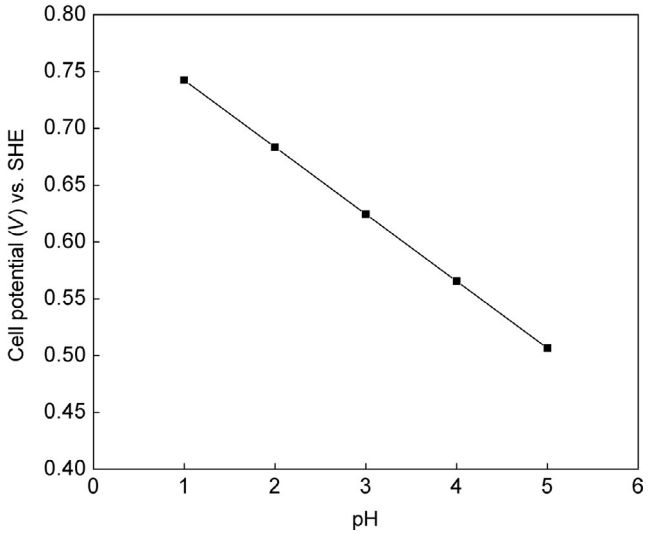

Fig. E2.5 Plot of pH vs. cell potential for corroding zinc cell.

Table E2.1 pH and Potential Relationship of Zn Cell

pH	$[H^+]$	[Zn]	Cell Potential (*V* vs. SHE)
1	0.1	0.05	0.741
2	10^{-2}	0.05	0.682
3	10^{-3}	0.05	0.623
4	10^{-4}	0.05	0.564
5	10^{-5}	0.05	0.505

Since the cell potential is positive, zinc will corrode at a pH of 1. Similarly, the cell potential for the remaining pH values can be calculated using the above expression. The results are presented in Fig. E2.5 and Table E2.1.

The cell potential is positive at all pH used. Therefore, zinc corrodes at these pHs. As shown in Table E2.1 and Fig. E2.6, the tendency of zinc to corrode increases with a decrease of pH.

E2.8. Plot the emf of an electrode constructed of zinc (anode) and a hydrogen electrode (cathode) immersed in 0.6 M $ZnCl_2$ at pH 0, 1, 2, 3, 4, and 5.

Solution:

Cell Notation: $Zn|Zn^{2+}, Cl^-, H^+|H_2|Pt$

Cell Reactions:

$$Zn \rightarrow Zn^{2+} + 2e^- (\text{anode})$$

$$2H^+ + 2e^- \rightarrow H_2 (\text{cathode})$$

$$Zn + 2H^+ \rightarrow Zn^{2+} + H_2 (\text{overall})$$

Zinc is oxidized at the anode and H^+ is reduced at the cathode. In the Nernst equation, we need to consider only the Zn^{2+} concentration and the H^+ concentrations. The activities of metal Zn and H_2 are assumed to be unity. Because Zn^{2+} is a product, it will appear in the numerator of the logarithm term, and H^+ will appear in the denominator of the logarithm term, where a_{H^+} is related to pH. The general Nernst equation for the overall reaction is

$$E_{\text{cell}} = e^{\circ}_{H^+|H_2} + e^{\circ}_{Zn|Zn^{2+}} - 2.303\frac{RT}{2F}\log\left(\frac{a_{Zn^{2+}}}{(a_{H^+})^2}\right)$$

For a pH of 0, the above equation becomes:

$$E_{\text{cell}} = 0 + 0.762 - \frac{0.059}{2}\log\left(\frac{a_{Zn^{2+}}}{(a_{H^+})^2}\right)$$

$$E_{\text{cell}} = 0.762 - \frac{0.059}{2}\log(0.6) - 0.059\text{pH}$$

$$E_{\text{cell}} = 0.769 \text{ V vs. SHE (for pH} = 0)$$

The equilibrium potential sign for $e^{\circ}_{Zn|Zn^{2+}}$ (Zn oxidation) is reversed because −0.762 V vs. SHE is the standard reduction potential for Zn^{2+}. Substituting the other pH values in the expressions, the emf of the cell is calculated. The plot of pH vs. the cell potential (Fig. E2.6) indicates that increasing the pH by 1 reduces the cell potential by 0.059 mV.

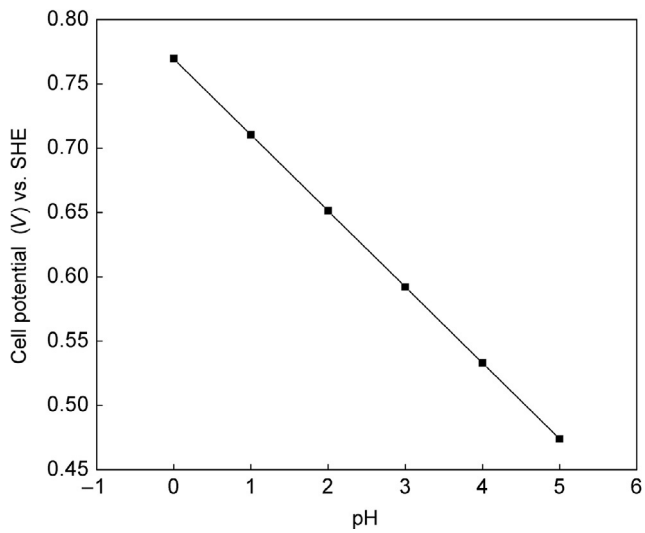

Fig. E2.6 Plot of pH vs. cell potential for the Zn system.

E2.9. Calculate the concentration of Zn^{2+} ions required to stop the zinc corrosion when Zn is immersed in a solution of $FeCl_2$ with activity of $Fe^{2+} = 0.1$ M.

Solution:

$$\text{Cell Notation}: Zn|Zn^{2+}, Cl^-, Fe^{2+}|Fe$$

Cell Reactions:

$$Zn \rightarrow Zn^{2+} + 2e^- \text{ (anode)}$$

$$Fe^{2+} + 2e^- \rightarrow Fe \text{ (cathode)}$$

$$Zn + Fe^{2+} \rightarrow Zn^{2+} + Fe \text{ (overall)}$$

The Nernst equations for the anode, cathode, and overall reactions are as follows:

$$e_{Zn|Zn^{2+}} = e^{o}_{Zn|Zn^{2+}} - 2.303\frac{RT}{2F}\log\left(\frac{a_{Zn^{2+}}}{a_{Zn}}\right)\text{(anode)}$$

$$e_{Fe^{2+}|Fe} = e^{o}_{Fe^{2+}|Fe} - 2.303\frac{RT}{2F}\log\left(\frac{a_{Fe}}{a_{Fe^{2+}|Fe}}\right)\text{(cathode)}$$

$$E_{cell} = e_{Fe^{2+}|Fe} + e_{Zn|Zn^{2+}} = e^{o}_{Fe^{2+}|Fe} + e^{o}_{Zn|Zn^{2+}} - 2.303\frac{RT}{2F}\log\left(\frac{a_{Fe}a_{Zn^{2+}}}{a_{Fe^{2+}}}\right)\text{(overall)}$$

For the iron activity given, the above equation can be written as:

$$E_{cell} = e^{o}_{Fe^{2+}|Fe} + e^{o}_{Zn|Zn^{2+}} - 2.303\frac{RT}{2F}\log\left(\frac{a_{Zn^{2+}}}{a_{Fe^{2+}}}\right)$$

$$E_{cell} = 0.762 - 0.440 + 2.303\frac{RT}{2F}\log\left(\frac{a_{Zn^{2+}}}{a_{Fe^{2+}}}\right) = 0 \text{ when the reaction stops}$$

For the reaction to stop, the cell emf should be equal to zero or positive

$$E_{cell} = 0 = 0.323 - \frac{0.059}{2}\log\left(\frac{a_{Zn^{2+}}}{0.1}\right)$$

The zinc activity of the above equation is the concentration of zinc when the corrosion reaction finishes.

$$\frac{0.646}{0.059} = \log\left(\frac{a_{Zn^{2+}}}{0.1}\right)$$

$$a_{Zn^{2+}} = \left(10^{0.646/0.059}\right)(0.1) = 8.9 \times 10^9 \text{ M}$$

E2.10. (a) Calculate the cell potential of a concentration cell constructed from a zinc electrode in 0.2 M $ZnSO_4$ and 0.6 M $ZnSO_4$ solution. Neglect the liquid junction potential.
(b) Write the spontaneous reaction of the cell and indicate which electrode is the anode.

Solution:
Assuming the Zn immersed in 0.2 M $ZnSO_4$ is the anode, while Zn immersed in 0.6 M $ZnSO_4$ is the cathode, the appropriate reactions are:

$$\mathrm{Zn} \rightarrow \mathrm{Zn}^{2+}(0.2\,\mathrm{M}) + 2\mathrm{e}^{-}(\text{anode})$$

$$\mathrm{Zn}^{2+}(0.6\,\mathrm{M}) + 2\mathrm{e}^{-} \rightarrow \mathrm{Zn}\ (\text{cathode})$$

$$\mathrm{Zn} + \mathrm{Zn}^{2+}(0.6\ \mathrm{M}) \rightarrow \mathrm{Zn} + \mathrm{Zn}^{2+}(0.2\ \mathrm{M})\ (\text{overall})$$

The cell potential is

$$E_{\mathrm{Cell}} = e^{\circ}_{\mathrm{Zn}|\mathrm{Zn}^{2+}} + e^{\circ}_{\mathrm{Zn}^{2+}|\mathrm{Zn}} - 2.303\frac{RT}{nF}\log\left(\frac{0.2}{0.6}\right) = 0 - \frac{0.059}{2}\log\left(\frac{0.2}{0.6}\right)$$

$$E_{\mathrm{Cell}} = 0.014\ \mathrm{V\ vs.\ SHE}$$

Since the potential is positive, the reaction proceeds spontaneously as written.

E2.11. If the concentration of H^+ decreases from 0.5 M to 10^{-6} M, estimate how much the oxidizing power of the (MnO_4^-/Mn^{2+}) couple will be reduced.

Solution:

$$\mathrm{MnO_4^-} + 8\mathrm{H}^{+} + 5\mathrm{e}^{-} \rightarrow \mathrm{Mn}^{2+} + 4\mathrm{H_2O}$$

$$e_{\mathrm{MnO_4^-}|\mathrm{Mn}^{2+}} = e^{\circ}_{\mathrm{MnO_4^-}|\mathrm{Mn}^{2+}} - \frac{0.059}{5}\log\left(\frac{a_{\mathrm{Mn}^{2+}}}{\left(a_{\mathrm{MnO_4^-}}\right)\left(a_{\mathrm{H}^+}\right)^8}\right)$$

When the concentration of H^+ is 0.5 M, the potential is:

$$e_{1,\mathrm{MnO_4^-}|\mathrm{Mn}^{2+}} = e^{\circ}_{\mathrm{MnO_4^-}|\mathrm{Mn}^{2+}} - \frac{0.059}{5}\log\left(\frac{a_{\mathrm{Mn}^{2+}}}{\left(a_{\mathrm{MnO_4^-}}\right)(0.5)^8}\right)$$

When the concentration of H^+ is 10^{-6} M, the potential is:

$$e_{2,\mathrm{MnO_4^-}|\mathrm{Mn}^{2+}} = e^{\circ}_{\mathrm{MnO_4^-}|\mathrm{Mn}^{2+}} - \frac{0.059}{5}\log\left(\frac{a_{\mathrm{Mn}^{2+}}}{\left(a_{\mathrm{MnO_4^-}}\right)(10^{-6})^8}\right)$$

So the oxidizing power can be estimated as the difference between the electrode potentials:

$$e_{2,MnO_4^-|Mn^{2+}} - e_{1,MnO_4^-|Mn^{2+}} = -\frac{0.059}{5}\log\left(\frac{(0.5)^8}{(10^{-6})^8}\right) = -0.538\,\text{V vs.SHE}$$

Thus, the oxidizing power was reduced by 0.538 V vs. SHE by decreasing the hydrogen ion concentration to 10^{-6} M.

E2.12. Determine whether iron is stable in aqueous solution at pH = 3, 5, and 7. Plot the driving EMF and the Gibbs free-energy as a function of pH. Assume $P_{H_2} = 1$ atm. and $[Fe^{2+}] = 10^{-6}$ M.

Solution:

Half-Cell Reactions:

$$Fe \rightarrow Fe^{2+} + 2e^-$$

$$2H^+ + 2e^- \rightarrow H_2$$

Overall Reaction:

$$Fe + 2H^+ \rightarrow Fe^{2+} + H_2$$

The Nernst equation for the anodic reaction can be written as:

$$e_{Fe|Fe^{2+}} = e^o_{Fe|Fe^{2+}} - \frac{0.059}{2}\log(a_{Fe^{2+}})$$

$$e_{Fe|Fe^{2+}} = 0.440 - \frac{0.059}{2}\log(10^{-6})$$

$$e_{Fe|Fe^{2+}} = 0.617\,\text{V vs.SHE}$$

$$E_{cell} = e_a + e_c$$

Because $\Delta G = -nFE_{cell}$

$$E_{cell} = e^o_{H^+|H_2} + e^o_{Fe|Fe^{2+}} - \frac{2.303RT}{2F}\log\left(\frac{a_{Fe^{2+}}}{(a_{H^+})^2}\right)$$

$$E_{cell} = -\frac{\Delta G}{nF} = \left[E^o_{H^+|H_2} + \frac{RT}{nF}\ln\left(\frac{(C_{H^+})^2}{P_{H_2}}\right)\right] - \left[E^o_{M^+|M} + \frac{RT}{nF}\ln(C_{M^{+n}})\right]$$

$$E_{cell} = e^o_{Fe|Fe^{2+}} - 0.059\text{pH}$$

By substituting the given pH values in the above equation, the potential of iron in aqueous solution at various pH values can be obtained. The Gibbs free-energy change can then be calculated from the cell potential (Table E2.2). The results are plotted in Fig. E2.7a and b.

Table E2.2 The Cell Potential and Gibbs Free-Energy for Iron as a Function of pH

pH	${}^{e}Fe\|Fe^{2+}$(V)	E_{cell} (V)	ΔG (kJ/mol)
3	0.617	0.440	−84.92
5	0.617	0.322	−62.15
7	0.617	0.204	−39.37

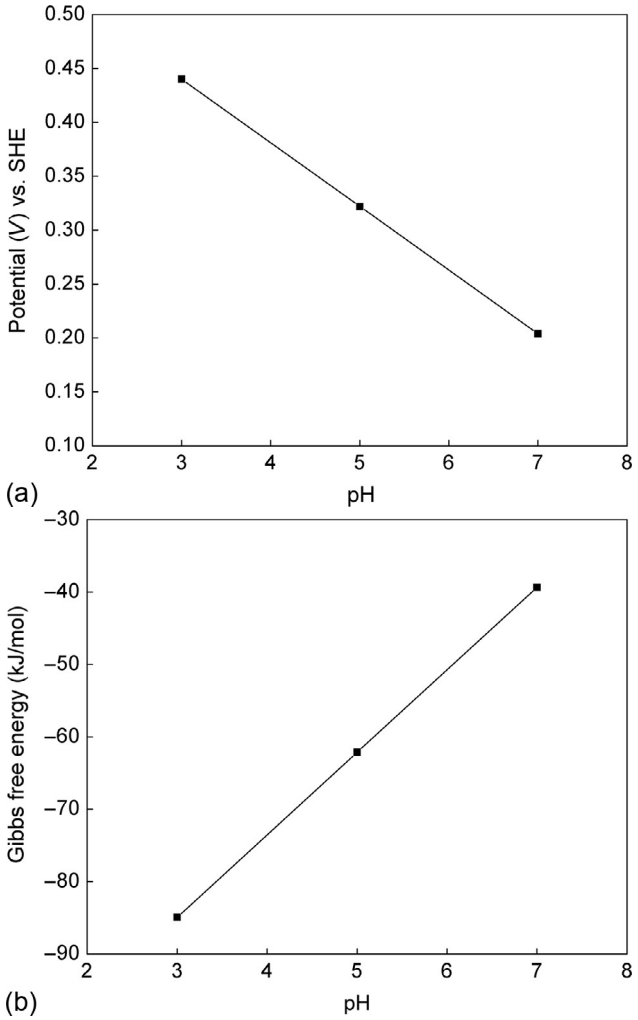

Fig. E2.7 (a) The potential and (b) Gibbs free-energy for iron as a function of pH.

SOLUTIONS GUIDE

CHAPTER 3: ELECTROCHEMICAL KINETICS OF CORROSION

E3.1. The potential of a zinc electrode on which Zn deposits from a 0.1 M $ZnSO_4$ solution is −1.1 V vs. SCE.

(a) Determine the zinc deposition voltage on the hydrogen scale.

(b) Determine whether zinc oxidation or reduction occurs at this potential.

Solution:

(a)
$$Zn^{2+} + 2e^- \rightarrow Zn, \quad e^o_{Zn^{2+}|Zn} = -0.762\,V \text{ vs. SHE}$$
$$e_{eq,Zn^{2+}|Zn} = -0.762 + 2.303\frac{RT}{2F}\log\left(\frac{a_{Zn^{2+}}}{a_{Zn}}\right)$$
$$= -0.762 + \frac{0.059}{2}\log(0.1)$$
$$= -0.792\,V \text{ vs. SHE}$$

(b) Since the applied potential is more cathodic than the equilibrium potential, Zn reduction will occur.

E3.2. Copper is immersed in a solution of AgCl where the activity of Ag^+ is 0.01 M. The following ion exchange reaction occurs during corrosion of copper:

$$Cu + 2Ag^+ \rightarrow Cu^{2+} + 2Ag$$

Estimate the concentration of Cu^{2+} that will halt copper corrosion.

Solution:

$$Cu \rightarrow Cu^{2+} + 2e^- (\text{anode}), \quad e^o_{Cu^{2+}|Cu} = -0.337\,V \text{ vs. SHE}$$
$$2Ag^+ + 2e^- \rightarrow 2Ag(\text{cathode}), \quad e^o_{Ag^+|Ag} = 0.799\,V \text{ vs. SHE}$$
$$e_{eq,Ag^+|Ag} = 0.799 - 2.303\frac{RT}{2F}\log\left(\frac{(a_{Ag})^2}{(a_{Ag^+})^2}\right)$$
$$e_{eq,Cu|Cu^{2+}} = -0.337 - 2.303\frac{RT}{2F}\log\left(\frac{a_{Cu^{2+}}}{a_{Cu}}\right)$$
$$E_{cell} = 0.799 - 0.337 - 2.303\frac{RT}{2F}\log\left(\frac{a_{Cu^{2+}}}{(0.1)^2}\right)$$

Corrosion Engineering
http://dx.doi.org/10.1016/B978-0-444-62722-3.09967-5

which simplifies to:

$$0 = 0.462 - \frac{0.059}{2}\log\left(\frac{a_{Cu^{2+}}}{(0.1)^2}\right)$$

$$\frac{0.924}{0.059} = \log\left(\frac{a_{Cu^{2+}}}{0.01}\right)$$

$$a_{Cu^{2+}} = \left(10^{0.924/0.059}\right)(0.01) = 4.58 \times 10^{13}\,\mathrm{M}$$

E3.3. Calculate the anodic exchange current density for tin for an overpotential of 0.2 V if the corrosion current is 0.5 A/cm^2. The anodic Tafel slope, b_a, is 0.05 V/decade.

Solution:

$$\eta_a = b_a \log\left(\frac{i}{i^o_{Sn}}\right)$$

$$0.2 = 0.05\log\left(\frac{0.5}{i^o_{Sn}}\right)$$

$$i^o_{Sn} = \frac{0.5}{\left(10^{0.2/0.05}\right)} = 5 \times 10^{-5}\,\mathrm{A/cm^2}$$

E3.4. Using the Tafel equations, derive:
(a) The corrosion current equation (dependence of I_{corr} on $i^o_{H_2}$ and i^o_M).
(b) The corrosion potential equation (dependence of E_{corr} on $i^o_{H_2}$ and i^o_M).

Solution:

According to the Tafel equation:

$$\eta = a + b\log(i)$$

From the Butler-Volmer equation:

$$\eta_a = b_a \log\left(\frac{I_{corr}}{i^o_M}\right) = E_{corr} - e_{eq,M^{2+}|M}$$

$$\eta_c = b_c \log\left(\frac{I_{corr}}{i^o_{H_2}}\right) = E_{corr} - e_{eq,H^{+}|H_2}$$

$$E_{corr} = e_{eq,M^{2+}|M} + b_a \log\left(\frac{I_{corr}}{i^o_M}\right)$$

$$E_{corr} = e_{eq,H^{+}|H_2} + b_c \log\left(\frac{I_{corr}}{i^o_{H_2}}\right)$$

Solving the last two equations for I_{corr} and E_{corr},

$$e_{eq,M^{2+}|M} + b_a\left[\log(I_{corr}) - \log\left(i^o_M\right)\right] = e_{eq,H^+|H_2} + b_c\left[\log(I_{corr}) - \log\left(i^o_{H_2}\right)\right]$$

$$e_{eq,H^+|H_2} - e_{eq,M^{2+}|M} = E_{cell} = b_a\left[\log(I_{corr}) - \log\left(i^o_M\right)\right] - b_c\left[\log(I_{corr}) - \log\left(i^o_{H_2}\right)\right]$$

$$E_{cell} = \log(I_{corr})(b_a - b_c) + b_c\log\left(i^o_{H_2}\right) - b_a\log\left(i^o_M\right)$$

$$\log(I_{corr})(b_a - b_c) = E_{cell} - b_c\log\left(i^o_{H_2}\right) + b_a\log\left(i^o_M\right)$$

$$\log(I_{corr}) = \left[\frac{\left(E_{cell} - b_c\log\left(i^o_{H_2}\right) + b_a\log\left(i^o_M\right)\right)}{(b_a - b_c)}\right]$$

$$I_{corr} = 10^{\left[\left(E_{cell} - b_c\log\left(i^o_{H_2}\right) + b_a\log\left(i^o_M\right)\right)/(b_a - b_c)\right]}$$

Substituting this result into either of the original two equations,

$$E_{corr} = \frac{b_a b_c\left(\log\left(i^o_M\right) - \log\left(i^o_{H_2}\right)\right) + \left(b_a e_{eq,H^+|H_2} - b_c e_{eq,M^{2+}|M}\right)}{(b_a - b_c)}$$

E3.5. Construct an Evans diagram (E vs. $\log i$) for the corrosion of silver in a hydrogen-saturated 0.1 M HCl solution in which the activity of Ag^{2+} is 10^{-18} M. The data for the reaction is as follows:

$$\left[Ag^{2+}\right] = 10^{-18}\,M \quad [H^+] = 0.1\,M \quad a_c = -0.0824\,V \text{ vs. SHE}$$

$$b_a = 0.100\ V/\text{decade} \quad b_c = -0.100\ V/\text{decade}$$

$$i^o_{Ag} = 0.8\,A/cm^2 \quad i^o_{H_2} = 0.15\,A/cm^2$$

Calculate:

(a) Exchange equilibrium potentials of the hydrogen and Ag redox reaction.
(b) Corrosion current and corrosion potential.
(c) Protection current to prevent corrosion.

Solution:

Equilibrium Potentials:

$$2H^+ + 2e^- \rightarrow H_2, \quad e^o_{H^+|H_2} = 0.00\,V \text{ vs. SHE}$$

$$2Ag^{2+} + 2e^- \rightarrow 2Ag, e^o_{Ag^+|Ag} = 0.799\,V \text{ vs. SHE}$$

$$e_{\mathrm{eq,H^+|H_2}} = e^{\circ}_{\mathrm{H^+|H_2}} - 2.303\frac{RT}{nF}\log\left(\frac{a_{\mathrm{H_2}}}{(a_{\mathrm{H^+}})^2}\right)$$

$$= 0 - \frac{0.059}{2}\log\left(\frac{1}{(0.1)^2}\right)$$

$$= -0.059\,\mathrm{V\ vs.\ SHE}$$

$$e_{\mathrm{eq,Ag^+|Ag}} = e^{\circ}_{\mathrm{Ag^+|Ag}} - 2.303\frac{RT}{nF}\log\left(\frac{a_{\mathrm{Ag}}}{(a_{\mathrm{Ag^+}})^2}\right)$$

$$= 0.799 - \frac{0.059}{2}\log\left(\frac{1}{(10^{-18})^2}\right)$$

$$= -0.263\,\mathrm{V\ vs.\ SHE}$$

Corrosion current and corrosion potential:

$$\eta_{\mathrm{a}} = b_{\mathrm{a}}\log\left(\frac{I_{\mathrm{corr}}}{i^{\circ}_{\mathrm{Ag}}}\right) = E_{\mathrm{corr}} - e_{\mathrm{eq,Ag^+|Ag}}$$

$$\eta_{\mathrm{c}} = b_{\mathrm{c}}\log\left(\frac{I_{\mathrm{corr}}}{i^{\circ}_{\mathrm{H_2}}}\right) = E_{\mathrm{corr}} - e_{\mathrm{eq,H^+|H_2}}$$

$$E_{\mathrm{corr}} = e_{\mathrm{eq,Ag^+|Ag}} + b_{\mathrm{a}}\log\left(\frac{I_{\mathrm{corr}}}{i^{\circ}_{\mathrm{Ag}}}\right)$$

$$E_{\mathrm{corr}} = e_{\mathrm{eq,H^+|H_2}} + b_{\mathrm{c}}\log\left(\frac{I_{\mathrm{corr}}}{i^{\circ}_{\mathrm{H_2}}}\right)$$

$$e_{\mathrm{eq,Ag^+|Ag}} + b_{\mathrm{a}}\left[\log(I_{\mathrm{corr}}) - \log\left(i^{\circ}_{\mathrm{Ag}}\right)\right] = e_{\mathrm{eq,H^+|H_2}} + b_{\mathrm{c}}\left[\log(I_{\mathrm{corr}}) - \log\left(i^{\circ}_{\mathrm{H_2}}\right)\right]$$

$$e_{\mathrm{eq,H^+|H_2}} - e_{\mathrm{eq,Ag^+|Ag}} = b_{\mathrm{a}}\left[\log(I_{\mathrm{corr}}) - \log\left(i^{\circ}_{\mathrm{Ag}}\right)\right] - b_{\mathrm{c}}\left[\log(I_{\mathrm{corr}}) - \log\left(i^{\circ}_{\mathrm{H_2}}\right)\right]$$

$$E_{\mathrm{cell}} = \log(I_{\mathrm{corr}})(b_{\mathrm{a}} - b_{\mathrm{c}}) + b_{\mathrm{c}}\log\left(i^{\circ}_{\mathrm{H_2}}\right) - b_{\mathrm{a}}\log\left(i^{\circ}_{\mathrm{Ag}}\right)$$

$$\log(I_{\mathrm{corr}})(b_{\mathrm{a}} - b_{\mathrm{c}}) = E_{\mathrm{cell}} - b_{\mathrm{c}}\log\left(i^{\circ}_{\mathrm{H_2}}\right) + b_{\mathrm{a}}\log\left(i^{\circ}_{\mathrm{Ag}}\right)$$

$$\log(I_{\mathrm{corr}}) = \left[\frac{\left(E_{\mathrm{cell}} - b_{\mathrm{c}}\log\left(i^{\circ}_{\mathrm{H_2}}\right) + b_{\mathrm{a}}\log\left(i^{\circ}_{\mathrm{Ag}}\right)\right)}{(b_{\mathrm{a}} - b_{\mathrm{c}})}\right]$$

$$I_{corr} = 10^{\left[\left(E_{cell} - b_c \log\left(i^o_{H_2}\right) + b_a \log\left(i^o_{Ag}\right)\right)/(b_a - b_c)\right]}$$

$$= 10^{\left[\left(0.204 - (-0.100)\log(0.15) + 0.100\log(0.8)\right)/(0.100 - (-0.100))\right]}$$

$$= 3.66\,\mathrm{A/cm^2}$$

$$E_{corr} = \frac{b_a b_c\left(\log\left(i^o_{Ag}\right) - \log\left(i^o_{H_2}\right)\right) + \left(b_a e_{eq,H^+|H_2} - b_c e_{eq,Ag^+|Ag}\right)}{(b_a - b_c)}$$

$$= \frac{(0.100 \times -0.100)(\log(0.8) - \log(0.15)) + (0.100 \times -0.059) - (-0.100 \times -0.263)}{(0.100 - (-0.100))}$$

$$= -0.197\,V \text{ vs. } SHE$$

Calculation of the protective current:
In order to reverse the corrosion reaction, $\eta_{prot} = 0$. To do this, the

$$E_{prot} = e_{eq,a}$$

In this case, it means that $E_{prot} = e_{eq,Ag^+|Ag}$

$$\eta_{prot} = E_{prot} - e_{eq,H^+|H_2}$$

$$= -0.263 - (-0.059)$$

$$= -0.204\,V$$

$$\log\left(i_{prot}\right) = \frac{\left(\eta_{prot} - a_c\right)}{b_c}$$

$$i_{prot} = 10^{\left(\eta_{prot} - a_c\right)/b_c}$$

$$= 10^{(-0.204 + 0.0824)/-0.100}$$

$$= 16.44\,\mathrm{A/cm^2}$$

An Evans diagram for the Ag system is shown in Fig. E3.1

E3.6. A lead electrode is immersed in an oxygen-saturated 0.1 M $PbSO_4$ solution. Calculate and plot the corrosion current at pH between 3 and 6. The Tafel constants are $b_a = -b_c = 0.10$ V/decade and the exchange current densities for lead and oxygen reduction are 10^{-1} and 10^{-2} A/cm^2, respectively.

Solution:

$$2Pb^{2+} + 4e^- \rightarrow 2Pb, \quad e^o_{Pb^{2+}|Pb} = -0.126\,V \text{ vs. SHE}$$

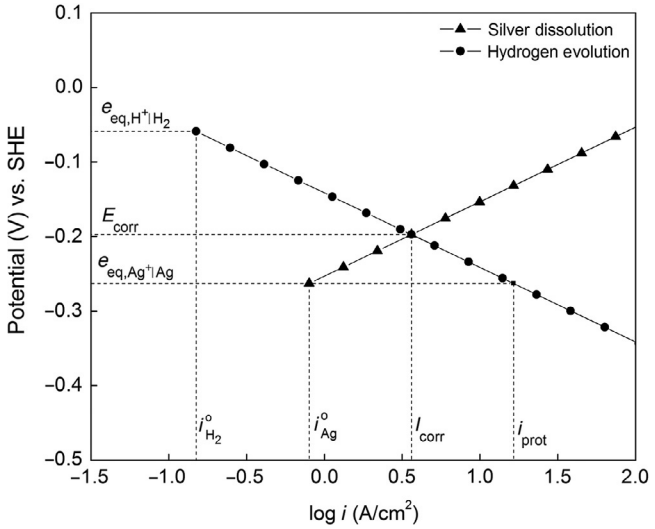

Fig. E3.1 Evans diagram for the Ag system.

$$e_{Pb^{2+}|Pb} = e^{o}_{Pb^{2+}|Pb} - 2.303\frac{RT}{nF}\log\left(\frac{1}{(a_{Pb^{2+}})^2}\right)$$

$$= -0.126 - \frac{0.059}{2}\log\left(\frac{1}{0.1}\right)$$

$$= -0.155\,\text{V vs. SHE}$$

$$O_2 + 4H^+ + 4e^- \rightarrow 2H_2O,\ e^{o}_{H^+|H_2O} = 1.23\ \text{V vs. SHE at pH} = 0$$

$$e_{H^+|H_2O} = e^{o}_{H^+|H_2O} - 2.303\frac{RT}{nF}\log\left(\frac{1}{(a_{H^+})^4}\right)$$

$$= 1.23 - 0.059(\text{pH})$$

$$\eta_a = b_a\log\left(\frac{I_{corr}}{i^{o}_{Pb}}\right) = E_{corr} - e_{eq,\,Pb^{2+}|Pb}$$

$$\eta_c = b_c\log\left(\frac{I_{corr}}{i^{o}_{H_2O}}\right) = E_{corr} - e_{eq,\,H^+|H_2O}$$

$$E_{corr} = e_{eq,\,Pb^{2+}|Pb} + b_a\log\left(\frac{I_{corr}}{i^{o}_{Pb}}\right)$$

$$E_{corr} = e_{eq,\,H^+|H_2O} + b_c\log\left(\frac{I_{corr}}{i^{o}_{H_2O}}\right)$$

$$e_{eq,\,Pb^{2+}|Pb} + b_a\left[\log(I_{corr}) - \log\left(i^{o}_{Pb}\right)\right] = e_{eq,\,H^+|H_2O} + b_c\left[\log(I_{corr}) - \log\left(i^{o}_{H_2O}\right)\right]$$

$$e_{\mathrm{eq,H^+|H_2O}} - e_{\mathrm{eq,Pb^{2+}|Pb}} = E_{\mathrm{cell}} = b_{\mathrm{a}}\left[\log\left(I_{\mathrm{corr}}\right) - \log\left(i^{\mathrm{o}}_{\mathrm{Pb}}\right)\right] - b_{\mathrm{c}}\left[\log\left(I_{\mathrm{corr}}\right) - \log\left(i^{\mathrm{o}}_{\mathrm{H_2O}}\right)\right]$$

$$E_{\mathrm{cell}} = \log\left(I_{\mathrm{corr}}\right)\left(b_{\mathrm{a}} - b_{\mathrm{c}}\right) + b_{\mathrm{c}}\log\left(i^{\mathrm{o}}_{\mathrm{H_2O}}\right) - b_{\mathrm{a}}\log\left(i^{\mathrm{o}}_{\mathrm{Pb}}\right)$$

$$\log\left(I_{\mathrm{corr}}\right)\left(b_{\mathrm{a}} - b_{\mathrm{c}}\right) = E_{\mathrm{cell}} - b_{\mathrm{c}}\log\left(i^{\mathrm{o}}_{\mathrm{H_2O}}\right) + b_{\mathrm{a}}\log\left(i^{\mathrm{o}}_{\mathrm{Pb}}\right)$$

$$\log\left(I_{\mathrm{corr}}\right) = \left[\frac{\left(E_{\mathrm{cell}} - b_{\mathrm{c}}\log\left(i^{\mathrm{o}}_{\mathrm{H_2O}}\right) + b_{\mathrm{a}}\log\left(i^{\mathrm{o}}_{\mathrm{Pb}}\right)\right)}{\left(b_{\mathrm{a}} - b_{\mathrm{c}}\right)}\right]$$

$$I_{\mathrm{corr}} = 10^{\left[\left(E_{\mathrm{cell}} - b_{\mathrm{c}}\log\left(i^{\mathrm{o}}_{\mathrm{H_2O}}\right) + b_{\mathrm{a}}\log\left(i^{\mathrm{o}}_{\mathrm{Pb}}\right)\right)/\left(b_{\mathrm{a}} - b_{\mathrm{c}}\right)\right]}$$

$$= 10^{\left[\left((1.23 - 0.059\mathrm{pH} - (-0.155)) - (-0.10)\log\left(10^{-2}\right) + 0.10\log\left(10^{-1}\right)\right)/(0.10 - (-0.10))\right]}$$

$$E_{\mathrm{corr}} = \frac{b_{\mathrm{a}}b_{\mathrm{c}}\left(\log\left(i^{\mathrm{o}}_{\mathrm{Pb}}\right) - \log\left(i^{\mathrm{o}}_{\mathrm{H_2O}}\right)\right) + \left(b_{\mathrm{a}}e_{\mathrm{eq,H^+|H_2O}} - b_{\mathrm{c}}e_{\mathrm{eq,Pb^{2+}|Pb}}\right)}{\left(b_{\mathrm{a}} - b_{\mathrm{c}}\right)}$$

$$= \frac{(0.10 \times -0.10)\left(\log\left(10^{-1}\right) - \log\left(10^{-2}\right)\right) + (0.10 \times (1.23 - 0.059\mathrm{pH})) - (-0.10 \times -0.155)}{(0.10 - (-0.10))}$$

The corrosion rates for pH 3-6 were calculated and plotted in Fig. E3.2.

E3.7. Iron corrodes in a solution saturated with oxygen. The pH of the solution is 7 and the partial pressure of oxygen is 1 atm.

(a) Calculate the corrosion current and corrosion potential of the system.

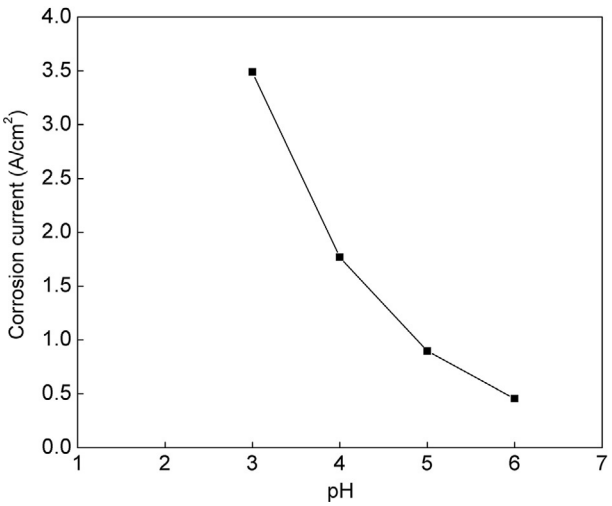

Fig. E3.2 Plot of pH vs. corrosion current for the Pb electrode.

(b) Calculate the protection current required to reduce the corrosion current to zero.

Additional information:

$$[\mathrm{Fe}] = 0.7\,\mathrm{M} \quad \mathrm{pH} = 7 \quad P_{\mathrm{O_2}} = 1\,\mathrm{atm}$$

$$b_{\mathrm{a}} = 0.08\,\mathrm{V/decade} \quad b_{\mathrm{c}} = -0.11\,\mathrm{V/decade}$$

$$i^{\mathrm{o}}_{\mathrm{Fe}} = 10^{-5}\,\mathrm{A/cm^2} \quad i^{\mathrm{o}}_{\mathrm{OH^-}} = 10^{-6}\,\mathrm{A/cm^2}$$

Solution:

Calculating the potentials

$$2\mathrm{Fe}^{2+} + 4\mathrm{e}^- \rightarrow 2\mathrm{Fe}, \quad e^{\mathrm{o}}_{\mathrm{Fe^{2+}|Fe}} = -0.440\,\mathrm{V\ vs.\ SHE}$$

$$\mathrm{O_2} + 2\mathrm{H_2O} + 4\mathrm{e}^- \rightarrow 4\mathrm{OH}^-, \quad e^{\mathrm{o}}_{\mathrm{O_2|OH^-}} = 0.401\,\mathrm{V\ vs.\ SHE}$$

$$\begin{aligned} e_{\mathrm{eq,O_2|OH^-}} &= e^{\mathrm{o}}_{\mathrm{O_2|OH^-}} - 2.303\frac{RT}{nF}\log\left(\frac{(a_{\mathrm{OH^-}})^4}{P_{\mathrm{O_2}}}\right) \\ &= 0.401 + 0.059(14-7) \\ &= 0.814\,\mathrm{V\ vs.\ SHE} \end{aligned}$$

$$\begin{aligned} \mathrm{e}_{\mathrm{Fe^{2+}|Fe}} &= \mathrm{e}^{\mathrm{o}}_{\mathrm{Fe^{2+}|Fe}} - 2.303\frac{\mathrm{RT}}{\mathrm{nF}}\log\left(\frac{\mathrm{a_{Fe}}}{(\mathrm{a_{Fe^{2+}}})^2}\right) \\ &= -0.440 - \frac{0.059}{4}\log\left(\frac{1}{(0.7)^2}\right) \\ &= -0.445\,V\ vs.\ SHE \end{aligned}$$

Calculate the E_{corr} and I_{corr}

$$\eta = b\log\left(\frac{i}{i^{\mathrm{o}}}\right)$$

$$\eta_{\mathrm{c}} = b_{\mathrm{c}}\log(I_{\mathrm{corr}}) - b_{\mathrm{c}}\log\left(i^{\mathrm{o}}_{\mathrm{OH^-}}\right)$$

$$\eta_{\mathrm{a}} = b_{\mathrm{a}}\log(I_{\mathrm{corr}}) - b_{\mathrm{a}}\log\left(i^{\mathrm{o}}_{\mathrm{Fe}}\right)$$

$$E_{\mathrm{corr}} = e^{\mathrm{o}}_{\mathrm{Fe^{2+}|Fe}} + b_{\mathrm{a}}\log\left(\frac{I_{\mathrm{corr}}}{i^{\mathrm{o}}_{\mathrm{Fe}}}\right)$$

$$E_{\mathrm{corr}} = e^{\mathrm{o}}_{\mathrm{O_2|OH^-}} + b_{\mathrm{c}}\log\left(\frac{I_{\mathrm{corr}}}{i^{\mathrm{o}}_{\mathrm{OH^-}}}\right)$$

$$E_{\text{corr}} = e_{\text{eq,Fe}^{2+}|\text{Fe}} + b_{\text{a}} \log\left(\frac{I_{\text{corr}}}{i^{\circ}_{\text{Fe}}}\right)$$

$$E_{\text{corr}} = e_{\text{eq,O}_2|\text{OH}^-} + b_{\text{c}} \log\left(\frac{I_{\text{corr}}}{i^{\circ}_{\text{OH}^-}}\right)$$

$$e_{\text{eq,Fe}^{2+}|\text{Fe}} + b_{\text{a}}\left[\log(I_{\text{corr}}) - \log\left(i^{\circ}_{\text{Fe}}\right)\right] = e_{\text{eq,O}_2|\text{OH}^-} + b_{\text{c}}\left[\log(I_{\text{corr}}) - \log\left(i^{\circ}_{\text{OH}^-}\right)\right]$$

$$e_{\text{eq,O}_2|\text{OH}^-} - e_{\text{eq,Fe}^{2+}|\text{Fe}} = b_{\text{a}}\left[\log(I_{\text{corr}}) - \log\left(i^{\circ}_{\text{Fe}}\right)\right] - b_{\text{c}}\left[\log(I_{\text{corr}}) - \log\left(i^{\circ}_{\text{OH}^-}\right)\right]$$

$$E_{\text{cell}} = \log(I_{\text{corr}})(b_{\text{a}} - b_{\text{c}}) + b_{\text{c}} \log\left(i^{\circ}_{\text{OH}^-}\right) - b_{\text{a}} \log\left(i^{\circ}_{\text{Fe}}\right)$$

$$\log(I_{\text{corr}})(b_{\text{a}} - b_{\text{c}}) = E_{\text{cell}} - b_{\text{c}} \log\left(i^{\circ}_{\text{OH}^-}\right) + b_{\text{a}} \log\left(i^{\circ}_{\text{Fe}}\right)$$

$$\log(I_{\text{corr}}) = \left[\frac{\left(E_{\text{cell}} - b_{\text{c}} \log\left(i^{\circ}_{\text{OH}^-}\right) + b_{\text{a}} \log\left(i^{\circ}_{\text{Fe}}\right)\right)}{(b_{\text{a}} - b_{\text{c}})}\right]$$

$$I_{\text{corr}} = 10^{\left[\left(E_{\text{cell}} - b_{\text{c}} \log\left(i^{\circ}_{\text{OH}^-}\right) + b_{\text{a}} \log\left(i^{\circ}_{\text{Fe}}\right)\right)/(b_{\text{a}} - b_{\text{c}})\right]}$$

$$I_{\text{corr}} = 10^{\left[\left(1.26 - (-0.11)\log(10^{-6}) + 0.08 \log(10^{-5})\right)/(0.08 - (-0.11))\right]}$$

$$I_{\text{corr}} = 11.7\,\text{A/cm}^2$$

$$E_{\text{corr}} = \frac{b_{\text{a}} b_{\text{c}}\left(\log\left(i^{\circ}_{\text{Fe}}\right) - \log\left(i^{\circ}_{\text{OH}^-}\right)\right) + \left(b_{\text{a}} e_{\text{eq,O}_2|\text{OH}^-} - b_{\text{c}} e_{\text{eq,Fe}^{2+}|\text{Fe}}\right)}{(b_{\text{a}} - b_{\text{c}})}$$

$$E_{\text{corr}} = \frac{(0.08 \times -0.11)(\log(10^{-5}) - \log(10^{-6})) + (0.08 \times 0.814) - (-0.11 \times -0.449)}{(-0.08 - (-0.11))}$$

$$E_{\text{corr}} = -0.037\,\text{V vs. SHE}$$

In order to reverse the corrosion reaction, $\eta_{\text{prot}} = 0$, or $E_{\text{prot}} = E_{\text{a}}$. In this case, it means that $E_{\text{prot}} = e_{\text{Fe}^{2+}|\text{Fe}}$

$$\eta_{\text{prot}} = E_{\text{prot}} - e_{\text{O}_2|\text{OH}^-} = -1.263\,\text{V}$$

$$\log\left(i_{\text{prot}}\right) = \frac{\left(\eta_{\text{prot}} - a_{\text{c}}\right)}{b_{\text{c}}}$$

$$i_{\text{prot}} = 10^{\left(\eta_{\text{prot}} - a_{\text{c}}\right)/b_{\text{c}}}$$

$$a_{\text{c}} = -b_{\text{c}} \log\left(i^{\circ}_{\text{c}}\right)$$

$$a_c = 0.11 \log\left(10^{-6}\right)$$

$$a_c = -0.66\,\text{V vs. SHE}$$

$$i_{\text{prot}} = 10^{(-1.263+0.66)/-0.11}$$

$$i_{\text{prot}} = 3.03 \times 10^5\,\text{A/cm}^2$$

An Evans diagram for the iron system is plotted in Fig. E3.3.

E3.8. Derive an expression for the slope of the corrosion rate vs. pH for zinc in a 0.01 M $ZnCl_2$ solution. Assume that all zinc acts as a cathode and assume that there is no concentration polarization.

Solution:

$$2H^+ + 2e^- \rightarrow H_2, \quad e^{\circ}_{H^+|H_2} = 0.00\,\text{V vs. SHE}$$

$$Zn^{2+} + 2e^- \rightarrow Zn, \quad e^{\circ}_{Zn^{2+}|Zn} = -0.762\,\text{V vs. SHE}$$

$$e_{\text{eq},H^+|H_2} = 0 - 2.303\frac{RT}{2F}\log\left(\frac{a_{H_2}}{(a_{H^+})^2}\right)$$

$$= -0.059(\text{pH})$$

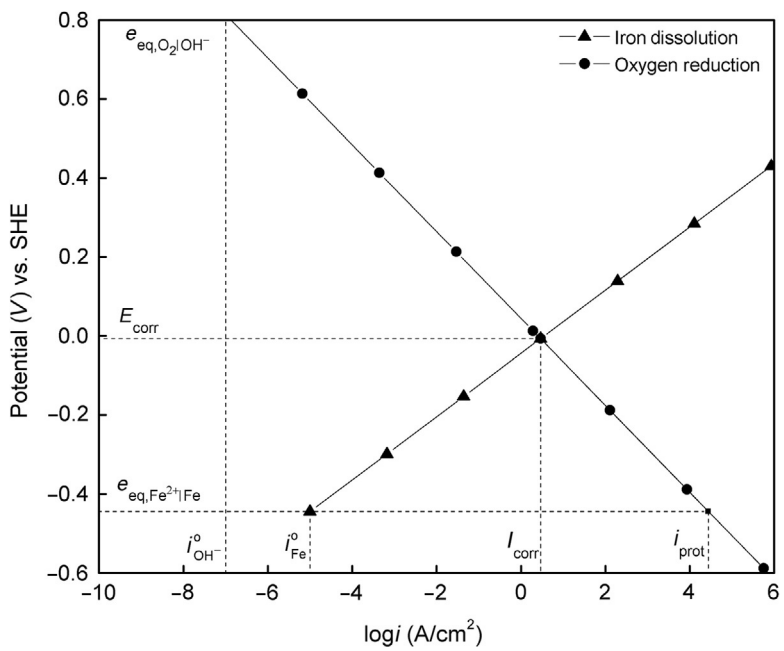

Fig. E3.3 Evans diagram for the iron system.

$$e_{\text{eq},Zn^{2+}|Zn} = e^{o}_{Zn^{2+}|Zn} - 2.303\frac{RT}{nF}\log\left(\frac{a_{Zn}}{a_{Zn^{2+}}}\right)$$
$$= -0.762 - \frac{0.059}{2}\log\left(\frac{1}{0.01}\right)$$
$$= -0.821\,\text{V vs. SHE}$$

For cathodic polarization:

$$\eta_c = e_{\text{eq},Zn^{2+}|Zn} - e_{\text{eq},H^+|H_2}$$
$$= -0.059(\text{pH}) - 0.821$$
$$\eta_c = -b_c\log\left(\frac{i}{I_{\text{corr}}}\right)$$
$$i = I_{\text{corr}}10^{-\eta_c/b_c}$$

Approximating 10^x

$$10^x = 1 + 2.3x + \frac{(2.3x)^2}{2!} + \ldots$$
$$10^{-\eta_c/b_c} = 1 - \frac{2.3\eta_c}{b_c}$$
$$i = I_{\text{corr}}\left(1 - \frac{2.3\eta_c}{b_c}\right)$$
$$= I_{\text{corr}}\left(1 - \frac{2.3(0.059\text{pH} - 0.821)}{b_c}\right)$$
$$\frac{di}{d\text{pH}} = \frac{-2.3(0.059)I_{\text{corr}}}{b_c}$$

E3.9. The exchange current density and cathodic Tafel slope (b_c) of platinum in a deaerated H_2SO_4 solution with a pH of 2.0 are 7.6×10^{-6} A/cm^2 and -0.025 V/decade, respectively. Calculate the current in A/cm^2 when platinum is polarized cathodically at -0.334 V vs. SCE.

Given:

$$e_{Pt^{2+}|Pt} = -0.334\,\text{V vs. SCE} \quad \text{pH} = 2$$
$$b_c = -0.025\,\text{V/decade} \quad i^{o}_{c} = 7.6\times10^{-6}\,\text{A/cm}^2$$

Solution:

$$2H^+ + 2e^- \rightarrow H_2$$
$$Pt^{2+} + 2e^- \rightarrow Pt$$
$$2H^+ + 2e^- \rightarrow H_2, \quad e^{o}_{H^+|H_2} = 0.00\,\text{V vs. SHE}$$

$$Pt^{2+} + 2e^- \rightarrow Pt, \quad e^o_{Pt^{2+}|Pt} = 1.2\,V \text{ vs. SHE}$$

$$e_{eq,H^+|H_2} = 0 - 2.303\frac{RT}{2F}\log\left(\frac{a_{H_2}}{(a_{H^+})^2}\right)$$
$$= -0.059pH = -0.118\,V \text{ vs. SHE } (pH = 2)$$

Convert the potential to the saturated calomel electrode scale:

$$e_{eq,H^+|H_2} = -0.118 - 0.241 = -0.359\,V \text{ vs. SCE}$$

For cathodic polarization of hydrogen evolution:

$$\eta_c = e_{H^+|H_2} - e_{Pt^2|Pt}$$

$$\eta_c = -0.359 - (-0.334) = -0.025\,V$$

$$\eta_c = b_c \log\left(\frac{i}{i_c^o}\right)$$

$$i = 10^{\eta_c/b_c} i_c^o$$
$$= 10^{(-0.025/-0.025)} \times 7.6 \times 10^{-6}$$

$$i = 7.6 \times 10^{-5}\,A/cm^2$$

E3.10. Calculate the limiting current density for oxygen reduction in an alkaline solution if the oxygen concentration is 0.4 mol/m^3, the diffusion coefficient, D_{O_2}, is equal to 5.0×10^{-10} m^2/s, and the diffusion layer thickness is 195.3 μm.

Solution:

$$i_L = \frac{nFD_{O_2}a_{O_2}}{\delta}$$
$$= \frac{4 \times 96500 \times 5.0 \times 10^{-10} \times 0.4}{1.953 \times 10^{-4}}$$
$$i_L = 0.395\,A/cm^2$$

E3.11. Nickel is deposited at a current density of 75 A/m^2. Calculate the limiting current if the reduction occurs at a concentration overpotential of −150 mV.

Solution:

$$Ni^{2+} + 2e^- \rightarrow Ni$$

$$\eta_d = \frac{RT}{nF}\ln\left(\frac{i_L - i}{i_L}\right)$$

Solving for $i_{L,}$

$$i_L = \frac{-i}{\exp\left(\frac{\eta_d nF}{RT}\right) - 1}$$

In this case,

$$= \frac{-0.0075}{\exp\left(\frac{-150 \times 10^{-3} \times 2 \times 96485}{8.314 \times 298}\right) - 1}$$

$$= 0.0075\,\mathrm{A/cm^2}$$

E3.12. Calculate the corrosion potential, corrosion current, and protection current needed to stop corrosion for cadmium in a deaerated corrosive medium.

Additional information:

$$\left[Cd^{2+}\right] = 10^{-5}\,\mathrm{M\ pH} = 1\ a_c = -0.360\,\mathrm{V\ vs.\ SHE}\ b_a = 0.100\,\mathrm{V/decade}\ b_c = -0.120\,\mathrm{V/decade}\ i^o_{Cd} = 10^{-3}\,\mathrm{A/cm^2}$$

Solution:

Calculations of the exchange current density for the cathodic reaction and the anodic intercept:

From the Bulter-Volmer equation:

$$\eta = E_i - E_{eq}$$

From the Tafel equation:

$$\eta = a + b\log(i)$$

At the equilibrium point of each reaction, $E_r = Ei$, therefore

$$\eta = 0\,\mathrm{V}$$

$$0 = a + b\log(i)$$

$$a = -b\log(i)$$

$$i = 10^{-a/b}$$

So

$$a_c = -b_c \log\left(i^o_c\right)$$

$$-0.360 = 0.120\log\left(i^o_c\right)$$

$$i^o_{H_2} = 10^{-0.360/0.120}$$

$$= 10^{-3}\,\mathrm{A/cm^2}$$

Calculation of Equilibrium Potentials:

$$2H^+ + 2e^- \rightarrow H_2;\ \ e^o_{H^+|H_2} = 0.00\,V \text{ vs. SHE}$$

$$Cd^{2+} + 2e^- \rightarrow Cd;\ \ e^o_{Cd^{2+}|Cd} = -0.402\,V \text{ vs. SHE}$$

$$e_{eq,H^+|H_2} = e^o_{H^+|H_2} - 2.303\frac{RT}{nF}\log\left(\frac{a_{H_2}}{(a_{H^+})^2}\right)$$

$$= -0.059(pH)$$

$$= -0.059\,V \text{ vs. SHE}$$

$$e_{eq,Cd^{2+}|Cd} = e^o_{Cd^{2+}|Cd} - 2.303\frac{RT}{nF}\log\left(\frac{a_{Cd}}{a_{Cd^{2+}}}\right)$$

$$= -0.402 - \frac{0.059}{2}\log\left(\frac{1}{10^{-5}}\right)$$

$$= -0.550\,V \text{ vs. SHE}$$

Calculation of the corrosion potential and the corrosion current:

$$\eta_a = b_a\log\left(\frac{I_{corr}}{i^o_{Cd}}\right) = E_{corr} - e_{eq,Cd^{2+}|Cd}$$

$$\eta_c = b_c\log\left(\frac{I_{corr}}{i^o_{H_2}}\right) = E_{corr} - e_{eq,H^+|H_2}$$

$$E_{corr} = e_{eq,Cd^{2+}|Cd} + b_a\log\left(\frac{I_{corr}}{i^o_{Cd}}\right)$$

$$E_{corr} = e_{eq,H^+|H_2} + b_c\log\left(\frac{I_{corr}}{i^o_{H_2}}\right)$$

$$e_{eq,Cd^{2+}|Cd} + b_a\left[\log(I_{corr}) - \log\left(i^o_{Cd}\right)\right] = e_{eq,H^+|H_2} + b_c\left[\log(I_{corr}) - \log\left(i^o_{H_2}\right)\right]$$

$$e_{eq,H^+|H_2} - e_{eq,Cd^{2+}|Cd} = b_a\left[\log(I_{corr}) - \log\left(i^o_{Cd}\right)\right] - b_c\left[\log(I_{corr}) - \log\left(i^o_{H_2}\right)\right]$$

$$E_{cell} = \log(I_{corr})(b_a - b_c) + b_c\log\left(i^o_{OH^-}\right) - b_a\log\left(i^o_{Pb}\right)$$

$$\log(I_{corr})(b_a - b_c) = E_{cell} - b_c\log\left(i^o_{H_2}\right) + b_a\log\left(i^o_{Cd}\right)$$

$$\log(I_{corr}) = \left[\frac{\left(E_{cell} - b_c\log\left(i^o_{H_2}\right) + b_a\log\left(i^o_{Cd}\right)\right)}{(b_a - b_c)}\right]$$

$$I_{corr} = 10^{\left[\left(E_{cell} - b_c\log\left(i^o_{H_2}\right) + b_a\log\left(i^o_{Cd}\right)\right)/(b_a - b_c)\right]}$$

$$= 10^{\left[\left(0.4905 - (-0.120)\log(10^{-3}) + 0.100\log(10^{-3})\right)/(0.100 - (-0.120))\right]}$$

$$= 1.697 \times 10^{-1}\,A/cm^2$$

$$E_{\text{corr}} = \frac{b_a b_c\left(\log\left(i^{\circ}_{\text{Cd}}\right) - \log\left(i^{\circ}_{\text{H}_2}\right)\right) + \left(b_a e_{\text{eq},\text{H}^+|\text{H}_2} - b_c e_{\text{eq},\text{Cd}^{2+}|\text{Cd}}\right)}{(b_a - b_c)}$$

$$= \frac{(0.100 \times -0.120)(\log(10^{-3}) - \log(10^{-3})) + (0.100 \times -0.059) - (-0.120 \times -0.5495)}{(0.100 - (-0.120))}$$

$$= -3.27 \times 10^{-1}\,\text{V vs. SHE}$$

In order to reverse the corrosion reaction, $\eta_{\text{prot}} = 0$ hence, $E_{\text{prot}} = e_a$. Thus, $E_{\text{prot}} = e_{\text{Cd}^{2+}|\text{Cd}}$.

$$\eta_{\text{prot}} = E_{\text{prot}} - e_{\text{H}^+|\text{H}_2} = -0.491\,\text{V}$$

$$\log\left(i_{\text{prot}}\right) = \frac{\left(\eta_{\text{prot}} - a_c\right)}{b_c}$$

$$i_{\text{prot}} = 10^{\left(\eta_{\text{prot}} - a_c\right)/b_c}$$

$$= 10^{(-0.491-(-0.360))/-0.12}$$

$$= 12.34\,\text{A/cm}^2$$

An Evans diagram for the Cd system is shown in Fig. E3.4.

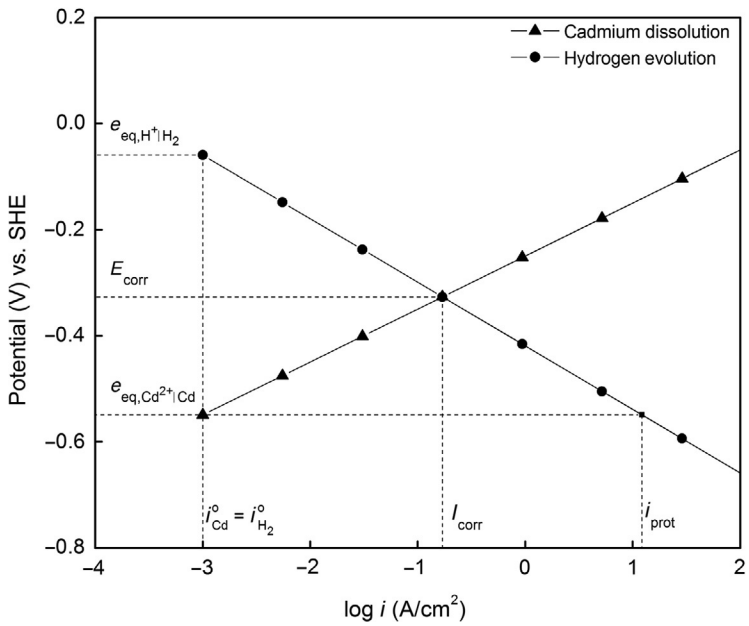

Fig. E3.4 Evans diagram for the Cd system.

SOLUTIONS GUIDE

CHAPTER 4: PASSIVITY

E4.1. Calculate and construct, using mixed potential theory, the critical passivation current density (a) potentiostatic and (b) galvanostatic polarization curve for anodic dissolution for active-passive metal that has the following electrochemical parameters: $E_{corr} = -0.5$ V vs. SCE, $E_{pp} = -0.4$ V vs. SCE, $I_{corr} = 10^{-4}$ A/cm^2, $b_a = 0.05$, $I_{pass} = 10^{-5}$ A/cm^2, and $E_{tr} = +1.0$ V vs. SCE.

Solution:

(a) The critical passivation current density is calculated by substituting the anodic current i_a density with I_{crit} and the anodic potential E with E_{pp} in Tafel equation (Fig. E4.1).

$$i_a = I_{corr} 10^{(\eta_a / b_a)}$$
$$\eta_a = E - E_{corr} \rightarrow E = E_{pp}$$
$$\eta_a = E_{pp} - E_{corr} = -0.4 - (-0.5)$$
$$I_{crit} = i_a = I_{corr} 10^{(\eta_a / b_a)} \rightarrow I_{crit} = 10^{-4} \times 10^{(0.1/0.05)} = 10^{-2} \text{A/cm}^2$$

The potential in potentiostatic mode is a single value as a function of current. The potentiodynamic and potentiostatic anodic polarization curves obtained at the same sweep rate are identical. They identify corrosion properties of passivating metals and alloys and are very useful in predicting the corrosion properties of material.

(b) In galvanostatic mode starting from the corrosion potential of the working electrode, the applied current, $i_{app} = i_a - i_c$, increased in anodic direction and the potential is measured at each galvanostatically controlled step. In this mode, the applied current above the critical current density increases the potential into the transpassive region of the anodic curve. In the back scan, the applied current initially decreases to passivation current I_{pass}. In the next step, with decrease of the current, the potential decreases into the active region. In galvanostatic mode, because the potential is not a single value as a function of current, this procedure cannot adequately define the corrosion properties of an active-passive metal or alloy (Fig. E4.2).

E4.2. For active-passive alloys A and B with electrochemical parameters given in Table E4.1, calculate the critical passivation current density and determine which is more easily passivated.

http://dx.doi.org/10.1016/B978-0-444-62722-3.09966-3

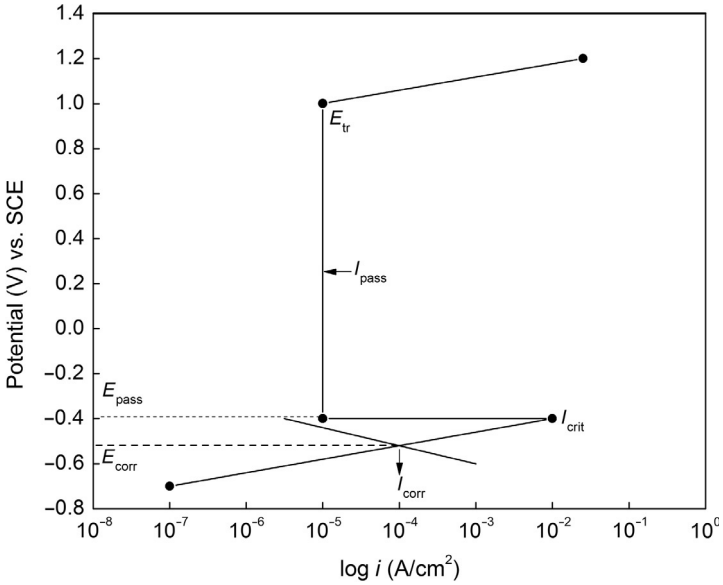

Fig. E4.1 Polarization curve for anodic dissolution for active passive metal.

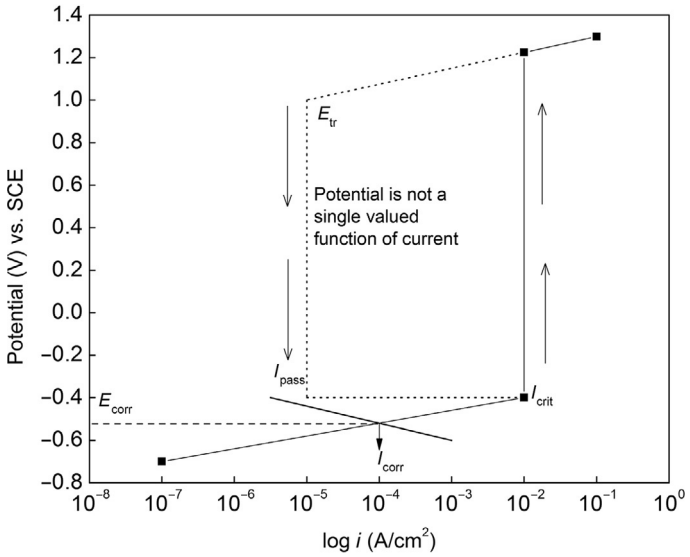

Fig. E4.2 Galvanostatically controlled polarization curve of an active-passive metal.

Table E4.1 Electrochemical Parameters for Active-Passive Alloys A and B

	I_{corr} (A/cm^2)	b_a (V/decade)	E_{corr} (V vs. SCE)	E_{pp} (V vs. SCE)
Alloy A	1×10^{-9}	+0.1	−0.300	0.2
Alloy B	7×10^{-8}	+0.1	−0.100	0.1

Solution:

Using mixed potential theory and Tafel equations, the critical current density for both alloys are calculated.

$$i_a = I_{corr} 10^{(\eta_a / b_a)}$$

$$\eta_a = E - E_{corr}$$

$$i_a = I_{crit}; \quad E = E_{pp}$$

$$I_{crit,A} = 1 \times 10^{-9} \times 10^{((0.2-(-0.3))/0.1)} = 10^{-4}\,\mathrm{A/cm^2}$$

$$I_{crit,B} = 7 \times 10^{-8} \times 10^{((0.1-(-0.1))/0.1)} = 7 \times 10^{-6}\,\mathrm{A/cm^2}$$

Alloy B is more easily passivated because it requires lower critical passivation current density.

E4.3. Construct an anodic polarization curve and calculate the critical passivation current density of an active-passive alloy using mixed potential theory with the folowing electrochemical parameters: $E_{corr} = -0.55$ V vs. SCE; $I_{corr} = 10^{-4}$ A/cm^2; $b_a = 0.1$, $E_{pp} = -0.3$ V vs. SCE; and $I_{pass} = 10^{-7}$ A/cm^2, $E_{tr} = +0.9$ V.

Using the given parameters, the anodic polarization curve was constructed (Fig. E4.3) and the critical passivation current density was calculated using mixed potential theory.

Solution:

$$I_{crit} = i_a = I_{corr} \exp^{((2.3 b_a nF/RT)\eta_a)} = I_{corr} 10^{((2.3 b_a nF/RT)\eta_a)}$$

$$I_{crit} = I_{corr} 10^{(\eta_a/(2.3 b_a nF/RT))} = I_{corr} 10^{(\eta_a / b_a)}$$

$$\eta_a = E - E_{corr}$$

$$E = E_{pp}$$

$$\eta_a = -0.3 - (-0.55) = 0.25$$

$$I_{crit} = 10^{-4} 10^{(0.25/0.1)} = 10^{-1.5}\,\mathrm{A/cm^2}$$

E4.4. Parameters of an active-passive metal are given in Table E4.2:

(a) Calculate the critical current density required to passivate the metal.

(b) Calculate the equilibrium potential of the corroding species given the exchange current density of the metal, $i^o = 10^{-9}$ A/m^2.

(c) Calculate the concentration of the metal-ion species at the equilibrium potential. Assume that one electron transfer reaction occurs during the corrosion of

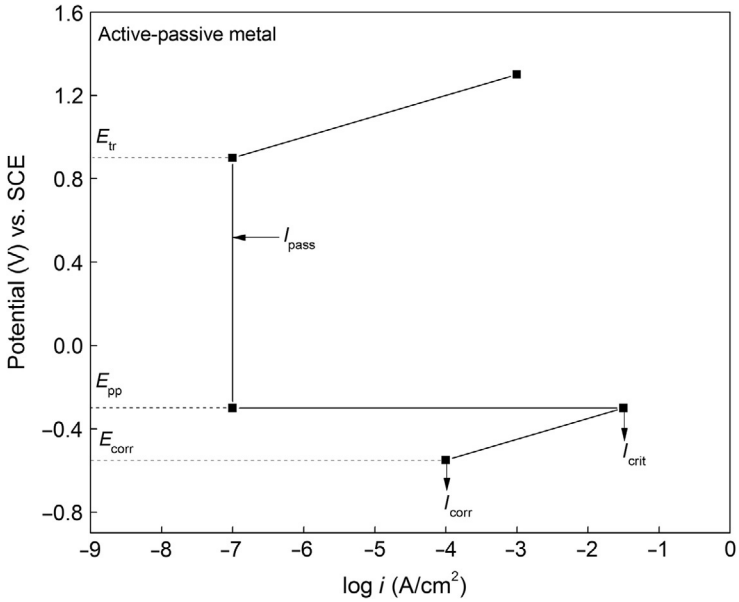

Fig. E4.3 Polarization curve for anodic dissolution for active-passive metal.

Table E4.2 Electrochemical Parameters of an Active-Passive Metal

E_{corr} (V vs. SCE)	I_{corr} (A/cm^2)	b_a (V/decade)	E_{pp} (V vs. SCE)	I_{pass} (A/cm^2)	E_{tr} (V vs. SCE)
-0.5	10^{-4}	0.05	-0.4	10^{-5}	1.0

the metal-ion species and the standard electrode potential of this reaction is -0.25 V vs. SCE.

(d) Assuming that the corrosive media is acidic, calculate the cathodic exchange current density if the cathodic reduction is hydrogen. Assume the pH of the solution is 2 and the cathodic Tafel slope is -0.12 V.

(e) Construct the Evans diagram using the electrochemical parameters of the active-passive metal.

Solution:

(a) The anodic curve of the metal follows the Tafel relation up to the passivation potential. Using the anodic Tafel equation, one can calculate the critical passivation current density

$$\eta_M = E_{pp} - E_{corr} = b_a \log\left(\frac{I_{crit}}{I_{corr}}\right)$$

$$\eta_M = -0.4 - (-0.5) = 0.05 \log\left(\frac{I_{crit}}{10^{-4}}\right)$$

$$I_{crit} = 10^{-2}\,A/cm^2$$

(b) The equilibrium potential is on the same Tafel line as in part a. Since the exchange current density is known, the equilibrium potential can be estimated using the relation:

$$\eta_M = E_{corr} - e_{eq,M} = b_a \log \frac{I_{corr}}{i^o_M}$$

$$\eta_M = -0.5 - e_{eq,M} = 0.05 \log \frac{10^{-4}}{10^{-9}}$$

$$e_{eq,M} = -0.75\,V\,vs.\,SCE$$

(c) The concentration at the equilibrium potential is estimated by using the Nernst relation.

$$e_{eq,M} = e^o_M + \frac{0.059}{1} \log (a_{M^{2+}})$$

$$-0.75 = -0.25 + \frac{0.059}{1} \log (a_{M^{2+}})$$

$$a_{Fe^{2+}} = 3.35 \times 10^{-9}\,M$$

(d) Since the pH of the solution is 2, one can calculate the equilibrium potential as

$$e_{eq,H_2} = -0.059\,pH = -0.059 \times 2 = -0.12\,V\,vs.\,SHE = -0.36\,V\,vs.\,SCE$$

Using the Tafel equation, the exchange current density for hydrogen evolution reaction can be calculated as:

$$E_{corr} - e_{eq,H} = b_c \log \frac{I_{corr}}{i^o_{H_2}}$$

$$-0.5 + 0.36 = -0.12 \log \frac{10^{-4}}{i^o_{H_2}}$$

$$i^o_{H_2} = 6.8 \times 10^{-6}\,A/cm^2$$

(e) The Evans diagram using the electrochemical parameters of the active-passive metal is shown in Fig. E4.4.

E4.5. Plot the polarization curve for anodic dissolution of the active passive metal that has the following electrochemical parameters given in Table E4.3:

(a) Calculate the critical current density to passivate the metal.

(b) Calculate the equilibrium potential of the anodic dissolution reaction if the exchange current density of the anodic reaction is 10^{-5} A/cm^2.

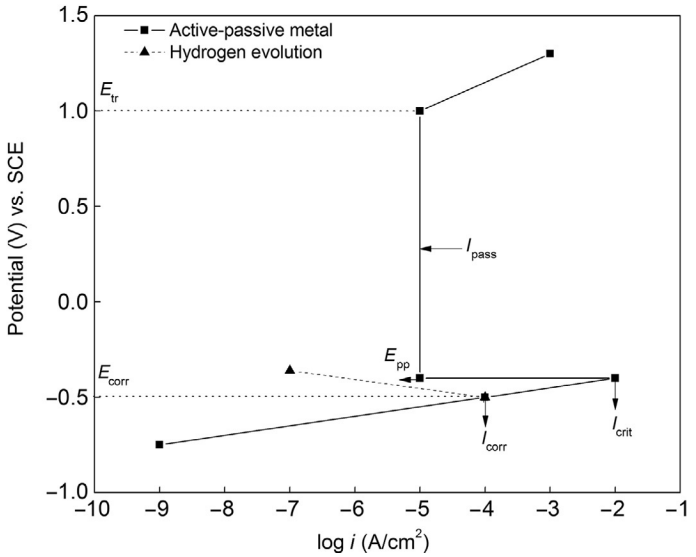

Fig. E4.4 Evans diagram for active-passive metal constructed using electrochemical parameters given in Table E4.2.

Table E4.3 Electrochemical Parameters of Anodic Dissolution of an Active-Passive Metal

E_{corr} (V vs. SCE)	I_{corr} (A/cm^2)	E_{pp} (V vs. SCE)	b_a (V/decade)	b_c (V/decade)	I_{pass} (A/cm^2)	E_{tr} (V vs. SCE)
−0.5	10^{-4}	−0.4	0.05	0.1	10^{-5}	1.05

(c) Assuming that the hydrogen evolution reaction is the only cathodic reaction in an acidic media with activity of H^+ and H_2 equal to 1.0, calculate the exchange current density for the hydrogen evolution reaction on the active-passive metal.

Solution:

The polarization curve was constructed (Fig. E4.5) using the electrochemical parameters values given in Table E4.3.

(a) Calculation of critical passivation current density

The Tafel equation applied to two points [log(I_{corr}), E_{corr}] and [log(I_{crit}), E_{pp}] is used to calculate the critical passivation current density:

$$E_{corr} - e_{eq,a} = a + b_a \times \log(I_{corr})$$

$$E_{pp} - e_{eq,a} = a + b_a \times \log(I_{crit})$$

By solving the equations:

$$I_{crit} = 10^{-2}\,\mathrm{A/cm^2}$$

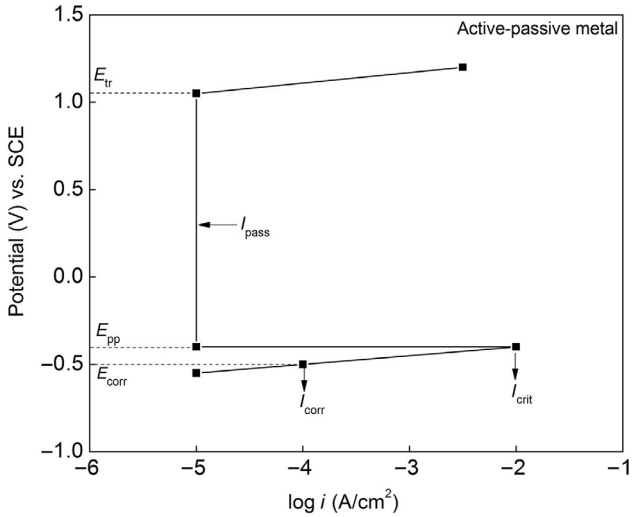

Fig. E4.5 Polarization curve constructed using the electrochemical parameters given in Table E4.3.

(b) Calculation of the equilibrium potential of the anodic dissolution reaction if the exchange current density of the anodic reaction is 10^{-5} A/cm^2,

$$\eta = E - e_{\mathrm{a}}^{\mathrm{o}}$$

$$\eta = a + b_{\mathrm{a}} \times \log(i)$$

$$\eta = b_{\mathrm{a}} \times \log\left(\frac{i}{i_{\mathrm{a}}^{\mathrm{o}}}\right)$$

At intersection point [log(I_{corr}), E_{corr}],

$$\eta = E_{\mathrm{corr}} - e_{\mathrm{eq,a}} = b_{\mathrm{a}} \times \log\left(\frac{I_{\mathrm{corr}}}{i_{\mathrm{a}}^{\mathrm{o}}}\right)$$

Solving the Tafel equation for $E_{\mathrm{corr}} = -0.5$ V vs. SCE and $I_{\mathrm{corr}} = 10^{-4}$ A/cm^2.

$$e_{\mathrm{eq,a}} = -0.55\,\mathrm{V\,vs.SCE}$$

(c) Hydrogen evolution was assumed to be the only cathodic reaction:

$$2\mathrm{H}^+ + 2\mathrm{e}^- \rightarrow \mathrm{H}_2$$

The equilibrium potential of the hydrogen evolution reaction is:

$$e_{\mathrm{eq,c}} = E_{\mathrm{H^+/H_2}} = e_{\mathrm{H^+|H_2}}^{\mathrm{o}} + \frac{RT}{2F} \ln[\mathrm{H}^+]^2$$

$$e_{\mathrm{eq,c}} = e^{\mathrm{o}}_{\mathrm{H^+|H_2}} = -0.24\,\mathrm{V\ vs.\ SCE}$$

The Tafel constant for the cathodic reaction is 0.10 V/decade

$$\eta_{\mathrm{c}} = E_{\mathrm{corr}} - e_{\mathrm{eq,c}} = b_{\mathrm{c}} \log\left(\frac{I_{\mathrm{corr}}}{i^{\mathrm{o}}_{\mathrm{c}}}\right) = -0.5 - (-0.24) = -0.1 \log\left(\frac{10^{-4}}{i^{\mathrm{o}}_{\mathrm{c}}}\right)$$

$$i^{\mathrm{o}}_{\mathrm{c}} = 2.5 \times 10^{-7}\,\mathrm{A/cm^2}$$

E4.6. Hypothetical active-passive alloys A and B have the following electrochemical parameters given in Table E4.4:

(a) Construct the polarization curves for both alloys and estimate their critical passivation current densities.

(b) Discuss the following:

1. Which alloy will be more easily protected by anodic protection?

2. Which will be more corrosion resistant in the reducing condition?

3. Which will be more corrosion resistant in the passive state?

4. Which will be more easily passivated by dissolved oxidizers?

Solution:

(a) The polarization curve was constructed (Fig. E4.6) using the electrochemical parameters values given in the table.

1. Because alloy B exhibits a voltage span of 0.9, 0.2 V larger than that of alloy A, alloy B will be more easily protected by anodic protection.

2. In the reducing or active region of the active-passive alloy, the alloy B will be more corrosion resistant due to its lower corrosion current.

3. In the passive state, alloy B will be more corrosion resistant due to its lower passivation current density.

4. Alloy A will be more easily passivated due to its lower critical passivation current density of $10^{-2}\,\mathrm{A/cm^2}$ and more negative passivation potential of 0.1 V vs. SCE when compared with critical passivation current density and passivation potential of alloy B of $10^{-1}\,\mathrm{A/cm^2}$ and 0.25 V vs. SCE, respectively.

Table E4.4 Electrochemical Parameters for Hypothetical Active-Passive Alloys A and B

	E_{corr} (V vs. SCE)	I_{corr} (A/cm^2)	b_{a} (V/decade)	E_{pp} (V vs. SCE)	I_{pass} (A/cm^2)	E_{tr} (V vs. SCE)
Alloy A	−0.5	1.0×10^{-7}	0.1	0.1	1×10^{-6}	+0.9
Alloy B	−2.3	7.0×10^{-8}	0.1	0.25	1×10^{-7}	+1.1

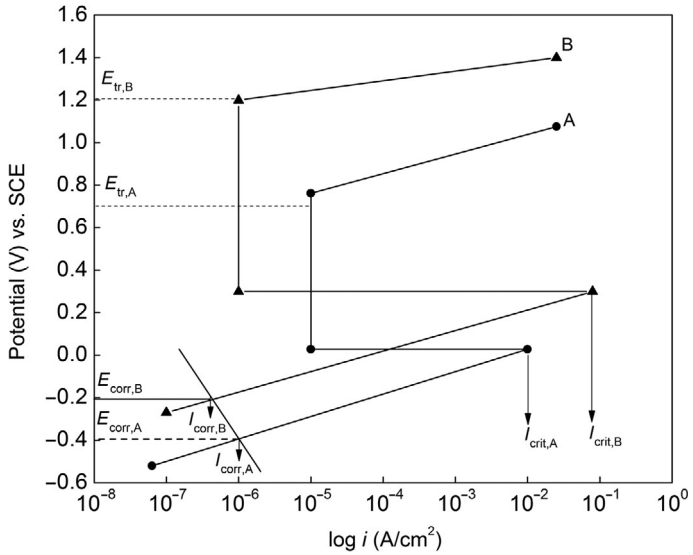

Fig. E4.6 Schematic of anodic polarization curves for hypothetical alloys A and B.

E4.7. Active-passive alloys A, B, and C have the following electrochemical parameters given in Table E4.5:

Calculate the critical current density and determine:

(a) Which alloy would be more easily protected by anodic protection?
(b) Which is more easily passivated in oxydizing electrolytes?
(c) Which will be the more corrosion resistant in the passive state?
(d) Which will be more corrosion resistant in the active state of the alloy in the presence of oxidizing solutions?

Solution:

Critical passivation current densities are calculated from the anodic polarization curve shown in Fig. E4.7. The passivation current density values calculated using mixed potenial theory are 89 A/cm^2, 9.4×10^{-3} A/cm^2, and 4.5×10^{-6} A/cm^2 for alloys A, B, and C, respectively.

Table E4.5 Electrochemical Parameters for Active-Passive Alloys A, B, and C

	i_{corr} (A/cm^2)	b_a (V/decade)	E_{pp} (V vs. SHE)	i_{pass} (A/cm^2)	E_{corr} (V vs. SHE)	E_{tr} (V vs. SHE)
Alloy A	2.8×10^{-4}	0.1	+0.1	3.8×10^{-5}	−0.43	1.00
Alloy B	4.4×10^{-5}	0.1	−0.1	5×10^{-6}	−0.35	0.85
Alloy C	4.5×10^{-6}	0.1	+0.14	1×10^{-6}	−0.24	0.90

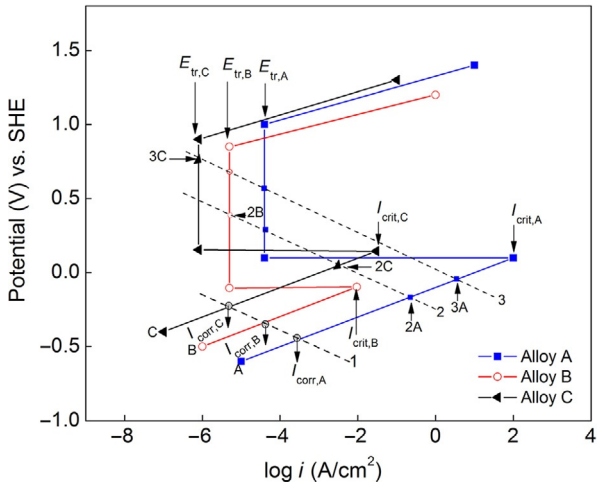

Fig. E4.7 Anodic polarization curves of hypothetical alloys.

Hypothetical alloys A, B, and C described in Fig. 4.17 are used to illustrate the alloy evaluation under reducing and oxidizing conditions. For reducing (or active state of the alloy) conditions (a), the alloy C is superior because of the lowest corrosion rates compared with the other two alloys in the active region.

For modestly oxidizing conditions (b), the alloy C is not recommended because the critical passivation current density is higher than the reduction curve 2. The intersection 2C indicates that this alloy is in a state of borderline passivity. Both, the active and passive states are possible. Alloy C is recommended in highly oxidizing conditions because the critical passivation current density doesn't exceed the reduction line 3. Also, this alloy has the lowest passivation current density. Alloy B is superior in modestly and highly oxidizing conditions because the reduction curves 2 and 3 exceed the critical passivation current density. Alloy A has very high critical current density for passivation and is very difficult to passivate. It is not recommended in modestly oxidizing conditions because the reduction line 2 is below the critical passivation current density. In strongly oxidizing conditions, this alloy is in a state of borderline passivity.

E4.8. An active-passive alloy corrodes in the active state in acidic solution in presence of the redox couple $Fe^{3+}|Fe^{2+}$. The corrosion potential and corrosion current are $E_{corr} = -0.35\,V$ vs. SHE and $I_{corr} = 10\,\mu A/cm^2$. If the reduction occurs under activation control with $b_c = -0.1\,V/decade$, $[Fe^{2+}]$ of 10^{-6} M, and exchange current density of the redox couple $i^o_{Fe^{3+}|Fe^{2+}} = 0.01\,\mu A/cm^2$, calculate the concentration of Fe^{3+} oxidizer necessary to passivate the alloy. Recalculate the oxidizer concentration for an exchange current density of 0.1 and 1 $\mu A/cm^2$ for the redox couple.

Solution:
The following cathodic reaction occurs in the redox system:

$$Fe^{3+} + e^{-} \rightleftharpoons Fe^{2+} \quad e^{o} = -0.44\,V$$

From the Tafel equation:

$$E_{corr} - E = b_c \log\left(\frac{I_{corr}}{i^{o}}\right)$$

For $E_{corr} = -0.35$ V, $I_{corr} = 10\ \mu A/cm^2$

$$E = -0.35 - (-0.1) \times \log\frac{10}{0.01} = -0.05\,V$$

$$E = e^{o} + \frac{RT}{F}\ln\frac{Fe^{3+}}{Fe^{2+}}$$

$$-0.05 = -0.44 + 0.059\log\frac{(Fe^{3+})}{10^{-6}}$$

$$\left(Fe^{3+}\right) = 4.08\ mol/l$$

The oxidizer concentration for an exchange current density of $0.1\ \mu A/cm^2$ for the redox couple:

$$E = -0.35 - (-0.1) \times \log\frac{10}{0.1} = -0.15\,V$$

$$E = e^{o} + \frac{RT}{F}\ln\frac{Fe^{3+}}{Fe^{2+}}$$

$$-0.15 = -0.44 + 0.059\log\frac{(Fe^{3+})}{10^{-6}}$$

$$\left(Fe^{3+}\right) = 0.082\ mol/l$$

The oxidizer concentration for an exchange current density of $1\ \mu A/cm^2$ for the redox couple:

$$E = -0.35 - (-0.1) \times \log\left(\frac{10}{1}\right) = -0.25\,V$$

$$E = e^{o} + \frac{RT}{F}\ln\frac{Fe^{3+}}{Fe^{2+}}$$

$$-0.25 = -0.44 + 0.059\log\frac{(Fe^{3+})}{10^{-6}}$$

$$\left(Fe^{3+}\right) = 0.0017\ mol/l$$

E4.9. Table E4.6 lists the parameters of the active-passive alloys A, B, C, and D. Calculate critical current densities of the active-passive alloys and determine:

(a) Which of the alloys will be more corrosion resistant in the reducing condition?

(b) Which will be more corrosion resistant in the passive state?

(c) Which will be more easily passivated by dissolved oxidizers?

(d) Which would be more easily protected by anodic protection?

Solution:

The polarization curve (Fig. E4.8) for alloys A, B, C, and D is constructed using the electrochemical parameters given in the table. Alloy D does not exhibit passivation. The polarization curve for this alloy is constructed using the Tafel equation by taking $e_{eq} = -0.2$ V vs. SCE.

$$I_a = I_{crit} = I_{corr} 10^{(\eta_a / b_a)}$$
$$\eta_a = E - E_{corr}$$
$$E = E_{pp}$$
$$I_a = I_{crit}$$

Table E4.6 Parameters of the Active-Passive Alloys A, B, C, and D

	E_{corr} (V vs. SCE)	I_{corr} (A/cm^2)	b_a (V/decade)	E_{pp} (V vs. SCE)	I_{pass} (A/cm^2)	E_{tr} (V vs. SCE)
Alloy A	−0.4	1.0×10^{-6}	0.1	0.0	1×10^{-5}	0.7
Alloy B	−0.2	7.0×10^{-7}	0.1	0.3	1×10^{-6}	1.2
Alloy C	−0.5	5.0×10^{-7}	0.1	−0.1	8×10^{-4}	0.3
Alloy D	−0.1	1×10^{-6}	0.06	-	-	-

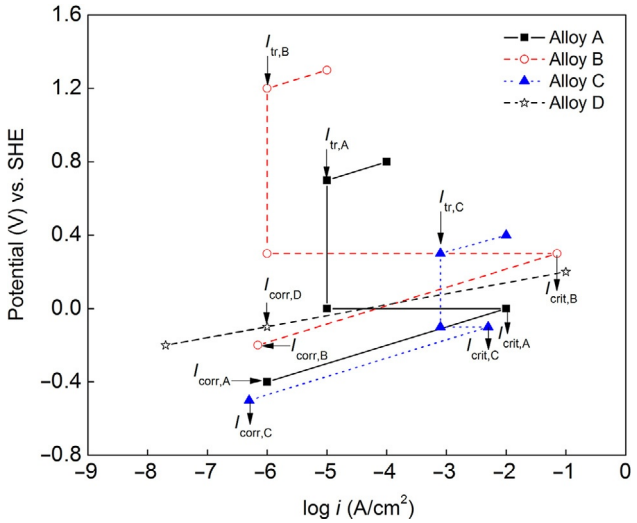

Fig. E4.8 Comparison of passive regions of different alloys.

Solving the Tafel equation:

$$I_{\text{crit, A}} = 1.0 \times 10^{-6} \times 10^{((0-(-0.4))/0.1)} = 1.0 \times 10^{-2}\,\text{A/cm}^2$$

$$I_{\text{crit, B}} = 7.0 \times 10^{-7} \times 10^{((0.3-(-0.2))/0.1)} = 7.0 \times 10^{-2}\,\text{A/cm}^2$$

$$I_{\text{crit, }C} = 5.0 \times 10^{-7} \times 10^{((-0.1-(-0.5))/0.1)} = 5.0 \times 10^{-3}\,\text{A/cm}^2$$

For alloy D,

$$E_{\text{corr}} - e_{\text{eq}} = b\log\left(\frac{I_{\text{corr}}}{i^{\text{o}}}\right)$$

$$-0.1 - (-0.2) = 0.06\log\left(\frac{10^{-6}}{i^{\text{o}}}\right)$$

$$i^{\text{o}} = 2.1 \times 10^{-8}\,\text{A/cm}^2$$

The results indicated that:

1. Alloy C would be more corrosion resistant under reducing conditions, because I_{corr} is the lowest for this alloy.
2. Alloy B would be more corrosion resistant in the passivation state because the passivity current (I_{pp}) is the lowest.
3. Alloy C would be easily passivated because the passivation potential (E_{pp}) and the critical current density are lower compared with other alloys.
4. Alloy B would be easily protected by anodic protection because the passive region extents from 0.3 to 1.2 V.
5. Alloy D cannot be protected by anodic protection because it doesn't have a passivation region.

E4.10. As a function of chromium content, Fe in Fe-Cr alloy has the following electrochemical properties shown in Table E4.7. The values of I_{corr} and b_a for pure iron are 5×10^{-5} A/cm^2 and 0.1 V/decade, respectively. Assume that b_a is constant for all alloy compositions.

Table E4.7 Electrochemical Properties of Fe in Fe-Cr Alloy as a Function of Chromium Content

Percentage of Cr in Fe-Cr Alloy	E_{corr} (V)	I_{crit} (A/cm^2)	I_{pass} (A/cm^2)	E_{tr} (V)
0%	−0.65	5×10^{-4}	1×10^{-5}	1.5
4%	−0.57	8×10^{-5}	1×10^{-6}	1.4
8%	−0.35	1×10^{-6}	1×10^{-8}	1.2

(a) Calculate the Flade potential for iron with no chromium as an alloying element.
(b) Calculate the corrosion current in the case of the alloys that contain 4% and the 8% Cr. The Flade potential of the corresponding alloys are −0.48 and −0.25 V, respectively.
(c) Plot the polarization curves.

Solution:

(a)

$$I_{crit} = i_a = I_{corr}\exp^{((\alpha_a nF/RT)\eta_a)} = I_{corr} \times 10^{((2.3\alpha_a nF/RT)\eta_a)}$$

$$I_{crit} = I_{corr} \times 10^{(\eta_a/b_a)}$$

$$\eta_a = E_F - E_{corr} = b_a \log\left(\frac{I_{crit}}{I_{corr}}\right)$$

$$E_F = E_{pp}$$

$$E_F = E_{corr} - b_a \log I_{corr} + b_a \log I_{crit}$$

(b) Because for 0% of Cr, the corrosion potential, E_{corr}, the corrosion current density, I_{corr}, and the critical current density, I_{crit}, are known, the Flade potential is calculated as:

$$E_F = -0.65 - 0.1\log\left(5 \times 10^{-5}\right) + 0.1\log\left(5 \times 10^{-4}\right)$$

$$E_F = -0.55\,\text{V vs.SCE}$$

In case of the 4% Cr alloy since the Flade potential is −0.48 V one can back calculate from the above expression the value of the corrosion current.

$$-0.48 = -0.57 - 0.1 \times \log I_{corr} + 0.1 \times \log\left(8 \times 10^{-5}\right)$$

$$I_{corr} = 10^{-5}\,\text{A/cm}^2$$

In the case of the 8% Cr alloy:

$$-0.25 = -0.35 - 0.1 \times \log I_{corr} + 0.1 \times \log\left(10^{-6}\right)$$

$$I_{corr} = 10^{-7}\,\text{A/cm}^2$$

(c) Based on the calculated values of the Flade potential, the corrosion current, corrosion potential, the slopes, the passivation currents, and the transpassive potentials, the passivation plots are constructed for each case as shown in Fig. E4.9.

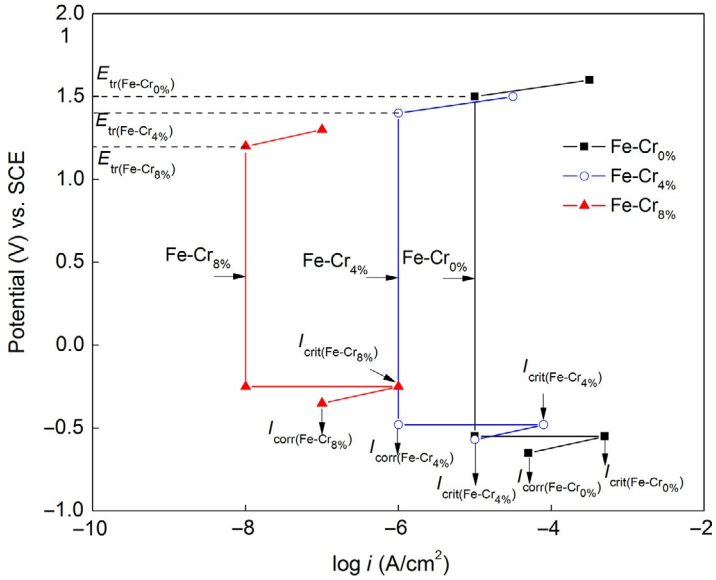

Fig. E4.9 Influence of Cr content on the passivity of Fe-Cr Alloys.

SOLUTIONS GUIDE

CHAPTER 5: BASICS OF CORROSION MEASUREMENTS

E5.1. For iron ($d = 7.8\ \text{g/cm}^3$) in a corrosive solution, the linear polarization slope at low current densities is 2 mV/(μA/cm^2). Assuming $b_a = b_c = \pm 0.1$ V/decade, calculate the corrosion current in mpy.

Solution:

$$\frac{\Delta E}{\Delta i} = \frac{b_a b_c}{I_{corr}(2.303)(b_a + b_c)}$$

$$I_{corr} = \frac{b_a b_c}{(2.303)(b_a + b_c)\dfrac{\Delta E}{\Delta i}}$$

$$I_{corr} = \frac{0.01\ \text{V}^2}{0.46\ \text{V}} \frac{1\ \mu\text{A/cm}^2}{2\ \text{mV}} \frac{1000\ \text{mV}}{1\ \text{V}} = 10.87\ \mu\text{A/cm}^2$$

$$\text{CR} = \frac{(0.131)(I_{corr})(\text{EW})}{d} = \frac{0.131 \times 10.87 \times 27.92}{7.8} = \text{CR(mpy)} = 5.09\ \text{mpy}$$

E5.2. Zinc ($d = 7.14\ \text{g/cm}^3$) corrosion rate in a deaerated solution of pH 1 is 2500 mpy. Calculate the corrosion potential of zinc vs. hydrogen reference electrode. The activity of the metal in the solution is 10^{-5} M. The value of the anodic (b_a) Tafel slope is 0.1 V/decade. The exchange current density for zinc is 10^{-5} A/cm^2.

Solution:

a) Anode: $Zn^{2+} + 2e^- \rightarrow Zn$ $e^o_{Zn^{2+}|Zn} = -0.762\ \text{V vs. SHE}$

$$e_{Zn^{2+}|Zn} = e^o_{Zn^{2+}|Zn} - \frac{0.0591}{n}\log\left(\frac{1}{[Zn^{2+}]}\right) = -0.762 - \frac{0.0591}{2}\log\left(\frac{1}{10^{-5}}\right)$$
$$= -0.910\ \text{V vs. SHE}$$

Calculation of corrosion current:

$$\text{CR(mpy)} = 2500 = \frac{0.131 \times I_{corr} \times (\text{EW})}{d} = \frac{0.131 \times I_{corr} \times (65.4/2)}{7.14}$$

$$\text{Solving for } I_{corr} \rightarrow I_{corr} = 4167\ \mu\text{A/cm}^2$$

http://dx.doi.org/10.1016/B978-0-444-62722-3.09965-1

Calculation of corrosion potential

$$E_{corr} - (-0.910) = 0.1 \log I_{corr} - 0.1 \log\left(10^{-5}\right)$$

$$E_{corr} = 0.1 \log I_{corr} - 0.1 \log\left(10^{-5}\right) - 0.910$$

$$E_{corr} = 0.1 \log\left(4167 \times 10^{-6}\right) - 0.1 \log\left(10^{-5}\right) - 0.910 = -0.648\,\text{V vs. SHE}$$

E5.3. For tin ($d = 7.3\ \text{g/cm}^3$) in a corrosive solution, the linear polarization, R_p, is $2\ \text{mV/}(\mu\text{A/cm}^2)$. Assuming $b_a = b_c = \pm 0.1$ V/decade, calculate the corrosion rate in mpy.

Solution:

$$I_{corr} = \frac{b_a b_c}{2.3(b_a + b_c)} \frac{1}{R_p};\quad R_p = \frac{\Delta E}{\Delta i}$$

$$I_{corr} = \frac{b_a b_c}{2.3(b_a + b_c)} \frac{\Delta i}{\Delta E} = \frac{0.01\,\text{V}^2}{2.3(0.1 + 0.1)\,\text{V}} \frac{1\,\mu\text{A/cm}^2}{2\,\text{mV}}$$

$$I_{corr} = \frac{0.01\,\text{V}^2}{0.46\,\text{V}} \frac{1\,\mu\text{A/cm}^2}{2\,\text{mV}} \frac{1000\,\text{mV}}{1\,\text{V}} = 10.87\,\mu\text{A/cm}^2$$

$$\text{CR} = \frac{0.131 \times I_{corr} \times \text{EW}}{d} = \frac{0.131[10.87\,\mu\text{A/cm}^2]\left[\frac{118.710\,\text{g/mol}}{2}\right]}{7.3\,\text{g/cm}^3}$$

$$= 11.57\,\text{mpy}$$

E5.4. By polarizing a corrosion redox system, a change in current of 8 mA was measured for a potential change of 2 mV. If the corrosion current is $1\ \text{A/m}^2$, estimate the electrochemically active area and the polarization conductance. (Assuming $b_a = b_c = \pm 0.1$ V/decade.)

Solution:

$$\frac{\Delta E}{\Delta i} = \frac{\Delta E}{\Delta I/A} = A\frac{\Delta E}{\Delta I} = A\frac{2}{8} = \frac{A}{4}$$

$$\text{Polarization conductance} = \frac{\Delta i}{\Delta E} = \frac{4}{A} = K_{corr}$$

$$I_{corr} = \frac{b_a b_c}{2.3(b_a + b_c)} \frac{\Delta i}{\Delta E} = \frac{0.01}{0.46} K_{corr}$$

$$1\,\text{A/m}^2 = \frac{0.01\,\text{V}^2 \times 4\,\text{A/V}}{A \times 0.46}$$

$$A = 0.087\,\text{m}^2$$

$$K_{corr} = 46.0\,\Omega^{-1}\text{m}^{-2}$$

E5.5. Assuming $b_a = b_c = \pm 0.1$ V/decade, $R_p = 4$ mV/(μA/cm^2), calculate the corrosion rate of zinc in a corrosive interface in gmd (grams per day).

Solution:

$$R_p = \frac{\Delta E}{\Delta i} = 4\frac{\text{mV}}{\mu\text{A/cm}^2}$$

$$I_{corr} = \frac{b_a b_c}{2.3(b_a + b_c)}\frac{\Delta i}{\Delta E}$$

$$I_{corr} = \frac{(0.01\text{V})^2}{0.46\text{V}}\frac{\mu\text{A/cm}^2}{4\text{mV}}\frac{1000\text{mV}}{1\text{V}}$$

$$I_{corr} = 5.435\mu\text{A/cm}^2$$

$$\frac{m}{t} = \frac{M \times \text{A} \times i_{corr}}{nF}$$

$$\text{CR} = \left[\frac{65.4\text{g/mol}}{2\text{eq/mol}}\right] \times \frac{1\text{eq}}{96,500\text{C}} \times \left[5.435\mu\text{A/cm}^2\right] \times 1\text{cm}^2 \times \frac{10^{-6}\text{C/s}}{1\mu\text{A}}$$

$$\text{CR} = 1.84 \times 10^{-9}\text{g/s} \times \frac{3600\text{s}}{1\text{h}} \times \frac{24\text{h}}{1\text{day}} = 1.59 \times 10^{-4}\text{g/day}$$

E5.6. Determine the corrosion potential, the corrosion current, and the corrosion rate in mpy for zinc ($d = 7.14$ g/cm^3) in a solution of pH = 1. The activity of the metal in the solution is 10^{-2} M. The values of both the cathodic and the anodic Tafel slopes are ±0.1 V/decade. The exchange current densities for the anodic and cathodic reactions are 10^{-5} and 10^{-7} A/cm^2, respectively.

Solution:

Calculation of the anode potential:

$$e_a = e^o_{Zn^{2+}|Zn} + \frac{0.0591}{2}\log\left(Zn^{2+}\right)$$

$$e_a = -0.76 + \frac{0.0591}{2}\log\left(10^{-2}\right)$$

$$e_a = -0.819\text{V}$$

Calculation of the cathode potential:

$$e_c = e^o_{H_2|H^+} + \frac{0.0591}{2}\log\left(a_{H^+}\right)^2$$

$$e_c = -0.059(\text{pH})$$

$$e_c = -0.059\text{V}$$

Solve simultaneously for E_{corr} and I_{corr}

$$\eta = b\log\left(\frac{i}{i^{o}}\right)$$

$$\eta_c = E_{corr} - e_c$$

$$\eta_a = E_{corr} - e_a$$

$$E_{corr} + 0.819 = 0.1\log\left(\frac{I_{corr}}{10^{-5}}\right)(\text{Anode})$$

$$E_{corr} + 0.059 = -0.1\log\left(\frac{I_{corr}}{10^{-7}}\right)(\text{Cathode})$$

$$E_{corr} = -0.539\,\text{V}$$

$$I_{corr} = 6309\,\mu\text{A/cm}^2$$

$$\text{CR} = \frac{0.131 I_{corr}\text{EW}}{d}$$

$$\text{CR} = \frac{0.131(6309\,\mu\text{A/cm}^2)\left(\frac{65.4\,\text{g/mol}}{2\,\text{eq/mol}}\right)}{7.14\,\text{g/cm}^3}$$

$$\text{CR} = 3785\,\text{mpy}$$

E5.7. Calculate the corrosion rate in gmd for zinc ($d = 7.14$ g/cm^3) in a solution of pH 3. The activity of the metal in the solution is 10^{-4} M. The values of the cathodic and the anodic Tafel slopes are -0.12 and 0.1 V/decade, respectively. The exchange current densities for hydrogen evolution on zinc and zinc dissolution are 10^{-7} and 10^{-4} A/cm^2, respectively.

Solution:

Calculation of anode potential:

$$e_a = e^{o}_{Zn^{2+}|Zn} + \frac{0.0591}{2}\log\left(Zn^{2+}\right)$$

$$e_a = -0.76 + \frac{0.0591}{2}\log\left(10^{-4}\right)$$

$$e_a = -0.878\,\text{V}$$

Calculation of cathode potential:

$$e_c = e_{H_2|H^+} + \frac{0.0591}{2}\log\left(a_{H^+}\right)^2$$

$$e_c = -0.059(\text{pH})$$

$$e_c = -0.177\,\text{V}$$

Solve for corrosion, current I_{corr}

$$\eta = b \times \log\left(\frac{i}{i^{o}}\right)$$

$$\eta_c = E_{corr} - e_c$$

$$\eta_a = E_{corr} - e_a$$

$$E_{corr} + 0.878 = 0.1 \log\left(\frac{I_{corr}}{10^{-4}}\right) (\text{Anode})$$

$$E_{corr} + 0.177 = -0.12 \log\left(\frac{I_{corr}}{10^{-7}}\right) (\text{Cathode})$$

$$I_{corr} = 3.55 \times 10^{-3}\,\text{A/cm}^2$$

$$\text{CR} = \frac{0.131 \times I_{corr} \times \text{EW}}{d} = \frac{0.131(3.55 \times 10^{-3}\,\text{A/cm}^2)\left(\frac{65.4\,\text{g/mol}}{2\,\text{eq/mol}}\right)}{7.14\,\text{g/cm}^3}$$

$$\text{CR} = 2128\,\text{mpy}$$

E5.8. Calculate the corrosion current and the corrosion rate if a tin ($d = 7.3$ g/cm^3, EW = 118.71 g/mol) sample with surface area of 100 cm^2 is exposed in a deaerated solution of pH 2 for 24 h loses 34 mg.

Solution:

$$I_{corr} = \frac{W \times F}{t(\text{EW})} = \frac{2 \times 34 \times 10^{-3} \times 96\,487}{118.71 \times 24 \times 3600 \times 100} = 6.4 \times 10^{-6}\,\text{A}$$

$$I_{corr} = 6.4\ \mu\text{A}$$

$$\text{CR} = \frac{0.13 \times 118.71 \times 6.4}{2 \times 7.3} = 6.76\,\text{mpy}$$

E5.9. Cadmium ($d = 8.65$ g/cm^3) activity in a deaerated corrosive solution with a pH of 4 is 10^{-1} M. The values of the cathodic and the anodic Tafel slopes are -0.12 and +0.1 V/decade, respectively. The cathodic intercept is $a_c = -1.4$ V. The exchange current density for cadmium, i^{o}, is 3×10^{-11} A/cm^2. Standard potential for hydrogen and cadmium are $e^{o}_{H^+|H_2} = 0$ V vs. SHE and $e^{o}_{Cd|Cd^{2+}} = 0.403$ V vs. SHE, respectively. Assume that all the cadmium surface acts as cathode. Calculate the hydrogen exchange current density, corrosion potential, and the corrosion rate in mm/year.

Solution:

Calculation of the cathode potential:

$$e_c = -0.059(\text{pH}) = -0.236\,\text{V}$$

Calculation of exchange current density for cathodic reaction using the Tafel equation:

$$\eta_c = b\log\left(\frac{I_{corr}}{i^o}\right)$$

$$\log i^o = \frac{-1.4}{-0.12} = 11.66$$

$$\eta_c = -1.4 - 0.12\log I_{corr}$$

Calculation of the anode potential:

$$e_a = -0.403 + \frac{0.059}{2}\log(0.1) = -0.432\text{V}$$

$$\begin{aligned}\eta_{a,Cd} &= -b_a\log i^o_{Cd} + b_a\log I_{corr}\\ &= -0.1\log(3\times10^{-11}) + 0.1\log I_{corr} = 1.05 + 0.1\log I_{corr}\end{aligned}$$

Solve simultaneously for E_{corr} and I_{corr}

$$\eta = b\log\left(\frac{i}{i^o}\right)$$

$$\eta_c = E_{corr} - e_c$$

$$\eta_a = E_{corr} - e_a$$

$$E_{corr,H_2} + 0.236 = -1.4 - 0.12\log I_{corr}$$

$$E_{corr,Cd} + 0.432 = 1.05 + 0.1\times\log I_{corr}$$

$$-e_c + e_a = -2.45 - 0.22\log I_{corr}$$

$$I_{corr} = 3.385\times10^{-11}\,\text{A/cm}^2$$

$$E_{corr} = -0.379\,\text{V vs. SHE}$$

The corrosion rate in mm/year can be calcuated from the estimated corrosion current (A/cm^2).

In terms of mpy, 1 mA/cm^2 = 3.28 M/nd mpy, where d is the density of cadmium. Thus converting mA/cm^2 to mm/year results in:

$$\text{CR} = \frac{(3.28)(I_{corr})(\text{EW})}{d} = \frac{3.28\times3.385\times10^{-8}\times(112.4/2)}{8.65} = 7.21\times10^{-7}\,\text{mm/year}$$

E5.10. Calculate the corrosion potential and corrosion rate of silver in grams per square meter per day (gmd). The concentration of silver in a 0.3 N H_2SO_4 is 10^{-26} M. The values of the cathodic and the anodic Tafel slopes are −0.09 and +0.12 V/decade, respectively. The exchange current density for silver and hydrogen are $i^o_{Ag} = 5 \times 10^{-6}\,A/cm^2$ and $i^o_{H_2} = 5 \times 10^{-7}\,A/cm^2$, respectively. Standard potential for hydrogen and silver are 0 V vs. SHE and 0.799 V vs. SHE, respectively. Assume that all the silver surface acts as cathode.

Solution:
Calculation of equilibrium potentials:

$$E_{H^+|H_2} = 0.0 - \frac{0.0591}{2}\log\frac{(1)}{(0.3)^2} = -0.031\,V \text{ vs. SHE}$$

$$E_{Ag^+|Ag} = 0.799 + 0.059\log\left(10^{-26}\right) = -0.7376\,V$$

Calculation of corrosion potential and corrosion current using the Tafel equation:

$$\eta = b\log I_{corr} - b\log i^o$$

$$\eta_c = 0.09\log\left(5 \times 10^{-7}\right) - 0.09\log I_{corr} = E_{corr} - E_{H^+|H_2}$$

$$\eta_a = -0.12\log\left(5 \times 10^{-6}\right) + 0.12\log I_{corr} = E_{corr} - E_{Ag^+|Ag}$$

$$E_{corr} = -0.385\,\text{vs. SHE}$$

$$I_{corr} = 4.32 \times 10^{-3}\,A/cm^2$$

$$\frac{m}{t} = \frac{MI_{corr}}{nF}$$

$$CR = \left[\frac{107.9\,g/mol}{1\,eq/mol}\right]\left[\frac{1\,eq}{96{,}500\,C}\right]\left[\frac{4.32 \times 10^{-3}\,A}{cm^2}\right]\left(1\,cm^2\right)\frac{1\,C/s}{1\,A}$$

$$CR = 4.83 \times 10^{-6}\,g/s \times \frac{3600\,s}{1\,h} \times 24\,h/day$$

$$CR = 0.417\,g/day$$

E5.11. Calculate the corrosion current (A/cm^2) and corrosion rate (mm/year) of Sn dissolution if the potential of the tin ($7.3\,g/cm^3$) anode undergoing corrosion

is −0.08 V vs. SHE in 0.5 M $SnSO_4$. The standard electrode potential, e^{o}_{Sn}, is −0.13 V vs. SHE. The anodic Tafel constant is 0.1 V/decade and exchange current density, $i^{o} = 10^{-8}$ mA/cm^2.

Solution:

$$\eta_a = b_a \log\left(\frac{i}{i^{o}}\right) = e - e^{o} = -0.08 - (-0.13) = 0.05\,\text{V}$$

$$\eta_a = 0.05 = 0.1 \log\left(\frac{I_{corr}}{10^{-8}}\right)$$

$$I_{corr} = 3.16 \times 10^{-5}\,\mu\text{A/cm}^2$$

$$\text{CR} = \frac{0.131 \times I_{corr} \times \text{EW}}{d}$$

$$\text{CR} = \frac{0.131 \times (3.16 \times 10^{-5})\left(\frac{118.71}{2}\right)}{7.30}$$

$$\text{CR} = 3.37 \times 10^{-5}\,\text{mpy}$$

Since 1 mpy = 0.0254 mm/year

$$\text{CR} = 8.56 \times 10^{-7}\,\text{mm/year}$$

E5.12. For an overpotential of 0.2 V, calculate the corrosion rate of zinc ($d = 7.14$ g/cm^3) in mmpy if the exchange current density is 5×10^{-3} A/m^2. (The anodic Tafel constant is 0.045 V/decade.)

Solution:

Corrosion Current

$$\eta_a = b_a \times \log\left(\frac{i}{i^{o}}\right)$$

$$0.2 = 0.045 \log\left(\frac{I_{corr}}{5 \times 10^{-3}}\right)$$

$$I_{corr} = 1.39 \times 10^{2}\,\text{A/cm}^2$$

$$I_{corr} = 1.39 \times 10^{8}\,\mu\text{A/cm}^2$$

Corrosion Rate (CR)

$$\text{CR} = \frac{0.131 \times I_{corr} \times \text{EW}}{d}$$

$$\text{CR} = \frac{0.131 \times (1.39 \times 10^{8}) \times \frac{65.4}{2}}{7.14}$$

$$\mathrm{CR} = 8.35 \times 10^7\,\mathrm{mpy}$$

Since 1 mpy = 0.0254 mm/year,

$$\mathrm{CR} = 211.8 \times 10^6\,\mathrm{mm/year}$$

E5.13. If the slope of the polarization curve for Ni is 2 mV/(μA/cm^2), assuming $b_a = b_c = \pm 0.1$ V/decade, calculate the corrosion rate in grams per second (g/s).

Solution:

$$R_p = \frac{\Delta E}{\Delta i} = 2\frac{\mathrm{mV}}{\mu\mathrm{A/cm^2}}$$

$$I_{corr} = \frac{b_a b_c}{2.3(b_a + b_c)}\frac{\Delta i}{\Delta E}$$

$$I_{corr} = \frac{0.01\,\mathrm{V}^2}{0.46\,\mathrm{V}} \times \frac{\mu\mathrm{A/cm^2}}{2\mathrm{mV}} \times \frac{1000\mathrm{mV}}{1\mathrm{V}}$$

$$I_{corr} = 10.87\,\mu\mathrm{A/cm^2}$$

$$\frac{m}{t} = \frac{MI_{corr}}{nF}A$$

$$\mathrm{CR} = \left[\frac{58.6934\,\mathrm{g/mol}}{2\,\mathrm{eq/mol}}\right] \times \left[10.87\,\mu\mathrm{A/cm^2}\right] \times \frac{1\,\mathrm{eq}}{96{,}500\,C} \times 1\,\mathrm{cm^2} \times \frac{1\,\mathrm{C/s}}{10^6\,\mu\mathrm{A}}$$
$$= 3.3 \times 10^{-9}\,\mathrm{g/s}$$

SOLUTIONS GUIDE

CHAPTER 6: GALVANIC CORROSION

E6.1. Predict the possibility of galvanic corrosion in sea water for the following coupled pairs of alloys and metals: (i) aluminum alloys and aluminum brass, (ii) cadmium and manganese bronze, (iii) zinc and tin, (iv) low alloy steel and stainless steel 410, (v) low alloy steel and stainless steel 430, (vi) nickel 200 and Ni-Cr-Mo-Cu-Si alloy G, (vii) nickel cast iron and nickel 200, (viii) manganese bronze and silver bronze alloys, (ix) graphite and Ni-Cr-Mo alloy C, and (x) zinc and lead.

Solution:

With reference to Fig. 6.1, the galvanic corrosion of the given pairs of alloys and metals can be predicted. The results are summarized in Table E6.1.

E6.2. Predict whether or not galvanic corrosion will cause the following alloys to be subjected to leaching: (i) carbon and carbon steel alloys in an oxidizing atmosphere, (ii) steel rivets in aluminum drain gutters, (iii) copper-nickel alloy in refinery condenser tubes, (iii) graphite fiber-reinforced aluminum composites, (iv) brass in water, (v) iron-chromium alloys, and (vi) carbon steel pipe in contact with the weld to stainless steel pipe.

Solution:

Figure 6.1 can be used to predict the galvanic corrosion behavior of the given alloys subjected to leaching.

(i) Carbon will leach due to decarburization.
(ii) Aluminum may corrode galvanically near the steel rivets. Al is anodic when coupled to steel.
(iii) Nickel may corrode galvanically in copper nickel alloys. Ni is anodic when coupled to copper.
(iv) Zinc may corrode in brass exposed to water.
(v) Chromium from iron chromium alloy forms a protective film on the surface.
(vi) Carbon steel is strongly anodic to stainless steel, therefore galvanic corrosion of carbon steel is likely to occur.

E6.3. Estimate the effect of 1% impurity of platinum on the corrosion rate of zinc in acidic and alkaline solutions. Use the values of Tafel constants for the hydrogen evolution on the respective metals from Table E6.2.

http://dx.doi.org/10.1016/B978-0-444-62722-3.09964-X

Table E6.1 Prediction of Galvanic Corrosion of Various Paired Alloys and Metals

	Will Corrode	Will Be Protected
(i)	Aluminum alloys	Aluminum brass
(ii)	Cadmium	Manganese bronze
(iii)	Zinc	Tin
(iv)	Low carbon steel	Stainless steel 410
(v)	Low alloy steel	Stainless steel 430
(vi)	Nickel 200	Ni-Cr-Mo-Cu-Si Alloy G
(vii)	Nickel cast iron	Nickel 200
(viii)	Manganese bronze	Silver bronze alloys
(ix)	Ni-Cr-Mo alloy C	Graphite
(x)	Zinc	Lead

Table E6.2 Tafel Constants for the Hydrogen Evolution on the Respective Metals

Metal	Zn Acidic Solution	Pt Acidic Solution	Zn Alkaline Solution	Pt Alkaline Solution
Tafel constant, *a*	−1.24	−0.10	−1.20	−0.31
Tafel constant, *b*	−0.12	−0.12	−0.12	−0.12

Solution:

Corrosion rate calculations in acidic solution:

Based on the data given, the hydrogen overpotentials in Tafel equation for zinc and platinum in acidic solution are:

$$\eta_{H_2}^{Zn} = -1.24 - 0.12\log[i_{Zn}]$$

$$\eta_{H_2}^{Pt} = -0.10 - 0.12\log[i_{Pt}]$$

Assuming equipotential electrode surface due to a small surface area of platinum, one can equate the hydrogen overpotentials for zinc and platinum given by the Tafel equation:

$$-1.24 - 0.12\log[i_{Zn}] = -0.10 - 0.12\log[i_{Pt}] \Rightarrow i_{Pt} = 10^{9.5} i_{Zn}$$

Thus, the total corrosion rate of 1% platinum impurity in zinc is:

$$I_{corr} = 0.99 i_{Zn} + 0.01 i_{Pt} = 3.16 \times 10^{7} i_{Zn}$$

By adding 1% of platinum to pure zinc, the zinc corrosion rate drastically increases from the corrosion rate for pure zinc (2×10^{-10} A/cm^2). This is mainly due to the large hydrogen evolution exchange current densities on Pt (10^{-3} A/cm^2).

Corrosion rate calculations in alkaline solution:
Tafel equations for zinc and platinum are:

$$\eta_H^{Zn} = -1.20 - 0.12\log[i_{Zn}]$$
$$\eta_H^{Pt} = -0.31 - 0.12\log[i_{Pt}]$$

or

$$-1.20 - 0.12\log[i_{Zn}] = -0.31 - 0.12\log[i_{Pt}] \Rightarrow i_{Pt} = 10^{7.4} i_{Zn}$$

Calculated corrosion current of zinc with 1% platinum impurity in alkaline solution is:

$$I_{corr} = 0.99 I_{Zn} + 0.01 I_{Pt} = 2.61 \times 10^5 i_{Zn}$$

E6.4. Assuming that the surface of the alloy is equipotential under corroding conditions, by what factors do the corrosion rates of the following alloys increase/decrease in comparison with the pure iron (100% Fe) in acidic medium? Use the values of Tafel constants for the hydrogen evolution on the respective metals from Table E6.3.
Alloy A: (25% Fe, 25% Zn, 25% Ag, 25% Pb)
Alloy B: (50% Fe, 25% Zn, 12.5% Ag, 12.5% Pb)
Alloy C: (5% Fe, 25% Zn, 30% Ag, 40% Pb)

Solution:
Since the surface of the metal is equipotential, the hydrogen reduction on the metal has the same overpotential. Thus, the Tafel equations for the cathodic reaction for each of the metals in the alloy are:

$$\eta_{H_2,Fe} = -0.7 - 0.12\log(i_{H_2,Fe})$$
$$\eta_{H_2,Zn} = -1.24 - 0.12\log(i_{H_2,Zn})$$
$$\eta_{H_2,Ag} = -0.95 - 0.12\log(i_{H_2,Ag})$$
$$\eta_{H_2,Pb} = -1.56 - 0.12\log(i_{H_2,Pb})$$

Equating the corresponding Tafel equations:

$$-0.7 - 0.12\log(i_{H_2,Fe}) = -1.24 - 0.12\log(i_{H_2,Zn}) \Rightarrow i_{H_2,Zn} = 10^{-4.5} i_{H_2,Fe}$$
$$-0.7 - 0.12\log(i_{H_2,Fe}) = -0.95 - 0.12\log(i_{H_2,Ag}) \Rightarrow i_{H_2,Ag} = 10^{-2.1} i_{H_2,Fe}$$

Table E6.3 Tafel Constants for Each of the Metals in the Alloy

Metal	Fe	Zn	Ag	Pb
Tafel constant, *a*	−0.7	−1.24	−0.95	−1.56
Tafel constant, *b*	−0.12	−0.12	−0.12	−0.12

$$-0.7-0.12\log\left(i_{H_2,Fe}\right)=-1.56-0.12\log\left(i_{H_2,Pb}\right)\Rightarrow i_{H_2,Pb}=10^{-7.2}i_{H_2,Fe}$$

The corrosion rates for each alloy estimated using the $i_{Fe}^{metal(Zn,Ag,Pb)}$ ratio are:

$$\begin{aligned}i_{alloy\,A}&=0.25i_{H_2,Fe}+0.25\times10^{-4.5}i_{H_2,Fe}+0.25\times10^{-2.1}i_{H_2,Fe}\\&\quad+0.25\times10^{-7.2}i_{H_2,Fe}=0.252i_{H_2,Fe}\end{aligned}$$

$$\begin{aligned}i_{alloy\,B}&=0.5i_{H_2,Fe}+0.25\times10^{-4.5}i_{H_2,Fe}+0.125\times10^{-2.1}i_{H_2,Fe}\\&\quad+0.125\times10^{-7.2}i_{H_2,Fe}=0.50i_{H_2,Fe}\end{aligned}$$

$$\begin{aligned}i_{alloy\,C}&=0.05i_{H_2,Fe}+0.25\times10^{-4.5}i_{H_2,Fe}+0.3\times10^{-2.1}i_{H_2,Fe}\\&\quad+0.4\times10^{-7.2}i_{H_2,Fe}=0.0525i_{H_2,Fe}\end{aligned}$$

E6.5. Sn and Pt are immersed in an acidic solution with unit hydrogen ion activity. Using the electrochemical parameters listed below, calculate the galvanic corrosion rate.

(a) When 1 cm^2 Sn is coupled to 1 cm^2 of Pt in acidic solution.

(b) When 10 cm^2 Pt is coupled to 1 cm^2 of Sn in the same solution.

The Tafel slope for tin dissolution is $b_a=0.1$ V/decade. The cathodic Tafel slope for hydrogen evolution reaction on both Sn and Pt is $b_c=-0.1$/decade. Exchange current density for hydrogen evolution on Sn, $i_{H_2,Sn}^{o}=1\times10^{-8}\,A/cm^2$ and on Pt, $i_{H_2,Pt}^{o}=1\times10^{-3}\,A/cm^2$. The concentration of dissolved species of $[Sn^{2+}]=10^{-12}$ M. Exchange current density for Sn dissolution is $i_{Sn}^{o}=1\times10^{-6}\,A/cm^2$. Tin equilibrium potential is -0.138 V vs. SHE. Assume that platinum dissolution is negligible.

Solution:

(a) Calculation of galvanic corrosion rate and galvanic potential when 1 cm^2 Sn is coupled to 1 cm^2 of Pt in acidic solution:

Cathode polarization curve

$$\text{Standard cathode potential}: e_c^o=0.0\,V\text{ vs. SHE}$$

To calculate the galvanic current using mixed potential theory, it is necessary to determine the sum of the hydrogen evolution exchange current densities on platinum and tin:

$$i_c^o=i_{Pt}^o+i_{Sn}^o$$

$$i_c^o=\left(10^{-8}\,A/cm^2+10^{-3}\,A/cm^2\right)\times1\,cm^2=10^{-3}\,A$$

Solving the cathodic Tafel equation:

$$E_{corr,\underline{Sn}-Pt(1\,cm^2)}-e_c^o=-0.1\log\left(\frac{I_{corr,\underline{Sn}-Pt(1\,cm^2)}}{i_{couple}^o}\right)$$

$$E_{\text{corr},\underline{\text{Sn}}-\text{Pt}(1\ \text{cm}^2)} = -0.1\log\left(I_{\text{corr},\underline{\text{Sn}}-\text{Pt}(1\ \text{cm}^2)}\right) + 0.1\log\left(10^{-3}\right) \quad \text{(E6.1)}$$

Anodic polarization curve:

$$\text{Sn}^{2+} + 2e^- \rightleftharpoons Sn, \text{e}^{o}_{Sn^{2+}/Sn} = -0.138\ V$$

Calculation of equilibrium potential for tin electrode:

$$e_{\text{eq,a}} = e^{\text{o}}_{\text{Sn}^{2+}|\text{Sn}} + \frac{0.059}{2}\log\left[\text{Sn}^{2+}\right] = -0.138 + \frac{0.059}{2}\times\log\left(10^{-12}\right)$$
$$= -0.492\text{V vs. SHE}$$

Assuming that only tin is dissolving (platinum dissolution in acidic solution is negligible), the anodic Tafel equation is:

$$E_{\text{corr},\underline{\text{Sn}}-\text{Pt}(1\ \text{cm}^2)} - e_{\text{eq,a}} = 0.1\log\left(I_{\text{corr},\underline{\text{Sn}}-\text{Pt}(1\ \text{cm}^2)}/i^{\text{o}}_{\text{a}}\right)$$

$$E_{\text{corr},\underline{\text{Sn}}-\text{Pt}(1\ \text{cm}^2)} - (-0.492) = 0.1\log\left(I_{\text{corr},\underline{\text{Sn}}-\text{Pt}(1\ \text{cm}^2)}\right) - 0.1\log\left(10^{-6}\right) \quad \text{(E6.2)}$$

Applying mixed potential theory, the corrosion current and corrosion potential when 1 cm^2 Sn is coupled to 1 cm^2 of Pt in an acidic solution are calculated by solving Eqs. (E6.1) and (E6.2).

$$E_{\text{corr},\underline{\text{Sn}}-\text{Pt}(1\ \text{cm}^2)} = -0.096\text{V vs. SHE}$$

$$I_{\text{corr},\underline{\text{Sn}}-\text{Pt}(1\ \text{cm}^2)} = 9.12\text{mA}$$

(b) Calculation of galvanic corrosion rate and galvanic potential when 1 cm^2 Sn is coupled to 10 cm^2 of Pt in an acidic solution.

Cathode polarization curve:

$$\text{Standard cathode potential}: e^{\text{o}}_{\text{c}} = 0.0\text{V vs. SHE}$$

Sum of the hydrogen evolution exchange current densities:

$$i^{\text{o}}_{\text{c}} = i^{\text{o}}_{\text{Sn}} \times 1\,\text{cm}^2 + i^{\text{o}}_{\text{Pt}} \times 10\,\text{cm}^2$$

$$i^{\text{o}}_{\text{c}} = 10^{-8}\,\text{A/cm}^2 \times 1\,\text{cm}^2 + 10^{-3}\,\text{A/cm}^2 \times 10\,\text{cm}^2 = 10^{-2}\,\text{A}$$

Cathode Tafel equation:

$$E_{\text{corr},\underline{\text{Sn}}-\text{Pt}(10\ \text{cm}^2)} - e^{\text{o}}_{\text{c}} = -0.1\log\left(\frac{I_{\text{corr},\underline{\text{Sn}}-\text{Pt}(10\ \text{cm}^2)}}{i^{\text{o}}_{\text{c}}}\right) \quad \text{(E6.3)}$$

Anode polarization curve:

$$\text{Equilibrium anode potential}: e_{\text{eq,a}} = -0.492\text{V}$$

Exchange current density for Sn dissolution : $i_a^o = 10^{-6}\,\text{A}$

Anode Tafel equation:

$$E_{\text{corr},\underline{\text{Sn}}-\text{Pt}(10\,\text{cm}^2)} - e_{\text{eq,a}} = 0.1\log\left(\frac{I_{\text{corr},\underline{\text{Sn}}-\text{Pt}(10\text{cm}^2)}}{i_a^o}\right)$$

$$E_{\text{corr},\underline{\text{Sn}}-\text{Pt}(10\,\text{cm}^2)} - (-0.492) = 0.1\log\left(I_{\text{corr},\underline{\text{Sn}}-\text{Pt}(10\,\text{cm}^2)}\right) - 0.1\log\left(10^{-6}\right) \quad \text{(E6.4)}$$

Solving Eqs. (E6.3) and (E6.4), the galvanic corrosion current and galvanic potential are calculated when 1 cm^2 Sn is coupled to 10 cm^2 of Pt in acidic solution.

$$E_{\text{corr},\underline{\text{Sn}}-\text{Pt}(10\,\text{cm}^2)} = -0.046\ \text{V vs. SHE}$$

$$I_{\text{corr},\underline{\text{Sn}}-\text{Pt}(10\,\text{cm}^2)} = 28.84\,\text{mA}$$

E6.6. Sn and Pt are immersed in an acidic solution with unit hydrogen ion activity. Using the electrochemical parameters listed below, construct the Evans diagram and evaluate the effect of the cathode-sacrificial anode electrode surface area ratio on galvanic corrosion of a tin-platinum galvanic couple (see Case Study 6.1).

(a) Determine the corrosion potential $E_{\text{corr,Sn}}$ and corrosion rate for tin when tin is not coupled $I_{\text{corr,Sn}}$.

(b) Estimate the corrosion potential $E_{\text{corr},\underline{\text{Sn}}-\text{Pt}(1\,\text{cm}^2)}$ and the galvanic corrosion rate $I_{\text{corr},\underline{\text{Sn}}-\text{Pt}(1\,\text{cm}^2)}$ when 1 cm^2 of Sn is coupled with 1 cm^2 of platinum in the same solution.

(c) Estimate the corrosion potential $E_{\text{corr},\underline{\text{Sn}}-\text{Pt}(10\,\text{cm}^2)}$ and the galvanic corrosion rate $I_{\text{corr},\underline{\text{Sn}}-\text{Pt}(10\,\text{cm}^2)}$ when 1 cm^2 of Sn is coupled with 10 cm^2 of platinum in the same solution.

(d) Estimate the hydrogen evolution current density $i_{\text{H}_2,\underline{\text{Sn}}-\text{Pt}(1\,\text{cm}^2)}$ on tin when 1 cm^2 of Sn is coupled with 1 cm^2 of platinum in the same solution.

(e) Estimate the hydrogen evolution current density $i_{\text{H}_2,\underline{\text{Sn}}-\text{Pt}(10\,\text{cm}^2)}$ on tin when 1 cm^2 of Sn is coupled with 10 cm^2 of platinum in the same solution.

The Tafel slope for tin dissolution is $b_a = 0.1$ V/decade. The Tafel slopes for hydrogen evolution reaction on both tin and platinum is $b_c = -0.1$/decade. Exchange current density for hydrogen evolution on Sn, $i_{\text{H}_2,\text{Sn}}^o = 1\times10^{-8}\,\text{A/cm}^2$ and on Pt, $i_{\text{H}_2,\text{Pt}}^o = 1\times10^{-3}\,\text{A/cm}^2$. The concentration of dissolved species of $[\text{Sn}^{2+}] = 10^{-12}$ M. Exchange current density for Sn dissolution is $i_{\text{Sn}}^o = 1\times10^{-6}\,\text{A/cm}^2$. Platinum dissolution is negligible. Sn equilibrium potential is -0.138 vs. SHE and that of hydrogen, e^o, is 0.00 vs. SHE. Assume that platinum dissolution is negligible.

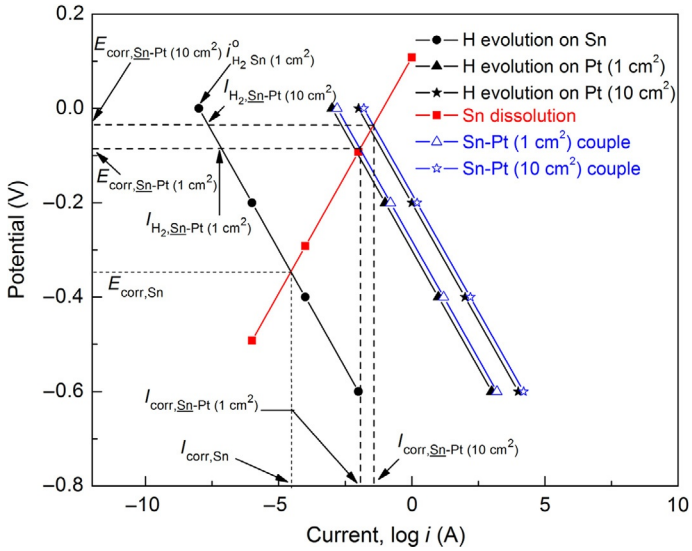

Fig. E6.1 Evans diagram for the effect of the cathode-sacrificial anode surface area on galvanic corrosion of a tin-platinum galvanic couple.

Solution:

From the given parameters, the Evans diagram for the Sn-Pt couple has been constructed and the electrochemical parameters are labeled in Fig. E6.1. The rate of hydrogen evolution current on the tin surface increases when it is coupled to a piece of inert platinum. The observed increase of the tin corrosion rate shown in Fig. E6.1 results from the difference of the exchange current densities of the coupled metals. The intersection of the tin dissolution polarization curve and the polarization curve corresponding to hydrogen evolution on tin results in a tin corrosion rate equal to $I_{corr,Sn}$. When an equal surface area of tin (1 cm^2) and platinum (1 cm^2) are coupled, the sum of the rates of the hydrogen evolution reaction on each metal is equal to the total rate of the hydrogen evolution reaction. Because the hydrogen ion exchange current density is very low (10^{-8} A/cm^2) on Sn, and very high on platinum (10^{-3} A/cm^2), the total rate of the hydrogen evolution reaction will be approximately equal to the rate of hydrogen evolution on the platinum surface. The polarization curves of hydrogen evolution of coupled Sn with 1 and 10 cm^2 of Pt^2 are labeled in Fig. E6.1 as a Sn-Pt (1 cm^2) couple and a Sn-Pt (10 cm^2) couple, respectively. The figure clearly illustrates that coupling of 1 cm^2 tin to 1 cm^2 platinum shifts the corrosion potential of Sn from $E_{corr,Sn}$ to $E_{corr,\underline{Sn}-Pt(1\ cm^2)}$ (the corrosion potential of the couple), resulting in an increase of the corrosion rate of Sn from $I_{corr,Sn}$ to $I_{corr,\underline{Sn}-Pt(1\ cm^2)}$. Hydrogen evolution on tin when tin is coupled with 1 cm^2 of

platinum is estimated at the intersection of the hydrogen polarization line on tin $i^{o}_{H_2,Sn(1\ cm^2)}$ with the line of corrosion potential of the couple $E_{corr,\underline{Sn}-Pt(1\ cm^2)}$. The rate of the hydrogen evolution reaction on Sn when coupled with 1 cm^2 platinum decreases from $I_{H_2,Sn}$ to $I_{H_2,\underline{Sn}-Pt(1\ cm^2)}$.

When platinum with a surface area of 10 cm^2 is coupled with 1 cm^2 of tin, the magnitude of the hydrogen current increases results in an increase in the Sn corrosion rate to $I_{corr,\underline{Sn}-Pt(10\ cm^2)}$. The rate of hydrogen evolution on Sn, as shown in the figure, decreases to $I_{H_2,\underline{Sn}-Pt(10\ cm^2)}$. Hydrogen evolution on tin, when tin is coupled with 10 cm^2 of platinum, is estimated at the intersection of the hydrogen polarization line on tin $i^{o}_{H_2,Sn(1\ cm^2)}$ with the line of corrosion potential of the couple $E_{corr,Sn-Pt(10\ cm^2)}$.

E6.7. Tin and gold are immersed in acidic solution with unit hydrogen ion activity. Using the electrochemical parameters listed below, calculate the galvanic corrosion rate when 1 cm^2 of Sn is coupled to 1 cm^2 of Au in acidic solution. Compare the results with those obtained in problem E6.6 when 1 cm^2 Sn is galvanically coupled with 1 cm^2 Pt. For Sn, the anodic Tafel constant, b_a, is 0.1 V/decade. The cathodic slopes for hydrogen evolution reaction on both Sn and Au is $b_c = -0.1$/decade. Hydrogen evolution current density on Sn is 1×10^{-8} A/cm^2 and on Au 1×10^{-6} A/cm^2. The concentration of dissolved species of $[Sn^{2+}] = 10^{-12}$ M. Exchange current density for Sn dissolution is 1×10^{-6} A/cm^2. Sn equilibrium potential is $e^{o}_{Sn^{2+}|Sn} = -0.138$V vs. SHE. The hydrogen reversible potential on tin is 0.00 vs. SHE. Assume that gold dissolution is negligible.

Solution:

Cathode polarization curve

$$\text{Standard cathode potential}: e^{o}_{c} = 0.0\ \text{V vs. SHE}$$

Sum of the hydrogen evolution exchange current densities:

$$i^{o}_{c} = i^{o}_{Sn} + i^{o}_{Au}$$

$$i^{o}_{c} = 10^{-8}\text{A/cm}^2 \times 1 + 10^{-6}\text{A/cm}^2 \times 1 = 1.01 \times 10^{-6}\text{A/cm}^2$$

$$E_{corr} - e^{o}_{c} = -0.1 \log\left(\frac{I_{corr}}{i^{o}_{c}}\right)$$

Cathode Tafel equation:

$$E_{corr} = -0.1 \log(I_{corr}) + 0.1 \log\left(1.01 \times 10^{-6}\right) \tag{E6.5}$$

Anode polarization curve

Equilibrium anode potential:

$$Sn^{2+} + 2e^{-} \rightleftharpoons Sn \quad e^{o}_{Sn^{2+}|Sn} = -0.138\text{V}$$

$$E_{a,eq} = e^{o}_{Sn^{2+}|Sn} + \frac{0.059}{2}\log\left[Sn^{2+}\right]$$
$$= -0.138 + \frac{0.059}{2} \times \log\left(10^{-12}\right) = -0.492\,V,$$

Exchange current density for Sn dissolution: $i^{o}_{a} = 10^{-6}\,A/cm^2$

Anode Tafel equation:

$$E_{corr} - E_{a,eq} = 0.1\log\left(\frac{I_{corr}}{i^{o}_{a}}\right)$$

$$E_{corr} - (-0.492) = 0.1\log(I_{corr}) - 0.1\log\left(10^{-6}\right) \quad \text{(E6.6)}$$

Solving Eqs. (E6.5) and (E6.6), one can calculate galvanic corrosion current and galvanic potential for 1 cm^2 Sn when it is coupled to 10 cm^2 of Au in an acidic solution.

$$E_{corr} = -0.246\ V \text{ vs. SHE}$$

$$I_{corr} = 0.29\,mA/cm^2$$

The corrosion current, I_{corr}, and corrosion potential, E_{corr}, when 1 cm^2 Sn is coupled to 1 cm^2 of Pt in an acidic solution estimated in Problem E6.6 are:

$$E_{corr} = -0.096\,V \text{ vs. SHE}$$

$$I_{corr} = 9.12\,mA/cm^2$$

The reversible potential of Au/Au^{+3} in the emf series is +1.498 V vs. SHE and is more positive than that of Pt/Pt^{+2} (+1.2 V vs. SHE). One can expect, considering the gold reversible potential that tin in the tin-gold galvanic couple should exhibit, more severe corrosion when compared to the tin-platinum galvanic couple. However, the corrosion rate of the Sn-Au couple, as calculated in this problem, is approximately 30 times smaller when compared to the Sn-Pt couple. Higher hydrogen exchange current density of Pt contributes to the severe galvanic effect when compared to gold; besides, gold has more positive reversible potential in the emf series.

E6.8. Equal 1 cm^2 areas of nickel and iron are immersed in 1 M acidic solution. Using the electrochemical parameters listed below:

(a) Calculate the corrosion potential and the corrosion rate for each metal, when they are uncoupled.

(b) Determine the potential and current passing in the galvanic couple when nickel and iron are electrically coupled.

(c) Determine the corrosion rates for nickel and iron when they are galvanically coupled.

The standard equilibrium dissolution potentials for nickel and iron are −0.25 and −0.44 V vs. SHE, respectively. The exchange current density for nickel

dissolution is 1×10^{-7} A/cm^2 and that for Fe is 1×10^{-6} A/cm^2. The concentrations of dissolved species of $[Ni^{2+}]$ is 4.13×10^{-4} M and that of $[Fe^{2+}]$ is 1 M. The exchange current densities for the hydrogen evolution reaction on nickel is 4×10^{-6} A/cm^2 and that on iron is 1×10^{-6} A/cm^2. Assume Tafel constants of ± 0.1 V/decade for the anodic and cathodic reactions.

Solution:

(a) Corrosion potential and corrosion rate for each metal, when they are uncoupled

$$\text{Standard cathode potential}: e_c^o = 0.0\,\text{V vs. SHE}$$

$$\text{Equilibrium anode potentials}: e_{eq,a(Ni)} = e_{Ni}^o + \frac{0.059}{2}\log\left(4.13 \times 10^{-4}\right) = -0.35\,\text{V vs. SHE}$$

$$e_{eq,a(Fe)} = e_{Fe}^o + \frac{0.059}{2}\log(1) = -0.44\,\text{V}$$

Nickel polarization curves

Anodic:

$$E_{corr,Ni} - (-0.35) = 0.1\log\left(\frac{I_{corr,Ni}}{10^{-7}}\right) \tag{E6.7}$$

Cathodic:

$$E_{corr,Ni} - 0 = -0.1\log\left(\frac{I_{corr,Ni}}{4 \times 10^{-6}}\right) \tag{E6.8}$$

Solving Eqs. (E6.7) and (E6.8), the corrosion potential and corrosion current for Ni are:

$$E_{corr,Ni} = -0.095\,\text{V}$$

$$I_{corr,Ni} = 3.55 \times 10^{-5}\,\text{A/cm}^2$$

Iron polarization curves

Anodic:

$$E_{corr,Fe} - (-0.44) = 0.1\log\left(\frac{I_{corr,Fe}}{10^{-6}}\right) \tag{E6.9}$$

Cathodic:

$$E_{corr,Fe} - 0 = -0.1\log\left(\frac{I_{corr,Fe}}{10^{-6}}\right) \tag{E6.10}$$

Solving Eqs. (E6.9) and (E6.10), the corrosion potential and corrosion current for Fe are:

$$E_{\text{corr,Fe}} = -0.22\text{V}$$

$$I_{\text{corr,Fe}} = 1.58 \times 10^{-4}\,\text{A/cm}^2$$

(b) Corrosion potential and galvanic current passing through the iron-nickel galvanic couple

Cathodic polarization curve for the couple

The hydrogen evolution exchange current density on the cathode is the sum of hydrogen evolution on nickel and iron.

$$i^{o}_{\text{c,couple}} = 4 \times 10^{-6} + 1 \times 10^{-6} = 5 \times 10^{-6}\,\text{A/cm}^2$$

Or

$$E_{\text{corr,couple}} - 0 = -0.1\log\left(\frac{I_{\text{corr,couple}}}{i^{o}_{\text{c,couple}}}\right)$$

$$E_{\text{corr,couple}} - 0 = -0.1\log\left(I_{\text{corr,couple}}\right) + 0.1\log\left(5 \times 10^{-6}\right) \tag{E6.11}$$

Calculation of the anodic polarization curve for the couple:

One can consider that the equilibrium potential for nickel $e_{\text{eq,Ni}} = -0.35$ V vs. SHE represents a point on the Fe-Ni couple anodic polarization line. To estimate the total anodic current of the couple at this potential, it is necessary to calculate the iron anodic current contribution at this point. Thus, by applying an overvoltage, $\eta = -0.35 - (-0.44)$ to Eq. (E6.9), one can calculate the iron contribution to the overall current density of the couple:

$$\eta = -0.35 - (-0.44) = 0.1\log\left(\frac{i_{\text{Fe}}}{10^{-6}}\right) \rightarrow i_{\text{Fe}} = 7.94 \times 10^{-6}\,\text{A/cm}^2$$

The total anodic current is the sum of the nickel exchange current density and the iron anodic current estimated at −0.35 V.

$$i_{\text{A}} = i^{o}_{\text{Ni}} + i_{\text{Fe}} = 10^{-7} + 7.94 \times 10^{-6} = 8.04 \times 10^{-6}\,\text{A/cm}^2$$

Therefore,

$$E_{\text{corr,couple}} - E_{\text{A}} = 0.1\log\left(\frac{I_{\text{corr,couple}}}{i_{\text{A}}}\right)$$

$$E_{\text{corr,couple}} - (-0.35) = 0.1\log\left(I_{\text{corr,couple}}\right) - 0.1\log\left(8.04 \times 10^{-6}\right) \tag{E6.12}$$

Solving Eqs. (E6.11) and (E6.12), one calculates the galvanic corrosion potential and galvanic current for Ni-Fe couple:

$$E_{\text{corr, couple}} = -0.185\,\text{V vs. SHE}$$

$$I_{\text{corr, couple}} = 3.57 \times 10^{-4}\,\text{A/cm}^2$$

(c) Individual corrosion rates for nickel and iron when they are galvanically coupled.

The corrosion rates for nickel ($I_{\text{corr, }\underline{\text{Ni}}-\text{Fe}}$) and iron ($I_{\text{corr, Ni}-\underline{\text{Fe}}}$) after galvanic coupling are calculated by substituting the corrosion potential of the iron-nickel galvanic couple $E_{\text{corr,couple}} = -0.185\,\text{V}$ vs. SHE in Eqs. (E6.7) and (E6.9), respectively.

$$(-0.185) - (-0.35) = 0.1 \log\left(\frac{I_{\text{corr, }\underline{\text{Ni}}-\text{Fe}}}{10^{-7}}\right)$$

$$I_{\text{corr, }\underline{\text{Ni}}-\text{Fe}} = 4.43 \times 10^{-6}\,\text{A/cm}^2$$

$$(-0.185) - (-0.44) = 0.1 \log\left(\frac{I_{\text{corr, Ni}-\underline{\text{Fe}}}}{10^{-6}}\right)$$

$$I_{\text{corr, Ni}-\underline{\text{Fe}}} = 3.52 \times 10^{-4}\,\text{A/cm}^2$$

E6.9. Construct the Evans diagram for a nickel and iron galvanic couple immersed in 1 M acidic solution. Using the electrochemical parameters listed in Exercise E6.8, estimate graphically the following parameters and tabulate the results:

(a) The corrosion potential and the corrosion rate for each metal, when they are uncoupled.

(b) The corrosion potential, $E_{\text{corr,Ni-Fe}}$, and the current passivating the galvanic couple, $I_{\text{corr,Ni-Fe}}$.

(c) The individual corrosion rates for nickel, $I_{\text{corr, }\underline{\text{Ni}}-\text{Fe}}$, and iron, $I_{\text{corr, Ni}-\underline{\text{Fe}}}$, when they are galvanically coupled.

Solution:

The Evans diagram was plotted, the values for (a), (b), and (c) are shown in Fig. E6.2, and the results are summarized in Table E6.4.

Table E6.4 Graphically Obtained Values of E_{corr} and I_{corr} for the Ni-Fe Galvanic Couple

Metal/Couple	E_{corr} (V)	I_{corr} (A/cm^2)
Ni	−0.095	3.55×10^{-5}
Fe	−0.22	1.58×10^{-4}
Ni-Fe couple	−0.185	3.57×10^{-4}
Ni-$\underline{Fe}$	−0.185	3.52×10^{-4}
$\underline{Ni}$*-Fe*	−0.185	4.43×10^{-6}

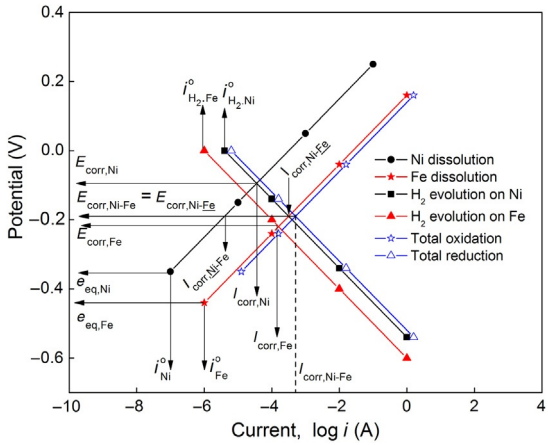

Fig. E6.2 Evans diagram for the galvanic couple between iron and nickel.

SOLUTIONS GUIDE

CHAPTER 7: PITTING AND CREVICE CORROSION

E7.1. The radius, r, of a growing hemispherical pit increases linearly with the time, t, while the true current density, I_{pit}, for metal dissolution in the pit remains constant with time. Derive the following relationship between the anodic current, I'_{pit}, and pit growth rate,

$$I'_{pit} = 2\pi r^2 (nF/V_{Me}) \frac{dr}{dt}$$

where V_{Me} is the atomic volume of the metal (1.4137×10^{-29} m^3 for Fe). The growth rate of the pit is equal to the rate of the volume change of the pit divided by the atomic volume of the metal $= (dV/dt) \times (1/V_{Me})$ [105].

Solution:

From Faraday's law, the rate of corrosion is given as:

$$\text{Rate of corrosion} = \text{I} \times \frac{\text{At.wt.}}{nF} = I'_{pit} \times \frac{\text{At.wt.}}{nF} \tag{E7.1}$$

The current is equal to I'_{pit}, while the area is equal to the inner surface area of the hemisphere $2\pi r^2$. During pitting corrosion the volume growth as a function of time is given by:

$$\frac{dV}{dt} = \frac{d\left(\frac{2}{3}\pi r^3\right)}{dt} = 2\pi r^2 \frac{dr}{dt} \tag{E7.2}$$

The number of iron ions dissolved is given by their total volume divided by the ionic volume. Thus, the iron dissolution rate is defined as:

$$\text{Rate of corrosion} = \left(\frac{\text{dissolution rate}}{v_{Me}}\right) = \frac{2\pi r^2}{v_{Me}} \frac{dr}{dt} \tag{E7.3}$$

where v_{Me} is the volume of the metal ion. The molar metal atomic volume is defined as:

$$V_{Me} = \text{At.wt.} v_{Me} \tag{E7.4}$$

Eqs. (E7.1) through (E7.4) the relationship between anodic pit current and the growth rate of the pit:

$$I'_{pit} = 2\pi r^2 (nF/V_{Me}) \frac{dr}{dt} \tag{E7.5}$$

http://dx.doi.org/10.1016/B978-0-444-62722-3.09963-8

E7.2. If the true current density, I_{pit}, is constant with time, estimate from the dependence of the apparent pitting current for steel on time (shown in Table E7.1) how rapidly the pit grows.

Solution:

It is known that,

$$I'_{pit} = I_{pit} \times \text{area} \tag{E7.6}$$

Since I_{pit} is constant, the rate of increase of I'_{pit} is essentially the rate of growth of the pit. A plot of pitting current vs. time is shown in Fig. E7.1.

Table E7.1 The Dependence of Apparent Pitting Current for Steel

Time (min)	Apparent Pitting Current for Steel (μA)
0	0.000
3	0.001
5	0.0025
7	0.02
9	0.01
11	0.05
13	0.110
15	0.240

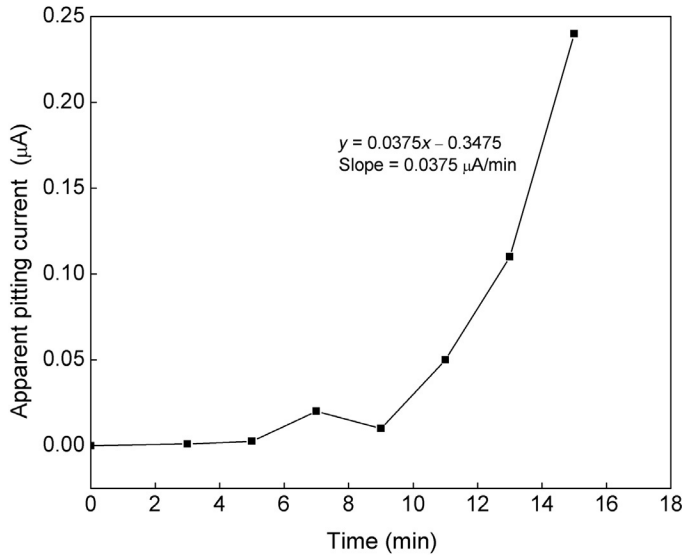

Fig. E7.1 Apparent pitting current of steel vs. time.

The rate of growth of the pit is given by the slope of the region of steep rise (from 9 to 15 min) in Fig. E7.1. The slope of steep rise region (11-15 min) is 0.0375 μA/min.

E7.3. A pit in an alloy exposed to a chloride solution grows to a depth of 0.25 cm in one month. Assuming an alloy density of 7.2 g/cm^3, calculate the current density, i_{pit}, at the interior of the pit. I_{pit} for metal dissolution remains constant with time. The alloy's molecular weight is 56 g/mol.

Solution:

The I_{pit} for the metal dissolution, when the pit remains constant with time, is calculated using Faraday's law and given values of depth of the pit, time, and the alloy density.

$$I_{pit} = \frac{\frac{0.25 \times 1 \times 7.2}{56} \times 96,487 \times 2}{30 \times 24 \times 3600} = 2.39 \times 10^{-3}\ \text{A/cm}^2$$

E7.4. If the radius of an iron atom is 1.5 Å and the thickness of iron corroding for five minutes is 15 Å, calculate the steady state passive current density for iron in 0.5 M HCl. The pitting current, I_{pit}, for the metal dissolution in the pit remains constant with time.

Solution:

The thickness of iron corroding in 5 min is:

$$h = 15\ \text{Å} = \frac{\frac{I_{pass} \times 5 \times 60}{96,485} \times 56}{2 \times 7.8}$$

$$I_{pass} = \frac{15\ \text{Å} \times 2 \times 7.8}{\frac{5 \times 60}{96,485} \times 56} = 1.34 \times 10^{-5}\ \text{A/cm}^2$$

E7.5. Corrosion of passive metals occurs by pitting in chloride solutions. This pitting can be prevented by the addition of anionic inhibitors. At a critical ratio of adsorbed chloride ions to adsorbed anion, the passive film is displaced by chlorides, allowing a pit to initiate.

(a) Derive an equation relating the minimum amount of anion necessary to inhibit pitting of a passive metal in chloride solutions to the activity of chloride ions.

Hint: Assume the amount of ion adsorbed per unit area follows the Freundlich adsorption isotherm [86].

(b) A set of experimental data relating the critical activity of nitrate anions inhibiting pitting of 18-8 stainless steel in $FeCl_3$ solutions and chloride activity is given in Table E7.2. Check if these experimental data fit the equation derived in (a) [86].

Table E7.2 Critical Activity of Nitrate Anions for the Inhibition of Pitting in 18-8 Stainless Steel

Activity of Nitrate Anions (M)	Activity of Chloride Ions (M)
0.049	0.069
0.103	0.265
0.16	0.62
0.27	1.23

(c) Relate the critical ratio of adsorbed chloride ions to adsorbed anion to the Freundlich adsorption isotherm constants.

Solution:

(a) The Freundlich adsorption isotherm for the adsorbed ions is given by

$$a_1 = k_1(\mathrm{Cl}^-)^{\frac{1}{n_1}} \tag{E7.7}$$

$$a_2 = k_2(\text{anion})^{\frac{1}{n_2}} \tag{E7.8}$$

where 'a_i' is the amount of ion adsorbed on the metal surface, and k_i and n_i are the Freundlich adsorption isotherm constants. At a specific ratio $a_1/a_2 = C$, the passive film breaks down locally. At lower ratios i.e. when more inhibitor is adsorbed, the passivity remains intact. Dividing the two equations we have;

$$\frac{a_1}{a_2} = \frac{k_1(\mathrm{Cl}^-)^{\frac{1}{n_1}}}{k_2(\text{anion})^{\frac{1}{n_2}}} \tag{E7.9}$$

Taking logarithm on both sides and simplifying we have,

$$\log(\mathrm{Cl}^-) = \frac{n_1}{n_2}\log(\text{anion}) + n_1 \log\left(\frac{Ck_2}{k_1}\right) \tag{E7.10a}$$

or

$$\log(\mathrm{Cl}^-) = k\log(\text{anion}) + \text{const} \tag{E7.10b}$$

where

$$k = \frac{n_1}{n_2} \tag{E7.10c}$$

and

$$\text{const} = \log\left(\frac{Ck_2}{k_1}\right)^{n_1} \tag{E7.10d}$$

(b) A plot of log(anion) vs. log(Cl^-) shown in Fig. E7.2 yields a straight line indicating that the experimental data fit the derived equations.

(c) In Eq. (E7.10d), the constant "a" is defined as:

$$\text{const} = \log\left(\frac{Ck_2}{k_1}\right)^{n_1}$$

$$\left(\frac{Ck_2}{k_1}\right)^{n_1} = 10^{\text{const}} \tag{E7.11a}$$

$$C = \left[10^{\text{const}}\left(\frac{k_2}{k_1}\right)^{-n_1}\right]^{\frac{1}{n_1}} \tag{E7.11b}$$

According to Eq. (E7.10d), the constant C is the intercept in Fig. E7.2. Thus, the ratio of the adsorbed ions could be estimated if the Freundlich adsorption isotherm constants are known.

E7.6. A set of experimental data relating critical activity of hydroxide anions inhibiting pitting of 18-8 stainless steel in $FeCl_3$ solutions and chloride activity is listed in Table E7.3 [13].

(a) Plot a graph of $\log(a_{OH^-})$ vs. $\log(a_{Cl^-})$ and determine the linearity. Estimate the slope and intercept value.

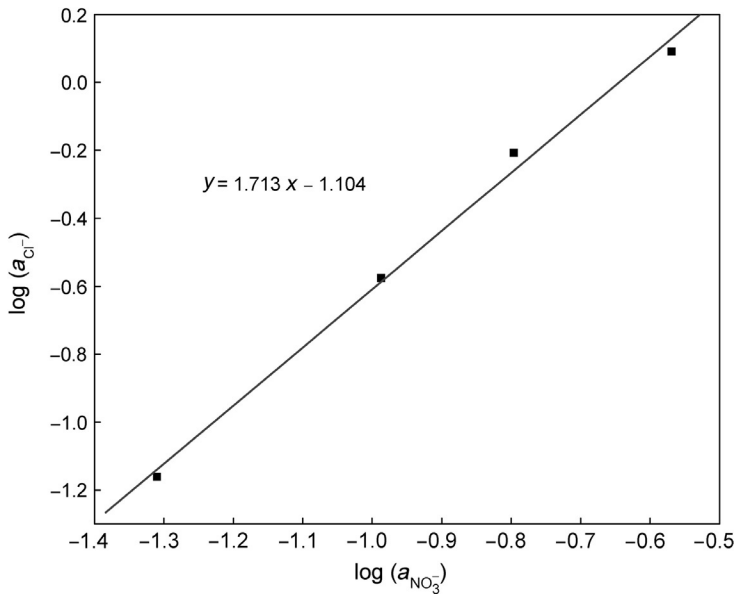

Fig. E7.2 Plot of log(anion) vs. log(Cl^-).

Table E7.3 Critical Activity of Hydroxide Anions for the Inhibition of Pitting in 18-8 Stainless Steel

Activity of Hydroxide Anions (M)	Activity of Chloride Ions (M)
0.033	0.26
0.1	1.55
0.2	5.12
0.32	9.89

(b) Calculate the critical concentration of the anion needed to suppress pitting when the activity of chloride ions is 0.15 M.

Solution:

(a) The plot in Fig. E7.3 is linear in agreement with Eq. (E7.10b). The slope and the intercept values are 1.6174 and 1.8135, respectively.

(b) From the plot, we can find the following relation between the concentration of chloride and hydroxide ions.

$$\log a_{Cl^-} = 1.6174 \log \left(a_{OH^-}\right)_{crit} + 1.8135$$

When $a_{Cl-} = 0.15$ M,

$$log\,(0.15) = 1.6174 \log \left(a_{OH^-}\right)_{crit} + 1.8135$$

The critical anion concentration to stop the pitting is:

$$a_{OH^-} = 0.0234\,\text{M}$$

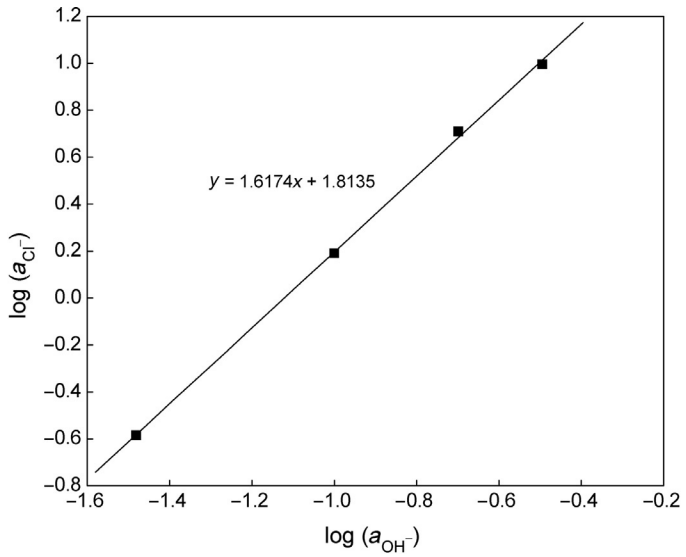

Fig. E7.3 Correlation between $\log(a_{Cl^-})$ vs. $\log(a_{OH^-})$.

E7.7. A set of experimental data relating critical activity of sulfate anions inhibiting pitting of 18-8 stainless steel in $FeCl_3$ solutions and chloride activity is given in Table E7.4.

(a) Plot $\log\left(a_{SO_4^{2-}}\right)$ vs. $\log\left(a_{Cl^-}\right)$ and check the linearity. Calculate the slope and intercept values.

(b) Estimate the activity of Cl^- ions when the minimum amount of the anion to suppress pitting is 0.2 M

Solution:

(a) A plot of $\log\left(a_{SO_4^{2-}}\right)$ vs. $\log\left(a_{Cl^-}\right)$ shown in Fig. E7.4 is linear. The slope and the intercept are calculated and given in the figure.

(b) From Fig. E7.4:

$$\log\left(a_{Cl^-}\right) = 0.848 \log\left(a_{SO_4^{2-}}\right)_{crit} - 0.0601$$

Table E7.4 Critical Activity of Sulfate Anions for the Inhibition of Pitting in 18-8 Stainless Steel

Activity of Sulfate Anions (M)	Activity of Chloride Ions (M)
0.031	0.046
0.1	0.12
0.16	0.19
0.31	0.32

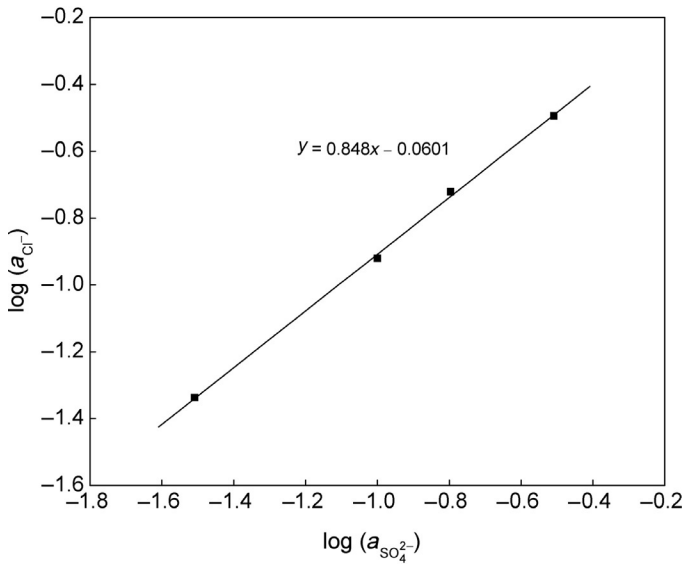

Fig. E7.4 Plot of $\log\left(a_{SO_4^{2-}}\right)$ vs. $\log\left(a_{Cl^-}\right)$.

For $\left(a_{SO_4^{2-}}\right) = 0.2$ M,

$$\log\left(a_{Cl^-}\right) = 0.848\log(0.2)_{crit} - 0.0601$$

Therefore,

$$a_{Cl^-} = 0.222\,\text{M}$$

E7.8. Electrokinetic parameters of an active-passive alloy are given in Table E7.5 and the anodic polarization curve of the active-passive alloy in the presence of chloride ions is shown in Fig. E7.5 (Figure 7.23 in Chapter 7). Pitting corrosion initiation occurs at 0.045 V vs. SHE.

Using the data given in Table E7.5 and Fig. E7.5,

(a) Determine the range of $[H^+]$ where the alloy is passive. The cathodic reaction is hydrogen evolution with the following kinetics parameters:

$$i_c^o = 5 \times 10^{-5}\,[H^+];\quad b_c = -0.05$$

(b) Estimate the pH at critical pitting potential of 0.045 V at which the alloy cannot be passivated.

Table E7.5 Electrokinetic Parameters of an Active-Passive Alloy

$I_{corr,a}$ (A/cm^2)	b_a (V/decade)	$E_{corr,a}$ (V)	E_{pp} (V)	I_{pp} (A/cm^2)	E_{tr} (V)
1×10^{-5}	0.1	−0.5	−0.3	1×10^{-6}	0.3

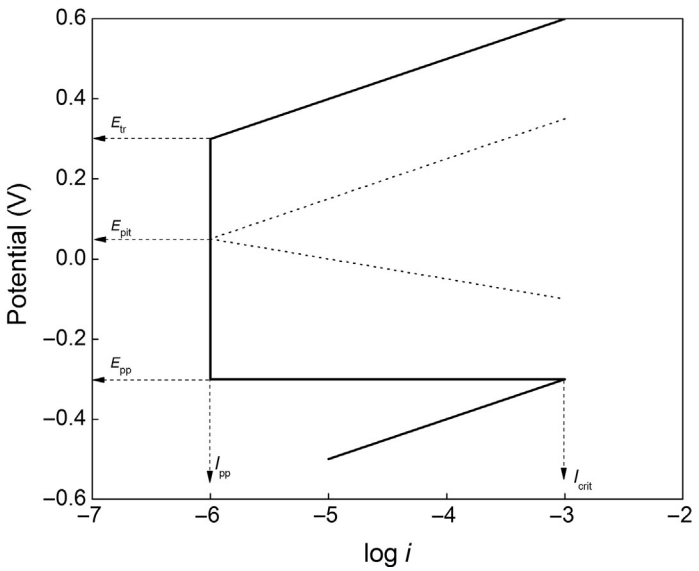

Fig. E7.5 Polarization curve of active-passive alloy in the presence of chloride ions.

Solution:

$$E - E_{eq} = b\log\frac{i}{i^o}$$

$$E + 0.059\,\text{pH} = -0.05\log i + 0.05\log\left(5\times10^{-5}\right) + 0.05\log\left(H^+\right)$$

$$0.109\,\text{pH} = -0.05\log i - 0.2151 - E$$

Minimum hydrogen ion concentration, $[H^+]$, that initiates alloy passivation is at I_{crit} and E_{pp}:

$$0.109\,\text{pH} = -0.05\log\left(10^{-3}\right) - 0.2151 - (-0.3)$$

$$\text{pH} = 2.16$$

The pH at E_{pit} and I_{pp} is calculated as:

$$0.109\,\text{pH} = -0.05\log\left(10^{-6}\right) - 0.2151 - (0.045)$$

$$\text{pH} = 0.366$$

E7.9. Pitting inhibitor effectiveness depends strongly on the type and anion concentration. The thermodynamic (critical) activity, a_I, required to inhibit pitting corrosion for a given activity of the aggressive anion is described by [13]:

$$\log\left(Cl^-\right) = a\log\left(a_{I(crit)}\right) + b$$

(a) From the data given in Table E7.6, estimate the minimum amount of anion necessary to suppress pitting when the activity of the Cl^- ions is 0.15 M.

(b) Calculate pitting inhibition potential for $(Cl^-) = 0.2$ M. $E_{pit(i)}$ is related to the concentrations of the Cl^- ion and the inhibitor in Eq. (E7.12) [13]:

$$E_{pit(i)} = 1.56 + 0.38\log\left[\left(Cl^-/ClO_4^-\right)\right] \tag{E7.12}$$

Table E7.6 Activities of Cl^- and ClO_4^- Anions

Cl^- (M)	ClO_4^- (M)
0.001	0.001
0.01	0.013
0.033	0.056
0.04	0.07
0.1	0.21
0.25	0.64
0.4	1.13

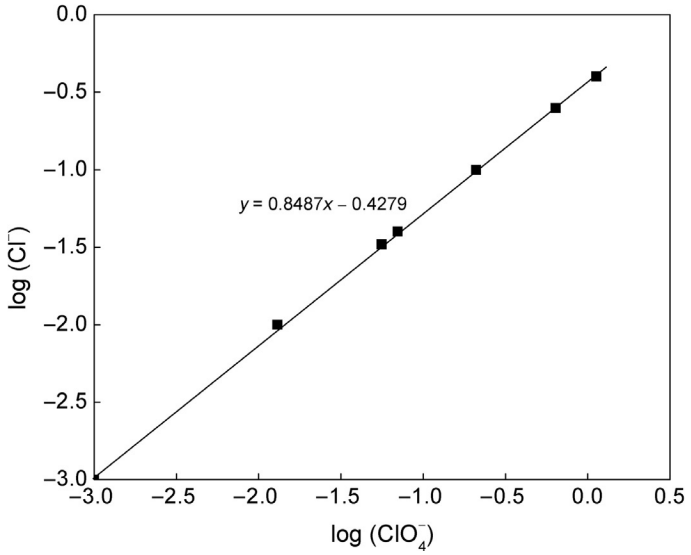

Fig. E7.6 Plot of log (Cl^-) vs. log (ClO_4^-).

Solution:

(a) Fitting the curve in Fig. E7.6 for the tabulated values of Cl^- and ClO_4^- concentrations, the values of "a" and "b" are 0.85 and −0.43, respectively.

For $(Cl^-) = 0.15$ M, the minimum amount of anions required is 0.34 M.

(b) The relationship between pitting inhibition potential, $E_{pit(i)}$ and the concentrations of the Cl^- ion and the inhibitor given in Eq. (E7.12) can be used to determine the pitting inhibition potential for $(Cl^-) = 0.2$ M.

For $(Cl^-) = 0.2$ M,

$$a_{(i)} = 0.479\,\text{M}$$

for which

$$E_{pit(i)} = 1.56 + 0.38\log\left[Cl^-/ClO_4^-\right] = 1.56 + 0.38\log[(0.2/0.479)] = 1.416\,\text{V}$$

E7.10. Compare pitting characteristics of the alloys listed in Table E7.7 [7], determine which alloy would pit, and why?

Solution:

Hastelloy C alone does not pit since its pitting potential is greater than its maximum corrosion potential.

E7.11. The critical activity of an inhibitor ($a_{crit,anion}$) essential for a given activity of chloride ions is given by an expression of the form:

$$\log(Cl^-) = a\log(a_{crit,anion}) + b$$

Table E7.7 Pitting Characteristics of Various Alloys [7]

Alloy Designation	E_{pit} (V vs. SCE)	Corrosion Potential (V vs. SCE)	
		Maximum	Minimum
Type 430 SS	−0.130	0.230	−0.310
Type 304 SS	−0.020	0.280	−0.140
Type 316 SS	0.100	0.385	0.090
Carpenter 20 Cb	0.050	0.520	0.120
Incoloy 825	0.525	0.530	0.180
Hastelloy C	0.900	0.530	0.530

Reproduced by permission of The Electrochemical Society.

The values of Freundlich isotherm parameters "*a*" and "*b*" for (Cl^-) concentrations between 0.1 and 1.0 M in the above equation are given in Table E7.8. Arrange the inhibitor anions in the order of increasing effectiveness.

Hint: The smaller the amount of anion required to passivate the metal for the chosen concentration of Cl^- the more efficient it is. Choose any value of (Cl^-) activity between 0.1 and 1.0 M. For example, 1.0 M and estimate the value of $\log(a_{crit,anion})$ for each of the anions.

Solution:

Choose any value of (Cl^-) activity between 0.1 and 1.0 M. For example 1.0 M and estimate the value of $\log(a_{crit,anion})$ for each of the anions. Calculated critical activities of the anions are listed in Table E7.9.

The hydroxide has the highest anion effectiveness to stop pitting corrosion: Estimated inhibitor anion effectiveness is: Perchlorate < Sulphate <Nitrate < Hydroxide.

Table E7.8 Values of Freundlich Isotherm Parameters "*a*" and "*b*" for Cl^- Concentrations Between 0.1 and 1.0 M

Anion	a	b
Nitrate	1.88	1.18
Sulphate	0.85	−0.05
Hydroxide	1.62	1.84
Perchlorate	0.83	−0.44

Table E7.9 Critical Activities of Various Anions

Anion Activity (M)	Critical Activity (M)
Nitrate	0.2357
Sulphate	1.1450
Hydroxide	0.0731
Perchlorate	3.3894

SOLUTIONS GUIDE

CHAPTER 8: HYDROGEN PERMEATION AND HYDROGEN-INDUCED CRACKING

E8.1. Values of the hydrogen cathodic current density, i_c, and steady state hydrogen permeation current, j_∞, as a function of the overpotential, η, measured using the Devanathan-Stachurski technique are given in Table E8.1.

Using the IPZ mechanistic model [13,14], calculate:

(a) The hydrogen diffusivity (D, cm^2/s) in AISI 4340 steel.

(b) The modified exchange current density (i_o' A/cm^2).

List of parameters:

Membrane thickness (L) = 0.01 cm

Temperature (T) = 293 K

Faraday constant (F) = 96,484 C/mol

Gas constant (R) = 8.314 J/(mol K)

Transfer coefficient (α) = 0.5

Half-rise time ($t_{1/2}$) = 52.43 s

Solution:

(a) Calculation of hydrogen diffusivity

Using Eq. (8.30):

$$t_{1/2} = \frac{0.14L^2}{D}$$

$$D = \frac{0.14L^2}{t_{1/2}}$$

$$D = \frac{0.14(0.01\,\text{cm}^2)}{52.43\,\text{s}}$$

$$D = 2.67 \times 10^{-7}\,\text{cm}^2/\text{s}$$

(b) Calculation of modified exchange current density

According to Eq. (8.40)

$$i_c e^{a\alpha\eta} = -\frac{bi_o'}{k''} j_\infty + i_o' \tag{8.40}$$

Corrosion Engineering
http://dx.doi.org/10.1016/B978-0-444-62722-3.09962-6

Table E8.1 Kinetic Data for Hydrogen Evolution and Hydrogen Permeation in AISI 4340 Steel

η (mV)	i_c (μA/cm^2)	j_∞ (μA/cm^2)
−248	894	22.5
−276	1491	27.5
−300	2360	34.5
−326	3727	43.5
−356	6708	53.7

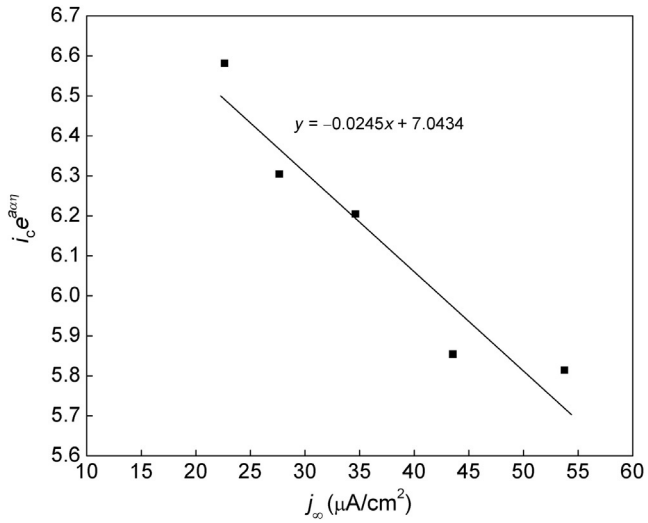

Fig. E8.1 Plot of $i_c e^{a\alpha\eta}$ as a function of the hydrogen permeation current through an AISI 4340 steel membrane of 0.01 cm thick.

As shown on Fig. E8.1, a plot of j_∞ vs. $i_c e^{a\alpha\eta}$, where $a = F/RT$, and $\alpha = 0.5$ is a straight line with slope $= bi_o'/k''$ and with an intercept of $i_o' = 7.04 \times 10^{-6}$ A/cm^2.

E8.2. Using the IPZ model and measured value of hydrogen cathodic current density, i_c, and steady state hydrogen permeation current, j_∞, as a function of the overpotential, η, given in Table E8.1, calculate:

(a) The thickness-dependent absorption-adsorption rate constant, (k'', mol/cm^3).

(b) The recombination rate constant, (k_3, mol/cm^2 s).

List of parameters:

Membrane thickness (L) = 0.01 cm

Temperature (T) = 293 K

Faraday constant (F) = 96,484 C/mol

Gas constant $(R) = 8.314\,\text{J/(mol K)}$

$$D = 2.67 \times 10^{-7}\,\text{cm}^2/\text{s}$$

$$b = L/FD$$

Transfer coefficient $(\alpha) = 0.5$
Half-rise time $(t_{1/2}) = 52.43\,\text{s}$

Solution:

(a) Calculation of the thickness-dependent absorption-adsorption rate constant, (k'', mol/cm^3).

The thickness-dependent absorption-adsorption rate constant, k'' is calculated from the slope of the plot in Fig. E8.1.

From

$$i_c e^{a\alpha\eta} = -\frac{bi_o'}{k''} j_\infty + i_o' \tag{8.40}$$

and $i_o' = 7.04 \times 10^{-6}\,\text{A/cm}^2$; $b = L/FD = 0.388\,\text{(A/cm)}$

$$k'' = -\frac{bi_o'}{\text{slope}} = \frac{0.388 \times 7.04 \times 10^{-6}}{0.0245} = 1.11 \times 10^{-4}\,\text{mol/cm}^3$$

(b) Evaluation of recombination rate constant (k_3, mol/cm^{2}s).

According to Eq. (8.38)

$$j_\infty = \frac{k''}{b\sqrt{Fk_3}}\sqrt{i_r}$$

A plot of j_∞ (μA/cm^2) vs. $\sqrt{i_r}$ (μA/cm^2) is a straight line through the origin with slope $= k''/b\sqrt{Fk_3}$. The slope in Fig. E8.2 of 0.6123 is used to calculate the recombination rate constant

$$k_3 = \left(\frac{k''}{b \times \text{slope}}\right)^2 \times \frac{1}{F} = \left(\frac{1.11 \times 10^{-4}}{0.388 \times 0.6123}\right)^2 \times \frac{1}{96,485} \times 10^6 = 2.26 \times 10^{-6}\,\frac{\text{mol}}{\text{s cm}^2}$$

E8.3. Using the IPZ model and measured value of hydrogen cathodic current density, i_c, and steady state hydrogen permeation current, j_∞, as a function of the overpotential, η, given in Table E8.1, calculate the hydrogen surface coverage, (θ_H).

List of parameters:
Membrane thickness $(L) = 0.01$ cm
Temperature $(T) = 293$ K
Faraday constant $(F) = 96,484$ C/mol
Gas constant $(R) = 8.314\,\text{J/(mol K)}$
Transfer coefficient $(\alpha) = 0.5$

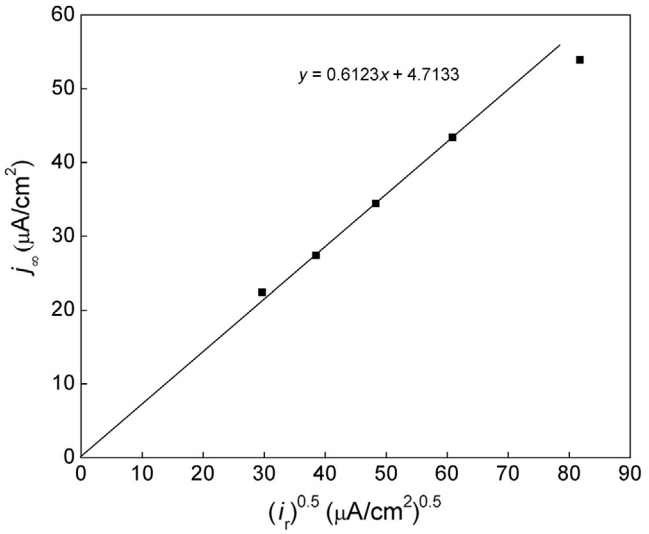

Fig. E8.2 Plot of the hydrogen permeation current through an AISI 4340 steel membrane of 0.01 cm as a function of $\sqrt{i_r}$.

Half-rise time $(t_{1/2}) = 52.43$ s

Solution:

Calculation of hydrogen surface coverage θ_H

Hydrogen surface coverage θ_H is calculated as a function of hydrogen overpotential by substituting the calculated value of k_3 estimated in exercise E8.2 and experimentally measured $i_r = i_c - j_\infty$ into Eq. (8.35):

$$i_r = Fk_3\theta_H^2 \tag{8.35}$$

E8.4. The hydrogen kinetic parameters were calculated by fitting the experimental data to the IPZ model. The results for samples A and B are presented in Table E8.2. Predict which sample shows better resistance to hydrogen permeation.

Solution:

The modified exchange current density, i_o' (A/cm^2), measures the extent of hydrogen evolution reaction. Using this parameter as criterion, the amount of hydrogen evolved on sample A is lower by two orders of magnitude than the hydrogen evolved on sample B. The thickness-dependent absorption-

Table E8.2 Kinetic Data for Hydrogen Evolution and Hydrogen Permeation for Samples A and B

Sample	i_o' (A/cm^2)	k'' (mol/cm^3)	k_3 (mol/s cm^2)
A	9.17×10^{-7}	1.11×10^{-6}	7.38×10^{-6}
B	6.30×10^{-5}	2.10×10^{-5}	5.73×10^{-6}

adsorption rate constant, k'' is larger for sample B than for sample A. The higher value of k'' indicates that more hydrogen atoms are adsorbed and permeate through the membrane. The recombination rate constant k_3 shows how much hydrogen is recombined, which is removed from the surface. Given that less hydrogen is evolved in sample A, the adsorption-desorption rate is smaller. More hydrogen is recombined and it is removed from the surface than in sample B. Sample A shows higher resistance to hydrogen atom permeation than sample B.

E8.5. Use the hydrogen atom direct mechanism [18,19] discussed in Ref. [16] to explain why the steady state hydrogen permeation current density, j_∞, is directly proportional to the cathodic current density, i_c, and is independent of the membrane thickness when the cathodic current density is small.

E8.6. The resistance to hydrogen permeation in Cd deposited on steel was evaluated by using the Devanathan-Stachurski technique. The hydrogen evolution current, i_c, and the permeation current, j_∞, were measured as a function of overpotential and are listed in Table E8.3.

Determine the applicability of the IPZ model to this data.

Solution:

If the IPZ model is applicable to the experimental data, a plot of $j_\infty\,(\mu A/cm^2)$ vs. $\sqrt{i_r}(\mu A/cm^2)^{0.5}$, Eq. (8.38) would be a straight line passing through the origin. The plot shown in Fig. E8.3 is not linear, indicating that the data are not in agreement with the IPZ model.

$$j_\infty = \frac{k''}{b\sqrt{Fk_3}}\sqrt{i_r} \tag{8.38}$$

The non-linearity is due to the apparent standard free-energy of hydrogen adsorption. Under these conditions, the Frumkin-Temkin (F-T) corrections should be applied to both, the discharge and the recombination currents [18,19]. The modified set of charging and recombination currents are:

$$i_c = i_o'(1-\theta_s)e^{-a\alpha\eta}e^{-af\theta_s} \tag{E8.1}$$

Table E8.3 Hydrogen Evolution and Hydrogen Permeation Data for Cd Deposited on Steel

η (mV)	i_c ($\mu A/cm^2$)	j_∞ ($\mu A/cm^2$)
−300	6.6	2.20
−400	51.0	4.83
−450	133.3	6.50
−500	317.6	8.0
−550	666.6	9.03

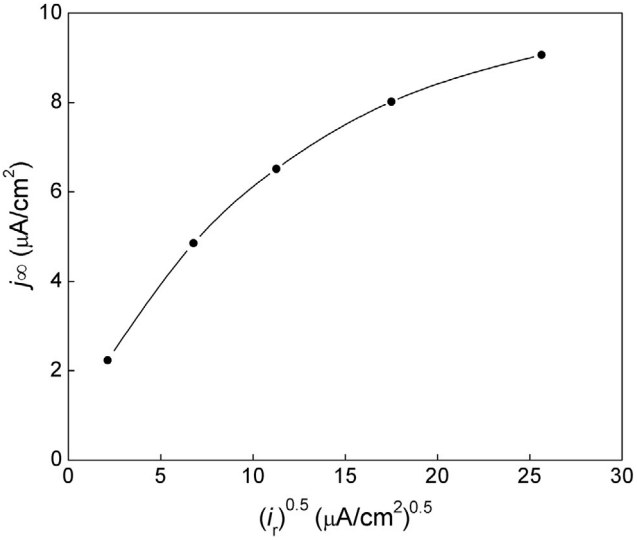

Fig. E8.3 Plot of j_∞ (μA/cm^2) as a function of $\sqrt{i_r}$ (μA/cm^2)$^{0.5}$ for Cd deposited on a steel membrane with a thickness of 0.01 cm.

$$i_r = Fk_3\theta_s^2 e^{2\alpha f\theta_s} \tag{E8.2}$$

where $f=\gamma/RT$, and γ is the gradient of the apparent standard free energy of adsorption with respect to coverage. The value of f is taken to be equal to 4.5. After suitable modification, Eqs. (E8.1) and (E8.2) can be rewritten to obtain Frumkin-Temkin (F-T) correction of Eq. (8.38):

$$\ln\left(\frac{i_c e^{\alpha fbj_\infty/k''}}{1-\dfrac{bi_\infty}{k''}}\right) = -\alpha a\eta + \ln\left(i_o'\right) \tag{E8.3}$$

$$\ln\left(\frac{\sqrt{i_r}}{j_\infty}\right) = \left(\frac{\alpha fb}{k''}\right)j_\infty + \ln\left(\frac{b\sqrt{Fk_3}}{k''}\right) \tag{E8.4}$$

E8.7. Using the Frumkin-Temkin (F-T) corrections to the IPZ model in exercise E8.6, calculate:

(a) The hydrogen evolution reaction coverage-dependent transfer coefficient, α.
(b) The modified exchange current density, i_o' (A/cm^2).
(c) The thickness-dependent absorption-adsorption rate constant, k'' (mol/cm^3).
(d) The recombination rate constant, k_3 (mol/cm^{2}s).

Use the following parameters:
Membrane thickness (L) = 0.01 cm
Temperature (T) = 293 K

Faraday constant $(F) = 96{,}484$ C/mol
Gas constant $(R) = 8.314$ J/(mol K)
Diffusion coefficient $(D) = 2.67 \times 10^{-7}$ cm^2/s
$f = 4.5$

$a = F/RT$

$b = L/FD$

Solution:

As shown in Fig. E8.4, a plot of $\ln\left(\sqrt{i_r}/j_\infty\right)$ vs. j_∞ (μA/cm^2) for Cd data is linear indicating the applicability of F-T corrections. The hydrogen kinetic parameters listed in exercise E8.4 are evaluated by plotting Eqs. (E8.4) and (E8.3). The correlations of $\ln\left(\sqrt{i_r}/j_\infty\right)$ vs. j_∞ and $\ln\left(i_c e^{\alpha f b j_\infty/k''}/(1-(bi_\infty/k''))\right)$ vs. η for Cd deposited on steel membrane were obtained by using an iterative procedure (Fig. E8.5). The value of α was assumed to be 0.5 for the first guess. With this value for α, the constant k'' is obtained from the slope of the plot shown in Fig. E8.4. The recombination rate constant k_3 is determined from the intercept of the same plot. The modified exchange current density i_o', is determined from the intercept of the plot shown in Fig. E8.5. With the value of i_o' from the intercept of the plot, we proceed to verify the assumed value of α. Using the value of α obtained from the slope of Eq. (E8.3), a new value for k'' was found by a regression analysis of Eq. (E8.4). The procedure was repeated until α converged.

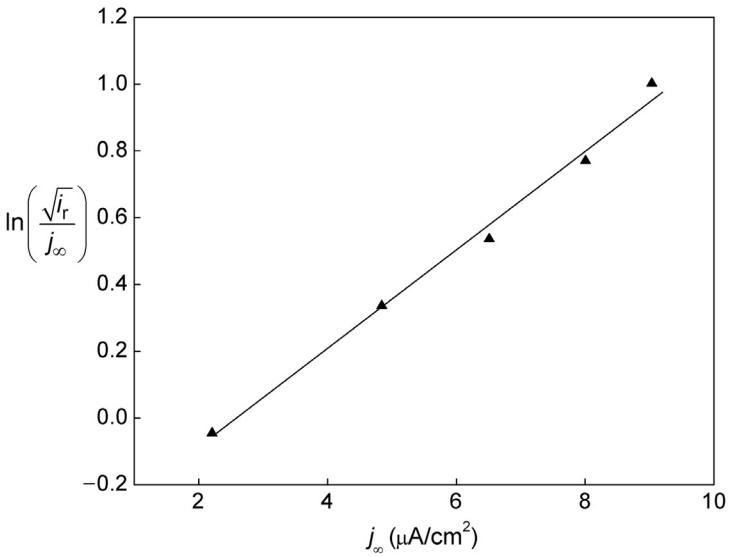

Fig. E8.4 Plot of $\ln\left(\sqrt{i_r}/j_\infty\right)$ vs. i_∞ (μA/cm^2) for Cd deposited on iron.

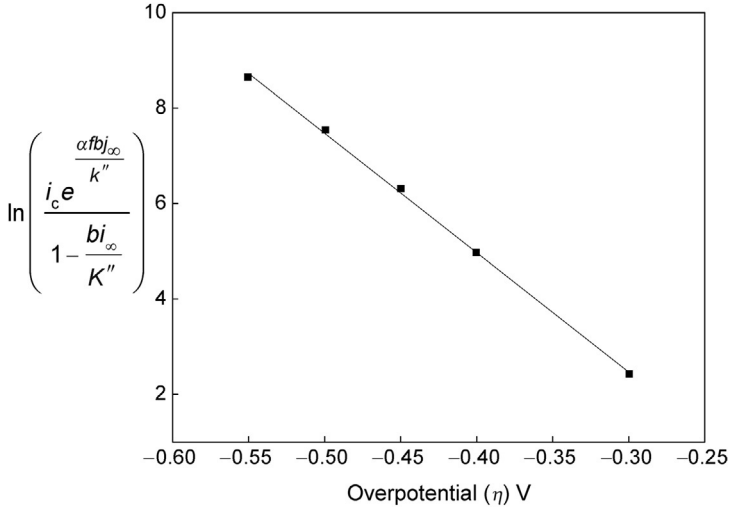

Fig. E8.5 Plot of $\ln\left(i_c e^{\alpha f b j_\infty / k''} / (1 - (b i_\infty / k''))\right)$ vs. η for Cd deposited on iron.

Table E8.4 Kinetic Parameters for Hydrogen Permeation Through Cd Coated Steel

α	i_o' (A/cm^2)	k'' (mol/cm^3)	k_3 (mol/s cm^2)
0.63	6.22×10^{-9}	7.32×10^{-6}	1.66×10^{-9}

The calculated values for the transfer coefficient, α, the modified exchange current density, i_o', the thickness-dependent absorption-adsorption rate constant, k'', and the recombination rate constant, k_3 are summarized in Table E8.4.

E8.8. Plot the hydrogen surface coverage for Cd deposited on steel as a function of overpotential. Use the data for permeation current and hydrogen evolution current as a function of overpotential listed in Table E8.3. The hydrogen surface coverage for Cd deposited steel was calculated using Eq. (E8.5), [81].

$$\theta_s = \frac{\left[k_{ads} + \left(\frac{D}{L}\right)\right]}{k_{abs}} C_s = \frac{C_s}{k''} = \frac{b j_\infty}{k''} \tag{E8.5}$$

where $b = L/FD$, membrane thickness $(L) = 0.01$ cm, temperature $(T) = 293$ K, Faraday constant $(F) = 96{,}485$ C/mol, gas constant $(R) = 8.314$ J/(mol K), diffusion coefficient $(D) = 2.67 \times 10^{-7}$ cm^2/s. Thickness-dependent absorption-adsorption constant, k'', calculated in Problem E8.7 $= 7.32 \times 10^{-6}$ mol/cm^3.

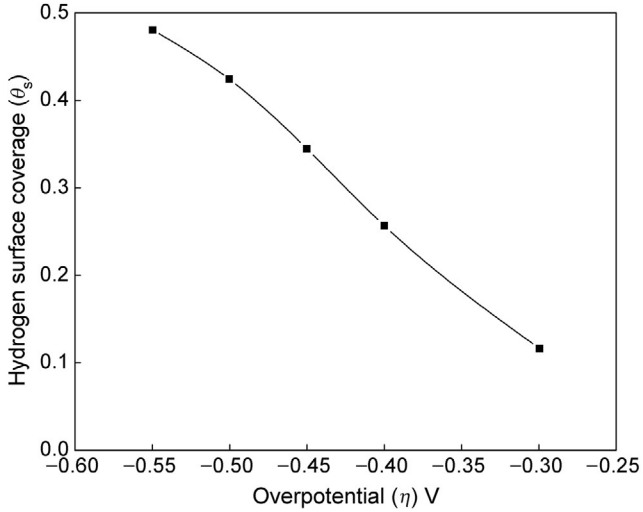

Fig. E8.6 Hydrogen surface coverage for Cd deposited on steel as a function of overpotential.

Solution:

The hydrogen surface coverage was calculated for the overpotentials and corresponding hydrogen permeation current values given in Table E8.3 using Eq. (E8.5) and the results are plotted in Fig. E8.6.

The hydrogen surface coverage on Cd coated steel is higher value than 0.1 which is in agreement with the Temkin isotherm.

SOLUTIONS GUIDE

CHAPTER 9: STRESS CORROSION CRACKING

E9.1 The critical stress intensity, K_{Ic}, is related to the magnitude of the stress, σ, at the tip of the crack by Eq. (E9.1)

$$K_{Ic} = Y\sigma\sqrt{\pi a} \tag{E9.1}$$

or

$$\sigma = \frac{K_{Ic}}{Y\sqrt{\pi a}}$$

where Y is a function of specimen crack geometry and "a" is crack length. Using Eq. (E9.1), calculate the critical stress intensity (materials fracture toughness) K_{Ic} of a specimen with a surface crack "a" of 0.45 mm exposed to a stress of $\sigma = 850$ MPa. Assume $Y = 1$.

Solution:

$$K_{Ic} = 1 \cdot 850\,\text{MPa} \cdot \sqrt{\pi(0.45 \times 10^{-3}\,\text{m})} = 31.96\,\text{MPa}\sqrt{\text{m}}$$

E9.2 If a material with fracture toughness, K_{Ic}, of 40 MPa$\sqrt{\text{m}}$ is exposed to stress (σ) levels of 600, 800, 1000, and 1200 MPa, compute the length of the surface cracks and correlate the estimated surface cracks values vs. stress levels. Assume $Y = 1$.

Solution:

$$a = \frac{1}{\pi}\left(\frac{K_{Ic}}{Y\sigma}\right)^2 \tag{E9.2}$$

Using Eq. (E9.2), the length of the cracks were estimated and the results are shown in Fig. E9.1.

E9.3 Using Eq. (E9.3):

$$Y = \frac{K_{Ic}}{\sigma\sqrt{\pi a}} \tag{E9.3}$$

(a) Estimate the parameter Y for a specimen with a fracture toughness, K_{Ic}, (plane strain fracture) of 30 MPa$\sqrt{\text{m}}$, and stress level of 420 MPa. The surface crack length is 1.5 mm.

(b) Estimate the parameter Y values for the same specimen with surface cracks of 0.5, 1, 2, and 3 mm.

http://dx.doi.org/10.1016/B978-0-444-62722-3.09961-4

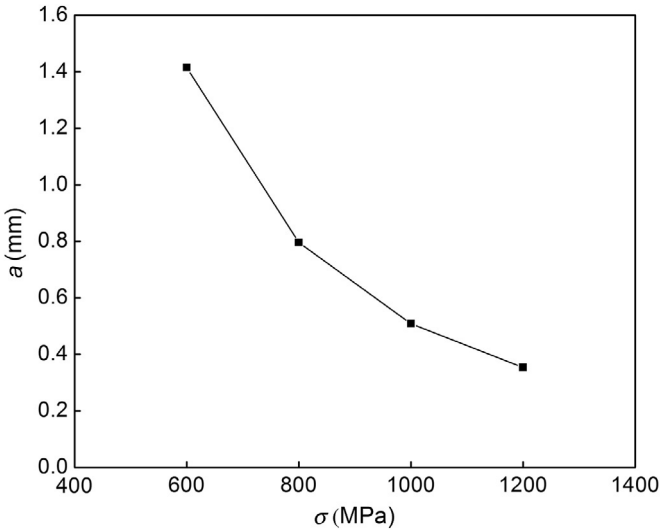

Fig. E9.1 Dependence of the surface cracks vs. stress levels.

(c) For the specimen in (a) with the same crack length of 1.5 mm, and the same parameter Y as calculated in (a), compute the fracture toughness, K_{Ic}, under 550 MPa of stress.

Solution:

(a)

$$Y = \frac{30\,\text{MPa}\sqrt{\text{m}}}{420\,\text{MPa}\sqrt{\pi(1.5\times10^{-3}\,\text{m})}} = 1.041$$

(b) Parameter Y values for the same specimen with surface cracks 0.5, 1, 2, and 3 mm are given in Table E9.1

(c) The fracture toughness, K_{Ic}, for the specimen with a crack length of 1.5 mm is:

$$K_{Ic} = 1.041\times550\,\text{MPa}\sqrt{\pi(1.5\times10^{-3}\,\text{m})} = 39.30\,\text{MPa}\sqrt{\text{m}}$$

E9.4 Compute the following.

(a) A specimen with a fracture toughness, K_{Ic}, of 60 MPa $\sqrt{\text{m}}$ is exposed to stress of 700, 900, 1100, and 1200 MPa. Assuming $Y=1$ and the largest surface crack of 1 mm, compute if the given stress levels between 700 and 1200 MPa will fracture the specimen.

Table E9.1 Dependence of Y Values for a Specimen with Surface Cracks of 0.5, 1, 2, and 3 mm

a (mm)	0.5	1.0	1.5	2.0	3.0
Y	1.802	1.274	1.041	0.901	0.736

(b) For the same conditions, estimate if the given stress levels in (a) will fracture the specimen when the largest surface cracks are 0.5 and 2.0 mm.

Solution:

(a)

$$K_{Ic} = Y\sigma_c\sqrt{\pi a}$$

$$\sigma_c = \frac{K_{Ic}}{Y\sqrt{\pi a}}$$

$$\sigma_c = \frac{60\,\text{MPa}\sqrt{\text{m}}}{1\sqrt{\pi \times 0.001\,\text{m}}} = 1070\,\text{MPa}$$

The specimen will fracture at stress level of 1070 MPa.

(b) When the largest surface cracks are 0.5 and 2.0 mm, the corresponding values of σ_c are 1514 and 757 MPa, respectively.

E9.5 An alloy specimen with a plane strain fracture toughness of 50 MPa $\sqrt{\text{m}}$ cracks with the maximum (critical internal crack length) of $2a = 3.0$ mm. Estimate the applied stress assuming $Y = 1$.

Solution:

The applied stress can be calculated using the following expression:

$$\sigma_c = \frac{K_{Ic}}{Y\sqrt{\pi a}}$$

where K_{Ic} 50 MPa $\sqrt{\text{m}}$ and $a = 1.5$ mm

$$\sigma_c = \frac{50\,\text{MPa}\sqrt{\text{m}}}{1\sqrt{\pi(1.5 \times 10^{-3}\,\text{m})}} = 728\,\text{MPa}$$

E9.6 The magnitude of the maximum stress existing at the tip of an external crack (σ_m) is defined by Eq. (E9.4):

$$\sigma_m = 2\sigma_o\left(\frac{a}{\rho_t}\right)^{1/2} \tag{E9.4}$$

where σ_o is tensile stress, "a" is the crack length, and ρ_t is the radius of the curvature. Estimate the value of the maximum stress σ_m that exists at the tip of an external crack with a radius of curvature ρ_t of 8.5×10^{-5} mm and critical crack length $2a = 3.0 \times 10^{-2}$ mm when a tensile stress σ_o of 220 MPa is applied.

Solution:

$$\sigma_m = 2 \times 220\,\text{MPa} \times \sqrt{\frac{1.5 \times 10^{-2}\,\text{mm}}{8.5 \times 10^{-5}\,\text{mm}}} = 5845\,\text{MPa}$$

E9.7 Compute the following:

(a) An alloy specimen with a plane strain fracture toughness of 80 MPa $\sqrt{\text{m}}$ cracks under stress with a minimum length of the surface crack of 35 mm, which

initiates formation of a fracture. Estimate the tensile stress. Assume a value of 1 for Y.

(b) An alloy specimen that exhibits a plane strain fracture toughness of 75 MPa $\sqrt{\text{m}}$ is exposed to a tensile stress of 300 MPa. Compute the minimum (critical) length (a_c) of the surface crack that initiates a fracture. Assume a value of 1.5 for Y.

Use Eq. (E9.5):

$$K_{Ic} = Y\sigma\sqrt{\pi a_c} \rightarrow a_c = \frac{1}{\pi}\left(\frac{K_{Ic}}{Y\sigma}\right)^2 \tag{E9.5}$$

where a_c is critical crack length.

Solution:

(a)
$$\sigma = \frac{80\,\text{MPa}}{1\sqrt{\pi(35\times10^{-3}\,\text{m})}} = 241.26\,\text{MPa}$$

(b)
$$a_c = \left(\frac{75\,\text{MPa}\sqrt{\text{m}}}{300\,\text{MPa}\times1.5\sqrt{\pi}}\right)^2 = 0.088\,\text{m} = 8.8\,\text{mm}$$

E9.8 In order to perform K_{Ic} testing on standard specimens, the following equation has been adopted:

$$a, B, (W-a) \geq 2.5\left(\frac{K_{Ic}}{\sigma_{ys}}\right)^2 \tag{E9.6}$$

The quantity $\left(\frac{K_{Ic}}{\sigma_{ys}}\right)^2$ is proportional to the plastic zone size. The minimum requirement for the specimen thickness, B, the crack length, "a", and ligament length, $(W-a)$, where W is the specimen width, should ensure that the plastic zone is sufficiently small for fracture to be controlled by the intensity of stress ahead of the crack tip, K_{Ic}. Materials with high-yield stress σ_{ys} and low-fracture toughness should have low thickness to satisfy the requirement of Eq. (E9.6) for the plane strain condition. Hydrogen embrittlement, stress corrosion cracking, and corrosion fatigue reduce the stress intensity. The methods used in linear elastic fracture mechanics developed in the last two decades can be used to test hydrogen embrittlement, stress corrosion cracking, and corrosion fatigue. These processes reduce the stress intensity to advance brittle cracks to low values of K_{Ic}. If a stainless steel alloy has yield strength, σ_{ys}, of 345 MPa and plain strain linear elastic fracture toughness, K_{Ic}, of 80 MPa $\sqrt{\text{m}}$, estimate the minimum specimen dimensions (a, B, W).

Solution:

$$a, B, (W-a) \geq 2.5\left(\frac{80\,\text{MPa}\sqrt{\text{m}}}{345\,\text{MPa}}\right) = 0.134\,\text{m}$$

$$a \geq 0.134\,\text{m}, \quad B \geq 0.134\,\text{m}, \quad W \geq a + 0.134\,\text{m} = 0.269\,\text{m}$$

E9.9 Corrosion fatigue testing is performed using a sinusoidal stress function. The stress cycle is characterized by the stress ratio, R, of minimum to maximum stress, $\left(R = \frac{S_{min}}{S_{max}}\right)$. The tensile stress and the compressive stress are taken as positive and negative, respectively. In the case when the stress is completely reversible ($S_{max} = S_{min}$), $R = -1$. R is a negative fraction if the stress is partially reversed. If both maximum and minimum stresses are tensile, R is a positive fraction. By cycling from tension to no load, R is equal to 0. A rotating cantilever beam apparatus is used for corrosion testing. The maximum stress level is defined as:

$$\sigma_m = \frac{\sigma_{max} + \sigma_{min}}{2} \tag{E9.7}$$

The stress amplitude is given by Eq. (E9.8)

$$\sigma_a = \frac{\sigma_{max} - \sigma_{min}}{2} \tag{E9.8}$$

The magnitude of the stress range, σ_r, is determined using Eq. (E9.9)

$$\sigma_r = \sigma_{max} - \sigma_{min} \tag{E9.9}$$

The single rotation of the bent-beam specimen shown in the figure represents one fatigue cycle. The specimen rotation results in tensile and compressive stress ($S_{max} = S_{min}$), $R = -1$. The results of the test as discussed under Corrosion Fatigue Testing in the chapter are plotted as the *S-N* curves as a maximum tensile stress vs. the number of cycles to failure. Examples of the calculations are given for a fatigue test in which the stress amplitude, σ_a, is 180 MPa and the mean stress, σ_m, is 65 MPa. Calculations are performed using Eqs. (E9.7) through (E9.9) to estimate (a) the maximum and minimum stress levels, (b) the stress ratio, and (c) the magnitude of the stress range.

Solution:

(a)

$$\sigma_a = \frac{\sigma_{max} - \sigma_{min}}{2} = 180\,\text{MPa};$$

$$\sigma_m = \frac{\sigma_{max} + \sigma_{min}}{2} = 65\,\text{MPa};$$

$$\sigma_{max} = 245\,\text{MPa} \rightarrow \sigma_{min} = -115\,\text{MPa}$$

(b)

$$R = \frac{S_{min}}{S_{max}} = \frac{-115\,\text{MPa}}{245\,\text{MPa}} = -0.469$$

(c)

$$\sigma_r = \sigma_{max} - \sigma_{min} = 245\,\text{MPa} - (-115\,\text{MPa}) = 360\,\text{MPa}$$

E9.10 In the cantilever beam apparatus shown in Fig. E9.2 (Fig. 9.67 in Chapter 9), a sample of stainless steel is exposed to a corrosion environment. If the minimum

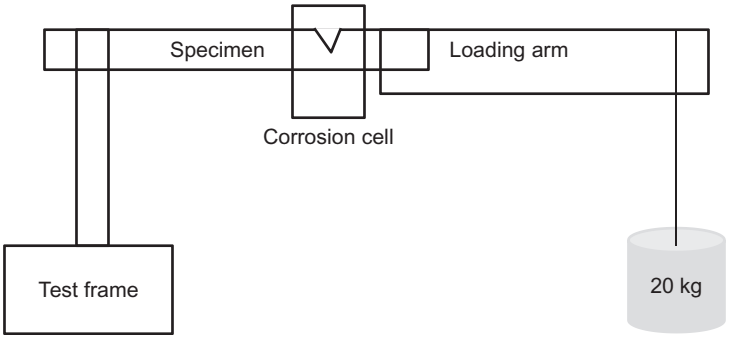

Fig. E9.2 Schematic of cantilever beam apparatus.

load of 20 kg is applied to a momentum arm of 2 m, estimate the fracture toughness value, K_{Ihic}, if the maximum crack length of 30 mm is caused from the applied stress. Assume the following specimen dimensions: width $B = 30$ mm, depth $W = 60$ mm, and reduced width across the side grooves $B_{\mathrm{N}} = 15$ mm.

Use Eq. (E9.10) to calculate the fracture toughness value, K_{Ihic}:

$$K_{\mathrm{Ihic}} = \frac{6MF}{\sqrt[3/2]{W-a}\sqrt{BB_{\mathrm{N}}}} \tag{E9.10}$$

where, M is bending moment, B is specimen width, B_{N} is net specimen with subtracting side grooves, a is crack length, and W is specimen width (Table E9.2).

Solution:

$$M = 20\,\mathrm{kg} \times 9.8\,\mathrm{m/s^2} \times 2\,\mathrm{m} = 392\,\mathrm{Nm}; \quad \frac{a}{W} = 0.5, \quad F = 0.72$$

$$K_{\mathrm{Ihic}} = \frac{6 \times 392\,\mathrm{Nm} \times 0.72}{\sqrt[3/2]{60\,\mathrm{mm} - 30\,\mathrm{mm}}\sqrt{30\,\mathrm{mm} \times 15\,\mathrm{mm}}} = 15.4\,\mathrm{MPa}\sqrt{\mathrm{m}}$$

E9.11 The material toughness properties are controlled by loading rate and constrained through:

K_{c} is the critical stress intensity factor for plain-stress conditions of variable constraint in the case of static loading. The value of K_{Ic} depends on specimen thickness, geometry, and on the crack size.

Table E9.2 Dependence of a/W and $F(a/W)$

a/W	$F(a/W)$
0.05	0.36
0.1	0.49
0.2	0.60
0.5	0.72

K_{Ic} is the critical stress intensity factor for static loading and plain-strain conditions of maximum constraint represents a minimum value for thick plates.

$$K_c, K_{Ic} = C\sigma\sqrt{a} \tag{E9.11}$$

where C is a function of specimen and crack geometry, σ is nominal stress (MPa), and "a" is flaw size, in (mm). Estimating the critical value of K_{Ic} for specific material with a given thickness, temperature, and loading rate, one can determine the flaw size for a given design stress level.

To estimate the crack growth in steel using fracture mechanics, it is necessary to:

(i) Estimate the maximum initial flow size a_o and K.
(ii) With given value of K_c or K_{Ic} and the maximum stress, calculate the critical flaw size a_c that would cause a brittle fracture.
(iii) The following expression can be used to estimate the fatigue crack growth rate per cycle of the steels:

$$\frac{d[a\,(m)]}{dN} = 1.354 \times 10^{-10}\left(\Delta K_I\left(\text{MPa}\sqrt{\text{m}}\right)\right)^{2.25} \tag{E9.12}$$

where $\frac{da}{dN}$ represents fatigue crack growth per cycle of loading, ΔK_I is the stress intensity range, MPa $\sqrt{\text{m}}$.

Assuming the following design specifications: $\sigma_{ys} = 700$ MPa; $K_{Ic} = 150$ MPa $\sqrt{\text{m}}$; $a_o = 8.0$ mm; $\sigma_{max} = 350$ MPa; $\sigma_{min} = 170$ MPa; $\Delta\sigma = 180$ MPa (live-load stress range); $\Delta a = 2.0$ mm; and $K_I = 1.12\sigma\sqrt{\pi a}$ and $\frac{d[a\,(m)]}{dN} = 1.354 \times 10^{-10}\left[\Delta K_I\left(\text{MPa}\sqrt{\text{m}}\right)\right]^{2.25}$.

Estimate:

(a) The critical flaw size (a_c) using the nominal maximum design stress K_{Ic} that would cause failure by brittle fracture.
(b) Derive ΔK_I using the appropriate expression.
(c) Numerically integrate the CGR expression between a_o and a_c to estimate the life of the structure before failing.

To calculate the critical flaw size (a_c) use Eq. (E9.13) derived from Eq. (E9.5).

$$a_c = \frac{1}{\pi}\left(\frac{K_{Ic}}{1.12\sigma_{max}}\right)^2 \tag{E9.13}$$

Solution:

(a) Estimate of a_c at σ_{max}:

$$a_c = \frac{1}{\pi}\left(\frac{K_{Ic}}{1.12\sigma_{max}}\right)^2 = \frac{1}{\pi}\left(\frac{150\,\text{MPa}\sqrt{\text{m}}}{1.12 \times 350\,\text{MPa}}\right)^2 = 0.0466\,\text{m} = 46.6\,\text{mm}$$

(b) Derive ΔK_I using the appropriate expression. K_I will change due to the change in stress loading and the resulting crack change per cycle:

$$\Delta K_I\left(\text{MPa}\sqrt{\text{m}}\right) = 1.12\Delta\sigma\sqrt{\pi a} = 1.985 \times 180\sqrt{a_{avg}} = 357.3\sqrt{a_{avg}}$$

where a_{avg} represents the average crack size between crack increments.

$$a_{avg} = \frac{a_i + a_j}{2}$$

(c) Solve for ΔN in terms of crack growth increments using the appropriate CGR expression:

$$\frac{d[a\,(\text{m})]}{dN} = 1.354 \times 10^{-10}\left(\Delta K_I\left(\text{MPa}\sqrt{\text{m}}\right)\right)^{2.25}$$

For numerical integration:

$$\frac{\Delta[a\,(\text{m})]}{dN} = 1.354 \times 10^{-10}\left(\Delta K_I\left(\text{MPa}\sqrt{\text{m}}\right)\right)^{2.25}$$

$$a_{avg} = \frac{a_1 + a_o}{2} = 9.0\,\text{mm}$$

$$\Delta N = \frac{\Delta a}{1.354 \times 10^{-10} \times \left(357.3\sqrt{(a_{avg})}\right)^{2.25}} \approx 5330\,\text{cycles}$$

Repeat for all intervals up to $a_c = 46.6$ mm. The calculated values are given in Table E9.3. A plot of "a" vs. cycles is shown in Fig. E9.3.

Table E9.3 Numerically Integrated Crack Growth Rate Expression Between a_o and a_c

a_o (mm)	a_f (mm)	a_{avg} (mm)	ΔK (MPa $\sqrt{\text{m}}$)	ΔN (cycles)	ΣN (cycles)
8.0	10.0	9.0	33.90	5330	5330
10.0	12.0	11.0	37.48	4250	9580
12.0	14.0	13.0	40.74	3520	13,100
14.0	16.0	15.0	43.76	3000	16,100
16.0	18.0	17.0	46.59	2600	18,700
18.0	20.0	19.0	49.25	2300	21,000
20.0	22.0	21.0	51.78	2050	23,060
22.0	24.0	23.0	54.19	1850	24,910
24.0	26.0	25.0	56.50	1690	26,600
26.0	28.0	27.0	58.71	1550	28,140
28.0	30.0	29.0	60.85	1430	29,570
30.0	32.0	31.0	62.91	1330	30,900
32.0	34.0	33.0	64.91	1240	32,130
34.0	36.0	35.0	66.85	1160	33,290
36.0	38.0	37.0	68.73	1090	34,370
38.0	40.0	39.0	70.57	1020	35,400
40.0	42.0	41.0	72.35	970	36,370
42.0	44.0	43.0	74.10	920	37,280
44.0	46.0	45.0	75.80	870	38,150

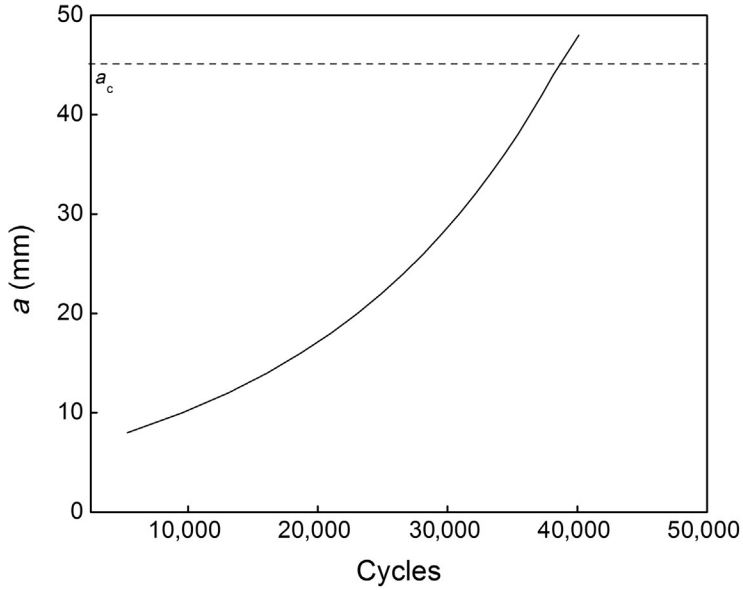

Fig. E9.3 Fatigue crack growth curve.

The required number of loading cycles decreases as the crack increases. Based on the given parameters, the structure will fail at approximately 38,000 cycles. Improving service life can be accomplished by increasing the critical crack size a_c, lower the design stress σ_{max}, lower the stress range $\Delta\sigma$ or improving fabrication, lowering the initial flaw size a_o. Change the parameters to see their influence on structure life.

SOLUTIONS GUIDE

CHAPTER 11: HIGH-TEMPERATURE CORROSION

E11.1. Experimentally determined weight gain data for oxidation of cobalt at 1200 °C are given in Table E11.1. Using the data:

(a) Plot graphs for parabolic, cubic, and quartic kinetics. Determine which rate equation best fits the data.

(b) Find the rate constant (k_{1200}) from the plot constructed in (a).

Solution:

(a) Oxidation kinetics follows the following equation:

$$W^m = k_m t \tag{E11.1}$$

where $m = 2, 3,$ or 4 for parabolic, cubic, and quartic kinetics, respectively, as shown in Fig. E11.1a–c. The data fits the parabolic rate equation best because W^2 vs. t is nearly a straight line. This is not the case for the plots of W^3 vs. t or W^4 vs. t.

(b) Cobalt oxidation follows the parabolic rate equation (E11.2):

$$W^2 = k_{p,1200} t \tag{E11.2}$$

Thus, the slope in Fig. E11.2 is used to estimate the rate constant. Linear least squares fit of the data (with zero intercept) is used to calculate the rate constant:

$$k_{p,1200} = 265.4 \text{mg}^2/\text{cm}^4\text{h}$$

E11.2. Using the rate constant for cobalt oxidation at 1200 °C obtained in exercise E11.1, calculate the rate constants at 900, 950, and 1150 °C using the Arrhenius equation. Assume that activation energy is 35 kcal/mol.

Solution:

The Arrhenius equation describes the temperature dependence of the oxidation rate constant:

$$k_p = k_o \exp\left(\frac{-E_a}{RT}\right)$$

where E_a is the activation energy (35 kcal/mol), R is the gas constant (0.001986 kcal/mol K), T is the temperature (K)

$$\ln k_{p,1200} = \ln k_o - \frac{E_a}{RT_{1200}}$$

Corrosion Engineering
http://dx.doi.org/10.1016/B978-0-444-62722-3.09973-0

Table E11.1 Weight Gain Data for Oxidation of Cobalt at 1200 °C

Time (h)	0	0.5	1.0	1.4	2.0	2.4	2.9	3.5	3.9	4.5	5.0
Weight gain (mg/cm^2)	0	11.1	15.6	19.2	22.4	25.2	27.7	30.3	32.2	34.1	36.4

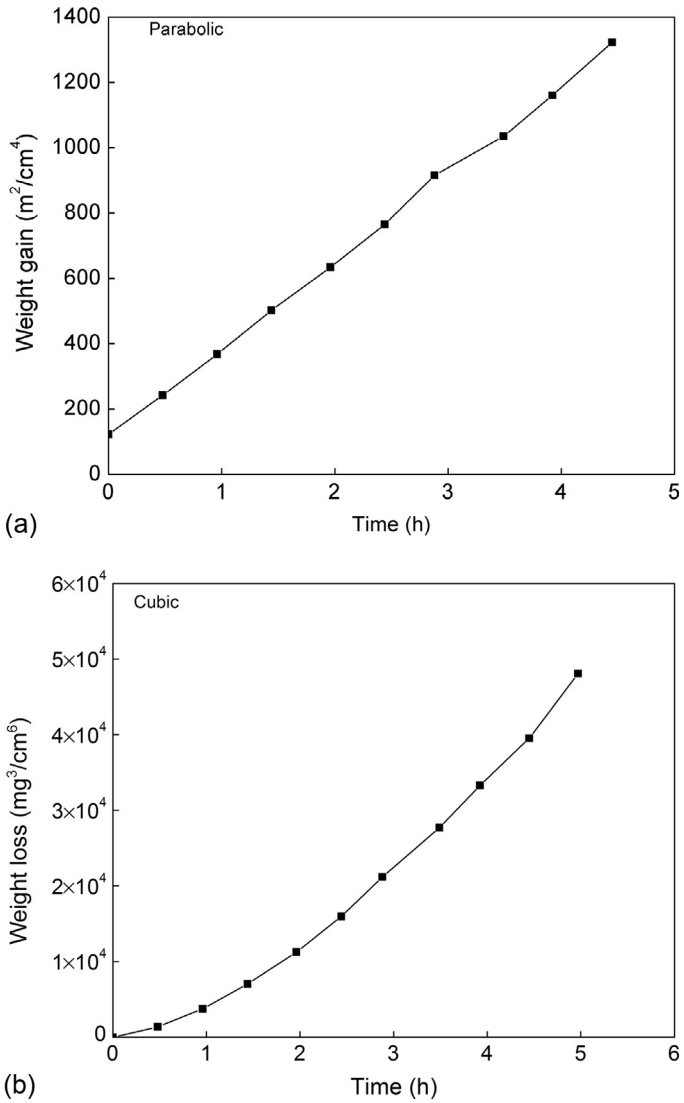

Fig. E11.1

Continued

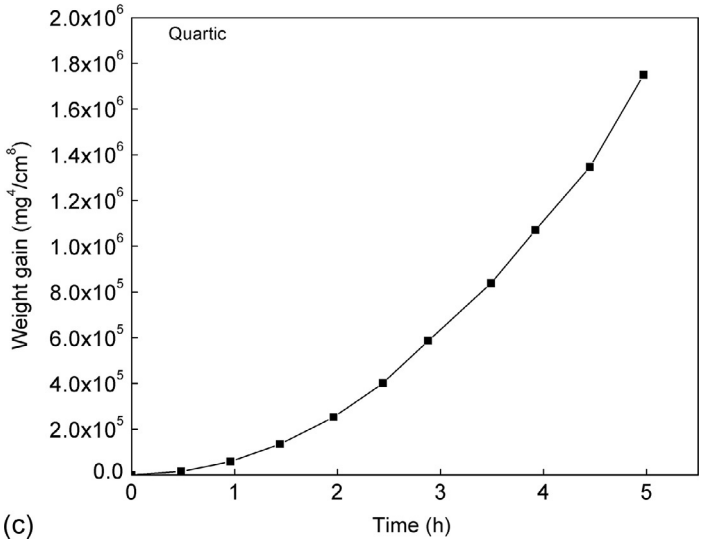

Fig. E11.1—Cont'd (a) Parabolic, (b) cubic, and (c) quartic rate laws for cobalt oxidation.

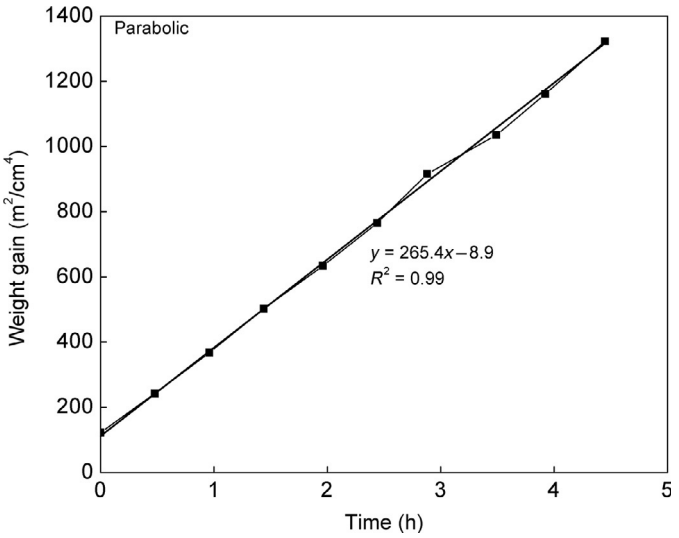

Fig. E11.2 Calculation of rate constant for cobalt oxidation at 1200 °C.

Similarly,

$$\ln k_{p,900} = \ln k_o - \frac{E_a}{RT_{900}}$$

$$\ln k_{p,900} - \ln k_{p,1200} = -\frac{E_a}{R}\left(\frac{1}{(900+273)\text{K}} - \frac{1}{(1200+273)\text{K}}\right)$$

$$\ln \frac{k_{p,900}}{k_{p,1200}} = -\frac{E_a}{R}\left(\frac{1}{1173\text{K}} - \frac{1}{1473\text{K}}\right)$$

$$\frac{k_{p,900}}{k_{p,1200}} = e^{-E_a/R((1/1173)-(1/1473))}$$

$$k_{p,900} = k_{p,1200}e^{-E_a/R((1/1173)-(1/1473))}$$

$$k_{p,900} = 265.4\frac{\text{mg}^2}{\text{cm}^4\text{h}}e^{[(-35\,\text{kcal/mol})(\text{mol K}/0.001986\,\text{kcal})((1/1173)-(1/1473))]}$$

$$k_{p,900} = 12.4\text{mg}^2/\text{cm}^4\text{h}$$

$$k_{p,950} = 23.0\text{mg}^2/\text{cm}^4\text{h}$$

$$k_{p,1150} = 174.3\text{mg}^2/\text{cm}^4\text{h}$$

E11.3. Calculate the weight gain (mg/cm^2) expected after 5 h at 900, 950, 1150, and 1200 °C by using information from exercises E11.1 and E11.2. Plot temperature vs. weight gain for 900, 950, 1150, and 1200 °C. Discuss the effects of temperature on the oxidation of cobalt.

Solution:

Cobalt oxidation follows the parabolic oxidation rate:

$$W^2 = k_p t$$

Weight gain at 900 °C:

$$k_{p,900} = 12.4\text{mg}^2/\text{cm}^4\text{h}$$

$$W_{900}^2 = (12.4)\times(5) = 62\text{mg}^2/\text{cm}^4$$

$$W_{900} = 7.87\text{mg}/\text{cm}^2$$

Weight gain at 950 °C:

$$k_{p,950} = 23.4\text{mg}^2/\text{cm}^4\text{h}$$

$$W_{950}^2 = (23.0)\times(5) = 115\text{mg}^2/\text{cm}^4$$

$$W_{950} = 10.7\text{mg}/\text{cm}^2$$

Weight gain at 1150 °C:

$$k_{p,1150} = 174.3\ \text{mg}^2/\text{cm}^4\text{h}$$

$$W_{1150}^2 = (174.3) \times (5) = 871.5\text{mg}^2/\text{cm}^4$$

$$W_{1150} = 29.5\text{mg}/\text{cm}^2$$

Weight gain at 1200 °C:

$$k_{p,1200} = 265.4\ \text{mg}^2/\text{cm}^4\text{h}$$

$$W_{1150}^2 = (265.4) \times (5) = 1327\text{mg}^2/\text{cm}^4$$

$$W_{1150} = 36.4\text{mg}/\text{cm}^2$$

Figure E11.3 shows that the oxide film weight increases with an increase in the temperature.

E11.4. The rate constants for cobalt with different temperatures are given in Table E11.2. Calculate the activation energy, E_a, in kcal/mol, and the constant, k_o, in mg^2/cm^4 h in the Arrhenius equation.

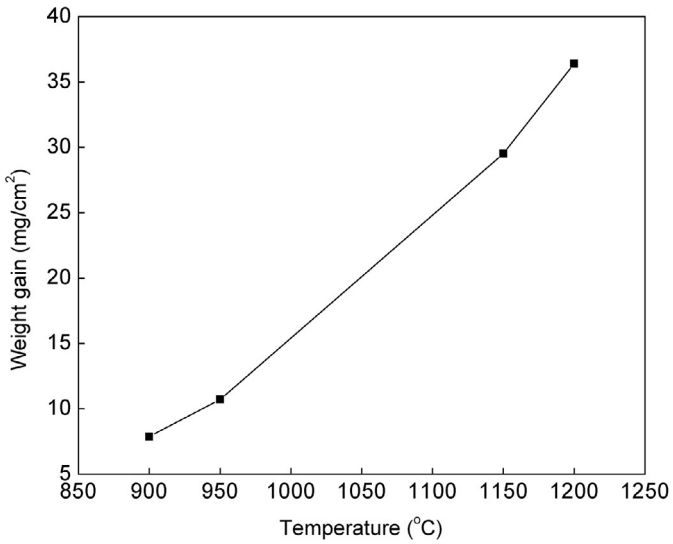

Fig. E11.3 Effect of temperature on the oxide film weight.

Table E11.2 Rate Constants for Cobalt as a Function of Temperature

Temp (°C)	900	950	1050	1100	1150	1200	1350
k_p (mg^2/cm^4 h)	12.45	23.00	68.36	111.00	174.30	265.40	801.91

Solution:
From the Arrhenius equation,

$$k_p = k_o \exp\left(\frac{-E_a}{RT}\right)$$

$$\ln(k_p) = \ln(k_o) - \frac{E_a}{R}\frac{1}{T}$$

When $1/T$ vs. $\ln(k_p)$ is plotted (Fig. E11.4), the slope is $-E_a/R$ and the intercept is $\ln(k_o)$

$$\ln(k_o) = 17.546$$

$$k_o = e^{17.546}$$

$$k_o = 41699513 \text{mg}^2/\text{cm}^4\text{h}$$

$$-\frac{E_a}{R} = -17623$$

$$E_a = 35.0 \text{kcal/mol}$$

E11.5. Oxidation of nickel at high temperatures follows the parabolic kinetics law. Using the oxidation constants given in Table E11.3, calculate the weight gain (g/cm^2) expected after 20 h for each of the alloys and plot the results as weight gain vs. weight % of Cr^{3+} in the alloy.

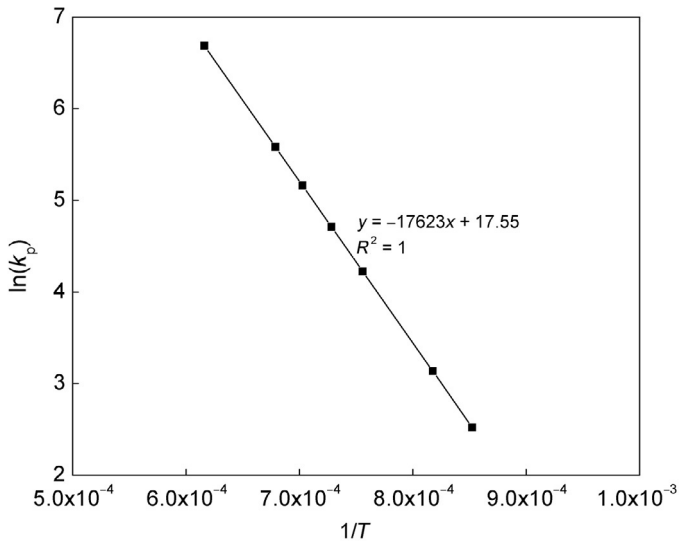

Fig. E11.4 $\ln(k_p)$ vs. $1/T$ for cobalt oxidation.

Table E11.3 Parabolic Oxidation Constant k_p (g^2/cm^4 h) at 900 °C for Different Weight % Cr^{3+}

Cr^{3+} Content (Wt. %)	Parabolic Oxidation Constant k_p at 900°C (g^2/cm^4 h)
0	3.8×10^{-10}
0.3	15×10^{-10}
1	28×10^{-10}
3	36×10^{-10}
10	5×10^{-10}

Solution:

Since nickel oxidation follows the parabolic oxidation rate:

$$W^2 = k_p t$$

For 0% Cr^{3+}

$$W_o^2 = \left(3.8 \times 10^{-10}\right) \times (20) = 7.6 \times 10^{-9}\,g^2/cm^4$$

$$W_o = 8.7 \times 10^{-5}\,g/cm^2$$

The weight gain can be calculated using the parabolic rate equation for chromium contents of 0.3, 1, 3, and 10%. The results are given in Table E11.4 and Fig. E11.5.

E11.6. Using the information in exercise E11.5, calculate the expected weight gain (g/cm^2) after 20 h at 1200 °C for 3% Cr^{3+} in the alloy, assuming an activation energy of 47.6 kcal/mol.

Solution:

The Arrhenius equation

$$k_p = k_o \exp\left(\frac{-E_a}{RT}\right)$$

where E_a is the activation energy (47.6 kcal/mol), R is the Gas constant (0.001986 kcal/mol K), T is the temperature (K)

Table E11.4 Weight Gain of Cr^{3+} for Different Chromium Contents Calculated Using Parabolic Rate Equation

Cr^{3+} (Wt.%)	Parabolic Oxidation Constant k_p at 900 °C(g^2/cm^4 h)	W^2 After 20 h (g^2/cm^4)	W After 20 h (g/cm^2)
0	3.8×10^{-10}	7.6×10^{-9}	8.7×10^{-5}
0.3	15×10^{-10}	3.0×10^{-8}	1.7×10^{-4}
1	28×10^{-10}	5.6×10^{-8}	2.4×10^{-4}
3	36×10^{-10}	7.2×10^{-8}	2.7×10^{-4}
10	5×10^{-10}	1.0×10^{-8}	1.0×10^{-4}

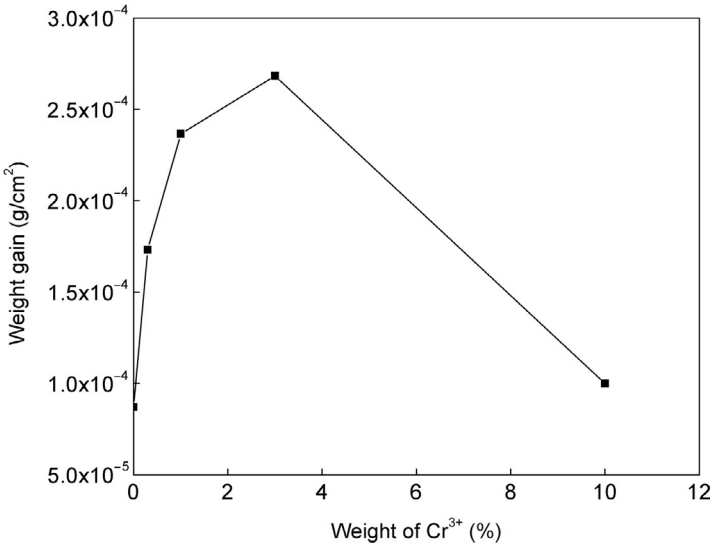

Fig. E11.5 Weight gain (g/cm^2) vs. weight percentages of Cr^{3+} in the alloy.

$$k_o = \frac{k_{p,900}}{e^{-E_a/RT_{900}}}$$

$$k_o = \frac{36 \times 10^{-10}\,g^2/cm^4h}{e^{[(-47.6(kcal/mol))/((0.001986(kcal/mol\,K))\times(900+273)\,K)]}}$$

$$k_o = 2.693\,g^2/cm^4h$$

$$k_{p,1200} = k_0 e^{-E_a/RT_{1200}}$$

$$k_{p,1200} = 2.693\,g^2/cm^4h \times e^{[-47.6\,kcal/mol/((0.001986\,kcal/mol\,K)\times(1200+273)\,K)]}$$

$$k_{p,1200} = 2.31 \times 10^{-7}\,g^2/cm^4h$$

$$W_{1200}^2 = 2.31 \times 10^{-7} \times 20$$

$$W_{1200}^2 = 4.62 \times 10^{-6}\,g^2/cm^4$$

$$W_{1200} = 2.15 \times 10^{-3}\,g/cm^2$$

E11.7. The oxidation of nickel at 200 and 340 °C was studied by Graham and Cohen [26]. The following approximate data were obtained for oxygen uptake as a function of time and presented in Table E11.5:

(a) Determine if the experimental data at 200 °C follow the logarithmic law.
(b) Determine if the experimental data at 340 °C follow the logarithmic law.
(c) If experimental data at 340 °C does not follow the logarithmic law at a whole range of data, determine the amount of oxygen uptake (μg/cm^2) at the point in the kinetic curve where the kinetics of nickel oxidation changes.

Table E11.5 Oxygen Uptake ($\mu g/cm^2$) as a Function of Time for Nickel at 200 and 340 °C

200 °C	Time (min)	0.121	0.249	0.5	1.005	2.017	3.024	4.087	5.027	6.07	7.058	8.047	9.007	10
	Oxygen uptake ($\mu g/cm^2$)	0.186	0.196	0.205	0.216	0.224	0.231	0.234	0.237	0.24	0.242	0.244	0.245	0.247
340 °C	Time (min)	0.121	0.245	0.502	1.01	2.049	3.075	4.079	5.166	6.126	7.125	8.051	9.192	10.1
	Oxygen uptake ($\mu g/cm^2$)	0.158	0.175	0.188	0.203	0.219	0.228	0.238	0.244	0.25	0.257	0.262	0.266	0.271

Solution:

(a) A plot of oxygen uptake (at 200 °C) vs. the logarithmic of time is a straight line. Therefore, the data follow logarithmic law at 200 °C as shown in Fig. E11.6.

(b) A plot of oxygen uptake (at 340 °C) vs. the logarithmic of time is a straight line only up to an oxygen uptake of 0.23 μg/cm^2 (Fig. E11.7). Therefore, the data do not follow the logarithmic law over the whole range.

(c) The kinetics of oxidation of nickel at 340 °C changes at an oxygen uptake of about 0.23 μg/cm^2.

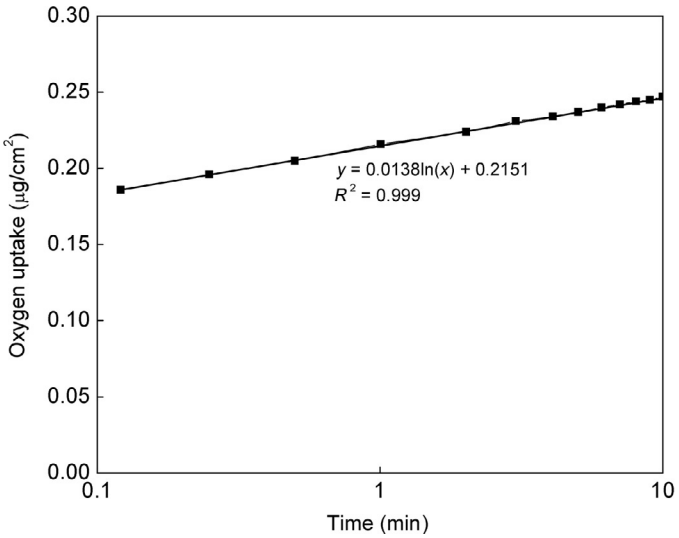

Fig. E11.6 Oxygen uptake as a function of time at 200 °C.

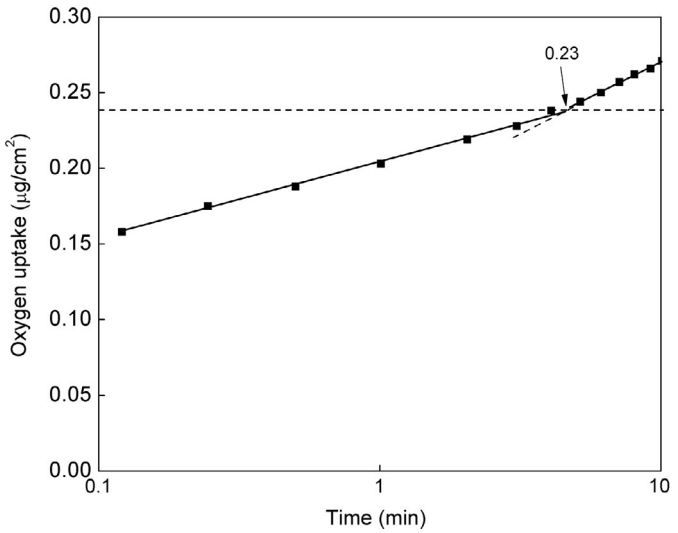

Fig. E11.7 Oxygen uptake as a function of time at 340 °C.

SOLUTIONS GUIDE

CHAPTER 15: CATHODIC PROTECTION

E15.1. Iron corrodes in a sea water solution of pH 7. Assuming corrosion proceeds by oxygen depolarization, calculate the minimum current required for complete cathodic protection. Exchange current density, i^o, for oxygen reduction is 10^{-8} mA/cm^2.

Solution:

Oxygen reduction is the predominant reduction reaction.

According to the Nernst equation,

$$e_{eq,O_2} = 1.227 - 0.059\,\text{pH}$$

$$\text{At pH } 7, e_{eq,O_2} = 0.814\,\text{V}$$

To calculate the minimum current required to protect the structure, the structure should be polarized to the equilibrium potential of iron to estimate the minimum protection current. Assuming $b_c = -0.1$ V/decade and $e_{eq,Fe} = -0.44$ V vs. SHE, the current required can be calculated using the Tafel equation:

Cathodic polarization reaction:

$$i_{prot} = i^o \times 10^{\left(\frac{e_{eq,Fe} - e_{eq,O_2}}{b_c}\right)}$$

Substituting the values,

$$i_{prot} = 34.7\,\text{A/cm}^2$$

E15.2. Using the following data for the corrosion of iron in hydrogen-saturated, oxygen-free solution, calculate (a) the corrosion rate and (b) the exchange current density for the hydrogen evolution reaction (HER) on iron.

pH 4; $a_{Fe^{2+}} = 0.02$ M; $i^o_{Fe} = 9 \times 10^{-7}$ A/cm^2; anodic $d\eta/d(\log i) = 0.04$ V/decade; the corrosion potential of iron is -0.215 V vs. RHE and $e^o_{Fe^{2+}|Fe} = -0.44$ V vs. SHE. For the HER, the cathodic $d\eta/d(\log i) = -0.12$ V/decade.

Given:

For Fe dissolution:

Exchange current density for iron dissolution $Fe^{2+}|Fe$, $i^o = 9 \times 10^{-7}$ A/cm^2

http://dx.doi.org/10.1016/B978-0-444-62722-3.09969-9

$$b_a = \frac{d\eta}{d(\log i)} = 0.04\,\text{V/decade}$$

$$E_{corr} = -0.215\,\text{V vs. RHE}$$

For hydrogen evolution:

$$H^+|H_2, \quad b_c = \frac{d\eta}{d(\log i)} = -0.12\,\text{V/decade}$$

Solution:

(a) Calculation of corrosion rate:

$$\eta_{Fe} = E_{corr} - e_{Fe^{2+}|Fe}$$

$$\eta_{H_2} = E_{corr} - e_{H^+|H_2}$$

$$i_{Fe} = i^o_{Fe} \exp\left(\frac{\alpha_a nF}{RT}\eta_{Fe}\right) \tag{E15.1}$$

$$i_{H_2} = i^o_{H_2} \exp\left(\frac{-\alpha_c nF}{RT}\eta_{H_2}\right) \tag{E15.2}$$

Write Tafel anodic and cathodic equations:

$$\eta_{Fe} = -\frac{RT}{\alpha_a nF}\ln i^o_{Fe} + \frac{RT}{\alpha_a nF}\ln i_{Fe}$$

$$\eta_{H_2} = \frac{RT}{\alpha_c nF}\ln i^o_{H_2} - \frac{RT}{\alpha_c nF}\ln i_{H_2}$$

Then, we have:

$$\eta_{Fe} = a_a + b_a \log i_{Fe}$$

$$b_a = \frac{2.3RT}{\alpha_a nF} = \frac{d\eta_{Fe}}{d\log i} = 0.04\,\text{V/decade}$$

$$a_a = -\left(\frac{RT}{\alpha_a nF}\right)\ln i^o_{Fe} = -\left(\frac{2.3RT}{\alpha_a nF}\right)\log i^o_{Fe} = -b_a \log i^o_{Fe}$$

$$= -0.04\log(9\times 10^{-7})$$

$$a_a = 0.242\,\text{V}$$

$$e_{Fe^{2+}|Fe} = -0.44 + \frac{0.0592}{2}\log(0.02) = -0.490\,\text{V vs. SHE}$$

The $e_{Fe^{2+}|Fe}$ is in SHE scale and needs to be converted into RHE scale before calculating $\eta_{Fe} = E_{corr} - e_{Fe^{2+}|Fe}$.

$$e^{o}_{H^+|H_2} = 0 - 0.0592 \times pH = 0 - 0.0592 \times 4 = -0.236\,V$$

$$e^{o}_{H^+|H_2} = 0\,\text{vs. RHE} = -0.236\,V\,\text{vs. SHE}$$

$$e_{Fe^{2+}|Fe} = -0.490 - (-0.236) = -0.254\,V\,\text{vs. RHE}$$

$$\eta_{Fe} = a_a + b_a \log i_{Fe}$$

$$0.039 = 0.242 + 0.04 \log I_{corr}$$

$$\log I_{corr} = -5.08$$

$$I_{corr} = 8.41 \times 10^{-6}\,A/cm^2$$

(b) Calculation of exchange current density for the HER on iron:

$$\eta_{H_2} = a_c + b_c \log i_{H_2}$$

$$b_c = -\frac{2.3RT}{\alpha_c nF} = \frac{d\eta_{H_2}}{d\log i} = -0.12\,V/\text{decade}$$

$$a_c = \left(\frac{RT}{\alpha_c nF}\right) \ln i^{o}_{H_2} = \left(\frac{2.3RT}{\alpha_c nF}\right) \log i^{o}_{H_2} = -b_c \log i^{o}_{H_2}$$

$$E_{corr} = -0.215\,V\,\text{vs. RHE}$$

$$\eta_{H_2} = E_{corr} - e^{o}_{H^+|H_2} = -0.215 - 0 = -0.215\,V$$

$$a_c = \eta_{H_2} - b_c \log I_{corr}$$
$$= -0.215 - (-0.12)\log(8.41 \times 10^{-6}) = -0.824\,V$$

$$\log i^{o}_{H_2} = -\frac{a_c}{b_c} = -\left(\frac{-0.824}{-0.12}\right) = -6.87$$

$$i^{o}_{H_2} = 1.36 \times 10^{-7}\,A/cm^2$$

E15.3. Using the data given in exercise E15.2, calculate the cathodic protection current required to reduce the corrosion rate to zero. (See Case Study 3.3, Chapter 3.)

Calculation of protection current, i_{prot}

Corrosion reaction is reversed at $\eta_{Fe} = 0$

$$\eta_{H_2} = e_{Fe^{2+}|Fe} - e_{H^+|H_2}$$

$$\eta_{H_2} = -0.490 + 0.236 = -0.254\,V$$

$$\log i_c = \left(\eta_{H_2} - a_c\right)/b_c = (-0.254 + 0.824)/(-0.12) = -4.75$$

$$i_c = i_{prot} = 1.78 \times 10^{-5}\ \text{A/cm}^2$$

To construct an E vs. log i diagram, one can calculate E values for iron dissolution reaction by assuming values for log i from -2 to -8 A/cm^2.

Since,

$$\eta = a_a + b_a \log i_a$$

$$\eta = E_{corr} - e_{Fe^{2+}|Fe}$$

$$E_{corr} - e_{Fe^{2+}|Fe} = 0.242 + 0.04 \log i_a$$

By substituting $E = E_{corr}$:

$$E = -0.490 + 0.242 + (0.04 \log i)$$

By solving the equation for different assumed log i values, one estimates the corresponding E values for the anodic reaction. By repeating the same procedure, E values for HER are obtained.

E15.4. During cathodic protection of iron under sea water conditions, the generation of OH^- leads to calcareous deposits by reaction with calcium and magnesium ions.

(i) List the reactions for scale formation. Does the limiting current density of oxygen increase or decrease with scale formation?

(ii) After 6 months, the limiting current for oxygen reduction changes by an order of two due to the formation of deposits. Calculate the current density required for the protection of the substrate before and after formation of the calcareous deposit.

(iii) If the applied current density is not changed, will it lead to overprotection or underprotection?

Given:

In absence of calcareous deposit, $i_{L,O_2} = 10^{-3}$ A/cm^2; $b_a = 0.04$ V/decade. For anode dissolution, $i^o = 10^{-6}$ A/cm^2.

Solution:

(i) The reduction reactions are:

$$Ca^{2+} + HCO_3^- + OH^- \rightarrow H_2O + CaCO_3$$

$$Mg^{2+} + 2OH^- \rightarrow Mg(OH)_2$$

Due to the formation of the calcareous deposit, the diffusion of oxygen decreases and consequently the limiting current for oxygen decreases. Thus, the cathodic current necessary for the protection decreases considerably.

(ii) Since the limiting current i_L,O_2 in the absence of calcareous deposit is 10^{-3} A/cm^2, the corresponding applied current necessary for cathodic protection is the same (Fig. E15.1). The oxygen reduction reaction is in the mass transfer region and is presented as a straight vertical line

When the limiting current changes by an order of two, that is, decreases to $i_L' = 10^{-5}$ A/cm^2, the applied current density required for cathodic protection also decreases by an order of two.

(iii) Since the applied current density decreases by two orders of magnitude, it will lead to overprotection, if we maintain the same current as in the absence of calcareous deposit.

E15.5. Calculate the mass of an anode and the number of anodes required for the protection of an iron tank for 7 years if an aluminum anode weighs 13.7 kg. Maintenance current demand in amps (I_m) = 1.52 A, utilization factor (u) = 0.85, and electrochemical capacity of the anode material (ε) = 2670 Ah/kg. The number of hours per year is 8760.

Solution:

Calculate the weight of the anode, W_a required for the protection of an iron tank for 7 years.

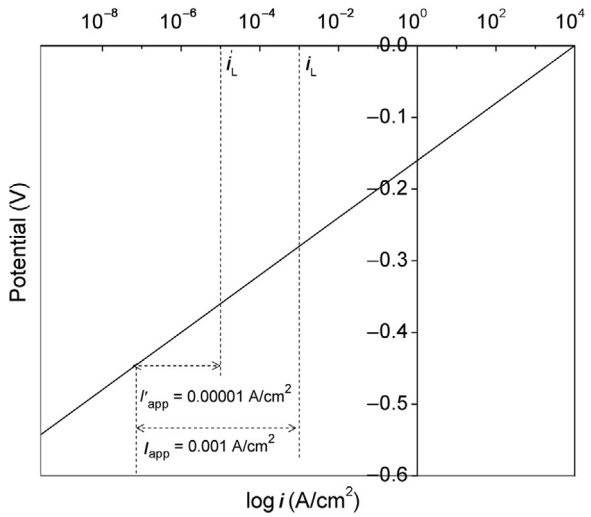

Fig. E15.1 Oxygen reduction kinetics during cathodic protection in sea water.

The total net weight of sacrificial anode material is determined from the following formula

$$W_a = \frac{I_m \times t \times 8760}{u \times \varepsilon} = \frac{1.52 \times 7 \times 8760}{0.85 \times 2670} = 41.07\,\text{kg}$$

The number of anodes

$$N = 41.07/13.7$$

$$N = 2.998$$

Hence 3 anodes are required to protect the iron tank for 7 years.

E15.6. For the cathodic protection of a steel pipeline, the following information has been obtained from the potential survey shown in Table E15.1. Calculate the following parameters:

(a) Calculate:

1. Potential at the drainage point. Compare it with the measured value.
2. Resistance of the pipe.
3. Current at drainage point.
4. Anode resistance
5. Number of anodes in the ground-bed.
6. Resistance of the anode ground-bed

Table E15.1 Potential Survey Data for the Cathodic Protection of a Steel Pipeline

Parameter	Drain Point 1	Drain Point 2
Drainage current measured, I_{om} (A)	16.6	9.8
Potential increase measured at the end of the section, $\triangle E_L$ (V)	0.26	0.26
Attenuation coefficient, α (km^{-1})	0.5	0.5
Protected pipe length, L (km)	3.86	3.86
Measured potential increase at the drainage point, $\triangle E_{om}$ (V)	0.83	0.83
Drainage current coefficient, k_i	1.5	1.5
Resistance of lead wire, ρ_w ($\Omega\,mm^2\,m^{-1}$)	0.0015	0.0015
Resistance of backfill, ρ_a ($\Omega\,mm^2\,m^{-1}$)	0.0052	0.0052
Resistance of soil, ρ_s ($\Omega\,mm^2\,m^{-1}$)	0.096	0.096
Length of lead wire, l_w (m)	375	375
Length of the anode, l_a (m)	1.1	1.1
Length of the anode with coke breeze backfill, l (m)	4.82	4.82
Depth of the anode ground-bed, t (m)	2	2
Wire cross section, a (mm^2)	15.5	15.5
Radius of the backfill, d_{bf} (m)	1.25	1.25
Radius of the anode, d_a (m)	0.28	0.28
Weight of a single anode of Fe-Si, W_a (kg)	68	68
Anode wear rate, R (kg/A year)	0.07	0.07
Accepted current per anode, I_a (A)	5.0	5.0

7. Lead wire resistance.
8. Rectifier power needed.
9. The anode wear and cycling life of the system.

Solution:

(a) All the necessary parameters and their units are given in Table E15.1.

1. Potential at the drainage points is calculated by:

$$E_{oc} = \Delta E_L \times \cosh(\alpha L)$$

For both drainage points, $\Delta E_L = 0.26$ V, $\alpha = 0.5$ km^{-1} and $L = 3.86$ km

So,

$$E_{oc} = 0.26 \times \cosh(0.5 \times 3.86) = 0.915\,\text{V}$$

2. Resistance of the pipe:

The resistance of the pipe is given by

$$R_c = E_{om}/I_{om}$$

So, at drainage point 1;

$$R_c = 0.83/16.6 = 0.050\,\Omega$$

and at drainage point 2;

$$R_c = 0.83/9.8 = 0.085\,\Omega$$

3. Current at the drainage points:

$$I_{oc} = k_i \frac{E_{oc}\tan(\alpha L)}{R_c} \quad (k_i \text{ being the drainage current coefficient})$$

So at drainage point 1,

$$I_{oc} = 1.5\frac{0.915\tanh(0.5 \times 3.86)}{0.05} = 26.3\,\text{A}$$

At drainage point 2,

$$I_{oc} = 1.5\frac{0.915\tanh(0.5 \times 3.86)}{0.085} = 15.5\,\text{A}$$

4. The anode resistivity is given by:

$$R_a = \frac{\rho_s}{2\pi L}\left(\ln\left(\frac{L}{2 \times d_{bf}}\right) + \frac{L}{2t} + \frac{\rho_a}{\rho_s} + \frac{4d_{bf}}{d_a\pi}\right)$$

$$= 3.87 \times 10^{-9}\,\Omega$$

5. Number of anodes:

Drainage point 1: $N_1 = I_{oc}/I_a = 26.3/5 = 5.26$

Therefore, the number of anodes is 6.

Drainage point 2: $N_2 = I_{oc}/I_a = 15.5/5 = 3.10$

Therefore, the number of anodes is 4.

6. Resistance of anode ground-bed:

The resistance of the anode ground-bed (R_{agb}) is given by

$$R_{agb} = R_a/N_a$$

N_a represents the number of anodes.

So, for drainage point 1: $R_{agb} = 6.45 \times 10^{-10}\ \Omega$

At drainage point 2: $R_{agb} = 9.68 \times 10^{-10}\ \Omega$

7. Lead wire resistance is given by

$$R_w = \frac{\rho_w \times l_w}{a} = \frac{0.0015\ \Omega \text{mm}^2\ \text{m}^{-1} \times 375\ \text{m}}{15.5\ \text{mm}^2} = 0.0363\ \Omega$$

8. Calculation of the rectifier power:

To calculate the total rectifier power, we first calculate the total resistance as:

$$R_{Tot} = R_{agb} + R_w + R_c$$

From this we find out the theoretical power requirement U_r as:

$$U_r = I_{oc} \times R_{Tot}$$

Allowing for safety factors, the applied power is

$$S_{min} = 2 \times I_{om} \times U_r$$

So, at drainage point 1 we have,

$$R_{Tot} = 6.45 \times 10^{-10} + 0.0363 + 0.050$$

$$R_{Tot} = 0.0863\ \Omega$$

$$U_r = 26.3 \times 0.0863$$

$$U_r = 2.27\ \text{V}$$

So, minimum rectifier output

$$S_{min} = 2 \times 16.6 \times 2.27$$
$$= 75.4\ \text{W}$$

At drainage point 2, we have $R_{Tot} = 0.121\ \Omega$, $U_r = 1.88$ V and so rectifier output = 36.8 W

9. Anode wear and cycle life:
Anode wear rate (R) = 0.07 kg/A year
Weight of anode used (W_a) = 68 kg
Cycle life (CL) = $W_a/(I_{om}\ R)$

At drainage point 1,

$$\begin{aligned} CL &= [68/(16.6 \times 0.07)] \\ &= 58.5 \text{ years} \end{aligned}$$

At drainage point 2,

$$\begin{aligned} CL &= [68/(9.8 \times 0.07)] \\ &= 99.1 \text{ years} \end{aligned}$$

INDEX

Note: Page numbers followed by *b* indicate boxes, *f* indicate figures and *t* indicate tables.

B

C

D

E

F

G

H

P

R

S

T

U